



XIX Riunione Nazionale di Elettromagnetismo

Rome, 10-14 September 2012

PROCEEDINGS

XIX Riunione Nazionale di Elettromagnetismo

Rome, 10-14 September 2012

PROCEEDINGS

Realized at “Roma Tre” University, Rome, Italy
Produced in Rome, Italy, September 2012

Copyright Società Italiana di Elettromagnetismo, 2012

ISBN: 978-88-907599-0-1

Summary

RiNEm 2012 – Introduction	4
RiNEm previous editions	4
Foreword	5
Prizes	6
Sponsors	7
RiNEm 2012 – Committees	8
XIX RiNEm – Timetable	9
XIX RiNEm – Scientific Program	10
Plenary lectures	28
Session 1 – Microwave components I	41
Session 2 – Bioengineering I	62
Session 3 – Electromagnetic theory	87
Session 4 – Electromagnetic imaging techniques	112
Session 5 – Numerical methods in electromagnetics	137
Session 6 – Synthetic aperture radar	164
Session 7 – Microwave components II	186
Session 8 – Ground penetrating radar	203
Session 9 – Antenna arrays	225
Session 10 – Propagation and scattering	250
Session 11 – Bioengineering II	271
Session 12 – Antenna design and measurements	292
Session 13 – Optical fibers	317
Session 14 – Radio frequency identification	338
Session 15 – Photonic crystals	363
Session 16 – Wireless communications, networks and systems	388
Session 17 – Photonic and plasmonic technologies and components	413
Session 18 – Energy and environment	438
Poster session I	463
Poster session II	537
Poster session III	607

RiNEm 2012 - Introduction

The *XIX Italian Meeting on Electromagnetics* takes place in Rome on 10-14 September 2012. This edition has been organized by the Applied Electromagnetics group of "Roma Tre" University.

The event represents an unique occasion for researchers working in the field and coming from different universities, research centers, and company/industries to meet and exchange their latest experiences and results. The contributions submitted for presentation to this edition of the meeting have been grouped in 18 oral and 3 poster sessions. The scientific program foresees also an URSI special session, a session devoted to the latest industrial developments, and 4 plenary sessions, where eminent invited experts coming from international universities will present their research achievements in different fields in electromagnetics from microwaves to optics.

This meeting represents also a great opportunity for students to be exposed to the country-wide state of the art in electromagnetics. To stimulate an active participation of young researchers and PhD students three different prizes (Barzilai Prize, Latmiral Prize, and Sannino Prize) will be also awarded and announced at the closing session.

Students attending the meeting can also attend the doctoral school, which is going to be held on 14-15 September 2012.

RiNEm: previous editions

- I. L'Aquila 24-25 Giugno 1976 (Coordinator: Prof. Fernando Bardati)
- II. Pavia, 2-4 Ottobre 1978 (Coordinator: Prof. Giuseppe Conciauro)
- III. Bari, 25-27 Giugno, 1980 (Coordinator: Prof. Roberto De Leo)
- IV. Firenze, 4-6 Ottobre, 1982 (Coordinator: Prof.ssa Annamaria Scheggi)
- V. Saint Vincent, 9-12 Ottobre 1984 (Coordinator: Prof. Mario Orefice)
- VI. Trieste, 22-24 Ottobre 1986 (Coordinator: Prof. Edoardo Carli)
- VII. Frascati, 5-8 Settembre 1988 (Coordinator: Prof. Fernando Bardati)
- VIII. Capri, 9-12 Ottobre 1990 (Coordinator: Prof. Giorgio Franceschetti)
- IX. La Cittadella, 5-8 Ottobre 1992 (Coordinator: Prof. Roberto Sorrentino)
- X. Cesena, 21-23 Settembre 1994 (Coordinator: Prof. Gabriele Falciasecca)
- XI. Firenze, 1-4 Ottobre 1996 (Coordinator: Prof.ssa Laura Ronchi Abbozzo)
- XII. Cetraro, 28 Settembre-1 Ottobre 1998 (Coordinator: Prof. Giuseppe Di Massa)
- XIII. Como, 25-28 Settembre 2000 (Coordinator: Prof. Carlo Capsoni)
- XIV. Ancona, 16-19 Settembre 2002 (Coordinator: Prof. Tullio Rozzi)
- XV. Cagliari, 13-16 Settembre 2004 (Coordinator: Prof. Giuseppe Mazzarella)
- XVI. Genova, 18-21 settembre 2006 (Coordinator: Prof. Matteo Pastorino)
- XVII. Lecce, 15-19 Settembre 2008 (Coordinator: Prof. Luciano Tarricone)
- XVIII. Benevento, 6-10 Settembre 2010 (Coordinator: Prof. Innocenzo Pinto)

Foreword

Ladies and Gentlemen,

Welcome to the XIX Riunione Nazionale di Elettromagnetismo (RiNEm), held in Rome, promoted by the Società Italiana di Elettromagnetismo (SIEm), hosted and organized by “Roma Tre” University of Rome. This event is realized in the year in which SIEm reaches its ten years of life, and “Roma Tre” University enters the third decade of its existence. We are particularly honored to host the RiNEm in coincidence with these two recurrences.

We are very glad of welcoming all of you to this venue and to host these four days of presentations in the exciting field of Electromagnetics. This prestigious event is a significant occasion for scientists coming from different universities to meet themselves and exchange their experiences and results. It is also an opportunity of formation for students, since it offer a complete background about the Italian state of the art in Electromagnetics and a Doctoral School on Friday and Saturday morning. To stimulate an active participation of young researchers and PhD students, several awards are assigned, and a limited number of undergraduate students are invited to freely participate.

We are very proud to have here five among the most internationally recognized scientists leading the research on the very wide field of Electromagnetics and areas of knowledge linked to it: *Prof. Andrea Alù*, from the University of Texas at Austin, USA; *Prof. Sébastien Lambot*, from the Université Catholique de Louvain, Louvain-la-Neuve, Belgium; *Prof. Leo Kempel*, from Michigan State University, USA; *Prof. Marian Marciniak*, from the National Institute of Telecommunications of Warsaw, Poland; *Prof. Evert Slob*, from the Delft University of Technology, Delft, The Netherlands.

We are deeply satisfied to have received also the contribution from experts of Scientific and Industry worlds of different but affine sections of the human knowledge. In fact we are very confident that a common cross-fertilization of ideas coming from different areas is very useful both for the advancement of scientific knowledge and for addressing the economic world to find new and successful ways of development and, in some cases, of real renaissance.

We would like to thank the Rector, the Administrative Manager, the Dean of the Faculty of Engineering, and the Director of the Department of Applied Electronics of “Roma Tre” University for having allowed us to use the academic structures in the best possible way, the President and the staff of the SIEm for a deep cooperation in the general and administrative organization of the Meeting, the Promoting Committee for the activity on the general structure, the Organizing and Local Committees for their enthusiastic and rich of energy contribution to the practical realization of the XIX RiNEm. Thanks to the efforts of all of them, it has been possible to render the XIX RiNEm an event rich in culture and at the same time pleasant and fruitful for all of us.

Finally we would like to thank all the financial and technical Sponsors, without their help several activities would not have been possible.

Welcome to Rome, and have a pleasant XIX RiNEm week!

Welcome to Rome!

Giuseppe Schettini and Lucio Vegni
Chairmen of the XIX Italian Meeting in Electromagnetics

Prizes

Barzilai Prize

Barzilai Prize is provided by SIEm (Italian Society of Electromagnetics) and will be awarded to authors under 35 years old who will present the best work. Giorgio Barzilai (1911 - 1987) was the initiator of the Electromagnetics School of "La Sapienza" University, in Rome. He created the specialization in Applied Electromagnetics and the PhD School in Applied Electromagnetics and Electrophysics Science. His 50 years of scientific activity (from 1935 to 1985) was founded on methodological rigor and constant research of practical applications of his work, combining both theoretical and practical aspects. From 1976 to 1985 Giorgio Barzilai was President of the Italian Committee of URSI. In 1978 he was appointed as Fellow of the Institute of Electrical and Electronic Engineers (IEEE) and in 1985 he received the Centenary Medal of IEEE.

Sannino Prize

Sannino Prize is provided by GAAS-MECSA in memory of Professor Mario Sannino, teacher of Electronics in the University of Palermo. The prize is awarded to the best work about millimetric waves and microwave circuits and devices by young researchers (under 35 years old) presented to the National Meetings of Electromagnetics.

Latmiral Prize

Latmiral Prize is provided by SIEm and will be awarded to authors under 35 years old who will present the best poster. Gaetano Latmiral (1909 -1995), together with Giorgio Barzilai and Mario Boella, was the initiator of Italian scientific research in Electromagnetics. He was born in Rome and graduated in Industrial Engineering at the Politecnico of Milan. During the Second World War contributed decisively to the development of radar and radar countermeasures. He was detained at the military prison at Tegel, where he established a special fellowship with the theologian Dietrich Bonhoeffer, subsequently a victim of Nazism. He escaped racial persecution after the war, and carried out his studies and research activity at CERN in Geneva, the Military Institute of Superior Transmissions, the National Research Council, the University of Rome "La Sapienza" (as Professor of Physics). In 1955 he became professor of "Theory and Techniques of Electromagnetic Waves," at the Institute of Naval University of Naples.

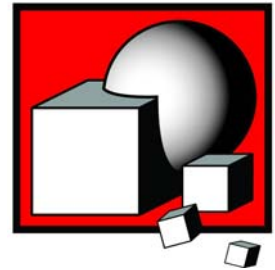
Sponsors



Agilent Technologies



CST



SELEX
Sistemi Integrati
A Finmeccanica Company



Technical Sponsors



IEEE



RiNEm 2012 - Committees

Chairmen

L. Vegni, *“Roma Tre” University*

G. Schettini, *“Roma Tre” University*

Promoting Committee

P. Bassi, *Bologna University*

P. Lampariello, *“Sapienza” University*

G. Leone, *II University of Napoli*

G. Pelosi, *Firenze University*

I. Pinto, *Sannio University*

L. Vegni, *“Roma Tre” University*

Organizing Committee

F. Bilotti, *“Roma Tre” University*

L. Pajewski, *“Roma Tre” University*

C. Ponti, *“Roma Tre” University*

G. Schettini, *“Roma Tre” University*

A. Toscano, *“Roma Tre” University*

L. Vegni, *“Roma Tre” University*

Local Committee

M. Barbuto, *“Roma Tre” University*

S. Ceccuzzi, *“Roma Tre” University*

R. Iovine, *“Roma Tre” University*

L. La Spada, *“Roma Tre” University*

S. Meschino, *“Roma Tre” University*

A. Monti, *“Roma Tre” University*

F. Napoli, *“Roma Tre” University*

D. Ramaccia, *“Roma Tre” University*

XIX RiNEm – Timetable

Day	Morning	Afternoon
Monday 10	-	12:00 - 14:00 <i>Registration</i> 14:00 - 14:30 <i>Opening Ceremony</i> - N11 14:30 - 15:30 <u>Plenary Lecture</u> – Marciniak - N11 15:30 - 16:00 <i>Coffee Break</i> 16:00 - 18:00 <i>URSI Session</i> - N11
Tuesday 11	09:30 - 11:00 <i>Session 1</i> - N11 09:30 - 11:00 <i>Session 2</i> - N13 11:00 - 11:30 <i>Coffee Break</i> 11:30 - 13:00 <i>Session 3</i> - N11 11:30 - 13:00 <i>Session 4</i> - N13	14:00 - 15:30 <i>Session 5</i> - N11 14:00 - 15:30 <i>Session 6</i> - N13 15:30 - 16:00 <i>Coffee Break</i> 16:00 - 17:30 <i>Poster Session I</i>
Wednesday 12	09:30 - 10:00 <u>Industry Lecture</u> - N11 10:00 - 11:00 <i>SIEm Meeting</i> - N11 11:00 - 11:30 <i>Coffee Break</i> 11:30 - 13:00 <i>SIEm Meeting</i> - N11 11:30 - 12:15 <i>CST Workshop</i> - N13 11:30 - 13:00 <i>Poster Session II</i>	14:00 - 15:30 <i>Session 7</i> - N11 14:00 - 15:30 <i>Session 8</i> - N13 15:30 - 16:00 <i>Coffee Break</i> 16:00 - 17:30 <i>Session 9</i> - N11 16:00 - 17:30 <i>Session 10</i> - N13 20:30 - <i>Social Dinner</i>
Thursday 13	09:30 - 11:00 <i>Session 11</i> - N11 09:30 - 11:00 <i>Session 12</i> - N13 11:00 - 11:30 <i>Coffee Break</i> 11:30 - 12:30 <u>Plenary Lecture</u> – Slob and Lambot - N11	14:00 - 15:30 <i>Session 13</i> - N11 14:00 - 15:30 <i>Session 14</i> - N13 15:30 - 16:00 <i>Coffee Break</i> 16:00 - 17:00 <i>Poster Session III</i> 17:00 - 8:30 <i>Session 15</i> - N11 17:00 - 18:30 <i>Session 16</i> - N13
Friday 14	09:00 - 10:30 <i>Session 17</i> - N11 09:00 - 10:30 <i>Session 18</i> - N13 10:30 - 11:00 <i>Coffee break</i> 11:00 - 12:00 <u>Plenary Lecture</u> – Alù – N11 12:00 - 13:00 <u>Plenary Lecture</u> – Kempel – N11 13:00 - 13:30 <i>Young Authors Award Ceremony and Closing Address</i>	<i>Doctoral School</i>
Saturday 15	<i>Doctoral School</i>	

Session 1 *Microwave Components I*
 Session 2 *Bioengineering I*
 Session 3 *Electromagnetic Theory*
 Session 4 *Electromagnetic Imaging Techniques*
 Session 5 *Numerical Methods in Electromagnetics*
 Session 6 *Synthetic Aperture Radar*
 Session 7 *Microwave Components II*
 Session 8 *Ground Penetrating Radar*
 Session 9 *Antenna Arrays*
 Session 10 *Propagation and Scattering*
 Session 11 *Bioengineering II*
 Session 12 *Antenna Design and Measurements*
 Session 13 *Optical Fibers*
 Session 14 *Radio Frequency Identification*
 Session 15 *Photonic Crystals*
 Session 16 *Wireless Communications, Networks, and Systems*
 Session 17 *Photonic and Plasmonic Technologies and Components*
 Session 18 *Energy and Environment*
 Poster Session I
 Poster Session II
 Poster Session III

Chairpersons: G. Marrocco, M. Mongiardo
 Chairpersons: G. d’Inzeo, S. Caorsi
 Chairpersons: G. D’Elia, G. Migliaccio
 Chairpersons: T. Isernia, M. Pastorino
 Chairpersons: G. Biffi Gentili, V. Galdi
 Chairpersons: C. Capsoni, P. Basili
 Chairpersons: R. Tascone, P. Tognolatti
 Chairpersons: E. Pettinelli, F. Soldovieri
 Chairpersons: G. Di Massa, R. Vescovo
 Chairpersons: R. Pierri, V. Fiumara
 Chairpersons: G. Sorbello, R. Olmi
 Chairpersons: A. Massa, C. Gennarelli
 Chairpersons: A. Galtarossa, S. Wabnitz
 Chairpersons: L. Tarricone, G. Mazzarella
 Chairpersons: S. Selleri, R. Orta
 Chairpersons: P. Nepa, D. Migliore
 Chairpersons: A. D’Orazio, S. Trillo
 Chairpersons: G. Cerri, L. Roselli
 Chairperson: L. Vincetti
 Chairperson: M. Midrio
 Chairperson: V. Degli Esposti

XIX RiNEm – Scientific Program

Monday 10 September 2012

- 12:00 – 14:00 Registration**
- 14:00 – 14:30 Opening Ceremony of XIX RiNEm – Aula N11**
Welcome address
Dean of the Faculty of Engineering, *“Roma Tre” University, Italy*
Introduction of the Conference Chairs
G. Schettini and L. Vegni, *“Roma Tre” University, Italy*
- 14:30 – 15:30 Plenary Lecture I – Aula N11**
Chairperson: G. Schettini, “Roma Tre” University, Italy
- Marian Marciniak**
National Institute of Telecommunications, Warsaw, Poland
Converged optical and wireless communications for the future
- 15:30 – 16:00 Coffee Break**
- 16:00 – 18:00 URSI Session – Aula N11**
Chairperson: R. Sorrentino, University of Perugia, Italy

Tuesday 11 September 2012

09:30 – 11:00 Session 1 – Microwave Components I – Aula N11

Chairpersons: *G. Marrocco, “Tor Vergata” University, Italy
M. Mongiardo, University of Perugia, Italy*

09:30-09:45

L. Ntubarikure, G. Pelosi, and S. Selleri

Harmonic balance Finite Element analysis of third order intermodulation products in ferrite devices

09:45-10:00

M. Oldoni, F. Seyfert, and G. Macchiarella

Tuning diplexers with rational filters

10:00-10:15

G. Virone, R. Tascone, O.A. Peverini, G. Addamo, Z. Farooqui, A. Tibaldi, and R. Orta

Synthesis strategy for broadband multiplexers

10:15-10:30

C. Tomassoni, S. Bastioli, and R. Sorrentino

TM dual-mode cavity filters with symmetric and asymmetric filtering functions

10:30-10:45

L. Zappelli

An equivalent circuit for microwave discontinuities

09:30 – 11:00 Session 2 – Bioengineering I – Aula N13

Chairpersons: *G. d’Inzeo, “Sapienza” University of Rome, Italy
S. Caorsi, University of Pavia, Italy*

9:30-9:45

A. Candiani, M. Sozzi, A. Cucinotta, R. Veneziano, R. Corradini, R. Marchelli, P. Childs, S. Pissadakis, and S. Selleri

DNA biosensor based on a double tilted fiber Bragg grating

9:45-10:00

E. Pievanelli, A. Plesca, R. Stefanelli, and D. Trincherò

Wearable self-powered wireless units for ultraviolet radiation dosimetry

10:00-10:15

M. Cavagnaro, F. Frezza, R. Laurita, M. Tannino, L. Manganaro, M. Marini, P. Sollazzo, A. Stagnitti, V. Lopresto, and R. Pinto

From magnetic resonance imaging to water content evaluation of a human tissue

10:15-10:30

B. Bisceglia, and V. Ivone

Health effects from cell phone radiations: the verdict of the court of appeal of Brescia

10:30-10:45

D. A. M. Iero

Optimal focusing of vectorial fields subject to arbitrary upper bounds

10:45-11:00

R. Iovine, L. La Spada, F. Bilotti, and L. Vegni

Gold nano-particles as a platform for biosensing

11:00 – 11:30 Coffee Break

11:30 – 13:00 Session 3 – Electromagnetic Theory – Aula N11

Chairpersons: **G. D’Elia, “Federico II” University of Naples, Italy**
G. Migliaccio, “Parthenope” University of Naples, Italy

11:30-11:45

K. Watanabe, Y. Nakatake, and G. Schettini

Plane-wave scattering from cylindrical objects

11:45-12:00

L. Infante, and S. Mosca

A closed-form estimation of the mutual coupling matrix applied to uniform circular arrays

12:00-12:15

P. Burghignoli

A phase-center study of Fabry-Pérot cavity antennas

12:15-12:30

M. Cametti, M. Bozzi, M. Pasian, and L. Perregrini

An analytical model to quantify the efficiency of arrays composed by high-gain reflector antennas

12:30-12:45

G. Castaldi, V. Galdi, A. Alù, and N. Engheta

Nonlocal transformation optics

12:45-13:00

F. Mangini

Electromagnetic scattering of an elliptically polarized plane wave by a buried sphere

11:30 – 13:00 Session 4 – Electromagnetic Imaging Techniques – Aula N13

Chairpersons: **T. Isernia, Università Mediterranea, Italy**
M. Pastorino, University of Genoa, Italy

11:30-11:45

M. Ferrara, P. Lucantoni, S. Mori, P. Nocito, G.M. Tosi Beleffi, E. Restuccia, F. Frezza, and F. S. Marzano

Atmospheric visibility through optical images

11:45-12:00

A. Guagliumi, M. Gnan, A. Liberato, L. De Marco, D. Bruni, F. Canini, and P. Bassi
System-level analysis and optimization of task-oriented imaging systems

12:00-12:15

D. Pinchera, M.D. Migliore, and F. Schettino
Through-wall communication by means of an ultra wide permittivity antenna (UWPA)

12:15-12:30

R. Solimene, A. D'Alterio, and R. Pierri
TWI for a lossless unknown wall

12:30-12:45

R. Scapaticci, L. Di Donato, I. Capatano, and L. Crocco
Differential microwave imaging from brain stroke monitoring

12:45-13:00

G. Bellizzi, O.M. Bucci, I. Capatano, L. Crocco, and R. Scapaticci
Advancements in microwave breast cancer imaging enhanced by magnetic nanoparticles as contrast agent

13:00 – 14:00 Lunch

14:00 – 15:30 Session 5 – Numerical Methods in Electromagnetics – Aula N11

Chairpersons: **G. Biffi Gentili, University of Florence, Italy**
 V. Galdi, University of Sannio, Italy

14:00-14:15

A. Fanti
A vector finite difference approach to the computation of modes in circular waveguide

14:15-14:30

G. Angiulli, D. De Carlo, and A. Sgrò
Nested BiCGStab for non-Hermitian linear systems arising from discretization of the EFIE

14:30-14:45

G. Valerio, S. Paulotto, P. Baccarelli, A. Galli, D. R. Jackson, and D. R. Wilton
Efficient computation of periodic Green's functions for printed structures with vertical elements

14:45-15:00

O. A. Peverini, A. Tibaldi, Z. Farooqui, G. Addamo, G. Virone, R. Orta, and R. Tascone
Analysis and design of passive waveguide devices by spectral element methods

15:00-15:15

D. Pinchera
An effective hybrid synthesis method for sparse plane wave generators

15:15-15:30

L. Ntibarikure
Model order reduction in Finite Element analysis of phased array antennas

14:00 – 15:30 Session 6 – Synthetic Aperture Radar – Aula N13

Chairpersons: *C. Capsoni, Polytechnic of Milan, Italy*
P. Basili, University of Perugia, Italy

14:00-14:15

G. Di Martino, A. Iodice, D. Riccio, G. Ruello, and I. Zinno

A novel high level SAR product: fractal dimension map

14:15-14:30

M. Picchiani, F. Del Frate, G. Schiavon, S. Stramondo, and M. Chini

DInSAR and neural networks for seismic source analysis

14:30-14:45

R.G. Avezzano, D. Latini, F. Del Frate, D. Velotto, and S. Lehner

Oil spill detection using X-band SAR data

14:45-15:00

A. Capozzoli, C. Curcio, and A. Liseno

SAR tomography with optimized track distribution and controlled resolution

15:00-15:15

N. Pierdicca, and L. Pulvirenti

Future use of the data from the ESA Sentinel-1 mission for operational soil moisture mapping: a multitemporal algorithm

15:30 – 16:00 Coffee Break

16:00 – 17:30 Poster Session I

Chairperson: *L. Vincetti, University of Modena and Reggio Emilia, Italy*

S. Ceccuzzi, S. Meschino

The role of evanescent modes excited inside the longitudinal corrugations of mode filters

F. Di Murro, M. Lucido, and F. Schettino

Electromagnetic scattering by a finite metallic cylinder

P. Imperatore, A. Iodice, and D. Riccio

Volume and roughness scattering effects: a unified perturbative approach

N. Tedeschi

Deep penetration of inhomogeneous plane waves in lossy media

F. Corsetti, M. Lucido, and G. Panariello

Analysis of propagation in coupled polygonal cross-section dielectric waveguides

P. Imperatore, A. Iodice, and D. Riccio

Perturbative approach for scattering in random media via distribution theory for discontinuous test functions

F. Chiadini, V. Fiumara, and A. Scaglione
A synthesis method for multi-section devices

A. Iodice, A. Natale, and D. Riccio
A novel interpretation for the Kirchhoff scattering from classical and fractal surfaces

G. Gradoni, T.M. Antonsen, and E. Ott
Random coupling model for wave chaotic cavities

L. Di Donato, D.A.M. Iero, I. Catapano, L. Crocco, G. Sorbello, and T. Isernia
Two approaches to field focusing in unknown environments

L. La Spada, R. Iovine, F. Bilotti, and L. Vegni
Infrared absorption measurements using metamaterials

F. Frezza, P. Nocito, and E. Stoja
A study on the fundamental mode characteristics sustained by the plasmonic slot waveguide

R. Ana Perez-Herrera, E. Coscelli, M. Sozzi, A. Cucinotta, S. Selleri, and M. Lopez-Amo
YB - doped photonic crystal fiber laser

C. Molardi, Masruri, E. Coscelli, F. Poli, A. Cucinotta and S. Selleri
FEM solver optimization for PCF design

A. C. Lesina, A. Vaccari, and A. Bozzoli
A modified RC - FDTD algorithm for plasmonics in Drude dispersive media

F. Baronio, M. Conforti, M. Levenius, K. Gallo, V. Pasiskevicius, F. Laurell, and C. De Angelis
Broadband optical parametric generation in LiTaO₃

R. Tumolo, G. Russo, S. Immediata, L. Timmoneri, M. D'Urso
Modeling and Simulating Wind Farm effects on Radar systems

P. Vinetti, M. D'Urso, M. Dispenza
Embedded Photonic Sensor Networks for Large Arrays Diagnostic

Wednesday 12 September 2012

09:30 – 10:00 Industry Lecture – Aula N11

Chairperson: F. Bilotti, “Roma Tre” University, Italy

Giancarlo Prisco

Selex S.I.

Receiving sparse signals in radar systems: blind recovery at minimum rate

10:00 – 11:00 SIEm Meeting – Aula N11

11:00 – 11:30 Coffee Break

11:30 – 13:00 SIEm Meeting – Aula N11

11:30 – 12:15 CST Workshop – Aula N13

11:30 – 13:00 Poster Session II

Chairperson: M. Midrio, University of Udine, Italy

S. Ceccuzzi, D. Milanese, and G.L. Ravera

Analysis of a flat, dielectric - loaded, ion cyclotron, test antenna by using three electromagnetic codes

R. Stefanelli and D. Trincherò

Full-analytical procedure for the design of micro-magnetic radiators

E. Di Salvo, F. Frezza, and S. Mosca

Analysis of cylindrical frequency selective surfaces for antenna radomes

P. Baccarelli, S. Paulotto, and D. R. Jackson

Matching techniques for efficient broadside radiation in 1D periodic printed leaky-wave antennas

A.F. Morabito and L. Di Donato

A canonical problem in multibeam antenna synthesis

S. Costanzo and A. Costanzo

Modified U-slot patch antenna with low cross-polarization for broadband applications

F. D’Agostino, F. Ferrara, C. Gennarelli, R. Guerriero, and M. Migliozzi

Direct far-field reconstruction from near-field data acquired through a helicoidal scanning

O. Leonardi, M. Pavone, G. Sorbello, and T. Isernia

A new compact monolithic patch antenna for dedicated short range communications systems

A. Galli, S. Mazzocchi, G. Valerio, M. Ciattaglia, and M. Zucca

UWB multifunctional arrays based on versatile printed rhombic antenna configurations

C. Occhiuzzi and G. Marrocco

Sensing-oriented design methodology for passive RFID antennas

A. D'Alessandro, A. Buffi, and P. Nepa

A new localization method for UHF-RFID smart shelves

S. Costanzo, G. Di Massa, and O.H. Moreno

Equivalent impedance retrieval of planar surfaces by open resonator technique

G. Monti, L. Tarricone, F. Congedo, and P. Arcuti

Wireless power transmission links: experimental results at the electromagnetic laboratory of Lecce

P. Rocca

Time-modulated arrays for next generation cognitive radio systems – potentialities and envisaged solutions

F. Viani

Array design in the correlation domain: a new paradigm

A. Buonanno, P. Vinetti, M.G. Labate, M.D'Urso, M. Albertini, L. Russo

Digital Multiple Beams Radars for Airport Monitoring and Surveillance

D.Pavone, G. Sorrentino, A.Buonanno, M. D'Urso

Surveillance of wide zones with Unattended Ground Sensors: from detection to alert

12:30 – 14:00 Lunch

14:00 – 15:30 Session 7 – Microwave Components II – Aula N11

Chairpersons: R. Tascone, CNR-IEIIT, Italy

P. Tognolatti, University of L'Aquila, Italy

14:00-14:15

G. Castaldi, V. Galdi, and I.M. Pinto

Short-pulsed wavepacket propagation in ray-chaotic enclosures: a random-plane-wave model

14:15-14:30

A. Sorrentino, and M. Migliaccio

The phase kurtosis index for reverberating chamber near LOS conditions

14:30-14:45

G. Grandoni, V. Mariani Primiani, and F. Moglie

Analysis of the entropy in fast time domain simulations of reverberation chambers

14:45-15:00

G. A. Casula, P. Maxia, G. Montisci, G. Mazzarella, and F. Desogus

Design of cavity resonators for chemical reactions

14:00 – 15:30 Session 8 – Ground Penetrating Radar – Aula N13

Chairpersons: *E. Pettinelli, “Roma Tre” University, Italy*
F. Soldovieri, CNR-IREA, Italy

14:00-14:30

A. Benedetto

Civil engineering applications of ground penetrating radar (invited)

14:30-14:45

D. Comite, A. Galli, F. Soldovieri, G. Valerio, P.M. Barone, S.E. Lauro, E. Mattei, and E. Pettinelli

Estimation of the geometrical features of buried objects from GPR analysis

14:45-15:00

F. Frezza, L. Pajewski, C. Ponti, G. Schettini, and N. Tedeschi

Plane wave scattering by a perfectly-conducting circular cylinder buried in a lossy medium

15:00-15:15

R. Persico, G. Leucci, and F. Soldovieri

Effect of the height of the measurement line on the diffraction curves in GPR prospecting

15:15-15:30

R. Monleone, M. Maffongeli, M. Pastorino, S. Poretti, A. Randazzo, and A. Salvadè

Detection of metallic bodies in dielectric structure by microwave imaging - Experimental results

15:30 – 16:00 Coffee Break

16:00 – 17:30 Session 9 – Antenna Arrays – Aula N11

Chairpersons: *G. Di Massa, University of Calabria, Italy*
R. Vescovo, University of Trieste, Italy

16:00-16:15

G. A. Casula, P. Maxia, G. Montisci, and G. Mazzarella

Design of printed UWB log-periodic dipole arrays

16:15-16:30

S. Mosca, and L. Infante

Tangram shaped subarrays for multiple beam array

16:30-16:45

A. F. Morabito, and A. R. Laganà

A size-tapered architecture for high performances isophoric direct radiating arrays

16:45-17:00

F. Venneri, S. Costanzo, G. Di Massa, E. Marozzo, A. Borgia, and M. Salzano

Implementation of a full-range varactor tuned element for the design of a reconfigurable reflectarray

17:00-17:15

G. Buttazzoni, and R. Vescovo

Co-polar and cross-polar pattern synthesis for reconfigurable antenna arrays

17:15-17:30

E.D. Di Claudio, G. Jacovitti, A. Laurenti

Hermite and Laguerre beamspaces for Ultra Wide Band antenna array processing

16:00 – 17:30 Session 10 –Propagation and Scattering – Aula N13

Chairpersons: *R. Pierri, Second University of Naples, Italy*
V. Fiumara, University of Basilicata, Italy

16:00-16:15

C. Capsoni, L. Luini, and R. Nebuloni

Preliminary assessment of site diversity schemes for earth-space optical links

16:15-16:30

A. Di Carlofelice, E. Di Giampaolo, M. Elaiopoulo, and P. Tognolatti

A study of radiowave propagation into collapsed buildings for rescue of trapped people

16:30-16:45

P. Imperatore, A. Iodice, and D. Riccio

The role of internal field approximation for scattering from layered rough interfaces

16:45-17:00

M. Carlin, L. Manica, G. Oliveri, L. Poli, P. Rocca, and A. Massa

Advances on inverse scattering methodologies and applications @ ELEDIA research center

17:00-17:15

L. Di Donato, I. Catapano, L. Crocco, and T. Isernia

A new framework for quantitative inverse scattering

20:30 Social Dinner

Thursday 13 September 2012

09:30 – 11:00 Session 11 – Bioengineering II – Aula N11

Chairpersons: *R. Olmi, CNR-IFAC, Italy*
G. Sorbello, University of Catania, Italy

09:30-09:45

R. Cicchetti, S. Pisa, E. Pittella, E. Piuze, and O. Testa
Analysis and design of a UWB radar for non-invasive breath activity monitoring

09:45-10:00

P. Russo, V. Mariani Primiani, A. De Leo, and G. Cerri
Radiated emission and susceptibility of breath monitoring system based on UWB pulses in spacecraft modules

10:00-10:15

G. Biffi Gentili, and M. Linari
A novel thermo-ablative microwave multi-applicator system

10:15-10:30

A. Denzi, F. Camera, A. Paffi, C. Merla, F. Apollonio, P. Marracino, G. d'Inzeo, and M. Liberti
Effects of nanosecond pulsed electric field on the activity of a Hodgkin and Huxley neuron model

10:30-10:45

A. Doria, G.P. Gallerano, E. Giovenale, G. Messina, A. Ramundo Orlando, and I. Spassovsky
Electromagnetic pulser for the investigation of cell membranes

09:30 – 11:00 Session 12 – Antenna Design and Measurements – Aula N13

Chairpersons: *A. Massa, University of Trento, Italy*
C. Gennarelli, University of Salerno, Italy

09:30-09:45

L. Lucci, R. Nesti, G. Pelosi, and S. Selleri
Design of circular corrugated horn with constant width corrugations

09:45-10:00

E. Bekele, R. Chirikov, M. Carlin, L. Manica, G. Oliveri, L. Poli, P. Rocca, and A. Massa
What's new on antenna synthesis @ ELEDIA research center

10:00-10:15

A.D. Capobianco, E. Autizi, A. Locatelli, D. Modotto, C. De Angelis, S. Boscolo, and M. Midrio
Printed CRLH omnidirectional loop antenna for mobile WLAN applications

10:15-10:30

M. Aldrigo, A. Costanzo, D. Masotti, and V. Rizzoli
A wearable UHF small patch antenna on a new magneto-dielectric material

10:30-10:45

O. Losito, M. Bozzetti, G. Cannone, F. Prudenzano, L. Mescia, A. Di Tommaso, P. Bia, V. Castrovilla, M. De Sario

Measurements of antenna factor with antenna impedance method

10:45-11:00

F. D'Agostino, F. Ferrara, C. Gennarelli, R. Guerriero, and M. Migliozzi

Spherical near-field to far-field transformation for quasi-planar antennas: an experimental validation

11:00 – 11:30 Coffee Break

11:30 – 12:30 Plenary Lecture II – Aula N11

Chairperson: L. Pajewski, “Roma Tre” University, Italy

Evert Slob

Delft University of Technology, Delft, The Netherlands

Full waveform inversion as a two-step linear process

Sébastien Lambot

Université Catholique de Louvain, Louvain-la-Neuve, Belgium

A closed form full-wave radar model for near-field layered media reconstruction

12:30 – 14:00 Lunch

14:00 – 15:30 Session 13 – Optical Fibers – Aula N11

*Chairpersons: A. Galtarossa, University of Padua, Italy
S. Wabnitz, University of Brescia, Italy*

14:00-14:15

L. Ursini, and M. Santagiustina

Applications of fiber optics dynamic Brillouin gratings in ultra wideband communications

14:15-14:30

M. Surico, A. Di Tommaso, P. Bia, L. Mescia, M. Bozzetti, O. Losito, M. De Sario, and F. Prudenzano

Large mode area fibers for high power and high beam quality lasers

14:30-14:45

L. Schenato, L. Palmieri, L. Vianello, G. Marcato, G. Gruca, T. van de Watering, D. Iannuzzi, A. Pasuto, and A. Galtarossa

Fiber optic sensor for precursory acoustic signals detection in rockfall events: feasibility analysis

14:45-15:00

L. Palmieri, A. Galtarossa, and L. Schenato

Distributed fiber optic sensor for intense magnetic field mapping

15:00-15:15

E. Balliu, A. Braglia, A. Califano, M. Olivero, A. Penna, and G. Perrone
A new pumping scheme for high power Tm-doped fiber laser

14:00 – 15:30 Session 14 – Radio Frequency Identification – Aula N13

Chairpersons: *G. Mazarella, University of Cagliari, Italy*
L. Tarricone, University of Lecce, Italy

14:00-14:15

G. Marrocco, and S. Caizzone
Electromagnetic properties of passive RFID networks

14:15-14:30

S. Manzari, C. Occhiuzzi, A. Catini, C. Di Natale, and G. Marrocco
Chemical loaded RFID antenna for humidity detection

14:30-14:45

D. De Donno, L. Catarinucci, R. Colella, and L. Tarricone
Performance evaluation of passive UHF RFID tags with software - defined radio

14:45-15:00

L. Catarinucci, R. Colella, and L. Tarricone
Innovative prototyping techniques for UHF RFID tags

15:00-15:15

A. Buffi, P. Nepa, and F. Lombardini
Localization of RFID tagged items on a conveyor belt

15:15-15:30

A. Michel, R. Caso, A. Buffi, and P. Nepa
Near-field UHF RFID antenna for desktop reader

15:30 – 16:00 Coffee Break

16:00 – 17:00 Poster Session III

Chairperson: *V. degli Esposti, University of Bologna, Italy*

D. Riccio and G. Ruello

A novel approach for the sampling of fractal surfaces in remote sensing

S. Meschino, L. Pajewski, M. Pastorino, A. Randazzo, and G. Schettini

Sub-array processing techniques applied to the detection of buried targets

Y. Pei, S. Yi, J. Zhou, R. Notarpietro, P. Savi, and M. Pini

GNSS reflectometry for Earth's surface monitoring exploiting an open-loop approach

S. Pompili, A. Di Carlofelice, P. Romano, and C. Sciannella

Spaceborne microwave interferometric radiometers: lunar sub-surface remote sensing, inverse problems and electromagnetic diagnostics

L. Pulvirenti, M. Chini, F.S. Marzano, N. Pierdicca, S. Mori, and L. Guerriero

Detection of floods and heavy rain using COSMO-SkyMed data

F. Nunziata and M. Montuori

Reflection symmetry to observe metallic targets at sea by a dual-polarimetric SAR

G. Di Martino, A. Iodice, D. Riccio, and G. Ruello

Electromagnetic characterization of speckle in SAR images

G. Olivieri

Contrast source Bayesian compressive imaging by a minimum norm formulation

M. Muzi

Resolution of MEG inverse problem via reweighted ℓ_1 minimization algorithm

A. Di Carlofelice, E. Di Giampaolo, and P. Tognolatti

Electromagnetic propagation inside a module of international space station: a numerical analysis

G. Bellizzi and O.M. Bucci

Criterion for the optimal choice of the operative conditions in magnetic nanoparticle hyperthermia: uncertainty analysis

B. Bisceglia, E. Avallone, A. Buonerba, E. Caliendo, F. Chiadini, A. Grassi, L. Incarnato, A. Scaglione, and L. Guerriero

Microwave treatment of tuff-stones. Structural analysis

P. Marracino, M. Migliorati, A. Paffi, M. Liberti, G. d'Inzeo, and F. Apollonio

Signal transduction on enzymes: the effect of electromagnetic field stimuli on superoxide dismutase (SOD)

M. Cavagnaro, S. Franco, V. Lopresto, and R. Pinto

Characterization of a microwave thermal ablation process

G. Monti, L. Tarricone, M. Dionigi, and M. Mongiardo

Artificial transmission line for wireless power transmission

M. Dal Forno, P. Craievich, R. Vescovo, and C. Serpico

Microwave design studies of linear accelerators for free electron laser photoinjectors

G.L. Ravera and S. Ceccuzzi

Analysis of the FAST ICRH antenna straps array with water load using HFSS code

17:00 – 18:30 Session 15 – Photonic Crystals – Aula N13

Chairpersons: *R. Orta, Polytechnic of Turin, Italy*
S. Selleri, University of Parma, Italy

17:00-17:15

S. Roy, M. Santagiustina, S. Combrié, A. De Rossi, A. Wilinger, and G. Eisenstein
Slow light engineered photonic crystal waveguide: propagation and parametric gain properties

17:15-17:30

D. Modotto, G. Manili, U. Minoni, S. Wabnitz, M. Andreana, V. Couderc, and A. Tonello
Giant dispersive wave generation in double core photonic crystal fiber

17:30-17:45

E. Coscelli, F. Poli, A. Cucinotta, and S. Selleri
Air-hole ring influence on the cut-off proprieties of 19-cell double-cladding photonic crystal fibers

17:45-18:00

S. Malaguti, G. Bellanca, S. Trillo, S. Combrié, and A. De Rossi
Filter design for OTDM and WDM receivers in PHC technology

18:00-18:15

A. Brancaccio, G. Leone, R. Solimene, and R. Pierri
Fault detection in a dielectric grid

18:15-18:30

A. Vaccari, A.C. Lesina, L. Cristoforetti, A. Chiappini, and M. Ferrari
A computational approach to the optical characterization of photonic crystals and photonic glasses

17:00 – 18:30 Session 16 – Wireless Communications, Networks and Systems – Aula N11

Chairpersons: *M.D. Migliore, University of Cassino, Italy*
P. Nepa, University of Pisa, Italy

17:00-17:15

A.A. Serra, R. Caso, A. Buffi, A. Guraliuc, A. D'Alessandro, A. Michel, and P. Nepa
Research activities on antenna design for wireless communication networks at the University of Pisa

17:15-17:30

F. Viani, M. Salucci, F. Robol, E. Giarola, and A. Massa
WSNs as enabling tool for next generation smart systems

17:30-17:45

S. Mori, P. Lucantoni, M. Ferrara, P. Nocito, G. M. Tosi Beleffi, E. Restuccia, F. Frezza, and F.S. Marzano
Hydrometeor scattering effects over near-infrared free-space urban links: model and experimental measurements

17:45-18:00

P. Imperatore, A. Iodice, and D. Riccio

Electromagnetic source localization in 3-D outdoor urban scenario using received signal strength

18:00-18:15

R. Stefanelli, N. Carvalho, D. Brunazzi, and D. Trincherò

Design of the wireless front-end for remote administration of domotic equipment

18:15-18:30

M. Dionigi, and M. Mongiardo

Wireless power transfer and near field magnetic communications by multi band resonators

Friday 14 September 2012

09:00 – 10:30 Session 17 – Photonic and Plasmonic Technologies and Components – Aula N13

Chairpersons: *A. D’Orazio, Polytechnic of Bari, Bari, Italy*
 S. Trillo, University of Ferrara, Italy

09:00-09:15

F. Morichetti, A. Canciamilla, S. Grillanda, P. Orlandi, S. Malaguti, M.J. Strain, M. Sorel, G. Bellanca, P. Bassi, and A. Melloni

SAPPHIRE: a generic foundry platform for silicon photonics

09:15-09:30

A. Parini, G. Calò, S. Malaguti, G. Bellanca, V. Petruzzelli, and S. Trillo

Photonics interconnect technology for chip multiprocessing architectures: the Photonica project

09:30-09:45

M.P. Bolzoni, G.G. Gentili, and S.M. Pietralunga

Grating-assisted coupling to strip plasmonic modes: 3D numerical analysis

09:45-10:00

M. Grande, G. Magno, R. Marani, G. Calò, V. Petruzzelli, and A. D’Orazio

Design of plasmonic directional couplers

10:00-10:15

F.M. Pigozzo, D. Modotto, and S. Wabnitz

Second harmonic generation in plasmonic waveguides

10:15-10:30

F. A. Bovino

Representation of a Spiral Phase Plate as a two mode Quantum Phase Operator

09:00 – 10:30 Session 18 – Energy and Environment – Aula N13

Chairpersons: *G. Cerri, Polytechnic University of Marche, Italy*
 L. Roselli, University of Perugia, Italy

09:00-09:15

A. Carta, R. Stefanelli, and D. Trincherò

Microwave electromagnetic sensors to estimate water density within snow

09:15-09:30

M. Montopoli, G. Vulpiani, and F. S. Marzano

The potential use of microwave weather radar for volcanic ash monitoring

09:30-09:45

M. Sozzi, C. Catellani, A. Cucinotta, S. Selleri, D. Menossi, R. Dharmadasa, A. Bosio, and N. Romeo

Laser scribing integration of polycrystalline thin film solar cells

09:45-10:00

S. Ceccuzzi, F. Napoli, L. Pajewski, G. Schettini, and A.A. Tuccillo

Antenna-plasma coupling calculations at lower hybrid frequencies by using a FEM code

10:00-10:15

R. Moro, S. Kim, M. Bozzi, and M. Tentzeris

Novel inkjet-printed substrate integrated waveguide (SIW) structures for eco-friendly low-cost application

10:15-10:30

A. Facchini, A. Zeffiro, P. Arcioni, and A. Buttafava

Preliminary studies on the microwave pre-treating of lignocellulosic biomasses

10:30 – 11:00 Coffee Break

11:00 – 12:00 Plenary Lecture III – Aula N11

Chairperson: L. Vegni, “Roma Tre” University, Italy

Andrea Alù

University of Texas at Austin, USA

Metamaterials and plasmonics: from RF to optical applications

12:00 – 13:00 Plenary Lecture IV – Aula N11

Chairperson: A. Toscano, “Roma Tre” University, Italy

Leo Kempel

Michigan State University, USA

Half-width Leaky-wave Antennas: A Progress Report

13:00 – 13:30 Young Authors Award Ceremony and Closing Address – Aula N11

Award announcement – P. Lampariello, “Sapienza” University of Rome, Italy

Chair closing – G. Schettini and L. Vegni, “Roma Tre” University, Italy

Proceedings of the XIX RiNEm

Plenary lectures

Marian Marciniak

National Institute of Telecommunications, Warsaw, Poland

Converged optical and wireless communications for the future

Evert Slob

Delft University of Technology, Delft, The Netherlands

Full waveform inversion as a two-step linear process

Sébastien Lambot

Université Catholique de Louvain, Louvain-la-Neuve, Belgium

A closed form full-wave radar model for near-field layered media reconstruction

Andrea Alù

University of Texas at Austin, USA

Metamaterials and plasmonics: From RF to optical applications

Leo Kempel

Michigan State University, USA

Half-width Leaky-wave Antennas: A Progress Report

Giancarlo Prisco

Selex S.I.

Receiving sparse signals in radar systems: Blind recovery at minimum rate

CONVERGED OPTICAL AND WIRELESS COMMUNICATIONS FOR THE FUTURE

Marian Marciniak^(1,2)

⁽¹⁾ National Institute of Telecommunications
Department of Transmission and Optical Technologies
1 Szachowa Street, 04-894 Warsaw, Poland

⁽²⁾ Kielce University of Technology
Faculty of Electrical Engineering, Automatics and Computer Science
Aleja Tysiaclecia Panstwa Polskiego 7, 25-314 Kielce, Poland
marian.marciniak@ieee.org

Abstract

The proposed converged network concept supports both circuit switched and packet switched traffic, real-time and non-real time services, and fixed and wireless communications. This is achieved by allocating necessary number of light wavelength channels for real time services according to the instantaneous demand, all remaining wavelengths are used for packet traffic. Transparency of the optical network allows to transmit Radio-over-Fibre signals on the dedicated optical wavelength channels as well.

Index Terms – Converged communications, Radio-over-Fibre, Transparent network

Nowadays communications target to transmit a variety of services as classical telephony, facsimile transmission, but also the Internet traffic, data transmission, radio and television broadcasting etc. Consequently, various transmission media are used as metal and fiber cables, and free space links for microwave, millimeter wave, and optical links. Owing to top performance of contemporary optical fibers there is a tendency to exploit optics as far as possible [1]. Thus a question arises: do we really need separate networks for different services? Or separate fibers in a single network? Why do not use separate optical wavelengths in a single fiber for that?

Here we propose a novel non-conventional approach to the future optical and wireless hybrid transport network that is capable to support current kinds of traffic as real time voice, wireless, and packet traffic in a single converged network. This hybrid network concept distinguish between real time and non-real time (packet or data) services. Those are physically transmitted on different optical wavelengths. Real time voice and wireless is carried on dynamically allocated wavelengths, according to instantaneous demand for real-time services. All remaining wavelengths are for the IP traffic. The two kinds of traffic are separated and interleaved in frequency (wavelength) domain, not in time domain. The microwave/millimeter wave signal transmission can be included in the transparent real-time part of the network by the means of modulating the optical carrier wavelength with the mobile signal in the 'Radio over Fiber' fashion. This is especially suited for transmitting 60 GHz signal which suffers of a high attenuation of 10 dB/km in the air [2]. On the other hand, the attenuation in silica glass fibres is below

0,2 dB/km at $\lambda = 1,55\mu\text{m}$ (so called 3rd transmission window). This approach allows to profit fully from both sophisticated SDH technology developed for real time - voice circuit switched service, and from IP protocol developed uniquely for packet-switched traffic but exposed to Quality of Service constraints [3].

Table 1 classifies characteristics for real-time and non-real time traffic within a hybrid converged network.

TABLE I
CHARACTERISTICS OF REAL-TIME AND NON-REAL TIME TRAFFIC.

Basic principle	Circuit-switched	Packet-switched
Service	Real-time - Voice, Video, Radio-over-Fiber	Non-real time: Internet (incl. VoIP), data
Cell/packet length	Constant length cells	Variable
Latency	Unnoticeable	Allowed
lost data	No retransmission	Retransmitted
Quality of Service	Guaranteed by over-provisioning	Best-effort
Traffic	Deterministic	Statistic
Other	Instantaneous bandwidth (# of λ s) controlled logically in IP routers	Intelligence
Transparency	Transparent	Incl. All-optical opacity
Bandwidth	Dedicated on demand	As wide as available
Security	Inherent	To be improved permanently

The converged network model resigns from the common approach to put the real-time traffic on top of packet network, and it claims to position them in parallel in the network rather. Consequently, it provides a space for inclusion of microwave signals via the Radio-over-Fibre technology. The model respects optimal conditions for Quality of Service and security requirements specific to different kinds of traffic, and it conserves the Quality of Service as well as security constraints for real-time traffic.

The presented hybrid optical & wireless network assures efficient use of the available bandwidth, and optimises the network availability for different traffic and services. This approach overcomes important drawbacks of an all-IP network, and it gently accommodates the real-time circuit-switched transmission of a high reliability and security with more flexible but highly vulnerable IP packet traffic.

REFERENCES

- [1] M. Marciniak, "Optical Fibres – Almost Ideal Transparent Propagation Medium?," *11th International Conference on Mathematical Methods in Electromagnetic Theory MMET*06 - Kharkiv Electromagnetics & Photonics Week 2006*, pp. 358-362, Kharkov, Ukraine, June 2006.
- [2] M. Marciniak, "Converged Optical and Wireless as enabling technology towards Future Networks", *The XXX General Assembly and Scientific Symposium of the International Union of Radio Science URSI GA 2011, Workshop on Advances in Optical-Wireless Communications*, Paper 04, Istanbul, Turkey, August 13-20, 2011.
- [3] M. Klinkowski, D. Careglio, J. Solé-Pareta, M. Marciniak, "A Performance Overview of Quality of Service Mechanisms in Optical Burst Switching Networks", in: *Current Research Progress of Optical Networks*, M. Ma (Ed.), Chapter 1, pp. 1-20, Springer, 2009.

LAYERED MEDIUM FULL WAVEFORM INVERSION AS A TWO-STEP LINEAR PROCESS

Evert Slob and Kees Wapenaar

Department of Geoscience & Engineering, Delft University of
Technology, Stevinweg 1, 2628 CN Delft, The Netherlands

e.c.slob@tudelft.nl

Abstract

Recently, Brogгинi et al. discussed several connections between wave field focusing, interferometry, and inverse scattering [1]. In different ways it is demonstrated how to construct the 1D seismic wave field measured in the homogeneous upper half space and generated by a source in the interior of an unknown medium. The input data is a reflection measurement from a source and a receiver in the homogeneous upper half space. In seismic interferometry [2] a physical receiver is necessary inside the unknown heterogeneous medium and physical sources must be present in both homogeneous half-spaces in which the heterogeneous medium is embedded. As an alternative approach focusing theory [3] is applied to reflection data to construct the wave field recorded at the receiver from a virtual source inside the heterogeneous medium [1]. Both methods do not require knowledge about medium properties other than assuming the waves propagate without dissipation. The important advantage of the second method over the first is that the location of the virtual source is obtained without having a physical receiver at that location. This creates data that is the starting point of the virtual source method of [4], but now without the need for borehole data. The data that is obtained from reflection data is a virtual Vertical Seismic Profile (VSP) data set. In a companion paper Wapenaar et al. showed how this could be extended to three-dimensional media [5]. Once the 3D wave fields are reconstructed with a virtual source in the subsurface, a dual VSP can be created that allows directional decomposition at the subsurface virtual source depth level followed by multi-dimensional deconvolution to create a 3D internal multiple-free image [6].

It is interesting that a number of successive data driven filter steps lead to creating wave fields as if they were generated, or measured, at locations where no physical source, or receiver, was placed and in addition lead to the construction of images free of internal multiples. The focusing theory of Rose, being a specific implementation of solving the Marchenko equation [7], is a linear data driven filter method of iteratively focusing a wave field at a specified one-way travel-time, or virtual depth level. This implies that the filter itself is a Green's function. In this talk it is shown that this filter contains the local reflection response for a source and receiver at the

virtual depth level. For 3D wave fields in a horizontally layered medium the obtained image contains the local reflection coefficients as a function of one-way intercept time and horizontal slowness. This is a non-recursive method, because the depth levels can be chosen independently. The solution to the Marchenko equation is analyzed for plane waves incident at arbitrary angles of incidence on a horizontally layered model. The image containing only local primary reflection coefficients at correct one-way travel times is extracted from the filter solution. Creating an image is the first step in an inversion approach. Once the image is obtained with local reflection coefficient amplitudes, the electric permittivity and magnetic permeability can be obtained from inverting the reflection coefficients for a number of slowness values. This is a direct matrix inversion solution that can be obtained in the least squares sense. The inversion step is recursive, because knowledge of the upper half space medium parameters is needed to start the scheme.

Index Terms – Focusing, Imaging, Inversion, Migration.

REFERENCES

- [1] F. Brogini, R. Snieder and K. Wapenaar, “Connection of scattering principles: focusing the wavefield without source or receiver”, *SEG Technical Program Expanded Abstracts, 81st Annual International Meeting of the Society of Exploration Geophysicists*, September 18-23, 2011, San Antonio, Texas, USA, pp. 3845-3850.
- [2] K. Wapenaar, J. Fokkema and R. Snieder, “Retrieving the Green’s function in an open system by cross correlation: A comparison of approaches” (L), *JASA*, 118(5), pp. 2783–2786, May 2005.
- [3] J.H. Rose, “Single-sided autofocusing of sound in layered materials”. *Inverse Problems*, 18, pp. 1923–1934, December 2002.
- [4] A. Bakulin and R. Calvert, “The virtual source method: Theory and case study”, *Geophysics*, 71(4), pp. SI139–SI150, July-August 2006.
- [5] K. Wapenaar, F. Brogini and R. Snieder, “A proposal for model-independent 3D wave field reconstruction from reflection data”, *SEG Technical Program Expanded Abstracts, 81st Annual International Meeting of the Society of Exploration Geophysicists*, September 18-23, 2011, San Antonio, Texas, USA, pp. 3788–3792.
- [6] K. Wapenaar, J. Thorbecke, J. van der Neut, E. Slob, F. Brogini and R. Snieder, “Integrated migration and internal multiple elimination”, *SEG Technical Program Expanded Abstracts, 82nd Annual International Meeting of the Society of Exploration Geophysicists*, November 4-9, 2012, Las Vegas, Texas, USA, to be published.
- [7] G.L. Lamb, “Elements of soliton theory”, John Wiley and Sons Inc., New York, 1980.

A CLOSED FORM FULL-WAVE RADAR MODEL FOR NEAR-FIELD LAYERED MEDIA RECONSTRUCTION

S. Lambot, A.P. Tran, F. André

Earth and Life Institute, Environmental Sciences,
Université catholique de Louvain
Croix du Sud 2 box L7.05.02, 1348 Louvain-la-Neuve, Belgium
sebastien.lambot@uclouvain.be

Abstract

A closed form near-field radar modeling approach for wave propagation in planar layered media is presented. The radar antennas are modeled using an equivalent set of infinitesimal electric dipoles and characteristic, frequency-dependent, global reflection and transmission coefficients. These coefficients determine through a plane wave decomposition wave propagation between the radar reference plane, point sources, and field points. Coupling between the antenna and layered medium is thereby inherently accounted for. The fields are calculated using three-dimensional Green's functions. We validated the model using frequency- and time-domain radars with antennas operating in different frequency ranges. The antenna characteristic coefficients were obtained from near- and far-field measurements over a copper plane. The proposed model provided unprecedented accuracy for describing near-field radar measurements collected over water and sand layers with frequency-dependent electrical properties. Medium properties could be retrieved through full-wave inversion. The proposed approach shows great promise for non-destructive testing of planar materials and soils, e.g., using ground-penetrating radar.

Index Terms – Full-wave inversion, ground-penetrating radar, Green's functions, layered media, near-field modeling.

REFERENCES

- [1] S. Lambot and F. André, 2012. Full-waveform modelling of near-field radar data to reconstruct planar layered media, *IEEE Transactions on Geoscience and Remote Sensing*, submitted.
- [2] S. Lambot, A.P. Tran and F. André. 2012. Near-field modeling of radar antennas for wave propagation in layered media: when models represent reality. In *Proceedings of The 14th Conference on Ground Penetrating Radar*, Edited by Y. Li, X. Xie, L. Liu, M. Sato and F. Kong, pp 42-46, 4-8 June 2012, Shanghai, China.

METAMATERIALS AND PLASMONICS TO CONTROL AND TAILOR ELECTROMAGNETIC WAVES

A. Alù

Department of Electrical and Computer Engineering, The
University of Texas at Austin
1 University Station C0803, Austin, TX 78712, USA
alu@mail.utexas.edu

Abstract

In this talk, I will discuss our recent progress and research activity in the fields of metamaterials and plasmonics, covering a wide range of topics, from theoretical approaches to model the anomalous wave propagation in metamaterials and plasmonic materials, to various applications at microwave and optical frequencies, including enhanced nonlinearities, sensing, imaging and energy harvesting. I will discuss our most recent theoretical and experimental results in these areas, including the concept of broadband ‘plasmonic Brewster’ light funneling [1] and ‘epsilon-near-zero’ metamaterials [2]. I will also show our recent near-field and far-field experimental measurements of 3-D radio-frequency cloaking, which represents the first experimental realization of a metamaterial cloak in 3-D for a free-standing object [3]. Finally, I will discuss the concept of twisted metamaterials and our experimental realization of ultrathin, broadband, planarized circular polarizers based on this idea, realized using stacked, lithographically printed optical metasurfaces [4]. Physical insights into these exotic phenomena will be discussed during the talk.

Index Terms – Metamaterials, plasmonics, scattering.

REFERENCES

- [1] A. Alù, G. D’Aguanno, N. Mattiucci, and M. J. Joemer, “Plasmonic Brewster angle: broadband extraordinary transmission through optical gratings,” *Physical Review Letters*, Vol. 106 (12), 123902 (4 pages), March 23, 2011.
- [2] J. Soric, S. Maci, N. Engheta, and A. Alù, “Omnidirectional small antennas based on ϵ -near-zero metamaterial channels,” *IEEE Transactions on Antennas and Propagation*, in press, 2012.
- [3] D. Rainwater, A. Kerkhoff, K. Melin, J. C. Soric, G. Moreno, and A. Alù, “Experimental verification of three-dimensional plasmonic cloaking in free-space,” *New Journal of Physics*, Vol. 14, 013054 (13 pages), January 25, 2012.
- [4] Y. Zhao, M. A. Belkin, and A. Alù, “Twisted optical metamaterials for planarized, ultrathin, broadband circular polarizers,” *Nature Communications*, Vol. 3, No. 870 (7 pages), May 29, 2012.

HALF-WIDTH LEAKY-WAVE ANTENNAS: A PROGRESS REPORT

L. Kempel¹), E. Rothwell¹), B. Shanker¹), P. Chahal¹)

⁽¹⁾ Dept. of Electrical & Computer Engineering, Michigan State Univ.
3410 Engineering Building, East Lansing, Michigan, USA, 48824
kempel@msu.edu

Abstract

Microstrip leaky-wave antennas have been a scholarly topic of interest for nearly three decades. Seminal work includes that of Oliner [1] and Menzel [2]. The former work presented an effective method for predicting the radiation properties of such antennas using the Transverse Resonance Method (TRM). The latter presented an effective method to physically realize such an antenna that utilized resonant and periodic slots near the feed. The slots provided a means to suppress the EH_{00} fundamental mode and hence provide power preferentially into the first higher-order (leaky) EH_{01} mode.

Although an useful antenna, the microstrip leaky-wave antenna was difficult to match due to the need to either carefully design the slots so as to not excessively impact the radiating current distribution (and hence the polarization purity of the antenna) or feed using a balanced structure that requires two feed points with 180° phase difference across the operational bandwidth of the antenna [3]. Hence, in either case, the realized bandwidth is always significantly lower than the theoretical bandwidth.

Schneider and Thiele introduced the concept of a half-width leaky-wave (HWLW) antenna to simplify the feed requirements [4]. The inclusion of a metallic septum results in the potential for using only one feed point since the septum suppresses the fundamental mode but not the first higher-order mode. Significant improvements have been made on this aperture over the past five years that enhanced understanding of the properties of such an antenna and facilitated greater functionality. Specifically, the most significant contributions are: arrays [5], inhomogeneous substrates ([6]-[7]), and both passive and active reactive loading to control the radiation properties ([8]-[9]), and inductive wall modeling [10].

During the evolution of this antenna design, better control over both bandwidth and radiation patterns has been obtained, and approaches to electronically controlling the beam has been investigated. The talk will present the results of these past five years and offer future perspective.

Index Terms – Microstrip leaky-wave antenna; end-fire radiation; wide bandwidth; electronic tuning.

REFERENCES

- [1] A. Oliner, "Leakage from Higher Modes on Microstrip Line with Applications to Antennas", *Radio Science*, 22, pp. 907-912, Nov. 1987.
- [2] W. Menzel, "A New Traveling-Wave Antenna in Microstrip", *Archiv fur Elektronik und Ubertragungstechnik (AEU)*, Band 33, Heft 4:137-140, April 1979.
- [3] W. Hong, T-L Chen, C-Y Chang, J-W Sheen, and Y-D Lin, "Broadband tapered microstrip leaky-wave antenna," *IEEE Trans. Antennas Propagat.*, 51, pp. 1922-1928, Aug. 2003.
- [4] G. M. Zelinski, G. A. Thiele, M. L. Hastriter, M. J. Havrilla, and A. J. Terzouli, "Half Width Leaky Wave Antennas," *IET Microwaves, Antennas & Propagation*, Vol. 1, No. 2, pp. 341-348, April 2007.
- [5] D. Killips, J. Radcliffe, L. Kempel, and S. Schneider, "Radiation by a linear array of half-width leaky-wave antennas," *ACES Journal*, 21, pp. 248-255, Nov. 2006.
- [6] C.A. Jaramillo-Henao, L.C. Kempel, and S.W. Schneider, "Simulation of microstrip leaky-wave antennas on inhomogeneous substrates using the transverse resonance and finite element methods," *Electromagnetics*, 28, pp. 27-41, Jan-Mar 2008.
- [7] H. Jiang, R. Penno, K.M. Pasala, L. Kempel, and S. Schneider, "Broadband microstrip leaky wave antenna with inhomogeneous materials," *IEEE Trans. Antennas Propagat.*, 57, pp. 1557-1561, May 2009.
- [8] M. Archbold, E.J. Rothwell, L.C. Kempel, and S.W. Schneider, "Beam steering of a half-width microstrip leaky-wave antenna using edge loading," *IEEE Antennas Wireless Prop. Lttrs*, 9, pp. 203-206, 2010.
- [9] H. Hejase, J. Myers, L. Kempel, and P. Chahal, "Design study of electronically steerable half-width microstrip leaky wave antennas," *61st IEEE Electronic Component and Technology Conf.*, pp. 1348-1353, 2011.
- [10] M.T. Corwin, Inductively Loading a Half Width Leaky Wave Antenna To Control the Main Beam Direction, M.S. Thesis, University of Dayton, 2012.

**RECEIVING SPARSE SIGNALS IN RADAR SYSTEMS:
BLIND RECOVERY AT THE MINIMUM RATE**

G. Prisco, R. Lalli, M. D'Urso, L. Timmoneri, F. De Stefani

SELEX Sistemi Integrati S.p.A., Via Circumvallazione Esterna di Napoli,
Loc. Pontericci zona ASI, I-80014 Giugliano, Napoli, Italy
(e-mail: gprisco@selex-si.com).

Abstract

In scenarios in which the carrier frequencies are unknown to the receiver, or vary in time, a challenging task is to design a spectrum-blind receiver at the minimum rate. In this context, a compressive sampling based technique is proposed as a down conversion solution that does not need Stable Local Oscillator (STALO) signal, and so it makes possible to eliminate a substantial analog section, obtaining a significant reduction of both dimensions and costs. In addition, such a scheme allows the transmission-receiving system to manage multiple signals, placed at different carrier frequencies, at the same time, in order to make the radar system more robust against external jammers.

Index Terms – Analog to digital conversion (ADC), compressive sampling (CS), radar receivers, spectrum blind reconstruction.

I. INTRODUCTION

In modern radar applications, an increasing number of functions is being pushed forward to sophisticated software algorithms, leaving only delicate finely tuned tasks for the circuit level. Sampling theory, the gate to the digital world, is the key enabling this evolution. Multifunctional wideband systems open a considerable gap with ADC devices. Furthermore one design goal is to put the ADC as close as possible to the antenna. Conversion speeds have become more and more difficult to obtain. Consequently, alternatives to high rate sampling are drawing considerable attention in both academia and industry. The most common way, especially in radar system, to avoid the sampling at the Nyquist rate, is the demodulation process wherein the signal is shifted from the high frequencies to the origin and then the lowpass version is sampled uniformly in time. This procedure must be repeated for each band individually and in sequential mode. In radar systems it is useful to highlight the difference between operative and instantaneous band. The first one represents the frequency range allocated for a specific system, in sense that no other deployments can use that frequencies. In general the operative band covers some hundreds of MHz. The second one instead is the effective bandwidth occupied by the radar signal at a given time, it is typically of the order of some MHz (e.g. 10 MHz), and so it can perform frequency hopping to defend itself against interference, jamming and other external signals. In this context, the radar system employs a small band inside a large

allocated frequency range. This means that the frequency domain representation of such a signals is intrinsically sparse.

Recently a number of “sampling” strategy have been proposed, exploiting the compressive sampling (CS) theory, an emerging research field for sampling and recovery sparse signals at the minimum rate. The mainstream line of CS papers studies sparsity for discrete and finite vectors [1]. In order to locate and reconstruct the instantaneous bands used by the radar signal a more effective signal model is needed. Based on the analog multiband model, within this analog framework, which studies signals from a truly continuous domain [2], we propose a sampling-reconstruction procedure that can locate the carrier frequencies and reconstruct the spectrum content, in the operative band, through a modified version of the Modulated Wideband Converter (MWC) [2] avoiding the use of the mixer devices.

The paper is divided in Sections. The first Section is the introduction. In the Section II the proposed technique is presented. In the section III numerical results are shown. Conclusions follows.

II. SPECTRUM RECOVERY SCHEME

For multiband signals, with N non overlapped bands of widths B , the minimal sampling rate is the sum of the bandwidths NB , given a fixed subspace description of known band locations [3]. If the Nyquist bandwidth actually occupied is assumed known, but not the band locations, the minimal sampling rate must be doubled to $2NB$ [4].

The traditional radar systems excites only one band at a time ($N=2$) and employ super-heterodyne demodulation scheme. The RF signal selection is performed by an agile Local Oscillator signal (STALO) that shifts the received signal around a lower frequency (see fig. 1). This analogical process is very expensive mainly because the STALO must be a very stable high frequency source. Typically STALO source and distributor represents one of the most expensive sections of the whole radar architecture. By using the MWC scheme [MWC], based on the fully-blind sampling framework, it is possible to extends the conventional demodulation to multiband inputs with unknown carriers.

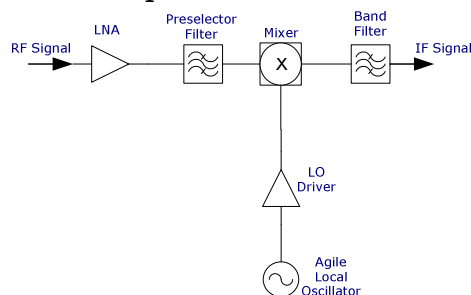


FIG. 1 – Typical demodulator scheme with agile STALO.

The conversion stage from analog to digital consists of a front-end of m channels, as depicted in Fig. 2 (a).

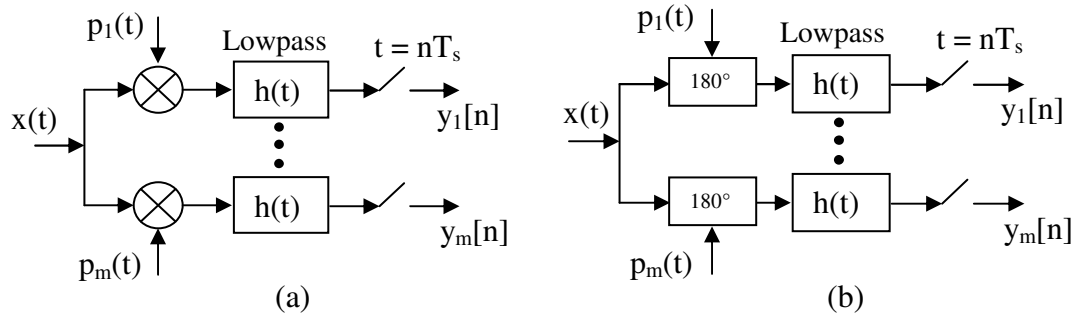


FIG. 2 – Front-end schemes: (a) MWC, (b) scheme with phase inverter.

With reference to the scheme in Fig. 2 (a), in the i th channel, the received RF signal $x(t)$ is multiplied by a periodic waveform $p_i(t)$ with period $T_p = 1/f_p$ that in each period is a piecewise constant function (different for each channel) that alternates between the levels ± 1 , lowpass filtered by $h(t)$, and then sampled at rate $f_s = 1/T_s$. In the basic version the sampling period T_s equals the aliasing period T_p , each channel samples at rate $f_s \geq B$ and the number of hardware branches $m \geq 2N$, so that the total sampling rate can be as low as $2NB$. These choices stem from necessary and sufficient conditions on the required sampling rate mf_s to allow perfect reconstruction. Since $p_i(t)$ is periodic, it has a Fourier series expansion

$$p_i(t) = \sum_{l=-\infty}^{+\infty} c_{il} e^{j2\pi l f_p t} \quad (1)$$

where c_{il} are a set of known coefficients. The result of the periodic mixing is the aliasing of the spectrum of $x(t)$, so that the product $\tilde{x}_i(t)$ contains shifted copies of the input spectrum $X(f)$

$$\tilde{X}_i(f) = \sum_l c_{il} X(f - lf_p) \quad f \in \left[-\frac{f_s}{2}, \frac{f_s}{2}\right] \quad (2)$$

The eq. (2) is the key to recovery of $x(t)$. By defining the unknown vector $z(f) = [z_1(f) \ z_2(f) \ \dots \ z_L(f)]$ where $z_i(f) = X(f - lf_p)$, eq. (2) in matrix form become $y(f) = A \cdot z(f)$. The sparsest solution $z(f)$ to such linear system provides the frequency carriers and the spectral behaviour of $x(t)$. The MWC requires to mix the input $x(t)$ simultaneously with the multiple sinusoids comprising the periodic waveforms, which poses an interesting circuit challenge. Since the mixing function $p_i(t)$ are a sign pattern it is possible, for non prohibitively high frequency, to replace the mixers with phase inverters (Fig. 2. (b)).

III. NUMERICAL RESULTS

In order to show the performance of the proposed architecture it is reported the results obtained simulating the sampling and reconstruction of a test signal composed of two linear frequency modulated carriers placed at $f_1 = 5.2\text{GHz}$ and $f_2 = 5.7\text{GHz}$, contaminated

by white Gaussian noise with SNR=10 dB. The signal consists of two pairs of bands ($N=4$), each of width $B=10$ MHz.

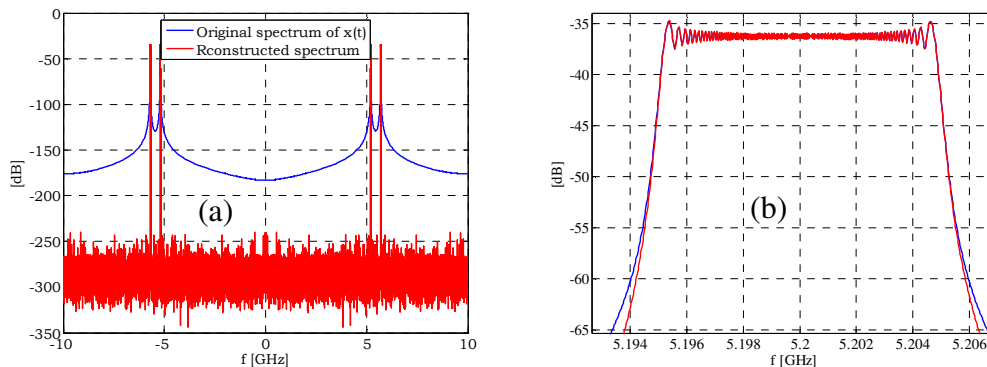


FIG. 3 – Original and reconstructed signals: (a) whole spectrum, (b) zoom around the frequency f_1 .

Coherently f_p has been chosen about 15Mz (slightly greater than B) and $f_s=f_p$. The carrier locations are correctly carried out as it can be seen in fig. 3. (a) and the spectral content of each band are well reconstructed as showed in fig. 3. (b) for the band centered around the frequency f_1 .

IV. CONCLUSION

A new receiver architecture, for radar systems, based the fully-blind recovery of multi-band signals, avoiding the use of the STALO and mixer have been presented. The preliminary tests show that potentiality it is possible to manage multiple carrier frequencies in the operative band, enabling the radar systems to operate with multiple antenna patterns at same time and make it more robust against external jammers.

REFERENCES

- [1] J. N. Laska, S. Kirolos, M. F. Duarte, T. S. Ragheb, R. G. Baraniuk, and Y. Massoud, "Theory and implementation of an analog-to-information converter using random demodulation," in Proc. IEEE Int. Symp. Circuits Syst., May 2007, pp. 1959–1962.
- [2] M. Mishali and Y. C. Eldar, "Xampling: Compressed sensing of analog signals," Compressed Sensing: Theory and Applications. Y. C. Eldar and G. Kutyniok, Eds. Cambridge University Press, Cambridge, U.K., no. 3, 2012.
- [3] C. Herley and P. W. Wong, "Minimum rate sampling and reconstruction of signals with arbitrary frequency support," IEEE Trans. Inform. Theory, vol. 45, no. 5, pp. 1555–1564, July 1999.
- [4] P. Feng and Y. Bresler, "Spectrum-blind minimum-rate sampling and reconstruction of multiband signals," in Proc. IEEE Int. Conf. ASSP, May 1996, vol. 3, pp. 1688–1691.

Session 1 – Microwave components I

L. Ntibarikure, G. Pelosi, and S. Selleri

Harmonic balance Finite Element analysis of third order intermodulation products in ferrite devices

M. Oldoni, F. Seyfert, and G. Macchiarella

Tuning diplexers with rational filters

G. Virone, R. Tascone, O.A. Peverini, G. Addamo, Z. Farooqui, A. Tibaldi, and R. Orta

Synthesis strategy for broadband multiplexers

C. Tomassoni, S. Bastioli, and R. Sorrentino

TM dual-mode cavity filters with symmetric and asymmetric filtering functions

L. Zappelli

An equivalent circuit for microwave discontinuities

HARMONIC BALANCE FINITE ELEMENT ANALYSIS OF THIRD ORDER INTERMODULATION PRODUCTS IN FERRITE DEVICES

L. Ntibarikure, G. Pelosi, S. Selleri

Department of Electronics and Telecommunications, University of Florence
Via di Santa Marta 3, 50139, Florence, Italy
stefano.selleri@unifi.it

Abstract

Results of a study of nonlinearities and intermodulation products for 3-port H-plane waveguide circulators are presented, based on a harmonic balance finite element analysis of the third-order nonlinearity in ferrites. Numerical results are derived for the field strength and the power level of the intermodulation signal.

Index Terms – Finite elements, harmonic analysis, ferrite, intermodulation, junction circulator, nonlinear interaction.

I. INTRODUCTION

Waveguide devices are widely used in high-power applications thanks to their low-losses. In high-power applications for waveguide devices with ferrite inserts, the motion of the magnetization vector can no longer be described by a linear set of equations. Considering higher-order terms of the permeability, echo signals in the time domain and intermodulation coupling in the frequency domain must be included in the nonlinear theory. In particular third-order nonlinearity in ferrites generate intermodulation noise in the signal bandwidth.

In a frequency domain analysis, conventional single-harmonic (SH) finite elements, does not allow for the computation of signal coupling between an in-band signal and a strong out-of-band interferer. A multiple-harmonics (MH) analysis would be an attractive alternative to time domain analysis.

The theory of harmonic balance finite element (HBFE) method, also known as multiharmonic finite element, is presented for the analysis of a generic H-plane microwave ferrite device. This technique has been successfully employed in magnetostatics problems [2]-[3] but not to high frequency ones. The final goal is to analyze a ferrite device affected by nonlinear behavior.

II. FORMULATION

Consider a waveguide circulator (Fig. 1). Due to the H-plane symmetry of the actual 3D device, a complete solution is attained by solving the associated 2D problem just for the out-of-plane component of the electric field (E_z)

$$\nabla \times [\mu_r]^{-1} \nabla \times (E_z \hat{\mathbf{z}}) + k^2 \epsilon_r (E_z \hat{\mathbf{z}}) = 0 \quad (1)$$

within the domain Ω , subdomain Ω_1 is fully linear while subdomain Ω_2 contains the nonlinear ferrite. Perfect electric conductor boundary conditions holds on Γ_0 while modal expansions are enforced at ports Γ_i , $i=1\dots 3$. k is the free space wavenumber, ε_r is the isotropic permittivity and $[\mu_r]$ has the form

$$[\mu_r] = \begin{bmatrix} \mu_r & -j\kappa_r & 0 \\ j\kappa_r & \mu_r & 0 \\ 0 & 0 & 1 \end{bmatrix}, \quad \begin{cases} \mu_r = 1 + \frac{\omega_0 \omega_m}{\omega_0^2 - \omega^2} \\ \kappa_r = -\frac{\omega \omega_m}{\omega_0^2 - \omega^2} \end{cases}, \quad \omega_0 = \gamma H_0, \quad \omega_m = \gamma M_s, \quad (2)$$

where ω is the angular frequency, γ the gyromagnetic ratio, H_0 the internal DC magnetic field and M_s the saturation magnetization. The conventional finite element formulation for anisotropic media can be retrieved in [4].

The diagonal permeability tensor coefficients can be expressed as

$$[\mu_r(E_z(\mathbf{r}), \mathbf{r}), \kappa_r(E_z(\mathbf{r}), \mathbf{r})] = \begin{cases} [1, 0] & \mathbf{r} \in \Omega_1 \\ [\bar{\mu}_r, \bar{\kappa}_r] + \xi(E_z(\mathbf{r})) & \mathbf{r} \in \Omega_2 \end{cases} \quad (3)$$

where $E_z(\mathbf{r})$ is the electric field in the generic point \mathbf{r} and $\xi(E_z(\mathbf{r}))$ is a quadratic scalar operator describing the nonlinear behavior.

Considering a two-tones problem, the MH behavior is introduced by approximating the electric field as

$$\hat{E}_z = e_1 \cos(\omega_1 t) + e_2 \cos(\omega_2 t) + e_3 \cos((2\omega_1 - \omega_2)t) + e_4 \cos((2\omega_2 - \omega_1)t) + e_5 \cos((2\omega_1 + \omega_2)t) + e_6 \cos((2\omega_2 + \omega_1)t) + e_7 \cos(3\omega_1 t) + e_8 \cos(3\omega_2 t) + \dots \quad (4)$$

where ω_1 is the in-band signal angular frequency and ω_2 is the angular frequency of the edge-band interfeerer, and the hat, here and in the following, denotes approximation deriving from the truncation of the series.

The complex harmonic amplitudes constitute the unknowns of a conventional finite element system, with k in (1) computed with the corresponding harmonic frequency

$$k_1 = \frac{\omega_1}{c_0}, \quad k_2 = \frac{\omega_2}{c_0}, \quad k_3 = \frac{2\omega_2 - \omega_1}{c_0}, \quad k_4 = \frac{2\omega_1 - \omega_2}{c_0}, \dots \quad (5)$$

being c_0 the speed of light in free space.

The harmonics retained in (4) are selected according to the quadratic operator $\xi(\cdot)$, which generates third order intermodulation products, the most critical being $(2\omega_1 - \omega_2)$ and $(2\omega_2 - \omega_1)$. Eight harmonic amplitudes in (4) will be considered.

The nonlinear behavior of the relative permeability tensor coefficients generates coupling between the previous harmonic signals at the frequencies that expand the electric field. The dependence can be explicitated on the magnetic field as:

$$\hat{\mu}_r = \bar{\mu}_r + \xi(E_z) = \bar{\mu}_r + \alpha \left(|\hat{H}_x(E_z)|^2 + |\hat{H}_y(E_z)|^2 \right) \quad (6)$$

which constitutes a wider sum of harmonics than that of the field, α being a constant. Quadratic permeability tensor coefficients leads to the following expression

$$\hat{\mu}_r = \mu_{r_0} + \sum_{m+n>0 \text{ even}} \mu_{r_{m,n}^+} \cos(m\omega_1 t + n\omega_2 t) + \mu_{r_{m,n}^-} \cos(m\omega_1 t - n\omega_2 t) \quad (7)$$

The harmonic amplitude μ_r of the permittivity is computed by testing its time evolving value (7) at the sought frequency

$$\begin{aligned} \mu_{r_0} &= \frac{\omega}{2\pi} \int_0^{2\pi} \bar{\mu}_r + \alpha \left(|\hat{H}_x|^2 + |\hat{H}_y|^2 \right) dt, \\ \mu_{r_{m,n}^\pm} &= \frac{\text{GCD}(m\omega_1, n\omega_2)}{\pi} \int_0^{2\pi} \left(\bar{\mu}_r + \alpha \left(|\hat{H}_x|^2 + |\hat{H}_y|^2 \right) \right) \cos(m\omega_1 t \pm n\omega_2 t) dt, \end{aligned} \quad (8)$$

being GCD the greater common divisor function.

Harmonic testing is then performed, leading to a large scale linear HBFE system which has formally the same structure as a conventional FE system, the nonlinearity being tackled via a Picard iteration.

III. NUMERICAL RESULTS

The device analyzed is sketched in fig. 1, the ferrite parameters are those presented in [5]. For a linear ferrite the devices operates correctly as shown in Fig. 2: Devices is matched at 10GHz and isolation (S31) is better than -15dB. In the case of a nonlinear ferrite, with $\alpha = 2 \times 10^{-7} \text{ m}^2 \text{ A}^{-2}$, analysis is performed with an impinging signal at $\omega_1 \in [2\pi 8 \times 10^9, 2\pi 12 \times 10^9]$ with an impinging power of (a) 0.5W; (b) 0.75W; (c) 1W; and an interferent signal at $\omega_2 = 2\pi 7.8 \times 10^9$ with a corresponding power level of (a) 50W; (b) 75W; (c) 100W. Graph clearly shows the effect of the nonlinearity both in a frequency shift and in the presence of an output power level at the third intermodulation product.

IV. CONCLUSION

A HBFE approach for waveguide devices containing nonlinear ferrites has been presented. The proposed method allows for the prediction, in frequency domain, of the amplitude of the intermodulation products and relative signal degradation.

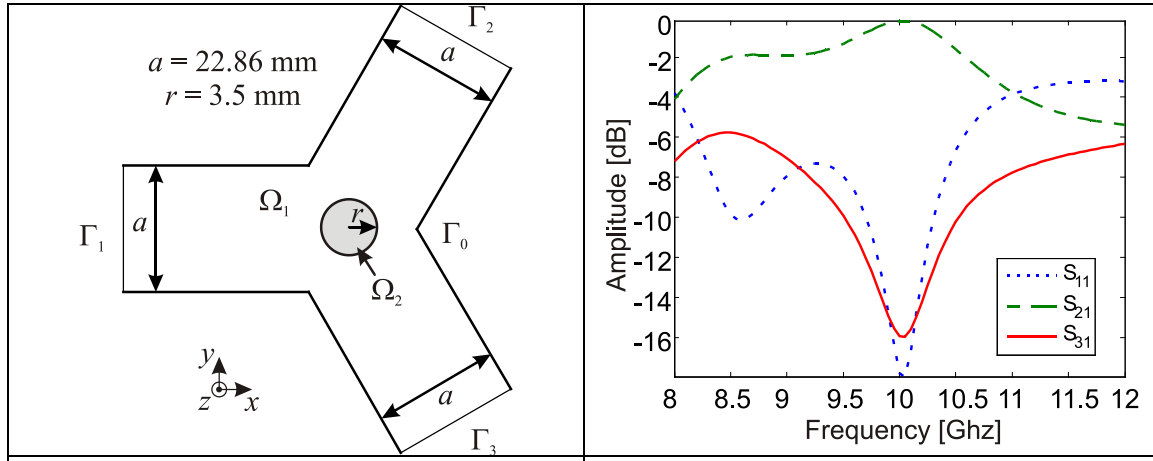


FIG. 1 – Sketch of the analyzed circulator H-plane cross-section. A cylindrical ferrite post of radius r is placed in the middle of the device.

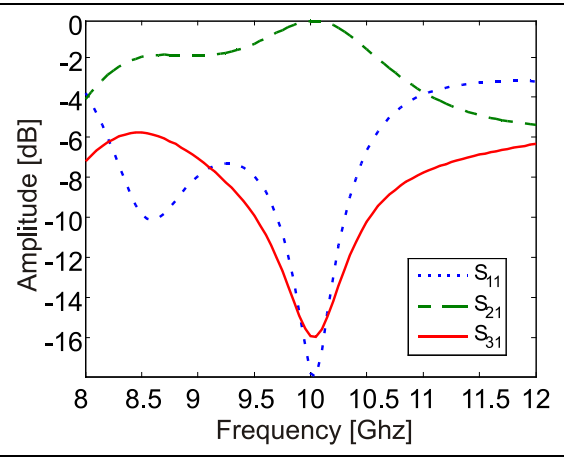


FIG. 2 – Amplitude of the three main scattering parameters for the linear case, for an impinging TE_{10} .

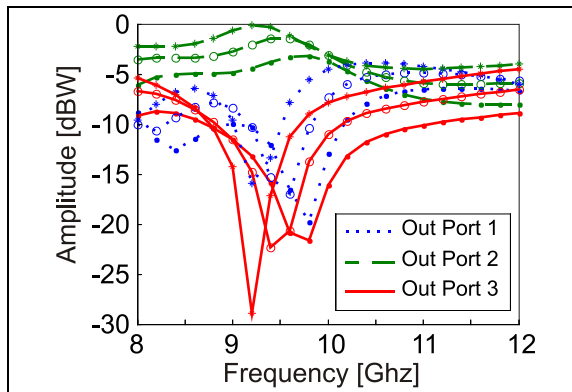


FIG. 3 – Amplitude of the output power at ω_1 nonlinear case. (a) bullets (b) empty circles (c) asterisks.

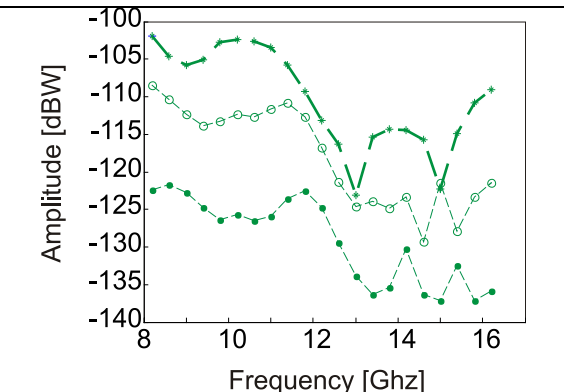


FIG. 4 – Amplitude of the output power at port 2 for the third harmonic $2\omega_1 - \omega_2$ for the nonlinear case. (a) bullets (b) empty circles (c) asterisks.

REFERENCES

[1] B. Razavi, RF Microelectronics, Upper Saddle River NJ: Prentice Hall, 1998, ch. 2, pp.14–25.
 [2] H. De Gerssem, H. Vande Sande, and K. Hameyer, “Strong coupled multi-harmonic finite element simulation package,” *COMPEL*, vol. 20, no. 2, pp. 535–546, 2001.
 [3] S. Yamada, K. Bessho, and J. Lu, “Harmonic balance finite element method applied to nonlinear AC magnetic analysis,” *IEEE Trans. Magn.*, vol. 25, no. 4, pp. 2971–2973, Jul. 1989.
 [4] M. Koshiba, and M. Suzuki, “Finite-Element Analysis of H-plane Waveguide Junction with Arbitrarily Shaped Ferrite Post,” *IEEE Trans. Microw. Theory Tech.*, vol.34, no. 1, Jan. 1986.
 [5] N. Okamoto, “Computer-Aided Design of H-plane Waveguide Junctions with Full-Height Ferrites of Arbitrary Shape,”

TUNING DIPLEXERS WITH RATIONAL FILTERS

M. Oldoni⁽¹⁾⁺, F. Seyfert⁽²⁾, G. Macchiarella⁽¹⁾

⁽¹⁾ Electronics and Information Department, Politecnico di Milano
32, p.zza L. Da Vinci, 20133, Milano, Italy

⁽²⁾ APICS Team, Institute National de Recherche en Informatique
et en Automatique (INRIA), Route des Lucioles,
BP 93 – 06902 Sophia Antipolis Cedex, France

+ oldoni@elet.polimi.it

Abstract

We describe an original technique to extract a polynomial model of the filters composing a diplexer based on the external measurements. This paper reports the theoretical basis and describes additional assumptions under which it can be applied successfully. Numerical examples are also shown to prove its practical behavior.

Index Terms – Deembedding, Rational model, Cauchy, Diplexer tuning

I. INTRODUCTION

Tuning microwave multiplexers is currently one of the bottlenecks in mass production of these devices. Several efforts have been devoted to generalizing techniques available for standard 2-port filters to multiplexers, but the complicated nature of the relationships among port measurements and internal components' currently allows only a few specific situations to be treated analytically. Most of them are based on a rational model of the overall diplexer which therefore must only include rational components ([1]-[4]). Another group of technique is based on extraction by optimization of a circuit model but convergence may not be guaranteed ([5], [6]).

In order to tune a filter there are usually some tuning elements (screws or similar) which may be acted upon to alter resonant frequencies and coupling coefficients. The exact tuning position can be obtained for standard 2-port filters in several ways, most of them based on the extraction of the characteristic polynomials or the coupling matrix. By comparing these with the reference filter, the tuning screws can be adjusted until the perfect alignment is obtained.

In a multiplexer whose measurement are known, de-embedding the filters is much more difficult and to this purpose we introduce an analytical technique designed for diplexers and capable of computing the filters' characteristic polynomials starting from the measurements of the diplexer and of the junction. The reference scheme is shown in Fig. 1 where the junction is modeled as a 3-port component with a generic frequency response, which may also be non-rational and/or lossy. Knowledge of the junction is a realistic assumption in several practical

situations, for example from previous measurements or from a precise circuit model or electromagnetic simulations of the fabricated structure. By converse filters must be tuned on a one-by-one basis due to their strict specifications and higher sensitivity to fabrication tolerances.

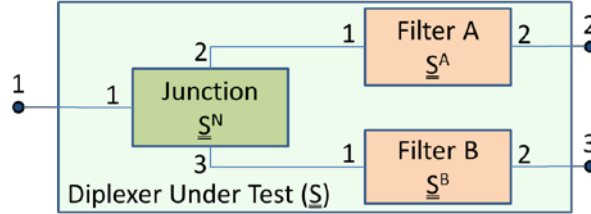


FIG. 1 – Reference model of the diplexer and its internal components.

II. ESTIMATION OF FILTERS POLYNOMIALS

One can easily compute the scattering parameters of the overall diplexer as a function of the junction ones and of the filters'. This leads in the reciprocal case to 6 equalities at each frequency. By assuming the diplexer measurements (S_{ij}) and the junction's parameters (S^N_{ij}) as known at these frequencies we are left with 6 unknowns (the values of the 3 scattering parameters of each filter S^A_{ij} , S^B_{ij}). By substitution it is possible to observe that there are actually only 5 independent equations which thus make the system underdetermined. It is in fact possible to manipulate the 5 equations to obtain the following form:

$$\begin{aligned}
 S_{21}^A &= a^A + b^A S_{11}^A & S_{21}^B &= a^B + b^B S_{11}^B \\
 S_{22}^A &= m^A + n^A S_{11}^A & S_{22}^B &= m^B + n^B S_{11}^B \\
 S_{11} - S_{11}^N &= \frac{S_{11}^A S_{21}^{N^2} + S_{11}^B S_{31}^{N^2} - S_{11}^A S_{11}^B v}{1 - S_{11}^A S_{22}^N - S_{11}^B S_{33}^N + S_{11}^A S_{11}^B z} \\
 v &= S_{21}^{N^2} S_{33}^N - 2S_{21}^N S_{31}^N S_{32}^N + S_{31}^{N^2} S_{22}^N, & z &= S_{22}^N S_{33}^N - S_{32}^{N^2}
 \end{aligned} \tag{1}$$

where expressions of the various coefficients a^X , b^X , m^X , n^X are reported in [7] and only depend on the known measurements.

To resolve the underdetermination we introduce rationality of the two filters, whose scattering parameters are consequently expressed as ratios of polynomials with a common denominator, $S^X_{ij} = N^X_{ij}/D^X$.

By using the four equations of (1) involving only one filter at a time, two homogeneous linear systems can be derived in the unknown polynomials of each and are extended to include measurements at several frequencies ω_k (system for filter A shown):

$$\begin{cases} a^A(\omega_k)D^A(\omega_k) + b^A(\omega_k)N_{11}^A(\omega_k) - N_{21}^A(\omega_k) = 0 \\ m^A(\omega_k)D^A(\omega_k) + n^A(\omega_k)N_{11}^A(\omega_k) - N_{22}^A(\omega_k) = 0 \end{cases} \tag{2}$$

The two systems can be rewritten in matrix form and the characteristic polynomials of each filter are stacked as a vector of coefficients which can be found by computing the SVD of the matrix and by taking the right vector(s) corresponding to null singular value(s).

When such a null singular value is unique then the solution vector is also unique and all the polynomials for that filter are known up to a common irrelevant constant scaling. Moreover, when at least one of the two filters can be determined uniquely in this way, the other can be also retrieved from it by using the common equation in (1).

It can be proven that, unless the junction is a very simple one, the number of different solutions to each of the two systems is one and thus the identification problem can be uniquely solved.

III. APPLICABILITY

Concerning practical applicability of the technique described in Sect. II, the rational assumption of the two filters plays a key role in the identification and therefore requires that distributed effects must be neglectable, implying a narrow frequency span. Note however that, as long as included in the measurements, the junction does not need to fulfill the rational assumption and thus can be practically arbitrary. However, in a practical situation, it is often the case of measurements where reference planes are not exactly coincident with those depicted in Fig. 1, for example when measuring equipment is not exactly calibrated or when such reference planes are not accessible. In these cases the lengths of these transmission lines, if not taken into account, violate the rational assumption and lead to unsatisfactory fitting results. As a consequence the additional unknown delays must be detected and estimated so that they can be included into or removed from the existing measurements. The detection and estimation can be achieved by setting up an optimization scheme which minimizes the misfit with respect to the diplexer measurements.

Another aspect important to outline the practical applicability is what can be done when the solution is not unique. Considering a simple parallel connection of the two filters to the common port, the junction is an ideal node. In this situation the number of different solutions for each filter can be found to be 2 and this describes the fact that one can actually “move” a constant shunt admittance from one filter to the other still fulfilling all the measurements. In this and similar cases the knowledge of the value at infinity of S_{11}^X of at least one of the filters can sufficiently constrain the solution to resolve the uncertainty.

IV. EXAMPLE

We applied the technique outlined in Sect. II to a set of data obtained by simulating a diplexer with a simple junction (an ideal node) and two 5-th order filters with 2 transmission zeros each. We also introduced a 1ns delay on each of the junction measurements and on the overall diplexer measurements to simulate misplaced reference planes and a noise floor of -90dB to model a real measurement setup. Without correcting the additional delays a bad fitting was obtained (Fig. 2, left: -21 dB of rms fitting error) whereas by estimating (within $\pm 10\%$) and correcting them a much better result was achieved (Fig. 2, right) with -

69dB of rms fitting error, where only attenuation levels below -80dB are not exactly fitted due to the effect of noise.

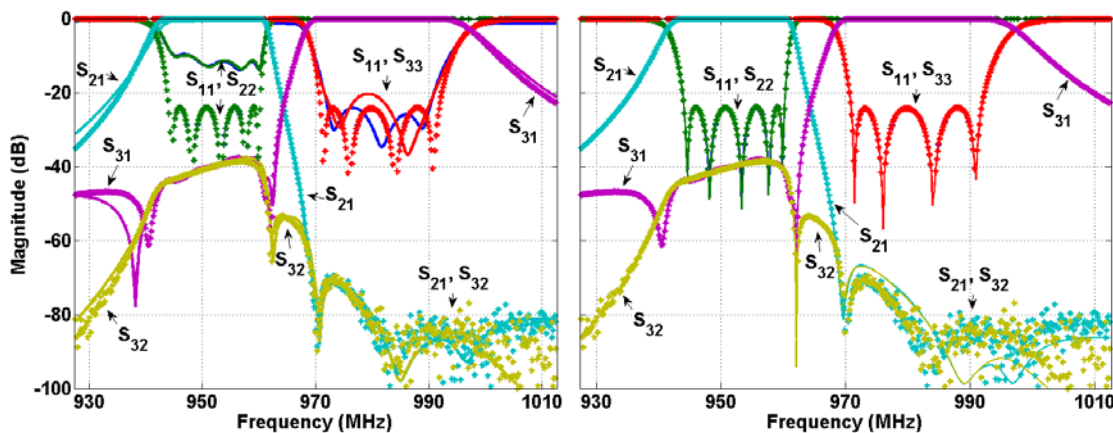


FIG. 2 – Comparison of the measured diplexer (crosses) with the measurements with same junction and fitted filters (solid lines)

V. CONCLUSION

This paper describes a technique suitable for extraction of filters' characteristic polynomials working from the measurements on the diplexer. This allows in-place tuning of these devices and was shown to be effective when additional delays are estimated and removed.

REFERENCES

- [1] D. Traina, G. Macchiarella, and J. Bertelli, "Computer aided tuning of GSM base-station filters – experimental results," in *Proc. IEEE Radio and Wireless Symp*, 2006, pp. 587–590.
- [2] F. Seyfert, L. Baratchart, J.-P. Marmorat, S. Bila, and J. Sombrin, "Extraction of coupling parameters for microwave filters: determination of a stable rational model from scattering data," in *Proc. IEEE MTT-S Int. Microwave Symp. Digest*, vol. 1, 2003, pp. 25–28.
- [3] A. Lamecki, P. Kozakowski, and M. Mrozowski, "Fast extraction of coupling matrix for optimization and CAD tuning problems," in *34th European Microwave Conference*, 2004, vol. 3, oct. 2004, pp. 1385–1388.
- [4] A. Garcia-Lamperez, S. Llorente-Romano, M. Salazar-Palma, and T. Sarkar, "Efficient electromagnetic optimization of microwave filters and multiplexers using rational models," *Microwave Theory and Techniques, IEEE Transactions on*, vol. 52, no. 2, pp. 508–521, Feb. 2004.
- [5] V. Mirafteb and R. R. Mansour, "Fully automated RF/microwave filter tuning by extracting human experience using fuzzy controllers," *IEEE Transactions on Circuits and Systems I*, vol. 55, no. 5, pp. 1357–1367, 2008.
- [6] P. Harscher, R. Vahldieck, and S. Amari, "Automated filter tuning using generalized low-pass prototype networks and gradient-based parameter extraction," *Microwave Theory and Techniques, IEEE Transactions on*, vol. 49, no. 12, pp. 2532–2538, dec 2001.
- [7] M. Oldoni, F. Seyfert, G. Macchiarella, D. Pacaud, "De-embedding of filters' responses from diplexer measurements," in *Proc. IEEE MTT-S Int. Microwave Symp. Digest*, 2011.

SYNTHESIS STRATEGY FOR BROADBAND MULTIPLEXERS

G. Virone⁽¹⁾, R. Tascone⁽¹⁾, O. A. Peverini⁽¹⁾, G. Addamo⁽¹⁾, Z. Farooqui⁽¹⁾,
A. Tibaldi⁽¹⁾, R. Orta⁽¹⁾

⁽¹⁾ Istituto di Elettronica ed Ingegneria dell'Informazione e delle
Telecomunicazioni – Consiglio Nazionale delle Ricerche (IEIIT-CNR) c/o
Politecnico di Torino, C.so Duca degli Abruzzi 24, 10129, Turin, Italy. Email:
riccardo.tascone@polito.it, giuseppe.virone@polito.it

Abstract

This paper presents a design method for wideband multiplexers. It is based on an aggregate discontinuity concept to keep the mutual loading effect of the various filters into account at the synthesis level. This method can provide the geometric parameters of the multiplexer starting from the desired polynomial frequency response.

The performance obtained in the case of a waveguide diplexer with a 1.4% band separation bandwidth is discussed.

Index Terms – Design Method, Filters, Multiplexers, Synthesis Technique

I. INTRODUCTION

Complex microwave multiplexers are required in the future communication systems in order to deal with the increased amount of services. Such filtering structures can be implemented with different technologies e.g. microstrip, stripline and metallic waveguide. As well known, the waveguide implementation is still the most suitable solution when both high power handling capabilities and low losses are required. The circuit scheme of a multiplexer is reported in Fig. 1.

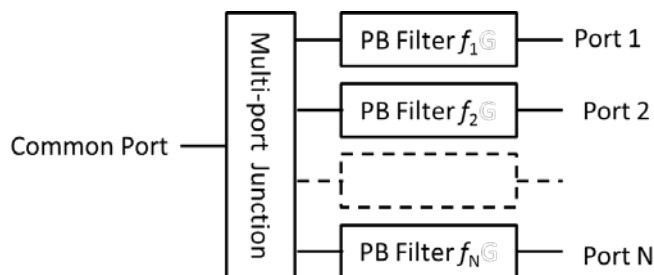


FIG. 1 – Circuit scheme for a multiplexer with passband filters.

The multiplexer is composed of N passband filters. Each one has a different passband with center frequency f_k , with $k = 1, 2, \dots, N$. The N

filters are connected to a multiport junction in order to provide a single common port.

The main electrical requirements are a high transmission coefficient from Common Port to Port k in the passband centered at f_k and a high attenuation to all the other ports. According to this, the Port k should exhibit a low reflection coefficient in the passband centered at f_k . The common port should instead be matched for all the considered passbands.

As reported in the literature, the multiplexer design strategy starts with the synthesis of the N passband filters. Subsequently, a multi-port junction is selected according to the required layout of the multiplexer (e.g. H-plane or E-plane for waveguide implementation). Such a junction with the corresponding connecting sections to the filters is then optimized to meet the above mentioned specifications [1].

Unfortunately, the mutual loading effect of the filters and the multi-port junction produces a degradation of the overall electrical performance. It should be noted that this phenomenon is particularly significant when broadband filters are combined. This performance degradation can be reduced if the geometry of the various filter is adjusted to compensate for the loading effect. Even if optimization algorithms are generally adopted to accomplish this task [2], their application is quite time consuming and can lead to suboptimum solutions owing to both the large number of parameters and the complexity of the goal function.

An alternative technique to compensate for the dispersive mutual loading effect of the various components is presented in section 2. The key point of this technique is the proper combination of the first filter discontinuities with the loaded multi-port junction to obtain a single aggregate discontinuity. Such an aggregate discontinuity is then used in the framework of the synthesis procedure reported in [3]. In other words, the synthesis technique is directly applied to a loaded configuration i.e. filter with the aggregate discontinuity to obtain the final geometrical parameters.

A design example in metallic waveguide is presented in section 3.

II. THE DESIGN STRATEGY

The equivalent circuit of the multiplexer is reported in Fig. 2. All the components are represented by their corresponding scattering matrices: \mathbf{S}^{MJ} represents the multi-port junction, \mathbf{S}^{f_k} represents the k^{th} filter. It should be noted that the filter f_1 has been described by the scattering matrices of all its M discontinuities $\mathbf{S}_i^{f_1}$.

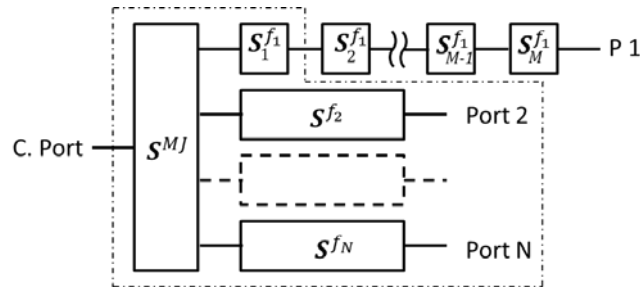


FIG. 2 – Scattering-matrix equivalent circuit for a multiplexer.

As far as the synthesis of the filter f_1 is concerned, it is possible to combine all the scattering matrices inside the dash-dotted contour (i.e. $S_1^{f_1}$, S^{MJ} and S^{f_k} with $k = 2, \dots, N$) into a single two-port scattering matrix. In this way, the loading effect of the multi-port junction and the other filters has been embedded in such an aggregate discontinuity. It should be noted that an analogous strategy can be adopted for the design of the other filters as well.

The aggregate discontinuity is more dispersive with respect to the basic building blocks (e.g. iris or septum for waveguide implementation) of the filter configuration. Nevertheless, it can still be managed in the framework of the linear-system identification technique reported in [3].

At this point, the design of the loaded filter is treated as an in-line filter with M discontinuities. In particular, the extraction technique in [3] is used to compute the scattering parameters of the various discontinuities and the cavity lengths from the desired frequency response in polynomial form. Finally, the geometrical parameters of the discontinuities are determined using a look-up-table.

According to the presented strategy, the design of the k^{th} loaded filter also depends on the other filters. However, the other filters exhibit a stop-band behavior in the k^{th} frequency band (the magnitude of their reflection coefficient approaches one). Therefore, their scattering matrix does not significantly depend on the subsequent design refinements. In conclusion, even if the synthesis technique has to be applied to all the N loaded filters in turn, only few iteration are required to reach the final results.

III. DESIGN RESULTS

A waveguide diplexer has been designed according to the proposed strategy. The adopted discontinuities are septa in rectangular waveguide [4]. A mitered T-junction has been introduced between the two filters to provide the common port. The full-wave analysis of the multiplexer has been performed using a proprietary simulation code [4].

The results obtained are reported in Fig. 3, where the vertical grey lines define the two operative bands. The reflection levels at the

common port S_{CC} are below -21 dB in both frequency bands. The transmission levels S_{1C} and S_{2C} are about -0.4 dB in the corresponding passbands (a silver-plated finish has been assumed). The transmission levels decrease to -50 dB in the adjacent frequency bands. It should be noted that the transition bandwidth is relatively narrow (1.4 %).

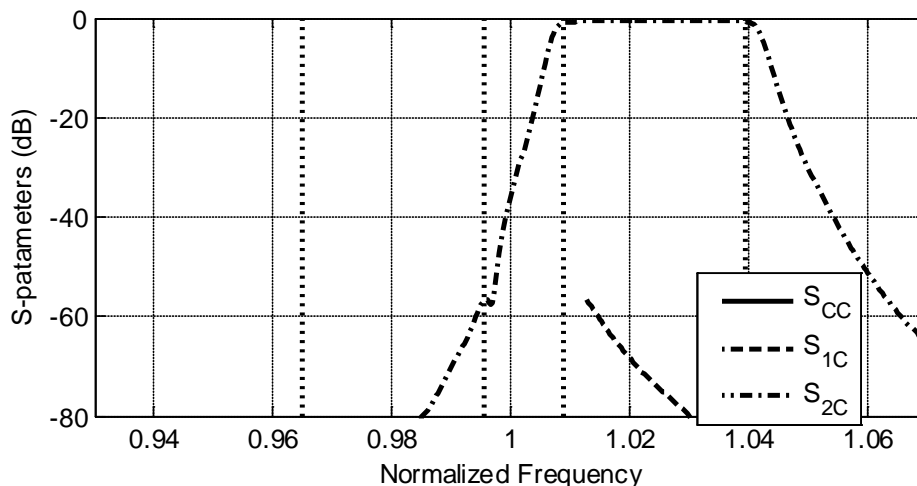


FIG. 3 – Scattering parameters of the designed multiplexer. The two operative frequency bands are highlighted with the vertical grey lines.

IV. CONCLUSION

The aggregate discontinuity concept has been presented for the synthesis of multiplexers. The design approach has been validated by applying it to a real configuration in metallic waveguide, showing good performance.

It should be pointed out that since the mutual loading effect is kept into account at the design stage, a reasonable mismatching of the multi-port junction can be tolerated. Thanks to this, simpler geometries (with less matching elements) can be adopted to reduce the manufacturing complexity of the overall multiplexer.

REFERENCES

- [1] R. Vahldieck, B. Varailhon de la Filolie, "Computed Aided Design of Parallel-connected Millimeter-wave Diplexers/Multiplexers", IEEE MTT-S Digest 1988, pp. 435-438.
- [2] J. Dittloff, F. Arndt, "Rigorous Field Theory of Millimeter-Wave E-plane Integrated Circuit Multiplexers", IEEE T-MTT Vol. 37, n. 2, Feb 1989, pp. 340-350.
- [3] R. Tascone, P. Savi, D. Trincherro, and R. Orta, "Scattering matrix approach for the design of microwave filters," IEEE T-MTT., vol. 48, no. 3, Mar. 2000 pp. 423-430.
- [4] O. A. Peverini, R. Tascone, M. Baralis, G. Virone, D. Trincherro and R. Orta, "Reduced-Order Optimized Mode Matching CAD of Microwave Waveguide Components", on IEEE Transactions on Microwave Theory and Techniques, Vol. 52, Issue 1, Jan. 2004, pp. 311-318.

TM DUAL-MODE CAVITY FILTERS WITH SYMMETRIC AND ASYMMETRIC FILTERING FUNCTIONS

C. Tomassoni⁽¹⁾, S. Bastioli⁽²⁾, R. Sorrentino⁽¹⁾

⁽¹⁾D.I.E.I, Univ. di Perugia, ⁽²⁾RS Microwave Co Inc., Butler, NJ, US
Tomassoni@diei.unipg.it

Abstract

In this paper we present TM dual-mode cavity filters exploiting nonresonating modes. The proper use of nonresonating modes allows filtering functions having a number of transmission zeros up to the number of poles. The design of such filters is very flexible in terms of number and position of transmission zeros, and both symmetric and asymmetric filtering functions can be obtained. Furthermore, with a moderate reduction of the Q-factor we can design TM filters extremely compact with respect to classical TE dual-mode filters.

I. INTRODUCTION

The tremendous growth of communication market requires filters with improved performances. Waveguide filters have excellent performances from the point of view of the loss, but they have the drawback to be heavy and bulky, and this represents a problem especially for satellite applications. In order to mitigate this problem, dual-mode filters have been introduced [1]-[2]. Several dual-mode waveguide filters have then been proposed in the literature.

Recently, in [3]-[4] the use of TM dual-mode cavities exploiting nonresonating modes have been introduced. Non resonating modes [5] are modes that resonate far away from the filter passband and are exploited to create an additional path for the EM energy bypassing the resonant modes. This allows the insertion of transmission zeros in the filtering function. As shown in [3]-[4], the use of the TM dual-mode cavity (instead of the classical TE dual-mode cavity) allows a dramatic reduction of the filter dimension with a moderate reduction of the Q-factor, while the proper use of non resonating modes allows a number of transmission zeros equal to the number of poles.

In this paper we explain the basic theory of the TM dual-mode filters and we show some results.

II. THEORY

In the TM dual-mode cavity of Fig.1, we exploit the TM_{120} and TM_{210} as resonant modes and the TE_{10} , TE_{01} and TM_{11} as nonresonating modes. The cavity realizes the transversal topology of Fig.1c. This topology allows both symmetric and asymmetric filtering functions with or

without transmission zeros (up to two zeros). Furthermore each transmission zero can be independently positioned.

Such a topology requires that the two resonators resonate at different frequencies (f_{120} and f_{210}). This can be obtained by properly selecting the transverse dimensions w and h of the cavity. In fact, the resonant frequencies are independent of the cavity length (the third index of the resonant modes is zero) and this allows the cavity to be very short and compact. The cavity length can be chosen so as to obtain a tradeoff between cavity dimension and Q-factor (the shorter the length the lower the Q). At the passband, the nonresonating mode propagates through the cavity carrying some energy from input to output that bypasses the resonant modes. This allows one to realize the source-to-load coupling M_{SL} of the topology. In any case, the topology parameters M_{S1} , M_{S2} and M_{SL} can be realized by properly selecting the cavity parameters [4] illustrated in Fig.1b: the major size of the iris (a_s), the iris rotation θ and the position of the iris centre along the cavity diagonals (p_s).

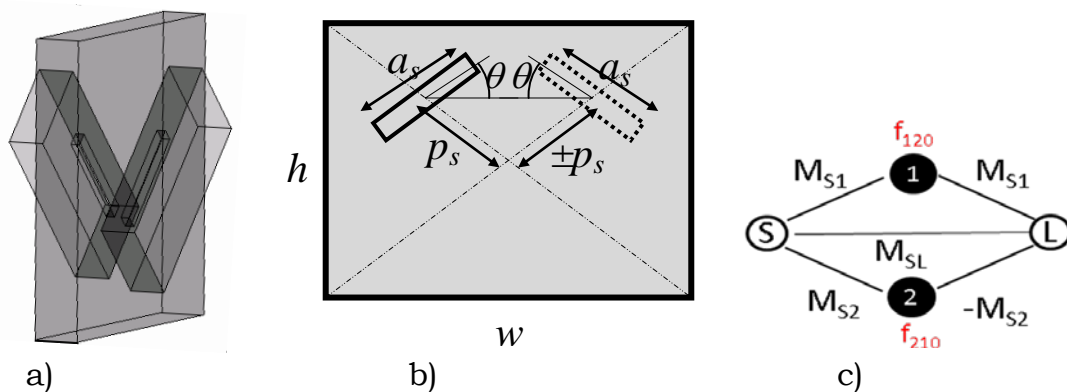


FIG. 1 – TM dual-mode cavity: (a) perspective view, (b) front view, (c) relevant topology.

In Fig.2 some examples showing the flexibility in the transmission zero positioning for the dual-mode cavity filtering functions are illustrated. The cases of one zero in the upper and the other in the lower stop-band are shown in Fig.2a and Fig.2b for symmetric and asymmetric filtering functions, respectively. The possibility to change the position of one zero leaving the other in the same position is shown in Fig.2c and Fig.2d in the case of both zeros in upper or lower stop-band, respectively.

Higher order filters can be obtained by cascading two or more cavities. In order to realize N^{th} order filters with N transmission zeros, the different cavities must be properly cascaded so as to guarantee that all the transmission zeros generated by each cavity will still appear in the overall filter response. This can be obtained under certain conditions, as detailed in [3]-[4]

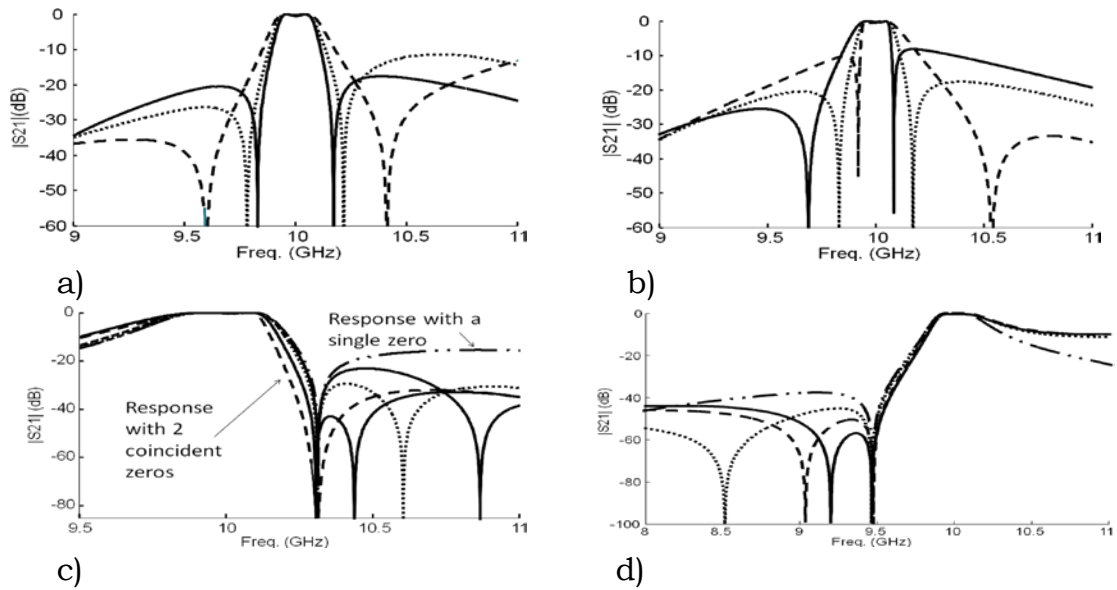


FIG. 2 – Filtering functions of dual-mode TM cavities.

III. RESULTS

In order to demonstrate the high flexibility of the presented approach, some four and six poles filters have been designed. Taking advantage of the simple geometry of such filters, the design is made by using the mode-matching that allows fast and accurate simulations.

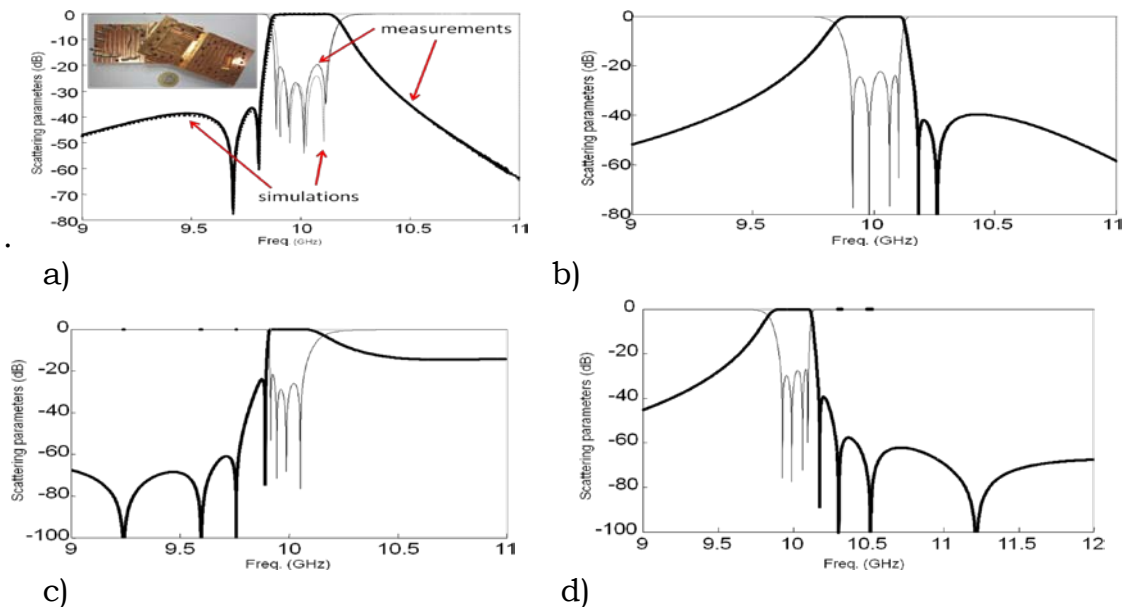


FIG. 3 – Fourth order filters having two (a-b) or four (c-d) transmission zeros. The filter in (a) has been manufactured and measured.

In Fig 3 the response of some fourth order filters are shown. In order to demonstrate the accuracy of the method, the filter of Fig.3a has been

manufactured and measured and the comparison with the simulation has been plotted, showing an excellent agreement.

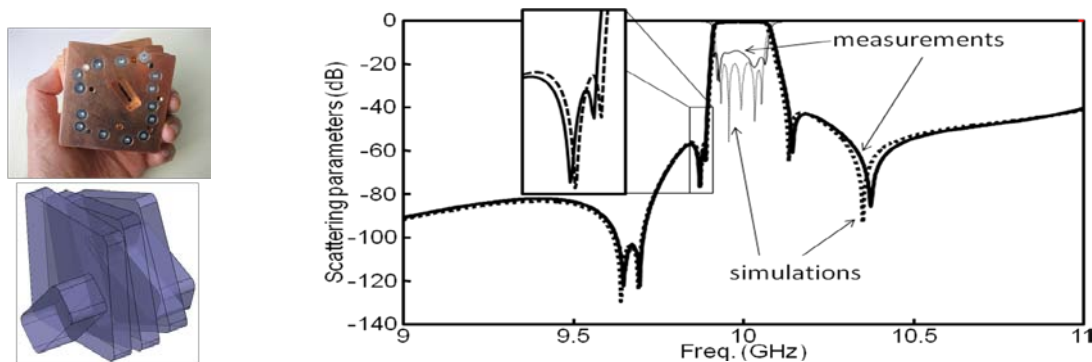


FIG. 4 – TM dual-mode cavity filter of sixth order having six transmission zeros. Comparison between simulations and measurements.

Finally, in Fig.4 the comparison between simulations and measurements for a six poles copper filter having four zeros in the lower stop-band and two zeros in the upper stop-band is shown. The filter is very compact (length: 19mm) and its unloaded Q-factor is about 5500.

IV. CONCLUSIONS

In this paper, filters obtained by cascading TM dual-mode cavities have been presented. The high flexibility in the transmission zero positioning has been demonstrated through several examples. A four pole filter and a six pole filter having zeros asymmetrically placed in lower and/or upper stop-band have been manufactured and measured showing the feasibility of the approach.

REFERENCES

- [1] A. E. Williams, "A four-cavity elliptic waveguide filter," *IEEE Trans. Microwave Theory Tech.*, (1970 Symposium Issue), vol. MTT-18, pp. 1109-1114, Dec. 1970.
- [2] A. E. Atia and A. E. Williams, "New Types of Waveguide Bandpass Filters for Satellite Transponders," *COMSAT Technical Review*, Vol. 1, No. 1, Fall 1971.
- [3] S. Bastioli, C. Tomassoni, R. Sorrentino, "A new class of waveguide dual-mode filters using TM and nonresonating modes," *IEEE Trans. Microwave Theory Tech.*, vol. 58, no. 12, pp. 3909-3917, Dec. 2010.
- [4] C. Tomassoni, S. Bastioli, R. Sorrentino, "Generalized TM Dual-Mode Cavity Filters" *IEEE Trans. Microwave Theory Tech.*, vol. 59, no. 12, pp. 3338-3346, Dec. 2011
- [5] S. Bastioli, "Multimode waveguide filters using nonresonating modes," *IEEE Microwave Magazine*, vol. 12, Issue 6, pp. 77-86, Oct. 2011.

AN EQUIVALENT CIRCUIT FOR MICROWAVE DISCONTINUITIES

L. Zappelli

Dipartimento di Ingegneria dell'Informazione,
 Università Politecnica delle Marche, Via Brecce Bianche, 60131 Ancona
l.zappelli@univpm.it

Abstract

An equivalent circuit for discontinuities exciting evanescent accessible modes is proposed. The key feature of this equivalent circuit is its capability for simplification if a port relative to an accessible evanescent mode is matched, or connected to a very long line. Circuit drawing is simple and fast and is based on a regular polygon with as many susceptances as the sides and the diagonals. Each side is connected with a line of electrical length θ_k to the terminal ports and, if the port refers to an evanescent accessible mode, a series reactance is added. This reactance is the key to the evanescent part of the circuit because it is able to cancel the effect of the evanescent mode if the port is matched or connected to a very long evanescent line, reducing the complexity of the circuit by one degree.

Index Terms – S-matrix theory, equivalent circuits, evanescent modes, generalized scattering matrix.

I. INTRODUCTION

The actual devices very often require a compact design, with the smallest overall dimensions, which is a cogent requirement for satellite equipment. Hence, the discontinuities in the devices are arranged so closely that the interactions between higher order evanescent, but accessible, modes must be taken into account. Moreover, the introduction of the accessible modes in electromagnetic representation increases the number of the modal ports required to describe the interactions. Hence, the “classic” approach based on equivalent circuits seems to be no longer effective because (a) the equivalent circuits do not contain the effects of the accessible evanescent modes and (b), even if any circuit describing these effects is defined, the number of ports needed to describe all the effects would produce a very complex topology of the equivalent circuits, which does not help the optimization process. For example, the presence of one evanescent accessible mode at the output section of a generic discontinuity would produce a three-port equivalent circuit (one input port and one output port for the input/output propagating modes plus the output port relative to the accessible evanescent mode), like the one reported in Fig. 1 [1], with a topology which is difficult to manage in an optimization process. To overcome this problem, in this paper we propose a general equivalent circuit made up of susceptances and electrical lines, which takes into account propagating and evanescent modes in a topologically simple

network. Moreover, under the hypothesis that the scattering matrix of the discontinuity has been evaluated with a commercial or self-developed software, some approximating functions for the electrical parameters of the circuit can be proposed which can be used to integrate the equations in [1,2] and to implement simple and fast software to perform optimization with very little runtime effort [3].

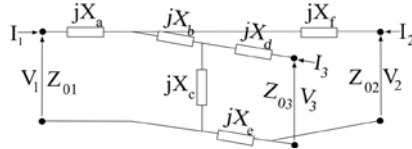


Fig. 1: The equivalent circuit of a generic three-port device as in [1].

II. THEORY

Our goal is to model an equivalent circuit that contains a “natural” representation of the evanescent modes. By “natural” representation of the evanescent mode, we mean an equivalent circuit where the effect of the evanescent mode disappears when its port is connected to its modal impedance. To that end, we propose the equivalent network shown in Fig. 2a, which replaces the circuit shown in Fig. 1, where the six independent parameters are the three susceptances $b_{12}^3, b_{23}^3, b_{13}^3$ and the three electrical lengths of the lines $\theta_1, \theta_2, \theta_3$. b_{ij}^n is the susceptance between nodes i and j and the apex represents the number of the ports (modes) in the circuit.

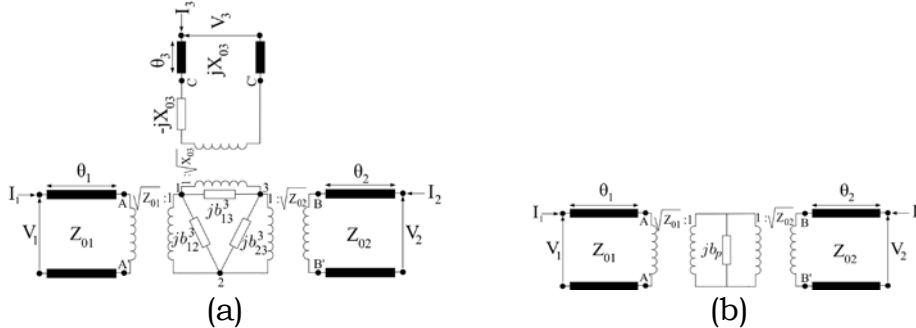


Fig. 2: (a) The equivalent circuit of a generic three-port device proposed in this paper. Ports 1 and 2 refer to propagating modes, while port 3 to the evanescent accessible mode. (b) The equivalent circuit of Fig. (a) if port 3 is matched to $Z_{03} = jX_{03}$ with $b_p = b_{23}^3 + b_{13}^3$.

The electrical lengths θ_1, θ_2 refer to propagating lines while θ_3 refers to an evanescent line. The transformers are introduced to normalize the susceptances contained in the kernel of the circuit (hereafter, quantities written in lowercase are dimensionless while those in uppercase are expressed in the proper dimension). The presence of the series reactance $-jX_{03}$, the conjugate of the modal impedance of the evanescent accessible mode, in front of the evanescent line of length θ_3 , should be noted since this is the key feature of the equivalent circuit. In fact, let us suppose that a very long transmission line relative to the

evanescent mode is connected to port 3 (or suppose the port is matched to its modal impedance): the equivalent load at the port is only the modal impedance $Z_{03} = jX_{03}$ and the input impedance seen at terminal C-C' is again jX_{03} . Due to the presence of the series reactance $-jX_{03}$, the equivalent load seen at terminal 1-3 is a short circuit that cancels the presence of the evanescent mode 3, reducing the whole equivalent network to the one shown in Fig. 2b, which contains electrical quantities relative only to the propagating modes 1 and 2, with $b_p = b_{23}^3 + b_{13}^3$. Apart from the transformers, the equivalent network shown in Fig. 2b is very similar to those used in microwave theory to represent a two-port network, for example an inverter. It should be noted that the electrical lengths θ_1, θ_2 do not change by reducing the circuit in Fig. 2a to that in Fig. 2b and that the value of $b_p = b_{23}^3 + b_{13}^3$ is perfectly known from b_{23}^3, b_{13}^3 . The equivalent circuit can be similarly defined to also take into account the presence of another evanescent accessible mode. The proposed equivalent circuit is represented in Fig. 3a and it has been drawn starting from the equivalent circuit proposed in [2].

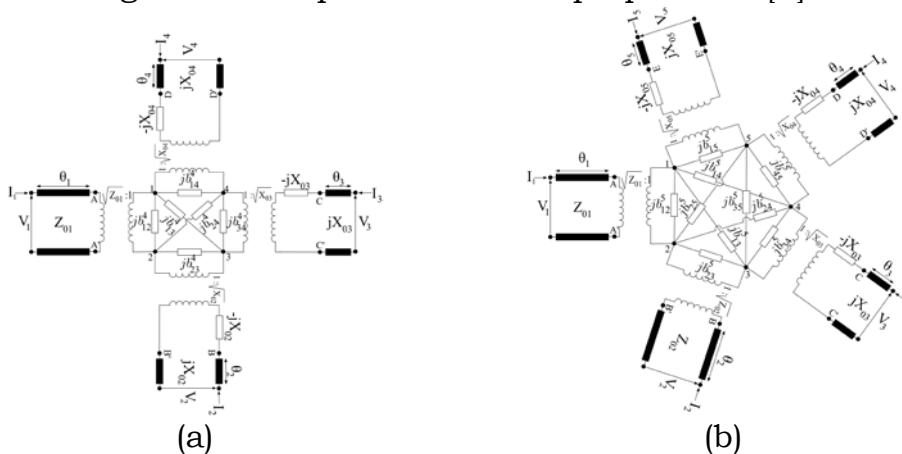


Fig. 3: The equivalent circuit of a generic four-port (a) and five-port (b) device. Ports 1 and 2 refer to propagating modes, while ports 3, 4 and 5 to evanescent accessible modes

It has been obtained by adding port 4, with modal impedance jX_{04} and electrical length θ_4 , with a series reactance $-jX_{04}$ and a shunt susceptance, relative to the evanescent mode, to the circuit relative to the three modes model. Moreover, two other susceptances across the diagonals of the square have been added. The susceptances contained in the circuit shown in Fig. 3a (four-mode model) can differ from those relative to the three-mode model shown in Fig. 2a, and this is emphasized by the apex of the susceptances, which refers to the number of the ports (modes) of the circuit.

The equivalent circuit relative to a four-port discontinuity can be extended to any number of ports relative to propagating or evanescent modes. The circuit is based on a regular polygon with the number of sides, n , equal to the number of the ports (modes). Each side has a

susceptance. Moreover, there are as many other susceptances as there are diagonals of the polygon. The $-jX_{ok}$ series reactances are added to the ports relative to the evanescent modes. Finally, n lines with proper electrical length θ_k are connected to the n sides. The case of the equivalent circuit with 5 ports (one input propagating mode, one output propagating mode and three output evanescent accessible modes) is shown in Fig. 3b. The ease in drawing this type of circuit should be noted. The electrical lengths $\theta_1, \theta_2, \theta_3, \theta_4$ do not change.

Once the equivalent circuit has been defined and its scattering matrix has been derived, we can use them to speed up the optimization process of a complex structure, like a passband filter or a diplexer. In fact, the optimization process starts from the knowledge of a prototype. Then, with the help of a commercial or self-developed electromagnetic analysis software, the dimensions of the irises, or posts, or screws, or any other discontinuity in the waveguide, are optimized in order to satisfy the requested performance. This process usually requires a considerable runtime because the interactions between the discontinuities must be analyzed, and they become stronger as the discontinuities grow closer. Hence, it is fundamental to take into account the presence of evanescent interacting modes to correctly optimize the device. The proposed equivalent circuit can help in this process. In fact, having fixed the dimension of the waveguide and the kind of discontinuities (posts, irises,...), we can evaluate the susceptances b_{ij}^n and the electrical lengths θ_k from our knowledge of the numerical value of the scattering matrix, obtained with a commercial or self-developed software for various values of the post or iris dimensions. Finally, we can extract some approximating functions for b_{ij}^n and θ_k , depending on the frequency and the dimensions, which integrate the formulae reported in [1,2], and we can use them to speed up the optimization process, as discussed in [3].

III. CONCLUSION

In this paper, an equivalent circuit for discontinuities exciting evanescent accessible modes has been proposed. The electrical susceptances and electrical lengths involved in the circuit can be approximated with simple series functions which make the analysis and the optimization of waveguide filters made with irises or posts cascades very easy and fast.

REFERENCES

- [1] Marcuvitz, N., "Waveguide handbook", Mc-Graw-Hill, 1951.
- [2] Montgomery, C. G. and Dicke, Robert H. and Purcell, Edward M., "Principles of microwave circuits", McGraw-Hill, 1948, I Ed.
- [3] L. Zappelli, "An equivalent circuit for discontinuities exciting evanescent accessible modes", *IEEE Transactions on Microwave Theory and Techniques*, V. 60, N.5, May 2012, pp.1197-1209.

Session 2 – Bioengineering I

A. Candiani, M. Sozzi, A. Cucinotta, R. Veneziano, R. Corradini, R. Marchelli, P. Childs, S. Pissadakis, and S. Selleri

DNA biosensor based on a double tilted fiber Bragg grating

E. Pievanelli, A. Plesca, R. Stefanelli, and D. Trincherò

Wearable self-powered wireless units for ultraviolet radiation dosimetry

M. Cavagnaro, F. Frezza, R. Laurita, M. Tannino, L. Manganaro, M. Marini, P. Sollazzo, A. Stagnitti, V. Lopresto, and R. Pinto

From magnetic resonance imaging to water content evaluation of a human tissue

B. Bisceglia, and V. Ivone

Health effects from cell phone radiations: the verdict of the court of appeal of Brescia

D. A. M. Iero

Optimal focusing of vectorial fields subject to arbitrary upper bounds

R. Iovine, L. La Spada, F. Bilotti, and L. Vegni

Gold nano-particles as a platform for biosensing

DNA BIOSENSOR BASED ON A DOUBLE TILTED FIBER BRAGG GRATING

A. Candiani⁽¹⁾, M. Sozzi⁽¹⁾, A. Cucinotta⁽¹⁾, R. Veneziano⁽²⁾, R. Corradini⁽²⁾,
R. Marchelli⁽²⁾, P. Childs⁽³⁾, S. Pissadakis⁽³⁾, S. Selleri⁽¹⁾

⁽¹⁾ Department of Information Engineering, University of Parma,
Parma 43100, Italy

⁽²⁾ Department of Organic and Industrial Chemistry, University of
Parma, Parma 43100, Italy

⁽³⁾ Foundation for Research and Technology-Hellas (FORTH), Institute
of Electronic Structure and Laser (IESL), Heraklion 70013, Greece
stefano.selleri@unipr.it

Abstract

A label-free DNA biosensor based on a double tilted fiber Bragg grating is presented. The outcladding of the fiber has been functionalized using peptide nucleic acid (PNA) probes able to recognize specific DNA strands. When the DNA binds to the PNA a refractive index change occurs at the cladding interface and the fringe visibility of the Fabry-Perot core-cladding closed loop cavity formed by the double tilted grating changes accordingly. The biosensor detects up to 10nM DNA solution, inducing a 10% modulation of the corresponding fringes visibility. The re-use of the fiber for multiple measurements and the selectivity of the sensor have been also demonstrated.

Index Terms – Biosensors, DNA detection, optical fiber sensors, tilted fiber Bragg gratings.

I. INTRODUCTION

A biosensor is an analytical device that couples an immobilized bio-specific recognition element to the surface of a transducer, which converts a molecular recognition event into a measurable signal. Different principles for detecting a biological molecule have been reported [1], including electrochemical, mechanical, optical and calorimetric measurements. Among the optical-based systems fiber optic biosensors offer the main advantage to have a small, flexible shape able to be placed in small vessels and in tissues, connecting a remote light source to a small in situ sensing element. There are two main detection protocols implemented in biosensor technology: fluorescence-based detection, where the analytes are labeled with fluorescent tags such as dyes [2], and label-free detection, where the target molecules are detected by attachment on a suitably functionalized substrate, inducing surface localized refractive index changes, optical absorption loss or scattering [3].

In the present work an optical fiber DNA label-free biosensor, utilizing a Double Tilted Fiber Bragg Grating (DTFBG) as a detector element, is reported. A specific functionalization of the external surface of the fiber has been performed. Significant spectral modulations in the visibility of

the fringes have been measured after harmonic analysis and repeatability has been proved by making several tests.

II. EXPERIMENTAL SET-UP AND RESULTS

The DTFBG structure is reported in Fig. 1. It consists of two identical blazed fiber gratings separated by a distance d , creating two interferences. At the Bragg wavelength the signal is reflected into the core, creating Fabry-Perot interference. At lower wavelengths the light is reflected from the core mode to the cladding modes then back into the original core mode, generating a ring cavity resonance.

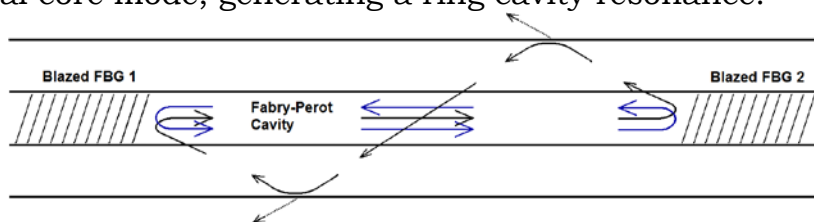


FIG. 1. DTFBG structure, showing the Fabry-Perot resonance at the Bragg wavelength (blue line), and the ring cavity resonance (black line).

Refractive index change measurements of the medium surrounding the fiber can be performed by using the resonant cavity structure [4], where the level of interference between the two tilted gratings will change according to how much light is lost from the counter-propagating cladding modes. Following a protocol already successfully used in our previous works [3], the sensitive region between the two tilted gratings has been functionalized using PNA molecules, which are well known to bind in a very effective way and have a high specificity to complementary DNA strands [5]. After the functionalization, the fiber was fixed into a sealed Teflon tubing system, together with another DTFBG fiber not functionalized to be used as a reference.

TABLE 1. PNA AND DNA SEQUENCES USED IN THE EXPERIMENT.

Oligo	Sequence	Role
PNA	5'-CTTATCCGGTGCC-3'	Probe
DNA	5'-CTGAAAAAGAAGCTAAAGCAGAGGCACCGGATAAG-3'	Target
DNA	5'-CTGAAAAAGAAGCTAAAGCAGAGGCACCAAGATAAG-3'	Mismatch

The DNA used for the experiments were commercially available oligonucleotides provided by Thermo Fisher Scientific. The sequences of PNA and DNA used are reported in Table 1. Measurement using mismatched DNA strands, containing a single nucleotide polymorphism (SNP), have been also made to prove that this device is able to recognize a DNA sequence with just one SNP. The visibility changes were analyzed using the Visibility parameter, which is the ratio between the average alternating component, caused by the ring cavity interference, and the average slowly-varying component, that describes essentially the DC

component of the spectrum. The Fourier transform of the transmission spectrum and the calculation of the visibility have been performed by a specifically designed software.

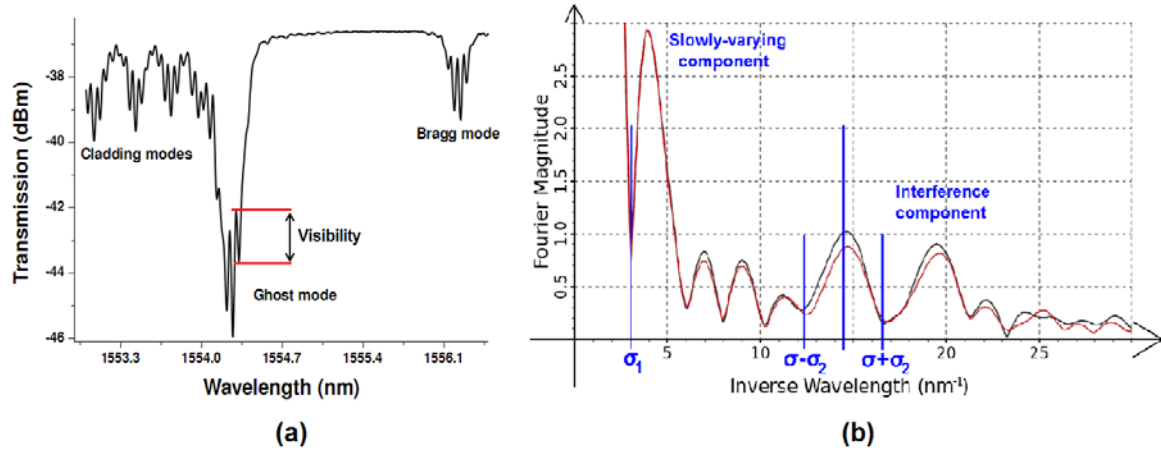


FIG. 2 (a) Transmission spectrum of the DTFBG, showing the visibility of one interference fringe of the ghost mode. (b) Details of the transmission spectra in the inverse wavelength domain for the initial (black line) and final (red line) spectra of the experiment done with a 10nM DNA solution.

In Fig. 2(b) the Fourier transform for two spectra recorded before and after the hybridization process is shown. At first a hybridization with a 10 nM DNA in Phosphate Buffer Saline (PBS) solution has been carried on. Measurements show a clear decrease of the visibility for the functionalized fiber in the first 50 min, while the non functionalized fiber shows no significant variation of the fringes visibility (Fig. 3(a)).

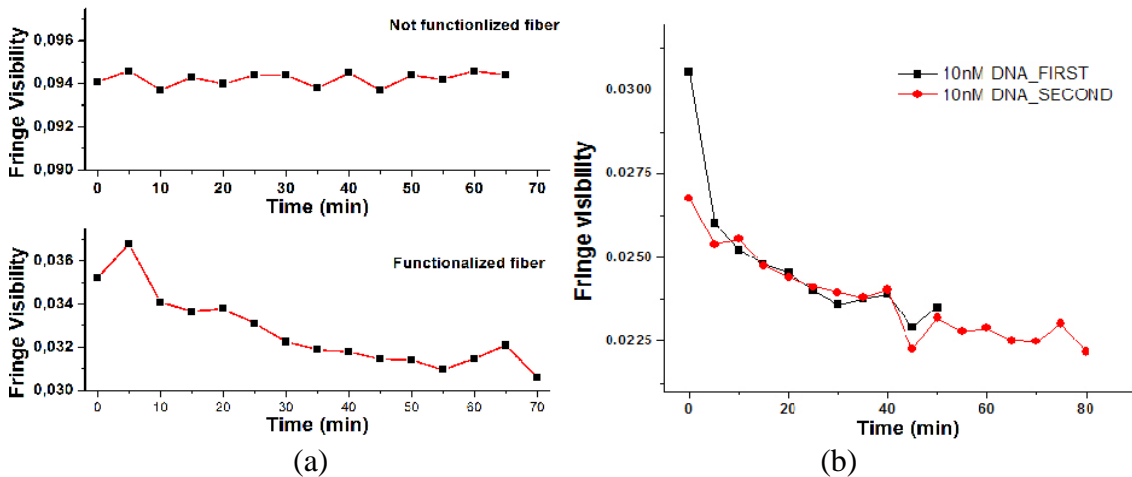


FIG. 3 (a) Visibility change obtained after a 10 nM DNA solution hybridization. (b) The fiber has been re-hybridized twice after being washed.

The change observed for the functionalized fiber must be attributed to the refractive index change due to the DNA-PNA binding. After washing the fiber for 24 h, other measurements with 10 nM DNA solution were carried on, to verify the reproducibility of a single measurement. The experimental data suggests that the specific effect of the DNA on the

fiber can still be visible for several hybridization steps, as reported in Fig. 3(b). Hybridizations with mis-matched DNA, which had just one base difference, were performed as well.

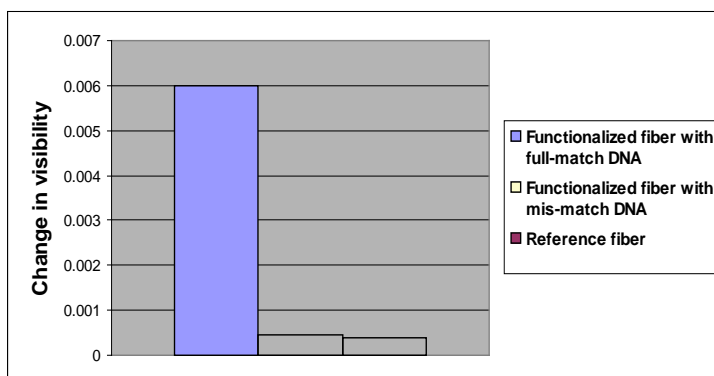


FIG. 4 The graph shows the average change in visibility for the functionalized fiber with full-match DNA, with mis-match DNA, and the reference fiber.

Two different tests done on the same fiber showed that the change in visibility for this additional test was of the same extent of the reference fiber, as shown in Fig. 4, proving the high sensor selectivity.

III. CONCLUSION

The present work shows for the first time the application of DTFBG fibers for the direct label-free DNA detection. The system was shown to give a specific response only when the fiber was functionalized, with good sensitivity and selectivity for a solution with a very low concentration of 10 nM. This approach can be extended to other recognition elements and can eventually be used in extremely narrow contexts where large and less flexible platforms cannot easily operate.

REFERENCES

- [1] L. A. Terry, S. F. White, and L. J. Tigwell, "The Application of Biosensors to Fresh Produce and the Wider Food Industry", *J. Agric. Food Chem.*, Vol. 53 Issue 5, pp. 1309–1316 (2005)
- [2] Y. Ruan, E. P. Schartner, H. Ebendorff-Heidepriem, P. Hoffmann, and T. M. Monro, "Detection of quantum-dot labelled proteins using soft glass microstructured optical fibers", *Optics Express*, Vol. 15, Iss.ue 26, pp. 17819-17826 (2007)
- [3] M. Sozzi, A. Cucinotta, R. Corradini, R. Marchelli, M. Konstantaki, S. Pissadakis, and S. Selleri, "Modification of a long period grating-based fiber optic for DNA biosensing", *SPIE Proceedings Vol. 7894, Optical Fibers, Sensors, and Devices for Biomedical Diagnostics and Treatment XI*, Israel Gannot, Editors, 78940J (2011).
- [4] P. Childs, A. C. L. Wong, I. Leung, G.-D. Peng, and Y. B. Liao, "An in-line in-fibre ring cavity sensor for localized multi-parameter sensing," *Meas. Sci. Technol.* 19(6), 065302 (2008).
- [5] P. E. Nielsen, "Peptide Nucleic Acids: Protocols and Applications", Copenhagen, Denmark: Horizon Bioscience, 2004.

WEARABLE SELF-POWERED WIRELESS UNITS FOR ULTRAVIOLET RADIATION DOSIMETRY

E. Pievanelli, A. Plesca, R. Stefanelli, D. Trincherò

iXem Labs – Politecnico di Torino
Department of Electronics and Telecommunications
Corso Duca degli Abruzzi, 24, 10129 Turin, Italy
info@ixem.polito.it

Abstract

The protection of workers and individuals exposed to physical phenomena impacting on health, represents a challenge for the next future. An ideal solution is represented by the use of non-invasive, low cost, wearable and washable devices, able to detect continuously personal exposure and activate alarms in case of hazardous events. The devices are miniaturized in dimensions and weight and provided with a radio interface, forming a set of wearable mobile nodes in a wireless network. Furthermore, the node embeds energy harvesting techniques for self-powering. The wireless device can connect to a standard wireless networks (Bluetooth, ZigBee), as well as to Ad-Hoc ones, by means a dedicated skin antennas. As an example, the methodology is applied to assess UltraViolet (UV) exposure to prevent diseases due to under- or over- exposition to UV rays. The preliminary studies confirm the feasibility of the project.

Index Terms – Micro antennas, dosimetry, electromagnetic exposure.

I. INTRODUCTION

In the last years, the monitoring of physical phenomena has been growing thanks to the use of small devices. It is possible to identify two main categories in such a field, depending on the type of devices used: fixed or mobile ones. Usually, the first ones are used to monitor the quality of the environment in fixed positions, they are installed in strategic places in order to cover a large area. They find application in monitoring the quality of air, moisture of the terrain, earth movements, rivers or volcanoes activity. On the other hand, the mobile devices are installed on moveable machines, objects or humans. In the last case, they can be used to monitor their vital signs or the quality of the environment that surrounds them: the so-called personal dosimeters.

In this paper a preliminary design of a small, low cost, wearable, washable and auto-rechargeable sensing unit is presented. Since it is wearable and very small, it is also not invasive so the subject can wear it even in critical conditions when also the esthetical aspect is important.

The system is composed by the sensor node and the wireless network that interconnects all devices. A centralized gateway collects all the data that can be analyzed automatically or by technicians.

II. SENSOR ARCHITECTURE

The main components of the sensor are: the sensing unit, the power supply and the radio interface.

The sensing unit is the responsible of the detection of the external phenomenon translating it into a voltage or current signal. As an applicative example, the UV sensor has been chosen. In this case the node is used to evaluate UV exposition for subjects potentially at risk of developing a pathology UV-related (like skin cancer or low level of vitamin D). Among all possible fabrication processes the devices based on Silicon Carbide (SiC) have been selected, Fig. 1. The main advantages of such a devices are the small size, high speed and good spectral response. Even if they are the best in their category, the output current of the photodetector is still very small (in the range of nA), so even a small external parasitic current could disturb its detection. In this context a deeper analysis of the electromagnetic compatibility of all the system has to be performed, as well as a protection to interferers. A metallic shield is necessary, but, again, interferes generated internally has to be avoided. The possibility to use a pre-amplified sensor has to be investigated, compatibly with the power available.



FIG. 1 – An UV sensor based on SiC (courtesy of Scitec Tocon Standard).

Another aspect to take into account, in order to reduce the maintenance of the node, is the power supply. All the system components are optimized in order to have low power consumption, nevertheless an energy harvester should be integrated to significantly extend the operating life of the sensor [1]. Several harvesters have been analyzed [2], the one based on the difference of temperature between the human body and the environment could be the best solution for the design of a small and wearable wireless sensors system. A well-know commercial device, the thermoelectric power generator MPG-D602 (Fig. 2) manufactured by Micropelt is one of the possible choices. This product, from datasheet, is able to provide an output voltage of 1.75 V per 1 Watt of thermal input. It works starting from only 10°C of

difference between hot and cold side, indeed it is very small, 3.375 mm x 2.5 mm x 1.07 mm [3].

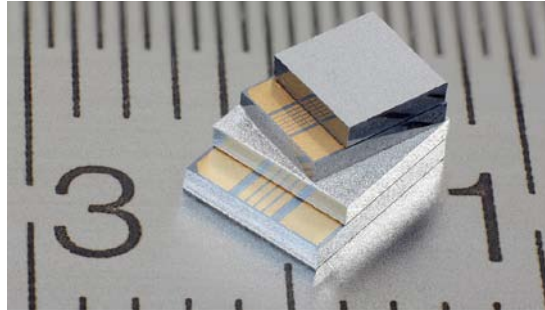


FIG. 2 –Two thermal energy harvesters, produced by Micropelt.

The radio component is expected to be the larger one, in terms of dimensions. The design of a new and innovative micro board could be unrealistic and time wasting, so a deep search in off-the-shelf market has to be done in order to identify the smallest one. Another critical aspect is the power consumption: it is reasonable to assume that the most consuming component is the radio, especially at the beginning of the communication.

In order to minimize the power consumption it may be possible that an intelligent firmware has to be built, as well as the minimization of data samples to be transmitted during the monitoring period.

III. WIRELESS NETWORK ARCHITECTURE

The wireless network architecture can be built according to two standard implementations, a Wireless Body Area Network (WBAN), exploiting either the Bluetooth and/or the ZigBee standards, or defining an Ad-Hoc transmission system, working at 400 MHz. The choice of the implementation method depends strongly on the application.

The WBAN radio is required when the subject can wear a mobile phone. Through a Bluetooth connection the node transmits to a mobile phone that forwards to the Internet. Alternatively, a ZigBee radio can be useful in a small confined environment. An Ad-Hoc network can represent the most efficient way to acquire data in large environments.

IV. THE ANTENNA

The node component that requires a dedicated rigorous analysis is the antenna. It has to be compact, light, and it needs to minimize any coupling effect with the human body. Two types of antennas are being investigated, one at 2.4 GHz either for the Bluetooth and ZigBee

standards, and another one at 400 MHz only for Ad-Hoc wireless networks. Several issues are in common with the two types, among them the maximizations of the efficiency and the minimization of the dimensions play a crucial role. Usually, radiators for WBAN radios are realized by means of patch antennas, they are efficient but too big for the specific applications. For this reason, we are applying a similar methodology to the one described in [4], based on the implementation of a resonant back-shielded loop. The dimensions are consequently reduced by applying some tricks that optimize the current path length, decreasing the space occupied by the antenna (a marguerite shape with more than 20 petals, Fig. 3).

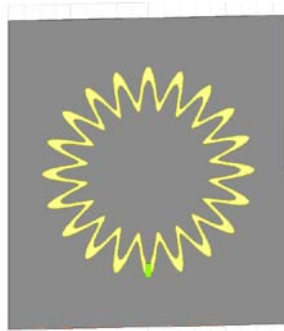


FIG. 3 – The back-shielded loop with 20 petals, a trick used to reduce the space occupation

V. CONCLUSION

The paper presents a preliminary design of an innovative wireless node for the monitoring of environmental physical phenomenon. All the components are presented, in particular the sensing unit embeds a UV. The node is self-powered, low cost, scalable, wearable and washable. The radiator is designed according to a dedicated synthesis procedure aimed to minimize its dimensions.

REFERENCES

- [1] Li Huang; Pop, V.; de Francisco, R.; Vullers, R.; Dolmans, G.; de Groot, H.; Imamura, K., "Ultra low power wireless and energy harvesting technologies — An ideal combination," *2010 IEEE International Conference on Communication Systems (ICCS)*, pp.295-300, 17-19 Nov. 2010
- [2] Adnan Harb, "Energy harvesting: State-of-the-art", *Renewable Energy*, Volume 36, Issue 10, October 2011, Pages 2641-2654
- [3] www.micropelt.com/download/datasheet_mpg_d602_d751.pdf
- [4] Stefanelli, R.; Trincherò, D.; "Full-Analytical Procedure For The Design Of Micro-Magnetic Radiators", submitted to RinEm 2012.

FROM MAGNETIC RESONANCE IMAGING TO WATER CONTENT EVALUATION OF A HUMAN TISSUE

M. Cavagnaro⁽¹⁾, F. Frezza⁽¹⁾, R. Laurita⁽¹⁾, M. Tannino⁽¹⁾, L. Manganaro⁽²⁾,
M. Marini⁽²⁾, P. Sollazzo⁽²⁾, A. Stagnitti⁽²⁾, V. Lopresto⁽³⁾, R. Pinto⁽³⁾

⁽¹⁾ Dept. of Information Engineering, Electronics and
Telecommunications, “La Sapienza” University, Rome, Italy
roberto.laurita@diet.uniroma1.it

⁽²⁾ Dept. of Radiological Science, “Umberto I” Polyclinic,
“La Sapienza” University, Rome, Italy

⁽³⁾ Unit of Radiation Biology and Human Health,
ENEA Casaccia Research Centre, Rome, Italy

Abstract

The scope of this article is to compare two methods to extrapolate the water content of human tissues from magnetic resonance imaging. Two different approaches to gain the same goal will be outlined and discussed in order to draw a roadmap for subsequent studies and refinements which will lead to dielectric properties finding. A quantitative benchmarking approach will be shown.

Index Terms – Quantitative imaging; water fraction; T1 mapping; proton density.

I. INTRODUCTION

Non-invasive measurements of the electromagnetic properties of biological tissues are necessary in several kinds of studies and biomedical applications. The electromagnetic properties of human tissues can be obtained from the water content of the tissue [1]. Correspondingly, the water content of a tissue can be obtained from Magnetic Resonance Imaging (MRI) data (e.g. [2]).

In this study, two different automatic procedures to evaluate water content of a tissue, using MRI, will be compared. The first procedure aims at the longitudinal relaxation time T1 of the tissue filling the corresponding body area. Then, from the evaluation of T1, the tissue water content is derived.

The second approach is based on a recently developed research [3] [4]. It is based on gradient echo like MRI sequences properly executed to extrapolate the signal intensity at zero echo time (TE=0) for the generic tissue. Considering that this signal is directly proportional to the proton density of the tissue and, therefore, to its water content, the water fraction (wf) of a generic tissue can be directly determined using pure water as a reference.

The results obtained applying both methods will be described from a quantitative point of view in the following paragraphs.

II. METHODS

A phantom composed by nine tubes (type falcon - 45 ml) filled with different percentages of water has been prepared by some of the authors (VL and RP). The analysis of the obtained data has been performed by others (RL and MT) who did not know the composition of the different samples under test. The MRI acquisitions have been done with a “Siemens Magnetom Avanto 1.5T” scanner at “Umberto I” Radiology Department. Two types of sequences have been used: Turbo Spin Echo (TSE) and Spoiled Gradient Recalled Echo (SGRE) modeled, respectively, by:

$$S = K \rho e^{\frac{TE}{T2}} \left(1 - 2e^{\frac{-TR+TE/2}{T1}} + e^{\frac{-TR}{T1}} \right) \quad (1)$$

$$S = \frac{K \rho \left(1 - e^{\frac{-TR}{T1}} \right) e^{\frac{-TE}{T2^*}} \sin(\alpha)}{1 - e^{\frac{-TR}{T1}} \cos(\alpha)} \quad (2)$$

where ρ means the proton density, $T1$ and $T2$ ($T2^*$) are the longitudinal and transversal relaxation times, TE and TR are the Echo and Repetition Time, K is an instrumental constant. A description of these parameters is provided in [2] and [5].

An MRI scanner produces a set of files stored in “Digital Imaging and Communication in Medicine (DICOM)” format [6].

To retrieve information from DICOM files, in this study, MatLab has been used.

When the first approach to evaluate water content is used, two acquisitions for the same slice with different TR are performed and the ratio of corresponding signals is evaluated according to the following equation:

$$\frac{S1}{S2} = K \frac{1 - 2e^{\frac{-TR1+TE/2}{T1}} + e^{\frac{-TR1}{T1}}}{1 - 2e^{\frac{-TR2+TE/2}{T1}} + e^{\frac{-TR2}{T1}}} \quad (3)$$

where $TR1$ must be shorter than $TR2$. Except K , all the other parameters are known, so that from Eq. (3) the corresponding $T1$ value can be obtained. In [7] a relation between water fraction and $T1$ has been derived, according to:

$$\frac{1}{wf} = A + \frac{B}{T1} \quad (4)$$

A and B parameters depend on the used static magnetic field and have been determined for brain tissues, i.e. for tissues with a high water content.

The second approach is based on a comparison of quantities proportional to the proton density between tissue and pure water and is based on a SGRE sequence. Applying different TE values and making

an extrapolation to the value TE=0, the signal obtained (labeled S0) is proportional to the proton density. Assuming to have a sample of pure water for reference, and repeating the extrapolation, the water content of tissue (voxel by voxel) is obtained dividing the tissue's extrapolated value for the corresponding water data:

$$Wf = \frac{S0(tissue)}{S0(ref)} \quad (5)$$

According to [3] several errors affect this measure, due to temperature, field inhomogeneities, imperfections of the receiver coil and T1 saturation. In this work, to remove the dependence of T1 from Eq. (5), a sequence with the same TE, but a different flip angle, has been done.

III. RESULTS

Totally, 27 DICOM files have been generated: 6 for Spin Echo (2 acquisitions for 3 slices) and 21 for FLASH (6 acquisitions with different TE for 3 slices and 1 acquisition with a different flip angle for 3 slices). The overall scan lasted about 21 minutes (7 min for Spin Echo and 14 min for SGRE). MRI setup is reported in Table I. Looking at Fig. 1, it is clear that tube 0, in the center, is empty.

TABLE I – SEQUENCES SETUP

Parameter	<u>TSE</u> Value	<u>SGRE</u> Value
<i>Echo Time</i>	22 ms	10.7, 20, 30,40, 50, 60 ms
<i>Repetition Time</i>	450, 2100 ms	1000 ms
<i>Flip Angle</i>	n.a.	90°, 45° (only for TE = 40 ms)
<i>Slice Thickness</i>	2 mm	2 mm
<i>Bits Stored/Allocated</i>	12 / 16	12 / 16
<i>Rows/Columns</i>	256 / 180	512 / 384
<i>Pixel Spacing</i>	1.25 mm	0.625 mm

From Table II it can be noted that T1 Method is well fitted (as expected) for water percentages higher than 60%, instead, the PD Method seems to provide good results only where the extrapolation algorithm worked properly without considering the error correction lack.

TABLE II - PHANTOM COMPOSITION AND BENCHMARKING

Tube Id	H2O (%g)	% err. T1 Method	% err. PD Method
0	0	0.0	0.0
1	50	9.5	0.9
2	30	5.6	35.6
3	100	0.2	6.0
4	80	1.6	2.3
5	30	14.2	18.2
6	80	1.5	16.0
7	50	10.0	9.5
8	100	0.1	14.9

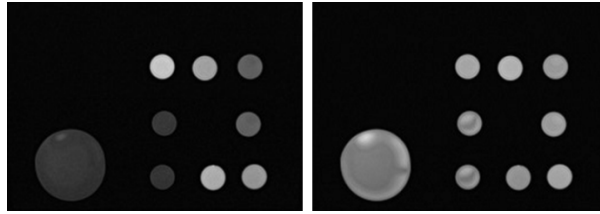


FIG. 1 – TSE acquisitions (DICOM Images) with different TR (450, 2100 ms).

IV. CONCLUSION

Results show that tubes with high percentage of water are better identified using a procedure based on spin echo sequences. The next step will be to optimize the same procedure in order to have good results (less than 3% of error) for all possible percentages of water content.

The sequence based on SGRE proved to be more difficult to apply. A first interpretation of the obtained results brings to a revision of smoothing and extrapolation algorithms and to a repetition of the test with more acquisitions and maybe an optimized sequence.

This quantitative overview is the prerequisite for a further study on dielectric properties evaluation (using MRI) of tissues. To reach this enhanced target, a faster way is to refine the first approach (water content from T1) which has also the important advantage to avoid the presence of a reference tube.

V. REFERENCES

- [1] J. L. Schepps and K. R. Foster, "The UHF and microwave dielectric properties of normal and tumour tissues: variation in dielectric properties with tissue water content," *Phys. Med. Biol.*, vol. 25, pp. 1149-1159, 1980.
- [2] M. Mazzurana, L. Sandrini, A. Vaccari, C. Malacarne, L. Cristoforetti and R. Pontalti, "A semi-automatic method for developing an anthropomorphic numerical model of dielectric anatomy by MRI," *Phys. Med. Biol.*, vol. 48, pp. 3157-3170, 2003.
- [3] H. Neeb, K. Zilles and N. J. Shah, "A new method for fast quantitative mapping of absolute water content in vivo," *NeuroImage*, vol. 31, pp. 1156-1168, 2006.
- [4] N. J. Shah, V. Ermer and A. M. Oros-Peusquens, "Measuring the Absolute Water Content of the Brain Using Quantitative MRI," *Methods in Molecular Biology*, vol. 711 part 2, pp. 29-43, 2011.
- [5] M. A. Bernstein, K. F. King and X. J. Zhou, *Handbook of MRI Pulse Sequences*, Elsevier Academic Press, 2004.
- [6] ACR-NEMA DICOM home page, <http://medical.nema.org/>, 1985.
- [7] P. Fatouros and A. Marmarou, "Use of magnetic resonance imaging for in vivo measurements of water content in human brain: method and normal values," *J. Neurosurg.*, vol. 90, pp. 109-115, 1999.

HEALTH EFFECTS FROM CELL PHONE RADIATIONS THE VERDICT OF THE COURT OF APPEAL OF BRESCIA

B. Bisceglia⁽¹⁾, V. Ivone⁽²⁾

(1) Department of Electronic and Computer Engineering,
University of Salerno
Via Ponte Don Melillo, 84084 Fisciano, Salerno, Italy
bbisceglia@unisa.it

(2) Dip. Di Studi Internazionali di Diritto e Etica dei Mercati
University of Salerno
Via Ponte Don Melillo, 84084 Fisciano, Salerno, Italy
vituliaivone@unisa.it

Abstract

The effect of mobile phone radiation on human health is the subject of recent interest and study. Many scientific studies have investigated possible health symptoms of mobile phone radiation. These studies are occasionally reviewed by some scientific committees to assess overall risks. The Court of Appeal of Brescia has recently recognized the occupational origin of a trigeminal schwannoma in a user of mobile telephones, and ordered the Italian Workers' Compensation Authority (INAIL) to award the applicant a compensation for a high degree (80%) permanent disability. We describe and discuss the salient aspects of this unprecedented ruling as a case-study in the framework of the use (and misuse) of scientific evidences in toxic-tort litigation. A comprehensive strategy to improve the quality of expert witness testimony in legal proceedings and promote just and equitable verdicts is urgently needed in Italy.

Index Terms – benign tumor, compensation, mobile telephone, occupational health.

I. INTRODUCTION

The exposure of a user to cell phone radiations depends on the technology of the phone, the distance between the phone's antenna and the user, the extent and type of use, and the user's distance from cell phone towers.

Studies thus far have not shown a consistent link between cell phone use and cancers of the brain, nerves, or other tissues of the head or neck. More research is needed because cell phone technology and how people use cell phones have been changing rapidly.

The effect of mobile phone radiation on human health is the subject of recent interest and study, as a result of the enormous increase in mobile phone usage throughout the world (as of June 2009, there were more than 4.3 billion subscriptions worldwide).

The WHO (World Health Organization) has classified mobile phone radiation on the IARC (International Agency for Research on Cancer) scale into Group 2B - possibly carcinogenic to humans on May 31, 2011. «Could be some risk» of carcinogenicity, so additional research into the long-term, heavy use of mobile phones needs to be conducted. The IARC seeks to identify environmental factors that can increase the risk of cancer in humans. IARC uses the following categories to classify environmental agents:

TABLE I - IARC CLASSIFICATION

Group	Description
1	Carcinogenic to humans
2A	Probably carcinogenic to humans
2B	Possibly carcinogenic to humans
3	Not classifiable as to its carcinogenicity to humans
4	Probably not carcinogenic to humans

IARC has classified radiofrequency fields in Group 2B, possibly carcinogenic to humans.

IARC interprets the 2B classification as meaning there is limited evidence showing radiofrequency carcinogenicity in humans and less than sufficient evidence of carcinogenicity in experimental animals.

IARC has classified the following other agents as *possibly carcinogenic to humans*:

- Coffee
- Extremely low frequency electromagnetic fields (power line frequency)
- Talc-based body powder

II. THE VERDICT. COURT OF APPEAL OF BRESCIA, 2009

Towards the end of 2009, the Court of Appeal of Brescia (as the authority invested to judge Occupational Health cases) awarded compensation to Mr. Innocent Marcolini, a company manager, in a decision against the INAIL (The National Insurance Institute for Accidents at Work) judging that Mr. Marcolini's disability of 80% was caused by his workplace and that the resulting onset of a neuroma of the ganglion of Gasser could be attributed to his professional environment, in particular, the constant exposure to electromagnetic waves when using the office cordless and mobile telephones. From 1981 until 1993 Mr. Marcolini had worked as a business manager, and in that capacity he claimed to have used the company's land-line, cordless and mobile telephones for an average of 5-6 hours a day for the period of 12 years. Being right handed, he regularly held the mobile

to his left ear while using his right hand either to answer the desk phone or to take notes.

According to the documents produced in court, in June 2002 Mr. Marcolini began to be affected by a benign tumor which had affected his cranial nerves, in particular the acoustic nerve, and on November 8th 2002 Mr. Marcolini underwent brain surgery for the removal of ganglion of Gasser. A postoperative MRI [1] showed that there was still a residual tumor.

The following symptoms were noted after the operation:

- Ulcer of the left cornea,
- Syndrome of algo-dystrophic to the left hemiface with severe chronic pain,
- persistent paraesthesia of the hemiface,
- disturbance to the masticatory mechanism,
- double vision,
- partial epilepsy,
- memory loss,
- reduced attention span,
- reduced adaptability,
- temporal lobe syndrome with disturbance to smelling, hearing, taste, balance, vision, and psychiatric.

Mr. Marcolini believed that his constant use of the telephone had caused him to have a serious health condition. As such, on the 17th of November 2003, he asked INAIL for compensation due to his health condition but was denied stating that there was no causal link between Mr. Marcolini's occupation and his health problems as reported. INAIL opposed the application, always in terms of the lack of causation and the lack of oral evidence supporting his claim. INAIL produced various documentation to support their refusal. Having fulfilled the preliminary testimony, the sitting judge, after confirming the claimant's intense use of cellular and cordless phones and involving technical experts for the Court, rejected the application for lack of causation, in accordance to the comments submitted by the Technical Consultant (CTU). During Mr. Marcolini's appeal, the INAIL reminded the court that there was no reliable scientific studies regarding the harmfulness of electromagnetic waves.

In 2004, after the diagnosis of an adrenal lesion, he underwent further surgery at the European Institute of Oncology. The histological diagnosis confirmed that he had a Pheochromocytoma, a rare tumor with possible secretion of catecholamines.

Mr. Marcolini applied to the Court of Brescia on the 7th of June 2007 citing his serious and complex brain disorder, which he believed to be of an occupational origin. In 2009 the Court of Appeal of Brescia, as an Occupational tribunal, issued a ruling recognizing the occupational

nature of his disease and approved the awarding of 80% disability to Mr. Marcolini. [1]

III. DOSIMETRIC REMARKS

The court appointed expert witness takes in account the use of mobile and cordless from Mr Marcolini. He has used such devices (800-1900 MHz) 5-6 hours in a day (Table II). [2]

«Nel periodo in cui ha lavorato c/o San Giacomo SPA per i primi 3 anni utilizzava telefono mobile – cordless (deposte 5-6 h al dì), dal 1993-4 al cordless fu associato l’uso di telefono cellulare fino al settembre 2003. I telefoni mobili (cordless) e i telefoni cellulari funzionano attraverso le onde elettromagnetiche» [2]

Table II - Court appointed expert witness

	Banda di Frequenza
Cordless (varie generazioni)	800- 1900 MHz
Tel. cellulari (varie generazioni)	800- 1900 MHz

«Il quesito proposto può essere così svolto: l’esposizione a Radiofrequenze, anamnesticamente per un tempo efficace (>10 anni), ha molto verosimilmente avuto un ruolo concausale nell’evoluzione della neplasia patita dal sig. Marcolini.

La menomazione dell’integrità fisica legata alla malattia ed ai suoi esiti si stima in misura dell’80%.»

IV. CONCLUSION

Is there some evidence from studies of cells, animals, or humans that radiofrequency energy can cause cancer? A limited number of studies have shown some evidence of statistical association of cell phone use and brain tumor risks, but most studies have found no association.

The verdict of the Court of Appeal of Brescia is paradigmatic in the controversial debate about health effects of exposure of humans to cell phone radiations.

REFERENCES

- [1] Sentenza di Merito, Corte di Appello di Brescia, 22.12.2009, n. 614.
 [2] Court appointed expert witness, CTU 2° grado.

OPTIMAL FOCUSING OF VECTORIAL FIELDS SUBJECT TO ARBITRARY UPPER BOUNDS

D. A. M. Iero⁽¹⁾

⁽¹⁾ DIMET, Univ. Mediterranea di Reggio Calabria, Via Graziella, Loc. Feo di Vito, 89100 Reggio Calabria
domenica.iero@unirc.it

Abstract

The paper introduces an effective method for the globally optimal focusing of vectorial fields by means of an array of antennas, which is of interest in a number of applications including microwave hyperthermia.

Index Terms – Energetic Applications of Microwaves, Optimal Focusing, Biomedical Applications of Microwaves, Hyperthermia, Antenna synthesis.

I. INTRODUCTION

As well known, power pattern synthesis is a classical problem in electromagnetics, that, in its widest sense, relies in the optimization of a cost function of the parameters' set specifying the antenna structure and excitations. In the general case, because its inherent non convexity, optimization algorithms can be trapped in one of its many local minima, leading the designer to a suboptimal solution that may not fulfill all the requirements and, even if the synthesis is successful, there is usually no way to judge if the design could be improved, (for instance, by using a smaller number of feeds, or a smaller antenna).

In some cases, some interesting and successful alternative formulation of the problem is possible, such as, for example, the optimal focusing of *scalar* fields by means of fixed-geometry arrays. In fact, one can recast the synthesis into a convex programming problem [1]. This approach allows the determination of the excitations of a given set of sources that will produce a maximum *scalar* field in a given direction subject to arbitrary sidelobe bounds elsewhere. It guarantees the achievement of the globally optimal solution for a large class of pencil beam synthesis problems in an effective and efficient way without recurring to global optimization techniques, which are extremely heavy from the computational point of view. Interestingly, the approach is very general, as it can be applied to any fixed geometry array as well as to the case of spatial [2] rather than angular [1] focusing, which is of interest when trying to optimize the power deposition in a given region of space [2]. Moreover, it can be argued, and it has been confirmed by a large set of experiments, that such an approach outperforms the well known Time Reversal technique [3]. As an example Fig.1 compares the field distributions achieved by the two approaches in a 2D anatomically realistic breast numerical phantom.

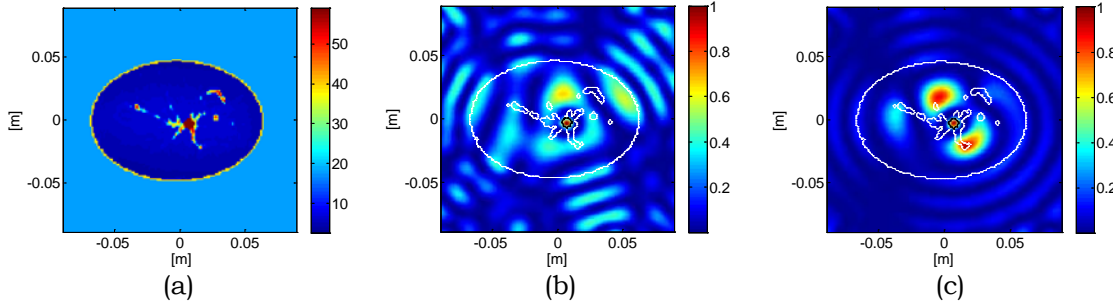


FIG. 1 – (a) Relative permittivity distribution (2 GHz) of a fatty breast (slice $s_1=155$, phantom ID: 071904), (b) EM field focused through the optimal *scalar* approach, (c) EM field focused through Time Reversal Method.

On the other side, such an approach cannot be applied to generic *vectorial* fields, which is obviously the most general case. Hence, the present communication is devoted to the optimal focusing of *vectorial* fields subject to arbitrary upper bounds. Due to its *vectorial* nature, the problem at hand has been tackled by formulating it as a multi-objective one, which can be solved by reducing it to a number of different convex programming problems [4]. As already stated, the problem is of interest any time one wants to optimize the power deposition in a given region of space, such as in hyperthermic treatments of cancer (which was our original motivation).

II. THE PROPOSED APPROACH

Considering a set of N sources, i.e. N -elements arbitrary (fixed-geometry) array, each radiating (under unitary excitation) a known vectorial field $\underline{\varphi}_n$, the focusing problem can be formulated as:

find the complex excitations I_n ($n = 1, \dots, N$) of the given sources such to

$$\text{Max} \quad |\underline{E}(\underline{r}_0)|^2 = \left| \sum_{n=1}^N I_n \underline{\varphi}_n(\underline{r}_0) \right|^2 \quad (1)$$

subject to

$$|\underline{E}(\underline{r})|^2 = \left| \sum_{n=1}^N I_n \underline{\varphi}_n(\underline{r}) \right|^2 \leq UB(\underline{r}) \quad \underline{r} \in \Omega \quad (2)$$

where $\underline{E}(\underline{r})$ is the radiated field, $UB(\underline{r})$ is a non-negative arbitrary function of the coordinate \underline{r} spanning the observation space Ω , and \underline{r}_0 is the target direction (i.e. maximum power deposition point).

Assuming, without any lack of generality, a 2D observation space Ω and a TE polarization, i.e. $\underline{E}(\underline{r}) = E_x(\underline{r}) \underline{i}_x + E_y(\underline{r}) \underline{i}_y$ and $\underline{\varphi}_n(\underline{r}) = \varphi_n^x(\underline{r}) \underline{i}_x + \varphi_n^y(\underline{r}) \underline{i}_y$, the problem becomes:

find the complex excitations I_n ($n = 1, \dots, N$) of the given sources such to

$$\text{Max} \quad \left(\Re\{E_x(\underline{r}_0)\}^2 + \Im\{E_x(\underline{r}_0)\}^2 + \Re\{E_y(\underline{r}_0)\}^2 + \Im\{E_y(\underline{r}_0)\}^2 \right) \quad (3)$$

subject to

$$|\underline{E}(\underline{r})|^2 = \left| \sum_{n=1}^N I_n \underline{\varphi}_n(\underline{r}) \right|^2 \leq UB(\underline{r}) \quad \underline{r} \in \Omega \quad (4)$$

In order to solve (3)-(4), it proves useful to consider the auxiliary multi-objective problem:

find the complex excitations I_n ($n = 1, \dots, N$) of the given sources such to

$$\text{Max } \Re\{E_x(\underline{r}_0)\}^2, \Im\{E_x(\underline{r}_0)\}^2, \Re\{E_y(\underline{r}_0)\}^2, \Im\{E_y(\underline{r}_0)\}^2 \quad (5)$$

subject to

$$|\underline{E}(\underline{r})|^2 = \left| \sum_{n=1}^N I_n \underline{\varphi}_n(\underline{r}) \right|^2 \leq UB(\underline{r}) \quad \underline{r} \in \Omega \quad (6)$$

Knowing that the phase reference in the target direction \underline{r}_0 is a degree of freedom, a convenient choice is to assume that one component of the field, e.g. $E_x(\underline{r}_0)$, in this direction is purely real. Then, the optimization task (5) can be decomposed in several single-objective sub-problems

find the complex excitations I_n ($n = 1, \dots, N$) of the given sources such to

$$\text{Max } \Re\{E_x(\underline{r}_0)\} \quad (7)$$

subject to

$$\Im\{E_x(\underline{r}_0)\} = 0 \quad (8)$$

$$\Re\{E_y(\underline{r}_0)\} = \psi_i \quad \psi_i \in \Psi \quad (9)$$

$$\Im\{E_y(\underline{r}_0)\} = \beta_i \quad \beta_i \in B \quad (10)$$

$$|\underline{E}(\underline{r})|^2 = \left| \sum_{n=1}^N I_n \underline{\varphi}_n(\underline{r}) \right|^2 \leq UB(\underline{r}) \quad \underline{r} \in \Omega \quad (11)$$

where $\Psi = \{\psi_i | -\psi_{max} \leq \psi_i \leq \psi_{max}\}$, $B = \{\beta_i | -\beta_{max} \leq \beta_i \leq \beta_{max}\}$, ψ_{max} and β_{max} are, respectively, obtained maximizing the real and imaginary part of $E_y(\underline{r}_0)$ subject to constraints (11).

It is worth to note that $|\underline{E}(\underline{r})|^2$ is a positive semidefinite quadratic form (as a function of the real and imaginary part of I_n). Hence, the corresponding constraints (11) defines a convex set (an hyperellipsoid) in the space of the unknowns, as well as constraints (8)-(10), (which define an hyperplane). As the intersection of convex sets is still convex, constraints (8)-(11) defines a convex set. Finally, we have also to stress that the objective function (7) is linear too, so that each single-objective problem is a convex one that admits a unique maximum, i.e. an optimal solution is guaranteed.

The convexity of each single-objective problem and a proper choice of Ψ and B make the Theorem1 hypothesis, in [4], be satisfied, allowing us to find *Pareto-optimal solutions of the multi-objective problem (5)-(6)*. After having found all the Pareto-optimal solutions of the multi-objective problem, we have just to define a criteria for an a posteriori articulation

of preference to identify the optimal solution of the original problem (1)-(2) among all the *Pareto-optimal solutions* provided by the multi-objective problem (5)-(6). Knowing that the focusing problem at hand relies in the maximization of the power deposition onto the target point, its best solution is the *Pareto-optimal* one whose corresponding $|\underline{E}(\underline{r}_0)|$ is the maximum one.

III. A NUMERICAL EXAMPLE AND ON GOING ACTIVITIES

To validate the overall approach from a numerical point of view, the described *vectorial* focusing approach has been implemented exploiting Fmincon Matlab function and Matlab parallel toolbox. In fact, the above formulation of the problem in many independent single object optimizations allows the use of parallel programming in order to improve performances further.

Fig.2 shows the amplitude of a focused *vectorial* field radiated by a circular array of 18 magnetic line sources in a 2D scenario ($0.2m \times 0.2m$) without any obstacle. The black grid represents the arbitrary upper bound constraints.

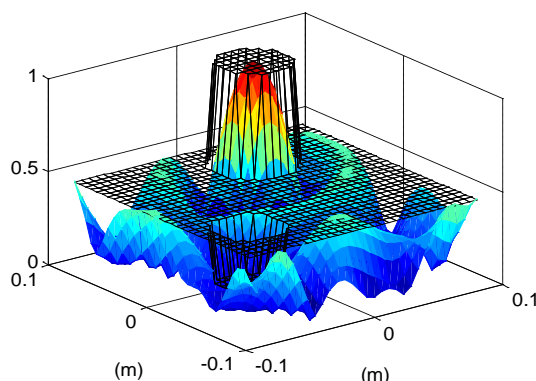


FIG. 2 – Amplitude of the focused *vectorial* field and upper bound mask.

The application of the above concepts and tools to non homogeneous scenarios will be presented at the conference.

REFERENCES

- [1] T. Isernia and G. Panariello, "Optimal focusing of scalar fields subject to arbitrary upper bounds," *El. Letters*, vol.34, no.2, pp.162-164, 22 Jan 1998.
- [2] D. Iero, T. Isernia, A. F. Morabito, I. Catapano, and L. Crocco, "Optimal Constrained Field Focusing for Hyperthermia Cancer Therapy: a Feasibility Assessment on Realistic Phantoms," *Progress In Electromagnetics Research, PIER*, vol. 102, pp. 125-141, 2010.
- [3] M. Fink, "Time reversal of ultrasonic fields. I. Basic principles," *Ultrasonics, Ferroelectrics and Frequency Control, IEEE Transactions on*, vol.39, no.5, pp.555-566, Sept 1992.
- [4] Jiguan Lin, "Multiple-objective problems: Pareto-optimal solutions by method of proper equality constraints," *IEEE Trans. on Automatic Control*, vol.21, no.5, pp. 641- 650, Oct 1976.

GOLD NANO-PARTICLES AS A PLATFORM FOR BIOSENSING

Renato Iovine, Luigi La Spada, Filiberto Bilotti, Lucio Vegni
Applied Electronics Department, “Roma Tre” University
Via della Vasca Navale 84, 00146 Rome, Italy
riovine@uniroma3.it

Abstract

In this contribution, a bio-electromagnetic sensor, based on Localized Surface Plasmon Resonance (LSPR) effects operating in the near-infrared frequency regime, is proposed. It consists in a planar array of gold nano-particles deposited on a silica substrate. The adopted geometry of the nano-particles leads to an enhancement of the localized electric field and can be used, thus, for sensing applications. The proposed structure is optimized to achieve the highest possible performance in terms of sensitivity and is designed to detect organic compounds by refractive index (RI) measurements. Sensitivity performances are evaluated also by varying the polarization of an incident plane-wave. Full-wave simulations confirm the effectiveness of the proposed sensor design.

Index Terms– Array of gold nano-particles, biosensing, LSPR sensors.

I. INTRODUCTION

Electromagnetic properties of gold nano-particles have been recently investigated by several research groups [1]. In particular, when nano-particles are much smaller than the wavelength of the incident field (e.g. at optical frequencies), free electrons of metal structures start oscillating collectively. These charge density oscillations, confined to metallic nano-structures and called Localized Surface Plasmon Resonances (LSPRs), are responsible for a strong enhancement of the field near the metallic surfaces. The resonance wavelength position and relative intensity are related to the type of metal, size and shape of the particles, as well as to the dielectric environment. This property makes such structures suitable for biomedical applications, such as light scattering microscopy-based imaging, sensing applications [2], and photothermal therapy for tumor treatments [3].

Current developments of nano-imprinting of gold nano-particles on a dielectric substrate allow the fabrication of planar sensors with high resolution and excellent sensitivity performances [4]. In fact, for an inter-particle distance much smaller than the incident field wavelength, electric near-field interactions between nano-particles may lead to a more uniform distribution of the electric field, increasing, thus, the active area of the sensor.

In this study, we exploit this phenomenon to propose the design of a new LSPR sensor, consisting of a 2D planar array of different nano-particles. Electromagnetic properties of the sensor are evaluated through proper full-wave simulations by using CST Studio Suite [5]. An optimization on the structure is also carried out to obtain high sensitivity performances. Finally, the sensor is numerically tested to show its ability to detect organic compound by RI measurements.

II. LSPR SENSOR DESIGN

The proposed sensor is shown in Fig.1. Its structure consists in a planar array of gold nano-particles deposited on a silica substrate. Different nano-particles have been considered: nano-cylinders and nano-crescents.

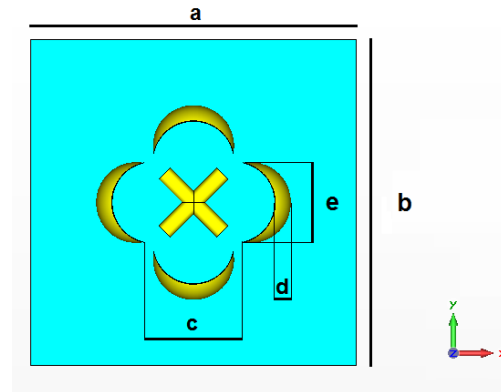


FIG. 1 – Top view of the unit-cell of 2D planar array: $a=b=400$ nm, $c=120$ nm, $d=20$ nm, $e=100$ nm, nano-cylinder radius=10 nm, nano-cylinder length=100 nm, nano-crescent thickness=50 nm, silica substrate thickness=60 nm.

The choice of these two particles allows maximizing sensor sensitivity. In fact, in order to enhance LSPR, three mechanisms are here combined [6]:

- coupling gold nano-particles with inter-particle distance much smaller than the incident field wavelength;
- use of gold nano-crescent to increase the polarizability by employing the multi-polar resonance;
- use of coupled nano-cylinders in cross (X) configuration to increase the sensitivity of the LSPR sensor, based on the plasmon hybridization.

The array is excited by a plane-wave, having the electric field parallel and the propagation vector \mathbf{k} perpendicular to the plane containing the structure. The degrees of freedom related to geometrical parameters were optimized (see caption of Fig. 1) to tune the resonance peak in the near infrared (NIR) region and to ensure a suitable electric field distribution on the sensor surface to achieve a good active area for sensing. The electromagnetic interaction between the proposed structure and the incident plane-wave results in a strong local electric field enhancement, localized nearby the surface (Fig.2). In the proposed configuration the strong localization of the electric field is due to the interactions among nano-particles of different shapes: nano-cylinders and nano-crescents. Therefore, the structure exhibits a few resonant frequencies (see Fig.3), whose position depends also on the electric field polarization.

The sensor behavior is related to the effective RI variation of the system "LSPR sensor-sample under test". When the sample is placed on the sensing platform, its presence changes the electromagnetic characteristics of the sensor. As a result, the structure exhibits a shift in the resonant frequency, with different values in terms of position, magnitude, and bandwidth. By observing a change in the resonant frequency, it is possible to detect a variation in the effective permittivity, which is useful to recognize different biological compounds (Fig.3).

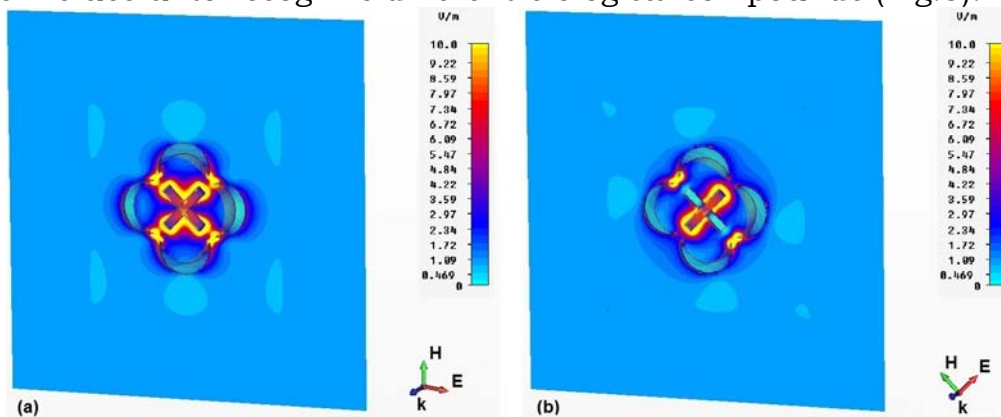


FIG. 2 – Electric field distribution on the sensor surface at the resonant wavelength without sample for two different polarizations (a-b). The incident electric field magnitude is 1V/m.

III. NUMERICAL RESULTS

The electromagnetic sensor response is evaluated in terms of extinction cross-section (magnitude, amplitude width, and position of its resonant wavelengths). For gold nano-particles, experimental values [7] of the complex permittivity function have been inserted in the full-wave simulator.

As shown in Fig. 2, the use of different shapes of nano-particles, arranged in array configuration, allows obtaining an electric field distribution that optimizes the active area of the sensing platform and an enhancement of the local electric field, caused by the inter-coupling of such structures.

To test the sensor sensitivity, the RI values of rat mammary adipose and tumor tissue have been used [8]. In Fig.3, the extinction cross-section spectra obtained from full-wave simulations are shown. As depicted in Fig.3a, the resonance peak shifts from 1030 nm for a tumor tissue to 1052 nm for a regular adipose tissue. The sensitivity value in terms of wavelength shift vs. refractive index unit (RIU) is 285 nm/RIU. For the polarization shown in Fig. 2b, the resonance peak shifts from 1075 nm (tumor tissue) to 1124 nm (adipose tissue) (see Fig. 3b). The sensitivity value is now 636 nm/RIU.

From the presented results, it is clear that the sensitivity of the proposed sensor is a function of the electric field polarization. In particular, higher sensitivity is obtained with the polarization shown in Fig. 2b, associated to a high field intensity between nano-crescent tips.

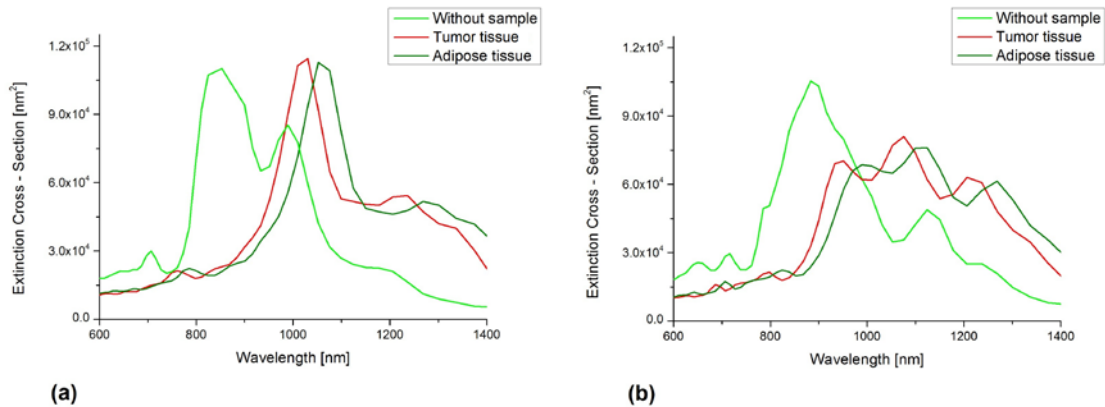


FIG. 3 – Extinction spectra of the sensor without sample (RI=1), rat mammary cancer (RI=1.39), and adipose tissue (RI=1.467). (a-b) Spectra are obtained by using the incident plane-waves as in Figs. 2a and 2b, respectively.

IV. CONCLUSION

In this contribution, we have proposed an LSPR sensor based on a new unit-cell, consisting of different coupled nano-particles (nano-cylinders and nano-crescents). By means of full-wave simulations, we have shown the ability of the proposed structure to be used as a high-sensitive sensor for biological samples working in the near-infrared frequency range.

REFERENCES

- [1] A. Moores and F. Goettmann, "The plasmon band in noble metal nanoparticles: an introduction to theory and applications," *New J. Chem.*, vol. 30, pp. 1121-1132, 2006.
- [2] W. Cai, T. Gao, H. Hong and J. Sun, "Application of gold nanoparticles in cancer nanotechnology," *Nanotechnology, Science and Application*, vol. 1, pp. 17-32, 2008.
- [3] J.L. Li and M. Gu, "Gold-nanoparticle-enhanced cancer photothermal therapy," *IEEE J. Selected Topics in Quantum Electronics*, vol. 16, pp. 989-996, 2010.
- [4] C.C. Liang, M.Y. Liao, W.Y. Chen, T.C. Cheng, W.H. Chang and C.H. Lin, "Plasmonic metallic nanostructures by direct nanoimprinting of gold nanoparticles," *Optics Express*, vol. 19, pp. 4768-4776, 2011.
- [5] CST Computer Simulation Technology, www.cst.com
- [6] T. Chung, S.-Y. Lee, E.Y. Song, H. Chun, and B. Lee, "Plasmonic nanostructures for nano-scale bio-sensing," *Sensors*, vol.11, pp. 10907-10929, 2011.
- [7] P.B. Johnson and R.W. Christy, "Optical constants of the noble metals," *Phys. Rev. B*, vol. 6, pp. 4370-4379, 1972.
- [8] A.M. Zysk, E.J. Chaney and S.A. Boppart, "Refractive index of carcinogen-induced rat mammary tumors," *Phys. Med. Biol.*, vol.51, pp. 2165-2177, 2006.

Session 3 – Electromagnetic theory

K. Watanabe, Y. Nakatake, and G. Schettini
Plane-wave scattering from cylindrical objects

L. Infante, and S. Mosca
A closed-form estimation of the mutual coupling matrix applied to uniform circular arrays

P. Burghignoli
A phase-center study of Fabry-Pérot cavity antennas

M. Cametti, M. Bozzi, M. Pasian, and L. Perregrini
An analytical model to quantify the efficiency of arrays composed by high-gain reflector antennas

G. Castaldi, V. Galdi, A. Alù, and N. Engheta
Nonlocal transformation optics

F. Mangini
Electromagnetic scattering of an elliptically polarized plane wave by a buried sphere

PLANE-WAVE SCATTERING FROM CYLINDRICAL OBJECTS BURIED UNDER PERIODICALLY CORRUGATED SURFACE

K. Watanabe⁽¹⁾, Y. Nakatake⁽²⁾, and G. Schettini⁽³⁾

⁽¹⁾ Department of Information and Communication Engineering,
Fukuoka Institute of Technology

3-30-1 Wajirohigashi, Higashi-ku, 811-0295 Fukuoka, Japan

⁽²⁾ Graduate School of Engineering, Fukuoka Institute of Technology

3-30-1 Wajirohigashi, Higashi-ku, 811-0295 Fukuoka, Japan

⁽³⁾ Applied Electronics Department, “Roma Tre” University

Via della Vasca Navale 84, 00146 Rome, Italy

koki@fit.ac.jp

Abstract

This paper formulates the plane electromagnetic wave scattering problem of cylindrical objects buried under periodically corrugated surface. The structure under consideration is an imperfectly periodic structure, in which the structural periodicity is locally broken, and the fields generally have continuous spectra in the wavenumber space. The present formulation is a spectral-domain method based on the pseudo-periodic Fourier transform, and combines the coordinate transformation method and the recursive transition-matrix algorithm.

Index Terms – imperfectly periodic structures, plane-wave scattering, pseudo-periodic Fourier transform, spectral-domain analysis.

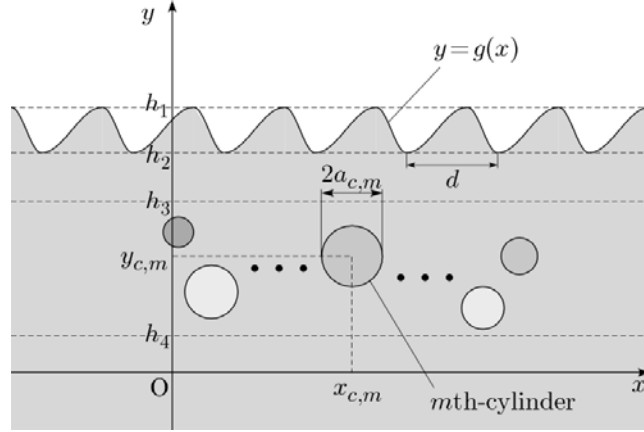
I. INTRODUCTION

This paper considers the plane-wave scattering problem of cylinders buried under periodically corrugated surface, and presents a formulation based on the coordinate transformation method (C-method) [1] and the recursive transition-matrix algorithm (RTMA) [2]. The C-method is for the scattering problem of the perfectly periodic surface-relief gratings, and the RTMA is for the problem of a finite number of cylindrical objects. These two methods can be combined with the use of the sampling in the wavenumber space. Here, we introduce the pseudo-periodic Fourier transform (PPFT) [3], which makes it possible to consider the sampling scheme inside the Brillouin zone. The PPFT also makes it easy to apply the conventional grating formulations, such as the C-method, to the problems of imperfectly periodic structures, because the transformed fields have a pseudo-periodic property.

II. SETTINGS OF THE PROBLEM

The present paper considers the scattering problem of electromagnetic fields with a time-dependence $\exp(-i\omega t)$ from a structure schematically shown in Fig. 1. The structure is uniform in the z -direction and the x -

axis is parallel to the periodicity direction of the surface. The equation of the corrugated surface is given by $y = g(x)$, where $g(x)$ is a known periodic function with a period d . For simplicity, $g(x)$ is supposed to be a continuous function with piecewise differentiable. The surrounding region $y > g(x)$ is filled with a homogeneous and isotropic medium with the permittivity ε_s and a permeability μ_s .



The substrate region $y < g(x)$ is also filled with a homogeneous and isotropic medium described by a permittivity ε_b and a permeability μ_b , and M circular cylinders are located in this region. The m th-cylinder ($m = 1, 2, \dots, M$) is described by the permittivity $\varepsilon_{c,m}$, the permeability $\mu_{c,m}$, the radius $a_{c,m}$, and the center position $(x, y) = (x_{c,m}, y_{c,m})$. The parameters are chosen not to overlap the cylinders. The fields are uniform in the z -direction and two-dimensional scattering problem is here considered. Two fundamental polarizations are expressed by TE and TM, in which the electric and the magnetic fields are respectively parallel to the z -axis. We sometimes denote the z -component of electric field for the TE-polarization and the z -component of magnetic field for the TM-polarization by $\psi(x, y)$ to express both polarizations simultaneously. The fields are excited by the plane-wave of unit amplitude and the angle of incidence $\theta^{(i)}$ is measured counter-clockwise from the x -axis.

III. OUTLINE OF FORMULATION

We introduce a curvilinear coordinate system $O-uvz$, which is related to the original coordinate system $O-xyz$ by continuous transformation equations: $u = x$ and $v = y - g(x)$. Also, we introduce the PPFT. The definition of the PPFT and its inverse transform are formally given by

$$\bar{\psi}(u; \xi, v) = \sum_{m=-\infty}^{\infty} \psi(u - m d, v) e^{i m d \xi}, \quad \psi(u, v) = \frac{1}{k_d} \int_{-k_d/2}^{k_d/2} \bar{\psi}(u; \xi, v) d\xi \quad (1)$$

where ξ is the transform parameter, and $k_d = 2\pi/d$ denotes the inverse lattice constant. Since the transformed fields are pseudo-periodic in terms of u , they can be expressed in the generalized Fourier series expansions as

$$\bar{\psi}(u; \xi, v) = \bar{\mathbf{x}}(x; \xi)^t \bar{\boldsymbol{\psi}}(\xi, v), \quad (\bar{\mathbf{x}}(x; \xi))_n = e^{i \alpha_n(\xi) x}, \quad \alpha_n(\xi) = \xi + n k_d \quad (2)$$

where $\bar{\boldsymbol{\psi}}(\xi, v)$ are column matrix generated by the Fourier coefficients. From Maxwell's curl equations and the constitutive relations, we may

derive a coupled differential-equation set for $\bar{\psi}(\xi, v)$ and $-i(\partial/\partial v)\bar{\psi}(\xi, v)$, and the general solution in each region ($y > g(x)$ for $r = s$ and $y < g(x)$ for $r = b$) is obtained in the following form:

$$\begin{pmatrix} \bar{\psi}(\xi, v) \\ -i\frac{\partial}{\partial v}\bar{\psi}(\xi, v) \end{pmatrix} = \begin{pmatrix} \bar{\mathbf{P}}_{r,1}^{(-)}(\xi) & \bar{\mathbf{P}}_{r,1}^{(+)}(\xi) \\ \bar{\mathbf{P}}_{r,2}^{(-)}(\xi) & \bar{\mathbf{P}}_{r,2}^{(+)}(\xi) \end{pmatrix} \begin{pmatrix} \bar{\mathbf{a}}_r^{(-)}(\xi, v) \\ \bar{\mathbf{a}}_r^{(+)}(\xi, v) \end{pmatrix} \quad (3)$$

$$\bar{\mathbf{a}}_r^{(\pm)}(\xi, v) = \bar{\mathbf{V}}_r^{(\pm)}(\xi, v - v') \bar{\mathbf{a}}_r^{(\pm)}(\xi, v'), \quad \left(\bar{\mathbf{V}}_r^{(\pm)}(\xi, v) \right)_{n,m} = \delta_{n,m} e^{i\eta_{r,n}^{(\pm)}(\xi)v} \quad (4)$$

where the matrix consisting of $\bar{\mathbf{P}}_{r,1}^{(\pm)}(\xi)$ and $\bar{\mathbf{P}}_{r,2}^{(\pm)}(\xi)$ is the diagonalization matrix for the coefficient matrix of the coupled differential-equation set, the column matrices $\bar{\mathbf{a}}_r^{(\pm)}(\xi, v)$ give the coefficients of the eigenmode expansion, and $\{\eta_{r,n}^{(\pm)}(\xi)\}$ denote the propagation constants of the eigenmodes that are given by the eigenvalues of the coefficient matrix. We arrange the eigenvalues so as to relate the $\{\eta_{r,n}^{(+)}(\xi)\}$ and $\{\eta_{r,n}^{(-)}(\xi)\}$ to the eigenmodes propagating in the positive and the negative v -directions, respectively. Considering the boundary conditions at $y = g(x)$ (namely $v = 0$), the relation between the coefficients of the incoming and the outgoing eigenmodes can be obtained in the following form:

$$\begin{pmatrix} \bar{\mathbf{a}}_s^{(+)}(\xi, 0) \\ \bar{\mathbf{a}}_b^{(-)}(\xi, 0) \end{pmatrix} = \begin{pmatrix} \bar{\mathbf{S}}_{11}(\xi) & \bar{\mathbf{S}}_{12}(\xi) \\ \bar{\mathbf{S}}_{21}(\xi) & \bar{\mathbf{S}}_{22}(\xi) \end{pmatrix} \begin{pmatrix} \bar{\mathbf{a}}_s^{(-)}(\xi, 0) \\ \bar{\mathbf{a}}_b^{(+)}(\xi, 0) \end{pmatrix} \quad (5)$$

where the expressions of the scattering-matrix is omitted in this paper.

When the plane-wave illuminates a perfectly periodic structure, the field has an equidistant discrete spectrum in the wavenumber space. The structure under consideration is an imperfectly periodic structure but, for the plane-wave incident problem, it may be necessary to decompose the field into that for the related structure with perfect periodicity and the residual. Here, the field in $y > g(x)$ is expressed as

$$\begin{aligned} \psi(x, y) &= e^{i(k_x x - \sqrt{k_s^2 - k_x^2} y)} \\ &+ \frac{1}{k_d} \int_{-k_d/2}^{k_d/2} \bar{\mathbf{x}}(x; \xi)^t \bar{\mathbf{P}}_{s,1}^{(+)}(\xi) \bar{\mathbf{V}}_s^{(+)}(\xi, y - g(x)) \left(\bar{\mathbf{a}}_s^{(g,+)}(\xi, 0) + \bar{\mathbf{a}}_s^{(c,+)}(\xi, 0) \right) d\xi \end{aligned} \quad (6)$$

where the superscripts g and c in parentheses indicate that the coefficient matrices are respectively related to the scattered field from the periodic surface without cylinders and the residual field. On the other hand, the field in $y < g(x)$ but outside the cylinders is expressed as

$$\begin{aligned} \psi(x, y) &= \sum_{m=1}^M \mathbf{g}_b^{(H^{(1)})}(x - x_{c,m}, y - y_{c,m})^t \mathbf{b}_m^{(c)} \\ &+ \frac{1}{k_d} \int_{-k_d/2}^{k_d/2} \bar{\mathbf{x}}(x; \xi)^t \bar{\mathbf{P}}_{b,1}^{(-)}(\xi) \bar{\mathbf{V}}_b^{(-)}(\xi, y - g(x)) \left(\bar{\mathbf{a}}_b^{(g,-)}(\xi, 0) + \bar{\mathbf{a}}_b^{(c,-)}(\xi, 0) \right) d\xi \end{aligned} \quad (7)$$

where the first term in the right-hand side is the scattered field from the cylinders in the cylindrical-wave expansions. The bases functions are given by column matrices $\mathbf{g}_r^{(Z)}(x, y)$ whose n th-components are given as

$$\left(\mathbf{g}_r^{(Z)}(x, y) \right)_n = g_{r,n}^{(Z)}(x, y) = Z_n(k_r \rho(x, y)) e^{in\phi(x, y)} \quad (8)$$

with $\rho(x, y) = (x^2 + y^2)^{1/2}$ and $\phi(x, y) = \arg(x + iy)$, where Z specifies the cylindrical functions associating to the cylindrical-wave bases in such a way that $Z = J$ denotes the Bessel function and $Z = H^{(1)}$ denotes the Hankel function of the first kind, and $\mathbf{b}_m^{(c)}$ is a column matrix generated by the expansion coefficients for the m th-cylinder.

The first term in the right-hand side of Eq. (6) expresses the incident field and yields $\bar{\mathbf{a}}_s^{(-)}(\xi, 0)$. From Eq. (5), the coefficient matrices $\bar{\mathbf{a}}_s^{(g,+)}(\xi, 0)$ and $\bar{\mathbf{a}}_b^{(g,-)}(\xi, 0)$ are given by $\bar{\mathbf{S}}_{11}(\xi) \bar{\mathbf{a}}_s^{(-)}(\xi, 0)$ and $\bar{\mathbf{S}}_{21}(\xi) \bar{\mathbf{a}}_s^{(-)}(\xi, 0)$, respectively. Since the first term of Eq. (7) yields $\bar{\mathbf{a}}_b^{(+)}(\xi, 0)$, Eq. (5) relates $\mathbf{b}_m^{(c)}$ to $\bar{\mathbf{a}}_b^{(c,-)}(\xi, 0)$. Simultaneously, since the second term in the right-hand side of Eq. (7) gives the incident field for the cylinders, manipulation of the RTMA yields an expression of $\mathbf{b}_m^{(c)}$ by $\bar{\mathbf{a}}_b^{(g,-)}(\xi, 0) + \bar{\mathbf{a}}_b^{(c,-)}(\xi, 0)$. From these relations, we may derive a coupled system of integral-equations for $\bar{\mathbf{a}}_b^{(c,-)}(\xi, 0)$. To solve the coupled integral-equations, we introduce a discretization in the transform parameter ξ . Considering the periodicity, we take L sample points in the Brillouin zone and assume that the coupled integral-equations are satisfied at these points. Also, the integrals are approximated by an appropriate numerical integration scheme with the use of same sample points. Then we may solve equations numerically.

IV. CONCLUSIONS

This paper has presented a spectral-domain formulation of the two-dimensional electromagnetic scattering from a finite number of cylindrical objects buried under periodically corrugated surface. The present formulation was based on the C-method and the RTMA, and they were combined with the help of the PPFT. The formulation will be verified by numerical experiments on the presentation though this paper does not include the results because of the page limitation.

REFERENCES

- [1] J. Chandezon, M. T. Dupuis, G. Cornet, and D. Maystre, "Multicoated gratings: a differential formalism applicable in the entire optical region," *J. Opt. Soc. Am.*, vol. 72(7), pp. 839–846, Jul. 1982.
- [2] W. C. Chew, *Waves and Fields in Inhomogeneous Media*, Van Nostrand Reinhold, New York, 1990.
- [3] K. Watanabe and K. Yasumoto, "Two-dimensional electromagnetic scattering of non-plane incident waves by periodic structures," *Prog. Electromagn. Res.*, vol. PIER 74, pp. 241–271, 2007.
- [4] M. A. Fiaz, F. Frezza, L. Pajewski, C. Ponti, and G. Schettini, "Scattering by a circular cylinder buried under a slightly rough surface: the cylindrical-wave approach," *IEEE Transactions on Antennas and Propagation* (in press).

A CLOSED-FORM ESTIMATION OF THE MUTUAL COUPLING MATRIX APPLIED TO UNIFORM CIRCULAR ARRAYS

L.Infante⁽¹⁾, S. Mosca⁽¹⁾

⁽¹⁾Antenna Dept. Selex Sistemi Integrati
Via Tiburtina km 12.400 00131 Rome, Italy
linfante@selex-si.com stmosca@selex-si.com

Abstract

It is known that the beamforming pattern is distorted in the presence of mutual coupling unless a mutual coupling compensation technique is used. In this paper we describe a fast procedure that provides an estimation of the dominant terms of the mutual coupling matrix for uniform circular array. The proposed method is obtained by perturbing the array elements with a single generic signal impinging on it from a known direction. By properly processing the array element signals an estimation of the mutual coupling matrix is provided.

Index Terms – Mutual coupling matrix, uniform circular array, indirect approach, closed form.

I. INTRODUCTION

In uniform circular array (UCA) the knowledge of mutual coupling matrix (MCM) is a crucial point to obtain high performance digital beamforming (DBF) antenna pattern. A typical architecture of an eight elements ($N=8$) receiving only system devoted to estimation of the direction of arrival is depicted in Fig.1; each antenna element is connected to a receiver and an AD converter that provide the digitalization of the signals.

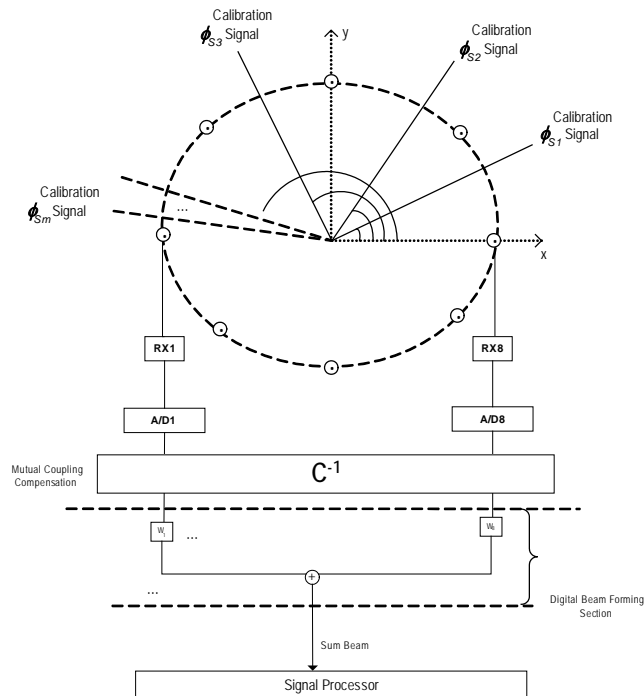


Fig. 1 Circular array architecture for DOA estimation with mutual coupling compensation and DBF section

Considering that the circular array has a radius R , the array factor related to this geometry at a generic but known angle ϕ along the azimuthal plane can be written in the form

$$\underline{AF} = \left[f_1(\phi) \exp(-jkR \cos(\phi - \phi_1)) \dots f_N(\phi) \exp(-jkR \cos(\phi - \phi_N)) \right]^T \quad (1)$$

where $\phi_n = 2\pi n/N$ according to the array geometry and $f_n(\phi)$ is the element pattern of one single element in the array. Supposing an incoming signal S_1 impinging on the array at a fixed direction ϕ_{s1} , the eight received signals by each elements after the AD converter can be written as

$$\underline{X}_{s_1} = S_1 \underline{C}_T \cdot \underline{AF}_1 \quad (2)$$

where the mutual coupling matrix \underline{C}_T including the receiver and digital section is estimated here by using an indirect approach. Once the mutual coupling matrix is known, the decoupling of the received signals is performed by applying \underline{C}_T^{-1} at the digital beam forming section and then the digital weights w_n can be applied as if the array is supposed ideal without the presence of mutual coupling. In this case, undistorted digital beams can be formed and elaborated by the signal processor.

II. MUTUAL COUPLING ESTIMATION

As described in [1] the mutual coupling matrix, can be measured via direct approach, where a network analyzer can be used to measure the self-impedance term and the mutual impedance term for each element of the array. Another way is to simulate the whole array by using a full-wave electromagnetic solver and then numerically obtain the coupling matrix [2]. These methods are called direct approaches that provide a good estimation of the effective mutual coupling phenomena via measurements or numerically. Some limitations are typical of direct approach: antenna elements must be driven in both transmitting and receiving mode, derivation of mutual coupling coefficients via network parameters requires that the feed line connecting the antenna elements are well matched, the measurement of the coupling matrix is usually done when the system is under test and not during the operative mode. This facts are big restrictions for mobile systems that require frequent calibration every time the system is deployed. To overcome the limitations of the direct approach new techniques have been developed in recent times in order to estimate the mutual coupling [3]-[4]. We call these techniques indirect approach since they use external signals impinging on the array while it is driven in its operative mode. These solutions have the advantage that can be performed on site while the systems is operative and are applicable to non reciprocal systems.

As suggested in [3]-[4], the mutual coupling matrix can be estimated by considering a set of M signals received by the array elements and minimize the following cost functional defined as

$$O(\underline{C}_T, S_1, S_2, \dots, S_M) = \min \sum_{m=1}^M \left\| \underline{X}_{s_m} - S_m \underline{C}_T \cdot \underline{AF}_m \right\|_2^2 \quad (3)$$

The estimation of a full rank mutual coupling matrix can be provided by iterative Quasi-Newton optimization method that requires large cpu time to find an accurate solution. This method provides a more and more accurate estimation of the MCM supposed that the incoming signals are a sufficient set, usually greater than the number of elements in the array, and impinging the array from very different angles. Both these capabilities can be achieved by using a rotating array and a transmitting probe located in the far-zone of the array. In the case of a not-rotating array the number of external transmitting probes should be increased up to the number of array elements. In those cases where it is not possible to use a large number of probes or a rotating array another strategy must be adopted. A quick estimation of the dominant

terms of the mutual coupling matrix can be provided in closed form by using some typical proprieties of the mutual coupling matrix in UCA.

It is possible to solve the previous non-linear system in closed form by considering the symmetry ($C_{ij} = C_{ji}$) and circular propriety of the mutual coupling matrix and considering that the dominant coupling coefficients extend over four adjacent element surrounding the active element while the remaining coupling coefficients are set to zero. Another assumption made is that the elements performs the same coupling coefficients taken diagonal-wise (Toeplitz propriety). Under these assumptions the unknowns reduce to the terms C_{11} , C_{21} and C_{31} of the MCM, that can be rewritten as

$$\underline{\underline{C}}_T = \begin{bmatrix} C_{11} & C_{21} & C_{31} & 0 & 0 & 0 & C_{31} & C_{21} \\ C_{21} & C_{11} & C_{21} & C_{31} & 0 & 0 & 0 & C_{31} \\ C_{31} & C_{21} & C_{11} & C_{21} & C_{31} & 0 & 0 & 0 \\ 0 & C_{31} & C_{21} & C_{11} & C_{21} & C_{31} & 0 & 0 \\ 0 & 0 & C_{31} & C_{21} & C_{11} & C_{21} & C_{31} & 0 \\ 0 & 0 & 0 & C_{31} & C_{21} & C_{11} & C_{21} & C_{31} \\ C_{31} & 0 & 0 & 0 & C_{31} & C_{21} & C_{11} & C_{21} \\ C_{21} & C_{31} & 0 & 0 & 0 & C_{31} & C_{21} & C_{11} \end{bmatrix} \quad (4)$$

By expressing the dominant tri-diagonal terms as $C_{11} = x$, $C_{21} = y$ and $C_{31} = z$ we can reformulate (3) as

$$\begin{cases} \min \sum_{m=1}^M \left\| \underline{X}_{s_m} - S_m \underline{\underline{C}}_T \cdot \underline{AF}_m \right\|^2 \\ \text{where } \underline{\underline{C}}_T = x \underline{I} + y \underline{\underline{C}}_1 + z \underline{\underline{C}}_2 \end{cases} \quad (5)$$

Where \underline{I} is the identity matrix and $\underline{\underline{C}}_1$ and $\underline{\underline{C}}_2$ can be written as

$$\underline{\underline{C}}_1 = \begin{bmatrix} 0 & 1 & 0 & 0 & 0 & 0 & 0 & 1 \\ 1 & 0 & 1 & 0 & 0 & 0 & 0 & 0 \\ 0 & 1 & 0 & 1 & 0 & 0 & 0 & 0 \\ 0 & 0 & 1 & 0 & 1 & 0 & 0 & 0 \\ 0 & 0 & 0 & 1 & 0 & 1 & 0 & 0 \\ 0 & 0 & 0 & 0 & 1 & 0 & 1 & 0 \\ 0 & 0 & 0 & 0 & 0 & 1 & 0 & 1 \\ 1 & 0 & 0 & 0 & 0 & 0 & 1 & 0 \end{bmatrix} \quad \underline{\underline{C}}_2 = \begin{bmatrix} 0 & 0 & 1 & 0 & 0 & 0 & 1 & 0 \\ 0 & 0 & 0 & 1 & 0 & 0 & 0 & 1 \\ 1 & 0 & 0 & 0 & 1 & 0 & 0 & 0 \\ 0 & 1 & 0 & 0 & 0 & 1 & 0 & 0 \\ 0 & 0 & 1 & 0 & 0 & 0 & 1 & 0 \\ 0 & 0 & 0 & 1 & 0 & 0 & 0 & 1 \\ 1 & 0 & 0 & 0 & 1 & 0 & 0 & 0 \\ 0 & 1 & 0 & 0 & 0 & 1 & 0 & 0 \end{bmatrix} \quad (6)$$

by defining

$$\begin{aligned} \underline{\underline{K}}_m &= [S_m \underline{AF}_m \underline{I}, S_m \underline{AF}_m \underline{\underline{C}}_1, S_m \underline{AF}_m \underline{\underline{C}}_2] \\ \underline{V} &= [x, y, z]^T \end{aligned} \quad (7)$$

(5) can be written in the form

$$\sum_{m=1}^M \left\| \underline{X}_{s_m} - \underline{\underline{K}}_m \underline{V} \right\|^2 \quad (8)$$

Showed that the function is quadratic and convex with respect to \underline{V} we can solve the Least-Square (LS) problem by using the pseudo-inverse formulation

$$\underline{V}_{LS} = \left(\sum_{m=1}^M \underline{\underline{K}}_m^T \underline{\underline{K}}_m \right)^{-1} \left(\sum_{m=1}^M \underline{\underline{K}}_m^T \underline{X}_{s_m} \right) \quad (9)$$

Thus the LS estimation of the MCM can written as

$$\underline{\underline{C}}_{LS} = V_{LS}(1)\underline{\underline{I}} + V_{LS}(2)\underline{\underline{C}}_1 + V_{LS}(3)\underline{\underline{C}}_2 \quad (10)$$

The closed form expression of the LS problem has been checked for the eight elements array in two particular cases reported in Fig. 2a-b, showing the effectiveness of the proposed method in the case where nine signals are incident on the array (Fig.2a) with respect to one single signal (Fig.2b).

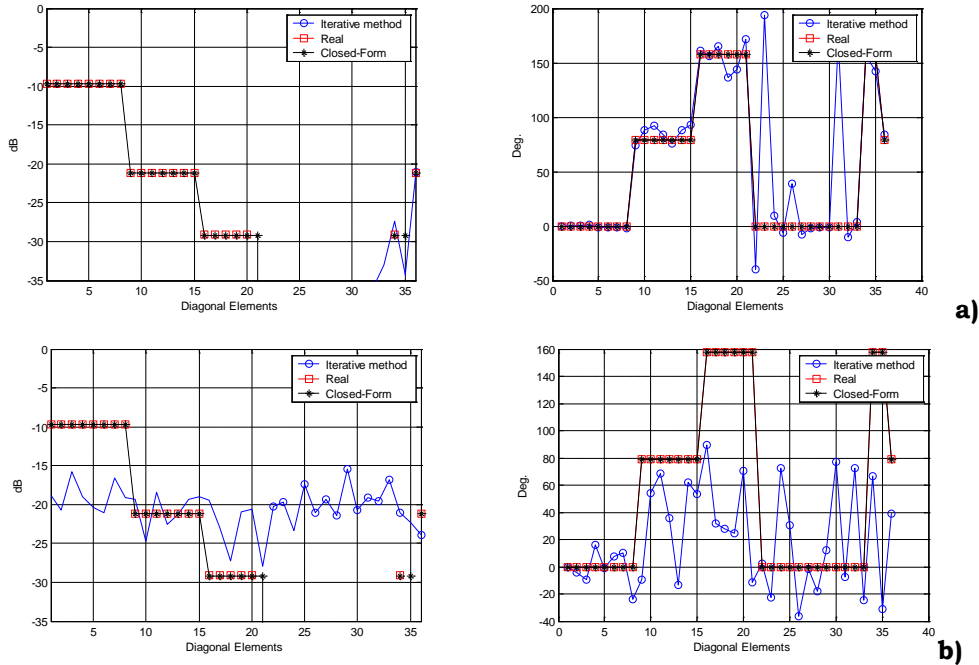


Fig. 2 Amplitude and Phase of the elements of the mutual coupling upper-matrix grouped diagonal-wise evaluated by using iterative (blu-line) and closed-form (black-line) methods for the case of **a)** nine signals located at $\phi=[11.25^\circ,47^\circ, 175^\circ,145.7^\circ, 153.2^\circ,211.25^\circ,254.4^\circ,275.8^\circ,361.23^\circ]$ and **b)** one signal at $\phi=[11.25^\circ]$

III. CONCLUSION

In the present paper we have proposed a fast method to estimate the dominant coupling coefficients of UCA by means of indirect approach. The strength of the proposed method lies under some typical proprieties of the mutual coupling matrix of circular array. In all those cases where it is not possible to get a large number of calibration signals the proposed method becomes more and more applicable. The proposed method is theoretically as well experimentally under investigation at the Antenna Dept. of Selex-SI Rome plant.

REFERENCES

- [1] H.Steyskal and J.S. Herd, "Mutual Coupling Compensation in Small Array Antennas," IEEE Trans. On Antennas and Propagation, Vol. 38, No.12, pp.1971-1975, Dec. 1990
- [2] Z.Huang, C.A. Balanis and C.R. Birtcher, "Mutual Coupling Compensation in UCAs: Simulations and Experiment", IEEE Trans. On A. and P. Vol. 54 No.11, Nov. 2006
- [3] M. Malanowsky, K. Kulpa, "Digital Beamforming for Passive Coherent Location Radar", IEEE Radar Conference 2008
- [4] F. Belfiori, S. Monni, W. Van Rossum, P. Hoogeboom "Mutual Coupling Compensation Applied to a Uniform Circular Array" Radar Symposium (IRS), 2010 11th International

A PHASE-CENTER STUDY OF FABRY-PÉROT CAVITY ANTENNAS

P. Burghignoli⁽¹⁾

⁽¹⁾ Department of Information Engineering, Electronics and Telecommunications, Sapienza University of Rome
Via Eudossiana 18, 00184 Rome, Italy
burghignoli@die.uniroma1.it

Abstract

The phase center is studied for Fabry-Pérot cavity antennas viewed as two-dimensional leaky-wave radiators, adopting both local and global definitions. Closed-form expressions are obtained for the phase-center location of broadside pencil beams, as a function of the attenuation constant of the leaky mode responsible for radiation and of the extension of the angular sector of interest. Numerical results that validate the proposed formulas are given for specific antenna structures.

Index Terms – Phase center, Fabry-Pérot cavity antennas, leaky-wave antennas, reflector antennas.

I. INTRODUCTION

Fabry-Pérot Cavity Antennas (FPCAs), comprised of a planar cavity delimited by a metal ground plane and a Partially Reflecting Surface (PRS), have a number of attractive features (e.g., feed simplicity, high directivity, low profile and cost) and have received considerable attention in the last decade (see, e.g., [1]-[3]).

In this contribution the main results of a phase-center (PC) study of FPCAs are reported, obtained adopting a leaky-wave model for their radiation mechanism [4]. In particular, analytical expressions are derived for the PC location in FPCAs radiating pencil beams at broadside, as a function of the relevant leaky-mode attenuation constant and of the extension of the angular region of interest. These may find application, e.g., in reflector antenna systems where the FPCA constitutes the feed, as recently proposed in [5].

II. ANALYSIS

As first shown in [6], directivity enhancement through the use of PRSs can be explained in terms of radiation from cylindrical leaky waves excited by the antenna feed placed inside the FP cavity. When the FPCA is designed to radiate a broadside pencil beam, the feed excites a pair of TE and TM leaky modes with the same phase and attenuation constants; the resulting co-polar far-field pattern is then, assuming the z axis as the broadside direction and standard spherical coordinates [7],

$$E_{\text{co}} = \left(\cos^2 \phi \cos \theta + \sin^2 \phi \right) \frac{2j\hat{\alpha}^2}{\sin^2 \theta + 2j\hat{\alpha}^2} \quad (1)$$

where $\hat{\alpha}$ is the leaky-mode attenuation constant normalized with respect to the free-space wavenumber k_0 . From (1) we have, for the antenna phase pattern,

$$\Psi = \Psi(\theta) = \arctan\left(\frac{\sin^2 \theta}{2\hat{\alpha}^2}\right) \quad (2)$$

which is strictly omnidirectional.

The PC of an antenna can be calculated adopting different approaches. A *local* approach defines the PC as the center of curvature of equiphase surfaces in the far field in the observation direction. For an omnidirectional broadside beam the PC is located on the z axis and it results $k_0 z_{\text{PC}} = -\Psi''(0)$, hence from (2) we find

$$\frac{z_{\text{PC}}}{\lambda_0} = -\frac{1}{2\pi\hat{\alpha}^2} \quad (3)$$

An alternative, *global* approach defines the PC as the phase reference point that minimizes the phase-pattern variance inside an angular region of interest Ω . For an omnidirectional broadside phase pattern and a conical region $\Omega \equiv \{0 \leq \theta \leq \theta_0\}$ it results (the derivation is omitted for brevity)

$$k_0 z_{\text{PC}} = \frac{12}{(1 - \cos \theta_0)^3} \int_0^{\theta_0} [\Psi(\theta) - \bar{\Psi}] \sin \theta \cos \theta \, d\theta \quad (4)$$

where the overbar stands for mean value. Once (2) is inserted into (4), the integral can be evaluated analytically, thus resulting in a closed-form formula for the PC location as a function of both $\hat{\alpha}$ and θ_0 :

$$\frac{z_{\text{PC}}}{\lambda_0} = -\frac{3}{\pi(1 - \cos \theta_0)^3} \left[f_1(\sin^2 \theta_0, \hat{\alpha}) - f_1(0, \hat{\alpha}) + f_2(1, \hat{\alpha}) - f_2(\cos^2 \theta_0, \hat{\alpha}) \right] \quad (5)$$

where

$$\begin{aligned} f_1(u, \hat{\alpha}) &= u \arctan\left(\frac{u}{2\hat{\alpha}^2}\right) - \hat{\alpha}^2 \ln(4\hat{\alpha}^2 + u^2) \\ f_2(u, \hat{\alpha}) &= (-1)^{1/4} \left[\sqrt{-j + 2\hat{\alpha}^2} \arctan\left(\frac{(-1)^{1/4} u}{\sqrt{-j + 2\hat{\alpha}^2}}\right) \right. \\ &\quad \left. + j\sqrt{j + 2\hat{\alpha}^2} \arctan\left(\frac{(-1)^{3/4} u}{\sqrt{j + 2\hat{\alpha}^2}}\right) \right] + u \arctan\left(\frac{1 - u^2}{2\hat{\alpha}^2}\right) \end{aligned} \quad (6)$$

III. RESULTS

In Fig. 1, amplitude and phase co-polar radiation patterns in the principal planes are reported for an FPCA designed to radiate a broadside beam at $f = 10$ GHz, comprised of an air cavity and a dielectric PRS with $\epsilon_r = 15$, excited by a horizontal electric dipole placed in the middle of the cavity. The exact patterns are in good agreement with the approximate ones calculated with (1), where the normalized attenuation constant of the leaky mode responsible for radiation has been estimated through the approximate formula $\hat{\alpha} \cong 1 / \sqrt{\pi\epsilon_r}$ [6].

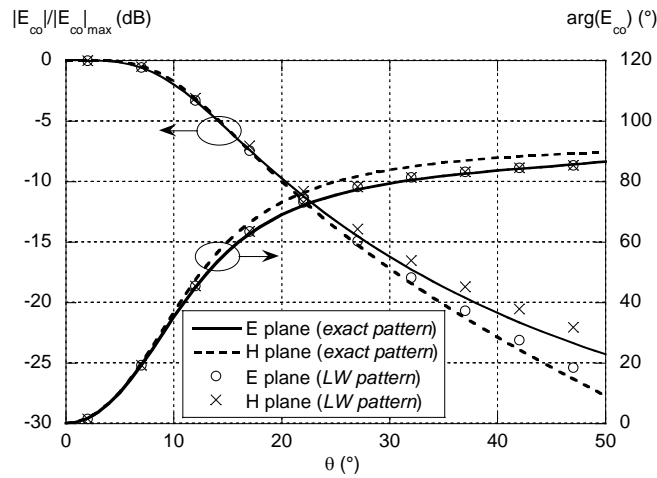


FIG. 1 – Normalized radiation patterns in the principal planes, both in amplitude and phase, for the co-polar component of the electric field radiated by a substrate-superstrate FPCA: comparison between the exact pattern and the leaky-wave (LW) approximate pattern (1).

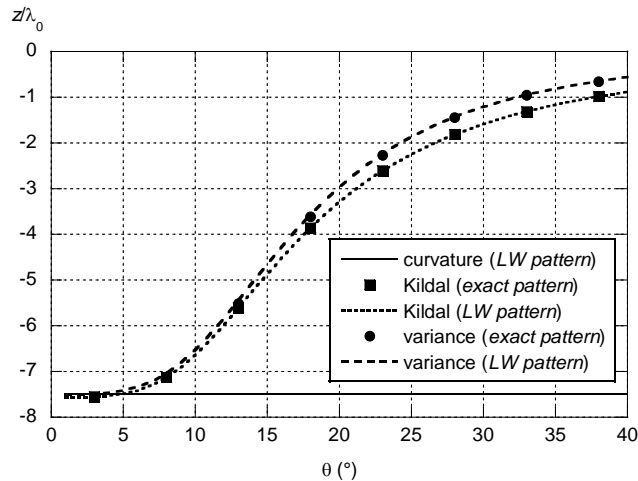


FIG. 2 – PC location for a substrate-superstrate FPCA as a function of the half-angle θ_0 : comparison between results obtained with different PC definitions using both the exact pattern and the leaky-wave (LW) approximate phase pattern (2).

In Fig. 2, results are reported for the PC location calculated with *i)* the curvature-based formula (3); *ii)* the well-known Kildal's definition (using the refined approach proposed by Rao and Shafai in [8]); and *iii)* via minimization of the phase-pattern variance. For the latter two approaches, both the exact antenna pattern and the approximate leaky-wave pattern (1) have been employed. A very good agreement can be observed between the global definition based on minimization of the phase-pattern variance (both calculated numerically with the exact pattern and through the proposed analytical formula (5)) and Kildal-Rao reference results. The local definition for the PC is instead valid only in the limit $\theta_0 \rightarrow 0$, i.e., for very small angular regions, as expected.

I. CONCLUSION

The global formula for the phase-center location based on the minimization of the phase-pattern variance is in good agreement with the standard Kildal's formula and produces accurate results also for wide angular regions, thus providing a useful design tool for reflector antenna systems. Further extensions of this work may concern, e.g., Fabry-Pérot cavity antennas radiating scanned conical beams.

REFERENCES

- [1] A. P. Feresidis and J. C. Vardaxoglou, "High gain planar antenna using optimised partially reflective surfaces," *IEE Proc. Microw. Antennas Propag.*, vol. 148(6), pp. 345-350, Dec. 2001.
- [2] R. Sauleau, P. Coquet, T. Matsui, and J.-P. Dan, "A new concept of focusing antennas using plane parallel Fabry-Perot cavities with nonuniform mirrors," *IEEE Trans. Antennas Propag.*, vol. 51(11), pp. 3171-3175, Nov. 2003.
- [3] H. Boutayeb, K. Mahdjoubi, A.-C. Tarot, and T. A. Denidni, "Directivity of an antenna embedded inside a Fabry-Perot cavity: Analysis and design," *Microw. Opt. Tech. Lett.*, vol. 48(1), pp. 12-17, Jan. 2006.
- [4] P. Burghignoli, "A leaky-wave analysis of the phase center in Fabry-Pérot cavity antennas," *IEEE Trans. Antennas Propag.*, vol. 60(5), pp. 2226-2233, May 2012.
- [5] N. Llombart, A. Neto, G. Gerini, M. Bonnedal, and P. De Maagt, "Leaky wave enhanced feed arrays for the improvement of the edge of coverage gain in multibeam reflector antennas," *IEEE Trans. Antennas Propag.*, vol. 56(5), pp. 1280-1291, May 2008.
- [6] D. R. Jackson and A. A. Oliner, "A leaky-wave analysis of the high-gain printed antenna configuration," *IEEE Trans. Antennas Propag.*, vol. AP-36(7), pp. 905-910, Jul. 1988.
- [7] A. Ip and D. R. Jackson, "Radiation from cylindrical leaky waves," *IEEE Trans. Antennas Propag.*, vol. 38(4), pp. 482-488, Apr. 1990.
- [8] K. S. Rao and L. Shafai, "Phase center calculations of reflector antenna feeds," *IEEE Trans. Antennas Propag.*, vol. AP-32(7), pp. 740-742, Jul. 1984.

AN ANALYTICAL MODEL TO QUANTIFY THE EFFICIENCY OF ARRAYS COMPOSED BY HIGH-GAIN REFLECTOR ANTENNAS

M. Cametti⁽¹⁾, M. Bozzi⁽¹⁾, M. Pasian⁽¹⁾, L. Perregrini⁽¹⁾

⁽¹⁾ Dipartimento di Ingegneria Industriale e dell'Informazione, University of Pavia, Via Ferrata 1, 27100 Pavia, Italy, marta.cametti@unipv.it

Abstract

Arrays composed by high-gain reflector antennas used for deep space communications require a precise knowledge of the degradation that phase, amplitude and pointing fluctuations impose on the capability of the array to combine coherently the signal received from each antenna.

In this paper an analytical model for the fluctuation of each parameter (phase, amplitude and pointing) is derived and it is used to predict the efficiency of an array composed by an arbitrary number of high-gain reflector antennas. The analytical models are verified by numerical simulations of an array designed for future upgrades of the European Space Agency ground segment.

Index Terms – antenna array, array efficiency, reflector antenna, excitation coefficient

I. INTRODUCTION

A key parameter of antennas used as ground station for deep space application is the antenna gain. To this aim, reflector antennas are widely adopted due to their large gain. However, practical limits to the maximum antenna diameter exist because for large dishes it is extremely difficult to provide a proper surface shape (e.g. parabolic reflectors) because of the gravity-induced loads. For this reason, arrays composed by reflector antennas are adopted when very high gains are required. Examples of arrays of reflector antennas already operating or under constructions are available in the literature [1-4]. All previous arrays have been primarily built for radio-astronomical purposes, although the potential benefit that an array of reflector antennas can provide to deep space communications was promptly recognized since the first deep space missions in the Seventies [5]. However, arrays are not yet fully exploited as ground station mainly due to the difficulties to achieve a good coherence between the antennas for all operating scenarios (e.g. strong atmospheric turbulence, rains, low elevation angles). In fact, ground stations must usually guarantee a time availability significantly higher than for radio telescopes. Nevertheless, all major space agencies, including NASA and ESA are funding projects aimed to analyze the feasibility of arrays of reflector antennas specifically devoted to deep space communications [6, 7]. For these reasons, it is important to develop analytical tools able to predict the level of coherence achievable for a given array.

This paper derives three analytical models for all possible sources of coherence degradation (i.e. phase, amplitude and pointing fluctuations), directly applicable to arrays composed by high-gain elements separated by multi-wavelength distances. In order to verify the analytical approach, the expected array degradation is also calculated by means of numerical simulation tools for a practical test case, currently proposed as possible future ground station for ESA.

II. ANALYTICAL FORMULATION

The gain of a generic antenna can be expressed by [8]:

$$G \approx \frac{4\pi}{2\eta_0} \frac{|r\bar{E}_0|^2}{P} \quad (1)$$

where E_0 is the electric field calculated at a distance r from the source, P is the input power and η_0 is the vacuum impedance. If high-gain reflector antennas are assumed, neglecting any mutual coupling between them, the array gain of N antennas can be written as:

$$G_{array} \approx \frac{4\pi}{2\eta_0} \frac{|r(\bar{E}_1 + \bar{E}_2 + \dots + \bar{E}_N)|^2}{P_1 + P_2 + \dots + P_N} \quad (2)$$

where E_i is the electric field generated by the i -th antenna and P_i is the input power at the i -th antenna. In order to introduce phase, amplitude and pointing errors, it is useful to express the electric field and the power associated with each antenna as function of a generic excitation coefficient. According to this formulation, the following equations hold:

$$\bar{E}_i = C_i \bar{E}_0 \quad C_i = A_i e^{j\varphi_i} f(\theta_i) \quad P_i = \frac{1}{2} \text{Re}\{Z_0\} |I_0|^2 A_i^2 \quad (3)$$

where A_i is the amplitude error (ranging from one to zero), φ_i is the phase error, $f(\theta_i)$ is a function accounting for the pointing error, I_0 and Z_0 are the input current and the input impedance of the antenna, respectively. Now, substituting (3) into (2) the generic array gain of N antennas affected by any kind of phase, amplitude or pointing errors, is obtained:

$$G_{array} \approx \frac{4\pi}{2\eta_0} \frac{2|r\bar{E}_0(A_1 e^{j\varphi_1} f(\theta_1) + \dots + A_N e^{j\varphi_N} f(\theta_N))|^2}{\text{Re}\{Z_0\} |I_0|^2 (A_1^2 + \dots + A_N^2)} \quad (4)$$

Eq. (4) is now re-arranged for three different cases, considering phase errors only ($A_i=1$; $f(\theta_i)=1$), amplitude errors only ($\varphi_i=1$; $f(\theta_i)=1$) and pointing errors only ($A_i=1$; $\varphi_i=1$). Three equations describing the array gain degradation versus phase, amplitude or pointing errors in terms of statistical formulation are obtained (mathematical steps are omitted for brevity):

$$\chi_f \approx 1 - \sigma_\varphi^2 \quad \chi_a \approx 1 - \frac{\sigma_A^2}{P} \quad \chi_p \approx 1 - 2\alpha(\sigma_\theta^{RMS})^2 \quad (5)$$

where σ_φ is the standard deviation for phase errors, σ_A is the standard deviation for amplitude errors, σ_θ^{RMS} is the root mean square (RMS) for pointing errors; χ_f , χ_a and χ_p are the array degradation (scalar real number from zero to one) for phase, amplitude and pointing errors, respectively; α is a scalar coefficient accounting for the beamwidth of the antenna and P is the mean power reduction suffered by the array:

$$\bar{P} = \frac{\sum_{i=1}^N A_i^2}{N} \quad (6)$$

III. TEST-CASE

An array of twelve 20m antennas is chosen as test case. This is the output of a detailed feasibility study promoted by ESA aimed to address all aspects related to a possible enhancement of the performances of the current single dish DS antennas [7]. The proposed array layout depicted in Fig. 1 (all the antennas aligned in north-south direction spaced 60 m apart) is a compromise between minimizing shadowing effects (by placing the antennas as far as possible) and maximize the signal correlation (amplitude and phase fluctuations due to bad weather conditions mitigated by placing the antennas as close as possible).

The proposed array is numerically simulated in order to verify the analytical formulation derived in section II. The radiated field generated by each 20-m antenna is calculated at 8.4 GHz by means of a commercial tool based on physical optics [9] and the array radiation pattern is calculated as the sum of the radiated field generated by each antenna (thus assuming that no mutual coupling is present between antennas, as per section II). To simulate phase, amplitude and pointing errors, a Montecarlo analysis is carried on, assigning a random phase/amplitude/pointing to each antenna excitation. The results are reported in Fig. 2.

For phase fluctuations, the maximum error can be around 30 degrees [10]. The agreement with numerical simulations can be considered good, with a maximum discrepancy of 0.2–0.3 dB.

For amplitude fluctuations, the maximum error can be around 50% (i.e. 3 dB less than nominal power) [11]. Three analytical curves are shown, each with a different mean power reduction \bar{P} (1, 0.6 and 0.5). In fact, the same amplitude fluctuation (i.e. the same standard deviation σ_A) returns different losses according to the mean power reduction \bar{P} . In particular, a top and a bottom limiting curve can be retrieved. The top curve is always associated with a mean power reduction \bar{P} equal to unity. Of course, this is an ideal asymptotic case ($\bar{P} = 1$ means no power reduction at all). The bottom curve depends on the distribution of the numerical simulation. For the case reported in Fig. 2, where the power collected by each antenna can be reduced to 50% of the nominal value, a mean power reduction \bar{P} equal to 0.5 represents the worst case condition. All other cases (e.g. $\bar{P} = 0.6$) indicates intermediate cases.

For pointing fluctuations, the maximum error can be 5 mdeg [12]. The agreement with numerical simulations can be considered good, with a slight discrepancy due to the polynomial approximation ($\alpha = 90 \text{ deg}^{-2}$) adopted to represent the 20-m antenna radiation pattern. Please note that for pointing errors the RMS is best suited (instead of standard deviation as for phase and amplitude errors) to take into account that an identical de-pointing for each antenna causes an array gain reduction (while an identical phase or amplitude value for each antenna does not).

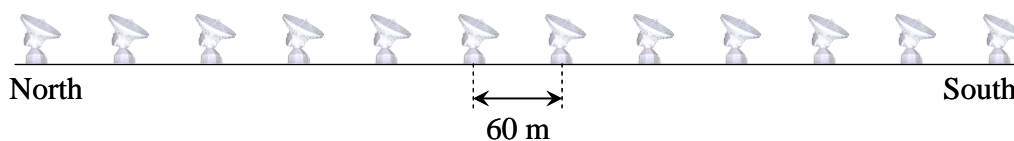


FIG. 1 - Proposed array layout composed by twelve 20-m antennas.

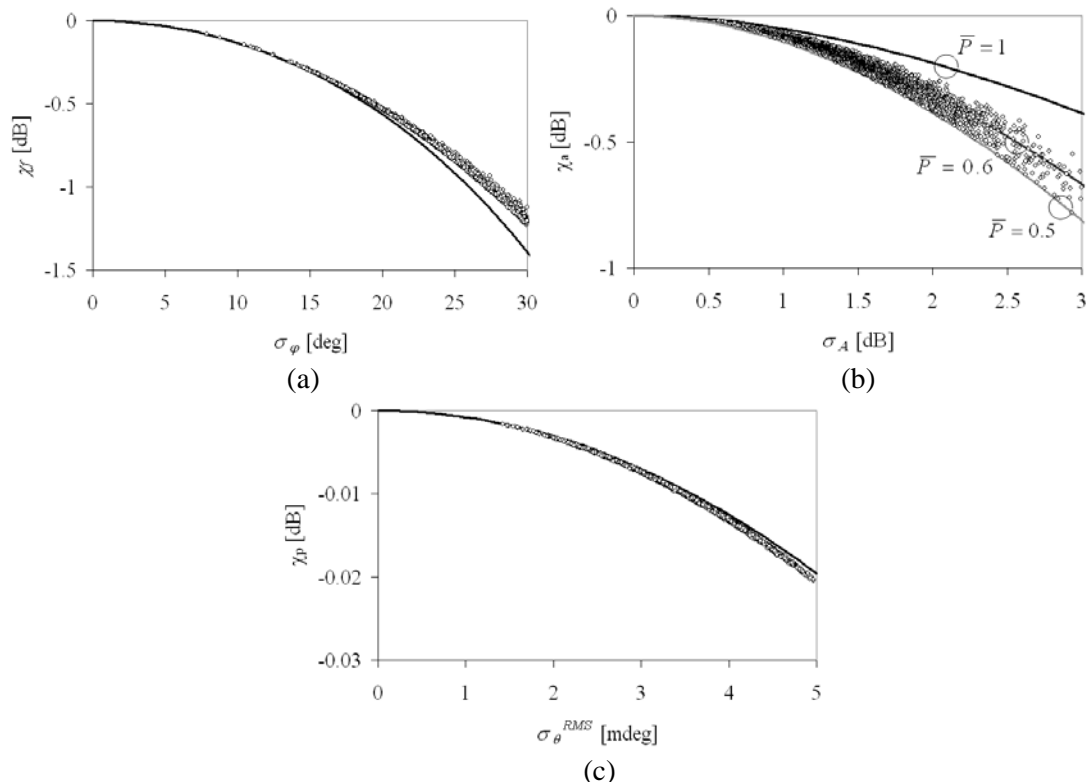


FIG. 2 - Array gain degradation at 8.4 GHz, comparison between analytical formulation (solid curves) and numerical simulation (dots). (a) phase errors; (b) amplitude errors; (c) pointing errors.

IV. CONCLUSION

This paper presented the analytical formulation adopted to describe the array gain degradation of array composed by high-gain reflector antennas. The mathematical models are verified by numerical simulations for a test case designed for future upgrades of the ESA ground segment.

V. REFERENCES

- [1] J. S. Ulvestad *et al.*, *The Very Large Array Observational Status Summary*, 2009.
- [2] ATA official website: <http://www.seti.org/ata>.
- [3] ALMA official website: <https://science.nrao.edu/facilities/alma>.
- [4] ATCA official website: <http://www.narrabri.atnf.csiro.au>.
- [5] W. A. Imbriale, *Large Antennas of the Deep Space Network*, U.S.A., Wiley, 2003.
- [6] R.J. Cesarone *et al.*, "Prospects for a Next-Generation Deep-Space Network," *Proceedings of the IEEE*, vol.95, no.10, pp.1902-1915, Oct. 2007.
- [7] S. Marti *et al.*, "Future Architectures for ESA Deep Space Ground Station Antennas," *EuCAP 2011*, Rome, Italy, April 11-15, 2011.
- [8] C. A. Balanis, *Antenna Theory, Analysis and Design*, U.S.A., Wiley, 2005.
- [9] GRASP9 official website: www.ticra.com.
- [10] F. Davarian, "Uplink Arraying Next Steps," *IPN Progress Report 42-175*, Nov. 2008.
- [11] A. Rogister *et al.*, "RAPIDS: RAdio Propagation Integrated Database System", *Meeting and Joint Workshop with COST272*, ESTEC, May 2003.
- [12] E. Vassallo *et al.*, "The European Space Agency's Deep-Space Antennas," *Proceedings of the IEEE*, vol.95, no.11, pp.2111-2131, Nov. 2007.

NONLOCAL TRANSFORMATION OPTICS

G. Castaldi⁽¹⁾, V. Galdi⁽¹⁾, A. Alù⁽²⁾, N. Engheta⁽³⁾

⁽¹⁾ CNR-SPIN and Waves Group, Department of Engineering, University of Sannio
Corso Garibaldi 107, I-82100, Benevento, Italy

castaldi@unisannio.it, vgaldi@unisannio.it

⁽²⁾ Dept. of Electrical and Computer Engineering, The University of Texas at Austin
1 University Station, C0803, Austin, TX 78712, USA

alu@mail.utexas.edu

⁽³⁾ Department of Electrical and Systems Engineering, University of Pennsylvania 200
South 33rd Street, Room 215, Moore Building, Philadelphia, PA 19104, USA

engheta@ee.upenn.edu

Abstract

We review our recently introduced nonlocal transformation optics framework based on coordinate transformations in the spectral (wavenumber) domain. Our approach allows a physically-incisive and powerful geometrical interpretation in terms of deformation of the equi-frequency contours, and may pave the way to new intriguing developments in dispersion engineering of electromagnetic metamaterials.

Index Terms \square Metamaterials, spatial dispersion, transformation optics.

I. INTRODUCTION

Transformation optics (TO), based on the form-invariant properties of coordinate-transformed Helmholtz [1] and Maxwell's equations [2], has rapidly established itself as a very powerful and versatile framework for designing metamaterials with prescribed field manipulation capabilities (see, e.g., [3] for a recent review). In spite of the several extensions and generalizations (see, e.g., [4]–[6]) insofar proposed, attention and applications have been essentially focused on *local* effects.

In a recent study [7], we have extended the potential of this approach by enabling the manipulation and control of *nonlocal* light-matter interactions [8,9], which are becoming increasingly relevant in metamaterial modeling and applications (see, e.g., [10-15]). In order to engineer desired *nonlocal* field manipulation effects, our approach is based on coordinate transformations in the *spectral* (wavenumber) domain, rather than in the conventional spatial domain.

II. SUMMARY OF NONLOCAL TO FRAMEWORK

We start from the algebraized form of Maxwell's curl equations in the time-harmonic $[\exp(-i\omega t)]$ spectral wavenumber domain

$$\begin{cases} i\mathbf{k}' \times \mathbf{E}'(\mathbf{k}') = i\omega\mu_0\mathbf{H}'(\mathbf{k}') - \mathbf{M}(\mathbf{k}'), \\ i\mathbf{k}' \times \mathbf{H}'(\mathbf{k}') = -i\omega\varepsilon_0\mathbf{E}'(\mathbf{k}') + \mathbf{J}(\mathbf{k}'), \end{cases} \quad (1)$$

describing the radiation of assigned electric and magnetic source distributions $(\mathbf{J}', \mathbf{M}')$ in an auxiliary vacuum space. Next, we apply a real-valued coordinate transformation to a new spectral domain \mathbf{k} ,

$$\mathbf{k}' = \underline{\underline{\Lambda}}^T(\mathbf{k}) \cdot \mathbf{k} = \mathbf{F}(\mathbf{k}), \quad (2)$$

where $\underline{\underline{\Lambda}}^T$ denotes (the transpose of) a second-rank tensor operator. Paralleling the standard (spatial-domain) TO approach [2], as we did in [7] we then exploit the form-invariant properties of Maxwell's equations in the mapped spectral domain \mathbf{k} in order to relate the corresponding fields, sources, and constitutive relationships to those in the original vacuum domain, obtaining

$$\begin{cases} \{\mathbf{E}, \mathbf{H}\}(\mathbf{k}) = \underline{\underline{\Lambda}}^{-T} \cdot \{\mathbf{E}', \mathbf{H}'\}[\underline{\underline{\Lambda}}^T \cdot \mathbf{k}], \\ \{\mathbf{J}, \mathbf{M}\}(\mathbf{k}) = \det^{-1}(\underline{\underline{\Lambda}})\underline{\underline{\Lambda}} \cdot \{\mathbf{J}', \mathbf{M}'\}[\underline{\underline{\Lambda}}^T \cdot \mathbf{k}], \\ \{\underline{\underline{\varepsilon}}, \underline{\underline{\mu}}\}(\mathbf{k}) = \det^{-1}(\underline{\underline{\Lambda}})\underline{\underline{\Lambda}} \cdot \underline{\underline{\Lambda}}^T, \end{cases} \quad (3)$$

where $\det(\cdot)$ denotes the determinant, $^{-T}$ the inverse transpose, and $\underline{\underline{\varepsilon}}, \underline{\underline{\mu}}$ the relative permittivity and permeability tensors of the generally anisotropic and *spatially-dispersive* transformation medium.

We note that the relationships in (3) correctly reproduce the standard (spatial-domain) TO results in the particular case of *linear* spectral mapping (i.e., \mathbf{k} -independent coordinate mapping), and generally yield *nonlocal* constitutive properties in the case of *nonlinear* spectral mapping. Accordingly, one can exploit the above spectral field/source transformations in order to systematically design a desired nonlocal field effect in a fictitious curved-coordinate spectral domain; such effects may be equivalently obtained in an actual physical space filled up by a spatially-dispersive transformation medium whose constitutive “blueprints” are explicitly given in (3).

Our spectral-domain TO approach admits a geometrical interpretation in terms of tailoring the dispersion characteristics via deformation of the *equi-frequency contours* (EFCs), which allows direct manipulation of the kinematical (wavevector and velocity) properties of the wave propagation and reflection/refraction [16]. Assuming an (x, z) two-dimensional (2-D) scenario, Fig. 1 exemplifies the deformation of the circular EFC pertaining to vacuum [Fig. 1(a)] $k_x'^2 + k_z'^2 = \omega^2/c_0^2$ (with c_0 denoting the corresponding speed of light) as an effect of the spectral mapping

$$F_x^2(k_x, k_z) + F_z^2(k_x, k_z) = \frac{\omega^2}{c_0^2}. \quad (4)$$

For instance, a *single-valued* mapping may yield a moderately deformed shape [cf. Fig. 1(b)], whereas a *double-valued* mapping may lead to the appearance of a *new*

branch [cf. Fig. 1(c)]. In [7], we exploited such a straightforward connection between the multi-valued character of the coordinate mapping in (4) and the presence of additional extraordinary waves was exploited in order to engineer a transformation medium with prescribed wave-splitting capabilities.

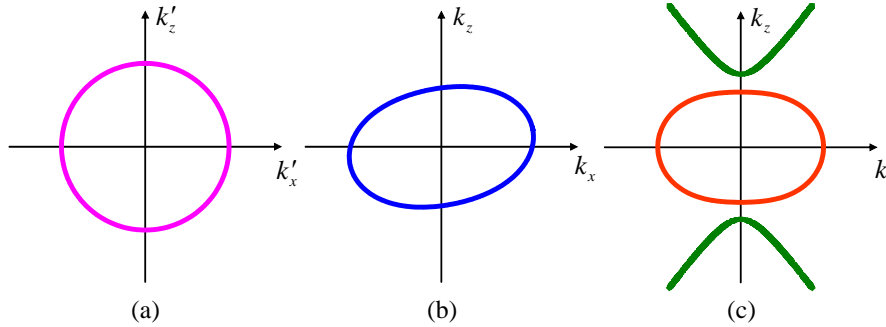


FIG. 1 (From [7]) Schematic illustration of the deformation of the circular EFC pertaining to vacuum (a) as an effect of a single-valued (b) and double-valued (c) spectral mapping (details in the text).

Moreover, for the same 2-D scenario as above, we showed in [7] that a desired *modulation transfer function* $T(k_x)$ relating the 1-D spatial spectra of the (x -dependent) aperture transverse field distributions at two z -constant planes separated by a distance d , may be in principle engineered via the spectral coordinate mapping

$$F_x(k_x) = \sqrt{\frac{\omega^2}{c_0^2} + \frac{1}{d^2} \log[T(k_x)]}, \quad F_z(k_z) = k_z. \quad (5)$$

III. CONCLUSIONS

As highlighted by the above examples, our proposed approach may open up new intriguing venues in the engineering of the spatial dispersion properties of EM metamaterials. Crucial to its practical applicability is the availability of nonlocal homogenized models as well as the synthesis of anisotropic, nonlocal artificial materials capable of approximating the arising constitutive blueprints within given frequency and wavenumber ranges. Further details, as well as an illustrative end-to-end example of application of these concepts, may be found in [7].

REFERENCES

- [1] U. Leonhardt, "Optical conformal mapping," *Science*, vol. 213(5871), pp. 1777-1780, June 2006.

- [2] J. B. Pendry, D. Schurig, and D. R. Smith, "Controlling electromagnetic fields," *Science*, vol. 312(5781), pp. 1780-1782, June 2006.
- [3] H. Chen, C. T. Chan, and P. Sheng, "Transformation optics and metamaterials," *Nature Materials*, vol. 9(5), pp. 387-396, May 2010.
- [4] L. Bergamin, "Generalized transformation optics from triple spacetime metamaterials," *Phys. Rev. A*, vol. 78(5), 043825, Oct. 2008.
- [5] S. A. Tretyakov, I. S. Nefedov, and P. Alitalo, "Generalized field-transforming metamaterials," *New J. Phys.*, vol. 10, 115028, Nov. 2008.
- [6] G. Castaldi, I. Gallina, V. Galdi, A. Alù, and N. Engheta, "Transformation-optics generalization of tunnelling effects in bi-layers made of paired pseudo-epsilon-negative/mu-negative media," *J. Opt.*, vol. 13(2), 024011, Feb. 2011.
- [7] G. Castaldi, V. Galdi, A. Alù, and N. Engheta, "Nonlocal transformation optics," *Phys. Rev. Lett.*, vol. 108(6), 063902, Feb. 2012.
- [8] P. Halevi (Ed.), *Spatial Dispersion in Solids and Plasmas*, North-Holland, Amsterdam, 1992.
- [9] V. M. Agranovich and V. Ginzburg, *Spatial Dispersion in Crystal Optics and the Theory of Excitons*, Wiley-Interscience, New York, 1966.
- [10] M. G. Silveirinha, "Generalized Lorentz-Lorenz formulas for microstructured materials," *Phys. Rev. B*, vol. 76(24), 245117, Dec. 2007.
- [11] M. Notomi, "Manipulating light with strongly modulated photonic crystals," *Rep. Progr. Phys.*, vol. 73(9), 096501, Sep. 2010.
- [12] A. Alù, "Restoring the physical meaning of metamaterial constitutive parameters," *Phys. Rev. B*, vol. 83(8), 081102R, Feb. 2011.
- [13] A. Alù, "First-principles homogenization theory for periodic metamaterials," *Phys. Rev. B*, vol. 84(7), 075153, Aug. 2011.
- [14] A. A. Orlov, P. M. Voroshilov, P. A. Belov, and Y. S. Kivshar, "Engineered optical nonlocality in nanostructured metamaterials," *Phys. Rev. B*, vol. 84(4), 045424, July 2011.
- [15] G. A. Wurtz, R. Pollard, W. Hendren, G. P. Wiederrecht, D. J. Gosztola, V. A. Podolskiy, and A. V. Zayats, "Designed ultrafast optical nonlinearity in a plasmonic nanorod metamaterial enhanced by nonlocality," *Nature Nanotechnology*, vol. 6(2), pp. 107-111, Jan. 2011.
- [16] E. H. Lock, "The properties of isofrequency dependences and the laws of geometrical optics," *Phys.-Usp.*, vol. 51(4), pp. 375-393, 2008.

ELECTROMAGNETIC SCATTERING OF AN ELLIPTICALLY-POLARIZED PLANE WAVE BY A BURIED SPHERE

F. Mangini

Department of Information Engineering, Electronics
and Telecommunications, "La Sapienza" University of Rome,
Via Eudossiana 18, 00184 Rome, Italy
mangini@diet.uniroma1.it

Abstract

A rigorous method to analyze the scattering of an elliptically-polarized plane wave by a perfectly-conducting sphere buried in a dielectric half-space, is presented. The electric field components are expanded in spherical harmonic series. The scattered-reflected field is computed through the plane-wave spectrum of the scattered field, considering the reflection of each elementary plane wave. The interaction between the scattered-reflected field and the sphere is taken into account by expanding the field in spherical harmonic series, to impose the boundary conditions on the sphere's surface. The procedure leads to an infinite linear system giving the unknown coefficients of the scattered field. To achieve a numerical solution, a Matlab code is implemented, where a suitable truncation of the system has been performed.

Index Terms – Electromagnetic scattering, buried sphere, spherical harmonics, plane-wave spectrum

I. INTRODUCTION

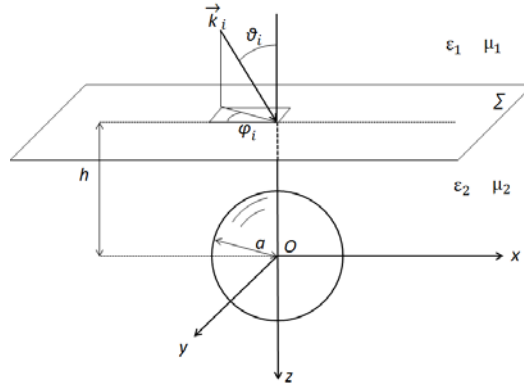
The scattering problem related to buried objects has a very wide area of applications and a huge number of publications can be found in the literature treating various aspects.

The geometry considered in this paper is shown in Fig. 1. A sphere of radius a is located at the center of a Cartesian coordinate system. The sphere is placed at a distance h below the interface between two media.

The impinging radiation is a plane wave traveling from medium 1 to medium 2, at an angle ϑ_i , with respect to the z axis, and lying on a plane passing through the z axis and forming an angle φ_i , with respect to the x axis. Let $\varepsilon_1, \mu_1, k_1$ and $\varepsilon_2, \mu_2, k_2$ be the permittivity, permeability and propagation wavenumber of the above ($z < -h$) and below ($z > -h$) media, respectively.

II. THEORETICAL ANALYSIS AND RESULTS OBTAINED

Assuming that the incident field is an elliptically-polarized plane wave with an electric field given by:


FIG. 1 – Geometry of the scattering problem.

$$\underline{E}_i(\underline{r}) = \underline{E}_{0i} e^{i\mathbf{k}_i \cdot \underline{r}} = \left(E_{\theta i} \underline{\theta}_{0i} + E_{\varphi i} \underline{\varphi}_{0i} \right) e^{i\mathbf{k}_i \cdot \underline{r}},$$

in the absence of the sphere the reflected \underline{E}_r and transmitted \underline{E}_t waves are given by

$$\begin{aligned} \underline{E}_r &= \left(R_H^{12} E_{\theta} \underline{\theta}_{0r} + R_E^{12} E_{\varphi} \underline{\varphi}_{0r} \right) e^{i\mathbf{k}_r \cdot \underline{r}} e^{-2ihk_1 \cos \theta_i} \\ \underline{E}_t &= \left(T_H^{12} E_{\theta} \underline{\theta}_{0t} + T_E^{12} E_{\varphi} \underline{\varphi}_{0t} \right) e^{i\mathbf{k}_t \cdot \underline{r}} e^{ih(k_2 \cos \theta_i - k_1 \cos \theta_t)} \end{aligned}$$

with R_E^{12} , T_E^{12} and R_H^{12} , T_H^{12} being the Fresnel reflection and refraction coefficients for parallel and perpendicular polarizations, respectively, referring to the interface between medium 1 and medium 2.

The general case of the scattering from a sphere behind an interface, can be treated [1] by the representation of the incident field as a series of regular spherical vector wave functions $\underline{M}_{mn}^{(1)}(\underline{k}_r) = \underline{m}_{mn}(\theta, \varphi) j_n(k_2 \underline{r})$ and

$$\underline{N}_n^m(\underline{k}_r) = \underline{n}_{mn}(\theta, \varphi) \frac{d[r j_n(k_2 \underline{r})]}{kr dr} + \underline{p}_{mn}(\theta, \varphi) \frac{j_n(k_2 \underline{r})}{kr} :$$

$$\underline{E}_t(\underline{r}) = \sum_{n=1}^{+\infty} \sum_{m=-n}^n a_{mn} \underline{M}_{mn}^{(1)}(\underline{k}_2 \underline{r}) + b_{mn} \underline{N}_{mn}^{(1)}(\underline{k}_2 \underline{r}) \quad (1)$$

where $j_n(k_2 \underline{r})$ are the spherical Bessel functions of the first kind.

The orthogonality of the vector spherical harmonics implies that the coefficients in the expansion may assume the following form:

$$a_{mn} = (-1)^m i^n \frac{2n+1}{n(n+1)} \frac{(n-m)!}{(n+m)!} e^{ih(k_2 \cos \theta_i - k_1 \cos \theta_t)} \left(T_H^{12} E_{\theta} \underline{\theta}_{0t} + T_E^{12} E_{\varphi} \underline{\varphi}_{0t} \right) \cdot \underline{m}_{mn}^*(\theta_t, \varphi_t)$$

$$b_{mn} = (-1)^m i^n \frac{2n+1}{n(n+1)} \frac{(n-m)!}{(n+m)!} e^{ih(k_2 \cos \theta_i - k_1 \cos \theta_t)} \left(T_H^{12} E_{\theta} \underline{\theta}_{0t} + T_E^{12} E_{\varphi} \underline{\varphi}_{0t} \right) \cdot \underline{n}_{mn}^*(\theta_t, \varphi_t)$$

The scattered field can also be expanded as [1]:

$$\underline{E}_s(\underline{r}) = \sum_{n=1}^{+\infty} \sum_{m=-n}^n e_{mn} \underline{M}_{mn}^{(3)}(\underline{k}_2 \underline{r}) + f_{mn} \underline{N}_{mn}^{(3)}(\underline{k}_2 \underline{r}) \quad (2)$$

In this case the radial functions are the spherical Hankel functions of the first kind, $h_n^{(1)}(k_2 \underline{r})$. The rest of our analysis concerns the calculation of the expansion coefficients e_{mn} and f_{mn} .

In addition to the two fields described by Eq. (1) and Eq. (2), a third field exists in the ambient medium. This field is the result of the scattered field reflecting off the surface and striking the particle: it can be described through an expansion of the scattered field in infinite plane waves traveling in various directions (α_i, β_i) , each multiplied by the appropriate Fresnel coefficient [1]:

$$\underline{E}_{sr}(\underline{r}) = \sum_{n=1}^{+\infty} \sum_{m=-n}^n \frac{i^{-n}}{2\pi} \left(e_{mn} \int_0^{2\pi\pi/2-i\infty} \int_0^{\pi/2-i\infty} \underline{E}_{Re}^{mn} e^{ik_r \cdot \underline{r}} d\alpha_i d\beta_i + f_{mn} \int_0^{2\pi\pi/2-i\infty} \int_0^{\pi/2-i\infty} \underline{E}_{Rh}^{mn} e^{ik_r \cdot \underline{r}} d\alpha_i d\beta_i \right)$$

with

$$\begin{aligned} \underline{E}_{Re}^{mn} &= e^{im\beta_i} \sin \alpha_i \left[iR_H^{21} \pi_n^m (\cos \alpha_i) \underline{\alpha}_{0r} - R_E^{21} \tau_n^m (\cos \alpha_i) \underline{\beta}_{0r} \right] e^{2ik_2 h \cos \alpha_i} \\ \underline{E}_{Rh}^{mn} &= e^{im\beta_i} \sin \alpha_i \left[iR_H^{21} \tau_n^m (\cos \alpha_i) \underline{\alpha}_{0r} - R_E^{21} \pi_n^m (\cos \alpha_i) \underline{\beta}_{0r} \right] e^{2ik_2 h \cos \alpha_i} \\ \pi_n^m &= m \frac{P_n^m (\cos \alpha_i)}{\sin \alpha_i} \quad \tau_n^m = \frac{dP_n^m (\cos \alpha_i)}{d\alpha_i} \end{aligned}$$

To determine the coefficients of the development, one must apply the boundary conditions, i.e. the cancellation of the tangential field along the surface of the sphere. It is useful to expand each plane wave in spherical harmonics:

$$\underline{E}_{sr}(\underline{r}) = \sum_{q=1}^{+\infty} \sum_{p=-q}^q \left[\underline{M}_{mn}^{(1)}(\underline{r}) \left(\sum_{n=1}^{+\infty} \sum_{m=-n}^{-n} e_{mn} C_{mn}^{pq} + f_{mn} D_{mn}^{pq} \right) + \underline{N}_{mn}^{(1)}(\underline{r}) \left(\sum_{n=1}^{+\infty} \sum_{m=-n}^{-n} e_{mn} G_{mn}^{pq} + f_{mn} H_{mn}^{pq} \right) \right]$$

with:

$$\begin{aligned} C_{mn}^{pq} &= i^{q-n} (-1)^{-q} \frac{2q+1}{q(q+1)} \frac{(q-p)!}{(q+p)!} \delta_{pm} \int_0^{\pi/2-i\infty} \left(R_H^{21} \pi_n^m \pi_p^q - R_E^{21} \tau_n^m \tau_p^q \right) \sin \alpha_i e^{2ihk_2 \cos \alpha_i} d\alpha_i d\beta_i \\ D_{mn}^{pq} &= i^{q-n} (-1)^{-q} \frac{2q+1}{q(q+1)} \frac{(q-p)!}{(q+p)!} \delta_{pm} \int_0^{\pi/2-i\infty} \left(-R_H^{21} \pi_n^m \tau_p^q + R_E^{21} \tau_n^m \pi_p^q \right) \sin \alpha_i e^{2ihk_2 \cos \alpha_i} d\alpha_i d\beta_i \\ G_{mn}^{pq} &= i^{q-n} (-1)^{-q} \frac{2q+1}{q(q+1)} \frac{(q-p)!}{(q+p)!} \delta_{pm} \int_0^{\pi/2-i\infty} \left(R_H^{21} \tau_n^m \pi_p^q - R_E^{21} \pi_n^m \tau_p^q \right) \sin \alpha_i e^{2ihk_2 \cos \alpha_i} d\alpha_i d\beta_i \\ H_{mn}^{pq} &= i^{q-n} (-1)^{-q} \frac{2q+1}{q(q+1)} \frac{(q-p)!}{(q+p)!} \delta_{pm} \int_0^{\pi/2-i\infty} \left(-R_H^{21} \tau_n^m \tau_p^q + R_E^{21} \pi_n^m \pi_p^q \right) \sin \alpha_i e^{2ihk_2 \cos \alpha_i} d\alpha_i d\beta_i \end{aligned}$$

Finally, an infinite linear system of equations is obtained for the unknown scattering coefficients of the field components, in the form:

$$\begin{pmatrix} e_{mn} \\ f_{mn} \end{pmatrix} = \begin{pmatrix} \delta_{mp} \delta_{nq} \frac{j_n(k_2 a)}{h_n^{(1)}(k_2 a)} + C_{mn}^{pq} & G_{mn}^{pq} \\ D_{mn}^{pq} & \delta_{mp} \delta_{nq} \frac{j_n(k_2 a)}{h_n^{(1)}(k_2 a)} + H_{mn}^{pq} \end{pmatrix}^{-1} \begin{pmatrix} -a_{pq} \\ -b_{pq} \end{pmatrix}$$

For numerical implementation purposes a suitable truncation criterion has been adopted, and its impact on the accuracy and the numerical efficiency of the code has been established via comparisons with analytical and numerical results reported in the literature [2]. The

truncation criterion which we propose is a Bohren-Huffman modified criterion:

$$N = x + 4x^{1/3} + 2$$

with

$$x = k_2 a (\sin \theta_i + 1) (\sin \varphi_i + 1) .$$

Moreover, the results of the method implemented in a Matlab code were compared with those of simulations done with a commercial software which implements the Finite Element Method. The comparison is presented in Fig. 2 for typical scenario of buried sphere detection.

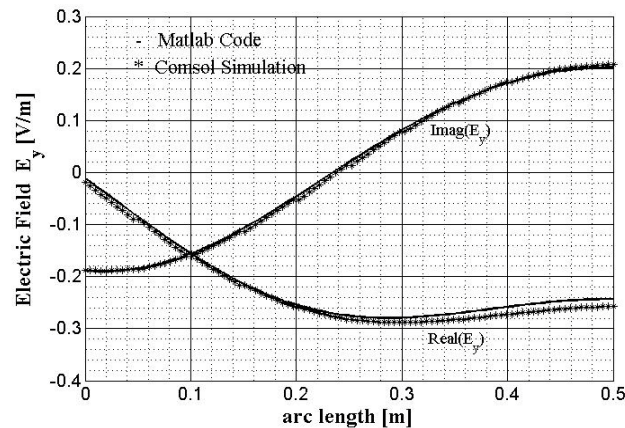


FIG. 2 – Comparison of numerical results obtained with Matlab and with Comsol simulations. A normal incidence, with electric field linearly polarized along y , on an air-glass interface, with a perfectly conducting sphere of radius $a=25$ cm buried at $h=80$ cm, is considered at 300 MHz. The scattered field is calculated along a line parallel to the x axis at a distance $2a$ from the center of the sphere. In this example, the series are truncated at $n=8$.

III. CONCLUSION

In this paper, we presented a rigorous method to determine the scattering of an elliptically-polarized plane wave by a perfectly conducting sphere buried in a dielectric ground. Comparisons with simulations performed with a commercial software showed good accordance. This method can be generalized to the case of various, conducting or dielectric buried spheres or shells in a dissipative half space, which will be object of future works. In this way, the method could found many applications in: buried objects detection, biomedical sensing, metamaterial analysis, microscopy.

REFERENCES

- [1] A. Doicu, T. Wriedt, Y.A. Eremin, *Light Scattering by Systems of Particles*, Springer, New York, 2006.
- [2] B. Esen, I. Akkaya, A.Yapar, “Scattering of a Plane Wave from a Perfectly Conducting Sphere Buried in a Conducting Dielectric,” *Electromagnetics*, vol. 24, pp. 607–621, May 2004.

Session 4 – Electromagnetic imaging techniques

M. Ferrara, P. Lucantoni, S. Mori, P. Nocito, G.M. Tosi Beleffi, E. Restuccia, F. Frezza, and F. S. Marzano

Atmospheric visibility through optical images

A. Guagliumi, M. Gnan, A. Liberato, L. De Marco, D. Bruni, F. Canini, and P. Bassi

System-level analysis and optimization of task-oriented imaging systems

D. Pinchera, M.D. Migliore, and F. Schettino

Through-wall communication by means of an ultra wide permittivity antenna (UWPA)

R. Solimene, A. D'Alterio, and R. Pierri

TWI for a lossless unknown wall

R. Scapaticci, L. Di Donato, I. Capatano, and L. Crocco

Differential microwave imaging from brain stroke monitoring

G. Bellizzi, O.M. Bucci, I. Capatano, L. Crocco, and R. Scapaticci

Advancements in microwave breast cancer imaging enhanced by magnetic nanoparticles as contrast agent

ATMOSPHERIC VISIBILITY THROUGH OPTICAL IMAGES

M. Ferrara^(1,2), P. Lucantoni^(1,2), S. Mori⁽¹⁾, P. Nocito⁽²⁾, G. M. Tosi Beleffi⁽²⁾, E. Restuccia⁽²⁾, F. Frezza⁽¹⁾, F. S. Marzano⁽¹⁾

⁽¹⁾ D.I.E.T., Sapienza University of Rome
Via Eudossiana 18, 00184 Rome, Italy
mori@die.uniroma1.it

⁽²⁾ I.S.C.O.M., Min. of Economic Development
Viale America 201, 00144 Rome, Italy
paolo.nocito@sviluppoeconomico.gov.it

Abstract

From telecommunications to transport application, visibility is a fundamental quantity to be estimated. To this end, there are many different instruments basing their estimation on measures of optical attenuation or scattering through the atmosphere. Unfortunately, this kind of instruments provides reliable results only for certain range of distances and is quite expensive. In this work is presented an experimental study on the use of a video camera for visibility estimation. Collected appraisals will be compared with a method of literature and with the measures of the attenuation of the optical carrier provided by the Free Space Optics (FSO) wide area set up realized in Rome (Italy) by DIET-Sapienza University and ISCOM-Ministry of Economic Development.

Index Terms – Free Space Optics, Visibility.

I. INTRODUCTION

Aim of this work is emulate the behavior of the human eye in visibility estimation. Given target at known different distances are chosen; then, we take pictures every minute and we ask camera to find (and then recognize) each target: the higher is the similarity, the better is the visibility. To validate these measures, we put the camera close to an optical transceiver, so both instruments “see” the same scene (Fig. 1).



Fig. 1 - (a) Optical transceiver and camera. (b) Scenario

We estimate the specific attenuation from visibility [3] and then we compare obtained results with the extinction of the optical carrier, measured from received power.

II. VISIBILITY ESTIMATION

As preliminary step, we choose in Fig. 1 four targets at known distances in condition of good visibility and we extract edges from them, obtaining that we will call “mask” (Fig. 2). Between these, relevant importance has the Eur “Mushroom”, because on his roof is placed a transceiver identical to the one on the roof of the Ministry of Economic Development. The distance between the two transceiver is about 800 m.

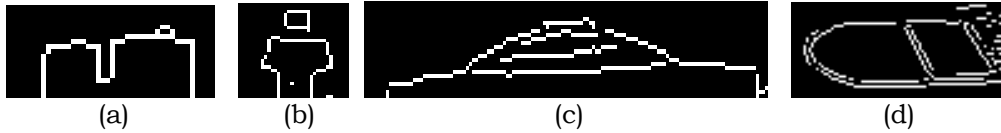


Fig. 2 – Masks: (a) 1600m; (b) 800m; (c) 550m; (d) 90m

We determine now the positions of the masks in the scene, so we collect three information about each target: shape, distance from camera, coordinates in the scene. Starting from that, we acquire new images and we proceed according to the diagram in Fig. 3.

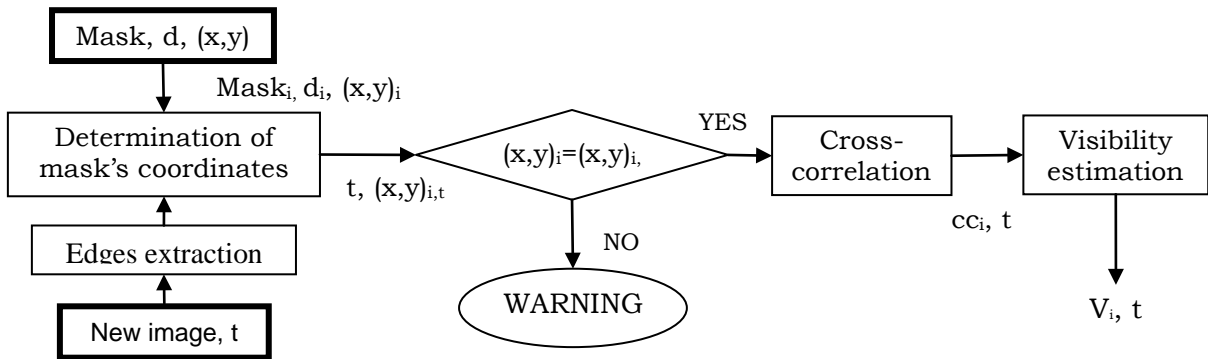


Fig. 3 – Flow chart for visibility estimation.

We look for every target in the new images; once it is found, we determine if his position is the one we expect. If it is so, we compute how much the target found in the new image is similar to the relative mask. Eventually, we estimate visibility according to (1):

$$\hat{V} = \sum_{i=1}^N \bar{d}_i \frac{\text{crosscorr}_i(t)}{\max(\text{crosscorr}_i)} \quad (1)$$

where \overline{d}_i are relative distances between targets defined as follows:

$$\overline{d}_i = \begin{cases} d_i - d_{i-1} & \text{if } i < N \\ d_i & \text{if } i = N \end{cases} \quad (2)$$

III. RESULTS

The observation period goes from 16/01/2012 to 08/02/2012. We compared the visibility estimation obtained using our method, based on masks, and a solution proposed in [1], based on probabilistic distribution of mean contrast in a scene with lambertian surfaces [2]. The results are shown in Fig. 4(a).

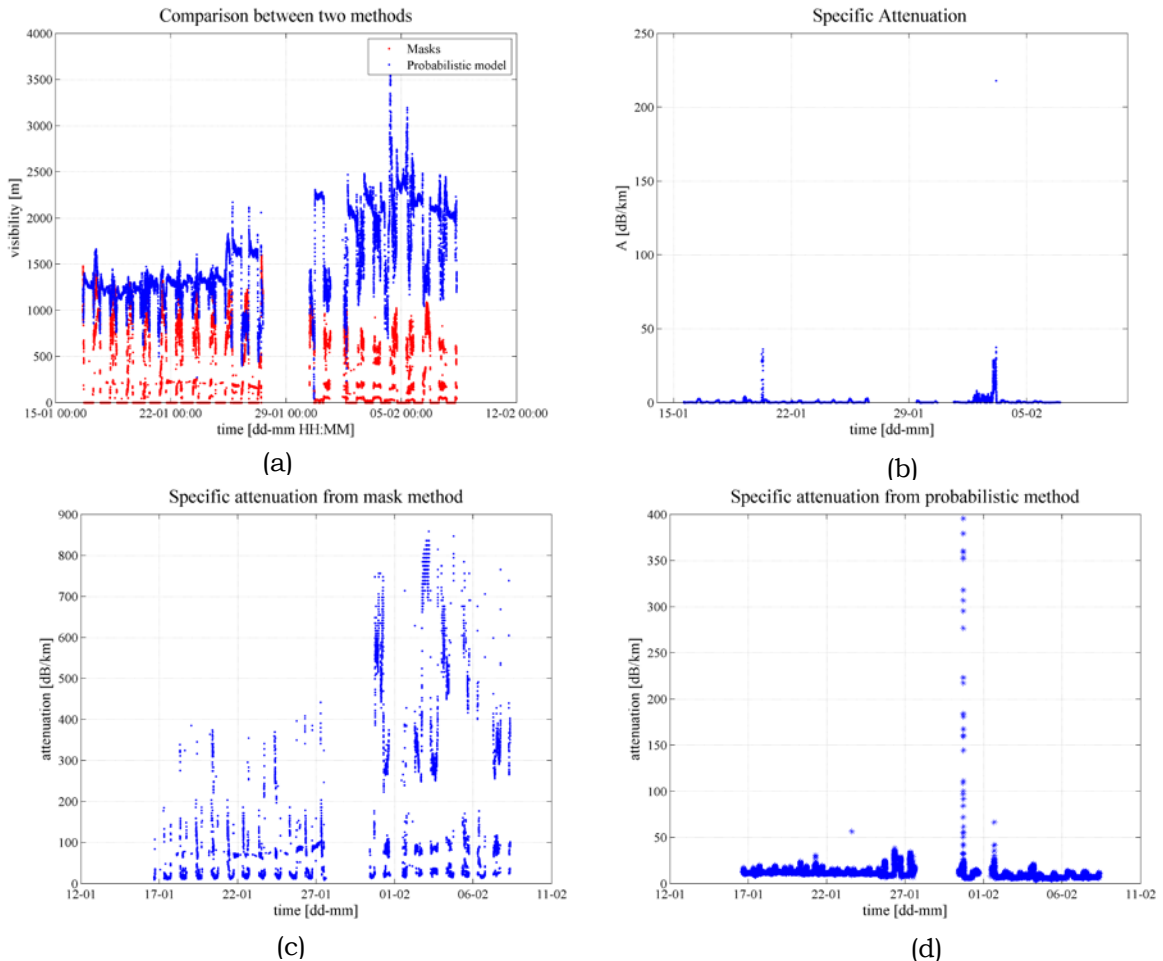


Fig. 4 – (a) estimated visibility in both method; (b) specific attenuation measured from received power of FSO; (c) specific attenuation from method based on masks; (d) specific attenuation from probabilistic method.

In Fig. 4 (b) is shown the measured specific attenuation, in (c) and (d) we obtain this quantity using the relation (3) [3]:

$$A_e[dB/km] = \frac{17}{V[km]} \left(\frac{0.55}{\lambda[\mu m]} \right)^q \geq 0 \quad (3)$$

IV. CONCLUSION

After comparison between different methods, it points out a good agreement in trends but different values, in particular regarding specific attenuation. This is due to the upper bound of visibility in the method based on mask, with consequent overestimation of attenuation. A proper calibration could lead to better appraisals.

ACKNOWLEDGEMENT

This work has been carried out within an ISCOM-University La Sapienza funded joint project. Authors are thankful to EUR SpA (Rome, Italy) for its kind availability. The authors deeply thank the staff of ISCOM for the technical support provided, particularly Roberto Dal Molin, Massimo Ferrante, Antonio Spaccarotella, Paolo Balducci and Mauro Piacentini. F. Consalvi of Fondazione Ugo Bordoni (FUB, Rome, Italy) is acknowledged for his support on technical activities.

REFERENCES

- [1] N. Hautière, R. Babari, É. Dumont, R. Brémond, e N.Paparoditis, “Estimating Meteorological Visibility using Cameras: a Probabilistic Model-Driven Approach”, 2010.
- [2] Giorgio Ficco, Lezioni del Corso “Tecnica del Controllo Ambientale”, lezione n.01, A.A. 2005-2006, Università degli Studi di Cassino Facoltà di Ingegneria -Polo di Frosinone.
- [3] H. Henniger, O. Wilfert, “An Introduction to Free-space Optical Communications”, Institute of Communications and Navigation, German Aerospace Center (DLR), 82230 Wessling, Germany, University of Technology Purkynova 118, CZ-61200 Brno, Czech Republic, Radioengineering, Vol. 19, No. 2, June 2010, pp. 203-212

SYSTEM-LEVEL ANALYSIS AND OPTIMIZATION OF TASK-ORIENTED IMAGING SYSTEMS

A. Guagliumi^(1,3), M. Gnan^(1,3), A. Liberato⁽¹⁾,
L. De Marco^(1,4), D. Bruni⁽²⁾, F. Canini⁽²⁾, P. Bassi⁽¹⁾

⁽¹⁾ DEIS, University of Bologna,
Viale del Risorgimento 2, I 40136 Bologna, Italy

⁽²⁾ Datalogic, Via San Vitalino 13,
I 40012 Lippo di Calderara di Reno BO, Italy

⁽³⁾ Present address: Datalogic, Lippo di Calderara di Reno BO, Italy

⁽⁴⁾ Present address: Automotive Lighting Italia SpA
Via Cavallo 18, I 10078 Venaria Reale TO, Italy

antonella.liberato@unibo.it

Abstract

The design of an electro-optical system such as a vision system is classically made by optimizing its constituting parts independently. However, because of the complexity of the overall system, the best performance of a single element may not correspond to that of the complete processing chain. In this paper a tool named SLALOM, acronym of “System Level AnaLysis and OptiMization” is proposed. SLALOM is a C-based extension to optical design software that includes the modeling of the electronic subsystem not encompassed by the software itself. It consists in two complementary tools that share a common core and can be executed independently to perform lens design at system level, and to simulate the overall system performance.

Index Terms – Analysis, Design, Imaging systems, Wavefront coding.

I. INTRODUCTION

In a digital imaging system, the optical part that collects the image is tightly linked to the electronic part that enhances it. The intertwining between the two blocks is especially evident in systems based on wavefront coding [1], such as task-oriented imaging systems (for example barcode readers or iris scanners), where a decoding block extracts the desired information out of the image. Because of the high complexity of the whole system, separate optimization of single parts may not lead to the best overall performance. This suggests that the design should be done at system level, taking into account also the interactions between the different parts during the optimization [2-3].

In this paper we propose a tool to analyze and design at system level that, rather than having general purpose as in [2-3], takes into account metrics appropriate for the requirements of the decoding block.

II. MODELING OF THE COMPLETE ELECTRO-OPTICAL SYSTEM

The blocks of the full electro-optical imaging system are shown in Fig. 1.

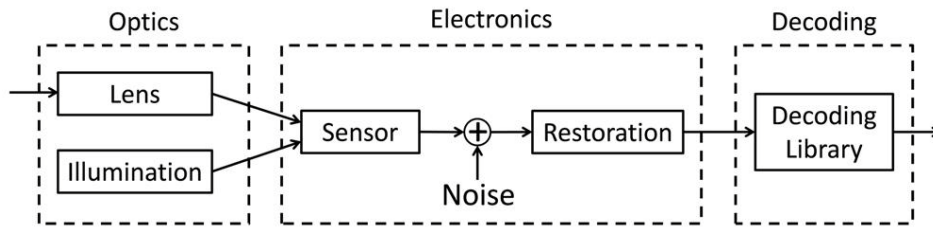


FIG 1. Model of the Electro-Optical system

The “Optics” block includes the lens and the external illumination system. The former creates the image of the object on the sensor plane and is described by an optical design software (ZEMAX [4] in our case). The latter is taken into account by considering the incident radiating power as being due to both room light and ad hoc illumination systems.

The “Electronics” block includes the Sensor converting the overall incident radiating power into current and the Restoration stage. Noise introduced by the detector [5] is also considered. Shot noise associated to the photo-generation of electrons and modeled by Poisson statistics is the dominant contribution for sufficiently large signals. The behavior of the sensor is modeled through its photon transfer curves that give the signal and noise levels as functions of the irradiance on the sensor plane. Since the detector surface is an array of pixels, the image provided by the detector is a sampled version of the original one. This sampling effect is considered too. The restoration stage enhances the image so that it is compatible with the image decoding routines of the following block. In the present case it is a Wiener filter: it inverts the Spatial Frequency Response (SFR) of the optical and electronic blocks preceding the reconstruction also taking noise into account. Other kinds of filters are anyway possible.

The “Decoding” block takes care of extracting the desired information from the restored image. In our case it is a proprietary software package developed in Datalogic. The sequence of blocks can be considered linear and therefore can be modeled either in the space or in the frequency domain.

Modeling in the space domain provides the output image as the convolution of the input image with the lens Point Spread Function (PSF), followed by sensor sampling, introduction of noise in each pixel and final convolution with the kernel of the reconstruction filter.

Modeling in the frequency domain uses of the transfer functions of all blocks and returns the SFR of the whole system. Also the noise is considered, estimating the Signal-to-Noise Ratio (SNR) analytically.

The two domains may be used effectively for the two goals of analysis and design, as it will be explained in the next section.

III. SYSTEM LEVEL ANALYSIS AND DESIGN

The tool SLALOM, acronym of “System Level AnaLysis and OptiMization”, implements the model described so far. It is a C-based extension to ZEMAX consisting into two complementary sets of routines sharing a common core. They can be run independently to simulate the overall system behavior (analysis) or optimize lens parameters (design).

The decoding block is indirectly included in SLALOM through parameters known as relevant for successful decoding, making the tool also applicable to diverse contexts.

The analysis functionality uses the spatial domain approach that directly and efficiently provides the creation of images generated by the system blocks. Such images can then be further decoded to extract the desired information. The long simulation time is not a concern since this functionality is used in independent single runs.

Conversely, the design functionality uses the frequency domain approach. Design is obtained by coupling SLALOM to the optimization engine of ZEMAX. Since optimization requires running the routines repeatedly, the execution time is a critical parameter. Moreover, images are not needed since the overall results are the system SFR and SNR, which must be compared to the requirements of the decoding library. Therefore, modeling in the frequency domain is now preferred.

As a validation of the performance of the tool before its application for system design, SLALOM was used to simulate the behavior of a commercially available bar code reader. Since the real system has no restoration stage, this block was omitted also in the simulations.

Images of two different barcodes generated by the SLALOM analysis routines were decoded and simulations results compared to experimental ones (Fig. 2). The green area defines the experimental decoding interval. The blue lines report successful (pass) and failed decoding of simulated images.

Fig. 2(a) refers to a 20 mils bar code. The overall Depth of Field (DoF) is correctly evaluated, except for a longitudinal offset. The failed decoding at 350 mm, in the mid of a successful decoding range, was not considered dramatic since single failures in reading may also occur in practice and can be overcome by simply reading the code again. Fig. 2(b) shows the results for a 5 mils bar code. In this case the DoF was underestimated by a 10% factor, which can be acceptable.

Similar results were obtained also in other cases. Considering both the difficulty to model external illumination - a critical factor for successful decoding - and the possible discrepancies between nominal and real barcode reader features, results can be considered satisfactory. This enables to use SLALOM in the design phase, with marked advantages in terms of time and cost savings: SLALOM not only allows system level design avoiding expensive prototype realization, but also permits overall performance optimization since the whole system is kept into account.

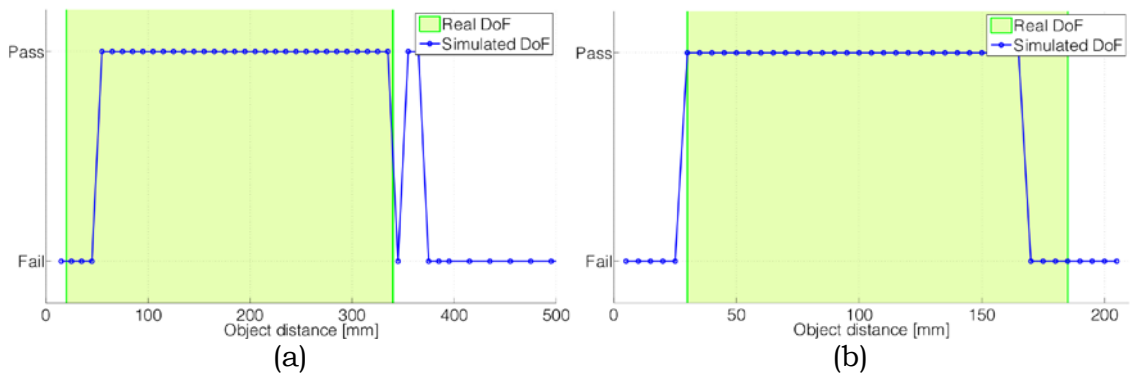


FIG. 2 – Comparison between real and simulated DoF of an existing barcode reader, working with (a) 20 mils bar codes and (b) 5 mils bar codes.

IV. CONCLUSIONS

A tool named SLALOM, acronym of “System Level Analysis and OptiMization”, allowing optimal design of task-based imaging systems has been proposed. It works at the system level taking into account the optical, electronic and decoding blocks that make up the system. The main characteristics and operation modes of the system have been described in view of both system analysis and design. An example of application of the SLALOM tool in the analysis operation mode has been shown that replicates the behavior of a real system. The good agreement of measured and simulated results proves the correctness of the approach and opens the way to the design of new systems considering the interactions of the different blocks and not optimizing each component one by one. This system-level design has the potential of greatly enhancing the performance of task-based imaging systems.

ACKNOWLEDGEMENTS

Work done in the framework of a cooperation between DLS and DEIS, also funded by the VIALAB Project of Regione Emilia Romagna.

REFERENCES

- [1] W. T. Cathey and E. R. Dowski, “New paradigm for imaging systems,” *Applied optics*, vol. 41, no. 29, pp. 6080-92, Oct. 2002.
- [2] D. G. Stork and M. D. Robinson, “Theoretical foundations for joint digital-optical analysis of electro-optical imaging systems,” *Applied Optics*, vol. 47, no. 10, p. B64-B75, Apr. 2008.
- [3] M. D. Robinson and D. G. Stork, “Comparing the extended depth-of-field imaging performance of spherical aberration and asymmetric wavefront coding,” 2009.
- [4] ZEMAX, Optical and illumination design software, available at <http://www.radiantzemax.com/> or <http://www.optima-research.com/>
- [5] J. R. Janesick, “Photon Transfer”, SPIE press, 2007.

THROUGH-WALL COMMUNICATION BY MEANS OF AN ULTRA WIDE PERMITTIVITY ANTENNA (UWPA)

D.Pinchera⁽¹⁾ , M.D.Migliore⁽¹⁾ , F.Schettino⁽¹⁾

⁽¹⁾ DIEI, Università degli Studi di Cassino e del Lazio Meridionale,
Via G.Di Biasio 43, 03043 Cassino, Italy

Abstract

In this contribution an antenna specifically designed for wireless Through-the-Wall communication is presented. By means of the presented system it is possible to transmit through walls with relative permittivity in the range 1-9 maintaining the reflections lower than -10dB. The antenna is simulated and experimentally tested in real working conditions, confirming its good performance.

Index Terms – Antennas, Permittivity, Attenuation Measurement.

I. INTRODUCTION

Communication in complex indoor environments is a very challenging field for ICT engineers; this is also due to the fact that many buildings were not built thinking to the need to provide a wireless coverage, so a wireless network design could be difficult for the limitations provided by the building itself.

One of the most troublesome conditions arises when we need to communicate between two areas separated by thick walls; in some cases we are not allowed to use wires because of security issues, so a *Through-the-Wall* communication is necessary [1-8].

Walls can be made of various materials, concrete (reinforced or not), stucco, marble and so on. For the sole case of concrete, according to aging and humidity, the relative permittivity can be in the range 2-8, so the design of an antenna for Through-the-Wall communication could change according to the particular wall chosen.

The aim of this contribution is the introduction of a novel antenna, exhibiting an ultra wide permittivity behavior, i.e. its reflection coefficient is kept below -10dB for a wide range of permittivities of the wall to which it is connected.

II. ANTENNA DESIGN

To the best knowledge of the authors, no antenna specifically designed according to ultra-wide-permittivity characteristics is described in the open literature. There is, however, a wide literature on the realization of ultra wide band antennas [9], and we are going to exploit some of the concepts of UWB antennas in our design.

Let us consider an antenna surrounded by a dielectric medium; the (working) resonating frequency f_r of the antenna depends on the permittivity of the dielectric medium and changes according to the formula $f_r=f_0/\sqrt{\epsilon_r}$, where ϵ_r is the relative dielectric permittivity of the medium and f_0 is the resonant frequency when $\epsilon_r=1$. Accordingly, roughly speaking, an antenna whose frequency response does not change within a suitable range is also capable of working in different materials.

This observation has been exploited in the design shown in Fig. 1, where an UWB patch antenna is stuck in direct contact with the wall and, to improve the transmission, a $\lambda_0/2$ metallic cavity is also added (λ_0 being the free space wavelength at 2.45GHz).

The optimization of the antenna has been achieved by means of CST Microwave Studio [10], starting from the design of an UWB printed monopole antenna. The substrate on which the monopole and the ground plane are realized is a 0.5 mm thick Arlon 25N ($\epsilon_r=3.38$).

To verify the quality of the design, in Fig. 2 the reflection coefficient at the ISM 2.45GHz is plotted as a function of the permittivity of the wall on which the antenna is placed, showing satisfactory performance.

III. PROTOTYPE REALIZATION AND TESTING

A prototype of the UWPA has been built (Fig. 3). The cavity is realized by means of a folded 0.5mm thick aluminum foil, with an additional layer of aluminum adhesive tape in order to improve the robustness of the whole structure.

The UWPA built has been tested when stuck on different materials (concrete, marble, plasterboard, free-space). In Fig. 4a the reflection coefficient measured in different working conditions is plotted.

These results confirm that the reflection coefficient of the antenna in the ISM band is lower than -10 dB for all the materials tested. The reflection coefficient of the antenna operating in free-space is in good agreement with the corresponding simulation.

To test the *Through-the-Wall* communication capabilities of the antenna in Fig. 4b we show the transmission coefficient between two UWP antennas (S21) placed on the sides of a 20 cm concrete wall, measured using a Vector Network Analyzer. The comparison with numerical simulations shows again a very good matching.

IV. CONCLUSION

A novel compact, low cost, light antenna, aimed at the optimization of through-the wall communications has been proposed. The antenna is designed to keep a suitably low reflection coefficient when operating on walls with relative dielectric permittivity in the range 1-9. In this sense the antenna has “ultra wide permittivity” properties.

The antenna has been tested in real working environments, and the results obtained in the measurement campaign confirmed the expectations.

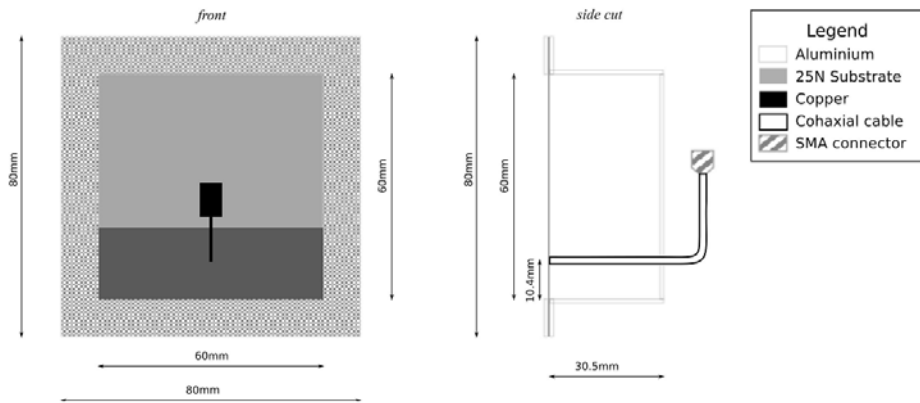


FIG. 1 – Scheme of the UWP Antenna

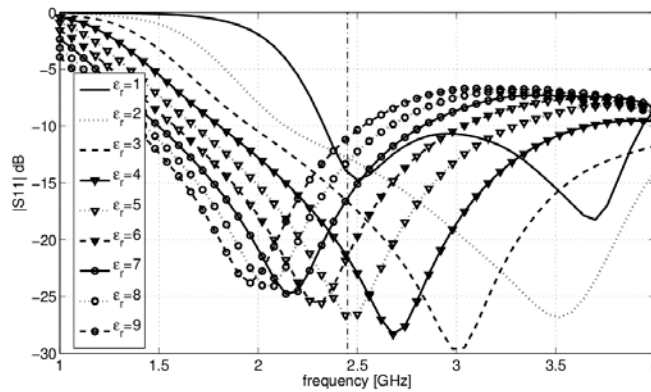


FIG. 2 – Simulation of the reflection coefficient for variable wall permittivity

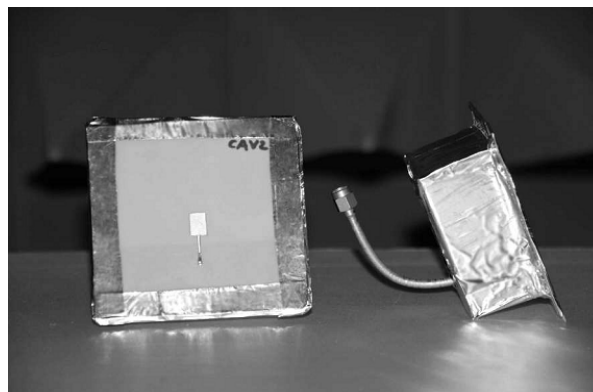


FIG. 3 – Photo of two realized prototypes

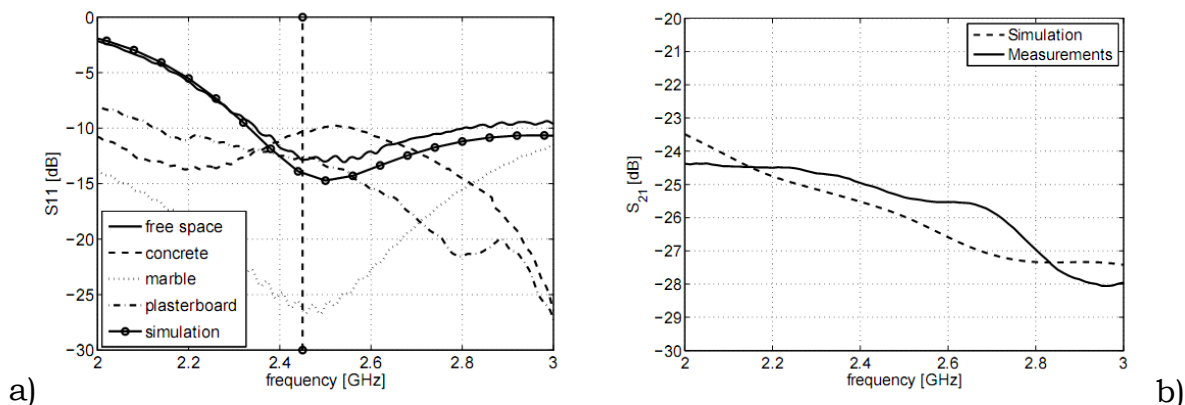


FIG. 4 – Measurements on the realized prototypes

REFERENCES

- [1] Y.P.Zhang and Y.Hwang, “Measurements of the Characteristics of Indoor Penetration Loss,” IEEE 44th Vehicular Technology Conference, 1994, pp.1741–1744
- [2] A.Ogunsola, U.Reggiani, and L.Sandrolini, “Modelling shielding Properties of concrete” 17th International Zurich Symposium on Electromagnetic Compatibility, 2006, pp.34–37
- [3] R.Dalke and C.L.Holloway and P.McKenna, “Rejection and Transmission Properties of Reinforced Concrete Walls,” IEEE Antennas and Propagation Society International Symposium, 1999, pp.1502–1505
- [4] D.Pea, R.Feick, H.D.Hristov and W.Grote, “Measurement and Modeling of Propagation Losses in Brick and Concrete Walls for the900-MHzBand,” IEEE Transactions On Antennas And Propagation, VOL.51, NO.1, January2003
- [5] P.Vlach, B.Segal, J.LeBel and T.Pavleseck, “Cross-Floor Signal Propagation Inside a Contemporary Ferro-Concrete Building at 434, 862, and 1705MHz” IEEE Transactions on Antennas and Propagation, VOL. 47, NO.7, July1999, pp.1230–1232
- [6] G.Knapp, “Microwave Coupler Feeds Outdoor Antenna Through Walls,” High Frequency Electronics, May2006, pp.58–62
- [7] S.Mizushina and A.Adachi “A Technique for Wireless LAN Connection through Building Concrete Wall at 2.4GHz,” IEEEIMS, 2010, pp.260–263
- [8] H.L.Bertoni, Radio Propagation for Modern Wireless Systems, Prentice Hall, 2000
- [9] B.H.Allen, Ultra-wideband: antennas and propagation for communications, radar and imaging, Wiley2007
- [10] CST Studio Suite <http://www.cst.com/>

TWI FOR A LOSSLESS UNKNOWN WALL

R. Solimene, A. D'Alterio, R. Pierri

Department of Information Engineering, Second University of
Naples, Via Roma 29, 81031, Aversa, Italy
rocco.pierri@unina2.it

Abstract

A TSVD based procedure to characterize the wall transmission coefficient in the framework of through-the-wall imaging is introduced. The procedure works for a symmetric lossless wall and does not rely on optimization schemes but requires a multistatic configuration.

Index Terms—Linear inverse scattering problem, obstacle estimation, singular value decomposition, through-wall imaging.

I. INTRODUCTION

Through-the wall imaging (TWI) is an emerging research field whose application ranges from civilian to military contexts [1].

What makes TWI problems different than free space imaging is the presence of the wall. Indeed, the wall is the primary source of clutter and must be accounted for by any imaging algorithm in order to avoid blurring and delocalization effect [2].

While clutter can be cancelled by gating and/or filtering procedure, to obtain focalized reconstructions, the wall parameters should be known. In practical situations, such parameters are unknown or known with some degree of uncertainty. Therefore, a wall estimation stage should be run before imaging.

Many methods cast the wall estimation problem as an optimization and benefit from the single-layer homogeneous assumption which leads to a limited number of unknowns (two or three) to be looked for [3]-[5].

However, in many other situations, such a hypothesis does not hold, and the typical problems of nonlinear optimization turn out to be relevant.

In this paper we present a new non-optimization-based wall characterization procedure in the case of walls varying only along the depth. The main idea is to estimate the wall transmission coefficient rather than its electromagnetic properties. This allows to cast characterization as a linear inverse problem we solve by a Truncated-Singular Value Decomposition (TSVD).

As measurements are collected in reflection mode configuration, the method can be applied only to symmetric lossless walls. However, the wall can be multilayered with the number of layers being unknown.

This approach has been already presented in [6]. Here, we extend it to the more realistic case of 3D.

I. PROBLEM FORMULATION

The scenario consists of a three-layered medium. The first and the third layers are assumed to be the free-space with ε_0 and μ_0 being its dielectric permittivity and magnetic permeability, respectively. The second layer is representative of the wall. It is assumed laterally homogeneous, lossless with a relative dielectric $\varepsilon_w(z) = \varepsilon_w(d-z)$, d being its thickness. The transmitting antenna is located in the first layer at a distance h from the front face of the wall in $P = (x_s, y_s, -d)$ so that the effect of the wall on the antenna radiation properties is negligible.

We consider a multistatic measurement configuration where the reflected field is collected over a set of different positions taken over a square region, the observation domain, $\Sigma = \Sigma_x \times \Sigma_y = [-X_o, X_o] \times [-Y_o, Y_o]$. Accordingly, the reflected field, $\underline{E}_r(x_o, y_o, k_o)$, can be expressed through the integral equation

$$\underline{E}_r(x_o, y_o, k_o) = \frac{1}{(2\pi)^2} \iint_D \underline{\Gamma}(k_x, k_y, k_o) \underline{f}_i(k_x, k_y, k_o) \times \exp[-jk_x(x_o - x_s)] \exp[-jk_y(y_o - y_s)] \exp(-j2k_z h) dk_x dk_y \quad (1)$$

where $\underline{\Gamma}(k_x, k_y, k_o)$ is the dyadic reflection coefficient of the wall, which is function of the Fresnel reflection coefficients Γ_{TE} and Γ_{TM} [7], that is

$$\underline{\Gamma}(k_x, k_y, k) = \begin{bmatrix} \left(\Gamma_{TE} \frac{k_y^2}{k_i^2} + \Gamma_{TM} \frac{k_x^2}{k_i^2} \right) & \left(\Gamma_{TM} \frac{k_x k_y}{k_i^2} - \Gamma_{TE} \frac{k_x k_y}{k_i^2} \right) & 0 \\ \left(\Gamma_{TM} \frac{k_x k_y}{k_i^2} - \Gamma_{TE} \frac{k_x k_y}{k_i^2} \right) & \left(\Gamma_{TE} \frac{k_x^2}{k_i^2} + \Gamma_{TM} \frac{k_y^2}{k_i^2} \right) & 0 \\ 0 & 0 & -\Gamma_{TM} \end{bmatrix} \quad (2)$$

$\underline{f}_i = (f_x, f_y, f_z)$ is the source plane-wave spectrum, $k_i^2 = k_x^2 + k_y^2$ and k_x, k_y, k_z are the wavenumber components corresponding to x, y, z , respectively, $k_o = \omega \sqrt{\varepsilon_0 \mu_0}$ is the free-space wavenumber. Note that the integration interval in eq. (1) has been restricted to the “visible domain”.

Accordingly, to retrieve the wall transmission coefficient, one has first to invert eq. (1) for Γ_{TE} and Γ_{TM} . If a sliced approach is used [5], as the 3D TWI reconstruction is obtained by solving a collection of two-dimensional and scalar problems, Fresnel coefficients are all we need to implement it [6]. Otherwise, once the Fresnel reflection coefficients are known, the dyadic transmission coefficient of the wall can be obtained as well.

II. NUMERICAL RESULTS

In this section, we report some numerical reconstructions of the Fresnel reflection coefficients obtained by exploiting synthetic data corrupted by an additive white Gaussian noise with SNR=30dB.

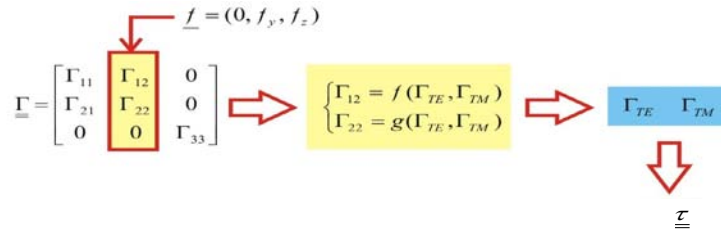


FIG. 1 –Flow chart of the overall wall characterization procedure.

As source, we consider a truncated rectangular wave guide with aperture 0.1m×0.05m in size and located at (0,0,-0.2). The reflected field is collected over 36 measurement points which uniformly span the measurement aperture $\Sigma = [-1,1] \times [-1,1] \text{m}^2$ located at the same distance (from the wall) as the source. A single frequency $f = 1.2 \text{GHz}$ is here employed. A three-layered wall is considered, with thicknesses 0.1m, 0.04m and 0.1m, respectively, and relative dielectric permittivity of 4, 1 and 4.

To invert eq. (1) one of the method discussed in [7] can be employed. Here, we consider the case in which the transversal source spectrum is linearly polarized along the y-axis, so that $\underline{f}_i = (0, f_y, f_z)$. This way, a couple of linear integral equations is obtained. Their inversion is achieved through a TSVD procedure whose outcomes are exploited to solve a system of two equations for Γ_{TE} and Γ_{TM} . The overall procedure is sketched in Fig. 1, whereas the reconstruction of the amplitude and phase of Γ_{TE} along with its actual behaviour are reported in Fig. 2. As can be seen, reconstruction is satisfactory achieved except for point where the scattering parameters exhibit numerical singularities [7]. Similar result are obtained for Γ_{TM} (not shown here).

III. COCLUSIONS

We proposed a new wall characterization procedure and validated it against synthetic data. The idea is to estimate the wall transmission coefficient instead of the electromagnetic properties (dielectric permittivity, thickness, etc.) of the wall. This allowed to cast the characterization as a linear inverse problem, thus avoiding optimization algorithms which can be time and resource consuming when the wall structure is not a mere single homogeneous slab.

The procedure works for lossless symmetric walls. However, layered walls (with the number of layers being unknown) can be dealt with.

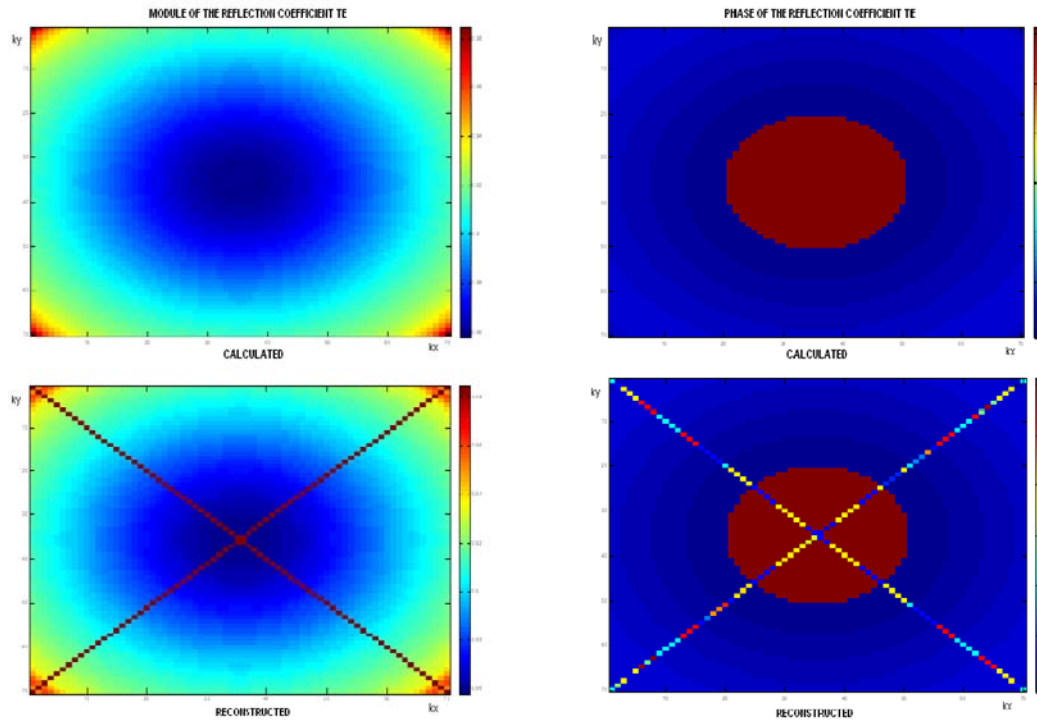


FIG. 2–Top row: actual TE reflection coefficient. Bottom row: retrieved one.

REFERENCES

- [1] M. Amin and K. Sarabandi, “Special issue on remote sensing of building interior,” *IEEE Trans. Geosci. Remote Sens.*, vol. 47, no. 5, May 2009.
- [2] G. Wang and M. G. Amin, “Imaging through unknown walls using different standoff distances,” *IEEE Trans. Signal Process.*, vol. 54, no. 10, pp. 4015–4025, Oct. 2006.
- [3] F. Ahmad, M. G. Amin, and G. Mandapati, “Autofocusing of through-the-wall radar imagery under unknown wall characteristics,” *IEEE Trans. Image Process.*, vol. 16, no. 7, pp. 1785–1795, Jul. 2007.
- [4] M. Dehmollaian and K. Sarabandi, “Refocusing through building walls using synthetic aperture radar,” *IEEE Trans. Geosci. Remote Sens.*, vol. 46, no. 6, pp. 1589–1599, Jun. 2008.
- [5] R. Solimene, F. Soldovieri, G. Prisco, and R. Pierri, “Three-dimensional through-wall imaging under ambiguous wall parameters,” *IEEE Trans. Geosci. Remote Sens.*, vol. 47, no. 5, pp. 1310–1317, May 2009.
- [6] R. Solimene, R. Di Napoli, F. Soldovieri, R. Pierri, “TWI for an unknown symmetric lossless wall,” *IEEE Trans. Geosci. Remote Sens.*, vol. 49, n.8, pp. 2876–2886, August 2011.
- [7] R. Solimene, A. D’Alterio, F. Soldovieri, “Determining the Fresnel Reflection Coefficients in 3D Half Space Geometry by GPR Multistatic Data,” *Near Surface Geophysics*, vol. 9, pp. 265–275, 2011

DIFFERENTIAL MICROWAVE IMAGING FOR BRAIN STROKE MONITORING

R.Scapaticci^(1,2), L. Di Donato⁽²⁾, I. Catapano⁽¹⁾, L. Crocco⁽¹⁾

(1) CNR-IREA, Consiglio Nazionale delle Ricerche – “Istituto per il Rilevamento Elettromagnetico dell’Ambiente”, Via Diocleziano 328, 80124 Naples, Italy
([scapaticci.r, catapano.i, crocco.l@irea.cnr.it](mailto:scapaticci.r,catapano.i,crocco.l@irea.cnr.it))

(2) DIMET, Università “Mediterranea” di Reggio Calabria, Via Graziella, Loc. Feo di Vito, Reggio Calabria 89100, Italy.
(loreto.didonato@unirc.it)

Abstract

The adoption of microwave imaging as a tool for non-invasive monitoring of brain stroke has recently gained an increasing attention. With respect to such a framework, in this communication, we propose a simple and effective imaging strategy for brain stroke monitoring, based on a modified formulation of the linear sampling method, which allows a quasi real time monitoring of the disease's evolution. The performance of the imaging technique is assessed through numerical examples dealing with an anthropomorphic phantom.

Index Terms – Microwave Imaging, Brain Stroke Imaging, Linear Sampling Method.

I. INTRODUCTION

A stroke is caused by a failed blood circulation into the brain due to a blocked or burst blood vessel and can cause serious diseases or even death if not timely detected. Currently, the main clinical imaging tools used to detect and diagnose brain strokes are computerized tomography (CT) and/or magnetic resonance imaging (MRI). These techniques are largely assessed and provide in a reliable way the stroke's location and kind. However, they are not cost effective, their operation is time consuming and the involved instrumentations are not portable. As such, they are not suitable for a continuous monitoring of the stroke's evolution. These circumstances motivate the interest for new technologies that can integrate the currently available ones to improve the overall efficiency of the diagnosis.

In the recent years, by relying on the evidence that ischemic tissue shows, in the microwave band, different electric properties with respect to healthy tissues [1], several research groups are investigating the possibility to use microwave tomography (MWT) for brain imaging, developing both MW exposure devices and imaging strategies [2-4].

With respect to such a framework, in this communication, we propose an imaging strategy for brain stroke monitoring based on the Linear Sampling Method (LSM) [5], and in particular on its modified formulation [6]. Such an imaging approach is meant as a cooperative tool with well assessed and current available diagnostics technique (e.g. from CT or MRI), as it assumes that the brain structure is (at least approximately) known. This is a reasonable assumption since, according to the current clinical protocols, these techniques are the ones routinely applied to patients showing stroke symptoms. On the other hand, the real time imaging capability of the proposed method, as well as the non ionizing (and therefore harmless) nature of microwaves let exploit the tool to perform a continuous monitoring of the stroke, which represents a crucial aspect for timely treatment of the disease.

II. IMAGING STRATEGY

The imaging approach we consider is based on the modified version of the LSM proposed in [6], which takes advantage of the knowledge of the brain structures provided by other diagnostic techniques. This method is worth to be considered since it is not demanding in terms of computational time and memory requirements. The knowledge about the electromagnetic features of the head tissues allows to formulate the imaging problem in a “differential” fashion, that is as the search of a perturbation with respect to a known scenario. Formally, this corresponds to sample the investigated area into an arbitrary number of sampling points \mathbf{r}_p and solve in each of them, the following equation in the unknown \mathbf{x}

$$\Delta \mathbf{E}_s \mathbf{x}(\mathbf{r}_p) = \tilde{\mathbf{G}}(\mathbf{r}_m, \mathbf{r}_p), \quad (1)$$

where $\Delta \mathbf{E}_s$ is the difference between the measured data (i.e., in presence of the stroke) and the data computed by simulating the known “unperturbed” reference scenario (i.e., the healthy brain), while the right hand side $\tilde{\mathbf{G}}$ expresses the Green function of the inhomogeneous scenario, i.e., the field radiated by an elementary source located in \mathbf{r}_p (in the brain) and evaluated at the receivers located at \mathbf{r}_m .

A stable solution of Eq.(1) can be achieved by exploiting the SVD of $\Delta \mathbf{E}_s$ and the Tikhonov regularization [5]. Hence, we can foresee that the L^2 norm of solution \mathbf{x} will assume large values when \mathbf{r}_p is outside of areas exhibiting anomalous properties with respect to the healthy brain and low values elsewhere. In order to enhance the readability of the imaging result, we consider a differential indicator defined as:

$$\Delta \Upsilon(\mathbf{r}_p) = \frac{\|\mathbf{x}(\mathbf{r}_p)\|^2}{\|\tilde{\mathbf{G}}(\mathbf{r}_p)\|^2} = \frac{1}{\|\tilde{\mathbf{G}}(\mathbf{r}_p)\|^2} \sum_{n=1}^N \left(\frac{\lambda_n}{\lambda_n^2 + \alpha^2} \right)^2 \left| \langle \tilde{\mathbf{G}}(\mathbf{r}_p), \mathbf{u}_n \rangle \right|^2 \quad (2)$$

In Eq. (2) the energy of the solution \mathbf{x} is weighted by the norm of the right hand side of Eq. (1) in each sampling point in order to compensate the attenuation of the field, due to the different location of the sampling points with respect to the receivers.

III. NUMERICAL ASSESSMENT

While referring the reader to [7] for more details concerning the choice of the working frequency and the adopted matching medium, in this Section we show the performance of the proposed imaging method with respect to a 2D scenario computed starting from a slice of the 3D anthropomorphic phantom taken from [8] and using the dielectric properties of biological tissues reported in [9]. The actual permittivity profile is shown in Fig.1a.

The head is probed at 1GHz, by means of 32 elementary line sources located on a circle surrounding the region under test, and working in a matching medium having electric properties $\epsilon_{mm}= 40$, $\sigma_{mm}= 0.01\text{S/m}$. Receiving probes are located in the same positions of the transmitting ones.

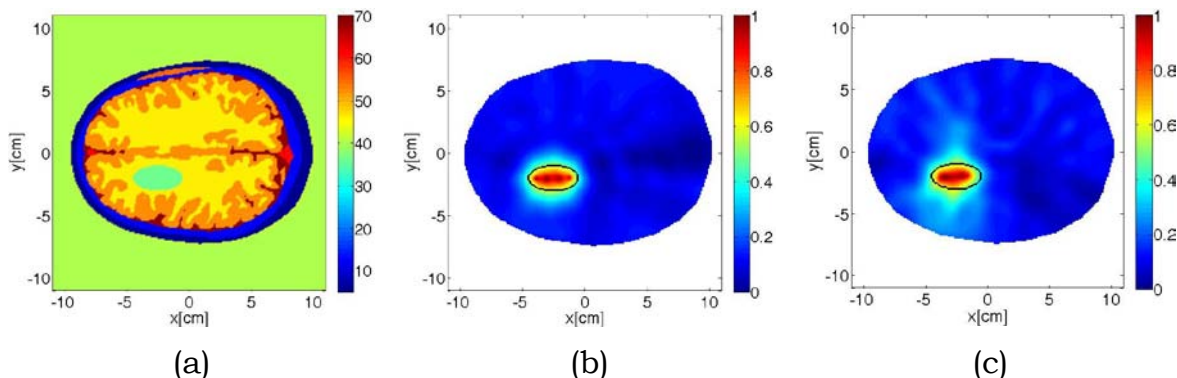


FIG. 1 – Validation of the proposed imaging approach: (a) reference permittivity profile; (b) differential indicator in ideal conditions; (c) differential indicator in realistic conditions.

First, let us observe the result obtained by using the proposed imaging strategy in ideal conditions, i.e., when the reference profile is exactly *a priori* known and noiseless data are processed, see Fig.1b as this gives an idea of the "best obtainable result". Then, to assess the capability of the approach in more realistic conditions, we have considered the unavoidable presence of uncertainties on the reference scenario and noise on data. In particular, we have processed simulated data corrupted by an additive gaussian noise (SNR=60dB) and we have introduced a $\pm 2,5\%$ random variability on the electromagnetic properties of the tissues in the phantoms, to simulate the natural

variability of actual tissues. Note that the average values of the electromagnetic properties of the tissues are instead used to evaluate the Green's function $\tilde{\mathbf{G}}$. Corresponding reconstruction is shown in Fig.1c.

As can be seen, these figures corroborate the capability of the proposed approach as an effective strategy for brain stroke imaging.

IV. CONCLUSIONS

This communication concerns with a feasibility study on Microwave Imaging for brain stroke monitoring. It is worth to note that microwaves are particularly suitable to perform a continuous monitoring, since they are not harmful for the patient, being non-ionizing radiations and they involve technologies which allows to design portable and cost-effective devices. The positive results obtained by the imaging strategy with a 2D anthropomorphic head phantom motivate the ongoing studies aimed at assessing the proposed tool in the more realistic 3D case.

REFERENCES

- [1] S. Y. Semenov et al., "Dielectrical spectroscopy of canine myocardium during acute ischemia and hypoxia at frequency spectrum from 100kHz to 6GHz", *IEEE Transactions on Medical Imaging*, Vol.21, pp. 547-550, 1994.
- [2] S. Y. Semenov and D. R. Corfield, "Microwave tomography for brain imaging: feasibility assessment for stroke detection", *International Journal of Antennas and Propagation*, Vol.2008, 8 pages, 2008.
- [3] D. Ireland and M. Bialkowski, "Microwave head imaging for stroke detection", *Progress in Electromagnetics Research M*, Vol. 21, pp.163-175, 2011.
- [4] A. Fhager, M. Persson, "A microwave measurement system for stroke detection", *Antennas and Propagation Conference*, Loughborough (UK), Nov. 2011.
- [5] F. Cakoni, D. Colton, "Qualitative Methods in Inverse Scattering Theory", Springer-Verlag Berlin Heidelberg, 2006.
- [6] I.Catapano and L. Crocco, "An imaging method for concealed targets", *IEEE Trans. Geosci. Remote Sens.*, Vol.47, pp. 1301-1309, 2009.
- [7] R. Scapaticci, L. Di Donato, I. Catapano, L. Crocco, "A feasibility study on Microwave Imaging for brain stroke monitoring", *Progress in Electromagnetic Research*, submitted.
- [8] I.G. Zubal, C.R. Harrell, E.O. Smith, Z. Rattner, G. Gindi, P.B. Hoffer, "Computerized three-dimensional segmented human anatomy", *Medical Physics*, Vol.21 (2), pp.299-302, 1994.
- [9] "Dielectric properties of body tissues in the frequency range 10 Hz - 100 GHz", [Online], Available: <http://niremf.ifac.cnr.it/tissprop/>.

ADVANCEMENTS IN MICROWAVE BREAST CANCER IMAGING ENHANCED BY MAGNETIC NANOPARTICLES AS CONTRAST AGENT

G. Bellizzi⁽¹⁾, O.M. Bucci^(1,2), I. Catapano⁽²⁾, L. Crocco⁽²⁾, R. Scapaticci^(2,3)

⁽¹⁾ DIBET, Università “Federico II” di Napoli, Via Claudio 28, 80125
Naples, Italy
(gbellizz, bucci@unina.it)

⁽²⁾ CNR-IREA, Consiglio Nazionale delle Ricerche – “Istituto per il
Rilevamento Elettromagnetico dell’Ambiente”, Via Diocleziano
328, 80124 Naples, Italy
(scapaticci.r, catapano.i, crocco.l@irea.cnr.it)

⁽³⁾ DIMET, Università “Mediterranea” di Reggio Calabria, Via
Graziella, Loc. Feo di Vito, Reggio Calabria 89100, Italy.

Abstract

This communication deals with Microwave Imaging of breast cancer and aims at presenting ongoing advancements on a recently proposed methodology, which exploits Magnetic Nanoparticles (MNP) as contrast agent able to selectively target cancerous tissues by modifying their magnetic permeability. In this framework, we discuss the performance of the imaging approach, in terms of reliability and sensitivity, against realistic conditions.

Index Terms – breast cancer imaging, contrast agent, magnetic nanoparticles, microwave imaging

I. INTRODUCTION

The relationship existing in the microwave frequency range between electric properties of human breast tissues and their physiopathological status motivates the investigation of microwave imaging (MWI) as a tool for cancer diagnosis. However, studies on the dielectric properties of human mammary tissues at microwave frequencies [1] have outlined that MWI may fail in discriminating malignant tissues from healthy fibroglandular ones. To overcome this drawback, a contrast enhanced MWI methodology has been recently proposed [2], which uses MNP as a selective contrast agent. Since the human tissues are non magnetic, the capability of inducing a magnetic anomaly localized only into the tumor allows to cast the cancer imaging as the reconstruction of a magnetic contrast from the corresponding scattered field. In this respect, since the induced magnetic contrast is embedded into a complex heterogeneous electric scenario, as the female breast, a key issue is to extract, from the measured data, the signal meaningful for the imaging

task, i.e., the backscattered field due to the MNP. To pursue this goal, the possibility of modulating the magnetic response of MNP at microwaves by means of an external polarizing magnetic field (PMF) has been exploited. In particular, the MNP response can be switched OFF and ON by applying or not an external PMF of sufficient intensity. In this way, the differential ON-OFF signal only accounts for the response of the MNP targeted tumor. This communication reports some recent results, which, starting from the encouraging ones reported in [2], aim at assessing the performances of the MNP enhanced MWI approach in realistic scenarios, i.e, considering the experimental characterization of MNP response [3] and anthropomorphic breast phantoms [4].

II. IMAGING STRATEGY

The low amount of MNP that can be selectively delivered to cancerous tissues implies that the induced magnetic anomaly can be actually modeled as a weak perturbation of the surrounding electric scenario. Accordingly, the differential scattered field ΔE_s , i.e. the difference of the signals measured when MNP are ON and OFF, is linearly related to the magnetic contrast χ_μ [2] and the imaging task can be cast as the inversion of the corresponding relationship:

$$\Delta E_s(r_m, r_v) = -j\omega\mu_o \int_{\Omega} \tilde{\mathbf{G}}^{EM}(r_m, r) \chi_\mu(r) \tilde{\mathbf{H}}_i(r, r_v) d \neq \quad v, m = 1, \dots, M \quad (1)$$

where, $\tilde{\mathbf{G}}^{EM}$ and $\tilde{\mathbf{H}}_i$ are the electric-magnetic Green's function and the incident magnetic field related to the reference electric scenario, respectively, r_m and r_v denote the locations of the M receiving and transmitting probes. A stable regularized solution $\hat{\chi}_\mu$ of Eq. (1) can be achieved by means of the Truncated Singular Value Decomposition (TSVD):

$$\hat{\chi}_\mu(r) = \sum_{n=1}^T \frac{1}{\sigma_n} \langle \Delta \hat{\mathbf{E}}_s, \mathbf{u}_n \rangle \mathbf{v}_n(r), \quad (2)$$

where $\Delta \hat{\mathbf{E}}_s$ is the collected data vector, while σ_n , \mathbf{u}_n and \mathbf{v}_n denotes the n -th singular value and singular vectors of the matrix L_{EM} , i.e. the discretized version of the integral operator in Eq. (1). The threshold T has to be chosen in such a way to assure a good trade-off between the accuracy of the approximation and the stability of the solution.

III. PERFORMANCE ANALYSIS

The presented numerical analysis is referred to an anthropomorphic phantom (ID 070604PA2 from <http://uwcem.ce.wisc.edu/home.htm>),

and takes into account experimental results on the MNP behavior [3]. The breast is immersed in a homogeneous lossless matching medium, whose relative permittivity is $\epsilon_b=25$. The domain Ω is probed by means of 24 z-directed electric dipoles and evenly spaced on three circumferences surrounding Ω . Transmitting and receiving probes are located at the same positions. The tumor, modeled as a spherical inclusion, has approximately the same electric features of the fibroglandular tissue. First, to study the sensitivity with respect to the size of the tumor and the adopted working frequency, we have observed the reconstruction capabilities of the proposed strategy at a fixed frequency and for a fixed value of SNR ($f=2\text{GHz}$ and $\text{SNR}=70\text{dB}$) and considering different sizes of the cancerous inclusion. As expected, the lower is the radius of the spherical inclusion the larger is the magnetic contrast that should be induced. In particular, we found that $|\chi_\mu| \propto \frac{c}{r^3}$, where r is the radius of the tumor and c is the concentration of MNP delivered into the tumor. A similar behavior is observed fixing the tumor's dimension and SNR ($r_t=0.5\text{cm}$ and $\text{SNR}=70\text{dB}$) and varying the working frequency. The theory of Rayleigh scattering suggests that the magnitude of the scattered field varies as the square of the frequency and, as a consequence, also the induced magnetic contrast should do the same. However, we observed that at lower frequencies a higher magnetic contrast, with respect to the one suggested by the theoretical model, is needed to obtain a reliable reconstruction (see Fig.1). This is due to the fact that at those frequencies the hypothesis of point scatterer fails.

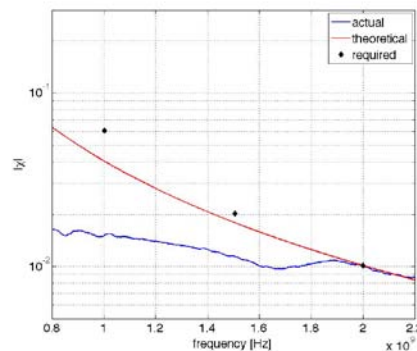


Fig.1 - Induced magnetic contrast against working frequency. The blue line represents the experimental measured response of MNP [3].

According to these results, in the second part of our analysis, concerning the assessment of the robustness of the method against uncertainties on the reference electric scenario, we have fixed the working frequency at 2GHz. Moreover we have supposed a concentration $c=10\text{mg/ml}$ of MNP delivered into a tumor, whose radius is $r_t=0.5\text{cm}$. Hence, based on the experimental result in [3], the magnitude of the induced magnetic contrast when MNP are switched ON is set to $|\chi_\mu| = 0.0094$. Since no a priori information on the breast are assumed, but for its outer shape and the skin extent, two approximated electric scenarios

have been considered to model the breast inner structure: a homogeneous adipose medium and a homogeneous fibroglandular one, shown in Figs.2.b,c, respectively.

Figures 2.e,f state that the reconstruction reliability is influenced by the adopted reference scenario. In particular, we have observed that, based on the location of the tumor, one of the two reference scenarios is preferable. However, whatever is the tumor location, an its reliable reconstruction is achieved by simply considering the intersection of the results provided by the two reference scenarios, see Fig.2.d.

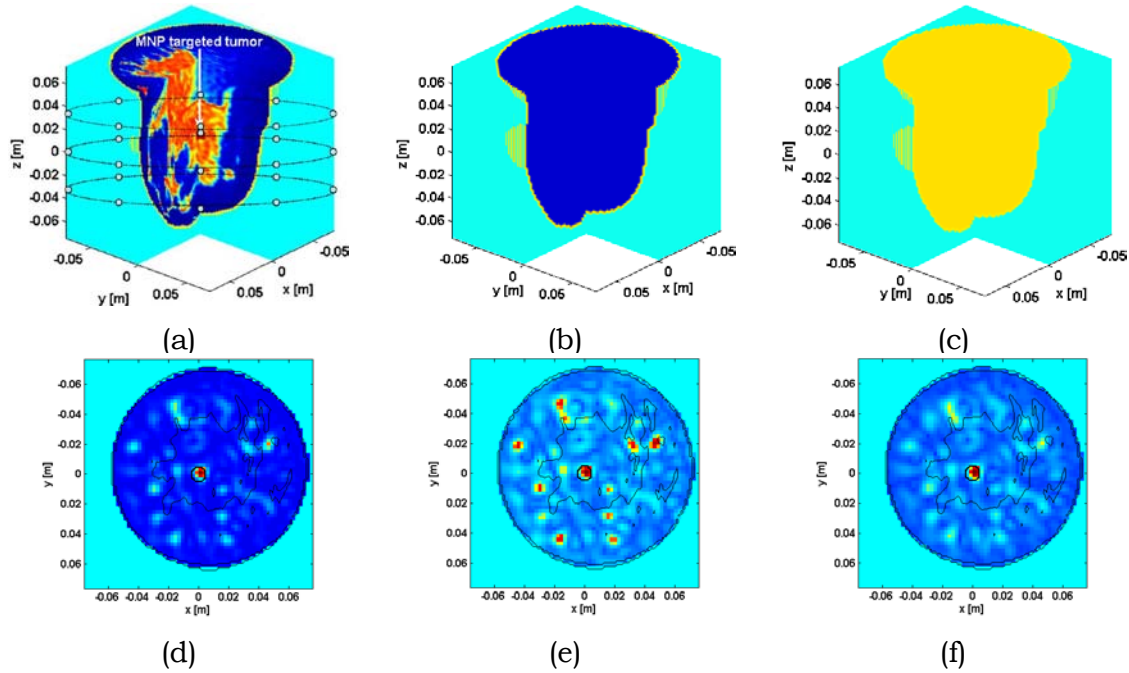


Fig.2 - Performances assessment against reference electric scenario: (a) reference permittivity profile; (b) adipose reference scenario; (c) fibroglandular reference scenario; (d) intersection of the reconstructions in (e) and (f); (e) normalized magnitude of $\hat{\chi}_\mu$ obtained with reference scenario in (b); (f) normalized magnitude $\hat{\chi}_\mu$ obtained with reference scenario in (c).

REFERENCES

- [1] M. Lazebnik et al., “A large-scale study of the ultra wideband microwave dielectric properties of normal, benign and malignant breast tissue obtained from cancer surgeries”, *Phys. Med. Biol.*, vol. 52, pp. 6093–6115, 2007.
- [2] G. Bellizzi, O. M. Bucci, I. Catapano, “Microwave Cancer Imaging Exploiting Magnetic Nanoparticles as Contrast Agent”, *IEEE Trans. On Biomed. Eng.*, vol. 58, no.9, pp.2528-2536, Sept. 2011.
- [3] G. Bellizzi and O. M. Bucci, “A novel measurement approach for the broadband characterization of diluted water ferrofluids”, *EuCAP 2012*.
- [4] O.M. Bucci, G. Bellizzi, I. Catapano, L. Crocco, R. Scapaticci, “Magnetic Nanoparticles Enhanced Microwave Imaging: a Feasibility Assessment”, *EuCAP 2012*.

Session 5 – Numerical methods in electromagnetics

A. Fanti

A vector finite difference approach to the computation of modes in circular waveguide

G. Angiulli, D. De Carlo, and A. Sgrò

Nested BiCGStab for non-Hermitian linear systems arising from discretization of the EFIE

G. Valerio, S. Paulotto, P. Baccarelli, A. Galli, D. R. Jackson, and D. R. Wilton

Efficient computation of periodic Green's functions for printed structures with vertical elements

O. A. Peverini, A. Tibaldi, Z. Farooqui, G. Addamo, G. Virone, R. Orta, and R. Tascone

Analysis and design of passive waveguide devices by spectral element methods

D. Pinchera

An effective hybrid synthesis method for sparse plane wave generators

L. Ntibarikure

Model order reduction in Finite Element analysis of phased array antennas

A VECTOR FINITE DIFFERENCE APPROACH TO THE COMPUTATION OF MODES IN CIRCULAR WAVEGUIDE

A. Fanti

Department of Electrical and electronic Engineering
University of Cagliari Piazza d'Armi, 09123 Cagliari, Italy
alessandro.fanti@diee.unica.it

Abstract

We describe here a Vector Finite Difference approach to the evaluation of waveguide eigenvalues and modes for circular waveguides. The FD is applied using a 2D polar grid, in the waveguide section. A suitable Taylor expansion of the vector mode function, allows to take exactly into account the boundary condition. The FD approximation results in a constrained eigenvalue problem, that we solve using a decomposition method. This approach has been evaluated comparing our results to the analytical modes of the circular waveguide.

Index Terms – constrained eigenvalue problem, equivalent magnetic current, finite-difference, waveguide modes

I. INTRODUCTION

An accurate knowledge of the cut-off frequency and mode vector is important in many waveguide problems. Among them, we quote here the analysis of waveguide slot and apertures using the methods of moments (MoM) [1], and the solution of waveguide junction problem using mode matching [2]. Standard Finite Differences (FD) approaches compute the eigenfunctions of Hertz potential, and so a numerical derivative is therefore required, to get the vector mode functions, which can result in reduced accuracy.

Aim of this work is to present the direct computation of vector eigenfunctions in a waveguide, using a finite difference (FD) approximation of the vector Helmholtz equation on a polar grid. Since we are mainly interested in using those modes in MoM, the entire development will be expressed in term of equivalent magnetic surface currents. This approximation leads to a matrix eigenvector problem, when suitable conditions are added. These come out from the boundary condition and the solenoidal or irrotational condition on mode vectors. The latter must be added as a separate constraint, and the resulting constrained eigenvalue problem can then be solved using linear algebra techniques [3].

II. DESCRIPTION OF THE TECHNIQUE

Let us consider a circular waveguide. The TE modes surface magnetic current \vec{M} , equivalent to the transverse field $\vec{e} = \vec{i}_z \times \vec{M}$, are the eigenfunction of the Helmholtz equation[3]:

$$\nabla_t^2 \vec{M} + k_t^2 \vec{M} = 0 \quad (1)$$

with additional conditions.

$$\nabla_t \times \vec{M} = 0 \quad \vec{M} \cdot \vec{i}_n \Big|_C = 0 \quad (2)$$

where C is the contour of the waveguide (see Fig.1a). FD approach to the solution of this problem is based on the replacement of problem (1) with a discretized version. In order to correctly include the boundary condition, a polar grid is selected, with spacing $\Delta r, \Delta \alpha$, and the equations are replaced by difference equations. For each internal grid point (see Fig.1b), a second order Taylor approximation allows to evaluate $\nabla_t^2 \vec{M}$ using surface magnetic current samples in terms of the neighboring, ampling points.

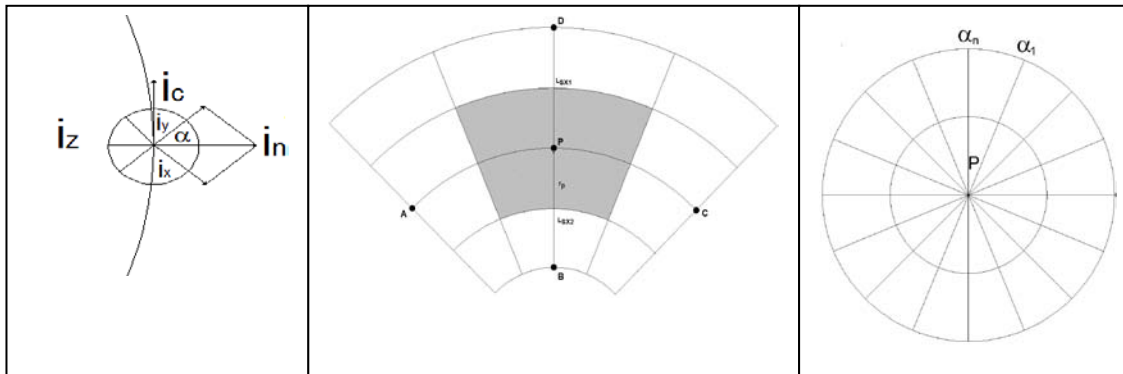


FIG. 1 – (a) Vectors geometry with respect to the contour of the conductor. (b) Internal point of polar framework. (c) Center of polar framework

The expression for an internal point P as in Fig.1b is :

$$\begin{aligned} \nabla_t^2 \vec{M}_P = & \left[M_{B,r} K_1 + M_{D,r} K_2 + M_{A,r} K_3 + M_{C,r} K_3 - M_{P,r} K_4 + M_{A,\alpha} K_5 - M_{C,\alpha} K_5 \right] \cdot \vec{u}_r + \\ & + \left[M_{B,\alpha} K_1 + M_{D,\alpha} K_2 + M_{A,\alpha} K_3 + M_{C,\alpha} K_3 - M_{P,\alpha} K_4 - M_{A,r} K_5 + M_{C,r} K_5 \right] \cdot \vec{u}_\alpha \end{aligned} \quad (3)$$

where $K_1 = \frac{1}{\Delta r^2} - \frac{1}{2r_p \Delta r}$ $K_2 = \frac{1}{\Delta r^2} + \frac{1}{2r_p \Delta r}$ $K_3 = \frac{1}{r_p^2 \Delta \alpha^2}$ $K_4 = K_1 + K_2 + 2K_3 + \frac{1}{r_p^2}$ $K_5 = \frac{1}{2r_p^2 \Delta \alpha}$.

which can be easily extended to a boundary point [4]. To discretize the first condition (2) we can use a first-order Taylor expression and get:

$$\nabla_t \times \overline{M} = \frac{1}{r} \cdot \left(\frac{\partial(rM_\alpha)}{\partial r} - \frac{\partial M_r}{\partial \alpha} \right) = \left(\frac{1}{r_p} \cdot M_{p,\alpha} + \frac{M_{D,\alpha} - M_{B,\alpha}}{2\Delta r} - \frac{1}{r_p} \cdot \frac{M_{C,r} - M_{A,r}}{2\Delta \alpha} \right) = 0 \quad (4)$$

It remains to consider the center of the circle, see Fig.1c. In this point it is not possible to use a Taylor expression since it is a point of singularity for the polar frame. Then we integrate (1) and apply the theorem of the gradient to the result to get:

$$\int_c \left[\left(\frac{\partial M_r}{\partial r} + \frac{1}{r} M_r \right) \cdot \frac{\Delta r}{2} + \frac{\partial M_\alpha}{\partial \alpha} \right] \cdot (i_x \cos(\alpha) + i_y \sin(\alpha)) \cdot d\alpha = -k_t^2 M \left(\pi, \frac{\Delta r^2}{4} \right) \quad (5)$$

After a numerical evaluation we get:

$$\begin{aligned} \sum_{q=1}^N M_{r,q} \cdot \cos(\alpha_q) \cdot \Delta \alpha + \sum_{q=1}^N \left[\frac{M_{\alpha,q} \cdot \sin(\alpha_q) + (M_{0,y}^q \sin(\alpha_q) \cos(\alpha_q) - M_{0,x}^q \sin^2(\alpha_q))}{2} \right] &= -k_t^2 M_x \left(\alpha, \frac{\Delta r}{2} \right) \\ \sum_{q=1}^N M_{r,q} \cdot \sin(\alpha_q) \cdot \Delta \alpha - \sum_{q=1}^N \left[\frac{M_{\alpha,q} \cdot \cos(\alpha_q) + (M_{0,y}^q \cos^2(\alpha_q) - M_{0,x}^q \sin(\alpha_q) \cos(\alpha_q))}{2} \right] &= -k_t^2 M_y \left(\alpha, \frac{\Delta r}{2} \right) \end{aligned} \quad (6)$$

The discretized version of the eigenvalue problem can therefore be expressed as a constrained eigenvalue problems:

$$Ax = \lambda x \quad C^T x = 0 \quad (7)$$

where A is a (2n,2n) matrix, (containing the discretized form of (1), i.e., (3) taking into account the B.C and the (6)) and C is (2n,m) with n>m (expressing the $\nabla_t \times \overline{M}$ condition), and $\lambda = -k_t^2$. Following [5], we can solve (7) by letting $x = Q \cdot y$ and where Q is an orthogonal (2n,2n) matrix obtained by the QR factorization of the matrix C. Then $A \cdot Q \cdot y = \lambda \cdot Q \cdot y \rightarrow Q^T \cdot A \cdot Q \cdot y = \lambda \cdot Q^T \cdot Q \cdot y$ i.e. $By = \lambda y$ where $B = Q^T \cdot A \cdot Q$ is a (2n,2n) matrix. The constrained becomes $(Q \cdot R)^T \cdot x = (Q \cdot R)^T \cdot Q \cdot y = R^T \cdot Q^T \cdot Q \cdot y = R^T \cdot y = 0$. This problem can then be recasted as:

$$\begin{cases} B \cdot y = \lambda \cdot y & \Rightarrow \begin{vmatrix} B_{11} & B_{12} \\ B_{21} & B_{22} \end{vmatrix} \cdot \begin{vmatrix} u \\ v \end{vmatrix} = \lambda \cdot \begin{vmatrix} u \\ v \end{vmatrix} \\ R^T \cdot y = 0 & \Rightarrow \begin{vmatrix} T_1 & 0 \end{vmatrix} \cdot \begin{vmatrix} u \\ v \end{vmatrix} = 0 \end{cases} \quad (8)$$

where B_{ij} is a (n,n) matrix. T_1 are (invertible) triangular matrix. Now $u=0$ [5] and therefore we need to extract the eigenvalues of B_{22} which is a (n,n) matrix. This discretized eigenvalues problem must be solved by numerical routine and, the full matrix routines of Matlab have been used. The waveguide modes can then be obtained as $x = Q \cdot \begin{pmatrix} 0 \\ v \end{pmatrix}$.

III. NUMERICAL RESULTS

The resulting technique gives results comparable (see table I) with analytic eigenvalue and eigenvectors. The last column shows the RMS difference between analytical mode vectors.

Table I - Comparison between our FD code and analytic results for TE modes in circular waveguides $r=4\text{mm}$ $\Delta r=0.03960$ $\Delta\alpha=0.5^\circ$.

n,p	Kta	Ktpv	ep%	RMS_error *1.0e-006
11	0,460296	0,460292	0,000793	0.0001
21	0,763559	0,763531	0,003656	0.0007
01	0,957927	0,957697	0,023982	0.0008
31	1,050297	1,050204	0,008831	0.0011

IV. CONCLUSION

A new FD approach to the computation of the modes of circular waveguide has been described. The typical full matrix obtained by the FD allows an effective computation of the eigenvalues, with a very good accuracy, as shown by our tests.

REFERENCES

- [1] G. Mazzarella, G. Montisci: "Accurate Characterization of the Interaction between Coupling Slots and Waveguide Bends in Waveguide slot Arrays," *IEEE Trans. Microwave Theory and Techniques*, vol.48, issue(7), pp 1154-1157, July 2000.
- [2] P.Matras, R.Bunger, F.Arndt : "Mode-matching analysis of the step discontinuity in elliptical waveguides," *IEEE Microwave and Guided Wave Letters*, vol.6, issue(3), pp 143-145, March 1996.
- [3] W. Gander, G. H. Golub, U. Von Matt: "A constrained eigenvalue problem", *Linear Algebra and its Applications*, Vol.114-115, pp 815-839, March-April 1989.
- [4] A.Fanti, G.Mazzarella. "Vector Finite Difference Approach to the Computation of TM Waveguide Modes.", *Proc.Int. Conf. Loughborough Antennas and Propagation Conference (LAPC2011)*, UK, 14-15 Nov. 2011
- [5] W. Gander, G. H. Golub, U. Von Matt: "A constrained eigenvalue problem", *Linear Algebra and its Applications*, Vol.114-115, pp 815-839, March-April 1989.

NESTED BiCGSTAB FOR NON-HERMITIAN LINEAR SYSTEMS ARISING FROM DISCRETIZATION OF THE EFIE

G. Angiulli⁽¹⁾, D. De Carlo⁽¹⁾, A. Sgrò⁽¹⁾

⁽¹⁾ Dimet, “Mediterranea” University
Via Graziella – Loc. Feo di Vito, 89121 Reggio Calabria, Italy
giovanni.angiulli, domenico.decarlo, annalisa.sgro@unirc.it

Abstract

Although in the last years the BiCGStab has been employed with success to handle large linear systems arising from the the RWG MoM discretization of electromagnetic scattering problems formulated by EFIE, its nested version, the N-BiCGstab, has received little attention. In this work, a numerical study on its performances is presented. Results demonstrate that N-BiCGStab is, at least in the examined cases, faster and more robust than the standard BiCGStab coupled with diagonal or ILU preconditioning.

Index Terms– Krylov Subspace Methods, EFIE, Method of Moments, N-BiCGStab.

I. INTRODUCTION

In Computational Electromagnetics (CEM) a number of alternative integral formulations are available to model the electromagnetic scattering and radiation phenomena. Among these, the standard form of the electric field integral equation (EFIE) still remains extensively exploited, even in spite of some well-known limitations (see [1] and references within). When a real life EM problem is tackled, the discretization of the EFIE provides a very large, dense and non-Hermitian linear system of equations that can be solved in an efficient way by using a Krylov subspace method (KSM) in conjunction with a suitable preconditioning technique (PT) [2]. During the years, many efforts have been done by researchers to define the best choice among the different couples {KSM, PT} available in literature. Nowadays, a good compromise seems reached by the use of the Generalized Minimal Residual method (GMRES), in combination with ILU preconditioning (see [2] and references within). Although the GMRES is optimal, in the sense that it leads to a minimal residual solution over the associate Krylov subspace, such a goal is achieved against a demand in memory space that grows linearly with the number of iterations and that could become rapidly prohibitive in term of memory requirements (see [2] and references within). Even if this limitation can be circumvented when GMRES is employed in its restarted version, the GMRES(m), it is a very difficult task to assign a priori value to the restart parameter m such

that both convergence and memory requirements are both optimized. Hence, especially when large and dense non-Hermitian linear systems are tackled on small workstation a technique involving a fixed amount of memory per iteration should be employed, if out-of-memory errors must to be avoided. This is the case of the Bi-Conjugate Stabilized (BiCGStab) method. In spite of being less popular than the GMRES, BiCGStab has been already exploited with success in CEM literature to treat large EM problems. However, as underlined in [3], the performances of the BiCGStab can be improved providing that the preconditioning step is treated by another KSM so realizing the Nested BiCGStab (N-BiCGStab) method. Although N-BiCGStab has been extensively employed in many others engineering fields (see for example [4] and references within), at the best of our knowledge little attention has been devoted to it in CEM. In this work, preliminary results of a numerical study on its performances for solving the dense non-Hermitian linear systems arising from discretization of EFIE, are presented.

II. THE N-BICGSTAB AT A GLANCE

In what follows we provide a brief account about the ideas and principles characterizing N-BiCGStab (see [3] and references within). Basically it searches for an approximate solution \mathbf{i}_n of the matrix system (i.e. the discretized EFIE)

$$\mathbf{Z}\mathbf{i} = \mathbf{v} \quad (1)$$

of the form

$$\mathbf{i}_n \in \mathbf{i}_0 + K_n(\mathbf{r}_0, \mathbf{Z}), \quad n = 1, 2, 3, \dots \quad (2)$$

where $\mathbf{i}_0 \in \mathbb{C}^n$ is any initial guess for the solution of Eq. (1), $\mathbf{r}_0 = \mathbf{v} - \mathbf{Z}\mathbf{i}_0$ is the residual vector, and $K_n(\mathbf{r}_0, \mathbf{Z})$, defined as $K_n(\mathbf{r}_0, \mathbf{Z}) = \text{span}\{\mathbf{r}_0, \mathbf{Z}\mathbf{r}_0, \dots, \mathbf{Z}^{n-1}\mathbf{r}_0\}$ is the n -th *Krylov subspace* generated by the couple $(\mathbf{r}_0, \mathbf{Z})$. It can be demonstrated that any vector in $K_n(\mathbf{r}_0, \mathbf{Z})$ can be written as a polynomial in \mathbf{Z} times \mathbf{r}_0 , and so Eq. (2) becomes

$$\mathbf{i}_n = \mathbf{i}_0 + q_{n-1}(\mathbf{Z})\mathbf{r}_0 \quad (3)$$

where q_{n-1} is a suitable polynomial of a degree at most $n - 1$. The above relation implies that at the residual $\mathbf{r}_n = \mathbf{v} - \mathbf{Z}\mathbf{i}_n$ is associated a polynomial p_n

$$\mathbf{r}_n = \mathbf{r}_0 - \mathbf{Z}q_{n-1}(\mathbf{Z})\mathbf{r}_0 = p_n(\mathbf{Z})\mathbf{r}_0 \quad (4)$$

of degree at most n , called *residual polynomial*. The approximate solution \mathbf{i}_n , or equivalently, the associate polynomial p_n , is founded by N-BiCGStab requiring that \mathbf{r}_n fulfils the following orthogonality condition

$$\mathbf{r}_n \perp K_n(\hat{\mathbf{r}}_0, \mathbf{Z}^H) \quad (5)$$

(where $\hat{\mathbf{r}}_0 \in \mathbb{C}^n$ is an arbitrary vector satisfying the condition $\langle \mathbf{r}_0, \hat{\mathbf{r}}_0 \rangle = 1$). More precisely N-BiCGStab tries to construct a sequence of vectors $\{\mathbf{i}_n\}$ such that $\mathbf{i}_n \rightarrow \mathbf{i}$ for $n = 1, 2, \dots$ in a given tolerance ε making the n -th iteration consist of two levels: an *outer level* implementing all the procedures that are necessary to compute \mathbf{i}_n starting from \mathbf{i}_{n-1} [3] and an *inner level* in which the preconditioning phase [3]

$$\mathbf{P}\mathbf{e}_{n-1} = \mathbf{r}_{n-1} \quad (6)$$

is solved in an “inexact way” by a secondary KSM (which is chosen by the user), so maintaining the asymptotic complexity $\mathcal{O}(N^2)$ of the overall procedure (at step n) unvaried [3].

III. NUMERICAL RESULTS

As a test case we considered the plane wave scattering by a perfect conducting metallic sphere with radius $r=0.5$ m at the frequency $f=150$ MHz. A computer code implementation of the MoM RWG and of the N-BiCGStab method has been developed exploiting the MATLAB framework. Simulations have been carried out using a PC with an Intel Core™ 2 Duo processor at 1.66 GHz and 4 GB of main memory. The conducting sphere has been discretized with $n = 11850$ edges. All the results have been obtained fixing an accuracy $\varepsilon=10^{-6}$ and a maximum number of iterations $\text{maxit}=500$ for the outer level, while fixing $\varepsilon= 10^{-1}$ and $\text{maxit} = 100$ for the inner level. The initial guess vector is set equal to the null vector for both levels. Different KSMs have been considered for the inner level but, due to lack of space, in what follows only results considering the BiCGStab as inner method are shown. Table (1) compares the performances of the N-BiCGStab, in which the preconditioning phase (6) is carried out exploiting the antihermitian component of \mathbf{Z} , with those provided by *i)* the standard BiCGStab algorithm and *ii)* some preconditioned implementations of it. Table (1) and figure (1) make apparent how the N-BiCGStab reduces significantly both the overall number of iterations and the computational time required to reach convergence.

IV. CONCLUSIONS

In this work a numerical study on the performances of the N-BiCGStab for non-Hermitian linear system arising from the discretization of the EFIE is presented. At least in the examined cases, numerical results show that this technique can reduce significantly the computational burden with respect the standard BiCGStab coupled with a diagonal or ILU preconditioner. Currently, we are working on an implementation of this technique for general purpose graphic processing units (GPGPU) following the guideline outlined in [5].

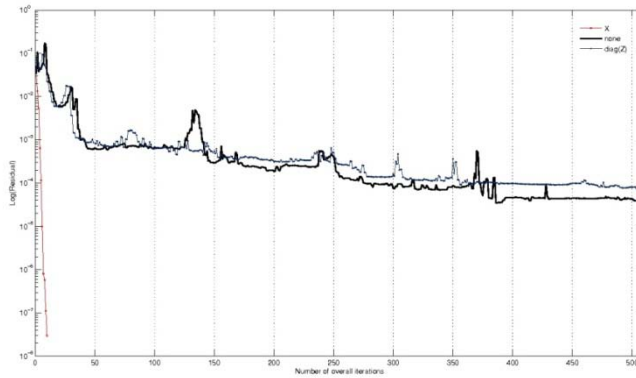


FIG. 1– Euclidean norm of the residual vector. Note that in the case under consideration the ILU-preconditioned BiCGStab saturates the available memory and so cannot be compared with the other techniques.

TABLE I – BiCGSTAB vs N-BiCGSTAB

Method	Convergence	Iterations	Time [Sec]	Residual
N-BiCGStab	Yes	10	150	$2.9 \cdot 10^{-8}$
BiCGStab	No	500	467	$2.9 \cdot 10^{-5}$
BiCGStab diag. precond.	Yes	486	697	$3.8 \cdot 10^{-7}$
BiCGStab ILU precondition	No (out of memory)	---	---	---

REFERENCES

[1] Angiulli G., Tringali S., “Stabilizing the E-Field Integral Equation at the internal resonances through the computation of its numerical null space,” *International Journal of Applied Electromagnetics and Mechanics*, n. 32, pp. 63-72, 2010.

[2] Bunse-Gerstner A., Cañas-Gutiérrez I., “A preconditioned GMRES for complex dense linear systems from electromagnetic wave scattering problems,” *Linear Algebra and Its Applications*, Vol. 416, pp. 135-147, 2006.

[3] Vogel J. A., “Flexible BiCG and flexible BI-CGSTAB for nonsymmetric linear systems”, *Applied Mathematics and Computation*, vol. 188, pp.226-233, 2007.

[4] Manguoglu M., Sameh A. H., Tezduyar T. E., and Sathe S., “A nested iterative scheme for computation of incompressible flows in long domains”, *Computational Mechanics*, vol.43, n.1, pp.73-80, 2008.

[5] Velamparambil S., MacKinnon-Cornier S., Perry J., Lemos R., Okoniewski M., Leon J., “GPU Accelerated Krylov Subspace Methods for Computational Electromagnetics”, *Proc. Of the 38th Microwave Conference*, pp. 1312-1314, 2008.

EFFICIENT COMPUTATION OF PERIODIC GREEN'S FUNCTIONS FOR PRINTED STRUCTURES WITH VERTICAL ELEMENTS

G. Valerio⁽¹⁾, S. Paulotto⁽²⁾, P. Baccarelli⁽³⁾, A. Galli⁽³⁾,
D. R. Jackson⁽⁴⁾, and D. R. Wilton⁽⁴⁾

⁽¹⁾ IETR UMR 6164, Institut d'Electronique
et de Télécommunications de Rennes – Rennes, France
guido.valerio@univ-rennes1.fr

⁽²⁾ Maxtena Inc. – Bethesda, MD, U.S.A.

⁽³⁾ Department of Information Engineering, Electronics and
Telecommunications, “Sapienza” University of Rome – Rome, Italy

⁽⁴⁾ Department of Electrical & Computer Engineering,
University of Houston – Houston, TX, U.S.A.

Abstract

The vertical components of the mixed-potential Green's functions due to one-dimensional (1-D) or bidimensional (2-D) phased array of dipoles in a layered medium are computed through suitable homogeneous-medium asymptotic extractions from the standard spectral series of Floquet's harmonics. The extracted terms can be expressed as potentials for a 1-D or 2-D array of half-line sources. Their computation requires a suitable modification of the Ewald method, thus resulting in new modified spectral and spatial series, having Gaussian convergence even in the case of complex modes and improper harmonics. Numerical comparisons have been performed to validate the proposed acceleration technique.

Index Terms – Acceleration methods, Ewald method, Green's functions, Mixed potentials, Periodic structures.

I. INTRODUCTION

Computational modeling tools for a fast and accurate design of guiding and radiating structures with 1-D and 2-D periodicity in layered media have recently found an increasing interest. Most of the available integral-equation approaches are based on the solution of a Mixed-Potential Integral Equation (MPIE) by means of the Method of Moments (MoM) [1], where currents can be expressed in terms of sub-domain basis functions [2]. This method leads to an efficient analysis that is based on the reduction of the computational domain to a single unit cell [3,4]. Nevertheless, since periodic Green's functions are usually expressed in terms of slowly-converging series, acceleration techniques are required for their computation [3,4]. In this work, effective methods are discussed for the faster computation of the dyadic and scalar periodic mixed-potential Green's function, which are suitable for the analysis of vertical elements and can take into account the presence of improper leaky waves supported by the periodic layered structures.

II. MIXED-POTENTIAL ACCELERATION

A mixed-potential formulation [1] is chosen here. Its milder spatial singularities lead to an easier integration over the testing and basis functions [2], with respect to field-based formulations. Both dyadic and scalar Green's functions are defined. They are usually expressed as spectral sum of harmonics, where the actual expressions depend on the kind of periodicity considered. With reference to the geometries shown in Fig. 1, we mention here two kinds of spectral series:

$$G(\mathbf{r}, \mathbf{r}') = \frac{1}{2\pi p} \sum_{n=-\infty}^{+\infty} e^{-jk_{x_n}\Delta x} \int_{-\infty}^{+\infty} \tilde{G}(\mathbf{k}_{t_n}; z, z') e^{-jk_y\Delta y} dk_y \quad (1)$$

$$G(\mathbf{r}, \mathbf{r}') = \frac{1}{A} \sum_{n=-\infty}^{+\infty} \sum_{m=-\infty}^{+\infty} \tilde{G}(\mathbf{k}_{t_{nm}}; z, z') e^{-j\mathbf{k}_{t_{nm}} \cdot \Delta \mathbf{r}} \quad (2)$$

where for 1-D periodic arrays along x , as in Fig. 1(a), p is the spatial period, $k_{x_n} = k_{x_0} + 2\pi n/p$ is the wavenumber along x of the n th harmonic, k_y is a continuous spectral integration variable, and $\mathbf{k}_{t_n} = k_{x_n}\mathbf{x}_0 + k_y\mathbf{y}_0$. For 2-D arrays, as in Fig. 1(b), A is the unit-cell area and $\mathbf{k}_{t_{nm}} = \mathbf{k}_{t_{00}} + (2\pi m\mathbf{z}_0 \times \mathbf{s}_1)/A + (2\pi n\mathbf{s}_2 \times \mathbf{z}_0)/A$ is the wavenumber of the (n, m) th harmonic, \mathbf{s}_1 and \mathbf{s}_2 being the spatial lattice vectors of the array. \tilde{G} is a spectral Green's function, known in closed form for any stratification.

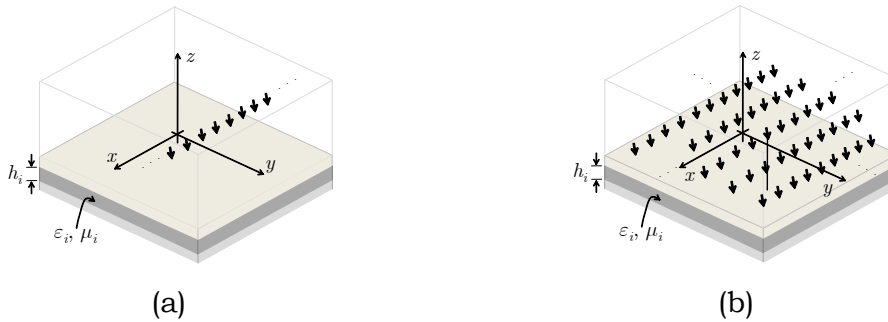


FIG. 1 – Stratified geometries with periodic distributions of sources analyzed here: (a) 3D problem with 1D periodicity; (b) 3D problem with 2D periodicity.

Depending on the direction of the currents, the computation of different components of the potentials is required. For instance, formulating an EFIE for purely planar periodic structures (such as periodic microstrips, with electric currents orthogonal to the axis of stratification) requires the computation of only two scalar potentials (the “transverse potentials”) [1]. For a more complex (non-planar) structure, the remaining “vertical potentials” should also be calculated (including the scalar potential P_z and the off-diagonal entries of the dyad \mathbf{G}_A) [1].

The convergence of the series and integrals in (1)-(2) becomes dramatically slow as $z \rightarrow z'$ at an interface between media. A common approach to accelerate the convergence of the transverse potentials is

the asymptotic extraction of direct and quasi-static images as (we refer here to the array 2-D point sources, but similar extractions can be performed for the other geometry):

$$G(\mathbf{r}, \mathbf{r}') = \frac{1}{A} \sum_{n,m=-\infty}^{+\infty} \left[\tilde{G}(\mathbf{k}_{t_{nm}}; z, z') - \sum_{i=-1}^{+1} C_i \tilde{g}(\mathbf{k}_{t_{nm}}; z_i) \right] e^{-j\mathbf{k}_{t_{nm}} \cdot \Delta \mathbf{r}} + \sum_{i=-1}^{+1} C_i g(\mathbf{k}_{t_{00}}; \mathbf{r}) \quad (3)$$

If the source and the observation points are in the same layer, three images are extracted: a spectral-domain homogeneous-medium Green's function \tilde{g} due to the “direct” path from the source to observation point, and due to the two reflections from the nearest interfaces. If the source and the observation points are in adjacent layers, only the direct image is extracted. The first series in (3), called “regularized Green's functions,” is faster converging due to the asymptotic cancellation between terms. Extracted terms are summed back to restore the original function G in the form of a homogeneous-medium periodic Green's function g . This is still expressed as a slowly-converging series, but it can be evaluated with the Ewald method [3] as the sum of two different series, g_E^{spectral} and g_E^{spatial} , each one with Gaussian convergence.

A more delicate extraction is required for vertical potentials, due to their different asymptotic behavior. The scalar vertical potential P_z (again only for the 2-D case for brevity) is computed with extraction [3]:

$$P_z(\mathbf{r}, \mathbf{r}') = \frac{1}{A} \sum_{n,m=-\infty}^{+\infty} \left[\tilde{P}_z(\mathbf{k}_{t_{nm}}; z, z') - \sum_{i=-1}^{+1} \frac{D_i}{jk_{z_{nm}}} \tilde{g}(\mathbf{k}_{t_{nm}}; z_i) \right] e^{-j\mathbf{k}_{t_{nm}} \cdot \Delta \mathbf{r}} + \sum_{i=-1}^{+1} D_i g^z(\mathbf{k}_{t_{00}}; \mathbf{r}) \quad (4)$$

where the extracted terms are spectral homogeneous-medium Green's functions divided by the factor k_z . Due to this factor, the functions g^z can be related to homogeneous-medium periodic Green's functions g through integration along the stratification direction (z):

$$g^z(\Delta \mathbf{r}) = \int_{|\Delta z|}^{+\infty} g d\zeta \quad (5)$$

The off-diagonal terms zx and zy of the dyad \mathbf{G}_A can be simply computed by differentiating the extracted terms in (4) with respect to the transverse coordinates x and y , respectively. From (5), the Ewald method can be applied by integrating the two original Ewald series along the z direction. This defines two modified Ewald series:

$$g^z(\Delta \mathbf{r}) = \int_{|\Delta z|}^{+\infty} g d\zeta = \int_{|\Delta z|}^{+\infty} g_E^{\text{spectral}} d\zeta + \int_{|\Delta z|}^{+\infty} g_E^{\text{spatial}} d\zeta = g_E^{z,\text{spectral}} + g_E^{z,\text{spatial}} \quad (6)$$

both again with a Gaussian convergence rate, which are valid also in the case of improper waves.

III. NUMERICAL RESULTS

We show here some numerical results to validate the computational methods described in the previous section. In Figs. 2(a) and 2(b), comparisons are given between the non-accelerated and the accelerated scalar vertical potential P_z and the off-diagonal term zx of \mathbf{G}_A for a 1-D array of sources over a grounded slab. A forward space-leaking $n = 0$ harmonic is chosen, with the spectral integration paths in (1) chosen according to [4]. As expected, the results are in perfect agreement, thus validating the method in the critical case of improper waves.

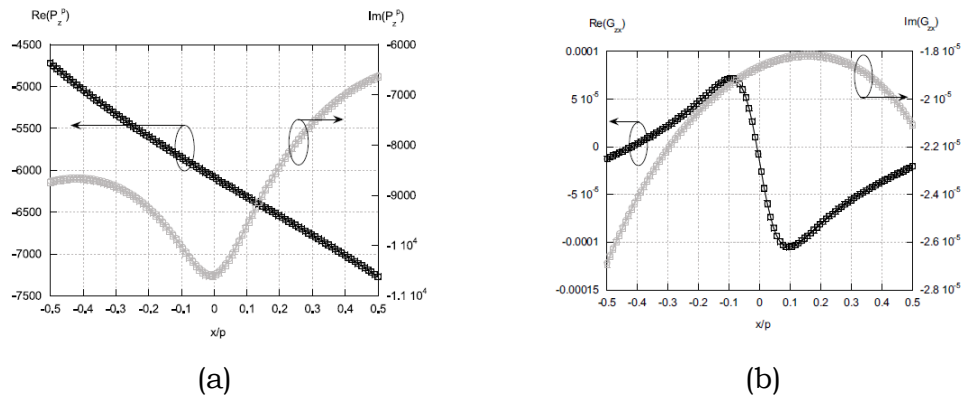


FIG. 2 – Real (black line) and imaginary (gray line) part of the potentials: (a) P_z and (b) G_{zx} . Computation without any acceleration (lines with squares) and with the asymptotic extraction (4) (lines with circles) in the segment $-p/2 < \Delta x < p/2$, $p = 2$ mm, $\Delta y = p/20$, $\Delta z = 0$, in a grounded slab with $\epsilon_r = 2.2$, height $h = 0.508$ mm, at frequency $f = 10$ GHz and a wavenumber of $k_x/k = 0.8 - j0.02$.

IV. CONCLUSION

Original techniques for the efficient evaluation of all the components of multilayered 1-D and 2-D periodic Green's functions have been proposed and tested. Even if related to the accuracy degree and the specific structure investigated, the time saving with these acceleration algorithms is remarkable (typically two or more orders of magnitude).

REFERENCES

- [1] K. A. Michalski and D. Zheng, "Electromagnetic scattering by sources of arbitrary shape in layered media, Part I: Theory," *IEEE Trans. Antennas Propag.*, vol. 38, Mar. 1990, pp. 335-344.
- [2] S. M. Rao, D. R. Wilton, and A. W. Glisson, "Electromagnetic scattering by surfaces of arbitrary shape," *IEEE Trans. Antennas Propag.*, vol. 30, May 1982, pp. 409-418.
- [3] G. Valerio, D. R. Wilton, D. R. Jackson, and A. Galli, "Acceleration of mixed potentials from vertical currents in layered media for 2-D structures with 1-D periodicity," *IEEE Trans. Antennas Propag.*, in press.
- [4] P. Baccarelli, C. Di Nallo, S. Paulotto, and D. R. Jackson, "A full-wave numerical approach for modal analysis of 1-D periodic microstrip structures," *IEEE Trans. Microw. Theory Tech.*, vol. 54, Apr. 2006, pp. 1350-1362.

ANALYSIS AND DESIGN OF PASSIVE WAVEGUIDE DEVICES BY SPECTRAL ELEMENT METHODS

O. A. Peverini, A. Tibaldi, Z. Farooqui, G. Addamo, G. Virone,
R. Orta, R. Tascone

CNR-IEIIT, c/o Politecnico di Torino
Corso Duca degli Abruzzi 24, 10129, Torino, Italy
oscar.peverini@ieiit.cnr.it

Abstract

This work will present a spectral-element method suitable for the efficient design of two-dimensional passive waveguide components. The method exploits different domain mappings in order to correctly model the singular behavior of the field close to sharp edges also in presence of curved sides. Several devices for satellite communication and scientific instrumentation have successfully been designed with the present technique. Detailed comparison between simulated and measured performance will prove the reliability of the method also when very demanding specifications are set on components design

Index Terms – Model-order reduction, passive waveguide devices, spectral-element methods.

I. INTRODUCTION

State-of-the-art microwave and millimeter-wave passive waveguide components have to exhibit wide/multi-band behavior along with demanding electrical performances that partly depend on the specific application, i.e. communications, scientific surveys and remote-sensing. As an example, in satellite communication systems, the broad-band and multi-band features have to be specifically traded-off against power-handling management and interference-signal suppression [1]. Hence, very accurate modeling and measurement procedures have to be applied during the design and testing of each component of the feed-chains. Since two-dimensional (2-D) devices are widely used in these systems, the development of very efficient analysis methods to be used in the design stage of 2-D waveguide structures is of practical interest.

In this work, the design of 2-D waveguide components is addressed by applying a spectral element method (SEM) in order to efficiently evaluate the multi-mode Generalized Scattering Matrices (GSMs) of E(H)-plane components with sharp edges and irregular shapes. The analysis of complex devices is efficiently achieved by cascading the multimode GSMs of their basic components, whose geometry is synthesized by means of the scattering matrix design approach described in [2]. In the SEM, the domain is subdivided into a few elements to gain flexibility in the geometry description, and at the same time the degree of the polynomials in each sub-domain is relatively high

to retain the exponential convergence typical of spectral-methods. However, the singular behavior of the fields close to sharp edges significantly degrade its convergence properties. In order to overcome this burden, as in the FEM [3], the set of polynomial functions can be augmented with singular functions. However, only a small number of singular functions can be introduced on each element, since they can become essentially linearly dependent on the polynomial basis set [4]. Moreover, the singular functions must be defined on elements with irregular boundaries, so that a small number of subdomains are needed to describe the geometry.

I. SPECTRAL ELEMENT METHOD

The analysis of a x -invariant structure with section Ω can be cast in the following weak integral form of the scalar Helmholtz equation [5]

$$\iint_{\Omega} \nabla_t \phi \cdot \nabla_t v \, d\Omega - k_t^2 \iint_{\Omega} \phi v \, d\Omega = \sum_{k=1}^{N_{\text{ports}}} \int_{\Gamma^{(k)}} \frac{\partial \phi_{\text{wg}}^{(k)}}{\partial n_{\text{wg}}^{(k)}} v \, d\Gamma_{\text{wg}}^{(k)} \quad \forall v \in X_v \quad (1)$$

where X_v is a suitable space of test functions, and the variables ϕ and ϕ_{wg} represent the scalar field component in the Ω domain and in the input waveguide ports, respectively. This scalar variable represents either the H_x or E_x field component, depending on the set of incident modes, i.e. LSE^(x) or LSM^(x). Therefore, the same geometry can be considered for the analysis of both E-plane and H-plane structures. The unknown ϕ has to satisfy the Neumann or Dirichlet boundary conditions on the metal walls (depending on the problem type) and the continuity condition through the waveguide ports.

The basic steps of the spectral element method to be presented are:

- Definition of a geometrically conforming partition in order to decompose the object region Ω into M subdomains Ω_i .
- Evaluation of an analytical linear blending mapping from each subdomain Ω_i to the unit square $S = (-1,1)^2$ in the reference σ -domain.
- Introduction of a companion structure in a χ -domain with rectified sides in order to correctly model the singular behavior of the field close to sharp edges also in presence of curved sides.
- Definition of a set of basis functions on each subdomain Ω_i as the tensor product of Chebyshev polynomials defined in the reference σ -domain that are weighted by singular functions defined in the χ -domain.
- Application of the basis-recombination strategy [6] in order to derive a set of a set of basis functions that satisfy the boundary conditions
- Ortho-normalization of the basis-functions set.

- Application of the mortar-matching technique [6], in order to glue together the functions defined on each subdomain Ω_i
- Introduction of a reduced-order model by evaluating a set of problem-matched functions [7].
- Computation of the generalized scattering matrix of the component by applying the Galerkin method (with the problem-matched basis functions) to (1).

II. RESULTS

Several devices have been developed by applying the present analysis method. As an example, Fig. 1 shows the comparison between the simulated and measured scattering coefficients of a Ku-band E-plane diplexer operating broadcast and fixed satellite services with two Rx channels. Although the transition band of the diplexer is narrower than 1 %, a very remarkable agreement between simulated and measured performance has been achieved.

I. CONCLUSION

The present method has successfully been applied to the analysis of E(H)-plane devices. Its extension to the analysis of cylindrical structures is currently under development. This is expected to be particularly effective in the design of dual-band high-efficiency smooth-wall feed-horns for multi-beam satellite systems.

ACKNOWLEDGEMENT

This work has been partly supported by Thales Alenia Space Italy and by the Italian Ministry of Education, University and Research (MIUR) under the PRIN grant 20097JM7YR .

REFERENCES

- [1] P. Perottino, P. Lepeltier, J. Maurel, K. Tossou, L. Salghetti Drioli, and P. Sarasa, "Multi-Frequency Feed for Telecommunications Satellite", *Proc. 32nd ESA Antenna Workshop*, October 2010, ESTEC, The Netherlands.
- [2] R. Tascone, P. Savi, D. Trincherro, and R. Orta, "Scattering matrix approach for the design of microwave filters", *IEEE Trans. Microwave Theory Tech.*, vol. 48(3), pp. 423-430, March 2000.
- [3] J.S. Juntunen and T. D. Tsiboukis, "On the FEM treatment of wedge singularities in waveguide problems", in *IEEE Trans. Microwave Theory Tech.*, vol. 48(6), pp. 1030-1037, June 2000.

- [4] J. P. Boyd, *Chebyshev and Fourier spectral methods*, New York: Dover Publications, 2000.
- [5] G. Pelosi, R. Coccioli, and S. Selleri, *Quick finite elements for electromagnetic waves*, Norwood, MA: Artech House, 1998.
- [6] C. Canuto, M. Y. Hussaini, A. Quarteroni, and T.A. Zang, *Spectral methods: evolution to complex geometries and applications to fluid dynamics*, Berlin, Germany: Springer-Verlag, 2007.
- [7] O. A. Peverini, R. Tascone, M. Baralis, G. Virone, D. Trincherro, and R. Orta, "Reduced-order optimized mode-matching CAD of microwave waveguide components", *IEEE Trans. Microwave Theory Tech.*, vol. 52(1), pp. 311-318, Jan. 2004.

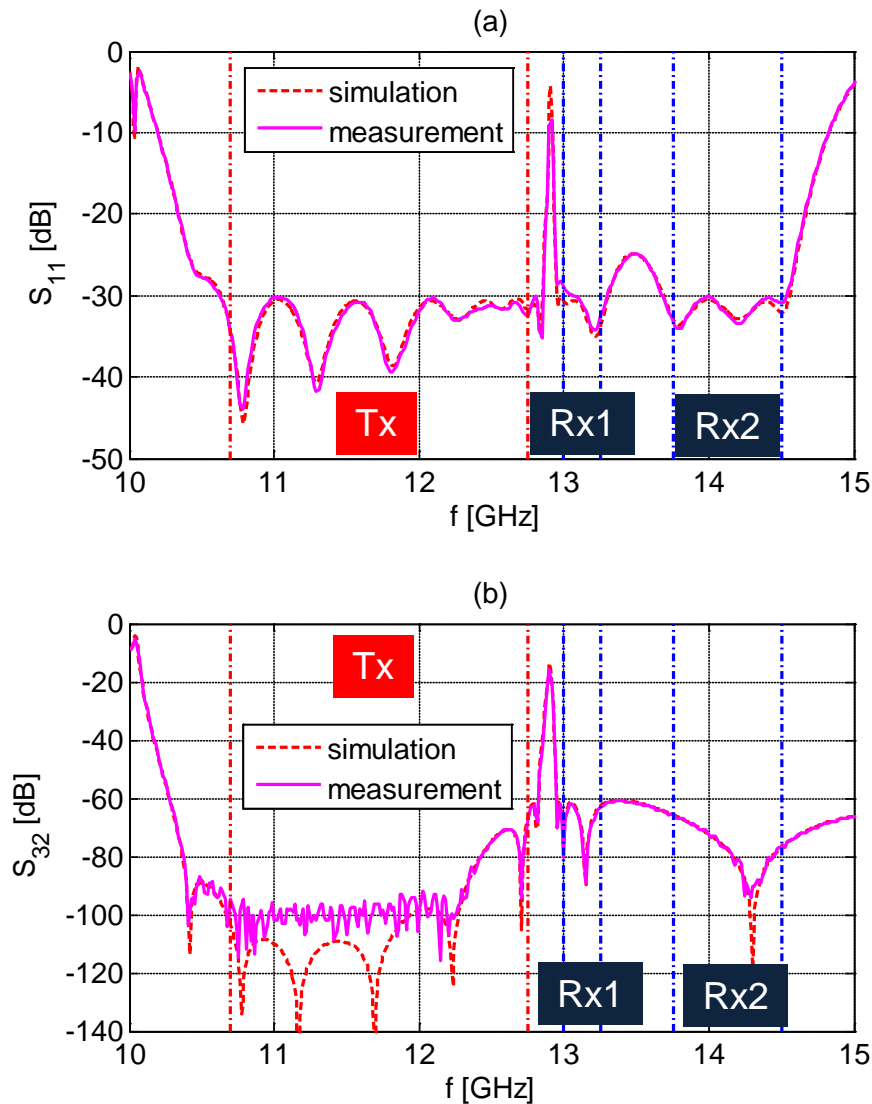


FIG. 1 – Simulated and measured scattering parameters of the Ku-band diplexer described in the text. (a) Reflection coefficient at the common port 1. (b) Transmission coefficient from the Tx port 2 to the Rx port 3 (Isolation).

AN EFFECTIVE HYBRID SYNTHESIS METHOD FOR SPARSE PLANE WAVE GENERATORS

D.Pinchera⁽¹⁾

⁽¹⁾ DIEI, Università degli Studi di Cassino e del Lazio Meridionale,
Via G.Di Biasio 43, 03043 Cassino, Italy

Abstract

In this contribution a novel synthesis approach for Plane Wave Generators is presented; the advantages of the hybrid method used for the synthesis are its numerical efficiency and the effectiveness of the solution found. The layouts found by the algorithms present also the advantage of a reduced complexity and a simplified construction of the achievable layouts.

Index Terms – Antenna Measurements, Antenna Arrays, Hybrid Numerical Methods

I. INTRODUCTION

Antenna testing is one of the most important paradigms of hi-performance antenna design [1]. Among the different solutions currently adopted (far-field ranges, compact ranges, near-field systems) Plane Wave Generators are attracting more and more interest in the last years [2-7]. A Plane Wave Generator (PWG) is an antenna array specifically designed to synthesize a plane wave, or a superposition of plane waves, in a near field volume. A PWG has several interesting advantages compared to other antenna testing systems. It shares with compact ranges the possibility of performing fast measurements in controlled indoor environments, while its size can be kept smaller, with clear advantages in the size and cost of the anechoic chamber.

In this paper a novel synthesis approach for Plane Wave Generators is summarized as well as the numerical analysis of some design examples; this contribution describes part of an extensive work [2,3], performed jointly by the Università di Napoli “Federico II” and Università degli Studi di Cassino e del Lazio Meridionale, within a research activity supported by Selex Sistemi Integrati [8].

II. FORMULATION OF THE PROBLEM AND THE ALGORITHM DEVELOPED

Let us consider the problem of synthesis of a plane wave on the PWA coming from broadside direction. Let \mathbf{P} the vector collecting the positions of the PWG elements, whose excitations are collected in the vector \mathbf{I} . The planar Plane Wave Area will be denoted by PWA, while the surface of the lateral walls of the anechoic chambers will be denoted by Ω (Fig.1). The optimal vectors \mathbf{I} and \mathbf{P} describing the PWG, under constraints on the level of the cross-polar component on the PWA, and the level of the field amplitude on the later walls of the anechoic chamber can be obtained solving the following problem:

$$\arg \min_{\mathbf{I}, \mathbf{P}} \|E_{cop}(\mathbf{I}, \mathbf{P}) - 1\|_2 \quad \text{on PWA} \quad (1)$$

with the following constraints:

$$\langle E_{cop}(\mathbf{I}, \mathbf{P}) \rangle = 1 \quad \text{on PWA} \quad (2)$$

$$|E(\mathbf{I}, \mathbf{P})| < a \quad \text{on } \Omega \quad (3)$$

$$|E_{cross}(\mathbf{I}, \mathbf{P})| < \varepsilon \quad \text{on PWA} \quad (4)$$

wherein E denotes the radiated field, E_{cop} and E_{cross} denote its copolar and crosspolar components, and $\|\cdot\|_p$ the L_p norm. As discussed in [2], in case of directive AUT $p=2$ is the most appropriate choice.

The considered formulation of the problem is difficult to handle, since the functional E is a strongly non linear function of the vector of positions \mathbf{P} ; furthermore there is an open question regarding the right number of radiating elements to use, that should be reduced as much as possible in order to keep manufacturing costs low.

This latter problem can be faced by choosing a number of radiating elements (approximately) equal to the number of degrees of freedom on the AUT of the most tilted plane wave that the PWG is going to radiate [2]. Once the number of radiating elements has been chosen an effective procedure of synthesis can be achieved exploiting as much as possible the linearity of the radiation operator respect to the PWG elements' excitations: an evolutionary algorithm searches for the optimal vector \mathbf{P} while the optimal excitations are found by means of fast convex programming techniques.

This approach requires a global search in a space with a number of dimensions proportional to the overall number of antennas, that could be cumbersome. According to the optimal continuous solutions found in [2], it could be reasonable to place the radiating elements according to a non-equispaced grid (Fig.2). This choice has two main advantages: first, the number of unknowns is strongly reduced (for a square PWG we have the square root of the number of feeds) so we can have a reasonably good synthesis with only 100 iterations; second, the synthesized layout can be manufactured with reduced costs thanks to the regular structure of the array.

Since it can be demonstrated that for directive AUTs the optimal metric for evaluating the quality of a PWG is δ_2 [2], defined as:

$$\delta_2 = 1/\sqrt{A} \|\delta E_{cop}\|_2 / \langle E_{cop} \rangle \quad (5)$$

the cost function adopted for the evolutionary algorithm is:

$$C = \begin{cases} \delta_2 & \text{if } |E| < a \text{ on } \Omega \\ \max(E(\mathbf{I}, \mathbf{P})) & \text{if } |E| \geq a \text{ on } \Omega \end{cases} \quad (6)$$

In this way the cost will be positive and equal to the maximum field exceeding the boundaries if the boundary constraints are not verified, and will be negative when such a constraint is verified. Also, the algorithm will try at first to find a position able to radiate a field in the PWA that does satisfies the constraints, then the solution will be further improved in order to achieve the minimum error on the PWA.

When fields from directions other than broadside are required the synthesis is achieved considering a number of incidence directions in a chosen range, and choosing as cost metric the index Φ , equal to the maximum cost function among the different incidences considered.

III. NUMERICAL EXAMPLES

As an example a synthesized layout made of 400 radiating elements will be shown; in this case $d=35\lambda$, $2a=28\lambda$ and $2b=25\lambda$. In Fig. 3 we have the elements' positions and relative excitations in the case of synthesis of a plane wave coming from broadside direction, while in Fig. 4 the field on the PWA plane is depicted. In the shown case we have a quality index $\delta_2=-33.8\text{dB}$. To verify the quality of the solution found, the reconstruction of the field radiated by a Chebyshev planar array is depicted in Fig.5, showing a very good agreement. The hybrid algorithm is numerically efficient, since it took less than 1 hour to synthesize the shown example on a PC with an Intel i7 2.3GHz processor and 6Gb RAM.

Finally in Fig.6 the performance index Φ of the optimized structures (in this case with 32×32 elements to match the correct number of degrees of freedom of the tilted plane wave on the PWA) when considering plane waves coming from variable incidence ranges is shown. More synthesis examples will be shown during the conference.

IV. CONCLUSIONS

The PWG synthesis algorithm presented allows to synthesize array layouts capable to perform a good antenna testing. The synthesis algorithm is quick, and allows to design arrays that are relatively simple and cheap to build, making the Plane Wave Generators an even more appealing solution for antenna testing

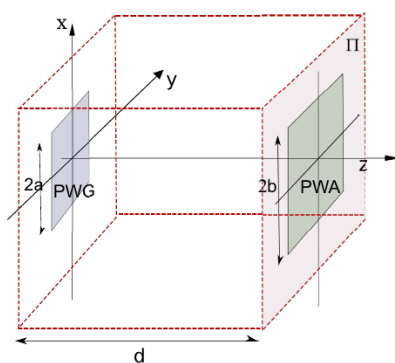


FIG. 1 – PWG scheme; Π is the surface on which the PWA is placed; PWA is the AUT Area

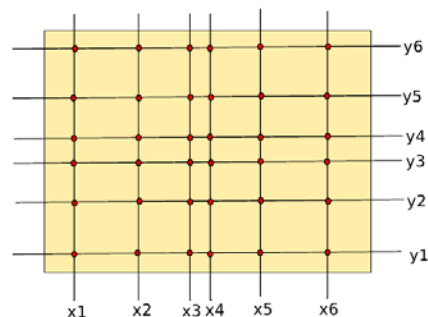


FIG. 2 – Scheme of the PWG elements' grid

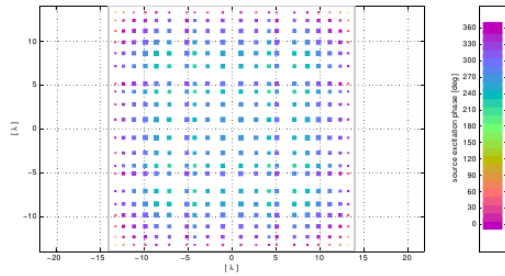


FIG. 3 – Layout of a PWG of 400 elements

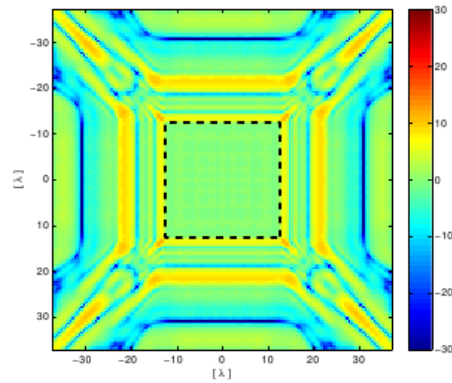


FIG. 4 – Field of the PWG on the PWA [dB]

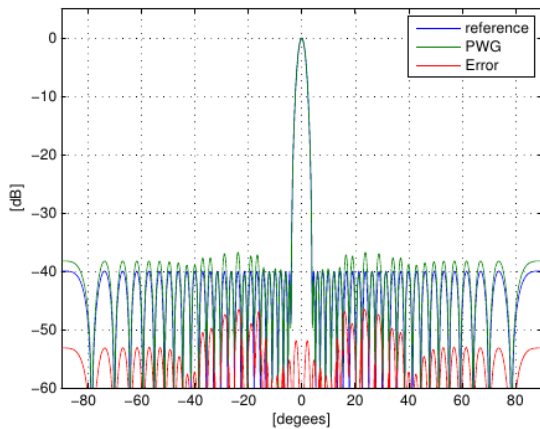


FIG. 5 – Reconstruction error in the case of the testing of a Chebyshev planar array

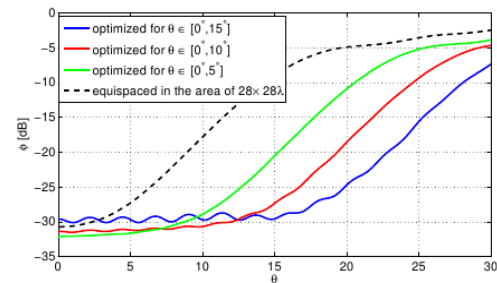


FIG. 6 – Performance index Φ in case of layouts optimized for variable angles of incidence

REFERENCES

- [1] G.E. Evans, *Antenna Measurement Techniques*, Artech-House, 1990
- [2] O.M. Bucci, M.D. Migliore, “Plane-Wave Generator Synthesis. Part 1: Design Criteria and Achievable Performances”, submitted
- [3] O.M. Bucci, M.D. Migliore, G. Panariello and D. Pinchera “Plane-Wave Generator Synthesis. Part 2: Effective Synthesis of Sparse PWG”, submitted
- [4] A. Capozzoli, Claudio Curcio and A. Liseno, “Time-Harmonic Echo Generation”, *IEEE Trans. on Antennas and Propagation*, Vol. 59, no.9, September 2011, pp. 3234-3245
- [5] D. A. Hill, A circular array for plane-wave synthesis, *IEEE Trans. Electromagn. Compat.*, vol. 30, no. 1, pp. 38, Feb. 1988.
- [6] R. Haupf, “Generating a Plane Wave With a Linear Array of Line Sources”, *IEEE Trans. on Antennas and Propagation*, Vol 51, n. 2, Feb 2003, pp. 273-278
- [7] A. Buonanno, M. Durso and G. Proscio, “Reducing Complexity in Indoor Array Testing”, *IEEE Trans. on Antennas and Propagation*, Vol. 8, Aug. 2010, pp. 2781 – 2784
- [8] Research Contract between Selex S. I. and University of Naples Federico II: “SINTESI DI ARRAY SPARSI PER LA REALIZZAZIONE DI UN PLANE WAVE GENERATOR (PWG)”

MODEL ORDER REDUCTION IN FINITE ELEMENTS ANALYSIS OF PHASED ARRAY ANTENNAS

Laurent Ntibarikure

Department of Electronics and Telecommunications
University of Florence
Via di Santa Marta 3, I-50139 Florence, Italy
laurent.ntibarikure@unifi.it

Abstract

The model order reduction technique is applied to the finite elements analysis of phased array antennas, leading to fast and accurate computation of the radiation pattern in front of a beam steering process. Computational timings and approximation error of the reduced order model are shown for a patch antennas array, proving the noticeable advantages of the presented approach.

Index Terms – Finite elements, phased array antennas, model order reduction, beam steering.

I. INTRODUCTION

In modern communication systems and many other applications such as radar utilization, large arrays of antennas are employed to form an electronically steerable antenna beam while completely avoiding mechanically moving parts. In order to adjust such a beam to the given dynamically changing needs, a large amount of consecutive full-wave field analysis runs would be necessary to process every emerging parameter set.

Due to the enormous computational effort that would be needed for such analysis, it is highly desirable to extract, in an off-line stage, a subset of information from those numerically accurate fully three dimensional results, enabling in an on-line stage, fast tuning of parameters at a lower accuracy level. In mathematical terms, the challenge is to reduce a very large linear system of equations, with typically millions of unknowns, to a comparatively small one with only thousands of unknowns, while necessarily keeping the relevant information. This kind of approach belongs to the group of model order reduction algorithms which are nowadays employed in many areas, in particular in electronic design processes [1].

Due its capability to handle materials inhomogeneity and geometrical complexity of modern antennas, to its formulation that allows antennas coupling analysis, the finite elements method results to be a suitable analysis tool for phased array antennas. Being usually

truncated by means of absorbing boundary conditions, the domain of analysis is restricted to the near fields. Radiation patterns must hence be computed in a post-processing step from the knowledge of the tangential near fields on the enclosing surface boundaries.

The finite elements formulation for the near-field computation, the near-field to far-field transformation method and the model order reduction technique employed are presented in Section II. Section III shows results obtained from the analysis of a 3-by-5 patch antennas array. Section IV draws some conclusions.

II. FORMULATION

The analyzed boundary value problem (Fig. 1) consists of solving the vector Helmholtz equation for the electric field:

$$\nabla \times \frac{1}{\mu_r} \nabla \times \mathbf{E} - k_0^2 \varepsilon_r \mathbf{E} = 0 \quad (1)$$

with perfect electric boundaries conditions on Γ_E , absorbing boundary conditions on Γ_R and wave ports conditions (keeping only fundamental mode) on Γ_{WG}^p , $p=1\dots P$. k_0 is the free-space wavenumber, μ_r and ε_r are, respectively, the relative permeability and permittivity of the utilized materials. For the sake of simplicity, all metallic parts that compose the antennas array are assumed to be perfect electric.

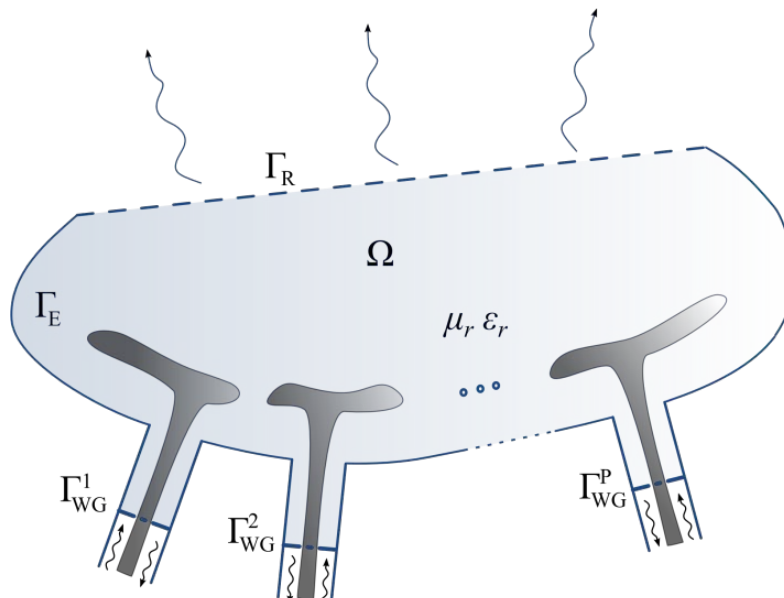


FIG. 1 – Sketch of the phased array antennas finite element analysis domain Ω .

Upon applying the conventional Galerkin finite elements (FE) method with edge basis functions [2], a linear system of the form $[\mathbf{A}]\mathbf{x}=\mathbf{b}$ is

obtained, where $[\mathbf{A}]$ is a sparse matrix, due to local character of the chosen basis functions. For the superposition principle, the right hand side \mathbf{b} can be expanded into a sum of vectors \mathbf{b}_p as much as the number of ports, in order to extrapolate from the system the complex excitations enforced at each port, allowing to set the excitations of the ports for a beam steering operation.

As the radiation pattern is sought for, Stratton-Chu formulas in Kottler's form [3]-[4] are used to compute the far-field from the FE solution on Γ_R , then, with the knowledge of the accepted power at antennas ports, the antenna gain can be retrieved all over the observation directions. This near-field to far-field transformation can be viewed as the application of an operator \mathbf{c}^H on the FE solution such that $g = \mathbf{c}^H \mathbf{x}$, with g the gain value in the selected observation direction and $[\cdot]^H$ is the hermitian transpose operator. For further reduction of the model [5], \mathbf{c} have been approximated in terms of truncated Fourier series, reducing the number of operations to compute the pattern. \mathbf{c} is thus written in terms of vectors \mathbf{c}_q associated to a given harmonic function.

A projection-based model order reduction technique [1], [5]-[7] is finally performed by properly choosing independent FE solutions computed for different scan angle excitation. Those solutions, which constitute global basis functions for the reduced system, are collected in a matrix \mathbf{V} that is used to project the full input (steering excitations)-output (gain) system matrices in the following manner:

$$\begin{aligned} [\mathbf{V}]^H [\mathbf{A}] [\mathbf{V}] &= [\tilde{\mathbf{A}}] \\ [\mathbf{V}]^H \mathbf{b}_p &= \tilde{\mathbf{b}}_p \\ \mathbf{c}_q^H [\mathbf{V}] &= \tilde{\mathbf{c}}_q^H \end{aligned} \quad (2)$$

leading to the reduced order system of full matrices of the form:

$$\left\{ \begin{aligned} [\tilde{\mathbf{A}}] \tilde{\mathbf{x}} &= \sum_p i_p \tilde{\mathbf{b}}_p \\ g &= \left(\sum_q o_q \tilde{\mathbf{c}}_q^H \right) \tilde{\mathbf{x}} \end{aligned} \right. \quad (3)$$

where i_p are the complex excitations for each antenna element and o_q are the harmonic functions that expand the near-field to far-field transformation operator. The system matrices of Eq. (3) are now full matrices with an order as low as the dimension of the space spanned by \mathbf{V} . The reduced system solution vector is related to the full system solution vector by $\tilde{\mathbf{x}} = [\mathbf{V}]^H \mathbf{x}$.

III. RESULTS

The array of 3 by 5 patch antennas shown in Fig. 2 have been analyzed with the proposed technique. The spacing between the antennas is of $\lambda_0/2$, λ_0 being the free space wavelength. First order basis functions have been chosen requiring, for a sufficient near-field accuracy, a mesh density of $\lambda_0/10$, leading to about 3.6×10^5 unknowns. 26 Fourier coefficients have been retained to approximate \mathbf{c} , being enough for an approximation error in the gain of 10^{-8} , relatively to the full operator pattern results. The main error introduced at this point is only attributable to the finite elements approximation and the numerical integration technique employed for the implementation of Stratton-Chu formulas.

To reduce the model by Eq. (2), 15 FE independent solutions were needed, that is for 15 different scan angles, leading to a relative error of the gain as low as 10^{-11} , while 14 and less solutions would have introduced a non-neglectable error ($\sim 10^{-1}$). To validate the FE code, the simulation has been run with the commercial package Ansys HFSS. Results, shown in Fig. 3, validate the present formulation.

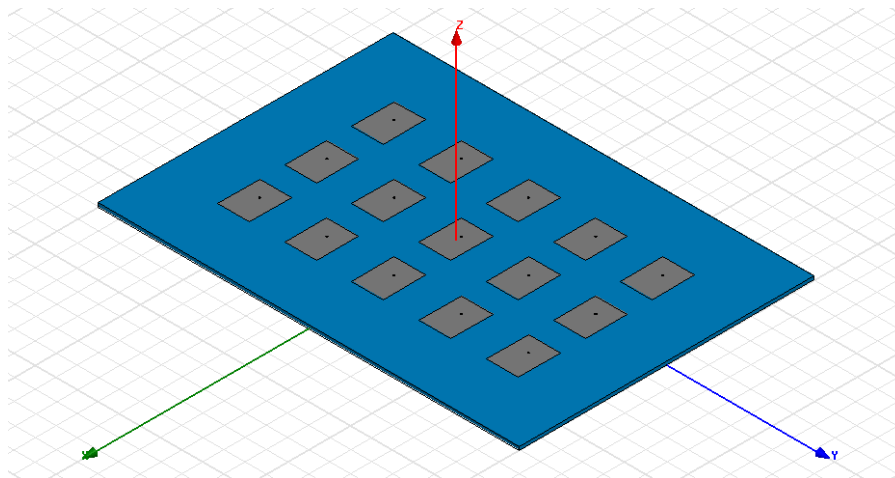


FIG. 2 – Array of 3 by 5 coaxial-fed rectangular patch antennas analyzed for fast beam steering computations.

To emphasize the advantages of the model order reduction, timings in the pattern computations have been compared (Table I). Ansys HFSS requires about 35 s to compute the patterns of Fig. 3 while the present code requires only 150 ms, 233 times lower than Ansys HFSS times.

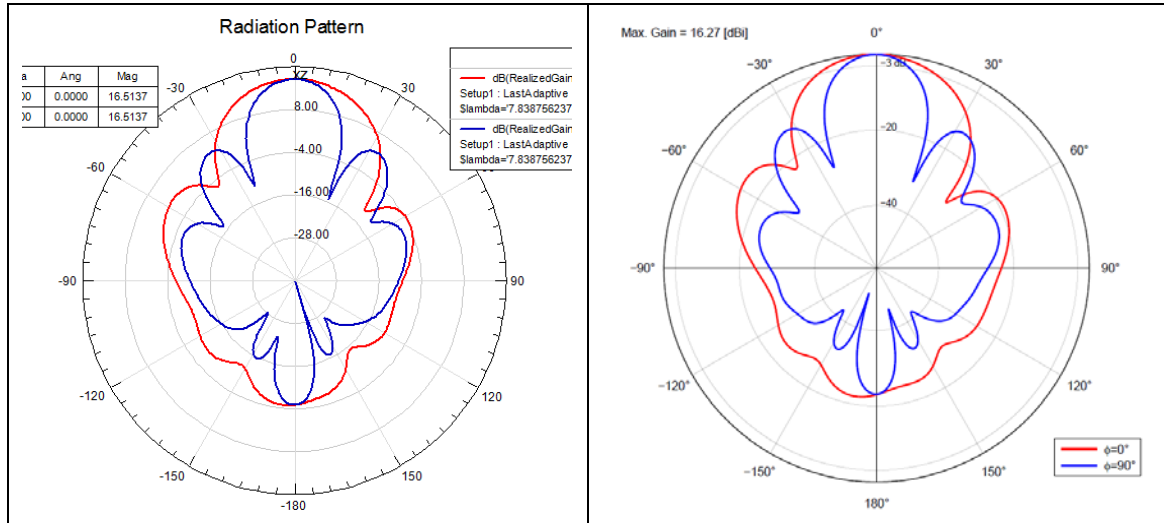


FIG. 3– Patterns computed on the XZ and YZ planes with (left) HFSS and (right) present FE code.

TABLE I – COMPUTATIONAL REQUIREMENTS

	Anslys HFSS	Present code
Full system assembly and solution timings (off-line)	38 min	45 min
Total memory requirements for full system (off-line)	1.5 GB	625 MB
Memory requirements for reduced system (on-line)	-	1.5 MB
Radiation pattern computation timings (on-line)	35 s	150 ms

IV. CONCLUSION

The model order reduction technique have been employed to speed-up the computation of the radiation patterns from finite elements analysis of phased array antennas. As the finite elements system has been parameterized in terms of port excitations, very fast computation of radiation patterns in front of a beam steering operation can be achieved.

It has been shown that the reduced order systems of dimensions as large as the number of array antennas contain all the necessary

information to retrieve the patterns with an error as low as numerical one. Fourier expansion of the near-field to far-field transformation operator reduces computational effort while keeping reasonable accuracy for pattern evaluation.

It is worth noticing that the presented technique might render practical pattern shaping optimization algorithms applied to full-wave simulations.

ACKNOWLEDGEMENT

The author acknowledges the contribution, guidance and the insight provided by discussions with Professor Romanus Dyczij-Edlinger and Dr. Ortwin Farle (*Lehrstuhl für Theoretische Elektrotechnik*, Saarland University, Saarbrücken, Germany) during his Master's thesis internship.

REFERENCES

- [1] A. C. Antoulas, *Approximation of Large-Scale Dynamical Systems*, Philadelphia, PA: SIAM, 2005, ch. 7, pp. 207-246.
- [2] G. Pelosi, R. Coccioli, and S. Selleri, *Quick Finite-Element for Electromagnetic Waves*, 2nd ed. Nordwood, MA: Artech House, 2009, ch. 7, pp. 172-188.
- [3] E. J. Rothwell, M. J. Cloud, *Electromagnetics*, New York, NY: CRC Press, 2001, ch. 6, pp 407-428.
- [4] P. Monk, "The near field to far field transformation", *COMPEL*, vol. 14, n. 1, pp. 41-56, 1995.
- [5] P. D. Ledger, J. Peraire, K. Morgan, O. Hassan, N. P. Weatherill, "Parameterised electromagnetic scattering solutions for a range of incident wave angles," *Comput. Meth. Appl. Mech. Eng.*, vol. 193, n. 33-35, pp. 3587-3605, 2004.
- [6] D. B. P. Huynh, A. T. Patera, "Reduced basis approximation and a posteriori error estimates for stress intensity factors," *Int. J. Numer. Meth. Eng.*, vol. 72, pp. 1219-1259, 2007.
- [7] G. Rozza, D. B. P. Huynh, A. T. Patera, "Reduced basis approximation and a posteriori error estimation for affinely parametrized elliptic coercive partial differential equations," *Arch. Comput. Meth. Eng.*, vol. 15, n. 3, pp. 229-275, 2008.

Session 6 – Synthetic aperture radar

G. Di Martino, A. Iodice, D. Riccio, G. Ruello, and I. Zinno

A novel high level SAR product: fractal dimension map

M. Picchiani, F. Del Frate, G. Schiavon, S. Stramondo, and M. Chini

DInSAR and neural networks for seismic source analysis

R.G. Avezzano, D. Latini, F. Del Frate, D. Velotto, and S. Lehner

Oil spill detection using X-band SAR data

A. Capozzoli, C. Curcio, and A. Liseno

SAR tomography with optimized track distribution and controlled resolution

N. Pierdicca, and L. Pulvirenti

Future use of the data from the ESA Sentinel-1 mission for operational soil moisture mapping: a multitemporal algorithm

A NOVEL HIGH LEVEL SAR PRODUCT: FRACTAL DIMENSION MAP

G. Di Martino⁽¹⁾, A. Iodice⁽¹⁾, D. Riccio⁽¹⁾, G. Ruello⁽¹⁾, I. Zinno⁽²⁾

⁽¹⁾Università di Napoli Federico II, Via Claudio 21, 80125, Napoli, Italy

⁽²⁾IREA, Italian National Research Council (CNR), 80124, Napoli, Italy

Abstract

In this paper the analysis of fractal dimension maps obtained from Synthetic Aperture Radar (SAR) images is presented. For the first time, it is shown that it is possible to extract from SAR data information related only to the roughness of the observed surface, i.e. presenting low dependence on the parameters of the considered incident field. Both natural and urban scenarios are considered and the behavior of the maps in case of different sensor look angles is discussed.

Index Terms – Fractals, rough surfaces, Synthetic Aperture Radar.

I. INTRODUCTION

Recently the authors developed an innovative electromagnetic model which allows the retrieving of information - dependent on the natural surface roughness component only - from the electromagnetic field scattered from a natural surface, as acquired by SAR sensors [1]. In fact, the fractal dimension is a significant geophysical parameter of natural surfaces, dictating the distribution of the roughness over different spatial scales [1]-[4]. For this reason, the possibility to estimate the fractal dimension from a single amplitude-only SAR image is of fundamental importance for geomorphologic and geophysical analysis.

This novel and unparalleled result has been obtained thanks to the appropriate electromagnetic model introduced in [1]. In fact, it allows the extraction of a map of the point-by-point fractal dimension of the observed scene. The fractal dimension of natural areas, due to the fact that it is related only to the roughness of the observed surface, shows a very interesting behavior: it is one of the few parameters which we expect to be very stable whenever illumination and radar conditions change. However, when the fractal estimation is performed in presence of man-made objects, non-fractal characteristics can be observed on the fractal map: these are mainly related to the bright signature and to the significant geometrical distortions present on SAR data when built-up areas are imaged. These non-fractal characteristics can heavily change for different acquisition parameters of the sensor (e.g. look angle).

These maps can lead toward the development of high level products to be used by geophysicists for earth surface modeling and monitoring.

II. THEORETICAL FRAMEWORK

The fractional Brownian motion (fBm) is a regular stochastic process that completely describes natural surfaces by means of only two independent parameters: the Hurst coefficient, H (which is linked to the

fractal dimension by the simple relation $D=3-H$) and the standard deviation of surface increments at unitary distance, s [m^{1-H}] [2], [3].

In order to retrieve the fractal dimension of a natural scene from its SAR image the authors developed a direct electromagnetic model which links the surface to its final amplitude SAR image [1]. The expression of the power spectral density (PSD) of image range cuts has been analytically evaluated. In an appropriate range of spatial frequencies, it presents a power law behavior, thus showing on a log–log plane a linear behavior with a slope related to the Hurst coefficient H of the observed surface:

$$S_p(k_y) = s^2 \Gamma(1 + 2H) \sin(\pi H) \frac{1}{|k_y|^{2H-1}} \quad (1)$$

where k_y is the wavenumber of the range cut of the image and $\Gamma(\cdot)$ is the Euler Gamma function.

III. EXPERIMENTAL SETUP

Exploiting the theoretical results presented in the previous section, a processing, based on a spectral elaboration of amplitude SAR images, is implemented. The output product of this processing is the fractal map relevant to the input SAR image, that provides - for each pixel of the starting SAR image - the fractal dimension, evaluated on a small patch selected through a sliding window centered in the pixel. To obtain this result, within each window the power spectral densities of the range cuts are averaged to get the PSD: finally, according to the expression in (1), the fractal dimension is evaluated through a linear regression on the graph of the spectrum in a log–log plane [1].

Note that, due to the fact that natural surfaces are characterized by a value of the fractal dimension $2 < D < 3$ [2], [3], all the man-made objects present in the SAR image can be identified through fractal processing, as they lead to fractal dimension values outside this fractality range. Moreover, the fractal dimension is a quantitative descriptor of the roughness and geomorphologic properties of natural surfaces and it could allow distinguishing between different geomorphic areas or recognizing geodynamic processes accountable for natural structures formation [4]. Finally, comparing fractal maps relevant to the same natural surface area, but obtained from SAR images acquired with different look angles, it turns out that the shapes of the histograms of the fractal maps do not significantly change as the viewing sensor geometry varies. Conversely, comparing the fractal maps obtained from SAR images with different look angles of the same urban area, the corresponding fractal dimension distributions show different behaviors.

In Fig. 1, two COSMO-SkyMed stripmap images of the Somma-Vesuvius volcanic complex (Naples, Italy) acquired with two different look angles ($\theta_1=22^\circ$ and $\theta_2=31^\circ$) are shown. In Fig. 2 their fractal

dimension maps, generated using a sliding windows of 51x51 pixels, are presented. Note that on the left and on the bottom of the fractal maps small very dark patches corresponding to man-made objects present on the scene are clearly visible: all dark features correspond to SAR image areas that are detected as non-fractal (see the grey level palettes). Note that also layover zones in the SAR images are detected as non-fractal.

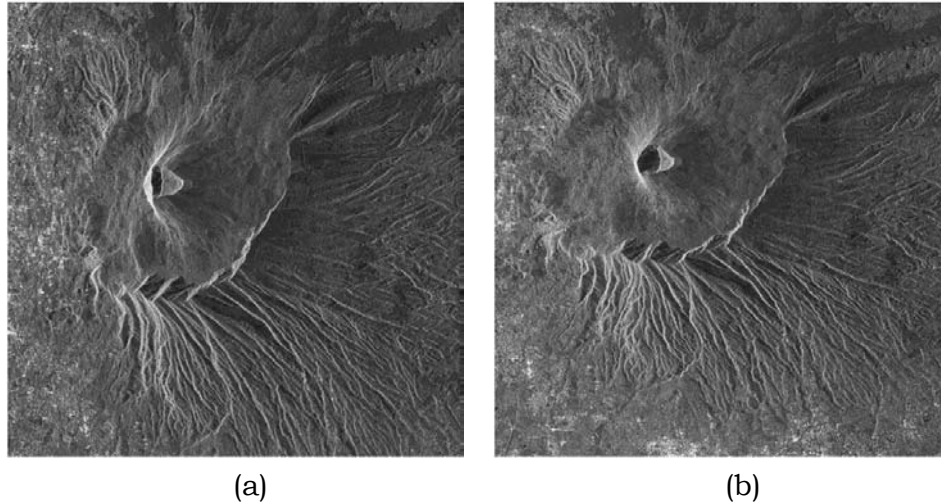


FIG. 1 – COSMO-SkyMed stripmap images of the Vesuvius acquired with look angles $\theta_1 = 22^\circ$ in (a) and $\theta_2 = 31^\circ$ in (b).

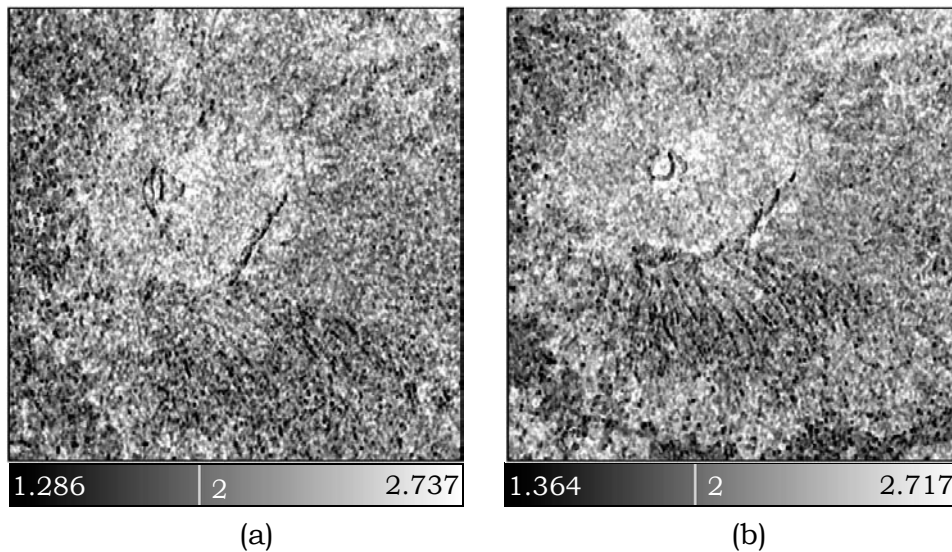


FIG. 2 – Fractal maps of the SAR images Fig. 1-(a) and Fig. 1-(b), respectively.

In Tab. I and in Fig. 3-(a) the statistics and the histograms of the fractal maps in Fig. 2 are reported: they show that, changing the sensor viewing geometry, the behavior of the estimated fractal dimension maps does not significantly change. For the sake of brevity, for the urban scenario case, we present in Tab. I and in Fig. 3-(b) only the statistics and the histograms: the SAR images and the relevant fractal maps acquired with the mentioned look angles over the same urban area (the

business center of Naples) are not reported. Note that, in this case, the statistics change significantly as the sensor viewing geometry varies.

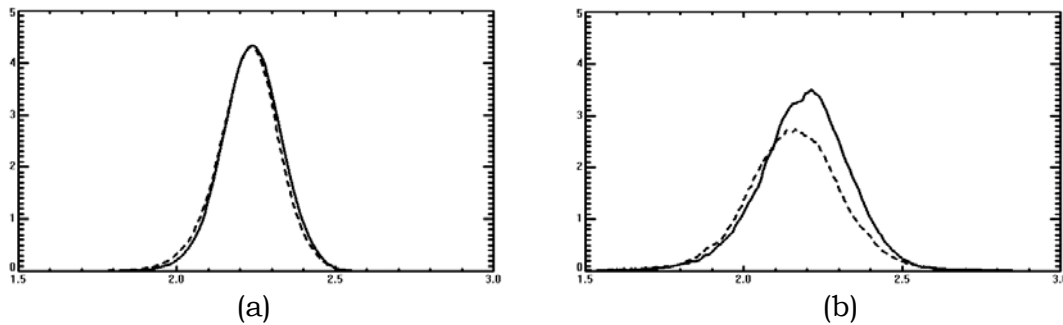


FIG. 3 – (a) Superposition of the histograms of the fractal maps in Fig. 2. (b) Superposition of the histograms of the fractal maps relevant to the urban area. In both cases: $\theta_1=22^\circ$ with continuous line and $\theta_2=31^\circ$ with dashed line.

Table I - STATISTICS OF THE FRACTAL DIMENSION MAPS

Figure	D_{min}	D_{max}	D_{mean}	D_{stdev}
Fig. 3-(a), $\theta_1=22^\circ$	1.286	2.737	2.240	0.095
Fig. 3-(a), $\theta_2=31^\circ$	1.364	2.717	2.230	0.098
Fig. 3-(b), $\theta_1=22^\circ$	1.063	3.738	2.196	0.150
Fig. 3-(b), $\theta_2=31^\circ$	1.013	4.316	2.166	0.171

IV. CONCLUSIONS

Thanks to the appropriate electromagnetic modeling introduced by the authors in [1], for the first time it is possible to extract from SAR data information related only to the roughness of the observed surface. The studies presented in the present paper strongly support the idea that fractal dimension maps can lead to the development of high level SAR products which can be positively used by geologists and geophysicists.

ACKNOWLEDGEMENT

This work has been supported in part by Agenzia Spaziale Italiana within COSMO/SkyMed AO, project ID 2202 and project ID 1200.

REFERENCES

- [1] G. Di Martino, D. Riccio, I. Zinno, "SAR Imaging of Fractal Surfaces," *IEEE Trans. Geosci. Remote Sens.*, vol.50, no.2, pp. 630-644, Feb. 2012.
- [2] G. Franceschetti, D. Riccio, Scattering, *Natural Surfaces and Fractals*. Academic Press, Burlington (MA), USA, 2007.
- [3] B.B. Mandelbrot, *The Fractal Geometry of Nature*. New York: Freeman, 1983.
- [4] D.L. Turcotte, *Fractals and Chaos in Geology and Geophysics* (second edition), Cambridge University Press, 1997.

DInSAR AND NEURAL NETWORKS FOR SEISMIC SOURCE ANALYSIS

M. Picchiani⁽¹⁾, F. Del Frate⁽¹⁾, G. Schiavon⁽¹⁾, S. Stramondo⁽²⁾, M. Chini⁽²⁾

⁽¹⁾Earth Observation Laboratory, Department of Computer Science, Systems and Production, Tor Vergata University, Via del Politecnico, 1 I-00133 Rome, Italy.

⁽²⁾Istituto Nazionale di Geofisica e Vulcanologia, Via di Vigna Murata, 605 I-00143 Rome, Italy.

picchian@disp.uniroma2.it

Abstract

Since the 1990s differential interferometry techniques have been applied to synthetic aperture radar images to measure the surface displacement field caused by earthquakes. Indeed the phase difference of the radar signals acquired after and before the event registers the variation of the electromagnetic path due to the displacement. Analytical formulation to model these changes in radar range exists, anyway the inverse problem, i.e. the retrieval of the seismic source parameters from the interferometric phase measured, is not of straightforward solution because of its intrinsic ill-posedness. A novel inversion technique, based on Neural Networks, harmonic analysis and non-linear principal component analysis, has been developed in previous studies obtaining encouraging results. Here the theoretical basis of the methodology is reviewed and applied to a new set of experimental data.

Index Terms – SAR Interferometry, Neural Networks, Nonlinear PCA

I. INTRODUCTION

Repeat pass Differential Interferometry (DInSAR) represents the most attractive technique available to measure, the surface displacement field caused by earthquakes [1]. The centimetric accuracy of the measure allows reconstructing the coseismic surface displacement field extracting the interferometric phase from the complex cross-multiplication of each pixel in the two Synthetic Aperture Radar (SAR) images, acquired before and after the event. The phase contains different contributions like the orbital and the topographic ones, that can be eliminated to obtain the deformation signal. The fringe pattern, i.e. the image representing the phase changes, carries information on the geometry of the source. The solution of inverse problem, i.e. the retrieval of fault parameters from the interferogram, cannot be written in closed analytical form, moreover the problem is ill-posed, since the parameter space can present several local minima. Neural Networks (NN) are particularly suited to the analysis of complex behaviours, of which we do not know the exact functional relationship, but of which we have available a sufficient number of examples. Indeed through supervised learning the NN implements a non-linear function approximation between inputs (the data) and outputs (the geophysical

parameter). In previous study [2] we proposed a new approach where the estimation of the fault parameters (Length, Width, Strike, Dip, Depth), starting from the wrapped interferogram, is obtained by chaining two different NN architectures: in the first one a dimensionality reduction is performed by a so called Auto-Associative Neural Networks (AANN) [3], while in the second stage the final inversion is carried out with a Multi-Layer Perceptron (MLP) NN [4].

II. MATERIALS AND METHODS

We applied the NN procedure to three different data sets. The interferograms have been obtained applying DInSAR to a coseismic pair of Envisat ASAR data for the L'Aquila event (April 6th 2009, Mw=6.3, Italy) and two coseismic pairs of ALOS PALSAR data for the Darfield (September 3rd, 2010, Mw=7.1, New Zealand) and Christchurch, (February 21st 2011, Mw=6.3, New Zealand) events (fig. 1).



FIG. 1 - Differential interferogram relative to the L'Aquila earthquake, (left).
 Differential interferogram relative to the Darfield earthquake (center).
 Differential interferogram relative to the Christchurch earthquake (right).

The displacement field represented by the fringes is the surface expression of the displacement among the fault blocks. The Okada formulation [5] expresses the surface displacement $u_i(x_1, x_2, x_3)$ due to a dislocation $\Delta u_j(\xi_1, \xi_2, \xi_3)$ across a surface Σ in an isotropic medium as:

$$u_i = \frac{1}{4\pi} \iint_{\Sigma} \left[\Delta u_j \left(\lambda \delta_{jk} \frac{\partial u_i^k}{\partial \xi_l} + \mu \left(\frac{\partial u_i^j}{\partial \xi_l} + \frac{\partial u_l^j}{\partial \xi_i} \right) \nu_k \right) \right] d\Sigma \quad (1)$$

In eq. 1 δ_{jk} is the Kronecker delta, λ and μ are Lamé's coefficients, specifying the elastic medium, ν_k is the direction cosine of the normal to the surface element $d\Sigma$. The term u_i^j is the i th component of the displacement at (x_1, x_2, x_3) due to the j th direction point force of magnitude F at (ξ_1, ξ_2, ξ_3) . The synthetic interferogram is obtained converting the displacement components u_i , projected onto the satellite Line Of Sight, into phase and applying a wrapper operator [1]. The fault geometry parameters are the inputs of the direct Okada model while

represents the outputs of the NN based inversion procedure. To train the NNs lacking of a proper set of real data a sets of synthetic interferograms, developed using the Okada model, have been used. However, giving to the network the whole interferogram as input can be very counterproductive and a procedure able to constrain the information in a lower dimensional space is required. For this reason a features extraction methodology, based on Discrete Fourier Transform (DFT) and AANN has been developed. The AANN architecture is characterized by a symmetrical topology in which the output layer is equal to the input layer and an internal “bottleneck” layer is included. The network is trained to approximate the identity mapping between inputs and output. Since the bottleneck layer is smaller than the output, its nodes must represent or encode the information in the inputs for the subsequent layers to reconstruct the input. We have first considered the phase spectrum of the interferometric image, from which we have extracted the DFT low frequency components. In this way it was possible to obtain a first reduction of dimensionality of the data, more exactly from 2250000 to 5000 input components. A further reduction was achieved by applying an AANN scheme to the signal produced by the DFT processing. The output of this phase is a final reduced vector composed by only 50 elements. These 50 elements were used as input in the training phase of the neural network algorithms dedicated to the inversion. Three NNs have been so trained and applied to retrieve the fault parameters from the considered real interferograms.

III. RESULTS AND CONCLUSIONS

The solution of the neural inversion shows interesting results (table 1), indeed the estimated geometric parameters are generally in agreement with the results from other authors [6]-[7]-[8] and the three models computed (shown in figure 2) are quite comparable with the real interferograms. The little overestimation for the fault geometrical parameters is due to the choice of considering a constant slip onto the fault plane. Moreover the source of Darfield is more complex than the other sources. Therefore the NNs result, at present, can be only considered for a sub-optimal representation of the source.

TABLE 1. Geometric parameters of the seismic source as retrieved by the neural network for the three considered interferograms

Seismic Event	Length (km)	Width (km)	Dip (deg)	Strike (deg)	Top/Bottom Depth (km)	Mean Slip (cm)
L’Aquila	13.58	6.88	63	135	3.7/9.8	100
Darfield	46.0	5.0	84	78	4.9/9.9	120
Christchurch	18.0	14.0	55	60	4.0/15.46	100

The NN approach can be very effective when a first characterization of the seismo-genetic fault is needed in a very short time. The obtained result can be considered like a basis to develop a more sophisticated

study on the earthquake evolution [9]. Moreover the inversion is applied directly on so called wrapped interferograms, not requiring to apply heavy unwrapping algorithms.

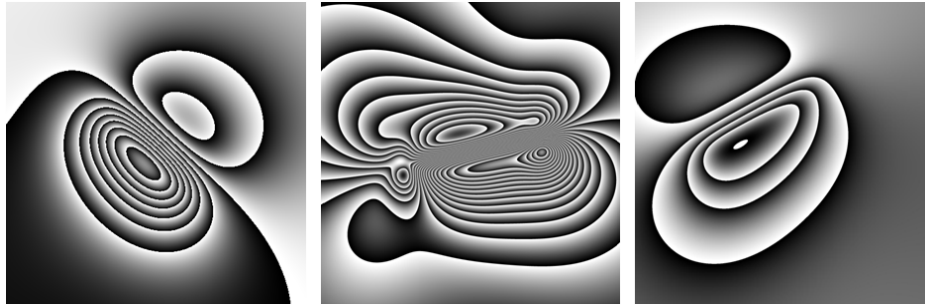


FIG. 2 - The models of the considered earthquakes: L'Aquila event (left). Darfield event (center). Christchurch event (right).

REFERENCES

- [1] Zebker, H. A., and R. M. Goldstein (1986), Topographic Mapping From Interferometric Synthetic Aperture Radar Observations, *J. Geophys. Res.*, 91(B5), 4993–4999, doi:10.1029/JB091iB05p04993.
- [2] Picchiani M., Del Frate F., Schiavon G., and Stramondo S., Chini M., Bignami, C., “Neural Networks for automatic seismic source analysis from DInSAR data”, Proc. SPIE 8179, DOI: 10.1117/12.898575
- [3] Kramer, M. A., “Nonlinear principal component analysis using autoassociative neural networks”, *J. Amer. Inst. Chem. Eng. (AIChE)*, Vol. 37, 233–243 (1991).
- [4] Bishop, C. M., [Neural Networks for Pattern Recognition], Oxford University Press, 296-297 (1995).
- [5] Okada Y., “Surface deformation due to shear and tensile faults in a half space”, *Bull. of the Seism. Soc. of America*, vol. 75, n.4, 1135-1154 (1985).
- [6] Walters R. J., Elliott J. R., D’Agostino N., England P. C., Hunstad I., Jackson J. A., Parsons B., Phillips R. J., and Roberts G., “The 2009 L’Aquila earthquake (central Italy): A source mechanism and implications for seismic hazard”. *Geophys. Res. Lett.*, VOL. 36, L17312, 6 (2009). doi:10.1029/2009GL039337.
- [7] Gledhill, K., Ristau, J., Reyners, M., Fry, B., Holden, C., “The Darfield (Canterbury) earthquake of September 2010: preliminary seismological report”. *Bulletin of The New Zealand Society For Earthquake Engineering* 43, 215-221 (2010).
- [8] Beavan J., Fielding E., Motagh M., Samsonov S., Donnelly N., Fault Location and Slip Distribution of the 22 February 2011 Mw 6.2 Christchurch, New Zealand, Earthquake from Geodetic Data *Seismological Research Letters*, November/December 2011, v. 82, p. 789-799
- [9] Stramondo, S., Kyriakopoulos, C., Bignami, C., Chini, M., Melini, D., Moro, M., Picchiani, M., Saroli, M., & Boschi, E. (2011). “Did the September 2010 (Darfield) earthquake trigger the February 2011 (Christchurch) event?”, *Scientific Reports*, 1 DOI: 10.1038/srep00098

Oil Spill Detection Using X-band SAR Data

Ruggero Giuseppe Avezzano⁽¹⁾, Daniele Latini⁽¹⁾, Fabio Del Frate⁽¹⁾,
Domenico Velotto⁽²⁾, Suzanne Lehner⁽²⁾

⁽¹⁾ D.I.S.P. – Tor Vergata University, Via del Politecnico 1, 00133
Rome, Italy - {avezzano,latini,delfrate}@disp.uniroma2.it

⁽²⁾ Remote Sensing Institute – DLR IMF GW, Munchner Str. 20,
Wessling, Germany

Abstract

The increased amount of Synthetic Aperture Radar (SAR) images acquired over the ocean represents an extraordinary potential for improving oil spill detection activities. To this purpose, the use of artificial Neural Networks (NN) has already been demonstrated to be profitable. However, the effective design of a NN algorithm relies on the availability of a statistically significant set of examples to be used for the training phase. In this paper the performance of NN is discussed for two different dataset provided by the last generation satellite missions: Cosmo-Skymed and TerraSAR-X. In the latter case, the use of an electromagnetic model has been considered to improve the statistical representation of the data. The results obtained are satisfactory as in both cases the overall accuracy of the classification, discriminating between oil spills and look-alikes, is more than 80%.

Index Terms – COSMO-Skymed, Damping Ratio, Neural Networks, PCNN, Two-scale Model.

I. INTRODUCTION

The damping of ocean waves by viscoelastic films has been subject of many studies. At incidence angles between 20 to 75 degrees the radar backscattered power depends on the power spectral density of Bragg waves, this process is described by the Bragg scattering theory [1]. Moreover the presence of a monomolecular surface film attenuates not only short gravity-capillary waves, but also long ocean waves, as described by Marangoni effect. For these reasons the presence of dark patches on SAR images can be often related to the presence of surface films. However, the origin of a dark spot in the SAR image can be also due to the presence of atmospheric effects or natural surface slicks. To allow effective oil spills surveillance using active radar techniques it is therefore important to correctly discriminate between actual oil spills and what are called “look-alikes”.

The use of neural networks in classification problems has increased over the years due to several advantages. In particular they do not require the knowledge of the probability distribution functions characterizing the variables of interest and they are robust in dealing with noisy data. The process of detecting oil pollution is generally composed of three steps [2]: segmentation of the dark object, extraction of significant features, classification of the oil spill candidate. The

features extracted from an oil spill candidate are generally divided into Geometric (Area, Perimeter, Complexity, Spreading) and Radiometric (Object Standard Deviation, Background Standard Deviation, Contrast values between Object and Background) ones.

In this study the topic introduced above has been addressed considering two types of X-band images . They have been provided by the COSMO-SkyMed and TerraSAR-X missions in the framework of an ASI Announcement of Opportunity and as a result of a collaboration with DLR, respectively. While the number of examples that could be extracted from Cosmo-Skymed imagery was considered statistically significant for the NN learning phase, this was not the case for the TerraSAR-X dataset. Therefore, as discussed in the following, a electromagnetic model based procedure was designed to generate additional examples.

II. DATA SIMULATION STRATEGY

To build a statistically significant dataset for TerraSAR-X data, the exploitation of C-band ground truth, already available in the context of previous ERS-SAR and ENVISAT-ASAR research projects, was considered. To this purpose, the simulation of new radiometric features has been investigated employing two different models. Background Standard Deviation values were obtained using a NRCS Two-Scale model of the sea, Contrast values were obtained using a Damping Ratio model of a viscoelastic substance spread on the sea surface.

Two-Scale approach is widely used to characterize sea surface. Its electromagnetic behavior is regarded as a sum of two principal components. Long waves' echoes are modeled using Geometric Optics Approximation and short scale waves are modeled using a Small-Perturbation Model. A drawback in two-scale models lies in arbitrariness of response depending on the cut-off frequency of the two approximations. In [4] the first order of the Small-Slope Approximation is used to characterize short waves, leading to a cut-off invariant model. Considering the simulated value, obtained choosing wind speed, wind direction, incidence angle and frequency, the standard deviation value of the sea surface intensity echo is easily derived from:

$$S.D.d = e^{\sqrt{\frac{4}{\pi} \nu - 1}} \cdot N \quad R \quad (1)$$

The model is quite complex, but it has been inverted using a look-up table of all possible NRCS values given wind velocity and incidence angle. Regarding Contrast Value, a model for biogenic slicks damping has been extracted from a series of experimental campaigns during 1994 [5]. The original model of damping ratio derived from Marangoni theory.

Rheological parameters representing the absolute value and the phase of complex dilation modulus of surface film are key parameters in describing the pollutant inside the model and are well known in literature.

This model has been improved after the SIR-C/X-SAR campaign including energy transfer effects from wind, wave breaking and viscous dissipation, obtaining the following form of contrast:

$$\frac{\sigma^{(0)}}{\sigma^{(s)}} = \frac{\beta^{(s)} - 2\Delta^{(s)}c_g}{\beta^{(0)} - 2\Delta^{(0)}c_g} m^{\Delta n - 4} \left(2u_* \sqrt{\frac{|c \phi| \mathfrak{d}}{g}} \right)^{\Delta n} \quad (2)$$

where the superscript (0) and (s) denote the slick-free and the slick-covered surface. σ is the NRCS of the sea surface, β is a function of wind conditions (direction, group velocity and friction velocity). c_g is the wave group velocity, g is the acceleration of gravity and u_* is the wind friction velocity. Damping ratio model emphasize a dependance growing with frequency, and X-band values have been derived with a similar inversion procedure.

III. RESULTS

A set of 60 COSMO-SkyMed ScanSAR images have been used. These images were acquired over well-known oil slick disasters, and contain several certified oil slicks. 188 examples of verified both oil spills and look-alikes were detected and used for the training and the test phase.

The TerraSAR-X dataset was composed of 47 StripMap and ScanSAR images acquired from November 2007 to September 2010, from which 94 examples of oil spills and look-alikes were extracted.

An automatic segmentation step was implemented using a Pulse Coupled Neural Network, a relatively new technique based on the computational implementation of the mechanisms underlying the visual cortex of small mammals [3].

After that a statistically significant set of examples was generated for both Cosmo-Skymed and TerraSAR-X products, a Feedforward Multi-Layer Perceptron (MLP) Neural Network was designed for the implementation of the classification step. For the Cosmo-Skymed data an 87% of correct classification over a validation dataset consisting of 46 examples was obtained. Regarding the TerraSAR-X data set, the net was trained over 55 examples stemming from scaled C-band features and it was capable to provide an accuracy of about 83% when tested on X-band features extracted from TerraSAR-X data.

ACKNOWLEDGEMENT

The research has been partially carried out within the framework of ASI contract L/020/09/0. COSMO-SkyMed data provided by ASI AO project 1483.

The TerraSAR-X data are provided by DLR over the science AO OCE1045 (PI: Domenico Velotto; Sector: Oceanography).

REFERENCES

- [1] W. Alpers, H. Huhnerfuss, "The Damping of Ocean Waves by Surface Films: A New Look at an Old Problem", *Journal of Geophysical Research*, vol. 94, NO. C5, pp. 6251-6265, 1989.
- [2] F. Del Frate, A. Petrocchi, J. Lichtenegger and G. Calabresi, "Neural Networks for Oil Spill Detection using ERS-SAR Data", *IEEE Transaction on Geoscience and Remote Sensing*, vol. 38, no. 5, pp. 2282-2287, 2000.
- [3] R. Eckhorn, H. J. Reitboeck, M. Arndt and P. Dicke, "Feature linking via synchronization among distributed assemblies: Simulations of results from cat visual cortex", *Neural Comput*, vol. 2, pp. 293-307, 1990.
- [4] G. Soriano, C.-A. Guerin, "A Cutoff Invariant Two-Scale Model in Electromagnetic Scattering From Sea Surfaces", *IEEE Geoscience and Remote Sensing Letters*.
- [5] M. Gade, W. Alpers, H. Huhnerfuss, H. Masuko, T. Kobayashi, "Imaging of biogenic and anthropogenic ocean surface films by the multifrequency/multipolarization SIR-C/X SAR", *Journal of Geophysical Research*, vol. 103, NO. C9, pp. 18851-18866, 1998.

SAR TOMOGRAPHY WITH OPTIMIZED TRACK DISTRIBUTION AND CONTROLLED RESOLUTION

A. Capozzoli, C. Curcio, A. Liseno

Università di Napoli Federico II, DIBET

Via Claudio 21, I 80125 Napoli (Italy)

a.capozzoli@unina.it

Abstract

In SAR tomography, the available information in the height direction is limited by the number of different tracks that can be flown in practice, so that the “few” possible acquisitions should be accurately selected.

We present an approach for the design of the “optimal” constellation for the desired degree of resolution.

Index Terms – Measurement configuration design, Multiresolution, Singular Value Optimization, Tomography.

I. INTRODUCTION

In many applications of inverse scattering, it is crucial to define the measurement configuration maximizing the collected information, given the degree of desired resolution and some knowledge on the Region of Interest (ROI).

A relevant (although not the only one) example is Synthetic Aperture Radar (SAR) tomography [1,2], allowing accessing 3D information on the ROI by several passes (tracks) of the sensor over the scene or by sensor constellations. Although the number of tracks is in principle related to the desired resolution, in this context it is practically limited by the difficulties and costs of realizing many passes of the sensor or of implementing sensor constellations. The issues then regard exploiting the minimum number of tracks to obtain reconstructions with a fixed degree of resolution, possibly non-uniform across the scene to allow enhancing the reconstruction capabilities wherever needed [5].

A method to face some of the above issues has been preliminary addressed in [3,4]. In this paper, the approach is generalized so to tackle all the above requirements.

II. THE APPROACH

The geometry of the tomographic problem, considered in a monostatic configuration, is depicted in Fig. 1(left).

On defining by x' the position of an elementary scatterer inside the investigation domain $(-H, H)$, by x_k the sensor position for the k -th track, and by λ the wavelength, the vector $\underline{s}=[s_1, \dots, s_N]$ of the received signals s_k can be expressed, after deramping, as [1,2]

$$s_k = s(x_k) = \int_{-H/2}^{H/2} \rho(x') e^{j \frac{4\pi}{\lambda} \frac{x_k x'}{r_0}} dx' \quad (1)$$

In eq. (1), $-H \leq x_k \leq H$ and ρ is the "vertical" reflectivity distribution [1-4] of the scene which is herein represented for example by Prolate Spheroidal Wave Functions (PSWFs) [6], properly filtered to a desired resolution limit [5], namely

$$\rho(x') = \sum_{i=1}^M \alpha_i \Psi_i[c, x'] * f(x'; \Omega). \quad (2)$$

In eq. (2), the Ψ_i 's are the PSWF's with space-bandwidth product $c=2\pi H'/\lambda$, $\underline{\alpha}=[\alpha_1, \alpha_2, \dots, \alpha_M]$ is the vector of the expansion coefficients of the scene with full resolution, $M=4H'/\lambda$, $*$ denotes convolution and $f(x')$ is the window controlling the desired resolution Ω , for instance, a Kaiser-Bessel one $f(x'; \Omega) = I_0((\pi/\Omega)\sqrt{H^2 - x'^2})$, where I_0 is the modified Bessel function of zero-th order.

The relation between \underline{s} and $\underline{\alpha}$ can be recast in the matrix form

$$\underline{s} = \underline{\Psi} \underline{\alpha}. \quad (3)$$

According to eq. (3), solving the tomographic problem amounts at finding the solution of a linear system, here determined by a regularized Singular Value Decomposition (SVD) approach, for instance, a Truncated SVD (TSVD).

As stressed in the Introduction, a key point in SAR tomography is the design of the measurement configuration. For a fixed resolution Ω , the positions of the tracks should be chosen to collect as much information as possible with the minimum number of acquisitions. This can be achieved by maximizing the Shannon number (which is a measure of such an information), namely, the quantity

$$\Phi = \sum_{j=1}^J \frac{\sigma_j}{\sigma_1}, \quad (4)$$

where σ_j are the singular values of the matrix $\underline{\Psi}$, and $J=\min\{M, N\}$. Being $\underline{\Psi}$ dependent on $\underline{x}=[x_1, x_2, \dots, x_N]$, Φ depends on the number and positions of the tracks too. The measurement constellation is then designed in terms of track number and positions, by a singular value optimization procedure [6]. More in detail, on denoting by $\Phi_{opt}(N)$ the maximum value of Φ for a given N against the track positions on the nominal aperture $(-H, H)$, further tracks must be added for a fixed Ω until a saturation behavior is observed, corresponding to the maximum amount of information that can be gathered from $(-H, H)$. The value of N at the saturation knee represents the minimum number of tracks needed to achieve all the available information in $(-H, H)$. Once the number of tracks for a given Ω has been defined, their position is determined as

the x providing $\Phi_{opt}(M)$. Obviously, the procedure returns different results for different values of Ω .

III. RESULTS

We here present two test cases corresponding to $\Omega=2\lambda$ and $\Omega=4\lambda$, being the working frequency $f=1\text{GHz}$, $H'=7\text{m}$, $H=150\text{m}$ and $r_0=1\text{km}$.

Fig. 1(right) depicts the behavior of $\Phi_{opt}(N)$ for both the cases. The saturation knee occurs at $N=11$ and $N=8$, respectively, thus showing that the saturation depends on the desired resolution. and Fig. 2 displays the track locations for both the cases. Notably, the tracks are allocated within an interval which is much narrower than $(-H,H)$.

Fig. 3 shows the reconstructions of a profile with rectangular window shape and support of 14m . As a reference, the representation of that profile on the first M PSWFs (without filtering function f) is also reported, representing the best achievable reconstruction for the selected representation. By comparing Figs. 3(left) and 3(right), the different reached resolutions can be appreciated. Also, both the reconstructions are comparable to those achieved by acquiring the data all over the continuous aperture coinciding with $(-H,H)$.

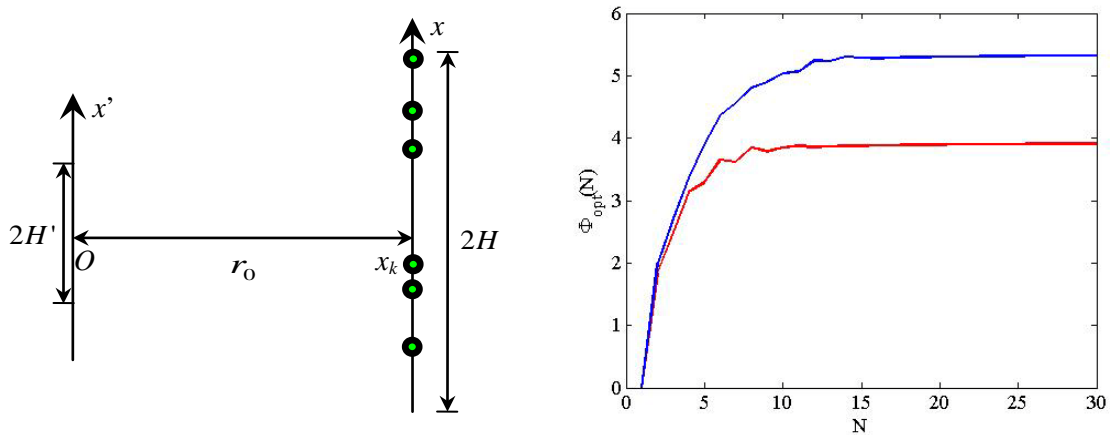


FIG. 1 – Left: Geometry of the problem. Right: Behavior of $\Phi_{opt}(N)$ for $\Omega=2\lambda$ (blue curve) and $\Omega=4\lambda$ (red curve).

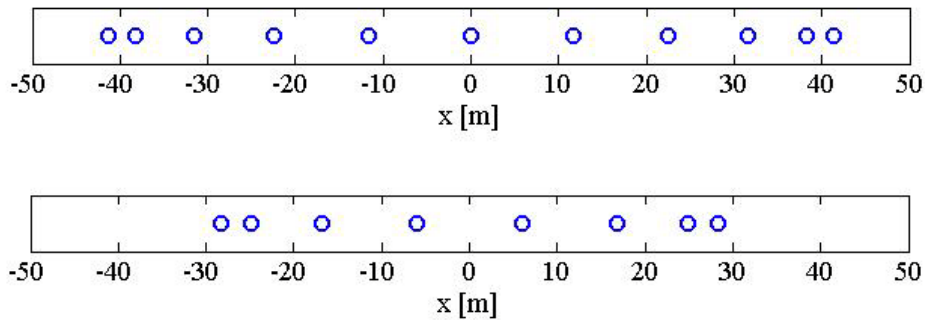


FIG. 2 – Measurement point locations for $\Omega=2\lambda$ (up) and $\Omega=4\lambda$ (down).

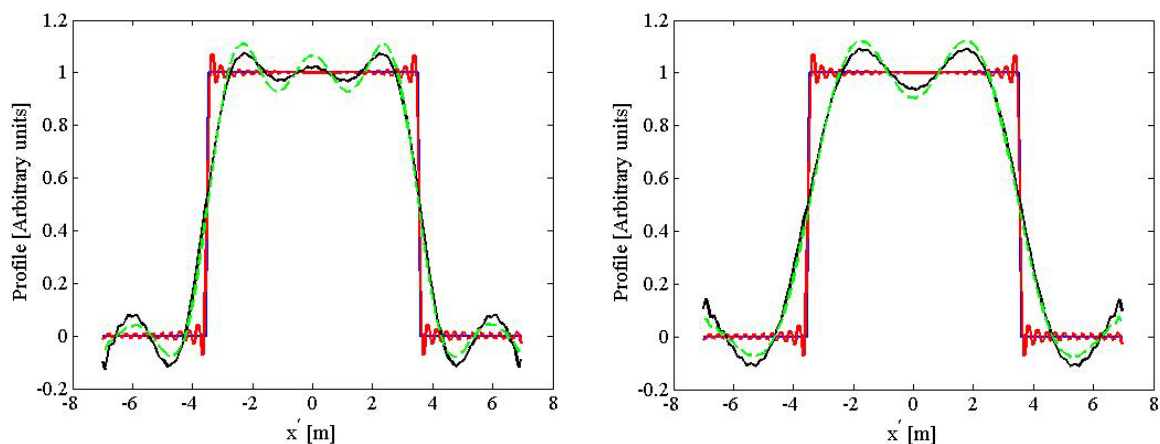


FIG. 3 – Profile reconstruction for $\Omega=2\lambda$ (left) and $\Omega=4\lambda$ (right). Blue: reference profile. Red: profile projected on the first M PSWF's. Black curve: reconstructed profile. Green dashed: reconstruction with continuous aperture.

IV. CONCLUSION

An approach for selecting the number and location of tracks to maximize the amount of collected information with the least possible number of acquisitions for a fixed resolution has been presented. Future developments regard a performance analysis when different degrees of resolution are desired within the same scene. The technique can be extended to the vector case and to multistatic configurations. Although it has been illustrated with reference to SAR tomography, it could be generalized to other possible applications of inverse scattering.

REFERENCES

- [1] A. Reigber, A. Moreira, "First demonstration of airborne SAR tomography using multi-baseline L-band data," *IEEE Trans. Geosci. Remote Sens.*, Vol. 38, No. 5, 2142-2152, Sep. 2000.
- [2] G. Fornaro, F. Serafino, F. Soldovieri, "Three-dimensional focusing with multipass SAR data," *IEEE Trans. Geosci. Remote Sens.*, Vol. 41, No. 3, 507-517, Mar. 2003.
- [3] V. Severino, M. Nannini, A. Reigber, R. Scheiber, A. Capozzoli, G. D'Elia, A. Liseno, P. Vinetti, "An approach to SAR tomography with limited number of tracks," *Proc. of the IEEE Int. Symp. on Geosci. Remote Sens.*, IV-216-IV-219, Cape Town, South Africa, Jul. 12-17, 2009.
- [4] A. Capozzoli, G. D'Elia, A. Liseno, P. Vinetti, M. Nannini, A. Reigber, R. Scheiber, V. Severino, "SAR tomography with optimized constellation and its application to forested scenes," *Atti Della Fondazione G. Ronchi*, Vol. LXV, No. 3, 367-375, May-Jun. 2010.
- [5] A. Capozzoli, C. Curcio, A. Liseno, "Controlling the far-field resolution in near-field antenna characterization," *Proc. of the Antenna Measur. Tech. Ass.*, 1-6, Englewood, CO, Oct. 16-21, 2011.
- [6] A. Capozzoli, C. Curcio, A. Liseno, and P. Vinetti, "Field sampling and field reconstruction: A new perspective," *Radio Sci.*, Vol. 45, RS6004, 31, 2010, doi:10.1029/2009RS004298.

FUTURE USE OF THE DATA FROM THE ESA SENTINEL-1 MISSION FOR OPERATIONAL SOIL MOISTURE MAPPING: A MULTITEMPORAL ALGORITHM

Nazzareno Pierdicca, Luca Pulvirenti

Dept. Information Engineering, Electronics and Telecommunications, Sapienza University of Rome, Italy

Abstract

The Sentinel-1 mission will offer the opportunity to obtain C-band radar data characterized by short revisit time, thus allowing the generation of frequent soil moisture maps. This paper presents a multitemporal algorithm that exploits such a short revisit time to perform an operational soil moisture mapping. The algorithm assumes the availability of a time series of SAR images that is integrated within a retrieval algorithm based on the Bayesian maximum posterior probability statistical criterion. Preliminary results show that the performances of the multitemporal algorithm are better than those provided by a standard monotemporal one.

Index Terms – Synthetic Aperture radar, Soil moisture, multitemporal, bare soil scattering

I. INTRODUCTION

Soil moisture content (mv) is a key parameter that influences both global water and energy budgets because it controls the redistribution of rainfall among infiltration, runoff, percolation in soil, and evapotranspiration. Its knowledge is therefore essential for hydrological applications, such as flood monitoring and weather forecasts, as well as for climatology and agronomy.

Synthetic Aperture Radar (SAR) measurements are sensitive not only to soil moisture, but also to surface roughness and, in the presence of vegetation, to biomass and canopy structure. This implies that mv retrieval is generally an ill-posed problem, especially if the observations from a single configuration (i.e. single frequency, polarization and incidence angle) system are used. Recent works have proved that such an ill-posedness can be tackled if a time-series of SAR observations is available. In these works both change detection techniques (e.g., [1]) as well as Bayesian approaches [2] have been used.

A time-series of SAR images can be presently obtained from the C-band ENVISAT/ASAR sensor in ScanSAR Global Mode mode, as well as from the X-band radars on board the COSMO-SkyMed constellation. However, the use of Global Mode implies a worsening of the spatial resolution (from 30 cm to 1 km), while X-band is not the best one for estimating mv because of the large effects of vegetation canopy. The future European Space Agency (ESA) Sentinel-1 mission, foreseen in the framework of the European GMES program, will provide C-band radar data characterized by short revisit time (the two-satellite constellation

will offer six days exact repeat), thus permitting the application of multitemporal inversion algorithms, that are expected to strongly increase the quality and the reliability of the mv retrievals, and to develop an operational mv product.

In this paper, a multitemporal algorithm conceived to be operationally used to map mv from Sentinel-1 data is presented. It has been designed in the framework of the “GMES Sentinel-1 Soil Moisture Algorithm Development” project funded by ESA. The algorithm assumes the availability of a time series of SAR images and is based on the hypothesis that a statistical relation exists among the soil conditions at the different times of the series (i.e., among some of the geophysical parameters involved in the problem). In particular, it is assumed that, considering a specific temporal interval in which a number of Sentinel-1 (S-1) images is available, the average characteristics of surface roughness do not substantially change, as opposed to soil moisture, whose temporal scale of variation is shorter than that of roughness.

As for the effects of vegetation canopy on the radar signal, they are taken into account by applying a well-established semi-empirical model [3]. The temporal series of radar data, possibly corrected for the vegetation effects, is integrated within the retrieval algorithm that is based on the Bayesian maximum posterior probability (MAP) statistical criterion.

To assess the proposed methodology, we have simulated a number of S-1 observations of an agricultural site composed by several fields having constant surface roughness and variable soil moisture. The results show that the application of the multitemporal algorithm improves the performances of a standard monotemporal one both at pixel scale and at field scale.

II. THE MULTITEMPORAL ALGORITHM

The theory on which the proposed multitemporal algorithm is founded is described in [2]. The MAP estimator maximizes the probability density function (pdf) $p(\Theta|\mathbf{Z})$ of the vector of soil parameters (moisture and roughness) Θ conditioned to the measurements vector \mathbf{Z} . Considering the availability of a temporal series of measurements acquired at the current time t and at M previous times $t-M, \dots, t-1$ and applying the Bayes theorem, it turns out:

$$p(\Theta^t | \mathbf{Z}^{t-M}, \dots, \mathbf{Z}^t) = \frac{p(\mathbf{Z}^{t-M}, \dots, \mathbf{Z}^t | \Theta^t) p(\Theta^t)}{p(\mathbf{Z}^{t-M}, \dots, \mathbf{Z}^t)} \quad (1)$$

where superscripts denote time. By assuming that the statistics of the measured \mathbf{Z} conditioned to the soil parameters Θ is represented by the Wishart distribution [4] and that $p(\Theta)$ is uniform, the MAP criterion reduces to minimize the following distance (or “cost function”) with respect to Θ^t [2]:

$$d = \left\{ n \text{Tr}[\mathbf{C}(\Theta^t)^{-1} \mathbf{Z}^t] + n \log |\mathbf{C}(\Theta^t)| \right\} - \sum_{i=t-M}^{t-1} \log \left[\int_{m_v} \exp\{-n \text{Tr}[\mathbf{C}(\Theta^i)^{-1} \mathbf{Z}^i] - n \log |\mathbf{C}(\Theta^i)|\} dm_v \right] \quad (2)$$

where $|\cdot|$ indicates the determinant, $\text{Tr}(\cdot)$ represents the trace operator, n is the number of looks and $\mathbf{C}=\mathbf{C}(\Theta)$ is the covariance matrix that describes the surface scattering for the general case of a polarimetric radar. The terms of the main diagonal of \mathbf{C} differ from the backscattering coefficients for a 4π factor [4], [5].

The first term between curly brackets in (2) is the cost function for a standard monotemporal MAP algorithm (hereafter denoted as d_{mono}^t) depending on the data at time t only, while the second term (the summation) is that related to the multitemporal approach and basically represents the marginal probabilities of the measurements, conditioned to surface roughness and cumulated over the M previous acquisitions so that:

$$d = d_{mono}^t - \sum_{i=t-M}^{t-1} \log \left[\int_{m_v} \exp(-d_{mono}^i) dm_v \right] = d_{mono}^t - d_{marg} \quad (3)$$

The minimum of d has been found using a Monte Carlo approach, that is by searching this minimum in a randomly generated database. The forward surface scattering model proposed by Oh et al. [5] has been used for matching Θ with \mathbf{C} .

III. RESULTS

To assess the proposed methodology we have accomplished a simulated test. We have supposed a simplified scenario in which S-1 observes a bare terrain consisting of 10×10 square fields (range and azimuth directions are considered) each one including 10×10 pixels. Every field has been characterized by average values of roughness and moisture and the roughness of each field has been assumed constant throughout the period of the observations, while random changes of the field volumetric moisture between subsequent images have been supposed. Ten S-1 observations have been simulated and, for this purpose, the model described in [5] has been used. The speckle noise has been accounted for as done in [4] and a multilook processing with $n=100$ has been assumed, which is similar to what is foreseen for the standard S1 product.

To the simulated S-1 images, the multitemporal algorithm has been applied. The results are shown in Figure 2 for the case of single (VV) polarization. Both the root mean square retrieval error ($RMSE$) of m_v and the determination coefficient R^2 are reported. The improvement achieved by applying the new multitemporal algorithm can be clearly seen. It can be noted that after five times (i.e., five SAR observations) the improvement of both $RMSE$ and R^2 tend to be less evident than that obtained from time 1 to time 5, so that a temporal series of $M=4-6$ images seems to be the best choice for the use of the multitemporal

algorithm (also to avoid that the hypothesis of constant roughness loses validity).

It must be mentioned that, in the framework of the ESA project, the algorithm has been also applied to real data and compared to ground observations of soil moisture. Although multitemporal sequences at C-band are difficult to be gathered until now, a few cases have demonstrated the validity of the approach.

ACKNOWLEDGEMENT

This work has been supported by ESA/ESTEC under contract No. 4000101351/10/NL/MP/ef

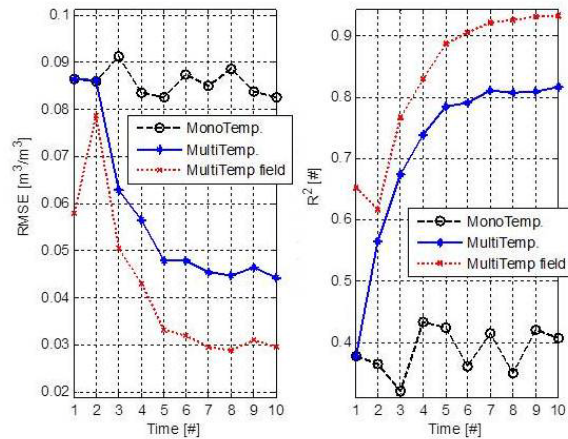


FIG. 1 - Root mean square retrieval error of mv (left panel) and R2 coefficient (right panel) for the simulated test. Black lines: monotemporal algorithm (pixel scale); blue lines: multitemporal algorithm (pixel scale); red lines: multitemporal algorithm (field scale).

REFERENCES

- [1] Pathe, C.; Wagner, W.; Sabel, D.; Doubkova, M.; Basara J. B.: Using ENVISAT ASAR Global Mo-de Data for Surface Soil Moisture Retrieval O-ver Oklahoma, USA. Ieee Transactions on Geoscience and Remote Sensing. Vol. 47, No. 2, pp. 468-480, 2009
- [2] Pierdicca, N.; Pulvirenti, L.; Bignami, C.: Soil moisture estimation over vegetated terrains u-sing multitemporal remote sensing data. Remo-te Sensing of Environment. Vol. 114, pp. 440-448, 2010
- [3] Attema, E. P. W.; Ulaby, F. T.: Vegetation mo-deled as a water cloud. Radio Science. Vol. 13, pp. 357-364, 1978
- [4] Pierdicca, N.; Castracane, P.; Pulvirenti, L.: In-version of Electromagnetic Models for Bare Soil Parameter Estimation from Multifrequency Po-larimetric SAR Data. Sensors. Vol. 8, pp. 8181-8200, 2008
- [5] Oh, Y.; Sarabandi, K.; Ulaby, F. T.: Semi-Empirical Model of the Ensemble-Averaged Dif-ferential Mueller Matrix for Microwave Back-scattering From Bare Soil Surfaces. Ieee Transactions on Geoscience and Remote Sensing. Vol. 40, No. 6, pp. 1348-1355, 2002

Session 7 – Microwave components II

G. Castaldi, V. Galdi, and I. M. Pinto

Short-pulsed wavepacket propagation in ray-chaotic enclosures: a random-plane-wave model

A. Sorrentino, and M. Migliaccio

The phase kurtosis index for reverberating chamber near LOS conditions

G. Grandoni, V. Mariani Primiani, and F. Moglie

Analysis of the entropy in fast time domain simulations of reverberation chambers

G. A. Casula, P. Maxia, G. Montisci, G. Mazarella, and F. Desogus

Design of cavity resonators for chemical reactions

SHORT-PULSED WAVEPACKET PROPAGATION IN RAY-CHAOTIC ENCLOSURES: A RANDOM-PLANE-WAVE MODEL

G. Castaldi, V. Galdi, I. M. Pinto

Waves Group, Department of Engineering, University of Sannio
 Corso Garibaldi 107, I-82100, Benevento, Italy
castaldi@unisannio.it, vgaldi@unisannio.it, pinto@sa.infn.it

Abstract

We review our recently proposed short-pulsed random-plane-wave statistical model of wavepacket propagation in a ray-chaotic enclosure. We show that this representation leads to analytical results that are in good agreement with predictions from full-wave numerical simulations.

Index Terms: Ray chaos, electromagnetic reverberation, short pulses.

I. INTRODUCTION

During the last decades, *ray chaos* has emerged as an intriguing paradigm with important implications in a variety of electromagnetic (EM) application scenarios, ranging from reverberating enclosures to microlasers (see, e.g., [1]–[7]).

In close analogy with *quantum chaos* (see, e.g., [8] and references therein), the presence of distinctive *footprints* in the time-harmonic high-frequency wave dynamics of ray-chaotic systems has been evidenced by many theoretical, numerical and experimental studies. Such footprints are not encountered in ray-regular (e.g., coordinate-separable) configurations.

In a recent study [9], we have dealt with ray-chaotic enclosures in the *short-pulsed* (SP) regime, for which only a few results (see, e.g., [5,7]) are available in the literature.

II. SP-RPW MODEL

Referring to Fig. 1, we consider a two-dimensional (closed, hollow) enclosure with perfectly-electric conducting walls and a Sinai-stadium-type geometry (i.e., quarter of stadium with an off-centered quarter-circle indentation) of characteristic size a . Figure 1(a) also shows a sample ray trajectory, from which the ray-chaotic behavior may be qualitatively understood (see [9] for more details). We assume that the enclosure is excited by an initially localized (“bullet”-like) SP wavepacket characterized by a waveform $s(t)$ of duration $T_s \ll a/c_0$ (with c_0 denoting the speed of light in vacuum), and z -directed electric field. Figure 1(b) shows a representative *late time* ($t_0 = 1000T_s$) field distribution computed via finite difference- time-domain (FDTD) [10] based numerical simulations, from which it can be seen that the wavepacket energy is eventually spread across the enclosure in a uniform, random-like fashion.

In [9], we proposed an effective and physically-insightful representation of the coarse features of the wavefield dynamics in this regime, based on an extension to the time-domain of the well-established time-harmonic *random-plane-wave* model [11]. In

our proposed model, with reference to a spatio-temporal domain of observation $r \equiv \sqrt{x^2 + y^2} \leq R$, $t_0 \leq t \leq t_0 + T$ (with $R \ll c_0 T_s$ and $T \ll T_s$), the electric field is expressed in terms of a superposition of independent SP-RPWs of the form

$$e_z(\mathbf{r}, t) \approx \sum_{n=1}^N a_n s[t - c_0^{-1}(\cos\phi_n x + \sin\phi_n y) - t_n], \quad (1)$$

where $\mathbf{r} \equiv (x, y)$, the number N of pulse arrivals is Poisson-distributed [12] with mean value $\bar{N}_{T,R}$, a_n are uncorrelated, zero-mean, unit-variance random variables, ϕ_n and t_n are uniformly and independently distributed random variables within the intervals $[-\pi, \pi]$ and $[t_0 - R/c_0, t_0 + R/c_0 + T]$, respectively; a formally similar expression holds for the magnetic field too (see [9] for details).

Paralleling the analysis of Poisson impulse noise processes in [12], we showed that in the limit $\bar{N}_{T,R} T_s \ll (T + 2R/c_0)$ (corresponding to *strongly overlapping* SP-RPWs, and hence intuitively well suited to model the late-time wavefield dynamics), the SP-RPW model in (1) yields a (zero-mean) spatio-temporal Gaussian random field, irrespective of the SP waveform shape and specific parameter distributions. Such field is therefore completely characterized by its spatio-temporal correlation, which can be expressed as [9]

$$c(\rho, \tau) \equiv \langle e_z(\mathbf{r}, t) e_z(\mathbf{r} + \boldsymbol{\rho}, t + \tau) \rangle \approx \left(\frac{\mathcal{E}_{EM}}{\mathcal{E}_0 \mathcal{A}_e} \right) \int_{-\infty}^{\infty} |\bar{S}(\omega)|^2 J_0 \left(\frac{\omega \rho}{c_0} \right) \exp(-i\omega\tau) d\omega, \quad (2)$$

where $|\bar{S}(\omega)|^2$ represents the normalized energy spectral density of the SP waveform, J_0 is the zeroth-order Bessel function [13], \mathcal{A}_e is the area of the enclosure, \mathcal{E}_{EM} is the (conserved) EM energy (per unit-length in z) initially injected in the enclosure, and isotropy and spatio-temporal stationarity are evident. For certain classes of SP waveforms, such as, e.g., analytic delta functions [14], the integral in (2) can be evaluated in closed form (see [9] for details).

As a representative example, assuming a second-derivative-analytic-delta-function SP waveform, Fig. 2(a) shows a Gaussian probability plot pertaining to the local temporal statistics (over an interval of duration $20T_s$) of the normalized wavefield observed at a fixed point ($x_c = 0.602a$, $y_c = 0.121a$) at a *late time* $t_0 = 1000T_s$, which is in very good agreement with the Gaussian prediction (dashed line). Similar results were observed for different observation points, as well as for the (local) spatial statistics (see [9] for details). For the same observation point and time, Fig. 2(b) shows a snapshot of the spatio-temporal correlation (estimated over a $4c_0 T_s \times 4c_0 T_s$ square domain), which, apart from weak fluctuations, appears essentially *isotropic*. A generally good agreement with the SP-RPW model can be observed from representative 1-D cut shown in Fig. 2(c). Conversely, early-time responses, not shown here for brevity (see [9] for details), show *markedly non-Gaussian* behaviors.

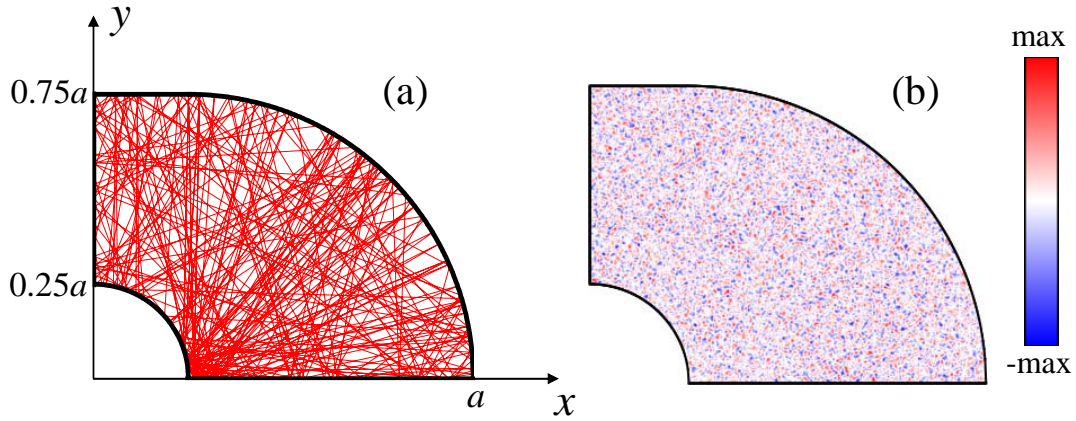


FIG. 1 (a) Schematic of the Sinai-stadium geometry and typical space-filling ray trajectory (after 250 reflections). (b) Representative FDTD-computed electric field map for SP-excitation ($c_0 T_s = a/20$) at a late time ($t_0 = 1000 T_s$).

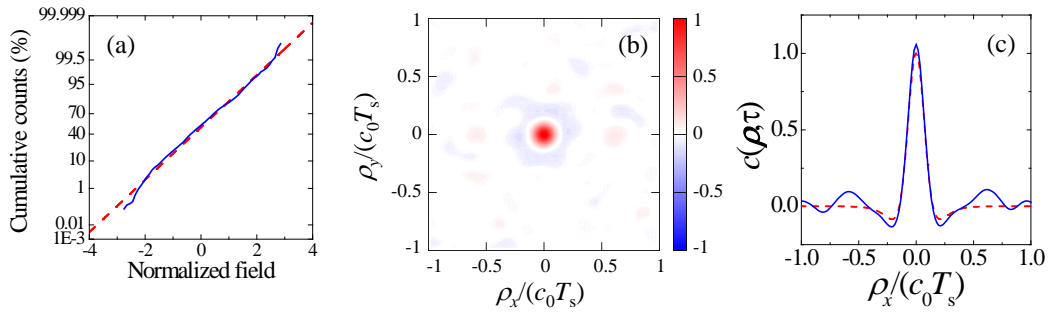


FIG. 2 (a) Gaussian probability plot of late-time temporal statistics (blue-solid curve) compared with Gaussian reference statistics (red-dashed line). (b) Spatio-temporal correlation snapshot at $\tau=0$, and (c) corresponding 1-D cut (blue-solid curve) at $\rho_y=0$ compared with SP-RPW prediction (red-dashed curve). Details in the text.

III. CONCLUSIONS

We reviewed here our recently proposed SP-RPW statistical model of SP wavepacket propagation in a ray-chaotic enclosure. Analytical predictions from this model, in good agreement with FDTD numerical simulations, indicate that the late-time response of a SP-excited ray-chaotic enclosure may be effectively modeled as a spatio-temporal random Gaussian field, whose parameters are simply related to coarse geometrical cavity properties, energy invariants, and the SP waveform.

REFERENCES

- [1] J. U. Nöckel and A. D. Stone, "Ray and wave chaos in asymmetric resonant optical cavities," *Nature*, vol. 385(6611), pp. 45-47, Jan.1997.
- [2] C. Gmachl, F. Capasso, E. E. Narimanov, J. U. Nöckel, A. D. Stone, J. Faist, D. L. Sivco, and A. Y. Cho, "High-power directional emission from microlasers with chaotic resonators," *Science*, vol. 280(5369), pp. 1556-1564, June 1998.
- [3] L. Cappetta, M. Feo, V. Fiumara, V. Pierro, and I. M. Pinto, "Electromagnetic chaos in mode stirred reverberation enclosures," *IEEE Trans. Electromagn. Compatibility*, vol. 40(3), pp. 185-192, Aug. 1998.
- [4] A. J. Mackay, "Application of chaos theory to ray tracing in ducts," *IEE Proc. Radar, Sonar Navig.*, vol. 164(6), pp. 298-304, Dec. 1999.
- [5] V. Galdi, I. M. Pinto, and L. B. Felsen, "Wave propagation in raychaotic enclosures: Paradigms, oddities and examples," *IEEE Antennas Propagat. Mag.*, vol. 53(2), pp. 635-644, Feb. 2005.
- [6] F. Seydou, T. Seppanen, and O. M. Ramahi, "Computation of the Helmholtz eigenvalues in a class of chaotic cavities using the multiple expansion technique," *IEEE Trans. Antennas. Propagat.*, vol. 57(4), pp. 1169-1177, Apr. 2009.
- [7] B. T. Taddese, J. Hart, T. M. Antonsen, E. Ott, and S. M. Anlage, "Sensor based on extending the concept of fidelity to classical waves," *Appl. Phys. Lett.*, vol. 95(11), 114103, Sept. 2009.
- [8] H.-J. Stöckmann, *Quantum Chaos. An Introduction*, Cambridge University Press, Cambridge, 1999.
- [9] G. Castaldi, V. Galdi, and I. M. Pinto, "Short-pulsed wavepacket propagation in ray-chaotic enclosures," accepted for publication in *IEEE Trans. Antennas Propagat.*, 2012 (preprint: arXiv:1112.6099v1 [physics.optics]).
- [10] A. Taflove and S. C. Hagness, *Computational Electrodynamics: The Finite-Difference Time-Domain Method*, 3rd Ed., Artech-House, Norwood (MA), 2005.
- [11] M. V. Berry, "Regular and irregular semiclassical wavefunctions," *J. Phys. A: Math. Gen.*, vol. 10(12), pp. 2083-2091, Dec. 1977.
- [12] D. Middleton, *An Introduction to Statistical Communication Theory*, IEEE Press, Piscataway (NJ), 1996.
- [13] M. Abramowitz and I. E. Stegun, *Handbook of Mathematical Functions*, Dover, New York, 1972.
- [14] E. Heyman and L. B. Felsen, "Weakly dispersive spectral theory of transients, part I: Formulation and interpretation," *IEEE Trans. Antennas Propagat.*, vol. 35(1), pp. 80-86, Jan. 1987

THE PHASE KURTOSIS INDEX FOR REVERBERATING CHAMBER NEAR LOS CONDITIONS

A. Sorrentino⁽¹⁾, M. Migliaccio⁽¹⁾

⁽¹⁾ Dipartimento per le Tecnologie, “Parthenope” University
Centro Direzionale Is C 4, 80143, Naples, Italy
antonio.sorrentino@uniparthenope.it

Abstract

This paper presents a simple and effective parameter able to unambiguously identify different channel conditions within a reverberating chamber (RC). The kurtosis index is first applied to characterize the phase of the received signal to discriminate the line-of-sight (LOS) or not (NLOS) conditions. Experiments undertaken over a large set of cases accomplished by emulating different propagation channel conditions at the RC of the Università di Napoli Parthenope, formerly Istituto Universitario Navale (IUN), confirm the soundness of the kurtosis index and its effectiveness from an operational point of view.

Index Terms – Kurtosis index, Reverberating Chamber, Propagation Channel.

I. INTRODUCTION

The mode-stirred reverberating chamber (RC) is basically an electrically large shielded room with metallic walls, in which one or more stirrers create continuously random changing boundary conditions of the electromagnetic field.

New interesting application of the RC as emulator of propagation channels is nowadays of paramount interest.

When only scattered waves arrive at the terminal, the signal envelope shows fast fading represented by a Rayleigh distribution. Such class of propagation channels is called Non-Line-of-Sight (NLOS) [1]. When a coherent component is present, the signal envelope shows a Rice distribution. Therefore, the class of the Line-of-Sight (LOS) propagation channel occurs [2].

The departure of the Rice field model from the Rayleigh one can be described by means of the Rice Factor, K , i.e. the ratio between the powers of the coherent and incoherent component of the field. The K factor is one of the most important parameter of Rice channels. It is a measure of the fading depth on the received signal.

When a small but significant direct link is present, it can be theoretically shown that the K factor is not granularly enough to unambiguously distinguish propagation channel conditions. This fact especially occurs in the near LOS critical conditions. To circumvent this problem one must employ a better descriptor. This is represented by the kurtosis index that has been recently applied to model wideband propagation channels [3]. Hence, this parameter is first applied to

characterize the RC channels conditions and to further enhance its granularity it is evaluated on the corresponding Rice phase distribution [4]. Experiments undertaken over a large set of cases accomplished by emulating different propagation channel conditions at the RC of the Università di Napoli Parthenope, formerly Istituto Universitario Navale (IUN), confirm the soundness of the kurtosis index and its effectiveness from an operational point of view.

II. THE PHASE OF THE ELECTROMAGNETIC FIELD

Let us consider a RC in which the electromagnetic field is partially stirred, i.e., a coherent field component is present. Due to the unstirred field component the resulting electromagnetic field must be seen as the complex superposition of a real and imaginary Gaussian field with different means, say \hat{E}_r and \hat{E}_i , respectively. It is possible to combine them in order to determine the probability density function (pdf) of the field amplitude which now results Rice distributed whereas the phase φ is distributed as follows [4]

$$p(\varphi) = \frac{1}{2\pi} \exp\left(-\frac{\hat{E}^2}{2\sigma^2}\right) \left\{1 + b\sqrt{\pi} \exp(b^2) [1 + \operatorname{erf}(b)]\right\} \quad (1)$$

wherein

$$b = \frac{1}{\sigma\sqrt{2}} (\hat{E}_r \cos \varphi + \hat{E}_i \sin \varphi) \quad (2)$$

\hat{E} is the amplitude of the unstirred component of the field and $\operatorname{erf}(f)$ is the error function.

Whenever \hat{E} is increased, i.e. we move from a LOS to NLOS condition, eq. (2) shows a peaked behavior that is centered on a φ value depending on \hat{E}_r and \hat{E}_i .

It is natural to employ the kurtosis index since it is a measure of the "peakedness" of the probability distribution of a real-valued random variable. Mathematically, the kurtosis is a statistical parameter that indicates the fourth order moment of the received signal. Once applied to the sample phased of the electromagnetic field in a RC, the kurtosis k is given by

$$k(\varphi) = \frac{1}{\sigma^4} \frac{\sum_i (\varphi_i - \bar{\varphi})^4}{N} \quad (3)$$

where σ is the standard deviation of the phase φ and $\bar{\varphi}$ is the mean value of φ . N is the number of samples of φ .

The kurtosis index k is expected to be close to zero in the NLOS cases while increasing to higher positive values as soon as we move to near LOS conditions.

III. EXPERIMENTAL RESULTS

In this section a meaningful set of experimental results are shown. The data analyzed are collected by making use of the reverberating chamber located at the IUN. It is a 2m size cubic chamber whose internal walls and stirrers are made of aluminum. Three stirrers are present at the IUN RC. The first stirrer (S1), placed on the left of the entrance door, has a rectangular shape of about 1.84m x 0.45m size; the second stirrer (S2) and the third stirrers (S3) have a Greek-cross shape. The former one has bars of about of 1.84m x 0.25m size; it is placed in front of the entrance door. The S3 stirrer has bars of about of 1.20m x 0.18m size and it is placed in the ceiling. A photo of the IUN RC is shown in Fig.1. The S1, S2 and S3 stirrers work in continuous mode with a maximum speed of 180, 390 and 320 rate per minute (rpm), respectively. Experiments are accomplished by using a monochromatic signal centred on 1.8 GHz. Two Ets-Lindgren double-ridged waveguide horn certified to work in the 1 – 18 GHz frequency range are employed. For each single measurement, a data set of 16000 samples in 3.66 s is acquired, that is a sample time equal to 2.29 ms. In all the experiments the three stirrers are operated together. A full calibration of the entire system is a priori accomplished. The scattering coefficient S_{21} is measured by making use of the Agilent Technologies Network Analyzer (VNA).



Fig. 1: The IUN RC

In Table I the results of the experimental data are listed. It can be noted that values of the kurtosis index smaller than 1 call for a NLOS RC condition. This is compatible with the underline electromagnetic field phase model described in section II. It is confirmed by the Rice factor values that are really close to 0. When a small coherent component is present, the kurtosis values become greater than 1, see Table 1. If one in practice consider 1 as the limiting value of the NLOS conditions it must be noted that small but significant coherent component values are

now detected by the new index while it was not possible by the classical procedure that evaluated the Rice factor over the complex amplitude of the received electromagnetic field. This fact is of operational interest since, as shown in Table I, one can now detect even near LOS conditions.

Table I – Kurtosis Parameter Values

RC Configuration	Kurtosis index values	Rice Factor
Case A	0.972	0.003
Case B	0.963	0.002
Case C	1.056	0.032
Case D	1.154	0.095
Case E	1.556	0.405
Case F	2.455	0.625

IV. CONCLUSIONS

In this paper the phase kurtosis index is first proposed and experimented over RC electromagnetic fields. Its enhanced granularity allows detecting near LOS conditions. This is of operational relevance.

V. REFERENCES

- [1] G. Ferrara, M. Migliaccio, A. Sorrentino, "Characterization of GSM Non-Line-of-Sight (NLOS) Propagation Channels Generated in a Reverberating Chamber by Using Bit- Error-Rates (BER)", *IEEE Trans. Electromagn. Compat.*, vol.49, no.3, pp.467-473, 2007.
- [2] A. Sorrentino, G. Ferrara, M. Migliaccio, "The Reverberating Chamber as a Line-of-Sight Wireless Channel Emulator", *IEEE Trans. Antennas Propag.*, vol.56, no.6, pp.1825-1830, 2008.
- [3] L. Mucchi, P. Marcocci, "A New Parameter for UWB Indoor Channel Profile Identification", *IEEE Trans. Wireless Communication*, vol.8, no.4, pp.1597-1602, 2009.
- [4] M. Migliaccio, "On the Phase of the Statistics of the Electromagnetic Field in Reverberating Chamber", *IEEE Trans. Electromagn. Compat.*, vol.43, no.4, pp.694-696, 2001.

ANALYSIS OF THE ENTROPY IN FAST TIME DOMAIN SIMULATIONS OF REVERBERATION CHAMBERS

G.Gradoni⁽¹⁾, V. Mariani Primiani ⁽²⁾, F. Moglie ⁽²⁾

⁽¹⁾ Institute for Research in Electronics and Applied Physics,
University of Maryland, Paint Branch Drive, College Park,
MD-20742, USA. Email: ggradoni@umd.edu

⁽²⁾ Dipartimento di Ingegneria dell'Informazione.
Università Politecnica delle Marche. 60131 Ancona . Italy.
Email: f.moglie@univpm.it, v.mariani@univpm.it

Abstract

In this contribution, we investigate the entropy growth in a mode-stirred cavity simulated by the FDTD method. The adopted reverberation chamber is efficiently stirred by paddles and excited by a Gaussian pulse. It is observed that the entropy starts growing quadratically in time, then it increases linearly during the energy buildup, and it saturates after a few nanoseconds, when the onset of disordered fields occur. This allows for terminating the numerical simulations well before the Richardson time, as the asymptotic entropy is rapidly achieved. The analysis is based on the eigenvalues of the correlation matrix, calculated over a dense grid of spatial points, thus supporting the perspective of the reverberation chamber as a statistical multivariate process.

Index Terms – Correlation matrix, Entropy, FDTD, Reverberation chambers.

I. INTRODUCTION

Reverberating chambers (RC) are large overmoded cavities wherein a stochastic electromagnetic field develops as driven by irregular (dynamic) boundaries [1]. Such boundaries are typically created by placing one or more mechanical mode-stirrers inside a cavity having simple (integrable) geometry. Full wave simulations of RC [2] allow for checking the performance of the stirrer(s) by using the ensemble theory. The standard IEC-61000-4-21 describes a few ensemble parameters such as independent positions and field uniformity to evaluate the goodness of a stirred environment. Finite difference time domain (FDTD) or transmission line matrix (TLM) can easily give all field components (full wave) at every spatial point of a chamber for every time instant. It must be remarked that the simulations in the time domain should run until the fields inside the RC do not vanish, or at least for the average time required by the excited cavity modes to fully develop, namely the Richardson time [3]. These two time scales are very long for cavities with a high Q-factor, leading to a high request of computer time. Therefore, a key point is how simulations can be optimized in terms of required time to maintain their reliability in terms of RC performance quantification. Here, we investigate the possibility of quantifying this

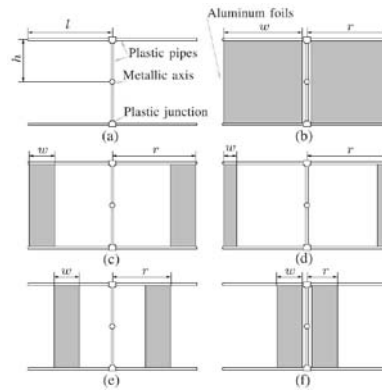
effect obtaining the RC performance after a small fraction, e.g., one hundredth, of the computation time normally required for these kind of structures

II. GEOMETRY OF THE ANALYZED CHAMBER AND STIRRER

The analyzed chamber is that present in our EMC laboratory: it is $6 \times 4 \times 2.5 \text{ m}^3$. We simulate this chamber assuming the presence of a horizontal stirrer, made of aluminum sheets. The axial support is made of a metallic tube used for the connection to the external motor. The supports were built using plastic pipes and junctions obtaining a “T” shape and then mounted on the metallic rotating axis. The picture reported in Fig. 1 shows all supports and the aluminum foils. The same Fig. 1 shows several front views of the analyzed stirrer dimension and shape.



(1.1)



(1.2)

FIG. 1 – Photo of the stirrer blades (1.1) and schematization of the simulated blade configurations (1.2) in front views.

III. NUMERICAL SIMULATIONS AND ENTROPY COMPUTATION

In the standard FDTD technique the time behavior of the incident field is a pulse modulated sine function. This source allows us to investigate a broad frequency range with only one FDTD computation run. All metallic parts are considered ideal, and volumetric losses are introduced to account for the actual chamber quality factor [4], [5]. If a full simulation is performed for our chamber, the pulse vanishes after $10 \mu\text{s}$. *If we apply our Entropy-based strategy, the simulations stop after 250 ns* recording the data for the entire $N=360$ simulations, obtained varying the angle of the mode-stirrer. The correlation array is computed for each twin of two stirrer positions on the magnitude of the electric field evaluated by the numerical code in a specified (dense) grid of spatial points inside the chamber volume. The Entropy is evaluated from the correlation matrix to quantify the influence of the stirrer on the cavity. From the square correlation matrix of dimension $N \times N = 360$ the first step is to evaluate its eigenvalues λ_n . After, the eigenvalues of the

correlation matrix are normalized to yield a unit summation. The information entropy H (of order α) is evaluated using the Renyi definition [6]. The case $\alpha=1$ is the Shannon H (information) Entropy, which can be evaluated using L'Hopital's Rule

$$H_\alpha = \frac{1}{1-\alpha} \ln \left(\sum_{m=1}^N \hat{\lambda}_m^\alpha \right) \quad H_1 = - \sum_{m=1}^N \hat{\lambda}_m \ln \hat{\lambda}_m \quad (1)$$

IV. RESULTS

Figs. (2.1), (2.2), and (2.3) show the total field in a section of the chamber. The first one refers to a time of 15 ns and for a fixed stirrer position (0°). The second one refers to the same position of the stirrer but at a time instant of 150 ns. The field pattern is strongly affected by the stirrer mixing of the chamber modes. The black zones refer to metal parts: stirrer and transmitting antenna. The last picture refers to the same time step but for a different stirrer position (135°): the pattern is completely different, point-by-point, highlighting the capability of the stirrer of creating field disorder.

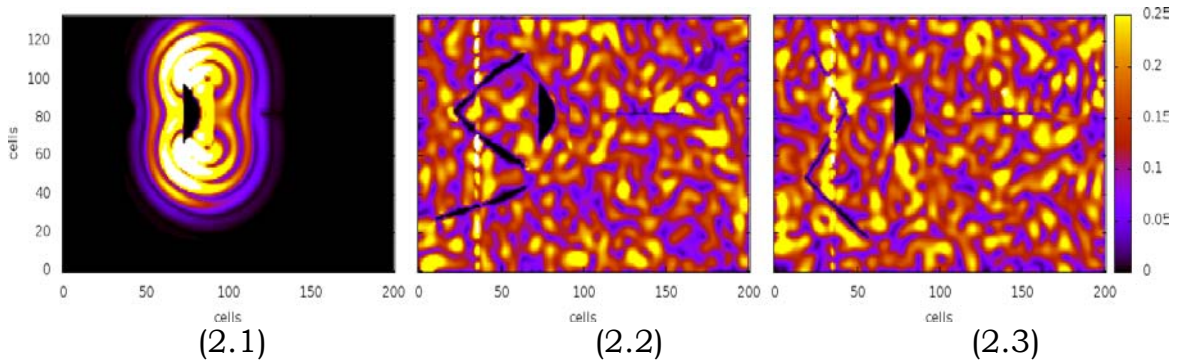


FIG. 2 – Electric field patterns in V/m. (2.1) stirrer at 0° and time = 15 ns, (2.2) same position and time = 150 ns, (2.3) stirrer at 135° and time 150 ns.

Fig. 3 reports the Entropy computed for different stirrer dimensions, referred to the notation of Fig. 1. As expected, the larger is the stirrer the higher is the Entropy.

After a rapid (quadratic) increase at early time, the Entropy shows a saturation behavior that confirms the possibility to stop the time domain simulation after about 200 ns obtaining reliable results on the random field distribution. The same figure reports the effect produced by the conductivity variation in the volumetric losses.

The loss increasing simulates a possible quality factor reduction. For σ less than 10^{-3} S/m, it can be noted that no effect is produced on the Entropy. The environment gets semi-open. For lower values, after an overlapping region, the Entropy progressively drops at earlier times.

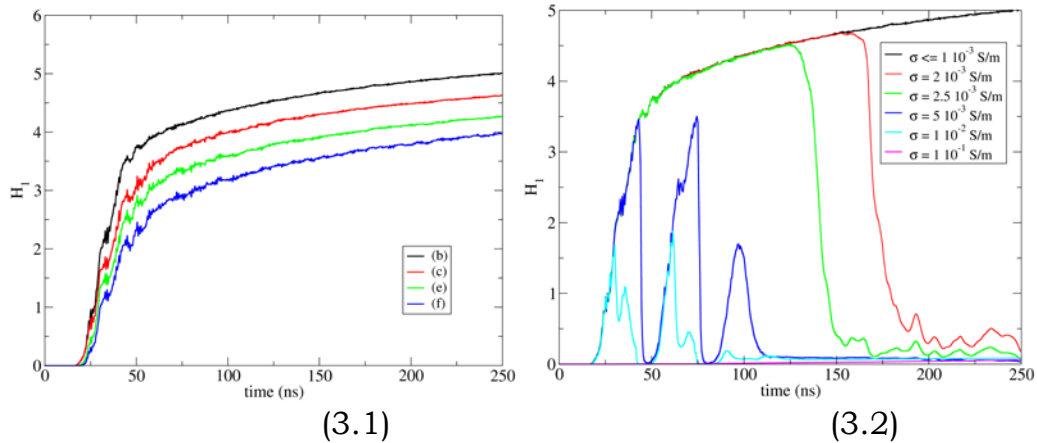


FIG. 3 – Entropy values as function of stirrer shape (3.1). Effect of the conductivity adopted for the volumetric losses (3.2).

V. CONCLUSION

A time domain fast computation for reverberation chamber field can be achieved analyzing the entropy within the working volume. In that way, the computation can be stopped at early times without affecting the result reliability in stirrer efficiency analysis. The introduction of volumetric losses allows for further accelerating the computation process. Metallic walls, and paddles, are assumed to be ideal.

REFERENCES

- [1] P. Corona, G. Ferrara, M. Migliaccio, “Reverberating chambers as sources of stochastic electromagnetic fields,” *IEEE Transactions on Electromagnetic Compatibility*, Vol. 38 (3), pp. 348-356.
- [2] V. Mariani Primiani and F. Moglie, “Numerical determination of reverberation chamber field uniformity by a 3-d simulation,” in *Proc. of the 10th Int. Symposium on Electromagnetic Compatibility (EMC Europe 2011)*, York, UK, Sep. 2011, pp. 829-832.
- [3] R. E. Richardson, “Mode-stirred chamber calibration factor, relaxation time, and scaling laws,” *IEEE Trans. Instrum. Meas.*, vol. 34, no. 4, pp. 571-580, Dec. 1985.
- [4] F. Moglie, “Convergence of the reverberation chambers to the equilibrium analyzed with the finite-difference time-domain algorithm,” *IEEE Trans. Electromagn. Compat.*, vol. 46, no. 3, pp. 469-476, Aug. 2004.
- [5] F. Moglie, V. Mariani Primiani, “Numerical analysis of a new location for the working volume inside a reverberation chamber,” *IEEE Trans. Electromagn. Compat.*, vol. 54, 2012, to be published, DOI: 10.1109/TEMC.2012.2186303.
- [6] R. J. Pirkl, K. A. Remley, and C. S. L. Patané, “Reverberation chamber measurement correlation,” *IEEE Trans. Electromagn. Compat.*, vol. 54, 2012, to be published, DOI: 10.1109/TEMC.2011.2166964.

DESIGN OF CAVITY RESONATORS FOR CHEMICAL REACTIONS

G. A. Casula⁽¹⁾, P. Maxia⁽¹⁾, G. Montisci⁽¹⁾, G. Mazzarella⁽¹⁾ and F. Desogus⁽²⁾

⁽¹⁾ Dipartimento di Ingegneria Elettrica ed Elettronica, Università di Cagliari, Italy

⁽²⁾ Dipartimento di Ingegneria Chimica e Materiali, Università di Cagliari, Italy

paolo.maxia@diee.unica.it

Abstract

We present in this work a microwave resonant cavity, used to evaluate the effect of the absorption of a low power electromagnetic field at microwave frequencies, designed using a commercial general purpose software for the electromagnetic simulation of three-dimensional high-frequency components.

Index Terms – Cavity Resonator, catalysis.

I. INTRODUCTION

The irradiation with electromagnetic fields at the microwave frequencies has a significant catalytic effect on the oxidation of organic compounds [1]. The general principle of catalysis is the change in reaction mechanisms followed by reagents to obtain the products. The effect of catalysis is kinetic in nature, and not thermodynamic: the action of the catalyst only modifies the intermediate states of a reaction, but does not change the final state. This means that the catalyst does not affect whether or not a reaction will take place, but only the reaction rate. The effects of microwaves in chemical reactions have been investigated using microwave ovens with power over 100 watts [2-3]. Following [4], a resonant cavity has been designed in order to study the effects of microwaves on organic reactions using low power (the feeding power is between 0.5 and 10 W).

The cavity resonator has been designed using a commercial general purpose software for the electromagnetic simulation of three-dimensional high-frequency components, CST Microwave Studio.

II. DESIGN OF THE RESONATOR

In this work, a rectangular cavity with copper walls working at 2.45 GHz is considered.

The resonant cavity must be designed providing that the reaction mixture, fed by an experimental multi-tube reactor placed inside a

cavity, is subjected to the maximum radiation from the cavity electromagnetic field.

As a first step we designed a cubic cavity filled with air. In this case the starting dimension is obtained by the equation [5]:

$$f_{nml} = c \cdot \left[\left(\frac{l}{2d} \right)^2 + \left(\frac{m}{2b} \right)^2 + \left(\frac{n}{2a} \right)^2 \right]^{\frac{1}{2}} \quad (1)$$

where l , m , n are integers and $d=b=a$ are the dimensions of the cavity sides.

Since only the fundamental mode TE_{110} must be excited, the corresponding cavity side is equal to 85 mm.

The aim of the cavity is to transfer as much electromagnetic energy as possible to a reaction mixture. A multi-tube reactor, consisting of two plexiglass structures where a mixture of water distilled to 90% circulates, is placed inside the cavity in order to maximize the surface of the reagent fluid exposed to the electromagnetic field.

The reactor is centered with respect to the cavity, ensuring a uniform absorption of the electromagnetic radiation by the liquid.

The insertion of the reactor modifies the resonant frequency of the fundamental mode TE_{110} of the cavity, which decreases at 1.31 GHz, due to the dielectric permittivity of plexiglass and water. As a consequence, the cavity side must be modified in order to maintain the operating frequency at 2.45 GHz. Furthermore, the imaginary part of water dielectric constant can't be neglected, therefore we use the Debye model [6] for the dielectric tangent of distilled water, which gives $\delta=0.15$ at the frequency of interest.

If we use the cavity in the fundamental mode at 2.45 GHz after the reactor insertion, and maintaining a cubic configuration, it will result in a significant reduction in the cavity size, making it unfeasible.

Even considering a higher mode, we did not find any field configuration able to ensure both a satisfying input matching and an acceptable field distribution in the region of the multitube reactor. Therefore we had to modify the three sizes of the cavity separately, aiming at a cavity with reasonable size.

The optimal configuration of the structure is shown in figure 1, with the following dimensions: $d=108$ mm, $b=130$ mm and $a=55$ mm. The resonant mode at the design frequency of 2.45 GHz is a higher order mode.

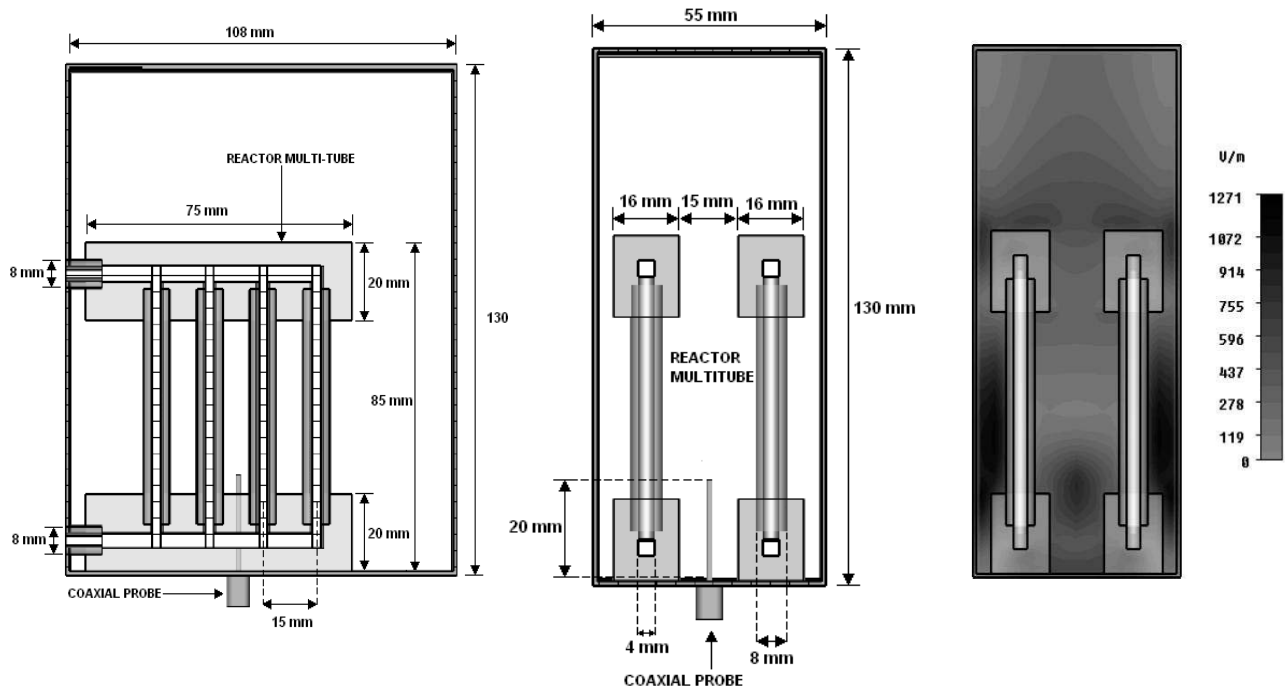


FIG. 1 – Cavity view and Field distribution inside the cavity.

III. RESULTS

The structure has been fed in the bottom side by a coaxial probe [7], as shown in Figure 1, with an input power of 0.5 W.

The performed simulation shows a good matching at the desired frequency with a return loss smaller than -20 dB (Figure 2).

Figure 3 shows the percentage of absorbed power at different frequencies. At the design frequency the structure absorbed power, expressed as $1 - |\Gamma|^2$, is greater than 90% with a Q factor equals to 29.

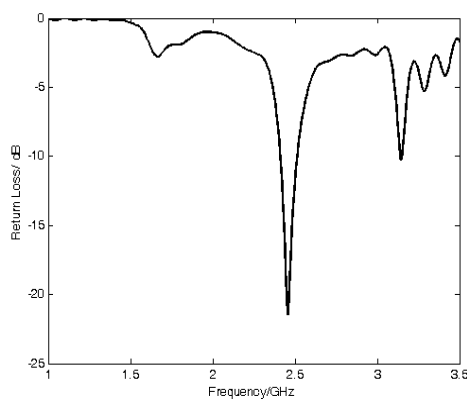


FIG. 2 – Return Loss

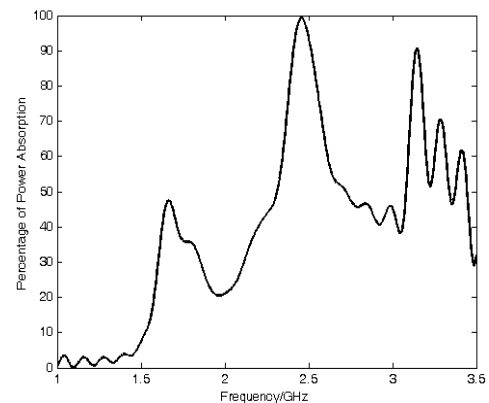


FIG. 3 – Percentage of power absorption.

The field distribution in a section of the cavity is shown in the right of Figure 1. Although the field appears to have the maximum intensity nearby the walls, the area of the multi-tube reactor is sufficiently radiated.

IV. CONCLUSION

We designed a resonant cavity, operating at 2.45 GHz and fed with low power, for evaluating the catalytic effect of the absorption of a low power electromagnetic field at microwave frequencies.

Further developments will include both the investigation if sterilization or pasteurization could be obtained by microwave irradiation at low power, and the study of other configurations for improving the absorption of radiation by the reaction mixture.

ACKNOWLEDGEMENT

Paolo Maxia gratefully acknowledges Sardinia Regional Government for the financial support of her PhD scholarship (P.O.R. Sardegna F.S.E. Operational Programme of the Autonomous Region of Sardinia, European Social Fund 2007-2013 - Axis IV Human Resources, Objective 1.3, Line of Activity 1.3.1.)

REFERENCES

- [1] N.Serpone, S.Horikoshi, A.V. Emeline, "Microwave in advanced oxidation processes for environmental applications. A brief review", *Journal of Photochemistry and Photobiology C: Photochemistry Reviews*, No. 11, pp. 114-131, 2010.
- [2] R. Luque, S.K. Badamali, J.H. Clark, M. Fleming, D.J. Macquarrie, "Controlling selectivity in catalysis: selective greener oxidation of cyclohexene under microwave condition", *Applied Catalysis A: General*, No. 341, pp. 154-159, 2008.
- [3] S.E. Mallakpour, A. Hajipour, A. Mahdavian, A. Zadhoush, F. Ali-Hosseini, "Microwave assisted oxidation of polyethylene under solid-state condition with potassium permanganate", *European Polymer Journal*, No. 37, pp. 1199-1206, 2001.
- [4] Carta R., Desogus F., "The effect of low-power microwaves on the growth of bacterial populations in a plug flow reactor", *AIChE Journal*, No. 56, pp. 1270-1278, 2010
- [5] R.E. Collin, "Foundation for Microwave engineering", *IEEE Press Series on Electromagnetic Wave Theory*, 2001.
- [6] R.Zajiček, , L.Oppl, J.Vrba, "Broadband measurement of Complex Permittivity using Reflection Method and Coaxial Probes", *Radioengineering*, Vol. 17, No. 1, April 2008
- [7] S.A. Long, M.W. McAllister, L.C. Shen, "The resonant Cylindrical Dielectric Cavity Antenna", *IEEE transaction on antenna and propagation*, Vol. AP-31, No. 3, May 1983.

Session 8 – Ground penetrating radar

A. Benedetto

Civil engineering applications of ground penetrating radar (invited)

D. Comite, A. Galli, F. Soldovieri, G. Valerio, P.M. Barone, S.E. Lauro, E. Mattei, and E. Pettinelli

Estimation of the geometrical features of buried objects from GPR analysis

F. Frezza, L. Pajewski, C. Ponti, G. Schettini, and N. Tedeschi

Plane wave scattering by a perfectly-conducting circular cylinder buried in a lossy medium

R. Persico, G. Leucci, and F. Soldovieri

Effect of the height of the measurement line on the diffraction curves in GPR prospecting

R. Monleone, M. Maffongeli, M. Pastorino, S. Poretti, A. Randazzo, and A. Salvadè

Detection of metallic bodies in dielectric structure by microwave imaging - Experimental results

**CIVIL ENGINEERING APPLICATIONS OF GROUND PENETRATING RADAR
INVITED TALK**

A. Benedetto

Sciences of Civil Engineering Department, “Roma Tre” University
Via Vito Volterra 62, 00146 Rome, Italy
benedet@uniroma3.it

Abstract

Ground Penetrating Radar (GPR) is a sensing equipment that is based on the principle of scattering of electromagnetic waves. In particular GPR transmits a signal pulse that travels through the material essentially as a non dispersive wave. It is reflected or scattered by any change of impedance. The signal that is received back by GPR looks like the transmitted signal and its time delay as well as the differences in phase, frequency and amplitude depend on the depth, shape and electromagnetic properties of the scattering or reflecting object.

The origin of this inspection technique can be discovered in the first applications of the radio wave propagation above and along the surface of the Earth (for a review see [1]). Beyond the most diffused research in the field of communication, direction finding and radar, probably the first documented application in the field of civil engineering was oriented to identify the ground water table depth [2], supported in Egypt by the National Research Council for the geophysical prospection of underground water in the Egyptian deserts.

During and after the second world war the research in radio frequency applications received a large attention especially with reference to the sounding of geological materials. Notwithstanding these researches were devoted to military scopes (e.g. [3]), they have had some relevant impacts for potential civil engineering uses.

A significant activity in the field of civil engineering started up in the sixties and has become mature in the seventies. The main surveys that were carried out using GPR investigated mines and underground deposit [4;5;6;7]. In this period, in the line of the lunar science missions, strong efforts have been spent to improve the available technologies that seemed very promising for the subsurface examinations [8;9;10].

At the end of seventies and from the eighties the use of GPR also for several applications in the field of civil engineering has increased massively. In 1978 Dolphin et al. documented probably one of the first archeological survey. Olhoeft [11;12] studied the electrical character of geological materials as well as the relationships between electrical conductivity and dielectric polarization. A very important application of GPR in borehole configuration was the inspection of the nuclear waste disposal sites [13].

Another important and essential incentive to the research came from the military and humanitarian applications for mines detection [14;15]. The success of GPR performance in this field is remarkably whereas there is a considerable contrast in dielectric properties between the landmine and the host soil [16] and attracted the most of the financial resources by governments all over the world but especially in the USA.

Therefore the equipment was strongly improved and the applications beyond the military scopes increased. In particular, referring to the civil engineering applications, a first overview was given by Ulriksen in 1982 [17]. Actually GPR is used in all the fields of civil engineering for inspection, monitoring and design purposes (e.g [18;19;20;21;22]).

The detection of utilities and buried objects as well as the inspection of road pavements and bridge decks as well as the measurement of moisture content in natural soils are the main applications of GPR in the civil engineering context. In addition very interesting examples of the use of GPR in structural, geotechnical engineering and railways inspections have to be mentioned.

Index Terms – Civil engineering, Ground Penetrating Radar, Road pavement survey, bridge inspection, water content evaluation, geomorphologic stability, structure monitoring.

REFERENCES

- [1] A. P. Annan “GPR—History, Trends, and Future Developments”, *Subsurface Sensing Technologies and Applications*, Vol. 3, No. 4, October 2002.
- [2] El Said, M.A.H., 1956, Geophysical prospection of underground water in the desert by means of electromagnetic interference fringes: *Pro. I.R.E.*, v. 44, p. 24–30 and 940.
- [3] Waite, A.H. and Schmidt, S.J., 1961, Gross errors in height indication from pulsed radar altimeters operating over thick ice or snow, *IRE International Convention Record*, Part 5, p. 38–54.
- [4] Cook, J.C., 1973, Radar exploration through rock in advance of mining: *Trans. Society Mining Engineers, AIME*, v. 254, p. 140–146.
- [5] Holser, W.T., Brown, R.J., Roberts, F.A., Fredriksson, O.A., and Unterberger, R.R., 1972, Radar logging of a salt dome: *Geophysics*, v. 37, p. 889–906.
- [6] Unterberger, R.R., 1978, Radar propagation in rock salt: *Geophys. Prosp.*, v. 26, p. 312–328.
- [7] Thierbach, R., 1973, Electromagnetic reflections in salt deposits: *J. Geophys.* (1974) v. 40, p. 633–637.
- [8] Annan, A.P., 1973, Radio interferometry depth sounding: Part I—Theoretical discussion: *Geophysics*, v. 38, p. 557–580.
- [9] Simmons, G., Strangway, D., Annan, A.P., Baker, R., Bannister, L., Brown, R., Cooper, W., Cubley, D., deBettencourt, J., England, A.W., Groener,

- J., Kong, J.A., LaTorraca, G., Meyer, J., Nanda, V., Redman, J.D., Rossiter, J., Tsang, L., Urner, J., Watts, R., 1973, Surface Electrical Properties Experiment, in Apollo 17: Preliminary Science Report, Scientific and Technical Office, NASA, Washington D.C., p. 15-1-15-14.
- [10] Ward, S.H., Phillips, R.J., Adams, G.F., Brown, Jr., W.E., Eggleton, R.E., Jackson, P., Jordan, R., Linlor, W.I., Peeples, W.J., Porcello, L.J., Ryu, J., Schaber, G., Sill, W.R., Thompson, S.H., and Zelenka, J.S., 1973, Apollo lunar sounder experiment, in Apollo 17: Preliminary Science Report, Scientific and Technical Office, NASA, Washington, D.C., p. 22-1-22-26.
- [11] Olhoeft, G.R., 1975, The electrical properties of permafrost, Ph.D. Thesis, University of Toronto., 172 pages.
- [12] Olhoeft, G.R., 1987, Electrical properties from 310 to 10⁹ Hz — physics and chemistry: *Proceedings of the 2nd International Symposium on the Physics and Chemistry of Porous Media*, American Institute of Physics Conference Proceedings, v. 154, p. 281–298.
- [13] Davis, J.L. and Annan, A.P., 1986, Borehole Radar Sounding in CR-6, CR-7 and CR-8 at Chalk River, Ontario. Technical Record TR-401, Atomic Energy of Canada Ltd.
- [14] MacDonald, J., Looockwood, J., Altshuler, T., Broach, T., Carin, L., Harmon, R., Rappaport, C., Scott, W., and Weaver, R.: Alternatives for landmine detection, RAND, USA, 336 pp., 2003.
- [15] D. J Daniels “GPR for Landmine Detection, an Invited Review Paper”, *Tenth International Conference on Ground Penetrating Radar*, 21 -24 June, 2004, Delft, The Netherlands.
- [16] Chen, C., Rao, K., and Lee, R.: “A tapered-permittivity rod antenna for ground penetrating radar applications”, *J. Appl. Geophys.*, 47, 309–316, 2001.
- [17] Ulriksen, C.P.F., 1982, “Application of impulse radar to civil engineering”: Unpublished Ph.D. Thesis, Dept. of Engr. Geol., U. of Technology, Lund, Sweden, p. 175.
- [18] Saarenketo T & Scullion T (2000) Road Evaluation with Ground Penetrating Radar. *Journal of Applied Geophysics* 43: 119–138.
- [19] F. Finck (2003). “Introduction of a ground penetrating radar system for investigations on concrete structures” *Otto-Graf-Journal* Vol. 14, 35-44
- [20] A. Benedetto, M.R. De Blasiis (2010). Applications of Ground Penetrating Radar to road pavement: state of the art and novelties, *Proc. 2nd GeoShanghai International Conference in Shanghai, China in 2010*
- [21] J Hugenschmidt (2010). “Geophysics and non-destructive testing for transport infrastructure, with special emphasis on ground penetrating radar”, PhD Thesis ETH ZURICH
- [22] A. Benedetto, G. Manacorda, A. Simi and F. Tosti (2012). “Novel perspectives in bridges inspection using GPR”, *Nondestructive Testing and Evaluation*, Vol. 27, No. 3, September 2012, 239–251

ESTIMATION OF THE GEOMETRICAL FEATURES OF BURIED OBJECTS FROM GPR ANALYSIS

D. Comite⁽¹⁾, A. Galli⁽¹⁾, F. Soldovieri⁽²⁾, G. Valerio⁽³⁾,
P. M. Barone⁽⁴⁾, S. E. Lauro⁽⁴⁾, E. Mattei⁽⁴⁾, E. Pettinelli⁽⁴⁾

(1) Department of Information Engineering, Electronics
and Telecommunications, “Sapienza” University of Rome –
Via Eudossiana 18, 00184 Rome, Italy
comite , galli@diet.uniroma1.it

(2) IREA, Istituto per il Rilevamento Elettromagnetico dell’Ambiente,
C.N.R. – Via Diocleziano 328, 80127 Naples, Italy
soldovieri.f@irea.cnr.it

(3) I.E.T.R., Institut d’Electronique et de Télécommunications
de Rennes, University of Rennes 1 –
Campus Beaulieu, Av. Générale Leclerc, 35000 Rennes, France
guido.valerio@univ-rennes1.fr

(4) Department of Physics “E. Amaldi”, Roma Tre University –
Via della Vasca Navale 84, 00146 Rome, Italy
pambarone , lauro , mattei , pettinelli@fis.uniroma3.it

Abstract

The ability of a Ground Penetrating Radar (GPR) to detect and reconstruct the location, size and shapes of buried objects by means of inverse data processing is addressed in this work. The choices of the relevant electromagnetic parameters, geometries, and operational frequencies are related to the investigations performed in the framework of the planetary ExoMars mission. The study shows to what extent the use of a frequency-domain microwave tomographic inversion algorithm allows us to recognize different kinds of canonical geometries, even in critical conditions where the scatterers have size comparable to the wavelengths of the probing signal and can be located close to the antennas. An extensive analysis has been carried out starting from radargrams derived both by measurements (a “sand-box” experimental setup) and by simulations (numerical data from ad-hoc implementation of a CAD tool).

Index Terms – CAD simulations, GPR instrument, Inverse problems, Scattering from objects.

I. INTRODUCTION

The main goal of the planned “ExoMars” mission will be to drill the shallow Martian subsurface and analyze the extracted samples on site, looking for evidence of life on the “red planet”. In order to prevent dangerous and energy-consuming drilling operations of the rover, it will be extremely significant to recover information about the geological features of the first few meters of the subsoil and, in particular, on the position and shapes of rocks buried in sandy regolith.

To this aim, a ground-penetrating-radar (GPR) instrument [1] will be the best candidate for providing fast and reliable analyses of the shallow subsurface, also relying on suitable inversion procedures on the data. In this frame, our study is developed to test what kind of knowledge can be derived on the location, size and shape of shallow buried targets by applying a microwave tomographic algorithm [2] to both measured and simulated radargrams [3] in critical operative conditions.

II. EXPERIMENTAL AND NUMERICAL GPR ANALYSIS

In order to acquire suitable data to be processed, an experimental setup has been expressly built, consisting of a $150 \times 100 \times 30$ cm dielectric box, filled with a mixture of a glass beads in which scatterers having different shapes can be buried [3]. Measurements have been performed using a commercial bistatic GPR instrument (“PulseEkko Pro” by Sensors and Software Co.) equipped with a pair of antennas having a 1 GHz bandwidth around the central frequency of 1 GHz. In order to complete a surface scanning, the instrument is swept along the major axis of the box at the soil smooth interface, with a fixed mutual distance between the transmitting/receiving antennas (chosen at 19 cm here).

In this study, preliminary measurements have been executed on targets made of hard wood wrapped with aluminum foils to firstly test the approach in the case of non-penetrable objects. Various canonical geometries of buried targets have been considered (sphere, cube, parallelepiped, cylinder, cone, pyramid, etc.). Radargrams (the typical output for this kind of analysis) are generated transmitting a Gaussian pulse from each position on the surface and collecting the signal scattered by the buried objects. A relevant example of a measured radargram is shown in Fig. 1 for a cube (9 cm side) and a square-based pyramid (9×9×10 cm), buried at a fixed depth from surface (9 cm here).

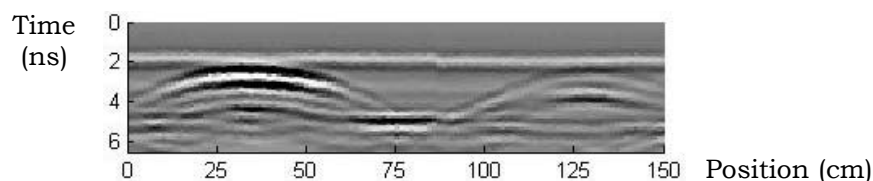


FIG. 1 – Example of a measured GPR radargram, generated converting on a gray scale the amplitude of the received signal from each position along the surface. These data are due to buried cube (left) and pyramid (right) scatterers.

The experimental setup just described has also been modeled by means of a commercial full-wave electromagnetic CAD, “CST Microwave Studio”, directly operating in the time domain. A flexible ‘simulated GPR environment’, including the Tx/Rx antenna system, has suitably been implemented in order to achieve numerical results comparable with the experimental setup [3].

Objects with the same shapes as those used in the measurements have then been simulated numerically in a host medium analogue to the sandy glass-bead mixture. As for the experimental data, a Gaussian pulse is radiated by the Tx antenna and the signal at the output of the Rx antenna is collected. It is worth noting that such traces consist of a first ‘direct’ wave, guided by the soil interface, followed later by that scattered from the buried objects. In order to emphasize the scattering contributions, when the superficial roughness can be neglected, a single direct signal has been evaluated in the absence of any buried rock and then subtracted from each received trace (such operation is named ‘background removal’). In Fig. 2, an example of simulated radargrams is shown for a cube, before (a) and after (b) this background removal.

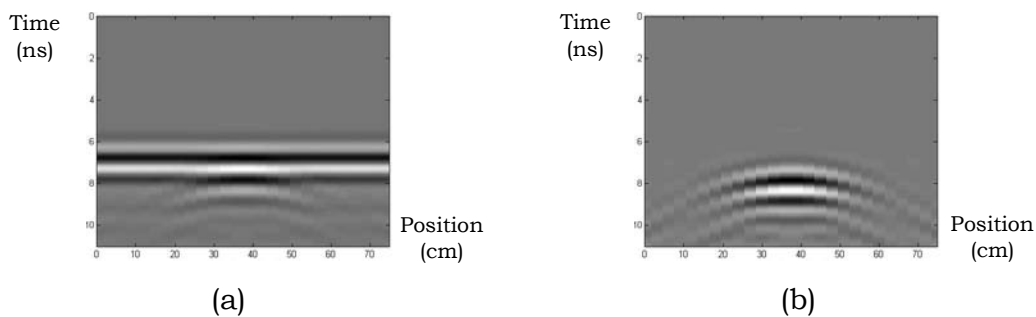


FIG. 2 – Simulated GPR radargrams for a cube with 9 cm side and 9 cm deep in a sandy soil: (a) before and (b) after the operation of background removal.

III. RESULTS FROM THE INVERSION APPROACH

In order to obtain location and shape estimations of the targets, a tomographic frequency-domain algorithm has been handled, based on the Born approximation to linearize the relevant inverse problem [2]. As is known, this approach can perform accurate reconstruction only when applied to a full observation for weak scatterers. Nevertheless, the relevant application to our GPR data is stimulating to test what kind of information can be recovered in critical cases. In the method, the targets are represented in terms of anomalies (‘contrast function’) of the dielectric permittivity and conductivity with respect to the properties of a background environment. First, a tomographic reconstruction has been obtained by starting from the raw measured GPR data, as shown in Fig. 3 for a 2D side view of the box with cube and pyramid of Fig. 1.

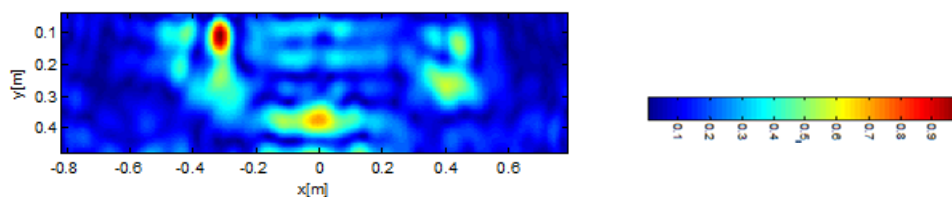


FIG. 3 – Tomographic reconstruction based on experimental data for cube and pyramid (as in Fig. 1): the contrast function is plotted through a color scale.

This result enables us to detect and well localize the targets and the bottom of the dielectric box, which is visible only in the central zone because the box is placed on two wooden lateral tables creating an air gap below the central lower part.

We finally present some reconstructions derived by processing the regularized GPR data from the simulated numerical setup. In Fig. 4, the results achieved for two cubes of different size are shown. Since these objects are not penetrable, we are able to well locate and reconstruct only their upper face, particularly clear for the bigger cube, in agreement with resolution limits imposed by the probing wavelengths.

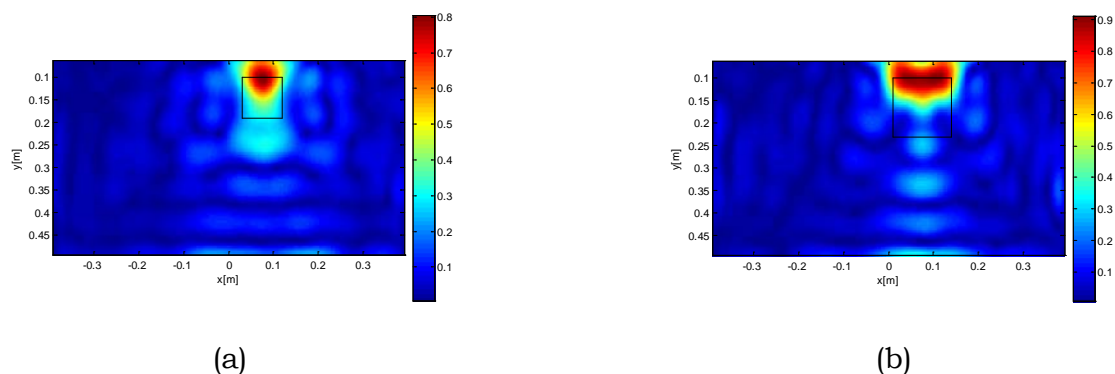


FIG. 4 – Tomographic reconstruction based on numerical radargram data for differently-sized cubes: (a) side of 9 cm; (b) side of 13 cm.

IV. CONCLUSION

GPR measurements and numerical simulations have been performed and processed to achieve information on buried targets with an inverse tomographic algorithm, tested in very challenging practical condition. Further studies are planned on the scattering effects of three-dimensional penetrable objects in different hosting environments.

ACKNOWLEDGEMENT

This work has been financially supported by the Italian Space Agency (ASI) through contract ASI-INAF n. I/029/08/0.

REFERENCES

- [1] D. J. Daniels (Ed.), *Ground Penetrating Radar*. IEE Press, 2004.
- [2] E. Pettinelli, A. Di Matteo, E. Mattei, L. Crocco, F. Soldovieri, J. D. Redman, and A. P. Annan, “GPR response from buried pipes: measurement on field site and tomographic reconstructions,” *IEEE Trans. Geosci. Remote Sensing*, vol. 47, Aug. 2009, pp. 2639-2645.
- [3] G. Valerio, A. Galli, P. M. Barone, S. E. Lauro, E. Mattei, and E. Pettinelli, “GPR detectability of rocks in a Martian-like shallow subsoil: a numerical approach,” *Planet. Space Sci.*, vol. 62, Mar. 2012, pp. 31-40.

PLANE WAVE SCATTERING BY A PERFECTLY-CONDUCTING CIRCULAR CYLINDER BURIED IN A LOSSY MEDIUM

F. Frezza⁽¹⁾, L. Pajewski⁽²⁾, C. Ponti⁽²⁾, G. Schettini⁽²⁾, and N. Tedeschi⁽¹⁾

⁽¹⁾ Department of Information Engineering, Electronics and
Telecommunications, “La Sapienza” University of Rome,
Via Eudossiana 18, 00184 Roma, Italy.

fabrizio.frezza@uniroma1.it

⁽²⁾ Applied Electronics Department, “Roma Tre” University,
Via della Vasca Navale 84, 00146 Roma, Italy

Abstract

The 2D electromagnetic scattering of a plane wave by a perfectly-conducting circular cylinder buried in a lossy medium, is presented. The problem of reflection and transmission of both the plane wave and the cylindrical wave at the interface with a dissipative medium has been faced taking into account the general case of inhomogeneous waves. The scattering problem has been solved with the Cylindrical-Wave Approach. The theoretical solution has been numerically implemented in a Fortran code and the numerical results have been compared with both the literature and simulations with a commercial software.

Index Terms – Buried objects detection, electromagnetic scattering, inhomogeneous plane waves, lossy media, spectral domain analysis.

I. INTRODUCTION

In this paper, the two-dimensional scattering of a plane wave by a perfectly-conducting circular cylinder buried in a dissipative medium is analyzed through the Cylindrical Wave Approach (CWA). The results presented in [1] are extended to media with complex electromagnetic constants. The problem of reflection and transmission between two lossy media is solved with the Fresnel coefficients of complex argument. The angles of the phase vector and the attenuation vector of the transmitted wave are computed through the methods presented in [2]. Finally, the reflection and transmission of the scattered cylindrical waves by the plane interface is obtained through the plane-wave expansion of the cylindrical functions in lossy media [3]. Numerical evaluation of the fields is obtained through a Fortran code. In Section II, the theoretical formulation of the problem is presented. The procedure leads to a linear system of equations that gives the coefficients of the scattered field. In Section 3, the numerical results of the Fortran code developed are reported. Comparisons with both results in the literature and simulations with a commercial software are shown, emphasizing the advantages of our technique in terms of computing time. Finally, in Section 4 conclusions are drawn.

II. THEORETICAL FORMULATION

The geometry of the problem is the following: a perfectly-conducting cylinder, with radius a , is buried in a medium 1, in the half-space $x > 0$, at a depth h . Let us suppose that the half-space $x < 0$ is filled with air. We consider an electromagnetic plane wave from air, impinging on medium 1. The time factor is taken to be $\exp[-i\omega t]$, which is omitted below. Let us assume that the medium 1 is a homogeneous medium, with relative electric permittivity $\varepsilon_1 = \varepsilon'_1 + i\sigma/(\omega\varepsilon_0)$. Similarly, we call n_1 the complex refractive index of the medium, defined as the square root of the complex relative permittivity.

Let us suppose that the incident plane wave has a propagation vector \mathbf{k}_i lying in the plane (x, z) . The polar coordinate system on this plane is taken to be (r, θ) , where θ is the angle formed with the x -axis and the origin coincides with the center of the cylinder. We use normalized variables and parameters, defined as: $\xi = k_0 x$, $\zeta = k_0 z$, $\chi = k_0 h$, $\rho = k_0 r$, $\alpha = k_0 a$. Here $k_0 = 2\pi/\lambda_0$ is the vacuum wave number. Similarly, the parallel and orthogonal components of the wave vector will be normalized: $n_{i\parallel} = k_{iz}/k_0$ and $n_{i\perp} = k_{ix}/k_0$.

The electromagnetic field is treated through the quantity V , which represents the y -component of the electric field in E-polarization ($TM^{(y)}$), and the y -component of the magnetic field in H-polarization ($TE^{(y)}$). The Fresnel coefficients, taking into account the reflection and transmission at the interface, are indicated as $\Gamma(n_{\parallel})$ and $T(n_{\parallel})$, respectively, where the indication of the relevant polarization has been omitted for the sake of brevity.

To calculate a rigorous solution of the scattering problem, the field has been decomposed in different contributions, as presented in [1]. To solve the problem of the reflection and transmission at the interface, we may consider the propagation vectors divided in their real and imaginary parts, e.g., the transmitted wave vector $\mathbf{k}_t = \boldsymbol{\beta}_t + i\boldsymbol{\alpha}_t$. To evaluate the transmitted propagation vector, in the general case of two lossy media, we use a generalization of the Snell's law, as shown in [2]. These relations give the transmitted wave vector components as phase and attenuation vectors.

The transmitted wave is an inhomogeneous wave except for a normally incident wave. To expand the transmitted inhomogeneous wave into a cylindrical waves superposition, we need to represent the complex propagation vector in terms of a complex angle $\varphi_t = \varphi_{tR} + i\varphi_{tI}$. The transmitted wave can be expressed as a superposition of Bessel functions. The scattered field by the cylinder can be written as a superposition of cylindrical waves, i.e., Hankel functions of order m , times an exponential factor, with unknown weights c_m . The Bessel and Hankel functions involved are of complex argument, and their behavior with respect to the index ensure the convergence of the series also with the exponential growth due to the complex angle φ_t .

The scattered-reflected and the scattered-transmitted fields are expressed through the plane wave spectrum in lossy media of the cylindrical functions, multiplying each elementary plane wave by the reflection and the transmission coefficient, respectively. By imposing the boundary conditions, we can find, for both the polarizations, the following linear system for the unknowns:

$$\sum_{m=-\infty}^{+\infty} A_{mn} c_m = B_n \quad \text{with: } n = 0, \pm 1, \pm 2, \dots \quad (1)$$

with:

$$A_{mn} = i^{m-n} e^{-im\phi_i} \left[G_n^{E,H} (n_1 \alpha) RW_{m+n} (-2n_1 \chi, 0) + \delta_{mn} \right]$$

$$B_n = -T_{01} (n_{i||}) G_n^{E,H} (n_1 \alpha) e^{in_1 n_{i||} \chi} e^{-in\phi_i}$$

where: δ_{mn} is the Kroenecker symbol, CW_n is the cylindrical wave of order n , RW_n is the cylindrical reflected wave of order n , G_n^E is the ratio between the Bessel function of the first kind and the Hankel function of order n , and G_n^H is the ratio of their derivatives.

III. NUMERICAL RESULTS

We implemented the analytical procedure on a Fortran code. To find a numerical solution of the system in Eq. (1), it is obviously needed the introduction of a truncation at a finite number of elements M . As a criterion for the choice of the maximum order, we find $M = 3\alpha \text{Re}[\epsilon_1]$ is a good compromise between accuracy and computational weight. The procedure is valid for any value of the losses, but the computational time increases with the losses, because of the presence of σ_1 inside the kernel of the integrals.

As a first result, a comparison between our code, the low-frequency scattering amplitudes presented in [4], and the simulations with the commercial software Comsol, based on the Finite Element Method, has been considered. In Fig. 1a) a comparison between Figure 5 of [4], the simulations with Comsol and the results of our code is shown ($\epsilon'_1 = 15$, $\sigma_1 = 0.001 \text{ S/m}$, $\alpha = 0.2$, $\chi = 1.26$ at frequency $f_0 = 30 \text{ MHz}$ and incident angle $\phi_i = 0^\circ, 30^\circ, 60^\circ$). In Fig. 1b), the amplitude of the scattered field when the incident wave impinges at $\phi_i = 0^\circ, 60^\circ$ is reported. The parameters considered are: $\epsilon'_1 = 10$, $\sigma_1 = 0.01 \text{ S/m}$, $\alpha = 1.4$, $\chi = 15$, at a frequency $f_0 = 600 \text{ MHz}$, at normal incidence. About the time of the simulations, Comsol returns the solutions in approximately 150 s, the Fortran code at 2 s. All the simulations have been implemented on a personal computer with two CPUs Intel i7 at 3.0 GHz and 2.8 GHz, and with 12 GB of RAM.

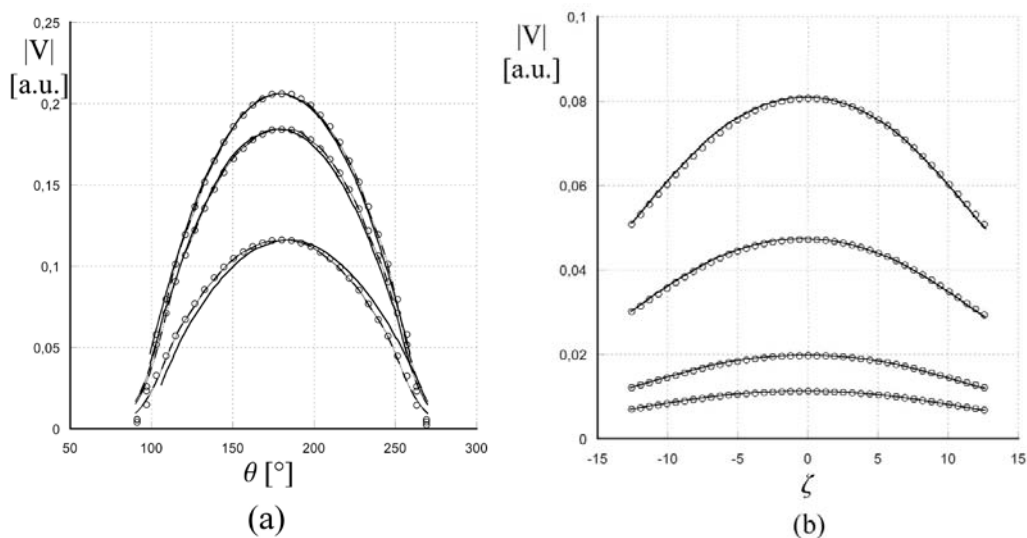


FIG. 1 – Amplitude of the scattered-transmitted field: (a) from Figure 5 of [4] (solid line), computed with Cmsol (dashed line), and with our code (circles), for (from top to bottom): $\varphi_i = 0^\circ, 30^\circ, 60^\circ$. (b) Scattered field by a buried cylinder computed with Cmsol (solid line) and with our code (circles), with (from top to bottom): $\sigma_1 = 0 \text{ S/m}$ and $\varphi_i = 0^\circ, 60^\circ$; $\sigma_1 = 0.01 \text{ S/m}$ and $\varphi_i = 0^\circ, 60^\circ$.

IV. CONCLUSIONS

In this paper, a spectral-domain solution has been employed to characterize the 2D scattering of a plane wave by conducting cylindrical structures buried in a half-space filled by a dissipative medium. We found a theoretical solution of the problem by a cylindrical harmonics expansion. The numerical evaluation of the theoretical solution has been developed through a Fortran code. Comparisons with both results in the literature and simulations with a commercial software have been reported.

REFERENCES

- [1] M. Di Vico, F. Frezza, L. Pajewski, and G. Schettini, “Scattering by a finite set of perfectly conducting cylinders buried in a dielectric half-space,” *IEEE Transactions on Antennas and Propagation*, vol. 53(2), pp. 719-727, Feb. 2005.
- [2] J.E. Roy, “New results for the effective propagation constants of nonuniform plane wave at the planar interface of two lossy media,” *IEEE Transactions on Antennas and Propagation*, vol. 51(6), pp. 1206-1215, Jun. 2003.
- [3] F. Frezza, G. Schettini, and N. Tedeschi, “Generalized plane-wave expansion of cylindrical functions in lossy media convergent in the whole complex plane,” *Optics Communications*, vol. 284(16-17), pp. 3867-3871, Apr. 2011.
- [4] J.D. Kanellopoulos and N.E. Buris, “Scattering from conducting cylinders embedded in a lossy medium,” *International Journal of Electronics*, vol. 57(3), pp. 391-401, Mar. 1984.

Effect of the height of the measurement line on the diffraction curves in GPR prospecting

R. Raffaele⁽¹⁾, G. Leucci⁽¹⁾ F. Soldovieri⁽²⁾

⁽¹⁾ Institute for Archaeological and Monumental Heritage
Via Monteroni, Campus Universitario, 73100, Lecce, Italy
r.persico@ibam.cnr.it, g.leucci@ibam.cnr.it

⁽²⁾ Institute for Electromagnetic Sensing of the Environment
Via Diocleziano 328, 80127 Naples, Italy
soldovieri.f@irea.cnr.it

Abstract

In this paper, the shape of the diffraction curves vs. the height of the observation line in the framework of GPR prospecting is analysed. Therefore, it is shown that the height of the measurement line is a critical factor.

Index Terms – Diffraction curves, GPR prospecting, measure of permittivity.

I. INTRODUCTION

In the framework of ground penetrating radar (GPR) prospecting, the diffraction curves (DC) are the most exploited method to estimate the propagation velocity (PV) of the e.m. waves in the soil. The method is based on GPR data in multi-bistatic configuration: it is user-friendly, fast and non-invasive, and does not require further tools, which is instead needed with time domain reflectometry (TDR) or common midpoint (CMP) [1]. The achievable accuracy is in general of the order of 10% [1]. This measure has an intrinsic value if the prospecting is specifically aimed to evaluate some characteristics of the soil (e.g. in hydro-geophysical applications [2] or in hydrocarbon contamination measurements[1]). In the other cases, this measure is a key-ingredient for a correct time-depth conversion and a reliable focusing by means of an inversion or a migration algorithm. In this work, we propose a study of the DC method in terms of height of the observation line [3]. In the next section, the equation of the DC for interface data and a fixed height data are retrieved. In section 3, the effect of the height of the observation line is discussed. Conclusions follow.

II. THE DC FOR INTERFACE DATA AND FIXED HEIGHT DATA

With reference to fig. 1, let us consider, in a 2D geometry, an electrically small buried target. First, let us consider interface GPR data.

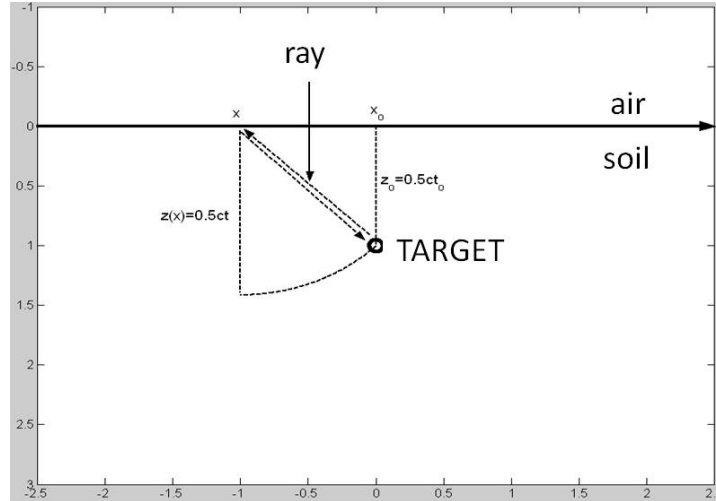


FIG. 1 – Measure of the PV from the DC for interface data.

The GPR antennas measure the scattered field in several points in air, placed along a finite length segment centred around the target. Considering a Cartesian system with the origin at the interface, and neglecting the offset between the GPR antennas, we have that the datum point is $(x,0)$ and the target point is (x_o, z_o) . The distance

between these two points is $\sqrt{(x-x_o)^2 + z_o^2}$, which also expresses the apparent depth $z_{app}(x)$ of the target at the observation abscissa x . The quantity actually measured is the corresponding return time of the signal, given by $t(x) = \frac{2z_{app}(x)}{c}$ (see fig. 1), so that we have $z_{app}(x) = \frac{ct(x)}{2}$,

where c is the PV of the e.m. waves in the soil and the factor 2 is due to the “round trip” of the signal. The point of the observation line at minimum distance from the target is at $x = x_o$, and here one records the minimum two-travel time $t_o = \frac{2z_o}{c} \Leftrightarrow z_o = \frac{ct_o}{2}$. Consequently we have:

$$\frac{ct}{2} = \sqrt{(x-x_o)^2 + \left(\frac{ct_o}{2}\right)^2} \Leftrightarrow t = \frac{2}{c} \sqrt{(x-x_o)^2 + \left(\frac{ct_o}{2}\right)^2} \Rightarrow \frac{t^2}{t_o^2} - \frac{(x-x_o)^2}{0.25c^2t_o^2} = 1 \quad (1)$$

Eq. (1) represents a hyperbola in the plane (x,t) , with vertex in (x_o, t_o) (only the branch for $t \geq 0$ is relevant). The equation is parametric in c , and this allows to work out c from a matching between the data and the model of eq. (1).

Let us now consider the case $h > 0$. With reference to fig. 2, due to the refraction at the interface, eq. (1) evolves into:

$$t(x) = \frac{2}{c_o} \sqrt{(x-x_1)^2 + \left(\frac{ct_{o1}}{2}\right)^2} + \frac{2}{c} \sqrt{(x_1-x_o)^2 + \left(\frac{ct_{o2}}{2}\right)^2} \quad (2)$$

where x_1 is the interface point of the refracted ray (see fig. 2), c_o e c are the PV in air and in the soil, $t_{01} = (2h)/c_o$ and $t_{02} = (2z_o)/c$ are the minimum two-travel times in air and in the soil, respectively.

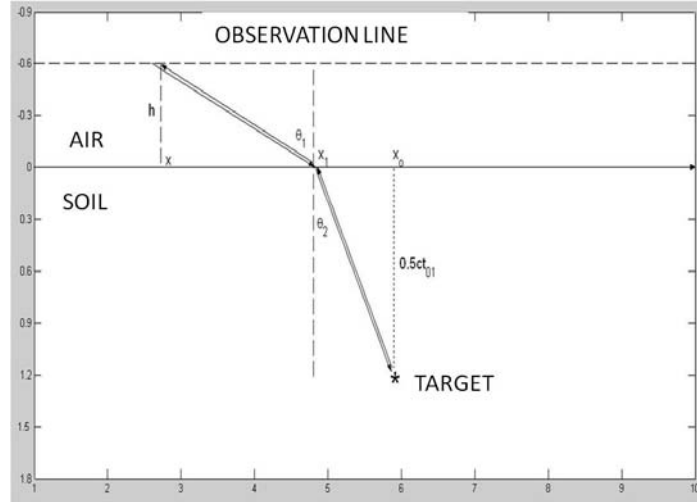


FIG. 2 – Ray in the case of measurement line at non-null height.

To express the DC, we can express x_1 vs. x by applying the Snell's refraction law, which implies (see fig. 2):

$$\sin(\theta_1) = \frac{c_o}{c} \sin(\theta_2) \Leftrightarrow \frac{|x - x_1|}{\sqrt{(x - x_1)^2 + h^2}} = \frac{c_o}{c} \frac{|x_1 - x_o|}{\sqrt{(x_1 - x_o)^2 + \left(\frac{ct_{02}}{2}\right)^2}} \quad (3)$$

with the physical constraint that x_1 belongs to the interval $[x, x_o]$ if $x \leq x_o$ or $[x_o, x]$ if $x \geq x_o$. It can be graphically recognised that eq. (3) has one and only one solution under this physical constraint. So, considering a numerical resolution of eq. (3), we formally achieve the DC as:

$$t(x) = \frac{2}{c_o} \sqrt{(x - x_1(x, x_o, c, t_{01}, t_{02}))^2 + h^2} + \frac{2}{c} \sqrt{(x_1(x, x_o, c, t_{01}, t_{02}) - x_o)^2 + \left(\frac{ct_{02}}{2}\right)^2} \quad (4)$$

III. THE RANGE OF VARIABILITY OF THE DC AT NULL AND NON-NULL HEIGHT

III.A – THE CASE OF NULL HEIGHT

The equation of the asymptotes of the DC are given by

$$t = \pm \frac{2}{c} (x - x_o) \quad (5)$$

Eq. (5) means that the asymptotes do not depend on the time-depth of the target. Some DC is shown in fig. 3: The hyperbolas degenerate into the asymptotes for $t_o \rightarrow 0$ and becomes progressively flatter around the vertex for $t_o \rightarrow +\infty$.

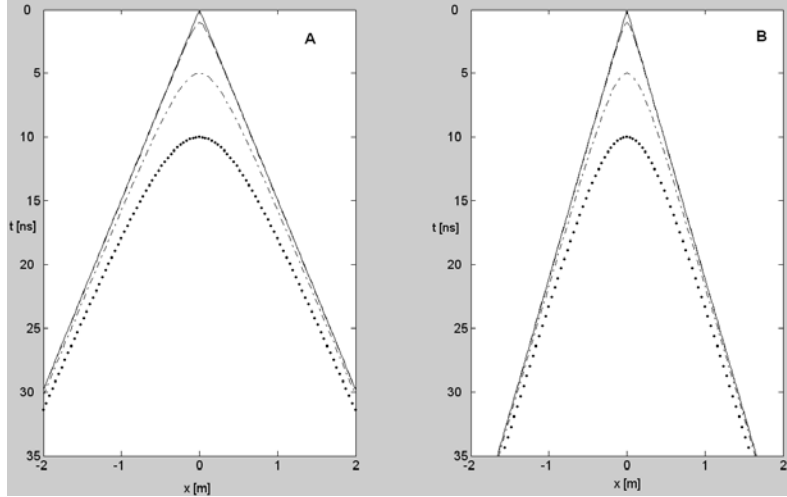


FIG. 3 – DC for a deeper and deeper target. Panel A: $c=1.34 \times 10^8$ m/s. Panel B: $c=0.95 \times 10^8$ m/s. In all panels: Solid line: the asymptotes. Dashed line: the curve for $t_0=1$ ns. Dashed-dotted line: the curve for $t_0=5$ ns. Dotted line: the curve for $t_0=10$ ns.

Moreover, since the slope of the asymptotes is $\pm 2/c$, the DC becomes progressively “narrower” while decreasing the PV. In fig. 3 we show some examples. In particular, panels A and B refer to the case of interface data. Please note that the case $c = \frac{c_o}{9} \approx 0.033 \text{ m/ns}$ corresponds to a relative dielectric permittivity equal to 81, which is approximately that of the fresh water and can be regarded as an extreme occurrence in most practical cases. The other side extreme case is represented by an ideal transparent air-made-soil ($c = c_o = 0.3 \text{ m/ns}$).

III.B – THE CASE OF NON-NULI HEIGHT

Let us preliminary consider the limit case of an interface target ($t_{02} \rightarrow 0$). This case can be discussed multiplying both the members of eq. (3) times the product of the denominators. So, we have:

$$|x - x_1| \sqrt{(x_1 - x_o)^2 + \left(\frac{ct_{02}}{2}\right)^2} \rightarrow |x - x_1| |x_1 - x_o| = \frac{c_o}{c} |x_1 - x_o| \sqrt{(x - x_1)^2 + h^2} \quad (6)$$

Since the condition $c|x - x_1| \rightarrow c_o \sqrt{(x - x_1)^2 + h^2}$ is impossible, eq. 6 involves

$$\lim_{t_{02} \rightarrow 0} x_1 = x_o \quad (7)$$

So, substituting eq. (7) in eq. (4), we achieve

$$t(x) = \frac{2}{c_o} \sqrt{(x - x_o)^2 + \left(\frac{c_o t_{01}}{2}\right)^2} \quad (8)$$

Eq. (8) is a DC in air, coherently with the fact that the propagation of the signal occurs exclusively in air. Coherently, eq. (8) does not depend on c , and so it is impossible to retrieve c from too shallow targets.

Let us now pass to the case $t_{02} > 0$. In this case, for an ideal air-made-soil ($c = c_o$) we have:

$$t(x) = \frac{2}{c_o} \sqrt{(x-x_1)^2 + \left(\frac{c_o t_{01}}{2}\right)^2} + \frac{2}{c_o} \sqrt{(x_1-x_o)^2 + \left(\frac{c_o t_{02}}{2}\right)^2} \quad (9)$$

Moreover, for $c = c_o$ eq. (4) is easily solved as $x_1 = \frac{x t_{02} + x_o t_{01}}{t_{01} + t_{02}}$, which substituted in eq. (9), with some manipulation, provides

$$t(x) = \frac{2}{c_o} \sqrt{(x-x_o)^2 + \left(\frac{c_o(t_{01}+t_{02})}{2}\right)^2} \quad (10)$$

Eq. (10) is the DC in air for a target at the time depth $t_{01} + t_{02}$. Let us now consider, the opposite ideal case $c \rightarrow 0$. In this case, from eq. (3), we work out again $x_1 \rightarrow x_o$. Substituting in eq. (4) we achieve

$$t(x) = \frac{2}{c_o} \sqrt{(x-x_o)^2 + \left(\frac{c_o t_{01}}{2}\right)^2} + t_{02} \quad (11)$$

Eq. (12) means that this limit curve is the same of eq. (8) rigidly shifted of the time t_{02} . Physically, this means that the limit trajectory of the ray is a broken line with a first segment from the source point (x, h) to the projection of the target at the interface $(x_o, 0)$, followed by a vertical segment from this point to the target-point $\left(x_o, \frac{c t_{02}}{2}\right)$. This means that

the limit ray maximizes the path of the signal in air and minimizes that in the soil, coherently the principle of Fermat. This makes poorer the information achievable from the data because the DCs tend to be less different from each other compared to the case of data at the air soil interface. This difficulty increases for shallower targets driving to the theoretical insolvability of the problem for interface targets, as shown. Let us now consider also the case $t_{02} \rightarrow +\infty$. In this case, from eq. (4) we see that $x_1 \rightarrow x$, and so eq. (4) evolves into

$$t(x) = \frac{2h}{c_o} + \frac{2}{c} \sqrt{(x-x_o)^2 + \left(\frac{c t_{02}}{2}\right)^2} = t_{01} + \frac{2}{c} \sqrt{(x-x_o)^2 + \left(\frac{c t_{02}}{2}\right)^2} \quad (12)$$

Eq. (12) is the DC relative to the soil at hand translated of the time t_{01} . Physically, this means that the limit trajectory of the ray is composed by a vertical segment from the source point (x, h) to its projection at the interface $(x, 0)$ and then from this point to the target-point $\left(x_o, \frac{c t_{02}}{2}\right)$.

From eq. (12), we have that, for deep targets the range of variability of the DCs is essentially the same as if the data were gathered at the interface. However, this “recover” occurs at quite high time depths, where even the diffraction curves derived from interface data provide a progressively poorer information, because of their progressive flattening.

In fig. 4 (panels C and D) two examples are provided. In particular, in both panels we have considered the case $t_{01} = 2ns \leftrightarrow h = 30cm$. In panel C the diffraction curves for $t_{02} = 0$ are shown (homologous to panel A), and in panel D the DCs for $t_{02} = 20ns$ are shown (homologous to panel B).

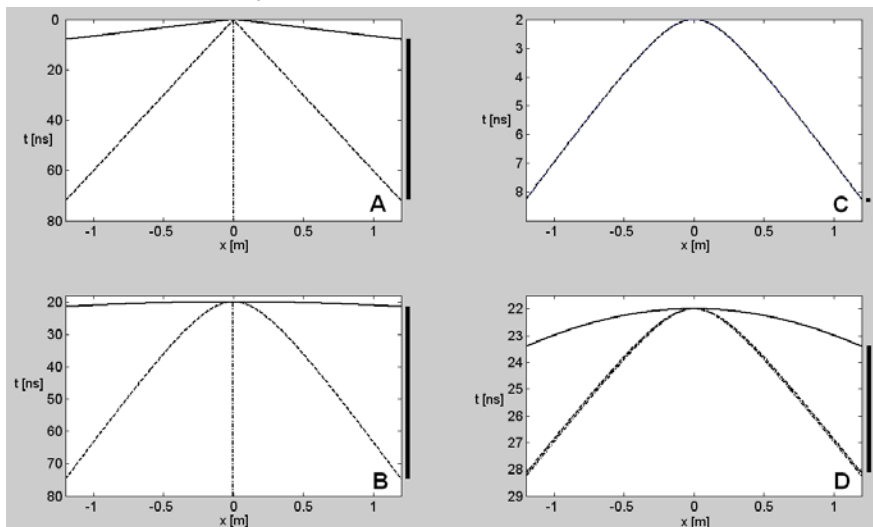


FIG. 4 – DCs compared. Panel A: $h = 0cm$, $t_o = 0ns$; Panel B: $h = 0cm$, $t_o = 20ns$; Panel C: $h = 30cm$, $t_{o2} = 0ns$; Panel D: $h = 30cm$, $t_{o2} = 20ns$; Solid line: $c = c_o$; dashed line: $c = c_o / 9$; dashed-dotted: $c = 0$.

On the right hand side of the curves, we have marked vertical segments that expresses the time-distance between the extreme physical cases of “air-made-soil” and “water-made-soil” at 1.2 m away from the target. This distance is 64 ns in panel A, but reduces to 53 ns in the case of panel B. In the case of observation line at 30 cm, instead, this distance is equal to 0 ns for an interface target (panel C), and increases “only” to 4.7 ns for a target at the time depth of 20 ns in the soil (panel D).

IV. CONCLUSIONS

We have shown preliminary calculations about the evaluation of the PV in the framework of GPR prospecting, and we have shown that the measure is potentially less reliable if the height of the observation line is larger than zero. A ray model for the propagation has been adopted. This is quite simple, but it is the model customarily exploited in GPR applications. At the conference, the theoretical results will be back-upped with FDTD simulations.

REFERENCES

- [1] H. Jol, Ground Penetrating Radar: Theory and applications, Elsevier, 2009.
- [2] F. Soldovieri, G. Prisco, R. Persico, Application of Microwave Tomography in Hydrogeophysics: some examples, Vadose Zone Journal, pp. 160-170, Feb. 2008.
- [3] I. Catapano, L. Crocco, Y. Krellmann, G. Trilitzsch, F. Soldovieri, "A Tomographic Approach for Helicopter-Borne Ground Penetrating Radar Imaging," *Geoscience and Remote Sensing Letters, IEEE*, vol.9, no.3, pp.378-382, May 2012.

DETECTION OF METALLIC BODIES IN DIELECTRIC STRUCTURE BY MICROWAVE IMAGING - EXPERIMENTAL RESULTS

R. Monleone⁽¹⁾, M. Maffongelli⁽¹⁾, M. Pastorino⁽²⁾, S. Poretti⁽¹⁾,
A. Randazzo⁽²⁾, A. Salvadè⁽¹⁾,

⁽¹⁾ TTHF Laboratory, Swiss University of Applied Sciences

⁽²⁾ CH-6928 Manno, Switzerland
asalvade@supsi.ch

⁽¹⁾ Dynatech Department, University of Genoa
Via Opera Pia 11A, 16145 Genova, Italy
{matteo.pastorino;andrea.randazzo}@unige.it

Abstract

This paper reports experimental results concerning the inspection of dielectric structures in which metallic inclusions are present. The investigation is based on a microwave imaging approach and the measured data have been obtained by using a prototype of a microwave tomograph. The reconstructed images of the structures under test have been constructed by using a nonlinear inverse scattering procedure based on a truncated Landweber method. The reported results concern in particular the inspection of wood materials with cylindrical metallic inclusions.

Index Terms – Inverse scattering, microwave imaging, wood industry.

I. INTRODUCTION

In industrial applications, it is often necessary to detect the presence of foreign bodies inside known structures. A significant example is represented by the wood industry [1], in which metallic objects (e.g., nails or splinters) can make the wood material unsuitable for the process and can also damage the cutting machinery. When a metallic object is included inside a dielectric structure, microwave nondestructive testing techniques can be satisfactory applied.

In [2], the present authors reported an inspection approach based on electromagnetic imaging for penetrable objects. The approach was specifically devoted to inspect wood slabs and trunks. Experimental results were also provided. They were obtained by using a prototype of a microwave tomograph developed at the Swiss University of Applied Sciences (SUPSI) and described in details in [3]. The system is able to illuminate the structure under test (SUT) in a frequency range of 1-6 GHz. The measured samples of the scattered electric field are “inverted” by using a procedure based on a truncated Landweber method, which has been developed and tested in [4][5]. The approach belongs to the class of electromagnetic inverse scattering methods, which has received

a significant attention from the electromagnetic community in the last years [6]-[15].

In this paper, for the first time, the proposed imaging system is applied to inspect dielectric targets including foreign metallic bodies, which, as previously mentioned, has a significant applicative relevance.

To simulate quite a complex scatterer, a composite target has been constructed. It is made by wood and some other dielectric materials with low electric conductivity. A metallic inclusion has been inserted in the structure. Since the system is working under tomographic conditions, the shape of the target is elongated in order to simulate a cylindrical object for which two-dimensional (2D) slides of the cross section are retrieved and visualized as pixelated images. No post-processing and filtering are applied to the final images.

The paper is organized as follow. In Section II the imaging system (hardware and software) is briefly reviewed, whereas the experimental results are reported and discussed in Section III. Some conclusions are drawn in Section IV.

II. THE IMAGING PROTOTYPE

The developed prototype [3] allows multiview multi-frequency acquisitions in the operating band of 1-6 GHz. It is composed by three major modules: The measurement and acquisition hardware; the movement control hardware; and the management system. The first one includes a vector network analyzer (VNA) equipped with a digital IF input filter configured at 300 Hz. The acquisition module is controlled by a custom software running on the management system PC, which is interfaced to the VNA by means of a standard LAN connection. The last block contains all the electronics needed to move the antennas and to rotate the platform. The transmitted and receiving antennas have 8.5 dBi gain and 60° beamwidth. The SUT is positioned on a rotating platform made of weakly scattering material.

The collected samples of the field are related to the dielectric properties of the SUT by the following nonlinear Fredholm equation for transverse magnetic (TM_z) incident polarization

$$\mathbf{e}_m = \mathbf{e}_i + L\{\tau\} \quad (1)$$

where \mathbf{e}_m is an array of M elements containing the values of the z -component of the total electric field; \mathbf{e}_i is an array of the same dimension containing the values of the known incident field at the same locations; $L\{\}$ is the nonlinear Lippmann-Swinger operator [6] and τ is the *scattering potential*, which is related to the distribution of the complex dielectric permittivity of the target, i.e., $\tilde{\epsilon} = \epsilon - j\omega^{-1}\sigma$. Equation (1) is discretized and solved (in a regularization sense) by using a truncated Landweber method [5], following the approach described in

[3]. A pixelated image of the dielectric parameters is then obtained. The final images (in particular the one related to the electric conductivity distribution) allow one to detect the possible presence of metallic inclusions inside the SUT.

III. EXPERIMENTAL RESULTS

The prototype has been used to acquire field samples in $M = 91$ measurement points, which are equally spaced along an arc of circumference of radius $R = 73$ cm and aperture $\Phi = 1.5\pi$. The TX antenna assumes $S = 16$ equally spaced positions (the antenna moves along the same circumference). 91×16 measured samples are collected and inverted. The cross section of the SUT (shown in Fig. 1) is located inside a square investigation area of side $L = 0.3$ m (discretized into $N = 63 \times 63$ square subdomains).

The reconstruction results are shown in Fig. 2. In particular, the distributions of the retrieved relative dielectric permittivity (Fig. 2(a)) and electric conductivity (Fig. 2 (b)) are reported. As can be seen, the two dielectric objects are reconstructed with quite good accuracy, both in terms of shape and dielectric permittivity. Moreover, the metallic inclusion is clearly identifiable in the conductivity map.

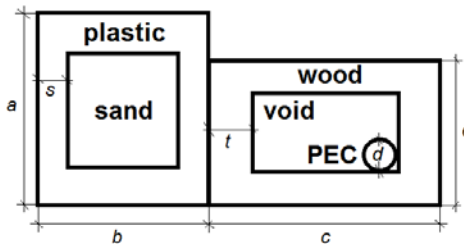


FIG. 1 – Cross section of the inspected target. Wood beam (11.5 cm × 7.5 cm) with a rectangular hole (5.5 cm × 3.5 cm); plastic box (11 cm × 9 cm) with a rectangular hole filled with sand (5.3 cm × 3.0 cm); circular metallic inclusion (11 mm in diameter).

IV. CONCLUSIONS

Experimental results concerning the detection of metallic bodies inside dielectric structures have been reported. They show the capability of microwave imaging to provide positions and shapes of inclusions with a rather good accuracy. Consequently, microwaves can be usefully considered in developing inverse-scattering based apparatuses for nondestructive testing and evaluation in industrial applications.

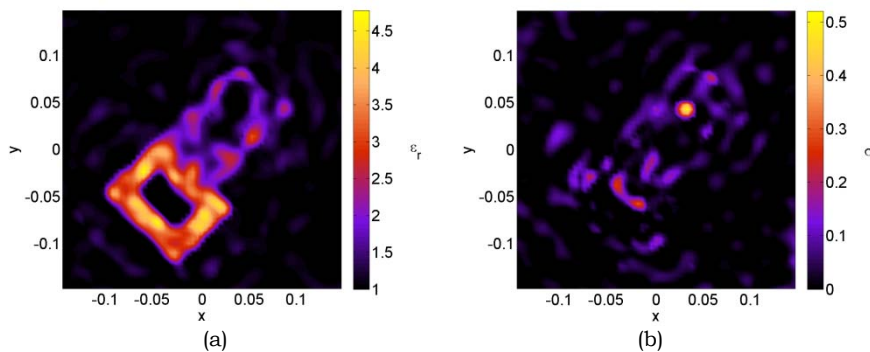


FIG. 2 – Distributions of the reconstructed (a) relative dielectric permittivity and (b) electric conductivity [S/m].

REFERENCES

- [1] V. Bacur, *Nondestructive Characterization and Imaging of Wood*. Springer, Berlin, 2003.
- [2] A. Salvadè, et al., “Tomografia a microonde in una applicazione di diagnostica non-invasiva nell'industria del legno”, *Atti XVI Riunione Nazionale di Elettromagnetismo (XVI RiNEM)*, pp. 400-403, Genova, 18-21 Sett. 2006.
- [3] - “A new microwave axial tomograph for the inspection of dielectric materials,” *IEEE Transactions on Instrumentation and Measurement*, vol. 58, pp. 2072-2079, 2009.
- [4] C. Estatico, G. Bozza, A. Massa, M. Pastorino, A. Randazzo, “A two-step iterative Inexact-Newton method for electromagnetic imaging of dielectric structures from real data,” *Inverse Problems*, vol. 21, no. 6, pp. S81-S94, Dec. 2005.
- [5] C. Estatico, G. Bozza, M. Pastorino, A. Randazzo, “An Inexact-Newton method for microwave reconstruction of strong scatterers,” *IEEE Antennas and Wireless Propagation Letters*, vol. 5, pp. 61-64, 2006.
- [6] M. Pastorino, *Microwave Imaging*. Hoboken, NJ: John Wiley & Sons, 2010.
- [7] G. Bellizzi, O. M. Bucci, I. Catapano, “Microwave cancer imaging exploiting magnetic nanoparticles as contrast agent,” *IEEE Transactions on Biomedical Engineering*, vol. 58, pp. 2528-2536, 2011.
- [8] G. Oliveri, L. Lizzi, M. Pastorino, and A. Massa, “A nested multi-scaling Inexact-Newton iterative approach for microwave imaging,” *IEEE Transactions on Antennas and Propagation*, vol. 60, no. 2, pp. 971-983, Feb. 2012.
- [9] L. Crocco, I. Catapano, L. Di Donato, T. Isernia, “The linear sampling method as a way to quantitative inverse scattering,” *IEEE Transactions on Antennas and Propagation*, 2012, in press.
- [10] K. Belkebir, R. E. Kleinman, and C. Pichot, “Microwave imaging-Location and shape reconstruction from multifrequency scattering data,” *IEEE Transactions on Microwave Theory and Techniques*, vol. 45, no. 4, pp. 469-476, Apr. 1997.
- [11] L. Zhang, J. Stiens, A. Elhawil, and R. Vounckx, “Multispectral illumination and image processing techniques for active millimeter-wave concealed object detection,” *Applied Optics*, vol. 47, no. 34, p. 6357, Nov. 2008.

Session 9 – Antenna arrays

G. A. Casula, P. Maxia, G. Montisci, and G. Mazzarella
Design of printed UWB log-periodic dipole arrays

S. Mosca, and L. Infante
Tangram shaped subarrays for multiple beam array

A. F. Morabito, and A. R. Laganà
A size-tapered architecture for high performances isophoric direct radiating arrays

F. Venneri, S. Costanzo, G. Di Massa, E. Marozzo, A. Borgia, and M. Salzano
Implementation of a full-range varactor tuned element for the design of a reconfigurable reflectarray

G. Buttazzoni, and R. Vescovo
Co-polar and cross-polar pattern synthesis for reconfigurable antenna arrays

E.D. Di Claudio, G. Jacovitti, A. Laurenti
Hermite and Laguerre beamspaces for Ultra Wide Band antenna array processing

DESIGN OF PRINTED UWB LOG-PERIODIC DIPOLE ARRAYS

G. A. Casula⁽¹⁾, P. Maxia⁽¹⁾, G. Montisci⁽¹⁾ and G. Mazzarella⁽¹⁾

⁽¹⁾ Dip. Ingegneria Elettrica ed Elettronica, Univ. di Cagliari,
Piazza d'Armi, 09123, Cagliari, Italy
paolo.maxia@diee.unica.it

Abstract

A wideband microstrip log periodic array operating between 4 and 18 GHz (thus working in C,X and Ku bands) has been designed. The proposed solution is remarkably simple and shows both SWR and gain better than likely structures present in the literature. The same antenna can also be used as an UWB antenna. The design has been developed using a general purpose and specialist tool for the 3D electromagnetic simulation of microwave high frequency components.

Index Terms – UWB antennas, Printed Log-Periodic dipole arrays.

I. INTRODUCTION

Log-periodic dipole arrays (LPDA) using cylindrical dipoles are well-known since the 50's, and their design rules are based on the works of Isbel and Carrell [1-3]. LPDA have a reasonable gain with a very large bandwidth (up to a decade) and therefore the LP concept has been used with different implementations. Among them, printed LP arrays are very promising since their low cost and weight, and a number of different realizations has been reported in the literature [4-10].

This work describes a simple implementation of LP printed arrays with a 4.5:1 bandwidth, and shows very good performances, not only as a standard LP antenna, but also as an UWB antenna. Actually, in the range 6-11 GHz, its gain and phase-center are remarkably constant with the frequency.

The design has been done using CST MICROWAVE STUDIO 2010, a general purpose software for the 3D electromagnetic simulation of microwave components.

II. LPDA DESIGN

The array structure is based on a two-wire printed transmission line on the two sides of a dielectric slab, where the array dipoles are connected, in an alternate way, on the two printed lines in a structure very similar to a standard (i.e., wire) LPDA. As a consequence, the design rules for wire LPDAs [1] can be used, with some suitable modifications.

Starting from the required bandwidth, 4-18 GHz, we get $N=14$ dipole elements, $2\alpha=30^\circ$ and $\tau=0.85$ for a directivity of 7.5 dBi.

The width of the metallization of the feeding lines has been calculated requiring a characteristic impedance of 50Ω , and considering a substrate with [10] a dielectric constant $\epsilon_r=2.54$ and a thickness of 0.51 mm. Since the feed line (Fig.1) has an anti-symmetric field configuration, we can insert a ground plane in the middle (Fig.1b), and design a 25Ω standard microstrip (with $h/2$ slab length) by evaluating its W assuming a quasi-static propagation.

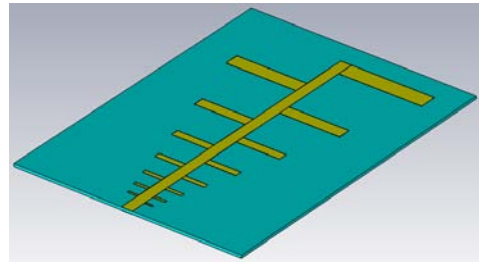
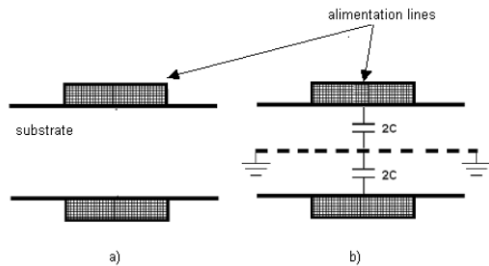


FIG. 1 – Section of the antenna feeding line.

FIG. 2 – 3D Antenna Layout

The length of the longest dipole is equal to half-wavelength at 4 GHz, while the length of the other dipoles can be obtained following (1):

$$\frac{l_{n+1}}{l_n} = \frac{1}{\tau} \quad (1)$$

where l_n is computed starting from the dielectric wavelength $\lambda_r = \lambda_0 / \sqrt{\epsilon_{\text{eff}}}$, since the antenna lies on a dielectric substrate. The effective dielectric constant on the feed line, ϵ_{eff} , is used to take into account the typical microstrip side-effects, due to the field overflow beyond the physical dimensions of the structure.

Since the effective dielectric constant on the feed line, ϵ_{eff} , is frequency dependent, the design has been made using ϵ_{eff} at the center of the band, i.e., 11 GHz. The resulting value $\epsilon_{\text{eff}} = 2.25$ is used to scale the whole geometry.

Finally, the dipole width W_d has been chosen from [10] to give a 50Ω equivalent impedance. Starting from the Carrell expression for cylindrical dipoles [3], we can compute the diameter for each dipole [10], which is then transformed to W by the requirement of equal perimeter $2\pi \cdot a = 2W$.

III. RESULTS

The antenna layout is shown in Fig.2. The direct use of Carrell equations leads to a design with an unacceptable performance at the lower end of the band, mainly in the SWR, which cannot be corrected with a circuitual remedy. Therefore we added a further dipole at the lower end of the band to cover the whole frequency range, getting a

return loss smaller than -10 dB (Fig.3). This solution results in a small size increase (around 20%).

The average directivity (Fig.4) is larger than the specified one, dropping below its value only at the edges of the frequency band.

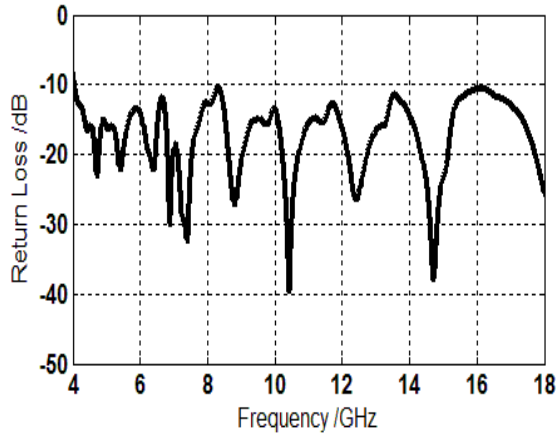


FIG. 3 – Reflection coefficient

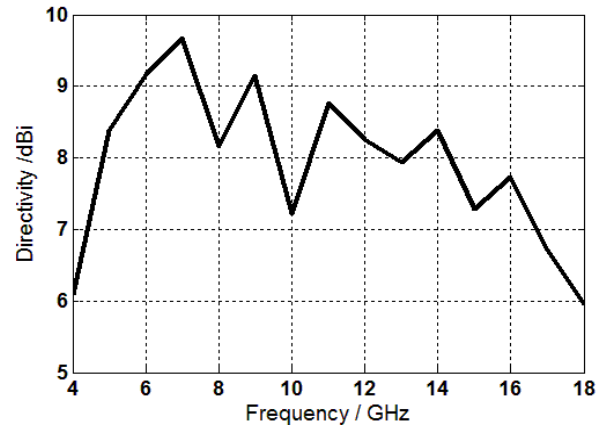


FIG. 4 – Average directivity

In the Table 1 we report also the position of the phase center of the antenna. In the central part of the frequency band (6-11 GHz) its variation is less than 20% of the free space wavelength (computed at the center frequency of 8.5 GHz). Therefore the proposed antenna can be used as an UWB antenna.

In Fig.5 the radiation patterns are shown at various frequencies. The main lobe is essentially the same at all frequencies, with a -3 dB beamwidth around 50° .

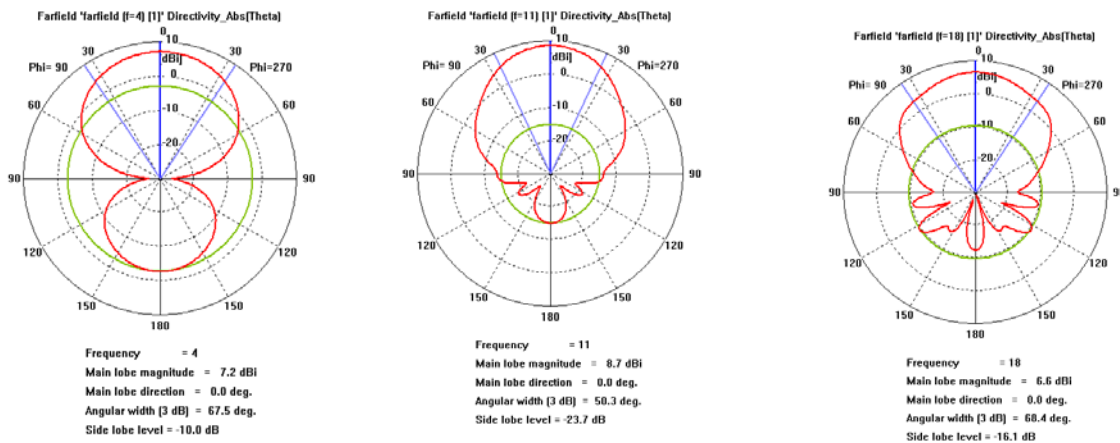


FIG. 5 – Radiated electric field at 4, 11 and 18 GHz.

Frequency/Ghz	X[mm]	Y[mm]	Z[mm]
6	0.80	0	-30.27
7	0.33	0	-37.39
8	0.25	0	-29.01
9	0.45	0	-34.15
10	0.30	0	-24.64
11	0.53	0	-37.31

Table 1 – Phase Center Position at 6-11 Ghz. [mm]

IV. CONCLUSION

A wideband microstrip printed Log-Periodic dipole array operating in a frequency band from 4 to 18 GHz has been designed using CST Microwave Studio. The proposed solution is remarkably simple and shows both SWR and gain better than likely structures present in the literature. It has a quite reduced size and very good performances if used as a UWB antenna (in the range 6-11 GHz).

ACKNOWLEDGEMENT

Paolo Maxia gratefully acknowledges Sardinia Regional Government for the financial support of her PhD scholarship (P.O.R. Sardegna F.S.E. Operational Programme of the Autonomous Region of Sardinia, European Social Fund 2007-2013 - Axis IV Human Resources, Objective 1.3, Line of Activity 1.3.1.)

REFERENCES

- [1] R.Carrel, "The Design Of Log-Periodic Dipole Antennas", IRE International Convention Record, March 1961, Vol.9, pp.61-75.
- [2] D.E.Isbell, "Log Peridic Dipole Arrays", IRE Transaction On Antennas and Propagation, vol. AP-8, pp. 260-267, may 1960.
- [3] R.Carrel, "Analysis and Design of the Log-Periodic Dipole Antenna", Ph.D. Dissertation, University of Illinois, 1961.
- [4] C.Donn, J.Lew, J.P.Scherer, "Microstrip Log-Periodic Dipole Array", Antennas and Propagation Society International Symposium, vol.23, 1986, pp. 709-712.
- [5] S.H. Kim, J.H. Choi, J.W. Baik and Y.S. Kim, "CPW-fed log-periodic dumb-bell slot antenna array", Electronics Letters, April 2006, vol. 42, n° 8.
- [6] A.A Gheethan, D.E. Anagnostou, "The design of reconfigurable Planar Log-periodic Dipole Array using switching elements", IEEE Antennas and propagation society International Symposium, June 2009, pp 1-4.
- [7] A.A Gheethan, D.E. Anagnostou, "Reduced Size Planar Log-Periodic Dipole Arrays using rectangular meander line elements", IEEE Antennas and propagation society International Symposium, July 2008, pp 1-4.
- [8] D.E. Anagnostou, J.Papaplymerou, C.Christodoulou, M.Tentzeris, "A Small Planar Log-Periodic Koch Dipole Antenna (LPKDA)", IEEE Antennas and propagation society International Symposium, July 2006, pp 3685-3688.
- [9] R.Kakkar, G.Kumar, "Stagger tuned microstrip log-periodic antenna", Antennas and Propagation Society International Symposium, July 2006, vol. 2, pp. 1262-1265.
- [10] C.K.Campbell, I.Traboulay, M.S. Suthers, H.Kneve, "Design Of A Stripline Log-Periodic Dipole Antenna", IEEE Transaction Antennas Propagation, vol. AP-25, September 1977, pp.718-721.

TANGRAM SHAPED SUBARRAYS FOR MULTIPLE BEAM ARRAY

S. Mosca, L. Infante

Antenna Department, SELEX Sistemi Integrati
Via Tiburtina, km. 12400, 00131, Rome, Italy
stmosca@selex-si.com, linfante@selex-si.com

Abstract

In phased array antennas which provide multiple beams using digital beamforming (DBF), the choice of the subarray shape is crucial. In this paper the shape of the subarrays is chosen according to an old Chinese puzzle game called Tangram. The choice of this shaping provides lower sidelobes with respect to square subarrays on offset beams obtained by means of DBF.

Index Terms—Digital Beamforming, Subarray shaping, Multiple beam antenna.

I. INTRODUCTION

Multiple beam phased array radars have higher performance with respect to single-beam phased array radars, in terms of refresh rate, etc. Several strategies can be used to design the phased array architecture to obtain multiple beams in reception using digital beam forming (DBF). Ideally a digital receiver per antenna element would allow to obtain a huge number of simultaneous receive beams, but this solution is not cost effective. In order to obtain a compromise among cost and performance, the elements are arranged into subarrays, each connected to a digital receiver. The choice of the size and shape of the subarray has been investigated by many authors according to different performance parameters [1]-[3]. The focus of the present paper is that of investigating a particular subarray shaping with the aim of obtaining multiple simultaneous beams (within a narrow angular region around the scanning direction) with low sidelobe level.

Section II describes the motivation and strategy of subarray shaping, section III describes the performance of such shaping by making some examples and section IV contains the conclusions.

II. SUBARRAY SHAPING

Throughout the paper it is assumed that the phased array architecture is that described by the block diagram shown in Fig. 1. If the antenna elements are phased (by proper phase settings on the phase shifters) in order to steer the beam to a nominal direction, other simultaneous beams (called offset beams) that are slightly steered away from the nominal direction can also be obtained.

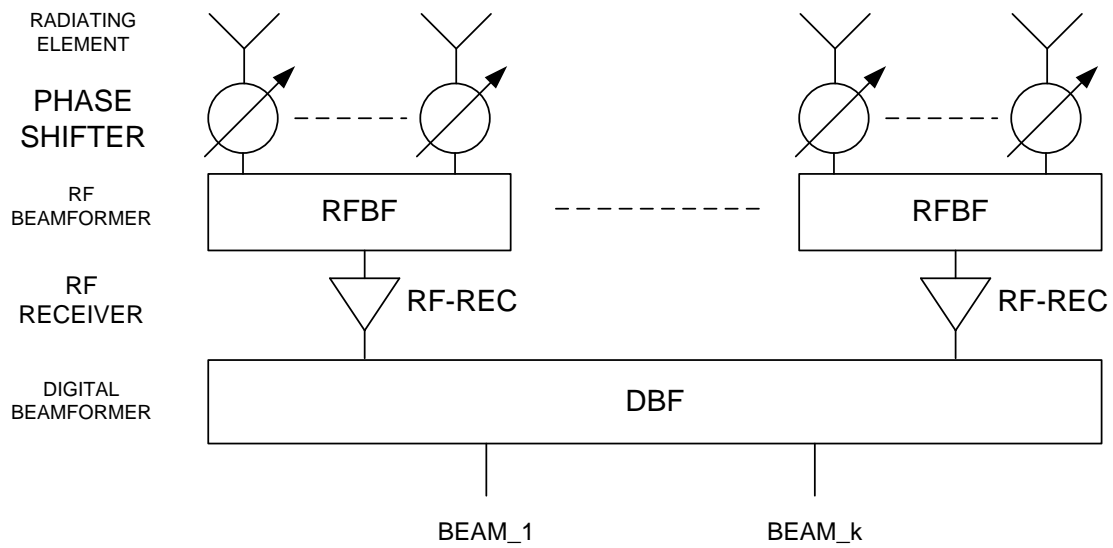


FIG. 1–Phased array block diagram.

Referring to Fig. 1 such beams can be obtained digitally by simply applying different phases to the DBF coefficients. The question is now how to divide the array into subarrays in order to get the best performance from the offset beams in term of sidelobes. The easiest way is to divide it in equally sized rectangular subarrays, taking into account that the sidelobe level of the offset beams gets worse as the size of the subarrays increases because of phase quantization. This happens because the phase centers are equally spaced on a rectangular lattice. In order to increase the sidelobe level, phase quantization must be reduced, and this can be obtained by making the phase centers of the subarray as random as possible. Many strategies have been developed by several authors to randomize the subarrays [1]-[3]. In the present paper the phase randomization is obtained by dividing the array in squares, each of which is divided according to the tangram puzzle. Tangram puzzle is an ancient Chinese puzzle where several shapes have to be arranged in order to obtain a square, or many other fancy shapes. The one that inspired this paper is the rectangle, which is obtained by joining two squares (see Fig. 2).

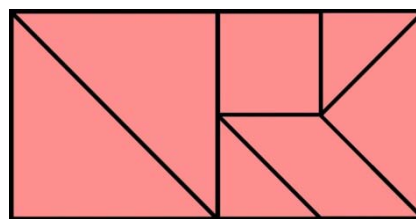


FIG. 2–Tangram subarrays.

In Fig.2, the right square is composed of five shapes, if each shape is associated to a subarray this can be used as the building block to construct an array of subarrays. In such an array the subarrays have their corresponding phase center not on a regular lattice (see for

example Fig. 3). The array is then composed of the necessary tangram squares. Each of the tangram squares which composes the array can be randomly rotated or mirrored in order to increase the randomness of the position of the phase centers.

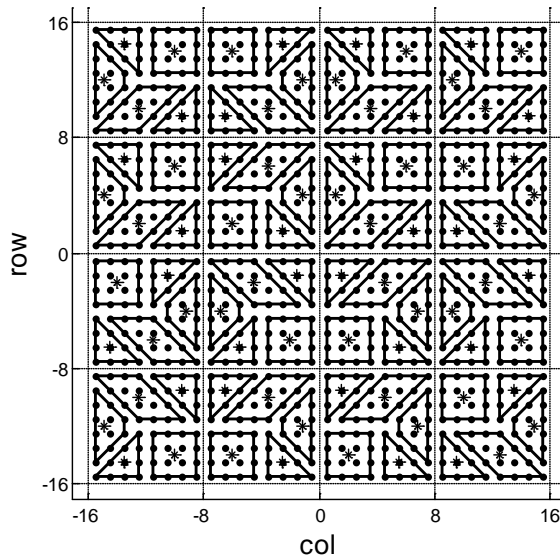


FIG. 3–Tangram subarrays. Dot (.) shows element position, star (*) indicates phase center of the subarrays.

III. NUMERICAL RESULTS

In order to verify the performance improvement of the tangram shaped subarrays with respect to the square ones, two examples are reported. Each configuration is compared according to the peak and RMS sidelobe level when an offset beam is scanned at an angle equal to one half-power beam-width (HPBW) from the nominal beam direction. The array is assumed to have a -30 dB sidelobe Taylor taper. The phase of each subarray to perform beam-steering by mean of DBF phases is computed according to the position of its phase center.

Assuming a square tile of 8 by 8 elements spaced by half wavelength, this is divided in 5 subarrays according to the tangram shaped patterns inspired by the right square of Fig. 2. An array, labeled TANG4 (see Fig. 3), of 4 by 4 tiles, thus made of 80 subarrays is simulated, and the performance in terms of sidelobes when scanned at one HPBW are reported in Table I. To compare the previous configuration with one with the same number of subarrays, but with square shape, an array of 9 by 9 square subarrays (each made of 4 by 4 elements), labeled SQUARE9, is simulated. The performances of such configuration are reported also in Table I. For further comparison an array of 5 by 5 tangram tiles (each tile is made of 8 by 8 elements divided in 5 subarrays according to tangram shapes), labeled TANG5, is compared

with respect to an array of 11 by 11 square tiles (each made of 4 by 4 elements), the performances of such configurations are also reported in Table I for comparison.

TABLE I – PERFORMANCE COMPARISON OF SIDELOBE LEVELS (SLL)

Configuration	Number of subarrays	SLL [dB]	SLL RMS [dB]
TANG4	80	-20.2	-29.3
SQUARE9	81	-16.0	-27.2
TANG5	125	-22.1	-31.9
SQUARE11	121	-18.0	-29.7

From Table I it can be noticed that maintaining approximately constant the number of subarrays (it is not possible to make a square array with tangram shaped subarrays have exactly the same number of subarrays as an array of square shaped subarrays), the array made with tangram shaped subarrays has lower sidelobes (when scanned at one HPBW from boresight) than the one made with square sidelobes. In detail, TANG4 configuration has sidelobes 4 dB lower than SQUARE9 configuration, and also TANG5 configuration has sidelobes 4 dB lower than SQUARE11 configuration.

IV. CONCLUSION

This paper introduced a new subarray shaping strategy inspired by the tangram puzzle. It has been shown that, in multiple beam arrays with DBF, the offset beams obtained by only setting the phase of the subarrays (without changing the phase of the phase shifters), have lower sidelobes for tangram shaped subarrays than square shaped subarrays.

REFERENCES

- [1] Bailey, C.D., Aalfs, D.D., "Design of digital beamforming subarrays for a multifunction radar," Radar Conference - Surveillance for a Safer World, 2009. RADAR. International , pp.1-6, 12-16 Oct. 2009
- [2] Hu Hang, Qin Weicheng, "Research on Subarray Partitioning of Planar Phased Array with Adaptive Digital Beamforming," Microwave, Antenna, Propagation and EMC Technologies for Wireless Communications, 2007 International Symposium on , pp.691-694, 16-17 Aug. 2007
- [3] Darren Ansell, Evan J. Hughes, "Use of Muti-Objective Genetic Algorithms to Optimise the Excitation and Subarray Division of Mutifunction Radar Antennas," Proc. IEE colloquium, England, 2001, pp.8/1-8/4

A SIZE-TAPERED ARCHITECTURE FOR HIGH-PERFORMANCE ISOPHORIC DIRECT RADIATING ARRAYS

A. F. Morabito, A. R. Laganà

LEMMA Research Group, DIMET Department, Università Mediterranea di Reggio Calabria, Via Graziella, Loc. Feo di Vito, I-89124 Reggio Calabria, Italy
{andrea.morabito, antonia.lagana}@unirc.it

Abstract

We propose a new architecture for high-gain isophoric arrays. The solution is able, by exploiting the feeds size as unique degree of freedom of the antenna design problem, to perfectly emulate the behaviour of given continuous aperture sources. Uniformly-excited arrays fulfilling by a wide margin the requirements recently established by the European Spatial Agency for the multibeam coverage of Europe are designed in a fast and deterministic fashion.

Index Terms – Power Synthesis, Isophoric Antennas, Direct Radiating Arrays.

I. INTRODUCTION AND MOTIVATIONS

Usual degrees of freedom in array synthesis are either the excitations of a fixed-geometry structure [1], or the locations and phase excitations of the fixed-amplitude radiating elements [2]-[7], or even both of them [8],[9]. In particular, the second of these problems is of interest in the design of Direct Radiating Arrays (DRA) for communications from satellites [2]-[7].

In fact, arrays easily lend themselves to multibeam and reconfigurability applications, and allows to exploit in an optimal fashion the available power by requiring that all the (identical) amplifiers work under the same optimal conditions, thus resulting in equi-amplitude entry points (leading to the so-called ‘isophoric’ arrays) [2]-[7].

As a matter of fact, such a circumstance, together with the need to keep the number of amplifiers (and antennas) as low as possible, has stimulated research activities aimed at the optimal synthesis of sparse arrays [3], thinned arrays [5], and clustered [4] arrays.

In all these cases, the quest for very low sidelobes can be fulfilled by emulating, through the array structure, an appropriate amplitude tapering on the antenna aperture [1]-[9]. For example, ‘density taper’ procedures can be applied for the synthesis of sparse arrays [3].

On the other side, each of these architectures has its own drawbacks. By leaving aside (because of the available space) the case of clustered arrays, it has to be noted that in both cases of thinned and sparse arrays the quest for low sidelobes leaves empty a large portion of the aperture plane, thus resulting in a reduction of the antenna gain with respect to the theoretical limitations [6],[7]. As the gain is of the utmost importance in satellite applications, such a circumstance led

researchers of LEMMA, in connection with close co-workers, to develop first in [7] and then in [6] the chance to exploit two different kinds of radiating elements (see Fig. 1.b) in an otherwise sparse array architecture (see Fig. 1.a). In fact, exploitation of two kinds of ‘aperture-like’ elements allows both a better filling of the available aperture, and a better emulation of (tapered) reference sources. Notably, for the same ‘filling’ reasons, the exploitation of square (rather than circular) elements was also suggested in [7].

In this communication, we further elaborate the basic concept introduced in [7] in order to develop and optimize a ‘size-tapered’ architecture for high-gain isophoric DRA.

Interestingly, an apparently similar concept had been introduced in [9] (see Fig. 1.c). In such a case, however, complex excitations are also used as degrees of freedom, and the elements dimensions are fixed in advance rather than being synthesized in some optimal fashion. As a consequence, contents of [9] are indeed very different from what follows. In fact, the proposed architecture exploits as degrees of the freedom of the synthesis problem only the elements dimensions, which are determined by the procedure described in the following Section.

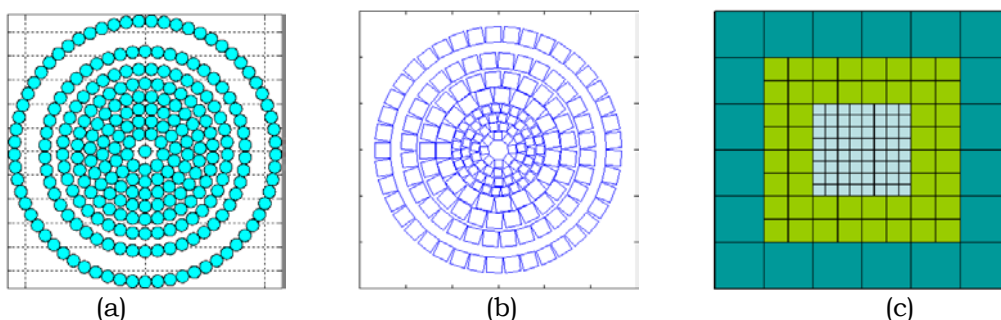


FIG. 1 – Different DRA architectures: density tapering (a) [2],[3]; density and element-size tapering (b) [6]; excitations and element-size tapering (c) [9].

II. THE SYNTHESIS PROCEDURE

The proposed approach assumes that the single array elements are aperture antennas, and hence that feeds carrying the same overall power but having different dimensions produce, on their aperture, different field levels. Consequently, a smart positioning of elements having a different size can allow to optimally fill the space at disposal and, at the same time, to realize the desired tapering on the overall array aperture. By taking into account all the concepts above, the following four-steps strategy has been devised:

1. choose the area A of the smallest DRA element to be employed;
2. synthesize a continuous source fulfilling at best the radiation requirements and having a quantized amplitude (see Fig. 2.a). The number of source levels will be equal to the number of feed’s sizes to be employed;

3. identify the area of each DRA element in such a way to perfectly emulate, in each portion of the aperture, the continuous source coming out from step 2. In particular, feeds of area $Q^2 \cdot A$ are placed in those regions where the aperture field's normalized amplitude is equal to $1/Q$. Note that feeds should emulate uniform-amplitude apertures, i.e., they should have an aperture efficiency as large as possible;
4. establish the elements locations and geometrical shapes such to 'completely' fill the aperture by just employing feeds having the areas identified in step 3.

III. APPLICATION TO THE DESIGN OF SATELLITE MULTIBEAM ANTENNAS

In order to test the devised procedure in an application of actual interest, we used it to solve the synthesis problem defined in [2], i.e., the design of an isophoric DRA for the multibeam coverage of the Europe from geostationary satellites (see [2]-[7] for a detailed description of the technical requirements). The achieved circular-ring DRA layout, fulfilling all the imposed constraints and being composed by 246 isophoric square feeds of areas 16, 25 and 64 λ^2 , being λ the wavelength in free space, is depicted in Fig. 2.a. The corresponding directivity is shown in Fig. 2.b.

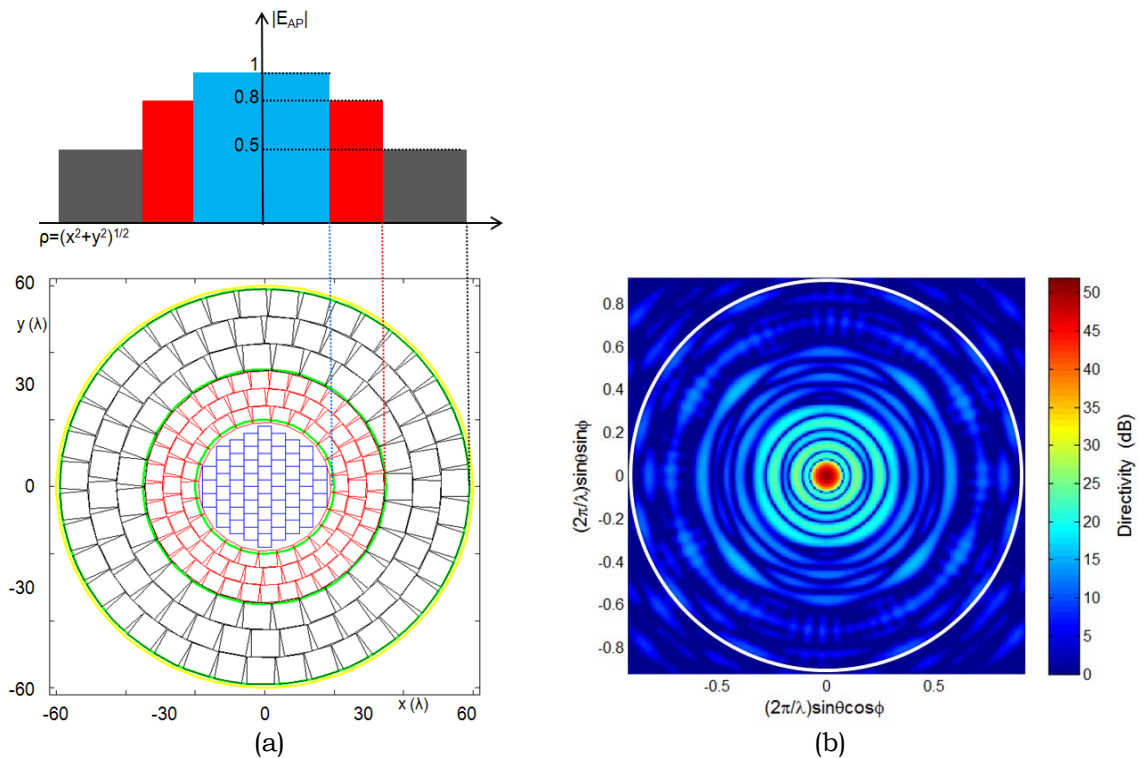


FIG. 2 – Synthesis approach: (a) reference source distribution and corresponding DRA layout; (b) achieved directivity (θ and ϕ respectively denoting the elevation and azimuthal observation angles).

Notably, the proposed architecture resulted able to achieve a directivity behavior very close to the ultimate feasible performance of the reference continuous source. The relevance of the achieved result can be proved also by comparing it with the performance achieved by a DRA proposed by [6] (in which not only the elements size but also the elements location is exploited as a degree of freedom of the synthesis problem) and composed by a 12-units lower number of elements. In fact, while the DRA in [6] achieves a slightly better performance in terms of peak sidelobe level, the present solution provides better results in terms of minimum directivity guaranteed inside a spot of width 0.65° . In particular, at the edge of a generic spot, the array shown in Fig. 2.a achieves a directivity equal to 46.2 dBi, which is 1 dB larger than the one provided by the DRA in [6]. Also, by evaluating the same directivity at a scanning angle of 1.12° , the result achieved by the DRA of Fig. 2.a, i.e., 45.8 dBi, turns out to be 0.8 dB larger than the one provided in [6]. Finally, the proposed solution allows to safely scan the beam, by still fulfilling all requirements on sidelobes, up to 1.68° . Such a circumstance allows to get a multibeam antenna realizing 37 different beams (as opposite to the 19 beams of [6]).

REFERENCES

- [1] T. Isernia, P. Di Iorio, and F. Soldovieri, "An effective approach for the optimal focusing of array fields subject to arbitrary upper bounds," *IEEE Trans. on Antennas and Propagation*, vol. 48 (12), pp. 1837-1847, 2000.
- [2] ESA ITT AO/1-5598/08/NL/ST, "Innovative architectures for reducing the number of controls of multiple beam telecommunications antennas".
- [3] O. M. Bucci, M. D'Urso, T. Isernia, P. Angeletti, and G. Toso, "Deterministic synthesis of uniform amplitude sparse arrays via new density taper techniques," *IEEE Transactions on Antennas and Propagation*, vol. 58 (6), pp. 1949-1958, 2010.
- [4] A. F. Morabito, T. Isernia, M. G. Labate, M. D'Urso, and O. M. Bucci, "Direct radiating arrays for satellite communications via aperiodic tilings," *Prog. In Electromagnetics Research*, vol. 93, pp. 107-124, 2009.
- [5] O. M. Bucci, T. Isernia, and A. F. Morabito, "A deterministic approach to the synthesis of pencil beams through planar thinned arrays," *Progress In Electromagnetics Research*, vol. 101, pp. 217-230, 2010.
- [6] O. M. Bucci, T. Isernia, A. F. Morabito, S. Perna, and D. Pinchera, "Density and element-size tapering for the design of sparse arrays with a reduced number of control points and high efficiency," *Proceedings of the Fourth European Conference on Antennas and Propagation*, 2010.
- [7] T. Isernia and M. D'Urso, "Improving sparse arrays performance by exploiting two kinds of square feeds," *DIMET Dept. Internal Report*, 2008.
- [8] D. Caratelli and M. C. Viganò, "A novel deterministic synthesis technique for constrained sparse array design problem," *IEEE Transactions on Antennas and Propagation*, vol. 59 (11), pp. 4085-4093, 2011.
- [9] A. K. Bhattacharyya, "Projection matrix method for shaped beam synthesis in phased arrays and reflectors," *IEEE Transactions on Antennas and Propagation*, vol. 55 (3), pp. 675-683, 2007.

IMPLEMENTATION OF A FULL-RANGE VARACTOR TUNED ELEMENT FOR THE DESIGN OF A RECONFIGURABLE REFLECTARRAY

F. Venneri, S. Costanzo, G. Di Massa, E. Marozzo, A. Borgia, M. Salzano

DEIS – University of Calabria
Via P. Bucci, 87036 Rende (CS), Italy
costanzo@deis.unical.it

Abstract

The implementation of a tunable reflectarray element based on the use of an aperture-coupled patch is presented. A full phase tuning range is achieved with a single varactor diode and proved by simulations and measurements. A 3x15 X-band reflectarray is fabricated and tested to demonstrate the beam-scanning capabilities of the proposed configuration.

Index Terms– Reconfigurable antennas, reflectarrays.

I. INTRODUCTION

Microstrip reflectarrays offer a valid solution for those applications requiring a certain degree of flexibility in the reconfiguration of the antenna radiation pattern. They consist of a low-profile reflector composed by an array of microstrip elements, which can be realized at low cost with a relative simple fabrication process. These features make reflectarrays very competitive with respect of traditional parabolic reflectors. Furthermore, by properly integrating the array elements with well suited tunable components, microstrip reflectarrays acquire also the ability to scan the radiation main beam or to reconfigure the radiation pattern shape. In such case, they could offer a good alternative to traditional phased arrays, as eliminating the need for complex beam-forming networks. Different reconfigurable reflectarray elements have been presented in literature, each one based on the use of tunable components or materials, such as MEMS switches, PIN/varactor diodes and liquid crystal substrates [1-4]. In this paper, a tunable reflectarray element based on the use of an aperture-coupled patch, integrated with a single varactor diode is considered [5]. The proposed element is successfully adopted for the design of an X-band reflectarray prototype composed by 3x15 radiating elements. The experimental validations, performed on the fabricated antenna, show the effectiveness of the proposed tunable reflectarray configuration.

II. DESIGN OF SINGLE TUNABLE REFLECTARRAY ELEMENT

The adopted reflectarray element consists of a rectangular patch slot-coupled to a varactor-tuned microstrip line (Fig. 1). By electrically changing the capacitance associated to the diode, a continuous

variation is introduced in the phase of the field reflected by the element. Usually, the phase shift introduced by a single diode varies within a limited 180° range, due to the capacitive nature of the diode reactance. However, the proposed antenna can be properly optimized in order to obtain a full variation of the reflection phase. As a matter of fact, the line length L_s+L_v (see Fig. 1) can be chosen with the purpose of introducing a proper inductive effect in the varactor-based tuning circuit, so improving the element phase agility. Besides the opportunity to obtain a full phase tuning range, the proposed configuration offers a uniform reflecting surface, due to the fact that the varactor diodes and the biasing circuitries are located below the ground plane. As a further advantage, the aperture-coupled reflectarray configuration provides also the possibility to improve its operating bandwidth [6].

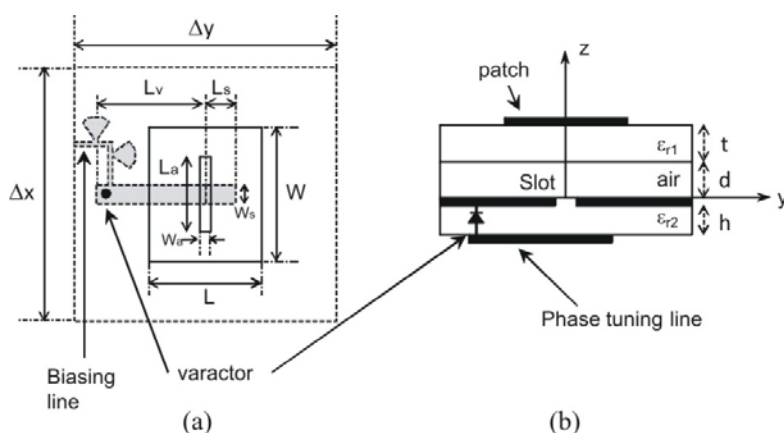


FIG. 1 – Single element geometry: (a) top view; (b) side view.

The proposed configuration is adopted to design a reflectarray cell operating at a frequency equal to 11.5 GHz. The antenna substrate is composed by a first layer of Diclاد870 ($\epsilon_r=2.33$) and a second one of air, having thickness $t=d=0.762$ mm (Fig. 1). The microstrip line is printed on a single layer of Diclاد870 with $h=0.762$ mm. The cell size is fixed to a value equal to $\Delta x=\Delta y=0.7\lambda_0$ at the operating frequency. A varactor is inserted between the ground plane and the microstrip line. The adopted diode (Microsemi MV31011-89) is characterized by a tunable reverse voltage varying from 0 V to 20 V which gives a variable capacitance ranging from 2 pF to 0.2 pF. The synthesized antenna dimensions are given as: $W=9.3$ mm, $L=8.2$ mm, $W_a=0.6$ mm, $L_a=5.8$ mm, $W_s=3.07$ mm, $L_v=6.5$ mm. The length of the stub L_s is chosen in order to maximize the phase agility of the element. As it can be observed in Fig. 2(a), this goal is achieved for a value of L_s equal to 7.8 mm. In Fig. 2(b) it is also evident that reflection losses increase by enhancing the phase tuning range of the element. This effect must be taken into account in order to obtain a good compromise between the phase agility and the efficiency of each reflectarray radiator. Anyway, a diode with a lower series resistance could reduce the amount of reflection losses. The proposed element is validated by performing the measurement of the

phase curves vs varactor reverse voltage for different frequencies (Fig. 3(a)). A good agreement between simulated and measured reflection phase curves can be observed in Fig. 3(b).

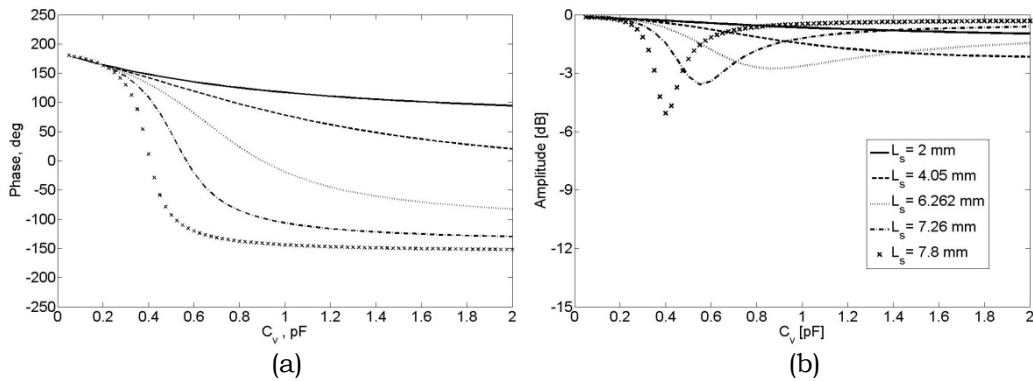


FIG. 2 – Simulated reflection coefficient vs varactor capacitance for different stub length: (a) phase; (b) amplitude.

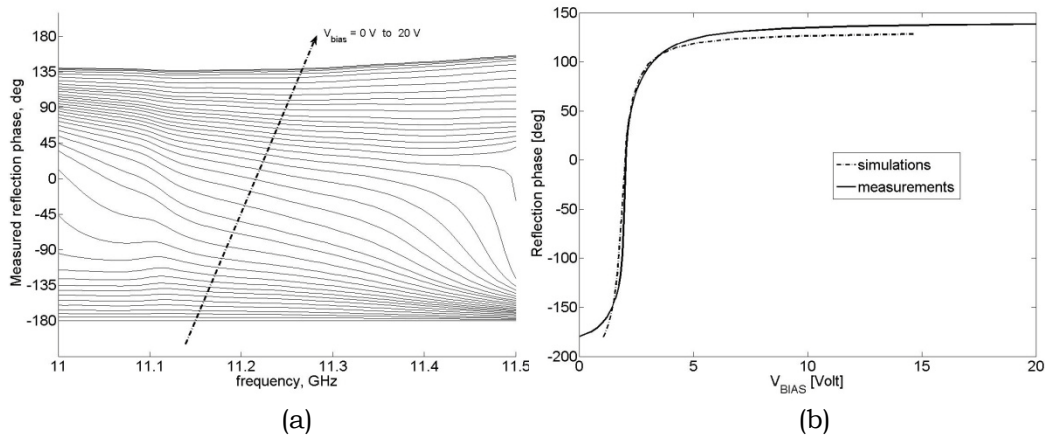


FIG. 3 – (a) Measured reflection coefficients vs frequency for different values of the bias voltage; (b) Comparison between measured and simulated reflection phase at the frequency $f = 11.25$ GHz.

III. DESIGN AND TEST OF RECONFIGURABLE REFLECTARRAY PROTOTYPE

A 3x15 reflectarray prototype is designed in order to prove the effectiveness of the proposed reconfigurable element. The array is illuminated by an X-band horn with an offset angle of 15° . The elements are controlled by a properly designed DACs-board, which imposes the desired bias voltages across the varactors. The fabricated antenna (Fig. 4(a)) is tested into the anechoic chamber of Microwave Laboratory at University of Calabria, by performing the radiation pattern measurements for different configurations of the bias voltages distributions. In particular, the varactor voltages are computed in order to scan the main beam θ_{mb} in the x-z plane (Fig. 4), from -20° to 20° with an angular step equal to 10° . As it can be observed in Fig. 4(b), the measured patterns confirm the validity of the implemented reconfigurable reflectarray.

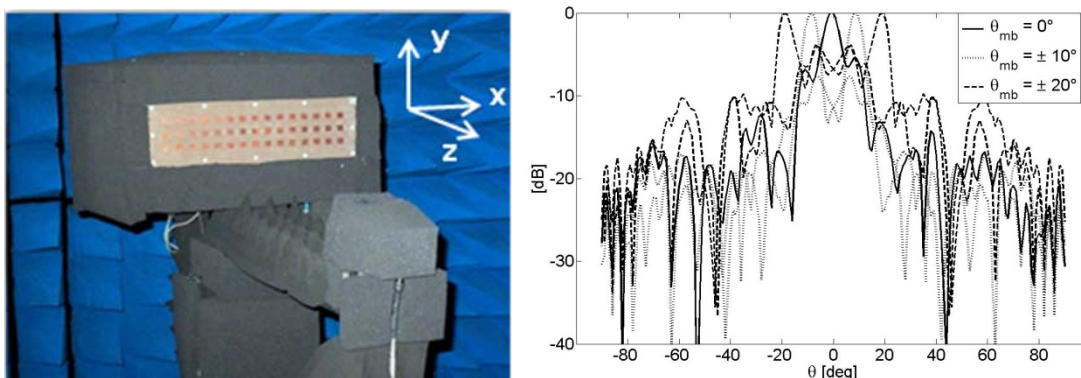


FIG. 4 – (a) Photograph of the reflectarray prototype into the anechoic chamber; (b) Measured radiation patterns for different biasing voltage distributions.

IV. CONCLUSION

A tunable reflectarray element based on the use of a single varactor diode has been presented. The proposed configuration has been successfully adopted for the implementation of a demonstrative reflectarray prototype. The experimental tests performed on the fabricated antenna have demonstrated the beam-scanning capabilities of the proposed reconfigurable element.

REFERENCES

- [1] S. V. Hum, M. Okoniewski, R. J. Davies, “Realizing an electronically tunable reflectarray using varactor diode-tuned elements”, *IEEE Microwave and wireless components letters*, vol. 15, no. 6, June 2005.
- [2] M. Riel, J. J. Laurin, “Design of an electronically beam scanning reflectarray using aperture-coupled elements”, *IEEE Trans. Antennas Propagat.*, vol. 55, no. 5, May 2007.
- [3] A. Moessinger, S. Dieter, W. Menzel, S. Mueller, R. Jakoby, “Realization and characterization of a 77 GHz reconfigurable liquid crystal reflectarray”, *13th Int. Symp. on antenna Technology and Applied Electromagnetics and Canadian Radio Sciences Meeting*, 2009
- [4] R. Sorrentino, R. V. Gatti, L. Marcaccioli, B. Mencagli, “Electronic steerable MEMS antennas”, *EuCAP 2006, European Conference on Antennas and Propagations*, nov. 2006.
- [5] F. Venneri, S. Costanzo, G. Di Massa, “Reconfigurable aperture-coupled reflectarray element tuned by a single varactor diode”, *Electronics Letters*, vol. 48, no. 2, January 2012.
- [6] S. Costanzo, F. Venneri, and G. Di Massa, “Bandwidth enhancement of aperture-coupled reflectarrays,” *IEE Electronics Letters*, Vol. 42, No. 23, 1320–1321, 2006.

CO-POLAR AND CROSS-POLAR PATTERN SYNTHESIS FOR RECONFIGURABLE ANTENNA ARRAYS

G. Buttazzoni, R. Vescovo

Department of Engineering and Architecture
University of Trieste
Via A. Valerio 10, 34127 Trieste, Italy
giulia.buttazzoni@phd.units.it
vescovo@units.it

Abstract

A numerical method is presented for the power synthesis of co-polar and cross-polar patterns of phase controlled reconfigurable arrays. The method is suitable for arrays of arbitrary geometry, including conformal ones.

Index Terms – Conformal reconfigurable arrays, Co-polar pattern, Cross-polar pattern, Phase control, Power synthesis.

I. INTRODUCTION

One of the most attracting features of antenna arrays is the possibility of realizing the reconfigurability, that is, their capability of generating different radiation patterns by suitably modifying the excitations of the array elements. Usually, the reconfigurability is obtained by modifying only the phase of the excitations, that is, keeping their amplitudes constant during the reconfiguration process. When antenna arrays are mounted on vehicles, their geometry is often dictated by the contour surfaces of such vehicles, and the radiating structures are referred to as conformal arrays. Many classical synthesis methods are not suitable for conformal arrays, as the radiating elements are usually directed in different directions, so that the radiation pattern cannot be expressed as the product of an array factor by an element factor. Furthermore, in some cases it is necessary to reduce the amplitude of the cross-polar patterns. Some synthesis techniques for reconfigurable conformal arrays are based on deterministic methods [1], [2], some others are based on stochastic techniques [3]. In this paper we present an iterative algorithm that allows the power synthesis of a number S of desired co-polar patterns and of the corresponding cross-polar patterns, with the capability of transforming a pattern into any of the others by phase-only control. The algorithm is based on an alternating projection approach, and is an evolution of the method presented in [4].

II. THE PROBLEM

With reference to a Cartesian system $O(x, y, z)$, the co-polar and the cross-polar patterns of an antenna array of N radiating elements are given, respectively, by:

$$F_{co}(\mathbf{a};\varphi) = \sum_{n=1}^N a_n f_{co}^n(\varphi) \quad (1), \quad F_{cr}(\mathbf{a};\varphi) = \sum_{n=1}^N a_n f_{cr}^n(\varphi) \quad (2)$$

where $\mathbf{a} = [a_1, \dots, a_N]^T$ is the excitation column vector, φ the generic azimuth direction in the xy -plane, $f_{co}^n(\varphi)$ and $f_{cr}^n(\varphi)$ the active co-polar and cross-polar element patterns, respectively, of the n -th array element [5]. Now, let us consider a number S of co-polar and cross-polar masks (M_{co}^s, M_{cr}^s) defined as: $M_{co}^s = \{f(\varphi) : f_{co,1}^s(\varphi) \leq |f(\varphi)| \leq f_{co,2}^s(\varphi)\}$, $M_{cr}^s = \{f(\varphi) : f_{cr,1}^s(\varphi) \leq |f(\varphi)| \leq f_{cr,2}^s(\varphi)\}$, where $f_{co,1}^s(\varphi)$, $f_{cr,1}^s(\varphi)$, $f_{co,2}^s(\varphi)$ and $f_{cr,2}^s(\varphi)$ are positive functions defining the lower and the upper bounds of the masks. We want to find S excitation vectors in such a way as to obtain S co-polar patterns belonging to the S co-polar masks, S cross-polar patterns belonging to the S cross-polar masks, with the capability of switching a pattern into the others by phase-only control. Note that the phase-only requirement does not imply a common amplitude for all the array elements, but it only means that the excitation amplitude of each array element keeps constant during the reconfiguration process. Thus, to radiate the S patterns, S different excitation phases are applied to each radiator, with a single excitation amplitude. This problem can be mathematically formulated as follows: determine S excitation vectors $\mathbf{a}_s = [a_{1s}, \dots, a_{Ns}]^T$ which simultaneously satisfy the following constraints:

$$F_{co}(\mathbf{a}_s; \varphi) \in M_{co}^s, \quad s = 1, \dots, S \quad (3)$$

$$F_{cr}(\mathbf{a}_s; \varphi) \in M_{cr}^s, \quad s = 1, \dots, S \quad (4)$$

$$|a_{n1}| = \dots = |a_{ns}| = \dots = |a_{nS}| = \alpha_n, \quad n = 1, \dots, N \quad (5)$$

The amplitudes α_n are not pre-assigned, but are optimized. At first, we formulate the synthesis problem as an intersection finding problem. To this aim, we introduce two sets U and V , as in [4]:

$$U = \{ \tilde{\mathbf{u}} : \tilde{\mathbf{u}} = ((f_{co}^1(\varphi), f_{cr}^1(\varphi)), \dots, (f_{co}^S(\varphi), f_{cr}^S(\varphi)), \mathbf{u}_1, \dots, \mathbf{u}_S) \}$$

$$V = \{ \tilde{\mathbf{v}} : \tilde{\mathbf{v}} = ((F_{co}(\mathbf{v}_1; \varphi), F_{cr}(\mathbf{v}_1; \varphi)), \dots, (F_{co}(\mathbf{v}_S; \varphi), F_{cr}(\mathbf{v}_S; \varphi)), \mathbf{v}_1, \dots, \mathbf{v}_S) \}$$

where $f_{co}^s(\varphi) \in M_{co}^s$, $f_{cr}^s(\varphi) \in M_{cr}^s$, the vectors $\mathbf{u}_s = [u_{1s}, \dots, u_{Ns}]^T$ satisfy condition (5), whereas the functions $F_{co}(\mathbf{v}_s; \varphi)$, $F_{cr}(\mathbf{v}_s; \varphi)$ are obtained by replacing \mathbf{a} with \mathbf{v}_s in (1) and (2), respectively. Thus, the elements of U satisfy all constraints of the problem (although the functions $f_{co}^s(\varphi)$ and $f_{cr}^s(\varphi)$ are not necessarily array patterns), while the elements of V represent the co-polar and the cross-polar array patterns and the corresponding excitation vectors. Now, it is evident that any element belonging to both sets, that is, to their intersection $U \cap V$, is a solution to our problem. After choosing a suitable distance between the points of U and V , and a suitable starting point $\tilde{\mathbf{u}}_0$, such solution can be found

with the alternating projection algorithm, which follows the iterative scheme:

$$\tilde{\mathbf{u}}_n = P_U P_V \tilde{\mathbf{u}}_{n-1}, \quad n=1,2,\dots \quad (6)$$

where P_U and P_V are the projection operators onto the sets U and V , respectively. Since P_U and P_V are projectors, and due to the properties of the distance, the points of the sequence $\{\tilde{\mathbf{u}}_n\}$ (belonging to U) are closer and closer to the set V , and therefore to a solution to our problem [4]. However, we here propose a modified version of this approach, obtained by modifying the projector P_V . Precisely we add, to the squared distance between the current point of U and the generic point of V , the sum of the power values radiated in the side lobe regions, of all the co-polar and cross-polar patterns, and minimize this new functional. So, we obtain a "corrected operator" P_V^c which is not a projector onto V anymore, but gives radiation patterns with small power in the side lobe region. The iteration scheme (6) becomes: $\tilde{\mathbf{u}}_n = P_U P_V^c \tilde{\mathbf{u}}_{n-1}$, $n=1,2,\dots$. Now, as P_V^c is not a projector, the sequence of distances $d_n = d(\tilde{\mathbf{u}}_n, V)$ is not guaranteed to decrease. However, the power requirement is consistent with the side lobe masks requirements, and this improves the results.

III. NUMERICAL EXAMPLE AND CONCLUSION

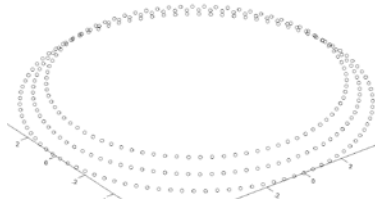


FIG. 1 – Array structure consisting of $N = 261$ Huygens radiators radially oriented.

With reference to the array of Fig. 1, let us consider the masks of Fig. 2. Firstly, we solve the synthesis problem in absence of constraint (4), obtaining the patterns in Fig. 2. Then, we solve the problem with the method proposed in [4] and with the method presented in this paper, obtaining the patterns in Fig. 3 and in Fig. 4, respectively. Table I summarizes the results. A comparison between Figs. 3 and 4, and the third and fourth columns of Table I, shows the considerable improvement obtained with the proposed algorithm.

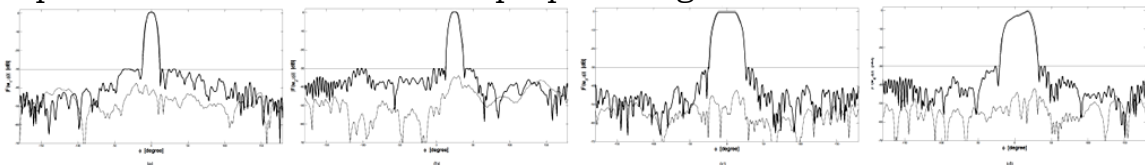


FIG. 2 – Co-polar patterns (solid thick lines) belonging to the co-polar masks (solid thin lines) and cross-polar patterns (dashed lines) obtained solving the problem without the constraint (4).

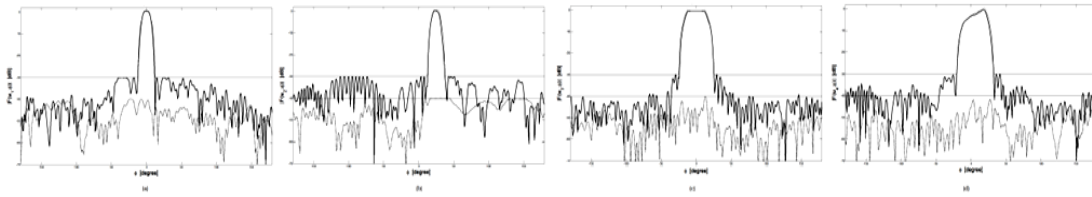


FIG. 3 – Co-polar patterns (solid thick lines) and cross-polar patterns (dashed lines) belonging to the corresponding masks (solid thin lines) obtained solving the problem with the algorithm in [4].

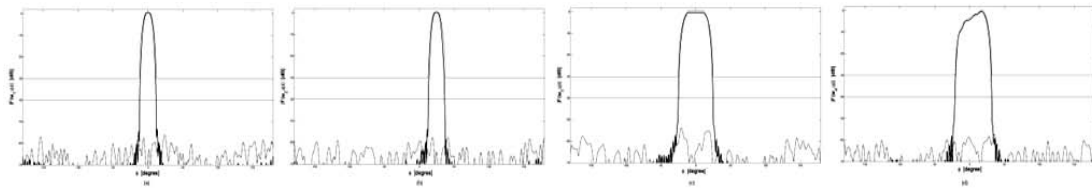


FIG. 4 – Co-polar patterns and cross-polar patterns obtained solving the problem with the proposed algorithm.

TABLE I - COMPARISON BETWEEN THE OBTAINED RESULTS

	Absence of (4)	Algorithm in [4]	Presented algorithm
Iterations	175	7098	23110
$PSLL$	$3.5 \cdot 10^{-3}$	$3.9 \cdot 10^{-3}$	$2.6 \cdot 10^{-6}$
PCR	$5.3 \cdot 10^{-3}$	$4.8 \cdot 10^{-3}$	$8.7 \cdot 10^{-6}$
max_{CR}	-33.9 dB	-40.0 dB	-53.8 dB

REFERENCES

- [1] O. M. Bucci, G. Mazzarella, and G. Panariello, "Reconfigurable arrays by phase-only control," *IEEE Transactions on Antennas and Propagation*, vol. 39, pp. 919-925, Jul. 1991.
- [2] L. Vaskelainen, "Iterative least-squares synthesis methods for conformal array antennas with optimized polarization and frequency properties," *IEEE Transactions on Antennas and Propagation*, vol. 45, pp. 1179-1185, Jul. 1994.
- [3] D. W. Boeringer and D. H. Werner, "Particle swarm optimization versus genetic algorithms for phased-array synthesis," *IEEE Transactions on Antennas and Propagation*, vol. 52, pp. 771-779, Mar. 2004.
- [4] G. Buttazzoni and R. Vescovo, "Synthesis of co-polar and cross-polar patterns with dynamic range ratio reduction for phase-only reconfigurable arrays," EUCAP 2012, *European Conference on Antennas and Propagation*, March 26-30 2012, Prague, Czech Republic
- [5] D.M. Pozar, "The active element pattern," *IEEE Transactions on Antennas and Propagation*, vol. 42, No. 8, pp. 1176-1178, Aug. 1994.

HERMITE AND LAGUERRE BEAMSPACES FOR ULTRA WIDE BAND ANTENNA ARRAY

E. D. Di Claudio⁽¹⁾, G. Jacovitti⁽²⁾, A. Laurenti⁽³⁾

⁽¹⁾⁽²⁾ DIET, Department of Information Engineering, Electronics and Telecommunications, “La Sapienza” University
Via Eudossiana 18, 00184 Rome, Italy

⁽¹⁾dic@infocom.uniroma1.it ⁽²⁾gjacov@infocom.uniroma1.it

⁽³⁾ GIAL S.r.l. company

Via Capodistria 12, 00198, Rome, Italy
ablaur@rmnet.it

Abstract

In this paper the use of 2-D Hermite-Gauss (HG) and Laguerre-Gauss (LG) expansions of the space-time signal delivered by an Ultra Wide Band (UWB) linear antenna array is outlined. Signatures of UWB incoming signals are confined within a finite rank signal subspace, parametrized by their direction of arrival (DOA), just as the steering vectors of narrowband array signals. Fast calculation of UWB DOA is allowed by polynomial rooting. To show the potential of this approach, the statistical performance of a Conditional Maximum Likelihood (CML) DOA estimator for a single UWB source in presence of spatially and temporally colored Gaussian noise is estimated with simulation trials. It results that, with a proper choice of the expansion parameters, accuracy approaches the Cramer-Rao bound.

Index Terms – Ultra Wide Band antenna array, Hermite-Gauss and Laguerre-Gauss expansions, direction finding, subspace fitting.

I. INTRODUCTION

Array based direction finding of UWB signals [1] is traditionally performed by analyzing differential Time Delays Of Arrivals (TDOA) between antennas [2][3] or by reducing UWB signals to multiple narrow band signals [4] through frequency *binning* of array outputs and optional focusing of individual bins onto a virtual array [5]. However, frequency binning produces considerable modeling errors, especially in the cases of short time signals and bandwidths exceeding half-octave [5][6].

To circumvent these drawbacks, a radically different approach is followed in this contribution. Starting from the fact that baseband (or heterodyned to baseband) UWB signals captured by a linear array form a *linear pattern* (or 1-D pattern) in the space-time support [7], it is shown [8] that the Cartesian separable *2-D Hermite-Gauss* (2-D HG) expansion of a linear pattern truncated to a finite order M defines a signal subspace in its coefficient space whose maximum dimension is $M + 1$. This subspace rotates in the space-time plane with the DOA of the impinging wavefront. Now, the truncated 2-D HG expansion is

linearly related to a truncated *Laguerre-Gauss* (LG) expansion of the same order by an unitary, block diagonal transformation matrix [8][9]. In particular, the polar separable LG functions and coefficients rotate through a simple multiplication by a phase factor with angle proportional to both the rotation angle and the *harmonic order* of the function itself [8][9].

This remarkable property enables a *Conditional ML* (CML) DOA estimator for deterministic, but unknown signals, which in the case of a single source admits fast computation with rooting techniques [7][8].

II. LINEAR PATTERN WAVEFRONT MODEL

A plane wavefront carrying the signal $s(t)$ is received by the generic omni-directional, unit gain sensor of a linear antenna array located at position $(x, 0)$ and produces the space-time baseband signal

$$u(x, t) = s \left[t - \sin(\theta) \frac{x}{c} \right] \quad (1)$$

where c is the wave propagation speed and θ is the azimuth angle, referred to array broadside. If $u(x, t)$ is sampled at times $\{t = nT; n = 0, 1, \dots, N-1\}$ and sensors are located at the equi-spaced abscissas $\{x_q = qdcT; q = 0, 1, \dots, Q-1\}$, the resulting $(Q \times N)$ *space time patch* is modeled as

$$u(q, r) = s \left\{ \frac{T}{\cos(\alpha)} [r \cos(\alpha) - q \sin(\alpha)] \right\} \quad (2)$$

i.e., the equation of a sampled linear pattern in 2-D [8], rotated by the angle

$$\alpha = \arctan[d \cdot \sin(\theta)] \quad (3)$$

with respect to the abscissa axis.

III. 2-D HG AND LG LINEAR PATTERN EXPANSIONS

It can be shown that the truncated, M th order 2-D HG expansion of scale σ of the patch (2), defined by [8][9]

$$u(q, r; \sigma) \cong \sum_{m=0}^{M-1} \sum_{l=0}^m x_{m-l, l} h_{m-l}(q; \sigma) h_l(r; \sigma) \quad (4)$$

where $1 \leq M < Q$ and

$$h_l(\xi; \sigma) = \frac{H_l\left(\frac{\xi}{\sigma}\right)}{\sqrt{2^l l! \sigma \sqrt{\pi}}} e^{-\frac{\xi^2}{2\sigma^2}}; \quad H_l(\nu) = (-1)^l e^{\nu^2} \frac{d^l(e^{-\nu^2})}{d\nu^l} \quad (5)$$

is the orthonormal 1-D Hermite-Gauss basis function of scale σ , obeys a matrix equation in the form

$$\mathbf{x} = \mathbf{T}_{L \rightarrow H} \mathbf{D}(-\alpha) \mathbf{E}_s(\sigma) \mathbf{c} \quad (6)$$

where the column vector \mathbf{x} of length $(M+1)(M+2)/2$ stacks the 2-D HG coefficients $\{x_{m-l,l}; m=0,1,\dots,M, l=0,1,\dots,m\}$, \mathbf{T}_{L-H} is the unitary *inter-conversion matrix* from the LG expansion of order M [8][9] to the linearly related (4), $\mathbf{D}(-\alpha)$ is a diagonal matrix with non-zero entries $e^{-jp\alpha}$, where p is the harmonic order of the LG functions involved, $\mathbf{E}_s(\sigma)$ is a $(M+1)$ th dimensional orthogonal matrix and the column vector \mathbf{c} stacks the modified 1-D Hermite signal expansion coefficients

$$c_m = \left[\sum_{h=0}^{M-m} \frac{(-1)^h \sigma \sqrt{\pi} H_h^2(0)}{2^{h-1} h!} \right]^{\frac{1}{2}} \int_{-\infty}^{+\infty} s \left[\frac{t}{\cos(\alpha)} \right] h_m(t; \sigma) dt; \quad m=0,1,\dots,M. \quad (7)$$

IV. CML DIRECTION FINDING

Equation (6) is the basis for the straight-forward definition of ML DOA estimators, by analogy with the narrowband array signal subspace [4]. Taking into account the covariance $\mathbf{R}_{vv} = \mathbf{C}_v \mathbf{C}_v^H$ of the 2-D HG noise coefficients, determined by background noise statistics and the method employed for estimating \mathbf{x} , the single-source, *LG Conditional ML* (LG-CML) estimator α_{CML} of α , used in passive DOA tracking, is given by [7]

$$\alpha_{CML} = \arg \min_{\alpha, \mathbf{c}} \left\| \mathbf{C}_v^{-1} \left[\mathbf{x} - \mathbf{T}_{L \rightarrow H} \mathbf{D}(-\alpha) \mathbf{E}_s(\sigma) \mathbf{c} \right] \right\|_2^2 \quad (8)$$

which can be efficiently solved by polynomial rooting [7] or parabolic local interpolation [3].

V. COMPUTER SIMULATION

In Fig. 1 the performance of (8) is compared with the *Cramer-Rao bound* (CRB) for estimation variance, the optimal *space-time CML* (ST-CML), based on frequency binning, and a state of the art TDOA algorithm [2]. A source located at $\theta = 35^\circ$ was captured by an uniform linear array with $d = 0.9$, $N = Q = 14$, using $M = 13$ and $\sigma = 1.4$. Batches of 140 samples were collected by a sliding patch. The proposed LG-CML estimator is the best at low signal to noise ratio (SNR). For medium to high SNR, ST-CML and TDOA estimators perform slightly better than LG-CML, because the latter one under-weights corner data in the space-time patches, due to the inherent circular symmetry of (4). On the other hand, LG-CML is much more flexible and computationally cheaper than accurate TDOA implementations [2][3]. Moreover, compared to frequency binning techniques, it can provide single patch DOA estimates, especially useful in the presence of pulsed signals.

VI. CONCLUSION

The presented approach is currently investigated for the optimal choice

of the array and expansion parameters and also for extension to multi-source UWB scenarios using subspace algorithms [4].

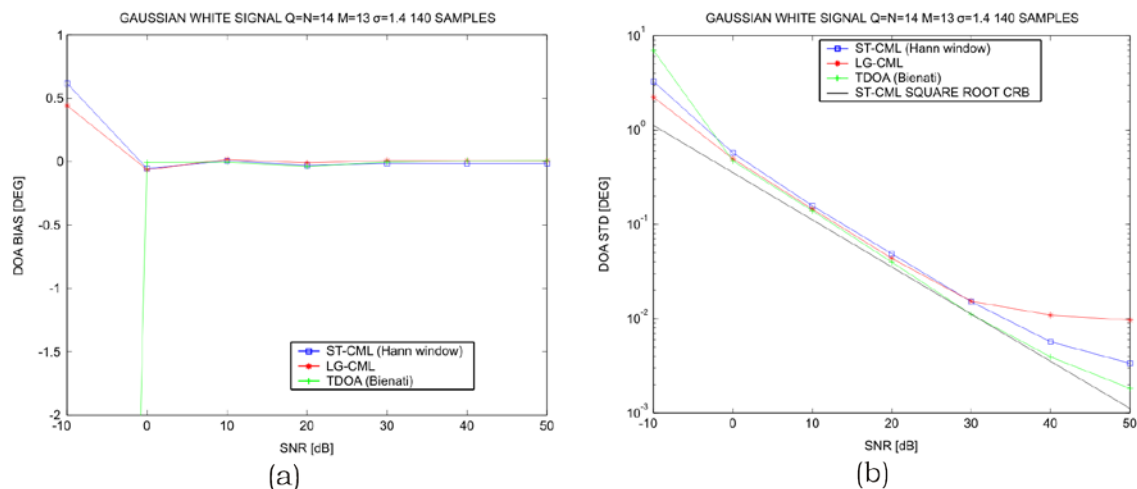


FIG. 1 – Performance comparison between the proposed LG-CML, some competing algorithms and the CRB; (a) DOA bias; (b) DOA standard deviation.

REFERENCES

- [1] M. G. M. Hussain, "Principles of space-time array processing for ultrawide-band impulse radar and radio communications," *IEEE Trans. On Vehicular Technology*, Vol. 51. No. 3, pp. 393-403, May 2002.
- [2] N. Bienati, N. U. Spagnolini, "Multidimensional wave-front estimation from differential delays," *IEEE Trans. on Geoscience and Remote Sensing*, vol. 39, no. 3, pp. 655 – 664, March 2001.
- [3] G. Jacovitti, G. Scarano, "Discrete time techniques for time delay estimation," *IEEE Trans. on Signal Processing*, vol. 41, no. 2, pp. 525-533 Feb. 1993.
- [4] M. Viberg, M. Ottersten & T. Kailath, "Detection and estimation in sensor arrays using weighted subspace fitting," *IEEE Trans. on Signal Processing*, Vol. 39, No. 11 , pp. 2436-2499, Nov. 1991.
- [5] E. D. Di Claudio, R. Parisi, "WAVES: weighted average of signal subspaces for robust wideband direction finding," *IEEE Trans. on Signal Processing*, vol. 49, no.10, pp. 2179-2191, Oct 2001.
- [6] E. D. Di Claudio, "Asymptotically perfect wideband focusing of multi-ring circular arrays", *IEEE Trans. on Signal Processing*, Piscataway, Vol. 53, No. 10, Part I, pp. 3661-3673, Oct. 2005.
- [7] E. D. Di Claudio, G. Jacovitti, A. Laurenti "Robust direction estimation of UWB sources in Laguerre-Gauss beamspaces," *Proc. of 2011 IEEE Int. Conf. on Acoustics, Speech and Signal Processing (ICASSP)*, pp. 2736-2739, Prague, 22-27 May 2011.
- [8] E. D. Di Claudio, G. Jacovitti, A. Laurenti "Maximum Likelihood orientation estimation of 1-D patterns in Laguerre-Gauss subspaces," *IEEE Trans. on Image Processing*, vol. 9, no. 5, pp. 1113-1124, May 2010.
- [9] E. D. Di Claudio, G. Jacovitti, A. Laurenti, "On the inter-conversion between Hermite and Laguerre local image expansions," *IEEE Trans. on Image Processing*, vol. 20, no. 12, pp. 3553-3565, Dec. 2011.

Session 10 –Propagation and scattering

C. Capsoni, L. Luini, and R. Nebuloni

Preliminary assessment of site diversity schemes for earth-space optical links

A. Di Carlofelice, E. Di Giampaolo, M. Elaiopoulo, and P. Tognolatti

A study of radiowave propagation into collapsed buildings for rescue of trapped people

P. Imperatore, A. Iodice, and D. Riccio

The role of internal field approximation for scattering from layered rough interfaces

M. Carlin, L. Manica, G. Oliveri, L. Poli, P. Rocca, and A. Massa

Advances on inverse scattering methodologies and applications @ ELEDIA research center

L. Di Donato, I. Catapano, L. Crocco, and T. Isernia

A new framework for quantitative inverse scattering

PRELIMINARY ASSESSMENT OF SITE DIVERSITY SCHEMES FOR EARTH-SPACE OPTICAL LINKS

C. Capsoni⁽¹⁾, L. Luini⁽¹⁾, R. Nebuloni⁽²⁾

- ⁽¹⁾ Dipartimento di Elettronica e Informazione, Politecnico di Milano,
Piazza Leonardo da Vinci 32, I-20133 Milan, Italy,
e-mail: {capsoni,luini}@elet.polimi.it
- ⁽²⁾ IEIIT-CNR, Via Ponzio 34/5, I-20133 Milan, Italy,
e-mail: roberto.nebuloni@ieiit.cnr.it

Abstract

Free Space Optical (FSO) links enable high-speed data transfer from Earth Observation satellites or deep space (DS) probes directly to ground stations. The presence on-board of remote sensing instruments with ever increasing accuracy and resolution fuels the need for transmitting large amounts of data. This contribution investigates the impairments to optical beam propagation due to clouds by exploiting radiosonde observation (RAOBS) data collected in two European sites. Long-term yearly statistics of path attenuation are calculated by first distinguishing between different cloud types and, afterwards, by integrating their contribution to the total attenuation along each vertical profile of RAOBS data. Finally, the effectiveness of a site diversity scheme, simultaneously employing both FSO links, is assessed. Results indicate that a dual-site diversity FSO system with target availability of 10% would require approximately a 40-dB fade margin to counteract cloud attenuation.

Index Terms – Free Space Optics, Laser communications, Earth-space propagation, Cloud attenuation.

I. INTRODUCTION

Spacecrafts for Earth observation (EO) and deep space (DS) missions embark complex remote sensing instruments, whose resolution and accuracy are continuously increasing. As a result, frequency bands traditionally employed for space-to-Earth data transfer (C- to Ka-band) are expected to reach saturation in the near future because of the large amount of data collected by such instruments. In this scenario, Earth-space optical links represent an appealing solution for next generation EO and DS missions because they offer extremely large bandwidths for data transfer to ground stations [1]. This paper investigates the usage of Free Space Optical (FSO) download links from a Geosynchronous Earth Orbit (GEO) satellite carrying high-resolution EO sensors. Specifically, the effects of the atmosphere on an FSO link are first outlined. Afterwards, a database of radiosonde observations (RAOBS) is processed to draw some results useful for the design of an Earth-space optical communication system. Finally it is shown that the extremely

high fade levels due to the presence of clouds can be mitigated by site diversity schemes.

II. EFFECTS OF THE ATMOSPHERE ON OPTICAL BEAM PROPAGATION

The propagation of optical waves through the atmosphere is undermined by gaseous absorption, interaction with atmospheric particles (fog, clouds, rain, etc.) and clear-air turbulence. Optical windows free from molecular absorption include the visible region, the wavelengths used in fiber optics (0.85 and 1.55 μm), and longer wavelengths such as the 10.6 μm IR window. As for particulates, fog and clouds produce the highest levels of laser attenuation, due to the high extinction efficiency of droplets and to their high number concentration.

The procedure to estimate cloud attenuation starts from a dataset of RAOBS collected twice a day (only in nonrainy conditions) in some sites worldwide [2]. High-resolution vertical profiles of temperature, pressure and relative humidity are provided as input to a cloud detection algorithm [3] to identify and characterize clouds in terms of Liquid Water Content (LWC) and Ice Water Content (IWC) in g/m^3 . Afterwards, based on Table I, each cloud is classified according to its vertical extent ΔH as suggested in [4]. Each cloud type is, in fact, associated to different microphysical properties, described by the Particle Size Distribution (PSD). By consequence, different cloud types have a different impact on the FSO link. The PSD for liquid water particles is usually modeled by a modified gamma function [5]:

$$n(r) = ar^\alpha e^{-br^\gamma} \quad (1)$$

where b , α and γ are parameters regulating the shape of eq. (1) (a is proportional to the LWC) and $n(r) dr$ is the number of particles per unit volume of air with radius comprised between r and $r+dr$.

Single-scattering theory is commonly applied to calculate cloud attenuation from the PSD. As the droplets within (liquid) water clouds are basically spherical in shape, their scattering properties are calculated through the Mie theory. The contributions of individual particles are added up to find the loss due to the entire population of cloud droplets along the propagation path.

TABLE I – CLOUD TYPES [4] AND ASSOCIATED PSD [5]

<i>Cloud type</i>	<i>b</i>	<i>α</i>	<i>γ</i>	<i>ΔH (km)</i>
Vertically developed cloud (Cumulonimbus)	0.5	5-6	0.3-0.5	3
Vertically developed cloud (Cumulus)	0.5	5-6	0.3-0.5	2
Mid-level (Nimbostratus)	0.425	4	1	0.8
Low-level (Stratus)	0.6	6	1	0.6

As for ice particles, the calculation of the volume extinction coefficient is complicated by the several different crystal shapes observed in ice clouds. In spite of the presence of diverse crystals, Platt [6] has shown that in the optical limit (i.e. if the extinction efficiency of individual particles is equal to 2), the specific attenuation γ_I due to ice clouds can be derived from the IWC (in g/m^3) through the following power-law relationship:

$$\gamma_I = 40.26 \text{ IWC}^{0.68} \quad (\text{dB/km}) \quad (2)$$

III. PERFORMANCE OF THE EARTH-SPACE OPTICAL COMMUNICATION SYSTEM

Two RAOBS sites have been considered to evaluate the performance of the Earth-space optical communication system. The left side of Fig. 1 shows the Complementary Cumulative Distribution Function (CCDF) of the optical attenuation A_{slant} at $10.6 \mu\text{m}$ experienced by two FSO links located in Milan and in Wien, each pointing to a GEO satellite (orbital position 16°E). CCDFs have been obtained by calculating A_{vert} as the integration of the specific attenuation due to liquid water and ice along the vertical LWC and IWC profiles, in turn obtained from RAOBS data (10 years). Finally, A_{vert} has been scaled according to the link elevation angle θ as $A_{slant} = A_{vert}/\sin(\theta)$, which assumes horizontal uniformity of clouds ($\theta = 37^\circ$ and 35° for Milan and Wien, respectively).

Also depicted in Fig. 1 is the joint CCDF of the optical attenuation that would be achieved by implementing site diversity between the above two stations. In practice this solution implies to dynamically select the link that is less affected by attenuation. The right side of Fig. 1 shows the diversity gain G as a function of the single-link availability level, being G the difference between dual- and single-link attenuation at the same probability level P . Results show that: a) extremely high attenuation values are obtained for most of the year (e.g. $A_{slant} > 200 \text{ dB}$ for 10% of the time in a year in both sites); b) site diversity is very effective in reducing the fade levels impairing the system; c) a dual-site diversity FSO system with target availability of 10% would require approximately a 40-dB fade margin to counteract cloud attenuation.

IV. CONCLUSION

The statistical distribution of cloud attenuation along an Earth-space optical communication link has been evaluated from radiosonde observations, and a simple two-site diversity scheme has been proposed to reduce link unavailability due to clouds. Preliminary results evidence that, by distancing the two ground stations (Milan and Wien) of about 500 km, a significant decorrelation of cloud occurrence is achieved, and as a consequence, a corresponding reduction in attenuation from the

single-site case. Future work will be addressed to obtaining comprehensive results from several different sites and to testing multiple site diversity schemes.

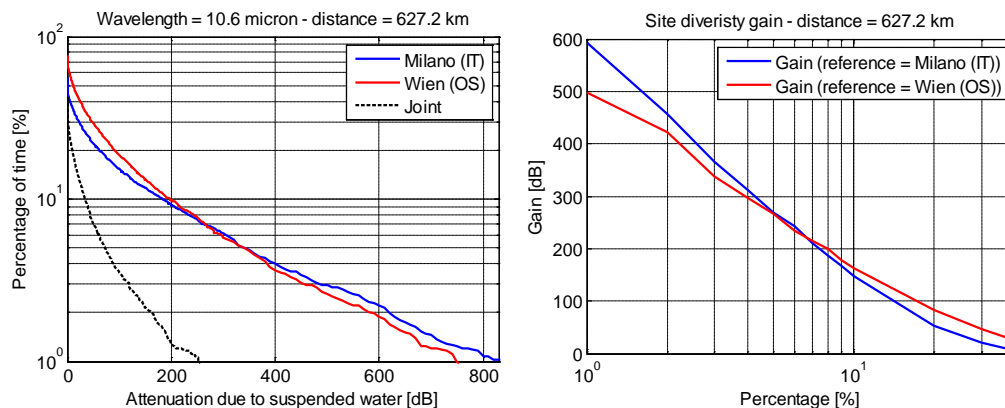


FIG. 1 – Left side: complementary cumulative distribution functions of cloud attenuation (single- and joint-link statistics). Right side: site diversity gain as a function of single-link availability level.

ACKNOWLEDGEMENT

The authors would like to thank Dr. Antonio Martellucci from the European Space Agency for kindly providing the FERAS database.

REFERENCES

- [1] H. Hemmati, A. Biswas, I. B. Djordjevic, “Deep-space optical communications: future perspectives and applications”, *IEEE Proceedings*, Vol. 99, No. 11, pp. 2020-2039, Nov. 2011.
- [2] COST Action 255 Final Report, Precipitation, Clouds and Other Related Non-Refractive Effects, J. P. V. Poiars Baptista, Ed. Noordwijk, The Netherlands: ESA Publication Division, ch. 3.2.
- [3] E. Salonen, W. Uppala, “New Prediction method of cloud attenuation”, *Electronics Letters*, vol. 27, No. 12, pp. 1106-08, June 1991.
- [4] A.W. Dissanayake, J.E. Allnut, F. Haidara, “A prediction model that combines rain attenuation and other propagation impairments along earth-satellite paths”, *IEEE Transactions on Antennas and Propagations* 1997; Vol. 45, pp.1546-1558.
- [5] E. P. Shettle, “Models of aerosols, clouds and precipitation for atmospheric propagation studies”, *AGARD conference* 454, pp. 1-13, 1989.
- [6] C.M.R. Platt, “A parametrization of the visible extinction coefficient of ice clouds in terms of the ice water content”, *J. Atmos. Sci.*, Vol. 54, pp. 2083-2098, 1997.

A STUDY OF RADIOWAVE PROPAGATION INTO COLLAPSED BUILDINGS FOR RESCUE OF TRAPPED PEOPLE

A. Di Carlofelice⁽¹⁾, E. Di Giampaolo⁽¹⁾, M. Elaiopoulos⁽²⁾ and P. Tognolatti⁽¹⁾

⁽¹⁾Dept. of Electrical Engineering and Information

⁽²⁾Dept. of Architecture and Urban Planning

University of L'Aquila

Via G. Gronchi, 18, 67100 L'Aquila, Italy

alessandro.dicarlofelice@univaq.it

Abstract

The paper deals with the localization of radio emitters into collapsed buildings after earthquake. A measurement campaign has been carried out in a typical European historical city, L'Aquila, which was recently stroke by a severe earthquake. Continuous wave radio transmitters operating at 434 and 868 MHz have been introduced under rubble and their signals have been measured at different points surrounding the debris to evaluate the path loss and the direction of arrival. An accurate reconstruction of the scenario has been also carried out using a laser scan. The obtained results demonstrate the possibility to localize a radio emitter under rubble with considerable accuracy.

Index Terms – Earthquake rubble characterization, direction of arrival, emergency responders, radio communication.

I. INTRODUCTION

Collapsed building structures constitute a very complex environment, for which no general model exists. Also, there is a large variety of possible scenarios because many different materials can be involved. The electromagnetic propagation strongly depends on the shape, dimensions, humidity and compression of debris which are highly variable [1]-[3].

In this work we study the electromagnetic characterization of a disaster scenario in a typical historical center of Italian towns.

Many measurements have been carried out to characterize electromagnetically the earthquake rubble in a number of buildings, collapsed or partially destroyed, in L'Aquila territory that was recently stroked by a severe earthquake. PL and DOA estimations are gathered using a portable network analyzer and a home-made direction finder. A very accurate modeling of the scenario has been carried out by a laser scan.

II. INSTRUMENTATION AND MEASUREMENTS

A. Transmitter

The Aurel transmitters (see Fig. 1) used in the experiments operate at the frequencies of 434 and 868 MHz. They can operate continuously for several hours, and are small sized. The Effective Radiated Power (E.R.P.) of these transmitters is 10 mW @ 434 MHz and 25mW @ 868 MHz, respectively. For both frequency bands, the Aurel transmitters were modified in order to: (a) switch between two different transmission mode

(CW or modulate carrier), (b) use a large battery pack. The modified transmitters and battery packs were placed in plastic cases for mobility and protection as shown in Fig. 2.



FIG. 1 – The Aurel transmitters used in measurement campaign: TX-4M10HA/V434 (left) and TX-8L25IA (right).

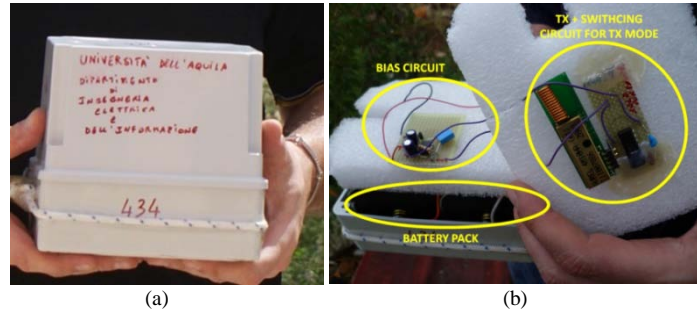


FIG. 2 – The grey plastic case of Aurel transmitter (a) and its interior (b).

B. Direction Finder Antenna and Receiving System

The method here employed is similar to the stereophonic identification of sound direction by human beings using their ears. Two axial-mode helical antennas possessing identical electrical properties with phase aligned polarizations are placed on a ground plane to form a two-element array. Having identical electrical properties, the antennas have identical bandwidths, radiation patterns, gains, polarizations and impedances. If the wave-front of the incoming signal is orthogonal to the axes of the antennas, no phase difference between received signals is observed. Otherwise a phase difference is detected.

A circuit, consisting in a SPDT PIN-diode switch, operating at an audio frequency (e.g. 1 kHz) alternatively connects each of the two antennas to the RF input of an FM audio communication receiver tuned to the frequency of interest (i.e. 434 or 868 MHz). This switching imposes phase modulation on the incoming signal whenever the DoA of incoming wave-front is not perfectly orthogonal to antenna baseline. This phase modulation is detected by the communication receiver and an audio tone is emitted. When the antenna array is rotated so that the DoA is orthogonal to the antenna baseline the audio-tone sharply disappears.

III. MEASUREMENT SYSTEM FOR A DOA EVALUATION

April 6, 2009, a devastating earthquake struck the city of L'Aquila and surrounding territories in the Abruzzo Region Italy. Onna is a small village in a valley near a river, about 6 km east of L'Aquila. It was close to the earthquake epicenter and many buildings either collapsed or were near collapse. The center of this small place was partially covered by collapses, reported material. The transmitter was placed in a 300

mm PVC pipe of nine meters, buried in the rubble. The amount of rubble that covered the tube varied between about 1 and 2 meters. Topographic methods based on optical instruments as laser scanner and total station have been used to measure the accuracy of the estimated DOA.



FIG. 4 The three-dimensional model of the test area created by laser scan.

The measurement results obtained at 432 MHz are shown in 1. In red the normal direction of each station made by the anter shown while in navy blue the signal real direction is drawn. The formed by the two directions is reported for each station. We can that most of the red lines pass through a circle with 1 meter radiu center on the emitter. This shows that DOA-based method gi highly probable localization of the emitter with uncertainty o Possible multipaths are evidenced in navy blue. Results for the frequency (i.e. 868 MHz) are similar.

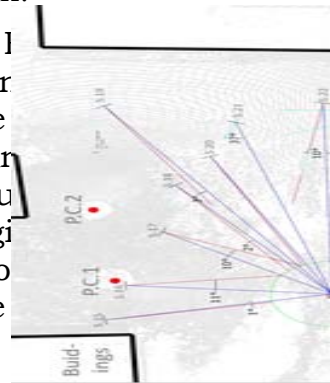


FIG. 5. Measurement results obtained at 434MHz. Red and blue lines show estimated DOA and true directions, respectively.

IV. MEASUREMENT SYSTEM FOR PATH LOSS EVALUATION

We also performed path loss measurement in Onna. The site is the same used for DOA estimation. The measurement setup is shown in Fig. 6.

Table I shows the path loss results for both vertical and horizontal polarizations. We can see a similarity between PL of the two polarizations, this is a consequence of the particular measurement site where volumetric scattering is the dominant propagation phenomena.

I. CONCLUSION

Experimental results of measurement campaigns for localizing a radio emitter into collapsed buildings after earthquake have been presented. Continuous wave radio transmitters operating at 434 and 868 MHz have been introduced under rubble and their signals have been measured at different points surrounding the debris to evaluate the path loss and the direction of arrival. An accurate reconstruction of the scenario has been also carried out using a laser scanner.

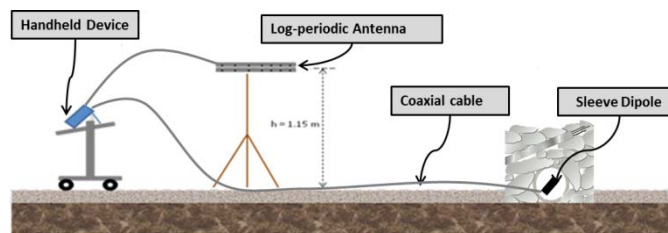


FIG. 6. Measurement setup in Onna.

TABLE I PATH LOSS RESULTS FOR THE ONNA SITE.

Dist. [m]	Vertical Polarization		Horizontal Polarization	
	PL [dB]	Std Dev.	PL[dB]	Std Dev.
12.9	81.37	2.93	74.86	2.32
16.1	77.93	2.18	84.54	6.87
10.2	70.73	1.94	68.73	1.39
14.7	87.53	4.43	82.69	2.24
19.1	76.40	1.39	83.04	2.54
29.0	86.03	3.45	90.06	2.24
28.0	90.80	3.76	90.81	4.89
27.0	99.72	2.54	105.65	4.46

ACKNOWLEDGEMENTS

The authors wish to thank the Italian Firefighters, Geomatics Laboratory of University of L’Aquila, A. Ambrosini, M. Feliziani and E. Rosciano, for the technical cooperation and the Carispaq Bank Foundation for the financial support to the Research Project “Laboratory for the development of RFID systems to search survivors buried under rubble of natural disasters”.

REFERENCES

- [1] Takemura, F. Enomoto, M. Denou, K. Erbatur, K. Zweirs, U. Tadokoro, S., “Proposition of a human body searching strategy using a cable-driven robot at major disaster”, Proceedings IEEE/RSJ International Conference on Intelligent Robots and Systems, 2004. (IROS 2004), Vol. 2, 2004, pp. 1456 – 1461.
- [2] Lidicky, L., “Fourier Array Processing for Buried Victims Detection Using Ultra Wide Band Radar with Uncalibrated Sensors”, IEEE International Geoscience and Remote Sensing Symposium, (IGARSS) 2008, Vol. 2, pp. 831-834.
- [3] K.M. Chen, Y. Huang, J. Zhang, and A. Norman, “Microwave Life-Detection Systems for searching Human Subjects Under Earthquake Rubble or Behind Barrier”, IEEE Trans. Biomedical Engineering, Vol. 27, no. 1, 2000, pp. 105-112.

THE ROLE OF INTERNAL FIELD APPROXIMATION FOR SCATTERING FROM LAYERED ROUGH INTERFACES

P. Imperatore⁽¹⁾, A. Iodice⁽²⁾, D. Riccio⁽²⁾

⁽¹⁾ Istituto per il Rilevamento Elettromagnetico dell'Ambiente, Italian National Research Council (CNR), 80124 Napoli, Italy

⁽²⁾ Department of Biomedical, Electronic and Telecommunication Engineering, University of Naples "Federico II", 80125 Napoli, Italy

imperatore.p@irea.cnr.it

Abstract

In this paper, the existing procedure to obtain the VPRT solution for scattering from rough multilayers is reformulated relying on a more physically sound way, avoiding the employing of the distribution theory. This also permits to shed light on the meaning of the involved approximation. Indeed, the "internal field approximation", arising in the context of electromagnetic cavities, is also implied.

Index Terms – Layered media, rough interfaces, electromagnetic scattering.

I. INTRODUCTION

Wave field scattered by layered rough media can be analytically treated by successfully employing appropriate perturbative formulations. In order to deal with layered structures with an arbitrary number of rough interfaces, two conceptually different approaches have been recently developed: The Boundary Perturbation Theory (BPT) [1] and the Volumetric-Perturbative Reciprocal Theory (VPRT) [2]. They employ different strategies to provide relevant closed-form solutions to the scattering problem. In this paper, we present a different formulation of the VPRT; in particular, we avoid the relevant perturbative expansion (see eq.(5)). This renders the procedure certainly longer, but also more physically sound, because it avoids the use of Dirac's delta function and distribution theory, allowing us recognizing that the approximation implied by the gently rough assumption is slightly different from the usual Born one. Indeed, the "internal field approximation", arising in the context of electromagnetic cavities, is also implied. Accordingly, we demonstrate that the analytical development which does not explicitly invoke the internal field approximation, is also susceptible of an interesting interpretation in terms of internal field, which is consistent with the gently rough assumption. The discussion is applied to the general case of a rough multilayer, which includes the case of rough surface as a particular case.

I. PERTURBATIVE FORMULATION

The VPRT formulation [2] considers a perturbation pertinent to the dielectric properties of the layered structure:

$$\varepsilon(\mathbf{r}_\perp, z) = \varepsilon_0 + \sum_{m=0}^{N-1} (\varepsilon_{m+1} - \varepsilon_m) \mathcal{U}(-z - d_m + \zeta_m(\mathbf{r}_\perp)), \quad (1)$$

$\mathcal{U}(\cdot)$ being the *Heaviside's* unit step function. Thus the rough multilayered can be modelled via an unperturbed medium with relative permittivity

$$\varepsilon^{(0)}(\mathbf{r}) = \varepsilon^{(0)}(z) = \varepsilon_0 + \sum_{m=0}^{N-1} (\varepsilon_{m+1} - \varepsilon_m) \mathcal{U}(-z - d_m), \quad (2)$$

to which a perturbation $\delta\varepsilon(\mathbf{r})$ is applied, so that $\varepsilon(\mathbf{r}) = \varepsilon^{(0)}(z) + \delta\varepsilon(\mathbf{r})$. Accordingly, the scattering problem is then treated by adopting suitable volumetric current distributions. As demonstrated in [3] the scattered field \mathbf{E}^s , at a generic position \mathbf{r}_0 in the upper half-space, can be written as

$$\mathbf{E}^s(\mathbf{r}_0) \cdot \hat{t} = -j \frac{k_0}{J\eta_0} \iiint_V \overline{\mathbf{E}}^{(0)}(\mathbf{r}) \cdot \delta\varepsilon(\mathbf{r}) \mathbf{E}(\mathbf{r}) d\mathbf{r}, \quad (3)$$

where $\overline{\mathbf{E}}^{(0)}$ is the (unperturbed) field radiated in the unperturbed medium by an auxiliary (fictitious) source $\overline{\mathbf{J}}(\mathbf{r}) = \hat{t} J \delta(\mathbf{r} - \mathbf{r}_0)$, located at \mathbf{r}_0 , $\delta(\cdot)$ being the *Dirac* delta function; k_0 and η_0 are the propagation constant and intrinsic impedance of vacuum, respectively; V is a volume enclosing all the sources. In the regime of small $\delta\varepsilon(\mathbf{r})$, the field $\mathbf{E}(\mathbf{r})$ in the integrand, see Eq.(3), can be estimated by the corresponding unperturbed field $\mathbf{E}^{(0)}(\mathbf{r})$, so that the scattered field $\mathbf{E}^{(1)}(\mathbf{r})$ turns out to be:

$$\mathbf{E}^{(1)}(\mathbf{r}_0) \cdot \hat{t} = -j \frac{k_0}{J\eta_0} \iiint_V \overline{\mathbf{E}}^{(0)}(\mathbf{r}) \cdot \delta\varepsilon^{(1)}(\mathbf{r}) \mathbf{E}^{(0)}(\mathbf{r}) d\mathbf{r}, \quad (4)$$

with

$$\delta\varepsilon^{(1)}(\mathbf{r}) = \left. \sum_{m=0}^{N-1} \frac{\partial \delta\varepsilon(\mathbf{r})}{\partial \zeta_m} \right|_{\zeta_m=0} \zeta_m = \sum_{m=0}^{N-1} (\varepsilon_{m+1} - \varepsilon_m) \zeta_m(\mathbf{r}_\perp) \delta(-z - d_m). \quad (5)$$

Equations (4) allows us evaluating the first-order scattered field from the knowledge of the medium perturbation $\delta\varepsilon^{(1)}$ and the two (unperturbed) field expressions, $\mathbf{E}^{(0)}(\mathbf{r})$ and $\overline{\mathbf{E}}^{(0)}$, respectively, radiated by actual and auxiliary (fictitious) sources in the unperturbed medium. The closed form solution obtained starting from eqs.(4)-(5) is introduced in[2].

II. INTERNAL FIELD APPROXIMATION

We reformulate the procedure to obtain the final VPRT closed form field expression from eq.(4). In particular, we avoid the perturbative expansion of $\delta\varepsilon(\mathbf{r})$ in eq.(5).

$\mathbf{E}(\mathbf{r}_\perp, z) \cong \mathbf{E}^{(0)}(\mathbf{r}_\perp, z)$; but it is intuitive that a better estimation of the actual field $\mathbf{E}(\mathbf{r})$ inside the perturbation volume V_m^+ can be obtained by considering the unperturbed field $\mathbf{E}^{(0)}$ just beneath the unperturbed interface: $\mathbf{E}(\mathbf{r}_\perp, z) \cong \mathbf{E}_{m+1}^{(0)}(\mathbf{r}_\perp, -d_m^-)$. This is sometimes referred to as “internal field approximation”. In addition, in compliance gently rough interface assumption, the approximation $\bar{\mathbf{E}}^{(0)}(\mathbf{r}) \cong \bar{\mathbf{E}}_m^{(0)}(\mathbf{r}_\perp, -d_m^+)$ can be also made inside the perturbation volume V_m^+ . Hence, we can write

$$\delta\varepsilon_m^+ \iint d\mathbf{r}_\perp \int_0^{\zeta_m^+} dz \bar{\mathbf{E}}^{(0)}(\mathbf{r}_\perp, z) \cdot \mathbf{E}(\mathbf{r}_\perp, z) \cong \delta\varepsilon_m^+ \iint d\mathbf{r}_\perp \int_0^{\zeta_m^+} dz \bar{\mathbf{E}}_m^{(0)}(\mathbf{r}_\perp, -d_m^+) \cdot \mathbf{E}_{m+1}^{(0)}(\mathbf{r}_\perp, -d_m^-). \quad (8)$$

Likewise, a better estimation of the actual field $\mathbf{E}(\mathbf{r})$ inside the perturbation volume V_m^- can be obtained by considering the unperturbed field $\mathbf{E}^{(0)}$ just above the unperturbed interface: $\mathbf{E}(\mathbf{r}_\perp, z) \cong \mathbf{E}_m^{(0)}(\mathbf{r}_\perp, -d_m^+)$. In addition, inside the perturbation volume V_m^- the approximation $\bar{\mathbf{E}}^{(0)}(\mathbf{r}) \cong \bar{\mathbf{E}}_{m+1}^{(0)}(\mathbf{r}_\perp, -d_m^-)$ can be made. Hence, we can write:

$$\delta\varepsilon_m^- \iint d\mathbf{r}_\perp \int_{\zeta_m^-}^0 dz \bar{\mathbf{E}}^{(0)}(\mathbf{r}_\perp, z) \cdot \mathbf{E}(\mathbf{r}_\perp, z) \cong \delta\varepsilon_m^- \iint d\mathbf{r}_\perp \int_{\zeta_m^-}^0 dz \bar{\mathbf{E}}_{m+1}^{(0)}(\mathbf{r}_\perp, -d_m^-) \cdot \mathbf{E}_m^{(0)}(\mathbf{r}_\perp, -d_m^+). \quad (9)$$

As a result, substituting (8) and (9) into equation (7), and taking into account that $\zeta_m^+ + \zeta_m^- = \zeta_m$, and $\mathbf{E}_{m+1}^{(0)}(\mathbf{r}_\perp, -d_m^-) = [\hat{x}\hat{x} + \hat{y}\hat{y} + \hat{z}\hat{z}(\varepsilon_m/\varepsilon_{m+1})]\mathbf{E}_m^{(0)}(\mathbf{r}_\perp, -d_m^+)$, whence

$$\begin{aligned} \mathbf{E}^{(1)}(\mathbf{r}_0) \cdot \hat{t} &= -j \frac{k_0}{J\eta_0} \iiint_V \bar{\mathbf{E}}^{(0)}(\mathbf{r}) \cdot \delta\varepsilon(\mathbf{r}) \mathbf{E}^{(0)}(\mathbf{r}) d\mathbf{r} \\ &= -j \frac{k_0}{J\eta_0} \sum_{m=0}^N (\varepsilon_{m+1} - \varepsilon_m) \iint d\mathbf{r}_\perp \zeta_m(\mathbf{r}_\perp) \bar{\mathbf{E}}_m^{(0)}(\mathbf{r}_\perp, -d_m^+) \cdot \mathbf{E}_{m+1}^{(0)}(\mathbf{r}_\perp, -d_m^-) \end{aligned} \quad (10)$$

which is essentially the same conclusion we directly obtained in [2] via a proper perturbative expression for $\delta\varepsilon(\mathbf{r})$ (see eq.(33) of [2]). Accordingly, we have demonstrated that the development in [2], which does not explicitly invoke the internal field approximation, is also susceptible of an interesting interpretation in terms of internal field, which is consistent with the gently rough assumption.

REFERENCES

- [1] P. Imperatore, A. Iodice, D. Riccio, “Boundary Perturbation Theory For Scattering in Layered Rough Structures” in *Passive Microwave Components and Antennas* (Ed. by V. Zhurbenko), INTECH, April 2010, pp. 1-25, ISBN 978-953-307-083-4.
- [2] P. Imperatore, A. Iodice, D. Riccio, “Volumetric-Perturbative Reciprocal Formulation for Scattering from Rough Multilayers”, *IEEE Trans. Antennas and Propag.*, vol.59, no.3, pp. 877-887, 2011.
- [3] P. Imperatore, A. Iodice, D. Riccio, “Consistency and Validity of Perturbative Formulations for Scattering from Rough Multilayers”, *IEEE Trans. Antennas and Propag.*, vol.60, no.4, pp.2019–2027, April 2012.

**ADVANCES ON INVERSE SCATTERING METHODOLOGIES AND
APPLICATIONS @ ELEDIA RESEARCH CENTER**

M. Carlin, L. Manica, G. Oliveri, L. Poli, P. Rocca, and A. Massa

ELEDIA Research Center @DISI, University of Trento
Via Sommarive 5, I-38123 Trento, Italy
andrea.massa@ing.unitn.it

Abstract

A concise overview of the most recent advances on the inverse scattering techniques developed at the ELEDIA Research Center of the University of Trento is reported. Different approaches comprising Evolutionary Algorithms and Iterative Multi-Resolution Subspace-Optimization Techniques are discussed. The use of the Compressive Sensing strategies is also considered as a suitable paradigm for the regularization of “sparse” microwave imaging problems. Some representative numerical examples are reported to assess the features of the discussed methods.

Index Terms– Linear Arrays, Array Synthesis, Autocorrelation.

I. INTRODUCTION

The problem of retrieving the dielectric profile of unknown objects starting from non-invasive electromagnetic measurements has a great importance in several applications including non-destructive-testing/non-destructive-evaluation, subsurface prospecting, and biomedical imaging [1]-[4]. Unfortunately, the associated inverse scattering problems are difficult to be solved because of their non-linearity and ill-posedness [5].

In the last two years, several research activities have been developed at the ELEDIA Research Center of the University of Trento with the aim of effectively solving such issues in different applicative domains. More in detail, global optimization strategies based on Evolutionary Algorithms [6][7] have been proposed and applied to mitigate the local minima issues caused by the non-linearity of inverse scattering problem [5]. Moreover, the use of subspace-based formulations has been considered in conjunction with multi-resolution strategies to address the ill-posedness of “contrast-source” inverse scattering problems [8].

More recently, the exploitation of Bayesian techniques coupled with sparseness regularization procedures has been proposed to counteract the ill-conditioning of sparse inverse problems [9].

This work is aimed at concisely reviewing the above advances discussing the features and advantages of each one of them in comparison with state-of-the-art methodologies.

II. INVERSION TECHNIQUES BASED ON EVOLUTIONARY ALGORITHMS

Evolutionary Algorithms (*EAs*) are stochastically-evolving techniques whose mechanisms are inspired by processes actually taking place in nature [6][7]. Thanks to their intrinsic capability to sample the solution space of arbitrary non-linear functionals in an efficient way, they have been adopted to solve several inverse scattering problems. In this context, members of the ELEDIA Research Center have proposed and developed *competitive* *EAs*, including Genetic Algorithms and Differential Evolution methods, as well as *cooperative* *EAs*, including the Particle Swarm algorithm and the Ant Colony Optimization [6][7]. These hill-climbing approaches have been selected because of the following features: (a) they do not require the differentiability of the cost function, (b) *a-priori* information on the solution can be easily introduced into the optimization procedure, (c) the values of the unknowns can be real, integer, or can be represented by a coded representation of the same unknowns, and (d) they can be easily integrated with deterministic methods based on gradient descent to improve the convergence [6][7].

III. MULTI-RESOLUTION SUBSPACE-OPTIMIZATION APPROACHES

Contrast source (*CS*)-formulation [10] techniques have received much attention due to the higher reconstruction accuracies and robustness which they allow with respect to the “contrast field” (*CF*) formulations of inverse scattering problems. In this framework, a subspace optimization method (*SOM*) has been recently introduced as a complement to the existing approaches [8]. In this technique, the contrast source is subdivided in a “deterministic” part, which is computed through singular value decomposition (*SVD*), and an “ambiguous” one, whose amplitude is determined by minimizing a cost functional including both “data” and “state” terms [8].

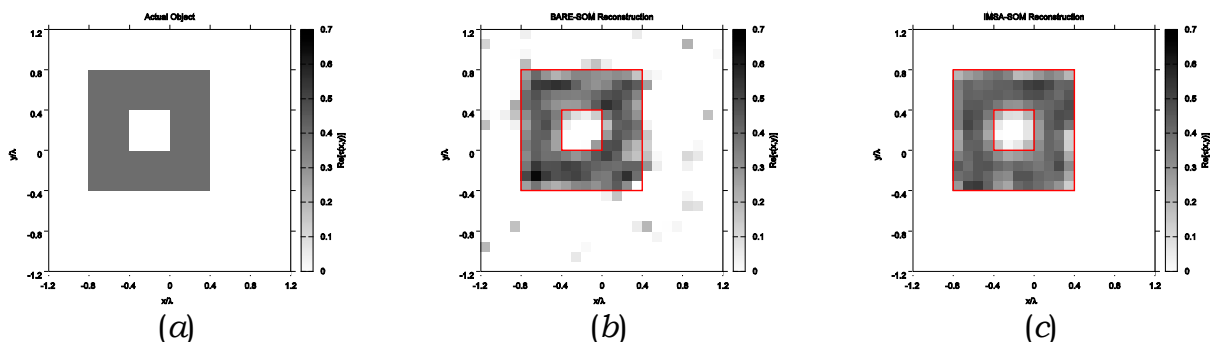


FIG. 1– [Hollow Cylinder, SNR=10 dB] Actual (a) and retrieved τ by (b) BARE-SOM and (c) IMSA-SOM.

The SOM method has been shown to share several merits of CSI-based inversion techniques, while also allowing faster convergences [8]. However, despite these interesting features, such an approach presents also some limitations when dealing with large solution spaces [8]. Indeed, it can yield to poor performances if several ‘local minima’ are at hand, since it is based on a deterministic minimization technique [8]. To overcome this and related drawbacks, the integration of a multi-focusing strategy, namely the iterative multi-scaling approach (*IMSA*), with the *SOM* method has been recently proposed and validated by members of the ELEDIA Research Center [8]. Indeed, the arising *IMSA-SOM* technique has been shown to achieve an increased effectiveness and accuracy in comparison with the state-of-the-art *SOM* approach [8]. As a representative numerical example, the reconstruction of a lossless hollow scatterer [Fig. 1(a)] by means of a standard *SOM* method [*BARE-SOM* - Fig. 1(a)] and by the *IMSA-SOM* approach [Fig. 1(c)] confirm that although both methods are able to identify the presence of a single object, the multi-focusing method yields to an higher accuracy in terms of retrieved contrast. Moreover, thanks to its zooming procedure, the *IMSA-SOM* completely avoids artifacts outside the object support, unlike the *BARE-SOM* [Fig. 1(b) vs. 1(c)].

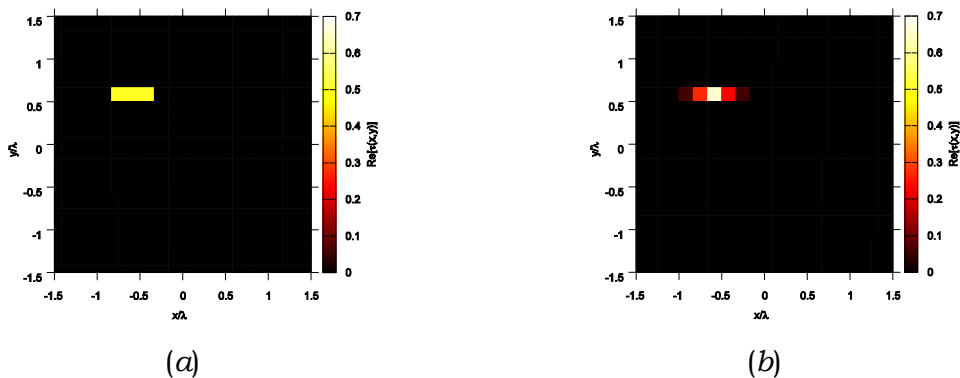


FIG. 2– Compressive Sensing Inversion [Line Object - $\tau=0.5$, SNR=5 dB] – Actual object (a) and BCS retrieved profiles (b).

IV. COMPRESSIVE SENSING STRATEGIES

Appraisal methodologies have been introduced to exploit the available information on the scattering process/unknowns in order to quantitatively retrieve the unknown objects’ features by means of significantly reduced computational resources. In this framework, members of the ELEDIA Research Center have recently proposed the exploitation of Compressive Sensing approaches to suitably comprise *a-priori* knowledge on the scatterers’ sparseness (either intrinsic or obtained thanks to a proper representation of the unknowns) [9]. More

specifically, the use of Bayesian formulations coupled with suitable sparseness-regularized formulations (i.e., Bayesian Compressive Sensing - *BCS*) have been investigated, and their effectiveness in the solution of 2D scattering problems in terms of reliability, effectiveness, and robustness to the noise has been shown [9]. To illustrate the effectiveness of such a technique also in low *SNR* scenarios, the retrieval of a non-homogeneous sparse cylinder with a “line” profile [Fig. 2(a)] by means of a 2D *CSI*-based *BCS* technique when *SNR*=5 dB is reported [Fig. 2(b)].

V. CONCLUSIONS

A review of the current activities carried out within the framework of inverse scattering approaches and techniques at the ELEDIA Research Center is presented. Different methodologies developed in the last two years (including EAs, IMSA-SOM, and *BCS*) are discussed, and some representative result is reported.

REFERENCES

- [1] D. Lesselier and T. Habashy, “Special issue on ‘Electromagnetic imaging and inversion on the Earth’s subsurface’,” *Inverse Probl.*, vol. 16, no. 5, Oct. 2000.
- [2] W. C. Chew and D. Lesselier, “Special issue on ‘Electromagnetic characterization of buried obstacles’,” *Inverse Probl.*, vol. 20, no. 6, pp. S1–S15, Dec. 2004.
- [3] T. Lasri and R. Zoughi, “Special issue on “Advances and applications in microwave and millimeter wave nondestructive evaluation”,” *Subsurf. Sens. Technol. Appl.*, vol. 2, no. 4, pp. 435–451, Oct. 2001.
- [4] S. Caorsi, A. Massa, M. Pastorino, and A. Rosani, “Microwave medical imaging: Potentialities and limitations of a stochastic optimization technique”, *IEEE Trans. Microwave Theory Tech.*, vol. 52, no. 8, pp. 1909-1916, 2004.
- [5] T. Isernia, V. Pascazio, R. Pierri, “On the local minima in a tomographic imaging technique,” *IEEE Trans. Geosci. Remote Sens.*, vol. 39, no. 7, pp. 1596-1607, Jul. 2001.
- [6] P. Rocca, M. Benedetti, M. Donelli, D. Franceschini, and A. Massa, “Evolutionary optimization as applied to inverse scattering problems,” *Inverse Problems*, vol. 25, no. 12, pp. 1-41, Dec. 2009.
- [7] P. Rocca, G. Oliveri, and A. Massa, “Differential Evolution as applied to electromagnetics,” *IEEE Antennas and Propagation Magazine*, vol. 53, no. 1, pp. 38-49, Feb. 2011.
- [8] G. Oliveri, Y. Zhong, X. Chen, and A. Massa, “Multi-resolution subspace-based optimization method for inverse scattering,” *Journal of Optical Society of America A*, vol. 28, no. 10, pp. 2057-2069, October 2011.
- [9] G. Oliveri, P. Rocca, and A. Massa, “A Bayesian Compressive Sampling-based inversion for imaging sparse scatterers,” *IEEE Transactions on Geoscience and Remote Sensing*, vol. 49, no. 10, pp. 3993-4006, October 2011.
- [10] P. M. van den Berg and A. Abubakar, “Contrast source inversion method: State of art,” *Progress Electromagn. Res.*, vol. 34, pp. 189–218, 2001.

A NEW FRAMEWORK FOR QUANTITATIVE INVERSE SCATTERING

L. Di Donato⁽¹⁾, I. Catapano⁽²⁾, L. Crocco⁽²⁾, T. Isernia⁽¹⁾

⁽¹⁾ DIMET – University Mediterranea di Reggio Calabria
Via Graziella, Loc. Feo di Vito, 89122 Reggio di Calabria, Italy
loreto.didonato, tommaso.isernia@unirc.it

⁽²⁾ IREA – Consiglio Nazionale delle Ricerche
Via Diocleziano, 80124 Napoli, Italy
catapano.i, crocco.l@irea.cnr.it

Abstract

In order to improve the accuracy and robustness of inverse scattering solution procedures, we introduce and address a new framework which is based on suitable ‘synthetic’ experiments. These latter, inspired and driven from the physical meaning of the Linear Sampling Method, allow to take advantage from some expected properties of the internal fields (and equivalent currents), thus allowing to simplify and speed up the inversion process. The broad applicability of the LSM allows to deal with a very wide class of unknown scatterers.

Index Terms – Inverse scattering, Linear Sampling Method, Microwave imaging.

I. INTRODUCTION

The estimation of morphologic and electromagnetic properties of an unknown scenario from the field it scatters when probed by means of known incident fields is relevant to many non-invasive imaging applications. However, such a goal requires to tackle a non-linear and ill-posed inverse problem, in which non trivial efforts are required to avoid the occurrence of ‘false solutions’ and to come to solutions as accurate as possible.

In this communication, an original application of the linear sampling method (LSM) [1] is given to address in a new fashion the quantitative inverse scattering problem. LSM is a popular approach which allows to retrieve the geometrical features of unknown targets. In this respect, it trades the difficulty of the inverse scattering problem with the possibility to gain information only about the geometrical features of the targets (thus neglecting its electromagnetic features). As a result, it is based on the solution of a linear exact equation, namely the far field equation (FFE), that, although still ill-posed, is free from false solutions [1,2]. The method is very effective in imaging the shape of unknown targets since it can deal with a large class of scatterers, involving non-weak, extended and not-convex or not-simply connected ones, and has a negligible computational burden.

On the other hand, the information explicitly gained from the LSM (i.e., the support of the scatterer) is not the only one which can be achieved. In fact, by relying on the physical meaning of the method [3], additional information can be gained, which allows to introduce a new

convenient procedure for quantitative imaging. In particular, ‘synthetic’ scattering experiments can be introduced such that the internal fields (and contrast sources) turn out to be localized (and circularly symmetric) around given sampling points. As internal fields (or induced currents) are one of the unknowns of inverse scattering problems, the exploitation of these expected properties allows indeed decisive advantages with respect to more usual inversion approaches. In fact, both accuracy and robustness against false solutions, as well as computational burden, take advantage from such a new framework.

II. BASICS OF THE LSM

Assuming the standard 2D scalar case for the electric field (TM polarization), the LSM consists in solving, in each point \underline{r}_s of an arbitrary grid which samples the investigated domain D , an auxiliary linear equation, namely the *far-field* equation (FFE):

$$\int_{\Gamma} F(\underline{R}_{\phi}, \theta_v) \iota(\theta_v, \underline{r}_s) d\theta = \frac{1}{j4} H_0^{(2)}(|\underline{r}_s - \underline{R}_{\phi}|) \quad (1)$$

In eq. (1), Γ denotes the measurement curve, \underline{R} and ϕ represent the distance from the center of D and the angular direction which identifies the measurement location, and θ_v denotes the n -th unitary incident field that probes the domain D . Under the above assumptions, $F(\underline{R}_{\phi}, \theta_v)$ is the multiview-multistatic scattered field data matrix, $\iota(\theta_v, \underline{r}_s)$ is the problem unknown, and the right hand side is the field radiated at the receivers by an elementary source located in sampling point. According to the LSM theory the FFE is ill-posed due to the properties of the kernel F [1] so that only a regularized solution can be sought. In doing so, one can conveniently exploit the singular value decomposition (SVD) of a matrix operator and the Tikhonov regularization to find:

$$\iota(\theta_v, \underline{r}_s) = \sum_{n=1}^{\infty} \frac{\sigma_n}{\sigma_n^2 + \alpha^2} \langle H_0^{(2)}(\underline{r}_s, \underline{R}_{\phi}), \mathbf{w}_n \rangle \mathbf{z}_n \quad (2)$$

wherein $\{\mathbf{w}_n, \sigma_n, \mathbf{z}_n\}$ represents the singular value system of F , α is the weighting regularization coefficient and ‘ \langle, \rangle ’ denotes the scalar product on Γ . The L^2 -norm of the solution (2) assumes high values when \underline{r}_s belongs to the scatterer’s support and low values elsewhere, thus acting as a support indicator when plotted over the sampling grid.

III. THE PROPOSED NEW FRAMEWORK

As extensively discussed in [4], the FFE can be seen as an attempt to recombine for each sampling point \underline{r}_s the scattered field as collected at the measurement locations in such a way to match (in the least square sense) the field radiated by an elementary source herein located. Moreover, due to the regularized nature of the sought solution, such a scattered field is supported by an induced contrast source focused in the neighborhood of the sampling point¹ [3]. This circumstance allows

¹ The regularization prevents to look for high energy super-directive sources.

to interpret the LSM as a focusing strategy of the secondary (or induced) sources. Furthermore, the linear relationship between the scattered fields and the incident ones, reveals that the focusing task corresponds to find a superposition (i.e., a linear combination) of the unitary-amplitude incident fields impinging from the different directions θ_ν such to induce into the target a focused contrast source radiating at the measurement locations just the field at the right hand side of eq.(1).

As a consequence, provided the sought solution fulfils the matching between the two sides of the FFE, it is possible to consider for any sampling point wherein this condition holds, an incident field synthetically build by ruling the primary fields through the FFE's solution, i.e. :

$$\int_{\Gamma} \mathbf{E}_{\text{inc}}(\underline{\mathbf{r}}, \theta_\nu) \iota(\theta_\nu, \underline{\mathbf{r}}_s) d\theta = \mathbf{u}_{\text{inc}}(\underline{\mathbf{r}}, \underline{\mathbf{r}}_s) \quad (3)$$

Such an incident field defines indeed a 'synthetic' scattering experiment where the corresponding internal field (and contrast source) are expected to be circularly symmetric around the sampling point $\underline{\mathbf{r}}_s$.

Now, let us consider a set of synthetic experiments built using a number of different sampling points $\underline{\mathbf{r}}_s$, $s=1, \dots, S$. By using a sufficiently large value of S , and a proper choice of the sampling points, such a set of experiments is fully equivalent to the original scattering experiments with respect to the original information content. In fact, the corresponding scattered fields can be easily computed by combining, according to the $\iota(\theta_\nu, \bullet)$ function, the measured scattered fields corresponding to the original experiments.

Then, while no property of the internal field can be exploited when tackling the original scattering experiments, symmetry properties around the sampling points can be instead exploited when dealing with the synthetic experiments. Saying it in other words, the LSM acts as a pre-processing allowing to perform a 'preconditioning' on the spatial distribution of the internal field unknowns. Moreover, because of the known behavior of the scattered field, some quantitative guess can also be made on the internal fields of the synthetic experiments.

This is in fact the basis of the new convenient quantitative inversion scheme presented and discussed in [4]. In this latter, the total internal fields are approximated by the sum of the incident fields (3) plus a scattered field given by a low pass version of the Green's function at the right hand side of eq. (1) originating at the considered sampling points. Such a novel approach is able to retrieve the dielectric properties of unknown targets for which the usual approximations, as for instance the Born one, cannot be adopted. Indeed such a new approximation takes into account the 'presence' and the 'nature' of the scatterer though a suitable preprocessing step based on the FFE solution.

However, the potential advantages arising from the physical meaning of the FFE (and the corresponding synthetic experiments) are not limited to the above discussed approximation.

In fact, at least a couple of alternative and stimulating possibilities do exist.

First, one can adopt approximation free inversion approaches, such as the one in [5], wherein, however, the contrast source unknowns are now expanded in suitable low dimensional representations reflecting their expected properties.

Second, by virtue of the localized nature of the contrast sources, the behavior of these latter is expected to be ruled by the local value of the contrast function. In fact, contrast source behavior will resemble the (angularly invariant) contrast source in a homogeneous cylinder having the same permittivity as the local value of the unknown target. Then, some analytical expressions of the contrast source behavior as a function of the local value of the contrast is possible, which suggests a number of interesting possibilities.

IV. CONCLUSION

The solution of the LSM, a *qualitative* method exploited (to date) for shape reconstruction of unknown scatterers, offers new opportunities in the solution of quantitative inverse scattering problem as it implicitly enforces a well-known focusing task of the induced currents. As such, through the introduction of convenient synthetic scattering experiments, it allows to gain additional information on the scattering phenomenon, such as the spatial behavior of the internal total field and of the induced contrast sources.

Theoretical details and validation proofs of the different possibilities arising from this framework will be addressed at the conference.

REFERENCES

- [1] D. Colton, H. Haddar, and M. Piana, "The linear sampling method in inverse electromagnetic scattering theory," *Inv. Probl.*, vol. 19, pp. 105–137, 2003.
- [2] T. Isernia, V. Pascazio, and R. Pierri, "On the local minima in a tomographic imaging technique," *IEEE Trans. Geosci. Remote Sens.*, vol. 39, no. 4, pp. 1596-1607, July 2001.
- [3] I. Catapano, L. Crocco, and T. Isernia, "On simple methods for shape reconstruction of unknown scatterers," *IEEE Trans. Antennas Propag.*, vol. 55, no. 5, pp. 1431–1436, May 2007.
- [4] L. Crocco, I. Catapano, L. Di Donato and T. Isernia, "The Linear Sampling Method as a way to quantitative inverse scattering," *IEEE Trans. Antennas Propag.*, vol. 60, no. 4, 1844-1853, April 2012.
- [5] T. Isernia, L. Crocco, and M. D'Urso, "New tools and series for forward and inverse scattering problems in lossy media," *IEEE Geosci. Remote Sens. Lett.*, vol. 1, no. 4, pp. 327–331, October 2004.

Session 11 – Bioengineering II

R. Cicchetti, S. Pisa, E. Pittella, E. PiuZZi, and O. Testa

Analysis and design of a UWB radar for non-invasive breath activity monitoring

P. Russo, V. Mariani Primiani, A. De Leo, and G. Cerri

Radiated emission and susceptibility of breath monitoring system based on UWB pulses in spacecraft modules

G. Biffi Gentili, and M. Linari

A novel thermo-ablative microwave multi-applicator system

A. Denzi, F. Camera, A. Paffi, C. Merla, F. Apollonio, P. Marracino, G. d’Inzeo, and M. Liberti

Effects of nanosecond pulsed electric field on the activity of a Hodgkin and Huxley neuron model

A. Doria, G. P. Gallerano, E. Giovenale, G. Messina, A. Ramundo Orlando, and I. Spassovsky

Electromagnetic pulser for the investigation of cell membranes

ANALYSIS AND DESIGN OF A UWB RADAR FOR NON-INVASIVE BREATH ACTIVITY MONITORING

P. Bernardi⁽¹⁾, R. Cicchetti⁽¹⁾, S. Pisa⁽¹⁾, E. Pittella⁽¹⁾, E. Piuzzi⁽¹⁾,
and O. Testa⁽¹⁾

⁽¹⁾ Department of Information Engineering, Electronics and
Telecommunications, Sapienza University of Rome
Via Eudossiana 18, 00184 Rome, Italy

pisa@die.uniroma1.it

Abstract

The design and realization of a ultra wideband (UWB) radar for non-invasive breath activity monitoring is presented. The radar structure is described and the design and realization of its various subsystems is shown. Finally, measurement results are presented, evidencing a sensitivity suitable to monitor the breath activity by detecting thorax movements.

Index Terms – Biomedical Monitoring, Breath Activity, UWB Radar Systems.

I. INTRODUCTION

Continuous monitoring of breath activity is of great importance for the diagnosis of many respiratory apparatus pathologies and for vital functions monitoring. The breath monitoring is usually performed either by means of inductive bandages or by airtight jackets, requiring a direct contact with the patient. By using the microwave electromagnetic radiation, it is possible to monitor any physiological activity, involving movements of parts of the body, carrying out a non-invasive monitoring. The systems proposed in literature for the remote sensing are mainly based on Doppler [1] or ultra wideband (UWB) [2]-[3] radar.

In this paper a UWB radar is designed, optimized, realized and tested. The introduced improvements with respect to the design proposed in [2] consist in the use of a very fast pulse generator based on a step recovery diode and in the implementation of a receiver based on very fast zero-bias Schottky diodes. Moreover, a suitable UWB drop-shaped antipodal dipole antenna is used to reduce the dispersive effects of the radiated field.

The paper is organized as follows. Section II describes the UWB radar block diagram, while in Section III the design and realization of the radar together with measurements on the various subsystems and on the whole prototype are discussed. Finally, in Section IV, some conclusions are drawn.

II. UWB RADAR BLOCK DIAGRAM

Fig. 1 shows a block scheme of the proposed UWB radar. The first block is a square wave generator whose output signal is split to obtain a square wave and its delayed replica. The repetition rate (RR = 1-10 MHz) generator drives a UWB generator that produces a monocycle pulse that excites the transmitting antenna and, once reflected by the human thorax, is captured by the receiving one. The RR delayed output drives a Gaussian pulse generator whose output acts as a strobe signal for the receiver. If this pulse, delayed of a time equal to the antenna-target round trip travel time, is present at the receiver strobe input together with the echo signal, the receiver output changes with the thorax movements. The receiver output is finally filtered and amplified.

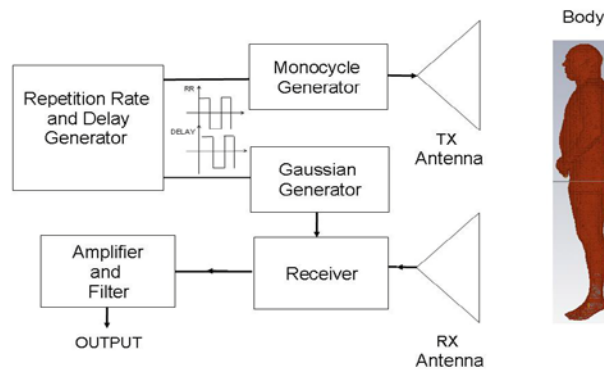


FIG. 1 – Block scheme of the UWB radar system.

III. UWB SUBSYSTEMS DESIGN AND REALIZATION

In this section a general description of the design and the realization of the subsystems previously described, together with some measurement results, are presented.

The repetition rate generator is composed by a relaxation oscillator based on the inverting Schmitt trigger 74HC14. The pulse repetition rate can be set from 1 to 10 MHz and the delayed output signal is obtained by means of a RC delay cell (delay range: 0 - 50 ns). The levels of the output square signal are ± 3 V with rise and fall time less than 5 ns.

The photo of the realized Gaussian generator, used to produce the strobe signal, is shown in Fig. 2a. The circuit consists of a step recovery diode (SRD DVB-6723) that, driven by the repetition rate generator signal, gives rise to a step with a fall time lower than 200 ps. A short-circuited transmission line converts the step into a pulse. A Schottky diode HSMS-2850 has been added to the circuit in order to reduce the pulse ringing, shaping the pulse and improving the symmetry. The Gaussian generator has been realized on a Rogers RO4003 substrate having relative permittivity $\epsilon_r = 3.38$ and thickness $h = 0.508$ mm.

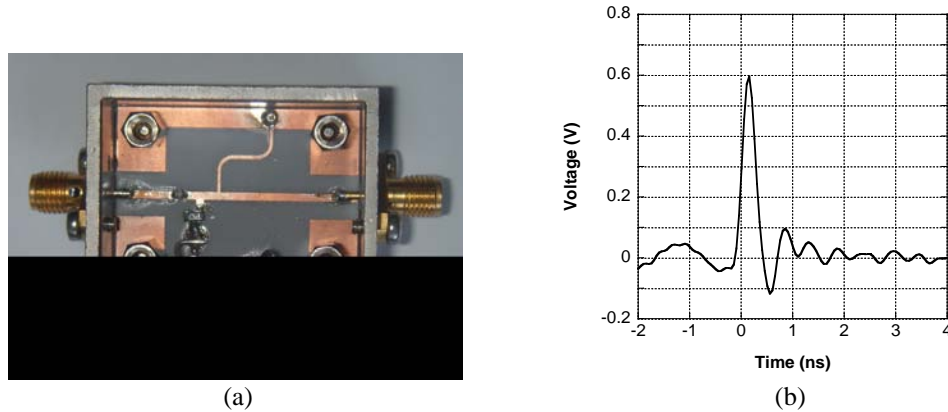


FIG. 2 – (a) Layout of the UWB Gaussian generator, (b) time behavior of the generated Gaussian pulse.

Fig. 2b shows the output signal measured by a LeCroy Oscilloscope WavePro 725Zi-A having a 2.5 GHz bandwidth. For the generation of the monocycle signal, a Gaussian pulse is first generated and then its time derivative is achieved by using a RC circuit.

The antennas, adopted for the realization of the radar, are printed planar structures suitably shaped in order to radiate UWB signals. The realized transmitting antenna belongs to the class of small element antennas characterized by a limited occupation area and by a large operating bandwidth with reduced dispersive effects [4]. In addition, this antenna presents a low field emission level in the direction of the feeding line. The geometry of the antenna is depicted in Fig. 3a. For the receiving unit, in order to obtain a balanced field probe, two planar antennas having half-heart shape geometry, have been adopted [5].

The receiver section of the UWB radar employs a “range gating” Schottky sampling diode circuit in which the Gaussian shaped pulse signal is used as strobe signal. In order to improve the receiver signal to noise ratio the circuit is designed to operate in differential mode. The output of the sampling circuit is sent to an integrator with a time constant great enough to allow the summation of many thousands of samples. The receiver adopts a couple of very fast zero bias Schottky diodes HSMS 2850.

The last block of the UWB radar consists of a differential instrumentation amplifier and a filtering unit, designed to increase the output signal in the operative band (0.01 – 10 Hz).

The measurement of the radar output signal obtained moving forward and backward a 30 cm × 30 cm flat metallic screen located about 50 cm far from the antennas is shown in Fig. 3b. As it can be noted from the figure, a total displacement of 2 cm gives rise to a voltage variation of about 10 mV. In conclusion, the realized UWB radar is able to monitor displacements comparable with human thorax movements resulting from the breath activity.

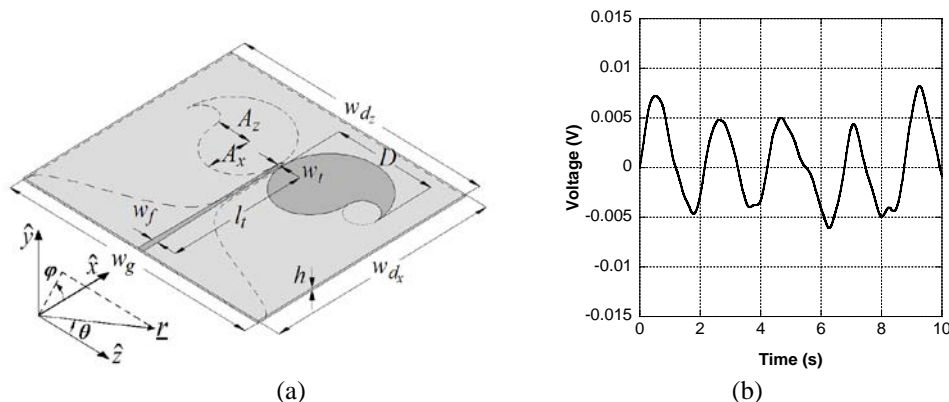


FIG. 3 – (a) Drop-shaped antipodal dipole antenna, (b) time behavior of the signal at the receiver output obtained moving forward and backward a flat metallic screen located about 50 cm far from the antennas.

IV. CONCLUSION

In this paper the design and the realization of a UWB radar for the breath activity monitoring has been presented. The design of the various subsystems, performed by using a commercial CAD tool, has been described. Measurements performed on the realized prototype prove the suitability of the realized UWB radar to monitor the breath activity.

ACKNOWLEDGEMENT

Work supported by the Italian Space Agency (ASI) under the Contract I/009/11/0 “Non Invasive Monitoring by Ultra wide band Radar of Respiratory Activity of people inside a spatial environment (NIMURRA)”.

REFERENCES

- [1] A. D. Droitcour, O. Boric-Lubecke, V. M. Lubecke, J. Lin, and G. T. A. Kovacs, "Range Correlation and I/Q Performance Benefits in Single-Chip Silicon Doppler Radars for Non-contact Cardiopulmonary Monitoring," *IEEE Trans. Microwave Theory Tech.*, vol. 52, pp. 838-848, 2004.
- [2] T.E. McEwan, "Ultra-wideband radar motion sensor," United States Patent 5,361,070, Nov. 1994.
- [3] S. Pisa, P. Bernardi, M. Cavagnaro, E. Pittella, and E. PiuZZi, "A circuit model of an ultra wideband impulse radar system for breath activity monitoring," *International Journal of Numerical Modelling: Elect. Net., Dev. and Fields*, vol.25, pp 46-63, 2012.
- [4] G. Cappelletti, D. Caratelli, R. Cicchetti, and M. Simeoni, "A Low-Profile Printed Drop-Shaped Dipole Antenna for Wide-Band Wireless Applications," *IEEE Trans. Antennas Propag.*, vol. 59, pp. 3526-3535, Oct. 2011.
- [5] E. Pittella, P. Bernardi, M. Cavagnaro, S. Pisa, and E. PiuZZi, "Design of UWB antennas to monitor cardiac activity", *J. Appl. Comput. Electromagn. (ACES)*, vol. 26, no. 4, pp. 267-274, April 2011.

RADIATED EMISSION AND SUSCEPTIBILITY OF BREATH MONITORING SYSTEM BASED ON UWB PULSES IN SPACECRAFT MODULES

P. Russo⁽¹⁾, V. Mariani Primiani⁽¹⁾, A. De Leo⁽¹⁾, G. Cerri⁽¹⁾

⁽¹⁾ Dipartimento di Ingegneria dell'Informazione, Università
Politecnica delle Marche
Via Brecce Bianche, 60131 Ancona, Italy
paola.russo@univpm.it

Abstract

The paper describes some EMC aspects related to a UWB radar for monitoring astronauts breathing activity. Compliance to EMC space standards forces some design aspects, in particular the peak voltage and the pulse waveform, as well as the receiver immunity.

Index Terms – radiated emission, radiated susceptibility, UWB

I. INTRODUCTION

This work is included in a project of ASI, which involves several Italian entities, universities and companies, called NIMURRA, that stands for “Non Invasive Monitoring by Ultra wide band Radar of Respiratory Activity of people inside a spatial environment”. It regards the placement of a UWB radar inside a spatial module to obtain information on the respiration of astronauts. Using a pulse characterized by a very wide bandwidth in a highly resonant environment, which contains electronic instrumentation, it is necessary to consider EMC issues relating to radiated emissions, but also with regard to the susceptibility of the UWB radar itself. The objective of the work is to give some useful information to the designer of the monitoring system that take into account the EMC problem. In particular considering the radiated emission and susceptibility problem we obtain some information on the maximum input signal that can be radiated by the system, and to the maximum electric field level that the system has to tolerate in order to fulfill the EMC standard.

II. EMC SPACE STANDARD

The standard applicable depends on the place where the radar will be placed. In particular two possible modules have been considered: Node 2 of the International Space Station (ISS), and Columbus module. The two modules however have different EMC standard requirements, for this reason at this stage of the project the limits considered are a worst combination between the limits prescribed for the COLUMBUS (COL) [1]

and for the US segment of the ISS [2]. Tests measurement procedures are defined by the MIL-STD 461 [3] and 462 [4].

Fig.1a reports the electric field limits for the radiated emission, and Fig.1b reports the electric field level to be radiated for the susceptibility tests.

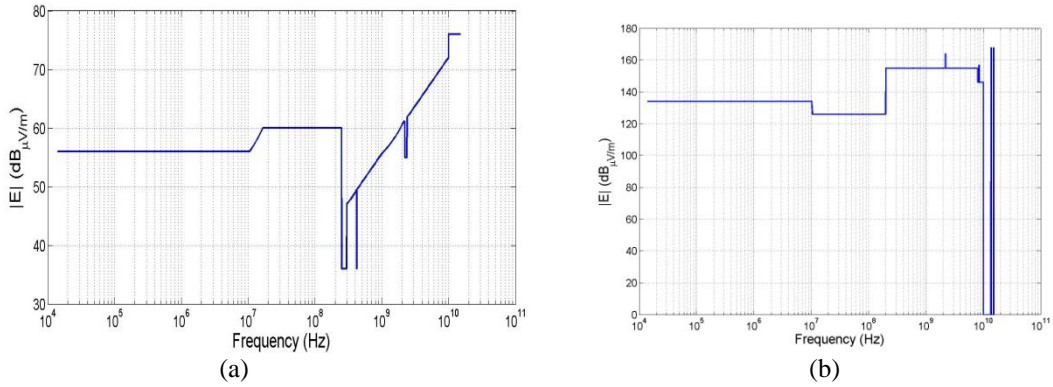


Fig. 1 – Electric field limits (a) and susceptibility levels (b). They are the worst combination between Columbus and Node 2 standards.

III. EVALUATION OF THE MAXIMUM INPUT VOLTAGE

Considering the standard emission level it is possible to calculate the maximum input signal that can be radiated by the antenna. To that purpose, a double ridge antenna placed in an empty space has been analyzed by means of a commercially available electromagnetic simulation software (CST). The applicable standard prescribed that the emission level has to be measured at 1m from the device, consequently a near field simulation is necessary.

The antenna is fed by the voltage pulse reported in Fig. 2a, and gives the electric field pulse reported in Fig. 2b.

After the application of a Fourier Transform, the transmitting transfer function $H(f)$ between the antenna input voltage and the corresponding electric field radiated at 1m is computed. This quantity is useful to recover the voltage spectral density limit $S(f)$ for the UWB pulse applicable to this antenna, in order to fulfill the electric field limits previously shown (Fig.1a):

$$|S(f)| = \frac{|E_{\text{limit}}|}{|H(f)| \cdot \text{RBW}} \quad [\text{V} / \text{Hz}] \quad (1)$$

In (1) we assume that the pulse repetition rate (PRF) is less than the instrument receiver bandwidth (RBW) prescribed by the standard, and so the emission level is proportional to the RBW of the instrument.

Fig. 3 reports the results for the application of (1) when $\text{RBW} = 1 \text{ MHz}$ and for a logarithmic scale representation.

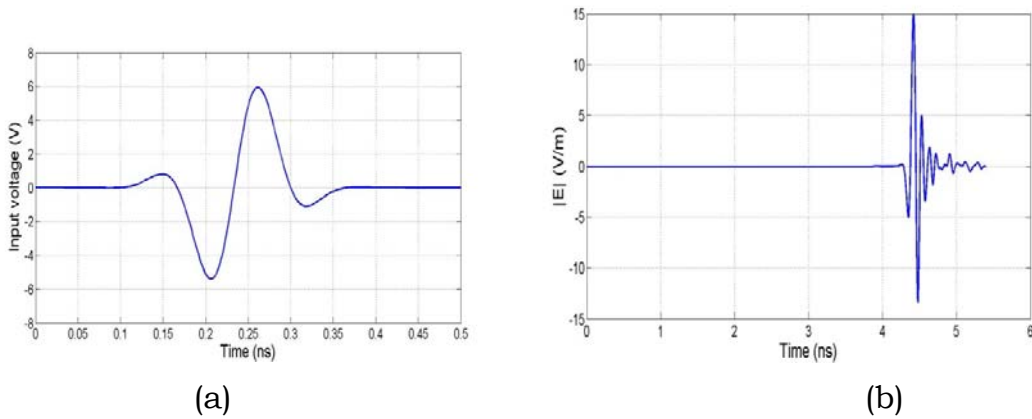


FIG. 2 – Applied voltage pulse (a); Electric field pulse produced at 1 m away from the antenna (b)

The result of Fig. 3 is useful for obtaining the information on the maximum input voltage applicable to the antenna input. For example, let's consider the possible pulses obtained as time derivatives of a Gaussian pulse:

$$p_n(\tau) = C_n \cdot (-1)^n \cdot \frac{1}{(\sigma\sqrt{2})^n} \cdot H_n\left(\frac{\tau}{\sigma\sqrt{2}}\right) \cdot \frac{1}{\sigma\sqrt{2\pi}} e^{-\frac{\tau^2}{2\sigma^2}} \quad (2)$$

where C_n is the amplitude, $H_n(x)$ is the Hermite's polynomial of n-th order.

Considering the first five time derivatives of the Gaussian pulse with $\sigma_1 = 75$ ps, $\sigma_2 = 75$ ps, $\sigma_3 = 60$ ps, $\sigma_4 = 55$ ps, $\sigma_5 = 50$ ps, it is possible to recover the constant C_n in (2) to fulfill the frequency limits of Fig 3. Fig. 4 shows the pulse time histories obtained.

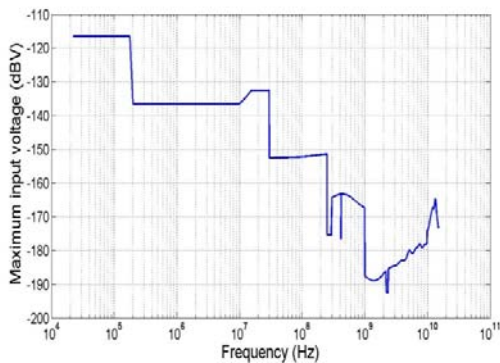


FIG. 3 – Spectral density limits for analyzed antenna input voltage.

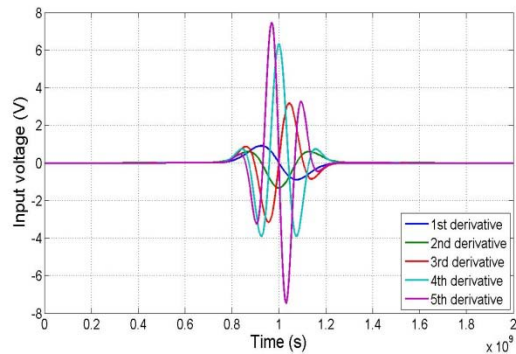


FIG. 4 – Applicable pulse time history for the first five derivatives of the Gaussian pulse.

IV. Maximum voltage induced in the UWB system

In order to make a device immune to the electric field level of Fig. 1b, the voltage received by the antenna during a susceptibility test is

calculated. Considering that the device has to be uniformly radiated by the same electric field level, an incident plane wave is used. Using a procedure similar to section III, the receiving transfer function $R(f)$ of the antenna between the electric field of the impinging plane wave and the corresponding received voltage can be calculated in order to transform the electric field level into the voltage received by the antenna. The receiving transfer function is calculated for the double ridge antenna used before, and the received voltage corresponding to the electric field of Fig. 1b is recovered. (see Fig. 4).

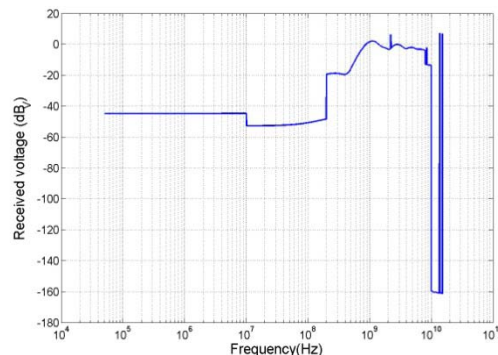


FIG. 4 – Susceptibility voltage level for the double ridge antenna.

The so obtained received voltage can be used by the designer of the monitoring system receiver to verify the front end components hazard and to establish proper countermeasures (limiters or suppressor devices for example).

V. Conclusion

A general procedure to recover useful parameter for the design of a UWB radar system has been presented. The electromagnetic environment and excitation prescribed by the EMC standard are simulated. For future development, more realistic environment and operating condition can be considered. As an example, the simulation of the effect of a disturbing source on the received signal will be useful to develop a robust signal processing algorithm that will be used to retrieve the respiratory rate.

References

- [1] COL-ESA-RQ-014. *Columbus EMC & Power Quality Requirements*. European Space Agency, Directorate of Manned Spaceflight and Microgravity
- [2] SSP 30237 (2011). *Space Station Electromagnetic Emission and Susceptibility Requirements*, NASA Space Station Programme document.
- [3] MIL-STD-461-E “*Requirements for the Control of Electromagnetic Interference Characteristics of Subsystems and Equipment*,” 20 august 1999
- [4] MIL-STD-462-D “*Test Method Standard for Measurement of Electromagnetic Interference Characteristics*”, 20 August 1999.

A NOVEL THERMO-ABLATIVE MICROWAVE MULTI-APPLICATOR SYSTEM

G. Biffi Gentili , M. Linari

Electronics and Telecommunication Department, University of
Florence

Via S. Marta 3, Florence, Italy
guido.biffigentili@unifi.it

Abstract

A novel minimally invasive thermoablative system that utilize an asynchronous array of up to four high efficiency microwave applicators is presented. The tumor ablation volume is optimized by adaptively distributing the available power among multiple applicators.

Index Terms—Thermoablation, Microwave, Applicator, Minimally invasive.

I. INTRODUCTION

In the recent years image-guided thermal ablation therapy in the interventional oncology is gaining attention in virtue of the refinement and significant development of several new, minimally invasive techniques for percutaneous, laparoscopic and intraoperative tumor destruction.

The rationale of the thermal ablation is to destroy the tumor either by heat (hyperthermal ablation) which include radiofrequency (RF), microwave (MW) and optical (Laser) energy sources or by cold (cryoablation or hypothermal ablation).

Thermoablative technologies are very promising for the curative, neoadjuvant and palliative treatments of liver, kidney, prostate, lung, bone and other primary or metastatic tumors. For selected patients these technologies offer a optimal treatment option given their availability in the outpatient setting and low associated morbidity and mortality.

II. MICROWAVE ABLATION

MW ablation represents the more recent addition to the growing armamentarium of the available ablative technologies but is still in a early stage and necessitates substantial methodological and technical improvements to ensure better flexibility, safety and effectiveness. MW ablative technology is also very promising for robotically assisted minimally invasive surgery.

MW tissue heating is mediated by the near field radiation emanating from the tip of a minimally invasive antenna [1] without the necessity of an electrical current passing through the patient's body, as in the RF

ablation technology that requires grounding pads for draining the RF current. The potential benefits of MW technology include higher intratumoral temperatures, larger tumor ablation volumes, faster ablation times, ability to use multiple applicators, optimal heating of cystic masses and less procedural pain [2]. The danger of heating tissue in unwanted areas is also reduced, especially at transition between anatomical structures having different electrical impedance such as near the vessel walls.

To increase coagulation volume multi-applicator approaches have been conceived. Preliminary studies and preclinical experience with multiple small-gauge antennas [3], [4] suggested that MW are highly conducive to the use of the multi-probe technology allowing very accurate tumor targeting through image-guided (robotically assisted) probes placing. Besides the synergistic use of multiple MW antennas in the treatment of a large solitary lesions, the ability to adaptively drive multiple antennas may be useful in preserving blood vessels and in the simultaneous treatment of multiple tumors.

III. THE MULTI-APPLICATOR SYSTEM

The Thermo Ablative Microwave Multi-applicator System (TAMMS) under development has been conceived to evolve from single to multi-applicator technology substantially improving flexibility, safety and effectiveness, in other words “usability”, and at the same time reducing patient discomfort with the following design objectives:

- Fully compliance with European CISPR 11 regulation and 60601-2-6 standard;
- Operation at 2.45 GHz frequency using a single solid-state MW generator with 100 W max total output power;
- Reduced treatment duration (< 10 min.).

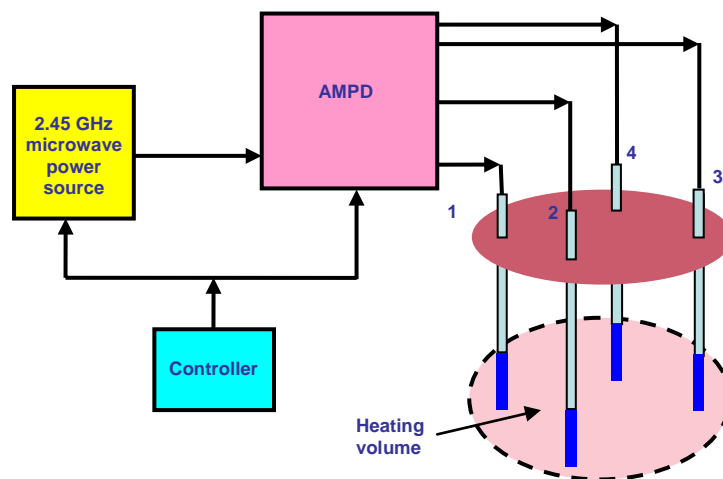


FIG. 1–The Thermo Ablative Multi-applicator System (TAMMS) architecture.

A key device of the new advanced thermo-ablative system is the APDU (Adaptive Power Distribution Unit) that adaptively distributes the available power of the generator among a maximum of four applicators suitably inserted into a solitary tumor or multiple nodules.

Depending on the tumor size, location and other relevant clinical parameters a single applicator or multiple applicator treatment can be planned.

A very accurate image guided 3D tracking of each applicator position and orientation can be obtained by the fusion of EM navigation technologies and image processing software [6], while impedance tomography can be used for internal tumor temperature monitoring.

IV. LOW LOSS APPLICATOR TECHNOLOGY

Existing MW applicators use very small commercial coaxial cables (typically 0.6 to 0.8 mm in diameter) passing inside a 11 to 16 gauge shaft tube to feed the radiating section, that consists of a simple isolated monopole or a couple of circumferential slots. The high power losses of such very miniaturized cables (about 2dB/m) are responsible for the applicator overheating when the input power exceeds a few watts. To maintain shaft temperature below the 40°C limit at high input power, water circulation is forced inside it, thus increasing mechanical complexity and catastrophic failure probability; furthermore radiation efficiency is reduced because part of MW power is wasted in warming the circulating water.

The new low loss applicator technology shown in Fig. 2 (patent pending) allows eliminating water cooling for an input power less than 25 W by substantially reducing cable losses and increasing radiation efficiency.

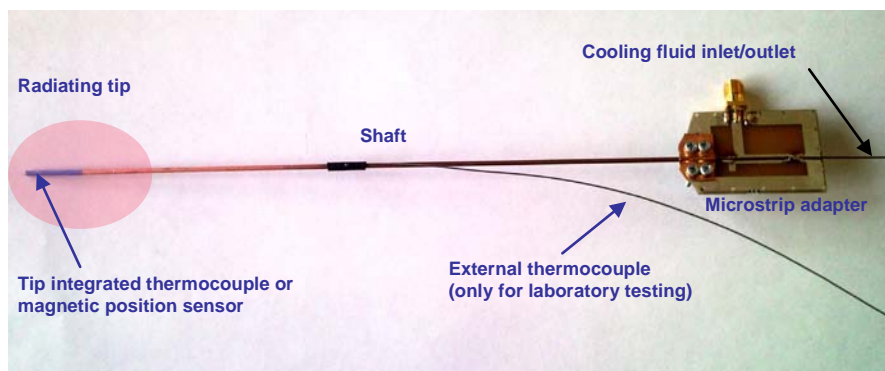


FIG. 2–Prototype of the new 16 gauge low-loss minimally invasive applicator.

V. EXPERIMENTS

Fig. 3. shows the result of a thermoablative ex-vivo procedure performed by employing a couple of 16 gauge high efficiency uncooled applicators immersed inside swine tissue at 25°C initial temperature.

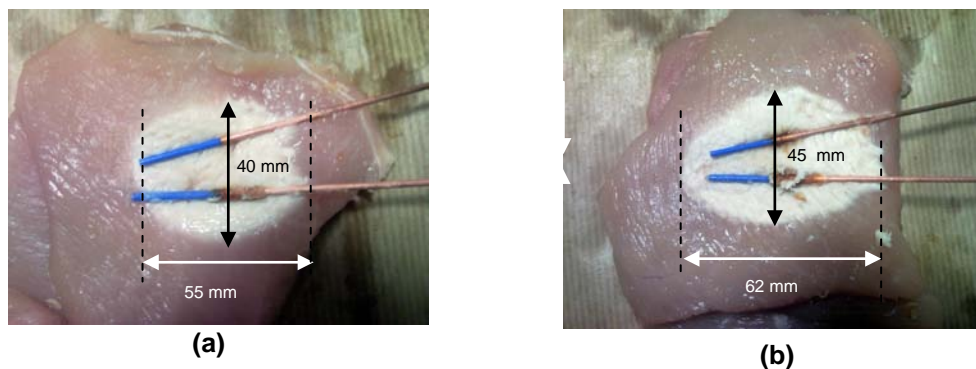


FIG. 3—Thermal ablation in swine ex-vivo tissue obtained by employing a couple of 16 gauge applicators and 40 W total input power with 50% duty cycle; (a) after 5 min., (b) after 8 min.

It is worth noting that to obtain a thermal lesion having the same dimensions of that of Fig. 3a using a single water cooled applicator, about 70 W for 10 min. should be applied.

VI. CONCLUSION

Preliminary experiments confirm that the proposed multi-applicator thermoablative system allows improving overall efficiency, extending the volume of the thermal ablation and reducing the ablation time. Furthermore if the APDU distributes the total power among multiple applicators and the average power for each applicator is maintained less than 25 W, the cooling system could be avoided with great advantages in term of usability, flexibility and procedural safety for the absence of tissue boiling, chimney effects and tissue carbonization.

REFERENCES

- [1] I.Longo, G. Biffi Gentili, M.Cerretelli, N. Tosoratti, "A Coaxial Antenna with Miniaturized Choke for Minimally Invasive Interstitial Heating", *IEEE Trans. On Biomedical Engineering*, vol. 50, no. 1, January 2003.
- [2] Caroline J. Simon et alii, "Microwave Ablation :Principles and Applications", *RadioGraphics* 2005; 25: S69-S83
- [3] Cristopher L. Brace et alii, "Microwave Ablation with Multiple Simultaneously Powered Small-gauge Triaxial Antennas: Results from an in Vivo Swine Liver Model", *Radiology*, 244, 151-156, July 2007.
- [4] Caroline J. Simon et alii, "Interoperative Triple Antenna Hepatic Microwave Ablation", *Interventional Radiology, AJR*:187, October 2006.
- [5] G. Biffi Gentili, M. Linari, "Design and Optimization of a Miniaturized Hyperthermic Microwave Applicator with Integrated Temperature Sensor", *ICHO 10th International Congress on Hyperthermic Oncology*, 9-12 April 2008, Munchen, Germany.
- [6] J. Wood Brandford et alii "Tecnologies for Guidance of Radiofrequency Ablation in the Multimodality Interventional Suite of the Future", *Journal of Interventional Radiology*, January 2007.

Effects of Nanosecond Pulsed Electric Fields on the Activity of a Hodgkin and Huxley Neuron Model

A. Denzi⁽¹⁾, F. Camera⁽¹⁾, A. Paffi⁽¹⁾, C. Merla⁽²⁾, F. Apollonio⁽¹⁾, P. Marracino⁽¹⁾, G. d’Inzeo⁽¹⁾ and M. Liberti⁽¹⁾

⁽¹⁾ Italian Inter-University Centre for the Study of Electromagnetic Fields and Biosystems (ICEmB) at “Sapienza” University of Rome, Rome 00184, Italy.

denzi@die.uniroma1.it

⁽²⁾ ICEmB at ENEA, Italian Agency for New Technologies, Energy and Sustainable Economic Development, Rome 00123, Italy

Abstract

The cell membrane poration is one of the main assessed biological effects of nanosecond pulsed electric fields (nsPEF). This structural change of the cell membrane appears soon after the pulse delivery and lasts for a time period long enough to modify the electrical activity of excitable membranes in neurons. Inserting such a phenomenon in a Hodgkin and Huxley neuron model by means of an enhanced time varying conductance resulted in the temporary inhibition of the action potential generation.

Index Terms – cell membrane, electroporation, Hodgking and Huxley neuron model, nanosecond pulsed electric fields

I. INTRODUCTION

In recent years, biological effects of nanosecond pulsed electric fields (nsPEF), characterized by durations in the nanosecond time scale and amplitudes in the MV/m range, have been investigated, evidencing promising applications in medical fields.

An important medical application of nsPEFs, which is currently under investigation, is based on the stimulation/inhibition of excitable tissues as the neuronal one [1].

Studies on nerve models reported the block of the conduction of the electric stimulation along a fiber, ascribed to the variation of membrane conductivity related to the pore formation in the plasma membrane [1], [2]. The membrane poration determines a change in the membrane permeability to ionic species. In neuronal cells, where the electrical activity results from the balance of ionic fluxes through the membrane, this effect is likely to affect the mechanisms of the action potential (AP) generation and transmission.

Aim of this work is to couple analytical expressions for the time behavior of conductance and capacitance of the porated membrane [3], [4] with a functional circuitual model of an excitable membrane patch. This will allow us to assess the effects of poration on neuronal electric activity and to quantify the observed modification as a function of

significant parameters, such as maximum poration level, pore resealing time, background stimulation level of the neuron model.

II. MODELS AND METHODS

In this section, the models used to describe both the passive properties (capacitance and conductance) and the functional ones (AP generation) of the porated membrane will be discussed.

The relative variation of the membrane capacitance (sum of the contributions of aqueous pores and the lipid bilayer [3]) is always below 2%, even for high values of pore density (N above 10^{15} m^{-2}), due to the small dimensions of pores; thus it can be disregarded. Different is the case of conductance where the flux of ions through the aqueous pores becomes the dominant contribution due to the higher conductivity of water with respect to the lipid bilayer. Such a pore contribution G_p is given by [4]:

$$\text{—————} \tag{1}$$

with r_p the pore radius, σ_w the water conductivity, h the membrane thickness, N the pore density, and A is a term accounting for the energy barrier experienced by the ions when flowing through the pore [4]. Both N and A depend on the transmembrane potential (TMP) and hence on time. A can be estimated on the bases of the TMP calculated as in [5]. Typically N exhibits a very sharp increase (in the time scale of ns) up to a maximum level (N_{MAX}), which, due to the resealing process of the pores, slowly decays (in a time scale up to s) to the initial value N_0 . In this paper, N_{MAX} has been calculated as in [5] and is of the order of 10^{15} m^{-2} . Pore resealing has been modeled as a single time constant (τ) process; τ has been chosen equal to 3, 10, 100 and 1500 ms. A value of $\sigma_w=1 \text{ mS/m}$ was used in Eq. (1).

To account for non-linear and active properties of the neuronal membrane, the well-known Hodgkin and Huxley (HH) circuitual model was considered [6]. The circuit is made of the parallel combination of the membrane capacitance C_m and three branches accounting for different ionic currents.

Variations induced by poration on the membrane conductivity have been accounted by inserting in the model a time varying leakage conductance, while C_m has been fixed to its typical value of $1 \text{ }\mu\text{F/cm}^2$ [6]. The leakage conductance has been modeled as a decreasing exponential function starting from the value assumed by the Eq. (1) after $1 \text{ }\mu\text{s}$ ($\approx 3 \text{ mS/cm}^2$) and with the time constant equal to τ .

The model has been implemented in the C++ environment using the direct Euler integration method with time step of $10 \text{ }\mu\text{s}$. Simulations have been carried out for stimulation currents I_s ranging from 6.3 up to $20 \text{ }\mu\text{A/cm}^2$.

III. RESULTS

The first effect induced by poration on the neuron activity is the introduction of a new electrical regime consisting in an initial inhibition period followed by the onset of a regular firing. In Fig. 1 such a behavior is shown, together with the exponential decay of $g_l(t)$, for $\tau=1500$ ms and $I_s= 20 \mu\text{A}/\text{cm}^2$.

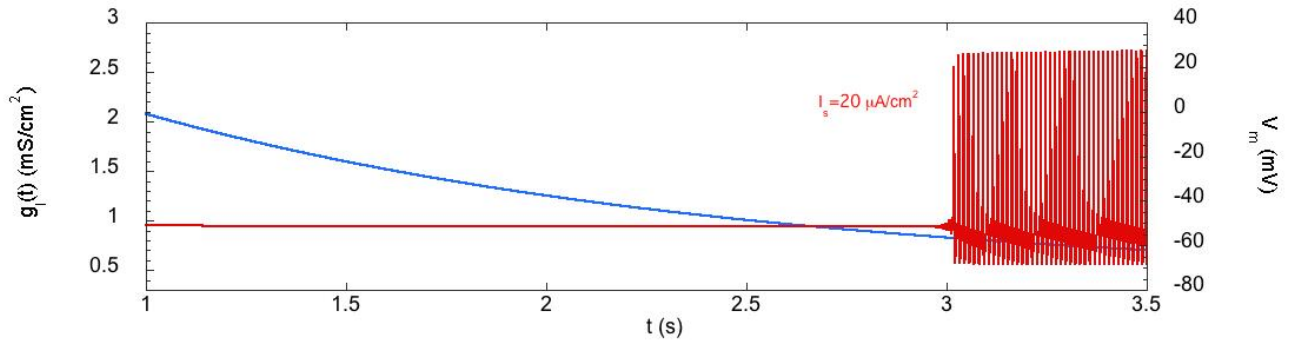


FIG. 1 – Time courses of the leakage conductance and of the transmembrane voltage for $I_s= 20\mu\text{A}/\text{cm}^2$, $\tau=1500$ ms, $N_{\text{MAX}}=10^{15} \text{ m}^{-2}$, $T=6.3^\circ\text{C}$.

To note that the firing activity restores before that $g_l(t)$ recovers to its initial value of $0.3 \text{ mS}/\text{cm}^2$. The possibility of temporarily silencing the neuron and the duration of such a reversible effect revealed to be dependent on the choice of I_s and τ , as reported in Fig. 2.

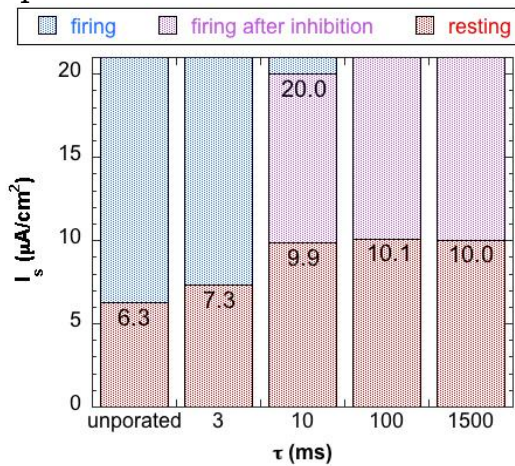


FIG. 2 – Electrical regimes exhibited by the HH model for the non-porated membrane and for the porated one.

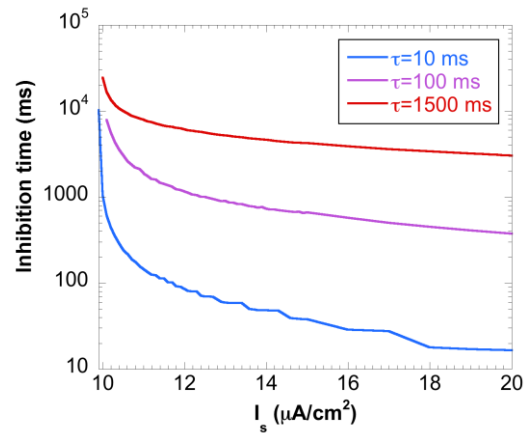


FIG. 3 – Inhibition time versus the stimulation current I_s for different resealing time constant.

The figure shows, for each time constant τ , the observed electrical regime in correspondence of each I_s value, highlighting those values representing the thresholds between two regimes. The first interesting effect is an enlargement of the resting regime with a translation of the threshold for the upper regime in all cases. Moreover, one can observe that the temporary silencing is possible only for $\tau > 10$ ms and $I_s > 10 \mu\text{A}/\text{cm}^2$.

Moreover, we observed that the longer the decay times of the membrane conductance, the longer the inhibition periods obtained (Fig.

3); this can be explained considering that the longer permanence of pores in their open state leads to a sort of membrane short circuit, which determines the TMP decrease under the threshold for the AP generation. However, it seems that higher stimulation currents I_s drive more quickly the neuron back to its regular firing state.

IV. CONCLUSIONS

We demonstrated how a temporary increase of the membrane conductance, due to the electroporation induced by nsPEFs, could disrupt the regular activity of a neuronal model. Such an effect has resulted in both a translation in the threshold between resting and firing regimes and in a temporary silencing of the neuron.

Further data would be necessary in order to fully elucidate the mechanism of the observed phenomenon also through molecular dynamic studies to obtain in depth knowledge of the membrane response to nsPEFs, in terms of variations in the ion flux through the pores.

However, the observed effects confirm the firing blocking shown in [1], [2] and suggest the possibility of modulating the electric activity of neurons by inhibiting the AP initiation through a suitable pulse train. Thus, the electroporation induced by nsPEFs could be used as an alternative approach to the direct electrical stimulation of neuronal system for medical application such as the chronic pain treatment.

V. REFERENCES

- [1] R. P. Joshi, A. Mishra, Q. Hu, K. H. Schoenbach, and A. Pakhomov, "Self consistent analyses for potential conduction block in nerves by an ultrashort high intensity electric pulse," *Physical Rev. E*, vol. 75, pp. 061 906–1–061 906–10, 2007.
- [2] R. P. Joshi, A. Mishra, J. Song, A. G. Pakhomov, K. H. Schoenbach, "Simulation Studies of Ultrashort, High-Intensity Electric Pulse Induced Action Potential Block in Whole-Animal Nerves," *Trans. On Biomed. Eng.*, Vol. 55, n. 4, pp. 1391-1398, 2008.
- [3] S. A. Freeman, M. A. Wang, J. C. Weaver, "Theory of electroporation of planar bilayer membranes: prediction of aqueous area, change in capacitance, and pore-pore separation," *Biophys. J.* 67, 42-56, 1994.
- [4] R. W. Glaser, S. L. Leikin, L. V. Chernomordik, V. F. Pastushenko, A. I. Sokirko, "Reversible electrical breakdown of lipid bilayers: formation and evolution of pores," *Biochimica et Biophysica Acta* 940, 275-287, 1988.
- [5] C. Merla, A. Paffi, F. Apollonio, P. Leveque, G. d'Inzeo, and M. Liberti, "Microdosimetry for nanosecond pulsed electric field applications: a parametric study for a single cell," *IEEE Trans. Biomed. Eng.*, vol. 58, no. 5, pp. 1294–1302, 2011.
- [6] A. L. Hodgkin and A. F. Huxley, "A quantitative description of membrane current and its application to conduction and excitation in nerve," *Journal of Physiology*, vol. 117, pp. 500-344, 1952.

ELECTROMAGNETIC PULSER FOR THE INVESTIGATION OF CELL MEMBRANES

A. Doria, G.P. Gallerano, E.Giovenale, G.Messina, A. Ramundo Orlando*
and I. Spassovsky

ENEA, Radiation Sources Laboratory, Via Enrico Fermi 45, 00044
Frascati (Rome) Italy

* CNR, Institute of Translational Pharmacology, Via Fosso del Cavaliere
100, 00133, Rome, Italy
andrea.doria@enea.it

Abstract

An electron based radiation source is presented with the aim of irradiating cell membrane models and biological cell membranes. The peculiarity of the device is that it can simultaneously generate short electromagnetic pulses, in the millimeter wave range, and electrostatic pulses with the same time structure.

Index Terms – Cell Membranes, Free Electron Laser, Electromagnetic Pulse.

I. INTRODUCTION

The device we present in this study is aimed at fulfilling the research objectives of a project for probing membrane dynamics with electromagnetic radiation and electric pulses. The basic idea of the proposal is to provide a unified view of ultrafast electromagnetic interactions with cellular systems. One of the most important questions in bio-electromagnetics today is whether cellular systems can rectify rapidly oscillating electric fields at frequencies which have pulse time durations ranging from pico-to-microseconds. It has been demonstrated [1] that short duration electric pulses produce significant changes in cell membrane potential. The project hypothesizes that similar effects may occur also from millimeter and THz waves. The cell membrane is, in fact, a complex polymolecular structure, whose transmembrane voltage controls the transport of chemicals into and out of the cell. The project will explore the interaction mechanisms using model membrane systems and electrically excitable cells (neurons) by applying electric pulses and RF carrier waves between 30 and 3000 GHz for possibly controlling cell function.

II. THE PULSER BASED FEL

ENEA has a long term experience in design and operation of electron-based electromagnetic sources, with particular importance for Free Electron Lasers [2], working in the long wavelength spectral range. The source to be realized is a novel Electro-Magnetic pulser, based on a previous prototype [3], capable of providing both nanosecond THz

electromagnetic (EM) radiation pulses as well as electrostatic (ES) pulses in the same device, with identical time duration. The pulser will allow, for the first time, direct comparison of EM and ES pulses on biological systems, a major goal of the project. The pulser will provide a core measurement capability for the program as it will produce peak electric fields in the samples that are significantly higher than any reported to date, while keeping the average power low enough to avoid sample heating.

The pulser diagram is schematically reported in Fig. 1. The electron gun is composed by a 20 kV power supply charging a capacitor bank C_0 that is the primary energy reservoir. A six-stage magnetic pulse compressor reduces the pulse from a discharge time of 1 μ s down to about 30 ns and rises the voltage up to 350 kV. The final condenser of the compressor is connected to a transmission-line transformer made by three coaxial cables charged in parallel and discharged in series on a mismatched diode load raising the voltage up to 1.5 MV.

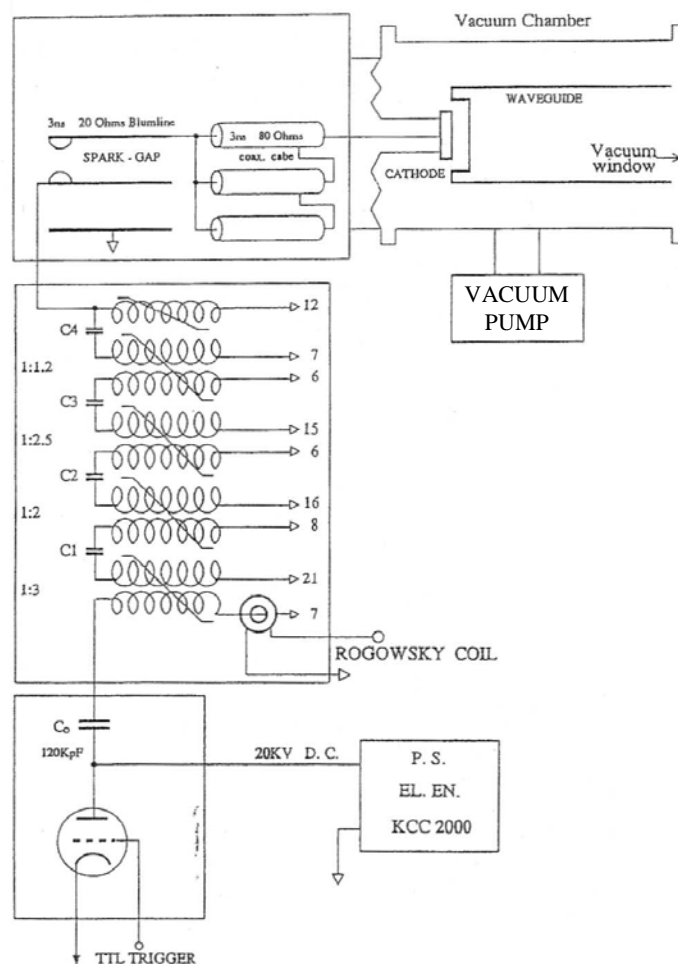


FIG. 1 – Pulser schematic diagram

A Free Electron Laser based on this accelerator can be assembled in a compact configuration as reported in Fig. 2:

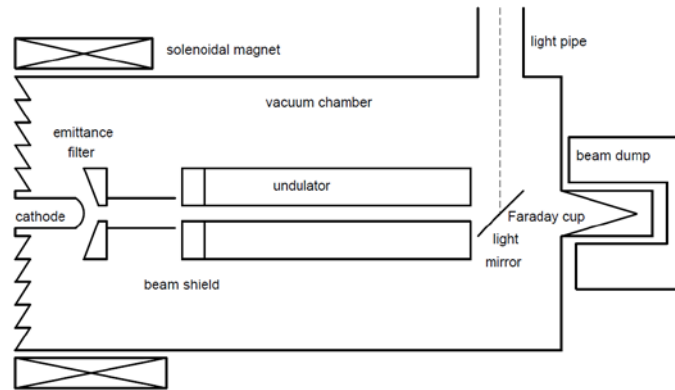


FIG. 2 – FEL block diagram

The electron beam, generated by the cathode is transported into the undulator by means of a solenoidal magnetic field to minimize the space-charge effects. The cathode and the magnetic undulator are contained inside a single vacuum chamber to simplify the e-beam transport system and the vacuum pumping system.

A peak current of about 5 kA allows the use of the pulser as a driver for an FEL. The quality parameter expected, like the emittance and the energy spread ($\epsilon_{x,y} = 30$ mm mrad, $\sigma_e = 1$ %) are good enough for long wavelength operation. The magnetic undulator considered in this study is a compact structure presently in use in the ENEA 2.5 MeV microtron based FEL (see Fig. 3).

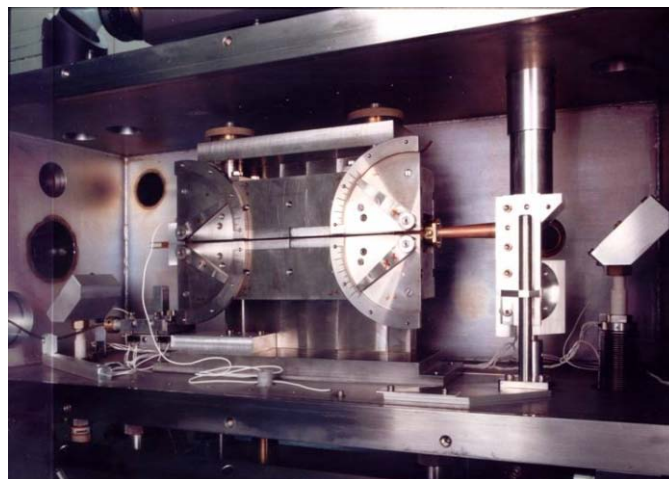


FIG. 3 – ENEA Compact Magnetic Undulator

The undulator consists of 8 periods of 2.5 cm of length with a variable gap; it can reach a parameter $K=0.8$ at a gap of $b=8$ mm generating, in this condition, an on-axis field of about 3.5 kgauss. The described FEL

source is capable to reach saturation at megawatt level at a central frequency of 200 GHz as reported in Fig. 4.

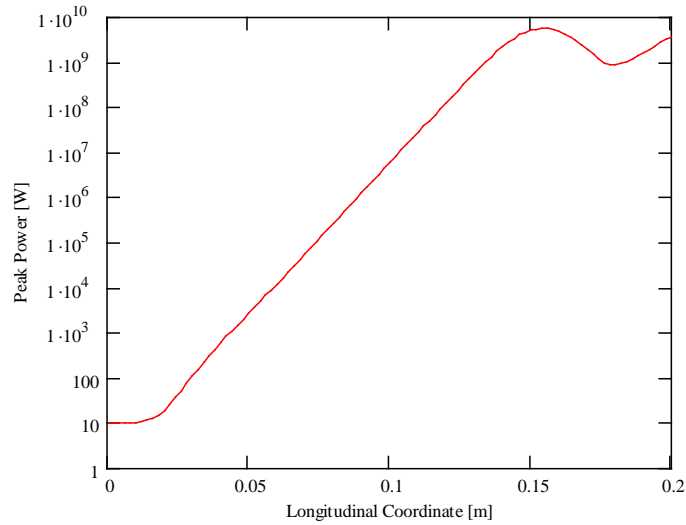


FIG. 4 – FEL radiation power evolution along the MU

REFERENCES

- [1] J. Teissie, “Biophysical effects of electric fields on membrane water interfaces: a mini review”, *Eur. Biophys. J.* 36, 967–972, (2007).
- [2] S.G. Biedron, J.W. Lewellen, S.V. Milton, J.F. Schneider, N.Gopalsami, L. Skubal, Y. Li, and M. Virgo, G.P. Gallerano, A. Doria, E. Giovenale, G. Messina, and I.P. Spassovsky, “Compact, High-Power Electron beam Based Terahertz Sources” - *Proceedings of the IEEE* - 95, No. 8, 1666-1678, (2007).
- [3] I.G. Yovchev, I.P. Spassovsky, N.A. Nikolov, D.P. Dimotrov, G. Messina, P. Raimondi, J.J. Barroso, R.A. Correa, “Numerical simulation of High Power Virtual Cathode reflex Triode Driven by Repetitive Short Pulse Electron Gun”, *IEEE Trans. On Plasma Science* – 24, No.3, 1015-1022, (1996).

Session 12 – Antenna design and measurements

L. Lucci, R. Nesti, G. Pelosi, and S. Selleri

Design of circular corrugated horn with constant width corrugations

E. Bekele, R. Chirikov, M. Carlin, L. Manica, G. Oliveri, L. Poli, P. Rocca, and A. Massa

What's new on antenna synthesis @ ELEDIA research center

A.D. Capobianco, E. Autizi, A. Locatelli, D. Modotto, C. De Angelis, S. Boscolo, and M. Midrio

Printed CRLH omnidirectional loop antenna for mobile WLAN applications

M. Aldrigo, A. Costanzo, D. Masotti, and V. Rizzoli

A wearable UHF small patch antenna on a new magneto-dielectric material

O. Losito, M. Bozzetti, G. Cannone, F. Prudenzano, L. Mescia, A. Di Tommaso, P. Bia, V. Castrovilla, M. De Sario

Measurements of antenna factor with antenna impedance method

F. D'Agostino, F. Ferrara, C. Gennarelli, R. Guerriero, and M. Migliozzi

Spherical near-field to far-field transformation for quasi-planar antennas: an experimental validation

DESIGN OF CIRCULAR CORRUGATED HORN WITH CONSTANT WIDTH CORRUGATIONS

L. Lucci⁽¹⁾, R. Nesti⁽²⁾, G. Pelosi⁽¹⁾, S. Selleri⁽¹⁾

⁽¹⁾ Department of Electronics and Telecommunications
University of Florence

Via Santa Marta 3, 50139 Florence, Italy

⁽²⁾ INAF, Arcetri Astrophysical Observatory,

Largo E. Fermi, 5, 50125 Florence, Italy

renzo.nesti@arcetri.astro.it

Abstract

In this contribution a novel design for circular corrugated horns is presented. The high performances typical of corrugated feeds is maintained even if design is constrained to have the corrugations' width uniform along the whole horn. The constant width corrugation property has a direct consequence on the mechanical design and fabrication, coming out easier and cheaper than in the well-known case of optimized - non uniform corrugation width - horns. The proposed horn can hence be fabricated using a pile of equal thickness layers, only machining a single circular stepped hole on each. The easy extension to arrays is straightforward in what are called platelet horn arrays. A particular design for a 43GHz corrugated horn is addressed and some results are shown.

Index Terms – Antennas, Corrugated horns, Arrays.

I. INTRODUCTION

Standard fabrication techniques, like milling from an aluminum ingot or electroforming, have since now set few limitations bound to machining tolerances, tool dimensions and minimum thickness, to the electromagnetic design of corrugated horns [1] for what concern the width of the corrugations, leaving the designer free to chose teeth and grooves for optimum performances.

The new interest in the development of focal plane arrays [2] comprising many identical feed horns is driving the research to cheaper and easier fabrication techniques both on the single feed element and on the array as a whole, having in mind in this last case some platelet solutions already tested with good results [3]. In this last case the constant width of the corrugation would give interesting perspectives since the platelet could be assembled by working metal sheets of equal thickness with clear advantage in material supplying. Furthermore the kind of machining for each plate would be very easy, requiring only the milling of a stepped circular hole representing the tooth and the groove of the corrugation.

A design of a constant width corrugation circular corrugated horn at 43GHz is presented in the following.

II. DESIGN

A phase study to develop a focal plane array receiver at 43GHz for the new Sardinia Radio Telescope (SRT) is currently being carried out. In this framework a design of a feed horn for the secondary Gregorian focus of the antenna has been done. Among standard feed specifications, a suitable geometry for low cost prototyping of an array with a significative number of elements (7 or 19) is required and the constancy of the corrugation width well addresses this point.

Optimization of the gain over system temperature of the SRT dual reflector antenna gives an 11dB@12° tapering specification at 43GHz. Other requirements are given for the whole Q-band (33-50GHz): return loss greater than 30dB and cross-polarization better than -30dB.

The corrugation width has been fixed to $w = 2.6\text{mm}$, about 0.36λ at center frequency and the groove and the tooth widths, g and t , respectively, are optimized under the constraint $w = g + t = 2.6\text{mm}$. Also the size of the horn must be minimized compatibly with the specifications and such an optimization is possible by adopting a curved profile for the corrugation envelope which allows more combinations of horn length-aperture diameter than in the standard linear horn case, to satisfy a given edge taper specification [4].

The resulting optimized horn is given in Fig. 1 where the typical dual profiled curve of the corrugations' envelope is shown.

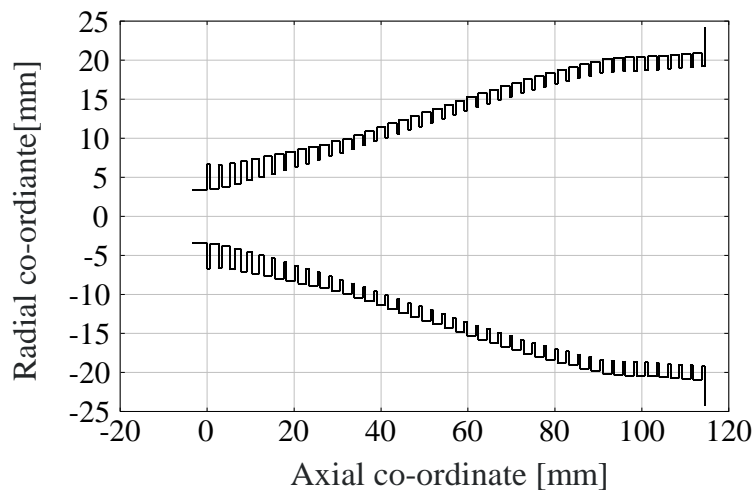


FIG. 1 – Optimized horn corrugation profile.

The total number of corrugations is $N_r = 44$, the throat transition region is formed by $N = 7$ corrugations with teeth and grooves linearly varying from the initial value $(t_0, g_0) = (2, 0.6)$ mm to a steady-state value of $(t_1, g_1) = (0.6, 2)$ mm.

The feed has been thought as a stack of disks to reduce even more the weight respect to the above mentioned platelet solutions, in which each

metal sheet encompasses the whole array cross section, and the assembly view of the executive drawing is shown in Fig. 2. The disks are grouped in three different sets of equal external diameters. A further step on both sides of each disk is required for precision alignment.

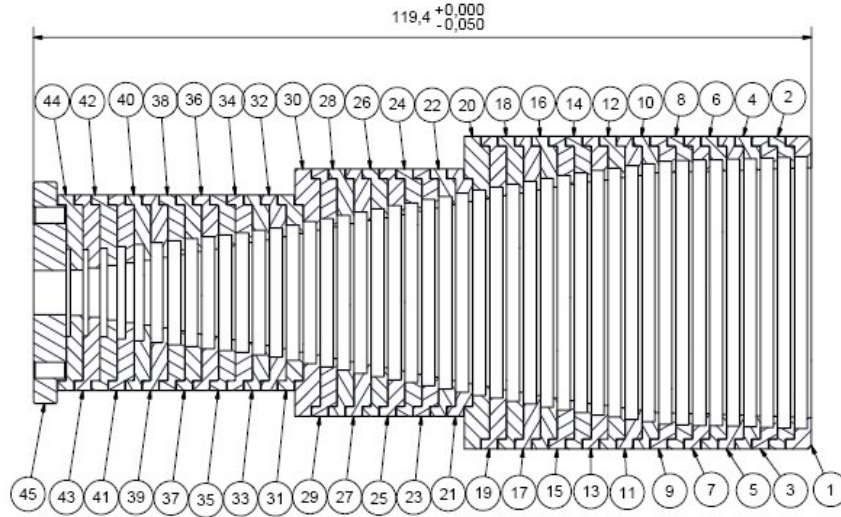


FIG. 2 – Drawing of the optimized horn assembled as a stack of disks.

The feed size is about 120mm in length and 50mm in diameter.

III. RESULTS

Optimized corrugated horn simulated results of the reflection coefficient and the maximum of the cross-polar component of the radiated field are given in Fig. 3.

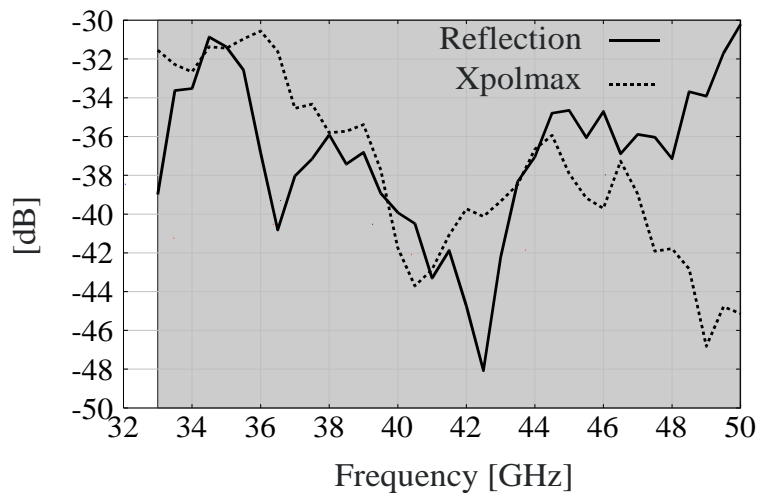


FIG. 3 – Reflection coefficient and cross-polarization maximum (Xpolmax).

Both performances are not appreciably degraded by the constant corrugation width over-constraint and fully satisfy the requirements.

The above statement also holds for the beam patterns as shown in the example plot of Fig. 4. The pattern cuts on the principal planes highlight very high beam symmetry having as a related effect the low cross-polar pattern on the 45° plane (where its maximum is).

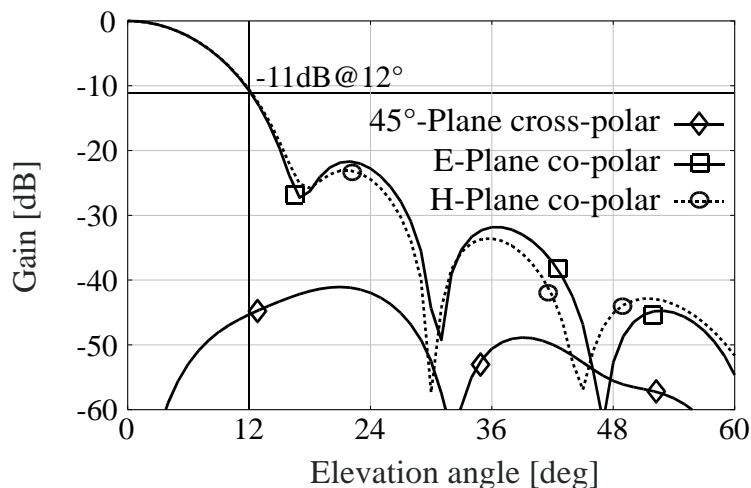


FIG. 4 – Patterns at 41.5GHz: E and H plane co-polar and 45° cut cross-polar.

Also in this case, it has to be noticed that the 11dB@12° taper requirement is satisfied on both principal planes.

IV. CONCLUSION

A novel constant width corrugation circular corrugated horn design has been presented. The horn shows very high performance satisfying the given requirements and is particularly suited to be cheaply and easily fabricated. This kind of corrugated horn has very attractive features as an element of a quite large focal plane array.

REFERENCES

- [1] P. J. B. Clarricoats and A. D. Olver, *Corrugated Horns for Microwave Antennas*, Peter Peregrinus, London, 1984.
- [2] B. Veidt and P. Dewdney, "Bandwidth Limits of Beamforming Networks for Low-Noise Focal-Plane Arrays," *IEEE Trans. Antennas Propagat.*, vol. 53, no. 1, pp. 450-454, 2005.
- [3] R. W. Haas, D. Brest, H. Mueggenburg, L. Lang, D. Heimlich, "Fabrication and Performance of MMW and SMMW Platelet Horn Arrays," *Int. J. . Infrared . Millimeter Waves*, vol. 14, pp. 2289-2293, 1993.
- [4] L. Lucci, R. Nesti, G. Pelosi, S. Selleri "Design of an Improved Profiled Corrugated Circular Horn at 320GHz," *J. Electromag. Waves Applic.*, Vol. 18, No. 2, 2004, pp. 387-396.

**WHAT'S NEW ON
ANTENNA SYNTHESIS @ ELEDIA RESEARCH CENTER**

E. Bekele, R. Chirikov, M. Carlin, L. Manica,
G. Oliveri, L. Poli, P. Rocca, and A. Massa

ELEDIA Research Center @ DISI, University of Trento
Via Sommarive 5, Povo 38123 Trento, Italy
andrea.massa@ing.unitn.it

Abstract

An overview of the innovative approaches for antenna design and optimization currently under development at the ELEDIA research center of the University of Trento are presented in this paper. The synthesis of non-conventional antenna arrays characterized by a non-regular disposition of the elements on the aperture and arrays using time as an additional degree of freedom for beam shaping as well as innovative methodologies for the synthesis of compact multi-band and broad-band antennas are described. The effectiveness and potentialities of the proposed techniques are illustrated by means of some representative examples.

Index Terms – Bayesian compressive sensing, Evolutionary optimization, Fractal antennas, Orthogonal array method, Sparse arrays, Time-modulated arrays.

I. INTRODUCTION

The design and optimization of antenna systems are still topics of great interest for both the scientific and industrial communities due to the proliferation of wireless applications and the growing number of end-users. In order to meet the specific requirements and the implementation constraints, the designer can consider a number of degrees of freedom available in the space, frequency, and time domains by controlling the electrical features of the individual radiating elements and/or the locations and feeding modality of a set of elements as for array antennas.

The techniques developed at the ELEDIA research center are devoted to the development and use of innovative optimization algorithms for the definition of the available antenna parameters and the study of new strategies in order to define a suitable environment for the application of the resolution algorithms. In order to identify the most suitable strategy for the different problem at hand, even in the case of large number of unknown parameters to be determined, various approaches have been developed based on deterministic approaches, global optimization algorithms, learning-by-example strategies, as well as hybrid solutions. In the following, the most recent results achieved with the research activity carried out at the ELEDIA Research Center are presented aimed at the design and synthesis of single radiating

elements as well as arrays for various applications ranging from the wireless communications up to radar systems.

II. SPARSE ARRAY DESIGN THROUGH BAYESIAN COMPRESSIVE SENSING

Sparse arrays are antenna structures where the radiating elements are non-uniformly located on the aperture. The possibility to exploit the element positions as additional degree of freedom allows to achieve the desired performance with a limited number of elements when compared to uniform arrangements. Although several strategies have been proposed in the literature, innovative approaches have been developed with the ELEDIA team based on the Bayesian Compressive Sensing (BCS). In [1], a method has been proposed for the design of sparse arrays with the aim of matching user-defined reference patterns. The main advantages of the BCS with respect to other state-of-the-art approaches are the flexibility, synthesis time, and reduction of number of array elements, while guaranteeing an excellent pattern matching. The approach in [1] devoted to the design of real element excitations have been extended to the synthesis of complex weighted arrays [2] by means of a multi-tasking version of the BCS (MT-BCS). Figure 1 shows an example of the synthesis of a sparse linear array generating a cosecant shaped beam pattern.

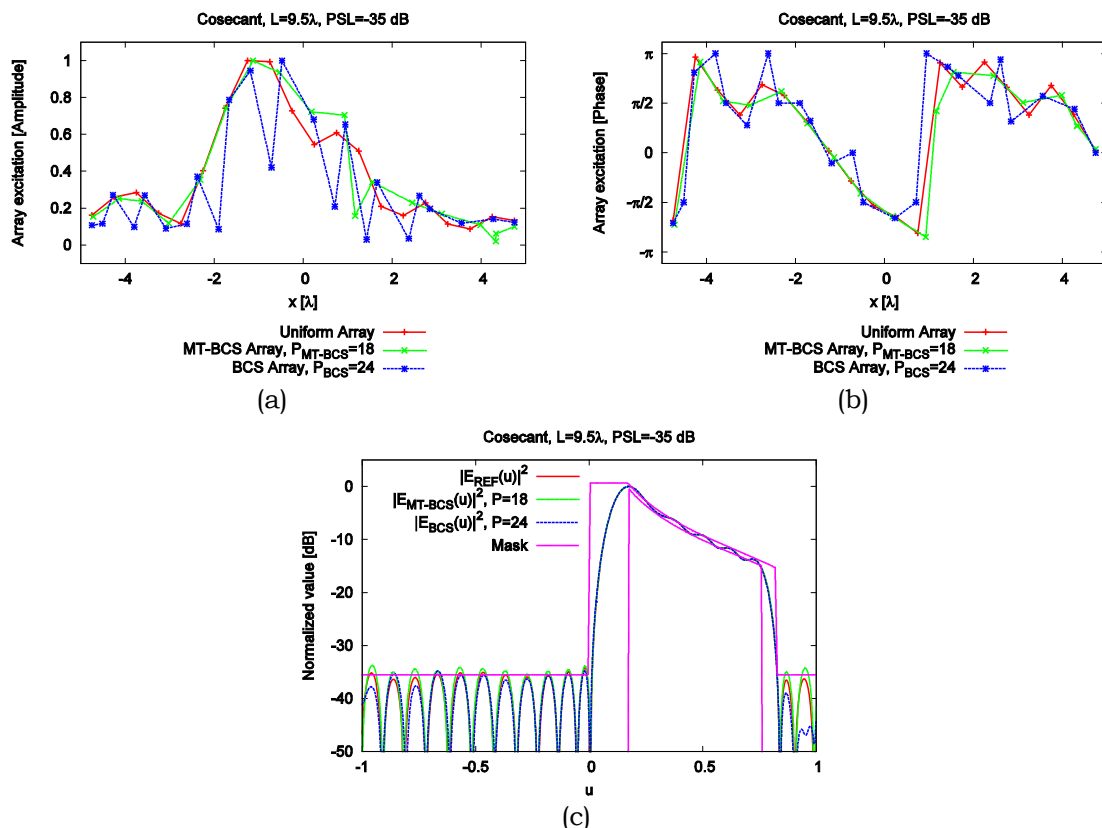


FIG. 1 – Plot of the reference and optimized (a) amplitude and (b) phase weights, and of the corresponding (c) beam patterns.

III. TIME-MODULATED ARRAY DESIGN AND OPTIMIZATION

Time-modulated arrays are antenna systems where, unlike classical phased arrays, a set of radio frequency (RF) switches are used in the feeding network to modulate the static element excitations. The switches are controlled by a periodic on-off sequence which allows to reconfigure the antenna radiation pattern. The unavoidable sideband radiations generated by the switches commutations, generally considered as power losses to be minimized [3], can be suitably exploit to synthesize simultaneous multiple beams. Therefore, the pulse sequence has to be properly optimized to obtain the desired radiation patterns [4]. As a representative example, the results of the design of a time modulated linear array for monopulse tracking applications generating a sum beam and a difference one at the carried frequency and the first harmonic, respectively, are reported in Fig. 2.

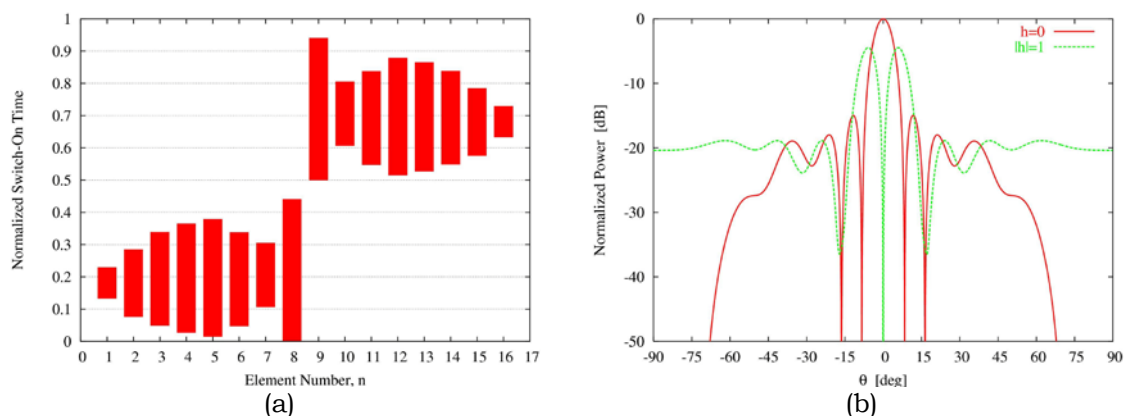


FIG. 2 – Plot of (a) the optimized pulse sequence and of (b) the corresponding beam patterns generated at $h=0$ (sum beam) and $h=1$ (difference beam).

IV. FRACTAL ANTENNAS SYNTHESIS THROUGH A HYBRID LBE-PSO METHOD BASED ON ORTHOGONAL ARRAYS

It has been shown that the design of multi-band antennas can be effectively addressed by means of perturbed fractal geometries [5]. As a matter of fact, the perturbation of the fractal parameters allows to tune in a selective way the antenna frequency bands thus avoiding the strict relationship between the resonating frequencies of classical fractal-shaped antennas. However, one of the main limitations in the optimization process is the computational burden required for the analysis when real antenna layouts are taken into account. To avoid this drawback, an innovative method has been proposed where the analysis is performed through a fast support vector machine (SVM) method where the antenna parameters are optimized by means of a particle swarm optimizer as in [6]. The training set of the SVM is properly determined by means of an orthogonal-array strategy allowing the definition of the minimum number of required samples.

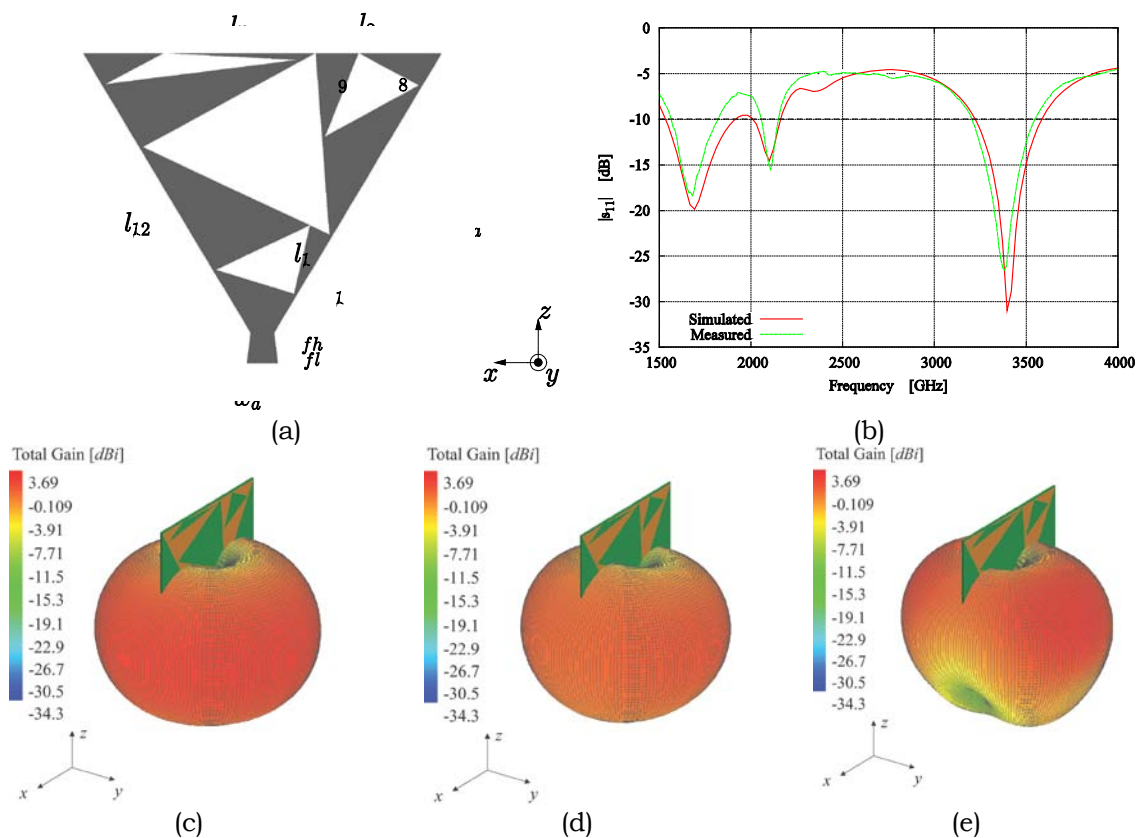


FIG. 3 – Plot of (a) the antenna geometry, of (b) the simulated and measured s_{11} values of the optimized antenna, and of (c) the radiation patterns.

REFERENCES

- [1] G. Oliveri, M. Carlin, and A. Massa, "Complex-weight sparse linear array synthesis by Bayesian compressive sampling," *IEEE Trans. Antennas Propag.*, 2012, in press.
- [2] G. Oliveri and A. Massa, "Bayesian compressive sampling for pattern synthesis with maximally sparse non-uniform linear arrays," *IEEE Trans. Antennas Propag.*, vol. 59(2), pp. 467-481, Feb. 2011.
- [3] L. Poli, P. Rocca, L. Manica, and A. Massa, "Handling sideband radiations in time-modulated arrays through particle swarm optimization," *IEEE Trans. Antennas Propag.*, vol. 58(4), pp. 1408-1411, Apr. 2010.
- [4] L. Poli, P. Rocca, G. Oliveri, and A. Massa, "Harmonic beamforming in time-modulated linear arrays," *IEEE Trans. Antennas Propag.*, vol. 59, no. 7, pp. 2538-2545, Jul. 2011.
- [5] R. Azaro, F. Viani, L. Lizzi, E. Zeni, and A. Massa, "A monopolar quad-band antenna based on a Hilbert self-affine prefractal geometry," *IEEE Antennas Wireless Propag. Lett.*, vol. 8, pp. 177-180, 2009.
- [6] L. Lizzi and A. Massa, "Dual-band printed fractal monopole antenna for LTE applications," *IEEE Antennas Wireless Propag. Lett.*, vol. 10, pp. 760-763, 2011.
- [7] Z. Bayraktar, D. H. Werner, and P. L. Werner, "Miniature meander-line dipole antenna arrays, designed via an orthogonal-array-initialized hybrid particle-swarm optimizer," *IEEE Antennas Propag. Mag.*, vol. 53(3), pp.42-59, Jun. 2011.

Printed CRLH Omnidirectional Loop Antenna for Mobile WLAN Applications

A.D. Capobianco⁽¹⁾, E. Autizi⁽¹⁾, A. Locatelli⁽²⁾, D. Modotto⁽²⁾,
C. De Angelis⁽²⁾, S. Boscolo⁽³⁾, M. Midrio⁽³⁾

⁽¹⁾ Dipartimento di Ingegneria dell'Informazione, University of Padova
Via Gradenigo 6/b, 35131 Padova, Italy

adc@dei.unipd.it

⁽²⁾ Dipartimento di Ingegneria dell'Informazione, University of Brescia
Via Branze 38, 25123 Brescia, Italy

⁽³⁾ Dipartimento di Ingegneria Elettrica, Gestionale e Meccanica
University of Udine, Via delle Scienze 208, 33100 Udine, Italy

Abstract

A printed loop antenna for mobile WLAN applications at 2.4GHz has been designed, fabricated and characterized. The structure is based on a composite right/left-handed (CRLH) transmission line that guarantees to achieve in-phase current even along a non small loop. Numerical simulations and measurements performed in anechoic chamber on fabricated prototypes confirm that the antenna exhibits good impedance matching and the radiation pattern is truly omnidirectional in the plane of the board, with high radiation efficiency and horizontal polarization of the radiated field.

Index Terms – Loop antenna, omnidirectional, printed antenna, WLAN.

I. INTRODUCTION

The pervasive diffusion of mobile wireless communications is one of the most important social phenomena of the last years. In this context, the widespread deployment of WLAN systems operating at 2.4GHz has pushed research in the field of antennas with the aim of selecting structures that can be efficiently integrated within mobile devices. Planar antennas characterized by omnidirectional radiation pattern in the plane of the board can be very attractive for many applications, in particular when integration of antenna and wireless card on the system board is a highly desired feature. It is well known that small (with respect to wavelength) loop antennas realize constant-current elements which behave as magnetic dipoles. As a consequence, they are characterized by omnidirectional pattern in the plane of the loop with horizontal polarization, but radiation efficiency is very poor. Larger loops permit to achieve an acceptable efficiency, but current along the loop is not constant and thus the radiation pattern deviates with respect to the omnidirectional shape. Only few works [1,2] concerning loop antennas for wireless communications designed to achieve omnidirectional radiation pattern have been reported in the literature. In this work we focus the attention on the analysis, design, fabrication and characterization of CRLH printed loop antennas for WLAN

applications at 2.4GHz. The proposed printed structure has been inspired by the loop antenna with left-handed loading described in [2], but in our case loading was obtained by using printed lumped elements instead of SMD inductors and capacitors.

II. ANTENNA DESIGN

A CRLH transmission line, which is characterized by a well known dispersion relation [3], can be implemented through left-handed loading of a printed bifilar line.

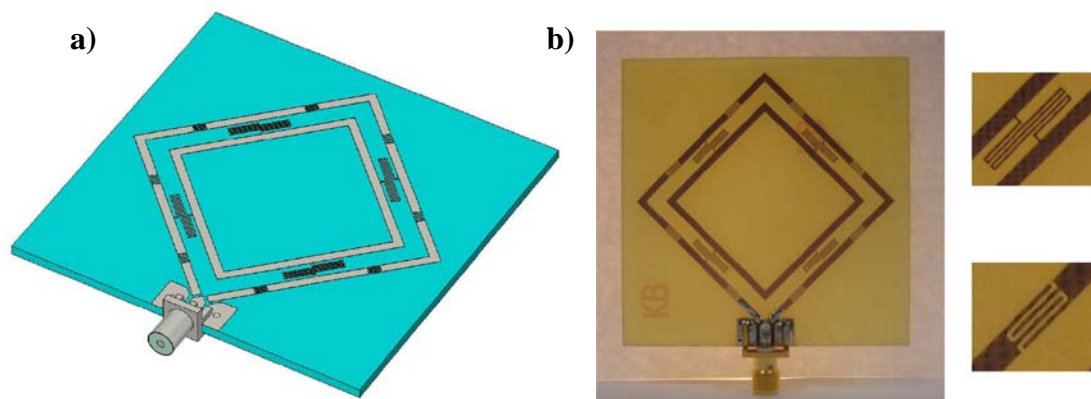


FIG. 1 – a) schematic view of the proposed CRLH loop antenna; b) photograph of one of the fabricated prototypes. The balun section and the SMA connector are visible on the bottom of the structure. A zoom onto a meander inductor and an interdigitated capacitor is also depicted.

One of the peculiar characteristics of this kind of structure is the possibility of obtaining a transmission line with null propagation constant, that can be used as a building block to realize a loop antenna wherein a constant current flows, in spite of the non-small size [2]. In our work, we exploit this principle in order to achieve a compact loop antenna operating at 2.4GHz and characterized by omnidirectional pattern in the plane of the FR4 substrate. Loading of the transmission line has been obtained by using printed lumped elements, in order to minimize losses and to exploit the geometrical degrees of freedom offered by this solution. A schematic view of the structure under exam is shown in Fig. 1a. The performance of the antenna has been optimized by resorting to extensive full-wave simulations through CST Microwave Studio [4]. The CRLH loop antenna has been designed to be printed on a standard FR4 substrate (thickness = 1.6mm, $\epsilon_r = 4.5$). A square loop composed of 4 CRLH unit cells with length equal to 35mm is printed on a $60 \times 60\text{mm}^2$ square PCB board. Each cell contains a bifilar printed line which is loaded through the insertion of two printed capacitors placed on the same strip, and a printed inductor connecting the two strips. Printed capacitors are characterized by an interdigitated

geometry [5] composed of 4 fingers. Printed inductors with meander geometry have been chosen [5]: the number of periods that forms the meander is 2. Excitation of the antenna is obtained by opening a gap in a corner of the loop, and by feeding the structure through a lattice balun. A prototype has been fabricated by using standard PCB milling techniques with a resolution up to 0.1mm (Fig. 1b).

III. NUMERICAL AND EXPERIMENTAL DESIGN

The CRLH loop antenna has been thoroughly analyzed through numerical simulations, and measurements on fabricated prototypes have been carried out in anechoic chamber by using an Agilent N5230A PNA-L network analyzer.

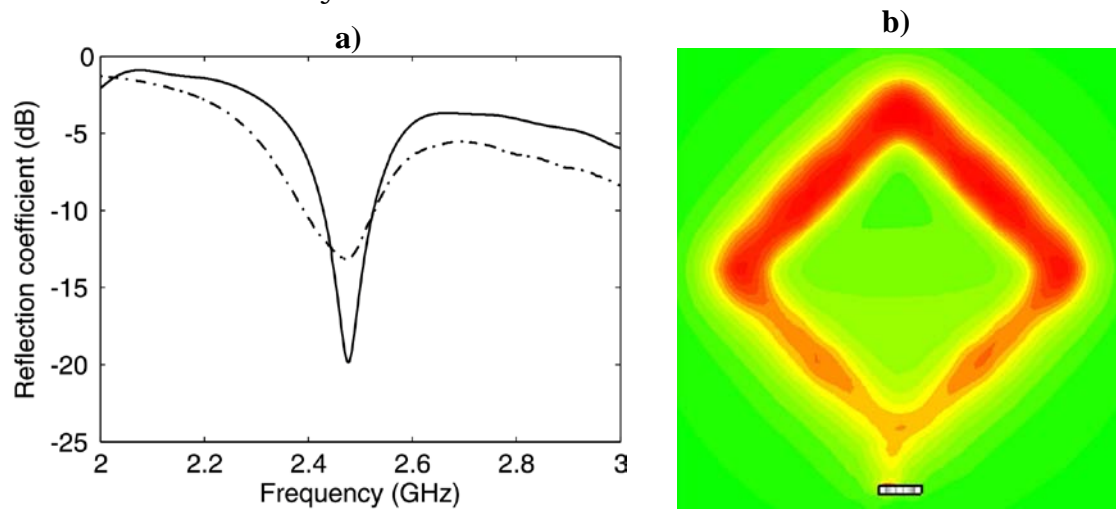


FIG. 2 – a) simulated (solid line) and measured (dashed-dotted line) reflection coefficient of the CRLH loop antenna; b) magnitude of the magnetic field close to the CRLH loop antenna.

In Fig. 2a we show the reflection coefficient of the designed antenna when the structure is connected with a 50-Ohm coaxial cable. It is worth noting that both simulations and measurements show that impedance matching is excellent around 2.4GHz, with a -10dB bandwidth which is about 100MHz. The magnetic field distribution in the near-field region has been numerically calculated (Fig. 2b) in order to verify that the antenna is really working in a condition of zeroth order resonance. In Fig. 3a we show the radiation solid, evaluated near the resonant peak. An almost ideal doughnut shape is clearly visible, with the axis which is normal to the plane of the FR4 substrate; polarization is horizontal and radiation efficiency is limited only by losses due to FR4 substrate and SMD components in the balun section. Moreover, in order to analyze in a quantitative way the quality of the omnidirectional radiator, we plot in Fig. 3b the radiation pattern in the plane of the board (gain is reported in decibel), with a display scale equal to 5dB per division. In spite of strong asymmetry of the structure, maximum

deviation of the measured pattern from an omnidirectional shape is around 2dB, thus the antenna can be considered a good starting point for the realization of smart antennas for WLAN applications.

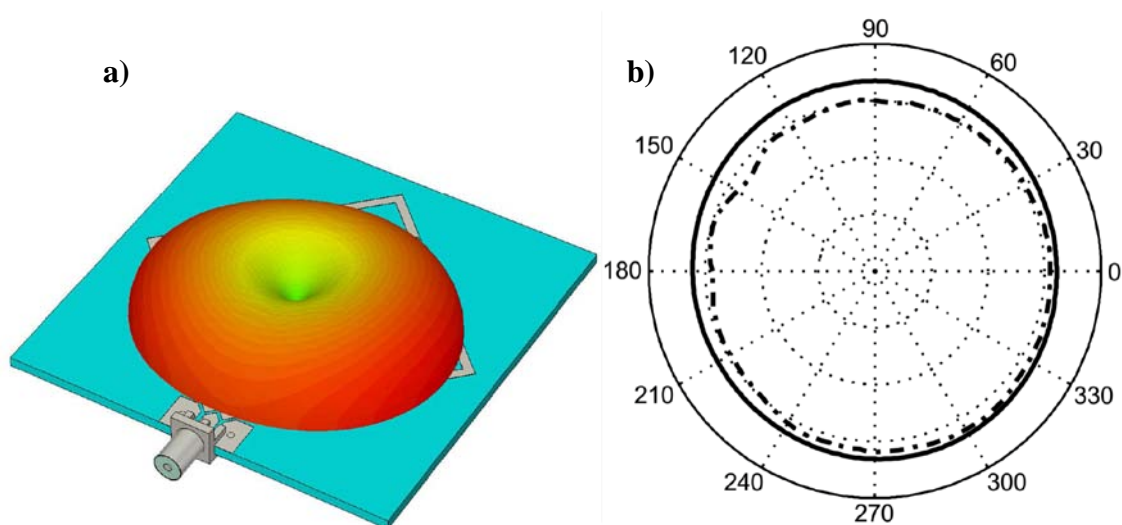


FIG. 3 – a) radiation solid (linear scale); b) simulated (solid line) and measured (dashed-dotted line) radiation pattern (in decibel) in the plane of the board. The scale of the plot is from 5 to -15 dB, with 5dB per division.

IV. CONCLUSION

We have described design, fabrication, and characterization of a printed CRLH loop antenna for mobile WLAN applications. We have reported numerical results and measurements in anechoic chamber which show that the antenna is characterized by a truly omnidirectional radiation pattern in the plane of the board, and that radiation efficiency is very high since antenna loading is achieved by using printed lumped elements.

REFERENCES

- [1] C.C. Lin, L.C. Kuo, and H.R. Chuang, "A Horizontally Polarized Omnidirectional Printed Antenna for WLAN applications", *IEEE Trans. Antennas Propagat.*, vol. 54, pp. 3551-3556, Nov. 2006.
- [2] A.L. Borja, P.S. Hall, Q. Liu, and H. Iizuka, "Omnidirectional Loop Antenna with Left-Handed Loading", *IEEE Antennas Wireless Propagat. Lett.*, vol. 6, pp. 495-498, Nov. 2007.
- [3] A. Lai, C. Caloz, and T. Itoh, "Composite Right/Left-Handed Transmission Line Metamaterials", *IEEE Microwave Magazine*, vol. 5, pp. 34-50, Sept. 2004.
- [4] CST Microwave Studio 2011, Darmstadt, Germany.
- [5] S.H. Kim, and J.H. Jiang, "Folded monopole LC-loaded antenna and its polarization reconfigurability", *Microwave Opt. Tech. Lett.*, vol. 53, pp. 1197-1201, June 2011.

A wearable UHF small patch antenna on a new magneto-dielectric material

Martino Aldrigo⁽¹⁾, Alessandra Costanzo⁽¹⁾,
Diego Masotti⁽¹⁾, and Vittorio Rizzoli⁽¹⁾

⁽¹⁾D.E.I.S., University of Bologna
Viale Risorgimento 2, 40136 Bologna, Italy
martino.aldrigo@unibo.it

Abstract

A new UHF small patch antenna for a wearable application at 868 MHz, built on an innovative magneto-dielectric material, is presented. Exploiting the miniaturization properties offered by values of permeability greater than unity, a barium-strontium hexaferrite has been synthesized in order to achieve the best compromise between antenna dimensions and performances. Once the electrical properties of the substrate were characterized, simulations and measurements of reflection coefficient and radiated far-field have been carried out, showing a good agreement and, consequently, a proof of the reliability of our design approach. Further improvements of the proposed design can be taken into account for applications in the 2.4 GHz ISM band.

Index Terms – Small antennas, UHF band, magneto-dielectric materials, wearable applications.

I. INTRODUCTION

In the last years, wearable and implantable devices have become of great interest, since they can be exploited for applications in the *Body Area Networks* (BANs), for real-time monitoring of health parameters. The challenge in the development of new integrated RF systems is the miniaturization of all components. The miniaturizing process also affects the radiating element(s): it requires a trade-off between small dimensions and performances of the antenna, since *electrically small antennas* do not exhibit radiation properties good enough to satisfy the link requirements in terms of power budget. By means of Magneto-Dielectric (MD) materials, antenna size can be strongly reduced by exploiting the value of relative permeability μ_r with lower values of ϵ_r , thus obtaining the same miniaturization factor: in fact, due to the refractive index definition $n = \sqrt{\epsilon_r \cdot \mu_r}$, the material intrinsic impedance is increased, since $\eta_i = \eta_0 \cdot \sqrt{\mu_r} / \sqrt{\epsilon_r}$, thus allowing an easier impedance matching. Furthermore, a radiating performance improvement, due to the increased radiation resistance, and a wider bandwidth can be observed. Our work was intended to synthesize an MD material to build a patch antenna with a reasonable size in order to be used in a wearable application.

II. MD MATERIAL CHARACTERIZATION AND MEASUREMENTS

The barium-strontium hexaferrite $\text{Ba}_{0.75}\text{Sr}_{0.25}\text{Fe}_{12}\text{O}_{19}$ [1] was chosen as the MD material under test: it was produced with the standard *Mixed Oxide* process and sintered at 1100°C to achieve a relative density of 93%. The choice for this type of MD material was made on the basis of its intrinsic

physical properties; in particular, M-type hexaferrites are strongly anisotropic and their values of μ_r can surpass Snoek's limitation:

$$(\mu_s - 1)\omega_{\text{res}} = \frac{4\pi}{3}\gamma 4\pi M_s \quad (1)$$

where μ_s is the static permeability, ω_{res} is the Ferro-Magnetic Resonance (FMR), $\gamma \approx 3 \text{ GHz/kOe}$ is the gyromagnetic constant and M_s is the saturation magnetization. It is of primary importance to utilize the MD substrate below the FMR, in order to avoid strong energy absorption and quick variations in the values of permeability. In Fig. 1, measured complex permittivity and permeability of the first prototype [2] are plotted all over the band of interest, i.e. 750 MHz – 1 GHz, to guarantee the best matching between the EM tool Drude model, and the measured values for ϵ' , ϵ'' , μ' and μ'' .

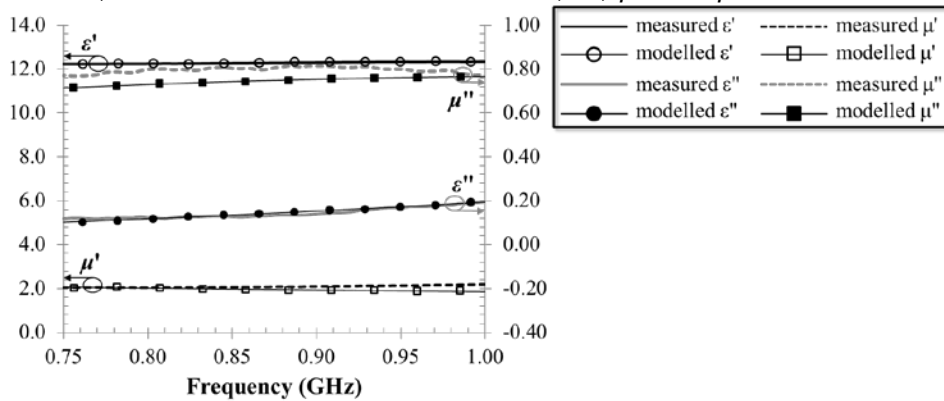


FIG. 1 – Comparison between measured and modelled values of permittivity and permeability in the band 750 MHz – 1 GHz.

III. ANTENNA DESIGN AND CONSTRUCTION

In agreement with our choice, an 868 MHz patch antenna has been designed to test the engineered substrate. The MD material sample used for our prototype is a disc, since round in shape devices are suitable for wearable applications thanks to the absence of sharp edges. For miniaturization purposes, a $\lambda_g/4$ -patch antenna has been built: since $\lambda_{\text{free-space}} \approx 345.62 \text{ mm}$ at 868 MHz, we have $\lambda_g/4 \approx 18 \text{ mm}$, consequently the chosen diameter for the disc is 33 mm, thus providing enough substrate for the patch antenna itself. Furthermore, we have tackled two problems: 1) the fragility of the ceramic composite; 2) the dielectrically dense material. For these two reasons, a value of 5 mm for the substrate thickness has been chosen as the best trade-off between robustness against mechanical stress and EM behavior of the antenna. The halving of the standard $\lambda_g/2$ -patch length has been obtained by means of a curved shorting plate mounted on the top of the substrate: this has turned out to be an easy-to-make solution that preserves the antenna radiating properties, since the radiating aperture faces a bigger portion of substrate w.r.t. a centered patch. The patch, the shorting plate and the ground plane are made of a 4 μm -thick silver film. The feeding technique is realized by inserting a micro-coaxial cable (50 Ω) into a via. The final prototype of the antenna is shown in Fig. 2.

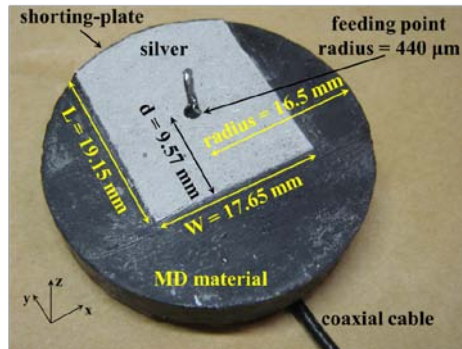


FIG. 2 – Wearable patch antenna: detailed view with the micro-coaxial cable.

In order to exploit the antenna for a wearable application, the device has been mounted on a 254 μm -thick EMC Shielding conductive fabric (conductivity $\sigma = 1 \times 10^7 \text{ S/m}$), to provide a ground plane which can be attached to any other desired fabric [3].

Fig. 3 shows a very good agreement between simulated and measured values of the reflection coefficient. In the band 750 MHz – 1 GHz the two curves exhibit the same bandwidth of about 250 MHz for $|S_{11, \text{MAX}}| = -10 \text{ dB}$: in the authors' opinion, this result is worth mentioning, since a typical characteristic of patch antennas is being narrow-band (about 4% of relative bandwidth in most cases), whereas in our work the relative bandwidth is at least about 29% (due to substrate properties). This could be considered a great advantage in terms of robustness of the antenna against mechanical tolerances: we proved by experiments that changes in the patch length of about 6% allow keeping a very good matching at the desired operating frequency. Furthermore, the impedance matching is very good: at 868 MHz, the simulated value of $|S_{11}|$ is around -24 dB, while the measured value is less than -40 dB, thus ensuring a great compatibility with standard feeding techniques.

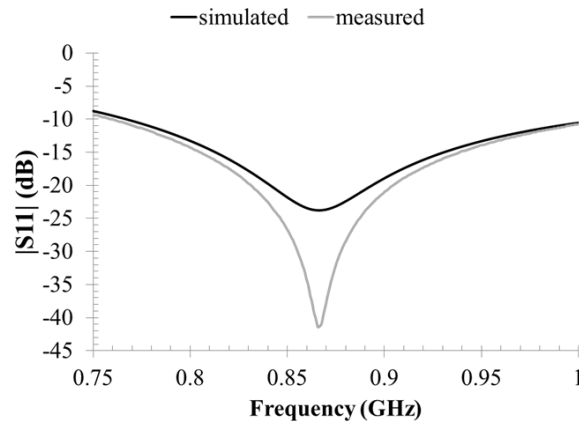


FIG. 3 – Simulated and measured reflection coefficient in the band 750 MHz – 1 GHz.

In Fig. 4, the E-plane (yz) and the H-plane (xz) simulated and measured radiation patterns of the normalized E-field at 868 MHz in polar coordinates are plotted, showing a very good correspondence. Simulated radiation efficiency has a value of about 1.5%, due to magnetic losses and to the very electrically-dense material. This has to be taken into account for further enhancements of MD material synthesis. Moreover, the designed antenna is electrically small, since its length is $\lambda_{\text{free-space}}/20$, and all electrically small antennas exhibit low values of efficiency. Despite this, due to the conductive

shielding, the matching and radiating properties of the whole system are independent of the presence of human body to which the system itself is attached. In particular, as is apparent in Fig. 4, the front-to-back ratio of the antenna is very low (the measured value is -16.34 dB), so that we can consider back-radiation negligible and not causing interactions with human tissues. The feasibility of the proposed solution was investigated by transmitting a power of -10 dBm: a received power of -48.4 dBm was measured in indoor environments at 1 m-distance, in good agreement with the results of the corresponding Friis calculations (-50.5 dBm). At a 3 m-distance the same quantity decreases to about -60 dBm. Hence our device can be easily exploited at a distance of some meters. For example, assuming a receiver sensitivity of -85 dBm, a 25 dB margin is preserved for potential scattering attenuation.

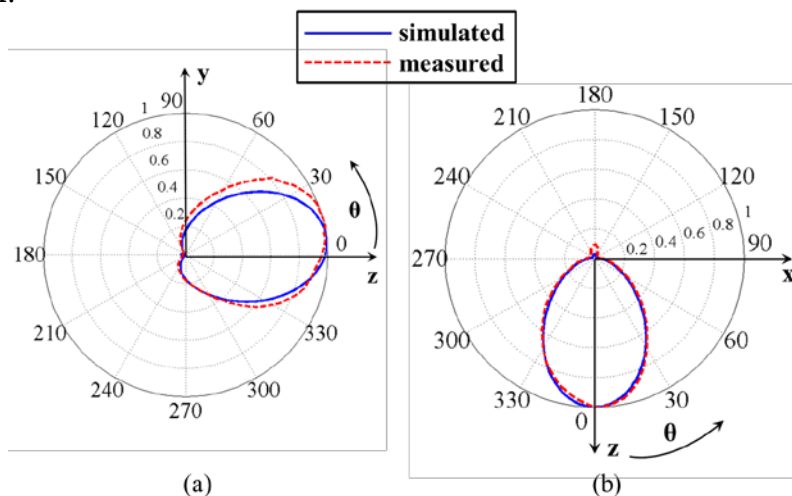


FIG. 4 – (a) E-plane and (b) H-plane simulated and measured radiation patterns of our MD antenna at 868 MHz.

IV. CONCLUSIONS

An innovative MD material has been presented. Its EM characterization has been the basis for the design of an electrically small patch antenna for wearable applications. Improvements in the MD material synthesis process are worth being investigated to create a new family of substrates for wearable/implantable antennas operating in the 2.4 GHz ISM band. Simulations and measurements of the prototype built on the MD material have shown a very good agreement and can be considered as the starting point for further researches in the field of magneto-dielectric antennas.

V. REFERENCES

- [1] F. M. M. Pereira et al., “Magnetic and dielectric properties of the M-type barium strontium hexaferrite ($Ba_xSr_{1-x}Fe_{12}O_{19}$) in the RF microwave (MW) frequency range”, *Journal of Material Science, Materials in Electronics* (2009).
- [2] C. E. Ciomaga et al., “Magnetolectric ceramic composites with double-resonant permittivity and permeability in GHz range: A route towards isotropic materials”, *Scripta Materialia*, Vol. 62, issue 8, April 2010.
- [3] A. Costanzo, F. Donzelli, D. Masotti, and V. Rizzoli, “Rigorous design of RF multi-resonator power harvesters”, *Proceedings of the Fourth European Conference on Antennas and Propagation (EuCAP)*, pp. 1-4, 2010.

MEASUREMENTS OF ANTENNA FACTOR WITH ANTENNA IMPEDANCE METHOD

O. Losito⁽¹⁾, M. Bozzetti⁽¹⁾, G. Cannone⁽¹⁾, F. Prudenzano⁽¹⁾, L. Mescia⁽¹⁾,
A. Di Tommaso⁽¹⁾, P. Bia⁽¹⁾, V. Castrovilla⁽²⁾, M. De Sario⁽¹⁾.

⁽¹⁾ DEE, Politecnico di Bari, Bari - Italy, Italy

losito@deemail.poliba.it

⁽²⁾ ITEL Telecomunicazioni S.r.l., Ruvo di Puglia (BA) – Italy

Abstract

In the fields of electromagnetic interference and electromagnetic compatibility, it is important to measure the strength of the electric field originating from electric devices. Knowledge of the antenna factor of a receiving antenna is necessary. In this paper, we discuss the antenna impedance method as a new calibration method measuring the free-space antenna factor. The experimental measurements are compared with both the standard field method and the data provided by the manufacturer of biconical, log-periodic and horn antennas. A good agreement with the technical regulation ANSI C63.5.

Index Terms – Antenna calibration, Antenna Factor, Standard Antenna Calibration Site.

I. INTRODUCTION

Antenna factors (AF) can be accurately obtained using different methods such as Standard Site Method (SSM), Reference Antenna Method (RAM) and so on [1]. The Standard Site Method (SSM) is specified in ANSI C 63.5 and is believed to yield the free-space value of the antenna factor [2]. However, because the antennas are assumed to be infinitesimal dipoles, improvement is considered necessary for this method to yield accurate antenna factors for tuned dipole antennas as well as for non-dipole antennas. To yield accurate antenna factors recently, a novel calibration method called the Antenna Impedance Method was developed (see papers [3]-[4]), for estimating the free-space antenna factor of an electromagnetic interference (EMI) antenna, especially for the very high frequency (VHF) range where traditional methods are difficult to apply. These method was summarize in the following section and the experimental measures of antenna factor made by this method were compared with the experimental data of Standard Field Method (SSM) showing a good agreement with the data and with the technical regulation ANSI C63.5.

II. ANTENNA IMPEDANCE METHOD

The Antenna Impedance Method (AIM) is a calibration method able to obtain the free-space antenna factor of an antenna under calibration. It is based on antenna impedance measurements of an antenna under calibration placed in a various heights above a metal ground plane. The

antenna input impedance is formulated in terms of the height-dependent radiation impedance and the effective length of the antenna. As well known the antenna factor of an antenna, AF, is defined by the ratio of the field strength of an incident plane wave, E, to the voltage induced at the antenna output port, V, (AF= E/V). An equivalent circuit of an antenna is shown in Fig. 1, where the radiation impedance is denoted by $Z_a(h)$.

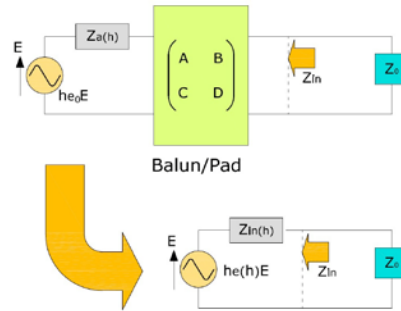


FIG. 1 - Equivalent circuit of an electromagnetic interference antenna

The antenna factor can be expressed as:

$$AF = \left| \frac{Z_{in}(h) + Z_0}{h_e(h)Z_0} \right| \quad \text{with} \quad Z_{in}(h) = \frac{Z_a(h)D + B}{Z_a(h)C + A} \quad \text{and} \quad h_e(h) = \frac{h_{e0}}{Z_a(h)C + A} \quad (1).$$

These parameters are defined in terms of the characteristics of radiating elements ($Z_a(h)$, h_{e0}), the transmission matrix (A, B, C, D) which representing various antenna circuits like a balun, and the impedance of a load of the antenna (Z_0). When an antenna is placed horizontally above a metal plane, the impedance of the antenna elements, $Z_a(h)$, can be expressed as the difference of a free-space component Z_{a_0} and a component $Z(h)$ accounting for the reflection at a metal plane:

$$Z_a(h) = Z_{a_0} - Z(h) \quad (2)$$

After some simple mathematical passages can be derived the characteristic AIM equation:

$$AF_{free} = \left| \frac{C_1 Z_0 - 1}{\Delta \cdot Z_0} \right| \quad \text{in which} \quad \Delta^2 = \begin{vmatrix} C_1 & -C_2 \\ -1 & C_3 \end{vmatrix}. \quad (3)$$

where C_1 , C_2 and C_3 can be determined from data on $Z_{in}(h)$.

III. SIMULATION AND EXPERIMENTAL RESULTS

The Standard Field Method (SFM) is certainly the most natural calibration method, because it can be derived directly from the defining equation of the antenna factor. The Standard Field Method consists of comparing voltages produced in an antenna by the field to be measured and by a standard field, the magnitude of which is computed from the dimensions of the transmitting antenna, its current distribution, the distance of separation, and effect of the ground.

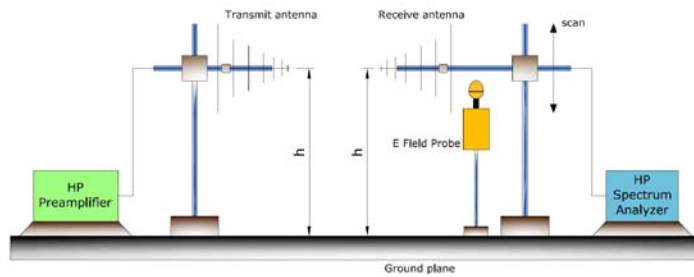


FIG. 2 - AF measure set-up made with Standard-Field Method

To determine the AF with the Antenna Impedance Method a simple code was developed in Matlab environment to solve the previous AIM equations. In the M-file script the input data were the frequency, the antenna impedance measurements on antenna under calibration and the antenna heights above the metal ground plane.

In detail the input impedance of antenna under calibration was measured in the semi-anechoic chamber of ITEL Telecomunicazioni srl EMC Test Lab scanning the antenna in seven heights from 1 m up to 4 m (step = 50 cm) in 26 points of the frequency range respectively: 20-300 MHz for the Biconical antenna, 200 – 1000 MHz for the Log-periodic antenna and 700 – 3000 MHz for Horn antenna.

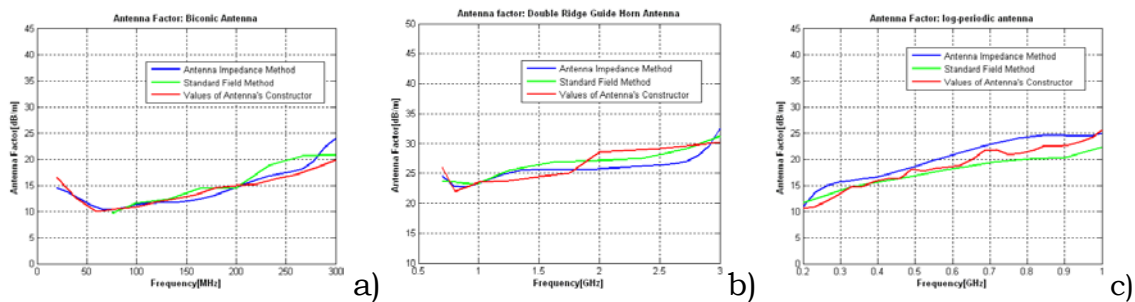


FIG. 3 -Experimental AF data obtained with AIM compared with SFM and calibrated data for a) Biconical antenna in the range of 20-300 MHz, for b) Horn antenna in the range of 700-3000 MHz and for c) log-periodic antenna in the range of 200-1000 MHz.

The values of the free-space antenna factor with antenna impedance method can be obtained solving a linear system of the input impedance of antenna measures for three corresponding antenna heights.

For each antenna we have compared the experimental fitting curve carried out by using both the calibrated data of the antenna provided by the manufacturer and with the experimental data of AF made by Standard Field Method previously discussed. As show in Fig. 3, we have found that the variation of the antenna factor in comparison to the data provided by the manufacturer is within ± 2.2 dB for Log-periodic and Biconical antennas while within ± 3.8 dB for Horn antenna.

IV. CONCLUSION

In this paper, a numerical method called Antenna Impedance Method (AIM) was performed for estimating the free-space antenna factor of an EMI antenna, for the frequency range from 20 to 3000 MHz using three different kinds of antenna. Biconical, Log-periodic and Horn antenna. The results of this method were compared with conventional EMI antenna calibration method such as the Standard Field Method and compared with the data provided by the manufacturer. The AF values obtained for this three antennas under calibration shown a variations within the range of [2.2 - 4.4] dB. The accuracy of the proposed estimation method was investigated by taking into account the probable errors associated with the conventional antenna calibration. It was concluded that the method could provide an estimation of the free-space antenna than is in a good agreement with the norm applicable to the calibration of antenna ANSI C63.5.

REFERENCES

- [1] MIL-STD-461D, Military Standard: Requirements for the Control of Electromagnetic Interference Emissions and Susceptibility (11 january 1993). SAE ARP 958 *The Engineering Society For Advancing Mobility Land Sea Air and Space 1999*, R. Nicole.
- [2] ANSI C63.5-1998 American National Standart for Electromagnetic Compatibility-Radiated Emission Measurements in Electromagnetic Interference (EMI) Control-Calibration of Antennas (9kHz-40 GHz)
- [3] S. Tsushima, K. Fujii, A. Sugiura, Y. Matsumoto, and Y. Yamanaka, "Determination of the Antenna Factor of Microwave Antennas Using the Antenna Impedance Measurement," *2004 Asia-Pacific Radio Science Conference (AP-RASC2004)*, Beijing, China, S2-06.
- [4] K. Fujii, S. Kaketa, A. Sugiura, Y. Matsumoto, and Y. Yamanaka, "Calibration of EMI Antennas in the VHF Band with Antenna Impedance Measurements," *2004 International Symposium on Electromagnetic Compatibility (EMC'04/Sendai)*, Sendai, Japan, 2C1-3, pp. 361 - 364.

SPHERICAL NEAR-FIELD TO FAR-FIELD TRANSFORMATION FOR QUASI-PLANAR ANTENNAS: AN EXPERIMENTAL VALIDATION

F. D'Agostino, F. Ferrara, C. Gennarelli, R. Guerriero, M. Migliozi

D.I.E.I.I., University of Salerno, via Ponte Don Melillo, 84084 Fisciano, Italy
 {fdagostino, flferrara, cgennarelli, rguerriero, mmigliozi}@unisa.it

Abstract

This work concerns the experimental validation of a near-field – far-field transformation with spherical scanning for quasi-planar antennas. Such a technique is based on the nonredundant sampling representations of the electromagnetic fields and on the optimal sampling interpolation expansions, and uses an oblate ellipsoid to model the antenna. It is so possible to remarkably lower the number of data to be acquired, thus reducing in a significant way the required measurement time. The effectiveness of such a technique is experimentally assessed at the UNISA Antenna Characterization Lab by comparing the far-field patterns reconstructed from nonredundant measurements on the sphere with those obtained from the near-field data directly measured on the classical spherical grid.

Index Terms – antenna measurements, near-field – far-field transformation with spherical scanning, nonredundant representations of electromagnetic fields.

I. INTRODUCTION

Among the near-field – far-field (NF–FF) transformations, that employing the spherical scanning (Fig. 1) is particularly interesting since it gives the full antenna pattern coverage [1-5]. The classical spherical NF–FF transformation technique [1] has been modified in [2] by taking into account the properties of spatial bandlimitation of electromagnetic (EM) fields [6]. In particular, the highest spherical wave to be considered has been rigorously fixed by these properties and the number of data on the parallels has resulted to be decreasing towards the poles. Moreover, the application of the nonredundant sampling representations of the EM fields [7] has allowed one to remarkably reduce the number of required NF data in the case of antennas having one or two predominant dimensions [2]. These results have been obtained by assuming the antenna under test (AUT) as enclosed in a prolate or oblate ellipsoid, respectively, and by developing an optimal sampling interpolation (OSI) formula, which allows the reconstruction of the data needed by the aforementioned NF–FF transformation. The ideal probe assumption in [2] has been then removed in [3] by developing an effective probe compensated spherical NF–FF transformation for elongated or quasi-planar antennas. At last, efficient spherical NF–FF transformations, suitable for these kinds of antennas and based on different and very flexible AUT modellings, have been proposed in [5].

Aim of this work is to provide the experimental validation of the NF–FF transformation with spherical scanning for quasi-planar antennas [2, 3] based on the oblate ellipsoidal AUT modelling. Such a validation has been carried out at the antenna characterization laboratory of the University of Salerno.

II. NONREDUNDANT SAMPLING REPRESENTATION ON A SPHERE

Let us consider a quasi-planar AUT and a probe scanning a spherical surface of radius d in the NF region. Since the voltage V measured by a nondirective probe has the same effective spatial bandwidth of the field, the nonredundant sampling representation of EM fields [7] can be applied to it. An effective

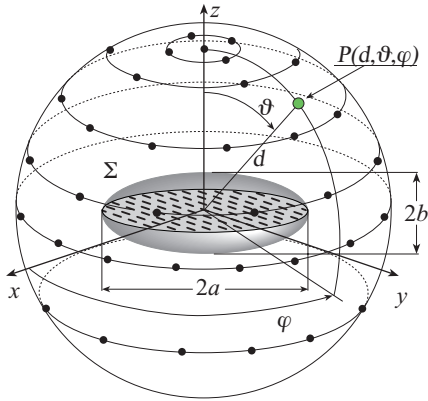


FIG. 1 – Spherical scanning for quasi-planar antennas.

modelling for such an AUT is obtained by choosing the surface Σ enclosing it coincident with the smallest oblate ellipsoid having major and minor semi-axes equal to a and b (see Fig. 1). The spherical coordinate system (r, ϑ, φ) is adopted to denote an observation point P . Inasmuch as the sphere can be represented by meridians and parallels, in the following we deal with the voltage representation on a curve C described by a parameterization $\underline{r} = \underline{r}(\xi)$. According to [7], let us introduce the “reduced voltage” $\tilde{V}(\xi) = V(\xi) e^{j\gamma(\xi)}$, where $V(\xi)$ is the voltage V_1 or V_2 measured by the probe or by the rotated probe and $\gamma(\xi)$ is a proper phase function. The error, occurring when $\tilde{V}(\xi)$ is approximated by a bandlimited function, becomes negligible as the bandwidth exceeds a critical value W_ξ [7]. Therefore, it can be effectively controlled by choosing a bandwidth equal to $\chi' W_\xi$, where $\chi' > 1$ is an enlargement bandwidth factor.

The bandwidth W_ξ and parameterization ξ relevant to a meridian, and the corresponding phase function γ are [2, 7]:

$$W_\xi = \beta \ell' / 2\pi ; \quad \xi = (\pi / 2) E(\sin^{-1} u | \varepsilon^2) / E(\pi / 2 | \varepsilon^2) \quad (1)$$

$$\gamma = \beta a \left[v \sqrt{(v^2 - 1) / (v^2 - \varepsilon^2)} - E(\cos^{-1} \sqrt{(1 - \varepsilon^2) / (v^2 - \varepsilon^2)} | \varepsilon^2) \right] \quad (2)$$

where β is the wavenumber, $\ell' = 4a E(\pi / 2 | \varepsilon^2)$ is the length of the ellipse C' (intersection between the meridian plane through P and Σ), $E(\cdot | \varepsilon^2)$ denotes the elliptic integral of second kind, and $u = (r_1 - r_2) / 2f$ and $v = (r_1 + r_2) / 2a$ are the elliptic coordinates, $r_{1,2}$ being the distances from P to the foci of C' . Moreover, $\varepsilon = f / a$ is its eccentricity and $2f$ its focal distance. The expression of the parameter ξ in (1) is valid when the angle ϑ belongs to the range $[0, \pi/2]$. For ϑ from $\pi/2$ to π , it results $\xi = \pi - \xi'$, where ξ' is the parameterization value corresponding to the point specified by the angle $\pi - \vartheta$. As shown in [2, 7], the curves $\gamma = \text{const}$ and $\xi = \text{const}$ are ellipses and hyperbolas confocal to C' .

When C is a parallel, the phase function γ is constant and it is convenient to choose the angle φ as parameter. The corresponding bandwidth [2, 7] is

$$W_\varphi(\xi) = \beta a \sin \vartheta_\infty(\xi) \quad (3)$$

wherein $\vartheta_\infty = \sin^{-1} u$ is the polar angle of the asymptote to the hyperbola passing through P .

According to the above results and by properly matching the OSI expansions along meridians and parallels, the following two-dimensional OSI formula results [2, 3]:

$$\tilde{V}(\xi, \varphi) = \sum_{n=n_0-q+1}^{n_0+q} \left\{ G(\xi, \xi_n, \bar{\xi}, N, N^n) \sum_{m=m_0-p+1}^{m_0+p} \tilde{V}(\xi_n, \varphi_{m,n}) G(\varphi, \varphi_{m,n}, \bar{\varphi}, M_n, M_n^n) \right\} \quad (4)$$

where $2q, 2p$ are the number of retained samples along ξ and φ , respectively, $n_0 = \text{Int}(\xi / \Delta\xi)$, $m_0 = \text{Int}(\varphi / \Delta\varphi_n)$,

$$\xi_n = n\Delta\xi = 2\pi n/(2N'' + 1); \quad N'' = \text{Int}(\chi N') + 1; \quad N' = \text{Int}(\chi' W_\xi) + 1 \quad (5)$$

$$\varphi_{m,n} = m\Delta\varphi_n = 2\pi m/(2M_n'' + 1); \quad M_n'' = \text{Int}(\chi M_n') + 1; \quad M_n' = \text{Int}[\chi^* W_\varphi(\xi_n)] + 1 \quad (6)$$

$$\chi^* = 1 + (\chi' - 1) [\sin \vartheta_\infty(\xi_n)]^{-2/3}; \quad N = N'' - N'; \quad M_n = M_n'' - M_n' \quad (7)$$

$\bar{\xi} = q\Delta\xi$, $\bar{\varphi} = p\Delta\varphi_n$, $\chi > 1$ is an oversampling factor needed to control the truncation error [7], $\text{Int}(x)$ denotes the integer part of x , and

$$G(\alpha, \alpha_k, \bar{\alpha}, L, L'') = \Omega_L[(\alpha - \alpha_k), \bar{\alpha}] D_{L''}(\alpha - \alpha_k) \quad (8)$$

Moreover,

$$D_{L''}(\alpha) = \frac{\sin[(2L'' + 1)\alpha/2]}{(2L'' + 1)\sin(\alpha/2)}; \quad \Omega_L(\alpha, \bar{\alpha}) = \frac{T_L[2\cos^2(\alpha/2)/\cos^2(\bar{\alpha}/2) - 1]}{T_L[2/\cos^2(\bar{\alpha}/2) - 1]} \quad (9)$$

are the Dirichlet and Tschebyscheff sampling functions, respectively, $T_L(\alpha)$ being the Tschebyscheff polynomial of degree L . The variation of χ^* with ξ is required to ensure a bandlimitation error constant with respect to ξ [6].

By using the expansion (4), it is possible to evaluate accurately the probe and rotated probe voltages at any point on the scanning sphere and, in particular, at the points needed by the classical NF-FF transformation with spherical scanning [1] as modified in [3, 5].

III. EXPERIMENTAL RESULTS

The described NF-FF transformation has been experimentally validated in the anechoic chamber available at the UNISA Antenna Characterization Lab, equipped with a roll over azimuth spherical NF facility system supplied by MI Technologies. The chamber, whose dimensions are $8m \times 5m \times 4m$, is provided with pyramidal absorbers ensuring a background noise lower than -40 dB. The amplitude and phase measurements are carried out by means of a computer-controlled vectorial network analyzer Anritsu. An open-ended WR90 rectangular waveguide is used as probe. The considered AUT is a MI-12-8.2 standard gain horn with aperture $19.4\text{cm} \times 14.4\text{cm}$, located on the plane $z = 0$ of the adopted reference system (Fig. 1) and operating at 10 GHz. Such an AUT has been modelled as enclosed in an oblate ellipsoid with $a = 12.3$ cm and $b = 4.5$ cm. The probe output voltages have been collected on a sphere of radius $d = 78.5$ cm.

The amplitudes of the reconstructed voltages V_1 and V_2 relevant to the meridians at $\varphi = 0^\circ$ and $\varphi = 90^\circ$, respectively, are compared in Figs. 2 and 3 with those directly measured on the same meridians, to assess the effectiveness of the two-dimensional OSI algorithm (4). At last, the FF patterns in the principal planes E and H obtained from the nonredundant spherical measurements are compared in Figs. 4 and 5 with those (references) obtained from the NF data directly measured on the classical spherical grid. In both the cases, the software package MI-3000 has been used to get the FF reconstructions. As can be seen, all the reconstructions are very accurate, thus confirming the effectiveness of the approach.

It is worth noting that the number of employed samples is 1 626, less than one half that (3 280) needed by the standard spherical scanning technique [1].

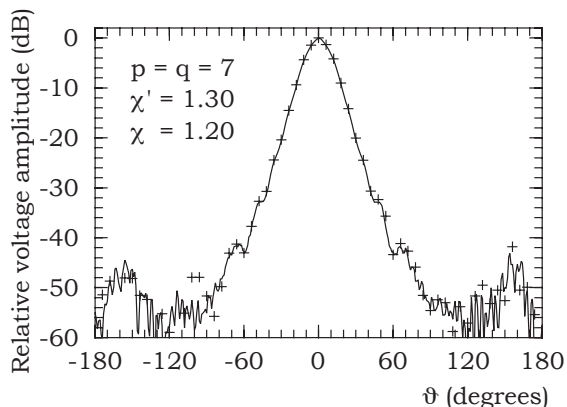


FIG. 2 – Amplitude of V_1 on the meridian at $\varphi = 0^\circ$. Solid line: measured. Crosses: recovered from nonredundant NF data.

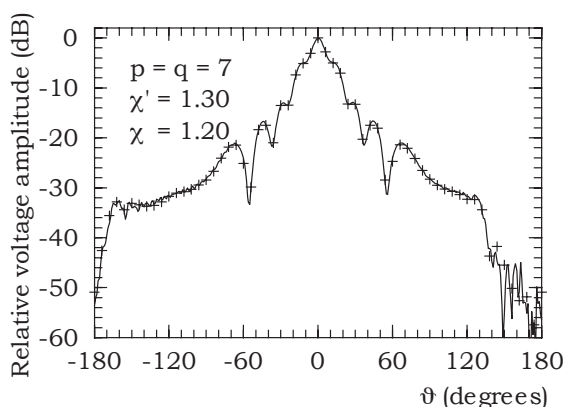


FIG. 3 – Amplitude of V_2 on the meridian at $\varphi = 90^\circ$. Solid line: measured. Crosses: recovered from nonredundant NF data.

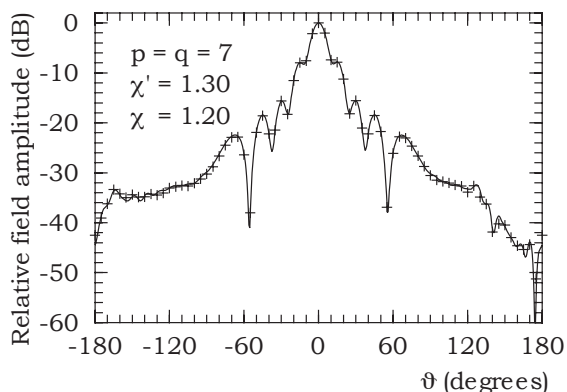


FIG. 4 – E-plane pattern. Solid line: reference. Crosses: reconstructed from nonredundant NF data.

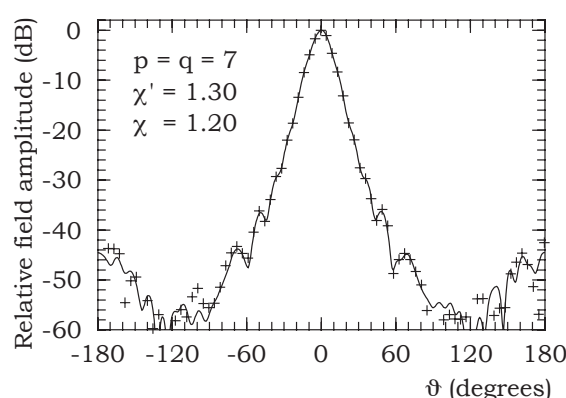


FIG. 5 – H-plane pattern. Solid line: reference. Crosses: reconstructed from nonredundant NF data.

REFERENCES

- [1] J. Hald, J.E. Hansen, F. Jensen, and F.H. Larsen, "Spherical near-field antenna measurements," J.E. Hansen Ed., Peter Peregrinus, London, 1998.
- [2] O.M. Bucci, C. Gennarelli, G. Riccio, and C. Savarese, "Data reduction in the NF-FF transformation technique with spherical scanning," *Journal of Electromagnetic Waves and Applications*, vol. 15, pp. 755-775, June 2001.
- [3] A. Arena, F. D'Agostino, C. Gennarelli, and G. Riccio, "Probe compensated NF-FF transformation with spherical scanning from a minimum number of data," *Atti della Fondazione G. Ronchi*, vol. 59, pp. 312-326, 2004.
- [4] T.B. Hansen, "Higher-order probes in spherical near-field scanning," *IEEE Transactions on Antennas and Propagation*, vol. 59, pp. 4049-4059, Nov. 2011.
- [5] F. D'Agostino, F. Ferrara, C. Gennarelli, R. Guerriero, and M. Migliozi, "Effective antenna modellings for a NF-FF transformation with spherical scanning using the minimum number of data," *International Journal of Antennas and Propagation*, vol. 2011, ID 936781, 11 pages.
- [6] O.M. Bucci and G. Franceschetti, "On the spatial bandwidth of scattered fields," *IEEE Transactions on Antennas and Propagation*, vol. AP-35, pp. 1445-1455 Dec. 1987.
- [7] O.M. Bucci, C. Gennarelli, and C. Savarese, "Representation of electromagnetic fields over arbitrary surfaces by a finite and nonredundant number of samples," *IEEE Transactions on Antennas and Propagation*, vol. 46, pp. 351-359, March 1998.

Session 13 – Optical fibers

L. Ursini, and M. Santagiustina

Applications of fiber optics dynamic Brillouin gratings in ultra wideband communications

M. Surico, A. Di Tommaso, P. Bia, L. Mescia, M. Bozzetti, O. Losito, M. De Sario, and F. Prudenzano

Large mode area fibers for high power and high beam quality lasers

L. Schenato, L. Palmieri, L. Vianello, G. Marcato, G. Gruca, T. van de Watering, D. Iannuzzi, A. Pasuto, and A. Galtarossa

Fiber optic sensor for precursory acoustic signals detection in rockfall events: feasibility analysis

L. Palmieri, A. Galtarossa, and L. Schenato

Distributed fiber optic sensor for intense magnetic field mapping

E. Balliu, A. Braglia, A. Califano, M. Olivero, A. Penna, and G. Perrone

A new pumping scheme for high power Tm-doped fiber laser

APPLICATIONS OF FIBER OPTICS DYNAMIC BRILLOUIN GRATINGS IN ULTRA WIDEBAND COMMUNICATIONS

L. Ursini, M. Santagiustina

CNIT – Dept. of Information Engineering, University of Padova
Via Gradenigo 6/B, 35131 Padova, Italy
marco.santagiustina@unipd.it

Abstract

By exploiting all-optical signal time differentiation and true time reversal, realized through dynamical Brillouin gratings in fiber optics, we propose a method to generate UWB Gaussian doublet (including higher-order) pulse and the implementation of an UWB time reversal mirror. Numerical predictions are reported.

Index Terms – Brillouin Scattering Fiber Optics, UWB communications.

I. INTRODUCTION

Dynamic Brillouin gratings (DBGs) in fiber optics are a powerful technique for light control and manipulation [1]. The stimulated Brillouin scattering between two counter-propagating optical beams, an input waveform (IW) and a short (ideally Dirac function) write pulse (WP), generates an acoustic wave (AW), that longitudinally modulates the fiber refractive index, thus creating a grating. The DBG, which retains the characteristics of the IW backscatters the read pulses (RPs), injected from the same side of the WP. If the RP is short (ideally Dirac function) the scattered output waveform (OW) is identical to the IW. In polarization maintaining (PM) fibers, the writing/reading processes can be decoupled by launching the WP and RP on orthogonal birefringence axes, and by properly satisfying frequency and phase matching conditions (see [1-5]). Recently, several potential applications of the DBGs, such as all-optical true time reversal (TTR) [2], all-optical time differentiation and integration [3], high resolution sensors [4] and microwave photonics filters [5], have been demonstrated. Here, we present two additional DBG applications in UWB communications [6] based on the DBG-assisted all-optical signal time differentiation and true time reversal. In particular, we propose a method to generate second- and higher-order derivatives of an UWB Gaussian pulse and a possible implementation of an UWB time reversal mirror (TRM). A numerical analysis is performed by integrating the SBS equations for the DBG [1] and through CST simulations for the microwave link.

II. UWB GAUSSIAN DOUBLET GENERATION

The generation of the first- (monocycle) or the second-order (doublet) derivatives of a Gaussian pulse is an efficient technique for UWB pulse

generation, following the U.S. Federal Communications Commission (FCC) specifications (PSD $< -41.3\text{dBm/MHz}$, bandwidth $>500\text{ MHz}$ or fractional bandwidth $>20\%$) [6]. Various methods have been presented in the optical domain, which provides high flexibility and huge bandwidth by exploiting microwave photonic filters [6], semiconductor optical amplifiers [7] and optical parametric amplification[8].

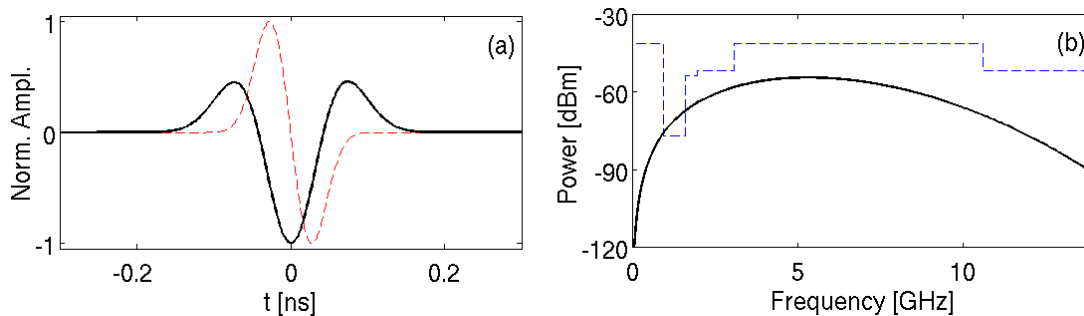


FIG. 1 – (a) WP/RP monocycle pulse (dashed line); OW doublet pulse (continuous line). (b) OW power spectrum (continuous line). FCC spectrum mask (dashed line).

As shown in [3], the time differentiation of arbitrary IWs can be obtained if the RP is the time derivative of a short pulse, so the OW is also the time derivative of the DBG-stored IW. Here, the second-order time derivative of a Gaussian pulse (IW) is achieved in two steps: first, if the WP is the first-order time derivative of a Gaussian pulse, the stored waveform retains IW first-order derivative; second, if the RP is the same as the WP, IW second-order derivative is eventually retrieved by the OW. By iterating the process, higher-order derivatives of IW can be obtained. Here, an example is presented. The IW is a 50 ps FWHM, Gaussian pulse. The WP is obtained by switching the phase of the IW [1,3] at the pulse peak, thus achieving a Gaussian monocycle pulse with a very good approximation (Fig. 1a, dashed line). The RP is the same as the WP. The OW is actually the Gaussian doublet, generated from the IW (Fig. 1a, continuous line). The generated UWB Gaussian doublet power spectrum (Fig. 1b) satisfies the FCC specifications, showing a peak centered at 6 GHz and a -10dB bandwidth of 7.7 GHz (from 1.94 to 9.67 GHz), with a fractional bandwidth of about 148%. These results are comparable to those previously obtained [6-8], but an advantage of this method is to easily obtain higher-order Gaussian pulse derivatives, to better fit the FCC specifications at low frequencies, by iteratively using the same setup.

III. UWB TIME REVERSAL MIRROR

TRMs exploit the phase conjugation process of time reversal: a signal, which propagates in a cluttered medium, is received at the TRM with high distortion and it is time reversed and re-transmitted back through the medium. The time reversed signal converges back to the source enabling multipath compensation, strong focusing, enhanced imaging

and target detection, and it is useful in communications as well as in medicine applications [9-11]. Here, by exploiting the DBG-based TTR, we propose a novel TRM for UWB signals. TTR through DBG has been demonstrated in [2]: if the RP is launched from the other side with respect to the WP TTR is achieved; in fact, the last part of the IW to be stored is the first to be retrieved. A numerical example is presented. The source (TX) and the receiver (RC) are horn-antennas with operational bandwidth from 5.5 to 7.5 GHz (Fig. 2). The RC is 7-elements array (Fig. 2). The TX-signal (Fig. 3a, blue dashed line) has a bandwidth of 2 GHz with a central frequency of 6.5 GHz. The radiated signal is scattered by 35 randomly distributed metallic and dielectric cylinders with 1.3 and 3.2 cm diameter, respectively [11]. The distorted signals at the RC (Fig. 3a, green continuous line shows the signal received by RC #6) is used to modulate a laser through which the DBG-based TTR is achieved. The WP and the RP are 50 ps FWHM pulses. The reversed signals are then retransmitted through the channel. A good refocusing on the TX is achieved when the TX combines the reversed signals coming from 7 (or more) elements in the RC (Fig. 3b). The quality of refocusing increases with the number of RC positions [9,10]. All-optical TRM has the advantage of the huge bandwidth.

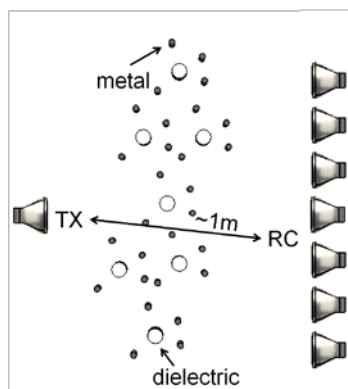


FIG. 2 – TRM setup scheme.

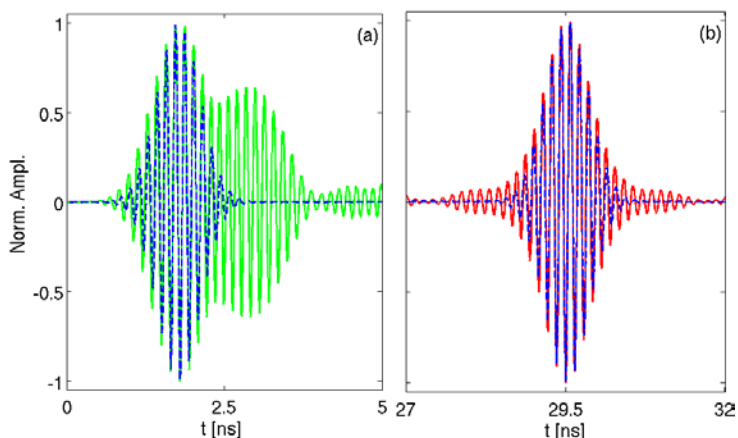


FIG. 3 – (a) TX signal (blue dashed line). RC #6 distorted signal (green continuous line). (b) TX reversed signal (blue dashed line). Focused signal at TX (red continuous line).

IV. CONCLUSIONS

We reported numerical tests on the possible applications of DBGs in UWB systems. In particular the performance for doublet Gaussian pulses generation and for time reversal mirrors have been assessed.

ACKNOWLEDGEMENT

The research has received funding from the EC, FP7 FET-Open Grant Agreement n. 219299, GOSPEL, the University of Padova (project "Signal processing and sensing based on dynamic Brillouin gratings in

optical fibers"), the Italian Ministry of Foreign Affairs (Direzione Generale per la Promozione del Sistema Paese) and was held within the agreement with ISCTI.

REFERENCES

- [1] M. Santagiustina, L. Ursini, "Slow light for signal processing and communications", *Information Photonics 2011*, Ottawa (Canada), May 18-20 2011, 275-FXbt-171.
- [2] S. Chin, N. Primerov, K-Y. Song, L. Thévenaz, M. Santagiustina, L. Ursini, "True Time Reversal via Dynamic Brillouin Gratings in Polarization Maintaining Fibers", *OSA Nonlinear Photonics 2010*, Karlsruhe (Germany), June 21-24 2010, NThA6.
- [3] N. Primerov, S. Chin, L. Thévenaz, L. Ursini, M. Santagiustina, "All-optical calculus based on dynamic Brillouin grating reflectors in optical fibers", *Slow and Fast Light (SL) 2011*, Toronto (Canada), June 12-16 2011, SLMA3.
- [4] K. Y. Song, S. Chin, N. Primerov, L. Thévenaz, "Time-domain distributed fiber sensor with 1 cm spatial resolution based on Brillouin dynamic grating", *J. Lightw. Techn.*, vol. 28, pp. 2062-2067, 2010.
- [5] J. Sancho, N. Primerov, S. Chin, Y. Antman, A. Zadok, S. Sales, L. Thévenaz, "Tunable and reconfigurable multi-tap microwave photonic filter based on dynamic Brillouin gratings in fibers", *Opt. Expr.*, vol. 20, pp. 6157-6162, 2012.
- [6] Q. Wang, J. Yao, "Switchable optical UWB monocycle and doublet generation using a reconfigurable photonic microwave delay-line filter", *Opt. Expr.*, vol. 15, pp. 14667-14672, 2007.
- [7] H. Chen, M. Chen, C. Qiu, S. Xie, "A novel composite method for ultra-wideband doublet pulses generation", *IEEE Phot. Techn. Lett.*, vol. 19, pp. 2021-2023, 2007.
- [8] J. Li, B. P. Kuo, K. K. Wong, "Ultra-wideband pulse generation based on cross-gain modulation in fiber optical parametric amplifier", *IEEE Phot. Techn. Lett.*, vol. 21, pp. 212-214, 2009.
- [9] G. Lerosey, J. de Rosny, A. Tourin, A. Derode, G. Montaldo, M. Fink, "Time reversal of electromagnetic waves and telecommunications", *Radio Science*, vol. 40, RS6S12, 2005.
- [10] G. Lerosey, J. de Rosny, A. Tourin, M. Fink, "Focusing beyond the diffraction limit with far-field time reversal", *Science*, vol. 315, pp. 1120-1122, 2007.
- [11] J. M. F. Moura, Y. Lin, "Detection by time reversal: single antenna", *IEEE Trans. Signal Processing*, vol. 55, pp. 187-201, 2007.

LARGE MODE AREA FIBERS FOR HIGH POWER AND HIGH BEAM QUALITY LASERS

M. Surico, A. Di Tommaso, P. Bia, L. Mescia, M. Bozzetti, O. Losito,
M. De Sario, F. Prudenzano

DEE- Dipartimento di Elettrotecnica ed Elettronica, Politecnico di Bari,
Via Orabona, 4, 70125 Bari
prudenzano@poliba.it

Abstract

Four different high power ytterbium doped fiber lasers are designed and compared via a home-made computer code. Their effective mode areas and beam qualities are numerically evaluated. A novel aperiodic fiber microstructure, very promising in order to construct high power and single mode lasers, has been identified.

Index Terms – beam quality, innovative fibers, laser modeling.

I. INTRODUCTION

Nowadays, fiber lasers are considered feasible sources in almost all the application fields where solid-state lasers are typically employed thanks to their excellent characteristics. Novel optical fibers, characterized by large cores, have been investigated with the aim to prevent nonlinearity and to allow high beam quality emission (i.e. beam quality factor M^2 close to the unit).

Large mode area (LMA) fibers and multicore fibers (MCFs) are the two approaches mainly followed to obtain the aforesaid goals [1-3]. In general, the increasing of the effective mode area decreases the optical power density but it causes both a decreasing of the beam quality and an increasing of bending sensitivity of single-mode (SM) fibers. In several LMA fiber lasers, single mode propagation and large mode area are reached by employing microstructured optical fiber (MOF) lattices instead of the step index ones (SIF). Therefore, a suitable trade-off between effective mode area and bending sensitivity requirements is obtained by exploiting the endlessly single-mode MOF behavior.

The MCF technology allows to obtain larger mode cross-section compared with that achievable via single core and single mode fibers. In MCF lasers, multiple rare earth doped cores are separated by un-doped regions. Therefore, thermal stress and nonlinearity drawbacks due to the high-power levels are strongly reduced. However, quasi-Gaussian emission profiles can be obtained via MCF lasers only if the propagation of the different supermodes are taken into account and appropriate techniques of supermode selection or combining or filtering are

adopted. In this paper, a home-made computer code is employed to investigate four different solutions optimized to obtain high brilliance and large mode area fiber lasers: the first two are based on i) a multimode (MM) 7 core SIF, and ii) a MM 19 core SIF, both adopting a Talbot cavity feedback; the other two solutions are based on iii) a single mode (SM) 19 core SIF and iv) a completely novel SM 1 core aperiodic and single material (quasi-crystal-fiber with air holes) fiber.

II. THEORY

The home-made computer code for simulation of ytterbium doped fiber lasers is implemented by considering the rate equations and the power propagation equations [4-5]. The propagation of all the supermodes is accurately taken into account. The supermode electromagnetic field profiles and the propagation constants are calculated by a commercial full vectorial finite element method FEM. The filling factor of the j -th core for the i -th mode is calculated as the ratio of power of the i -th mode inside the j -th core to the total power of the i -th mode [4-5]. All supermodes in MCFs compete with each other and give their contribute to the total population inversion.

For the lasers based on: i) the MM 7 core SIF and ii) the MM 19 core SIF, both adopting the Talbot cavity feedback, the far field is calculated by using the Rayleigh–Sommerfeld diffraction equation via the FFT method. Among all supermodes, only the in-phase mode has a good far-field intensity profile; it is selected via the Talbot cavity between the fiber end and the feedback mirror. Self and cross coupling coefficients are calculated as in [6]. For iii) the SM 19 core SIF and iv) the novel SM 1 core aperiodic MOF the Talbot cavity is not required. The beam quality is evaluated via the expression reported in [7].

III. RESULTS

Fig. 1 illustrates a sketch of the four fiber sections. For the fiber iv) a quarter of the section is reported. The design of the fiber sections has been performed via a large number of simulations in order to obtain similar effective mode areas A_{eff} , and to optimize the laser performance.

Table I reports the main parameters of the designed fibers. The emission and absorption cross sections of the ytterbium ions in silica glass and the losses are reported in [4]. Ytterbium ion concentration is 5×10^{25} ions/m³. The distance between the mirror and fiber end, $Z_M/2$, of the Talbot cavity has been optimized to obtain the in-phase propagation. Fiber iii) and iv) are designed to be single mode at the signal wavelength.

As an example, Fig. 2 illustrates the variation of the laser output versus the pump power (bidirectional) for the designed lasers with fiber length $L=10$ m.

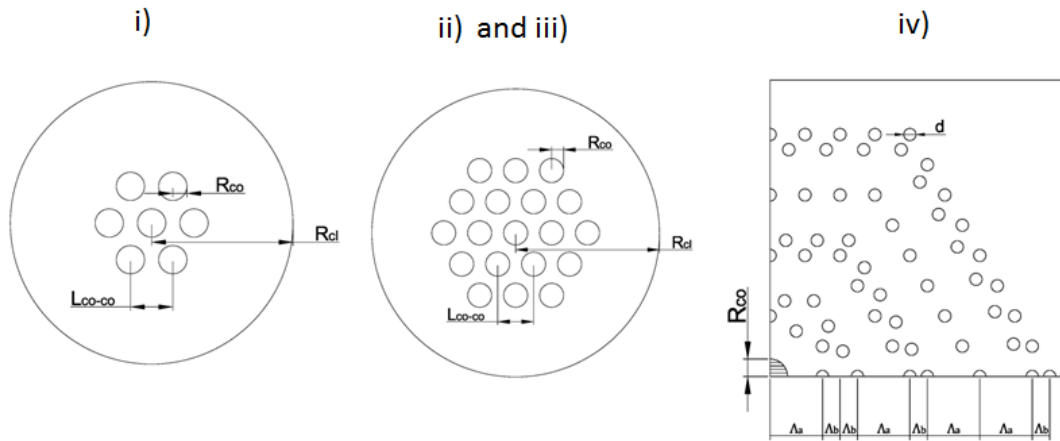

FIG. 1 – Fiber sections.

Table II reports the main output laser characteristics, i.e. the effective mode area A_{eff} , the beam quality M^2 and the slope efficiency η_s for the fiber length $L=10\text{m}$.

TABLE I – LASER PARAMETERS

Kind of fiber	i)	ii)	iii)	iv)
Number of cores	7	19	19	1
Cladding radius R_{cl}	250 μm	250 μm	250 μm	250 μm
Core radius R_{co}	5 μm	4.2 μm	2 μm	13 μm
Air hole radius	#	#	#	0.5 μm
Centre to centre distance L_{co-co}	17 μm	9.0 μm	5.5 μm	#
Pitch Λ_a	#	#	#	20 μm
Pitch Λ_b	#	#	#	5 μm
Cladding refractive index n_{cl} at λ_s	1.4497	1.4497	1.4497	1.4497
Core refractive index n_{co} at λ_s	1.4511	1.4527	1.4502	1.4497
Air refractive index n_A	#	#	#	1
R_1 reflectivity	0.99	0.99	0.99	0.99
R_2 reflectivity	0.04	0.04	0.04	0.04
$Z_m/2$	0.438 mm	1.167 mm	#	#

IV. CONCLUSION

Four fiber lasers have been designed and compared via simulation. High performance lasers based on the fibers of the same kind of i), ii), iii) have been reported in recent literature [1-2], [5-6].

The aperiodic fiber laser iv) is novel and it seems very promising and competitive with respect to the state of the art. In fact, it exhibits a high effective mode area and a high beam quality.

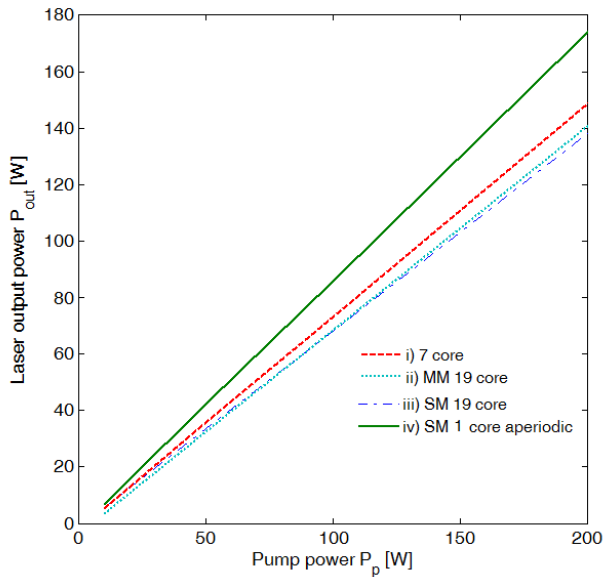


TABLE II – OUTPUT SIGNAL PARAMETERS

fiber	A_{eff} [μm^2]	M^2	η_s
i)	830	2.58	0.75
ii)	957	2.79	0.71
iii)	703	1.05	0.70
iv)	822	1.18	0.88

FIG. 2 – Laser outputs versus the pump power, fiber length $L=10$ m.

REFERENCES

- [1] B.M. Shalaby, V. Kermene, D. Pagnoux, A. Desfarges-Berthelemot, A. Barthélémy, M. Abdou Ahmed, A. Voss and T. Graf, “Quasi-Gaussian beam from a multicore fibre laser by phase locking of supermodes,” *Appl Phys B*, vol. 97, pp. 599–605, May 2009.
- [2] M.M. Vogel, M. Abdou-Ahmed, A.Voss, and T. Graf, “Very-large-mode-area, single-mode multicore fiber,” *Optics Letters*, vol. 34 (18), pp. 2876–2878 Sept. 2009.
- [3] F. Poli, E. Coscelli, T. T. Alkeskjold, D. Passaro, A. Cucinotta, L. Leick, J. Broeng, and S. Selleri, “Cut-off analysis of 19-cell Yb-doped double-cladding rod-type photonic crystal fibers” *Optics Express*, vol. 19, (10), pp. 9896–9907 2011
- [4] F. Prudenzano, L. Mescia, T. Palmisano, M. Surico, M. De Sario, G. C. Righini, “Optimization of pump absorption in MOF lasers via multi-long-period gratings: design strategies” *Applied Optics*, Vol. 51, (9), pp. 1410–1420, March 2012.
- [5] Y. Huo and P. K. Cheo, “Analysis of transverse mode competition and selection in multicore fiber lasers,” *J. Opt. Soc. Am. B*, vol. 22, (11), pp. 2345–2348, Nov. 2005.
- [6] C. Guan, L. Yuan and J. Shi, “Supermode analysis of multicore photonic crystal fibers” *Optics Communications*, vol. 283, pp. 2686–2689, 2010
- [7] A. Mafi and J. V. Moloney, “Beam Quality of Photonic-Crystal Fibers,” *J. of Lightwave Technology*, vol. 23 (7), pp. 2267–2270 July 2005

FIBER OPTIC SENSORS FOR PRECURSORY ACOUSTIC SIGNALS DETECTION IN ROCKFALL EVENTS: FEASIBILITY ANALYSIS

L. Schenato⁽¹⁾, L. Palmieri⁽²⁾, L. Vianello⁽²⁾, G. Marcato⁽¹⁾, G. Gruca⁽³⁾,
T. van de Watering⁽³⁾, D. Iannuzzi⁽³⁾, A. Pasuto⁽¹⁾ and A. Galtarossa⁽²⁾

⁽¹⁾ Research Institute for Hydrogeological Protection, Consiglio
Nazionale delle Ricerche, Padova (IT)

⁽²⁾ Dept. of Information Engineering, Univ. of Padova, Padova (IT)

⁽³⁾ Dept. of Physics and Astronomy & LaserLaB, VU Amsterdam (NL)
luca.schenato@cnr.it

Abstract

Two fiber optic sensors (FOSs) for detection of precursory acoustic emissions in rockfall events are proposed and experimentally characterized. Both sensors are interferometric, but the first one is made of a fiber coil that acts as sensing element, whereas the second sensor exploits a micro-machined cantilever carved on the top of a ferrule. Preliminary experimental tests aimed at comparing the performance with standard piezo-electric transducers show the viability of such FOSs for acoustic emission monitoring in rock masses.

Index Terms – Acoustic emission, fiber optic sensor, interferometry, rock monitoring.

I. MOTIVATION

Landslides generated by the collapse of rock masses represent a major source of hazard in mountain areas: they occur at the apex of a process of stress accumulation in the unstable rock, during which part of the accumulated energy is released in small internal cracks[1]. These cracks and the related acoustic emissions (AE) can, therefore, be used as precursory signals, through which the unstable rock could be monitored. In particular, preliminary geological surveys have suggested to monitor AE in the range 20÷100 kHz[2].

With respect to traditional AE sensors, such as accelerometers and piezoelectric transducers, FOS may provide a reliable solution, potentially offering more robustness to electromagnetic interference, smaller form factor, multiplexing ability and increased distance range and higher sensitivity.

To explore this possibility, in this work we have experimentally analyzed two interferometric fiber-based optical sensors for AE detection in rock masses. Performance have been compared with those from a standard piezo-electric transducer (PZT) and results , while not yet conclusive, confirm that FOSs may represent a viable approach to AE detection for unstable rock masses monitoring.

II. THE FIBER OPTIC SENSORS

The fiber optic AE sensors considered in this work are basically interferometric devices. The first sensor is made of 100 m of G.657 optical fiber, tightly wound on an aluminum flanged hollow mandrel (inner diameter 30 mm, height 42 mm) that is isolated from the environment with acoustic absorbing material. A 4-cm-long M10 screw, which acts also as the main mean of acoustic coupling between the rock and the sensor, is used to fasten the sensor to the rock. This fiber coil sensor (FCS) is inserted in the sensing arm of a fiber Mach-Zehnder interferometer according to the scheme proposed in [3].

The second sensor consists in a micro cantilever carved on the top of a cylindrical silica ferrule [4], with a marked mechanical resonance at about 12.5 kHz (Q-factor of about 400). A standard single mode fiber is housed in the same ferrule and the gap between the cantilever and the fiber end face acts as a vibration-sensitive Fabry-Perot cavity, interrogated with a low-coherence laser, tuned at the quadrature point of the cavity. The sensor is housed in a 2-cm-long M10 bored bolt.

III. THE EXPERIMENT

In order to achieve realistic coupling conditions, we have tested the sensors on a block of Classic Gray Montemerlo Trachyte (50 × 50 × 15 cm in size, about 100 kg in weight). The FOSs could be screwed into an internally threaded chemical anchor, housed in a hole drilled in the center of one of the 50 × 50 cm faces. The block was arranged so that the sensor under test was housed in the bottom face of the block, while the top face was left clear allowing the excitation of AEs. An amplified PZT (VS30-SIC-46dB from Vallen Systeme GmbH, 46 dB of electrical amplification) was used during the tests to compare its performance with those of the FOSs.

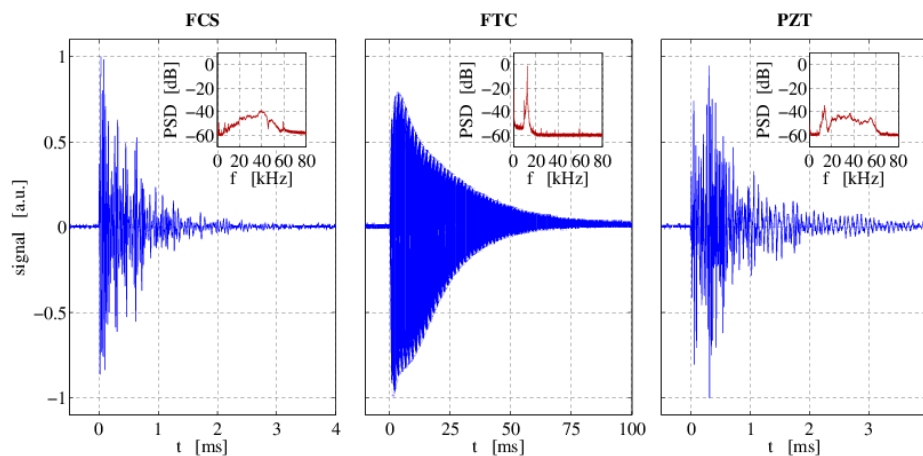


FIG. 1 – Typical signals (top row) and corresponding PSDs (bottom row) recorded by the three sensors (FCS, fiber coil sensor; FTC, ferrule-top cantilever; PZT, piezo-electric transducer).

Acoustic signals have been induced in a repeatable way by dropping a 5-mm-diameter steel ball along a steep slide [5]. Figure 1 shows, for each of the three sensors (the two FOSs and the PZT), a sample signal and the corresponding power spectral density (PSD), recorded when the ball is dropped at the center of the upper face of the trachyte block. We may notice that the signals recorded by the FCS and the PZT are close to the actual AE, while the FTC produces basically a damped oscillation: however, this feature of the FTC is not at all a limitation, since the bare detection and counting of AEs is enough from the present geological application[6].

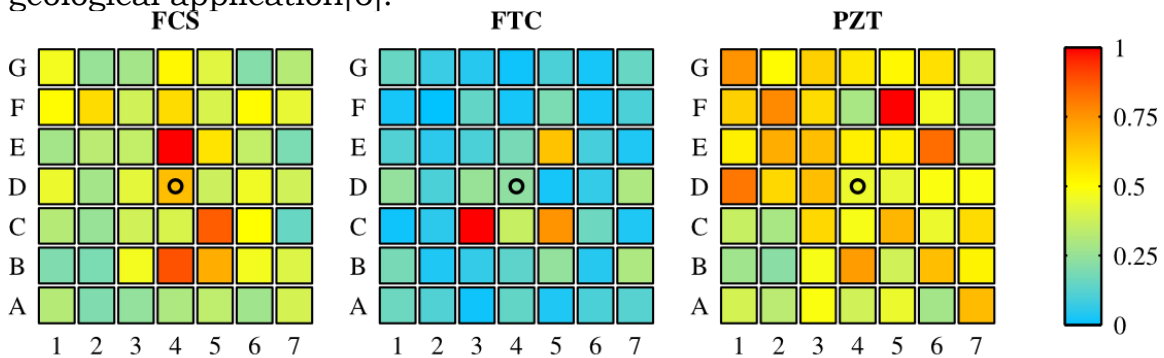


FIG. 2 – Normalized intensities recorded by the sensors as a function of the position of impact (FCS, fiber coil sensor; FTC, ferrule-top cantilever; PZT, piezo-electric transducer; markers indicate sensor position).

To compare the sensors, we have performed several tests by dropping the ball at different positions on an uniform 7×7 grid, drawn on the top 50×50 cm face of the block. The recorded signal, $V(t)$, from each sensor has been used to calculate the “acoustic energy” of the AE over

an arbitrary window T accordingly to $Y(t) = \int_t^{t+T} V^2(\tau) d\tau$, where T is the

average length of the event (T is 2.5 ms for FCS and PZT, whereas for the FTC T is 50 ms). Then, we define the intensity of the detected AE as $\max_t \{Y(t)\}$. Results of these tests are represented in Fig. 2.

The following consideration can be drawn from Fig. 2: (i) higher amplitudes occur nearby the center, where the ball is dropped, with some uncertainties due to rock inhomogeneity; (ii) PZT exhibits the least marked dependency on the excitation position, while the FTC the most one, and the FCS performs in between; this can be explained in term of different sensitivity of the sensors to surface waves (PZT and FTC are more likely sensitive to surface and volume waves, respectively). Regarding absolute performance, the FCS is the least sensitive of the three sensors (but FTC and PZT include at the receiver an electrical amplification of 20 dB and 46 dB, respectively). Noise performances are comparable: SNR is about 30 dB for all sensors.

IV. CONCLUSIONS

In this paper we have reported some preliminary experimental analyses aimed at exploring the applicability of FOSs to the monitoring of unstable rock masses. Two different interferometric sensors have been studied and compared with a standard PZT. Taking into account the differences in electrical amplification, the most sensitive sensor is the FTC, although FTC is also the one with the least temporal resolution. Experimental results suggest also that FOSs (FTC, in particular) could be intrinsically more sensitive to volumes waves, whereas PZT seems more sensitive to surface waves. While preliminary, this analysis has shown that FOSs represent a viable solution for this field of application.

ACKNOWLEDGEMENT

The research was supported by Fondazione Cassa di Risparmio di Padova e Rovigo under the project SMILAND, by Ministero degli Affari Esteri, Direzione Generale per la Promozione del Sistema Paese, by the European Research Council under the European Community's Seventh Framework Programme (FP7/ 2007-2013)/ERC grant agreement 201739, by the European COST Action TD1001 "OFSeSa", and by the Stichting voor Fundamenteel Onderzoek der Materie (FOM) under the Valorization grant number 11VAL11C.

REFERENCES

- [1] D. Amitrano, "Rupture by damage accumulation in rocks," *International Journal of Fracture*, vol. 139, no. 3, pp. 369–381, 2006.
- [2] G. Manthei, J. Eisenblätter, and T. Spies, *Acoustic Emission in Rock Mechanics Studies in Acoustic Emission - Beyond the Millennium*, Y. S. Kishi T., Ohtsu M., Ed. Elsevier, 2000.
- [3] K. Kageyama, H. Murayama, K. Uzawa, I. Ohsawa, M. Kanai, Y. Akematsu, K. Nagata, and T. Ogawa, "Doppler effect in flexible and expandable light waveguide and development of new fiber-optic vibration/acoustic sensor," *IEEE/OSA Journal of Lightwave Technology*, vol. 24, no. 4, pp. 1768–1775, 2006.
- [4] G. Gruca, S. de Man, M. Slaman, J. H. Rector, and D. Iannuzzi, "Ferrule-top micromachined devices: design, fabrication, performance," *Measurement Science and Technology*, vol. 21, no. 9, p. 094033, 2010.
- [5] N. Carino, "The impact-echo method: an overview," in *Proceedings of the 2001 Structures Congress & Exposition*, P. C. C. Editor, Ed. Washington, D.C.,: American Society of Civil Engineers, May 21-23 2001.
- [6] A. Lavrov, "The kaiser effect in rocks: principles and stress estimation techniques," *International Journal of Rock Mechanics and Mining Sciences*, vol. 40, no. 2, pp. 151–171, 2003.

DISTRIBUTED FIBER OPTIC SENSOR FOR INTENSE MAGNETIC FIELD MAPPING

L. Palmieri⁽¹⁾, A. Galtarossa⁽¹⁾, L. Schenato⁽²⁾, M. Guglielmucci⁽³⁾

⁽¹⁾ University of Padova, Department of Information Engineering,
Via Gradenigo 6/B, Padova, Italy,
luca.palmieri@dei.unipd.it

⁽²⁾ Research Institute for Hydrogeological Protection, CNR,
Corso Stati Uniti 4, 35127 Padova, Italy

⁽³⁾ Istituto Superiore delle Comunicazioni e delle Tecnologie
dell'Informazione, Viale America 201, 00144 Roma, Italy

Abstract

We describe a novel distributed fiber optic sensor, which is able to map both strength and orientation of intense static magnetic fields in the area spanned by the fiber. The sensor is based on Faraday rotation and on polarization analysis of the field backscattered by the fiber due to Rayleigh scattering. The small Verdet constant of standard silica fibers makes the proposed technique most suited to intense magnetic fields.

Index Terms – Fiber optic sensor, magnetic field, polarization, reflectometry, Faraday rotation

I. INTRODUCTION

One of the earliest application of fiber optic sensors (FOS) is the measurement of magnetic field, based on either Faraday rotation of polarization or magneto-strictive materials [1–6]. In general FOSs offer many advantages with respect to other sensors, one being the ability of performing distributed sensing. Nevertheless, none of the MFOS proposed so far is able to perform a truly distributed analysis.

In this paper we report a novel distributed MFOS based on Faraday rotation and polarization sensitive reflectometry (PSR) of Rayleigh scattering. The proposed sensor is able to map both strength and orientation of the magnetic field in the area spanned by the sensing fiber [7]. In this work, we report the successful mapping of the 1.5 T static magnetic field of a magnetic resonance imaging (MRI) scanner for medical application. The sensors, although not optimized for the specific aim, has sensitivity of 100 mT, accuracy of about 7% and spatial resolution of about 3 cm.

II. POLARIZATION SENSITIVE REFLECTOMETRY

Polarization sensitive reflectometry aims at measuring of the local birefringence of a fiber, by analyzing the state of polarization (SOP) of Rayleigh backscattering when the fiber is probed with a known optical signal [8]. In particular, in polarization-sensitive optical frequency domain reflectometry (POFDR) the fiber is probed by a frequency-swept continuous wave signal, and spatial resolution of few millimeters can be achieved. The

measurement range is however limited to few hundreds of meters (or even less) by the coherence length of the optical source. The measured round-trip SOP does not directly provide, however, local information about the fiber. Rather, it carries a cumulative information, for the detected field has undergone a round-trip. Nevertheless, the sought local information can be extracted from the data by means of a specific theoretical model and analysis algorithm, as detailed in Ref. [7].

All the asymmetries of a fiber and the perturbations acting along it (including Faraday effect) can be summarized by the 3-dimensional, real-valued birefringence vector, $\vec{\gamma}(z)$, which is in general a function of the position z along the fiber [9]. In general we may set $\vec{\gamma}(z) = \vec{\beta}(z) + \vec{\eta}(z)$, where $\vec{\beta}(z) = (\beta_1, \beta_2, \beta_3)^T$, is the reciprocal birefringence, which accounts for geometric asymmetries and stress-induced anisotropy, and $\vec{\eta}(z)$ is the nonreciprocal circular birefringence, which accounts for magnetic-field induced Faraday rotation. More explicitly, $\vec{\eta}(z) = (0, 0, \eta)^T$, where $\eta(z) = 2V B(z) \cos \psi(z)$, $B(z)$ is the amplitude of the magnetic induction (possibly varying along the fiber), $\psi(z)$ is the angle subtended by the direction of magnetic induction and the direction of forward propagation of light, and V is the Verdet constant, which for silica fibers reads $V \simeq 1.43/(\lambda_{[\mu\text{m}]})^2$ rad/T/m, λ being the wavelength of the probe field [9]. At 1550 nm the Verdet constant is about 0.60 rad/T/m.

PSR can measure the round-trip SOP $\hat{s}_R(z)$ as a function of the scattering point z , but this is related to $\vec{\gamma}(z)$ in a nontrivial way. Therefore, to extract local information on local Faraday rotation, the following algorithm must be implemented [7]: (1) measure the round-trip SOP $\hat{s}_R(z)$ for at least two different input SOPs; (2) calculate the vector $\vec{\gamma}_R(z)$ using $d\hat{s}_R/dz = \vec{\gamma}_R(z) \times \hat{s}_R(z)$ [8]; (3) solve the differential equation $d\mathbf{B}/dz = (1/2)\vec{\gamma}_R(z) \times \mathbf{B}(z)$, with $\mathbf{B}(0) = \mathbf{I}$; (4) calculate $\vec{\gamma}_A(z) = (1/2)\mathbf{B}^T(z)\vec{\gamma}_R(z)$. The key point is that $\vec{\gamma}_A(z) = (\beta_1, \beta_2, \eta)^T$, so its third component singles out the effect of magnetic field along the fiber, enabling their measurement. In particular, this component is completely decoupled from the local reciprocal birefringence of the fiber, which is the main cause of impairment in the Faraday-rotation based MFOSs previously considered [3].

III. EXPERIMENTAL RESULTS

The above theory as been tested by measuring the static magnetic field of an MRI scanner. To this aim we have built a planar sensor, made of three fibers, laid on three parallel planes along the paths shown in fig. 1(a). The three planes were stack one upon the other at a distance of about 5 mm. The sensor has been placed in the MRI scanner parallel to the bore axis, as shown in fig. 1(b). In a central section of the bore (about 60 cm long) the magnetic induction is nominally 1.5 T and parallel to the bore axis, whereas outside it quickly decreases.

The SOP backscattered by the sensing fibers has been measured with a POFDR schematically shown in fig. 1(c). The core of the setup is a customized commercial OFDR, modified to control and change the input

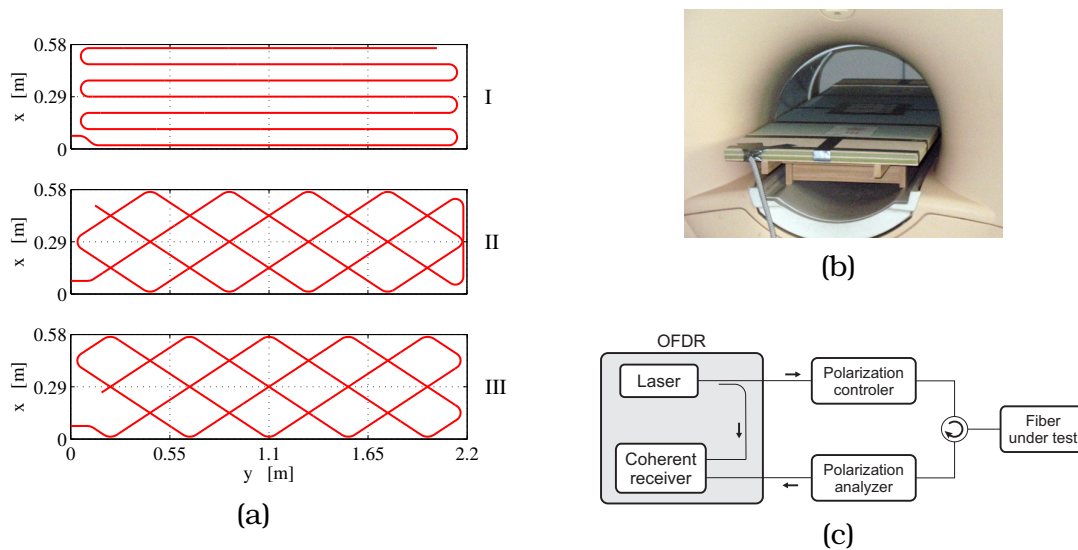


FIG. 1 – (a) Paths along which the fibers of the planar sensor are laid. (b) Picture of the experimental arrangement. (c) POFR setup.

SOP, and to analyze the backscattered SOP [7]. SOP measurement uncertainty, spatial resolution along the fiber, and measurement range are about 1%, 3 cm and 30 m, respectively. Measurements last about 10 s.

The magnetic induction measured along each sensing fiber is shown in figs. 2(a)-2(c). As we can see, there is a good agreement with the expected nominal values, marked by dashed lines. We remark, in particular, that fibers II and III are tilted at an (absolute) angle of 33.4° with respect to the bore axis (i.e. the y axis).

The main advantage offered by this configuration is that fibers cross themselves and each other at several positions. Actually, by overlapping the three paths we get 135 useful crossing points at which the magnetic induction can be measured in two different directions. This allows to map both strength and orientation of the component of the magnetic induction parallel to the sensor plane. The result is the bi-dimensional map shown in fig. 3: vectors represent the direction of the magnetic induction calculated at each intersection; colors encode field amplitude.

IV. CONCLUSIONS

We have described a novel distributed MFOS, which enables the mapping of both strength and orientation of intense and static magnetic field, in the area spanned by the fiber. The sensor is based on Faraday rotation and polarization sensitive reflectometry. Experimental tests performed on a 1.5 T MRI scanner have successfully confirmed the reliability of the proposed technique, showing that the sensor has spatial resolution (along the fiber) of 3 cm, uncertainty of about 7% and sensitivity of 100 mT.

ACKNOWLEDGMENTS

Authors are grateful to Policlinico Abano Terme, Italy, for kindly providing access to the MRI scanner. Partial support from the Italian Min-

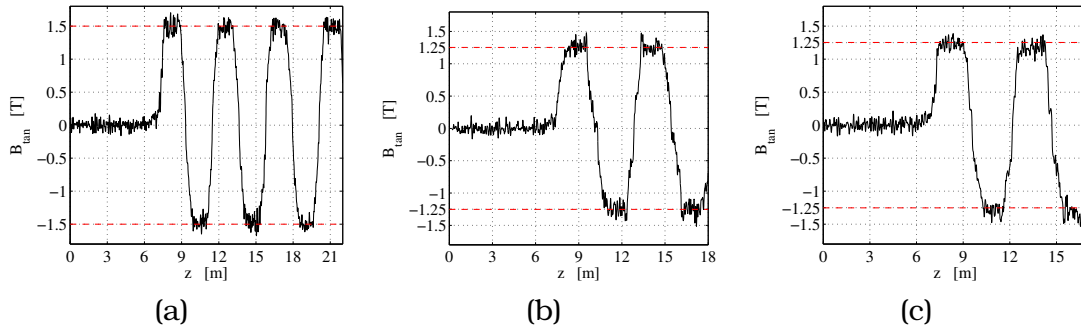


FIG. 2 – (a)-(c) Magnetic induction in the direction of the fiber measured on fibers I-III, respectively. Dashed lines represents the expected nominal values.

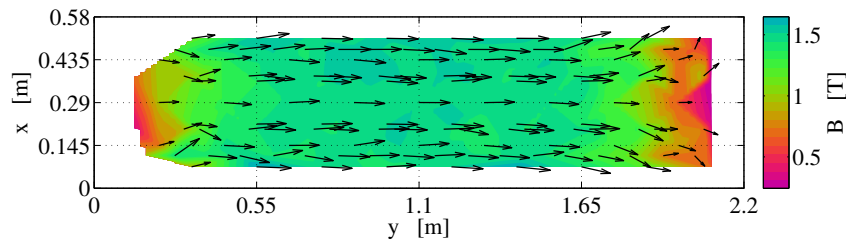


FIG. 3 – Bi-dimensional map of strength and orientation of the magnetic induction field tangent to the sensor plane.

istry of Foreign Affairs (Direzione Generale per la Promozione del Sistema Paese), the Italian Ministry of Instruction, University and Research (project PRIN 2008MPSSNX), Fondazione Cassa di Risparmio di Padova e Rovigo (project SMILAND) and ISCOM, Rome, Italy, is acknowledged.

REFERENCES

- [1] S. C. Rashleigh, "Magnetic-field sensing with a single-mode fiber," *Opt. Lett.* **6**, 19–21 (Jan 1981).
- [2] J. N. Ross, "Measurement of magnetic field by polarisation optical time-domain reflectometry," *Electronics Letters* **17**, 596–597 (1981).
- [3] V. Annovazzi-Lodi, S. Donati and S. Merlo, "Coiled-fiber sensor for vectorial measurement of magnetic field," *J. Lightw. Technol.* **10**, 2006–2010 (1992).
- [4] J. Lenz and S. Edelstein, "Magnetic sensors and their applications," *Sensors Journal, IEEE* **6**, 631–649 (2006).
- [5] V. Passaro, F. Dell'Olio and F. Leonardis, "Electromagnetic field photonic sensors," *Progress in Quantum Electronics* **30**, 45–73 (2006).
- [6] D. Davino, C. Visone, C. Ambrosino, S. Campopiano, A. Cusano and A. Cutolo, "Compensation of hysteresis in magnetic field sensors employing fiber bragg grating and magneto-elastic materials," *Sensors and Actuators A: Physical* **147**, 127–136 (9/15 2008).
- [7] L. Palmieri and A. Galtarossa, "Distributed polarization-sensitive reflectometry in nonreciprocal single-mode optical fibers," *J. Lightw. Technol.* **29**, 3178–3184 (2011).
- [8] L. Palmieri, "Accurate distributed characterization of polarization properties in optical fibers," in [*Optical Communication (ECOC), 2010 36th European Conference and Exhibition on*], 1–6 (2010).
- [9] R. Ulrich and A. Simon, "Polarization optics of twisted single-mode fibers," *Appl. Opt.* **18**, 2241–2251 (1979).

A NEW PUMPING SCHEME FOR HIGH POWER Tm-DOPED FIBER LASERS

E. Balliu⁽¹⁾, A. Braglia⁽¹⁾, A. Califano⁽¹⁾, M. Olivero⁽¹⁾, A. Penna⁽¹⁾,
G. Perrone⁽¹⁾

⁽¹⁾ Department of Electronics and Telecommunications
Politecnico di Torino
C.so Duca degli Abruzzi 24, 10129 Torino, Italy
guido.perrone@polito.it

Abstract

Tm-doped high power fiber lasers are attracting an increasing interest for their perspective industrial and medical applications, despite their maximum output power is currently limited mainly by the lack of specific high power pump sources at the most relevant Tm absorption peak. The paper presents a new pumping scheme that, exploiting another Tm absorption region, allows taking advantage of the enormous progress in terms of delivered power made by Yb-doped fiber lasers. Both Yb- and Tm-doped fiber lasers have been designed and realized in our labs, including some key components, such as the pump and output combiners. Preliminary results demonstrate that the proposed approach may be suitable for the realization of CW lasers able to emit well above 100 W at about 2 μm .

Index Terms – Fiber lasers, Tm-doped fibers, Industrial laser applications, Medical laser applications, Yb-doped fibers.

I. INTRODUCTION

Fiber lasers are rapidly becoming the most popular type of laser for high power applications, replacing both gas lasers traditionally used in the macro processing, such as cutting and welding, and solid-state lasers, which, instead, dominated the marking and micro machining applications. This success is due to a unique mix of peculiar characteristics, such as higher efficiency joined with better beam quality, simplified thermal management, improved mechanical stability and reliability, and possibility to deliver the beam where needed being already guided in a fiber [1].

Today, kilowatt range CW and pulsed lasers typically rely on Yb-doped silicate fibers, so their emission is at about 1 μm , with a pump around 900 nm. These very large output powers are possible thanks to the high efficiency of Yb ions and to the off-the-shelf availability of fiber-pigtailed single emitter diodes with power exceeding tens of watts, so that several hundred watt pumps can be obtained by combining a reasonable number of diodes through specific pump combiners.

There is, however, a growing interest also for the development of high power fiber lasers emitting at longer wavelengths, in the so called “eye-safe” region, because these would require less complex enclosures

with a subsequent simplification in the laser processing machine mechanical setup. Among these eye-safe lasers, the most promising is that using Tm-doped fibers, with emission at about 2 μm , since this wavelength allows processing new types of materials, besides for having relevant applications in medicine. Currently available Tm-doped fiber lasers are, however, practically limited to power levels in the order of 100 W because of the lack of specific high power pump sources at about 975 nm that is where the Tm exhibits the most relevant absorption peak. For example, diodes emitting around this wavelength have very low output powers and, moreover, a cost per watt that is almost ten times that of the diodes used to pump Yb-doped fibers. Therefore, some research groups are starting exploring other alternatives, pumping the Tm-doped lasers at wavelengths where more powerful sources can be available, even if the efficiency might be lower. Of particular interest is considering the possibility to pump at about 1 μm [2], where Nd- and Yb- doped active materials emit, and at about 1.5 μm , where Er-doped materials emit [3]. However, to the best of our knowledge, so far only few experiments, moreover not taking advantage of the high power levels delivered by Yb-doped fiber lasers, have been carried out.

This paper proposes an alternative pumping scheme for CW high power Tm-doped fiber lasers, in which the output of a high power Yb-doped fiber laser module is used for pumping the Tm-active fiber. Then, it describes the work in progress toward the realization of this laser system, including the fabrication of some key components such as the pump combiner for the Yb-doped laser and the combiner/adapter between the Yb- and the Tm-doped lasers.

II. THE LASER DESIGN

The proposed laser system is made by the cascade of a high power Yb-doped fiber laser, which is pumped by semiconductor laser diodes, and a Tm-doped fiber laser, which is pumped by the signal coming from the previous laser (Fig. 1).

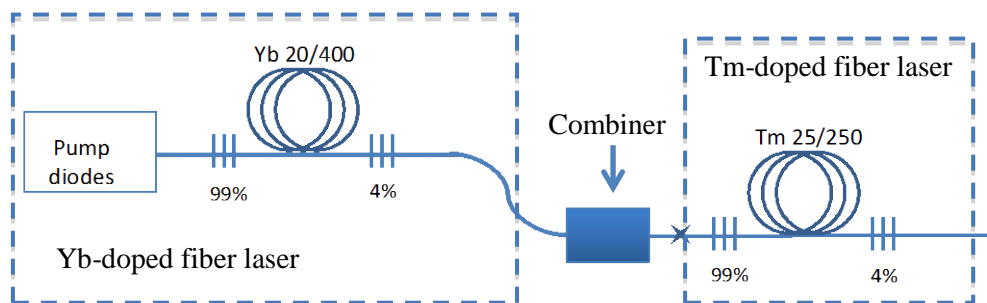


FIG. 1 – Schematic representation of the proposed two laser configuration in which the Yb-doped laser is used to pump the Tm-doped laser.

Both lasers, working in CW conditions, have been designed using a simplified steady-state model for three-level laser systems, in which a set of propagation equations for the progressive pump and the forward and backward propagating signals is simultaneously solved with the rate equations for the populations in just two laser levels. Practical considerations, and the uncertainty with which the parameters of commercial active fibers are known, make unnecessary to use more complex models; indeed, the results of the simulations can mainly be used to identify trends in the laser characteristics, but proper experiments are required to optimize its behavior. Given the expected working power, for both lasers large mode area double cladding fibers have been considered. These are certainly multimode fibers; however, in the design phase a single mode operation has been assumed because in the practical realization the active fibers are deployed in the package in such a way to minimize the losses of the fundamental mode only, so reducing the possibility of higher order modes to lase. Fig. 2 shows an example of the simulations results for about 20 m and 15 m of Yb-doped and Tm-doped fibers, respectively: the blue dotted curve represents the predicted output power from the Yb-doped laser versus the pump diode power, whereas the red solid curve is for the expected output power of the whole laser system, that is the power from the Tm-doped laser when it is pumped by the output of the Yb-doped laser. Results like those in Fig. 2 demonstrate that with the proposed approach it should be possible to obtain several hundred watts at 2 μm , although with a reduced wall-plug-efficiency due to the double conversion, from the diode to the Yb and finally to the Tm.

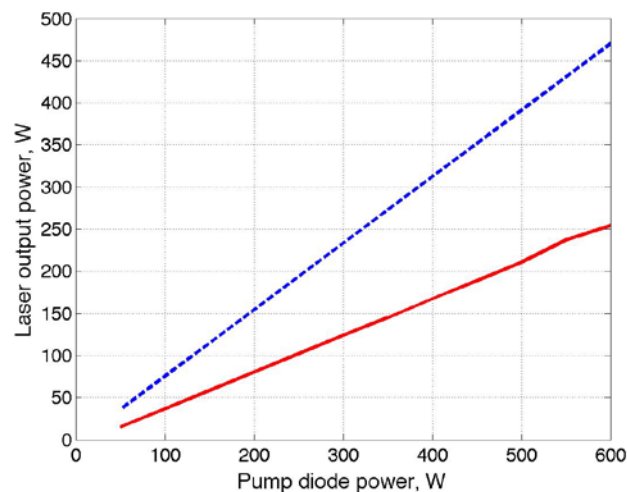


FIG. 2 – Simulation of the two laser system in which the first laser (Yb-doped active fiber, blue dotted curve) absorbs the power provided by the pump diodes and its emission acts as the pump is for the second laser (Tm-doped active fiber, red solid curve).

III. EXPERIMENTAL RESULTS

The scheme in Fig. 1 has been implemented and is currently under optimization. Commercial fibers and gratings have been acquired, while the pump combiner for the Yb-doped laser and the output combiner, which is used both to protect the Yb- doped laser from unwanted back-propagating signals and to adapt its output to the Tm-doped fiber, have been realized in our lab using a specific glass processing machine to taper, fuse and splice the fibers. In both cases extremely low loss devices have been obtained: for example, the output combiner has a transmission larger than 98%. All the components in Fig.1 have been positioned on a cold-plate to control the dissipation and prevent temperature induced damages. The Yb-laser has already been fully characterized obtaining a maximum “safe” output power of about 350 W, while the Tm-laser part is still under preliminary characterization and updated results will be given at the Conference.

IV. CONCLUSION

A laser system able to deliver over than 150 W at 2 μm has been designed and it is currently under experimental optimization. Preliminary results have proved the feasibility of the proposed approach and have demonstrated also that key components such as pump and output combiners with high transmission efficiency can be fabricated.

ACKNOWLEDGEMENT

The authors acknowledge the support of Regione Piemonte under the projects Hipernano and Life.

REFERENCES

- [1] D. J. Richardson, J. Nilsson, and W. A. Clarkson, “High power fiber lasers: current status and future perspectives,” *JOSA B*, Vol. 27, pp. 63-92, 2010
- [2] S. D. Jackson, F. Bugge, G. Erbert, “High-power and highly efficient Tm³⁺-doped silica fiber lasers pumped with diode lasers operating at 1150 nm,” *Optics Letters*, Vol. 32, pp. 2873 – 2875, 2007.
- [3] M. Meleshkevich, N. Platonov, D. Gapontsev, A. Drozhzhin, V. Sergeev, V. Gapontsev, “415W Single-Mode CW Thulium Fiber Laser in all-fiber format”, *European Conference on Lasers and Electro-Optics*, 1p, 2007.

Session 14 – Radio frequency identification

G. Marrocco, and S. Caizzone

Electromagnetic properties of passive RFID networks

S. Manzari, C. Occhiuzzi, A. Catini, C. Di Natale, and G. Marrocco

Chemical loaded RFID antenna for humidity detection

D. De Donno, L. Catarinucci, R. Colella, and L. Tarricone

Performance evaluation of passive UHF RFID tags with software - defined radio

L. Catarinucci, R. Colella, and L. Tarricone

Innovative prototyping techniques for UHF RFID tags

A. Buffi, P. Nepa, and F. Lombardini

Localization of RFID tagged items on a conveyor belt

A. Michel, R. Caso, A. Buffi, and P. Nepa

Near-field UHF RFID antenna for desktop reader

Electromagnetics Properties of Passive RFID Networks

G.Marrocco and S. Caizzone

University of Roma Tor Vergata, Via del Politecnico 1, 00133 Roma,
marrocco@disp.uniroma2.it

Abstract

The UHF passive Radio Frequency Identification technology generally enables an asymmetric interaction between the reader and the tag, the latter only being able to respond to the query of the reader through backscattering modulation. Very recently some experiments put into evidence the possibility to set up a tag to tag communication by using a simple illuminator. The key issues and the physical limitation of such a cross-link are here investigated both theoretically and numerically by fully accounting for the mutual coupling among the tags, their radiation properties and the impedance modulation.

Index Term: RFID, mutual coupling, wireless communications

I. INTRODUCTION

Radio frequency Identification (RFID) is a fast growing technology with countless applications in the control of items, the security assessment, the pervasive monitoring of environmental parameters and the biomedical sensing [1]. Within the current communication modality, tags are interrogated by a standalone reader or by a radio unit embedded into a more complex device such as a smartphone. The tags are usually passive and the communication is only possible between the reader and the tag that replies to the reader itself by means of reflection, on changing its radar cross-section. Tags are therefore not directly aware of the presence of other tags. The inter-tag communication is possible only in case of active devices acting as wireless sensor nodes.

The concept of tag to tag (T2T) communication between passive UHF RFID tags has been introduced very recently by Nikitin et al. in [2]. Two tags placed in close proximity may in principle directly communicate even in the absence of an RFID reader.

Although a preliminary indirect proof has been given in [2], the physical potentiality and limitations of T2T communication are still to be discovered. In this view this contribution presents a theoretical investigation aimed to characterize the inter-tags channel and to derive the performance parameters useful to set up some design guidelines. In particular it is of interest to define the modulation depth and its relationship with the inter-tag distance, geometry, and impedance matching. The modulation depth can be assumed as a merit factor of the T2T channel since it should be high enough (more than 50%) to enable the microchip comparator to discriminate the binary states.

A full understanding of the phenomena is carried out by the help of the mathematical formalism of RFID Grids in [3], [4].

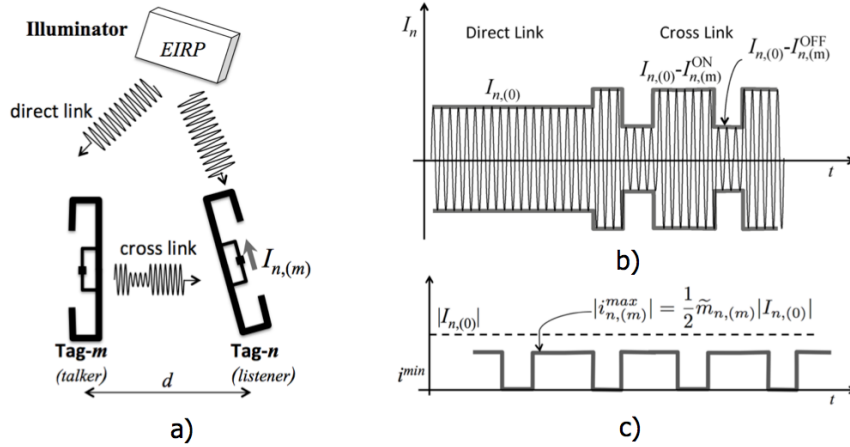


Figure 1. a) Scheme of tag to tag communication wherein the required power for the cross link is provided by and external illuminator. b) Induced current at n th microchip as superposition of unmodulated current (direct link) and modulated current (cross link). c) Demodulated signals after carrier suppression.

II. THE RFID CROSS-LINK

With reference to Fig.1a, a T2T communication requires at least an external e.m. power source, denoted as illuminator. The illuminator is here electromagnetically characterized by its effective length \underline{h}^R and by the radiated $EIRP_R$. For the sake of simplicity, just two tags are here visualized, but the proposed formulation may describe any number of elements. It is assumed that the m th tag, denoted as *talker*, is performing backscattering modulation at the considered time-instant, and hence it acts as the transmitter, while the n th tag is the *listener*. The radiating properties of the two tags are summarized throughout the embedded effective lengths and gains $\{h_n\}$ and $\{G_n\}$, respectively.

The close interaction between tags is such that they have to be regarded as a unique electromagnetic loaded receiver/scatterer provided with multiple ports. This object can be fully described as a distributed multi-port network, an *RFID Grid* [3], characterized by the impedance matrix \mathbf{Z} and by the diagonal impedance matrix

$$\mathbf{Z}_C^{ON/OFF} = \text{diag}(Z_{C,n}^{ON/OFF}) \quad (1)$$

of loading RFID microchips, where the superscript indicates the impedance modulation state enforced by the microchips. Through some calculations, it can be proved that the current over the receiving n th tag when the m th is modulating its impedance may be rewritten as linear superposition of two contributes

$$I_{n,(m)} = I_{n,(0)} - I_{n,(m)}^{ON/OFF} \quad (2)$$

The term $I_{n,(0)} = \beta(r)[Y_G]_n \cdot \mathbf{g}_{n,(0)}$, (with $[Y_G]_n$ the n th row of the admittance matrix of the system $[\mathbf{Z} + \mathbf{Z}_C]^{-1}$, and \mathbf{g}_n the system gain referred to n th port) is the induced current over the n th port due to the direct link (e.g. without modulation), which accounts for the mutual orientation between the tags and the illuminator. The second contribute

$$I_{n,(m)}^{ON/OFF} = \alpha_m^{ON/OFF} \beta(r) Y_{G,mn} [Y_G]_m \cdot \mathbf{g} \quad (3)$$

with $\alpha_m^{ON/OFF}$ a constant depending on modulation state, describes instead the cross-link e.g. the modulated field due to the impedance switch at the m th tag (Fig.1bc).

III. THE MODULATION DEPTH OF THE CROSS-LINK

It is now introduced the *modulation depth* for the cross link between the n th tag and the m th (talker) tag which describes the distance between the ON/OFF electrical states.

$$\tilde{m}_{n,(m)} = \frac{|I_{n,(m)}^{ON} - I_{n,(m)}^{OFF}|}{|I_{n,(0)}|} \quad (4)$$

$$= |Y_{G,mn}| \cdot \left| \frac{[Y_G]_m \cdot \mathbf{g}}{[Y_G]_n \cdot \mathbf{g}} \right| |\alpha_m^{ON} - \alpha_m^{OFF}| \quad (5)$$

The smaller is $\tilde{m}_{n,(m)}$, the more tricky the discrimination of the data-bit for the listener will be.

It is worth noticing that the modulation depth is definitely dependent on the tag-to-tag distance through the coupling matrix Y_G . This is a different behavior with respect to a standalone tag performing backscattering modulation toward the reader, and it is due to the close interaction between direct- and cross-links.

IV. NUMERICAL EXAMPLE

Two simple dipole-like tags with T-match layout (size in Fig.2) are here considered to discuss the above concepts. The assumed microchip impedance is $Z_C = 15 - j135\Omega$ (that of a commercial NXP chip). In a first example the T-match parameters have been optimized to achieve the usual conjugate matching in standalone configuration, so that $Z_{stand} = 15 + j126\Omega$. Accordingly, the modulation depth produces the diagram in Fig.2 (gray line), when the inter-antenna distance is increased up to a wavelength. The diagram has a maximum value of $\tilde{m}_{1,(2)} = 0.55$, now corresponding to an inter-antenna distance of about $d = 0.15\lambda$ which hence is the optimum separation for T2T communication, at least according to this impedance matching strategy.

The same geometry is next re-designed so that the new T-match transformers are suited to achieve Hermite impedance matching $Z_{11}(d_0) + Z_{12}(d_0) = Z_C^*$ for $d_0 = 0.15\lambda$ and to approach the theoretical limit of $\tilde{m}_{1,(2)} = 1$ (see again Fig.2, continuous line). In this case the modulation depth stays

higher than 50% up to inter-tag distance $d=0.25\lambda$, roughly corresponding to {7cm, 8cm} at the US and European RFID frequencies, respectively.

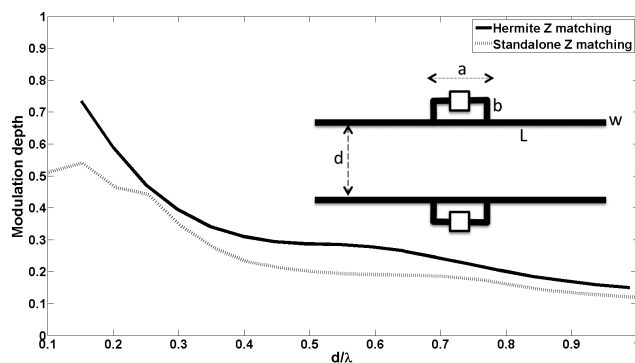


Figure 2. Two T-match tags with different kind of impedance matching: modulation depth vs. antenna separation. Wavelength corresponding to frequency $f=870\text{MHz}$. Size (in [mm]): $w=2$; Conjugated matching: $L = 148, a=20, b=8$. Hermite matching $L = 156, a=20, b=10$.

V. DISCUSSION AND CONCLUSIONS

The main achievements from the above theoretical and numerical analysis are resumed next.

i) The possibility that the listener tag may decode the information coming from the talker tag is dependent on the mutual coupling and on the distance. Such a property is described by the modulation depth parameter.

ii) The modulation depth strongly decays along with the distance between tags due to the interaction between direct- and cross-links. The modulation depth may be improved by a proper antenna matching strategy that directly accounts for the T2T coupling according to the Hermite condition.

iii) Moving to networks of interacting tags, it is possible to demonstrate that the T2T range is limited to the neighboring elements due to a shadowing effect, but the communication paths could be in principle extended to the whole grid by a multi-hop cooperative routing strategy.

A true implementation of the T2T link will require a change in the microchip hardware and new communication protocols. Some preliminary ideas about the latter issue may be found in [5] while the evolution of the microchip is still fully to be considered.

REFERENCES

- [1] G. Marrocco, "Pervasive electromagnetics: sensing paradigms by passive RFID technology", *IEEE Wireless Comm.*, vol. 17, no. 6, pp. 10-17, Dec. 2010
- [2] P. V. Nikitin, K.V.S. Rao, S. Lam, "RFID Paperclip Tags", *IEEE Int. Conf. on RFID* 2011, pp. 162-169
- [3] G. Marrocco, "RFID Grids: Part I - Electromagnetic Theory", *IEEE Trans. Antennas Propag.* Vol.59, N.3, pp. 1010-1026, Mar. 2011
- [4] S. Caizzone, G. Marrocco, "RFID Grids: Part II - Experimentations", *IEEE Trans. Antennas Propag.* Vol. 59, N. 8, pp. 2896-2904, Aug. 2011
- [5] "Stochastic communication protocol method and system for RFID tags based on coalition formation, such as tag-to-tag communication", *US patent application* 20080252424.

CHEMICAL LOADED RFID ANTENNA FOR HUMIDITY DETECTION

S.Manzari, C. Occhiuzzi, A. Catini, C. Di Natale, G. Marrocco

University of Roma Tor Vergata, Via del Politecnico,1, 00133, Roma
(ITALY)

Abstract

Passive UHF RFID tags, beside item labeling, are also able to exploit capability to sense the physical state of the tagged object as well as of the surrounding environment. Here a new family of polymer-doped tags are proposed and fully characterized for the detection of ambient humidity. A sensitive chemical species based on PEDOT:PSS is used to load a shaped slot, carved into a folded-like patch tag. The communication and sensing capabilities of the resulting radio-sensor are here investigated, showing how to control opposite requirements by a proper deposition of the sensitive material. The device could have several interesting applications in the assessment of the air quality and food conservation.

Index Terms – RFID, Sensor, humidity, polymer, PEDOT:PSS.

I. INTRODUCTION

The possibility to use passive RFID tags as sensors [1] has been very recently investigated for the wireless observation of several process in evolutions. In particular, sensitive materials may be integrated together with the tag's antenna at the purpose to transduce chemical/physical variation into changes of the tags' radiation performances. Some preliminary experiments with dipoles loaded by carbon nanotubes demonstrated the possibility to sense the presence of toxic gas in the air [2] while the use of shape memory alloys enabled the threshold monitoring of environmental temperature [3]. It is hence feasible to imagine many applications for the monitoring of the environmental conditions.

Another interesting parameter to be sensed is the humidity. Early prototypes involve sensitive coating or substrates [4, 5] whose electric parameters change because of the absorption of water. As a consequence, the electromagnetic variation of the tag's response (related to impedance and gain) can be remotely detected by the reader. However no attempt was done to relate the achievable sensitivity to the amount of sensing materials and to characterize the dynamic response of such class of devices to cyclic exposures.

This work explores the integration of ad-hoc designed UHF (870MHz) RFID tags together with sensitive polymers to achieve a fully controllable wireless humidity sensor, reducing the amount of chemical matter to small regions in the close proximity of the microchip. The effective sensing performances are moreover finally experimented during cyclic exposures which permit to evaluate the phenomena of recovery and hysteresis.

THE H-SLOT LOADED TAG

The proposed device is a folded planar antenna, over a teflon substrate 4 mm thick, provided with a radiating edge and sensing “glasses-like” slots wherein gas-sensitive polymers can be spread (Fig.1A). The central part of the slots host the RFID IC and it is the most critical area for the determination of the antenna's input impedance, because of the high values of local electric field. The current is forced to flow with opposite phases along the outer and inner perimeters of the slot and hence each half “glasses-like” slots profile may be considered as a combination of six slotlines whose characteristic impedances are affected by the dielectric properties of the polymer spread on top. Since the water absorption produces a change of the polymer's permittivity and conductivity, a variation of both input impedance and losses of the antenna is in turn expected and may be remotely detected by the reader as a modification of the tag's activation power and operative frequency.

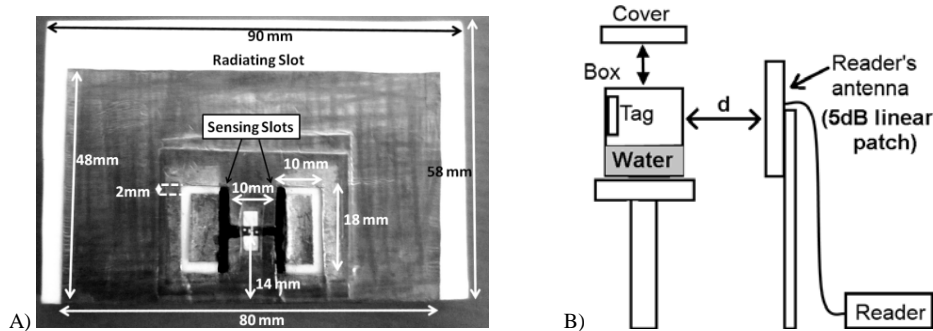


FIG. 1 – A) RFID sensor prototype over a Teflon substrate. Here an NXP IC is used, with $Z_{chip}=25-j237\text{ohm}$ and power sensitivity $P_{chip}=-18\text{dBm}$. Part of the two Teflon rings are coated by a PEDOT/PSS layer (black area). B) Humidity measurement set-up ($d=50\text{cm}$).

In this prototype, the sensing window of the Tag is coated by PEDOT/PSS [5], a commercially available conductive organic polymer. PEDOT is interesting for its conductive feature, whereas PSS exhibits the water's absorption capacity.

II. EXPERIMENTAL CHARACTERIZATION

The RFID sensor is experimentally evaluated when inserted into a closed plastic chamber partially filled with water (Fig. 1B). When the chamber is closed, the humidity percentage tends to $RH=100\%$ (wet air), while in case the cover is removed the humidity is that of the ambient dry air ($RH=50\%$). The former case is referred as exposure, while the latter as recovery. Cyclic exposures may be easily achieved by opening/closing the cap.

The sensing performances of the RFID tag have been preliminary analyzed versus the amount of polymer deposited into the “glasses-like” slots. Fig.2 shows the measured variation of the turn-on power, e.g the

power feeding the reader required to activate the RFID IC, with respect to the increase of humidity for three different polymer depositions.

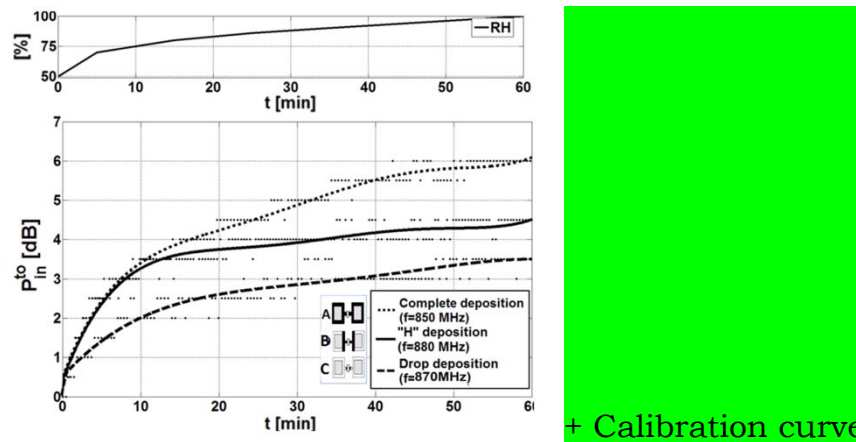


FIG. 2 – Top) Measured variation of humidity inside the plastic box containing the RFID radio-sensor. Bottom) Turn-on power normalized with respect to its initial value, e.g at ambient RH, for three different polymer depositions into the glasses-like slots. Measured data (discontinuous dots) have been fitted by a mean square interpolation.

In each case the frequency that guarantees the largest range of variation, i.e the frequency of the minimum turn-on power, has been selected for the measurement. During the exposure process ($0 < t < T_1 = 60 \text{ min}$) the turn-on power increases of about 3.5dB-6dB depending on the specific PEDOT deposition. It is clearly visible that the wider is the area covered by the polymer, the greater is the water absorption and thus the variation of the radiation performances of the sensor. It is moreover worth noticing that during the early grade of the exposure, e.g. for $50\% < RH < 75\%$ ($t < 10 \text{ min}$) the slopes of the curves A and B are completely overlapped, and hence a similar response may be achieved by using just half the maximum amount of the polymer. Finally, by observation of curve C) it is apparent that even a single drop of polymer placed right under the IC offers the possibility to detect the humidity's change even if with a smaller sensitivity.

Reproducibility, recovery, and hysteresis of the proposed RFID sensor have been tested by set up a cyclic exposure of humidity with two periods of different durations between wet and dry air. An intermediate tag layout (case B of Fig.2) has been considered for the purpose of turn-on power and backscattered power measurements. The achieved profiles are visible in Fig.3 for the selected frequency 880MHz. The change of the RFID powers reasonably follows the variation of the humidity. The recovery process at $RH=50\%$ takes place after the two cycles of humidity exposure during $T_1 < t < T_2$ and $T_3 < t < T_4$. As the box is removed the relative humidity drops down to the value of ambient air and hence the radio sensor starts its recovery. After 60min the recovery can be considered completed. However, just 5min are enough for the sensor to recover 3dB of turn-on power and 4dB of the backscattered

power. The effects are reversible, with a negligible hysteresis. Once the baseline value has been reached, the response remains stable with only 1dB difference between the beginning and the end of the process.

Finally, to double-check the true effectiveness of the doped tag against other external bias, not depending on the polymer itself, also a “blank” tag subjected to the same cyclic exposure as before has been considered. The overall measured change, for instance concerning the backscattered power (see again Fig.3), is negligible in comparison with the measured dynamics of the true polymer-doped tags.

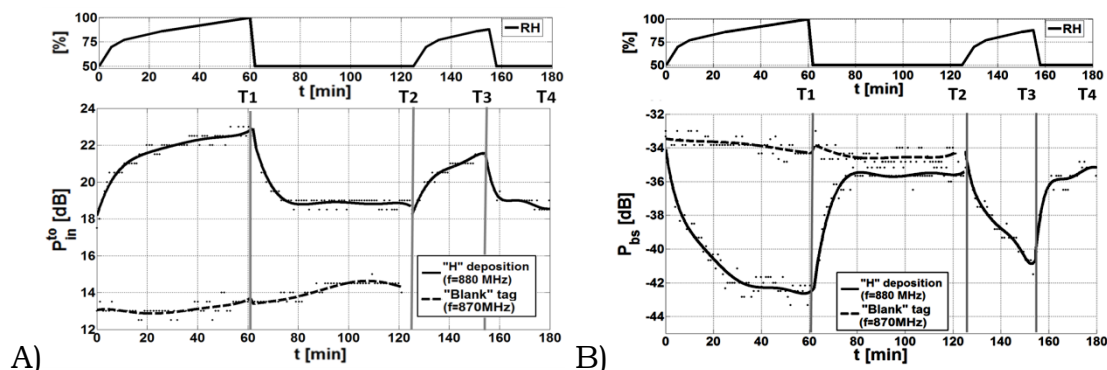


FIG. 3 – Measured turn-on (A) and backscattered power (B) normalized with respect to the turn-on power during cyclic exposures. Also the power from the “blank” tag is visible. Here $T_1=60$ min, $T_2=120$ min, $T_3=150$ min, $T_4=180$ min.

III. CONCLUSIONS

The complete integration of PEDOT:PSS into RFID tag has been here reported for the first time aiming to design and test a passive radio-sensor suitable to monitor the local humidity. Sensing performances and cyclic exposures have been jointly analyzed, leading to a fully working prototype, whose sensitivity and dynamic range can be controlled by the amount and the displacement of polymer into the sensing slots.

REFERENCES

- [1] Marrocco, G.; , "Pervasive electromagnetics: sensing paradigms by passive RFID technology," *Wireless Communications, IEEE* , vol.17, no.6, pp.10-17, December 2010.
- [2] Occhiuzzi, C.; Rida, A.; Marrocco, G.; Tentzeris, M.; , "RFID Passive Gas Sensor Integrating Carbon Nanotubes," *Microwave Theory and Techniques, IEEE Transactions on* , to appear.
- [3] Caizzone, S.; Occhiuzzi, C.; Marrocco, G.; , "Multi-Chip RFID Antenna Integrating Shape-Memory Alloys for Detection of Thermal Thresholds," *Antennas and Propagation, IEEE Transactions on* , vol.59, no.7, pp.2488-2494, July 2011.
- [4] J. Siden, G. Jinlan, and B. Neubauer, “Microstrip antennas for remote moisture sensing using passive RFID,” in *Asia-Pacific Microw. Conf.*, Singapore, Dec. 2009, pp. 2375–2378.
- [5] J. Virtanen, L.Ukkonen, T. Bjorninen, A.Z. Elsherbeni, L. Sydänheimo, “Inkjet-Printed Humidity Sensor for Passive UHF RFID Systems”, *IEEE Transactions on Instrumentation and Measurement*, 2011, Vol. 60, n. 8, pp. 2768 - 2777.
- [6] A. Elschner, S. Kirchmeyer, W. Lovenich, U. Merker, K. Reuter, *PEDOT: Principles and Applications of an Intrinsically Conductive Polymer*, CRC Press, Taylor and Francis Group, LLC, 2011.

PERFORMANCE EVALUATION OF PASSIVE UHF RFID TAGS WITH SOFTWARE-DEFINED RADIO

Danilo De Donno, Luca Catarinucci, Riccardo Colella,
and Luciano Tarricone

Department of Innovation Engineering – University of Salento
Via per Monteroni, 73100, Lecce, Italy
firstname.lastname@unisalento.it

Abstract

Performance evaluation of passive Radio Frequency Identification (RFID) Tags is a very challenging task and commercially available solutions for Tag testing are very expensive and not totally flexible. In this work, we propose a novel approach for the characterization of RFID Tags with Software-Defined Radio (SDR). We show how a cheap (below 1000\$) and flexible SDR-based RFID Reader can be turned into an accurate tool for measuring the goodness of the conjugate matching between the RFID chip and the antenna which primarily affects the Tag sensitivity. We test our platform by analyzing the performance of two built-in-lab Tags: measurements show a strong agreement with theoretical and simulation results.

Index Terms – RFID, Software-Defined Radio, Tag, sensitivity, performance.

I. INTRODUCTION

The adoption of passive Radio Frequency Identification (RFID) technology in the UHF band (865-868 MHz in Europe, 902-928 MHz in US, 952-954 MHz in Japan) is increasing rapidly. Due to low cost and ease of use, RFID based on the EPC Class-1 Generation-2 (Gen2) standard is now the reference technology for a wide range of applications requiring auto-identification, item traceability or access control. The working principle of RFID systems is simple and effective. A wired device called “Reader” transmits a modulated RF signal to a low-cost wireless “Tag” to retrieve the identification number (EPC code) stored into its data memory. A Tag is composed of an antenna and a chip with processing and storage capabilities. The effectiveness of the overall system is driven by the Tag performance, which ultimately depends on the chip sensitivity and on the goodness of the conjugate matching between chip and antenna. The Tag is a purely passive device, whose operating power is supplied by the Reader during the Continuous Wave (CW) transmission phase. Therefore, the main limitation is the energization range (forward link, from Reader to Tag) which depends on the capability of the Tag to harvest RF energy, and specifically on the Tag sensitivity, i.e. the minimum power required to turn-on the Tag.

Commercially available RFID test equipments are typically very expensive. The LabVIEW-controlled PXI RF platform by National

Instruments [1] and the Voyantic Tagformance Lite tool [2] function as enhanced RFID Readers with variable frequency, power, and controllable protocol settings. Such systems are extremely accurate but cost several tens of thousands of dollars. A considerably cheaper option is to resort to commercial RFID Readers, but at the cost of reduced flexibility and accuracy. In fact, Readers return only high-level data and offer very poor configurability.

In this paper, we propose a third alternative approach that combines flexibility, accuracy and cost-effectiveness. The idea is to use an open-source Software-Defined Radio (SDR) implementation of a Gen2 RFID Reader. Indeed, SDR technology provides high flexibility and control of the whole Gen2 communication stack, down to physical layer functions. The freely available Gen2 Reader by Buettner [3], based on GNUradio [4] and the Universal Software Radio Peripheral (USRP) [5], was chosen as the starting point to develop our Tag performance evaluation system. We extensively modified the original Buettner's code by implementing new features in order to obtain a cheap and flexible Tag testing platform. More details about the SDR equipment are given in Section II, while in Section III the consistency of our approach is tested on two built-in-lab Tags.

II. THE SDR TESTING PLATFORM

In recent years the number of chip and Tag vendors has grown considerably. RFID users need accurate and cost effective tools to test and characterize the performance of the large variety of Tags available on the market. Moreover, designers of Tag antennas require flexible platforms to test their prototypes in combination with different chips and in different RFID bands, in real-time, and under different operating conditions. In this work, we propose to consider the Software-Defined Radio (SDR) technology as a valid alternative to the expensive Tag testing equipments available on the market [1], [2]. The aim of SDR is to move the software domain as close as possible to the antenna in order to "turn hardware problems into software problems" and enabling radio engineers to work in a more accessible domain. We consider the freely available SDR Gen2 Reader by Buettner [3], built upon the GNUradio-USRP architecture, as the basis for building a cheap and versatile testing platform for passive RFID Tags. We modified considerably the original Buettner's code. First, the receive chain has been improved with major upgrades at the synchronization and decoding stages. Second, an automatic power control technique was implemented to stabilize the transmit power and ensure a constant power level across the 860-960 MHz frequency band. Finally, we consolidated all these features in a single measurement tool that automatically performs a precise evaluation of Tag performance in terms of sensitivity.

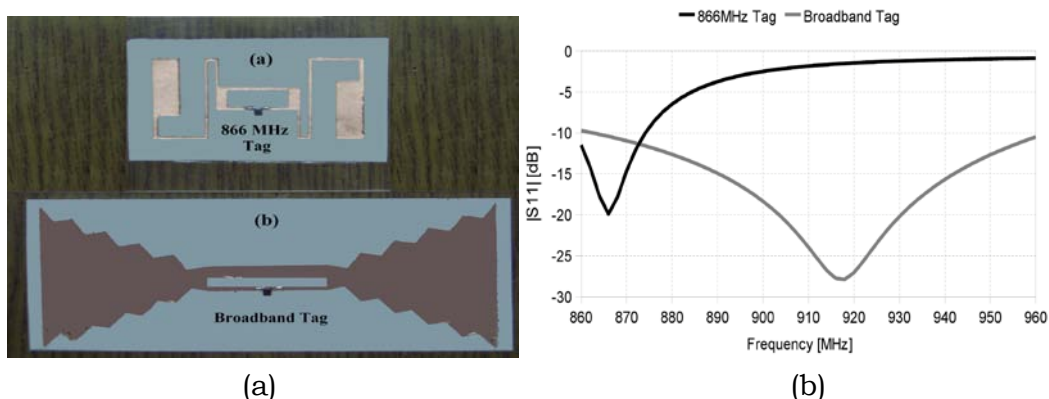


FIG. 1 – Designed Tag antennas (a) and their simulated return loss (b).

III. EXPERIMENTAL RESULTS

In this section, we present some experiments conducted with the SDR testing platform. Two different built-in-lab Tags mounting the Impinj Monza3 chip were evaluated. The antenna of the first Tag (see Fig. 1a) was specifically designed to be compact and narrowband around 866 MHz (European UHF RFID band). On the contrary, for the second Tag (see Fig. 1a) we designed a broadband antenna having best performance around 920 MHz. Figure 2b shows the S11 parameters of both antennas obtained by CST-MW Studio. In order to verify the theoretical behaviour of the developed Tags, we connected two circularly polarized antennas with 5.5 dBi gain to the USRP and run our testing tool on a QuadCore PC under Linux OS. We emulated an ideal free-space environment by taking the measurements in a large outdoor area, with antennas and Tags kept 1.5 meters above the ground.

The tag has been placed at a fixed distance $d=1$ meter from the Reader Tx/Rx antennas and oriented in the direction of maximum gain. The minimum Equivalent Isotropically Radiated Power ($EIRP_{ON}$) required to communicate with the Tag has been recorded at different frequencies in the 860-960 MHz band with 1 MHz spacing. Then, the Tag sensitivity ($P_{TH,tag}$) was estimated according to the following equation (see [6] for more details):

$$P_{TH,tag} = EIRP_{ON} \left(\frac{\lambda}{4\pi d} \right)^2 \eta_{plf}$$

where λ is the wavelength and $\eta_{plf} = 0.5$ is the polarization loss factor.

Results reported in Fig. 2 confirm the expected outcomes. The first Tag is narrowband: it performs extremely well around 866 MHz and its sensitivity degrades rapidly moving away the European band. The second Tag presents a broadband behaviour: its sensitivity is everywhere below -14 dBm with the lowest value (-18 dBm) around 920 MHz. Note that the Monza3 chip has a constant sensitivity of -15 dBm

in the 860-960 MHz band, therefore results in Fig. 4 remark the impact of antenna design in the frequency dependance of Tag sensitivity.

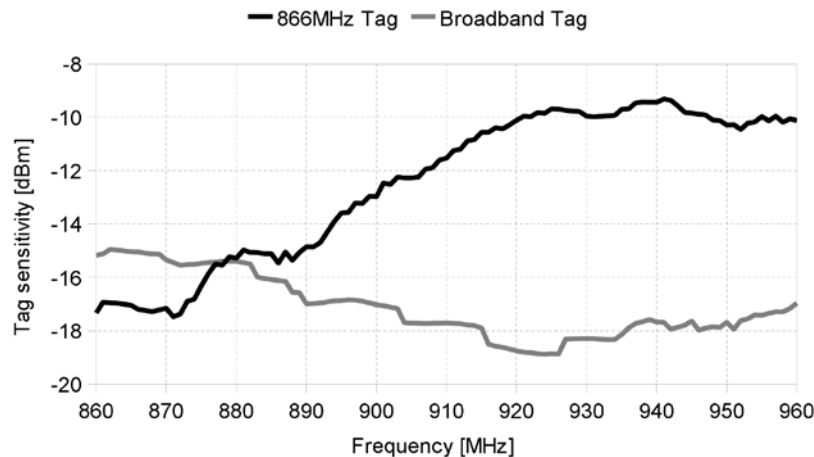


FIG. 2 – Measured Tag sensitivity.

IV. CONCLUSION

In this work, a SDR-based tool for performance analysis of passive UHF RFID Tags has been presented. The use of the Universal Software Radio Peripheral, along with the open-source toolkit GNUradio, leads to a total cost of the equipment below 1000\$. The SDR technology, vice versa, guarantees strong versatility since the effect of Gen2 protocol parameters, operating frequency, and interrogation power on RFID Tag performance can be completely evaluated. Preliminary sensitivity measurements on two built-in-lab Tags demonstrate the appropriateness of the proposed approach.

REFERENCES

- [1] National Instruments, “Using NI Software and Hardware to Develop and Test RFID Tags”, Online: <http://www.ni.com/-automatedtest/rfid.htm>.
- [2] Voyantic Ltd., Voyantic Tagformance Lite, Online: <http://www.voyantic.com/>.
- [3] M. Buettner and D. Wetherall, “A Flexible Software Radio Transceiver for UHF RFID Experimentation”, UW TR: UWCSE-09-10-02, 2009.
- [4] GNUradio, Online: <http://gnuradio.org>.
- [5] Ettus Research LLC, Online: <http://www.ettus.com/products>.
- [6] L. Catarinucci, D. De Donno, R. Colella, F. Ricciato, L. Tarricone, “A Cost-Effective SDR Platform for Performance Characterization of RFID Tags”, IEEE Transactions on Instrumentation and Measurement, vol. 61, no. 4, 2012.

INNOVATIVE PROTOTYPING TECHNIQUES FOR UHF RFID TAGS

L. Catarinucci⁽¹⁾, R. Colella⁽¹⁾, L. Tarricone⁽¹⁾

⁽¹⁾ Innovation Engineering Department, University of Salento
Via per Monteroni, 73100 Lecce, Italy
{[luca.catarinucci](mailto:luca.catarinucci@unisalento.it); [riccardo.coella](mailto:riccardo.coella@unisalento.it); [luciano.tarricone](mailto:luciano.tarricone@unisalento.it)}@unisalento.it

Abstract

Radio Frequency Identification (RFID) technology is increasingly adopted in many contexts where tags customized for specific applications are needed. Nevertheless, in many practical cases, electromagnetic labs which realize RFID tags use either very rudimentary methods, by shaping the tag antenna on a copper film through a handy cutter, or photolithography methods based on rigid PCB. In this work two innovative prototyping techniques suitable for built-in-lab flexible tags based on are presented. The former is based on the joint use of solid ink printers and flexible PCBs, the latter consists of using a cutting plotter on adhesive copper. A rigorous electromagnetic validation is then proposed, demonstrating the appropriateness of the proposed solutions.

Index Terms – Flexible PCB, Prototyping Techniques, RFID, UHF.

I. INTRODUCTION

Over the last few years, the growing interest in Radiofrequency Identification (RFID) technology has stimulated a conspicuous research activity involving design and realization of passive label-type UHF RFID tags customized for specific applications [1-3]. In most of the literature, presented and discussed tags are prototyped by using either rough-and-ready procedures or the here called PL_RPCB — photolithography on rigid Printed Circuit Boards (PCBs) [4]. However, for different reasons, such approaches are not the most indicated, since they are rather time-consuming and, moreover, they give rise to low quality devices in one case, and to cumbersome and rigid tags in the other. In this work, two alternative prototyping techniques suitable for cost-effective, time-saving and high-performance built-in-lab tags, are introduced and discussed. The former is based on the joint use of solid ink printers and flexible PCBs (SI_FPCBs). The latter consists of shaping the tag antenna on flexible adhesive copper sheets by using a machine called Cutting Plotter, and of removing the extra copper manually. The acronym CP_FACS (Cutting Plotter on flexible adhesive copper sheet) will be used from now on to refer to such a technique. Afterwards, a selection of tags, designed and manufactured by using both traditional and alternative techniques, is rigorously characterized and results compared, thus guiding the tag designer towards the most appropriate technique on the basis of specific needs.

II. ALTERNATIVE RFID TAG PROTOTYPING TECHNIQUES

In this section the two proposed RFID Tag antenna prototyping approaches, namely the SI_FPCB and the CP_FACS, are presented and discussed.

A. Solid Ink Based Tag Prototyping on Flexible PCBs: SI_FPCB

In order to realize flexible RFID tags and, at the same time, reduce the prototyping time, a new alternative solution, named SI_FPCB, can be introduced. Differently from the PL_RPCB, where rigid substrates such as FR4, CEM1 or CEM2 are used, this technique is based on flexible substrates of a particular material called DuPont Pyralux [5]. Typically, Pyralux is distributed as thin laminate sheets. Each sheet is composed of a flexible substrate of polyamide of thickness ranging from 12 to 45 μm and a copper-clad laminate of thickness varying between 12 and 35 μm . The basic idea of SI_FPCB technique has been just inspired by the extreme flexibility of Pyralux. Indeed, it becomes reasonable to think that the mask of the tag antenna could be directly printed on a standard Pyralux sheet as easily as printing on paper. In this way, the prototyping process is greatly accelerated and simplified, as time consuming and tedious steps such as UV exposure and sodium hydroxide etching, typically adopted in PL_RPCB, are not required anymore. Moreover, materials and costs are significantly reduced.

From an implementation point of view, it is worth highlighting that the common ink-jet and laser printers are not adequate for this purpose. The former because liquid ink does not adhere on copper, the latter because laser printers cannot print on reflecting surfaces. A very practicable solution, exhaustively tested and validated, consists in using solid ink printers which, differently from traditional printers, deposit a layer of a wax-based ink which perfectly adheres on the copper layer of the Pyralux sheet and, at the same time, shields the copper from subsequent ferric chloride etchings.

B. Cutting Plotter Based Tag Prototyping on Flexible Adhesive Copper Sheets: CP_FACS

CP_FACS is a novel and particularly time-saving technique useful to prototype extremely flexible and high-performing RFID tags through the use of a cutting plotter. This machine is regularly used in the graphic industry for cutting and shaping vinyl foils. Indeed, a cutting plotter is similar to a printer, but it is equipped with a precise cutting tip. In the antenna realization context, the use of cutting plotters is substantially new. The idea is to use flexible adhesive copper sheets instead of vinyl foils. In this way, in a first step the tag antenna layout can be straightforwardly shaped on the copper sheet surface. In the second and last step, the extra adhesive copper is manually removed.

The use of this prototyping technique promises immediate advantages especially in terms of average prototyping time. Indeed, only a few seconds are required to incise the tag antenna on the support and about a couple of minutes to remove the extra copper, depending on the tag complexity. Therefore, less than 5 minutes including soldering are necessary to obtain a functioning tag. Moreover, this technique could be also attractive thanks to the very low cost of both installation and management.

III. DESIGN AND REALIZATION OF UHF RFID TAGS FOR THE EVALUATION OF PROTOTYPING TECHNIQUES

In this section two examples of UHF RFID Tags, suitable for the evaluation of the main properties of above described PL_RPCB, SI_FPCB, and CP_FACS prototyping techniques are designed (Fig. 1). The first one is a narrowband dipole based on meander-line technique working in European dedicated RFID band (865 - 868 MHz). The other is an example of meandered bow-tie wideband antenna designed to work in both UE and USA RFID band (865 -

928 MHz), so to evaluate the appropriateness of the prototyping methods also in a wide range of frequencies. Three different sets of the proposed antennas, properly optimized for PL_RPCB, SI_FPCB and CP_FACS techniques respectively, have been simulated through the full wave simulator CST Microwave Studio®. All the designed antennas have been carefully matched to the Impinj Monza 3 chip having a measured input impedance equal to $Z_{\text{chip_UE}} = 31 - j157 \Omega @ 866 \text{ MHz}$ (central frequency in the UE band). Moreover, it is worth clarifying that, without loss of generality, FR4 (thickness $800 \mu\text{m}$; $\epsilon_r = 3.7$), polyamide (thickness $35 \mu\text{m}$; $\epsilon_r = 2.6$) and paper (thickness $35 \mu\text{m}$; $\epsilon_r = 1.8$) have been used as substrates for PL_RPCB, SI_FPCB, and CP_FACS approaches respectively.

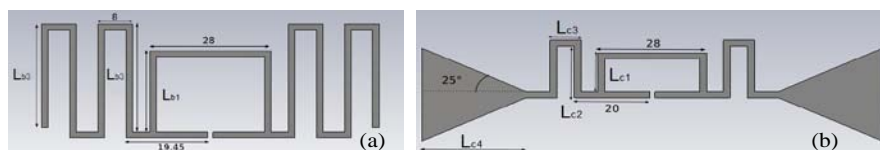


FIG. 1 – Layouts of the two studied tag antennas: narrowband meandered dipole (a), and wideband bow-tie (b). Dimensional parameter varies according to the method.

IV. RESULTS

In this Section, in order to classify PL_RPCB, SI_FPCB, and CP_FACS prototyping methods and to allow a fair comparison among them, the three groups of tags designed and realized in Section III, are exhaustively characterized and compared. Specifically, several measurements of tag antenna impedance have been carried out by adopting the rigorous method described in [6] and results compared.

In Fig. 2a, for instance, both the real and imaginary part of the impedance of the meandered dipole antenna are reported. More specifically, the two simulated results — one for the PL_RPCB case and one valid for both SI_FPCB and CP_FACS alternative approaches — are compared with experimental data. The very good agreement among results in the RFID UHF band (highlighted in the figure) demonstrates that none of the prototyping methods substantially affects the expected antenna properties. In addition, results shown in Fig. 2b confirm such a corollary also for the more complex case of meandered bow-tie.

V. CONCLUSIONS

In this work, two alternative prototyping techniques have been presented, discussed and validated from an electromagnetic point of view. Thanks to the joint use of flexible PCBs and a wax-based solid ink printer, the first proposed method produces flexible and physically robust tags in less than 30 minutes, making use, de facto, only of the last step of the photolithography process (chemical exposure to ferric chloride). The second method, simple but very effective, is even much more rapid: it takes only 5 minutes including RFID chip soldering. It consists of engraving the tag shape on adhesive copper sheets through a numerical control cutting plotter, and of removing the extra copper manually. Such a technique guarantees the desired tag flexibility and it is extremely cost-effective.

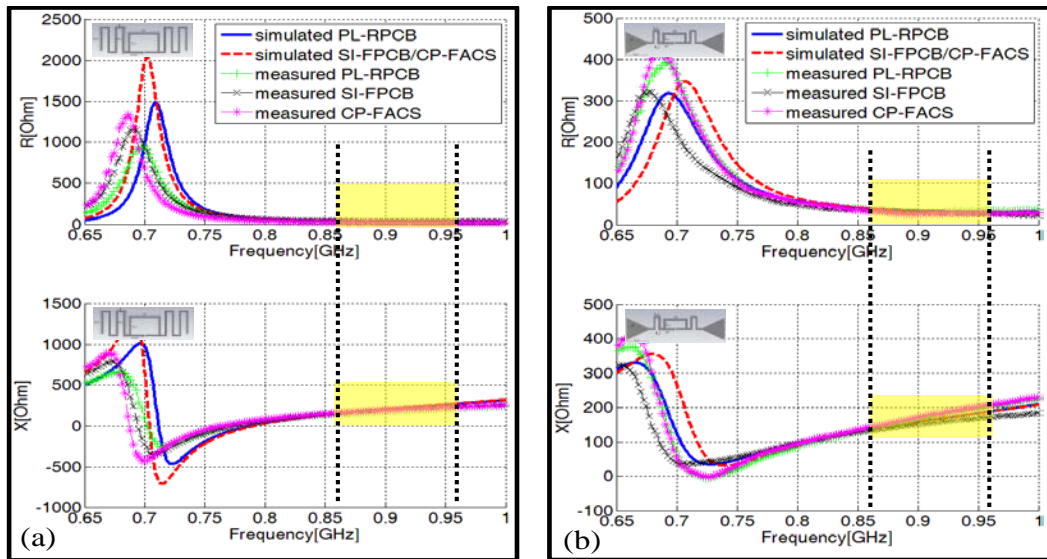


FIG. 2 – Comparison between simulated and measured tag antenna impedance by varying the prototyping method for the two studied antenna layouts: meandered dipole (a), and meandered bow-tie (b).

In order to investigate the quality of tags realized by means of these three approaches two example of narrowband and broadband tag layouts have been designed by taking into account the characteristics of each prototyping method. Then, each tag has been realized through both traditional and proposed alternative processes, and a comparison in terms of tag antenna impedance has been performed. Results are impressive. In spite of a greater simplicity, rapidity and cost-effectiveness, the two proposed prototyping methods generate label-type tags with performance as good as the rigid photolithography-based ones. Case by case, physical robustness, cost, processing time and simplicity, rather than tag performance, will dictate the most appropriate prototyping choice.

REFERENCES

- [1] K.H. Kim, J.G. Song, D.H. Kim, H.S. Hu, J.H. Park, "Fork-shaped RFID tag antenna mountable on metallic surfaces," *Electron. Lett.*, Vol. 43, No. 25, 1400-1402, 2007.
- [2] C. Occhiuzzi, C. Paggi, G. Marrocco, "Passive RFID Strain-Sensor Based on Meander-Line Antennas," *IEEE Trans Antennas Propagat*, vol. 59, Issue 12, pp. 4836–4840, Dec. 2011.
- [3] Y.C. Or, K.W. Leung, R. Mittra, K.V.S. Rao, "Analysis on the platform-tolerant radio-frequency identification tag antenna," *IET Microwave Antennas and Propagation*, Vol. 3, Issue 4, pp. 601–606, 2009.
- [4] Pui-Yi Lau; Yung, K.K.-O.; Yung, E.K.-N.; , "A Low-Cost Printed CP Patch Antenna for RFID Smart Bookshelf in Library," *Industrial Electronics, IEEE Transactions on*, vol.57, no.5, pp.1583-1589, May 2010.
- [5] Dupont Products homepage (last accessed: April, 2012), <http://www2.dupont.com/home/en-us/index.html>.
- [6] K.D. Palmer, M.W. Rooyen, "Simple broadband measurements of balanced loads using a network analyzer," *IEEE Transactions on Instrumentation and Measurement*, Vol. 55, No. 1, pp. 266–272, Feb. 2006.

LOCALIZATION OF RFID-TAGGED ITEMS ON A CONVEYOR BELT

A. Buffi, P. Nepa, F. Lombardini
Department of Information Engineering, University of Pisa
Via G. Caruso 16, 56122 Pisa, Italy
[\[a.buffi, p.nepa, f.lombardini\]@iet.unipi.it](mailto:a.buffi@iet.unipi.it)

Abstract

A new knowledge-based method to locate tagged items on a moving conveyor belt is presented, which is based on a synthetic array technique. System performance is presented through a simplified numerical model and performance analysis is shown with particular attention to the effects of thermal noise and environmental clutter.

Index Terms—UHF-RFID system, tag location, synthetic-array technique

I. INTRODUCTION

Radio Frequency Identification (RFID) technology applications for logistics, intelligent transportation systems, warehouse asset management, anti-counterfeiting in fashion and pharmaceutical industries, access control, security surveillance, airport baggage management and many other authentication and management processes are continuously increasing. Specifically, UHF-band RFID systems allow for remote and simultaneous detection/identification of all the tags illuminated by the reader antenna beam. Recently, not only tag detection and identification but also localization and tracking of tagged items is attracting interest for a large number of location-aware based applications. Therefore, a proliferation of RFID tag localization and tracking solutions and their integration in either commercial RFID readers or ad-hoc data processing systems is expected in the near future, to develop RFID-based Real Time Location Systems (RTLS) [1]. Localization techniques for RFID scenarios (the latter are often crowded indoor scenarios) are required to show high robustness and reliability with respect to multipath and (fixed/mobile) clutter phenomena. The main goal is to obtain a spatial resolution comparable to the size of the tagged items, by resorting to minimal modifications of existing readers (with no modifications of the RFID chipset at all). The latter aspect represents a must for implementing new services in those scenarios where RFID technology is already used, by resorting just to a reader upgrade, and with no changes in terms of number of readers and antennas, antenna positioning and configuration. The application of conventional location techniques (*e.g.* TDOA, RSSI, or PDOA) can be taken into consideration, but standardized RFID systems have some limitations such as the relatively small bandwidth, the limited number of available frequency channels and the short-range characteristics. Furthermore the signal-to-noise ratio is extremely low (especially for passive tags) and the signal amplitude profile is strongly influenced by multipath phenomena. In some RFID portal applications the basic approach consists in forcing the reader to read one tag at a time

(without querying previous and next tags), and then the detected tag will be just the one right under the RFID portal at that time. This aim can be obtained by using reader antennas optimized for near-field coupling, or near-field focused arrays able to maximize the field amplitude in a limited spot region [2].

The authors of this paper recently conceived a knowledge-based method to locate tagged items on a moving conveyor belt (patent pending), which is based on a synthetic array phase-based technique [3]. In Section II a brief overview of the proposed technique is presented, and a preliminary performance analysis is shown in Section III.

II. THE NOVEL PHASE-BASED LOCALIZATION TECHNIQUE

The proposed phased-based localization technique [3] exploits information known *a priori*, namely the conveyor belt path and speed, to simplify localization and tracking of moving tagged items. The belt path can be of any shape and not limited to a rectilinear one. Due to the anti-collision algorithms implemented in UHF RFID protocols, parallel processing of multiple tags can be easily implemented, so allowing for a real-time location of all the tags that a conventional wide-beam reader antenna can radiate simultaneously. When a tag is moving along the conveyor belt, the phase variations of the reflected signal complex envelope (of a reading with respect to a reference one) are related to the variation of the relative distance between reader antenna and tag. Phase-variation history can be measured at the output of the I-Q receiver at the reader side and compared with nominal phase variations. Finally, a matching operator can be applied to determine the nominal history that best fits the measured phase variation history, resembling a (knowledge-based) synthetic array approach. The position associated to the so selected nominal history is chosen as the more likely position of the tag at the reference time. It worth noting that the proposed method works with common wide-beam reader antennas without requiring any hardware modification if the system is implemented in readers that include an I-Q receiver.

III. LOCALIZATION CAPABILITIES

The algorithm spatial resolution has been studied through a simplified RFID radio link simulator taking into account thermal noise, environmental clutter and multipath phenomena. A simplified geometry of a RFID conveyor belt scenario is represented in Fig. 1. The following system parameters have been considered throughout the paper: working frequency, $f_0=866$ MHz, belt speed, $v=1$ m/s, interrogation repetition time, $IRT=100$ ms, reader antenna -3 dB beam-width, $HPBW=60^\circ$, minimum reader-tag distance $r_M=2$ m, tag position at the reference time $x_0=-1.1$ m, and consequently readings number, $N_r=23$. While the tag passes through the reader interrogation region, it can happen that some reader interrogations fail. It is due to several phenomena as thermal noise, tag radar cross section variations,

multipath and clutter phenomena, null directions in reader antenna radiation pattern. Missed readings correspond to a non-uniform spatial sampling of the phase variation history, so resulting in a location performance loss. Fig. 2 shows how algorithm resolution changes as a function of the number of missed readings. Percentage of missed readings are denoted as $s_m = N_{mr}/N_r$, with N_{mr} number of the missed readings. In Fig. 2, $s_m = 0\%$ corresponds to the case of all readings available, while $s_m = 26\%$ means that six readings are missed on a total of $N_r = 23$ (missed readings are randomly distributed inside the observation spatial interval D). Spatial resolution does not change significantly since the spatial interval along the conveyor belt in which the reader identifies the tagged item has been assumed to be the same for any percentage of missed readings: $D = 2.2$ m (the reader antenna illuminates a spatial interval $-1.1\text{m} < x < 1.1$ m). The non-uniform spatial sampling just causes higher side-lobe levels with a negligible resolution loss, as soon as some signal samples are available as inputs of the spatial correlation.

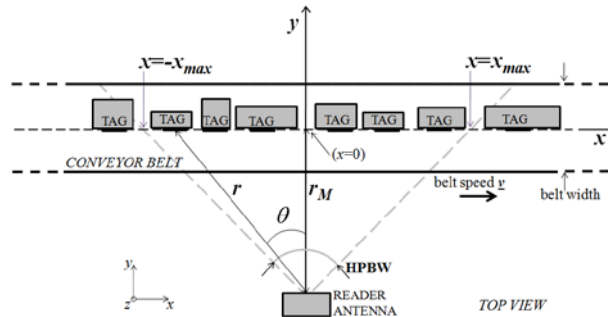


FIG. 1 – A simplified RFID localization scenario (top view).

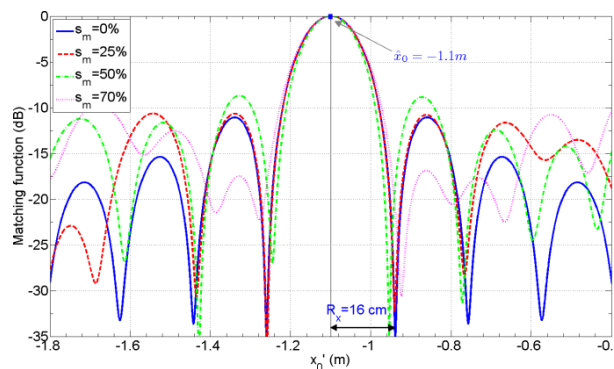


FIG. 2 – Matching function vs. the hypothetical tag position x_0' (actual tag location at the time of the first available reading: $x_0 = -1.1$ m), for different percentages of missed readings $s_m = N_{mr}/N_r$: N_{mr} is the number of the missed readings and $N_r = 23$ represents the maximum number of available readings.

Some interference sources exist that can affect the system performance: the backscattering from fixed obstacles in the scenario (*e.g.* furniture, pillars) or from moving obstacles (*e.g.* objects the tag is attached to). This mobile clutter can be constant or variable from one reading to another. An example of the effect of these interferences on the phase

history and consequently on the matching function is shown in Fig. 3 and Fig. 4, respectively. However, clutter contributions can be easily filtered and separated from the tag response as the latter is characterized by a modulated back-scattering depending on the unique tag identifier. The valuable effect of a conventional average filtering is clearly visible in Fig. 4.

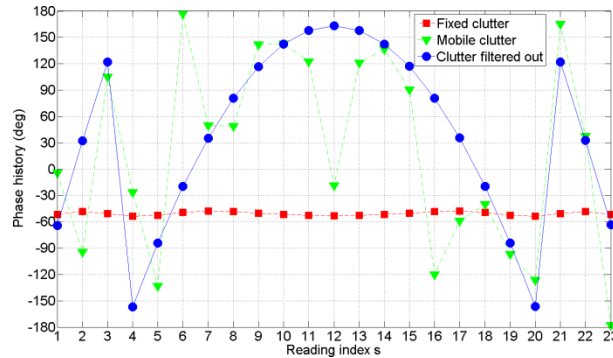


FIG. 3 – A set of phase histories of the I-Q signal at the reader, versus the reading index s , for different clutter contributions.

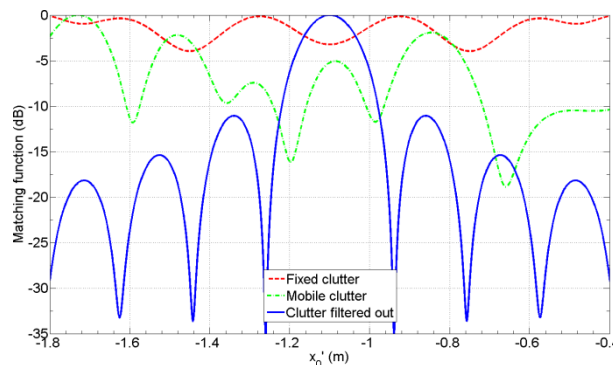


FIG. 4 – Matching function versus the hypothetical tag position x_0' for different clutter contributions; the solid line show how algorithm output is significantly improved after clutter contributions have been filtered out.

IV. CONCLUSIONS

Preliminary results of the performance analysis of a knowledge-based method to locate RFID-tagged items on a moving conveyor belt have been presented. Additional results will be shown at the conference, also including multipath effects on localization accuracy.

REFERENCES

- [1] N. Moayeri, J. Mapar, S. Tompkins, and K. Pahlavan, Special Issue on “Emerging opportunities for localization and tracking,” *IEEE Wireless Communication*, Vol. 18, No. 2, April 2011.
- [2] A. Buffi, A. A. Serra, P. Nepa, H.-T. Chou, and G. Manara, “A Focused Planar Microstrip Array for 2.4 GHz RFID Readers”, *IEEE Transactions on Antennas and Propagation*, Vol. 58, No. 5, pp. 1536-1544, May 2010.
- [3] P. Nepa, F. Lombardini, and A. Buffi, “Location and tracking of UHF-RFID tags”, *Proc. of IEEE-APS APWC*, Turin, Italy, 2011, pp. 1062-1065.

NEAR-FIELD UHF RFID ANTENNA FOR DESKTOP READER

A. Michel⁽¹⁾, R. Caso⁽¹⁾, A. Buffi⁽¹⁾, P. Nepa⁽¹⁾ and G. Isola⁽²⁾

⁽¹⁾Department of Information Engineering, University of Pisa

Via Caruso 16, 56122 Pisa, Italy

andrea.michel, roberto.caso, alice.buffi, p.nepa@iet.unipi.it

⁽²⁾C.A.E.N. RFID s.r.l.

Via Vetraia 11, 55049 Viareggio (LU), Italy

g.isola@caenrfid.it

Abstract

A travelling wave antenna for near-field UHF (865-928MHz) RFID desktop reader applications is proposed. A meandered coplanar waveguide line is properly designed in order to get an almost homogeneous magnetic field amplitude; thus, the detection of a tagged item in an arbitrary position and orientation is possible, ensuring a high read rate. Results in terms of reflection coefficient, gain, and effective isotropic field factor are discussed. Finally, the overall RFID system performance is evaluated in terms of tag detection, considering commercial RFID tags.

Index Terms—UHF RFID, near-field reader antenna, desktop reader.

I. INTRODUCTION

In recent years, RFID systems operating in the UHF (865-960MHz) band rapidly attracted a considerable attention in various applications for item-level tagging in supply chain managements and retail stores. In order to reduce environmental sensitivity to the nearby objects, Near-Field (NF) UHF RFID systems have been proposed [1]. In this case the electromagnetic coupling between reader and tag antennas occurs in the near-field region instead of the far-field region [2], with the benefits of high read rate and data rate typical of UHF-RFID systems. Solutions with both a strong electric or magnetic field near the antenna surface have been proposed in the open literature[3], for applications such as smart shelves or desktop readers.

In this paper a novel NF-UHF RFID reader antenna for desktop reader is presented. In Section II, the antenna design and performance are described, while measurements of the overall RFID system performance in terms of tag detection is presented in Section III, by considering two commercial RFID tags.

II. RFID READER ANTENNA DESIGN AND PERFORMANCE

This paper is aimed to design a UHF (865-928 MHz) RFID reader antenna able to shape the electromagnetic field amplitude in the antenna near-field region, in order to detect tags in a distance range up to around 10cm from

the antenna surface. A travelling wave antenna has been designed. In particular, a coplanar waveguide (CPW) line has been chosen such that is able to generate a relatively strong electromagnetic field in proximity of the reader antenna, but with a relatively low far-field gain. The higher the CPW line characteristic impedance, the stronger is the magnetic field near the reader antenna; therefore, a 150Ω CPW line has been chosen instead of a conventional 50Ω one.

A $275 \times 135 \text{ mm}^2$ planar and thin antenna has been realized on a 0.8-mm-thick FR4 substrate. The internal conductor width has been set to 2mm. In order to obtain a magnetic field distribution as uniform as possible above the antenna surface, an asymmetrical meandered CPW line has been designed (Fig. 1a), referred as *Snake Antenna* in the following. A quarter-wave impedance transformer has been introduced to match the CPW line to the required 50Ω input impedance. The CPW line is terminated on a 50Ω matched load, to avoid a standing wave (non-uniform) field pattern on the antenna surface, and to minimize the antenna far-field gain. Furthermore, a reflector plane is placed at a distance $H=12\text{mm}$ from the FR4 laminate (Fig. 1b), making the reader quite independent from the desk material properties. Both simulation and measurement results for the *Snake Antenna* reflection coefficient are shown in Fig. 1c, and they show a good agreement. The reflection coefficient is less than -14dB (VSWR <1.5) in the UHF RFID band (a percentage impedance bandwidth of 7%). The simulated antenna gain is equal to -13dBi .

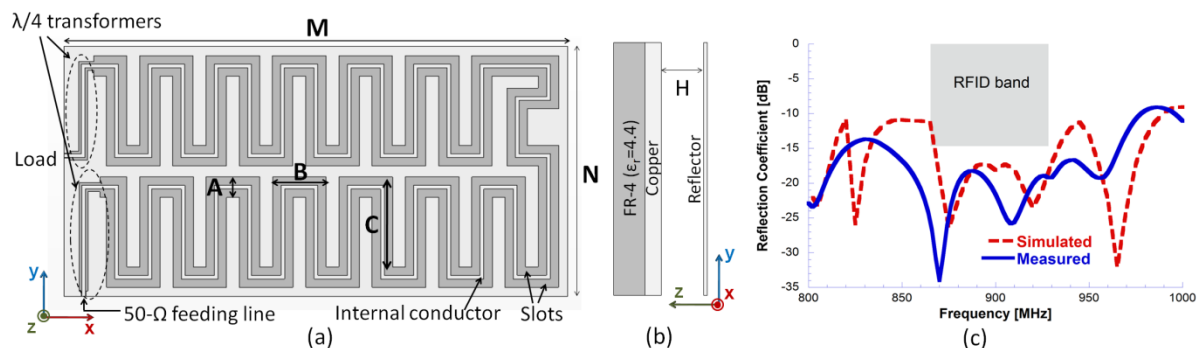


FIG. 1 – (a) Top and (b) lateral views of the proposed Snake Antenna. (c) Simulated and measured reflection coefficient. Antenna geometrical parameters: $M=275\text{mm}$, $N=135\text{mm}$, $A=11\text{mm}$, $B=29\text{mm}$, $C=49\text{mm}$, $P=0.753\text{mm}$, $H=12\text{mm}$.

An important NF RFID reader antenna parameter is the Effective Isotropic Field Factor (EIFF), which represents the ratio between the radiated field in the far-field region with respect to that radiated in the near-field region, normalized to the same quantity for an isotropic radiator. At a distance of 1cm, the *Snake Antenna* exhibits an EIFF equal to 10dB, demonstrating good near-field performance. In Fig. 2, the magnetic field intensity on the plane parallel to the reader antenna, at a distance of 1cm, is shown, for a 30dBm input power. It is worth noting that the field is almost uniform on the whole reader antenna area ($275 \times 135 \text{ mm}^2$). Despite the considerable size of the antenna surface, the maximum of the magnetic field intensity

reaches up to -15dBA/m . In Fig. 3, the amplitude of the H -field components is shown, when the reader is fed with 30dBm input power. It should be noted that, thanks to the adopted meandered structure of the CPW line, all H -field components exhibit an almost homogeneous amplitude distribution on the antenna surface, so allowing a good readability of tags arbitrarily oriented.

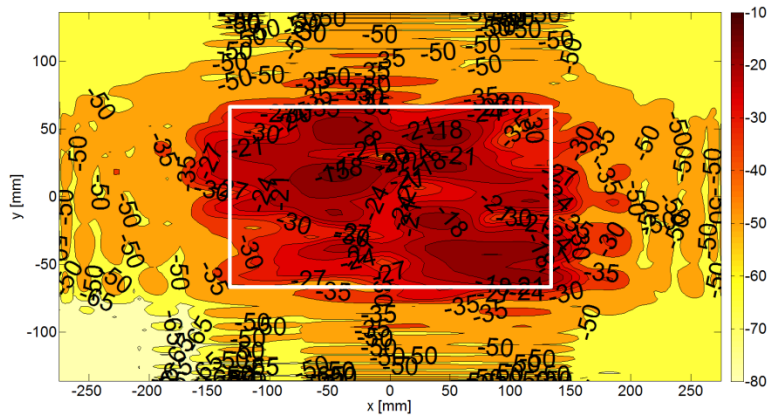


FIG. 2 – Magnetic field intensity (dBA/m) on the plane parallel to the reader antenna, at a distance of 1cm, when the antenna is fed with a 30dBm input power. The white line indicates the reader antenna border.

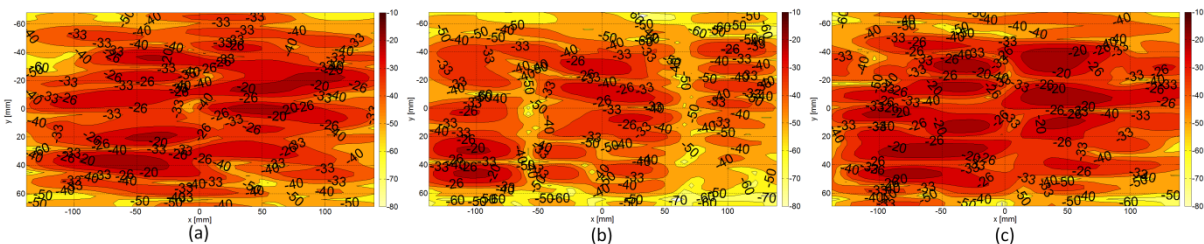


FIG. 3 – Magnetic field intensity (dBA/m) on the $275 \times 135 \text{ mm}^2$ plane, at a distance of 1cm from the reader: (a) H_x , (b) H_y and (c) H_z .

III. MEASUREMENTS OF TAG DETECTION

The performances of the proposed *Snake Antenna* have been tested also considering the overall RFID system. In particular an UHF RFID reader (CAEN R1260I Slate) has been employed to obtain measurements of tag detection range by varying the orientation, the position and the distance of the tag with respect to the antenna surface. Two different tags have been used: the Inlay UH113, Lab-ID (oriented to near-field applications), and the ALN 9640 Squiggle Inlay, Alien Technology (optimized for far-field applications). For this test, the US RFID band (902-928 MHz) has been considered, setting the reader input power equal to 23dBm (200mW). A plane with the same size of the antenna surface ($275 \times 135 \text{ mm}^2$) has been divided in 4×9 cells, and the readability test has been repeated in each cell, for both tags. Fig. 4 shows the average percentage of the whole area in which the tags can be detected, by varying the distance from the antenna

surface. It should be noted that the tag readability strictly depends on the particular tag and its sensitivity to the direction of the incoming electromagnetic wave. Anyway, the proposed *Snake Antenna* is able to generate a field such that is possible to detect both the near-field and the far-field tags up to 10cm, with only 23dBm of input power, in more than 50% of the antenna surface.

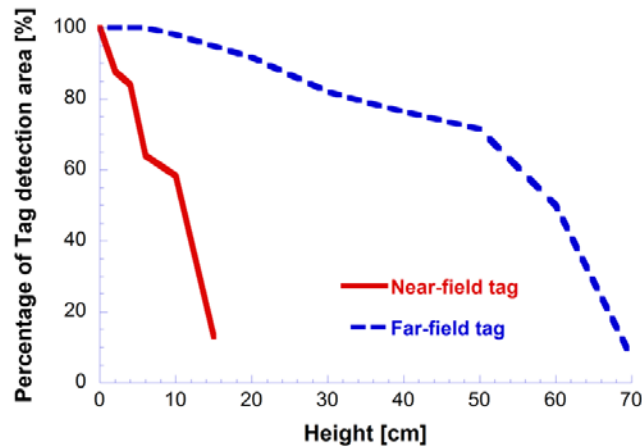


FIG. 4 – Average percentage of the entire area ($275 \times 135 \text{ mm}^2$) in which the tags can be detected, by varying the distance from the antenna surface.

IV. CONCLUSIONS

A travelling wave antenna design for a near-field RFID desktop reader, operating in the 865-928 MHz band, has been presented. The CPW meandered line has been realized to obtain a magnetic field distribution as homogeneous as possible, for all the field components, so allowing the detection of a tagged item placed in an arbitrary position on the antenna surface, and for any tag orientation. Simulated results have been shown in terms of reflection coefficient, gain, EIFF and magnetic field distribution. An experimental analysis of the tag detection area has been also presented, showing good performance of the entire RFID system with only 23dBm of input power.

REFERENCES

- [1] F. Fuschini, C. Piersanti, L. Sydanheimo, L. Ukkonen, and G. Falciasecca, “Electromagnetic analyses of near field UHF RFID systems”, *IEEE Transactions on Antennas and Propagation*, Vol. 58, No. 5, pp. 1759-1770, May 2010.
- [2] A. Buffi, P. Nepa, and G. Manara, “Analysis of Near-Field Coupling in UHF-RFID Systems”, *Proceedings of 2011 IEEE-APS Topical Conference on Antennas and Propagation in Wireless Communications (APWC 2011)*, pp. 931-934, 2011.
- [3] H.-W. Liu, C.-F. Yang, C.-H. Weng, H.-L. Kuo, K.-H. Wu, and Y.-S. Lin, “An UHF Reader Antenna Design for Near-field RFID Applications”, *2009 Asia Pacific Microwave Conference (APMC 2009)*, pp. 2394-2397, 2009.

Session 15 – Photonic crystals

S. Roy, M. Santagiustina, S. Combrié, A. De Rossi, A. Wilinger, and G. Eisenstein
Slow light engineered photonic crystal waveguide: propagation and parametric gain properties

D. Modotto, G. Manili, U. Minoni, S. Wabnitz, M. Andreana, V. Couderc, and A. Tonello
Giant dispersive wave generation in double core photonic crystal fiber

E. Coscelli, F. Poli, A. Cucinotta, and S. Selleri
Air-hole ring influence on the cut-off properties of 19-cell double-cladding photonic crystal fibers

S. Malaguti, G. Bellanca, S. Trillo, S. Combrié, and A. De Rossi
Filter design for OTDM and WDM receivers in PHC technology

A. Brancaccio, G. Leone, R. Solimene, and R. Pierri
Fault detection in a dielectric grid

A. Vaccari, A.C. Lesina, L. Cristoforetti, A. Chiappini, and M. Ferrari
A computational approach to the optical characterization of photonic crystals and photonic glasses

SLOW-LIGHT ENGINEERED PHOTONIC CRYSTAL WAVEGUIDE: PROPAGATION AND PARAMETRIC GAIN PROPERTIES

S. Roy⁽¹⁾, M.Santagiustina⁽¹⁾, S. Combrié⁽²⁾, A. De Rossi⁽²⁾, A. Willinger⁽³⁾,
G. Eisenstein⁽³⁾

⁽¹⁾ CNIT –DEI, Università di Padova,
Via Gradenigo 6b, 35131 Padova, Italia
marco.santagiustina@unipd.it

⁽²⁾ Thales Research and Technology,
Route Départementale 128, 35131 Palaiseau, Francia

⁽³⁾ Department of Electrical Engineering, Technion,
32000 Haifa, Israel.

Abstract

The linear and nonlinear properties of GaInP photonic crystal waveguides engineered for slow light application are presented. A full vectorial mode analysis method has been used. The dispersion of the nonlinearity and of the losses is taken into account for estimating parametric gain in degenerate four wave mixing. Narrowband optical parametric amplification is achieved in the slow light regime.

Index Terms–Photonic crystal waveguide, Dispersion property, Four wave mixing, Narrowband optical parametric amplification

I. INTRODUCTION

Semiconductor photonic crystal waveguides (PhCWs) attribute an enormous flexibility in light guiding mechanism and attracts a great attention in the current research of guided wave optics. Particularly in the slow light (SL) regime [1], a proper designing of the geometry of the PhCW structure enables numerous linear and nonlinear physical processes to interact and lead to interesting potential applications for a new generation of optical communications and microwave photonic system [1]. In particular, very efficient four wave mixing (FWM) can be achieved due to the huge nonlinearity and the dispersion engineering of specially designed SL PhCWs. In this article, we theoretically study an engineered PhCW realized with III-V semiconductor (GaInP) for degenerate FWM. In the theoretical model all dispersive linear and nonlinear terms have been considered. Eventually, a regime narrowband optical parametric amplification (NBOPA) is predicted, which can find applications for tuneable SL, or in parametric oscillators.

II. STRUCTURE AND PROPAGATION CHARACTERISTIC DESIGN

The proposed design of an engineered PhCW for FWM application achieves the relevant characteristics of the slow mode propagation, i.e.

large group index and low group velocity dispersion which favors phase matching, by coupling the TE fundamental even mode to a TE odd mode. Such design, proposed in [2], is very simple and repeatable, and enables a good confinement of the resulting quasi-even Bloch mode, thus fostering nonlinear effects.

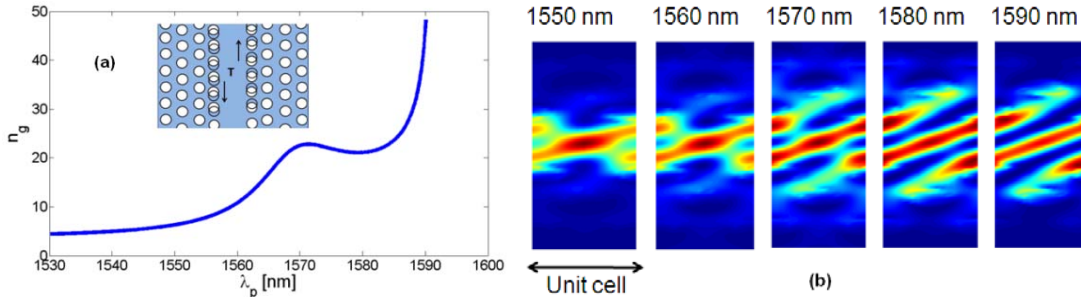


Fig. 1(a) Group index (n_g) as a function of wavelength (λ_p) (inset the refractive index profile of PhCW, showing translation (T) in innermost row of air holes) (b) Scalar fields for different wavelengths in the unit cell of the PhCW

The results that will be presented here refer to a membrane PhCW having the air-holes in a triangular lattice with parameters $a=484$ nm (crystal period), $d=0.25 a$ (hole diameter), and $h=185$ nm (slab height). The air holes of the innermost row have a diameter $d_1=0.24 a$ and are shifted outward by $0.18 a$. The linear dispersion is tailored here by means of a structural modification that entails a shift along the propagation axis of the innermost air-holes rows, on opposite directions on each side of the PhCW. Here, the translation parameter $T=0.08 a$ is used for the innermost rows of air holes. A schematic diagram of such structure is presented in the inset of Fig. 1a. All the properties (modes, group indexes etc.) have been calculated through a full vectorial mode analysis with the MPB code [3]. The group index, n_g , for the propagating Bloch mode in such designed structure is shown in Fig. 1a. The field amplitude, in the unit cell of the PhCW, is presented as a function of the wavelength in Fig. 1b. The evolution of field shapes clearly show the strong dispersion effects arising in this range of wavelengths.

III. MODELING THE DISPERSION IN NONLINEAR COEFFICIENTS

The highly dispersive nature of the field presented in Fig. 1b must be incorporated in the nonlinear coefficients, especially when effects involving different frequencies are considered (e.g. FWM, but also cross-phase modulation, XPM). The dispersion of the nonlinear response due to the overlap integrals of the mode at different frequencies has been generally overlooked, also because of the difficulty of accurately taking this effect into account. We have derived [3] a simplified approach to estimate the field overlap integrals in PhCWs. In particular the self-phase modulation (SPM) overlap integral can be interpolated by:

$$I_{SPM}(\lambda_p) = A \left\{ 1 + \exp[-2B(\lambda_p - \lambda_0)] - 2 \exp[-B(\lambda_p - \lambda_0)] + C \right\} \quad (1)$$

where A , B , C , and λ_0 are the fitting parameters to be determined.

The four-parameter formula bears similarity to the Morse potential and so the parameters can be related to specific properties of PhCW. XPM and FWM coefficients can then be derived from the self-phase one, through geometric means [3], slightly corrected to account for the interacting wave detuning. So, the complete modeling of nonlinear dispersion is achieved.

IV. PROPAGATION LOSS

The propagations losses in such nano-photonic structure also exhibits a high dispersive nature. For an accurate estimation of FWM gain, the losses should be incorporated. Here, the experimentally measured loss parameters of the manufactured PhCW has been also fitted as function of group index, as shown in Fig. 2a.

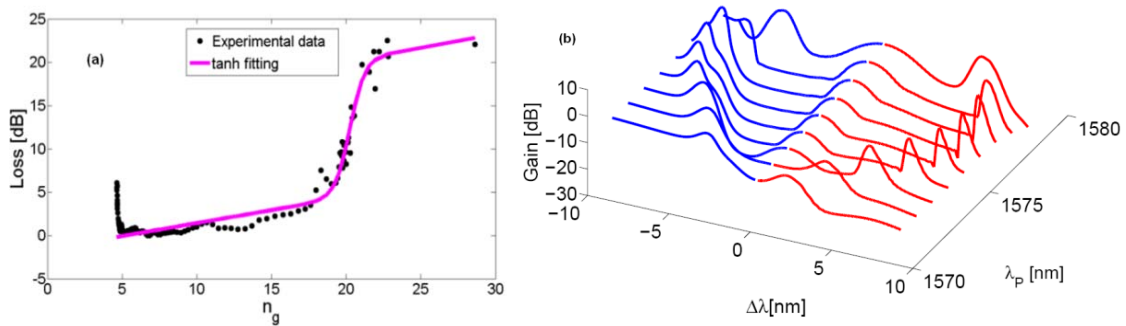


Fig. 2(a) Fitting of the experimental losses vs. group index in engineered PhCW (b)The parametric gain as a function of the pump wavelength and the pump signal detuning ($P_0=1$ W; $L=1.3$ mm).

V. PARAMETRIC GAIN PROPERTIES

Incorporating the dispersive nonlinearity and losses, an exact formula of the parametric gain for the PhCWs has been derived by extending the results of ref. [4] and is presented as:

$$G_s = \left| \frac{A_s(z=L)}{A_s(z=0)} \right|^2 = \exp(-\alpha_m L) |\bar{W}(y_0)|^{-2} \times \\ \times \left| (W'_{k,m}(y_0) - DW_{k,m}(y_0))M_{k,m}(y_L) + (DM_{k,m}(y_0) - M'_{k,m}(y_0))W_{k,m}(y_L) \right|^2 \quad (2)$$

where L is the waveguide length, $\alpha_m = (\alpha_1 + \alpha_2)/2$ and $\Delta\alpha = (\alpha_2 - \alpha_1)/2$ account for the loss dispersion, $M_{k,m}$, $W_{k,m}$ are the Whittaker confluent hypergeometric functions (and $M'_{k,m}$, $W'_{k,m}$ their derivatives) of parameters $k = i(\Delta\alpha + i\Delta\beta)\gamma_{pm}P_0/(\alpha_p^2 y_0)$, $m = (\alpha_p + \Delta\alpha + i\Delta\beta)/(2\alpha_p)$, $\gamma_{pm} = \gamma_p - \gamma_{1p} - \gamma_{2p}$ is the effective

nonlinear coefficient contributing to the phase matching condition, $y_0 = 2(\gamma_{F1}\gamma_{F2}^* - \gamma_{pm}^2)^{1/2} P_0 / \alpha_p$, $y_L = y_0 \exp(-\alpha_p L)$, $\bar{W}(y_0) = M_{k,m}(y_0)W'_{k,m}(y_0) - W_{k,m}(y_0)M'_{k,m}(y_0)$, $D = 1/2 y_0 \times (1 + (-\alpha_p + \Delta\alpha + i\Delta\beta) + i2\gamma_{pm}P_0) / \alpha_p$. The parametric gain from Eq. 2 is presented in Fig. 2b for different pump wavelengths λ_p and pump-signal detunings $\Delta\lambda = \lambda_1 - \lambda_p$. In particular, the pump wavelength is tuned from 1570 nm to 1578 nm, i.e. in the flat band of the dispersion curve of Fig. 1, in steps of 1 nm. The NBOPA regime can be easily recognized. Here, by increasing the pump wavelength the detuning between the pump and the gain peak initially grows but then diminishes. Note that the gain bandwidth can be tuned by changing λ_p and the larger is the detuning between the pump and the gain peak the narrower is the gain bandwidth. This characteristic might be very interesting to achieve tunable slow light effects.

VI. CONCLUSION

In conclusion, by using a vectorial mode analysis tool, we have derived the group indices, the fields, and the dispersive nonlinear coefficients of an engineered PhCW. Finally incorporating the dispersive losses we have obtained the gain characteristics, which exhibits NBOPA tuneable with the pump wavelengths. These results have potential applications in SL, parametric oscillation, all-optical signal processing.

ACKNOWLEDGEMENT

The research leading to these results has received funding from EC FET-Open programme under grant agreement n. 219299 GOSPEL. The research was held in the framework of the agreement with ISCTI, Roma and with the partial support from the Italian Ministry of Foreign Affairs (Direzione Generale per la Promozione del Sistema Paese).

REFERENCES

- [1] *Slow Light: Science and Applications*, J. B. Khurgin and R. S. Tucker, Eds., (CRC Press, Boca Raton, 2009).
- [2] S. Roy, M. Santagiustina, A. De Rossi, S. Combrié, and P. Colman "Modeling the Dispersion of the Nonlinearity in Slow Mode Photonic Crystal Waveguide", *IEEE Photonics Journal*, vol. 4 (1), pp. 224-233, Feb 2012.
- [3] <http://ab-initio.mit.edu/photons/>
- [4] M. E. Marhic, *Optical parametric amplifiers, oscillators, and related devices* (Cambridge University Press, 2008).

GIANT DISPERSIVE WAVE GENERATION IN DOUBLE CORE PHOTONIC CRYSTAL FIBER

D. Modotto⁽¹⁾, G. Manili⁽¹⁾, U. Minoni⁽¹⁾, S. Wabnitz⁽¹⁾,
M. Andreana⁽²⁾, V. Couderc⁽²⁾, A. Tonello⁽²⁾

⁽¹⁾ Dipartimento di Ingegneria dell'Informazione,
Università di Brescia, via Branze 38, 25123 Brescia, Italy

⁽²⁾ Université de Limoges, XLIM, UMR CNRS 7252,
123 Av. A. Thomas, 87060 Limoges, France
daniele.modotto@ing.unibs.it

Abstract

A soliton perturbed by higher-order dispersion terms can transfer power to a dispersive wave when they share a common phase velocity. This dispersive wave can be located several hundreds of nanometers away from the soliton carrier wavelength. We numerically study this phenomenon in a double-core photonic crystal fiber pumped at 1064 nm: the presence of a large quantity of short pulses due to the pump pulse break-up and the dispersion profile lead to the growth of a dispersive wave at 1535 nm whose amplitude is comparable to the pump. Preliminary experiments confirm our predictions.

Index Terms – Giant dispersive wave, nonlinear optics, photonic crystal fibers, supercontinuum generation.

I. INTRODUCTION

Intense optical pulses travelling along a glass fiber experience different nonlinear phenomena due to the combined effect of cubic instantaneous (Kerr) and delayed (Raman) responses. In particular, when the pulse is propagating in the anomalous dispersion regime, modulation instability (MI) sidebands can be observed nearby the pulse central frequency. It is also well known that, if the pulse wavelength is close to the fiber zero-dispersion wavelength (ZDW), the interplay between nonlinear effects and dispersion can foster a dramatic spectral broadening over bandwidths extending a full octave. This phenomenon is known as supercontinuum (SC) generation [1]. The possibility of creating optical spectra extending from the visible to the infrared spectral regions is obviously intriguing from a fundamental viewpoint, but it is also useful in many applications where light sources emitting several wavelengths are necessary. Since fiber dispersion tailoring is of paramount importance in the SC generation process, it is convenient to use photonic crystal fibers (PCFs) which offer great design freedom and allow for flexible ZDW positioning. Moreover, whenever optical solitons propagate in optical fibers a resonant energy transfer into dispersive waves (DWs) may take place. Two conditions must be satisfied for a

resonant transfer to a DW to exist: the soliton and the DW must be phase-matched, and the spectral tails of the soliton must overlap with the DW wavelength [1],[2].

II. DOUBLE CORE FIBER

In order to effectively generate a phase-matched DW, we used a double-core PCF fabricated by PERFOS with anomalous dispersion around 1064 nm. The waveguide was designed by starting from an hexagonal lattice of holes and by introducing a central core and a concentric ring of solid glass: this structure with two high index regions is inspired by the refractive index profiles which are used in dispersion shifted fibers [3]. Fig. 1(a) shows a scanning electron microscope (SEM) image of the fiber cross-section. We extracted the refractive index profile from this image, and calculated the fundamental mode profile and its propagation constant $\beta(\omega)$ by means of a commercial Finite Element Method (FEM) mode solver. The mode group velocity dispersion (GVD) $\beta_2(\omega)$ is plotted in Fig. 1(b): its dispersion is anomalous between 1018 nm and 1353 nm; a remarkable feature is the presence of a large peak of normal GVD centered around 1515 nm.

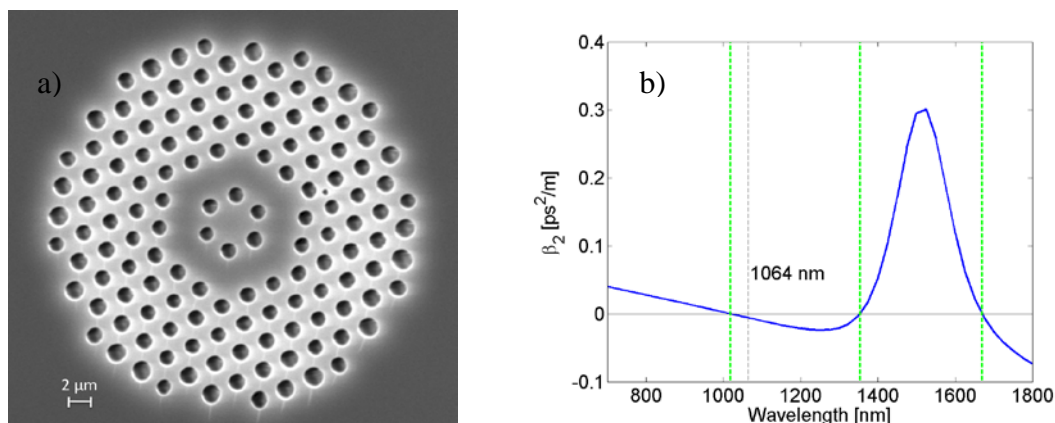


FIG. 1 – a) Photonic crystal fiber cross-section image; b) blue line: numerically calculated GVD in the spectral range of interest; green lines: ZDWs.

III. NUMERICAL RESULTS

Due to the GVD profile that cannot be approximated by a truncated Taylor series and the long pump pulse duration (hundreds of ps), it is difficult to make analytical predictions on the spectrum evolution along the fiber. We base our analysis on the Generalized Nonlinear Schrödinger Equation (GNLSE) which includes all relevant linear and nonlinear terms, and we solve it numerically via a standard split-step approach. We emphasize that the numerical burden is considerable due

to the large number of time steps required to model the wide spectral domain with an acceptable resolution. Extensive simulations show that after a few centimeters of propagation the pulse has already developed MI bands: the band at longer wavelengths (around 1100 nm) is considerably more intense. We remind that the onset of these frequency bands means that the pulse breaks-up in many short and extremely intense pulses which can be regarded as perturbed solitons. After propagation on long distances, these pulses experience a spectral red-shift caused by the Raman effect. As soon as the central part of the initial long pulse has turned into a train of short pulses, a large peak starts to grow around 1575 nm: this value agrees with the phase matching wavelength if we assume that the majority of the solitons involved in the energy transfer are located around 1100 nm. In order to show the evolution of both the temporal profile and the spectrum, we illustrate in Fig. 2 the propagation of a 100 ps long input pulse with a peak power of 1.5 kW. Fig. 2(a) and Fig. 2(b) show the spectrograms at distances $z=0.5$ m and $z=4$ m, respectively. In Fig. 2(a) we may observe that only the tails of the initial pulse are still intact, whereas the central part of the pulse has evolved into an irregular train of short pulses. The formation of a weak spectral peak around 1575 nm can already be noticed: we verified that this peak starts to grow as soon as the short pulses of the MI peak around 1100 nm are fully formed. Fig. 2(b) shows both the generated SC extending from around 800 nm to 1500 nm, and emergence of a strong DW which extends in time for more than 100 ps. In fact, the group velocity at 1575 nm is larger than at 1100 nm. Fig. 3(a) displays the numerically calculated output spectrum for $z=4$ m in a linear scale.

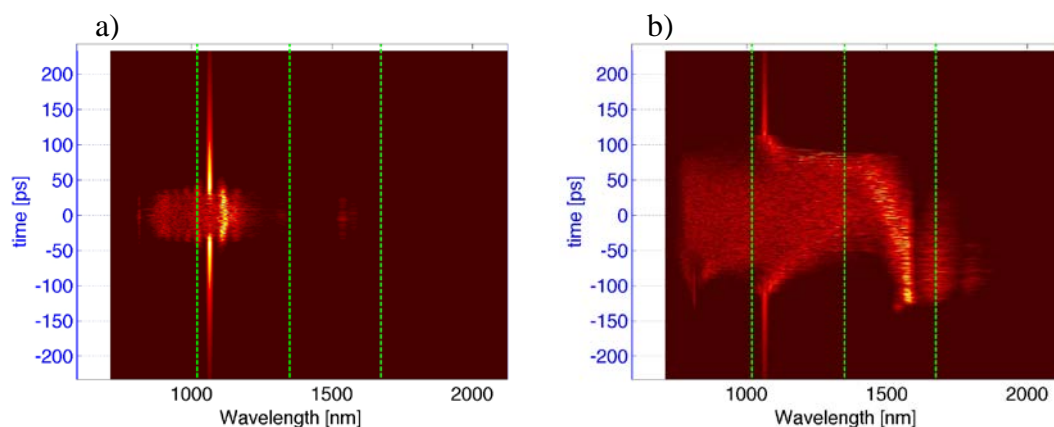


FIG. 2 – Numerically calculated spectrograms: a) $z=0.5$ m; b) $z=4$ m.

IV. EXPERIMENTAL RESULTS

The previously described PCF was experimentally tested: our light source was a Q-switched Nd:YAG laser, emitting pulses with a duration

of 600 ps and the peak power of 6 kW. The PCF was 4 m long, and the output spectra were measured by an optical spectrum analyzer (whose range is 600-1750 nm). The collected spectra show both SC generation and a giant DW peak formation around 1535 nm. The measured spectrum at the maximum power is shown in Fig. 3(b): as in the simulations, the generated DW peak at the fiber output had a spectral density which is comparable with that of the residual pump. The discrepancy between the predicted (1575 nm) and the measured (1535 nm) DW wavelength can be explained by errors introduced when estimating the fiber refractive index profile from the SEM image

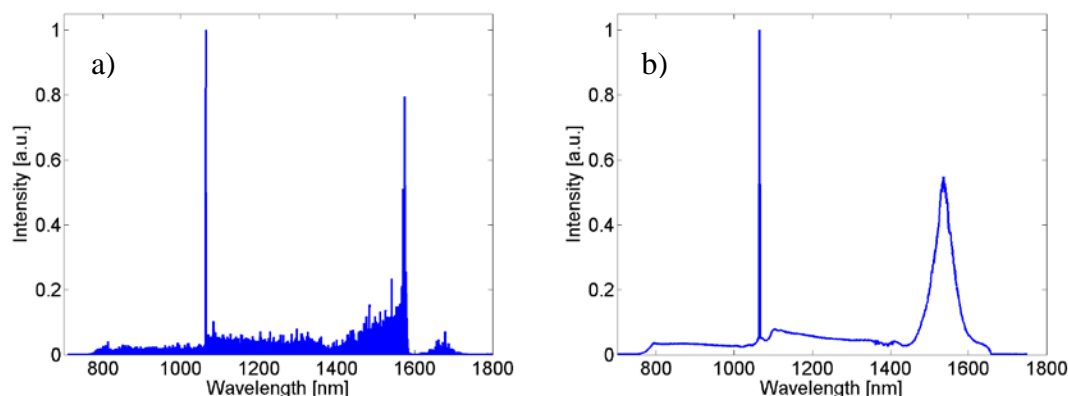


FIG. 3 – a) numerically calculated output spectrum for $z=4$ m and peak power 1.5 kW; b) measured output spectrum at the maximum laser power.

V. CONCLUSION

Subnanosecond pulses with a peak power of a few kW injected into a specially designed double-core PCF gave rise to a giant DW generation around 1535 nm. Such type of PCFs may enable new light sources operating in the telecom 1500-1650 nm spectral range.

REFERENCES

- [1] B.H. Chapman, J.C. Travers, S.V. Popov, A. Mussot, and A. Kudlinski, "Long wavelength extension of CW-pumped supercontinuum through soliton-dispersive wave interactions," *Optics Express*, vol. 18(24), pp. 24729-24734, Nov. 2010.
- [2] N. Akhmediev and M. Karlsson, "Cherenkov radiation emitted by solitons in optical fibers," *Physical Review A*, vol. 51(3), pp. 2602-2607, March 1995.
- [3] F. Gérôme, J.L. Auguste, and J.M. Blondy, "Design of dispersion-compensating fibers based on a dual-concentric-core photonic crystal fiber," *Optics Letters*, vol. 29(23), pp. 2725-2727, Dec. 2004.

AIR-HOLE RING INFLUENCE ON THE CUT-OFF PROPERTIES OF 19-CELL DOUBLE-CLADDING PHOTONIC CRYSTAL FIBERS

E. Coscelli, F. Poli, A. Cucinotta, S. Selleri

Information Engineering Department, University of Parma
 Viale G. P. Usberti 181/A, 43124 Parma, Italy
enrico.coscelli@nemo.unipr.it

Abstract

Yb-doped double-cladding photonic crystal fibers have become key components for power scaling in fiber laser systems. A careful design of such large core active fibers is mandatory to obtain a single-mode behavior, a necessary requirement for high quality laser beams. In this paper the new avoided-crossing approach has been applied to investigate the cut-off properties of 19-cell photonic crystal fibers, by changing the number of air-hole rings in the fiber inner cladding. Simulation results have shown that, double-cladding photonic crystal fibers with larger inner-cladding provide better cut-off properties of the guided-modes, which can have positive effects on the amplification process in practical applications.

Index Terms – Finite element method, high-power fiber lasers, Yb-doped double-cladding photonic crystal fibers, single-mode regime.

I. INTRODUCTION

High-power fiber laser market is currently dominated by Yb-doped fiber-based systems, whose power scaling requires the development of active optical fibers capable of providing a very large effective area. However, this enlargement can be detrimental for the fiber Single-Mode (SM) behavior, which is mandatory for the high laser beam quality required in many applications. Double-Cladding Photonic Crystal Fibers (DC-PCFs) have been demonstrated to be a valuable solution to these issues, being capable to support SM guiding even with very large active core diameters [1]. In particular, rod-type Yb-doped DC-PCFs, which have an outer diameter in the 1-mm range and are therefore inflexible [2], have been realized with core diameters up to 100 μm , by removing 19 air-holes from the center of the triangular lattice in the photonic crystal cladding. A careful design is mandatory to obtain SM guiding in such ultra-large core fibers.

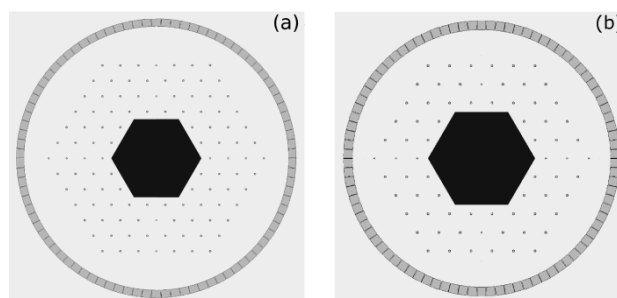


FIG. 1 – Cross-section of DC-PCF with (a) 4 and (b) 3 rings of air-holes.

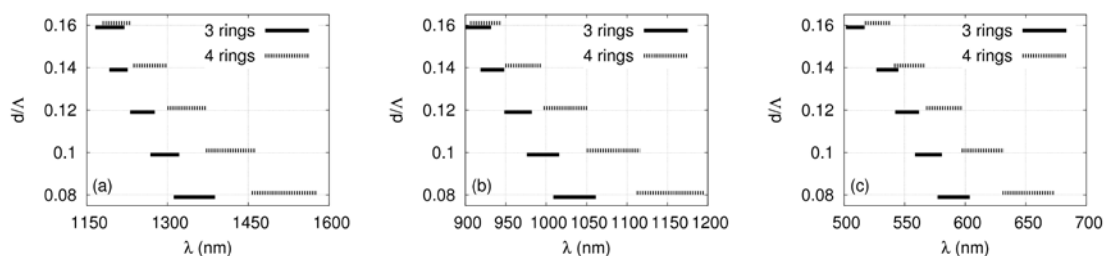


FIG. 2 – Comparison of SM wavelength ranges of fibers with 3 and 4 air-hole rings and different d/Λ , for (a) $n_{\text{core}} = 1.44975$, (b) 1.44985 and (c) 1.44995 .

Recently, it has been demonstrated that a new approach, based on the avoided-crossing of the guided modes with the first cladding mode of the actual fiber, must be considered to correctly define the single-mode regime in these fibers [3]. In this paper the avoided-crossing approach has been extensively applied to study the effects on the 19-cell Yb-doped DC-PCF cut-off properties of the inner cladding air-hole ring number. Simulation results have shown that 19-cell fibers with larger inner-cladding provide better cut-off properties in terms of SM range and of Fundamental Mode (FM) confinement into the Yb-doped core, with positive effects on the amplification process, even if with a worsening of the pump absorption efficiency.

II. NUMERICAL ANALYSIS

Fig 1(a) and (b) show, respectively, the cross-section of the 19-cell core DC-PCF with 4 and 3 air-hole rings in the inner cladding studied in the present analysis. The hole-to-hole spacing is $\Lambda = 16.6 \mu\text{m}$ and the air-hole diameter is d . The doped core region has a hexagonal shape, with edge of $(5/2)\Lambda = 41.5 \mu\text{m}$. Different values of doped core refractive index n_{core} , that is 1.44975 , 1.44985 and 1.44995 , have been considered, which are lower than the one used for silica, equal to 1.45 . The air-cladding surrounding the whole structure has an inner radius of $122.5 \mu\text{m}$ and $100 \mu\text{m}$ for DC-PCF with 4 and 3 air-hole rings, respectively. The cut-off properties of these two fiber designs have been compared, in order to verify the effect of the air-hole ring number on the SM regime. As already discussed in a previous work [3], the wavelength of the avoided-crossing between the dispersion curves of FM or Higher-Order Mode (HOM), and of the first cladding mode in the actual fiber structure has been considered as the cut-off one. The FM, HOM and first cladding mode guiding properties have been calculated by applying a full-vector modal solver based on the Finite Element Method [4]. The overlap integral Γ on the hexagonal doped core [4] has been used to evaluate the mode confinement, which is related to the achievable amplification [3]. In order to describe the cut-off properties of 19-cell Yb-doped DC-PCFs, it has been considered the SM wavelength range $\Delta\lambda_{\text{SM}} = \lambda_{\text{c,HOM}} - \lambda_{\text{c,FM}}$, being $\lambda_{\text{c,FM}}$ and $\lambda_{\text{c,HOM}}$ the FM and the HOM cut-off wavelength, respectively, and the overlap integral of the FM and the HOM at $\lambda_{\text{c,HOM}}$, which influence the efficiency of the amplification process.

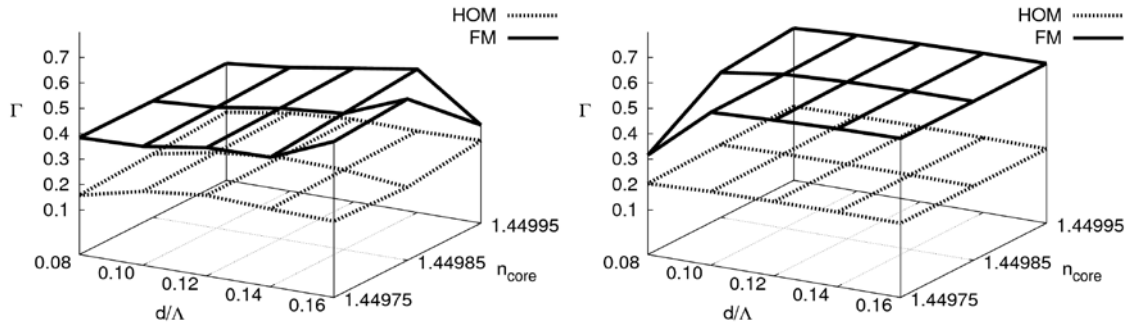


FIG. 3 – Overlap integral Γ of the FM and HOM at $\lambda_{c,HOM}$ for DC-PCFs with (a) 3 and (b) 4 air-hole rings, as a function of d/Λ and n_{core} .

III. 19-CELL DC-PCF CUT-OFF PROPERTIES

The number of air-hole rings in the DC-PCF inner-cladding has a great influence on the efficiency of the pump absorption, which increases if the inner cladding diameter decreases [5]. For this aspect, 19-cell Yb-doped DC-PCFs with 3 rings are better than the ones with 4 rings. However, it is important to investigate if the air-hole ring reduction has a positive effect also on the SM regime. Fig. 2 reports the SM range $\Delta\lambda_{SM}$ obtained for the 3- and 4-ring DC-PCFs, as a function of d/Λ , for different n_{core} values. Notice that the most relevant effect of the removal of the outermost air-hole ring is the blue-shift of the cut-off wavelengths of the guided modes. In fact, for both FM and HOM the cut-off occurs at longer wavelengths in the DC-PCFs with 4 air-hole rings, regardless of the other design parameters. A larger shift has been observed when smaller air-holes and a lower core refractive index are considered, reaching a maximum of 189 nm and 145 nm for $\Delta\lambda_{c,HOM}$ and $\Delta\lambda_{c,FM}$, respectively, when $d/\Lambda = 0.08$ and $n_{core} = 1.44975$. On the contrary, the cut-off wavelength difference is lower than 37 nm and 16 nm for HOM and FM, respectively, for all the 19-cell fibers with $d/\Lambda = 0.16$. It is important to underline that, in all the considered 19-cell fibers, the HOM cut-off wavelength decrease, due to the outermost air-hole ring removal, is higher than the FM one. Therefore, the SM range is narrower for the DC-PCFs with 3 air-hole rings, with respect to the 4-ring ones. Regardless to the inner cladding dimension, a wider SM range can be obtained in DC-PCFs with smaller air-holes and lower core refractive index. The maximum $\Delta\lambda_{SM}$ value of 120 nm has been calculated for the 4-ring fiber with $d/\Lambda = 0.08$ and $n_{core} = 1.44975$. Notice that, as the air-hole diameter and the core refractive index increase, the effect of the outermost air-hole ring removal on $\Delta\lambda_{SM}$ becomes less relevant. In fact, the lowest difference between the SM range of 4-ring and 3-ring 19-cell fibers has been obtained when $n_{core} = 1.44995$, regardless of the air-hole diameter value, with a minimum of about 5 nm for $d/\Lambda = 0.16$. Finally, the overlap integral of FM and HOM at $\lambda_{c,HOM}$ of the 3- and 4-ring DC-PCFs are reported in Fig. 3(a) and (b), respectively. Notice that for 3-ring DC-PCFs $\Gamma_{c,HOM}$ values are less constant, with respect to the 4-ring fiber case. However, they are all in

the range between 0.16 and 0.25, thus confirming the weak HOM confinement at cut-off condition. Moreover, differently from the 4-ring fibers, Γ_{FM} of the 3-ring DC-PCFs increases with the air-hole size, regardless of the core refractive index. With the exception of the DC-PCFs with $d/\Lambda = 0.16$, Γ_{FM} values are lower than those obtained for the corresponding 4-ring fibers, with a minimum of about 0.38 for the DC-PCFs with $d/\Lambda = 0.08$. When $d/\Lambda = 0.16$, the value of the FM overlap integral at $\lambda_{\text{c,HOM}}$ is very close to the one obtained for the 4-ring design, thus suggesting that for this air-hole size the number of cladding rings does not significantly affect the guided-mode properties.

IV. CONCLUSION

Simulation results have demonstrated that 4-ring 19-cell fibers have better properties in terms of width of the SM wavelength range and of FM confinement into the doped core at the HOM cut-off. These characteristics, together with the lower pump absorption efficiency, due to the larger inner-cladding, can significantly influence the performances of the amplification process in practical applications. The DC-PCFs with fewer air-hole rings become more convenient for large air-holes, especially for high core refractive index, when the guided-mode properties are not significantly affected by the inner-cladding dimension.

ACKNOWLEDGEMENT

The Authors acknowledge the support of the EU funded FP7 ALPINE Project, n. 229231.

REFERENCES

- [1] K. P. Hansen, C. B. Olausson, J. Broeng, K. Mattson, M. D. Nielsen, T. Nikolajsen, P. M. W. Skovgaard, M. H. Sørensen, M. Denninger, C. Jakobsen, and H. R. Simonsen, "Airlad fiber laser technology," *Proc. SPIE*, vol. 6873, 2008, pp. 687 307-1 – 687 307-12.
- [2] J. Limpert, N. Deguil-Robin, I. Manek-Hönninger, F. Salin, F. Röser, A. Liem, T. Schreiber, S. Nolte, H. Zellmer, A. Tünnermann, J. Broeng, A. Petersson, and C. Jakobsen, "High-power rod-type photonic crystal fiber laser," *Optics Express*, vol. 13[4], pp. 1055-1058, Feb. 2005.
- [3] F. Poli, E. Coscelli, T. T. Alkeskjold, D. Passaro, A. Cucinotta, L. Leick, J. Broeng, and S. Selleri, "Cut-off analysis of 19-cell Yb-doped double-cladding rod-type photonic crystal fibers," *Optics Express*, vol. 19[10], pp. 9896-9907, May 2011.
- [4] F. Poli, A. Cucinotta, and S. Selleri, *Photonic Crystal Fibers. Properties and Applications*, ed. by Dordrecht: Springer (Series in Material Science), 2007
- [5] A. Tünnermann, T. Schreiber, and J. Limpert, "Fiber lasers and amplifiers: an ultrafast performance evolution," *Applied Optics*, vol. 49[25], pp. F71-F78, Sep. 2010.

FILTER DESIGN FOR OTDM AND WDM RECEIVERS IN PhC TECHNOLOGY

S. Malaguti⁽¹⁾, G. Bellanca⁽¹⁾, S. Trillo⁽¹⁾, S. Combrié⁽²⁾, A. De Rossi⁽²⁾

⁽¹⁾ Dipartimento di Ingegneria, Università degli Studi di Ferrara,
via Saragat 1, Ferrara 44100, Italy
stefania.malaguti@unife.it

⁽²⁾ Thales Research and Technology, Palaiseau, France

Abstract

The always growing demand for high-bandwidth low-consumption data routing in the future communications, foregrounds the arrangement of new disruptive optical technologies. In the framework of the EU Copernicus project, we develop ultra-high performances signal-processing devices based on photonic crystal technology. Modeling, design and prototype fabrications of both, a WDM and an OTDM receiver will be proposed.

Index Terms – Photonic Crystals, Photonic Crystal Filters, WDM, OTDM, Nonlinear optics, FDTD.

I. INTRODUCTION

One of the most important functionality in a optical network is the routing of the data stream from a source to a destination node. This operation can be accomplished by relying on the multiple features of the light flow such as, for example, polarization, carrier frequency, interaction with the matter, and so on. Among the different technologies exploiting the light properties, photonic crystals (PhCs) have attracted considerable attention because of their effectiveness in the manipulation of light over scales comparable with the working-wavelength. Remarkably, the last advancements in the manufacturing skills, have made available well-established fabrication processes for creating 2D PhC membranes in semiconductor compounds that allow unprecedented signal control in ultra-compact integrated devices which will play a key role in future optical communications and interconnects. COPERNICUS (Compact Otdm/wdm oPtical rECiveRs based on photoNic crystal Integrated CircUitS) is a European project which brings together 7 different partners from academy and industry with high profiles in photonics, nanotechnology, modeling and developing new technologies for telecommunications and aerospace. The aim of this Project is to develop a cutting-edge photonic crystal technology for the high density integration of basic optical functions. The Project focuses, in particular, on development and integration of PhC devices for the realization of demultiplexing receivers for 100Gb/s optical time division multiplexed (OTDM) and wavelength division multiplexed (WDM) signals, including high-speed integrated photodetectors [1]. In this work, results concerning the design of the key components of both the WDM and the OTDM receivers are presented and discussed.

II. PHC FILTER FOR THE WDM RECEIVER

The first key device for COPERNICUS is a four channel WDM filter operating at 25Gb/s per channel. Two different versions for both the C (1550 nm) and O (1300 nm) bands are being developed. The filter specifications require a maximum insertion loss of 2 dB and a minimum isolation between adjacent channels of 30 dB. The key element of this component is the selective-wavelength drop filter.

The proposed design is based on a couple of L_n cavities used in mirror configuration [2], in order to increase the drop efficiency of the filter. For a single cavity, in fact, the maximum theoretical value of 50% is allowed [3]. L cavities are obtained by removing n adjacent holes (so they are named L_n cavities) from the PhC crystal structure. These cavities are simple to realize and to couple with bus and drop waveguides. When properly ‘tuned’ (by shifting the holes at the extremities or by reshaping the positions of the holes in the two sides of the resonator), these cavities guarantee a very high quality factor Q , thus increasing the selectivity of the filter. Q grows also with the length (i.e. the number of removed holes) of the resonator. Unfortunately, longer cavities easily support higher order modes, that can strongly interfere with other channels when the cavity is used as a filter for a WDM system. The distance between the resonances of these modes (i.e. the available Free Spectral Range of the cavity) decreases by increasing n . Therefore, a proper choice of the number of removed holes n to reach a compromise between the quality factor Q and the free spectral range FSR must be found. For the four channel WDM filter, a L_5 cavity is a possible solution; this cavity has a quiet high isolated quality factor ($Q \approx 100000$) and a FSR which satisfy the required specification ($FSR > 20\text{nm}$).

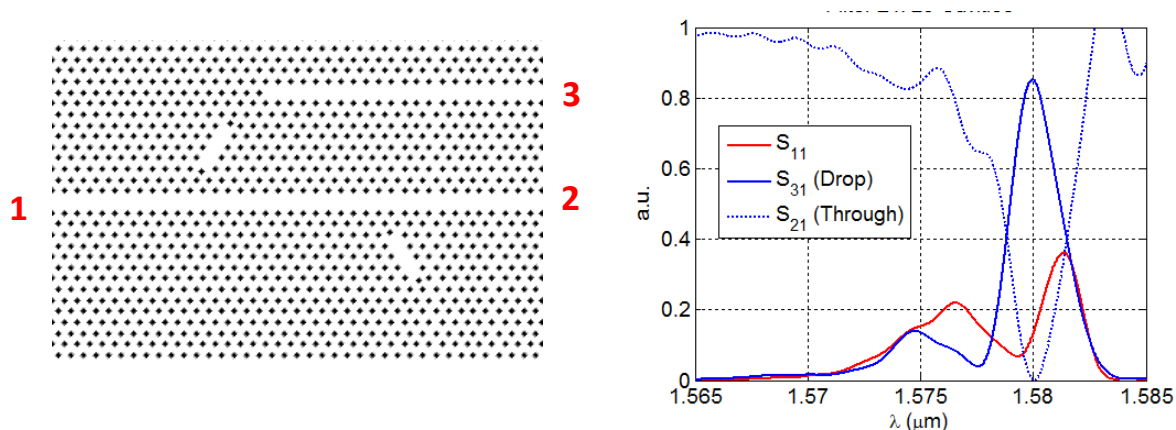


Fig. 1: Sketch of a two cavity filter realized with two coupled L_3 cavities (on the left) and S parameters of the filter (on the right).

In the mirror configuration set-up, the first cavity acts as resonant tunnelling-based channel drop filter, whereas the second resonator realizes a wavelength-selective reflection feedback in the bus waveguide. Detailed Coupled Mode Theory analysis and intensive FDTD simulations have allowed the design and optimization of different topologies based

on this concept. As an example, Fig. 1 (on the left) shows the topology of the filter used for both C and O bands. For each configuration, the value of the period a of the PhC membrane must be properly chosen. The response of this filter obtained via 3D-FDTD simulations is reported on the right hand side of the same figure. These curves show the reflection coefficient at the input port (S_{11}) and the transmission through the bus (S_{21}) and drop (S_{31}) ports respectively. The drop efficiency is of about 80% and the linewidth is close to 3 nm. Next figure shows the pattern of the $|H_z|$ for both resonant and not resonant wavelengths. In the former case, the field is dropped whereas, in the latter, the propagation flows on the bus waveguide.

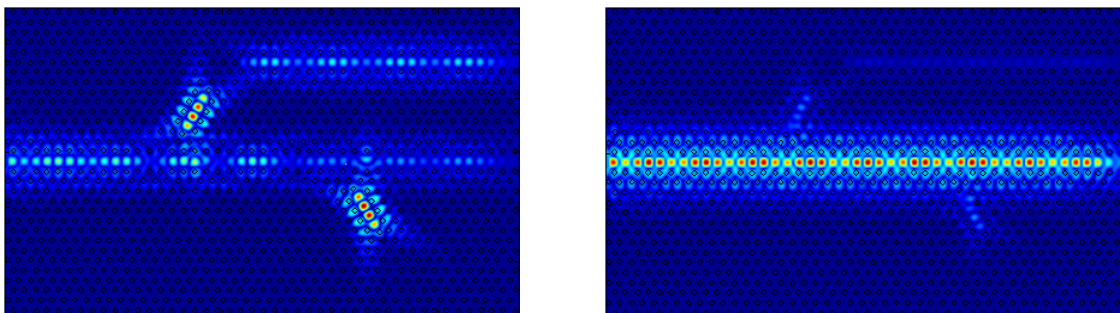


Fig. 2: $|H_z|$ field pattern at the resonance (on the left) and out of the resonance (on the right). In the first case, the field is dropped whereas, in the second one, the propagation flows straight on the bus.

III. OTDM RECEIVER

The design of an all-optical time domain receiver operating at 100Gb/s is a real challenge. In this case, the extraction of the output signal from the input section is obtained by triggering the nonlinear effects of the semiconductor by means of a high power control. In particular, for III-V compounds, the main nonlinearities are ruled by two-photon absorption (TPA) processes and its related effects such as free-carrier absorption (FCA), free-carrier dispersion (FCD), carrier diffusion. Numerical modeling of the complex nonlinear dynamics in PhC has been performed by implementing a 2D-FDTD code fully accounting for the aforementioned nonlinearities. The configuration of the investigated three-port device is illustrated in the right section of Fig. 3. In this set-up, the input waveguide (bus) and output (drop) waveguides are coupled with a resonator which, in the normal configuration, is detuned respect to the wavelength of the input signal. Tuning is obtained through a pump-probe operation by using a high power pump signal, which triggers the nonlinear effects in the cavity, shifts the resonance and causes the switching of the data signal (probe) from the input to the output section. The switching contrast (SC) is used as figure of merit to evaluate the performances of the device. This parameter is defined as the ratio between the probe power measured at the drop port when the pump is ON respect to the case in which the pump is OFF. As shown in

Fig. 3 (left), by suitable design of the PhC topology, high SC can be obtained with relative low input power on the pump.

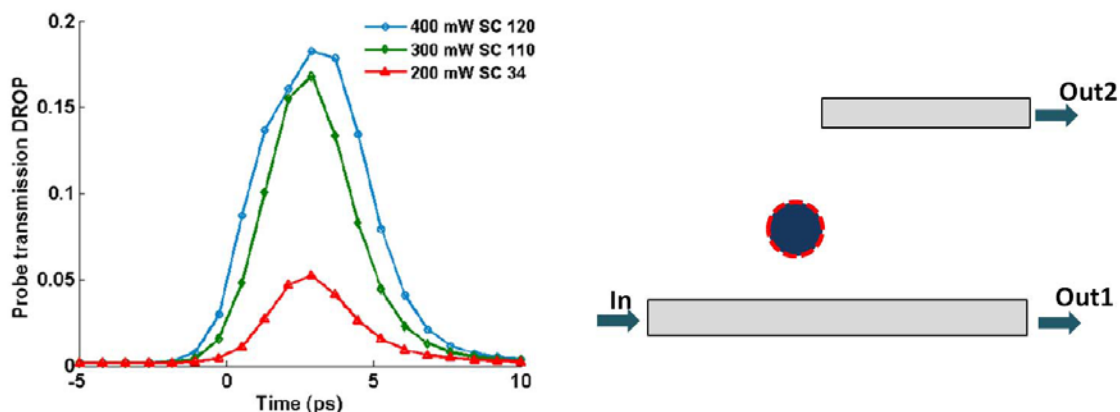


Fig. 3: Schematic representation of the AOG (on the right). Pump-probe operations in a three-ports AOG optimized design (on the left). The curves show the probe efficiency at the drop port for different control power injected into the structure. The corresponding values of the switching contrast (SC) are also indicated.

IV. CONCLUSIONS

In this contribution design of filters to be used as basic components for both, a WDM and a OTDM receiver in PhC technology have been presented. For the WDM receiver, a single stage of the filter based on two L3 cavities in mirror configuration is proposed. For the OTDM receiver, on the contrary, a design based on a pump-probe operation with high switching contrast and low pump power is presented.

ACKNOWLEDGEMENT

The authors acknowledge funding from the EC under the Project COPERNICUS (<http://www.copernicusproject.eu>).

REFERENCES

- [1] S. Malaguti, A. Armaroli, G. Bellanca, S. Trillo, S. Kaunga-Nyirenda, J. Lim, E. Larkins, P. Trost-Kristensen, K. Yvind, J. Mork, Y. Dumeige, M. Gay, P. Colman, S. Combr   and A. De Rossi, "Numerical modelling in photonic crystals integrated technology: the COPERNICUS Project," in Proceedings of the 11th International Conference on Numerical Simulation of Optoelectronic Devices (NUSOD), p. 133, Rome, Italy, 5th-8th September (2011).
- [2] Z. Zhang, M. Qiu, "Coupled mode analysis of in-plane channel drop filters with resonant mirrors", *Photonics and Nanostructures - Fundamentals and Applications.*, vol. 3, pp. 84-89, 2005.
- [3] A. Shinya, S. Mitsugi, E. Kuramochi, M. Notomi, "Ultrasmall multi-channel resonant-tunneling filter using mode gap of width-tuned photonic-crystal waveguide", *Optics Express*, vol. 13, n. 3, pp. 4202-4209, 2005.

FAULT DETECTION IN A DIELECTRIC GRID

A. Brancaccio, G. Leone, R. Solimene, R. Pierri

Dipartimento di Ingegneria dell'Informazione, Seconda Università di
Napoli
Via Roma 29, 81031 Aversa, Italy
adriana.brancaccio@unina2.it

Abstract

The canonical problem of detecting and localizing missing scatterers (faults) inside a known grid of small cross section dielectric cylinders is dealt with. The case of a TM scalar two-dimensional geometry is considered. The scattering by a fault is modeled as the radiation of a proper equivalent volumetric source, by exploiting the Green's function of the complete grid. An approximated linear model of the scattering is proposed, validated by means of numerical results, also in the case of two faults, and checked against model error and noisy synthetic data.

Index Terms – dielectric grid; fault detection; inverse scattering.

I. INTRODUCTION

Grid structures can be met in different applicative contexts, for instance in photonics where some types of artificial materials consist of a lattice of identical inclusions embedded within a host medium.

Electromagnetic scattering by periodic structures implies well-known dispersion and passband/stopband properties and their optimal use requires the availability of a full (although truncated) grid [1], [2]. The absence of one or more elements leads to frequency dependent scattering phenomena which are different from the expected behavior. Therefore, in literature, attention has been devoted to developing numerical methods in order to predict the field scattered by the grid when such a circumstance occurs [3]–[5].

A complementary issue concerns the need to test such structures in a nondestructive way. To this end, in order to detect and localize wanted and/or unwanted defects, the grid structure can be interrogated by an electromagnetic wave at a passband frequency, so that the diagnostics can be cast as an inverse scattering problem.

In this contribution, the problem of detecting and localizing a fault inside a grid of thin dielectric cylinders is dealt with in a two dimensional geometry. We follow the same approach used in [6] for perfect electrical conducting scatterers. The knowledge of the grid geometrical parameters, that is number and position of the scatterers, allows to compute the pertinent Green's function. Then, a fault is modeled as a perturbation of the background medium (i.e. the full grid). The scattered field, defined as the difference between the fields

scattered by $N - 1$ and N cylinders, depends in principle on the fault's position inside the grid. A suitable approximation of the excitation coefficients allows to formulate the problem as a linear one. The presence of more than one fault can be treated by the same algorithm if mutual coupling between two faults is neglected.

II. MATHEMATICAL MODEL

We consider a grid consisting of N small cross section identical dielectric scatterers, whose relative dielectric permittivity is denoted as ε_r , embedded into a dielectric homogeneous medium. The scatterers are z -parallel cylinders with radius $a \ll \lambda_0$, where λ_0 is the host medium wavelength, positioned at \mathbf{r}_n , $n = 1, \dots, N$. The illumination is provided by a z -directed filamentary current of amplitude I located at \mathbf{r}_s . The field scattered by the fault can be calculated as the one radiated by the equivalent source $J(\mathbf{r}_m) = j \frac{\beta_0}{\zeta_0} (1 - \varepsilon_r) E_{N-1}(\mathbf{r}_s, \mathbf{r}_m)$ where E_{N-1} indicates the field inside the lacking cylinder (in presence of the remaining $N - 1$ ones) assumed to be constant over the (small) cylinder's section.

By exploiting cylindrical harmonics and their approximation for small argument (for $\beta_0 a = 2\pi a / \lambda_0 \ll 1$) the Green's function of the full grid can be written as:

$$G^N(\mathbf{r}, \mathbf{r}') = \frac{-j}{4} \left[H_0^{(2)}(\beta_0 |\mathbf{r} - \mathbf{r}'|) + \sum_{n=1}^N a_n(\mathbf{r}) H_0^{(2)}(\beta_0 |\mathbf{r}' - \mathbf{r}_n|) \right], \quad (1)$$

when \mathbf{r}' varies outside the cylinders and

$$G^N(\mathbf{r}, \mathbf{r}') = \frac{-j}{4} b_m(\mathbf{r}) J_0(\beta_1 |\mathbf{r}' - \mathbf{r}_m|), \quad (2)$$

when \mathbf{r}' varies inside the m -th cylinder. In Eqs. (1) and (2) $H_0^{(2)}(\cdot)$ is the Hankel function of zero order and second kind, $J_0(\cdot)$ is the Bessel function of zero order, $\beta_1 = \beta_0 \sqrt{\varepsilon_r}$ and coefficients a_n and b_n represent the "excitation" of the external and internal, respectively, electric field for each cylinder, depending on both the illuminating field and the grid scatterers positions.

The scattered field can then be written as:

$$E_s(\mathbf{r}, \mathbf{r}_s) = \beta_0^2 (1 - \varepsilon_r) E_{N-1}(\mathbf{r}_s, \mathbf{r}_m) \iint_m G^N(\mathbf{r}, \mathbf{r}') d\mathbf{r}', \quad (3)$$

where integration ranges over the m -th scatterer's section.

When a fault occurs, excitation coefficient values change. However, in this work we assume that they are not significantly affected by the presence of a fault inside the grid. Accordingly, it can be shown that Eq. (3) can be recast as:

$$E_s(\mathbf{r}, \mathbf{r}_s) = \left\{ j\beta_0^2 \alpha \frac{\pi \zeta_0 l (1 - \sqrt{\epsilon_r})}{8 \sqrt{\epsilon_r}} \left[\frac{J_0(\beta_0 \alpha) H_1^{(2)}(\beta_0 \alpha) - \sqrt{\epsilon_r} J_1(\beta_1 \alpha) H_0^{(2)}(\beta_0 \alpha)}{J_1(\beta_0 \alpha) H_0^{(2)}(\beta_0 \alpha) - J_0(\beta_0 \alpha) H_1^{(2)}(\beta_0 \alpha)} \right] J_1(\beta_1 \alpha) \right\} b_m(\mathbf{r}_s) b_m(\mathbf{r}), \quad (4)$$

Normalizing by the factor in brace brings to

$$E_s(\mathbf{r}_h, \mathbf{r}_{sl}) = \sum_{n=1}^N b_n(\mathbf{r}_h) b_n(\mathbf{r}_{sl}) \gamma_n \quad (5)$$

where $\gamma_n = 0, \forall n \neq m$ and $\gamma_m = 1$, $h = 1, \dots, N_{oss}$ denotes N_{oss} different observation points and $l = 1, \dots, N_s$ denotes N_s different source positions.

Eq. (5) can be compactly rewritten in matrix notation as:

$$\mathbf{E} = \mathbf{L} \cdot \boldsymbol{\gamma} \quad (6)$$

Therefore the problem of retrieving the fault position amounts at solving Eq. (6) for $\boldsymbol{\gamma}$ by a linear inversion approach.

III. NUMERICAL ANALYSIS

We apply the inversion algorithm to the case of a square grid made of equally spaced cylinders. The host medium is free space and $\epsilon_r = 4$. Measurements are uniformly taken over a circle (shown in green in the following figures) with $N_{oss} = 100$ and $N_s = 3$.

First example, shown in Fig. 1, concerns a single fault deeply located inside a grid with $N = 41 \times 41$. The grid space step is $\lambda/8$. Fig. 1(b) reports the reconstruction obtained for data corrupted by additive white gaussian noise with SNR=10 dB, after a Truncated Singular Value Decomposition inversion procedure [6]. As can be seen the fault is correctly localized. Results can be further improved by applying a properly defined detection threshold that can be analytically derived as shown in [6].

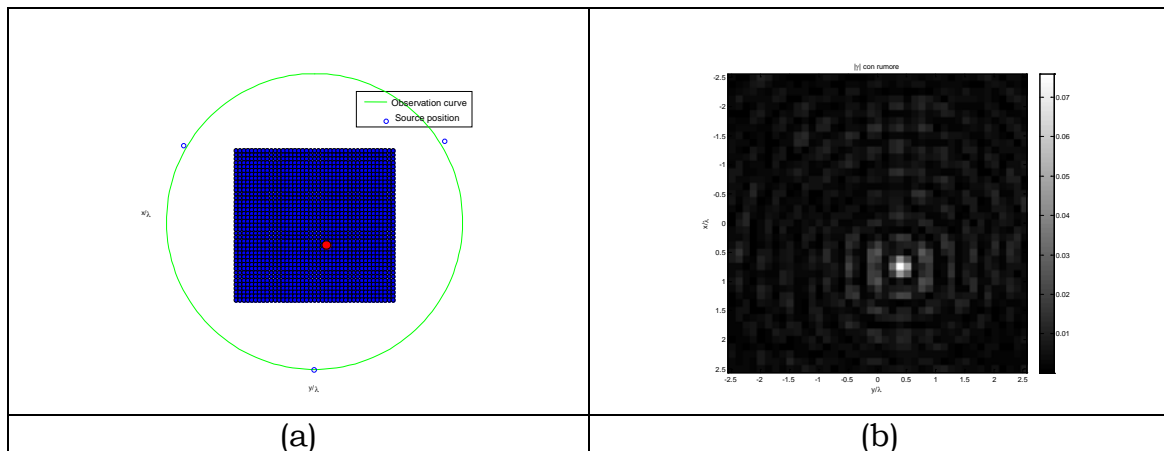


FIG. 1 – A grid of 41×41 cylinders spaced at $\lambda/8$. Fault position is indicated in red (a); reconstructed image (b).

As a further example, shown in Fig. 2, we now consider two faults in a $N = 21 \times 21$ grid with space step $\lambda/4$. In this case a model error occurs, due to the multiple scattering between the faults. However, the method succeeds in locating both faults as well.

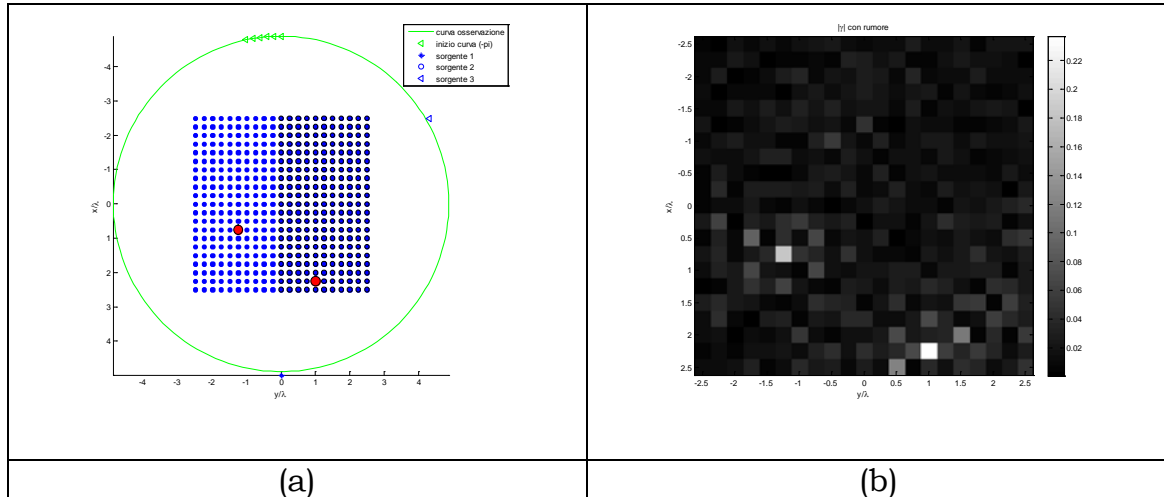


FIG. 2 – A grid of 21×21 cylinders spaced at $\lambda/4$. Fault positions are indicated in red (a); reconstructed image (b).

REFERENCES

- [1] K. Yasumoto, “Electromagnetic Theory and Applications for Photonic Crystals”, *Optical Engineering* (CRC, 2005).
- [2] C. Elachi, “Waves in active and passive periodic structures: a review,” *IEEE Trans. Microwave Theory Tech.*, 24, pp. 1666–1698, 1976.
- [3] G. Tayeb, D. Maystre, “Rigorous theoretical study of finite-size two-dimensional photonic crystals doped by microcavities,” *J. Opt. Soc. Am. A*, 14, pp. 3323–3332, 1997.
- [4] A. Ludwig and Y. Leviatan, “Analysis of bandgap characteristics of two-dimensional periodic structures by using the source model technique,” *J. Opt. Soc. Am. A*, 20, pp. 1553–1562, 2003.
- [5] A. Ludwig and Y. Leviatan, “Analysis of arbitrary defects in photonic crystals by use of the source-model technique,” *J. Opt. Soc. Am. A* 21, pp. 1334–1343, 2004.
- [6] A. Brancaccio, G. Leone, R. Solimene, “Fault detection in metallic grid scattering”, *J. Opt. Soc. Am. A*, 28, pp. 2588-2599, 2011.

A COMPUTATIONAL APPROACH TO THE OPTICAL CHARACTERIZATION OF PHOTONIC CRYSTALS AND PHOTONIC GLASSES.

Alessandro Vaccari⁽¹⁾, Antonino Cala' Lesina⁽¹⁾, Luca Cristoforetti⁽²⁾,
Andrea Chiappini⁽³⁾, Maurizio Ferrari⁽³⁾

⁽¹⁾ FBK (Fondazione Bruno Kessler), Renewable Energies and Environmental Technologies, via Sommarive 18, Trento, Italy.

⁽²⁾ Dipartimento della Conoscenza, Provincia Autonoma di Trento.

⁽³⁾ IFN-CNR, Institute of Photonics and Nanotechnology, CSMFO Lab., Via alla Cascata 56/c, Trento, Italy.

vaccari@fbk.eu

Abstract

The present paper describes a computational physics approach to the analysis of the light scattering from a three dimensional face-cubic centered lattice of spherical particles. The scattered electromagnetic field distribution is obtained after development of a parallelized FDTD (Finite Difference Time Domain) MPI code for the full numerical solution of the Maxwell's equations, with an impinging plane wave and assigned permittivity of the various spherical particles in the lattice. The aim is to numerically calculate the reflectance and transmittance of a crystal sample in the 500÷1000 nm wavelength range by determining, via the near-to-far field transforming Kirchhoff formula, applied to the FDTD scattered results, the angular distribution of the reflected and transmitted light. This study is suitable for the predictive optical characterization/simulation of large ordered photonic structures and, as a possible further development, of disordered distributions such as glasses.

Index Terms – MPI parallel computing, FDTD numerical method, face-cubic centered, photonic crystals.

I. INTRODUCTION

The analytical solution for the scattered field from a single dielectric sphere in a plane monochromatic wave is well-known [1]-[2], and expressed as a series expansion which can be evaluated, after retaining a finite number of terms only, to get field values with any accuracy, apart finite floating point numbers representation errors at the various space positions. However, for a high number of very close spherical scatterers forming a slab of given thickness along the propagation direction of the incident beam, the resulting electromagnetic field, which can now be separated into reflected and transmitted field, cannot be obtained by simple superposition from the various scatterers, because of their strong cooperative effect. In this case, a way to obtain an approximate solution converging to the correct one is through a

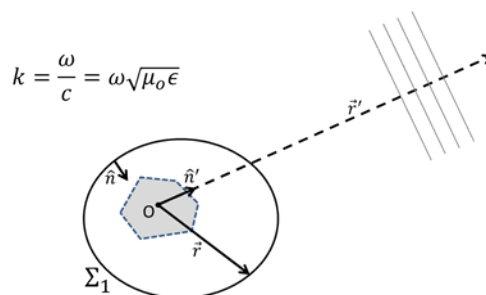
computational approach in which the governing equations, i.e. the Maxwell's equations, are directly solved in a numerical fashion.

II. THEORETICAL AND COMPUTATIONAL APPROACH

In the present paper a Finite Difference Time Domain (FDTD) method [3]-[4] is used, with an impinging plane electromagnetic pulse of finite duration (compact pulse) representing a light beam, which interacts with a distribution of many spherical objects, each one characterized by a permittivity value different from ϵ_0 . The resulting field is calculated in a discretized fashion on a three dimensional grid of sampling points.

Frequency Domain results are obtained by means of a Discrete Fourier Transform (DFT) of the system response to the transient excitation of the impinging pulse. The eventual frequency dependence of the objects' permittivity is accounted for in the time domain by modifying the formulation of the Ampère–Maxwell equation with a convolution integral describing the temporal dispersion in the relation between the \mathbf{D} and \mathbf{E} fields. Such a convolution integral can be calculated in a recursive way at every FDTD sampling point and then, with a single run of the FDTD code, one is able to get an entire frequency spectrum of results, at the cost of the computer memory needed to store the transformed electric field values at the various frequencies.

In the present paper it is considered the response of a particular three-dimensional distribution of spherical scatterers namely, an ordered face-cubic centered lattice with a high filling fraction, which is useful in the predictive optical characterization of certain photonic crystals. This target distribution, representing the crystal sample slab, is embedded in a volume of empty space at the exterior boundary of which a special absorbing boundary condition [5] is applied, in such a way that any back-reflected waves are cancelled, thus emulating an ideal infinite space around the crystal target sample under study. The optical characterization of the sample slab consists in the predictive calculation of his reflectance and transmittance in the 500÷1000 nm wavelength range. To pursue this task the calculations are performed by differentiating between a total field inner sub-volume and a scattered field only outer part. Inside the latter, a closed surface Σ_1 is selected and the \mathbf{E} and \mathbf{H} — FDTD obtained — near field values on it are used in the Kirchhoff integral formula [1], [6]

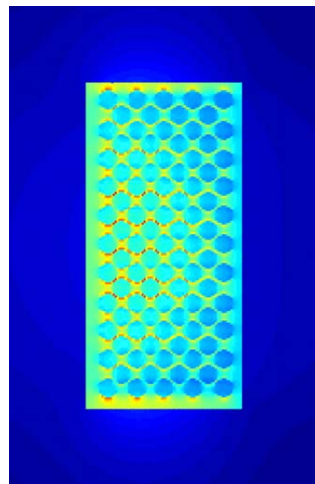
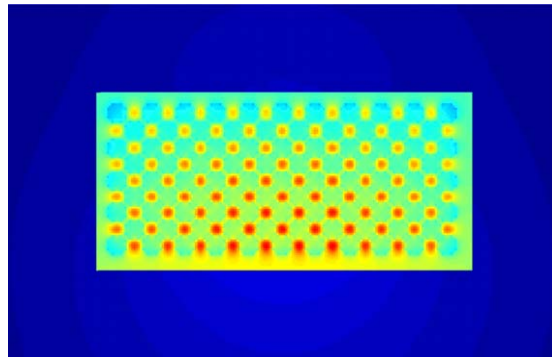


$$\vec{E}(\vec{r}') = \frac{e^{ikr'}}{r'} \frac{k\hat{n}'}{4\pi i} \times \oint_{\Sigma_1} \left[\sqrt{\frac{\mu_0}{\epsilon}} (\hat{n}' \times (\hat{n} \times \vec{H})) - \hat{n} \times \vec{E} \right] e^{-ik\hat{n}' \cdot \vec{r}} dS$$

The calculations based on this formula finally allows the angular distribution determination, at any given frequency of analysis, of the far transverse field values and the related Poynting power flux estimation, on the entire solid angle around the crystal sample. This amounts to the optical characterization of the sample.

III. SIMULATIONS

The simulations are performed with parallelized code making use of the Message Passing Interface (MPI) library for multiprocessors machines [7]. The possibility of running on high performance computers allows for large and highly resolved simulations. At the base of the parallelization scheme there is a decomposition of the FDTD numerical lattice in a three-dimensional grid of sub-lattices, each constituting a distinct process. Data at the six surfaces of each sub-lattice is passed between topologically neighboring processes, to recover the overall lattice integrity. Qualitative examples of the electric field from an array of spherical particles in a color scale are given below. The darker frames correspond to the scattered field only regions, from which data has taken for use in the Kirchhoff formula for near to far field transformation.



IV. CONCLUSION

This paper demonstrates the effectiveness of a computational analysis conducted with an appropriate model for the electromagnetic interaction of photonic crystals on the ground of the very basic governing laws, i.e., Maxwell's equations, which on the other hand are analytically unsolvable in the presence of complex structures. The paper is aimed to an "a priori" global optical characterization and to a parameterized predictive study of the behavior by varying the dimension of the scatterers, their shape, their spatial distribution and their electromagnetic properties. The chosen computational approach is already parallelized and ready for high demanding simulations.

Possible further developments could consist:

i) response analysis of random structures suitable for photonic glasses modeling [8]; ii) inclusion of a computational analysis of the quantum behavior of doping atoms located inside the matrix of scatterers, which have to be coupled through their Hamiltonians with the electromagnetic field temporal evolution just described in the present paper. The quantum evolution of the atomic systems would require the solution of the Time Dependent Schrödinger Equation, which could also be accomplished by using a finite difference time domain approach, according to [9].

REFERENCES

- [1] J. A. Stratton, *Electromagnetic Theory*, McGraw-Hill, New York and London, 1941.
- [2] A. Paris, A. Vaccari, A. Cala' Lesina, E. Serra, L. Calliari, "Plasmonic Scattering by Metal Nanoparticles for Solar Cells", *Plasmonics*, pp. 1-10, Springer, 2012.
- [3] K. S. Yee, "Numerical solution of initial boundary value problems involving Maxwell's Equations in isotropic media", *IEEE Transactions on Antennas and Propagation*, vol. 14, no. 3, pp. 302-307, 1966.
- [4] A. Taflove, S. C. Hagness, *Computational Electrodynamics: The Finite-Difference Time-Domain Method* 3rd ed., Norwood, MA: Artech House, 2005.
- [5] J. A. Roden, S. D. Gedney, "Convolution PML (CPML): An efficient FDTD implementation of the CFS-PML for arbitrary media", *Microwave and Optical Technology Letters*, vol. 27, no. 5, pp. 334-339, 2000.
- [6] W. C. Chew, "Waves and Fields in Inhomogeneous Media", IEEE Press, 1995.
- [7] A. Vaccari, A. Cala' Lesina, L. Cristoforetti, and R. Pontalti, "Parallel implementation of a 3D subgridding FDTD algorithm for large simulations," *Progress In Electromagnetics Research*, Vol. 120, 263-292, 2011.
- [8] W. S. Jodrey and E. M. Tory, "Computer simulation of close random packing of equal spheres", *Phys. Rev. A*, vol. 32, no. 4, pp. 2347-2351, 1985.
- [9] I. Wayan Sudiarta and D. J. Wallace Geldart, "Solving the Schrödinger equation using the finite difference time domain method", *J. Phys. A: Math. Theor.* 40, pp. 1885-1896, 2007.

Session 16 – Wireless communications, networks and systems

A.A. Serra, R. Caso, A. Buffi, A. Guraliuc, A. D'Alessandro, A. Michel, and P. Nepa
Research activities on antenna design for wireless communication networks at the University of Pisa

F. Viani, M. Salucci, F. Robol, E. Giarola, and A. Massa
WSNs as enabling tool for next generation smart systems

S. Mori, P. Lucantoni, M. Ferrara, P. Nocito, G. M. Tosi Beleffi, E. Restuccia, F. Frezza, and F.S. Marzano
Hydrometeor scattering effects over near-infrared free-space urban links: model and experimental measurements

P. Imperatore, A. Iodice, and D. Riccio
Electromagnetic source localization in 3-D outdoor urban scenario using received signal strength

R. Stefanelli, N. Carvallo, D. Brunazzi, and D. Trincherro
Design of the wireless front-end for remote administration of domotic equipment

M. Dionigi, and M. Mongiardo
Wireless power transfer and near field magnetic communications by multi band resonators

RESEARCH ACTIVITIES ON ANTENNA DESIGN FOR WIRELESS COMMUNICATION NETWORKS AT THE UNIVERSITY OF PISA

A.A.Serra, R.Caso, A.Buffi, A.Guraliuc, A.D'Alessandro, A.Michel, P.Nepa
Department of Information Engineering, University of Pisa, Italy

Via Caruso 16, 56122 Pisa, Italy

[[andrea.serra](mailto:andrea.serra@iet.unipi.it), [roberto.caso](mailto:roberto.caso@iet.unipi.it), [alice.buffi](mailto:alice.buffi@iet.unipi.it), [anda.guraliuc](mailto:anda.guraliuc@iet.unipi.it), [andrea.dalessandro](mailto:andrea.dalessandro@iet.unipi.it), [andrea.michel](mailto:andrea.michel@iet.unipi.it), [p.nepa](mailto:p.nepa@iet.unipi.it)][@iet.unipi.it](mailto:p.nepa@iet.unipi.it)

Abstract

An overview of the most recent antenna research activities at the Department of Information Engineering, University of Pisa, in the area of antenna design for wireless communication systems at UHF and microwave frequencies, is presented. Main results are on planar microstrip antennas for wideband communication systems, for both base stations and subscriber units, integrated PIFAs for DVB-T receivers and GPS terminals, near-field focused microstrip arrays, wearable antennas for body-centric communications. Most of the activities on antennas design, characterization and prototyping have been carried out in collaboration with either SMEs or international research centers.

I. INTRODUCTION

The pervasive development of wireless communication networks has determined a greater than ever need for high-performance antennas for large-scale production. Mass-production antennas must be simple, low-cost, easy-to-assembly, compact and low-weight. Nevertheless, they are also required to meet demanding electrical specifications: high-efficiency in compact antennas, shaped radiation patterns for base-station antennas, reconfigurability features for opportunistic communication systems, easy integration for mobile terminal antennas, electrical and mechanical robustness in wearable textile antennas for body-centric communications, as well as high isolation in dual-polarization antennas, as well as in antennas for MIMO applications and diversity schemes. The EM research group at the Microwave and Radiation Laboratory of the Department of Information Engineering, University of Pisa, has gained a valuable experience in designing, prototyping and characterizing planar antennas in the frequency range from a few hundred MHz up to 10 GHz. In the following, a brief overview of the antenna work carried out during the last few years is briefly summarized (more details can be found in the list of referenced journal papers).

II. WIDEBAND ANTENNAS FOR WIRELESS COMMUNICATIONS

The advantages of microstrip technology in terms of easy-fabrication, low-weight and reliability in mass production, determined an extensive utilization of printed antennas for the realization of planar antennas for base stations (or access points) and subscriber units (CPE, customer premises equipment) of wireless communication networks, as for example wireless local networks (WLANs) at the 2.4 GHz ISM band (IEEE 802.11b/g), WiMAX systems in the 3.3-3.8GHz frequency range, and high-data rate communications at 5-6GHz (Hiperlan, IEEE 802.11a). In this context, the authors presented a novel

feeding technique for dual-polarized patch antennas, where the patch and the feeding line are coupled through a resonant square ring slot [1]. In [2]-[3], it has been shown that the above technique is effective in realizing single-feed and double-feed circularly polarized antennas. Prototypes operating at the WiMax frequency band have been realized and prototyped [1]-[3]. Moreover a stacked-version [4] of the dual linearly polarized patch has been used to get up to 45% percentage impedance bandwidth, with a 2x1 array working in the GSM 1800-1900 band (1710-1910 MHz), UMTS band (1920-2170 MHz), ISM band (2400-2484 MHz), and UMTS 3G expansion band (2500-2690 MHz). Most of the work on ring slot coupled patch antennas has been carried out in collaboration with the University of Oviedo, Spain.

III. PIFAS FOR DVB-T RECEIVERS AND GPS TERMINALS

DVB-T (Digital Video Broadcasting-Terrestrial) standards are rapidly becoming very popular and they are nowadays the only terrestrial television service available in many regions. Next generation terminals will be required to have an integrated antenna in order to avoid cabled connections and to make them relatively portable (at least within an indoor scenario). In addition to this, a web access could be provided to guarantee access to on-demand services. A couple of dual-band antennas that can guarantee access to both TV and internet services has been presented in [5]-[6]. They are dual-band PIFAs (Planar Inverted-F Antennas) properly designed to fit in monitor-equipped devices with relatively stringent mechanical and aesthetic constraints; they exhibit the second resonance at the 2.4 GHz [5] or WiMAX frequency band [6]. A linearly-polarized PIFA has been also proposed for a commercial handheld GPS terminal [7]. A measurement campaign on GPS receiver performance (time to first fix, C/N distribution and horizontal dilution of precision) has also been carried out to compare the proposed antenna with a more complex commercial quadrifilar helix antenna and a conventional nearly-square patch. All the above cited PIFAs are low-cost solutions as they can be made out of a cut and bent single metallic sheet. A dual-band PIFA taking advantage of a similar simple construction technique has been designed for the implementation of a two-branch diversity reception scheme in laptop computers [8].

IV. NEAR-FIELD FOCUSED MICROSTRIP ARRAYS

A Near-Field (NF) focused array can be used to maximize the electric field amplitude in a limited-size spot around a given focal point located nearby the antenna aperture (in the antenna near-field region). NF focused antennas have been applied in several areas such as local hyperthermia and imaging in biomedical systems, as well as in non-contacting subsurface inspections and temperature monitoring in microwave industrial applications (see [9] for an extended and updated review of NF focused antennas realizations and applications, as well as for a discussion on related design criteria and performance parameters). In microwave focused antennas, a proper phase tapering of the aperture equivalent currents (or feeding currents of the array elements) is used to get an in-phase summation of the aperture contributions at the given focal point. NF focused antennas can be realized by pyramidal or conical horns with a focalizing lens in front of the antenna aperture, or Fresnel Zone antennas. On the other hand, lightweight, low profile, as well as low-cost NF focused antennas can be obtained by using planar microstrip arrays with a feeding network exhibiting relatively small differences with respect to a

corporate feeding network of a conventional broadside array. In the FOCUS project, which is funded by the University of Pisa in the framework of the Support Action on International Academic Collaborations, research on NF focused antennas is developed in collaboration with the Yuan-Ze University, Taiwan. In [10], the design of a circularly-polarized NF focused 8x8 microstrip array for RFID readers operating in the 2.4 GHz ISM band (2.4-2.48 GHz) has been presented, and its performance compared with those of the corresponding conventional far-field focused array (same size and number of elements, but with a uniform-phase distribution).

V. ANTENNAS FOR BODY-CENTRIC COMMUNICATIONS

The most innovative implementations of mobile communication systems include the possibility of using wearable devices that are attached to clothes, carried in small pockets and installed in clothes' accessories. Wearable terminals require a number of relatively challenging mechanic and electromagnetic specifications that system designers have to face with. Wearable antennas have to be compact, low-profile and unobtrusive to the user movements, especially if they are sewn or stitched straight onto clothes. Moreover, the radiating system must be compliant with operational standards such as those relevant to SAR (Specific Absorption Rate) limits and HAC (Hearing Aid Compatibility) recommendations. A novel dual-polarization/dual-pattern stripline-fed annular-ring slot antenna for body-centric communication systems, working in the IEEE 802.11a frequency band at 5.725-5.825 GHz, has been presented in [11]. Through a collaboration with the University of Birmingham, UK, antenna performance in terms of achievable diversity gain values have been measured in an experimental diversity reception set-up [12]. More recently, a wearable two-antenna system to be integrated on a life jacket and connected to Personal Locator Beacons (PLBs) of the Cospas-Sarsat system has been presented in [13]. Each radiating element is a folded meandered dipole resonating at 406 MHz and includes a planar reflector made a metallic foil. The folded dipole and the metallic foil can be attached on the opposite sides of the floating elements of the life jacket itself, so resulting in a mechanically stable antenna. Prototypes have been realized and a measurement campaign has been carried out when the life jacket with the antenna was worn by a user. Antenna compliance with the Cospas-Sarsat system specifications (in terms of coverage requirements and Effective Isotropic Radiated Power, EIRP, profiles) has been verified through radiation pattern measurements performed in the Satimo SG 3000F system available at Ce.R.Ca., Calero's research centre in Vicenza, Italy.

VI. CONCLUSIONS

A synthetic overview of the most recent results on antenna design activities at the Department of Information Engineering of the University of Pisa has been presented. Work in progress is about spiral wideband antennas realized through metallic strips vertically oriented with respect to the antenna plane [14] (in collaboration with the ElectroScience Laboratory, Ohio State University, USA). Moreover, planar reader antennas for NF coupling with UHF-RFID tags are being designed, accounting for specific requirements on magnetic and electric field distribution on the antenna plane, further than the EIRP limitations (in collaboration with CAEN RFID, Viareggio, Italy). Finally, slot antennas to be integrated in photovoltaic panels have been designed and

characterized, and tests on antenna prototypes will be presented at the conference [15].

REFERENCES

- [1] R. Caso, A. Serra, A. Buffi, M. R. Pino, P. Nepa, and G. Manara, "A Dual-Polarized Slot-Coupled Patch Antenna Excited by a Square Ring Slot", *IET Microwaves, Antennas, Propag.*, vol. 5, pp. 605-610, 2011.
- [2] A. Buffi, R. Caso, M. Rodriguez-Pino, P. Nepa, and G. Manara, "Single-Feed Circularly Polarized Aperture-Coupled Square Ring Slot Microstrip Antenna", *Electronics Letters*, vol. 46, pp. 268-269, 2010.
- [3] R. Caso, A. Buffi, M. Rodriguez-Pino, P. Nepa, G. Manara, "A novel dual-feed slot-coupling feeding technique for circularly polarized patch arrays", *IEEE Antennas Wireless Prop. Lett.*, vol. 9, pp. 183-186, 2010.
- [4] R. Caso, A.A. Serra, M.R. Pino, P. Nepa, and G. Manara, "A Wideband Slot-Coupled Stacked-Patch Array for Wireless Communications", *IEEE Antennas and Wireless Propagation Letters*, vol. 9, pp. 986-989, 2010.
- [5] R. Caso, A. D'Alessandro, A.A. Serra, P. Nepa, and G. Manara, "A Compact dual-band PIFA for DVB-T and WLAN applications", *IEEE Trans. on Antennas and Propagation*, vol. 60, pp. 2084-2087, 2012.
- [6] R. Caso, A. D'Alessandro, A.A. Serra, P. Nepa, G. Manara, "An Integrated Dual-Band PIFA for DVB-T and WiMAX Applications", *IEEE Antennas and Wireless Propag. Lett.*, vol. 10, pp.1027-1030, 2011.
- [7] A.A. Serra, P. Nepa, G. Manara and R. Massini, "A Low-Profile Linearly Polarized 3D PIFA for Handheld GPS Terminals", *IEEE Trans. on Antennas and Propagation*, vol. 58(4), pp. 1060-1066, April 2010.
- [8] A.A. Serra, P. Nepa, G. Manara, I. Dotto, "Performance evaluation of diversity schemes for laptop computers", *IET Microwaves, Antennas & Propagation*, vol. 4(12), pp. 2024-2030, 2010
- [9] A. Buffi, P. Nepa, and G. Manara, "Design Criteria for Near-Field Focused Planar Arrays", *IEEE Antennas and Propagation Mag.*, vol. 54(1), pp. 40-50, 2012.
- [10] A. Buffi, A.A. Serra, P. Nepa, H.-T. Chou, and G. Manara, "A Focused Planar Microstrip Array for 2.4 GHz RFID Readers", *IEEE Transactions on Antennas and Propagation*, vol. 58(5), pp. 1536-1544, May 2010.
- [11] A.A. Serra, A. Guraliuc, P. Nepa, I. Khan, and P.S. Hall, "Dual-polarisation and dual-pattern planar antenna for diversity in body-centric communications", *IET Microwaves, Antennas & Propagation*, vol. 4(1), pp. 106-112, January 2010.
- [12] P.S.Hall, Y. Hao, V.I. Nechayev, A. Alomainy, C.C..Constantinou, C. Parini, M.R. Kamarudin, T.Z. Salim, D.T.M. Heel, R. Dubrovka, A.S. Owadall, W. Song, A.A. Serra, P. Nepa, M. Gallo, M. Bozzetti, "Antennas and propagation for on-body communication systems", *IEEE Antennas and Propagation Magazine*, vol. 49(3), pp. 41-58, June 2007
- [13] A.A. Serra, P. Nepa, and G. Manara, "A wearable two-antenna system on a life jacket for Cospas-Sarsat Personal Locator Beacons", *IEEE Transactions on Antennas and Propagation*, vol. 60, pp. 1035-1042, 2012.
- [14] A. Guraliuc, R. Caso, P. Nepa, and J. L. Volakis, "Numerical Analysis of a Wideband Thick Archimedian Spiral Antenna", *IEEE Antennas and Wireless Propagation Letters*, vol. 11, pp. 168-171, 2012.
- [15] R. Caso, A. D'Alessandro, A. Michel and P. Nepa, "Integration of slot antennas in commercial photovoltaic panels for stand-alone communication systems", submitted to *IEEE Transactions on Antennas and Propagation*, 2012.

WSNs AS ENABLING TOOL FOR NEXT GENERATION SMART SYSTEMS

F. Viani, M. Salucci, F. Robol, E. Giarola, and A. Massa

ELEDIA Research Center @DISI, University of Trento
Via Sommarive 5, I-38123 Trento, Italy
andrea.massa@ing.unitn.it

Abstract

The development of smart environments is becoming more and more feasible thanks to the rapid advances in wireless and networking technologies, along with ubiquitous computing and communications. Heterogeneous functionalities of integrated smart systems based on Wireless Sensor network (WSN) technology have been recently developed at the ELEDIA Research Center of the University of Trento. In this work, a review of the most recent advancements developed at the ELEDIA Research Center in this framework are reviewed.

Index Terms– Wireless Sensor Networks, Smart Environments, Energy Management, Elderly Monitoring, Smart Home, Exposure Assessment.

I. INTRODUCTION

In the last decade, the vision of ubiquitous computing as emerging model for the next-generation smart systems [1] has become relevant thanks to the growth in computing and communication capabilities as well as in interactions with end users. The miniaturization of multi-features and portable devices has contributed to the diffusion of customized terminals able to proactively communicate with distributed networks for communications and information acquisition. In this framework, the ELEDIA Research Center of the University of Trento has investigated Wireless Sensor Networks [2,3] as enabling technology for next generation intelligent networks and services that can satisfy the arising user needs. One of the main strength behind WSNs devoted to smart systems is that, while the capabilities of each single sensor node is limited, the implementation of cooperative schemes throughout the whole network enables the solution of even complex tasks [4]. Moreover, the multi-sensor characteristic permits the integration of heterogeneous functionalities that can coexist, thus enabling multiple applications within the same hardware backbone.

Because of the well-known features of the WSN technology, the design of a cross-layer architecture has been investigated for the implementation of smart systems where multiple and heterogeneous functionalities can be integrated for the solution of different user needs in the field of smart environments.

This work is aimed at reviewing the recent applications of WSNs in the field of smart systems able to intelligently manage the content and the delivery of information acquired through heterogeneous nodes installed in smart spaces. Selected and representative results from real

implementations are presented to give some indications about the implemented solutions.

II. DISTRIBUTED POWER METERING FOR ENERGY MANAGEMENT

Nowadays, efficient energy saving and awareness about the resources management are important social and economic aspects. The traditional power grids and the lack of automation and monitoring tools are becoming limiting factors for the arising evolutions of the energy distribution schemes. In this framework, the ELEDIA Research Center has proposed and developed an intelligent system for the centralized management of energy consumptions in smart grid scenarios. Dedicated sensors for power metering belong to the WSN infrastructure installed in smart homes and manage the appliances for energy consumption optimization [Fig 1(a)].

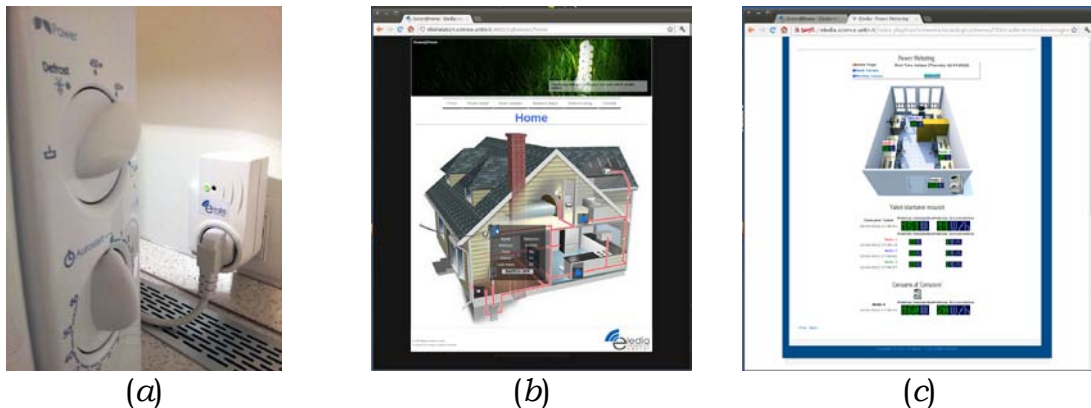


FIG. 1– Power metering sensor (a) and web services for system control in smart home (b) and smart office (c) scenarios.

From the provider point of view, the presence of local energy generation can be profitably monitored and remotely managed by means of WSN nodes installed in large number of residential units. On the other hand, the end user is involved in a process of improved awareness about long-term consumptions and optimal behaviors for cost reduction. The functionalities of the developed WSN-based system have been integrated in a decentralized control unit that can be easily managed through dedicated user-friendly web services for data visualization as graphically shown in Fig. 1(b) (smart home scenario) and Fig. 1(c) (ELEDIA laboratory consumptions management).

III. ELDERLY PEOPLE MONITORING AND BEHAVIOR ESTIMATION

The advantages of the WSN technology have been exploited for unobtrusive monitoring of elderly people in daily life scenarios. Passive real-time strategies for localization and continuous tracking of people [5,6] or undesired intruders in homeland security [7] have been already

proposed by members of the ELEDIA Research Center and recently improved for elders activities monitoring in ambient assisted living (AAL) scenarios. The wireless links for data transmission within the network have been exploited since the presence of targets inside the monitored domain perturbs the electromagnetic field generated by the radio modules of the nodes. The perturbations are then processed for the estimation of the probability of target presence. Starting from the estimation of elders positions, further online processing based on the customization of Kalman filtering procedures have been studied. The extraction of information about human behavioral activities and the estimation of health markers like walking speed, accelerations and trajectory evolution have been investigated as useful indicators of pathologies degeneration. The performance of the system has been experimentally verified in controlled environments as well as in real assisted living scenarios where WSNs have been installed for patient monitoring.

IV. ELECTROMAGNETIC FIELD MONITORING FOR EXPOSURE ASSESSMENT

In the last years, the exposure to electromagnetic fields is attracting more and more attention and systems for prolonged exposure assessment are rapidly growing in the field of residential smart environments. Usually, standard monitoring techniques are based on the experience of operators that perform measurements by means of professional and expensive instrumentations in limited time intervals and in a finite number of positions. In order to overcome these limitations, a distributed and inexpensive system for real-time exposure assessment based on WSN technology has been developed by the ELEDIA Research Center [8][9] and recently installed for long-term monitoring of the electromagnetic exposure of residential areas. A completely passive and small EM probe has been designed for a suitable integration in the WSN node backbone [Fig. 2(a)] that can be easily distributed in indoor and outdoor environments. A hybrid network typology has been designed to increase coverage and guarantee a reliable field measurement. To this end, a dedicated acquisition procedure has been implemented in order to synchronize the data acquisition and transmission phases. The values measured by the probe and acquired by the WSN node are locally stored and successively transmitted to the gateway unit according to the guidelines of the regulations imposed for field measurements.

The three orthogonal components of the electric field [Fig. 2(b)] as well as the monthly statistics of the total field measurements [Fig. 2(c)] can be easily seen through a web service available on the ELEDIA website [10].

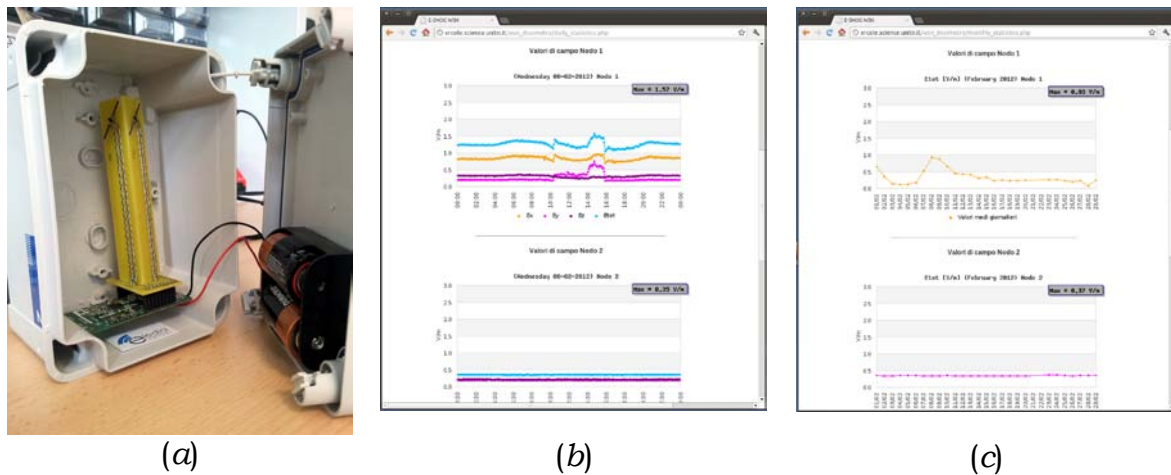


FIG. 2– Prototype of the WSN node for exposure assessment (a) and graphical representation of daily (b) and monthly (c) EM field statistics.

REFERENCES

- [1] M. Weiser, “The computer for the 21st century,” *Scientific Am.*, vol. 265, no. 3, pp. 94-104, Sep. 1991.
- [2] F. Viani, P. Rocca, G. Oliveri, and A. Massa, “Pervasive remote sensing through WSNs,” 6th *European Conference on Antennas and Propagation 2012* (EUCAP2012), Prague, March 26-30, 2012.
- [3] M. Benedetti, L. Ioriatti, M. Martinelli, and F. Viani, “Wireless sensor network: a pervasive technology for earth observation,” in *IEEE Journal of Selected Topics in App. Earth Obs. And Remote Sens.*, vol. 3, no. 4, pp. 488-497, 2010.
- [4] I. F. Akyildiz, W. Su, Y. Sankarasubramaniam, and E. Cayirci, “Wireless sensor networks: a survey,” *Computer Networks*, vol. 38, pp. 393-422, 2002.
- [5] F. Viani, M. Donelli, P. Rocca, G. Oliveri, D. Trincherò, and A. Massa, “Localization, tracking and imaging of targets in wireless sensor networks,” *Radio Science*, vol. 46, no. 5, 2011.
- [6] F. Viani, P. Rocca, M. Benedetti, G. Oliveri, and A. Massa, “Electromagnetic passive localization and tracking of moving targets in a WSN-structured environment,” *Inverse Problems - Special Issue on “Electromagnetic Inverse Problems: Emerging Methods and Novel Applications,”* vol. 26, pp.1-15, 2010.
- [7] F. Viani, G. Oliveri, and A. Massa, “Real-time tracking of transceiver-free objects for homeland security,” 39th *European Microwave Conference 2009* (EuMC2009), Rome, Italy, September 28 – October 2, 2009.
- [8] L. Ioriatti, M. Martinelli, F. Viani, M. Benedetti, and A. Massa, “Real-time distributed monitoring of electromagnetic pollution in urban environment,” in *Proc. 2009 IEEE International Symposium on Geoscience and Remote Sensing*, Cape Town, South Africa, July 13-17, 2009.
- [9] F. Viani, M. Donelli, G. Oliveri, D. Trincherò, and A. Massa, “A WSN-based system for real-time electromagnetic monitoring,” *Proc. 2011 IEEE AP-S International Symposium*, Spokane, Washington, USA, July 3-8, 2011.
- [10] ELEDIA website, demo gallery section, www.eledia.ing.unitn.it.

HYDROMETEOR SCATTERING EFFECTS OVER NEAR-INFRARED FREE-SPACE URBAN LINKS: MODEL AND EXPERIMENTAL MEASUREMENTS

S. Mori⁽¹⁾, P. Lucantoni^(1,2), M. Ferrara^(1,2), P. Nocito⁽²⁾, G. M. Tosi Beleffi⁽²⁾, E. Restuccia⁽²⁾, F. Frezza⁽¹⁾, F. S. Marzano⁽¹⁾

⁽¹⁾ D.I.E.T., Sapienza University of Rome
Via Eudossiana 18, 00184 Rome, Italy
mori@die.uniroma1.it

⁽²⁾ I.S.C.O.M., Min. of Economic Development
Viale America 201, 00144 Rome, Italy
paolo.nocito@sviluppoeconomico.gov.it

Abstract

Wireless communications through free space using optical carrier (Free Space Optics, FSO) represent a promising technology for peer-to-peer connections and urban area networks. Unfortunately FSO links are quite sensitive to atmospheric conditions. Extinction due to fog droplets and hydrometeors such as raindrops and snowflakes can drastically reduce the availability of the channel. In this work will be presented a parametric model to simulate droplets scattering effects over the FSO link. Experimental measurements will be shown for two study cases relative to the FSO wide area set up realized in Rome (Italy) by DIET-Sapienza University and ISCOM-Ministry of Economic Development.

Index Terms – Free space optics, hydrometeor effects modeling, near-infrared measurements, water content.

I. INTRODUCTION

FSO technology is a promising [1] “wireless” communication system in which modulated near-infrared (NIR) beams of collimated light are transmitted through the atmosphere and focused by lens on highly sensitive detectors at the receiver [2]. Even if in optimal conditions optical wireless systems can cover distances of several km, to ensure an acceptable Quality of Service (QoS) a shorter range has to be considered. FSO high data rates can be reached with relatively low error rates, while the extremely narrow laser beam-widths ensure channel spatial density, potential spatial diversity and high reliability [2].

Optical wireless link are sensitive to water-based atmospheric particles, which can introduce severe attenuations to the transmitted beam. Fog is the most deterrent attenuating factor, but also snowflakes and raindrops imposes a non negligible path attenuation [3].

This work will show a model of the absorption and scattering effects due to fog droplets and hydrometeor particles, where the link attenuation is function of the particle water content. The effects of water particles over the FSO link will be illustrated also by two measurements study cases collected in 2012 by the experimental setup realized in Rome, Italy [4].

II. HYDROMETEOR EFFECTS MODELING

Atmospheric hydrometeors can have various shapes depending on their microphysics and thermodynamical development. In this work, non-spherical particles have been modeled as equi-volume spherical particles. This assumption does not introduce significant errors in our analysis and allows the use of the Mie scattering theory to determinate the extinction σ_e , scattering σ_s and absorption σ_a cross sections.

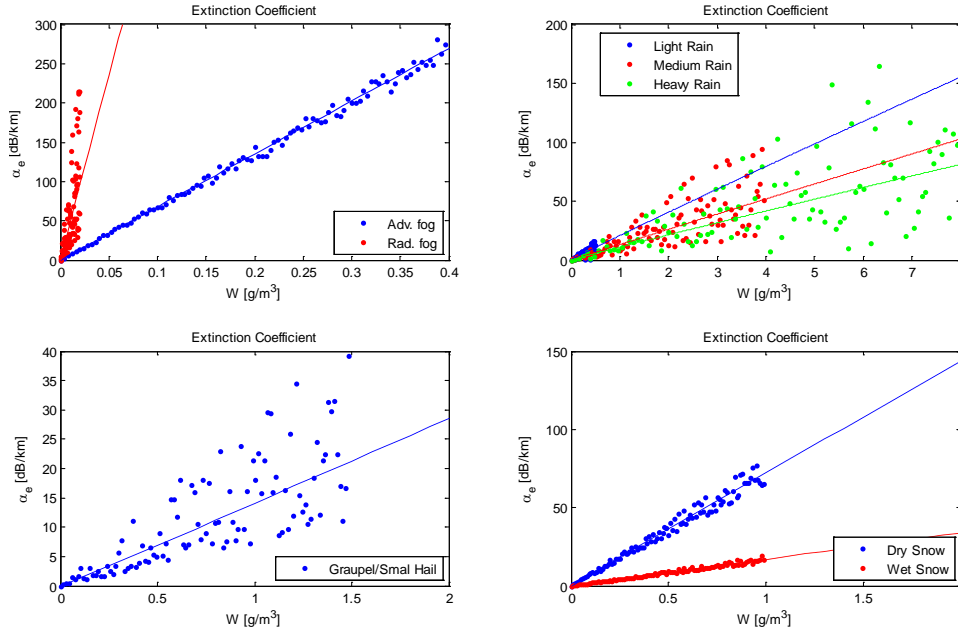


FIG. 1 – Extinction coefficient for the defined particles against water content under constrained random variability. Regression curves are shown.

The extinction coefficient k_e (usually expressed as $10\log_{10}(k_e)$ in dB/km) at a given frequency ν and for unpolarized radiation is then [5]:

$$k_e = \int_{r_m}^{r_M} \sigma_e(r) N_p(r) dr = \int_{r_m}^{r_M} [\sigma_a(r) + \sigma_s(r)] N_p(r) dr \quad (1)$$

where r_m and r_M are minimum and maximum of the volume-equivalent particle spherical radius r , and $N_p(r)$ the Particle Size Distribution (PSD). We have adopted the Scaled Gamma (SG) PSD as a general model for hydrometeor particles p (Eq. 2). Parameters N_e and Λ_e are expressed as function of shape parameter μ_e , effective radius r_e [mm], specific density ρ_p [g·cm⁻³] and water content W [g·m⁻³] of the particle.

$$N_p(r) = N_e \left(\frac{r}{r_e}\right)^{\mu_e} e^{-\Lambda_e \left(\frac{r}{r_e}\right)} = 10^3 \left(\frac{3W\Lambda_e^{4+\mu_e}}{4\pi\rho_p r_e^4 \Gamma(\mu_e+4)}\right) \left(\frac{r}{r_e}\right)^{\mu_e} e^{-\frac{\Gamma(\mu_e+4)}{\Gamma(\mu_e+3)} \left(\frac{r}{r_e}\right)} \quad (2)$$

We have defined 8 hydrometeor classes (advection and radiation fog, light, medium and heavy rain, dry and wet snow, graupel, [6], [7])

characterized by refraction index (using Maxwell-Garnett approximation for snow), density, and a range for μ_e , r_e , W . Simulations have been performed by random generation of particles varying μ_e , r_e , W uniformly within their range. An example is Fig. 1, that shows $k_e=f(W)$ at 1550 nm.

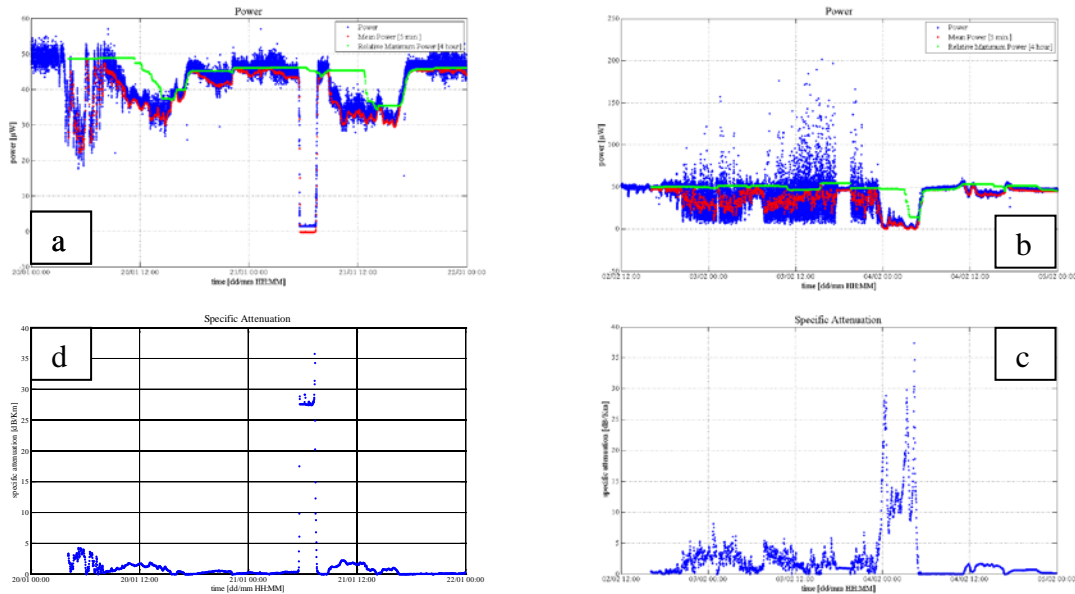


FIG. 2 – FSO Link A→B, Rome, Italy: received power [µW] (a, b) compared to the specific attenuation [dB/km] (c, d) by raingauge, for the fog event of 21/01/12 (a, d), and the snow event of 2-4/02/12 (b, c).

III. EXPERIMENTAL MEASUREMENTS

The experimental setup, located in EUR area of Rome (IT), connects the optical instruments on the roof of the Communications Dept. building of the Ministry of Economic Development (“A”) and the headquarter of the Dept. of Foreign Trade (“C”) via two optical transceivers on top of the so called “EUR Mushroom” tower (“B”). The distance between “A” and “B” is 750 m, whereas “B” and “C” are 900 m far apart. Instrumentation include the fSONA-SONAbeam® 1250-E optical transceiver operating at 1550 nm and (on “A”) a meteorological station, a particle disdrometer, a visibilimeter, an AXIS P1344-E video camera (for visibility analysis) [4]. As example of atmospheric effects, two case study for the “A”→”B” link have been selected, one occurred on 21 January 2012 (Fog event) and one occurred on 2-4 February 2012 (Snow event). In Fig. 2 are shown the FSO power [µW] received and the specific attenuation α [dB/km] derived by rain rate R through $\alpha=1.076R^{0.67}$ [4].

IV. CONCLUSION

A parametric model of water droplets scattering effects has been illustrated. Extinction simulations have been shown for fog droplets,

raindrops, snowflakes and graupel. A quantitative evidence of the droplets effects over the FSO link has been presented using the meteorological and optical data collected by the experimental setup realized in Rome, Italy. Plans foresight to collected at least a full year of measures, to cover the seasonal and diurnal variability of atmospheric conditions. Measurements will be used to improve the characterization of the atmospheric particles over the FSO link and to refine the presented model, with the objective of realize a generalized parametric modeling of extinction, scattering asymmetry and volumetric albedo respect of water content, fall rate or visibility.

ACKNOWLEDGEMENT

This work has been carried out within an ISCOM-University La Sapienza funded joint project. Authors are thankful to EUR SpA (Rome, Italy) for its kind availability. The authors deeply thank the staff of ISCOM for the technical support provided, particularly Roberto Dal Molin, Massimo Ferrante, Antonio Spaccarotella, Paolo Balducci and Mauro Piacentini. F. Consalvi of Fondazione Ugo Bordoni (FUB, Rome, Italy) is acknowledged for his support on technical activities.

REFERENCES

- [1] COST Action IC1101, "Optical Wireless Communications - An Emerging Technology", see Memorandum Of Understanding:
http://www.cost.esf.org/domains_actions/ict/Actions/IC1101
- [2] A.K. Majumdar and J.C. Ricklin "Free-Space Laser Communications, Principles and Advantages", *Springer Science LLC*, 233 Spring Street, New York, NY 10013, U.S.A., 2008.
- [3] R. Nebuloni and C. Capsoni, "Effect of Hydrometeor Scattering on Optical Wave Propagation Through the Atmosphere", *Proc. of 5th European Conference on Antennas and Propagation (EuCAP)*, Rome (IT), 11-15 April 2011.
- [4] F. S. Marzano, S. Mori, F. Frezza, P. Nocito, G. M. Tosi Beleffi, G. Incerti, E. Restuccia, F. Consalvi, "Free-Space Optical High-Speed Link in the Urban Area of Southern Rome: Preliminary Experimental Set Up and Channel Modelling", *Proc. of 5th European Conference on Antennas and Propagation (EuCAP)*, Rome (IT), 11-15 April 2011.
- [5] A. Ishimaru, "Wave propagation and scattering in random media", *IEEE Press*, Piscataway, NJ, 1997.
- [6] F.S. Marzano, D. Scaranari, and G. Vulpiani, "Supervised fuzzy-logic classification of hydrometeors using C-band dual-polarized radars", *IEEE Trans. Geosci. Rem. Sensing*, n. 45, pp. 3784-3799, 2007.
- [6] M. Gebhart, E. Leitgeb, S. Sheikh Muhammad, B. Flecker, C. Chlestil, "Measurement of Light attenuation in dense fog conditions for FSO applications", *Proc. of SPIE*, vol. 5891, 2005.

ELECTROMAGNETIC SOURCE LOCALIZATION IN 3-D OUTDOOR URBAN SCENARIO USING RECEIVED SIGNAL STRENGTH

P. Imperatore⁽¹⁾, A. Iodice⁽²⁾, D. Riccio⁽²⁾

⁽¹⁾ Istituto per il Rilevamento Elettromagnetico dell'Ambiente, Italian National Research Council (CNR), 80124 Napoli, Italy

⁽²⁾ Department of Biomedical, Electronic and Telecommunication Engineering, University of Naples "Federico II", 80125 Napoli, Italy

imperatore.p@irea.cnr.it

Abstract

This paper investigates how, by using only received signal strength information, the radio-localization in urban scenario can be achieved with sufficient accuracy, by adopting a methodologically new approach that incorporates a priori information about detailed structure of the 3-D propagation environment. We first formally introduce the localization as a nonlinear inversion problem, then we reformulate it as a global nonlinear optimization one. Accordingly, suitable cost functions are considered and discussed, with reference to both collaborative and non-collaborative scenarios.

Index Terms – Radio-localization, electromagnetic propagation, ray-tracing.

I. INTRODUCTION

Conventional radio-localization methods assume idealized situations, so that the specific character of the propagation environment is commonly disregarded [1]. In addition, most of the advanced radio localization methods hitherto proposed conceive the multipath phenomenon as detrimental and several strategies have been devised to combat against it. As a result, these methods lack an adequate model accounting for the electromagnetic propagation environment, which hinders their effectiveness in realistic scenarios. In this regard, it is worth to be emphasized that accurate EM propagation prediction cannot be achieved by relying on empirical model, not even in rural environment [2]. When urban scenario is concerned, most of the realistic situations are so complicated that the application of conventional localization methods turns out to be unsatisfactory. Solving the localization problem in a realistic environment, therefore, necessarily requires the developing of more sophisticated methods [3].

This paper investigates how, by using only received signal strength information, the radio-localization in urban environment can be achieved with sufficient accuracy, by adopting a methodologically new approach that incorporates a priori information about detailed structure of the 3-D propagation environment [4]-[6]. More specifically, given the

Received Signal Strength measured at certain prescribed sampling points within the operative scenario, we treat the localization of an unknown EM sources as an inverse problem in which the determination of location of an unknown EM source is appropriately accomplished by implicitly taking into account the pertinent signal propagation in the multipath environments [3]-[5]. We first formally introduce the localization as a nonlinear inversion problem, then we reformulate it as a global nonlinear optimization one. Accordingly, suitable cost functions are considered and discussed: Specifically, both collaborative and non-collaborative scenarios are addressed. In the collaborative case, one has prior knowledge about the input power of the (unknown) source to be localized. Nonetheless, this information is not available in a non-collaborative transmitter scenario. In order to cope with the lack of direct information on the input power at the transmitting antenna, the problem is properly re-formulated and a *co-linearity* criterion is established. In order to deal with pertinent minimization of the objective function, we successfully employ a simple and straightforward search strategy based on the Hooke-Jeeves method [6], which falls into a class of direct search methods known as pattern search algorithms. In order to demonstrate the efficacy of the proposed localization method, simulation experiments are carried out for a realistic environment. In addition, robustness with respect to several parameters is also evaluated. Finally, it is worth to emphasize that the proposed localization approach is intrinsically *site-specific*, since it appropriately exploits solutions to the direct electromagnetic propagation problem that are obtained by employing a suitable ray-tracing based solver [4]-[5].

II. RATIONALE OF THE LOCALIZATION METHOD

The relevant localization problem can be formalized as follows. The functional description of the dependence of EM field levels at M points of the scenario (whose locations are denoted by the vectors $\mathbf{x}_1, \mathbf{x}_2, \dots, \mathbf{x}_M \in \mathbb{B} \subset \mathbb{R}^3$) on the location \mathbf{r} of the a certain radiating source (forward problem) can be expressed in terms of the transformation

$$\boldsymbol{\varphi}: \mathbf{r} \in \mathbb{B} \subset \mathbb{R}^3 \rightarrow \boldsymbol{\varphi}(\mathbf{r}) = [\varphi(\mathbf{x}_1, \mathbf{r}), \dots, \varphi(\mathbf{x}_M, \mathbf{r})] \in \mathbb{R}_+^M, \quad (1)$$

where the vector-valued function $\boldsymbol{\varphi}(\mathbf{r})$ is the image into M -dimensional space of the corresponding source location \mathbf{r} . It should be emphasized that the mapping (1) is inherently nonlinear. Furthermore, given a specific operative scenario, and assuming the transmitter located in the unknown position \mathbf{r}^* , by gathering the experimental observations (received signal strength), acquired in M points of the scenario, we can construct the M -by-1 vector

$$\boldsymbol{\varphi}(\mathbf{r}^*) = [\varphi(\mathbf{x}_1, \mathbf{r}^*), \dots, \varphi(\mathbf{x}_M, \mathbf{r}^*)]. \quad (2)$$

The number of measurement locations M constitutes the dimension of the input data set (observable). We emphasize that the information about the unknown emitter position \mathbf{r}^* is embedded in the observed vector $\boldsymbol{\varphi}(\mathbf{r}^*)$. Here we are interested in constructing an inverse procedure that produces the location \mathbf{r}^* of an unknown transmitter in response of the vector $\boldsymbol{\varphi}(\mathbf{r}^*)$. To this aim, a suitable ray-tracing based solver [4]-[5] can be used to compute the field levels $\hat{\boldsymbol{\varphi}}(\mathbf{r})$ at the M measurement locations, produced by a source placed at \mathbf{r} . Then, by using a minimum squares criterion, the nonlinear optimization problem assumes the form

$$\hat{\mathbf{r}}(\boldsymbol{\varphi}(\mathbf{r}^*)) = \arg \min_{\mathbf{r}} \left\| \boldsymbol{\varphi}(\mathbf{r}^*) - K\hat{\boldsymbol{\varphi}}(\mathbf{r}) \right\|^2 \quad (3)$$

where $\hat{\mathbf{r}}$ identifies the source position such that simulations best match measurements; K^2 is the ratio between the actual input power and the one adopted by the solver to calculate $\hat{\boldsymbol{\varphi}}(\mathbf{r})$. We distinguish two different cases: in a collaborative scenario the transmitted power is known, so that K can be assumed unitary ($K^2=1$); in a non-collaborative environment K is unknown and it should be estimated. It is possible to demonstrate that, when the parameter K is unknown, the optimization problem (2) can be re-formulated, so obtaining the following co-linearity criterion

$$\hat{\mathbf{r}}(\boldsymbol{\varphi}(\mathbf{r}^*)) = \arg \max_{\mathbf{r}} \left(\frac{\hat{\boldsymbol{\varphi}}(\mathbf{r}) \cdot \boldsymbol{\varphi}(\mathbf{r}^*)}{\|\hat{\boldsymbol{\varphi}}(\mathbf{r})\| \|\boldsymbol{\varphi}(\mathbf{r}^*)\|} \right)^2 \quad (4)$$

This is equivalent to maximize the cosine of the angle between measurement and simulation vectors.

In both scenarios, minimization (or maximization) is achieved by using the Hooke-Jeeves method [6]

III. SIMULATION EXPERIMENTS

We consider a typical urban scenario, in which the unknown source to be localized is assumed positioned as depicted in Fig.1. The arrangement of the considered measurement points is depicted in Fig.2.



FIG. 1 – 3-D model of the considered operative scenario. Antenna height: 49.00[m]. Area dimension: 667x667 [mxm].

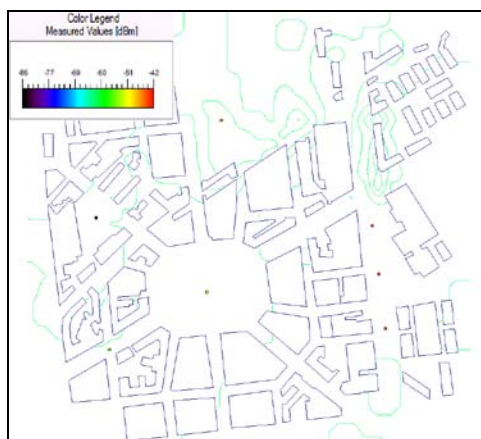


FIG. 2 – Measurement points ($M = 7$) arrangement; the corresponding measured values (dBm) are also shown.

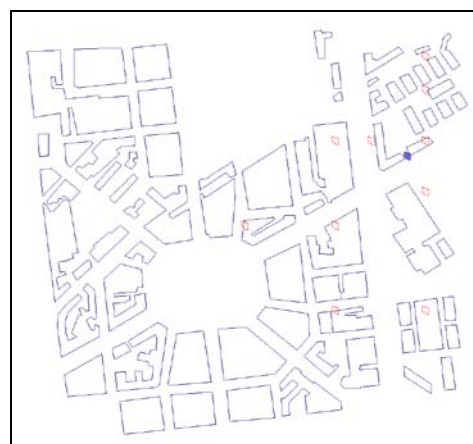


FIG. 3 – Employed ($N = 11$) candidate sources (red symbols); the actual source location is also shown (blue symbol)

By employ (3) or (4), the localization is successfully achieved with very high accuracy. The criterion (4) leads also to an accurate estimation of the actual transmitted power. Only a limited number of iterations, and hence of simulations, is needed by the Hook-Jeeves algorithm to converge, as shown in Fig.3, where the source positions employed in simulations are reported.

ACKNOWLEDGEMENT

His work was supported in part by LINCE project: “un sistema di Localizzazione/georeferenziazione degli INCidEnti stradali a basso costo”, funded by FARO (Finanziamento per l’Avvio di Ricerche Originali).

REFERENCES

- [1] G. L. Stuber, J. J. Caffery, “Radiolocation Techniques”, Mobile Communications Handbook, CRC Press LLC, 1999.
- [2] P. Imperatore, E. Salvadori, I. Chlamtac, “Path Loss Measurements at 3.5 GHz: A Trial Test WiMAX Based in Rural Environment,” in *Proc. of 3rd International Conference on Testbeds and Research Infrastructures for the Development of Networks and Communities (TRIDENTCOM)*, May 21-23, 2007.
- [3] P. Imperatore, A. Iodice, D. Riccio, “Radio Localization of Unknown Transmitter based on the propagation simulation in urban environment”, in *Proc. of XVIII RiNEM-1st National URSI B Meeting*, Benevento, 6-10 Sept. 2010.
- [4] G. Liang, H.L. Bertoni “A new approach to 3-D ray tracing for propagation prediction in cities”, *IEEE Trans.Antennas Propagat.*, vol 46, pp. 853-863, 1998.
- [5] G. Franceschetti, P. Imperatore, A. Iodice, D. Riccio, “Radio-Coverage Parallel Computation on Multi-Processor Platforms”, *Proc. of European Microwave Conference*, EuMC 2009, pp.1575-1578, 2009.
- [6] R.A. Hooke, T.A. Jeeves, “Direct Search Solution for Numerical and Statistical Problems”, *J. Assoc. Comp. Mach.*, vol.8, pp. 212-229, April 1961.

DESIGN OF THE WIRELESS FRONT-END FOR REMOTE ADMINISTRATION OF DOMOTIC EQUIPMENT

R. Stefanelli, N. Carvallo, D. Brunazzi, D. Trincherò

iXem Labs - Politecnico di Torino
Department of Electronics and Telecommunications
corso Duca degli Abruzzi 24, 10129 Turin, Italy
info@ixem.polito.it

Abstract

This paper introduces open-hardware wireless equipment designed for a medium scale Internet of Things and Internet of Services experiment, in a rural - digitally divided - village in the Italian Countryside. A wide band wireless network has been built, to provide several remote services: Internet access, intelligent house (garden) control, security surveillance. Internet of Things and Internet of Services activities are realized by means of low cost, open hardware wireless technology. The results obtained during the first eighteen months of experimentation demonstrate a strong participation of the local population, a reduction of the house management costs, together with an increase of safety and security.

Index Terms – Domotics, Wireless Sensors, Internet of Things, Smart-housing

I. INTRODUCTION

The digital gap in remote regions is considered a strategic issue for Developing and Developed Countries, a clear limitation of living conditions, and one of the most significant causes of emigration and loss of traditions. The connection to the digital World represents the most significant way to provide access to information and cultural exchange, but also to basic social services like telemedicine and distance learning. Additionally, in the very last years, a digital channel is more and more requested to transport information related to Things and Services. In rural scenarios, the possibility to acquire, share and control information associated to house and/or environment may signify not only additional comfort, but also energy saving, costs reduction, improved life quality, advanced security, health assistance [1]. Nonetheless, transforming a rural living place into an intelligent one does not make real sense, without a network. When a network is available, Things and Services may be inserted in a virtual social network, as the Humans do [1]: the inhabitants may share, compare, and optimize house managing. Bringing a networked intelligent platform to rural places is normally limited by bandwidth availability and end-users technological skills.

Starting from these basic concepts, we have developed an implementation scheme to facilitate adoption of intelligent systems in the Countryside: it is based on the realization of a very low cost, wideband last-mile Intranet network, on the construction of extremely

low cost wireless sensors and controllers, on a strong participation of the inhabitants and on the enrolment of University students during the design, realization and technological transfer phases. The scheme is being successfully implemented in a peculiar location in the Italian Countryside.

II. THE NETWORK REALIZATION

The experiment is being developed in the Municipality of Verrua Savoia, at 50 kilometers from Torino, Italy: it is located in a hilly area, on the plain border along the Po river; it covers a territory of about 16 square kilometers, where about 1400 inhabitants live. Most of the people are commuters and stay outside for a large part of the day. The relative distance from the city and the significant presence of commuters make the selected location a representative case of application for a general remote rural context.

At first, a wireless network has been realized, in order to interconnect all the hamlets of the village. The network topology is shown in Fig 1: five Hiperlan BSs, installed in strategic positions, guarantee the 99% territory coverage; the BSs are connected through P2P-links with high directivity antennas. At February 2012, 190 users are connected to the network.

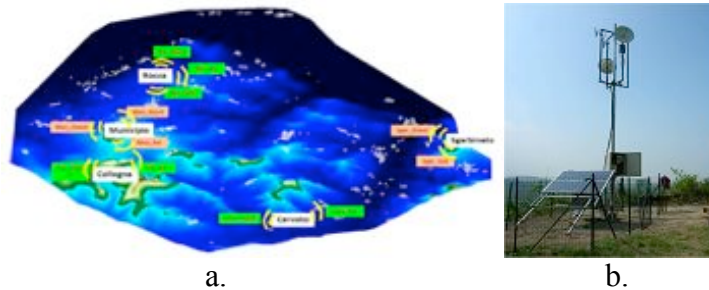


FIG. 1 – a. Hyperlan 802.11n coverage b. example of BS installation

III. WIRELESS SENSING SYSTEMS

In the preliminary test-phase, started during winter 2010-2011, one house has been selected, where a commercial device has been installed and connected to three remote temperature sensors and one remote humidity sensor [2].

Then, in the winter season 2011-2012, we have started developing home automation facilities for each subscriber: citizens have been provided with one wireless controller that can be connected to several sensors, a large number of personal Ethernet devices, and actuators. The controller, the sensors and the actuators have been designed and

built using extremely-low-cost devices. They have been operative for the whole winter season, even if they are still in the prototyping phase. Fig. 2 shows a couple of realizations, the microcontroller is realized by means an open-hardware board, the “Arduino Uno”. The board has been chosen because of its low cost, but also because it allows connection to many sensors and actuators: the basic version is equipped with 14 digital input/output pins and 6 analog inputs.

Among the several parameters that can be monitored are: temperature and humidity of rooms, gas/water leakages in the living environments, ground humidity. The list of Ethernet devices comprises cameras, loudspeakers, light etc. As actuators, the controller is able to manage thermostats, fuel burners, automated wells, alarming units and any kind of Ethernet based actuator.

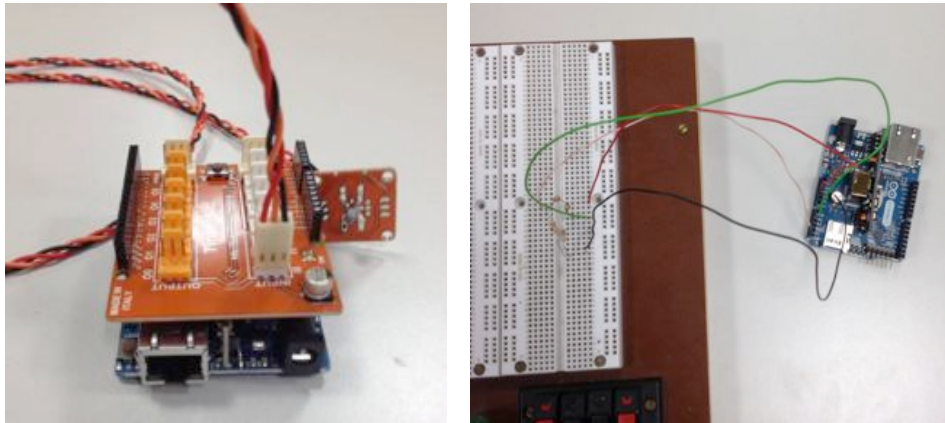


FIG. 2 – An example of thermostat and temperature sensor prototypes

The largest part of sensors and actuators are not directly wired to the controller, since they are deployed in different rooms. For this reason, these devices are equipped with a wireless front end, working at 433 MHz, in the same frequency band used to control gates and alarms by radiofrequency. Even if the available bandwidth is limited to 500 kHz, this characteristic does not represent a limitation: the amount of data collected and transmitted is extremely restricted. Fig.3 shows an example of radiator, designed according to the analytical scheme described in [3].

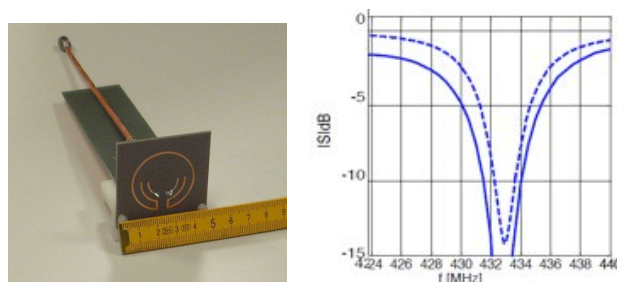


FIG. 3 – A 433 MHz antenna designed for a wireless temperature sensor

In the same time, a customized network environment, together with a dedicated web platform, has been developed, to favor an easy and integrated management of the sensing and controlling components. The web interface allows the user (or the remote manager) to monitor in real time the information detected by the sensors and to activate or deactivate the fuel burner. Thanks to the free connectivity provided to every users, and the static IP public address assigned to each device, they are remotely controllable and reachable from the Internet network.

IV. CONCLUSIONS

The paper introduces an experiment aimed to facilitate the daily home management, be remotely monitoring and controlling many activities. The combination of localized domotics equipment with Internet management optimizes living costs and energy consumption in remote locations, inhabited by elder people and commuters. A fundamental component is represented by the use of small, and efficient radiators useful to interconnect sensors and actuators in the whole house.

The preliminary results measured in the house that has been automated since the beginning of winter 2010-2011 are showing dramatic money savings, primarily due to the remote control of the sensing equipment. They exhibit a reduction of almost the 50% of the heating energy consumption and about 25% of garden watering. Data regarding the winter season 2011-2012 are more representative, as they are been applied to a larger number of houses. Unfortunately, they are affected by an unpredictable trigger: winter 2011-2012, which has not finished yet, has been the coldest of the last 100 years in Europe. Nevertheless, for the moment, we have still measured an average reduction of the 10% of the expenditures, between early November and late February. This datum should be analyzed and disaggregated, or, even more, compared to further data acquire in the next winter periods.

REFERENCES

- [1] Nugent, C. D. Finlay, D. D. Fiorini, P. Tsumaki, Y. Prassler, E., "Home Automation as a Means of Independent Living," *IEEE Transactions on Automation Science and Engineering*, Vol. 5, Issue 1, 2008, p. 1-9.
- [2] Trincherro, D.; Stefanelli, R.; Brunazzi, D.; Casalegno, A.; Durando, M.; Galardini, A., "Integration of smart house sensors into a fully networked (web) environment," *Sensors, 2011 IEEE*, Page(s): 1624 - 1627.
- [3] Stefanelli, R.; Trincherro, D.; "Full-Analytical Procedure For The Design Of Micro-Magnetic Radiators", submitted to RinEm 2012.

WIRELESS POWER TRANSFER AND NEAR FIELD MAGNETIC COMMUNICATIONS BY MULTI BAND RESONATORS

M. Dionigi⁽¹⁾, M. Mongiardo⁽¹⁾

⁽¹⁾ DIEI, Perugia University
Via G. Duranti 93, 06125 Perugia, Italy
marco.dionigi@unipg.it

Abstract

Resonant Wireless Power Transfer (WPT) can be realized by using coils coupled via their magnetic fields; such systems can exchange energy in the mid-range. Information can also be exchanged via Near-Field Magnetic Communications (NFMC), which is currently receiving considerable attention for several possible applications. We present a structure that can be used for realizing both WPT and NFMC; this structure shows separate frequency channels for the simultaneous transmission of power and data. A test system with one band for power exchange and two separate bands for data transmission is designed, simulated, and measured to show the effectiveness of the proposed structure.

Index Terms – wireless energy transfer, wireless power transmission, magnetic coupling, resonators, near field magnetic communications. About four key words or phrases in alphabetical order, separated by commas.

I. INTRODUCTION

Wireless Power Transfer (WPT) obtained via magnetically coupled resonators is currently receiving considerable attention and it is currently investigated for a variety of applications: from medical sensors and implanted devices, to immortal sensor networks; for wireless charging Electric Vehicles (EVs), to wireless powering of singlechip systems, etc. [1]

While it seems that resonant WPT is an interesting and viable approach for several applications, the same principles are also used in Near-Field Magnetic Communication (NFMC) where the reactive, evanescent, magnetic fields are employed for non contact short range communication [2]. However, using both WPT and NFMC would, in general, require two separate circuits, with increased complexity, weight, physical dimensions and costs.

We introduce a single physical structure capable to transmit power and exchange data over different frequency bands. Some examples [3], [4], [5] already exist on how to apply to the same system simultaneous power and data exchange for purely inductive (non resonant) links. Such systems usually adopt the same frequency for data and power transmission by proper choice of the modulation strategy. We present in this work a novel resonator that allows one to use a multiple band configuration taking advantage of the frequency separation of the

power channel from the data channels. In our system the loop inductance, which realizes the mutually coupled inductors, is used at all frequencies, thus allowing relatively efficient power and data transfer.

II. THE MULTI BAND RESONATOR

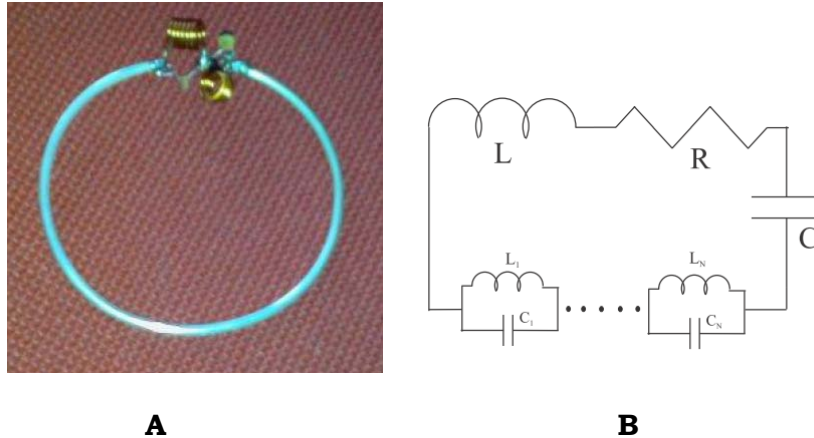


FIG. 1 – A) example of a multi band resonator. The main loop is made of mm diameter silver plated wire and mica capacitor, the higher frequency resonators are made of 1mm diameter insulated copper wire coils and ceramic capacitors. B) The multi band resonator circuit.

The basic structure of the multiband resonator is illustrated in Fig. 1A; it is composed of a large conducting loop and a number of parallel resonators equal to the number of the desired transmission bands. The equivalent circuit of the dual band resonator is reported in Fig. 1B. The resonator impedance, expressed as a function of frequency, is given by the following expression:

$$Z = R + j\omega L + \frac{1}{j\omega C} + \sum_{n=1}^N \frac{1}{\left[j\omega C_n + \frac{1}{j\omega L_n} \right]} \quad 1)$$

It is apparent from eq. (1) that the isolated resonator impedance Z presents $N+1$ zeros at different positive frequencies. This fact allows the main loop of the resonator to be used as a coupling element for both the power and data band. Due to efficiency considerations the lower frequency can be used for power transmission while the higher ones are suitable for data transmission.

III. THE MULTIBAND WPT SYSTEM

The multiband WPT system can be obtained by using the resonator introduced in the previous section. We consider the WPT structure given in Fig. 2A.: the latter is an indirect coupled system where the

two resonator are coupled to each other loop of the system. The input and output loops are used to obtain the matching from the resonator to the source and load resistance. The transmission properties of the system depend on the mutual inductance M_{23} and the quality factor of the resonators; the system can be designed in such a way that an optimal transmission can be obtained for a given M_{23} as described in [1]. We can add to the resonators the parallel resonant circuits of Fig. 2B in order to add multiple data transmission bands. In this case no coupling is considered between these resonators, due to their dimensions and distances.

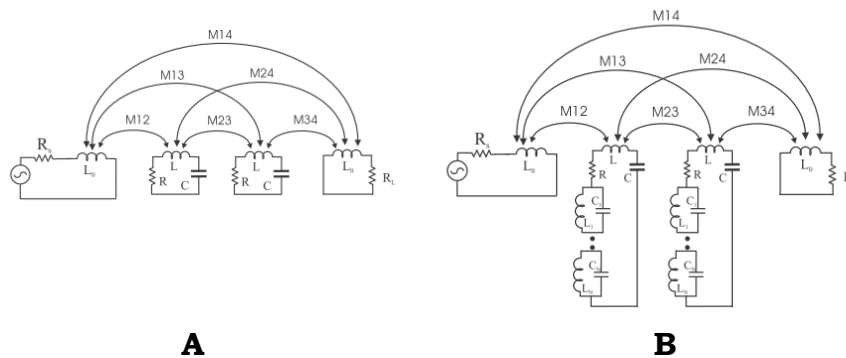


FIG. 2 – A) a single band WPT; B) multi band circuit capable of transferring frequency on one resonant frequency and informations on other.

In order to make it possible to separate the data bands from the power signal a proper signal filtering network must be used at the input and output ports of the WPT system.

IV. RESULTS

Based on the results of the previous section an entire WPT system has been realized. We have used 3 mm silver plated wire for the main loop and insulated copper wire for the inductance of higher frequency resonators. The main loop diameter is 72 mm while the two inductance made of 1 mm diameter copper wire are made respectively of 4 and 6 turn on a diameter of 7 mm with length 6mm and 9 mm. The power channel is in the 12 MHz frequency band while the first data channel is at 90 MHz and in the second data channel is at 135 MHz. The capacitors are made of silvered mica for the low frequency resonator and ceramic capacitors. The WPT system is constituted by the input and output coupling loops of 50 mm diameters and coplanar with the resonator’s loops and a couple of three band resonators tuned to be as similar as possible. Fig. 8 shows the system with the resonators placed at 35 mm distance; source and load resistance are of 50 Ohm. Figure 3 shows the comparison of the measured and simulated transmission scattering parameters for the system when the distance between the resonators is 35 mm.

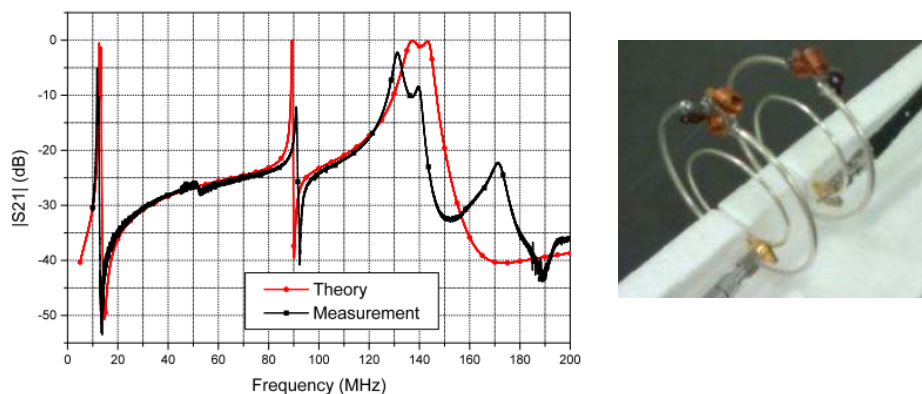


FIG. 3 – Measured and simulated response of the WPT system shown in the picture

V. CONCLUSIONS

We have introduced a single physical structure capable of realizing resonant wireless power transfer and near field magnetic communication at separate frequency bands. We have also presented network models suitable for the analysis and design of this class of structures. The dependence of the efficiency with the characteristics of the resonators has been investigated, and a complete system has been designed and measured showing fairly good agreement between measured and theoretical values.

REFERENCES

- [1] M. Dionigi, A. Costanzo, M. Mongiardo, "Network Methods for the Analysis and Design of Resonant Wireless Power Transfer Systems," Chapter of the book "Wireless Power Transfer - Principles and Engineering Explorations", <http://www.intechweb.org/>, 2011.L.
- [2] Agbinya, J.I.; Masihpour, M.; , "Near field magnetic induction communication Link Budget: Agbinya-Masihpour model," Broadband and Biomedical Communications (IB2Com), 2010 Fifth International Conference on , vol., no., pp.1-6, 15-17 Dec.2010.
- [3] Hirai, J.; Tae-Woong Kim; Kawamura, A.; , "Wireless transmission of power and information and information for cableless linear motor drive," Power Electronics, IEEE Transactions on , vol.15, no.1, pp.21-27, Jan 2000.
- [4] R Puers, R Carta and J Thon, "Wireless power and data transmission strategies for next-generation capsule endoscopes," Journal of Micromechanics and Microengineering, vol.21 no.05, 2011.
- [5] Rathge, C.; Kuschner, D.; , "High efficient inductive energy and data transmission system with special coil geometry," Power Electronics and Applications, 2009. EPE '09. 13th European Conference on , vol., no., pp.1-8, 8-10 Sept. 2009.

Session 17 – Photonic and plasmonic technologies and components

F. Morichetti, A. Canciamilla, S. Grillanda, P. Orlandi, S. Malaguti, M.J. Strain, M. Sorel, G. Bellanca, P. Bassi, and A. Melloni

SAPPHIRE: a generic foundry platform for silicon photonics

A. Parini, G. Calò, S. Malaguti, G. Bellanca, V. Petruzzelli, and S. Trillo

Photonics interconnect technology for chip multiprocessing architectures: the Photonica project

M.P. Bolzoni, G.G. Gentili, and S.M. Pietralunga

Grating-assisted coupling to strip plasmonic modes: 3D numerical analysis

M. Grande, G. Magno, R. Marani, G. Calò, V. Petruzzelli, and A. D'Orazio

Design of plasmonic directional couplers

F.M. Pigozzo, D. Modotto, and S. Wabnitz

Second harmonic generation in plasmonic waveguides

F. A. Bovino

Representation of a Spiral Phase Plate as a two mode Quantum Phase Operator

SAPPHIRE: A GENERIC FOUNDRY PLATFORM FOR SILICON PHOTONICS

F. Morichetti⁽¹⁾, A. Canciamilla⁽¹⁾, S. Grillanda⁽¹⁾,
P. Orlandi⁽²⁾, S. Malaguti⁽³⁾, M. J. Strain⁽⁴⁾, M. Sorel⁽⁴⁾,
G. Bellanca⁽³⁾, P. Bassi⁽²⁾, A. Melloni⁽¹⁾

⁽¹⁾Dipartimento di Elettronica e Informazione, Politecnico di Milano,
Via Ponzio 34/5, Milano 20133, Italy, morichetti@elet.polimi.it

⁽²⁾ Dipartimento di Elettronica, Informatica e Sistemistica,
Università di Bologna, Viale Risorgimento 2, Bologna 40136, Italy

⁽³⁾ Dipartimento di Ingegneria, Università degli Studi di Ferrara,
via Saragat 1, Ferrara 44100, Italy

⁽⁴⁾ School of Engineering, University of Glasgow, United Kingdom

Abstract

A Shared Access Platform to Photonic Integrated Resources (SAPPHIRE) is presented, which aims to become the first national infrastructure enabling a shared access of different users to a generic silicon photonic foundry. The platform is based on the concept of high-level circuit design for photonic integrated circuits (PICs), where complex architectures can be designed without a specific knowledge of either electromagnetic (EM) or technological issues, but simply operating at the circuit level on a selected set of elementary functional elements, named building blocks (BBs). The main roles of the SAPPHIRE platform in the foundry-Users interactions are discussed, as well as the concept of photonic BBs and circuit simulation. Results on a proof-of-concept device are shown to demonstrate the validity of the high-level circuit design for PICs.

Index Terms – Circuit Design, Photonic Generic Foundry, Photonic Integrated Circuit, Silicon Photonics

I. INTRODUCTION

The production of PICs has been traditionally driven by a substantially application-oriented methodology, where technology processes were finely tuned to fulfill the needs of specific products. This led to the fragmentation of resources over many different technologies, which has hindered a sustainable growth of the PICs market. In the European scenario, this way of thinking is slowly but radically changing. In the last years the bases for the creation of application-blind photonic integration technologies have been set, for instance for Indium Phosphide [1] and Silicon-on Insulator [2] photonic platforms. This new trend is based on the concept of generic foundry, the same scheme that boosted the success of microelectronics and microwave technologies.

In this contribution, we present our recent advances in the development of the SAPPHIRE (Shared Access Platform to Photonic Integrated Resources) platform, which aims to originate the first national infrastructure able to make available silicon photonic technologies to different users through a shared access scheme.

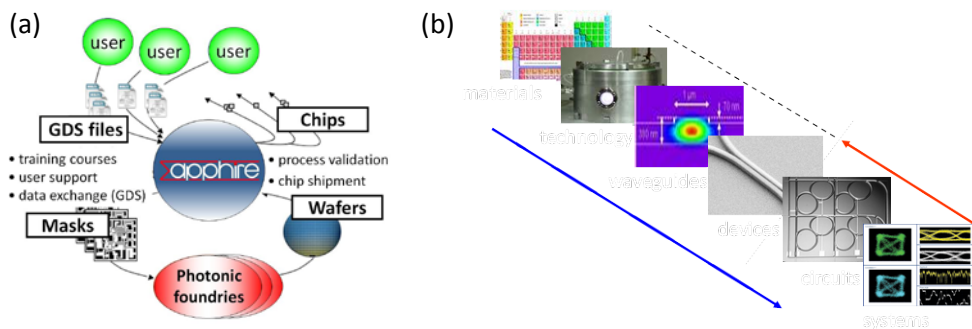


FIG. 1 – Schematics of (a) the generic photonic platform and (b) the high level circuit design concept for PICs.

THE SAPPHIRE PLATFORM

The SAPPHIRE platform is an infrastructure that is being created to facilitate the access of different kind of users (universities, small-medium enterprises, research centers) to the technology services of silicon photonic foundries. A first partnership has been set with the James Watt Nanofabrication Center (JWNC) at the University of Glasgow, but the platform architecture can be extended to include other foundries in the future. As shown in Fig. 1(a), the photonic foundry can serve many users, whose projects are collected and processed simultaneously in multi-project wafers runs, with a wafer- and cost-sharing scheme. The interaction between users and the foundry is eased by the SAPPHIRE platform interface, which offers a variety of services, such as: development of dedicated Design Kits (DKs) for the foundry technology; support for the design of PICs and for the generation of mask layouts compliant with foundry standards; assembly of the users' mask layouts; chip delivery to users; qualifications of the fabrication runs.

In the shared-access platform scheme, even users with no expertise in optical technologies can access foundry services, because PICs design is based on a new concept of “high-level” circuit design. Figure 1(b) shows that, compared to the classic “low level” design approach (blue arrow), where a deep knowledge at physical and EM level is required, in the circuit design approach complex PICs can be designed by operating at the circuit level only (red arrow), that is by acting over a selected set of elementary functional elements, namely building blocks (BBs), according to well defined rules contained in the foundry DKs.

II. BUILDING BLOCKS AND CIRCUIT SIMULATION

PICs design in a generic integration technology is based on the concept of BBs. A BB is a functional entity representing the model of a physical device. It describes its behavior through a mathematical representation, e.g. a scattering matrix. Figure 2(a) shows a few examples of silicon photonic BBs that are being developed within the SAPPHIRE platform and their representation in the circuit simulator Aspic™ [3]. The BB model is the result of extensive analytical studies, EM simulations and experimental characterization, and guarantees the behaviour of the BB

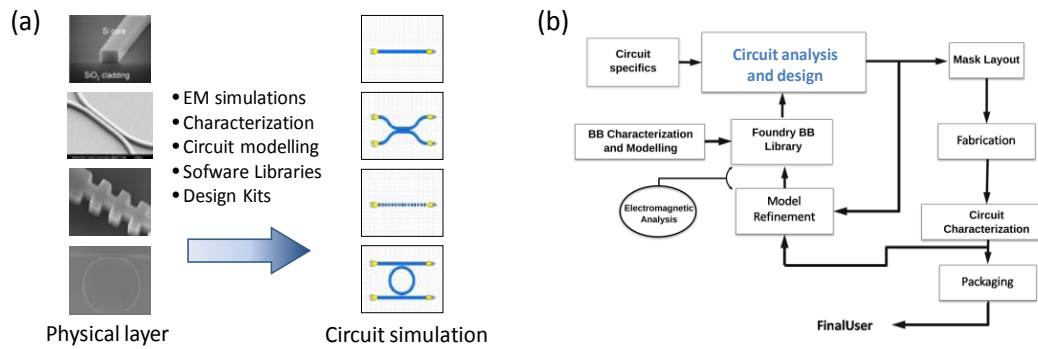


FIG. 2 - (a) Photographs of some silicon photonic BBs and their representation in the circuit simulator Aspici™. (b) Block diagram of the design and fabrication process in a generic foundry approach.

within well-defined ranges of validity [4]. The model accuracy can be tailored according to the specific phase of the design process: for proof-of-concept evaluations, a simple model with only basic optical properties permits higher simulation speed, whereas design optimization requires advanced parameters and parasitic effects (such as polarization sensitivity, spurious backreflections, non-linear effects), as well as information on tolerance sensitivity and statistical distribution of the parameters.

As shown in Fig. 2(b), the core of the “high level” PICs design is a circuit simulator. In a circuit simulator complex PICs can be designed by assembling an arbitrary number of basic BBs, whose models are encoded into software “Foundry BB Libraries”, containing also the design rules to properly connect different BBs. EM analysis is a fundamental support for the BB model definition and calibration, but is not required as a PIC design tool as far as the BBs are used within their limits of validity and assembled according to the design rules fixed by the foundry. As a main advantage, circuit simulators are usually much faster and less memory consuming than any EM approach, enabling more sophisticated investigations, such as optimizations, sensitivity studies, design on tolerance, yield optimization, and so on [5].

III. A PROOF OF CONCEPT DEVICE

The validity of the circuit design approach was demonstrated by realizing a proof-of-concept silicon photonic device. The realized PIC, shown in Fig. 3(a), is a variable bandwidth filter (VBF) consisting of an unbalanced Mach Zehnder interferometer (MZI), with 3dB input/output directional couplers, loaded with two ring resonators (RRs) on the shorter arm. The power coupling ratio between the bus waveguide and the RRs is 70% and the MZI unbalance ΔL is equal to the ring circumference L_r . Bandwidth tunability is achieved controlling the mutual phase shift of the two RRs by using thermo-optic phase shifters. The design of the VBF was entirely carried out by assembling the constitutive BBs of the circuit, namely straight and bent waveguides, directional couplers and RRs, with the circuit simulator [see Fig. 3(b)],

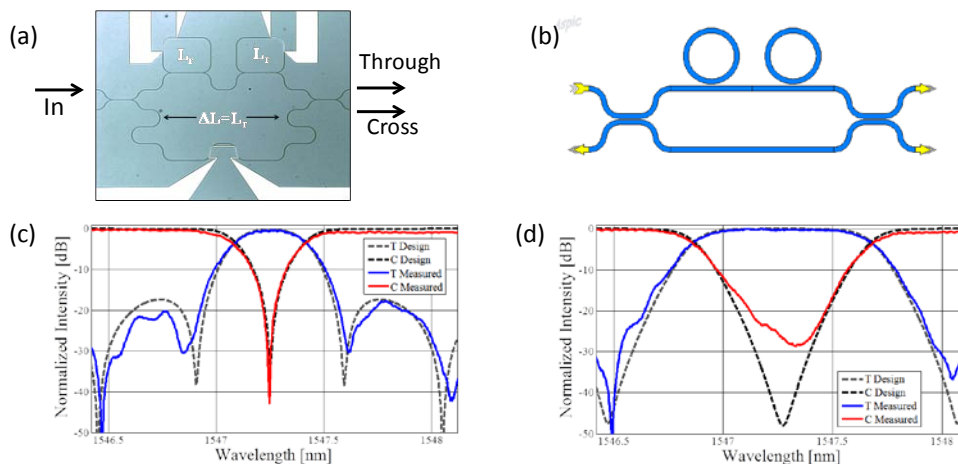


FIG. 3 – (a) Optical microscope photograph with design parameters and (b) Aspici™ layout of the silicon VBF. Simulated (dashed) and measured (solid) response of the filter at the trough (T) and cross (C) port: (c) 40 GHz and (d) 100 GHz bandwidth configuration.

containing the BB libraries of the foundry. The agreement between circuit simulations and experiment is shown in Figs. 3(c) and 3(d), where two configurations of the filter, with a bandwidth of 40 GHz and 100 GHz, respectively, are shown at the trough (T) and cross (C) port.

IV. CONCLUSIONS

We have presented our recent progress in the development of a shared access platform to silicon photonic technology. A number of silicon photonic BBs have been created and software libraries have been embedded in a photonic circuit simulator (Aspici™), enabling a high-level design of photonic circuits. The reliability of the BB models and the validity of the circuit simulation approach have been demonstrated by realizing a proof-of-concept device. Our results prove that the design tools developed in the SAPPHERE platform are ready to be used by external users as a valid interface to the silicon photonic foundry.

ACKNOWLEDGEMENT

The Authors thank the Italian PRIN 2009 project SAPPHERE (<http://sapphire.dei.polimi.it/>) for funding this research activity.

REFERENCES

- [1] Photonic Advanced Research and Development for Integrated Generic Manufacturing (PARADIGM), EU - 7th FP; <http://paradigm.jeppix.eu>.
- [2] ePIXfab, web site: : <http://www.epixfab.eu>.
- [3] Web sites: Filarete srl, Italy, <http://www.aspicdesign.com>; Phoenix BV, The Netherlands, <http://www.phoenixbv.com>.
- [4] A. Melloni et al. "Design kits and circuit simulation in integrated optics", Proc. Integrated Photonic Research, 2010 .
- [5] A. Melloni, et al. "Statistical design in integrated optics," Proc. European Conference on Lasers and Electro-Optics 2009, 14-19 June 2009.

PHOTONIC INTERCONNECT TECHNOLOGY FOR CHIP MULTIPROCESSING ARCHITECTURES: THE PHOTONICA PROJECT

A. Parini⁽¹⁾, G. Calò⁽²⁾, S. Malaguti⁽³⁾,
G. Bellanca⁽³⁾, V. Petruzzelli⁽²⁾, S. Trillo⁽³⁾

⁽¹⁾Laboratorio di Micro e Submicro Tecnologie abilitanti
dell'Emilia-Romagna (MIST E-R) c/o Dipartimento di Ingegneria,
Università degli Studi di Ferrara, Via Saragat 1, 44122 Ferrara, Italy,
alberto.parini@unife.it

⁽²⁾Dipartimento di Elettrotecnica ed Elettronica, Politecnico di Bari,
Via Re David 200, 70125 Bari, Italy

⁽³⁾Dipartimento di Ingegneria, Università degli Studi di Ferrara,
Via Saragat 1, 44122 Ferrara, Italy

Abstract

A Network-on-Chip (NoC) is an architectural paradigm where several independent computational cores, physically located on the same chip, can execute multiple concurrent processes, thus exploiting the potentialities of shared computing inside a single VLSI processor. As the number of interconnected cores increases, the needs in terms of communication bandwidth and power consumption grow exponentially, imposing unrealistic constraints for a practical realization. To overcome these limitations, Optical Networks-On-Chip (ONoCs) seem to be a promising solution. The aim of PHOTONICA is to develop a design platform for photonic on-chip interconnections. In this paper some of the main results obtained during the first year of activity are presented.

Index Terms – Photonic Integrated Circuits, Optical Networks-on-Chip, Micro-Ring Resonators, Mach-Zehnder Interferometers, CMOS Photonics,

I. INTRODUCTION

Chip multiprocessors (CMPs) architectures are currently the state-of-the-art in the design of high performance embedded systems. Following this architectural paradigm, multiple computational cores are manufactured on the same circuit die, hence reaching a high grade of parallelism and scalability. Due to the large number of interconnected modules, a data exchange system realized by using a traditional bus configuration is not applicable. From a system design point of view, a natural alternative is to implement, at the chip level, a network of links (Network-on-Chip) to route the traffic between the cores. Unfortunately, as the number of interconnected units located on the same physical substrate increases, the issues of bandwidth availability and dynamic power scavenging become crucial. The NoC paradigm can take advantage of the fully compatible CMOS silicon photonic integration; in fact, optical (instead of electrical) interconnections between cores can provide a huge communication bandwidth, with a power dissipation

that depends only on the circuitry topology [1]. This contribution presents the recent advances of the PHOTONICA FIRB 2008 project in the development of a unified design platform for multi-chip architectures with optical link interconnections.

II. THE PHOTONICA PROJECT

To perform an effective design of an Optical Network-on-Chip (ONoC), a wide set of expertise are needed. For this reason, different research units are cooperating in PHOTONICA: one team of the University of Siena, with skills on computer architecture and software optimization, one team of the Politecnico di Bari, for the design and the optimization of photonic devices, and two teams of the University of Ferrara, with expertise on both network architecture and photonics. Some test devices will be realized at the James Watt Nanofabrication Center of the University of Glasgow, and to access the facilities of this foundry the approach proposed in the SAPPHIRE PRIN 2009 Project (<http://sapphire.dei.polimi.it/>) will be pursued.

An efficient analysis and design of an ONoC at topological and architectural levels requires specific tools that are not directly compatible with the ones commonly used in electromagnetics (FDTD, FEM, BPM). The idea of PHOTONICA is to exploit an analytical intermediate model as an interface between the physical and the architectural layers [2]. An arbitrary complex ONoC is decomposed into elementary blocks, the Photonic Switching Elements (PSEs). Each PSE can be considered as a black box, whose input-output relations are described by means of a scattering matrix whose elements, described in an analytic form, depend on some parameters of the optical circuit (optical lengths, coupling coefficients, propagation losses) which are properly tuned through a numerical fitting procedure, in order to fully mimic the behavior obtained with the electromagnetic simulation. The next step in the bottom-up abstraction process is to export the analytical model of each PSE into the architectural modeling tool (SystemC); this is achieved by implementing in the software the routines able to manage complex algebra and matrix manipulation. With these extensions, SystemC becomes an hybrid electronic-optical architecture-level simulation framework capable of assembling complex optical switching fabrics while, at the same time, assessing the practical feasibility and effectiveness of these fabrics on the specific technology platform.

III. THE SWITCHING FABRICS

The routing functionality inside an ONoC can be implemented by means of resonance-based effects (wavelength-selective routing). In this case, the PSEs are realized with microring resonators cascaded with waveguide intersections. The most simple ring-based PSE (one input two outputs - 1×2 PSE) is sketched in the two insets of Fig. 1(a). If the wavelength of the carrier signal is resonant with the ring, the input is

routed in the perpendicular waveguide; on the contrary, if the signal is not in resonance, the propagation continues along the straight waveguide. These basic elements can be combined to form 2×2 PSE and more complex networks as, for example, the one illustrated in Fig. 1(a), which represents a switch with 4 possible input and 4 possible output ports [3]. To verify the design approach proposed by PHOTONICA, the transmission between the different ports have been calculated via FDTD, by simulating the whole original network topology. Then, these results have been compared with the ones obtained by the cascading of the analytical models of the individual PSEs. As one can observe (Fig.1(b) and Fig.1 (c)), the agreement is very good.

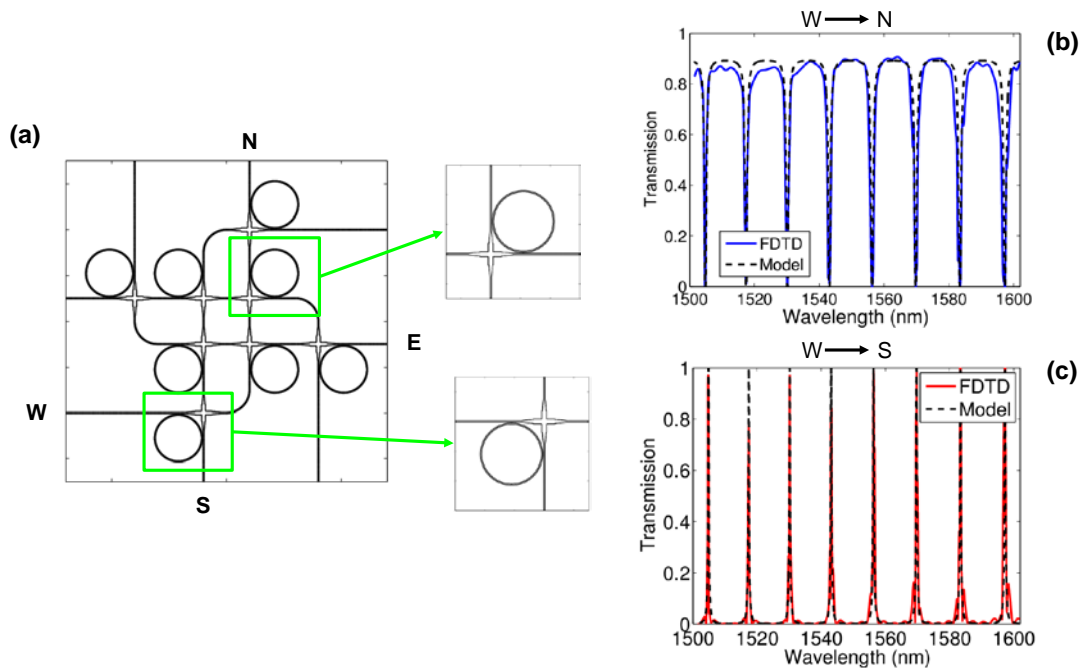


FIG. 1–Scheme of an optical router with 4 input and 4 output ports (a); the insets show two of the 1×2 PSE composing the network. Simulated (dashed line) and modeled (solid line) transmission curves for the path linking the W port with the N port (b), and for the path linking the W port with the S port (c).

The routing functionality can be also implemented by means of interference-based devices (non wavelength-selective routing). In this case the basic building blocks are broadband Mach-Zehnder Switches (MZSs) [4]. The MZS, whose scheme is illustrated in Fig. 2(a), is made of two coupled waveguide sections with an interposed phase-shifting region. The chosen waveguides, the cross section of which is sketched in Fig. 2(b), are silicon ribs embedded in SiO₂. The switching behavior can be simply described as it follows. In the OFF-state, being no phase shift applied, the input optical signal at port 1 is collected at port 4. Conversely, in the ON-state, a phase shift equal to π (at $\lambda=1.55 \mu\text{m}$) is induced in the phase shifter by plasma dispersion, causing the input optical signal to switch to port 3. Fig. 2(c) shows the crosstalk (CT) of the MZS in the OFF (solid curve) and ON (dashed curve) states

respectively. The bandwidth of the MZS, defined as the wavelength range in which the CT is lower than -15 dB and the insertion loss is lower than 1.1 dB, is equal to 115 nm, which allows the contemporary switching of 57 WDM channels with a required energy of 4.6 fJ/bit.

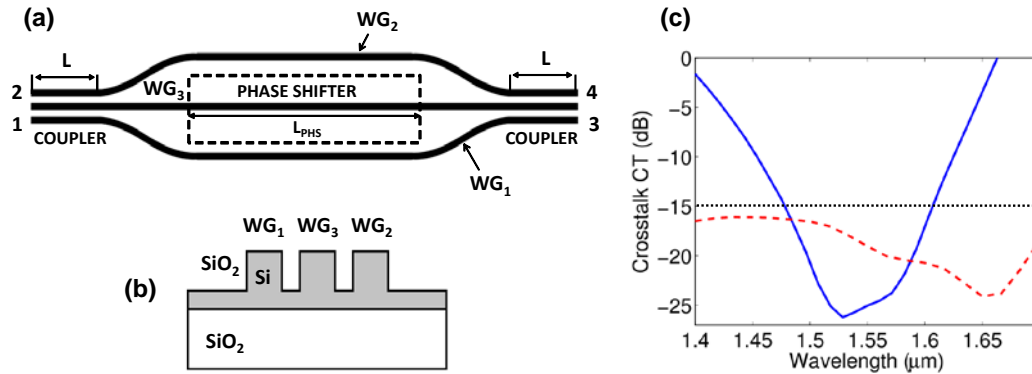


FIG. 2—Scheme of the MZ (a) and cross section of the coupler (b). Crosstalk in the OFF (solid curve) and ON (dashed curve) states.

IV. CONCLUSIONS

In this contribution, the recent achievements of the PHOTONICA FIRB 2008 project in the development of a unified framework for the design of Optical Network on Chip architectures have been presented. The research activity has dealt with ONoCs based on ring resonators and on Mach Zehnder type interferometers. The analytical models describing the fundamental building blocks have been derived and successfully exported to an architectural modeling software (SystemC).

ACKNOWLEDGEMENT

The authors thank all the members of the PHOTONICA consortium. This work is supported by the Italian Ministry of the University and Research (MIUR) through PHOTONICA FIRB 2008 and SAPPHIRE PRIN 2009 Projects. Alberto Parini thanks the Programma Operativo FESR 2007-2013 of the Emilia-Romagna Region – Attività I.1.1. for the financial support to his research activity.

REFERENCES

- [1] A. Shacham et al., “On the Design of a Photonic Network-on-Chip”, Proceedings of the First International Symposium on Networks-on-Chip (NOCS'07).
- [2] A. Parini et al., “Abstract modelling of switching elements for optical networks-on-chip with technology platform awareness”, 5th Interconnection Network Architecture: On-Chip, Multi-Chip, INA-OCMC 2011 Workshop.
- [3] J. Chan et al., “Insertion Loss Analysis in a Photonic Interconnection Network for On-Chip and Off-Chip Communications”, IEEE Lasers and Electro-Optics Society, 2008, LEOS 2008.
- [4] G. Calò et al., “Broadband Mach-Zehnder Switch for Photonic Networks on Chip”, IEEE J. Lightwave Technology, 2012.

GRATING-ASSISTED COUPLING TO STRIP PLASMONIC MODES: 3D NUMERICAL ANALYSIS

M.P. Bolzoni⁽¹⁾, G.G. Gentili⁽¹⁾, S.M. Pietralunga⁽²⁾

⁽¹⁾ Politecnico di Milano, Dip. Elettronica e Informazione
P.za L. da Vinci 32, 20133 Milano
gentili@elet.polimi.it

⁽²⁾ CNR-IFN, c/o Politecnico di Milano
P.za L. da Vinci 32, 20133 Milano

Abstract

Grating-assisted optical coupling into long-range modes of strip plasmonic waveguides is analyzed by a 3D numerical simulation with a full wave FEM software. A comparison with results obtained using the common 2D approximated analysis is shown, in case of 1D grating coupler and input Gaussian beam. Excited diffracted modal field distribution is calculated, as it evolves in propagation.

Index Terms – plasmonics, grating-assisted coupler, 3D numerical simulation.

I. INTRODUCTION

In recent years a considerable amount of literature has been published dealing with long-range propagation of surface plasmon polariton modes in strip waveguides (LRSPP) [1, 2]. Actually, plasmonics is a rather hot topic in advanced electro-magnetism, also because it appeals to various application fields, such as sensors, nanoantennas, photovoltaics and optical signal processing [1-6]. Even if aspects like LRSPP modal propagation properties [1], modal spectrum [7] and mode coupling [8-10] have been widely investigated in late years, the subject is far from being exhaustively analyzed. One major issue, in view of the design and fabrication of plasmonic lightwave circuits, is input and output light coupling to LRSPP modes. The most simple way to couple SPP modes either to free-space propagating optical beams or to modes of dielectric waveguides, is end-fire coupling [2], and actually efficient end-fire couplers have been designed and experimentally characterized [3, 8]. A 2D numerical approach, typically based on Finite Element Method or Finite-Difference-Time-Domain simulations is usually exploited in the search for best coupling conditions.

However, lateral optical coupling into plasmonic waveguides is also of paramount appeal, particularly for the field of 2D and 3D optical interconnects in planar lightwave circuits and whenever a strong redirection of light wavevector is addressed. Besides evanescent field coupling, efficient lateral couplers can be based on diffractive gratings.

Up to now however, the design of optimized grating has been performed in 2D , therefore relating optimization to coupling either with metallic layers or to slabs. The plasmonic propagation is then treated either by FDTD simulation [8-10, 11] or modeled by FEM [12]. In all cases, a 3D simulation, which is necessary to properly estimate the coupling efficiency in case of SPP modes of strip geometry, is still lacking.

In this work we introduce a 3D FEM analysis of LRSPP excitation in strip-like structures by means of binary grating couplers.

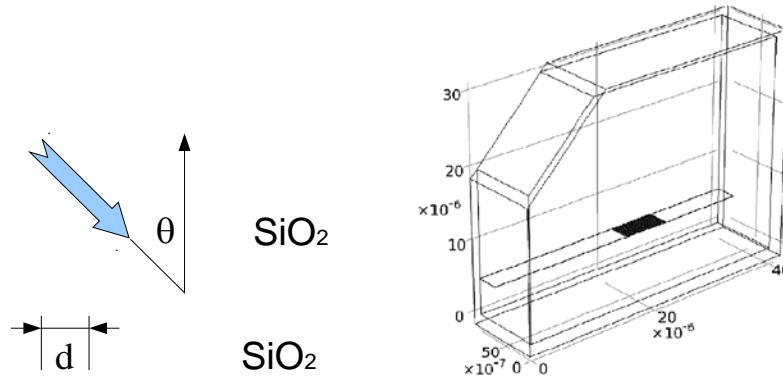


Fig. 1. Grating launcher and geometrical parameters. The full 3D structure is shown on the right.

II. DISCUSSION

Grating launchers are an interesting solution to the problem of LRSPP excitation, because of the simple structure, the availability of simple design formulas and the rather good simulated performances. As hinted in the Introduction, all the results available in the literature use a full-wave 2D analysis. This is commonly considered a good approximation to the “true” 3D problem, because the main aspects of light coupling to the grating are correctly represented. The design is in fact based on the following simple formula (see Fig. 1):

$$\beta_{\text{eff}} = k \sin \theta + m \frac{2\pi}{d}$$

where β_{eff} is the LRSPP propagation constant, k is the wavenumber, m is an arbitrary integer index (usually $m=\pm 1$) and d is the grating period. The main reason to use a 2D analysis is the large computer memory requested by a 3D analysis. On the other hand there are several aspects of LRSPP excitation by grating that necessarily require a 3D analysis, such as finite grating and beam size in the transverse direction, cutoff conditions for LRSPP mode and excitation of higher order modes. The LRSPP mode can be cutoff under specific combinations of physical parameters such as metal thickness, strip width and upper and lower cladding refractive index mismatch [13]. Since none of these phenomena are described by a 2D analysis a full 3D modeling has been carried out.

III. Results

The 3D modeling of a grating Plasmon coupler is very demanding in terms of simulation time and storage. The 3D FEM model required a box of large size as shown in Fig. 1. The analysis presented in this paper refers to a coupler designed at $\lambda=1.55 \mu\text{m}$ and this corresponds to a box size of about 40λ along the propagation direction, 30λ along the height and only 4λ along the transverse direction (by using the symmetry condition). The domain is finally bound by PML as an adsorbing boundary condition. The half-strip in fig. 1 is $3 \mu\text{m}$ wide and the metal thickness is 20 nm . Finally, after trying several configurations, the scattered field formulation was used [14]. In Fig. 2 we show a plot of the LRSPP field being excited by the grating. In Fig. 3 we show a set of mode plots obtained after the excitation of the Plasmon. The plots represent a LRSPP field excited by the Gaussian beam as it propagates along the strip and away from the grating. There is trace of higher order modes being excited, since the field pattern changes as it propagates. Avoiding the excitation of these higher order modes is a very difficult task, since they have a propagation constant similar to that of the LRSPP mode.

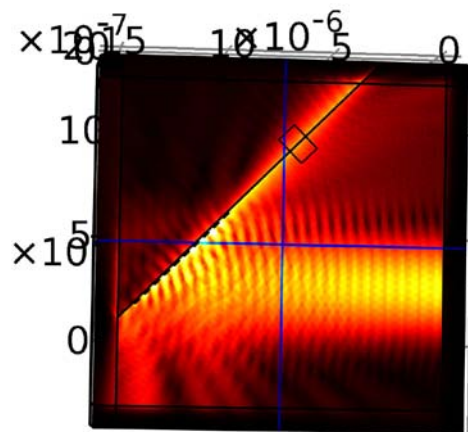


Fig. 2. 3D plot of Plasmon excitation.

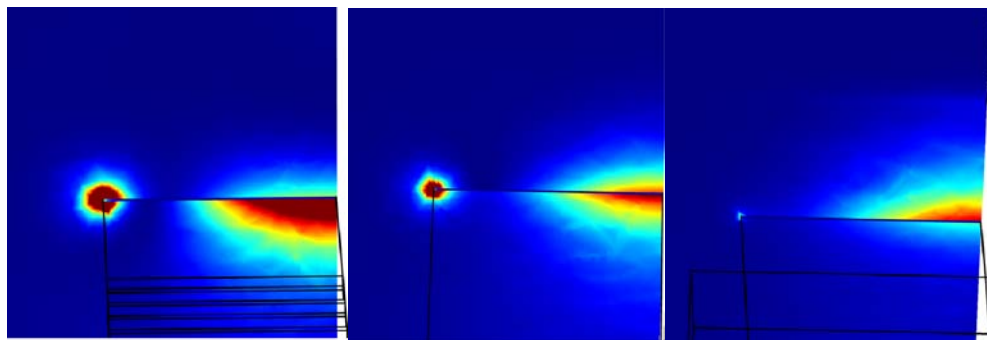


Fig. 3. In-coupled LRSPP field as it propagates away from the grating. Left: $1 \mu\text{m}$ from the grating. Center: $3 \mu\text{m}$. Right: $7 \mu\text{m}$.

REFERENCES

- [1] P. Berini “Plasmon-polariton waves guided by thin lossy metal films of finite width: bound modes of symmetric structures”, *Physical Review B*, 61, 2000, pp. 10484-10503.
- [2] R. Charbonneau, N. Lahoud, G. Mattiussi and P. Berini, “Demonstration of integrated optics elements based on long-ranging surface plasmon polaritons”, *Opt. Express*, Vol. 13, No. 3, (2005) pp.977-984
- [3] J. Jin Ju, S. Park, Min-su Kim, J. Tae Kim, S. K. Park Y. J. Park and Myung-Hyun Lee, “Polymer-Based Long-Range Surface Plasmon Polariton Waveguides for 10-Gbps Optical Signal Transmission Applications”, *J. Lightw. Technol.*, vol. 26, No. 11, (2008), pp. 1510-1518
- [4] H. A. Atwater, and A. Polman, “Plasmonics for improved photovoltaic devices”, *Nature Mat.*, 9, 205 (2010).
- [5] M. E. Stewart et al., “Nanostructured plasmonic sensors”, *Chem. Rev.*, Vol.108, 494 (2008).
- [6] S. Kawata, et al., *Nat. Phot.*, “Plasmonics for near-field nano-imaging and superlensing”, Vol. 3, 388, (2009).
- [7] I. Breukelaar, R. Charbonneau, P. Berini “Long-range surface plasmon-polariton mode cutoff and radiation”, *Appl. Phys. Lett.* 88, 051119 (2006).
- [8] P. Berini, C. Chen, “Broadside excitation of long range surface plasmons via grating coupling” *IEEE Photonics Technology Letters*, Vol. 21, no. 24, Dec. 2009, pp. 1831-1833.
- [9] P. Berini, C. Chen. “Grating couplers for broadside input and output coupling of long-range surface plasmons”, *Opt. Express*, Vol. 18, No 8, (2010) pp. 8006-8018.
- [10] Z. Fu, et al. “Numerical Investigation of a Bidirectional Wave Coupler Based on Plasmonic Bragg Gratings in the Near Infrared Domain” *J. Lightw. Technol.* Vol. 26, No. 22 (2008) pp. 3699- 3703.
- [11] M.J. Preiner, et al., “Efficient optical coupling into metal-insulator-metal plasmon modes with subwavelength diffraction gratings”, *Appl. Phys. Lett.*, Vol. 92 (2008), pp. 113109.
- [12] J.Lu, C. Petre and E. Yablonovitch, “Numerical optimization of a grating coupler for the efficient excitation of surface plasmons at an Ag–SiO₂ interface”, *J. Opt. Soc. Am. B*, Vol. 24, No. 9 (2007), pp. 2268-2272.
- [13] M. P. Bolzoni, G. G. Gentili, S.M. Pietralunga, “LR-SPP Mode Cutoff in Strip Waveguides as Affected by Technologically Induced Asymmetries: a Numerical Study”, *IEEE Photnocs. Tech. Lett.*, Vol. 23, No. 15, Aug. 2011, pp. 1082-1084.
- [14] COMSOL Multiphysics, ver. 4.2a, <http://www.comsol.com>.

DESIGN OF PLASMONIC DIRECTIONAL COUPLERS

M.Grande, G.Magno, R.Marani, G.Calò, V.Petruzzelli, A.D’Orazio

Dipartimento di Elettrotecnica ed Elettronica, Politecnico di Bari
Via Re David, 200, 70125 Bari
grande@deemail.poliba.it

Abstract

We propose and numerically investigate a novel kind of nanoscale plasmonic vertical directional couplers constituted by a polymeric waveguide and a surface plasmon polariton waveguide coupled through a metallic strip grating. By using finite-difference-time-domain simulations it is found that it is possible to design plasmonic couplers with high efficiency and very short coupling length in both visible and NIR range.

Index Terms – Plasmonic circuitry, directional coupler.

I. INTRODUCTION

Plasmonics is an exciting field of nanophotonics that explores the excitation of collective oscillations of conduction electrons – called surface plasmons - confined near noble metal/dielectric interfaces and their interactions with photons. When such metal dielectric nanostructures are illuminated with visible to near-infrared light, it is possible to generate strongly enhanced local electromagnetic fields which can be exploited for a large number of applications including near-field scanning optical microscopy, high-efficiency light emitting diodes and lasers, high-resolution imaging, extremely sensitive bio- and chemical sensors and photovoltaics [1-7].

Unlike conventional dielectric optical waveguides, surface plasmons are also capable of capturing, guiding, splitting with right angle, bend and focusing electromagnetic energy in deep-subwavelength length-scales, i.e. smaller than the diffraction limit of the light, making a technological reality the idea of a very compact and intrinsically large bandwidth plasmonic circuitry suitable for communication systems.

During the last years, active and passive plasmonic components, such as modulators, beam splitters, couplers, switches, demultiplexers, nanoantennas, based on different technologies such as metal-insulator-metal (MIM) and insulator-metal-insulator (IMI) structures, metallic nanohole arrays, hybrid plasmonic and integrated optical waveguides, channel plasmon polaritons, metallic nanowires, dielectric-loaded surface plasmon polariton (SPP) and long-range SPP waveguides, have been demonstrated [8-15].

In this paper a new kind of high performance nanoplasmonic vertical coupler is proposed and numerically investigated. The structure is constituted by a polymeric waveguide coupled through a metallic strip grating to a long-range and short-range surface plasmon polariton waveguide.

II. DESIGN OF PLASMONIC COUPLERS

The structure under examination, illustrated in Fig.1, can be considered as a cascade of two different building block: the input block A is a traditional polymeric waveguide constituted by a core region in SU8 (n=1.57) having thickness $W_{\text{SU8}} = 500 \text{ nm}$, deposited over a SiO_2 layer (n=1.44) while the coupling region B is constituted by the SPP waveguide realized by means of gold strips, immersed in SiO_2 , having width equal to 540 nm, inter-strip slit distance equal to 60 nm and a thickness of 30 nm.

The numerical simulations have been performed by means of a freely available software package based on the FDTD method [16] by considering a Gaussian source which excites a TM mode in the polymeric waveguide in the wavelength range 450 – 1100 nm. Gold regions are represented through a Drude model assisted by two Lorentz oscillators to fit the experimental data [17]:

$$\varepsilon_m(\omega) = \varepsilon_\infty - \frac{\omega_D^2}{\omega^2 + j\omega\gamma_D} - \sum_{k=1}^2 \frac{\delta_k \omega_k^2}{\omega^2 - \omega_k^2 + 2j\omega\gamma_k} \quad (1)$$

where the high-frequency complex dielectric constant of the metal ε_∞ is 5.398, the plasma frequency ω_D and the collision frequency γ_D of the Drude model are $1.398 \cdot 10^{16}$ and $1.033 \cdot 10^{14} \text{ rad/s}$, respectively. The parameters describing the contribution of each Lorentz oscillator are the amplitude δ_k , the resonant angular frequency ω_i and the damping constant γ_k , $k = 1, 2$, which are set accordingly to 17: $\delta_1 = 0.681$, $\omega_1 = 4.274 \cdot 10^{16} \text{ rad/s}$, $\gamma_1 = 4.353 \cdot 10^{14} \text{ rad/s}$, $\delta_2 = 1.861$, $\omega_2 = 5.225 \cdot 10^{16} \text{ rad/s}$ and $\gamma_2 = 6.608 \cdot 10^{14} \text{ rad/s}$.

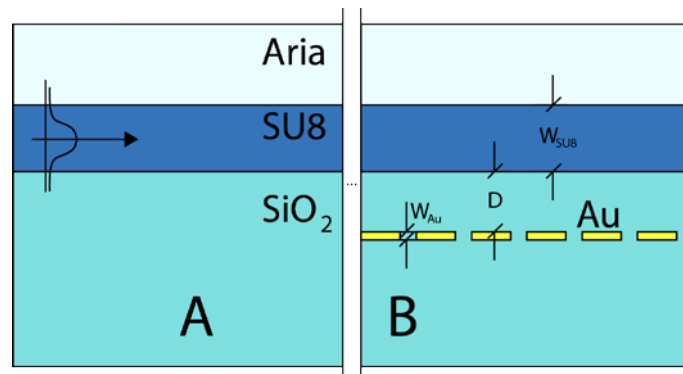


FIG. 1 – Scheme of the vertical plasmonic coupler.

The wavelengths, at which the maximum coupling occurs, have been identified through a spectral analysis by means of several power monitors centred at the gold strips showing a width equal to 200 nm. Tab.I resumes the results in terms of coupling efficiency η and coupling length L_C as a function of maximum coupling wavelength λ_c .

TABLE I –COUPLING EFFICIENCY AND COUPLING LENGTH AS A FUCNTION OF SOURCE WAVELENGTH

λ_c [nm]	η [%]	L_c [μm]
936.4	91	7.5
883.7	53.4	7.5
784	40	9.5
655	16.5	9.5

The short-range and long-range nature of the SPP mode has been determined by analyzing the symmetry of the mode excited on the grating. Fig.2 shows the longitudinal component of the Poynting vector evaluated for the wavelength λ_c equal to 936.4 nm and 883.7 nm that correspond to the short-range and long-range SPP mode, respectively.

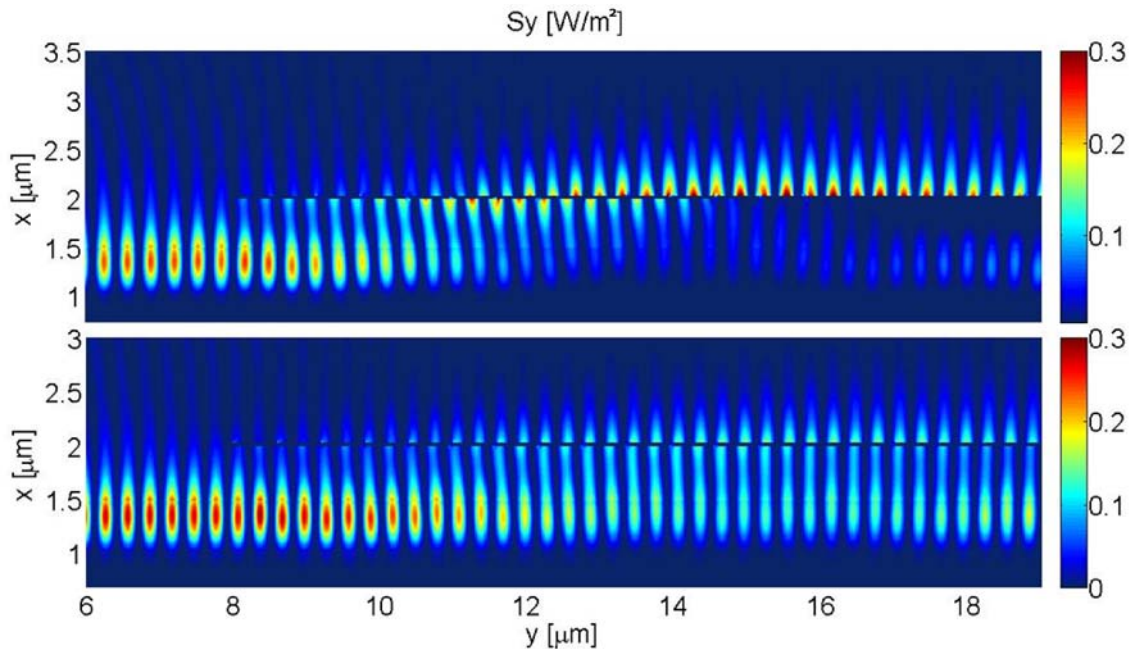


FIG. 2 – Longitudinal component of Poynting vector for (top) $\lambda_c= 936.4$ nm and (bottom) $\lambda_c= 883.7$ nm.

III. CONCLUSION

The coupling characteristics between a long-range and short-range SPP waveguides and a dielectric waveguide coupled through a metallic grating have been analyzed. We demonstrate that the coupling efficiency (coupling length) can reach 91% (7.5 μm) and 53.4% (7.5 μm) for the short-range and long-range, respectively. These results pave the way for the design and the optimization of a new class of plasmonic circuitry that could be integrated with passive and active devices in both visible and NIR range.

ACKNOWLEDGEMENT

The authors acknowledge the CINECA Award for the project *SPMAPS - Surface Plasmon Management in Active and Passive Systems 2011*.

IV. REFERENCES

1. Y.Wang, W.Srituravanich, C.Sun, X. Zhang: "Plasmonic Nearfield Scanning Probe with High Transmission", *Nanoletters*, vol.8, n.9, 2008, pp.3041-3045.
2. K.Quang Le, P.Bienstman: "Optical Modeling of Plasmonic Nanoparticles Enhanced Light Emission of Silicon Light-Emitting Diodes", *Plasmonics*, Vol.6, n. 1, 2010, pp. 53-57.
3. A.M.Lakhani, M.Kim, E.K.Lau, M.C.Wu: "Plasmonic crystal defect nanolaser", *Optics Express*, vol.19, n.19, 2011, pp.18237-18245.
4. R.Kotynski, T.Stefaniuk, A.Pastuszczak: "Sub-wavelength diffraction-free imaging with low-loss metal-dielectric multilayers", *Applied Physics A: Materials Science and Processing*, vol.103, n.3, 2011, pp. 905-909.
5. M.Grande, M. A.Vincenti, T.Stomeo, G.Morea, R.Marani, V. Marrocco, V.Petruzzelli, A.D'Orazio, R.Cingolani, M. De Vittorio, D. de Ceglia, M. Scalora: "Experimental demonstration of a novel bio-sensing platform via plasmonic band gap formation in gold nano-patch arrays", *Optics Express*, vol.19, n.22, 2011, pp. 21385-21395.
6. M. Grande, R. Marani, F. Portincasa, G. Morea, V. Petruzzelli, A. D'Orazio, V. Marrocco, D. de Ceglia, M.A. Vincenti: "Asymmetric plasmonic grating for optical sensing of thin layers of organic materials", *Sensors and Actuators B*, vol.160, n.1, 2011, pp.1056-1062.
7. V Marrocco, R Marani, M Grande, G Morea, G Calò, V Petruzzelli, A D'Orazio: "Modification of the scattering of silver nanoparticles induced by Fabry-Pérot resonances rising from a finite Si layer", *Journal of Optics*, 13, 2011, doi:10.1088/2040-8978/13/1/015004.
8. Y.Liu, J.Kim: "Plasmonic modulation and switching via combined utilization of Young interference and metal-insulator-metal waveguide coupling", *J.of Optical Society of America B*, vol.28, n.11, 2011, pp.2712-2716.
9. R. Marani, A.D'Orazio, V.Petruzzelli, S.G.Rodrigo, L. Martin-Moreno, F.J. Garcia-Vidal, J. Bravo-Abad: "Gain-assisted extraordinary optical transmission through periodic arrays of subwavelength apertures", *New Journal of Physics*, 2012, doi:10.1088/1367-2630/14/1/01302.
10. Q.Li, S.Wang, Y.Chen, M.yan, l.Tong, M.Qiu: "Experimental demonstration of plasmon propagation, coupling and splitting in silver nanowires at 1550-nm wavelength", *IEEE J. of Selected Topics in Quantum Electronics*, vol.17, no.4, 2011, pp.1107-1111.
11. A.V.Krasavin, A.V.Zayats: "Silicon-based plasmonic waveguides", *Optics Express*, vol.18, no.11, 2010, pp.11791-11799.
12. H.Lu, X.Liu, Y.Gong, D.Mao, L.Wang: "Enhancement of transmission efficiency of nanoplasmonic wavelength demultiplexer based on channel drop filters and reflection nanocavities: *Optics Express*, vol.19, no.14, 2011, pp.12885-12890.
13. T.Dattoma, M.Grande, R.Marani, V.Marrocco, G.Morea, A.D'Orazio: "Resonance wavelength dependence and mode formation in gold nanorod optical antennas with finite thickness", *PIER B*, vol.30, 337-353, 2011.
14. R. Marani, M. Grande, V.Marrocco, A. D'Orazio, V. Petruzzelli, M.A.Vincenti, D.de Ceglia: "Plasmonic Band Gap formation in two-dimensional periodic arrangements of gold patches with sub-wavelength gaps", *Optics Letters*, vol.36, no.6, March 15, 2011, pp.903-905.
15. R. Marani, V. Marrocco, M. Grande, G. Morea, A. D'Orazio, V. Petruzzelli: "Enhancement of extraordinary optical transmission in a double heterostructure plasmonic bandgap cavity", *Plasmonics*, 12 March 2011, DOI 10.1007/s11468-011-9225-4.
16. A. F. Oskooi, D. Roundy, M. Ibanescu, P. Bermel, J. D. Joannopoulos, and S. G. Johnson, "MEEP: A flexible free-software package for electromagnetic simulations by the FDTD method," *Computer Physics Communications* 181, 687-702 (2010).
17. E.D.Palik, Handbook of Optical Constants of Solids, Acad. Press, San Diego, CA., 1998.
18. J. M. McMahan, J. Henzie, T. W. Odom, G. C. Schatz and S. K. Gray, "Tailoring the sensing capabilities of nanohole arrays in gold films with Rayleigh anomaly-surface plasmon polaritons", *Optics Express*, Vol. 15, 18119, 2007.

SECOND HARMONIC GENERATION IN PLASMONIC WAVEGUIDES

F.M. Pigozzo⁽¹⁾, D. Modotto⁽¹⁾, S. Wabnitz⁽¹⁾

⁽¹⁾ Dipartimento di Ingegneria dell'Informazione,
 Università di Brescia, via Branze 38, 25123 Brescia, Italy
daniele.modotto@ing.unibs.it

Abstract

In this work we demonstrate theoretically that modal phase matching for second harmonic generation can be obtained in AlGaAs plasmonic waveguides by means of the Type II interaction: one pump is carried by a plasmonic mode, whereas the other pump and the second harmonic signals are carried by optical modes confined inside AlGaAs layers. The phase matched wavelength can be tuned in the near infrared by changing the physical dimensions of the waveguides.

Index Terms – Second harmonic generation, plasmonics, integrated optics.

I. INTRODUCTION

Quadratic nonlinear interactions involving plasmonic modes localized at the interface between a nonlinear material and a metal have recently been studied: the possibility of achieving modal phase matching (PM) among plasmonic modes has been demonstrated [1,2]. Nevertheless, the reported conversion efficiencies are very low since the second harmonic is carried by a plasmonic mode whose losses deplete the signal after a propagation distance of only a few microns. In this paper we show that the conversion efficiency can be improved by demonstrating that PM for second harmonic generation (SHG) can also be obtained by taking advantage of the high effective index of a plasmonic fundamental frequency (FF) pump which transfers energy to a low-loss second harmonic (SH) mode guided by total internal reflection.

We chose as the reference structure a multilayer composed of AlGaAs layers with different fractions of aluminum and therefore with different refractive indices (as in Fig. 1a): the core is $\text{Al}_{0.18}\text{Ga}_{0.82}\text{As}$ and cladding and substrate are made of $\text{Al}_{0.2}\text{Ga}_{0.8}\text{As}$ and $\text{Al}_{0.4}\text{Ga}_{0.6}\text{As}$, respectively. This slab can be etched to a depth of 1550 nm with respect to the surface to obtain a ridge waveguide having a width of $5\ \mu\text{m}$. Finally, this waveguide is covered by a layer of gold. Adachi's model [3] and Ung's code [4] have been used to evaluate the refractive indices of AlGaAs and gold, respectively, and a Finite Element Method was used to calculate the phase velocities of FF and SH modes.

When taking into account the tensorial nature of the quadratic interaction in AlGaAs, and considering that the plasmonic mode is TM polarized [1], when plasmonic fundamental modes are involved only the Type II interaction can be phase matched. In fact, the Type I interaction would require a TE polarized fundamental. As a consequence, we study

the PM of quadratic nonlinear mixing between a TM polarized FF plasmonic mode, a second optical TE polarized FF pump mode and an optical TE SH mode. We demonstrate the presence of the required PM between the TM polarized plasmonic mode at $\lambda_{FF} = 1603 \text{ nm}$, as a first pump, the optical TE_{00} mode with negligible losses, as a second pump, and the optical TE_{02} mode (also characterized by negligible losses) as the second harmonic.

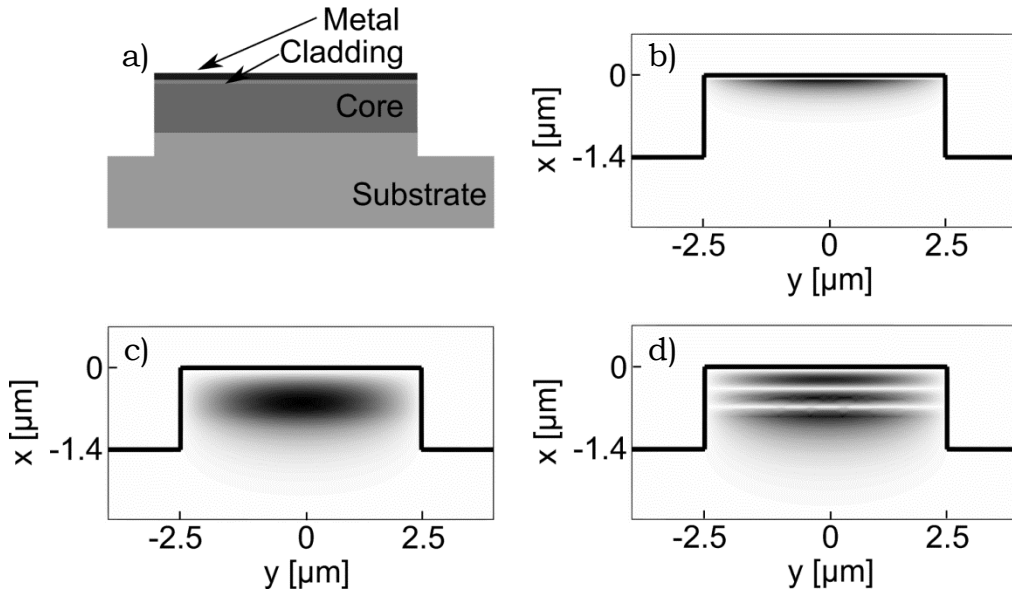


FIG. 1 – a) Waveguide structure. Absolute values of the main transverse components of the involved electric fields: b) pump plasmonic mode (TM), c) optical pump mode (TE_{00}), d) second harmonic mode (TE_{02}).

II. Conversion efficiency and tuning

The guided modes can be written in the form $E(x,y,z)=A(z)\xi(x,y)$, where $\xi(x,y)$, with dimensions m^{-1} , is the transverse profile normalized to 1 (i.e. $\int |\xi|^2 dx dy = 1$).

The equations which govern the quadratic interaction among the three modes are well known and we model the linear losses of the plasmonic FF mode by introducing an exponential decay along the z coordinate. After some mathematical steps, it is possible to obtain the absolute value $|A_{SH}|$ of the SH amplitude as a function of the propagation distance z :

$$|A_{SH}(z)| = \frac{\omega_{SH}}{c_0 n_{SH}} |A_{FF,p}| |A_{FF,o}| S \exp\left(-\frac{\alpha z}{2}\right) \left| \frac{\sinh\left(\frac{\alpha + i\Delta\beta}{2} z\right)}{\frac{\alpha + i\Delta\beta}{2} z} \right| z \quad (1)$$

where $\Delta\beta = \beta_{SH} - \beta_{FF,p} - \beta_{FF,o}$ is the phase mismatch, $\alpha = 0.1 \mu m^{-1}$ is the linear loss coefficient of the plasmonic mode, $d_{eff} = 90 \text{ pmV}^{-1}$ is the second-order

nonlinear optical susceptibility and $S = |\int d_{eff} \xi_{SH} \xi_{FF,p} \xi_{FF,o} dx dy = 1|$ is the overlap integral. Finally, ω_{SH} and n_{SH} are the angular frequency and the real part of SH modal effective index, respectively.

Whenever the phase mismatch is negligible, the SH power at the output of a waveguide of length L reads as:

$$P_{SH}(L) = \eta_0 \exp(-\alpha L) \left| \frac{\sinh\left(\frac{\alpha}{2} L\right)}{\frac{\alpha}{2} L} \right|^2 L^2 P_{FF,p} P_{FF,o} \quad (2)$$

$$= \eta(L) L^2 P_{FF,p} P_{FF,o}$$

where $P_{FF,p}$ and $P_{FF,o}$ are the input pump powers and

$$\eta_0 = \frac{32\pi^2}{\lambda_{FF}^2} \frac{1}{c_0 \epsilon_0} \frac{1}{n_{FF,p} n_{FF,o} n_{SH}} S^2 \quad (3)$$

In the absence of pump losses, i.e. if $\alpha=0$, the normalized conversion efficiency is given by equation (3). In the presence of losses, $\eta(L)L^2 \approx \eta_0/\alpha^2$ for sufficiently large values of L .

The profiles of the modes involved in the nonlinear interaction are shown in Fig. 1. The PM wavelength is $\lambda_{FF}=1603 \text{ nm}$ and it does not differ significantly from the PM wavelength of the slab obtained by considering a ridge of infinite width. Using Eq. (3), the normalized conversion efficiency value is $\eta_0=3.53 \cdot 10^4 \text{ W}^{-1}\text{m}^{-2}$. As well argued in the literature (for instance in [1]), since the losses in the metal attenuate the propagating plasmonic modes (and only marginally the optical modes), the conversion efficiency depends on the propagation distance. Fig. 2a) shows the product $\eta(L)L^2$ as defined in Eq. (2): for relatively large values of L this quantity tends to the value $\eta_0/\alpha^2=3.40 \cdot 10^{-6} \text{ W}^{-1}$, which is reached after about $L=50 \text{ }\mu\text{m}$. Although frequency conversion only takes place at the beginning of the guide, the second harmonic is associated with an optical mode with low losses ($\alpha = 0.0012 \text{ }\mu\text{m}^{-1}$), so that the converted energy can propagate for significant distances. We checked a posteriori the validity of the analytical results (1)-(3) by numerically integrating the relevant coupled field equations, including the losses of all modes.

We may test the tunability of the PM wavelength by varying the thickness of the core or of the cladding or the waveguide width without modifying other geometrical parameters; for example, as shown in Fig. 2b), the PM wavelength can be selected in a 80 nm range by changing the core thickness from 800 to 1200 nm . We may note instead that cladding thickness variations generate only small changes in PM wavelength. Similarly we can verify that the variation of the waveguide width from 4 to $9 \text{ }\mu\text{m}$ leads to a decrease in PM wavelength of only 3 nm , i.e., from 1605 to 1602 nm .

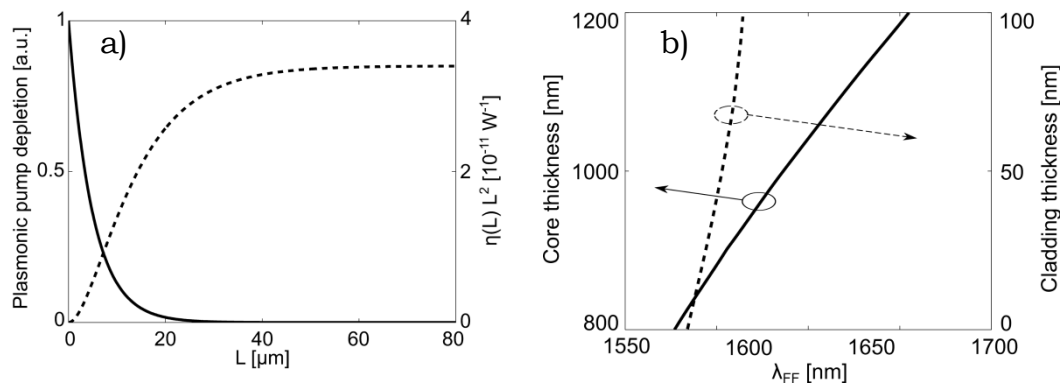


FIG. 2 – a) Plasmonic pump depletion (continuous line) and conversion efficiency multiplied by squared waveguide length (dashed line); b) relations between phase matched pump wavelength λ_{FF} and core thickness or cladding thickness while keeping other dimensions unchanged.

III. CONCLUSION

We demonstrated that modal PM among optical and plasmonic modes can be obtained in waveguides made of AlGaAs and covered by a gold layer. The interface between semiconductor and gold supports the propagation of a plasmonic mode. Whenever this mode is used in a Type II quadratic interaction as one of the two fundamental pumps, it is possible to obtain relatively efficient SHG. We designed realistic planar devices that fulfill the PM condition for pump wavelengths longer than 1580 nm . The maximum conversion efficiency is only limited by the losses of the plasmonic pump since the second harmonic is carried by a low-loss guided mode.

ACKNOWLEDGEMENT

The authors gratefully acknowledge the financial support given by the Fondazione Cariplo, project number 2009-2730.

REFERENCES

- [1] A. R. Davoyan, I. V. Shadrivov, and Y. S. Kivshar, “Quadratic phase matching in nonlinear plasmonic nanoscale waveguide,” *Opt. Express* 17, 20063 (2009).
- [2] Z. J. Wu, X. K. Hu, Z. Y. Yu, W. Hu, F. Xu, and Y. Q. Lu, “Nonlinear plasmonic frequency conversion through quasiphase matching,” *Phys. Rev. B* 82, 155107 (2010).
- [3] S. Adachi, “GaAs, AlAs and $\text{Al}_x\text{Ga}_{1-x}\text{As}$: materials properties for use in research and device applications,” *J. Appl. Phys.* 58, R1 (1985).
- [4] B. Ung and Y. Sheng, “Interference of surface waves in a metallic nanoslit,” *Opt. Express* 15, 1182 (2007).

Representation of a Spiral Phase Plate as a two mode Quantum Phase Operator

Fabio Antonio Bovino
 Quantum Optics Lab, Selex-SI, via Puccini 2, 16154, Genova
fbovino@selex-si.com

We introduce a quantum-like representation of a Spiral Phase Plate as a two mode phase operator. The representation is based on the Newton binomial expansion and on properties of rational power of quantum operators.

1. Introduction

Optical vortices (OV) in light beams are tightly bound to phase dislocations (or singularities): due to the continuous spatial nature of a field, the presence of these defects implies the vanishing of the field's amplitude in the singularity. In some types of dislocations the phase circulates around the singularity and creates a vortex [1]. Nye and Berry [2] used the term "phase dislocation" to define the locus of the zero amplitude of a field. Similarly to crystallography, phase dislocations can be classified in edge, screw and mixed screw-edge [3]. Recently the interest in OV increased because of the fact that fields in which they are included show an helical wave-front structure - developing around the screw dislocation line – entailing the presence of an orbital angular momentum (OAM). This is an important feature, which can be exploited in several applications, from optical tweezers to the generation of N-dimensional quantum states (q-nits) for quantum information applications.

A screw wave dislocation can be defined by means of the integer topological charge Q , which represents the phase winding number, and can be found through a circulation integral around the dislocation line:

$$Q = \frac{1}{2\pi} \oint df \quad (1)$$

where f is the phase of the field.

The most used method of generating OAM in an optical beam is by imprinting one or more vortices on its transverse field distribution, in practice by passing a fundamental Gaussian beam through a device that modifies only the phase, such as a Spiral Phase Plate (SPP). When a Gaussian beam is diffracted off such an SPP, the resulting mode can be viewed as a superposition of Laguerre–Gaussian (LG) modes. It is known that a Laguerre-Gaussian beam of paraxial light has a well-defined orbital angular momentum [4–7].

In Ref. [6] Nienhuis and Allen employed operator algebra to describe the Laguerre-Gaussian beam, and noticed that Laguerre-Gaussian modes are laser mode analog of the angular momentum eigenstates of the isotropic 2-d harmonic oscillator. In Ref. [10] Simon and Agarwal presented a phase-space description (the Wigner function) of the LG mode by exploiting the underlying phase-space symmetry. Li-Yun Hu and Hong-yi Fan have shown that LG mode is just the wave function of the common eigenvector of the orbital angular momentum operator and the total photon number operator of 2-d oscillator in the entangled state representation [11, 12], which is based on the first formulation of Einstein-Podolsky-Rosen quantum entanglement (EPR paradox).

In the Quantum Mechanics picture it is useful to search a quantum operational representation of a SPP because, according to Dirac, there should exist a formal correspondence between quantum optics operators and classical optics transformations. Aiello et al [13] proposed a quantum operator representing the action of the SSP on a Gaussian Beam: it is the analog of the quantum phase operator.

The issue of defining a quantum phase operator for the electromagnetic field is a great challenge in quantum mechanics and quantum optics. Quite few proposals were made to

define quantum phase operators consistent with quantum mechanics and coinciding with an experimental measurement. The most frequently discussed are those proposed by Susskind and Glogower [14], Pegg and Barnett [15], Paul [16], Noh, Fougires and Mandel [17], and Shapiro and Wagner (SW) [18]. The last ones are based on the simultaneous detection of quadrature components using a heterodyne detection method. In this paper we express the quantum phase operator related to a SPP in a novel way, which allows its application directly to Fock States without using Phase Space representation.

2. The Spiral Phase Plate Quantum Operator

A unitary SPP is a transparent dielectric plate with an edge dislocation that can be freely rotated around the plate axis. Let z be the axis of the plate, φ the azimuth angle and without loss of generality, let us suppose that the edge dislocation is at $\varphi = 0$. When a light beam with transverse profile $V(z\bar{z})$ crosses such a SPP, it acquires an azimuthal-dependent phase $e^{i\varphi}$, i.e., in terms of wave function :

$$\Psi(z\bar{z}) \Rightarrow e^{iq\varphi} \langle z, \bar{z} | \Psi \rangle \quad (2)$$

Let us introduce the quantum operator

$$\hat{e}^{i\varphi} = \frac{z}{|z|} = \sqrt{\frac{\hat{a}_+^\dagger + \hat{a}_-}{\hat{a}_+ + \hat{a}_-^\dagger}} = \sqrt{\frac{\hat{Y}}{\hat{Y}^\dagger}}, \quad (3)$$

with the commutator $[\hat{Y}, \hat{Y}^\dagger] = 0$. The operator associated to a generic SPP, $\hat{e}^{iq\varphi}$, with $q \in \mathbb{R}$, can be expanded in the form

$$\hat{e}^{iq\varphi} = \sum_{k=-\infty}^{\infty} C_{qk} \hat{e}^{ik\varphi}, \quad (4)$$

where

$$C_{qk} = \frac{1}{2\pi} \int_0^{2\pi} e^{i(q-k)\varphi} d\varphi = \frac{e^{i(q-k)\pi} \text{Sin}[(q-k)\pi]}{(q-k)\pi} \quad (5)$$

and

$$\hat{e}^{ik\varphi} = \left(\frac{\hat{a}_+^\dagger + \hat{a}_-}{\hat{a}_+ + \hat{a}_-^\dagger} \right)^{\frac{k}{2}} \quad (6)$$

with $k \in \mathbb{N}$. Following [19], or better, Isaac Newton (1665), the general operator $\hat{e}^{ik\varphi}$ can be formally expanded as

$$\begin{aligned} \hat{e}^{ik\varphi} &= (\hat{a}_+^\dagger + \hat{a}_-)^{\frac{k}{2}} (\hat{a}_+ + \hat{a}_-^\dagger)^{-\frac{k}{2}} = (\hat{a}_+ + \hat{a}_-^\dagger)^{-\frac{k}{2}} (\hat{a}_+^\dagger + \hat{a}_-)^{\frac{k}{2}} \\ &= \sum_{m=0}^{\infty} \sum_{h=0}^{\infty} \binom{k/2}{m} \binom{-k/2}{h} \hat{a}_+^{\dagger m} \hat{a}_-^{-\frac{k}{2}-m} \hat{a}_+^h \hat{a}_-^{\frac{k}{2}-h}, \end{aligned} \quad (7)$$

where

$$\binom{k/2}{h} = \frac{(k/2)_h}{h!},$$

and $(r)_h$ is the Pochhammer symbol. Moreover, to provide the application of the high non-linear operator directly to Fock States, without using Phase Space representations, we introduce the following selection rules:

$$\hat{a}^\alpha \hat{a}^{\dagger\beta} |n\rangle = \frac{\Gamma(1+n+\beta)}{\sqrt{n!\Gamma(1+n+\beta-\alpha)}} |n+\beta-\alpha\rangle, \quad (8)$$

and

$$\hat{a}^{\dagger\beta} \hat{a}^\alpha |n\rangle = \frac{\sqrt{n!\Gamma(1+n+\beta-\alpha)}}{\Gamma(1+n-\alpha)} |n+\beta-\alpha\rangle, \quad (9)$$

where $\alpha, \beta \in \mathbb{R}$, with the constrain $n+\beta \in \mathbb{N}^+$, $n+\beta-\alpha \in \mathbb{N}^+$. As an example, we apply the quantum operator $\hat{e}^{ik\varphi}$, corresponding to a SPP with topological charge $q=2.5$ to the displaced vacuum state of a 2-d Harmonic Oscillator, namely $\hat{D}(\alpha_+) \hat{D}(\alpha_-) |0,0\rangle = e^{\alpha \hat{a}_+^\dagger} e^{\bar{\alpha} \hat{a}_-^\dagger} |0,0\rangle$. That a state is the analogue of a Displaced Gaussian beam in paraxial approximation with $r_0^2 = |\alpha|^2$. In terms of wavefunction we obtain

$$\Psi(r, \varphi) = \sum_{p=0}^{\infty} \sum_{l=-\infty}^{\infty} e^{-\frac{r_0^2}{2w_0^2}} \left(\frac{r_0^2}{2w_0^2} \right)^{p+\frac{|l|}{2}} \frac{(-1)^p e^{-il\varphi_0}}{\sqrt{p!(p+|l|)!}} \sum_{h=0}^{\infty} \sum_{k=-\infty}^{\infty} C_{plhk} LG_h^k(r, \varphi) e^{ik\varphi}, \quad (10)$$

with

$$C_{plhk} = e^{i(q+l-k)\pi} \sqrt{\frac{p!h!}{(p+|l|)!(h+|k|)!}} \frac{\text{Sin}[(q+l-k)\pi]}{\pi(q+l-k)} I_{p,h}(l, k), \quad (11)$$

and

$$I_{p,h}(l, k) = (-1)^{p+h} \Gamma\left(\frac{|l+|k||}{2} + 1\right) \sum_{r=0}^{\text{Min}\{p,h\}} \binom{\frac{|k|-|l|}{2}}{p-r} \binom{\frac{|l|-|k|}{2}}{h-r} \binom{\frac{|l+|k|}{2} + r}{r}. \quad (12)$$

LG_h^k are the generalized Laguerre-Gaussian modes.

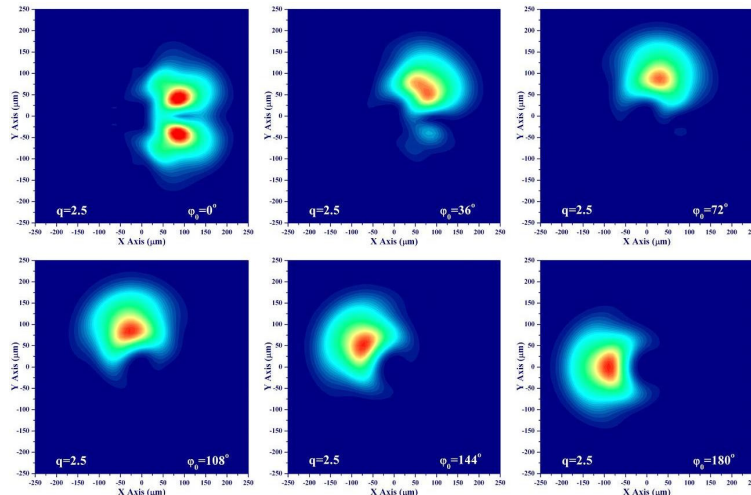


Figure 1: Contour plot of the diffracted field generated by a Displaced Gaussian Beam impinging on a Spiral Phase Plate at different angles in respect to the phase dislocation. The SSP is characterized by a topological charge $q=2.5$. and, in the particular case, the displacement is equal to the waist, $w_0=100\mu\text{m}$.

5. Conclusions

We identified the quantum operator, representing a SPP acting on an electromagnetic field, as the two mode phase operator and we introduced a novel representation based on the Newton binomial expansion and on the properties of rational power of lowering and raising operators of electromagnetic field. This method provides to handling nonlinear operators without using auxiliary picture such as P-representation in phase-space. Moreover, by exploiting the one-to-one correspondence between the state of the two-dimensional harmonic oscillator and a monochromatic paraxial beam of light, we considered the action of a Spiral Phase Plate on a displaced gaussian mode (a displaced vacuum state in quantum picture).

Bibliografia

- [1] M. Soskin, M. Vasnetsov, "Singular Optics", *Progress in Optics* **42**, 221-272 (2001).
- [2] J.F. Nye, M.V. Berry, "Dislocations in wave trains", *Proc. R. Soc. Lond. A* **336**, 165-190 (1974).
- [3] I.V. Basistiy, M. Soskin, M. Vasnetsov, "Optical wavefront dislocations and their properties", *Optics Commun.* **119**, 604-612 (1995).
- [4] J. Visser and G. Nienhuis, "Orbital angular momentum of general astigmatic modes", *Phys. Rev. A*, **70** (2004) 013809.
- [5] Gabriel F. Calvo, "Wigner representation and geometric transformations of optical orbital angular momentum spatial modes", *Opt. Lett.*, **30** (2005) 1207
- [6] G. Nienhuis and L. Allen, "Paraxial wave optics and harmonic oscillators", *Phys. Rev. A*, **48** (1993) 656.
- [7] R. Gase, "Representation of Laguerre-Gaussian Modes by the Wigner Distribution", *IEEE J. Quantum Electron.*, **31** (1995) 1811.
- [8] M. VanValkenburgh, "Laguerre-Gaussian modes and the Wigner transform", *J. Mod. Opt.*, **55** (2008) 3537.
- [9] L. Allen, S.M. Barnett and M.J. Padgett, "Optical Angular Momentum" (IOP Publishing, Bristol, UK, 2003).
- [10] R. Simon and G.S. Agarwal, "Wigner representation of Laguerre-Gaussian beams", *Opt. Lett.* **25** (2000) 1313.
- [11] H.-Y. Fan and J. R. Klauder, "Time evolution of the Wigner function in the entangled-state representation", *Phys. Rev. A*, **49** (1994) 704.
- [12] H.-Y. Fan and Y. Fan, "Representations of two-mode squeezing transformations", *Phys. Rev. A*, **54** (1995) 958.
- [13] A. Aiello, S. S. R. Oemrawsingh, E. R. Eliel, and J. P. Woerdman, "Unravelling two-photon high dimensional entanglement", <http://arXiv:quant-ph/0503034> (2005).
- [14] L. Susskind and J. Glogower, "Quantum mechanical phase and time operator", *Physics* **1** (1964) 49.
- [15] D.T. Pegg and S.M. Barnett, "Unitary Phase Operator in Quantum Mechanics", *Europhys. Lett.* **6** (1988) 483.
- [16] H. Paul, "Phase of a Microscopic Electromagnetic Field and Its Measurements", *Fortschr. Phys.* **22** (1974) 657.
- [17] J.W. Noh, A. Fougères and L. Mandel, "Measurement of the quantum phase by photon counting", *Phys. Rev. Lett.* **67** (1991) 1426; "Measurements of the probability distribution of the operationally defined quantum phase difference", **71** (1993) 2579.
- [18] J.H. Shapiro and S.S. Wagner, "Phase and amplitude uncertainties in heterodyne detection", *IEEE J. Quan. Electron.* **QE-20** (1984) 803.
- [19] A. Lukš, V. Peřinová and J. Křepelka, "Rotation angle, phases of oscillators with definite circular polarizations, and the composite ideal phase operator", *Phys. Rev. A* **50** (1994) 818.

Session 18 – Energy and environment

A. Carta, R. Stefanelli, and D. Trincherò

Microwave electromagnetic sensors to estimate water density within snow

M. Montopoli, G. Vulpiani, and F. S. Marzano

The potential use of microwave weather radar for volcanic ash monitoring

M. Sozzi, C. Catellani, A. Cucinotta, S. Selleri, D. Menossi, R. Dharmadasa, A. Bosio, and N. Romeo

Laser scribing integration of polycrystalline thin film solar cells

S. Ceccuzzi, F. Napoli, L. Pajewski, G. Schettini, and A.A. Tuccillo

Antenna-plasma coupling calculations at lower hybrid frequencies by using a FEM code

R. Moro, S. Kim, M. Bozzi, and M. Tentzeris

Novel inkjet-printed substrate integrated waveguide (SIW) structures for eco-friendly low-cost application

A. Facchini, A. Zeffiro, P. Arcioni, and A. Buttafava

Preliminary studies on the microwave pre-treating of lignocellulosic biomasses

MICROWAVE ELECTROMAGNETIC SENSORS TO ESTIMATE WATER DENSITY WITHIN SNOW

A. Carta, R. Stefanelli, D. Trincherò

iXem Labs – Politecnico di Torino
Department of Electronics and Telecommunications
corso Duca degli Abruzzi 24, 10129 Torino, Italy
info@ixem.polito.it

Abstract

The paper introduces a compact sensing topology based on a distributed alignment of electromagnetic radiators, deployed in a predefined distance to form an ad-hoc network, able to reveal the differential variation of humidity inside snowfields. By monitoring the relative attenuation among two separate alignments of vertical antennas, the relative permittivity and electrical conductivity of the snow can be deduced with sufficient precision. The two terms can be used as a precise indicators of dramatic events such as avalanches and landslides. The simulation results show that the dynamic of the signal attenuation is enough to reveal the snow water density.

Index Terms – Avalanche sensors, propagation in snow and ice, radiofrequency sensors, wireless sensor networks.

I. INTRODUCTION

The dramatic event of an avalanche is the result of a complex phenomenon determined by many factors, including the slope characteristics (inclination, roughness, etc), the weather conditions and the corresponding snowpack variations.

The evaluation of the liquid water content into the snowpack constitutes one of the variables to take into account in the identification of possible avalanche hazard. In fact, it can influence the snowpack mechanical properties and significantly reduce the snow cohesion and strength, [1]. The evaluation of the liquid water content can be performed by the so-called “hand” test: an expert observer makes the estimation by examining the sensing snow sample from each layer of the considered snowpack. Such technique is time-consuming, it requires the collection of a huge number of snow profiles that give just a relative quantification of the snow wetness level, [2]. Another technique is based on the use of the freezing calorimeter, [3]. Such method allows to obtain accurate results but it requires the use of a freezing agent, which arises safety issues. Moreover it is a time consuming procedure and requires large snow samples, making almost impossible the evaluation of the snow stratification with a vertical profiling. However, as demonstrated by many authors, the liquid water content and the density of snow can be directly related to its dielectric constant, [4].

Therefore instruments for the assessment of the complex dielectric constant have been developed during the years, [5]. In particular an instrument called the “Snow Fork” allows the evaluation of both the real and imaginary part of the dielectric constant, obtaining a corresponding reliable estimation of the snow liquid content and density, [5]. The resulting measurement can be performed in a nearly non-destructive way. However the realization of a complete wetness profile requires several spatially distributed measurements whereas it would be better to perform a continuous monitoring of the snowpack.

II. RELATION BETWEEN COMPLEX PERMITTIVITY AND WETNESS

Dry snow can be considered, from the electromagnetic point of view, as a heterogeneous medium composed of ice and air. The real part of the dielectric constant of dry snow is characterized by a linear dependency on its density, whereas the imaginary part, instead, is quite small, [4]. On the other hand, wet snow is a dielectric mixture of ice, liquid water and air whose behavior depends both on frequency and density. The relation between the dielectric constant and the snow wetness is a transcendental function that can be expressed in terms of Taylor series expansion. The approximation to the first order term can be considered sufficient for the purpose of this work, even if the introduction of a quadratic dependence allows to achieve more consistent results. In particular the real and the imaginary part of the dielectric constant have the following expressions, in agreement with the studies reported in [5]-[7]:

$$\varepsilon'(f, m_v) = \varepsilon'(f, m_v = 0) + \alpha'_1(f)m_v + \alpha'_2(f)m_v^2 \quad (1)$$

$$\varepsilon''(f, m_v) = \sigma(f, m_v = 0) + \alpha''_1(f)m_v + \alpha''_2(f)m_v^2 \quad (2)$$

where m_v is the liquid water content, expressed in percent per volume, and the α terms assume, with respect to the frequency of interest, the following values:

TABLE I – α COEFFICIENTS

	α_1'	α_2'	α_1''	α_2''
f = 2.45 GHz	0.1	0.005	0.01	0.0005
f = 900 MHz	0.092	0.83	0.012	0.104

Applying Eq. (1) and Eq. (2) with the proper α terms, it is possible to obtain the snow dielectric characteristics, reported in the following table.

TABLE II – DIELECTRIC PROPERTIES OF SNOW

Medium	Water Content (Vol. %)	f = 2.45 GHz		f = 900 MHz	
		ϵ'	σ	ϵ'	σ
Dry Snow	0	1.47	0.0001	1.6	0.0001
Moist Snow	0-3	1.71	0.0068	1.85	0.0005
Wet Snow	3-8	2.1	0.0299	2.2	0.0045
Very Wet Snow	8-15	2.9	0.0708	2.7	0.0070
Soaked Snow	>15	3.3	0.0953	3.6	0.0150
Water	/	81	2.8583	81	0.49

III. SENSING ARCHITECTURE

The proposed system for the estimation of the dielectric properties of the snow and the corresponding evaluation of its water content is based on the alignment of electric and magnetic radiators, as reported in Fig. 1

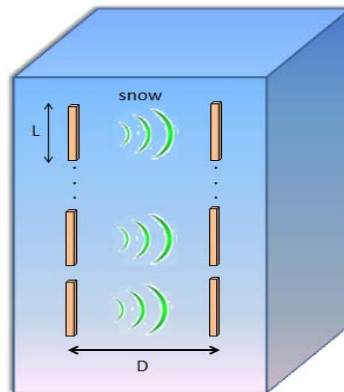


FIG. 1 – Schematic view of the sensors buried into the snow.

Each radiator is fed individually, as the whole alignment is not intended as an array. By monitoring the relative attenuation among the two separate alignments of vertical antenna it is possible to deduce information about the relative permittivity and electrical conductivity with sufficient precision. The realization of two alignments of radiators guarantees the continuous monitoring of the snow wetness, as well as the evaluation of the dielectric parameters at different depths, taking into account the possible presence of layers with different characteristics. The resulting compact design has the aim of reducing any possible modification to the snow status due to the introduction of the device itself. The preliminary testing activity has been performed by means of the software HFSS, by Ansoft. The system has been simulated

first considering two dipoles and then two loops, in order to identify the best radiator and the corresponding design to use. Moreover the performed analysis has been done considering different frequencies, spacings between the alignments and radiator sizes. The obtained results show a dependence of the received power from the snow water content. With both radiators, the availability of, at least, 10 dB of dynamic, in terms of received power, makes possible the identification of the snow characteristics using such parameter. The results for the dipole are reported in the following table, where D is the distance between the radiators and L is the dipole length. The same behavior has been observed for the loop. The values of received power are expressed in dB, they are all normalized with respect to the power received considering as medium the free space.

TABLE III – POWER DYNAMICS OF THE DIPOLE.

	f= 900MHz D = $\lambda/5$ L = $\lambda/2$	f= 2.45 GHz D = $\lambda/5$ L = 0.7λ	f= 900MHz D = $\lambda/4$ L = λ	f= 2.45 GHz D = λ L = $\lambda/2$
Medium	P _{RX} [dB]	P _{RX} [dB]	P _{RX} [dB]	P _{RX} [dB]
Dry Snow	-0.2653	-4.7569	-6.3034	-2.3287
Moist Snow	-0.4689	-7.9195	-8.4833	-3.7902
Wet Snow	-2.7080	-12.8903	-13.8059	-7.3849
Very Wet Snow	-6.0703	-20.8426	-16.0781	-12.9715
Soaked Snow	-10.8786	-21.8537	-16.1558	-13.1729
Water	-47.4341	-38.7873	-46.6324	-44.6983

REFERENCES

[1] Colbeck, S.: An Overview of Seasonal Snow Metamorphism, Rev.Geophys., 20, 45–61, 1982.

[2] Techel, F. and Pielmeier, C.: “Point observations of liquid water content in wet snow – investigating methodical, spatial and temporal aspects,” The Cryosphere, 5, 405-418, 2011.

[3] E. B. Jones, A. Rango. and S. M. Howell, “Snowpack liquid water determinations using freezing calorimetry,” Nordic Hydro], vol. 14, pp, 113-126. 1983.

[4] Tiuri, M.; Sihvola, A.; Nyfors, E.; Hallikaiken, M.; , "The complex dielectric constant of snow at microwave frequencies," Oceanic Engineering, IEEE Journal of , vol.9, no.5, pp. 377- 382, Dec 1984.

[5] Denoth, A.; Foglar, A.; Weiland, P.; Matzler, C.; Aebischer, H.; Tiuri, M.; Sihvola, A.; , "A comparative study of instruments for measuring the liquid water content of snow," Journal of Applied Physics , vol.56, no.7, pp.2154-2160, Oct 1984.

THE POTENTIAL USE OF MICROWAVE WEATHER RADAR FOR VOLCANIC ASH MONITORING

M. Montopoli^(1,2), G. Vulpiani⁽³⁾ and F. S. Marzano^(4,2)

(1) Dept. of Geography, University of Cambridge
Downing place, Cambridge, UK

(2) Center of excellence CETEMPS, University of L'Aquila
via Vetoio, L'Aquila, Italy

(3) Presidency of the Council of Ministers
Department of Civil Protection, Rome, Italy

(4) Dept. of Information Engineering, Sapienza University
Via Eudossiana 18, 00184 Rome, Italy

Abstract

In this work the experimental evidence together with modeling outcomes are considered to support the capability and shows the limitations of microwave weather radars to detect and monitor volcanic ash. Detection, classification and quantitative estimation of volcanic ash is the main challenges that scientist are facing to fully exploit the exiting weather radar systems. This paper briefly shows the state of the art on these aspects.

Index Terms – weather radars, remote sensing, volcanic eruptions.

I. INTRODUCTION

In the last few years, several volcanic activities, have reminded, especially to the European community, the threat represented by the volcanic eruptions. The main effects of this natural manifestation include: climate variations, threats to citizens that live close to the volcanoes and, due to the effects of dispersal winds on the erupted ash, the limitation and or cancellation of air traffic routes [1].

With respect to the observations of *Plinius the Elder* who described the famous Vesuvio eruption in the 79 AD, the state-of-the-art countermeasures to alleviate the consequence of a volcanic eruption is nowadays based on direct ground inspections, remote sensing observations and modeling efforts. In this context, remote sensing observations make use of instruments that transmit and receive electromagnetic and/or acoustic waves to infer key properties of eruptions. The output of such instruments is essential to feed physical models of atmospheric ash dispersal. Model outputs can be seen as the synthesis of observations and physical process to describe, as better as possible, the state of an erupting activity with time. This usually can support civil protection activities devoted to issue timely warnings, to monitor the ash plume during its evolution and to quantitatively

estimate tephra (i.e. the fragmented material produced by a volcanic eruption).

Among the variety of instruments that are under the attention of the scientific community for their operative use, weather radars are particularly appealing [3]. This is due to several aspects which are: i) the existence of permanent radar installations and their satisfactory coverage with respect to active volcanoes; ii) fine temporal and spatial resolution of the order of 5 min and 500m, respectively; iii) capability of microwaves to penetrate into the ash clouds giving to the volcanic experts an unprecedented point of view of eruptions. Among the drawbacks should be mentioned the limited spatial scale coverage. This implies, at the most used weather radar frequencies in the range of 4 - 10 GHz, a small sensitivity to very fine ash particles (of the order of μm) that show a longer residence time in the atmosphere and for this reason can travel for far distances across countries.

In this paper, examples of the potential of microwave weather radar to monitor volcanic ash are given using experimental evidence and modeling tools, which are able to describe the electromagnetic radar response to ash particles. The organization of the paper foresees some examples of ash detection in section II, quantitative estimation in section III, conclusion and remarks in section IV.

II. VOLCANIC ASH DETECTION

An effective use of weather radars for ash monitoring passes through two main steps: Ash detection and its quantitative estimation. The detection is needed to limit the analysis to regions where ash is mainly present and distinguish ash backscatter radar returns from undesired ones (all others sensible targets, i.e. hydrometeors). **Figure 1** shows an eruption case on May 25th occurred in Iceland at the Grimsvoth volcano as seen by an X band radar at about 70 km far from the volcano vent. The work frequency, the spatial and temporal resolutions and the maximum range are equal to 10 GHz, 10 min, 400 m and 120 km, respectively.

In the case shown in Figure 1, the detection of volcanic ash is quite straightforward due to the unequivocal ash plume over the volcano vent. In general, the radar signature of ash can be comparable with that typically shown by hydrometeors. In those cases the spatial and temporal texture of the observed scene is used to perform an optimal detection.

III. VOLCANIC ASH ESTIMATION

The estimation step can be addressed using the Volcanic Ash Radar Retrieval (VARR) methodology extensively described in previous works [2].

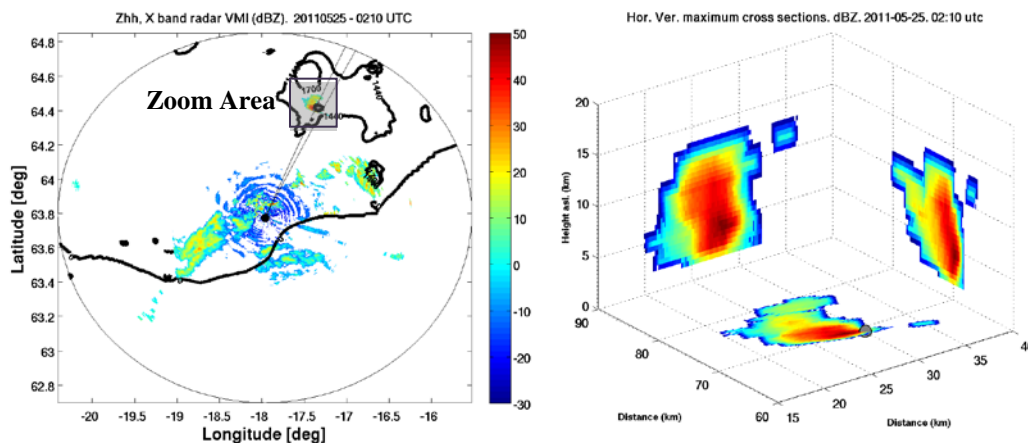


FIG. 1 – Left panel: 2D Vertical maximum indicator in [dBZ] of the scene for the Grmsivotn volcano eruption (Iceland) on May 25th, 2011 at 2:10 UTC. Right panel: A 3D zoom, at the same instant, around the volcano vent.

The VARR methodology, which belongs to the physically-based inversion algorithm class, is organized in further 2 basic steps: i) ash classification; ii) ash estimation. Both steps are trained by a physical-electromagnetic forward model, characterized by particle size distribution (PSD) of ash species and a radar backscattering model. PSD is usually modeled as a Scaled Gamma Particle Size Distribution (SG-PSD) whose main parameters are the number concentration N_n , number-weighted diameter D_n , and the shape parameter μ . These parameters are estimated from available PSD samples taken at the ground after experimental campaigns or alternately treated as random variables and constrained by a priori (experimental and physical) information. **Table 1** lists the typical range of diameters of ash categories whereas **Figure 2** shows an example of the modeled relation between the radar reflectivity and the volumetric ash concentration in the case of coarse ash and small, medium and intense concentration when oblate orientation is chosen for modeling ash particles. It is worth mentioning, as the synthetic signature of radar observables to ash particles is not limited to the radar reflectivity. The advent of orthogonal polarimetric radar systems has required modeling efforts (not shown here for brevity) able to describe the behavior of such systems. Two examples of the outcome of the processing chain just mentioned is shown in **Figures 3 and 4**. The first one plots the temporal evolution of the instantaneous mass in [kg] retrieved by a C band weather radar 260 km far from the Grimsvotn volcano during its eruption in May 2011. Figure 4 shows, for the same days, the estimated plume height.

TEPRHA	Particle type	Particle size
Ash	Fine ash (FA)	Less than 64 μm
	Coarse ash (CA)	From 64 μm to 532 μm
Lapilli	Small lapilli (SL)	From 0.532 mm to 2.56 mm
	Large lapilli (LL)	From 2.56 mm to 32 mm
Blocks	Blocks and bombs (BB)	Greater than 32 mm

TAB. 1 – classification of ash particles and their characteristic diameters

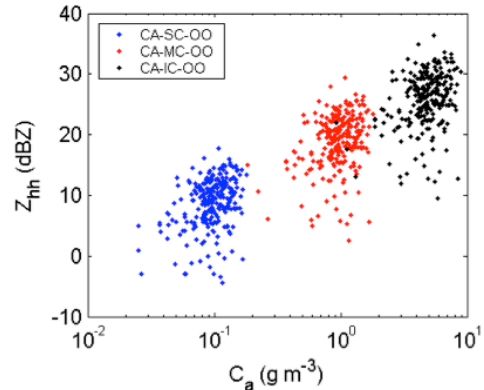


FIG. 2 – Correlation of radar reflectivity and coarse ash concentration

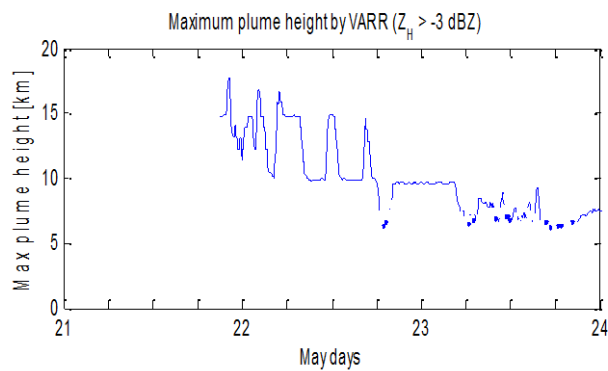
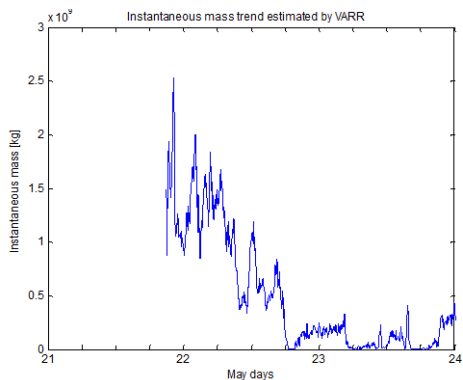


FIG. 2 – Left panel: Instantaneous mass. Right panel: Volcanic plume height.

IV. CONCLUSION

Weather radar systems have demonstrated to have some potential to bring an important contribution to the community of volcanology. Single polarization radar systems have been so far more popular and for this reason more exploited for ash monitoring. Dual polarization systems capability is under investigation even the low repetition frequency of volcanic eruptions and the lack of ground measurements makes the validation of the developed models problematic.

ACKNOWLEDGEMENT

We are grateful to B. Palmason and S. Karlsdóttir (Iceland Meteorological Office, Reykjavik, Iceland) for providing radar data.

REFERENCES

- [1] Sparks, R. (1986). The dimensions and dynamics of volcanic eruption columns. *Bulletin of Volcanology*, 48 (1), 3-15.
- [2] Marzano, F. S., Vulpiani, G., & Rose, W. I. (2006a). Microphysical characterization of microwave radar reflectivity due to volcanic ash clouds. *IEEE Transactions on Geoscience and Remote Sensing*, 44 (2), 313-327.
- [3] Harris, D. M., & Rose, Jr., W. I. (1983). Estimating particle sizes, concentrations, and total mass of ash in volcanic clouds using weather radar. *Journal of Geophysical Research*, 88 (C15), 10969-10983.

LASER SCRIBING INTEGRATION OF POLYCRYSTALLINE THIN FILM SOLAR CELLS

M. Sozzi⁽¹⁾, C. Catellani⁽¹⁾, A. Cucinotta⁽¹⁾, S. Selleri⁽¹⁾, D. Menossi⁽²⁾,
R. Dharmadasa⁽²⁾, A. Bosio⁽²⁾, N. Romeo⁽²⁾

⁽¹⁾ Dipartimento di Ingegneria dell'Informazione,
Università di Parma, Viale G.P. Usberti n.181/A, 43124, Parma

⁽²⁾ Dipartimento di Fisica,
Università di Parma, Viale G.P. Usberti n.7/A, 43124, Parma
stefano.selleri@unipr.it

Abstract

The growing demand for high productivity in the thin-film module industry, together with the request for more and more efficient photovoltaic devices, requires high-performance laser-scribing. We report a study of laser-scribing on CdTe thin-film modules.

Index Terms – laser scribing, thin film solar cells, photovoltaic cells

I. INTRODUCTION

Low cost photovoltaic modules production is the main aspect for reducing the costs of electrical energy produced by renewable sources to be competitive with fossil based energy sources. To provide a good alternative to mono and poly-silicon based modules it is necessary to develop devices with a comparable or even better efficiency/cost ratio. Mono and poly-silicon based modules are produced by assembling by hand a high number of different cells, which adds more time to the production process. On the other hand thin film solar cells with excellent results in efficiency/cost ratio have been obtained. The two most innovative materials are CdTe (cadmium telluride) and CIGS (CuInGaSe₂), with which solar cells efficiencies of 17.3% [1] and 20.3% [2] have been respectively obtained. These values are comparable to the highest efficiency obtained so far with silicon solar cells, 25% [3]. Unlike wafers, thin films are continuous layers of material which cover the whole substrate surface and if cut, they permit the creation of integrated connections. Interconnection process is carried out by scribing, that can be performed with laser radiation. The laser scribing process fits very well into the thin film modules production line, where working speed and operations easiness are basic requirements for large scale production. Nowadays poly-Si based modules are sold at 0.88 €/W, mono-Si based modules at 0.99 €/W, while thin film modules, like CdTe, are sold at 0.89 €/W [4]. It's then easy to understand that thin film photovoltaic modules are really competitive with silicon ones. This is possible because of the lower production costs for thin films, which is

also due to the integration of laser scribing into the production line. With the constant technological growth in thin film photovoltaic production it is possible to foresee that within the next few years (2015) modules with lower production costs, like 0.5-0.6 €/W, will be fabricated [5,6]. In this work the laser scribing has been carried out with a commercial solid state laser, and a fiber laser developed in the Optical Devices laboratory of the University of Parma. The use of a fiber laser can bring the advantage of having a better beam quality than a solid state one. The production steps of CdTe based solar cells and the results of laser scribing will be then presented.

II. CDTE POLYCRYSTALLINE THIN FILM SOLAR CELL

CdTe is a semiconductor with excellent photovoltaic characteristics, that make it suitable for being used as an absorber material in thin film solar cells. It has an energy gap of 1.45 eV and, unlike silicon, it is a direct gap semiconductor, which means that few microns of material are enough to absorb 90% of incident sun light. CdTe based solar cell, shown in Fig. 1, is fabricated in superstrate configuration. The soda lime glass (SLG) substrate used is covered with a film of Transparent Conductive Oxide (TCO), that constitutes the *n*-type (negative) front contact of the device. Then, to form the *p-n* junction, a film of CdS (cadmium sulphide) and CdTe are deposited on the TCO film. To increase the CdTe crystallinity and to form a good junction region, this structure is treated with a high temperature annealing in the presence of chlorine. Finally, the cell is completed by depositing the *p*-type back contact (positive), composed of As₂Te₃, Cu and Mo films.

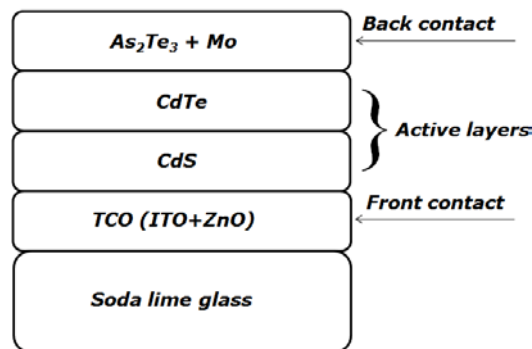


FIG. 1 – CdTe/CdS solar cell in superstrate configuration.

III. LASER SCRIBING

The laser scribing process is composed by three different stages, P1, P2 and P3. The P1 and P3 separate the electrical contacts of the nearby cells, while P2 defines the areas of the different cells. Everything is done

in such a way that all the cells are connected in series during the production process, as described in Fig.2.



FIG. 2 – Production stages of a thin film module.

The scribing process was carried out by using two kinds of lasers, a solid state laser emitting at wavelengths of 1064 nm and 532 nm, and a Ytterbium doped fiber laser working at a wavelength of 1064 nm. Both lasers worked in the nanosecond regime. The scribing has been performed on samples of CdTe/CdS photovoltaic cells, provided at different stages of the production process.

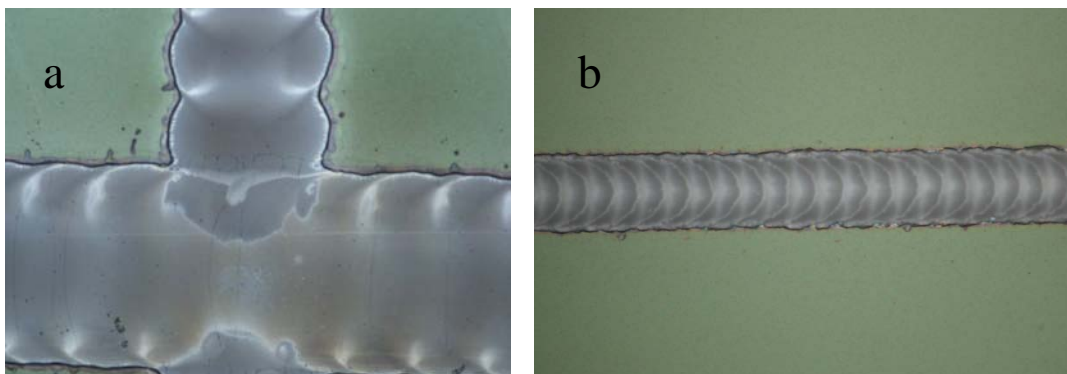


FIG. 3 – **a)** P1 scribe. Vertical scribe obtained with the solid state laser operating at a RR of 10kHz, and pulse width of 47ns, comparable to the horizontal one obtained during the industrial process. **b)** P1 Scribe obtained with the fiber laser operating at a RR of 100kHz, and pulse width of 20ns.

Fig. 3(a) is the optical microscope image of a P1 scribe performed on TCO with the solid state laser, while Fig. 3(b) represents a P1 scribe performed with the fiber laser.

From the image of Fig. 3(a) it is possible to notice that the scribing obtained in laboratory (vertical) is comparable with the one (horizontal) obtained during a standard scribing process made with a solid state commercial laser. The vertical scribing appears clean, sharp, and on the edges there is no presence of material re-deposition that can lead to short circuits. The scribing obtained with the fiber laser is still clean, and sharp, and there are no re-deposition effects, moreover compared to the ones obtained with the solid state laser there is a lower thermal effect on the edges and they appear cleaner, even if some micro-cracks are still visible. A further proof of the successful scribing is the insulation between the different scribed lines; a resistance on the order

of magnitude of about 100 M Ω has been measured. The main reason of the better scribing quality may be due to the value of the M², the laser beam quality factor that is about 1.1 for the fiber laser, and 1.6 for the solid state laser. Further improvements can be achieved by employing a fiber laser working with very short pulses.

In particular in this case there would be no heated affected zone at the edges of the scribing, due to the excessive heating of the material during the ablation process. In this area, the high temperatures induce the melting and the mixing of the nearby materials causing the short circuit of the *p-n* junction. Using very short pulses, 10 ps for example, the melting of the materials can be avoided.

IV. CONCLUSION

In this work the possibility to interconnect thin films solar cells, by means of laser scribing, has been demonstrated. The use of a fiber laser can lead to a better quality scribing. Further improvements can be obtained by using a fiber laser working with short pulses, for example in the pico-second regime. This would avoid all the problems related to the heating of the material and lead to the fabrication of more efficient devices.

ACKNOWLEDGEMENT

The Authors acknowledge the support of the EU funded FP7 ALPINE Project, n. 229231.

REFERENCES

- [1]<http://investor.firstsolar.com/releasedetail.cfm?ReleaseID=639463>.
- [2]http://www.zswbw.de/fileadmin/ZSW_files/Infoportal/Presseinformationen/docs/pi11-2010-e_ZSW-Weltrekord-DS-CIGS.pdf.
- [3]<http://www.smh.com.au/news/environment/energy-smart/quantum-leap-for-solar-cells/2008/10/22/1224351351197.html>
- [4]SolarBuzz, Solar Market Research and Analysis, January 2012.
- [5]First Solar,
<http://investor.firstsolar.com/releasedetail.cfm?ReleaseID=639463>.
- [6] <http://www.trefis.com/stock/fslr/articles/60278/first-solar-can-hit-144-with-rock-bottom-production-costs/2011-07-01>.

ANTENNA-PLASMA COUPLING CALCULATIONS AT LOWER HYBRID FREQUENCIES BY USING A FEM CODE

S. Ceccuzzi^(1,2), F. Napoli⁽²⁾, L. Pajewski⁽²⁾, G. Schettini⁽²⁾, A.A. Tuccillo⁽¹⁾

⁽¹⁾ Euratom-ENEA Association for fusion, C.R. Frascati
Via Enrico Fermi 45, 00044, Frascati, Italy

⁽²⁾ Applied Electronics Department, “Roma Tre” University
Via della Vasca Navale 84, 00146 Rome, Italy
silvio.ceccuzzi@enea.it

Abstract

This paper illustrates how a commercial software can be successfully employed to solve coupling problems between cold plasmas and grill antennas at Lower Hybrid frequencies (1-8 GHz). The FTU conventional grill, presently installed in ENEA-Frascati laboratories, is used as a test case to calculate antenna scattering matrix and launched power spectrum.

Owing to the high computational effort required by the simulations, a 2-D planar symmetry is enforced considering infinite length waveguides in poloidal direction. Simulation results are validated by comparison with experimental data in terms of average reflection coefficient, showing remarkable agreement. Pros and cons of the tool as well as possible improvements are discussed.

Index Terms – FEM, LH antenna, modeling.

I. INTRODUCTION

The excitation of Lower Hybrid (LH) waves by means of a phased waveguide array was proposed by Lallia [1] in 1974. A systematic study of this launching structure was firstly done by Brambilla in 1976 (i.e., the grill theory [2]) and pursued on by many researchers, leading to the development and validation of 3-D advanced coupling codes like GRILL3D-U [3], ALOHA [4] and TOPLHA [5]. Recently, the full-wave commercial software COMSOL Mutiphysics™ has been applied to solve this kind of problems too [6].

COMSOL is a 3-D solver based on the Finite Element Method (FEM), initially developed for structural mechanics and enhanced to properly manage multiphysics problems. It allows to model inhomogeneous, anisotropic and dispersive materials like cold plasmas. Furthermore it presents a user-friendly interface and its usage can be quickly learnt, while present codes are often terminal-based tools requiring the knowledge of some programming language and a specific training at the laboratories where they were developed.

The computational cost of LH antenna simulations get the user to simplify the problem, switching towards planar equivalent geometries. Although this 2-D approach is dated as compared with present codes, COMSOL looks very promising for fusion research thanks to its great

flexibility that allows anyone to introduce physical equations, e.g., to self-consistently simulate non-linear effects [7].

II. IMPLEMENTATION GUIDELINES

A cold slab plasma model can be implemented within the RF module of COMSOL through a proper characterization of the material electric tensor, whose expression has been derived for a x-directed static magnetic field, using the physics convention for harmonic regime (i.e., $e^{-i\omega t}$). Adopting Stix notation, it assumes the following form:

$$\underline{\underline{\varepsilon}} = \begin{pmatrix} P & 0 & 0 \\ 0 & S & -iD \\ 0 & iD & S \end{pmatrix} \quad \text{where} \quad \begin{aligned} S &= (R+L)/2 \\ P &= 1 - \sum_s \omega_{ps}^2 / \omega^2 \quad \text{and} \\ D &= (R-L)/2 \end{aligned} \quad \begin{aligned} R &= 1 - \sum_s \frac{\omega_{ps}^2}{\omega(\omega + \omega_{cs})} \\ L &= 1 - \sum_s \frac{\omega_{ps}^2}{\omega(\omega - \omega_{cs})} \end{aligned}$$

being ω_{cs} and ω_{ps} the cyclotron and plasma frequencies for the S plasma species. They are respectively related to the magnetic field \mathbf{B} and to the particles' densities n_s . The former varies like the inverse of the tokamak radius, while, as for the latter, a Deuterium plasma has been used enforcing the following profile for both ions and electrons:

$$n = (n_c - n_0) \cdot (1 - r^{p1})^{p2} + n_0 \quad (1)$$

being n_c and n_0 the central and edge densities, r the normalized minor radius, $p1$ and $p2$ the exponents defining the parabolic profile and its peaking factor.

Outward radiation conditions have been introduced through a damping term as in [6]. In COMSOL much attention has to be paid to mesh generation since element sizes along the two geometrical dimensions have been bound to a fraction of the parallel and perpendicular wavelengths of the LH waves. These values have been calculated solving the cold plasma dispersion relation in the simulated scenarios.

An important parameter of LH antennas is the launched power spectrum in the n_{\parallel} (\mathbf{B} -parallel refractive index) space. To calculate it, electric and magnetic fields at the antenna mouth have been exported from COMSOL and Fourier-transformed in Matlab.

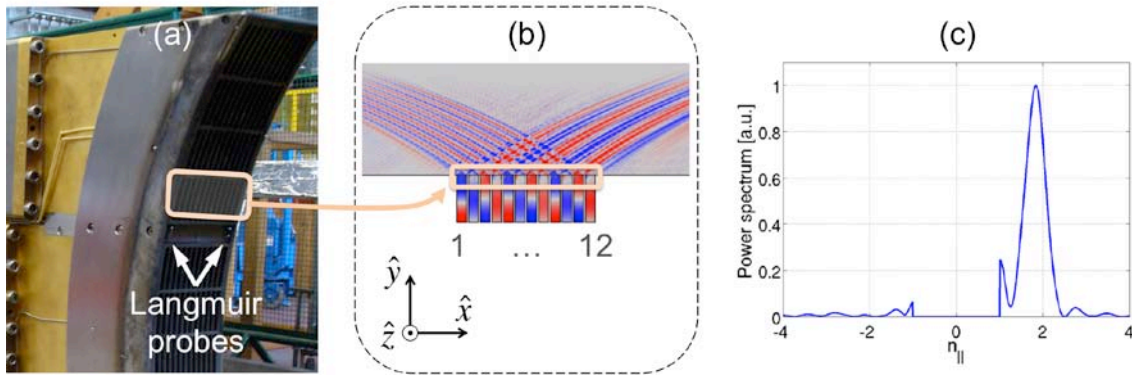


FIG. 1 – Real antenna (a), simulated geometry with E_x overlay (b) and normalized power spectrum (c) when edge density is $2.5 \times 10^{18} \text{ m}^{-3}$.

III. APPLICATION AND VALIDATION

One row of the FTU, 8 GHz conventional grill has been simulated: it is an array of twelve, reduced size, rectangular, active waveguides (width = 4.2 mm, septum = 0.8 mm). Measured reflection coefficients have been taken from the bottom row of the upper grill installed in the FTU 2nd port (see Fig. 1a). This choice was driven by several reasons like the gyrotron reliability, the attempt of avoiding rows with stronger poloidal curvature and the availability and closeness of Langmuir probes.

The operational scenarios have been derived from the FTU shots whose experimental data have been used for the tool validation. They are characterized by a toroidal magnetic field of 5.9 T and a waveguide phasing of 90 deg, giving a power spectrum peaked at $n_{\parallel} \cong 1.88$. As for the edge electron density, eight different values, varying in the range $[0.8 \div 6] \times 10^{18} \text{ m}^{-3}$, have been used. The other parameters of Eq. (1) have been estimated by fitting measured density profiles.

In Fig. 1 simulated geometry, including the parallel electric field overlay, and calculated power spectrum are also reported for one of the simulated scenarios. Two waves launched from the grill can be seen clearly: that traveling towards the right is the main peak of spectrum.

The comparison between measured and COMSOL-predicted average reflection coefficients is reported in Fig. 2. Taking into account the uncertainties of measurement, the difficulties in density profile estimation and the model approximations, the agreement can be considered as good.

IV. CONCLUSION AND PERSPECTIVES

Guidelines on the implementation of a tool for antenna-plasma coupling calculations at LH frequencies through COMSOL Multiphysics™ have been given. The tool has been used to simulate one row of the FTU LH conventional grill in some realistic operational scenarios. Results are

compared to experimental data in terms of average reflection coefficient, showing good agreement.

As next steps, the tool could be enhanced to handle tilted magnetic fields with respect to the antenna axis or, on a long-term scale, to introduce non-linear phenomena at the plasma edge.

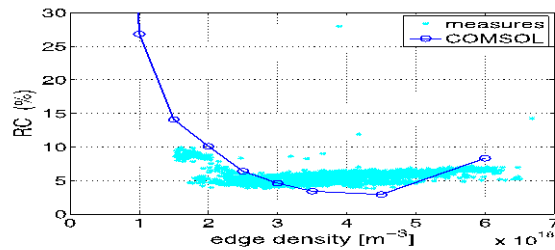


FIG. 2 – Comparison between measured and predicted average reflection coefficient for all simulated scenarios.

REFERENCES

- [1] P. Lallia, “A LHR heating slow wave launching structure suited for large toroidal experiments”, *2nd Topical Conference on RF Plasma Heating*, 1974, Lubbock, USA, 7pp.
- [2] M. Brambilla, “Slow-wave launching at the lower hybrid frequency using a phased waveguide array”, *Nuclear Fusion*, vol. 16(1), pp. 47–54, Feb. 1976.
- [3] M.A. Irzak, and O.N. Shcherbinin, “Theory of waveguide antennas for plasma heating and current drive”, *Nuclear Fusion*, vol. 35(11), pp. 1341–1356, Nov. 1995.
- [4] J. Hillairet, D. Voyer, A. Ekedahl, M. Goniche, M. Kazda, O. Meneghini, D. Milanesio, and M. Preynas, “ALOHA: an advanced LOWER hybrid antenna coupling code”, *Nuclear Fusion*, vol. 50(12), Dec. 2010, 17pp.
- [5] D. Milanesio, O. Meneghini, R. Maggiore, S. Guadamuz, J. Hillairet, V. Lancellotti, and G. Vecchi, “TOPLHA: an accurate and efficient numerical tool for analysis and design of LH antennas”, *Nuclear Fusion*, vol. 52(1), Jan. 2012, 7pp.
- [6] M.C. Kaufman, “Lower Hybrid experiments using an interdigital line antenna on the reversed field pinch”, Ph. D. in Physics at the University of Wisconsin-Madison, 2009.
- [7] O. Meneghini, S. Shiraiwa, and R. Parker, “Full wave simulation of lower hybrid waves in Maxwellian plasma based on the finite element method”, *Physics of Plasmas*, vol. 16(9), Sep. 2009, 4pp.

NOVEL INKJET-PRINTED SUBSTRATE INTEGRATED WAVEGUIDE (SIW) STRUCTURES FOR ECO-FRIENDLY LOW-COST APPLICATIONS

Riccardo Moro⁽¹⁾, Sangkil Kim⁽²⁾, Maurizio Bozzi⁽¹⁾, Manos Tentzeris⁽²⁾

⁽¹⁾ Dipartimento di Ingegneria Industriale e dell'Informazione,
University of Pavia, 27100 Pavia, Italy
riccardo.moro@unipv.it , maurizio.bozzi@unipv.it

⁽²⁾ Georgia Institute of Technology, Atlanta, GA 30309 USA
ksangkil3@gatech.edu , etentze@ece.gatech.edu

Abstract

The implementation of Substrate Integrated Waveguide (SIW) structures in paper-based inkjet-printed technology is presented in this paper for the first time. SIW interconnects and components have been fabricated and tested on a multilayer paper substrate, which permits to implement low-cost and eco-friendly structures. Paper-based fabrication appears very suitable for the realization of SIW components, as it allows for arbitrary geometry, conformal shape, and multilayered configuration. Paper is a widely available, low cost material and, moreover, it is environmental friendly: for this reason, it is currently investigated for several potential applications in wireless systems and wearable devices.

Index Terms—Substrate integrates waveguide, paper-based inkjet-printed technology, eco-friendly material.

I. INTRODUCTION

The realization of planar microwave circuits (in microstrip or coplanar technology) is traditionally based on the chemical etching of plastic or ceramic substrates, metalized on both faces. This fabrication technique produces a significant environmental impact, both during the production of the circuit and at the end of its life-time. For this reason, since long time there is a significant activity aiming to reduce the environmental impact of the fabrication of electronic circuits [1]. Among the proposed solutions, the use of paper looks like a good candidate. Paper is a widely available and very low cost material, and above all it is completely eco-friendly, both during its production that at the time of its disposal. The implementation of electronic circuits on paper can be performed by ink-jet printing [2], with no need of chemical etching or use of acids.

In this paper, the implementation of substrate integrated waveguide (SIW) components on paper substrates is presented for the first time. SIW structures are similar to traditional rectangular waveguides, and are implemented in dielectric substrates by using two rows of metalized holes that connect the two ground planes of the substrate [3]. The main advantage of SIW technology is the possibility to monolithically integrate all

components in a single substrate, with no need of interconnects or transitions between elements fabricated with different technologies. This feature dramatically reduces losses and parasitic, according to the “System on Substrate” (SoS) concept. SIW technology combines the advantages of classical microstrip circuits (low cost, easy fabrication, compact size, low weight) and metallic waveguides (low losses, complete shielding, high power handling capability).

II. PAPER-BASED INK-JET PRINTED TECHNOLOGY

Ink-jet printed technology is adopted to fabricate SIW structures on paper substrate. It does not produce any byproducts because it drops conductive ink on the desired position while conventional etching technique subtracts metals from the substrate surface using strong acids. Therefore, the ink-jet printing is cost effective and environmentally friendly [2].

The procedure is simple: the printer produces a droplet of conductive ink from a nozzle (typically silver, chosen for its high conductivity), which is placed in the desired position. This procedure guarantees a resolution in the order of 20 μm , which is compatible with many microwave circuits. The paper used for this application is commercially available and must have a hydrophobic coating. The thickness of a single paper layer is around 230 μm and multilayer configurations can be achieved by heat bonding. The electromagnetic characteristics of the paper were measured in the frequency range 0.5-2.5 GHz, obtaining a relative dielectric permittivity in the order of 3.2-3.3 and a loss angle of about 0.07. For the fabrication, the DMP2800 ink-jet printer with the Dimatix 10 pL cartridge (DMC-11610) was used. Cabot conductive ink CCI-300 was jetted at a temperature of 36°C, while the paper substrate was maintained at 50°C. The printed pattern was sintered in a thermal oven for 8 hours at 120°C. After sintering, the pattern has consistent DC conductivity in the range 9×10^6 S/m~ 1.5×10^7 S/m [4]. It is possible to realize metalized holes in the paper substrate: the procedure requires making the holes by a micro-drill, filling them with silver epoxy, and finally sintering the conductor ink (Fig. 1).



FIG. 1–Fabrication procedure to realize metalized holes.

III. PRELIMINARY IMPLEMENTATION OF PAPER-BASED SIW COMPONENTS

As a first step, straight SIW interconnects on paper have been implemented. The SIW lines have been designed for operation frequency of 5 GHz. This performance is achieved by selecting the geometrical parameters of the SIW structure: the width of the SIW is $w=24$ mm, the diameter of metal vias is $d=0.8$ mm and their longitudinal spacing is

$s=1.6$ mm. The substrate thickness is 0.69 mm, which is obtained by stacking 3 layers of paper; this thickness has been chosen to reduce the conductor loss, due to the relative low conductivity of the ink [3].

The design of SIW structures has been performed by using the full-wave electromagnetic simulator Ansys HFSS. The design of the SIW interconnects includes the transitions from 50- Ω microstrip line to SIW to allow the experimental characterization. The structures have been designed, considering the relative dielectric permittivity $\epsilon_r=3$, the loss tangent $\tan\delta=0.06$, and the ink conductivity $\sigma=1.5 \cdot 10^7$ S/m. Three transmission lines with different length (13, 20, and 27 unit cells, respectively) have been fabricated Fig. 2(a).

The electrical characteristics of the material have been experimentally verified by comparing the measured scattering parameters of two SIW interconnects with different length, according to the method described in [5]. The measured data permitted to determine the propagation constant of the SIW, and therefore the permittivity of the dielectric substrate, which results close to the nominal value of $\epsilon_r = 3$ over the entire frequency band of interest. In addition, the attenuation was estimated: the insertion loss of the SIW is 0.85 dB/cm at 5 GHz, while each microstrip-to-SIW transition and connector introduces an additional attenuation of approximately 0.2 dB. The comparison between simulations and measurements is reported in Fig. 2(b), in the case of the shortest interconnect.

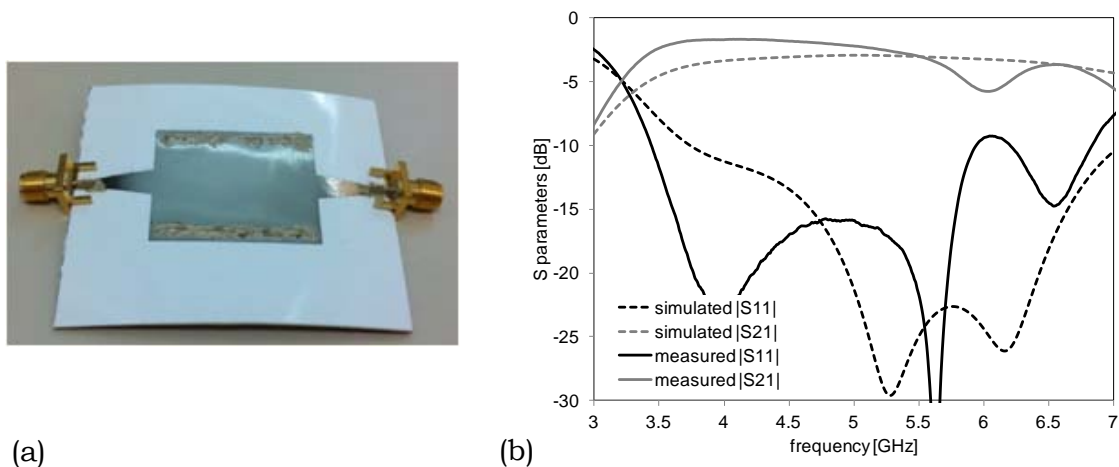


FIG. 2–(a) Photograph of the SIW transmission line. (b) Simulated and measured scattering parameters of SIW transmission line.

Furthermore, an SIW two-pole filter has been designed, fabricated and measured, to investigate the feasibility of SIW components on paper substrate. The filter includes two cavities, connected by an iris coupling aperture, and the dimensions are optimized for band-pass operation around 5 GHz (Fig. 3(a)). The simulated and measured frequency response of the component is reported in Fig. 3(b), with a measured insertion loss of approximately 5 dB at 5 GHz.

These results demonstrate how the performance of the filter is affected by the significant losses of the material. For this reason, the most suitable

filter topology needs to be carefully selected, and possibly configurations based on the pre-distorted concept need investigated [6].

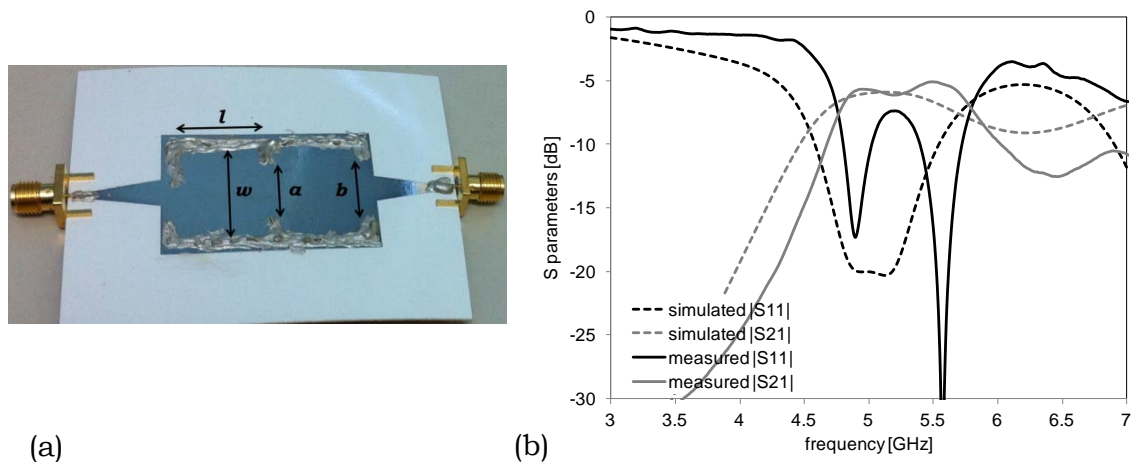


FIG. 3—(a) Photograph of the SIW filter ($w=24$ mm, $a=14.27$ mm, $b=15.89$ mm, $l=19.17$ mm). (b) Simulated and measured scattering parameters of SIW filter.

IV. CONCLUSION

SIW interconnects and components have been implemented by ink-jet printing on paper substrate for the first time. Straight interconnects and a filter have been fabricated and tested, demonstrating the applicability of paper-based technology to SIW structures.

While the achievable performance of paper-based SIW components is still inferior to components based on commonly used dielectric material, the implementation of SIW structures on paper substrate represents a significant step: it is the groundwork for future wireless systems and wearable devices, as it combines the advantages of low cost, flexible and eco-friendly material with the integration potential of SIW technology.

REFERENCES

- [1] D. Harrison et al., "Novel circuit fabrication techniques for reduced environmental impact," International Conference on Clean Electronics Products and Technology, pp. 174-175, 1995.
- [2] V. Lakafosis et al., "Progress Towards the First Wireless Sensor Networks Consisting of Inkjet-Printed, Paper-Based RFID-Enabled Sensor Tags," Proc. IEEE, vol. 98, no. 9, pp. 1601-1609, Sept. 2010.
- [3] M. Bozzi, A. Georgiadis, and K. Wu, "Review of Substrate Integrated Waveguide (SIW) Circuits and Antennas," IET Microwave Antennas and Propagation, Vol. 5, No. 8, pp. 909-920, June 2011.
- [4] G. Shaker et al., "Inkjet Printing of Ultrawideband (UWB) Antennas on Paper-Based Substrates," IEEE AWPL, Vol. 10, pp. 111-114, 2011.
- [5] F. Xu and K. Wu, "Numerical multimode calibration technique for extraction of complex propagation constants of substrate integrated waveguide," IEEE MTT-S Int. Microwave Symp., 2004.
- [6] F. Mira et al., "Substrate Integrated Waveguide Predistorted Filter at 20 GHz," IET MAP, Vol. 5, No. 8, pp. 928-933, June 2011.

PRELIMINARY STUDIES ON THE MICROWAVE PRE-TREATING OF LIGNOCELLULOSIC BIOMASSES

A. Facchini⁽¹⁾, A. Zeffiro⁽²⁾, P. Arcioni⁽¹⁾, A. Buttafava⁽²⁾

- (1) Dipartimento di Ingegneria Industriale e dell'Informazione, University of Pavia, Via Ferrata 1, 27100 Pavia, Italy
andrea.facchini01@ateneopv.it
- (2) Dipartimento di Chimica Generale, University of Pavia, Via Taramelli 12, 27100 Pavia, Italy
zeffiro.chem@gmail.com

Abstract

In this paper, a measurement setup to derive the complex permittivity of biomasses vs. temperature is presented. A TM_{010} cylindrical cavity resonator with heating system operating at 2.45 GHz has been designed. Complex permittivity is obtained by measuring transmission coefficient, while sample temperature is monitored by a thermocouple. Measurements of lignin, starch, cellulose and sewage sludge at room temperature are reported, as well as complex permittivity of lignin and cellulose in a temperature range of 25-200°C. Finally, the design of a microwave heater, intended to treat these materials in a pyrolysis process, is discussed.

Index Terms – Biomasses, complex permittivity measurement, microwave applicator, microwave processing.

I. INTRODUCTION

Recent studies have shown the positive effect of microwave heating to pretreat lignocellulosic materials and sewage sludge for the production of bioethanol [1-2]. It has been hypothesized that microwaves generate a rapid and selective heating, improving the destruction of structures that hinder the process of the digestion of lignocellulose. Cheapness and easy availability of commercial generators (magnetron) operating at 2.45 GHz, allow to think about applicators which take advantage of microwave heating to pretreat these materials. Designing applicators which maximize the interaction between microwaves and biomasses, requires the knowledge of their complex dielectric constant as a function of the temperature, data that are not readily available in the literature. For this reason we assembled an experimental setup, where a sample is placed into a cylindrical cavity (TM_{010} mode) and perturbation expressions are used to derive dielectric constant [3-5]. The cavity design allow for heating of the sample, to provide data at different temperatures. Connecting the cavity to a network analyzer HP 8510 through small loops and coaxial cables, the complex permittivity is obtained by elaborating the frequency dependent S-parameters around the resonating frequency of the cavity with and without sample, whereas the temperature of materials is observed with a thermocouple.

II. MEASUREMENT SETUP

Fig. 1 shows the TM_{010} cavity, used in the measurement setup. The cavity has a diameter of 94 mm and a height of 30 mm. The sample is placed in a quartz pipe (inner diameter = 4 mm; outer diameter = 5 mm), which is inserted into another quartz pipe (i.d. = 11 mm; o.d. = 12 mm), used to confine the heating flow. The quartz pipes are held in position along the axis of the cavity by two metal pipes (diameter of 12 mm and length of

20 mm). These dimensions have been chosen to reduce the leakage of the e.m. field from the cavity to a value that is so small that it doesn't affect the measurement.

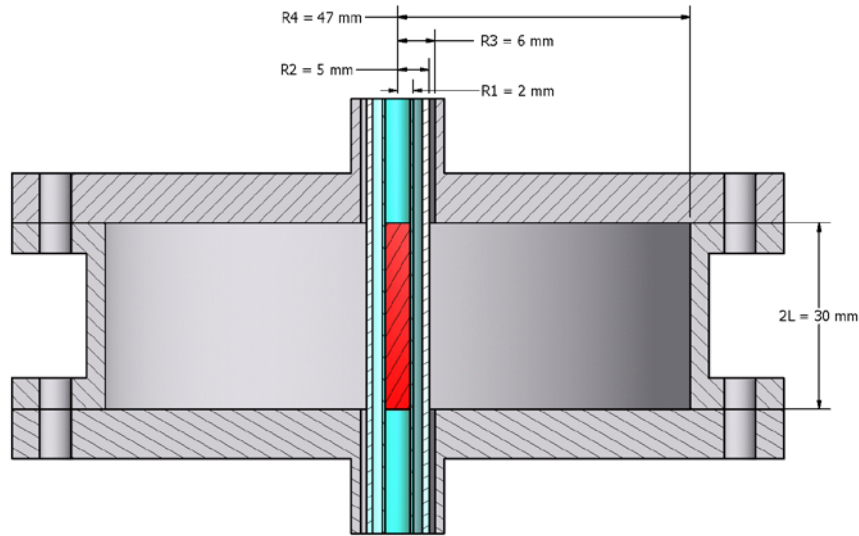


Fig. 1 The TM_{010} cylindrical cavity used in the measurement setup.

According to perturbation formulas [3-6] ϵ_r and $\tan\delta$ are obtained from the following expressions:

$$\epsilon_r = 1 + \frac{1}{a} \frac{f_0 - f_1}{f_1} \left(\frac{D}{d}\right)^2 \qquad \tan\delta = \frac{1}{2a\epsilon_r} \left(\frac{D}{d}\right)^2 \left(\frac{1}{Q_{u1}} - \frac{1}{Q_{u0}}\right)$$

where the constant a has a value of 1.855 for the mode TM_{010} , D is the cavity diameter, d is the sample diameter, and f_1 , Q_{u1} , f_0 , Q_{u0} are the resonant frequency and the unloaded quality factor measured for the cavity with and without sample, respectively.

To speed-up the measurement procedure, S-parameters are recorded by a simple LabView package, which also performs all the computation and stores the measured values into a file. Fig. 2 shows a typical set of values of S_{21} vs. frequency recorded by the package.

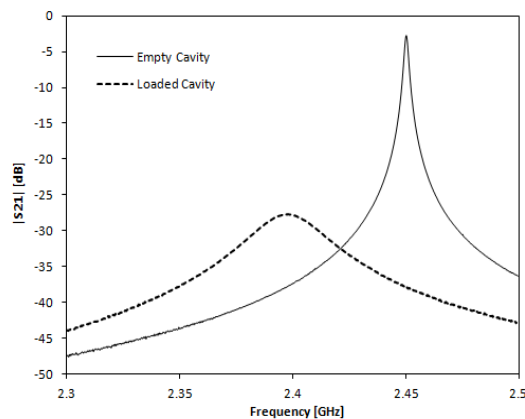


Fig. 2 Frequency response of the cavity with and without sample.

III. MEASURED RESULTS

Complex permittivity of typical sample of lignin, starch, cellulose and sewage sludge at room temperature are reported in Table I. These values are in good agreement with those reported in the literature for cellulose and starch [8-9].

Table I. Relative permittivity and loss tangent of some biomasses.

Material	ϵ_r	$\tan\delta$ ($\times 10^2$)
Lignin	1.885	3.04
Microcrystalline Cellulose	1.577	4.97
Starch	2.668	11.15
Sewage Sludge	5.407	16.69

Fig. 3 shows the complex permittivity vs. temperature in the case of lignin and fibrous cellulose. In both cases, loss tangent initially decreases with increasing temperature, due to water loss (this effect is more evident in the lignin sample, which had a higher water content at room temperature). At higher temperature, both relative permittivity and loss tangent increase with temperature, a fact that may cause thermal runaway during treatment [7].

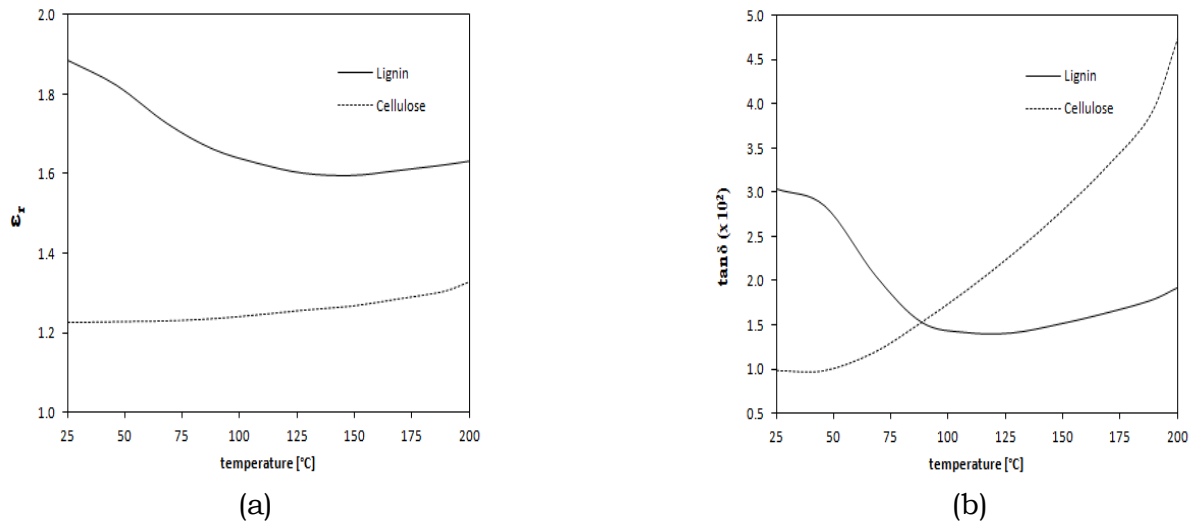


Fig. 3 Relative permittivity (a) and loss tangent (b) vs. temperature of lignin and cellulose.

IV. MICROWAVE APPLICATOR

On the basis of the measured permittivity of biomasses, a microwave reactor has been designed, to treat small quantities of material (~50 cc) inserted in a dielectric vessel. The applicator has to be connected to a commercial microwave generator working at 2.45 GHz with adjustable power output. The vessel is exposed to the e.m. field inside a short circuited rectangular waveguide (WR 340). An inductive iris and an adjustable tuning screw are used to minimize the reflection coefficient when different biomasses are inserted into the vessel. Fig. 4 shows the designed applicator (the lateral wall of the waveguide is transparent to show the inside of the structure). The vessel is included into a shielding structure to prevent leakage of e.m. field. To allow for monitoring of pressure and temperature of the biomass, two dielectric probes can be inserted into the vessel through small metal pipes, designed as waveguide well below cutoff at the operating frequency. At present, the structure is under manufacturing. Results of its testing will be presented at the conference.

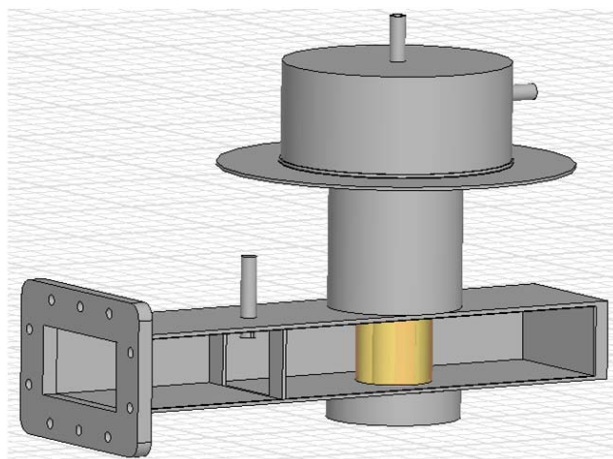


Fig. 4 Microwave Heater.

REFERENCES

- [1] Z. Hu and Z. Wen, "Enhancing enzymatic digestibility of switchgrass by microwave-assisted alkali pretreatment," *Biochem. Eng. J., Elsevier*, (2008), vol. 38, Issue 3, pp. 369–378.
- [2] S. Zhu, et al., "Pretreatment by Microwave/Alkali of Rice Straw and its Enzymic Hydrolysis," *Byosyst. Eng.* (2005), 93(3), 279-283.
- [3] H. Kawabata, T. Kobayashi, Y. Kobayashi and Z. Ma, "Measurement accuracy of a TM_{0m0} mode cavity method to measure complex permittivity of rod samples," *Microwave Conference, 2006. APMC 2006. Asia-Pacific*, vol., no., pp.1465-1470, 12-15 December 2006.
- [4] H. Kawabata, Y. Kobayashi, "Accurate measurements of complex permittivity of liquid based on a TM_{010} mode cylindrical cavity method," *Microwave Conference, 2005 European*, vol.1, no., pp.4, 4-6 October 2005.
- [5] H. Kawabata, H. Tanpo and Y. Kobayashi, "An improvement of the perturbation method for the complex permittivity measurements of liquids," in *Proceedings of the 2003 Asia-Pacific Microwave Conference*, WEP-65, pp.576-579, Seoul, November 2003.
- [6] H.E. Bussey and A.J. Estlin, "Errors in Dielectric Measurements Due to a Sample Insertion Hole in a Cavity," *Microwave Theory and Techniques, IRE Transactions on*, vol.8, no.6, pp.650-653, November 1960.
- [7] A.C. Metaxas, *Foundations of electroheat a unified approach*: John Wiley and Sons, 1996.
- [8] P.-F. Sung, Y.-L. Hsieh, K. Angonese, D. Dunn, R. J. King, R. Machbitz, A. Christianson, W. J. Chappell, L. S. Taylor, and M. T. Harris, (2011), "Complex dielectric properties of microcrystalline cellulose, anhydrous lactose, and α -lactose monohydrate powders using a microwave-based open-reflection resonator sensor," *Journal of Pharmaceutical Science*, vol.100, pp. 2920–2934, July 2011.
- [9] M.K. Ndife, G. Şumnu, L. Bayindirli, "Dielectric properties of six different species of starch at 2450 MHz," *Food Research International*, vol.31, Issue 1, pp. 43-52, January 1998.

Poster session I

S. Ceccuzzi, S. Meschino

The role of evanescent modes excited inside the longitudinal corrugations of mode filters

F. Di Murro, M. Lucido, and F. Schettino

Electromagnetic scattering by a finite metallic cylinder

P. Imperatore, A. Iodice, and D. Riccio

Volume and roughness scattering effects: a unified perturbative approach

N. Tedeschi

Deep penetration of inhomogeneous plane waves in lossy media

F. Corsetti, M. Lucido, and G. Panariello

Analysis of propagation in coupled polygonal cross-section dielectric waveguides

P. Imperatore, A. Iodice, and D. Riccio

Perturbative approach for scattering in random media via distribution theory for discontinuous test functions

F. Chiadini, V. Fiumara, and A. Scaglione

A synthesis method for multi-section devices

A. Iodice, A. Natale, and D. Riccio

A novel interpretation for the Kirchhoff scattering from classical and fractal surfaces

G. Gradoni, T.M. Antonsen, and E. Ott

Random coupling model for wave chaotic cavities

L. Di Donato, D.A.M. Iero, I. Catapano, L. Crocco, G. Sorbello, and T. Isernia

Two approaches to field focusing in unknown environments

L. La Spada, R. Iovine, F. Bilotti, and L. Vegni

Infrared absorption measurements using metamaterials

F. Frezza, P. Nocito, and E. Stoja

A study on the fundamental mode characteristics sustained by the plasmonic slot waveguide

R. Ana Perez-Herrera, E. Coscelli, M. Sozzi, A. Cucinotta, S. Selleri, and M. Lopez-Amo
YB - doped photonic crystal fiber laser

C. Molardi, Masruri, E. Coscelli, F. Poli, A. Cucinotta and S. Selleri

FEM solver optimization for PCF design

A. C. Lesina, A. Vaccari, and A. Bozzoli

A modified RC - FDTD algorithm for plasmonics in Drude dispersive media

F. Baronio, M. Conforti, M. Levenius, K. Gallo, V. Pasiskevicius, F. Laurell, and C. De Angelis

Broadband optical parametric generation in LiTaO₃

R. Tumolo, S. Immediata, G. Russo, M. D'Urso, and L. Timmoneri

Wind farm impact of primary radars

P. Vinetti, M. D'Urso, M. Dispenza

Embedded photonic sensor networks for large arrays diagnostic

THE ROLE OF EVANESCENT MODES EXCITED INSIDE THE LONGITUDINAL CORRUGATIONS OF MODE FILTERS

S. Ceccuzzi^(1,2) and S. Meschino⁽²⁾

⁽¹⁾ Euratom-ENEA Association for fusion, C.R. Frascati
Via Enrico Fermi 45, 00044, Frascati, Italy

⁽²⁾ Applied Electronics Department, “Roma Tre” University
Via della Vasca Navale 84, 00146 Rome, Italy
silvio.ceccuzzi@enea.it

Abstract

Mode filters for high-power oversized rectangular waveguides are usually based on corrugations partially filled with absorbing materials. In this paper the modal content excited at the input of longitudinal corrugations is calculated through an approximate model, whose reliability and limitations are assessed by comparison with a full-wave commercial code.

Wave amplitudes inside the absorbing material and power loss by Joule effect are computed by enforcing proper boundary conditions. Modes under cut-off are demonstrated to contribute to the total absorption when the lossy dielectric is located close enough to the waveguide slots. Useful guidelines for the design of mode filters are derived.

Index Terms – Corrugation, high-power microwaves, mode filter.

I. INTRODUCTION

High-power microwave transmissions over long distances are realized through oversized waveguides in a number of applications like fusion engineering and accelerators. Even with a careful design of the relevant components, spurious modes are unavoidably excited and propagate, owing to the intrinsic overmoded nature of these transmission structures.

Mode filters are intended for absorbing the unwanted modal content, avoiding dangerous effects like trapped mode resonances. At high power corrugated waveguides, with corrugations partially filled with an absorbing material, are generally used. Their study, started and soon abandoned in the 1960s [1], has been recently resumed within the conceptual design of a 5 GHz heating and current drive system for the International Thermonuclear Experimental Reactor (ITER) [2, 3].

In this scenario, a first approximate theoretical model was proposed in [4], where filter performance has been directly related to the reflection of modes propagating inside the corrugations. Here the role of under cut-off modes, excited at waveguide slots, is investigated using a rectangular waveguide with a longitudinal corrugation as a test case. Results can be generalized to different configurations.

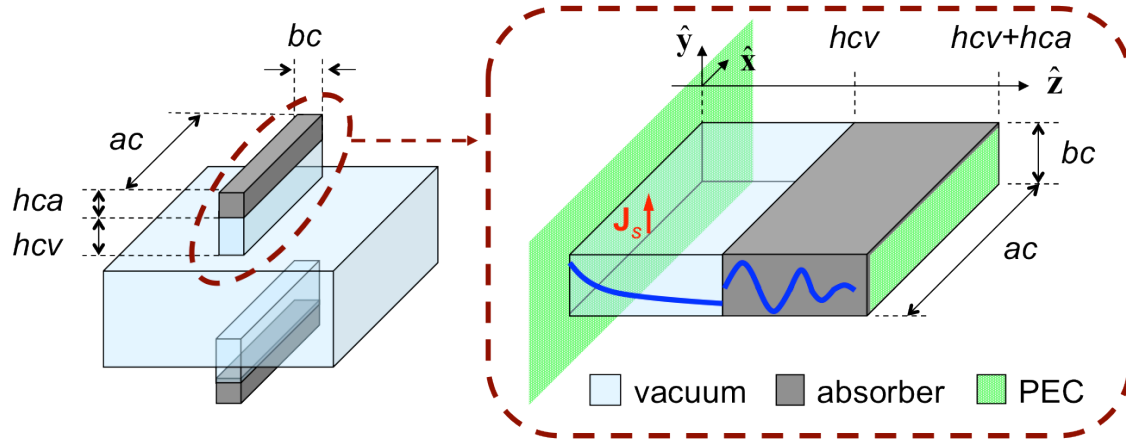


FIG. 1 – Reference geometry.

II. MODE EXCITATION

The leading idea behind this study is that modes under cut-off in vacuum-filled waveguides exhibit an imaginary part in their propagation constant (k_{zn}) when crossing lossy dielectrics. Referring to the geometry depicted in Fig. 1, these waves undergo an exponential decay in the vacuum region of the corrugation, but, if they reach the absorbing material without being excessively attenuated, they can give an effective contribution to the total absorption.

Modes excited at the input of the corrugation can be estimated starting from the magnetic field distribution at the wall of the un-slotted waveguide (perturbation method). The field for $z > 0$ can be expressed as a summation over all possible TE and TM modes with eigenvectors \mathbf{h}_{zn} and \mathbf{e}_{zn} respectively:

$$\mathbf{E} = \sum_n C_n^+ (\mathbf{e}_n + \mathbf{e}_{zn}) e^{-k_n z} + C_n^- (\mathbf{e}_n - \mathbf{e}_{zn}) e^{k_n z}$$

$$\mathbf{H} = \sum_n C_n^+ (\mathbf{h}_n + \mathbf{h}_{zn}) e^{-k_n z} + C_n^- (-\mathbf{h}_n + \mathbf{h}_{zn}) e^{k_n z}$$

where C_n^+ and C_n^- represent the unknown amplitudes of forward and backward waves. By filling the half-space enclosing the main waveguide ($z < 0$) with a perfect electric conductor (PEC), equivalent surface currents can be derived as $\mathbf{J}_s = 2 \cdot \hat{\mathbf{z}} \times \mathbf{H}|_{\text{wall}}$. At this point, the wave amplitudes C_n^+ can be approximately derived by an application of the Lorentz reciprocity formula as follows [5]:

$$C_n^+ = -\frac{1}{P_n} \int_{\text{slot}} \mathbf{E}_n^- \cdot \mathbf{J}_s dS \quad \text{being} \quad P_n = 2 \int_{\text{slot}} \mathbf{e}_n \times \mathbf{h}_n \cdot \hat{\mathbf{z}} dS$$

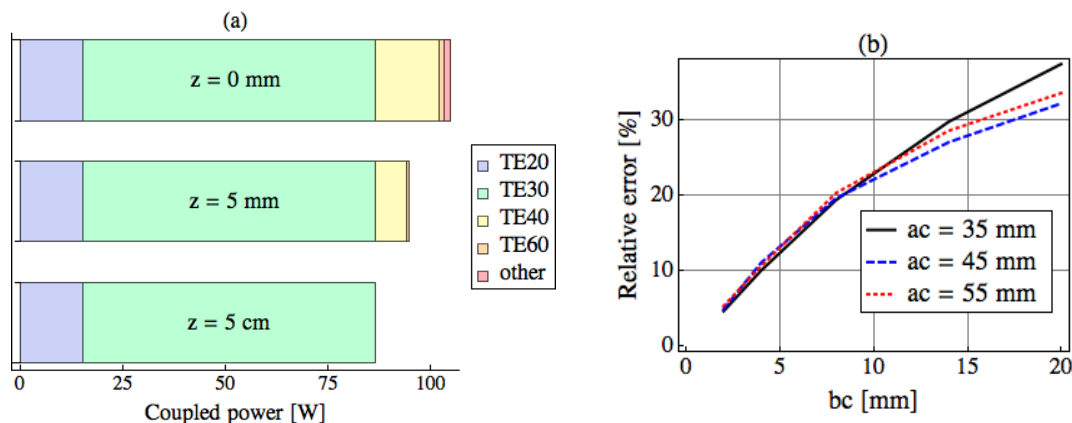


FIG. 2 – (a) Modal content excited by the TE_{20} mode (1 kW) in a corrugation with $ac = 100$ mm and $bc = 5$ mm. (b) Relative error between the TE_{20} -to- TE_{10} coupling predicted by this model and HFSS for different slot sizes.

This model has been applied to a standard waveguide WR-430 (cross-section 109.22 mm x 54.61 mm), working at 5 GHz and provided with a longitudinal slot having $ac = 100$ mm and $bc = 5$ mm. In this situation only 3 modes are above cut-off in the corrugation, namely the TE_{10} , TE_{20} and TE_{30} . The wave amplitudes of 150 modes with the lowest cut-off frequency have been calculated assuming that the main waveguide is fed with 1 kW of the TE_{20} mode. Results are reported in Fig. 2a: it can be observed that a significant part of the power (almost 30%) is coupled to evanescent modes, in particular the TE_{40} , that exponentially decay going away from the aperture.

Similar computations have been performed when the WR-430 is fed by the TE_{01} mode that, together with the TE_{20} , is the main responsible for the excitation of longitudinal corrugations. These two modes are degenerate in the WR-430 and their \mathbf{H} patterns are very similar close to the slot, so they excite the same modes.

Performed calculations are not self-consistent since wave amplitudes are derived from the unperturbed magnetic field in the main waveguide, but they are expected to be meaningful if corrugations are thin enough. Their reliability has been indeed checked as compared to a finite element solver (i.e., HFSSTM) and shown in Fig. 2b.

III. MODE ABSORPTION

The electromagnetic field in the absorber of Fig.1 is given by an infinite set of TE and TM modes, whose wave amplitudes can be calculated by using the proper boundary conditions as in [4]. Once they have been derived, the power loss in the lossy dielectric can be computed. It has been done for the same case of Fig. 2a, using a doped Silicon Carbide (SiC) as absorbing material.

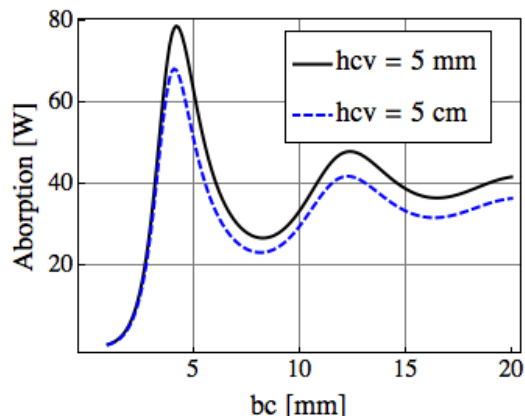


FIG. 3 – Power absorption versus corrugation width for different vacuum depths when the main waveguide is fed by a TE_{20} of 1 kW. Silicon Carbide ($\epsilon_r = 13.5$, $\tan \delta = 0.44$) has been used as absorber.

Results are plotted in Fig. 3, where the evanescent TE_{40} mode is seen to enhance the total absorption of a 15 %, when the vacuum section of the corrugation is thin enough.

IV. CONCLUSIONS

Evanescence modes coupled into a longitudinal corrugation from a rectangular waveguide have been demonstrated to play a role in the performances of mode filters, when the absorbing material is close enough to the slot. Their amplitudes have been estimated through an approximate model based on the perturbation method, whose reliability has been compared with a full-wave solver.

REFERENCES

- [1] H.J. Butterweck, "Mode Filters for Oversized Rectangular Waveguides", *IEEE Transactions on Microwave Theory and Techniques*, vol. 16(5), pp. 274-268, May 1968.
- [2] S. Meschino, S. Ceccuzzi, F. Mirizzi, L. Pajewski, and G. Schettini, "Microwave components for the lower hybrid transmission line of ITER", *Asia-Pacific Microwave Conference Proc.*, Dec. 7-10 2010, Yokohama, Japan, 4pp.
- [3] F. Mirizzi, and S. Ceccuzzi, "Optimized bends and mode filters for the main Transmission Lines of an ITER-relevant LHCD system", *24th Symposium on Fusion Engineering*, Jun. 26-30 2011, Chicago, USA, pp. 1-5.
- [4] S. Ceccuzzi, S. Meschino, F. Mirizzi, and G. Schettini, "Mode Filters for Oversized Corrugated Rectangular Waveguides", *XVIII Riunione Nazionale di Elettromagnetismo*, Sep. 6-10 2010, Benevento, Italy, 4pp.
- [5] R.E. Collin, "Foundations for Microwave Engineering," 2nd ed., John Wiley & Sons Inc, Hoboken NJ, 2001, pp. 276-281.

ELECTROMAGNETIC SCATTERING BY A FINITE METALLIC CYLINDER

F. Di Murro⁽¹⁾, M. Lucido⁽¹⁾, F. Schettino⁽¹⁾

⁽¹⁾ DIEI, Università degli Studi di Cassino e del Lazio Meridionale
Via G.Di Biasio 43, 03043 Cassino, Italy
schettino@unicas.it

Abstract

A full wave analysis of the electromagnetic scattering by a finite metallic cylinder is presented. The Electric Field Integral Equation (EFIE) related to the problem is solved by means of the Method of Moments (MoM) employing entire domain basis functions. Such functions have been chosen so as to reconstruct the correct edge behavior of fields and currents near the sharp edges of the cylinder. As a consequence, fast convergence of the series is obtained, only few expansion terms being necessary to achieve prescribed accuracy.

Index Terms □ Method of Moments, scattering, finite cylinder.

I. INTRODUCTION

The analysis of the electromagnetic scattering by 3D conducting objects is usually addressed by means of integral equation methods, solved resorting to Finite Elements (FE). It is well known that the presence of sharp edges leads to inaccuracies and/or instabilities in the solution, making it necessary the introduction of suitably modified elements near the edge [1]-[3].

This contribution is aimed at proposing a MoM formulation of the scattering by a PEC finite cylinder employing entire domain basis functions reconstructing the correct edge behavior of the electromagnetic field. The factorization of the singular behavior of the electromagnetic field at edges leads to a fast converging series, thus leading to a very small dimension of the scattering matrix and therefore of the computational effort needed.

The formulation of the problem and the expansion adopted are briefly presented in Section II. Some results showing the fast convergence of the method are given in Section III, whilst conclusions are drawn in Section IV.

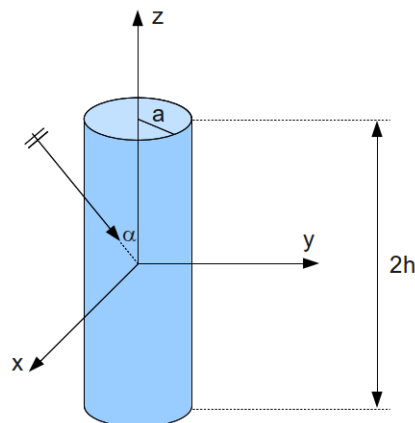


Fig. 1 - Geometry of the problem: a plane wave propagating in the xz plane impinges with an angle α onto a finite PEC cylinder of radius a and height $2h$.

II. FORMULATION OF THE PROBLEM

Let us consider a finite PEC cylinder, of radius a and height $2h$, as depicted in Fig. 1. The reference system is chosen so that the cylinder axis is along the z axis. A plane wave propagating in the xz plane impinges onto the cylinder with an angle α with respect to z axis. Due to cylindrical symmetry, the problem is formulated in cylindrical harmonics and solved separately for each harmonic. In particular an EFIE in the spectral domain has been obtained by imposing the boundary conditions on the cylinder surface for each harmonic of the electric field. As a matter of fact, the mentioned spectral domain is twofold: the Vector Hankel Transform (VHT) has been used for the components of fields and currents orthogonal to the z axis, and the Fourier Transform (FT) has been introduced for the fields and currents components along the z axis. Unfortunately due to the lack of space no more details of the formulation can be given here.

As outlined in the Introduction, we propose to solve the EFIE by means of Galerkin Method employing entire domain basis functions reconstructing the correct edge behavior of the fields and the surface currents. To this end, the Meixner conditions [4] prescribing the behavior of the electromagnetic fields near sharp edges have to be taken into account. Such conditions can be summarized in the following equation

$$J_{ir}(t), \frac{\partial J_{long}(t)}{\partial t} \underset{t \rightarrow 0}{\approx} t^{\frac{\psi - \pi}{2\pi - \psi}} \quad (1)$$

where $J_{ir}(t)$ and $J_{long}(t)$ are the surface current components transverse and longitudinal with respect to the wedge respectively, t is the distance from the wedge, and $\psi \leq 3\pi/2$ is the wedge angle. The longitudinal current edge behavior can be obtained by integrating Eq. (1) and taking into account that it has to be continuous across the wedge.

All the aforementioned requirements have been fulfilled in the adopted current expansions. As an example, the 0-th order harmonic currents on the disks and on the lateral cylinder, have been expanded by means of the following series

$$\begin{aligned} J_{disk}(r) &= r(1 - r^2/a^2)^\alpha \sum_{m=0}^{\infty} a_m P_m^{(1,\alpha)}(1 - 2r^2/a^2) \\ J_{cylinder}(z) &= (1 - z^2/h^2)^\beta \sum_{m=0}^{\infty} b_m C_m^{(\beta+1/2)}(z/h) \end{aligned} \quad (2)$$

where $P_m^{(a,b)}$ and $C_m^{(a)}$ are the Jacobi and Gegenbauer polynomials respectively, and α and β are parameters to be chosen so as to factorize the desired edge behavior. In particular they have to be chosen equal to $-1/3$ for the components which have to diverge on the wedge, and equal to $2/3$ for the remaining components. In order to enforce the continuity of the current components orthogonal to the wedge, the related expansions have to be supplemented by means of the following term

$$\chi(r, z) = \begin{cases} r/a & r \leq a \\ 0.5(z/h + 1) & -h \leq z \leq h \end{cases} \quad (3)$$

which can be obtained by Eq. (2) by using $\alpha=\beta=0$. It is worth noting that the current on the disk exhibits also the correct zero at the origin, as prescribed by the cylindrical harmonic expansion. The VHT of the disk current, as well as the FT of the cylinder current, can be analytically evaluated, so that the elements of the scattering matrix are single integrals to be numerically calculated.

The edge behavior factorized in expansions (2) dramatically speeds up the convergence of the series, as will be demonstrated by means of numerical results given in the following Section.

III. NUMERICAL RESULTS

Many simulations have been performed in order to verify the convergence of the method. Due to the lack of space only few results are shown here, for an incidence angle $\alpha = \pi/2$, and for the 0 order harmonic currents. In Fig. 2a and 2b the absolute value of the current coefficients are plotted, normalized to the first coefficient of the radial disk current, for different geometry dimensions in the TM case.

IV. CONCLUSION

An effective full-wave method for analyzing the scattering by a PEC finite cylinder has been presented. The method relies on the use of expansion functions reconstructing the correct behavior of the fields at edges, thus obtaining accurate results with only few expansion terms. In future work the generalization to the scattering by finite dielectric cylinders will be presented.

REFERENCES

- [1] N. Stevens, and L. Martens, "An efficient method to calculate surface currents on a PEC cylinder with flat end caps," *Radioscience*, vol. 38(1), pp. 6/1-6/10, 2003.
- [2] W.J. Brown, and D.R. Wilton, "Singular basis functions and curvilinear triangles in the solution of the electric field integral equation," *IEEE Transactions on Antennas and Propagation*, vol. 47(2), pp. 347-353, 1999.
- [3] M. Lucido, G. Panariello, and F. Schettino, "Electromagnetic scattering by multiple perfectly conducting arbitrary polygonal cylinders," *IEEE Transactions on Antennas and Propagation*, vol. 56(2), pp. 425-436, 2008.
- [4] J. Meixner, "The behavior of electromagnetic fields at edges," *IEEE Transactions on Antennas and Propagation*, vol. 20(4), pp. 442-446, 1972.

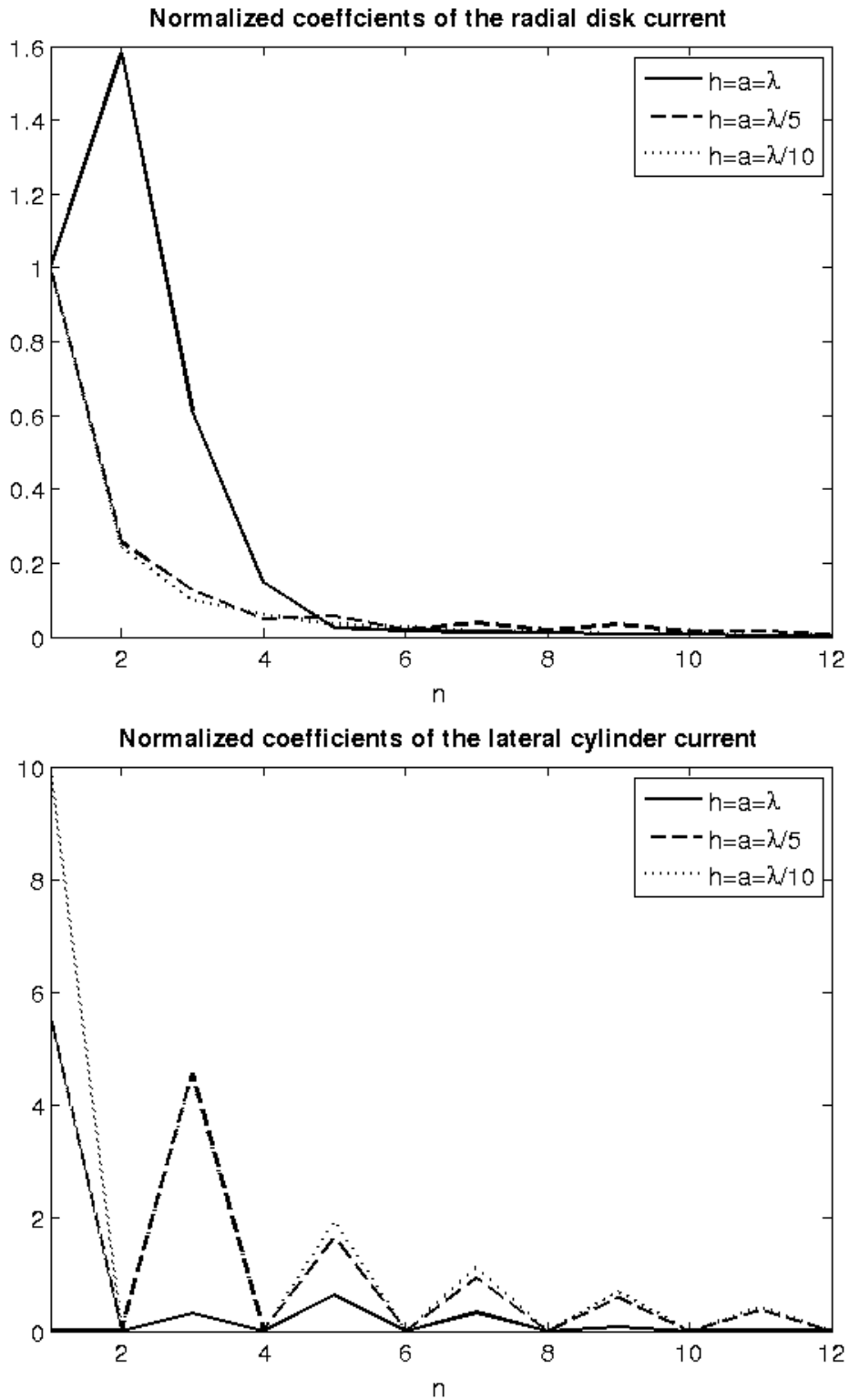


Fig. 2 – Absolute value of the normalized coefficients in the TM case for $\alpha = \pi/2$ and 0 order harmonic: a) radial disk current; b) longitudinal cylinder current.

VOLUME AND ROUGHNESS SCATTERING EFFECTS: A UNIFIED PERTURBATIVE APPROACH

P. Imperatore⁽¹⁾, A. Iodice⁽²⁾, D. Riccio⁽²⁾

⁽¹⁾ Istituto per il Rilevamento Elettromagnetico dell'Ambiente, Italian National Research Council (CNR), 80124 Napoli, Italy

⁽²⁾ Department of Biomedical, Electronic and Telecommunication Engineering, University of Naples "Federico II", 80125 Napoli, Italy

imperatore.p@irea.cnr.it

Abstract

We propose a comprehensive analysis for the evaluation of the scattering from randomly inhomogeneous semi-infinite media, including both interfacial roughness and volume inhomogeneities, by applying the methodological approach of the Volumetric Perturbative Reciprocal Theory (VPRT). An unifying perspective on the scattering phenomenon considered in its entirety is gained and an analytic scattering model is obtained.

Index Terms – Electromagnetic scattering, random media, perturbation theory.

I. INTRODUCTION

Whenever the scattering phenomena occur in actual media, whose volume structure can be inhomogeneous and possibly stratified, the scattering contributions arising from both interfacial roughness and volume inhomogeneities should be taken into account, because the electromagnetic waves significantly penetrate inhomogeneous media as roughly predicted by the values of the penetration depth. In order to properly establish a complete formulation for the relevant problem, including jointly both interfacial and volumetric scattering phenomena in the analytical investigation, we adopt the methodological approach of the Volumetric Perturbative Reciprocal Theory (VPRT) that was introduced in [1]-[2], which offer a certain inherent analytical convenience and can be effectively applied to the considered problem. Accordingly, we derive the formalism necessary for the theoretical description of the scattering processes, providing a mathematically consistent scheme that has the important result of the uniformity in the treatment of the two different types of scattering phenomena.

Therefore, in this paper we propose a comprehensive perturbative analysis for the evaluation of the scattering from randomly inhomogeneous semi-infinite media. The developed unified perturbative formulation permits to treat consistently both these mentioned

inhomogeneities and evaluate on an analytic playground, in the weak fluctuation approximation, the contributions pertinent to the two corresponding scattering mechanisms involved in a unitary theoretical framework.

We first introduce a proper description for the specific spatial 3D structure considered in this paper. Then, a general expression for the first-order scattering field is obtained by applying VPRT formulation. The obtained perturbative solution is given in closed-form for a bi-static configuration, clearly showing the common underlying analytical structure for both the scattering processes. Finally, the analytical solution is expressed in terms of the experimentally relevant quantities such as the scattering cross sections, whose expressions are directly related in terms of microscopic entities such as the structural correlation functions. Numerical simulation results are provided with reference to a canonical case.

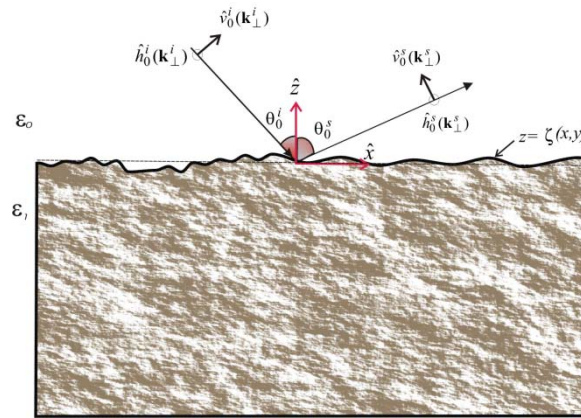


FIG. 1 – Geometry of the scattering problem: Bistatic configuration.

II. SCATTERING FORMULATION

The considered structure (Fig.1) can be regarded as obtained by a proper perturbation of the unperturbed structural properties. The unperturbed structure is constituted of two half-spaces, separated by a flat interface, each one assumed to be homogeneous and characterized by arbitrary and deterministic dielectric relative permittivity ε_0 and ε_1 , respectively. In order to characterize the inherent morphology, the description of statistical fluctuations occurring in the actual spatial structures can be achieved by employing different quantities: The perturbed medium is now obtained by assuming that topography of the interfacial irregularities is characterized by a *zero-mean* two-dimensional stochastic process, $\zeta(x, y) = \zeta(\mathbf{r}_\perp)$, and the *space-variant* morphological features of the lower half-space volume are characterized by a *zero-mean* three-dimensional stochastic process, $\chi_1(\mathbf{r})$, such that the relative permittivity of the lower half-space is described by $\varepsilon_1(\mathbf{r}) = \varepsilon_1 + \chi_1(\mathbf{r})$. Accordingly, the perturbed medium can be seen as the

truncation by the rough interface $\zeta(\mathbf{r}_\perp)$ of an infinite volume, whose permittivity fluctuations are described by a process $\chi_1(\mathbf{r})$. Therefore, the perturbed permittivity distribution is modeled by

$$\varepsilon(\mathbf{r}_\perp, z) = \varepsilon_0 + (\varepsilon_1(\mathbf{r}) - \varepsilon_0) \mathcal{U}(-z + \zeta(\mathbf{r}_\perp)), \quad (1)$$

where $\mathcal{U}(\cdot)$ is the *Heaviside's* step function, and the perturbation of the dielectric permittivity is $\delta\varepsilon(\mathbf{r}_\perp, z) = \varepsilon(\mathbf{r}_\perp, z) - \varepsilon^{(0)}(z)$; $\varepsilon^{(0)}(z)$ describes the unperturbed dielectric profile. We assume that roughness heights ζ and volumetric fluctuation χ_1 are small enough to perform a series expansion of the perturbation and truncate it to its first-order:

$$\delta\varepsilon(\mathbf{r}_\perp, z) \cong (\varepsilon_1 - \varepsilon_0)\delta(z)\zeta(\mathbf{r}_\perp) + \mathcal{U}(-z)\chi_1(\mathbf{r}) \quad (2)$$

where $\delta(\cdot)$ is the *Dirac's* delta function.

The expression of the field scattered by the structure can be obtained by applying general VPRT formulation with reference to the aforementioned structural description. After some manipulation we obtain the following expression for the overall bi-static normalized radar cross section (RCS) for the pertinent structure

$$\sigma_{qp}^0 = \pi k_0^4 |\varepsilon_1 - \varepsilon_0|^2 \left| \gamma'_{qp}(\mathbf{k}^s, \mathbf{k}^i) \right|^2 W(\mathbf{k}_\perp^s - \mathbf{k}_\perp^i) + \pi k_0^4 \left| \gamma''_{qp}(\mathbf{k}^s, \mathbf{k}^i) \right|^2 \hat{W}_1(\mathbf{k}_1^s - \mathbf{k}_1^i) \quad (3)$$

where k_0 is the propagation constant of vacuum; $W(\boldsymbol{\kappa})$ is the pertinent PSD (Power Spectral Density) of the rough interface; \hat{W}_1 has to be regarded as an *effective PSD*, being expressed as the convolution of the PSD $W_1(\boldsymbol{\kappa})$ of the medium volumetric fluctuation $\chi_1(\mathbf{r})$ with a Lorentzian function; \mathbf{k}^s and \mathbf{k}^i are the vector wave-numbers in the upper medium for the scattering and incident directions, respectively; $\mathbf{k}_\perp^s - \mathbf{k}_\perp^i$ is the projection on the x - y plane of the vector $\mathbf{k}^s - \mathbf{k}^i$; \mathbf{k}_1^s and \mathbf{k}_1^i are the vector wave-numbers in the lower (unperturbed) medium for the scattering and incident directions, respectively. Expressions for γ'_{qp} and γ''_{qp} are obtained in closed-form, and the convolution of the PSD $W_1(\boldsymbol{\kappa})$ and the Lorentzian function can also be analytically evaluated in closed form for a Gaussian PSD, so that a fully analytical solution is achieved, at variance with solutions available in literature [3]. Finally, it should be noted that the two terms in (3) correspond to the two pertinent scattering contributions (from rough interface and volume fluctuations), respectively.

III. NUMERICAL SIMULATIONS

The following description is considered. We assume the rough interface $\zeta(\mathbf{r}_\perp)$ described by a Gaussian 2D random process with *Gaussian correlations*: σ and l are the surface height standard deviation and

correlation length, respectively. The volumetric fluctuations $\chi_1(\mathbf{r})$ are described by using a isotropic 3-D random process with exponential correlation: ρ and a are the standard deviation and correlation length of the fluctuation, respectively. Relevant RCS (3) evaluation for prescribed parameters is depicted in Fig.2.

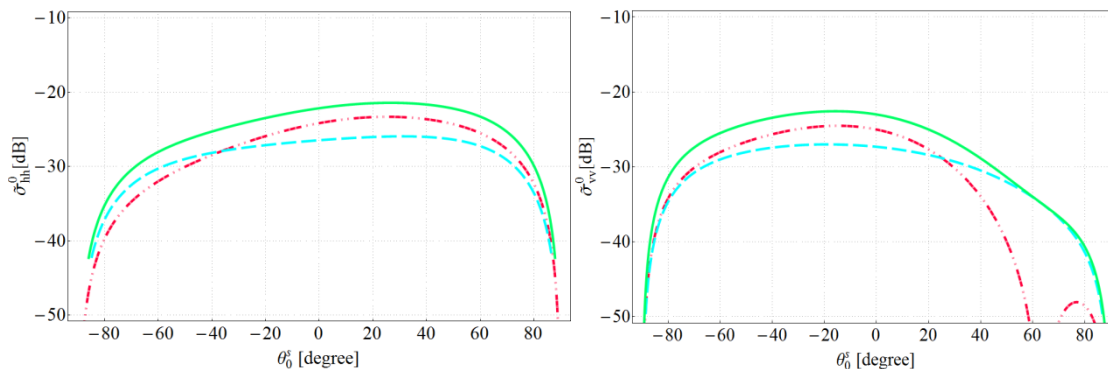


FIG. 2 – RCS for hh and vv polarization, with $f=1.6$ GHz, $k_0\sigma=0.15$, $k_0l=1.5$, $k_0\rho=0.2$, $k_0a=2.0$, $\varepsilon_1=2.2+j0.05$, $\theta_0^i = 50^\circ$: interfacial roughness (dotted-dashed line), volumetric (long-dashed line) and (solid line) overall contributions.

IV. CONCLUSION

This paper provides a canonical model for electromagnetic wave interactions with semi-infinite structure with random fluctuations. As a matter of fact, it is intellectually more satisfying to treat consistently elementary scattering mechanisms (i.e. interfacial and volumetric scattering) on the same conceptual and formal footing. Therefore, the twofold final purpose is to furnish an analytical treatment useful to gain a unifying perspective on the scattering phenomenon considered in its entirety and to provide an analytic model to be profitably used in applications.

REFERENCES

- [1] P. Imperatore, A. Iodice, D. Riccio, “Reciprocity, Coupling and Scattering: A New Look at SPM for Rough Surface”, *Proc. of European Microwave Conference*, 2009, EuMC 2009, pp.994-997, Sept. 29 2009-Oct. 1 2009.
- [2] P. Imperatore, A. Iodice, D. Riccio, “Volumetric-Perturbative Reciprocal Formulation for Scattering from Rough Multilayers,” *IEEE Transaction on Antennas and Propagation*, vol. 59, no. 3, pp.877-887, March 2011.
- [3] O. Calvo-Perez, A. Sentenac, J.-J. Greffet, “Light scattering by a two-dimensional, rough penetrable medium: a mean-field theory,” *RadioScience*, vol.34, pp.311-35, Mar. 1999.

DEEP PENETRATION OF INHOMOGENEOUS PLANE WAVES IN LOSSY MEDIA

N. Tedeschi

Dpt. of Information Engineering, Electronics and Telecommunications,
“La Sapienza” University of Rome,
Via Eudossiana 18, 00184 Roma, Italy.
nicola.tedeschi@uniroma1.it

Abstract

The incidence of an inhomogeneous plane wave on the interface between two lossy media is analyzed. The analytical expressions of the incidence angle of the phase vector, for which the transmitted wave has the phase or the attenuation vector parallel to the interface, are obtained. The transmitted wave with the attenuation vector parallel to the interface is physically interpreted, finding a wave in a lossy medium without attenuation away from the interface. The same effect appears at the interface between a lossless medium and a lossy one. In both cases the amplitude of the Poynting vector is analyzed to show the absence of attenuation away from the interface.

Index Terms – Inhomogeneous plane waves, Interfaces, Lossy media

I. INTRODUCTION

In the present paper the interaction of an inhomogeneous plane wave with the interface between two lossy media is considered. We calculate the analytical expressions of the incident angles for which the transmitted phase and attenuation vectors, respectively, are parallel to the interface. Afterwards, we try a physical interpretation of the transmitted waves at these critical angles. We find the transmitted wave with attenuation vector parallel to the interface is a plane wave, in a lossy medium, that does not attenuate away from the interface. This effect is significant, because allows us to deeply explore the lossy medium without energy losses. Moreover, we find this effect is possible also at the interface between a lossless medium and a lossy one, by impinging on the interface with an inhomogeneous wave, e.g., a leaky wave [1].

II. THE CRITICAL ANGLES

Let us consider an interface between two lossy media, medium 1 and medium 2, and let us call x the direction orthogonal to the interface. Assume an electromagnetic plane wave coming from medium 1 with expression $\exp [i(\mathbf{k}_i \cdot \mathbf{r} - \omega t)]$, where the propagation vector is a complex vector: $\mathbf{k}_i = \boldsymbol{\beta}_1 + i\boldsymbol{\alpha}_1$. The incident phase, $\boldsymbol{\beta}_1$, and attenuation, $\boldsymbol{\alpha}_1$, vectors form the angles ξ_1 and ζ_1 , respectively, with the normal to the interface. The angle between the two vectors is $\eta_1 = \xi_1 + \zeta_1$. Similarly,

the transmitted wave vector, \mathbf{k}_t , has phase and attenuation vectors forming angles ξ_2 and ζ_2 , and η_2 . Let us define the wave numbers k_0 , k_1 , and k_2 , associated to vacuum, medium 1 and medium 2, respectively. In [2], the transmission of an inhomogeneous plane wave at the interface between two lossy media is considered. The transmitted angles of the phase and attenuation vectors were found to match $\pi/2$ for given incident angles called ξ_1^{ξ} and ξ_1^{ζ} , respectively. These angles were computed by means of a numerical root-searching routine. By considering the Snell law, and imposing $\xi_2 = \pi/2$ or $\zeta_2 = \pi/2$, the following condition is obtained:

$$(\chi - 1) \tan^2 \xi_1 - \tan \eta_1 \tan \xi_1 + \chi = 0 \quad (1)$$

where the parameter χ is the ratio between the losses of the two media. In the particular case of non-magnetic and when only conduction losses are considered, the parameter reduces to the conductivities ratio: $\chi = \sigma_2/\sigma_1$. By solving eq. (1), we find two angles $\xi_{1,2}$ that coincide with ξ_1^{ξ} or ξ_1^{ζ} , depending on the value of the real part of the component of the incident propagation vector tangential to the interface, k_{it} .

III. DEEPLY PENETRATING WAVE

Now that the expressions of ξ_1^{ξ} and ξ_1^{ζ} have been computed, let us try to get a physical interpretation of the transmitted wave for these particular angles. When the incident wave, at a fixed η_1 , has a phase vector with $\xi_1 = \xi_1^{\xi}$, the transmitted phase vector is parallel to the interface, and the attenuation vector forms an angle ζ_2 with the normal to the interface. This wave has the constant phase planes orthogonal to the interface, and its purely real power flow is orthogonal to α_2 , if a TE wave is considered [3]. One could say that this is, for an interface between two lossy media, the wave closest to the surface wave. More interesting is the other case, for a phase incident vector with $\xi_1 = \xi_1^{\zeta}$. The transmitted wave, in this case, has the constant amplitude plane orthogonal to the interface, and the phase vector with an angle $\xi_2 \in [0, \pi/2]$. That means the wave is not attenuated in the direction orthogonal to the interface, and its purely real power flow, in the case of TE polarization, is orthogonal to the interface, too. This result is surprising, because we achieved a transmitted wave in a lossy medium which is not attenuated in the direction where the medium extends. In Fig. 1 the amplitude of the Poynting vector $\mathbf{\Pi}$, for a TE polarized incident wave impinging at $\xi_1 = \xi_1^{\zeta}$, is shown, for an interface between two lossy media, with $\epsilon_1 = 4$, $\sigma_1 = 0.01 \text{ S/m}$, and $\epsilon_2 = 10$, $\sigma_2 = 0.001 \text{ S/m}$, at frequency $f_0 = 600 \text{ MHz}$, for different values of η_1 . The power is plotted as a function of x/λ_0 , for $y = 0$, where λ_0 is the vacuum wavelength. We consider a field with unit amplitude. The field has been computed with

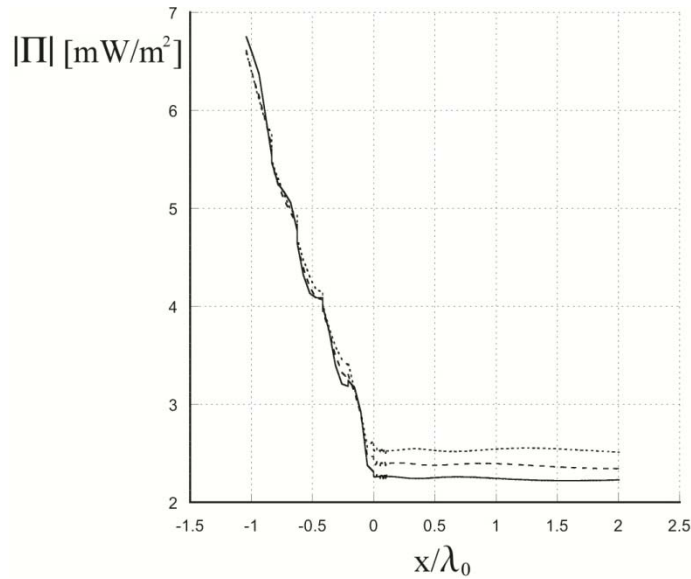


FIG. 1 – Amplitude of the Poynting vector near the interface, for different values of η_1 : -5° (solid line), 10° (dashed line), 40° (dotted line).

simulations performed on the commercial software Comsol, using the Finite Element Method in the frequency domain. The amplitude of the Poynting vector is attenuated in the first medium, i.e., $x < 0$, with weakly oscillations due to the reflected wave. In the second medium, the amplitude is constant, so that the transmitted wave can propagate indefinitely in the orthogonal direction to the interface.

The same effect can be obtained at the interface between a lossless medium and a lossy one, by considering an inhomogeneous incident plane wave, i.e., $\eta_1 = \pi/2$, e.g. a leaky wave [1]. In the literature it has been widely investigated how to generate this kind of waves at microwave frequencies, with the so called leaky-wave antennas [4]. In recent years, leaky-wave antennas at optical frequencies have been proposed, too [5]. Analyzing the Snell law in this case, we found the following critical angle:

$$\xi_c = \frac{1}{2} \arcsin \left[\frac{\text{Im}(k_2^2)}{\beta_1 \alpha_1} \right] \quad (2)$$

The values assumed by ξ_c decrease dramatically as a function of β_1 . The associated transmitted angle shows an equally sudden decrease. Moreover, we could see that, increasing β_1 , the amplitude of the Fresnel transmission coefficient tends to one, and the attenuation amplitude, in both media, increases. In Fig. 2, the amplitude of the Poynting vector is shown, as a function of x/λ_0 , for $y = 0$, near the interface, and compared with the amplitude of the Poynting vector for a homogeneous plane wave incident at the same angle. The inhomogeneous incident wave is taken with the minimum value of β_1 , i.e., when $\xi_c = \pi/4$. As medium 1 a vacuum and as medium 2 the same second medium of Fig. 1, are considered. These powers are obtained through simulation implemented on Comsol. We see the amplitude after the interface is constant when

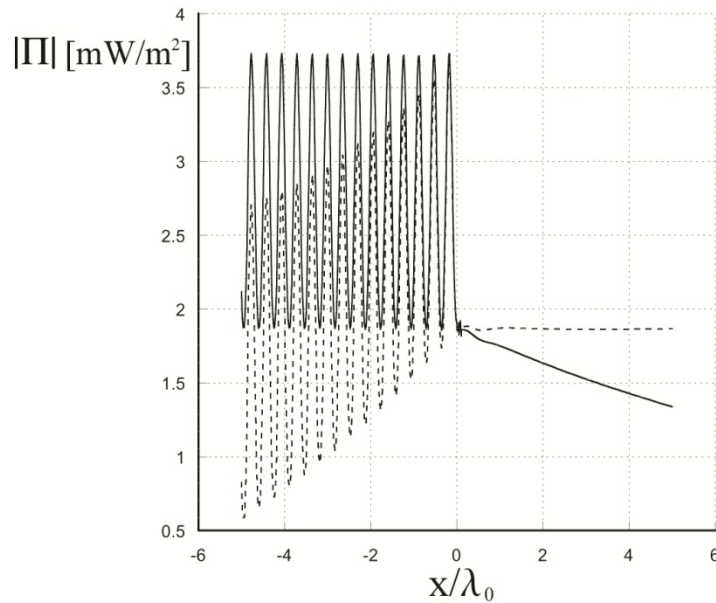


FIG. 2 – Amplitude of the Poynting vector near the interface, for an incident homogeneous wave (solid line) and an incident inhomogeneous wave (dashed-line).

the inhomogeneous wave is considered. Therefore the transmitted wave propagates indefinitely away from the interface.

IV. CONCLUSIONS

In this paper, we showed the possibility to obtain a transmitted wave in a lossy media with attenuation parallel to the interface. The effect to have a non-attenuated wave, away from the interface, in a lossy medium can be very useful, for information transmission, detection of buried objects, analysis of materials, microscopy, interaction with biological samples, etc.

REFERENCES

- [1] T. Tamir, "Inhomogeneous wave types at planar interfaces: III-Leaky waves," *Optik*, vol. 38(3), pp. 269-297, 1973.
- [2] J.E. Roy, "New results for the effective propagation constants of nonuniform plane wave at the planar interface of two lossy media," *IEEE Transaction on Antennas and Propagation*, 51(6), pp. 1206-1215, Jun. 2003.
- [3] R.B. Adler, L.J. Chu, and R.M. Fano, *Electromagnetic Transmission and Radiation*, Wiley, New York, 1972.
- [4] D.R. Jackson and A.A. Oliner, "Leaky-Wave Antennas," Ch. 7 in *Modern Antenna Handbook*, C.A. Balanis, Editor, Wiley, New Jersey, 2008.
- [5] Y. Wang, A.S. Helmy, and G.V. Eleftheriades, "Ultra-wideband optical leaky-wave slot antennas," *Optics Express*, 19(13), pp. 12392-12401, Jun. 2011.

ANALYSIS OF PROPAGATION IN COUPLED POLYGONAL CROSS-SECTION DIELECTRIC WAVEGUIDES

F. Corsetti⁽¹⁾, M. Lucido⁽¹⁾, G. Panariello⁽¹⁾

⁽¹⁾ DIEI, University of Cassino
Via G. Di Biasio 43, 03043 Cassino, Italy
lucido@unicas.it

Abstract

Aim of this paper is the accurate and efficient analysis of the propagation in coupled polygonal cross-section dielectric waveguides. The problem is formulated as a system of surface integral equations and discretized by means of Galerkin's method with analytically Fourier transformable expansion functions factorizing the behavior of the fields on the wedges. The presented numerical results show the accuracy and the efficiency of the proposed technique.

Index Terms – Coupled dielectric waveguides, edge behavior, Galerkin's method, surface integral equation.

I. INTRODUCTION

A considerable variety of coupling dielectric devices and structures is employed in the construction of modern optical integrated circuits. Among them there is the dielectric waveguide directional coupler, which is the building block of signal dividers, multiplexers, modulators and switches. As a consequence, accurate analyses of these structures are essential to the design of devices that meet specific requirements and criteria. Several methods of analysis have been proposed in the dedicated literature. The approximate ones are mostly based on the effective-index method (EIM) approximation [1] and the coupled mode theory [2]. For more accurate results, the finite element method (FEM) or finite difference method (FDM) in the frequency and in the time-domain are used [3]. However, these approaches generally require a high computational effort, and become cumbersome for situations more complicated than that of two identical closely coupled guides.

In this contribution an accurate and efficient analysis of the propagation in coupled polygonal cross-section dielectric waveguides is presented. In order to achieve a fast convergence, the problem formulated as a system of surface integral equations in the spectral domain, opportunely devised to be valid for objects with edges, is discretized by means of Galerkin's method with analytically Fourier-transformable basis functions factorizing the correct edge behavior and the continuity conditions of the unknowns.

II. FORMULATION AND SOLUTION OF THE PROBLEM

Let us consider a couple of parallel polygonal cross-section homogeneous and isotropic lossless dielectric waveguides dipped in a homogeneous and isotropic lossless medium. A coordinate system with the z axis parallel to the cylinders axes is introduced and a behavior of the fields with z of the kind $e^{-jk_z z}$ is assumed, where k_z is the propagation constant of the generic mode. Let us number the L sides of the cylinders progressively and introduce a local coordinate system (x_i, y_i, z) on the i th side with the origin at the centre of the side itself and y_i oriented in the outward direction.

Fictitious electric and magnetic surface current densities are introduced

$$\underline{J}_i(x_i) = \hat{y}_i \times \underline{H}_1|_{y_i=0} = -\hat{y}_i \times \underline{H}_2|_{y_i=0}, \underline{J}_{mi}(x_i) = -\hat{y}_i \times \underline{E}_1|_{y_i=0} = \hat{y}_i \times \underline{E}_2|_{y_i=0} \quad (1)$$

for $i = 1, 2, \dots, L$, where $h = 1, 2$ indicates the field outside and inside the dielectric cylinders respectively. Therefore, it is possible to show [4] that the magnetic vector potential in the two media can be written as

$$\underline{A}_h(x, y, z) = (-1)^h j \frac{\mu_h}{2} e^{-jk_z z} \sum_{i=1}^L \int_{-\infty}^{+\infty} \tilde{J}_i(u) \frac{e^{-j|y_i| \sqrt{k_h^2 - k_z^2 - u^2}}}{\sqrt{k_h^2 - k_z^2 - u^2}} e^{-ju x_i} du \quad (2)$$

where $\tilde{J}_i(u)$ is the Fourier transform of the electric current on i th side, k_h is the wave number and μ_h the magnetic permeability of the medium h . An analogous expression can be obtained for the electric vector potential $\underline{F}_h(x, y, z)$ by substituting $\tilde{J}_i(u)$ with $\tilde{J}_{mi}(u)$, and μ_h with ε_h (dielectric permittivity).

Thus, the fields in the two media can be written by means of the well-known differential relations between the fields and the potentials and a system of integral-differential equations can be obtained by imposing the continuity of the tangential components of the electric and magnetic fields on the cylinder surfaces. The behavior and continuity conditions at the edges of the unknowns [5] allow to reduce the obtained system of integral-differential equations to a system of integral equations by using the procedure outlined in [6].

A matrix equation can be obtained by means of Galerkin's method. To this end, suitable expansion functions for the longitudinal components and the derivative of the transverse components of the surface current densities factorizing the behavior of the fields on the wedges are the following [4]

$$\varphi_n^{(\alpha, \beta)}(x/c) = (1 - x/c)^\alpha (1 + x/c)^\beta \frac{P_n^{(\alpha, \beta)}(x/c)}{c \xi_n^{(\alpha, \beta)}} \prod (x/c) \quad (3)$$

for $n \geq 0$, where $P_n^{(\alpha,\beta)}(\cdot)$ is the Jacobi polynomial of order n and parameters α, β chosen to factorize the edge behavior of the unknowns, $\xi_n^{(\alpha,\beta)}$ is a normalization quantity and $\Pi(\cdot)$ is the unitary rectangular window. The Fourier transform of (3) is analytical and can be expressed in terms of the confluent hypergeometric function of first kind [4].

By means of reciprocity, it is possible to show that the coefficients' matrix has many symmetries [7] that reduce the number of the elements to be numerically evaluated. Moreover, all the coefficients can be reduced to single integrals, which can be efficiently evaluated by using the analytical acceleration technique proposed in [8].

III. NUMERICAL RESULTS

In order to appreciate the accuracy and efficiency of the presented technique, in Table I the propagation constant normalized to k_1 for the E_{21}^y mode of two coupled rectangular waveguides (of width $2a$, thickness $2b$ and separation between the centers $2d$) at a given normalized frequency $V = a\sqrt{k_2^2 - k_1^2}$ is reported as a function of the number of expansion functions used. It can be seen that an accuracy for the solution of 4 significant figures is achieved by using only 1 expansion function for each component of the surface current densities on each side of the cylinders. Moreover, only 3 expansion functions are needed to guarantee an accuracy for the solution of 8 significant figures.

For the same structure, in Table II the normalized coupling coefficients defined as

$$C_p = \frac{V(k_{z,11p}^2 - k_{z,21p}^2)}{4(k_2^2 - k_1^2)} \quad (4)$$

with $p = x, y$, where $k_{z,mnp}$ is the propagation constant for the E_{mn}^p mode reconstructed with 5 expansion functions are compared with those obtained in [1] by means of the effective-index method with built-in perturbation correction (EIMPC). Despite the efficiency of the approximated method presented in [1], the accuracy which allows to obtain in the evaluation of the normalized coupling coefficients is always between 1% and 5%.

IV. CONCLUSION

In this paper an accurate and efficient method for studying the propagation in coupled polygonal cross-section dielectric waveguides has been proposed. Future perspective is the extension of the method to the analysis of propagation of leaky modes in single and coupled dielectric waveguides.

REFERENCES

- [1] C. H. Kwan and K. S. Chiang, "Study of Polarization-Dependent Coupling in Optical Waveguide Directional Couplers by the Effective-Index Method With Built-in Perturbation Correction," *J. Lightwave Technol.*, vol. 20(6), pp. 1018-1026, Jun. 2002.
- [2] A. Hardy and W. Streifer, "Coupled mode solutions of multiwaveguide systems," *IEEE J. Quantum Electron.*, vol. 22, pp. 528-534, Apr. 1986.
- [3] M. J. Robertson, S. Ritchie and P. Dayan, "Semiconductor waveguides: analysis of optical propagation in single rib structures and directional couplers," *IEE Proc., Pt. J*, vol. 132(6), Dec. 1985.
- [4] M. Lucido, G. Panariello and F. Schettino, "Analysis of the Electromagnetic Scattering by Perfectly Conducting Convex Polygonal Cylinders," *IEEE Trans. On Antennas and Propagation*, vol. 54, pp. 1223-1231, Apr. 2006.
- [5] J. Meixner, "The Behavior of Electromagnetic Fields at Edges," *IEEE Trans. Antennas Propag.*, vol. 20, pp. 442-446, Jul. 1972.
- [6] M. Lucido, G. Panariello, and F. Schettino, "TE scattering by arbitrarily connected conducting strips," *IEEE Trans. Antennas Propag.*, vol. 57, pp. 2212-2216, Jul. 2009.
- [7] M. Lucido, G. Panariello, and F. Schettino, "Scattering by Polygonal Cross-Section Dielectric Cylinders at Oblique Incidence," *IEEE Trans. Antennas Propag.*, vol. 58, pp. 540-551, Feb. 2010.
- [8] M. Lucido, G. Panariello and F. Schettino, "Electromagnetic Scattering by Multiple Perfectly Conducting Arbitrary Polygonal Cylinders," *IEEE Trans. on Antennas and Propagation*, vol. 56, pp. 425-436, Feb. 2008.

TABLE I – NORMALIZED PROPAGATION CONSTANT FOR THE MODE OF TWO COUPLED RECTANGULAR WAVEGUIDES FOR DIFFERENT NUMBER OF EXPANSION FUNCTIONS USED ()

$(a/b = 1.0, d/a = 1.5, (k_2^2 - k_1^2)/k_2^2 = 0.02, V = 1.4)$

N	k_z/k_1
1	1.0017373
2	1.0016004
3	1.0016059
4	1.0016059
5	1.0016059
12	1.0016059

TABLE II - NORMALIZED COUPLING COEFFICIENTS FOR TWO COUPLED RECTANGULAR WAVEGUIDES

$(a/b = 1.0, d/a = 1.5, (k_2^2 - k_1^2)/k_2^2 = 0.02, \bar{C}_p = 100C_p)$

V	EIMPC -method		Proposed Method	
	\bar{C}_x	\bar{C}_y	\bar{C}_x	\bar{C}_y
1.4	5.94	5.89	5.832	5.809
1.6	4.76	4.72	4.842	4.823
1.8	3.71	3.68	3.839	3.826
2.0	2.84	2.82	2.968	2.960
2.2	2.16	2.15	2.263	2.258
2.4	1.63	1.62	1.710	1.708
2.6	1.23	1.22	1.287	1.287
2.8	0.92	0.92	0.968	0.968
3.0	0.70	0.69	0.727	0.728

PERTURBATIVE APPROACH FOR SCATTERING IN RANDOM MEDIA VIA DISTRIBUTION THEORY FOR DISCONTINUOUS TEST FUNCTIONS

P. Imperatore⁽¹⁾, A. Iodice⁽²⁾, D. Riccio⁽²⁾

⁽¹⁾ Istituto per il Rilevamento Elettromagnetico dell'Ambiente, Italian National Research Council (CNR), 80124 Napoli, Italy

⁽²⁾ Department of Biomedical, Electronic and Telecommunication Engineering, University of Naples "Federico II", 80125 Napoli, Italy

imperatore.p@irea.cnr.it

Abstract

We present the second-order volumetric perturbative reciprocal theory (VPRT), which has a direct theoretical interest to scattering in random and layered media including up to second-order effects. Distribution theory for discontinuous test functions provides the rigorous mathematical backbone of the general VPRT formulation, so conferring conceptual elegance to the theoretical construct.

Index Terms – Scattering, random media, reaction, distribution theory.

I. INTRODUCTION

This paper discusses a conceptual and mathematical method of interest in electromagnetic scattering analysis. Specifically, we present the second-order volumetric perturbative reciprocal theory (VPRT)[1][2], which has a direct theoretical interest to scattering in random and layered media including up to second-order effects. VPRT is methodologically based on volumetric perturbations of the scattering medium dielectric properties, so encompassing both interfacial roughness and volume inhomogeneities; its derivation is systematic, by using the reciprocity theorem, so providing meaningful reaction-based general expression for the scattering field; its results are rigorously and easily derived under the purview of distribution theory for discontinuous test functions. The last important point is worth to be emphasized. The use of the traditional distribution theory (DT) in electromagnetic problems treatment is widespread, and the traditional DT is usually regarded as generally and reasonably applicable. Nonetheless, little attention was paid to the recognition of pathological cases in which the classical DT does not apply. Some analytical expressions encountered in the aforementioned context can come out meaningless in the context of DT: the inherent inconsistency that can arise, although might result subtle, however is sometimes overlooked, so lacking the mathematical rigor [3]. These considerations might appear as purely mathematical in nature; however, the inherent implications are crucial in applications perspective. In this paper,

especially new is the application of the powerful distribution theory for discontinuous test functions, for the correct and rigorous treatment of singular perturbation, so overcoming the inadequateness of the classical distribution theory (DT) for analyzing perturbation theory for electromagnetic scattering problems. The emphasis in the paper is not on the specific results but on methods of analysis. We show also how the adoption of the VPRT solution results in a greatly simplified derivation of the classical second-order SPM solution.

II. SECOND-ORDER VPRT SCATTERING FORMULATION

Let us consider a source current density $\mathbf{J}(\mathbf{r})$ radiating an electromagnetic field $\mathbf{E}(\mathbf{r})$, $\mathbf{H}(\mathbf{r})$, in an inhomogeneous medium characterized by a relative dielectric permittivity distribution $\varepsilon = \varepsilon(\mathbf{r})$. The vector wave *Helmholtz* equation governing the electric field \mathbf{E} in a volume V is

$$\nabla \times \nabla \times \mathbf{E}(\mathbf{r}) - k_0^2 \varepsilon(\mathbf{r}) \mathbf{E}(\mathbf{r}) = jk_0 \eta_0 \mathbf{J}(\mathbf{r}) \quad (1)$$

where k_0 and h_0 are the wave-number and the impedance of the vacuum, respectively. We consider, in the regime of small $\delta\varepsilon(\mathbf{r})$, the following field representation $\mathbf{E}(\mathbf{r}) = \mathbf{E}^{(0)}(\mathbf{r}) + \mathbf{E}^{(1)}(\mathbf{r}) + \mathbf{E}^{(2)}(\mathbf{r}) + \dots$ and medium permittivity description $\varepsilon(\mathbf{r}) = \varepsilon^{(0)}(\mathbf{r}) + \delta\varepsilon^{(1)}(\mathbf{r}) + \delta\varepsilon^{(2)}(\mathbf{r}) + \dots$ where the parenthesized superscript indicates the perturbation order, and $\mathbf{E}^{(0)}(\mathbf{r})$ is the (unperturbed) field radiated by the actual source in the unperturbed medium. To supplement the original problem, we also introduce an associated *auxiliary* problem, whose symbols are hereafter indicated with an over-bar. The auxiliary (fictitious) test source is located at the observation point, $\bar{\mathbf{J}}(\mathbf{r}) = \hat{t}J\delta(\mathbf{r} - \mathbf{r}_0)$, \hat{t} is an arbitrarily oriented unit vector, and $J = 1 \text{ A}\cdot\text{m}$ is a unitary constant introduced for dimensional consistency reasons. Decomposing the problem in terms of suitable hierarchy of equations for both actual and auxiliary problems and by systematically making use of reciprocity theorem, we obtain the final expression for the second-order scattered field $\mathbf{E}^{(2)}(\mathbf{r}_0) \cdot \hat{t}J = R_{NL} + R_L$ [5], with

$$R_{NL} = -jk_0\eta_0^{-1} \iiint_V \mathbf{E}^{(1)}(\mathbf{r}) \cdot \delta\varepsilon^{(1)}(\mathbf{r}) \bar{\mathbf{E}}^{(0)}(\mathbf{r}) d\mathbf{r} = \iiint_V \mathbf{E}^{(1)}(\mathbf{r}) \cdot \bar{\mathbf{J}}^{(1)}(\mathbf{r}) d\mathbf{r} = \langle \mathbf{E}^{(1)}, \bar{\mathbf{J}}^{(1)} \rangle \quad (2)$$

$$R_L = -jk_0\eta_0^{-1} \iiint_V \bar{\mathbf{E}}^{(0)}(\mathbf{r}) \cdot \delta\varepsilon^{(2)}(\mathbf{r}) \mathbf{E}^{(0)}(\mathbf{r}) d\mathbf{r} = \iiint_V \bar{\mathbf{E}}^{(0)}(\mathbf{r}) \cdot \mathbf{J}_b^{(2)}(\mathbf{r}) d\mathbf{r} = \langle \bar{\mathbf{E}}^{(0)}, \mathbf{J}_b^{(2)} \rangle \quad (3)$$

The second-order scattering field expression consists of two terms which clearly outline, from a physical point of view, the effects of the medium perturbation on the scattered field. It should be noted that R_{NL} is linked to the reaction $\langle \mathbf{E}^{(1)}, \bar{\mathbf{J}}^{(1)} \rangle$ between the first-order scattering field $\mathbf{E}^{(1)}$ in the medium, due to the actual source, and the current $\bar{\mathbf{J}}^{(1)}$ induced into the perturbation volume $\delta\varepsilon^{(1)}$ by the unperturbed field $\bar{\mathbf{E}}^{(0)}$

due to the auxiliary source. R_L is linked to the reaction $\langle \bar{\mathbf{E}}^{(0)}, \mathbf{J}_b^{(2)} \rangle$ between the unperturbed field $\bar{\mathbf{E}}^{(0)}$, produced in the unperturbed medium by the auxiliary source, and the second-order current $\mathbf{J}_b^{(2)}$ induced into the perturbation volume $\delta\mathcal{E}^{(2)}$ by the unperturbed field $\mathbf{E}^{(0)}$ due to the actual source. The salient point that need to be emphasized is that the integrals in (2) and (3) can include the product of delta function (or its derivative) and a function presenting a jump discontinuity at the origin. It is important to note that when this kind of formal evaluation is carried out via a *naïve* application of the classical distribution theory, as it sometimes has been erroneously done in the past to deal with scattering problems (see for instance [3], where an expression different from the correct SPM one is obtained for scattering from gently rough surfaces), incorrect results are obtained.

III. DISTRIBUTION THEORY FOR DISCONTINUOUS TEST FUNCTIONS

In classical sense infinitely smooth test functions are usually adopted; however, recent mathematical works show that it is also possible to formally consider a distribution theory with the set of discontinuous test functions. This extension has been discussed by *Kurasov* [4] and is here briefly recalled. The set of the test functions K is defined as the set of all functions with compact support having uniformly bounded derivatives of all orders outside the origin. In this framework, a distribution f is a linear form on K . In [4] two fundamental distributions are introduced. The β distribution (the derivative of the unit distribution) is defined as $\beta(\varphi) = \varphi(0^+) - \varphi(0^-)$. The delta distribution is defined as $\delta(\varphi) = (\varphi(0^+) + \varphi(0^-))/2$. The generalized derivative $D_z f$ of a distribution f is defined by the equation $(D_z f)(\varphi) = -f\left(\frac{d}{dz}\varphi\right)$ where $\varphi \in K$ stands for the discontinuous test function. According to this theory, two different derivatives can be defined for a given $\psi \in K_{loc}$, where K_{loc} is the set of all bounded functions which are infinitely differentiable outside the origin with possibly a jump discontinuity at the origin: 1) Ordinary derivative $d\psi/dz$, i.e. the derivative calculated as an ordinary function at every point outside the origin. 2) Generalized derivative $D_z \psi$. Ordinary and generalized derivatives of a $\psi \in K_{loc}$ are related as:

$$D_z \psi = \frac{d}{dz} \psi + \beta(\psi)\delta + \delta(\psi)\beta, \quad (4)$$

$$D_z^2 \psi = \frac{d^2}{dz^2} \psi + \delta(\psi)D_z \beta - D_z \delta(\psi)\beta + \beta(\psi)D_z \delta - D_z \beta(\psi)\delta. \quad (5)$$

It is important to note that, in this framework, the derivative of a distribution does not coincide with the derivative defined in the sense of traditional distribution theory.

IV. SINGULAR PERTURBATION: THE CASE OF SURFACE SCATTERING

In order to give a simple demonstration of the power of the proposed scheme, we then apply it to a canonical scattering problem (gently rough surface $\zeta = \zeta(\mathbf{r}_\perp)$). This represents an instructive canonical case, since it involves the treatment of singular interaction, which is properly done by invoking mathematical results discussed in Section III. In fact, in this case we get $\delta\varepsilon^{(1)}(\mathbf{r}_\perp, z) = -\zeta(\mathbf{r}_\perp)D_z\varepsilon^{(0)}$ and $\delta\varepsilon^{(2)}(\mathbf{r}_\perp, z) = \frac{\zeta^2(\mathbf{r}_\perp)}{2}D_z^2\varepsilon^{(0)}$, with the unperturbed permittivity distribution $\varepsilon^{(0)}(z)$ exhibiting an abrupt discontinuity. Indeed, the classical derivation of the second-order SPM solution is commonly obtained with extremely intricate and bulky manipulations. On the contrary, by applying VPRT, it is possible to demonstrate that the same solution can be attained in concise and physically transparent way [5]. To save space, the derivation is not reported here.

V. CONCLUSION

VPRT is methodologically based on volumetric perturbations of the scattering medium structural dielectric properties so encompassing both interfacial roughness and volume inhomogeneities; its derivation is systematic by making use of the reciprocity theorem. Finally, DT for discontinuous test functions provides the rigorous mathematical backbone of the general VPRT formulation, so conferring conceptual elegance to the theoretical construct. It is worth to mention that the adopted perturbative methodology can be applied in other branches of physics and engineering as well.

REFERENCES

- [1] P. Imperatore, A. Iodice, D. Riccio, "Reciprocity, Coupling and Scattering: A New Look at SPM for Rough Surface", *Proceedings of European Microwave Conference, EuMC 2009*, pp.994-997, Sept. 29-Oct. 1, 2009, Rome, Italy.
- [2] P. Imperatore, A. Iodice, D. Riccio, "Volumetric-Perturbative Reciprocal Formulation for Scattering from Rough Multilayers", *IEEE Trans. Antennas and Propag.*, vol.59, no.3, pp. 877-887, March 2011.
- [3] A. A. Maradudin, D. L. Mills, "Scattering and absorption of electromagnetic radiation by a semi-infinite medium in the presence of surface roughness", *Physical Review B*, vol.11, no.4, pp.1392-1415, 1975.
- [4] P. Kurasov, "Distribution theory for the discontinuous test functions and differential operators with the generalized coefficients", *J. Math. Anal. Appl.*, 201, pp. 297-323, 1996.
- [5] P. Imperatore, A. Iodice, D. Riccio, "Second-Order Volumetric-Perturbative Reciprocal Scattering Theory", *IEEE Trans. Antennas and Propag.*, vol.60, no.3, pp.1505-1520, March 2012.

A SYNTHESIS METHOD FOR MULTI-SECTION DEVICES

F. Chiadini⁽¹⁾, V.Fiumara⁽²⁾, A.Scaglione⁽¹⁾

⁽¹⁾ Department of Electronic and Computer Engineering,
University of Salerno

fchiadini@unisa.it

⁽²⁾ Department of Environmental Engineering and Physics,
University of Basilicata

vfiumara@unibas.it

Abstract

We propose a synthesis method to design quarter-wave multi-section devices which exhibit reflection properties approximating a given reflection spectrum.

Index Terms—N-band devices, synthesis methods.

I. INTRODUCTION

Several devices, operating both at microwave and optical frequencies, can be modeled as a cascade of transmission line sections where TEM waves propagate. As examples, optical dielectric multilayers or microwave impedance transformers can be considered. Generally, these devices are used to obtain frequency selective reflection (or transmission) properties, e.g. forbidden transmission bands or matching bands. Several synthesis methods allow the characteristics of the device sections to be determined to obtain a given reflection spectrum [1],[2]. Generally, the strategy of each synthesis procedure depends on the particular reflection spectrum which the device is requested to exhibit.

In this paper we present a method to design quarter-wave multi-section lossless devices which, in principle, works whatever the requested reflection spectrum may be. Our method is based on the classical Riblet method, which was introduced in the 1950s as a design procedure for microwave impedance transformer, and allows a device exhibiting a behavior which approximates a given reflection spectrum to be designed.

II. SYNTHESIS METHOD

Consider a transmission line with characteristic impedance Z_C feeding a load with impedance Z_L (both Z_C and Z_L are assumed to be positive real valued). A quarter-wave multi-section lossless device consists of a cascade of N uniform, loss free, transmission line sections with characteristic impedance Z_i and lengths $\ell_i = \lambda_{0i}/4$, $i = 1, 2, \dots, N$, λ_{0i} being the wavelength in the i^{th} section at a given frequency f_0 , which inserted between the feeding line and the load makes the input reflection coefficient exhibit a given frequency profile. Let us consider the power loss ratio P_{LR} , namely:

$$P_{LR}(\theta) = \frac{P_G(\theta)}{P_L(\theta)} = \frac{1}{1 - |\Gamma(\theta)|^2} \quad (1)$$

where θ is the electrical length, i.e. $\theta = \ell_i \beta_i = \pi f / 2f_0$, f being the frequency and β_i the propagation constant in the i^{th} section, $P_G(\theta)$ and $P_L(\theta)$ are the power available from the generator and the power delivered to the load, respectively, and $\Gamma(\theta)$ is the reflection coefficient. It can be shown that P_{LR} can be expressed in the following form [1],[3]:

$$P_{LR}(\theta) = 1 + Q_N^2(\cos\theta) \quad (2)$$

where Q_N is an even or odd polynomial of order N in the variable $\cos\theta$. Given the polynomial Q_N , the Riblet procedure allows to compute the characteristic impedances Z_i of the sections giving the desired profile of P_{LR} [3]. The Riblet procedure is used in the classical theory of the impedance transformers, where Q_N is expressed either as an N -order Chebyshev polynomial in $\cos\theta$ or is proportional to $(\cos\theta)^N$ to obtain an equi-ripple or flat profile of $|\Gamma(\theta)|$ in a single matching band, respectively [1].

Now, consider the problem of designing a quarter-wave dielectric multilayer, consisting of $N=2M$ sections, with a reflection spectrum with amplitude $|\Gamma(\theta)|=G(\theta)$. Obviously, the function $G(\theta)$ must be periodic with period π and its restriction to $[0, \pi]$ must be symmetric with respect to $\theta=\pi/2$. Moreover, $G(0)=\Gamma_0=|(Z_L-Z_C)/(Z_L+Z_C)|$ and $0 \leq G(\theta) \leq 1$. In terms of the function $G(\theta)$, the power loss ratio can be written

$$P_{LR}(\theta) = \frac{1}{1 - |\Gamma(\theta)|^2} = 1 + \frac{G(\theta)^2}{1 - G(\theta)^2} = 1 + A(\theta)^2 \quad (3)$$

Let us consider the function $A_M(\theta)$, which is the trigonometric Fourier series of $A(\theta)$ truncated at the term $M=N/2$, and define the function

$$\bar{A}_M(\theta) = A_M(\theta) - A_M(0) + A(0) \quad (4)$$

which fulfills the physical constraint $\bar{A}_M(0) = \Gamma_0 / (1 - \Gamma_0^2)^{1/2}$. Because of the symmetry of $A(\theta)$ with respect to $\theta = \pi/2$, $\bar{A}_M(\theta)$ consists in a sum of weighted cosine functions $\cos(2k\theta)$, $k=1, 2, \dots, M$. As a consequence, $\bar{A}_M(\theta)$ can be expressed as a polynomial of order $N=2M$ in $\cos\theta$ by using the trigonometric multiple-angle formulas. Finally, the Riblet procedure can be applied with $Q_N(\cos\theta) = \bar{A}_M(\theta)$.

III. EXAMPLES

Let us consider the problem of designing a multi-section device which, inserted between a feeding line with characteristic impedance $Z_C=50\Omega$ and a load $Z_L=250\Omega$, gives two separated matching bands

$\Theta_1 = [\theta_1 - \Delta\theta/2, \theta_1 + \Delta\theta/2]$ and $\Theta_2 = [\theta_2 - \Delta\theta/2, \theta_2 + \Delta\theta/2]$. As an example, we consider $\theta_1 = 0.5$, $\theta_2 = \pi - \theta_1$, and $\Delta\theta = 0.3$. We choose

$$G(\theta) = \begin{cases} 0, & \theta \in \Theta_1 \cup \Theta_2 \\ \Gamma_0, & \text{otherwise} \end{cases} \quad (5)$$

If our synthesis procedure is applied with $N=8$, it gives the impedance values reported in Table I(a). The reflection coefficient at the input section of the so designed 8-section device can be exactly computed by using the characteristic matrix method [4]. In Fig.1 the reflection coefficient amplitude is plotted as a function of θ together with the function $G(\theta)$. For sake of brevity, results for different values of N are not reported.

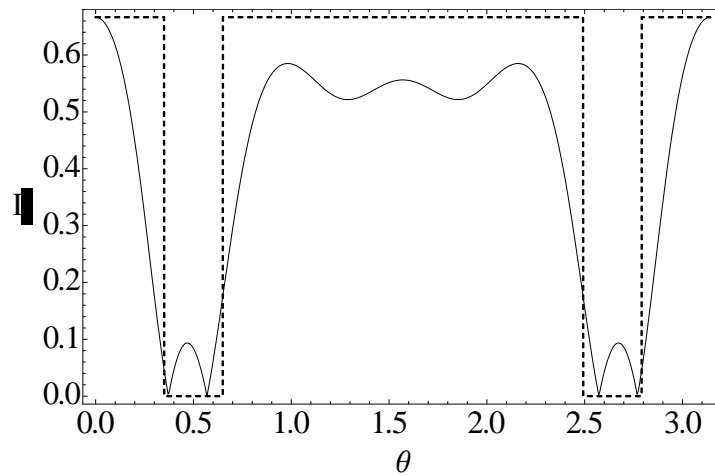


FIG. 1– Dual band 8-section matching device: reflection coefficient amplitude obtained by the proposed synthesis (solid line). The desired amplitude spectrum $G(\theta)$ is also plotted (dashed line).

Now we consider the design of a device which, inserted between two lines with the same characteristic impedance $Z_C=50\Omega$, gives two separated forbidden bands Θ_1 and Θ_2 . We consider $\theta_1 = 0.6$, $\theta_2 = \pi - \theta_1$, and $\Delta\theta = 0.5$ and choose

$$G(\theta) = \begin{cases} 1-10^{-3}, & \theta \in \Theta_1 \cup \Theta_2 \\ 0, & \text{otherwise} \end{cases} \quad (6)$$

The computed impedance values for $N=10$ are reported in Table I(b). In Fig.2 the transmittance T of the designed device is plotted as a function of θ .

IV.CONCLUSION

We have introduced a synthesis method of quarter-wave multi-section devices which applies to the design of devices exhibiting a given reflection spectrum. Some examples have been illustrated confirming that

our method allows to obtain devices exhibiting a reflection spectrum which can be considered a valid approximation to the requested one.

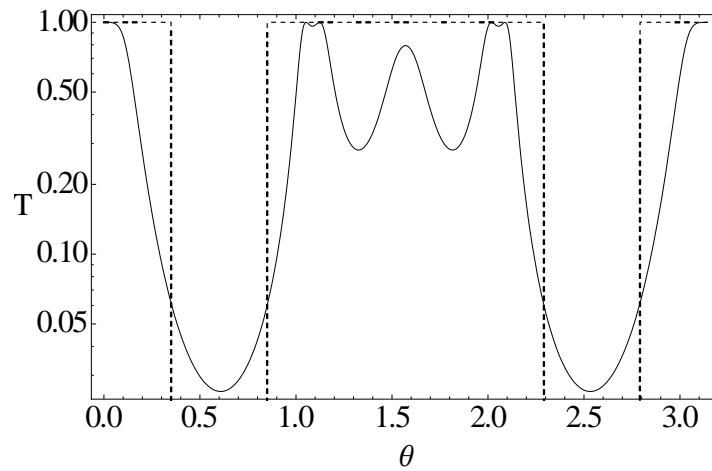


FIG. 2– Dual band 10-section bandgap device: transmittance obtained by the proposed synthesis (solid line). The desired transmittance is also plotted (dashed line).

TABLE I – IMPEDANCE VALUES

	(a) Matching device Impedance values [Ω]	(b) Bandgap device Impedance values [Ω]
Z_1	58.27	21.13
Z_2	76.29	34.96
Z_3	86.86	157.27
Z_4	72.48	299.45
Z_5	172.46	224.18
Z_6	143.92	11.15
Z_7	163.84	8.35
Z_8	214.54	15.90
Z_9		71.51
Z_{10}		118.30

REFERENCES

[1] R. E. Collin, "Foundations for microwave engineering", McGraw-Hill, New York, 1992.
 [2] S. J. Orfanidis, "Electromagnetic Waves and Antennas", URL: <http://www.ece.rutgers.edu/~orfanidi/ewa>, 1998.
 [3] H. J. Riblet, "General synthesis of quarter-wave impedance transformers", IEEE Transactions of Microwave Theory and Techniques, vol. MTT-5, pp. 36-43, 1957.
 [4] M. Born and E. Wolf, Principles of Optics, Cambridge, 1980.

A NOVEL INTERPRETATION FOR THE KIRCHHOFF SCATTERING FROM CLASSICAL AND FRACTAL SURFACES

A. Iodice⁽¹⁾, A. Natale⁽¹⁾, D. Riccio⁽¹⁾

⁽¹⁾ Dipartimento di Ingegneria Biomedica, Elettronica e delle Telecomunicazioni, Università degli Studi di Napoli Federico II, Via Claudio 21, 80125 Napoli, Italia

[iodice; antonio.natale; daniele.riccio}@unina.it](mailto:{iodice; antonio.natale; daniele.riccio}@unina.it)

Abstract

Electromagnetic models for surface scattering represent a handy analytical tool for any application founded on numerical methods which exploit the prediction of the scattered field. In addition, it is widely recognized that statistical scale-invariance properties exhibited by natural surfaces within a wide observation scale range are very efficiently described by means of fractal geometry and, of course, the better is the surface model employed to compute the electromagnetic scattering, the more accurate are the forecasts on the scattered field, provided that closed form solutions for the statistics of the field are attainable. Accordingly, here the focus is on the Kirchhoff scattering integral pertinent to a rough surface modeled as a fractional Brownian motion stochastic process. Such analysis led us to reconsider the meaning of the Kirchhoff solution for the scattering from both classical and fractal surfaces, so allowing us to provide a novel physical interpretation of the Kirchhoff scattering integral in terms of the probability density function of an equivalent rough surface.

Index Terms – Electromagnetic scattering, fractals, Kirchhoff Approach.

I. INTRODUCTION

Fractal geometry exhibits statistical scale-invariance properties which are distinctive of natural objects and so it is widely recognized that natural surfaces are very properly modeled by using the 2D fractional Brownian motion (fBm) stochastic process [1], [2]. Accordingly, for those applications that involve the electromagnetic scattering from natural surfaces (e.g., remote sensing data processing or wireless networks planning), it is certainly of interest to devise electromagnetic methods to evaluate the field scattered by a surface whose roughness is described via an fBm process.

Concerning this, in last decades several works have been addressed to formalize and solve the electromagnetic scattering from dielectric fBm surfaces [3]-[6] and, as expected, these analysis lead to a synthetic description of the scattered field which is in better agreement with measurements than those obtained by using classical, non-fractal, surface models [4], [5].

Within this framework, the Kirchhoff Approach (KA) is one of the most common used tools to analytically compute the scattering integral relevant to a rough surface; as stated in [3]-[6], in the case of fBm surfaces, its evaluation allows to express the scattered power density through two series, which are somehow complementary (in terms of convergence) and whose truncation criteria are detailed in [7].

Here the focus is on the Kirchhoff integral itself and on its physical reading instead of its closed form solution. In particular, we highlight that the KA integral for an fBm surface is proportional to a Symmetric alpha-Stable (S α S) distribution and, moreover, in order to provide a physical interpretation of this intriguing result we revisit the meaning of the KA solution for both classical and fractal surfaces.

II. KIRCHHOFF SCATTERING FROM ROUGH SURFACES

Let us consider a source illuminating a rough surface that separates air (or vacuum) from a homogeneous medium with complex relative permittivity ϵ_r .

Concerning the scattering surface $z(x,y)$, let us assume that the tangent plane approximation holds irrespective of the geometry employed to model it (criteria for the application of the KA for classical or fractal surfaces can be found in [8], [9] or [5], [6], respectively). Accordingly, the Kirchhoff approximation states that the mean square value of the generic component of the diffuse field is proportional to $p(-u_x/u_z, -u_y/u_z)$, with $p(a,b)$ defined as:

$$p(a,b) = \frac{1}{(2\pi)^2} \iint \exp\{jat_x + jbt_y\} \exp\left\{-\frac{1}{2}u_z^2 Q\left(\frac{t}{u_z}\right)\right\} dt_x dt_y, \quad (1)$$

wherein $Q(\tau)$ is the surface structure function, $t = \sqrt{t_x^2 + t_y^2}$ and $\mathbf{u} = (u_x, u_y, u_z) = \mathbf{k}_i - \mathbf{k}_s$, being \mathbf{k}_i and \mathbf{k}_s the incident and scattering propagation vectors, respectively, and their modulus k the wavenumber. Assuming a classical description for the scattering surface (a stationary, isotropic zero-mean, σ^2 -variance Gaussian stochastic process, with a Gaussian autocorrelation function), by letting $k\sigma \gg 1$ we can easily get the Geometrical Optics solution for the scattering, i.e. $p(a,b)$ becomes the probability density function (pdf) of the surface slopes and so the scattered power density results to be proportional to the probability that the local specular direction coincides with the scattering direction.

Conversely, assuming that the rough surface is modeled by an fBm process, with Hurst coefficient H and incremental standard deviation s [1, 2], we can state that the scattering integral expressed in (1) represents the distribution of an isotropic bivariate S α S random variable [10] with $\alpha=2H$ and dispersion coefficient proportional to the

variance of the fBm surface slope as observed at the wavelength scale. However, any attempt to interpret this result as the fBm counterpart of the GO solution for regular surfaces does not hold, as no GO limit has been used to obtain the fBm KA scattering pattern and, above all, because fBm surface slopes are not S α S random variables, but they are Gaussian.

Therefore, to give an interpretation of this result, the meaning of the Kirchhoff solution has to be revisited even for regular surfaces.

Accordingly, for a classical model of surface, we can state that a physical interpretation similar the one of the GO case can be given without letting $k\sigma \gg 1$. In particular, by expanding the structure function in MacLaurin series, we can read the integral in (1) as the convolution between the surface slopes' pdf and the local surface scattering diagram.

This alternative formalization suggests us to give a novel interpretation of the Kirchhoff solution: the overall rough surface can be seen as composed of many rough surface elements large with respect to the wavelength, with random Gaussian slopes and a proper scattering pattern, so that the mean square value of the field scattered by the overall surface is obtained by averaging the local scattering diagram over the surface elements' slopes. In addition, even for $k\sigma$ not large, $p(a,b)$ turns out to be positive and with unitary integral, so that it can be seen as the pdf of the slopes of an equivalent rough surface whose GO scattered power density is equal to the scattered power density of the actual rough surface.

Let us now move to consider scattering from an fBm surface. In this case a similar interpretation can be given to the Kirchhoff in scattering integral, but now we have to note that in this case GO cannot be achieved by decreasing the wavelength, because, due to the scale-invariance properties of the fBm (i.e., self-affinity), as the observation scale is reduced, finer and finer surface details appear, and the surface never appears smooth at any observation scale. Accordingly, the only way to obtain a smooth fBm surface is to let the surface fractal dimension tend to 2 ($D \rightarrow 2$), i.e. expanding the Kirchhoff integration kernel around $D=2$ (i.e., $H=1$), so that it can be read in terms of an intrinsic two-scale behaviour of the scattering surface: the mean square value of the overall scattered field is obtained by averaging the scattering diagrams of rough surface elements over their (Gaussian, according to the fBm model) slopes, as observed at a scale of the order of the wavelength. Moreover, in agreement with the previous discussion, the overall Kirchhoff scattering pattern of an fBm surface can also be interpreted as the S α S probability density function of the slopes of an equivalent rough surface whose GO scattered power density is equal to the scattered power density of the actual fBm surface.

III. CONCLUSION

In this paper we deal with the Kirchhoff solution for the scattering relevant to both classical and fractal surfaces from a new viewpoint. After some analytical manipulations of the Kirchhoff scattering integral we conclude that, irrespective of the model employed to describe the rough scattering surface, let it be classical or fractal, the scattered power density can be seen as proportional to the probability density function of the slopes of an equivalent rough surface whose GO scattered power density is equal to the scattered power density of the actual surface.

REFERENCES

- [1] B. B. Mandelbrot, *The Fractal Geometry of Nature*, New York: W.H.Freeman & C., 1983.
- [2] K. Falconer, *Fractal Geometry*, Chichester, UK: John Wiley & Sons, 1990.
- [3] O. Y. Yordanov and K. Ivanova, "Kirchhoff Diffractals", *J. Phys. A Math. Gen.*, vol.27, pp.5979-5993, 1994.
- [4] G. Franceschetti, A. Iodice, M. Migliaccio, D. Riccio, "Scattering from natural rough surfaces modelled by fractional Brownian motion two-dimensional processes", *IEEE Trans. Antennas Propagat.*, vol.47, no.9, pp. 1405-1415, 1999.
- [5] G. Franceschetti, A. Iodice, D. Riccio, "Fractal models for scattering from natural surfaces" in *Scattering*, edited by R.Pike and P.Sabatier, London: Academic Press, pp. 467-485, 2001.
- [6] G. Franceschetti and D. Riccio, *Scattering, Natural Surfaces and Fractals*, Academic Press, Burlington, (MA) USA, 2007.
- [7] S. Perna and A. Iodice, "On the Use of Series Expansions for Kirchhoff Diffractals", *IEEE Trans. Antennas Propagat.*, vol.59, no.2, pp. 595-610, 2011.
- [8] F. T. Ulaby, R. K. Moore and A. K. Fung, *Microwave Remote Sensing: Active and Passive*, Reading, MA: Addison-Wesley, 1982.
- [9] L. Tsang, J. Kong and K. Ding, "Scattering of Electromagnetic Waves – Theory and Applications", John Wiley & Sons, Inc, New York, 2000.
- [10] G. Samorodnitsky and M. S. Taqqu, *Stable Non-Gaussian Random Processes*. New York: Chapman & Hall, 1994.

RANDOM COUPLING MODEL FOR WAVE CHAOTIC CAVITIES

G. Gradoni⁽¹⁾, T. M. Antonsen⁽¹⁾, E. Ott⁽¹⁾

⁽¹⁾ Department of Physics & IREAP, University of Maryland
Paint Branch Drive, College Park, MD 20742, USA
Email: ggradoni@umd.edu

Abstract

The quest of a physical model for complex electromagnetic cavities is a vivid topic in modern engineering. In this contribution, we present a derivation of the random coupling model that describes the coupling of an external radiation into and out of electrically large enclosures through apertures (ports). A connection between deterministic and statistical theories is demonstrated in terms of cavity admittance (impedance) matrix. Our model makes use of the wave chaos theory to extend, and preserve, the classical modal description of the cavity field in presence of irregular boundaries.

Index Terms –Admittance matrix, aperture, random matrix theory, quantum and wave chaos, statistical electromagnetics.

I. INTRODUCTION

The study of aperture radiation inside electromagnetic enclosures has been pursued since a long time ago. More recently, several efforts have been made to model the field distribution inside complex enclosures. Several investigators came up with successful statistical models, most of them based on reasonable statistical assumptions driven by phenomenology of mode-stirred reverberation chambers. So far, it seems to be still necessary to relate the deterministic “system dependent” details of sources (sinks), such as apertures or antennas, to the fluctuation law describing the disordered behavior of fields inside irregular cavities.

In this contribution, we explain how this behavior can be tamed by wave chaos theory. In particular, we derive a model where the deterministic *radiation* admittance (impedance) of apertures (ports) naturally appears in the fluctuating *cavity* admittance, along with a random mode expansion describing the chaotic regime inside the cavity. This regime occurs in presence of irregular boundaries. We solve the boundary-value problem for an irregular, wave-chaotic, cavity by involving physical concepts developed in the frame of the random matrix theory for complex quantum mechanical systems.

A general formulation of the random coupling model (RCM) is presented and discussed, showing a connection between deterministic and statistical theories preserving the classical modal description. This is shown to be valid for three-dimensional cavities with apertures of arbitrary geometry, thus extending previous findings for isolated and interconnected microwave billiards [1], [2].

II. PHYSICAL CONSIDERATIONS

We investigated the rather canonical framework of an electrically large cavity exchanging energy with the external environment through apertures. We further assumed a cavity with boundary of arbitrary irregular shape.

It is known, from quantum chaos explorations of particles in a confined system with irregular *convex* boundaries, that motion trajectories exhibit exponential divergence in phase space, i.e., two particles originating from the same *position* with slightly different linear *momentum* follow very different paths after a few bounces on the boundary. This dynamic effect has an impact to the spectrum of complex systems subject to chaotic regime, which can be modeled by an unpredictable (random) Hamiltonian. In 1950, Eugene Wigner proved that the spectrum structure of several different compound nuclei could be reproduced by the eigenvalues of large random matrices with properly fluctuating elements. This line of inquiry is nowadays well established as the random matrix theory (RMT). About twenty years later, Sir Michael Berry conjectured that in semiclassical chaotic systems the particle wavefunction loses its “unperturbed” distribution, and it can be described by a superposition of plane-wave like solutions of the Schrödinger equation with random amplitude, polarization, and directions.

Our attack in deriving the random coupling model exploits both the Wigner surmise and the Berry hypothesis. This is valid if the dimensions of the cavity are much greater than the excitation wavelength, whence the semiclassical regime holds, and the propagation can be thought as made of *rays whose trajectories are chaotic*. The field dynamics is extremely sensitive to the cavity boundary, and the inner mixing regime rapidly destroys mode topologies. We can thus expand the mode amplitude in random plane waves, while preserving its resonant behavior, provided RMT is used to generate mode wavenumbers. Here, we use eigenvalues of a random matrix with Gaussian distributed elements (Gaussian Orthogonal Ensemble). We call the associated eigenvectors “chaotic modes”, to remark they are undistinguishable each other. The presented approach is not phenomenological as the ensemble we invoke when using RMT expresses the symmetry properties of the chaotic class a cavity belongs to.

III. RANDOM ADMITTANCE MATRIX

In order to involve sources and sinks in the model of a chaotic cavity, we first identify a suitable set of voltages and currents that are linearly related, and that can be used to describe the interaction of the fields within the cavity with radiations to and from the outside world. In case of localized ports, this identification is straightforward and also accessible in practice, while for apertures the transverse fields can be

expressed as a superposition of a basis of modes $e_s(x_\perp)$, viz.,

$$E_t = \sum_s V_s e_s(x_\perp); \quad H_t = -\sum_s I_s \hat{n} \times e_s(x_\perp), \quad (1)$$

where \hat{n} is the outward normal to the aperture, hereafter $\hat{n} \equiv \hat{z}$ for a planar aperture in the plane xy . Then, RCM provides a model for the linear relation between magnetic amplitudes I_s and electric amplitudes V_s that mimics the behavior of fields in the cavity $I_s = \sum_{s'} Y_{ss'}^{cav}(k_0) V_{s'}$,

where $Y_{ss'}^{cav}(k_0)$ is an element of the *cavity admittance* in k -space. The derivation of the admittance is based on the following approach. First one represents the cavity field in a complete basis of modes, and calculates the excitation of these modes due to coupling to the fields (1). Then one derives the formal expression for the cavity admittance that involves the modes and their resonant frequencies. In particular, the mode amplitudes are calculated by solving Maxwell's equations with boundary conditions of Eq. (1) on the aperture, and $E_t = H_t = 0$ elsewhere on the cavity boundary. Finally, by projecting fields onto the basis functions for electromagnetic (*em*) and magnetostatic modes (*ms*), yields

$$Y_{ss'}^{cav}(k_0) = \sqrt{\frac{\epsilon}{\mu}} \sum_n \left(\frac{ik_0}{k_0^2 - k_n^2} \frac{w_{sn}^{em} w_{s'n}^{em}}{V^{em}} + \frac{i}{k_0} \frac{w_{sn}^{ms} w_{s'n}^{ms}}{V^{ms}} \right), \quad (2)$$

which is exact, and where $w_{sn}^{(\cdot)} = \int_{aperture} d^2 x_\perp e_s(x_\perp) \cdot \hat{z} \times h_n^{(\cdot)}$ is the projection of

the n -th cavity mode onto the s -th aperture field mode, and $V^{(\cdot)}$ is a normalization factor for the cavity eigenfunctions.

At this point, according to the physical considerations discussed in the previous Section, we let the random coupling hypothesis intervene in Eq. (2). Specifically, we replace the exact eigenmodes with "chaotic modes" near the plane $z = 0$

$$h_{n\perp} = \lim_{N \rightarrow \infty} \frac{2}{\sqrt{N}} \sum_{j=1}^N b_{j\perp} \cos(k_j \cdot \hat{n} z) \cos(\theta_j + k_j \cdot x_\perp), \quad (3)$$

where $b_{j\perp}$, θ_j , and k_j are random variables. Using Eq. (3), and according to central limit theorem, for $N \rightarrow \infty$ we find that w_{sn}^{em} becomes a zero mean Gaussian variable. Furthermore, by diagonalizing the correlation matrix $\langle w_{sn}^{(\cdot)} w_{s'n}^{(\cdot)} \rangle$, and repeating the same procedure for the magnetostatic part, yields the RCM formulation for the cavity admittance

$$\underline{\underline{Y}}^{cav} = \mathcal{F}(\underline{\underline{Y}}^{rad}) + \left[\Re(\underline{\underline{Y}}^{rad}) \right]^{1/2} \cdot \underline{\underline{\xi}} \cdot \left[\Re(\underline{\underline{Y}}^{rad}) \right]^{1/2}, \quad (4)$$

where the statistical part is expressed by the fluctuation matrix

$$\underline{\underline{\xi}} = \frac{i}{\pi} \sum_n \frac{\underline{W}_n \tilde{\underline{W}}_n}{(K_0^2 - K_n^2 + i\alpha)}, \quad (5)$$

with $\alpha = k_0 / (\Delta k^2 Q)$ loss parameter, and $K_{(c)}^2 = k_{(c)}^2 / \Delta k^2$, and

$$\underline{Y}_{ss'}^{rad}(k_0) = \sqrt{\frac{\varepsilon}{\mu}} \int \frac{d^3 k}{(2\pi)^3} \frac{2ik_0}{k_0^2 - k^2} \bar{\mathbf{e}}_s(\mathbf{k}_\perp) \cdot \underline{\underline{\Delta}} \cdot \bar{\mathbf{e}}_{s'}(\mathbf{k}_\perp) \quad (6)$$

$$\underline{\underline{\Delta}} = \frac{\mathbf{k}_\perp \mathbf{k}_\perp}{k_\perp^2} \sqrt{\left(\frac{k^2 - k_\perp^2}{k^2} + \frac{(k_0^2 - k^2)k_\perp^2}{k^2 k_0^2} \right)} \frac{(\mathbf{k}_\perp \times \mathbf{n})(\mathbf{k}_\perp \times \mathbf{n})}{k_\perp^2} \quad (7)$$

The decomposition theorem in Eq. (4) shows the connection between (deterministic) radiation admittance and (fluctuating) cavity admittance of the aperture. The modal description of the cavity is preserved through Eq. (5), also emphasizing the role of distributed losses, and of the chaotic behavior of the system through the mean spacing of modes. The model predicts fluctuation laws in the range from superconducting ($\alpha = 0$) to semi-open cavities ($\alpha \gg 1$). In the asymptotic case where $\alpha \rightarrow \infty$, the magnitude of fluctuation tends to zero, and we get $\underline{\underline{Y}}^{cav} \approx \underline{\underline{Y}}^{rad}$, while it is always true $\langle \underline{\underline{Y}}^{cav} \rangle = \underline{\underline{Y}}^{rad}$, where Eq. (6) and Eq. (7) can be used.

IV. CONCLUSION

The random coupling model is derived for three-dimensional wave chaotic cavities with arbitrary apertures. The fluctuating cavity admittance matrix gets decomposed as the product of the radiation conductance and a universal matrix given by the summation of chaotic modes. The universal fluctuation depends on the chaotic class the electromagnetic cavity belongs to, through the average spacing between modes. Integral expressions are also found for the deterministic conductance and susceptance matrix of the aperture.

ACKNOWLEDGEMENT

Financial support by AFOSR, ONR, and NSF under MURI framework.

REFERENCES

- [1] S. Hemmady, X. Zheng, E. Ott, T. Antonsen, and S. Anlage, "Universal impedance fluctuations in wave chaotic systems," *Physical Review Letters*, vol. 94(1), pp. 014102--1-4, 2005.
- [2] G. Gradoni, T. Antonsen, and E. Ott, "Impedance and power fluctuations in linear chains of coupled wave chaotic cavities," accepted for publication, *Physical review E*.

TWO APPROACHES TO FIELD FOCUSING IN UNKNOWN ENVIRONMENTS

L. Di Donato⁽¹⁾, D. A. M. Iero⁽¹⁾, I. Catapano⁽²⁾,
L. Crocco⁽²⁾, G. Sorbello⁽³⁾, T. Isernia⁽¹⁾

- ⁽¹⁾ DIMET, Università Mediterranea di Reggio Calabria, via Graziella,
Loc. Feo di Vito, 89100 Reggio Calabria
loreto.didonato@unirc.it, domenica.iero@unirc.it,
tommaso.isernia@unirc.it
- ⁽²⁾ Istituto per il Rilevamento Elettromagnetico dell'Ambiente (IREA-CNR), Via Diocleziano 328, 80124 Napoli
catapano.i@irea.cnr.it, crocco.l@irea.cnr.it
- ⁽³⁾ DIEEI, Università degli Studi di Catania, Viale Andrea Doria 6,
95125 Catania gino.sorbello@dieei.unict.it

Abstract

The paper introduces two effective methods, based on the Linear Sampling Method, to tackle the problem of focusing an electromagnetic field onto a target point in unknown environments. Besides its theoretical relevance, the problem is of interest in applications spanning from biomedical engineering to security monitoring.

Index Terms – Electromagnetic focusing, Synthesis problems, Linear Sampling Method, Antenna synthesis.

I. INTRODUCTION

The Linear Sampling Method (LSM) [1] is an effective approach to retrieve the morphology (qualitative imaging) of an unknown object by means of simple processing of the field it scatters, without requiring any a priori information about the electromagnetic properties of the scatterer or any approximation. Nowadays, thanks to its robustness and low computational burden, it is well known in the inverse scattering community also as a valuable initial processing step for quantitative characterizations of unknown scatterers.

In this contribution we propose two different strategies based on the LSM processing to tackle another electromagnetic inverse problem, i.e. the synthesis of an array of antennas able to focus the radiated field onto a target point located in unknown environments. Obviously, although it requires that the antennas are able to sense the surrounding environment, no quantitative imaging procedure of the unknown scenario is involved. Both the proposed methods are based on the physical interpretation of the LSM given in [2], which shows the analogy between the linear inverse problem tackled by the LSM and the problem of focusing an electromagnetic wave into a penetrable scatterer. Moreover, it also takes advantage from a further insight, recently provided in [3], on the characteristics of the total internal field induced by LSM driven primary sources. Such an information allows then, by means of a suitable approximation on the induced fields, to apply the well known theory of pencil beams [3] to the problem at hand. Notably,

such a second approach allows indeed to look for a constrained focusing, i.e., it allows to enforce upper bounds on the level of sidelobes. Of course, both approaches do not guarantee the solution optimality, but, as shown by some numerical results, they can focus the field much better than just applying the above cited theory of pencil beams to the incident fields, (which just can work within the applicability of the Born approximation).

Solving the focusing problem tackled in this communication has a great impact on all those applications in which it is necessary to concentrate the energy of a field into a given region, while taking into account multiple interactions arising from the surrounding environment. This is for instance the case of security monitoring (e.g., motion tracking) and non-invasive medical treatments (e.g. hyperthermia).

II. FOCUSING APPROACHES

Let us consider the canonical 2-D scalar electromagnetic problem, wherein an unknown possibly not connected scatterer, whose cross section Σ is invariant along the z -axis, lies in the domain under test Ω and it is probed by means of transmitting and receiving antennas polarized along the target's axis of invariance. The LSM tackles the inverse scattering problem by solving an auxiliary inverse linear problem relying on the far field integral equation (FFIE):

$$F[\xi] = \int_{\Gamma} E_s(\theta, \underline{R}) \xi(\underline{r}_s, \theta) d\theta = G(\underline{R}, \underline{r}_s) \quad (1)$$

where ξ is the unknown function, $F[\bullet] : L^2(\Gamma) \rightarrow L^2(\Gamma)$ is the far-field operator [4], Γ is the curve where the antennas are positioned, E_s is the scattered field due to the incident field E_i , and G is the Green's function pertaining to the background scenario. By the sake of simplicity, a homogeneous reference scenario is considered from now on, but the approach can be extended in a straightforward fashion to any reference scenario.

After sampling the region under test Ω with an arbitrary grid of points \underline{r}_s and solving (1) for each of them, an estimate of the target's shape is achieved by plotting the energy of the (regularized) solution $||\xi||$. In fact, it assumes large values when $\underline{r}_s \in \Sigma$, and low values (with respect to its overall dynamic range) elsewhere [2].

Both focusing approaches we are proposing rely on the linear relationship between the incident and scattered fields, according to which the scattered field $F[\xi]$, defined by the first equality in eq.(1), can be thought as generated from a probing incident field given by :

$$\psi_i(\underline{r}_s, \underline{r}) = \int_{\Gamma} E_i(\underline{r}, \theta) \xi(\underline{r}_s, \theta) d\theta \quad (2)$$

More precisely, as long as (1) can be solved in a sampling point \underline{r}_s , ξ defines an incident field ψ_i , whose corresponding scattered one $F[\xi]$ is the field radiated by an elementary source located in \underline{r}_s (i.e. the Green's function G).

Strategy I

The first way to exploit the LSM in the focusing problem we are considering is based on its physical interpretation [2], according to which the linear inverse problem defined through the FFIE (1) is equivalent to focusing in the sampling point at hand the volumetric current induced by the interaction between a suitable probing wave and the target. Let us denote by $J_p(\theta)$ the (known) sensing excitation of a primary elementary source located on Γ in the direction θ and $E_{inc}(\underline{r}, \theta)$ the incident wave it radiates in Ω when no target is present. According to (2) and to the linear relationship between the array excitations and the incident fields, it is clear that the solution of the FFIE provides the direct knowledge of the array excitations required to enforce the scattered field $F[\xi]$ on Γ , that are given by :

$$J'_{foc}(\underline{r}_s, \theta) = \xi(\underline{r}_s, \theta) J_p(\theta) \quad (3)$$

In fact, the primary sources (3) will give rise to the incident field (2), which, by virtue of (1), correspond to a focusing in \underline{r}_s of the induced volumetric currents and hence of the total field.

Strategy II

The second proposed focusing strategy relies on a further insight into the LSM: while the incident field (2) depends on the unknown scatterer through ξ , the scattered one does not, as it matches the field G (in L^2 - norm) regardless the nature of the scatterer. In particular, assuming that equation (1) admits a solution, let us consider an incident field equal to ψ_i , so that the corresponding scattered field is a cylindrical wave pattern in the whole space external to the sampling point \underline{r}_s at hand. Then, the total field can be approximated as follows:

$$\Psi_{ts}(\underline{r}_s, \underline{r}) = \Psi_i(\underline{r}_s, \underline{r}) + F_{2D}^{-1} \left\{ \Lambda[\tilde{r}] \cdot F_{2D} \left[-\frac{j}{4} H_0^2(k_b |\underline{r} - \underline{r}_s|) \right] \right\} \quad , \quad (4)$$

wherein the second addendum at the right hand side is a low pass version of zero order second kind Hankel function, F_{2D} denotes the Fourier transform with respect to the spatial variable \underline{r} , \tilde{r} is the spectral variable, and Λ is a low-pass circular filter of radius $|\underline{r}| = k_b \cdot a_s$, a_s being the radius of the minimum circle enclosing the scatterer, as estimated from LSM. Notably, expression (4) only makes sense when the sampling point belongs to the scatterer. By using different sampling points \underline{r}_s , $s=1, \dots, S$, the desired possibly focused field can be given by a linear combination of a set of approximated fields (4) according to:

$$\Psi_t(\underline{r}) = \sum_{s=1}^S A_s \cdot \Psi_{ts}(\underline{r}_s, \underline{r}) \quad , \quad (5)$$

Then, we can apply the well known theory of pencil beams [4] to such an approximated total field solving the following constrained convex programming problem:

Find the complex coefficients A_s ($s = 1, \dots, S$) of the representation (5) such to

$$\text{Max } \Re\{\Psi_t(\underline{r}_0)\} \quad (6)$$

subject to

$$\Im\{\Psi_t(\underline{r}_0)\} = 0 \quad (7)$$

$$|\Psi(\underline{r})|^2 \leq UB(\underline{r}) \quad \underline{r} \in \Omega \quad (8)$$

wherein UB denotes a mask function for the adopted constrains. Then, if A_1, \dots, A_S is the solution of such a problem, the solution of the overall focusing problem will be given by:

$$J''_{foc}(\theta) = \sum_{s=1}^S A_s \cdot \xi(r_s, \theta) \cdot J_p(\theta) \quad (9)$$

III. A NUMERICAL EXAMPLE AND CONCLUSIONS

Fig.1 reports the kind of focusing performances one is able to achieve by using the first (a) and the second (b) proposed procedure, as well as the focusing which is achieved when approximating the total fields with the incident ones (c), i.e. adopting a backpropagation approach.

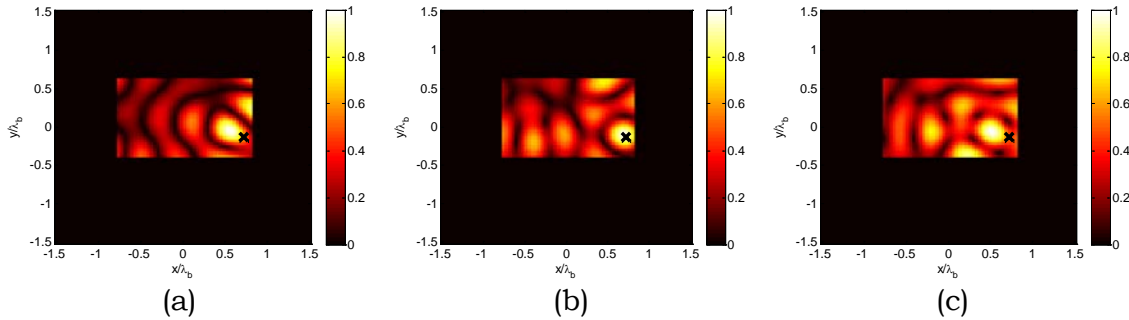


FIG. 1 Normalized amplitude of the field focused in a target point, identified by a cross marker, inside a rectangular scatterer ($\epsilon_r=2.25$, $\sigma=5\text{mS/m}$), embedded in vacuum.

As it can be seen in Fig.1, the second LSM focusing approach (b) provides a focused field characterized by the smallest target point mismatch and a side lobes' amplitude which, as well as that corresponding to the field focused by the first LSM procedure (a), is lower than the one obtained by mean of backpropagation approach (c).

REFERENCES

- [1] L. D. Colton and R. Kress, *Inverse Acoustic and Electromagnetic Scattering Theory*, Springer-Verlag, Berlin, Germany, 1992.
- [2] I. Catapano, L. Crocco, and T. Isernia, "On simple methods for shape reconstruction of unknown scatterers," *IEEE Trans. Antennas Propagat.*, vol. 55, pp. 1431-1436, 2007.
- [3] L. Crocco, I. Catapano, L. Di Donato and T. Isernia, "The Linear Sampling Method as a Way to Quantitative Inverse Scattering," *IEEE Trans. Antennas Propagat.*, vol.60, pp.1844-1853, 2012.
- [4] T. Isernia and G. Panariello, "Optimal focusing of scalar fields subject to arbitrary upper bounds ," *El. Letters* , vol.34, no.2, pp.162-164, 1998.

INFRARED ABSORPTION MEASUREMENTS USING METAMATERIALS

Luigi La Spada, Renato Iovine, Filiberto Bilotti, and Lucio Vegni
Department of Applied Electronics, "Roma Tre" University
Via della Vasca Navale 84, 00146 Rome, Italy

Abstract

In this study, a low cost, compact metamaterial-based sensor, operating in the mid-infrared frequency range, is proposed. The sensor is able to detect the presence of (in)organic compounds by absorption measurements. In particular, the proposed sensor is designed to recognize the presence of water content in biological samples. For this aim a new analytical model is developed useful to describe the resonant behaviour of the sensor. Good agreement between the numerical values, obtained through full-wave simulations, and the theoretical ones, obtained by using the proposed model is achieved. Results confirm the possibility to use the proposed structure as a sensor for water content recognition in an high selective way. This sensor may find application in medical diagnostics, in the detection of normal and cancer tissue by water absorption measurements.

Index Terms – Metamaterials, bio-electromagnetic sensor, absorption measurements, cancer tissue.

I. INTRODUCTION

Nowadays bio-electromagnetic sensors have assumed a crucial role in many application fields, such as biological sensing and detection, proteins analysis, cell membrane function [1,2]. In particular, sensors based on absorption measurements, have a great importance in biomedical applications. In fact, through absorbance measurements it is possible to extract different information from the biological sample under study, in particular the type of substance and its concentration. It is well known that each material has a characteristic spectrum that depends on the corresponding molecular structure [3]. The vibrational states of a molecule describe changes in the sample at molecular levels, leading to a particular sample spectral signature. Therefore, precise measurements of such spectrum allow the identification of a specific substance. These vibrational states can be probed in a variety of ways. The most direct way is through infrared (IR) spectroscopy. In particular, water exhibits different absorption peaks at such frequencies. New methods to identify such vibrational transitions are necessary. For this aim it is crucial to illuminate the sample in a selective way in order to excite only specific resonant frequencies, without affecting the sensor response by the absorption bands of other molecular species existing in the sample under study. Exploiting water absorption properties, the proposed research attempts to design a new selective filter suitable to recognize different water content in biological matter. To address these requirements we propose to use metamaterials, which exhibit several interesting electromagnetic properties, suitable for such purposes [4]. The main target of this paper is to propose the design of a new metamaterial-based sensor for water content detection in biological

tissues. The rest of the paper is structured as follows. First, a conceptual framework explaining the sensor behaviour is presented. Next, an equivalent quasi-static circuit model, describing the sensor resonant behavior is developed. Finally, as an application of the sensor, the water content recognition in biological samples is presented in the results paragraph.

II. THE COMPLEMENTARY SENSOR BEHAVIOUR

Absorption bands of water are related to molecular vibrations involving various combinations of water molecule fundamental vibrational modes. When an electromagnetic wave is transmitted through a medium containing water molecules, portions of the electromagnetic energy are absorbed by such molecules. This water absorption occurs preferentially at certain characteristic frequencies, while the rest of the spectrum is transmitted with minimal effects. Strong absorbance by water occurs at IR frequencies. Therefore, evaluating such spectral signatures (in terms of peak position, magnitude and amplitude width) allows to study the water content in the compound under test.

To exploit such phenomena, it is necessary to illuminate the biological compound in a selective way. For this purpose the metamaterial sensor is designed to have its resonant frequencies tuned to the main water absorption peaks in the IR spectrum. This can be done by using the Complementary Split-Ring Resonator configuration (CSRR). The material under test is placed not in direct contact to the sensor, but at a certain distance from it. The system "sensor-sample" is, then, irradiated by an IR electromagnetic field. When the resonance of the sensor is close to that of the material under test, the sensor response will have the same frequency positions, but its shape is greatly modified, especially in terms of magnitude and amplitude width, because of the water strong absorption.

III. THE QUASI-STATIC EQUIVALENT CIRCUIT MODEL

To design the sensor with its resonant frequencies tuned to specific absorption peaks, the following equivalent quasi-static circuit model must be used. The sensor consists in a metallic (e.g. silver in this case) planar array of complementary resonating inclusions, as shown in Figure 1a, where only the unit-cell is depicted. The structure is excited by a TE-wave. According to [5, 6], the equivalent LC resonant circuit describing the electromagnetic behaviour of the unit-cell is the one reported in Figure 1b. In the following, we describe each of the terms.

The magnetic and electric reactive phenomena can be described as follows: the total inductance can be written as the sum of two terms, the kinetic one (depending on the metal electromagnetic properties) and the geometric term, such as the gap and the square inductance (as a function of the inclusion geometrical parameters).

On the other hand, the total capacitance can be evaluated as the series of the geometrical (square capacitance) and the additional capacitance. Thus the resonant frequency is given by:

$$f_0 = \frac{1}{2\pi} \left\{ \left[L_{geom}(l, w, t) + L_{add}(l, w, t, \omega_p, \gamma, \omega) \right] \frac{C_{geom}(l, w, t, g) \cdot C_{add}(l, w, t, g, \omega_p)}{C_{geom}(l, w, t, g) + C_{add}(l, w, t, g, \omega_p)} \right\}^{-1/2}$$

In order to maximize the electromagnetic performance of the sensor, an optimization process is necessary. In particular, by exploring the relation linking electromagnetic and geometrical parameters with the resonant frequency, it is possible to accurately define the resonance positions and their bandwidth. In this way, the highest possible selectivity and the same magnitude in terms of transmission coefficient were obtained. Results are depicted in Figure 2.

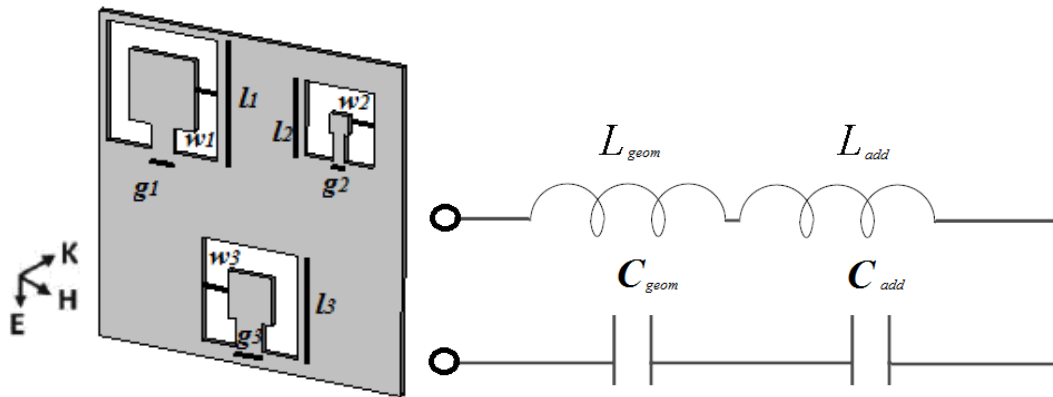


FIG. 1 – (a) Metamaterial unit-cell: side length $l_1=880$, $l_2=544$, $l_3=760$; strip width $w_1=180$, $w_2=200$, $w_3=205$; gap length $g_1=180$, $g_2=80$, $g_3=205$; all dimensions are expressed in nm. (b) Quasi-static equivalent circuit model

IV. RESULTS

A metamaterial-based sensor was designed by using the guidelines presented in the previous section. The sensing platform presents multiple resonant frequencies, tuned to ones of water molecule vibrational modes, such as 50, 66, and 100 THz. As a result, the sensor allows recognizing different water content in biological tissues. In the simulated experiment, the sensing platform is illuminated by an IR electromagnetic field and the output signal is revealed through a detector placed after the sample. To describe the absorption behaviour of water, water absorbance characteristics have been used. The corresponding full-wave numerical results are shown in Figure 2, where the sensor response without the biological compound and the transmission coefficient for different water content are shown. The results clearly reveal that the changes in the transmission coefficient magnitude and amplitude width are significantly related to the absorption rate of the hydrogen bonds of water molecules. Therefore, it is possible linking the transmission coefficient bandwidth to the water content in the biological sample. More specifically, the results demonstrate that all the transmission peaks significantly absorb in a

different way, in line with the absorption behaviour of water at such frequencies.

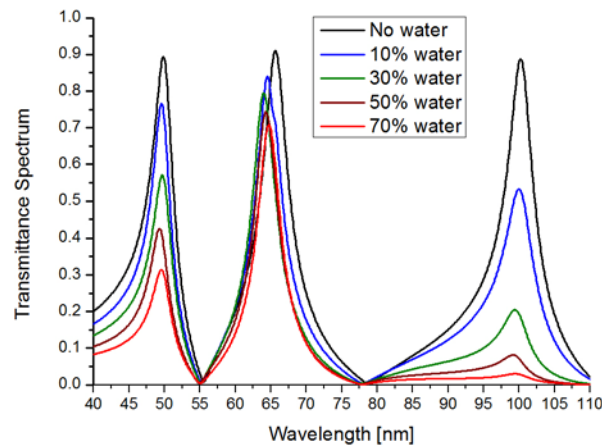


FIG. 2 – Transmission coefficient for different water content in a tissue.

V. CONCLUSIONS

In this contribution, we have shown that a metamaterial-based structure can be successfully used as a sensor working in the IR regime to detect water content in biological compounds.

A new analytical circuit model of the metamaterial structure has been proposed, leading to a good agreement (above 95%) between full-wave numerical and analytical results. The sensor has been optimized in order to obtain the highest selectivity performance. In addition, the results of this research suggest that, starting from the magnitudes and amplitude widths of the three water resonant peaks and their combinations, it is possible to recognize the different water content in the material under test. The proposed structure may find applications, for example, in the recognition of a healthy tissue from a malignant one through water content measurements.

REFERENCES

- [1] T. Vo-Dinh, and L. Allain, "Biosensors for Medical Applications," Biomedical Photonics Handbook, CRC Press, 2003.
- [2] M. Hu, J. Chen, Z.Y. Li, L. Au, G.V. Hartland, X. Li, M. Marquez, and Y. Xia, "Gold nanostructures: Engineering their plasmonic properties for biomedical applications," *Chem. Soc. Rev.*, vol. 35, pp. 1084–1094, 2006.
- [3] R.M. Silverstein, F.X. Webster, and D.J. Kiemle, *Spectrometric Identification of Organic Compounds*, 7th edition, Wiley, 2005
- [4] L. La Spada, F. Bilotti, L. Vegni, "Metamaterial resonator arrays for organic and inorganic compound sensing," *Proc. of SPIE 8306*, 83060I-1-10, 2011.
- [5] F. Bilotti, A. Toscano, L. Vegni, K. Aydin, K.B. Alici, E. Ozbay, "Equivalent-Circuit Models for the Design of Metamaterials Based on Artificial Magnetic Inclusions," *IEEE Trans. Microw. Theory Tech.*, vol. 55, 2865-2873, 2007.
- [6] T. Zentgraf, T. P. Meyrath, A. Seidel, S. Kaiser, and H. Giessen, "Babinet's principle for optical frequency metamaterials and nanoantennas", *Physical Review B*, vol 76, 033407-1-4, 2007.

A STUDY ON THE FUNDAMENTAL MODE CHARACTERISTICS SUSTAINED BY THE PLASMONIC SLOT WAVEGUIDE

F. Frezza⁽¹⁾, P. Nocito⁽²⁾, E. Stoja⁽¹⁾

⁽¹⁾ Department of Information Engineering, Electronics and Telecommunications, “La Sapienza” University of Rome, Via Eudossiana 18, 00184 Rome, Italy

⁽²⁾ ISCTI, Department of Communications, Ministry of the Economic Development, Viale America 201, 00144 Rome, Italy

stoja@diet.uniroma1.it

Abstract

We investigate and compare the characteristics of the fundamental guided mode sustained by a subwavelength plasmonic slot waveguide for three types of metals: gold, silver and aluminum. This is done in terms of mode effective index, propagation length, confinement and, as the mode under study is quasi-TEM, we also develop a transmission line model that can be employed in the design of optical components making use of slot waveguides.

Index Terms – plasmonics, subwavelength waveguide, modal study, integrated optics

I. INTRODUCTION

By exploiting the properties of metals at optical frequencies, plasmonic waveguides, which confine propagating electromagnetic energy in structures of subwavelength dimensions, may be designed. As this is of fundamental importance in the development of optical integrated circuits, many types of waveguides have been proposed [1] and, among these, the slot waveguide [2] seems to offer the best confinement of the propagating mode in the cross-section which allows for higher integration.

The symmetric slot waveguide (Fig. 1) is composed of a metallic film embedded in a homogeneous dielectric which, in all our simulations, is assumed to be silica with refractive index $n = 1.44$. On the other hand, for the asymmetric structure, the upper medium is supposed to be air, having $n = 1$.

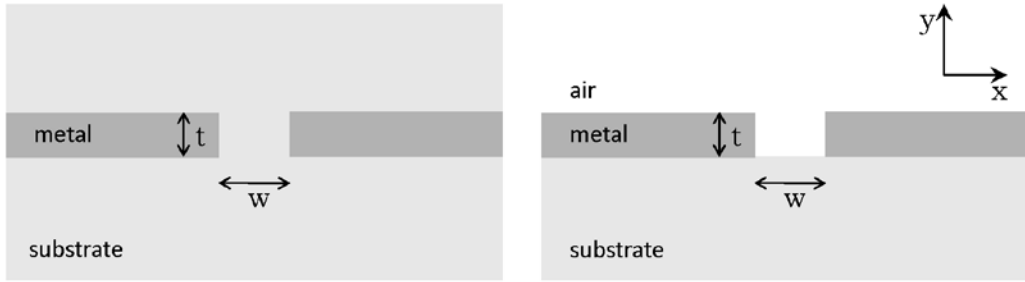


FIG. 1 – Cross-section of the slot waveguide: symmetric structure (right) and asymmetric structure (left). The reference system is also depicted.

II. MODE CHARACTERIZATION AND SIMULATION MODEL

As the structure is invariant along the propagation direction z (out of plane, Fig. 1), we can assume a $e^{-\gamma z}$ dependence along this direction with $\gamma = \alpha_z + j\beta_z$, α_z and β_z being the damping and phase constants respectively. The effective refractive index of the mode is defined as $n_{\text{eff}} = \beta_z / k_0$, and the mode propagation length as the length for which the mode power decays of $1/e^2$, $L_p = 1/2\alpha_z$.

We define the confinement factor F_c as the ratio between the power within the $w \times t$ slot area and the total power carried by the mode:

$$F_c = \frac{\int_{-w/2}^{w/2} \int_{-t/2}^{t/2} E_x(x, y) H_y^*(x, y) dx dy}{\int_{-\infty-\infty}^{+\infty+\infty} \int E_x(x, y) H_y^*(x, y) dx dy}.$$

Borrowing from microwave engineering, a characteristic impedance model would be very useful for the design of plasmonic waveguide components. From our analysis, we have noted that the fundamental mode of the symmetric structure is a quasi-TEM mode, as the dominant transverse field components E_x and H_y are at least three and four orders of magnitude greater than the longitudinal ones, for the electric and magnetic case, respectively. The electric field is tightly confined in the dielectric region and E_x is almost constant in the slot area. Consequently, we can define an equivalent impedance Z_o as the ratio of

an effective voltage $V = \int_{-\infty}^{+\infty} E_x dx$ and effective current $I = \int_{-\infty}^{+\infty} H_y dy$ retrieved

by integrating the dominant field components E_x and H_y along the horizontal ($y=0$) and vertical ($x=0$) symmetry lines of the structure, respectively [3]. The integrals can be truncated at the simulation domain dimensions as the fields are negligibly small at the boundaries.

For the same reason, the effective current I corresponds to the circuitation of H_y as the integration path may be “closed” by integrating along the simulation’s domain boundary where this component is negligible.

To search for the modes sustained by the structure, we run a 2D mode analysis in COMSOL Multiphysics which implements the Finite Element Method (FEM). While the substrate is not dispersive, metals in the optical regime present a plasmonic behavior. To take this into account a Drude-Lorentz model [4] was adopted for the electric permittivity of silver, gold, and aluminium. The metal film thickness is assumed to be 50 nm in all simulations. The dispersion of the fundamental mode is thoroughly investigated with respect to slot width w and operation wavelength λ_0 , for our three metals of choice.

III. RESULTS

In our wavelength range of interest, the slot dimensions are much smaller than the wavelength, so, as no other higher order bounded mode can propagate, the waveguide operates in the unimodal regime.

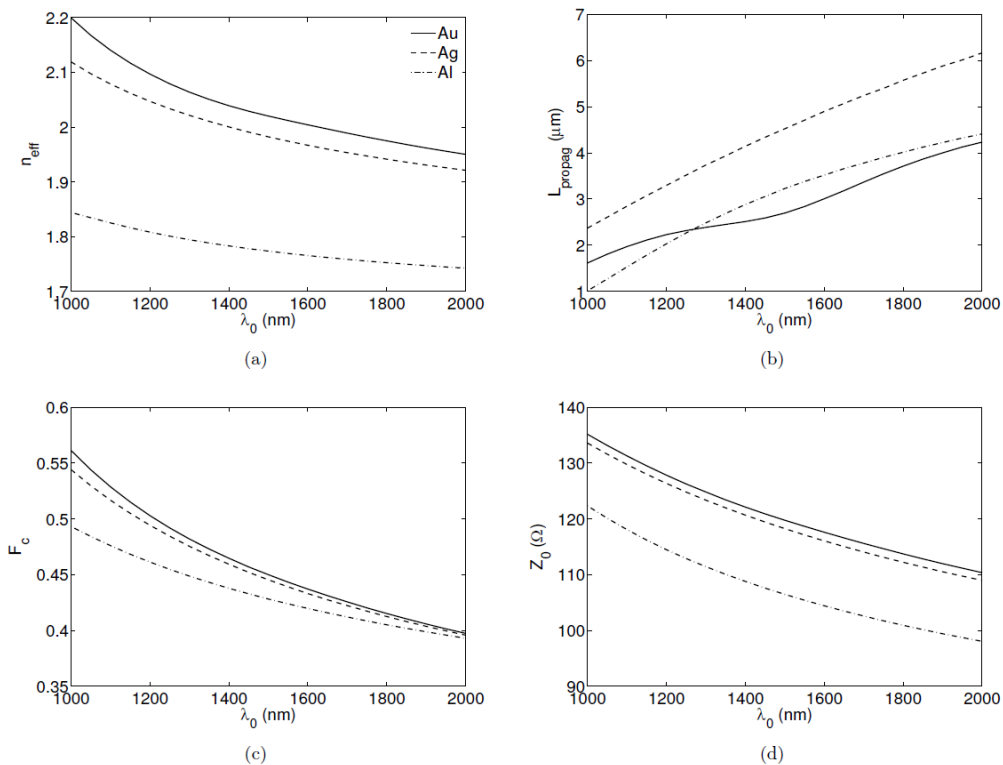


FIG. 2 – The effective refractive index (a) and propagation length (b) of the fundamental guided mode for a symmetric $50 \times 50 \text{ nm}^2$ slot waveguide as a function of free space wavelength; (c) mode confinement factor and (d) real part of the equivalent characteristic impedance.

Looking at the dispersion characteristics of the mode for a $50 \times 50 \text{ nm}^2$ symmetric slot waveguide (Fig. 2), we can observe that at longer wavelengths the mode becomes less confined and propagates farther. A similar behavior is presented in the asymmetric case, but conversely from a particular wavelength the mode becomes leaky. The same happens for the dispersion behavior with respect to the slot width. Physically, this behavior is related to the overlap of the mode profile with the metal region as the ohmic losses grow proportionally to the overlap.

Another interesting result to note is the fact that, at certain wavelengths, the propagation length of the mode in the case of aluminium is greater than the case of gold even if the ohmic losses are significantly lower in the latter case. Depending on the application of interest, this information can provide insight on the choice of the proper metal to be employed.

IV. CONCLUSION

A thorough investigation on the mode characteristics of the plasmonic slot waveguide is presented. The span of the characteristic impedance with respect to the slot width is promising in terms of the design of impedance matched plasmonic components.

In the asymmetric case, a cut-off wavelength/slot width for which the mode becomes leaky exists. This feature may be exploited for the design of plasmonic leaky-wave antennas.

REFERENCES

- [1] D. K. Gramotnev and S. I. Bozhevolnyi, "Plasmonics beyond the diffraction limit," *Nature Photonics*, vol. 4, pp. 83-91, 2010.
- [2] G. Veronis and S. Fan, "Guided subwavelength plasmonic mode supported by a slot in a thin metal film," *Optics Letters*, vol. 30, pp. 3359-3361, 2005.
- [3] W. Cai, W. Shin, S. Fan and M. L. Brongersma, "Elements for plasmonic nanocircuits with three dimensional slot waveguides," *Advanced Materials*, vol. 22, pp. 5120-5124, 2010.
- [4] A. D. Rakic and S. Fan, "Optical Properties of Metallic Films for Vertical-Cavity Optoelectronic Devices," *Applied Optics*, vol. 25, pp. 2511-2521, 2007.

YB-DOPED PHOTONIC CRYSTAL FIBER LASER

Rosa Ana Perez-Herrera⁽¹⁾, Enrico Coscelli⁽²⁾, Michele Sozzi⁽²⁾,
Annamaria Cucinotta⁽²⁾, Stefano Selleri⁽²⁾, Manuel Lopez-Amo⁽¹⁾

- (1) Departamento de Ingeniería Eléctrica y Electrónica, Universidad Pública de Navarra, Campus Arrosadía, ES-31006 Pamplona, Spain
- (2) Dipartimento di Ingegneria dell'Informazione, University of Parma, Viale G.P. Usberti 181/A, IT-43124 Parma, Italy
stefano.selleri@unipr.it

Abstract

An Ytterbium-doped Photonic Crystal Fiber (PCF) laser has been experimentally assembled. The issue of splicing PCFs with conventional fibers has been addressed, two solutions for splicing an air-clad Ytterbium-doped PCF with a conventional one have been proposed, and their losses have been measured. The performances of the laser have been evaluated.

Index Terms – Fiber Lasers, Large mode area fiber, Photonic Crystal Fiber, Splicing.

I. INTRODUCTION

High and medium power applications of fiber laser are gaining interest day by day in many different fields ranging from spectroscopy to medicine, from monitoring and sensing to micromachining and material processing [1]. The well-established fiber and doped fiber technology is one of the keys to this success. In addition, the advent of Photonic Crystal Fibers (PCFs) with their novel optical properties [2] has further boosted this process. Photonic crystal fibers are a new class of optical fibers in which the core can be either solid or hollow while the cladding is formed by a distribution of air-holes running along the entire fiber length. Large Mode Area (LMA) Double Cladding (DC) rare-earth-doped PCFs seems to be particularly promising. In these fibers, the Yb-doped inner core, with a LMA, is surrounded by a microstructured inner cladding region, which is in turn surrounded by a ring of large air-holes. Light from diode pumps having a poor beam quality is efficiently coupled into the inner cladding region, where it is gradually absorbed in the inner core, and thus leads to single-mode signal amplification and lasing. The advantages of PCF technology, over more conventional DC fibers with doped inner core and polymer outer cladding, are that it allows the fabrication of very large single-mode cores, and that the damage of the outer cladding due to the high fiber surface temperature [3] is not a problem, since air-holes are used instead of polymers. Double clad PCFs are known also as air-clad fibers [4]. Due to the greatly enhanced index contrast, the air-clad can provide very large

numerical apertures determined by the bridge-width in the air-clad. The extremely high numerical aperture for the pump core/inner cladding allows efficient pumping with inexpensive and high power broad area emitting pumps. The large mode area for the single mode signal facilitates high power levels while avoiding nonlinearities and providing a good overlap between the pump guide and the signal guide area.

However high quality splicing of PCFs with traditional fiber devices may be challenging and requires special attention to conserving optical properties at the splice interface.

In this paper the experimental set-up of a PCF based laser is described focusing on the issue of splicing the LMA air-clad Yb-doped fiber with the output fiber of a commercial pump combiner. Two splicing techniques are described and the laser performances are reported.

II. EXPERIMENTAL SET-UP

In Fig. 1 the experimental set-up of the laser is reported. A pig-tailed laser diode emitting at 1064nm is used as seed laser. An isolator and an optical circulator are inserted in order to protect the seed laser from reflected light that is monitored by mean of an Optical Spectrum Analyzer (OSA). The 915nm multimode pump light is coupled in the PCF together with the 1064 nm radiation by a pump combiner. A commercially available PCF has been used as active fiber, the DC-135/15-PM-Yb. Where the 15 μm large polarization-maintaining core is strictly single-mode, the inner cladding diameter is 135 μm , whereas the outer cladding diameter is 280 μm . The described set-up is quite simple, but it involves the issue of splicing the DC-135/15-PM-Yb with the output fiber of the pump combiner which is a standard DC fiber with core diameter equal to 5 μm .

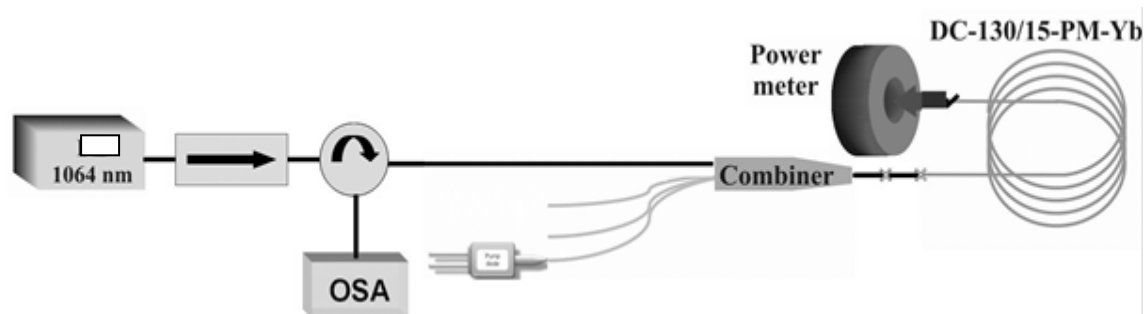


FIG. 1 – Experimental set-up of the PCF laser. The 1064nm seed laser radiation is combined with the pump one into a double cladding polarization maintaining PCF.

First of all the two fibers to be spliced together have been stripped and cleaved to high quality. The PCF is equipped with a standard single layer acrylate coating. The coating has been removed with conventional fiber stripping tools. All fibers have been cleaved with conventional high

precision cleaver Fujikura FK-11-LDF. Air-clad features presents an increased challenge for the cleaving procedure. In fact the air-clad is a ring of closely spaced air holes, which, when cleaved, acts as an efficient barrier for the shock wave associated with the cleave. Special care has been taken to use an appropriate amount of tension. Using too little tension results in no cleave occurring. Using too much tension, results in a time delay between the cleaving of the outer and inner cladding. In this case the inner cladding experiences too much stress during cleave and glass debris can be seen at the facet.

In order to reduce splice losses between the 5 μm core standard DC fiber and 15 μm core air-clad PCF, an intermediate LMA standard DC fiber with 10 μm core has been used. Thus the critical splicing is between the 15 μm air-clad PCF and a 10 μm core DC fiber.

III. RESULTS

PCF splices are different from standard fiber splices as the core cannot be seen through the side of the fiber and the power must be reduced to avoid hole collapse. Typical splice powers are about 25% less than what would be used for comparable solid fibers. However the lower splice power increases the risk of low mechanical strength and when optimizing the splice parameter, the goal is, therefore, to find the best compromise between transmission loss and mechanical strength.

When splicing is performed between fibers of different mode field diameter, there is a lower limit to the splice loss. We made the critical splice with two different setting of the splice machine Fujikura FSM-45PM-LDF. The results are reported in Fig.2.

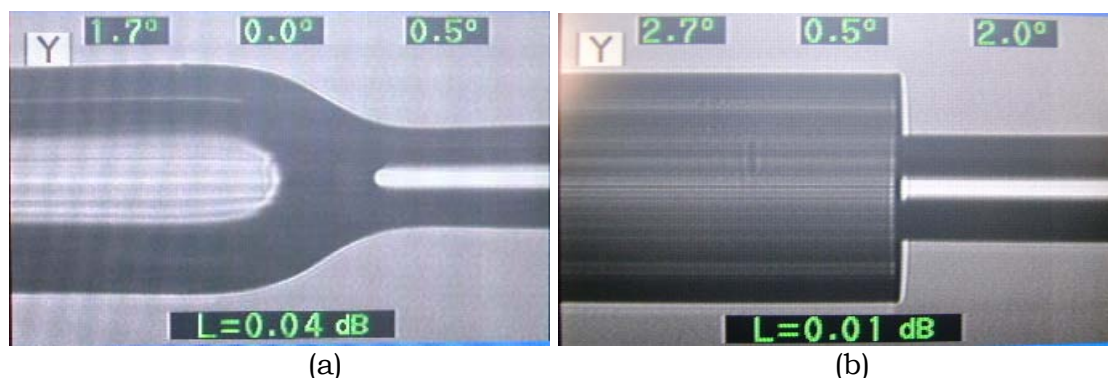


FIG. 2 –Comparison between the two different splicing methods used with the splice machine Fujikura FSM-45PM-LDF. (a): standard fiber tapering technique with partially collapsed holes. (b) Low power splice.

In Fig. 2(a) it is reported the result obtained by a standard fiber tapering technique. The loss estimated by the splice machine is about 0.04dB, but from the image it is clear that the holes are partially collapsed.

In Fig. 2(b) the splice obtained with reduced power is shown. The fiber microstructure is substantially unchanged, the estimated loss is about 0.01 dB. In order to verify the actual value of splice loss, more test have

been performed. The splice loss of Fig. 2(a) resulted to be 1.5 dB, whereas the loss of the splice shown in Fig.2 (b) is 7 dB. This value is considerably high and it must be considered that this splice shows very low mechanical strength also. The splice of Fig. 2(a) demonstrated high resistivity to mechanical strength test and it was selected as the most appropriate. The laser performances are shown in Fig.3. The air-clad fiber length was 15m. The pump power at 915nm was varied in the range 0-9 W. A gain of 22 dB was obtained for a pump power of 9W.

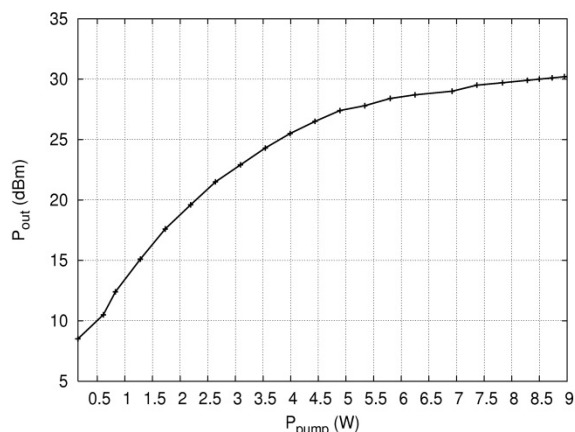


Fig. 3 - Laser output power. The Yb-doped PCF DC-135/15-PM-Yb- is 15m long and is pumped at 915 nm.

IV. CONCLUSION

The experimental set-up of a PCF laser has been presented. The attention has been focused on the challenging issue of splicing PCFs. Further activity might explore the possibility to improve the splice quality and loss thus increasing the laser gain.

ACKNOWLEDGEMENT

The Authors acknowledge the support of the EU funded FP7 ALPINE Project, n. 229231.

REFERENCES

- [1] F. Poli, A. Cucinotta, and S. Selleri, Photonic Crystal Fibers. Properties and Applications, ed. by Dordrecht: Springer (Series in Material Science), 2007
- [2] P. St. J. Russell, "Photonic-Crystal Fibers," IEEE/OSA J. Lightwave Technology., vol. 24, pp. 4729–4749, December 2006.
- [3] J. Limpert, T. Schreiber, A. Liem, S. Nolte, H. Zellmer, T. Peschel, V. Guyenot, A. Tunnermann, "Thermo-optical properties of air-clad photonic crystal fiber laser in high power operation", Optics Express, vol. 11, pp. 2982-2990, 2003.
- [4] K. P. Hansen, C. B. Olausson, J. Broeng, K. Mattson, M. D. Nielsen, T. Nikolajsen, P. M. W. Skovgaard, M. H. Sørensen, M. Denninger, C. Jakobsen, and H. R. Simonsen, "Airclad fiber laser technology," Proc. SPIE, vol. 6873, 2008, pp. 687 307–1 – 687 307–12.

FEM SOLVER OPTIMIZATION FOR PCF DESIGN

C. Molardi, Masruri, E. Coscelli, F. Poli, A. Cucinotta, S. Selleri

Information Engineering Department, University of Parma,
Viale G. P. Usberti 181/A, 43124 Parma, Italy
stefano.selleri@unipr.it

Abstract

The need to simulate electromagnetic field in complex optical devices, such as photonic crystal fiber, leads to use suitable numerical tools. Not always commercial software products cover this need. A full-vector modal solver, based on finite element method, has been updated and optimized for application to photonic crystal fiber design. First the electromagnetic problem is explained, paying attention to the numerical issues, such as fill-in, spurious solutions, memory requirement, and showing the chosen solutions to these issues. Then some tests have been displayed to prove the reliability of the solver, in particular a rod-type photonic crystal fiber has been simulated to investigate the solutions correctness and the performance in term of required memory space and execution time. Finally the solver results have been compared with the results obtained from commercial solver.

Index Terms – FEM, fill-in issue, full vector modal solver, photonic crystal fibers.

I. INTRODUCTION

Photonic Cristal Fibers (PCFs), have a very elaborate design in term of geometry and refractive index profile. The high number of PCF features, make them suitable to an increasing number of applications, such as sensors, communication, fiber lasers [1],[2]. Because of the high cost to manufacture new and innovative optical structures, a preventive simulated analysis is essential. Since the exact solution of the Maxwell equations in the PCFs is nearly impossible, a numerical method must be used. The Finite Element Method (FEM) is particular useful for this purpose.

In this paper the FEM based full-vector modal solver, developed and used at the Information Engineering Department of University of Parma, is optimized, highlighting the performances in term of use of memory and execution time. Comparative tests are shown in order to prove the reliability of the solutions, with particular emphasis on PCF design.

II. THE NUMERICAL APPROACH

The modal analysis of the electromagnetic field in optical structures starts from the well-known curl-curl equation:

$$\bar{\nabla} \times \left(\bar{p} \bar{\nabla} \times \bar{H} \right) - k_0^2 \bar{q} \bar{H} = 0 \quad (1)$$

where H is the magnetic field, k_0 is the wavenumber of the vacuum, p is the inverse of relative permittivity tensor, q the relative permeability tensor. The 2D domain can be discretize with a triangular element mesh. Considering the variational Rayleigh-Ritz [3] approach, the edge elements formulation has been chosen, in particular the T1.5 formulation proposed by Webb [4], which avoids the spurious solutions. The FEM discretization leads to this generalized eigenvalues problem:

$$([T] + n_{eff}^2 [S])\{h\} = 0 \quad (2)$$

where $[S]$ and $[T]$ are large, sparse, symmetric and not positive definite matrices, and the eigenvalues are the square of the effective index. A good method to find only some particular eigenvalues, near an expected value, is the Implicitly Restarted Arnoldi Method (IRAM), an evolution of the Arnoldi method, implemented in the Arpack library [5]. IRAM spans a basis of the Krylov subspace in witch are located the unknown solutions. This operation involves a large number of resolution of linear systems, whose matrices have the same attributes of sparsity and width of the matrices $[S]$ and $[T]$. A solid direct method of resolution is important because iterative methods, in this particular problem, don't reach convergence. The multifrontal method proposed by Duff and Reid [6], implemented in the Harwell library, has been chosen. The main issue of direct methods is the "fill-in" problem, which means that, after factorization, system matrix loses its sparsity. So the primary aim is the wise use of memory space, because the request of memory can rapidly overcomes the hardware capacity.

To aim this the solver has been written in C programming language, taking advantage of its good dynamical use of memory. In particular a C-coded framework manages the memory, the assembly of FEM matrices, the forcing of boundary condition and the interfaces with some Fortran subroutine, Arpack and Harwell, used for the high calculation efficiency. Furthermore some simple, but effective, tricks are used to take down the request of memory. First, it's important to delete every spurious non-zero entries in the matrix assembly; second, to free the workspace memory when no longer used; third, the run-time knowledge of the FEM matrices dimension, give the ability to allocate a sharper memory space respect the raw use of Harwell subroutines. These choices allow more than 60% memory saving.

III. SOLVER TESTING

The developed full-vector solver can be applied to the real and complex electromagnetic problems, implementing the Perfectly Matched Layers

(PML), and has been provided with features important for PCF analysis. In fact, it can simulate the structure bending, calculate the dispersion, the overlap integrals of the field with the proper regions, and can include Sellmeier equation.

For the first test, a rod-type, large mode area PCF has been chosen. This PCF, used for lasers and amplifiers, has a double cladding structure and the core is doped with ytterbium. The structure has been solved over a 99618 nodes mesh shown in Fig.1(a), searching for the Fundamental Mode (FM) effective index at various wavelengths. Then the mesh detail has been, step by step, increased, reaching 499.367 nodes. As shown in Fig.1(b) the n_{eff} curves converge to a stable value as expected. This test has been performed on a 64-bit server, with Xeon Quad Core 2.83 GHz processor and 8 GByte RAM. On this machine a VMware hypervisor was installed.

In Table I it's possible to see the performance in term of required memory space and execution time, searching for different pools of modes. A further test has been made on a step index fiber, with 10 μ m core diameter, 1.456 core refractive index, 125 μ m cladding diameter and 1.45 cladding refractive index. C-solver solutions, examining the FM around the third window, have been compared with the one obtained from COMSOL Multiphysics. The solutions has been calculated over a 27386 triangular elements mesh, paying attention to create with COMSOL a mesh the most similar to that used with the C-solver. Result are shown in Table II.

IV. CONCLUSION

The performed tests show that the developed solver achieves correct solutions for the electromagnetic problem in optical devices, and achieves excellent performance in term of required memory space and execution time, allowing more thick meshes and more accurate solutions. Thanks to this optimization the solver has been successfully applied to the design of doped double cladding PCFs. Memory requirement, caused by the fill-in, is still an open issue. To reach even better performances it's possible to investigate new FEM formulations, and test other numerical methods to solve the algebraic system.

TABLE I – C-MODAL SOLVER PERFORMANCES

N° of Nodes	Memory Space (MByte)			Execution Time (m:s)		
	6 modes	8 modes	10 modes	6 modes	8 modes	10 modes
99618	380	386	394	0:26	0:27	0:29
199557	914	925	945	1:28	1:30	1:35
299508	1380	1400	1430	2:30	2:36	2:44
399731	1920	1950	2000	3:56	4:04	4:10
499367	2500	2530	2570	6:10	6:20	6:34

TABLE II – FM n_{EFF} COMPARISON ON A STEP INDEX FIBER

$\lambda(\text{nm})$	FM n_{eff} (C-Solver)	FM n_{eff} (Comsol)	$ \Delta n_{\text{eff}} $
1500	1,45365717	1,45365760	$4,3 \times 10^{-7}$
1520	1,45361464	1,45361507	$4,3 \times 10^{-7}$
1540	1,45357218	1,45357262	$4,4 \times 10^{-7}$
1560	1,45352980	1,45353024	$4,4 \times 10^{-7}$
1580	1,45348750	1,45348796	$4,6 \times 10^{-7}$
1600	1,45344531	1,45344577	$4,6 \times 10^{-7}$

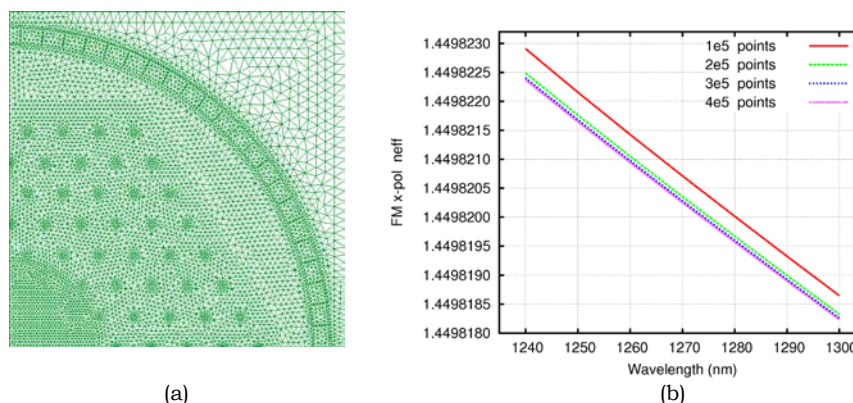


FIG. 1 – (a) 99618 points mesh, on the rod-type PCF used for the test. **(b)** FM n_{eff} curves at the increase of the accuracy of the mesh on the rod-type PCF.

ACKNOWLEDGEMENT

The Authors acknowledge the support of the EU funded FP7 ALPINE Project, n. 229231.

REFERENCES

[1] F. Poli, E. Coscelli, T. T. Alkeskjold, D. Passaro, A. Cucinotta, L. Leick, J. Broeng, S. Selleri, “*Cut-off analysis of 19-cell Yb-doped double-cladding rod-type photonic crystal fibers*”, (Optics Express, Vol. 19 Issue 10, 2011).

[2] E. Coscelli, F. Poli, T.T. Alkeskjold, D. Passaro, A. Cucinotta, L. Leick, J. Broeng, S. Selleri, “*Single-mode analysis of Yb-doped double-cladding distributed spectral filtering photonic crystal fibers*”, (Optics Express, Vol. 18 Issue 26, 2010).

[3] J. Jin, “*The Finite Element Method In Electromagnetics*”, (John Wiley & Sons Inc. 1993).

[4] J.P. Webb, “*Hierarchical Vector Based Functions Of Arbitrary Order For Triangular And Tetrahedral Finite Elements*”. (IEEE Antennas Propagation, Vol. 47, No. 8, 1999).

[5] Z. Bai, J. Demmel, J. Dongarra, A. Rhue, H. Van der Vorst, “*Templates for the Solution of Algebraic Eigenvalue Problems: a Practical Guide*”, (Draft 1999).

[6] I.S. Duff, J.K. Reid, “*Multifrontal Solution Of Indefinite Sparse Symmetric Linear Equations*”, (ACM Transaction on Mathematical Software, Vol. 9, No. 3, 1983).

A MODIFIED RC-FDTD ALGORITHM FOR PLASMONICS IN DRUDE DISPERSIVE MEDIA.

Antonino Cala' Lesina, Alessandro Vaccari, Alessandro Bozzoli

Renewable Energies and Environmental Technologies,
Fondazione Bruno Kessler, via Sommarive 18, 38121 Povo (TN),
Italy

[lesina, vaccari, bozzoli}@fbk.eu](mailto:{lesina, vaccari, bozzoli}@fbk.eu)

Abstract

A widespread approach in the FDTD analysis of dispersive media is the Recursive Convolution (RC) method. In the Drude version it shows a not so good accuracy in describing the electromagnetic field at the plasmonic resonance frequencies. We propose here a modified RC algorithm which, by minimizing the time truncation error, guarantees a better accuracy of the solution at parity of memory requirements and number of time iterations. We test the modified RC algorithm proposed by analyzing the behavior of gold and silver noble metal nanospheres exposed to an optical plane wave with respect to the standard RC approach and the analytical solution.

Index Terms – RC-FDTD method, Drude dispersion, plasmonics, Laplace transform.

I. INTRODUCTION

We focus here on the explicit Finite-Difference Time-Domain (FDTD) numerical solution method of the Maxwell's equations [1][2], with the Convolutional Perfectly Matched Layer (CPML) boundary conditions formulation [3]. To analyze Drude dispersive media, we start with the Recursive Convolution (RC) traditional algorithm [4]. It time-discretizes directly the convolution integral expressing the temporal non-locality between the \mathbf{D} and \mathbf{E} fields. In order to minimize the truncation error, we propose here to find a closed form solution of the Ampère-Maxwell, and only after to proceed with the time discretization. We calculate explicitly the kernel of such a closed form solution in the case of Drude media, and show how it can be updated recursively with the same memory requirements than the traditional RC scheme [4]. The evaluation of some error parameters and the comparison of the fields highlight a better accuracy of the proposed modified algorithm with respect to the standard RC algorithm [4]. The test has been done for Au and Ag noble metals [5], in the optical frequency range, and makes the modified RC algorithm suitable for plasmonics.

II. THEORETICAL APPROACH

A closed form solution for the electric field \mathbf{E} is found in the Laplace domain. Going back to the time domain and developing the time discretization we obtain a recursive expression for the electric field for the FDTD method at parity of memory requirements, as shown in [6][7].

III. SIMULATIONS

To test the modified RC algorithm previously proposed, we apply it to a 96 nm radius nanosphere, made of gold or silver, in a monochromatic light beam. We have tested our modified algorithm for Au at $\lambda=480$ nm and for Ag at $\lambda=336$ nm and $\lambda=380$ nm, i.e. the resonance wavelengths evidenced through the extinction coefficient defined in [8]. We used a $N \times N \times N$ cubic Yee cell discretization, with $N=200$, to accommodate the nanosphere. The cell edge (space step δ) amounts to 2 nm for a good representation of the geometrical details. The time step was set to $\delta/(2c_0)$, with c_0 the vacuum light velocity, to satisfy the Courant stability condition [2] in three dimensions. We also used a total field/scattered field (TFSF) source [2], placed 8 cells inward from the outer boundary of the FDTD lattice, to create a plane wave linearly polarized (along the z -axis), impinging along the positive y -direction on the nanostructure. The FDTD lattice was completed with an extra layer, 15 cells thick, supporting the CPML boundary conditions [3] to simulate an open to infinity surrounding media. We used a compact pulse exciting signal, i.e. of finite duration and with zero values outside a given time interval [9][10]. The signal duration is suitably chosen to get spectral distribution results in the range 200-1000 nm, as obtained by the Discrete Fourier Transform (DFT) which is updated at every FDTD time iteration, until the excitation is extinguished inside the whole numerical lattice. To get valid field values on that range with a single program run, we included the correct dispersive media behavior in the standard FDTD code by the above described modified RC algorithm. The Drude parameters for Au and Ag were taken from the literature [5].

The numerical results have been compared with those from the standard RC method [4] and with the analytical solution which we obtained by implementing the method described in [8].

To evaluate the deviation from the exact solution we considered the average error for each component

$$L_{\xi,\eta} = \frac{1}{N^3} \sum_{i,j,k=1}^N |E_{\eta}^{\xi}(i,j,k) - E_{\eta}^a(i,j,k)| \quad (1)$$

and the average error for the electric field module

$$L_{\xi} = \frac{1}{N^3} \sum_{i,j,k=1}^N \left| |E^{\xi}(i,j,k)| - |E^a(i,j,k)| \right| \quad (2)$$

where $\eta = \{x, y, z\}$ indicates the Cartesian component, $\xi = \{s, m\}$, and the letters s, m, a denote standard, modified and analytical electric field. The electric field, by means of the DFT, is expressed at the frequency of interest and is normalized with respect to the incident electric field at the same frequency. The values in Table I were obtained with 12000 time iterations simulations.

For the gold resonance are also reported the error parameters (1) and (2) calculated for E_x, E_y, E_z and $|\mathbf{E}|$ as a function of the simulation

duration (overall number of FDTD iterations) for standard RC and modified RC with respect to the analytical solution [8] (Fig. 1). Moreover the better numerical accuracy is evidenced with a comparison of the electric field for standard RC, modified RC and analytic solution extracted from the lattice along one direction in x, y and z (Fig. 2, 3, 4). In each figure the three components of the electric field (E_x on the left, E_y in the middle and E_z on the right) are represented: green for the analytical solution, blue for the standard RC-FDTD method and red for the modified RC-FDTD algorithm.

Table I - Modified (Standard) RC-FDTD Algorithm Deviation from the Analytical Solution

	<i>Au(480nm)</i>	<i>Ag(336nm)</i>	<i>Ag(380nm)</i>
$L_{m,x} (L_{s,x})$	0.0386 (0.0548)	0.1275 (0.1533)	0.0374 (0.0421)
$L_{m,y} (L_{s,y})$	0.0592 (0.0872)	0.2085 (0.2485)	0.0585 (0.0687)
$L_{m,z} (L_{s,z})$	0.0440 (0.0633)	0.1718 (0.2024)	0.0430 (0.0478)
$L_m (L_s)$	0.0693 (0.1011)	0.2670 (0.3282)	0.0594 (0.0684)

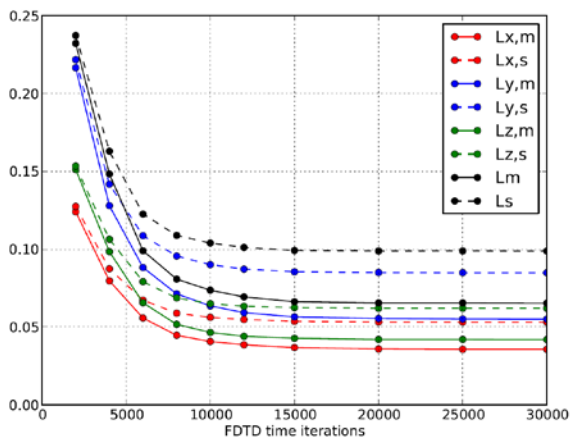


FIG. 1 – Error parameters $L_{\xi,\eta}$ and L_{ξ} comparison for Au ($\lambda=480\text{nm}$).

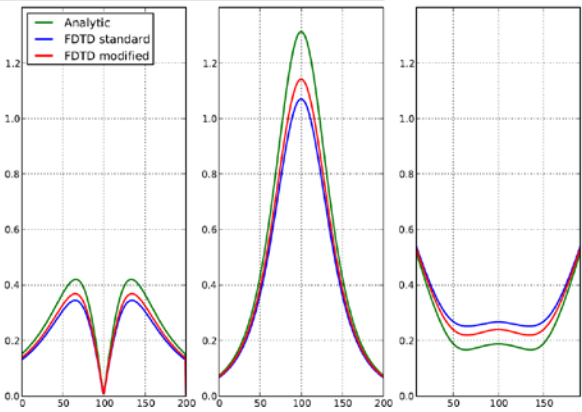


FIG. 2 – E_x, E_y, E_z comparison for Au nanosphere ($\lambda=480\text{nm}$) along the x axis.

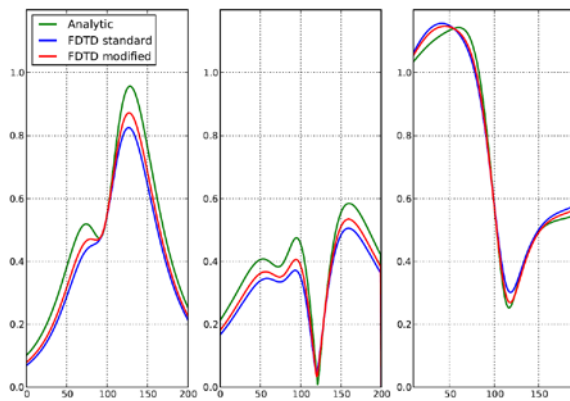


FIG. 3 – E_x, E_y, E_z comparison for Au nanosphere ($\lambda=480\text{nm}$) along the y axis.

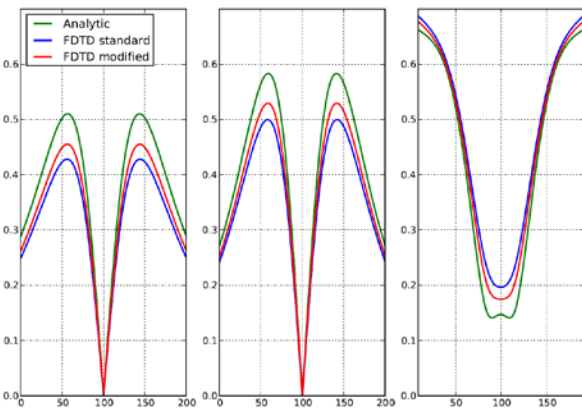


FIG. 4 – E_x, E_y, E_z comparison for Au nanosphere ($\lambda=480\text{nm}$) along the z axis.

IV. CONCLUSION

We proposed a modified Recursive Convolution algorithm for the FDTD analysis of Drude dispersive media in the plasmonic resonance regions. The algorithm has been evaluated by comparing its deviation from the analytical solution for gold and silver nanospheres at the resonance frequencies and evidencing an improvement with respect to the traditional RC method.

REFERENCES

- [1] K. S. Yee, "Numerical solution of initial boundary value problems involving Maxwell's Equations in isotropic media", *IEEE Transactions on Antennas and Propagation*, vol. 14, no. 3, pp. 302-307, 1966.
- [2] A. Taflove, S. C. Hagness, *Computational Electrodynamics: The Finite-Difference Time-Domain Method 3rd ed.*, Norwood, MA: Artech House, 2005.
- [3] J. A. Roden, S. D. Gedney, Convolution PML (CPML): "An efficient FDTF implementation of the CFS-PML for arbitrary media", *Microwave and Optical Technology Letters*, vol. 27, no. 5, pp. 334-339, 2000.
- [4] R.J. Luebbers, F. Hunsberger, K.S. Kunz, "A frequency-dependent finite-difference time-domain formulation for transient propagation in plasma", *IEEE Transactions on Antennas and Propagation*, vol. 39, no. 1, pp. 29-34, 1991.
- [5] K. Kolwas, A. Derkachova, M. Shopa, "Size characteristics of surface plasmons and their manifestation in scattering properties of metal particles", *Journal of Quantitative Spectroscopy & Radiative Transfer*, 110 (2009), pp. 1490-1501.
- [6] A. Cala' Lesina, A. Vaccari, and A. Bozzoli, "A novel RC-FDTD algorithm for the Drude dispersion analysis", *Progress In Electromagnetics Research M*, Vol. 24, 251-264, 2012.
- [7] A. Cala' Lesina, A. Vaccari, A. Bozzoli, "A Modified RC-FDTD Algorithm for Plasmonics in Drude Dispersive Media Nanostructures", IEEE, 2012, pp. 687-690, *6th European Conference on Antennas and Propagation (EUCAP 2012)*, Prague, 26-30/03/2012.
- [8] J. A. Stratton, *Electromagnetic Theory*, McGraw-Hill, New York and London, 1941.
- [9] R. Pontalti, L. Cristoforetti, L. Cescatti, "The frequency dependent FDTD method for multi-frequency results in microwave hyperthermia treatment simulation", *Phys. Med. Biol.*, vol. 38, pp. 1283-1298, 1993.
- [10] A. Vaccari, R. Pontalti, C. Malacarne, and L. Cristoforetti, "A robust and efficient subgridding algorithm for finite-difference time-domain simulations of Maxwell's equations", *J. Comput. Phys.*, vol. 194, pp. 117-139, 2003.

BROADBAND OPTICAL PARAMETRIC GENERATION IN LiTaO_3

F. Baronio⁽¹⁾, M. Conforti⁽¹⁾, M. Levenius⁽²⁾, K. Gallo⁽²⁾, V. Pasiskevicius⁽²⁾,
F. Laurell⁽²⁾, and C. De Angelis⁽¹⁾

⁽¹⁾ Department of Information Engineering, University of Brescia
Via Branze 38, 25123 Brescia, Italy

⁽²⁾ Department of Applied Physics, KTH-Royal Institute of Technology
Roslagstullsbacken 21, 10691 Stockholm, Sweden

baronio@ing.unibs.it

Abstract

We investigate theoretically and experimentally multistep parametric processes in broadband optical parametric generators based on periodically poled 1 mol % MgO-doped stoichiometric LiTaO_3 . We demonstrate that parametric collateral processes may deplete or enhance spectral portions of the optical parametric generation output, depending on pump pulse duration.

Index Terms – Nonlinear Optics; Parametric Generation; Quadratic Crystals.

I. INTRODUCTION

A wide range of applications, encompassing ultrafast spectroscopy, high energy physics, frequency combs and remote sensing, spurs current research on broadband optical sources in the infrared [1]. Coherent ultra-broadband parametric gain suitable for ultrashort pulse generation and amplification in such spectral region can be afforded by quadratic frequency down-conversion in Quasi Phase-Matched (QPM) materials operated close to their zero group velocity dispersion point. Broadband optical parametric generation (OPG) has been achieved in periodically patterned GaAs, KTiOPO_4 , LiNbO_3 , and, recently, LiTaO_3 , exhibiting a record (180 THz) gain bandwidth [2]. The spectral flatness of the parametric gain curves is a feature almost as important as the breadth of its spectral coverage. However, multistep quadratic processes triggered by broadband OPG, such as sum-frequency generation (SFG), often contribute to disrupting the flatness of gain profiles in QPM media [2]. Here, we consider both theoretically and experimentally the impact of multistep quadratic processes on broadband OPG in the pulsed regime, in periodically poled LiTaO_3 .

II. CASCADED PROCESSES IN OPG

In a quadratic material, the optical pump at λ_P excites parametric generation in the infrared region (λ_{OPG}) via first order QPM. High-order resonances of the QPM grating can simultaneously enable SFG between the pump and specific components in the broadband OPG spectrum. The SFG process ($1/\lambda_P + 1/\lambda_S \rightarrow 1/\lambda_{\text{SF}}$) subtracts energy from the OPG band, carving a gain dip at λ_S . This is the situation typically

encountered in the experiments [2]. The deleterious effects of spurious SFG processes on the parametric gain could in principle be alleviated through more sophisticated QPM grating designs, yet this option becomes ever more challenging as OPG spectra get wider. Alternatively, instead of trying to remove the QPM resonances responsible for upconversion, one could exploit SFG cascading to re-route power into the OPG band via difference frequency generation (DFG). According to the theory of quadratic cascading for non-degenerate frequency upconversion [3], one can expect the direction of energy flow in the SFG step to be reversible, even at perfect phase-matching, through a suitable choice of the optical excitation, i.e. the input power at λ_P .

III. THEORETICAL INVESTIGATION

To assess the impact of SFG cascading on broadband parametric generation, we performed a systematic numerical analysis based on a recently developed mathematical model [4], which can account rigorously for all the spectral components and multiple interactions. We explored the device response in the pulsed regime under experimentally viable conditions [2], referring to OPG in a 1cm-long periodically poled nearly stoichiometric LiTaO₃ crystal, doped with 1 mol% MgO (PPMgSLT), with a QPM period of 25 μm , operated at temperature $T = 80^\circ\text{C}$ and pumped close its zero-dispersion point ($\lambda_P = 860 \text{ nm}$) by Gaussian pulses at 1kHz, with peak intensities in the range 1-10 GW/cm^2 and pulse durations ranging between 0.5 and 30 ps. We simulated OPG from a classical Gaussian pump and a semiclassical pulse shot noise of one photon per mode with random phase on each spectral discretization bin. The OPG response was statistically evaluated over the ensemble of multiple simulations, performed with different random noise seeds. We typically used an average of 30 realizations, which compares well with the experimental conditions described in what follows. Fig. 1 illustrates key features of

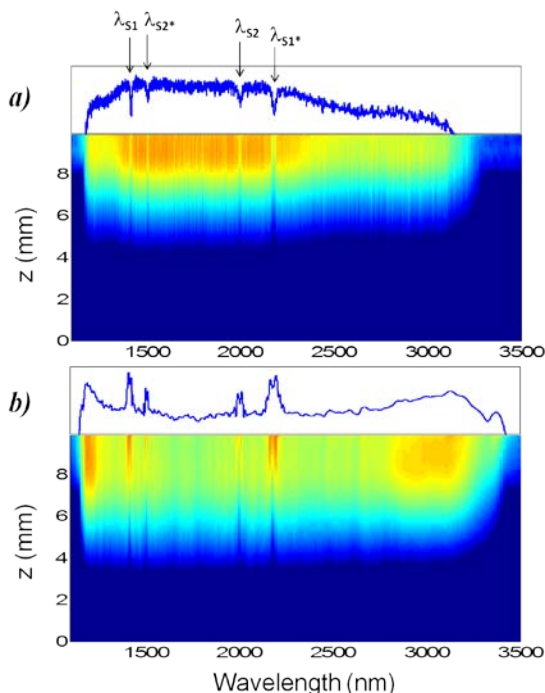


Fig. 1 Simulated OPG response of a 1cm-long PPMgSLT device in the presence of cascaded processes, with a Gaussian pump at $\lambda_P = 860 \text{ nm}$ of peak intensity $I = 7 \text{ GW}/\text{cm}^2$. Input pulse durations: a) 10ps and b) 0.7ps. Output spectra (1D plots) and OPG signal evolution inside the device (contour plots) in decibels.

an average of 30 realizations, which compares well with the experimental conditions described in what follows. Fig. 1 illustrates key features of

the calculated response, considering OPG in PPMgSLT with a pump at 860 nm, with a peak intensity $I_P = 7 \text{ GW/cm}^2$. In each picture, the upper plot shows the ultra-broadband OPG spectrum (sweeping from 1 to 3.5 μm) at the device output, while the contour plot illustrates its evolution in propagation (along z) in the QPM medium. Fig. 1a and b concern two different pump pulse durations, amounting to 10 ps and 0.7 ps, respectively. Fig. 1a refers to the situation generally encountered in the experiments, where SFG induces localised dips in the gain spectra. In this specific case the dips are located at 1.4, 1.5, 1.95 and 2.2 μm and represent the spectral signatures of two distinct SFG processes occurring in the PPMgSLT device, namely: SFG between λ_P and $\lambda_{S1} = 1.4 \mu\text{m}$, generating a wave at $\lambda_{SF1} = 533\text{nm}$ via 3rd-order QPM; SFG between λ_P and $\lambda_{S2} = 1.95 \mu\text{m}$, generating a wave at $\lambda_{SF2} = 600\text{nm}$ via 2nd-order QPM. The two processes affect also the gain at the conjugate signal wavelengths: $\lambda_{S1}^* = 2.2 \mu\text{m}$ [$= \lambda_{S1} \lambda_P / (\lambda_{S1} - \lambda_P)$] and $\lambda_{S2}^* = 1.5 \mu\text{m}$ [$= \lambda_{S2} \lambda_P / (\lambda_{S2} - \lambda_P)$], respectively. Fig. 1b shows the simulation results obtained for the same device of Fig. 1a, when pumped with Gaussian pulses of the same peak intensity, but with a much shorter duration (0.7ps). As apparent from the output spectrum of Fig. 1b, a gain enhancement now occurs at the very same spectral locations (λ_{S1} , λ_{S2} , λ_{S1}^* , λ_{S2}^*) where SFG was carving dips in the gain curve of Fig. 1a. With short pulses, the OPG dips are indeed removed by the onset of SFG cascading, which brings power back into the OPG band by activating the DFG channel. The result points out to a crucial role played by the pulses' temporal walk-off on in the onset of SFG cascading. As the pump pulse duration is decreased, the walk-off among the spectral components involved in the SFG process increases. Accordingly, as the components at λ_P , λ_{SF} and λ_S lose their overlap upon propagation, the SF wave begins to back-convert its power to λ_P and λ_S , yielding an enhancement of the OPG output.

IV. EXPERIMENTS

Seeking experimental confirmation for the predicted cascading phenomena, we investigated under varying pumping conditions the response of ultra-broadband parametric generation in PPMgSLT crystals. The samples used in the experiments were 500 μm -thick, 1 cm-long, z -cut substrates poled with a constant period of 25 μm . As pump, we employed a tunable picosecond Ti:sapphire amplifier system, consisting of a Nd:YVO₄-pumped femtosecond source which seeded a regenerative chirped pulse amplifier, delivering micro-joule pulses at 1 kHz with bandwidths of 2 nm, tunable from 820 to 900 nm. We could vary the final pump pulse duration in the OPG experiments by adjusting the group delay dispersion introduced by the final compressor stage of the amplifier. The crystal was kept at 80 °C. At its output, we recorded the signal spectra with a 0.55 m spectrometer (Horiba Jobin

Yvon iHR550, PbSe detector) sensitive up to 4.8 μm , averaging over 900 pulses. In the experiments we explored the impact of the input pulse duration on the output OPG spectra, while maintaining the peak pump intensity constant. Key features of the observed response are illustrated by Fig. 2, which compares measurements made with an input peak intensity of 6 GW/cm^2 for pump pulse durations of 6.1 and 1.7 ps (red and black curves, respectively). The experimental results agree with the theoretical expectations. The spectrum recorded with long pump pulses (red curve in Fig. 2), bears the characteristic signature of SFG, exhibiting a marked depletion of the OPG output at four signal

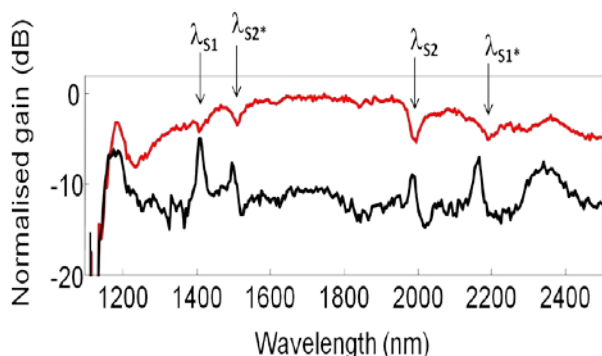


Fig. 2 OPG spectra measured with a pulsed pump at 860 nm, with Gaussian pulse durations of 6.1 ps (red line) and 1.7 ps (black line), at 6 GW/cm^2 in a 1 cm PPMgSLT crystal.

wavelengths (1.4, 1.5, 1.95 and 2.2 μm , highlighted by the arrows in Fig. 2), which match well the theoretical predictions (Fig. 1a). On the other hand, the short pump pulses (black curve in Fig. 2), trigger SFG cascading in the PPMgSLT device, yielding a significant enhancement of the OPG output at the same spectral locations where a gain reduction was apparent with long pulses, as expected from Fig. 1b.

V. CONCLUSION

In conclusion, we studied the interplay of multistep quadratic processes with broadband OPG in quadratic QPM media in the pulsed regime. We demonstrated the possibility to counteract the impact of spurious SFG on the parametric gain by triggering SFG-cascading to channel energy back into the OPG band.

ACKNOWLEDGEMENT

The present research is supported by the Swedish Research Council (VR fellowship 622 2010 526, VR grant 621 2011 4040), by MIUR (PRIN 2009P3K72Z) and Fondazione CARIPLO (2010-0595).

REFERENCES

- [1] G. Cerullo and S. De Silvestri, *Rev. Sci. Instrum.* 74, 1 (2003).
- [2] M. Levenius, V. Pasiskevicius, F. Laurell, and K. Gallo, *Opt. Expr.* 19, 4121 (2011).
- [3] A. L. Belostotsky, A. S. Leonov, and A. V. Meleshko, *Opt. Lett.* 19, 856 (1994)
- [4] M. Conforti, F. Baronio, C. De Angelis, *Phys. Rev. A* 81, 053841 (2010).

WIND FARM IMPACT ON PRIMARY RADARS

R. Tumolo, S. Immediata, G. Russo, M. D'Urso, L. Timmoneri

SELEX Sistemi Integrati S.p.A., Via Circumvallazione Esterna di Napoli,
Loc. Pontericci zona ASI, I-80014 Giugliano, Napoli, Italy
(e-mail: rtumolo@selex-si.com).

Abstract

The growing need for renewable energy sources has led to an increasing massive utilization of wind energy. Each year new wind farms arise, consisting of wind turbines (WT) bigger and bigger. Wind turbines are a very complex source of radar clutter to characterize and have an impact on air traffic control particularly difficult to mitigate. Wind turbines are often enormous structures, able to either re-irradiate a significant portion of the radar energy, and, because of blades motion, give rise to a Doppler effect very similar to that due to a flying airplane. In this work the steps towards the development of suitable wind turbine clutter mitigation techniques are presented.

Index Terms: clutter, Doppler, radar, wind farm, wind turbines

I. INTRODUCTION AND MOTIVATION

It is claimed that the motion of WT blades affects the correct performances of both military and civilian radars. This results in a number of adverse effects including:

- radar blind zones: the echo may dominate and mask those originating from aircraft resulting in a “radar blind zone” and missed detections;
- track seduction: the aircraft track may be seduced away from its correct path due to an association with an echo originating from the wind farm;
- high false alarm rate: the echoes originating from the wind farm may result in high rate of false reports in the vicinity of the farm.

II. MATHEMATICAL MODEL

The WT is typically constituted by a tower, a nacelle and a rotor with the blades [1]; the contribute pertinent to the tower and the nacelle can be represented in the signal model simply by a constant value, since they can be cancelled by the MTI or MTD devices thanks to their negligible motion in terms of Doppler. To describe the contributions from the blades, every blade has been supposed to be in the far field of the radar and assimilated to a linear antenna. With reference to the geometry represented in Figure 1, the signal backscattered by the blades is:

$$s(t) = \sum_{n=1}^N ALe^{j\left\{\omega_r t - \frac{4\pi}{\lambda} \left[R + \frac{L}{2} \cos \vartheta \cos(\varphi + \beta) \sin \left(\alpha_0 + \omega_r t + \frac{2\pi(n-1)}{N} \right) \right] \right\}}$$

$$\cdot \text{sinc} \left[\frac{2\pi}{\lambda} L \cos \vartheta \cos(\varphi + \beta) \sin \left(\alpha_0 + \omega_r t + \frac{2\pi(n-1)}{N} \right) \right] \quad [Eq.1]$$

where: A is a scale factor depending on the RCS of each blade, L is the blade length, N is the number of blades, ω_c is the radian frequency of the transmitted signal, ω_r is the blade rotation speed [rad/s], R is the distance of the centre of rotation from the radar, λ is wavelength of the transmitted signal, ϑ is the angle between the plane of blade rotation and the line of sight from the radar to the centre of rotation (yaw angle), ϕ is the elevation angle of the centre of rotation of the blades with respect to the radar, α_0 is an angle which accounts for the initial position of the blades, β takes into account any possible blade tilt with respect to the tower axis, f_r is the frequency of blade rotation ($\omega_r = 2\pi f_r$).

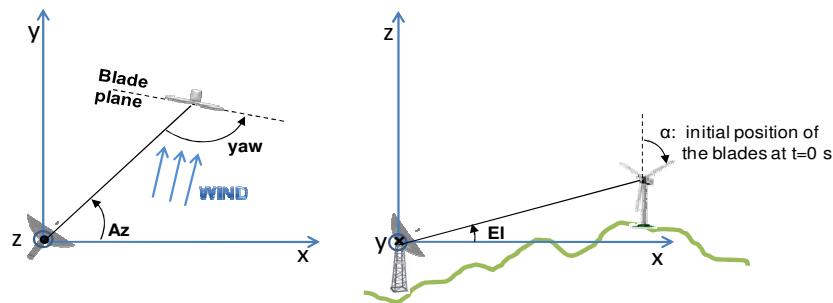


Figure 1: geometry of the radar Vs the WT position: (a) top view, (b) front view

The contribution of each blade is a phase term that accounts for the Doppler shift due to the tangential speed of the tip of each blade and a sinc function which accounts for the amplitude modulation introduced by the blades. Notice that in Eq.1 RCS is assumed to be a constant but in section IV the simulations are done considering several values (from 15dBsm to 24 dBsm).

III. POSSIBLE SOLUTIONS

The Fine Doppler Maps (FDM) are able to maintain CFAR conditions in wind turbine areas, while maintaining good Probability of Detection (PD) of real targets with different doppler content. They operate at the MTD-output, and compare the current echo pertaining to each cell (and for each filter) to a background estimate for this specific cell, based on the previous scan from that cell only.

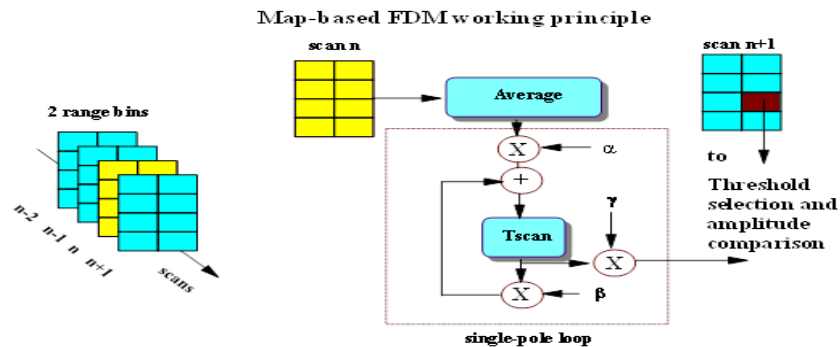


Figure 2: Principle of operation of FDM

The FDM process adapts the thresholds estimated filter by filter to avoid detections by the blades. The single FDM cell is constituted by the number of pulses within the Coherent Processing Interval (CPI) and a specific number of range cells, and the maps are created according to the following algorithm (see Fig. 2): calculation of the modules of each sample at each filter output; selection of the average modulus of the samples belonging to the same range within a fixed range window and to the same azimuth sector given by the CPI length; by indicating with j the j -th CPI and with N_j and N_r the number of pulses within it and the number of range cells included in the FDM cell respectively, with \mathbf{M}_{MTD} the $N_j \times N_j$ MTD matrix, and with $\mathbf{s}(i)$ the $N_j \times N_r$ received signal, the algorithm continues performing integration from scan to scan through the formula:

$$\mathbf{c}_j(i) = \alpha \mathbf{M}_{MTD} \bar{\mathbf{s}}(i) + \beta \mathbf{c}_j(i-1)$$

Where i denotes the i -th scan, α denotes a real scalar defined in the interval $]0,1[$, $\mathbf{c}_j(i)$ is the value to be assigned to the fine Doppler cell at the i -th scan, $\bar{\mathbf{s}}(i)$ is the $N_j \times 1$ vector obtained by performing the average of the moduli of $\mathbf{s}(i)$.

IV. PRELIMINARY RESULTS ON SYNTHETIC DATA

To assess the FDM performances in terms of blades and target PD, a scenario with a single Wind Turbine (WT) in a single range cell has been chosen. A very long observation time has been fixed and asynchronous target crossing over the Cell Under Test (CUT), in the order of one thousand, has been considered. More specifically, 1000 Montecarlo trials have been carried out, each of which considers 301 radar scans wherein the WT is always present, the target, a small class of airliners type Cessna 310B [3] with an rcs 4m^2 , occurs in the same range cell only for the last scan. Generally H_0 is the hypothesis associated to a false alarm; in our case it refers to the detection of only wind turbine. H_1 , as usual, is the hypothesis associated to the target detection.

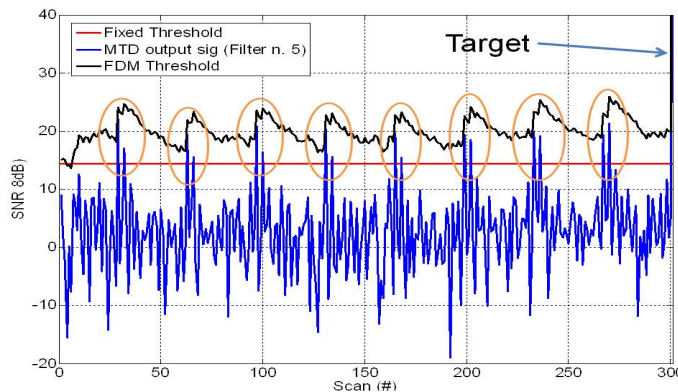


Figure 3: Blade flashes and FDM Thresholds

Fig. 3 depicts the FDM threshold capability of adaptation to the blade flashes that occur along the time of observation allowing the possibility to detect the target when it is present.

Further simulations of both target and blades PD have been carried out for different values of α and blades RCS; in figure 4 the main results of such simulations are shown.

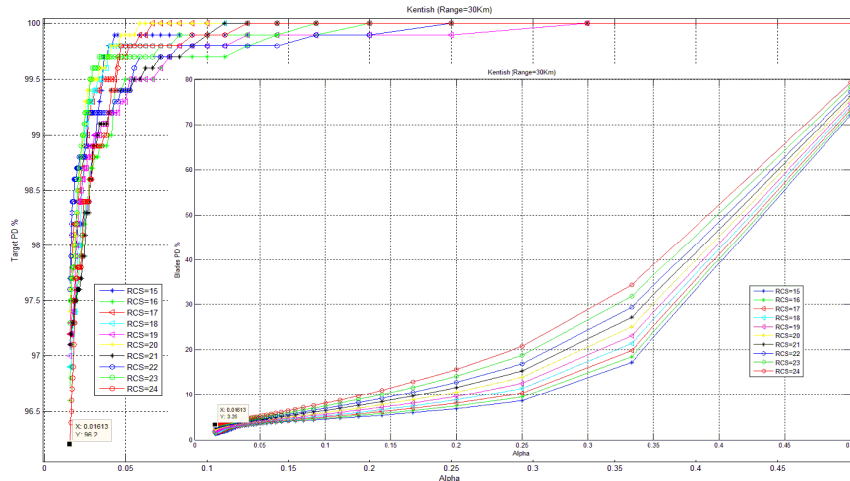


Figure 4: Target and Blades PD Vs α

In Figure 4 it can be seen that to achieve a target PD of 96.2%, α must be $\approx \frac{1}{62}$, and such a value corresponds to a blade PD of 3.35%.

V. CONCLUSION

In this paper the importance of wind farms impact on primary radars has been presented in terms of useful targets as well as WT clutter PD when FDM are operative, and a comparison between these two performance parameters has been done for different values of α and RCS of the blades. Since the simulations have been carried out without any real radar data and in the hypothesis of far field between radar and WT, which is not verified in the cases of interest, the next step, in order to prove the effectiveness of the model used in this paper, aims to acquire data from live recordings of radars in the vicinity of wind farms. Furthermore, a more precise WT RCS characterization is supposed to be done for providing the simulations with a more realistic model of the return signal backscattered from a WT.

REFERENCES

- [1] <http://www.trade.nsw.gov.au/energy/sustainable/renewable/wind>
- [2] EUROCONTROL “Guidelines on how to assess the potential impact of Wind Turbines on Surveillance Sensors”, 09 June 2010 Edition
- [3] Radar Engineer’s Sourcebook (Artech House Radar Library) by W. Morchin, 1992
- [4] TECHNICAL MEMO Mitigation process of ASR/SSR performance degradation from Wind Farm
- [5] J. Martin and B. Mulgrew, “Analysis of the theoretical radar return signal from aircraft propeller blades”, University of Edinburgh, Scotland, U.K.

EMBEDDED PHOTONIC SENSOR NETWORKS FOR LARGE ARRAYS DIAGNOSTIC

P.Vinetti⁽¹⁾, M. D'Urso⁽¹⁾ and M. Dispenza⁽²⁾

SELEX Sistemi Integrati

⁽¹⁾ Giugliano in Campania, Italy

⁽²⁾ Rome, Italy

pvinetti@selex-si.com; mdurso@selex-si.com; mdispenza@selex-si.com

Abstract

A feedback control network based on photonic sensors has been exploited to increase resiliency of large phased arrays for radar and space applications has been proposed. The sensor network is embedded in the antenna array front-end such to provide a a real-time control of the failures/calibration errors of system components. The feedback system dynamically acts on the weights of the Beam Forming Network thanks to accurate and effective synthesis methods, allowing minimizing the mismatch between the actual pattern and the reference one.

Index Terms – radar systems, dynamic beamforming, antenna arrays, phased array, photonic sensors, radar resiliency.

I. INTRODUCTION

Phased array antennas and, particularly, active antenna front-ends adopted for multifunctional radars, are high costs, very complex and electrically large systems. The overall performances are affected by the actual radiated beam, and a mismatch between the expected and the actual aperture field distribution can lead significant performance degradation [1-2]. When performance degradation becomes unacceptable, system maintenance is mandatory, which implies undesired temporarily interruption of the normal service.

This paper proposes a solution able to improve resiliency of array systems, enabling the capability to dynamically adapt the system to possible failures. The proposed method exploits an embedded non invasive Photonic Sensors Network (PSN), properly integrated in the radiating antenna front-end, and an adaptive beam-forming algorithm, embedded in the array control unit. The PSN is made of electrically small probes, aimed at continuously measuring the actual field on the array aperture thus providing an estimation of failure or calibration errors. Sensor data are properly processed and allow to determine the actual status of the array front-end (beam diagnosis phase). A second phase aimed at dynamically minimizing the mismatch between the actual pattern and the reference one by acting on the weights of the BFN is also implemented, if required (beam correction phase). Different from previous contributions[3], the photonic devices proposed in the paper are organized into a sensor network, able to detect the array failures, and integrated into a control system able to mitigate pattern degradations.

II. SYSTEM ARCHITECTURE

The system architecture is reported in Fig.1 (a). It is composed of two main sub-systems: the PSN and BFN feedback control unit.

BFN Feedback control is the system component aimed at analyzing the signals coming from the PSN and at applying possible corrections to the BFN in order to mitigate the effect of undesired failures and/or calibration errors. The feedback system can be tuned according to the considered system, taking into account desired performances, robustness, resiliency, and, moreover, the overall costs. The feedback control unit is made of two main sub-blocks. The first one, the beam diagnosis block, optically interrogates the photonic sensors embedded in the array front-end, in order to estimate calibration mismatches or components failures (status of the antenna front-end). In particular, it polls the integrated photonic network to retrieve the field distribution over the aperture. According to the required correction strategies different levels of complexity can characterize the logic of the block: diagnosis logics can concern direct comparisons between estimated field distribution and the expected one (through binary marks as OK/KO). More sophisticated logics can be adopted, based on specific test sequences aimed at retrieving information about the type/features of the anomalies, such as calibration errors, hardware component failures, impedance mismatch, etc. The beam correction block (see fig.1 (a)) addresses the mitigation of the retrieved failures/calibration errors. It contains effective algorithms able to synthesize the required patterns, by properly mitigating the undesired effects of failures. More in details, the beam correction block accomplishes a constrained BFN synthesis. Constraints are represented by a binary mask which excludes element failures from the synthesis, or bounds on the amplitude of the complex weights. This problem can be solved by adopting Convex Programming algorithms [4-5]. Note that, thanks to their convex nature, constraints on the weights corresponding to failing elements can be easily inserted in the adopted synthesis algorithm, particularly fast and effective thanks to a joint use of convex programming algorithms and NUFFT transforms, enabling to efficiently evaluate the array factor in case of arbitrary lattices.

The PSN of the beam diagnosis block is based on Electro- Optic (EO) techniques for field sensing [6]. The photonic sensor is an electrically small, dielectric electromagnetic field probe, embedded into the array element. The probe is made of a LiNbO₃ crystal substrate, wherein an optical circuit has been properly integrated to take advantage from the crystal's EO effect in order to modulate an optical carrier travelling through it. A Mach-Zehnder interferometer has been realized in the sensor optical circuit, according to [7]. Since such a device has to be integrated into the antenna element, its design cannot be generalized to any case and shall be optimized taking into account the specific features of the array element. Indeed, the actual electromagnetic field distribution inside the element, its physical properties and, possibly, the manufacturing procedure of the radiating element impose

limitations to size, positioning and installation approach of the photonic device.

The physical dimensions of the designed and realized probe are 1mm (width) x 3mm (length), which make it electrically small when compared to free space wavelength at L, S and C-band. A Wavelength Division Multiplexing (WDM) can be also added in order to simplify the integration (as shown in Fig.1(a)).

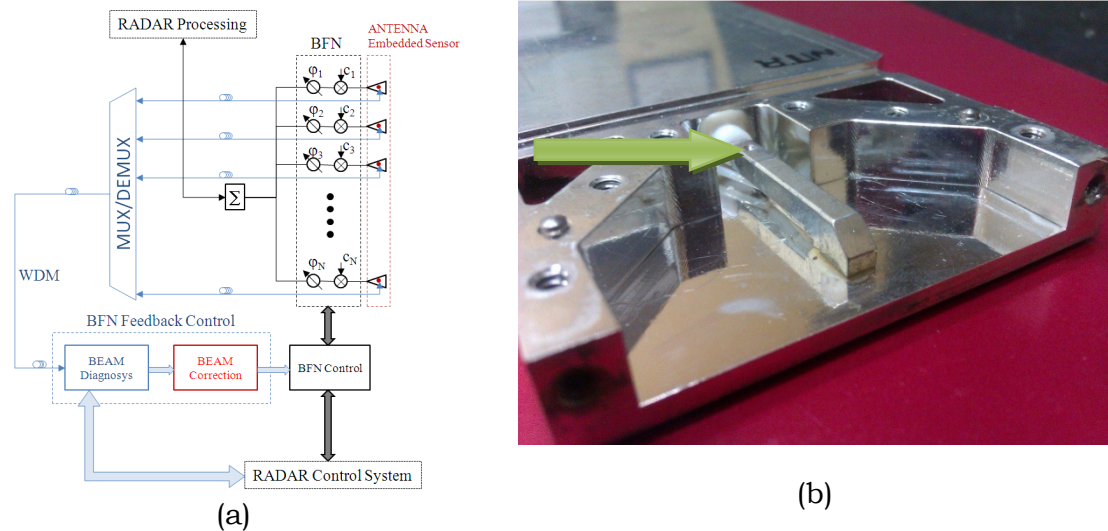


FIG. 1 – (a) The proposed system architecture **(b)** TRM with the integrated photonic sensor (green arrow indicating the region of the sensor deployment).

III. SYSTEM VALIDATION

The proposed system has been validating in two steps. The first one is aimed at validating the integration of the photonic network into the active radiating element of the considered radar system. Note that, in the considered system, the radiating element is a part of the transmit/receive module (TRM) of a commercial C-band radar system. The photonic sensor has been attached longitudinally under the metallic central ridge of the active radiating element, together with its (white) connecting fiber. Fig. 1(b) presents a picture of the integration photonic devices in the TRM. The TRM with the embedded photonic device has been tested with the extensive standard procedure, required to qualify the fabricated module before the integration into the radar system. For sake of brevity, this paper do not reports results of the tests of the experimental validation of the integration. By the way, the comparison between standard TRM module and modified one, i.e. with the embedded photonic sensor, for both receiving (Rx) mode and transmitting (Tx) mode, did not present significant differences.

The second step demonstrates the effectiveness of the proposed system in mitigating the effect of failures. To this aim, a failure has been introduced into the radar system, by switching off all the active modules belonging to a specific array row: a number nearly equal to 3.2 % of the overall number of elements has been assumed to be in failure. The

array diagram in presence of failures is shown in Figs. 2, where the compensated one, i.e. the array factor determined by applying the synthesis procedure described above is also reported. Fig.2 also show the pattern mask specifications.

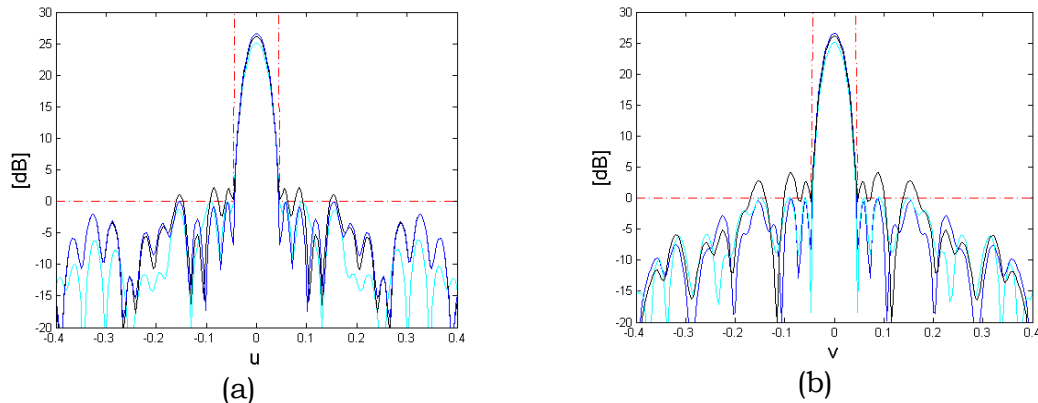


FIG. 2 – Pattern comparison: reference (blue), uncorrected (black) and corrected pattern (cyan line): **(a)** (v- cut), **(b)** u-cut.

IV. CONCLUSIONS

An innovative system based on a proper designed photonic sensors embedded in the antenna front-end has been proposed for on-site, real-time diagnosis and correction strategies. The system has been effectively integrated into TRMs of real world radar, manufactured by SELEX Sistemi Integrati S.p.A

REFERENCES

- [1] A. Buonanno, M. D’Urso, “A Novel Strategy for the Diagnosis of Arbitrary Geometries Large Arrays”, *IEEE Trans. Ant. Prop.*, 60, 2, pp. 880-885, February 2012.
- [2] J. Hoon Han, Sang-Ho L., N. Myung, “Array Antenna TRM failure compensation using adaptively weighted beam pattern mask based on genetic algorithm”, *IEEE Ant. Wireless Prop. Letters*, 11, 18-21, 2012.
- [3] R. B. Waterhouse, D. Novak, “Integrated Antenna/Electro-Optic Modulator for RF Photonic Front-Ends”, *Proceedings of 2011 International Microwave Symposium*, Baltimore, MD, June 2011.
- [4] O. M. D’Urso, T. Isernia, “Solving some array synthesis problem by using an hybrid approach”, *IEEE Trans. Ant. Propag.*, 55, 3, 2007.
- [5] T. Isernia, G. Panariello, “Optimal Focusing of scalar fields subject to arbitrary upper bounds” *Elec. Letters*. 34, 1998, pp. 162-164, 1998.
- [6] T. Nagatsuma, H. Togo, K. Narahara et Al., “Recent progress in optical measurement of radio-wave signal from GHz to THz”, *Microwave Papers*, 13, 20, 2004.
- [7] P. Vinetti, “Innovative Near Field and Very Near Field Antenna Test Ranges”, (Ph.D. thesis c/o University Federico II of Naples, Engineering Department), LAP LAMBERT Academic Publishing, 2011.

Poster session II

S. Ceccuzzi, D. Milanesio, and G.L. Ravera

Analysis of a flat, dielectric - loaded, ion cyclotron, test antenna by using three electromagnetic codes

R. Stefanelli and D. Trincherò

Full-analytical procedure for the design of micro-magnetic radiators

E. Di Salvo, F. Frezza, and S. Mosca

Analysis of cylindrical frequency selective surfaces for antenna radomes

P. Baccarelli, S. Paulotto, and D. R. Jackson

Matching techniques for efficient broadside radiation in 1D periodic printed leaky-wave antennas

A.F. Morabito and L. Di Donato

A canonical problem in multibeam antenna synthesis

S. Costanzo and A. Costanzo

Modified U-slot patch antenna with low cross-polarization for broadband applications

F. D'Agostino, F. Ferrara, C. Gennarelli, R. Guerriero, and M. Migliozzi

Direct far-field reconstruction from near-field data acquired through a helicoidal scanning

O. Leonardi, M. Pavone, G. Sorbello, and T. Isernia

A new compact monolithic patch antenna for dedicated short range communications systems

A. Galli, S. Mazzocchi, G. Valerio, M. Ciattaglia, and M. Zucca

UWB multifunctional arrays based on versatile printed rhombic antenna configurations

C. Occhiuzzi and G. Marrocco

Sensing-oriented design methodology for passive RFID antennas

A. D'Alessandro, A. Buffi, and P. Nepa

A new localization method for UHF-RFID smart shelves

S. Costanzo, G. Di Massa, and O.H. Moreno

Equivalent impedance retrieval of planar surfaces by open resonator technique

G. Monti, L. Tarricone, F. Congedo, and P. Arcuti

Wireless power transmission links: experimental results at the electromagnetic laboratory of Lecce

P. Rocca

Time-modulated arrays for next generation cognitive radio systems – potentialities and envisaged solutions

F. Viani

Array design in the correlation domain: a new paradigm

D.Pavone, G. Sorrentino, A. Buonanno, M. D'Urso

Surveillance of wide zones with unattended ground sensors: from detection to alert

A. Buonanno, P. Vinetti, M.G. Labate, M.D'Urso, M. Albertini, L. Russo

Digital multiple beams radars for airport monitoring and surveillance

ANALYSIS OF A FLAT, DIELECTRIC-LOADED, ION CYCLOTRON, TEST ANTENNA BY USING THREE ELECTROMAGNETIC CODES

S. Ceccuzzi^(1,3), D. Milanese⁽²⁾, G.L. Ravera⁽¹⁾

⁽¹⁾ Euratom-ENEA Association for fusion, C.R. Frascati
Via Enrico Fermi 45, 00044, Frascati, Italy

⁽²⁾ Electronic Department, Politechnic of Turin
Corso Duca degli Abruzzi 24, 10129, Turin, Italy

⁽³⁾ Applied Electronics Department, “Roma Tre” University
Via della Vasca Navale 84, 00146 Rome, Italy

silvio.ceccuzzi@enea.it

Abstract

The present work compares the results coming out from the following three Ion Cyclotron antenna tools: HFSS, COMSOL Multiphysics and the TOPICA code. A simplified flat antenna geometry, working at 30 MHz, is used as benchmark.

The comparison is carried out with respect to the scattering matrix and the RF potentials, i.e., the line integrals of the electric field along the flux tubes of the equilibrium magnetic field. Various operational configurations characterized by different antenna-load clearance are considered.

Very good agreement can be observed among the codes for all the simulated configurations in terms of scattering parameters. RF potentials also match as regards to patterns, trends as well as absolute values.

Index Terms – computational electromagnetics, ICRH antenna, modelling.

I. INTRODUCTION

Ion Cyclotron (IC) heating in magnetic confinement devices for thermonuclear fusion has proven to be an effective technique that directly increases fast ion populations [1]. Antennas represent the most critical part of the RF system due to the harsh environment they are called to operate, so a reliable prediction of their behaviour is of paramount importance in designing experiments and heating systems.

The electromagnetic performances of IC antennas are generally expressed by means of two main parameters, i.e., coupled power and RF potentials. The former is related to the antenna scattering matrix, while the latter is given by the integrals of the electric field component parallel to the equilibrium magnetic field along the magnetic field lines.

The aforementioned figures-of-merit can be computed by several codes, each one adopting its own formulation and modelling of the antenna load. Numerous authors have compared different antenna tools in terms of coupled power, showing very good agreement between them [2]-[4]. On the other hand RF potentials have been rarely compared and sometimes their results are said to miss a perfect match [5].

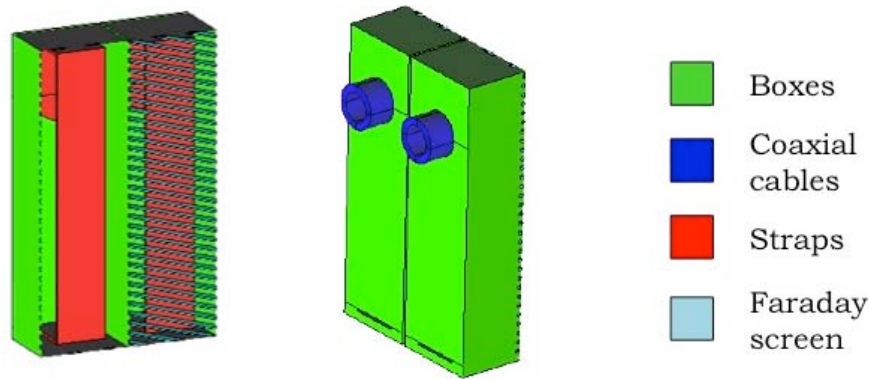


FIG. 1 – Flat antenna model; one half of the Faraday screen has been removed to let the interior visible.

This paper aims at filling this gap, presenting a comparison between three different, widely used, IC antenna tools in terms of both scattering matrix and RF potentials. A flat test antenna model, working at 30 MHz, is used as benchmark and the load is simulated through a dielectric, whose electromagnetic properties resemble the plasma behaviour.

II. BENCHMARK SETUP AND CODE DESCRIPTION

Antennas meant for working at IC frequencies (10-100 MHz) consist of short-circuited current straps, hosted in boxed and protected by conducting rods (Faraday Shield or FS) and a protruding frame (limiters). In general FS bars are slightly rotated to be aligned with the equilibrium magnetic field \mathbf{B} : it allows the reduction of the RF electric field components parallel to \mathbf{B} (E_{\parallel}), which play a deleterious role during IC plasma operations.

A simplified flat antenna model, without limiter tiles, has been used for simulations (see Fig. 1). In place of the plasma load, a dielectric with equivalent complex permittivity $\epsilon_r = 81 - 2397j$ has been used [6]. Five different configurations with vacuum gap, namely the FS-dielectric distance, ranging from 1 cm to 5 cm have been studied. Simulations have been performed with three different codes: HFSS, COMSOL Multiphysics and TOPICA.

The High Frequency Structure Simulator (HFSSTM) is a worldwide used, commercial software, based on the Finite Element Method (FEM). It's a 3-D full-wave electromagnetic field simulator, which solves a weak formulation of the partial differential equations. It automatically generates an appropriate mesh, determined by the physics and refined iteration-by-iteration during the simulation run.

COMSOL MultiphysicsTM is a 3-D FEM solver that looks very promising for fusion research. Enhanced to manage multiphysics problems, it allows great flexibility, letting the user introduce his equations and model inhomogeneous, anisotropic and dispersive

materials like cold plasmas [4]. Mesh has to be properly set by the user and convergence is found acting on basis function order.

The TORino Polytechnic Ion Cyclotron Antenna (TOPICA) code [7] is among the most advanced IC antenna tools. The electromagnetic problem is formulated by a set of multiple coupled integral equations, enforcing field continuity at the interface between antenna and plasma regions. A sparse algebraic system is finally derived applying a hybrid spatial-spectral Method of Moments (MoM) based on triangular basis functions. It can simulate dielectric, cold plasma and hot plasma loads.

III. RESULTS

The comparison of scattering parameters is reported in Fig. 2; due to matrix symmetry only two out of four parameters have been reported.

As for RF potentials, a $0-\pi$ phasing at the straps has been used. The complete patterns, calculated at the plasma-dielectric interface, are shown in Fig. 3a for a single configuration. In addition, the integrals of the absolute value of E_{\parallel} along the magnetic field lines have been calculated 5 mm far from the launcher and their average values have been compared in Fig.3b for all cases to give an overall picture.

IV. CONCLUSION

A benchmark between HFSS, COMSOL Multiphysics and the TOPICA code has been carried out with a flat, dielectric loaded, 30 MHz, test antenna in terms of scattering matrix and RF potentials.

There is an excellent agreement in terms of both module and phase for all studied configurations. Also RF potentials are very similar, though the match is not perfect. As a next step the comparison could be performed using plasma-loaded, more complex, ion cyclotron antennas.

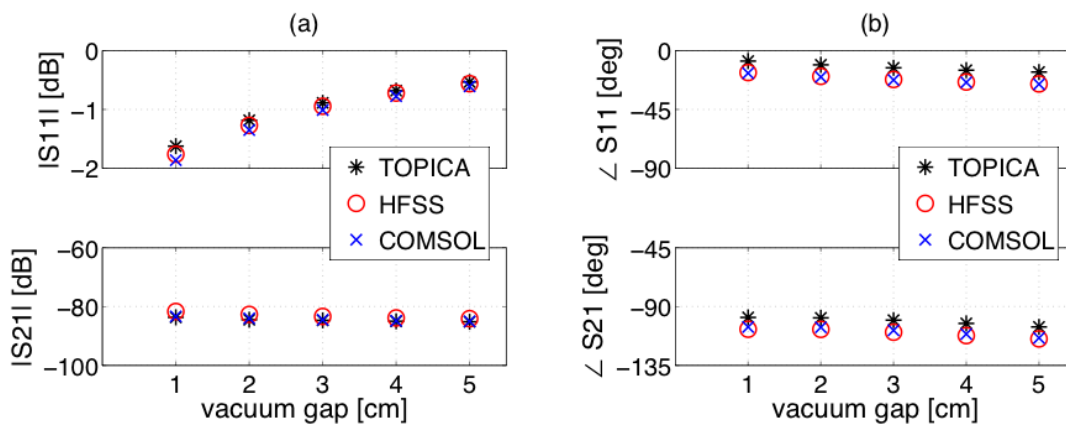


FIG. 2 – Module (a) and phase (b) of the scattering parameters S_{11} and S_{21} as predicted by the codes for different FS-dielectric clearances.

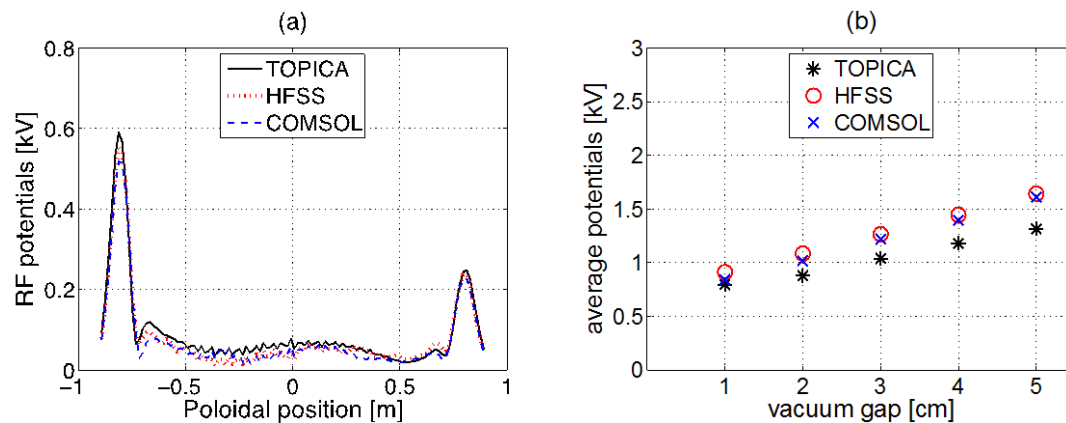


FIG. 3 – Comparison between the integrals of E_{\parallel} along flux tubes at the dielectric interface when vacuum gap = 3 cm (a) and between the mean values of the integrals of $|E_{\parallel}|$ along flux tubes at 5 mm in front of the launcher for all scenarios (b). All potentials are normalized to 1 MW of input power.

REFERENCES

- [1] J. Jacquinet, and the JET team, “Deuterium-tritium operation in magnetic confinement experiments: results and underlying physics,” *Plasma Physics and Controlled Fusion*, vol. 41 (3A), pp. A13-A46, March 1999.
- [2] M. El Khaldi, D. Milanesio, R. Maggiora, R. Magne, and K. Vulliez, “Electromagnetic Modelling of Dielectric Loads in front of an ICRH ITER Array using TOPICA and HFSS codes for comparison,” *AIP Conf. Proc.*, vol. 1187, pp. 273-276, 2009.
- [3] F. Louche, P. Dumortier, F. Durodié, A. Messiaen, R. Maggiora, and D. Milanesio, “3D modeling and optimization of the ITER ICRH antenna,” *AIP Conf. Proc.*, vol. 1406, pp. 69-72, 2011.
- [4] K. Crombe, V. Kyrtsya, R. Koch, and D. Van Eester, “Simulations of ICRF antenna near- fields in dielectric media and cold plasmas with COMSOL,” *AIP Conf. Proc.*, vol. 1406, pp. 97-100, 2011.
- [5] S. Ceccuzzi, R. Cesario, A. Krivska, F. Mirizzi, G.L. Ravera, A.A. Tuccillo, R. Maggiora, D. Milanesio, V. Bobkov, F. Braun, J-M. Noterdaeme, I. Zammuto and ASDEX Upgrade team, “Assessment of ion cyclotron antenna performance in ASDEX Upgrade using TOPICA”, *15th International Symposium on Applied Electromagnetics and Mechanics Proc.*, Sep. 7-9 2011, Naples, Italy, 2pp.
- [6] P.U. Lamalle, A.M. Messiaen, P. Dumortier, and F. Louche, “Recent developments in ICRF antenna modelling,” *Nuclear Fusion*, vol. 46 (4), pp. 432-443, Apr. 2006.
- [7] V. Lancellotti, D. Milanesio, R. Maggiora, G. Vecchi, and V. Kyrtsya, “TOPICA: an accurate and efficient numerical tool for analysis and design of ICRF antennas,” *Nuclear Fusion*, vol. 46 (7), pp. S476-S499, Jul. 2006.

FULL-ANALYTICAL PROCEDURE FOR THE DESIGN OF MICRO-MAGNETIC RADIATORS

R. Stefanelli, D. Trinchero

iXem Labs – Politecnico di Torino
Department of Electronics and Telecommunications
corso Duca degli Abruzzi, 24, 10129 Turin, Italy
info@ixem.polito.it

Abstract

Recently, small magnetic radiators are becoming more and more important for a large variety of applications involving the use of narrow transmission bandwidth in wireless sensor networks, data tracking, or environment monitoring, where they can be used not only in free-space conditions, but also inside complex electromagnetic media. As a matter of fact, the antenna is an essential component that impacts the efficiency of the transmission, the size of the device, and the bandwidth operability. In this paper an analytical procedure is introduced, that allows the design of magnetic antennas with arbitrary shape and extremely reduced dimensions. Since the design procedure is analytical, it can be efficiently applied to synthesize antennas in the free space, but also in general media. Simulations and measurements exhibit a good agreement.

Index Terms – small antennas, magnetic antennas, narrow band communications, wireless sensors

I. INTRODUCTION

Narrowband communication devices are being implemented for a larger and larger variety of applications, e.g. radio frequency identification (RFID), wireless sensor networks (WSNs), electromagnetic sensing (EMS) [1]. For these applications, the electromagnetic front-end (antenna, matching circuits, connecting cables) should be miniaturized, even if transmission properties should be optimized, to provide the maximum radiating efficiency to the system.

In the last years our group has introduced wireless devices into water, to sense the physical characteristics of the liquid, identify singularities, and provide information about the position of anomalies [2]. More recently, we have developed a new application that involves displacement of micro-sensors inside glaciers and snowfields, to monitor the wateriness and forecast avalanche events [3]. In all the mentioned scenarios, the transmitter is embedded in a dissipative medium, and the design of its RF part must take into account the electromagnetic characteristics of the medium, as well as its dimensions. For this reason, we have been working on the definition of a miniaturized antenna geometry, as well as the identification of a procedure for the design of radiators in lossy media [4]. In the following,

an effective progress is presented. The technique is based on a multi-conductor transmission lines approach; the matching impedance is computed analytically, without any optimization procedure, by a multi conductor model. The procedure can be applied to any antenna geometry, even very complex ones, e.g., with fractal shape.

II. ANTENNA DESIGN

The typology chosen for the mentioned application is the small magnetic radiator, which is significantly efficient in lossy media, as the field region is characterized by a wave impedance as small as the one of the medium surrounding the antenna.

Unfortunately, small radiators are characterized by a narrow transmission bandwidth that makes them unsuitable for standard communications. In RFID and WSNs technology, this limitation does not affect the performance of the system, as data are mainly characterized by a limited bandwidth.

For all the mentioned reasons, we have proposed an efficient magnetic antenna that allows the realization of small loop radiator, by embedding the matching circuit inside the loop [4]. An example is shown in Fig.1a, where the antenna is a standard circular loop and the two curvilinear transmission lines are inserted in series, to cancel the imaginary part of the impedance that can be measured at the loop terminals.

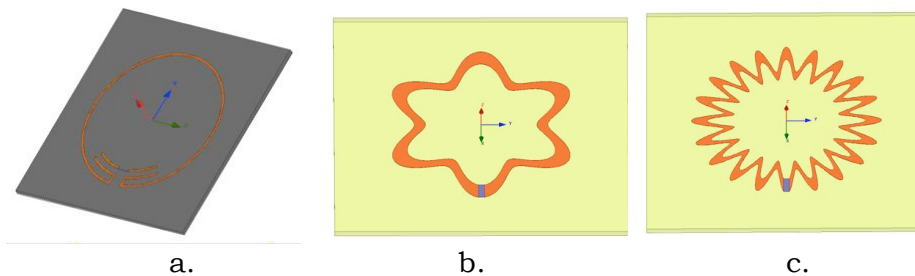


FIG. 1 – HFSS model of different antenna's design. a. small loop matched antenna. b and c: flower antennas with increased current path and smaller diameter.

To reduce the dimensions of the antenna, allowing an extended minimization of space occupation, more complex geometries have been investigated. In this way, it has been possible to synthesize small antennas, embedded inside circumferences having a radius down to 60% of a standard circular loop. To this purpose, a geometrical shape similar to a flower, where the number of petals is optimized to increase the current path, has been introduced, Fig. 1b,c.

III. THE ANALYTICAL METHOD

The design of the antenna is affected by the coupling between the radiating components (external loop, of any form) and the circuital ones (stubs). Hence, the simplified procedure described in [5] must be complemented by an iterative process or an optimization method. Since the analysis of these antennas requires the application of full wave methods, heavy computational resources and long running times should be introduced. For this reason, a new design method has been adopted that avoids the use of optimization techniques and converges in maximum two steps. Initially, the geometry of the loop is chosen and for that geometry the antenna impedance is calculated. Secondary, a multi-wire transmission line model is introduced to evaluate the coupling between the stubs and the loop. This model is used to compute the impedances Z_{11} , Z_{22} , Z_{31} and Z_{32} of the circuit shown in Fig. 2, once the length of the stubs has been determined.

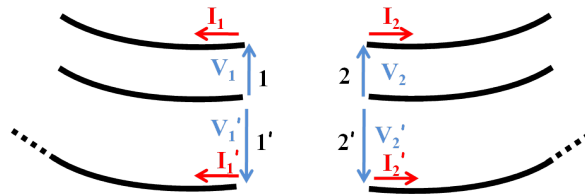


FIG. 2 – Transmission line model. The stubs are fed at natural ports 1 and 2 and left open at the terminal ports. The passive transmission lines are short-circuited at the feeding ports and left open at the terminal ports.

Once the parameters of the impedance matrix are known, the antenna impedance can be easily derived as:

$$Z_{ant} = \frac{V_{in}}{I_{in}} = Z_{11} + Z_{22} - 2Z_{21} + \frac{2(Z_{31} - Z_{32}) + Z_{33} \cos(kL)}{\cos(kL) + jY_{\infty} Z_{33} \sin(kL)} + j\sin(kL) \frac{Z_{\infty} - Y_{\infty} (Z_{31} - Z_{32})^2}{\cos(kL) + jY_{\infty} Z_{33} \sin(kL)} \quad (1)$$

where k , Z_{∞} and L are the propagation constant, the characteristic impedance and the length of the transmission line that interconnects the loop to the stubs. By applying a simple inversion, one can calculate the impedance of the radiating part that realizes the desired Z_{ant} , namely 50Ω .

Following the presented method, several samples have been realized, at different frequency carriers. For all cases, measurements of reflection coefficient (antenna impedance), radiation pattern, were performed. Fig. 3a and Fig. 3b show two examples (simulations and measurements),

performed on antennas with 16 petals working respectively at 900 Mhz and. Results exhibit a satisfactory agreement between simulated and measured data.

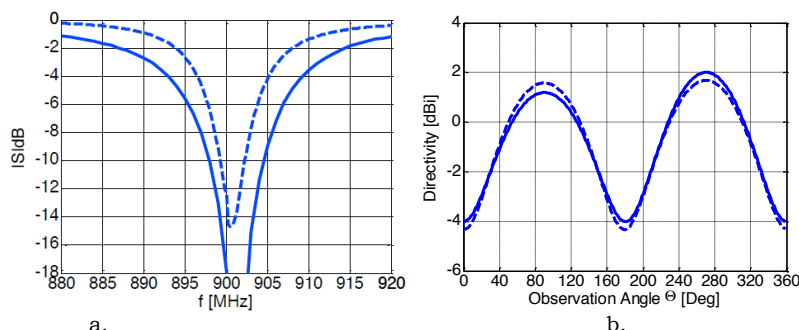


FIG. 3 – Simulations (continuous line) and measurement (dashed line) of the antenna impedance (a) and antenna radiation pattern (b) for a sample with 16 petals working at 900 MHz.

IV. CONCLUSION

The paper presents an improved design technique that allows the realization of extremely compact magnetic antennas. Unfortunately, the result usable bandwidth is extremely limited, but it is sufficient to efficiently cover a number of applications.

ACKNOWLEDGEMENT

This publication was made possible by NPRP grant # [NPRP 08-372-2-142] from the Qatar National Research Fund (a member of Qatar Foundation). The statements made herein are solely the responsibility of the authors.

REFERENCES

- [1] Kamoun, F.; , "RFID system management: state-of-the art and open research issues," *IEEE Transactions on Network and Service Management*, vol.6, no.3, pp.190-205, September 2009.
- [2] D. Trincherò, R. Stefanelli, "Microwave Architectures for Wireless Mobile Networking Networks Inside Water Distribution Conduits," *IEEE Transactions on Microwave Theory and Technique*, vol. no. 12, December 2009.
- [3] D. Trincherò, A. Carta, "Wireless Sensor Nodes for a dynamical monitoring of snow and ice conditions", *IEEE APS 2012*.
- [4] L. Cisoni, D. Trincherò, "An efficient technique for the design of miniaturized wireless sensors within liquids", *IEEE RWS 2011*, Phoenix 19/24 January 2011.

ANALYSIS OF CYLINDRICAL FREQUENCY-SELECTIVE SURFACES FOR ANTENNA RADOMES

E. Di Salvo⁽¹⁾, F. Frezza⁽¹⁾, S. Mosca⁽²⁾

⁽¹⁾ Department of Information Engineering, Electronics and
Telecommunications, “La Sapienza” University, Rome, Italy
eliadisalvo@gmail.com

⁽²⁾ SELEX Sistemi Integrati S.p.A., Reparto Antenne, Rome, Italy

Abstract

An analysis technique is described for cylindrical frequency selective structures, useful for antenna radome applications. The structures are made by free-standing conducting rectangular patches, or slots. Approximate relations are employed to study in particular structures with many elements. A comparison is reported with previous results given in the literature. The opacity, or transparency, of the surface for a suitable frequency range is shown.

Index Terms – Antenna Radomes, Cylindrical Floquet modes, Electromagnetic Scattering, Frequency Selective Surfaces (FSS).

I. INTRODUCTION

Frequency Selective Surfaces (FSS) have been an extensive research topic since a long time [1],[2]. The case of Cylindrical Frequency Selective Surfaces (CFSS), which may be of interest for antenna radome applications, has been less studied in the literature [3],[4]. In the present paper an analysis technique is described, particularly useful for structures with many constitutive elements.

II. METHOD EMPLOYED AND RESULTS OBTAINED

Figure 1 shows the infinitely long cylindrical structure we have considered. It may consist of free-standing conducting rectangular patches, or of a perfectly conducting circular cylinder perforated with axial slots. Patches or slots are located periodically along the circumferential direction φ (T_φ periodicity) and along the axial direction z (T_z periodicity).

Because of periodicity, the scattered fields are computed by analyzing the unit cell shown in Fig. 1b). Scattered fields are calculated according to the procedure described in [4]: however, we have extended this formulation for structures with a larger number of circumferential patches/slots (e.g., more than 64). This improvement has been obtained using approximated expressions of Bessel functions products [5],[6] and symbolic calculations performed with Matlab, to avoid overflow and underflow problems due to large-order and large-argument functions.

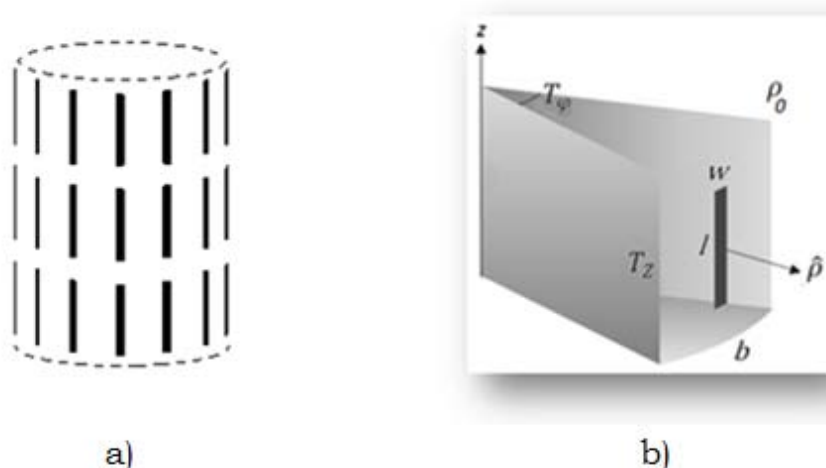


FIG. 1 – a) Cylindrical Frequency Selective Surface, made by conducting patches or slots; b) relevant unit cell parameters.

For the case of free-standing conducting patches, a cylindrical wave with TM polarization ($E_\varphi=0$; $H_z=0$), generated by an electric line current located on the cylinder axis, is considered. It is assumed $w < l/10$ and $w < \lambda/20$ where λ is the wavelength of the incident field. With these hypotheses the φ component of the electric surface current is considered constant: consequently, only the z component of the electric field and the φ component of the magnetic field are taken into account.

Being the structure under consideration periodical along φ and the z axis, the scattered fields are written as infinite sums of cylindrical Floquet modes. The amplitude coefficients of the cylindrical waves that compose the scattered field depend on the surface current on the conducting patch. This relation is found applying the boundary conditions on the tangential component of the electric field, that should be continuous at $\rho=\rho_0$, and on the tangential component of the magnetic field, that should be discontinuous at $\rho=\rho_0$ by an amount equal to the induced current density J_z .

Finally, equating the total tangential electric field to zero on a strip surface, an integral equation is obtained, where the unknown quantity is the current distribution. This integral equation may be solved numerically by using a method of moments technique. To obtain a numerical solution, the current is expanded into seven entire domain sinusoidal basis functions for narrow strips.

For the case of free-standing slots, a cylindrical wave with TE polarization ($E_z=0$; $H_\varphi=0$) generated by a magnetic line current located on the cylinder axis is considered. The slot size is the same as for the patch case and the conclusions for the field components are dual. For the numerical solution, the electric slot field is expanded into seven entire domain sinusoidal basis functions.

Figure 2 shows a comparison between a plot in [4] and our result obtained with a Matlab code using the above-mentioned approximated forms. Figure 3 is the same as Fig. 2, but with a larger cylinder radius.

In both we can see that near $l=0.5\lambda$ the CFSS does not allow the power to flow out.

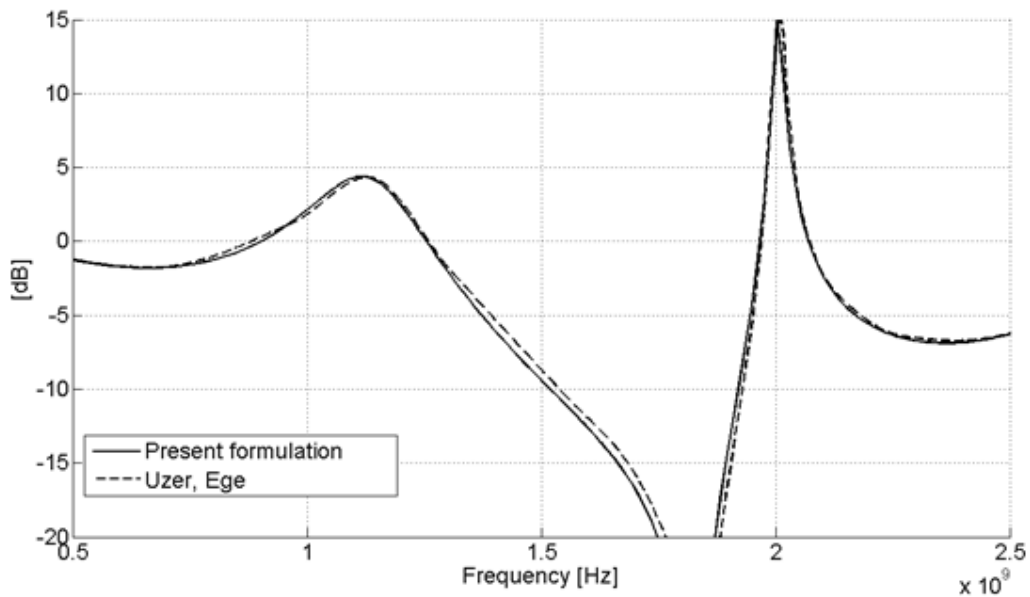


FIG. 2 – Ratio (dB) between radiated power measured away from the electric line current, with and without the CFSS, with $N = 16$ circumferential patches and unit cell parameters: $b = 50$ mm, $T_z = 100$ mm, $l = 90$ mm, $w = 4$ mm.

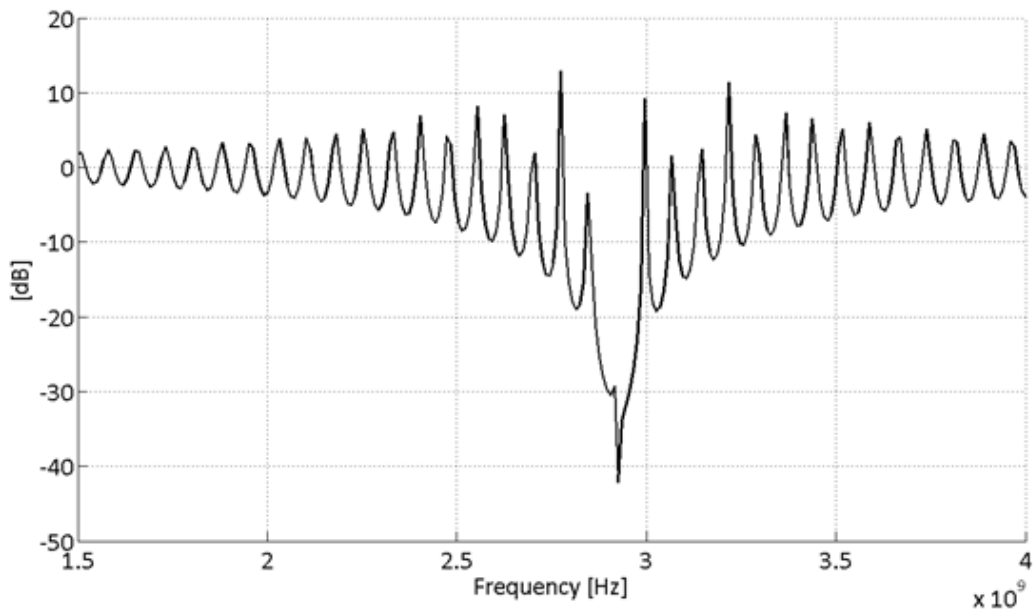


FIG. 3 – Same as in Fig. 2, for $N = 250$ circumferential patches, and unit cell parameters: $b = 50$ mm, $T_z = 55$ mm, $l = 50$ mm, $w = 4$ mm.

The plot in Fig. 4 is related to a conducting cylinder periodically drilled with axial slots. Near $l=0.6\lambda$ the CFSS allows the whole longitudinal magnetic field to flow out.

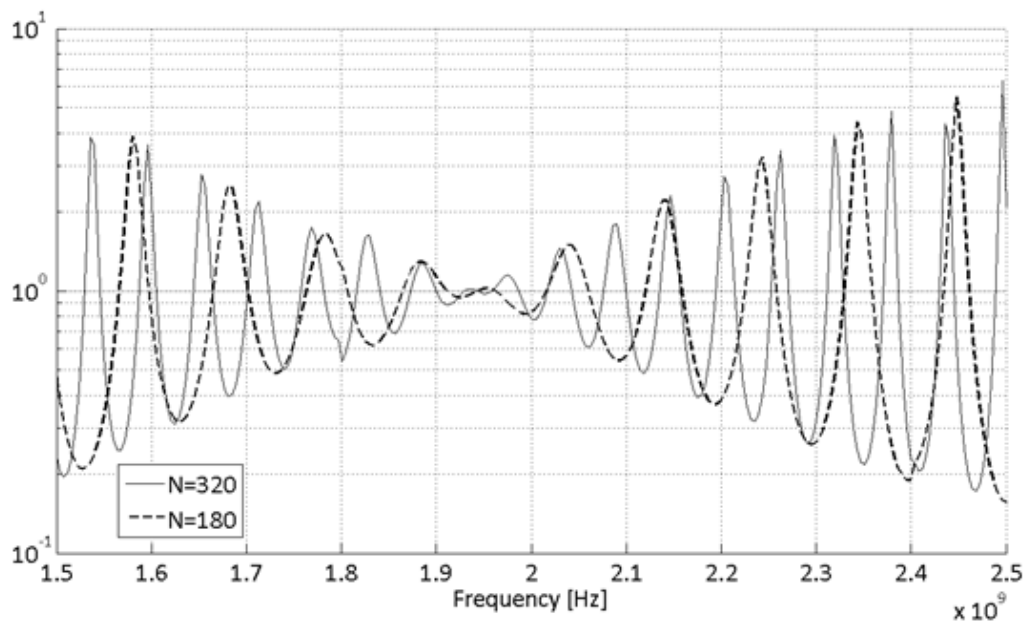


FIG. 4 – Ratio between longitudinal magnetic field (magnitude) measured away from the magnetic line current, with and without the CFSS, presenting 180 or 320 circumferential slots and: $b = 50$ mm, $T_z = 100$ mm, $l = 90$ mm, $w = 4$ mm.

III. CONCLUSION

The described technique is able to analyze cylindrical frequency selective structures with a large number of elements, useful for antenna radome applications. Further developments may concern the application of the technique to different patch/slot geometries.

REFERENCES

- [1] J. C. Vardaxoglou, *Frequency Selective Surfaces: Analysis and Design*, Wiley, New York, 1997.
- [2] B. A. Munk, *Finite Antenna Arrays and FSS*, Wiley, New York, 2003.
- [3] T. Cwik, "Coupling into and scattering from cylindrical structures covered periodically with metallic patches," *IEEE Transaction on Antennas and Propagation*, vol. 38, pp. 220-226, February 1990.
- [4] A. Uzer and T. Ege, "Radiation from a current filament located inside a cylindrical frequency selective surface," *ETRI Journal*, vol. 26(5), pp. 481-485, October 2004.
- [5] M. Abramowitz and I. A. Stegun (editors), *Handbook of mathematical functions: with formulas, graphs, and mathematical tables*, Dover, New York, 1972.
- [6] G. N. Watson, *A treatise on the theory of Bessel functions*, Cambridge University Press, London, 1962.

MATCHING TECHNIQUES FOR EFFICIENT BROADSIDE RADIATION IN 1-D PERIODIC PRINTED LEAKY-WAVE ANTENNAS

P. Baccarelli⁽¹⁾, S. Paulotto⁽²⁾, and D. R. Jackson⁽³⁾

⁽¹⁾ Dept. of Information Engineering, Electronics and
Telecommunications, 'Sapienza' University of Rome
Via Eudossiana 18, 00184 Rome, Italy,
baccarelli@die.uniroma1.it

⁽²⁾ Maxtena Inc., Bethesda, MD, USA

⁽³⁾ Dept. of Electrical & Computer Engineering,
University of Houston, Houston, TX, USA

Abstract

Symmetric π -matching networks are presented for suppressing the open stopband (OSB) and obtaining efficient broadside radiation in one-dimensional (1-D) periodic printed leaky-wave antennas (LWAs). The elimination of the OSB is achieved by matching the Bloch-wave impedance of the structure to a desired (non-zero) value at broadside frequency. Three different matching conditions can be applied. The effectiveness of the proposed techniques are demonstrated with numerical simulation on real structures.

Index Terms – Broadside scanning, leaky-wave antennas, one-dimensional (1-D) periodicity, open stopband.

I. INTRODUCTION

Printed periodic leaky-wave antennas (LWAs) are low-profile and suitable for various scanning applications, where the main radiated beam scans from the backward to the forward quadrants as the frequency increases [1]. A fundamental problem of these antennas has been the existence of an “open stopband” (OSB) in a narrow frequency region around broadside [1,2]. Within this narrow angular region the amount of the radiated power drops substantially and most of the signal is reflected back to the source. Techniques to suppress the OSB are thus of great importance, since they would enable a continuous beam scan through broadside [2]. In this paper, the use of π networks for matching the Bloch-wave impedance and eliminating the open stopband at broadside is presented.

II. π -MATCHING NETWORKS

In Figs. 1(a) and 1(b) network representations of the unit cell of general 1-D periodic printed LWAs are shown, where a transmission line of length ℓ is followed by a two-port π -matching network. Let us assume that the Bloch impedance looking into the π -matching networks

is Z_{B1} . This impedance is transformed through a length of line ℓ (with propagation wavenumber k_z and characteristic impedance Z_0) where $\ell = p - w_\pi$, with p the period and w_π the length of the π -matching network. The transformed impedance is denoted as Z_{B2} . At the OSB frequency, the π -matching circuits transform the impedance Z_{B2} back to Z_{B1} . In principle, the OSB will be eliminated for any choice of Z_{B1} , though ideally Z_{B1} is the value of the Bloch impedance for frequencies slight below and above the OSB frequency (hence, the Bloch impedance will not to vary much when the LWA scans through broadside) [2]. Consider the symmetric π -matching networks shown in Figs. 1(a) and 1(b). After some algebra, the condition for the transformation is obtained in terms of capacitance C and inductance L' for the networks in Fig. 1(a) and 1(b), respectively, as follows:

$$C = \frac{1}{2\omega Z_G} \frac{1 + (\omega L/Z_G)^2 + j(\Delta Z_B/Z_G)(\omega L/Z_G)}{(\omega L/Z_G) + j0.5(\Delta Z_B/Z_G)(\omega L/Z_G)^2} \quad (1.a)$$

$$L' = \frac{2Z_G}{\omega} \frac{1 - j0.5(\Delta Z_B/Z_G)[1/(\omega C' Z_G)]}{(1 + \omega^2 C'^2 Z_G^2)/(\omega C' Z_G) - j(\Delta Z_B/Z_G)} \quad (1.b)$$

where we denote the differences of the Bloch impedances as $\Delta Z_B \equiv Z_{B1} - Z_{B2}$ and the geometric mean of the Bloch impedances as $Z_G \equiv \sqrt{Z_{B1} Z_{B2}}$. We require that the capacitance C and inductance L' given by (1) be real-valued. This can happen in several different ways, which are described below.

a. Quarter-Wave Transformer

Here we require that $\ell = (2m-1)(\lambda_g/4)$, $m=1,2,\dots$, where $\lambda_g = 2\pi/k_z$ is the guided wavelength of the line. This condition implies that $Z_{B2} = Z_0^2/Z_{B1}$ (see Fig. 1), which also leads to $Z_G = Z_0$. The following relations are then determined for both networks:

$$L^{(\cdot)} = Z_0 \omega^{-1} \quad C^{(\cdot)} = (\omega Z_0)^{-1} \quad (2)$$

where the conditions on L and C' are needed to obtain real-valued capacitance and inductance in (1). The inductance and the capacitance in the π networks are unique and completely determined by (2); they can be properly designed once the value of Z_0 and frequency are specified. Furthermore, they do not depend explicitly on the Bloch impedance Z_B ; however, Z_B is affected by the value of Z_0 .

b. Half-Wavelength Transformer

In this case we have $\ell = m(\lambda_g/2)$, $m=1,2,\dots$, which corresponds to $Z_{B2} = Z_{B1} = Z_B$, which implies $Z_G = Z_B$ and $\Delta Z_B = 0$. It follows that the

capacitance and inductance from (1.a) and (1.b) are

$$C = (2\omega Z_B)^{-1} \left[1 + (\omega L / Z_B)^2 \right] (\omega L / Z_B)^{-1} \quad (3.a)$$

$$L = (2Z_B / \omega) (\omega C' Z_B) \left[1 + (\omega C' Z_B)^2 \right]^{-1}, \quad (3.b)$$

respectively. We note that the values of the inductance L and the capacitance C' are arbitrary, and hence, the solution is not unique. For a given L (C'), (3) determines the solution for C (L'), which depends explicitly on the Bloch impedance, and hence will be real only for real values of Z_B .

c. Perfectly Matched System

Here we assume that $Z_{B1} = Z_{B2} = Z_0$, which implies $Z_G = Z_0$, and $\Delta Z_B = 0$. In this case the length ℓ of the line is arbitrary, even though it affects the OSB frequency; the design equations are given from (3), where $Z_B = Z_0$.

III. DESIGN EXAMPLES AND DISCUSSION

Printed periodic microstrip LWAs, whose unit cell are shown in Figs. 1(a) and 1(b), have been optimized for eliminating the OSB following the design cases b and c, respectively. The Bloch impedances (which are almost real for the chosen unit cells) are shown in Figs. 2(a) and 2(b) and present a quite flat behavior across the broadside frequencies $f_B = 5.29$ GHz and 10.05 GHz, respectively, thus confirming the suppression of the OSB [2]. Values of the elements of the π networks at the broadside frequencies (where $Z_B \approx 71 \Omega$ and 50Ω , for the case of Figs. 1(a) and 1(b), respectively) are obtained by simulating the relevant discontinuities of width w_π with Ansys Designer® and are reported in Table I. Excellent agreement is observed between the design formulas and numerical simulations (reported in bold font in Table I), which validates the design approach based on simple π -matching networks. Finally, the dispersion behavior of the phase and attenuation constants around the broadside frequencies and the numerical radiation patterns, not shown here for brevity, illustrate the desired continuous scanning of the radiated beam through broadside for both the considered LWAs.

REFERENCES

- [1] D. R. Jackson and A. A. Oliner, "Leaky-wave antennas," in *Modern Antenna Handbook*, C.A. Balanis, Ed. New York: Wiley, 2008, ch. 7.
- [2] S. Paulotto, P. Baccarelli, F. Frezza, and D. R. Jackson, "A novel technique for open-stopband suppression in 1-D periodic printed leaky-wave antennas," *IEEE Trans. on Antennas and Propagation*, vol. 57, pp. 1894-1906, July 2009.

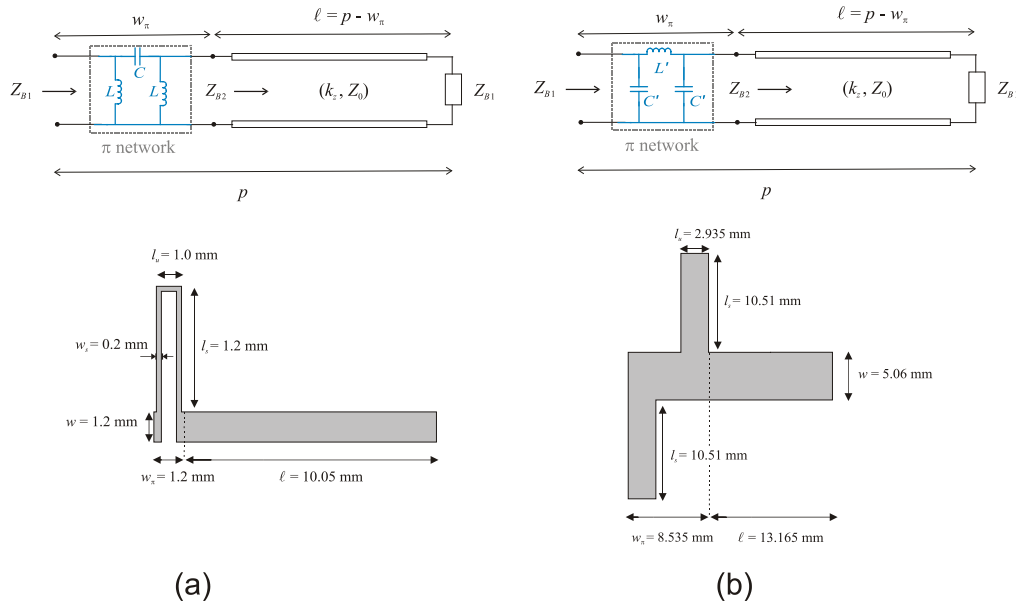


FIG. 1 – (a) Network representation and relevant unit cell of a 1-D periodic microstrip LWA loaded with long lengths of line folded as a *u*-stub. Dielectric substrate: Arlon AD1000 ($\epsilon_r = 10.35$), thickness 0.762 mm. (b) Network representation and relevant unit cell of a double-stub microstrip LWA. Dielectric substrate: Rogers RT/duroid 5880 ($\epsilon_r = 2.2$), thickness 1.575 mm.

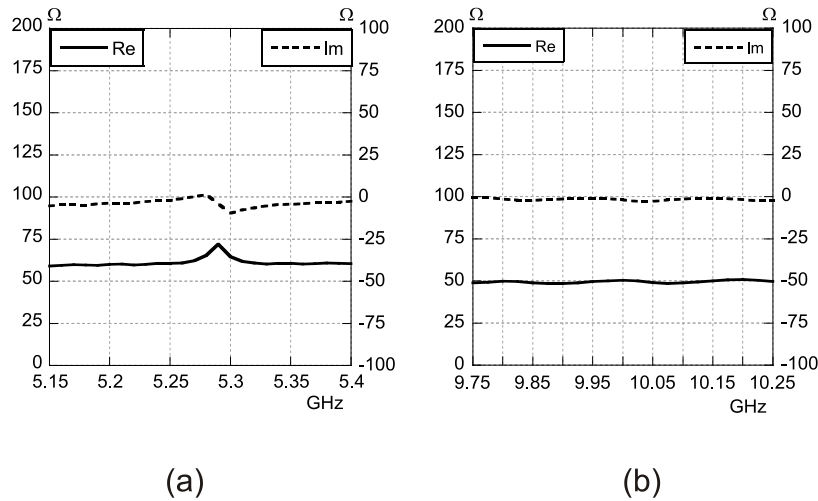


FIG. 2 – (a) Bloch impedance obtained by simulating with Ansys Designer® 60 unit cells of the LWA as in Fig. 1(a). (b) Bloch impedance obtained by simulating with Ansys Designer® 30 unit cells of the LWA as in Fig. 1(b). Legend: real part (solid lines) and imaginary part (dashed lines).

TABLE I

f_B (GHz)	$L^{(j)}$ (nH): (3.b)	$L^{(j)}$ (nH): sim.	$C^{(j)}$ (pF): (3.a)	$C^{(j)}$ (pF): sim.	$l/(\lambda_g/2)$
5.29	--	0.045	10.04	10.01	0.97
10.05	0.35	0.35	--	1.36	--

A CANONICAL PROBLEM IN MULTIBEAM ANTENNA SYNTHESIS

A. F. Morabito, L. Di Donato

LEMMA Group @ DIMET, Università ‘Mediterranea’ di Reggio Calabria,
Via Graziella, Località Feo di Vito, I-89124 Reggio Calabria, Italy
{andrea.morabito, loreto.didonato}@unirc.it

Abstract

The problem of the optimal synthesis of ‘four-color’ multi-beam antennas is formulated and solved. The proposed approach exploits at best all the degrees of freedom of the synthesis scenario at hand, and allows to formulate the design problem as a convex programming optimization. The achievement of the maximum feasible radiation performance is guaranteed in a large number of applications of actual interest.

Index Terms – Antenna Synthesis, Aperture Antennas, Multibeam Antennas.

I. THE PROBLEM AT HAND AND THE BASIC IDEA

The next satellite services will offer multimedia applications exhibiting higher and higher data rate performances [1]. To pursue such a goal, an overlapped beam spot coverage of the Earth will be provided, with high gain performances (such to guarantee adequate figures of merit in terms of EIRP and G/T) on each beam. Moreover, a sufficiently large isolation will be required amongst possibly interfering beams [1].

A canonical mission scenario is shown in Fig. 1, wherein the region to be covered results hexagonally sampled into a number of circular spots having a constant angular width and a constant center-to-center spacing. Each beam has assigned a specific frequency sub-band and polarization in order to avoid interferences amongst adjacent spots [1]. The ‘iso-frequency and iso-polarization’ spots are indicated by the same color, and two different frequency bands and polarizations are adopted, leading to the well known ‘four-color’ re-use scheme. Notably, by virtue of the well known Four Color Theorem [2], four is the minimum number of different channels which can be used in any re-use scheme.

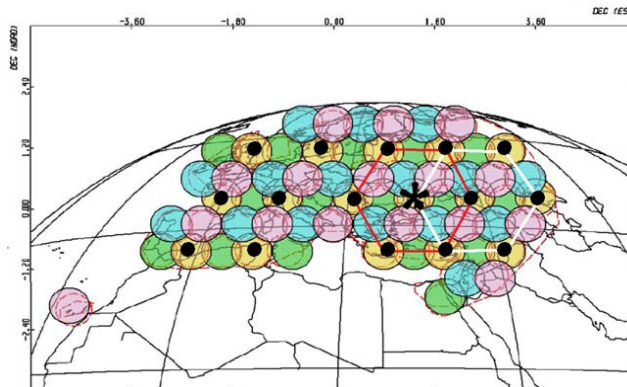


FIG. 1 – ‘Four-color’ multibeam coverage of the Europe. The gain must be maximized in the ‘*’ spot subject to sidelobe upper bounds in the ‘•’ spots.

Once a mission scenario is defined, the problem can be formulated as that of synthesizing one or more antennas able to maximize the minimum directivity inside the coverage zone while ensuring an adequate carrier-to-interference performance in the other beams (see Fig. 1).

Recently, it has been shown that, whatever the choice of the final antenna, the identification of a continuous aperture source fulfilling 'at best' the required specifications allows to establish the ultimate achievable radiation performances as well as a reference and a guide in the synthesis of the actual radiating system [3].

Up to now, effective procedures have been developed for the synthesis of circularly symmetric aperture fields able to fulfill (and optimize) given far field performances [3]. In particular, the approach in [3] provides a convex programming procedure for the fulfillment of circularly symmetric directivity constraints and the 'automatic' discard of superdirective fields. Notably, such a canonical result has been then exploited in the optimal synthesis of (multibeam) sparse arrays, thinned arrays, and clustered arrays [1],[3].

On the other side, considering the canonical multibeam scenario of Fig. 1, for each color the nearest interfering spots are located just in six equispaced angular directions (and those besides the nearest ones in other well-defined directions). As a consequence, for a fixed elevation angle, the imposition of a given sidelobe level constraint in all the azimuthal directions goes well beyond the actual antenna requirements. Saying it in other words, a circularly symmetric source tends, by definition, to fulfill the mission requirements not only on the 'iso-color' regions but also on the non-interfering spots, which unnecessarily over constrains the optimization problem.

Then, the basic idea proposed and developed herein is to solve the above design problem by exploiting sources having, for each value of the radial coordinate, an hexagonally symmetric behaviour in terms of azimuthal angle. In fact, such an hexagonal symmetry, which will however vary with the radial coordinate, will result in an hexagonal symmetry of the far field in the azimuthal variable.

Such a kind of dependency will allow to enforce the radiation constraints only where actually needed, i.e., just on the interfering spots. Therefore, these sources will lead to the best possible exploitation of the antenna synthesis degrees of freedom, and hence to the achievement of the maximum feasible performance in terms of carrier-to-interference ratio. Interestingly (see below), the final patterns will result in a sort of 'smart interlocking' amongst the higher sidelobes and the 'iso-color' regions. In the following, a convex programming strategy able to identify in a fast and effective fashion the globally optimal solution of such a canonical problem is outlined and tested.

II. THE SYNTHESIS PROCEDURE

Basically, by exploiting the guidelines of [4], the approach amounts to expand the aperture field in a suitable convenient basis, and then to find the coefficients of this expansion in such a way to maximize the directivity while guaranteeing the fulfillment of given upper bounds on the sidelobes, or to maximize the separation amongst main beam and sidelobes for a given beamwidth.

In the latter case, reasoning by the sake of simplicity for the beam pointing at boresight, the problem can be formulated as:

Maximize:

$$\text{Re}[E(\theta=0)] \quad (1.a)$$

Subject to:

$$\text{Im}[E(\theta=0)]=0 \quad (1.b)$$

$$|E(\theta,\phi)|^2 \leq UB(\theta,\phi) \quad (1.c)$$

wherein E denotes the far field distribution as a function of the elevation and azimuthal angles θ , ϕ , while the ‘upper bound’ mask UB takes into account the actual location of the iso-color beams, and the reference phase of the field is fixed to 0 in the target direction.

By so doing, the problem is reduced to a convex programming optimization, and hence, unless the constraints are so strict to prevent the existence of a solution, the fast achievement of its global optimum (which is unique) is guaranteed.

As far as the choice of the basis function of the aperture field is concerned, any (complete) expansion enforcing an ‘hexagonally symmetric’ azimuthal behavior (as defined above) can be used. In this work, as they allow both a closed-form expression for the far field and some control of radial variations along the aperture, we use the TE_{6n} propagation modes (with $n=1, \dots, N$) of a circular waveguide having a radius equal to that of the aperture at disposal. Therefore, our continuous aperture field E_{AP} defined over an aperture of radius a is written as:

$$E_{AP}(\rho, \varphi) = \sum_{n=0}^N \left\{ \sum_{m=1}^{M_n} [A_m \cos(6n\varphi) + A_{m+M_n} \sin(6n\varphi)] J_{6n} \left(\Phi_{6n,m} \frac{\rho}{a} \right) \right\} \quad (2)$$

wherein ρ and φ respectively denote the radial and azimuthal coordinates spanning the aperture, J_x is the Bessel function of first kind and order x , $\Phi_{x,m}$ is the m -th root of the derivative of J_x , $2M_n$ is the number of unknown coefficients in the basis J_{6n} (which must be chosen according to the number of degrees of freedom of the radiated field), and $N+1$ corresponds to the number of exploited TE_{6n} modes.

III. AN EXAMPLE OF PERFORMANCES

With reference to the optimization problem 1(a-c), an example of the achievable performance is shown in Fig. 2, where the same parameters

as in [1] have been used. By the sake of understanding, the location of the iso-color beams have also been reported in Fig. 2.b.

As it can be seen, the higher sidelobes are located midway amongst the iso-color beams, whereas, instead, the radiated field fulfills all the given constraints. Therefore, advantage is taken from azimuthal variations, which would have not been the case with circularly symmetric sources.

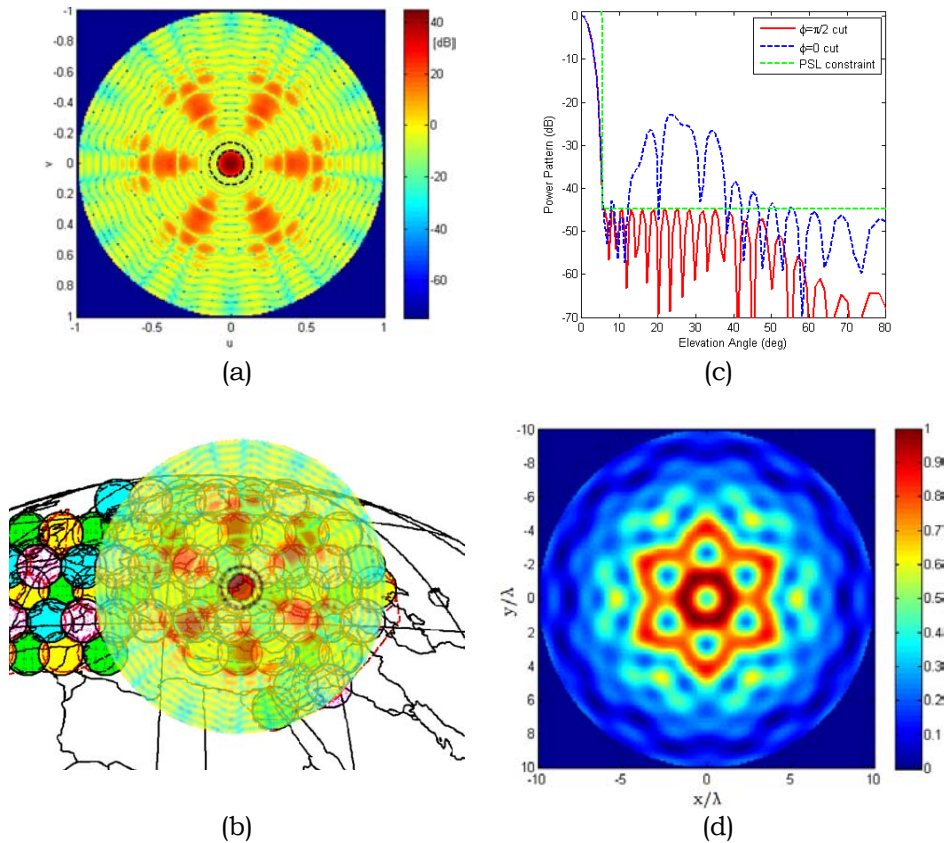


FIG. 2 – Synthesis results: power pattern plotted in the spectral plane (a) and along the main cuts (c); corresponding real aperture field distribution (d); achieved multibeam Europe coverage (b).

REFERENCES

- [1] ESA/ESTEC Tender AO/1-5598/08/NL/ST, “Innovative architectures for reducing the number of controls of multiple beam telecommunications antennas”.
- [2] K. Appel and W. Haken, “Every planar map is four colorable, Part I: discharging,” *Illinois Journal of Mathematics*, vol. 21, pp. 429–490, 1977.
- [3] O. M. Bucci, T. Isernia, and A. F. Morabito, “Optimal synthesis of directivity constrained pencil beams by means of circularly symmetric aperture fields,” *IEEE Ant. and Wireless Propag. Letters*, vol. 8, 2009.
- [4] T. Isernia and G. Panariello, “Optimal focusing of scalar fields subject to arbitrary upper bounds,” *Electronics Letters*, n. 34, pp. 162-164, 1998.

MODIFIED U-SLOT PATCH ANTENNA WITH LOW CROSS-POLARIZATION FOR BROADBAND APPLICATIONS

S. Costanzo, A. Costanzo

DEIS – University of Calabria
Via P. Bucci, 87036 Rende (CS), Italy
costanzo@deis.unical.it

Abstract

The basic U-slot shape usually adopted for enhancing the bandwidth response of a microstrip patch antenna is properly modified in this work to significantly reduce unwanted cross-polarization effects. A wideband impedance matching is obtained by introducing a proper annular gap around the feed probe, in order to compensate for the large inductive reactance due to the presence of a thick substrate. A compact P-band prototype with a 15% bandwidth is realized and experimentally tested.

Index Terms – Broadband antennas, compact antennas, U-slot antennas.

I. INTRODUCTION

The U-slot patch antenna configuration provides a useful single-layer structure to achieve broadband and/or multi-band features [1]. The basic idea is to exploit the reactive cancellation between the U-slot capacitance and the feed inductance, as well as the additional U-slot resonances to obtain a broadband frequency response. Several studies exist in literature which confirm the possibility to achieve impedance bandwidths in the range 10%-40% for both linear and circular polarization, with a larger frequency band in the presence of an air or foam substrate. The antenna behavior is strongly sensitive to the variations of different parameters describing the U-slot geometry and the substrate features. A significant attempt to establish design criteria for the standard U-slot patch configuration are provided in [1], where empirical formulas are presented on the basis of an accurate analysis of all structure resonances and their relations with the geometry parameters. However, design rules proposed in [1] give an approximate tool which may not work in all situations, and provide only a good starting point for successive optimizations to be performed for achieving the prescribed broadband features. Starting from the insight study of the antenna behavior described in [1], the original U-slot geometry is properly modified in this contribution to accomplish for a wideband response, but strongly reducing cross-polarization effects due to the complex combination of antenna and slot modes. These unwanted resonant modes are faced in [1] by imposing a specific constraint on the ratio between the U-slot vertical and horizontal arms, thus limiting in various cases the achievable bandwidth. Further problems arise in those applications, such as P-sounding radar, which require thick

substrates to satisfy the bandwidth requirements while guaranteeing at the same time the antenna compactness. In these cases, reliable design criteria do not exist, as the empirical formulas provided in [1] have limited applications to electrically thin substrates. In this contribution, the cross-polarization effects of the standard U-slot patch antenna are avoided by introducing a modified U-shape slot which minimizes the paths of unwanted currents. Furthermore, the problem of large probe inductance due to the presence of thick substrates is accurately faced by adopting a proper annular gap around the feed probe to reach a good impedance matching in the broadband frequency range. Experimental results on a compact P-band prototype are discussed to illustrate the validity of the proposed approach.

II. ANTENNA CONFIGURATION

The antenna configuration proposed in this contribution is illustrated in Fig. 1. The basic U-slot geometry is properly modified to improve its bandwidth features, but reducing at the same time the high cross-polar radiation often present at some frequencies within the operating range [1]. As discussed in [1], antenna and slot modes combinations give rise to undesired x-directed currents which produce a high cross-polar component unless the ratio between the vertical arm C and the horizontal arm D does not satisfy a specific criterion. This means that bandwidth requirements cannot always be satisfied while guaranteeing, at the same time, a low cross-polar effect.

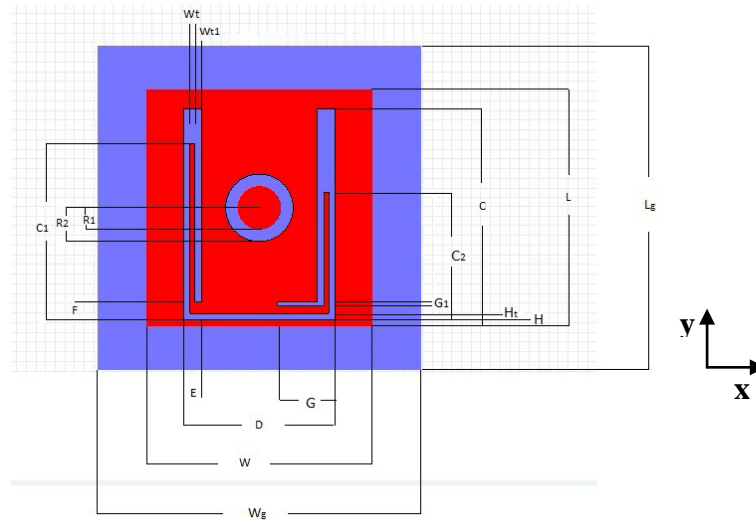


FIG. 1 – Layout of modified U-slot antenna.

As illustrated in Fig.1, the U-slot arms are properly shaped to minimize the paths of unwanted x-directed modes. In particular, a cut is realized along the horizontal U-slot direction, thus reducing the extent H_t of the new horizontal arm. To have a better tuning of the operating bandwidth, unequal lengths are chosen for the two U-slot vertical arms. As a further variation with respect to the original U-slot

design [1], a proper annular ring is introduced to compensate for the large probe inductance due to the presence of thick substrates, which could prevent the impedance matching.

III. DESIGN OF COMPACT P-BAND PROTOTYPE

Empirical formulas presented in [1] are adopted to have a starting point of the original U-slot antenna dimensions, by imposing a center design frequency $f_0 = 450$ MHz and an operating bandwidth of about 15%, useful for P-sounding radar. A foam substrate having thickness equal to 60 mm is assumed, with an upper thin layer (0.762 mm) of dielectric DiClad870 ($\epsilon_r = 2.33$) adopted uniquely for robustness reasons, to better support the U-shaped slot. Design rules proposed in [1] give a U-slot patch configuration ('Design 1') whose dominant dimensions are reported in Table I.

TABLE I – REFERENCE U-SLOT PATCH CONFIGURATIONS

Configuration Name	Patch Width W [cm]	Patch Length L [cm]
Design 1	49.26	27.50
Design 2	36.10	26.12

The simulated return loss (Fig. 2(a)) shows a reduced bandwidth of about 5.7% with respect to the imposed constraint, thus requiring an optimization refinement to obtain the 'Design 2' configuration reported in Table I. A larger bandwidth of about 11% is obtained in this case, but lower again with respect to the prescribed goal of 15%. Furthermore, when approaching to the frequency band extremes, a crosspolar field level in the H-plane comparable to the copolar component is produced (Fig. 2(b)), as yet observed in [1], thus indicating a reduction of the effective useful bandwidth.

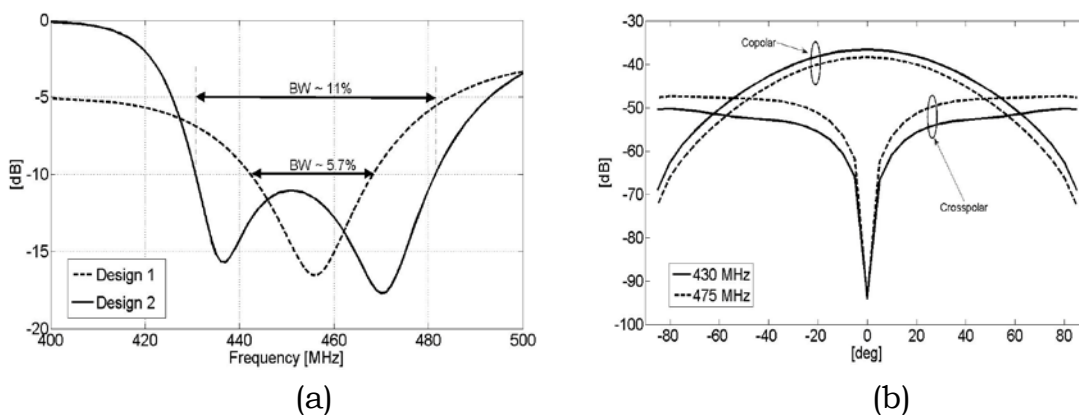


FIG. 2 – Simulated return loss (a) and field pattern (b) of U-slot configurations in Table I.

To overcome the limits of standard U-slot structure, the modified layout of Fig. 1 is considered, and accurate design formulas, taking into

account for all geometrical parameters, have been developed. A full description of the design rules will be provided in a future extended version of the work, as well as in the conference presentation. The final dimensions of P-band prototype with the layout of Fig. 1 are reported in Table II, and the realized structure is shown in Fig. 3.

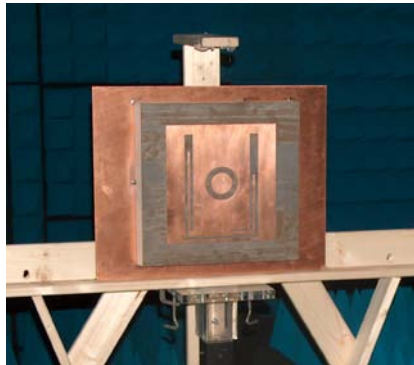


TABLE II – DIMENSIONS OF P-BAND MODIFIED U-SLOT ANTENNA

Parameter	Dimension [cm]	Parameter	Dimension [cm]
L_g	33.50	L	24.34
W_g	33.50	W	23.11
D	15.60	F	1.80
E	1.80	W_t	0.50
C	21.80	G	5.92
C_1	18.15	R_2	3.50

FIG. 3 – Photograph of P-band prototype.

The antenna has been tested into the Microwave Laboratory at University of Calabria, in terms of both return loss and radiation pattern measurements. A bandwidth of about 15% has been successfully obtained, and the wideband response is also confirmed by the radiation features, with a crosspolar component properly below the copolar field.

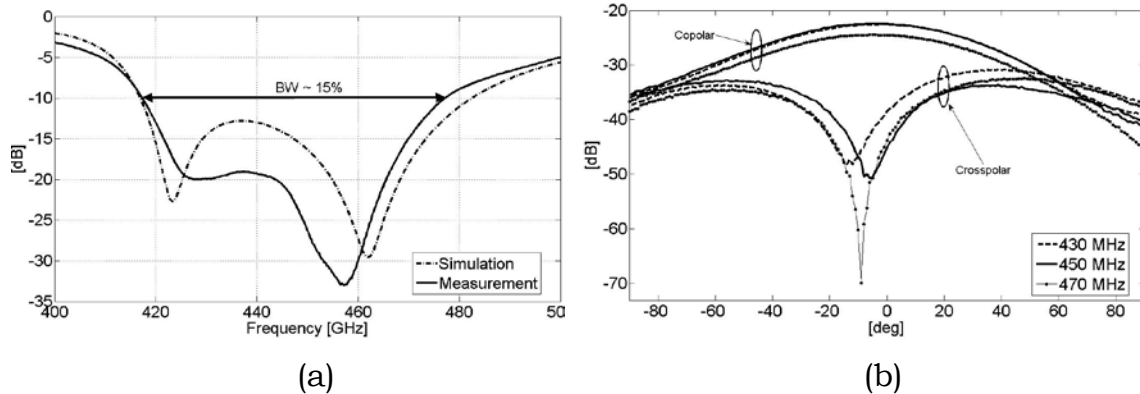


FIG. 4 – Measured return loss (a) and field pattern of Modified U-slot antenna.

IV. CONCLUSION

A modified U-shaped slot patch has been proposed in this work to guarantee a broadband response with low cross-polarization levels. A P-band prototype has been designed and tested to validate the approach.

REFERENCES

[1] S. Weigand, G. H. Huff, K. H. Pan, and J. T. Bernhard “Analysis and design of broad-band single-layer rectangular U-slot microstrip patch antennas,” *IEEE Trans. Antennas Propag.*, vol. 51, pp. 457-468, 2003.

DIRECT FAR-FIELD RECONSTRUCTION FROM NEAR-FIELD DATA ACQUIRED THROUGH A HELICOIDAL SCANNING

F. D'Agostino, F. Ferrara, C. Gennarelli, R. Guerriero, M. Migliozi

D.I.E.I.I., University of Salerno, via Ponte Don Melillo, 84084 Fisciano, Italy
{fdagostino, flferrara, cgennarelli, rguerriero, mmigliozi}@unisa.it

Abstract

A near-field – far-field transformation with helicoidal scanning for elongated antennas, which allows the evaluation of the antenna far field directly from a nonredundant number of data without interpolating them, is here proposed. It relies on a nonredundant sampling representation of electromagnetic fields and employs a flexible source modelling suitable for long antennas to determine the number of helix turns. Instead, the number of data on each turn is fixed by the minimum cylinder rule, as in classical cylindrical scan, in order to reduce the computational effort and simplify the mechanical scanning. Numerical results assessing the effectiveness of the proposed technique are shown.

Index Terms – antenna measurements, direct near-field – far-field transformation, helicoidal scanning, nonredundant representations of electromagnetic fields.

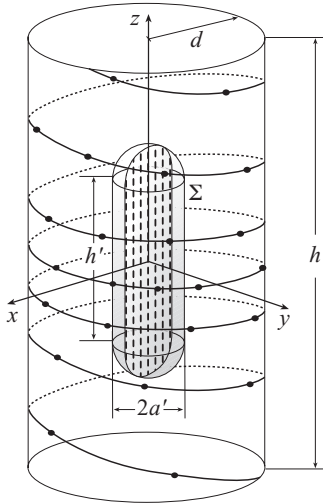
I. INTRODUCTION

Helicoidal scanning techniques exploiting continuous and synchronized movements of the positioning systems of the probe and antenna under test (AUT) have been proposed [1-3] to significantly reduce the measurement time. They are based on the nonredundant sampling representations of electromagnetic (EM) fields [4] and employ optimal sampling interpolation (OSI) formulas to efficiently recover the data required by the classical cylindrical near-field – far-field (NF–FF) transformation [5] from the acquired helicoidal ones. A direct NF–FF transformation with helicoidal scanning for volumetrical antennas, which allows the evaluation of the antenna far field directly from a nonredundant number of NF data without interpolating them, has been recently proposed [6]. Unfortunately, this last is not suitable for elongated antennas. In fact, the adopted spherical source modelling does not allow to consider measurement cylinders with a radius smaller than one half the AUT maximum size and this reflects in an increase of the error due to the scanning surface truncation.

Aim of this work is to develop a direct NF–FF transformation with helicoidal scanning tailored for elongated antennas. To this end, the AUT is considered as enclosed in a cylinder ended in two half spheres (Fig. 1), a shape suitable to deal with long antennas, but which remains quite general and contains the spherical modelling as particular case.

II. NONREDUNDANT SAMPLING REPRESENTATION ON A CYLINDER

Let us consider an elongated AUT enclosed in a surface Σ formed by a cylinder of height h' ended in two half-spheres of radius a' and a nondirective probe scanning a proper helix lying on a cylinder of radius d in the NF region (Fig. 1). The spherical coordinate system (r, ϑ, φ) is used to denote an observation point P . According to [4], when dealing with the representation on a curve C , it is convenient to adopt a proper analytical parameterization $r = r(\eta)$ for describing C and to introduce the “reduced voltage” $\tilde{V}(\eta) = V(\eta)e^{j\psi(\eta)}$, where V is the probe voltage and $\psi(\eta)$ is a proper phase function. The error, occurring when $\tilde{V}(\eta)$ is approximated by a bandlimited function, is negligible as the bandwidth ex-


FIG. 1 – Helicoidal scan.

ceeds a critical value W_η [4] and, accordingly, it can be effectively controlled by choosing a bandwidth equal to $\chi' W_\eta$, where $\chi' > 1$ is the bandwidth enlargement factor. The bandwidth W_η and parameterization η relevant to a generatrix, and the corresponding phase function ψ are [3]:

$$W_\eta = \beta \ell' / 2\pi ; \quad \eta = (\pi / \ell') [R_1 - R_2 + s'_1 + s'_2] \quad (1)$$

$$\psi = (\beta / 2) [R_1 + R_2 + s'_1 - s'_2] \quad (2)$$

where β is the wavenumber, ℓ' is the length of the curve C' , intersection between the meridian plane passing through P and Σ , $R_{1,2}$ are the distances from P to the tangency points $P_{1,2}$ on C' , and $s'_{1,2}$ are their arclength coordinates. As shown in [3], it results:

$$\ell' = 2(h' + \pi a') ; \quad R_{1,2} = [(z \mp h' / 2)^2 + d^2 - a'^2]^{1/2} \quad (3)$$

$$s'_1 = a' \sin^{-1} \left(\frac{a'd + R_1((h' / 2) - z)}{R_1^2 + a'^2} \right) ; \quad s'_2 = h' + a' \left[\pi - \sin^{-1} \left(\frac{a'd + R_2((h' / 2) + z)}{R_2^2 + a'^2} \right) \right] \quad (4)$$

According to [3], the helix is obtained by projecting on the cylinder a proper spiral wrapping Σ . The helix step is equal to the sample spacing $\Delta\eta = 2\pi / (2N'' + 1)$ needed to interpolate the voltage along a generatrix. Note that $N'' = \text{Int}(\chi N') + 1$, where $\text{Int}(x)$ denotes the integer part of x , $N' = \text{Int}(\chi' W_\eta) + 1$, and $\chi > 1$ is an oversampling factor [4]. The projection is obtained via the curves at $\eta = \text{const}$ [3]. Thus, the equations of the helix, when imposing its passage through a point Q_0 of the generatrix at $\varphi = 0$, are: $x = d \cos(\phi - \phi_s)$, $y = d \sin(\phi - \phi_s)$, $z = d \cot[\theta(\eta)]$, wherein ϕ is the parameter describing the helix, ϕ_s is the ϕ value at Q_0 , and $\eta = k\phi$, with $k = \Delta\eta / 2\pi = 1 / (2N'' + 1)$. A nonredundant representation on the helix is then got by choosing the optimal parameter ξ to describe it equal to β / W_ξ times the arclength of the projecting point on the spiral wrapping Σ and the phase function γ coincident with ψ . Moreover, W_ξ is β / π times the length of the spiral wrapping Σ from pole to pole [3].

According to the above results, the voltage at P on the generatrix at φ can be recovered via the following OSI expansion [3]:

$$\tilde{V}(\eta(\vartheta), \varphi) = \sum_{n=n_0-q+1}^{n_0+q} \tilde{V}(\eta_n) \Omega_N(\eta - \eta_n) D_{N''}(\eta - \eta_n) \quad (5)$$

where $\eta_n = \eta_n(\varphi) = \eta(\phi_s) + k\varphi + n\Delta\eta = \eta_0 + n\Delta\eta$, $2q$ is the number of the retained samples $\tilde{V}(\eta_n)$, $n_0 = \text{Int}[(\eta - \eta_0) / \Delta\eta]$, $N = N'' - N'$, and $D_{N''}(\cdot)$, $\Omega_N(\cdot)$ are the Dirichlet and Tschebyscheff sampling functions [4]. The samples $\tilde{V}(\eta_n)$ could be retrieved [3] via an expansion along the helix, similar to (5), thus allowing the reconstruction of the voltage at any point on the cylinder. However, the proposed direct NF–FF transformation avoids the explicit interpolation of the nonredundant acquired data to recover those required by the classical one [5].

III. THE DIRECT NF–FF TRANSFORMATION TECHNIQUE

According to [5], the cylindrical wave expansion coefficients a_ν and b_ν of the

AUT field are related to: i) the two-dimensional Fourier transforms

$$I_V^{1,2}(\sigma) = \int_{-\infty}^{\infty} \int_0^{2\pi} V^{1,2}(\varphi, z) e^{-jv\varphi} e^{j\sigma z} d\varphi dz \quad (6)$$

of the probe voltage for two sets of measurements (the probe is rotated by 90° in the second set); ii) the wave expansion coefficients c_m, d_m and c'_m, d'_m of the field radiated by the probe and the rotated probe, when used as transmitting antennas. Once the modal coefficients have been determined, the FF components of the electric field can be evaluated by using the FFT [5].

By taking into account (5), the integrals (6) can be rewritten in the form:

$$I_V^{1,2}(\sigma) = \int_{n \in N_r} \int_0^{2\pi} \left\{ \tilde{V}^{1,2}(\eta_n, \varphi) e^{-jv\varphi} \int_{-\infty}^{\infty} D_{N^n}(\eta(z) - \eta_n) Q(\eta(z) - \eta_n) e^{-j\psi(z)} e^{j\sigma z} dz \right\} d\varphi \quad (7)$$

where N_r is the set of indexes of all considered NF turns, $\tilde{V}^{1,2}(\eta_n, \varphi)$ are the reduced voltages samples at the intersection points between the generatrix at φ and the scanning helix, and $Q = \Omega_N$, if $|\eta(z) - \eta_n| \leq q\Delta\eta$, or $Q = 0$, otherwise. Let us first consider the integration over z . For any fixed φ , it results

$$G_{n\sigma}(\varphi) = \int_{z_i}^{z_f} D_{N^n}(\eta(z) - \eta_n) \Omega_N(\eta(z) - \eta_n) e^{-j\psi(z)} e^{j\sigma z} dz \quad (8)$$

where $z_i = z(\eta_n + q\Delta\eta)$ and $z_f = z(\eta_n - q\Delta\eta)$. Thus relation (7) can be rewritten as

$$I_V^{1,2}(\sigma) = \sum_{n \in N_r} \int_0^{2\pi} \tilde{V}^{1,2}(\eta_n, \varphi) G_{n\sigma}(\varphi) e^{-jv\varphi} d\varphi \quad (9)$$

This last involves an integration over φ that can be efficiently solved via the FFT, provided that the number of the voltage samples on each helix turn be always the same and equal to the smallest integer M_H , product of powers of 2, 3 and 5 equal or greater than $2[\text{Int}(\chi'\beta\rho_{\max}) + 1]$, $2\rho_{\max}$ being the AUT maximum transverse dimension. In such a way, the samples lying on the helix at $\varphi_m = m\Delta\varphi = 2\pi m/M_H$ with $m = 0, \dots, M_H - 1$ are all aligned. Accordingly, we get:

$$\int_0^{2\pi} \tilde{V}^{1,2}(\eta_n, \varphi) G_{n\sigma}(\varphi) e^{-jv\varphi} d\varphi = \frac{2\pi}{M_H} \sum_{m=0}^{M_H-1} \tilde{V}^{1,2}(\eta_{m,n}, \varphi_m) G_{n\sigma}(\varphi_m) e^{-j(2\pi mv/M_H)} \quad (10)$$

where $\eta_{m,n} = \eta_n(\varphi_m) = \eta(\phi_s) + k\varphi_m + n\Delta\eta$. The summation can be efficiently performed via a direct FFT algorithm.

It is worth noting that the $G_{n\sigma}(\varphi_m)$'s can be precalculated for given sets of antennas, since they depend only on the measurement cylinder radius and on the AUT modelling. Moreover, it is convenient to use this method to evaluate only the FF samples needed to reconstruct the antenna pattern via the far-field OSI expansion in [7]. It is so possible to evaluate the antenna far field in any cut plane directly from the helicoidal NF data without interpolating them.

IV. NUMERICAL TESTS

The following simulation refers to a uniform planar array of $\lambda/2$ spaced elementary Huygens sources, polarized along the z axis and covering a zone in

the plane $y = 0$, formed by a rectangle ended in two half-circles (λ being the wavelength). The rectangle sizes are: $2a' = 14\lambda$ and $h' = 46\lambda$. An open-ended WR-90 rectangular waveguide, at the frequency of 10 GHz, is chosen as probe. The helix wraps a cylinder with radius $d = 14\lambda$ and height $h = 160\lambda$. Figures 2 and 3 show the FF pattern reconstruction in the principal planes obtained by using the proposed direct helicoidal NF-FF transformation. As can be seen, the exact and recovered fields are practically indistinguishable, thus assessing the effectiveness of the technique.

Note that the number of used samples is 20 213, significantly less than that (34 668) needed by the classical cylindrical scanning and the helicoidal NF-FF transformation technique [8].

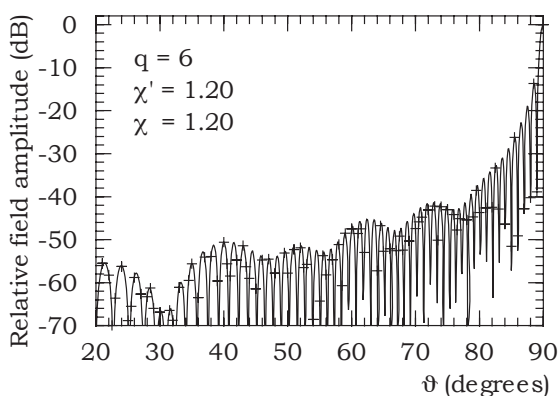


FIG. 2 – E-plane pattern. Solid line: exact. Crosses: recovered via the direct helicoidal NF-FF transformation.

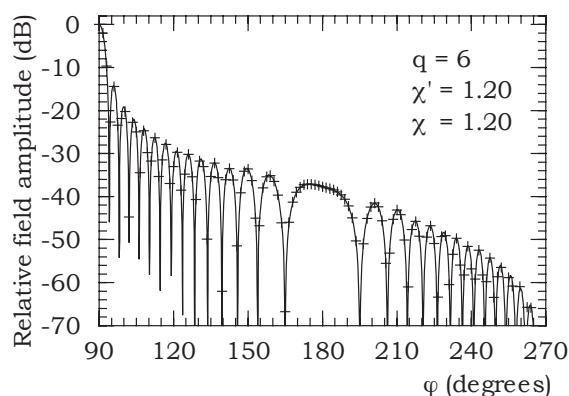


FIG. 3 – H-plane pattern. Solid line: exact. Crosses: recovered via the direct helicoidal NF-FF transformation.

REFERENCES

- [1] O.M. Bucci, C. Gennarelli, G. Riccio, and C. Savarese, “Nonredundant NF-FF transformation with helicoidal scanning,” *Journal of Electromagnetic Waves and Applications*, vol. 15, pp. 1507-1519, Nov. 2001.
- [2] F. D’Agostino, F. Ferrara, C. Gennarelli, R. Guerriero, and M. Migliozzi, “Near-field – far-field transformation technique with helicoidal scanning for elongated antennas,” *Progress in Electromagnetic Research B*, vol. 4, pp. 249-261, 2008.
- [3] F. D’Agostino, F. Ferrara, J.A. Fordham, C. Gennarelli, R. Guerriero, M. Migliozzi, G. Riccio, and C. Rizzo, “An effective NF-FF transformation technique for elongated antennas using a fast helicoidal scan,” *IEEE Antennas & Propagation Magazine*, vol. 51, pp. 134-141, Aug. 2009.
- [4] O.M. Bucci, C. Gennarelli, and C. Savarese, “Representation of electromagnetic fields over arbitrary surfaces by a finite and nonredundant number of samples,” *IEEE Transactions on Antennas and Propagation*, vol. 46, pp. 351-359, March 1998.
- [5] W.M. Leach Jr., and D.T. Paris, “Probe compensated NF measurements on a cylinder,” *IEEE Transactions on Antennas Propagation*, vol. AP-21, pp. 435-445, July 1973.
- [6] F. D’Agostino, F. Ferrara, C. Gennarelli, R. Guerriero, and M. Migliozzi, “An innovative direct NF-FF transformation technique with helicoidal scanning,” *International Journal of Antennas and Propagation*, vol. 2012, Article ID 912948, 9 pages, 2012.
- [7] O.M. Bucci, C. Gennarelli, G. Riccio, and C. Savarese, “NF-FF transformation with cylindrical scanning: an effective technique for elongated antennas,” *IEE Proceedings Microwaves, Antennas and Propagation*, vol.145, pp. 369-374, Oct. 1998.
- [8] S. Costanzo and G. Di Massa, “Far-field reconstruction from phaseless near-field data on a cylindrical helix,” *Journal of Electromagnetic Waves and Applications*, vol. 18, pp. 1057-1071, Aug. 2004.

A NEW COMPACT MONOLITHIC PATCH ANTENNA FOR DEDICATED SHORT RANGE COMMUNICATION SYSTEMS

O. Leonardi⁽¹⁾, M. Pavone⁽²⁾, G. Sorbello⁽¹⁾, T. Isernia⁽³⁾

⁽¹⁾ Dip. di Ingegneria Elettrica Elettronica e Informatica,
Catania University

Viale A. Doria 6, 95125 Catania, Italy

gino.sorbello@dieei.unict.it

ornella.leonardi@dieei.unict.it

⁽²⁾ ST Microelectronics Stradale Primo Sole 50 95125 Catania, Italy

mario.pavone@st.com

⁽³⁾ Dip. di Informatica, Matematica, Elettronica e Trasporti

Univ. Mediterranea di Reggio Calabria, 80100 Reggio Calabria, Italy

tommaso.isernia@unirc.it

Abstract

Dedicated Short Range Communications (DSRC) is a novel short- to medium-range wireless protocol designed for automotive use. The DSRC signals are circularly polarized and allocated in the 5.8 GHz band. This communication describes the development of a monolithic and compact microstrip antenna with left-hand circular polarization intended for the On-Board Unit (OBU) equipment of a DSRC system. The $0.773\lambda_0 \times 1.16\lambda_0$ fabricated prototype exhibits a circularly-polarized gain of about 5.52 dBi with an Cross Polarization Discrimination (XPD) greater than 10 dB.

Index Terms – *Left-Hand Circularly Polarized (LHCP), Dedicated Short Range Communication (DSRC), Microstrip Antenna.*

I. INTRODUCTION

Circularly polarized waves have many advantages for short-range communication. They can be used to reduce the interference due to reflections and allow a polarization match independent of the antennas angular orientation. For example, the electronic toll collection (telepass) is based on the wireless communication standard known as Dedicated Short-Range Communications (DSRC), which may employ circularly polarized antennas.

The standard [1] specifies the antenna requirements for the On-Board Unit (OBU) and for the Road-Side Unit (RSU) of a DSRC system. In this communication, we report on the development of a microstrip patch antenna suitable for integration on a circuit board. The antenna is realized in a monolithic configuration with a reduced total height and area. According to the standard [1] the antenna should have a 20 MHz bandwidth [5.795-5.815 GHz] and a unidirectional radiation pattern with a main lobe width of 70° in the vertical plane. For the OBU a reduced size and a low cost are mandatory furthermore a Cross

Polarization Discrimination (XPD) greater than 10 dB in boresight direction and greater than 6 dB within the -3 dB area are required for the OBU.

In literature there are several examples of circularly polarized antennas in the 5.8 GHz range that satisfying the conditions dictated by the standard, but these are often not monolithic structures [2] and therefore not suitable for series production. On the other hand, simpler configurations, require the use of antenna array to meet the characteristics required by the standard [3]. The small size patch antenna are less studied at 5.8 GHz [4], besides this often have suspended patch and ad hoc feeding networks with power divider and branch coupling lines [5] - [6]. A circularly-polarized miniaturized monolithic antenna compliant to the DSRC standard has not been proposed so far [7].

II. ANTENNA LAYOUT

The DSRC circularly polarized antenna is designed and realized on Arlon 450, a substrate with relative permittivity $\epsilon_r=4.5$ and $\tan\delta=0.0035$. The Arlon substrate has the same permittivity of the standard FR4, but exhibits a very stable behavior at 5.8 GHz and a better loss tangent.

The antenna proposed is a slot coupled patch antenna, which uses a two-layer configuration in which the layers are both Arlon 450 with different height, $h_1=0.015\lambda_0$ and $h_2=0.030\lambda_0$ respectively.

The use of two layers with the same permittivity allows to replace the second substrate region with two substrates of thickness h_1 . This involves a cost reduction in the case of mass production of the antenna.

The antenna has been designed with total size of $0.773\lambda_0 \times 0.773\lambda_0 \times 0.045\lambda_0$. The feeding microstrip line is realized on the $0.015\lambda_0$ thick layer to be with a 50Ω characteristic impedance, while the radiating patch on the $0.030\lambda_0$ one. The layout and antenna parameters are shown in Fig. 1.

TABLE II – ANTENNA PARAMETERS

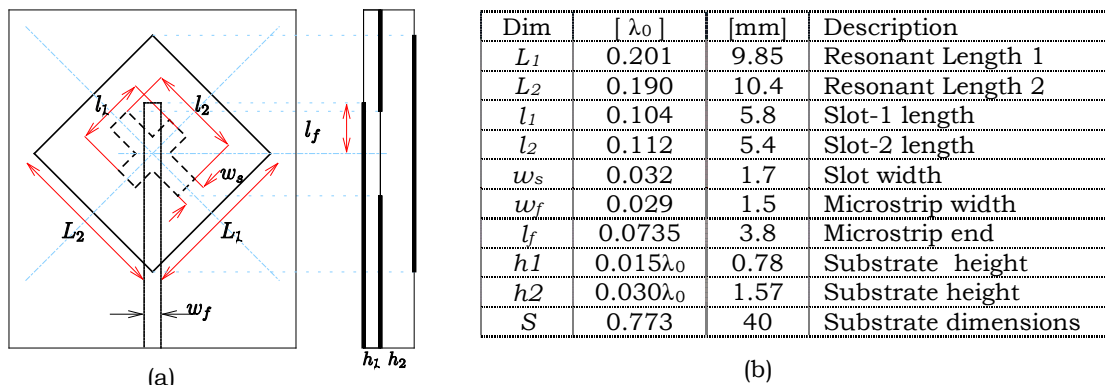


FIG. 1 – (a) Antenna layout: patch (continuous line), slot in the ground (dashed line), and feeding microstrip (dotted line). (b) Antenna parameters

The microstrip feed line and the slotted ground plane are etched on the opposite sides of the first substrate and the feeding structure (strip and slot) is assembled to be centered below to an almost square patch printed on the second substrate. The common ground plane has a cross slot with slightly unequal slot lengths inclined with respect to the microstrip feed line with an angle of 45° . For ease of fabrication and assembly, the ground plane has been replicated on the $0.030\lambda_0$ thick substrate, but the two grounds form electrically a single metal layer.

III. OPTIMIZATION AND EXPERIMENTAL RESULTS

The antenna has been optimized by means of numerical simulation [8] with the target to achieve circular polarization at 5.8 GHz. The CP is obtained exciting two orthogonal modes with equal magnitudes and in phase quadrature. Different patch lengths, L_1 and L_2 , and slot lengths, l_1 and l_2 , are used to balance the mode amplitudes as well as to control their phase difference. The stub length l_f was adjusted to match the antenna.

For ease of connectorization it was decided to increase the $0.015\lambda_0$ thick substrate of 2 cm along the y axis achieving a layout with total size of $0.773\lambda_0 \times 1.160\lambda_0$ (4 x 6 cm). The measured and simulated $|S_{11}|$ and Input Impedance are shown in Fig. 2. The simulation results are in good agreement with the experimental characterizations.

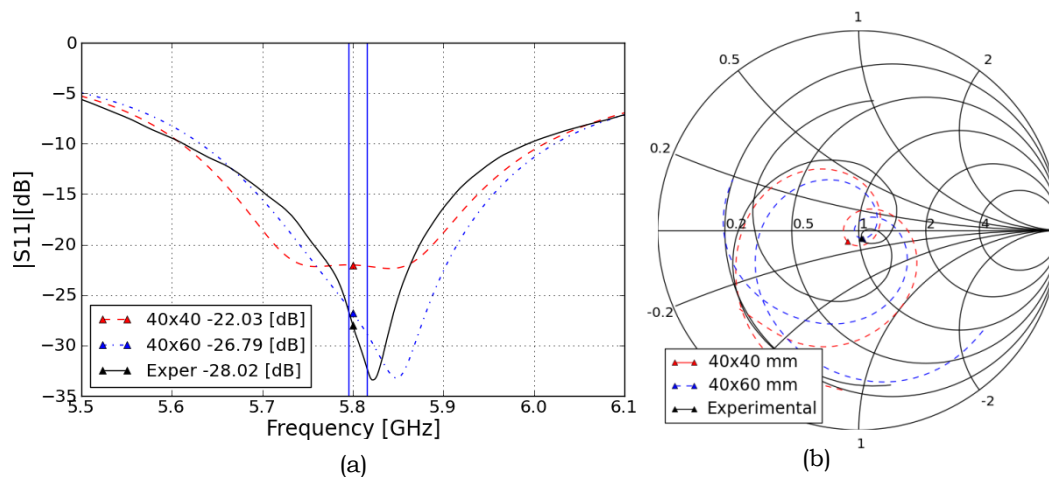


FIG. 2 – (a) $|S_{11}|$: Experimental (continuous line) and simulations result (dashed line). Vertical lines show the DSRC band. (b) Input impedance on a Smith Chart.

The gain measurement confirms the simulation and a good XPD below 10 dB in boresight direction is achieved. The measured gain patterns, with the test antenna rotated at 0° , 45° and 90° degree, are reported in Fig. 3.

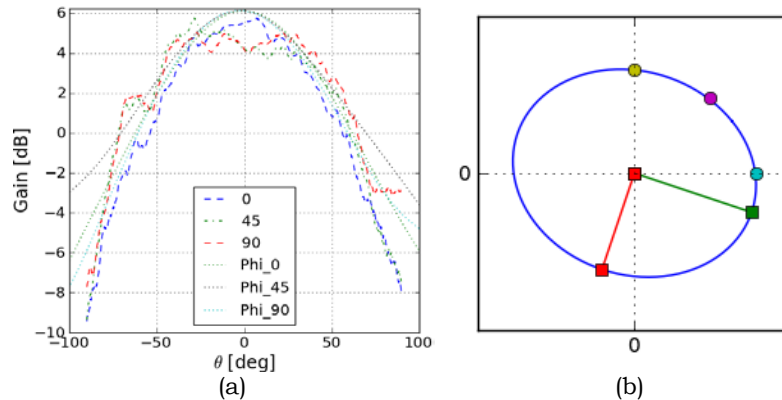


FIG. 3 – (a) Measured (dashed line) and simulated (dotted line) gain pattern for three different cut angles 0° , 45° and 90° . (b) Polarization ellipse for the electric field in the boresight direction (on the patch antenna axis).

IV. CONCLUSIONS

In this paper a compact monolithic DSRC patch antenna has been studied and optimized by simulations. The experimental characterization confirms a gain of 5.52 dBi. The circularly polarized antenna exhibits a good XPD compatible with the DSRC standards.

ACKNOWLEDGEMENT

The authors wish to thank Eng. Tindaro Cadili from Selex-ELSAG for the use of the anechoic chamber facility.

REFERENCES

- [1] European Standard EN 12253, Comité Européen de Normalisation (CEN), Jul., 2004 and ETSI ES 200 674-1 V2.2.1 (2011-02) Dedicated Short Range Communications (DSRC).
- [2] Megnet D., Mathis H. , "Circular polarized patch antenna for 5.8 GHz dedicated short-range communication" Microwave Conference, 2009. EuMC 2009. European , vol., no., pp.638-641, Sept. 29 2009-Oct. 1 2009.
- [3] Tiago Varum, João Matos, Pedro Pinho, Ricardo Abreu, Arnaldo Oliveira, Jorge Lopes , "Microstrip antenna array for multiband dedicated short range communication systems" Microwave and Optical Technology Letters, Volume 53, Issue 12, pages 2794–2796, December 2011.
- [4] Iwasaki, H. "A circularly polarized small-size microstrip antenna with a cross slot", IEEE Trans. on Ant. and Propagation vol.44, pp.1399-1401, 1996.
- [5] T. Vlasits, E. Korolkiewicz, A. Sambell, B. Robinson, "Performance of a cross-aperture coupled single feed circularly polarised patch antenna", Electronics Letters, vol.32, pp.612-613, March 1996.
- [6] Y. Xia and JL, "RHCP Patch Antenna for Automotive DSRC System", Wireless Communications Networking and Mobile Computing (WiCOM), 2010 6th International Conference on (2010).
- [7] Tiago Varum, João Nuno Matos, Pedro Pinho, "Printed antenna for On-Board Unit of a DSRC System", Antenna and Propagation. (APSURSI), 2011 IEEE International Symposium on.
- [8] Computer Simulation Technology, Germany.

UWB MULTIFUNCTIONAL ARRAYS BASED ON VERSATILE PRINTED RHOMBIC ANTENNA CONFIGURATIONS

A. Galli⁽¹⁾, S. Mazzocchi⁽¹⁾, G. Valerio⁽²⁾, M. Ciattaglia⁽³⁾, M. Zucca⁽³⁾

⁽¹⁾ Department of Information Engineering, Electronics
and Telecommunications – “Sapienza” University of Rome
Via Eudossiana 18, 00184 Rome, Italy
galli@diet.uniroma1.it , mazzocchi@diet.uniroma1.it

⁽²⁾ I.E.T.R., Institut d’Electronique et de Télécommunications
de Rennes – University of Rennes 1
Campus Beaulieu, Av. Générale Leclerc, 35000 Rennes, France
guido.valerio@univ-rennes1.fr

⁽³⁾ Sistemi Radianti – SELEX Sistemi Integrati S.p.A.
Via Tiburtina 1231, 00131 Rome, Italy
mciattaglia@selex-si.com , mzucca@selex-si.com

Abstract

Based on recently-proposed Ultra-Wide-Band planar antenna configurations having strips in suitable rhombic shapes, innovative configurations of printed arrays are presented and tested for typical multifunctional applications (radar, communications, sensing) ranging from C to K bands. By means of advanced parametric analyses, the radiative features are analyzed to design single structures and then arrays with small and large number of elements. Attention is paid to low-cost, compact and light-weight solutions, also accounting for realization issues. Stimulating performances are observed in terms of matching and radiation patterns, as a function of frequency and of phase shift.

Index Terms – Multifunction radar arrays, Planar printed antennas, Ultra-wide-band applications.

I. INTRODUCTION

Among the various applications of Ultra-Wide-Band (UWB) systems, noteworthy attention has recently been devoted to multifunction arrays, capable to perform several tasks in the same radiating structure (involving, e.g., radar surveillance, communication links, remote sensing, etc.). In some cases, thousands of radiating elements could be required, so that new versatile and low-cost antenna solutions are envisioned [1],[2]. Printed technology usually enables for a number of desirable advantages, such as manufacturing simplicity and economy, compactness, flatness, conformability, etc.

For typical applications ranging from C to K bands, very low-cost, simple and flexible configurations of printed UWB elements have recently been proposed, based on printed strips suitably arranged in rhombic shapes [3]. On this ground, the design and the performance of new variously-sized planar array configurations are investigated here.

II. PRINTED RHOMBIC-SHAPED ELEMENTS

New simple and low-cost UWB printed antenna configurations have recently been proposed and tested by the authors [3], based on sets of printed dipoles with different lengths, forming approximately rhombic shapes. The central patch is the longest and can suitably be fed at its ends with coaxial probes, whilst the side patches have smaller dimensions and are parasitic. In the configuration of Fig. 1, two orthogonal structures are placed on different substrates of a three-layer grounded structure, able to accomplish compact dual polarization.

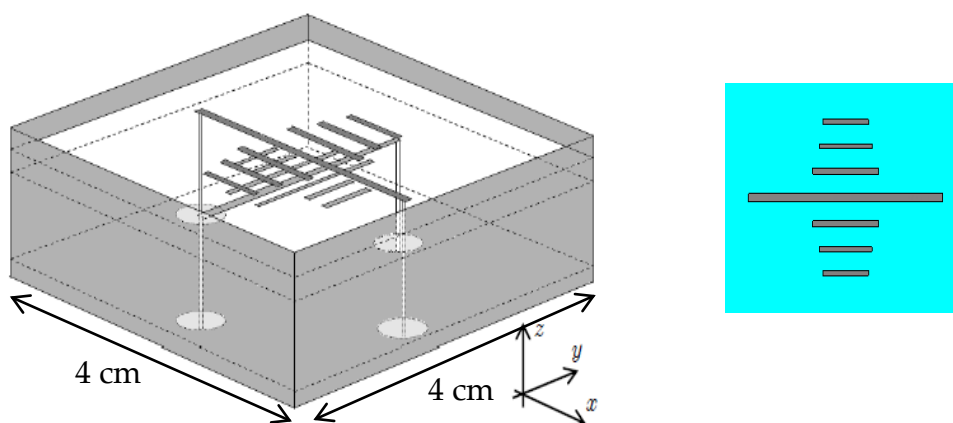


FIG. 1 – 3D view (left) and top view (right) of the basic topology of the antenna printed element for the UWB arrays, based on a rhombic alignment: two rotated sets of strips (the central ones are properly fed through probes) placed on two levels of a three-layered structure to provide dual pol.

The antenna operational performances in terms of return loss, efficiency and radiation patterns are strongly affected by the choices of the various geometrical and physical parameters involved (dimensions and locations of the various strips, layers' parameters, etc.). Moreover, with fine-tuning of the pair of probes on the opposite sides of each main strip and proper selection of the phase shift between the feeders, it is possible to achieve a direct control of the current configuration excited on the lines, thus suitably influencing the directional features of the radiated beam.

A solution for the single radiating dual-pol element, aimed at operating in the 5-25 GHz range, has been analyzed and designed numerically, using mainly “CST Microwave Studio” in conjunction with specific optimization tools. An outcome that shows the wide-band behavior of the return loss in the desired frequency range is presented in Fig. 2(a). An example of the radiation patterns with gain features for different frequencies is given in Fig. 2(b). A lateral shielding of the single radiating elements can be implemented through metallic side walls, thus enabling a reduction of adverse effects related both to possible launching of surface and leaky waves in the layered structure and to mutual element coupling in the array environment.

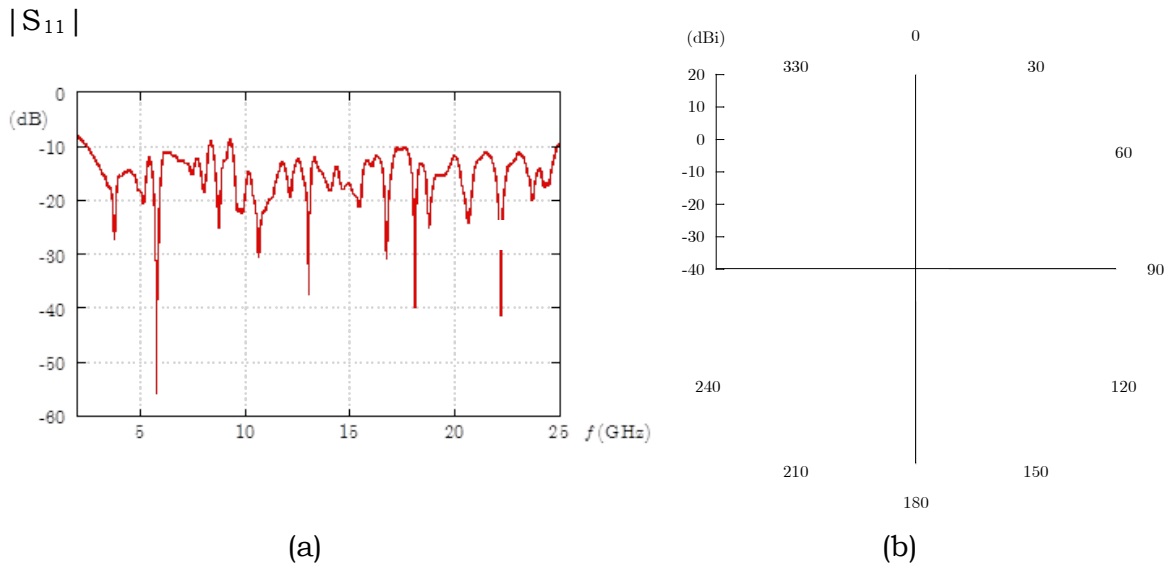


FIG. 2 – Behaviors of the rhombic-shaped printed antenna of Fig. 1. Ports 1 and 2 feed the upper element; ports 3 and 4 feed the lower element. (a) Return loss $|S_{11}|$ (dB) vs. frequency f (GHz); (b) Directional gain in polar form vs. θ on the principal elevation plane $\phi = 0^\circ$ at different frequencies in the operational bandwidth 5-25 GHz, with the ports 1 and 2 exciting an E -field along the θ direction: 5 GHz (blue line), 10 GHz (green), 20 GHz (red).

In the design process, attention has been paid to the use of simple commercially-available dielectric substrates in order to strongly reduce the costs of large array implementation through well-established manufacturing techniques for printed circuits (PCB).

III. ARRAY PERFORMANCES

Based on the element topology previously optimized and on the relevant radiation features achieved, different analyses have been led to obtain information on the scanning-beam features of variously-sized arrays. To this aim, the radiation pattern of an array of 140x140 elements has been computed first with an array-factor approximation, for diverse values of the pointing angle of the main beam, depending on the selected phase shift between adjacent elements of the array. The gain at the main lobe direction is fairly regular (around 50 dBi), and the side-lobe levels are rather reduced (about 20 dB below the main lobe). The same quantities have been computed for different pointing elevation angles of the main beam. Effects related to grating lobes can be present in connection of the element spacing as phase shift and frequency are varied in a quite wide range.

In order to properly evaluate the element coupling effects in an array environment without approximations, the performances of both 1D and 2D arrays made of a smaller number of elements have been analyzed by means of a full-wave CAD implementation of the overall structure.

Demonstrative features of a linear array of 3 adjacent cells are reported in Fig. 3. In Fig. 3(a), the radiation patterns on the two principal planes are shown when the three upper or the lower sets of patches are fed in phase. The patterns are quite regular and a fan beam is obtained, as typical of these linear arrays. The relevant coupling amount among cells has also been analyzed: in Fig. 3(b), the magnitude of the active reflection coefficients, as a function of the frequency for all in-phase elements, shows that a good input matching is achieved in this array configuration as well. The matching and scanning capabilities of this array have then been evaluated in terms of the frequency and of the phase shift for pointing angles on the elevation plan until about 45° .

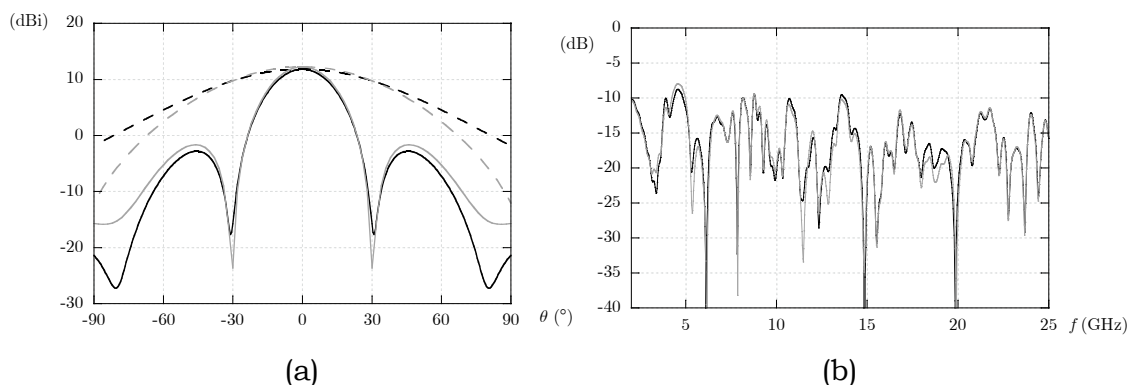


FIG. 3 – Linear array of 3 adjacent elements as in Fig. 1: directive gain in polar form on the principal elevation planes $\phi = 0^\circ$ (solid lines) and $\phi = 90^\circ$ (dashed lines) at 5 GHz: beam pointing at broadside for in-phase fed upper elements (black lines) and lower elements (gray lines). (b) Magnitude of the active reflection coefficient (dB) vs. frequency f at the middle cell of the array (black line) and at one side cell (gray line), with the three lower elements fed in phase.

IV. CONCLUSION

Original types of UWB planar arrays based on rhombic-shaped printed dipoles have been investigated for radar, communication and dual-pol sensing applications. In the design process, practical implementation aspects have been considered, such as the choice of low-cost dielectric layers commonly used in PCB technology and the most appropriate feeding. The proposed topology is characterized by quite inexpensive reproducibility, compactness, high modularity and scalability.

REFERENCES

- [1] J. J. Lee, "Ultra wideband arrays," in *Antenna Engineering Handbook*, J. L. Volakis, Ed. McGraw-Hill, 2007.
- [2] W. Wiesbeck, G. Adamiuk, and C. Sturm, "Principles of UWB antennas basic properties and design," *Proc. IEEE*, vol. 97, no. 2, Feb. 2009.
- [3] S. Mazzocchi, G. Valerio, M. Zucca, M. Ciattaglia, A. De Luca, and A. Galli, "A new multifunctional UWB planar antenna based on printed dipoles in rhombic configuration," *Proc. EuCAP*, Apr.11-15, 2010, Barcelona, Spain, 3pp.

SENSING-ORIENTED DESIGN METHODOLOGY FOR PASSIVE RFID ANTENNAS

C.Occhiuzzi⁽¹⁾, G. Marrocco⁽²⁾

DISP: Dipartimento di Informatica, Sistemi e Produzione,
“Tor Vergata” University, Via del Politecnico 1, 00133 Rome
⁽¹⁾occhiuzzi@disp.uniroma2.it ⁽²⁾marrocco@disp.uniroma2.it

Abstract

RFID passive tags are nowadays starting to be considered more than simple labeling devices: by properly analyzing the two-ways communication link it is possible to collect information about the state of a tagged object, without any specific embedded sensor or local power supply. A design methodology is here proposed to simultaneously account for the opposite requirements of sensing and communication. The method is based on a proper representation of the antenna response to varying boundary conditions over an impedance chart that permits to identify the theoretical limit of the design and to fully shape the response of the tag.

Index Terms – RFID Sensor, optimization, design chart

I. INTRODUCTION

The possibility to use passive tags as sensing devices of objects, people and environment is nowadays one of the most interesting and challenging application of passive UHF Radio Frequency Identification (RFID) technology. Many different employments have been already envisaged and experimented that demonstrated the feasibility of the idea but, at the same time, the limitation of the actual design methodologies [1]. The rationale of the *tag-as-sensor* is based on the fact that, since the tag's input impedance and gain depend on the surrounding environment, any of its physical or chemical variation could affect the tag's performance and be remotely detected by the reader. The generality of this basic principle potentially allows any passive tag to be used as a sensor of “effective” permittivity changes with respect to reference condition. However, this class of devices should be able to properly track the evolution of the phenomena under observation, being for example monotonic, single valued and sensitive enough at least in the most critical ranges. Communication and sensing features demand for opposite requirements, since the sensitivity of the tag-as-sensor to the variation of the process under observation is usually paid in terms of a worsening of the power scavenging capabilities and hence of the read distance.

Since there is no decoupling from the operative and structural point of view between antenna and sensor, the traditional design procedures have to be revisited or even rethought in order to handle, at the same time, both sensing and communication needs. In this paper the

optimization problem is formalized in terms of the shaping of the tag's response to the change of the observed process by means of convenient matching charts that permit to understand the physical limitation of the sensing capability and to set up a proper global design. The feasibility of the method is evaluated by an example concerning the sensing of objects with time-varying permittivity.

II. METHOD

RFID platforms exploit a two-way communication link: a direct one, wherein the key-issue is the scavenging of power at the chip's port so that the tag may activate and perform actions, and a reverse link wherein the tag transmits its data to the reader by changing its reflectivity through impedance modulation. Generally, the direct link imposes the bottleneck of the whole tag-reader communication and it limits the maximum read range. The parameter that represents the tag's scavenging features is the realized gain $G_{\tau} = G\tau$, e.g the gain of the tag's antenna scaled by the mismatch to the RFID IC. A trade-off solution to the sensing-communication problem is to observe the state of the object $\Psi(t)$ (chemical/physical process in evolution) through a measurable quantity whose variation is not necessarily associated to a worsening of the communication performance. Such an indicator should be optimally a parameter of the reverse-link such as the backscattered power which is however orientation- and position-dependent. If some degradation can be accepted, the Analog IDentifier (AID) [1] is also a convenient metrics since combines both the direct and the reverse links to provide a sensing information independently on the reader-tag position and orientation as well as on the interaction with the surrounding environment.

Due to the small size of the UHF tag's antenna, there are very few degrees of freedom in shaping the gain: the direct and reverse links could be therefore analyzed in term of the only input impedance by considering the power transmission coefficient $\tau(\Psi)$ and the AID(Ψ). These parameters are usefully expressed [2] in terms of normalized input impedance $r_a = R_A/R_{IC}$, $x_a = X_A/X_{IC}$, with $Z_{IC} = R_{IC} + jX_{IC}$ the RFID chip's impedance and $Q = |X_{IC}|/R_{IC}$ the chip quality factor:

$$\tau[\Psi] = \frac{4r_a}{|1+r_a+jQ(1+x_a)|^2} \quad (1) \quad AID[\Psi] = \sqrt{\frac{\tau}{r_a}} = \frac{2}{|1+r_a+jQ(1+x_a)|} \quad (2)$$

A chart of $\{AID, \tau\}$ isolines can be produced so that the communication and the sensing characteristics of the tag are expressed over a same plane (Fig.1). The point (1,-1) corresponds to the perfect matching condition between antenna and IC, for which $AID = \tau = 0dB$. The eccentricity of the ellipses depends on the quality factor Q of the microchip. The AID- τ diagram can be considered as a kind of *Sensing Smith Chart*, in which the role of the frequency is replaced by the

process realization. Each process in evolution from an initial to a final state, involving a modification of input impedance, can be hence traced over such a plane by a sequence of couplets $[r_a(\Psi_\square), x_a(\Psi_\square)]$ describing an oriented curve $\vec{Z}(\Psi) = r_a(\Psi)\hat{i} + x_a(\Psi)\hat{j} \in \mathbb{R}^2$.

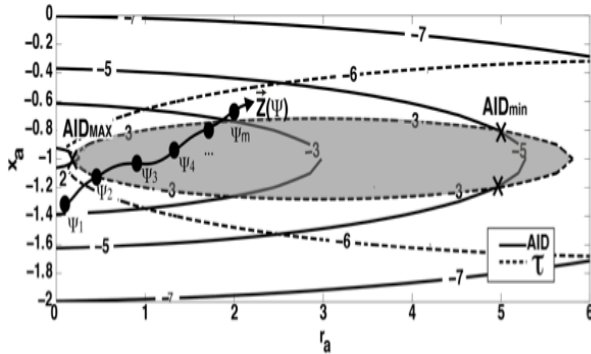


Figure 1 : Iso-line of constant AID and τ on normalized antenna impedance plane.

Moreover, the same condition will fix the maximum variation of AID, in the specific: $5\text{dB} < \text{AID}[\Psi] < 2\text{dB}$ as observed by the intersections between the isocurves. In general, the path $\vec{Z}(r_a, x_a)$ can totally, partially or even not belong to such an area: only the process dynamics inside the shadowed ellipse will be observed by the radio sensor. The slope of the curve $\vec{Z}[\Psi]$ with respect to the r_a -axis will affect the sensitivity of the tag's response to the process' evolution.

The design procedures has to confine $\vec{Z}(r_a, x_a)$ inside the $\tau[\Psi] > \tau_{\min}$ region. Once defined an ideal response curve $\vec{Z}_0[\Psi]$, fully compliant with the specific requirements, the geometrical parameters $\{p_1, p_2, \dots, p_n\}$ of the tag can be optimized by minimizing the following error function by means of any kind of optimization methods, e.g. Genetic Algorithms,

$$\sum_n \left\| \vec{Z}(\Psi_n)[p_1, p_2, \dots, p_N] - \vec{Z}_0(\Psi_n) \right\|_2 \rightarrow 0 \quad (3)$$

III. NUMERICAL EXAMPLE

The method is demonstrated over a simple tag for the wireless monitoring of the filling level of a perspex box containing sugar (Fig.2) [1]. The first guess for the tag-as-sensor is a simple half-wave dipole @870MHz. The considered RFID IC has impedance $Z_{IC} = 17 - j190\Omega$ and the corresponding $\{\text{AID}, \tau\}$ chart is shown in Fig.2 (left). The communication performances are preserved by enforcing the constrain $\tau_{\min} = -1\text{dB}$ (less than 10% reduction in the read range). Accordingly, the maximum variation of the AID could be at most $\Delta\text{AID} = 1 - (-2\text{dB}) = 3\text{dB}$. The simulated impedance response of the tag $\vec{Z}_A[\Psi]$ lies outside the useful area, it exhibits a non monotonic profile and hence it is not suited to sensing and neither to communication; an impedance T-match

To preserve a stable read-range of the tag during the whole evolution of the process, it is required that $\tau[\Psi] > \tau_{\min}$. For instance the choice $\tau_{\min} = 3\text{dB}$ will permit not to degrade the read range below the 30% of its maximum value corresponding for example to the initial (or final) state of the process. Above constraint enforces the vector $\vec{Z}(r_a, x_a)$ to belong to the shadowed elliptical

adapter is thus added to reshape the curve (Fig.2 left). The form factor $\{a, b\}$ of the T-match is optimized with the aim to move the tag's response (now denoted as $\bar{Z}_B[\Psi]$) inside the shadowed region $\tau > 1\text{dB}$ and to achieve a monotonic profile.

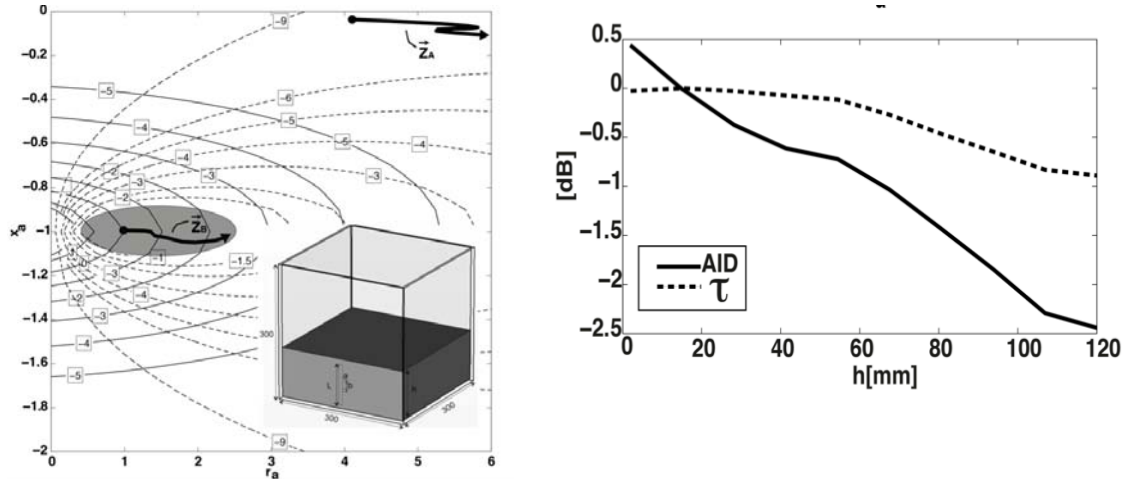


Figure 2: Left) $\{AID, \tau\}$ chart. In grey the area corresponding to $\tau_{\min}=-1\text{dB}$. Right) AID and τ profiles versus the filling level $h[\text{mm}]$.

Fig.2 (right) shows the corresponding AID and τ profile versus the sugar's height for the optimized tag with $a=13\text{mm}$, $b=20\text{mm}$. As expected, the power transfer coefficient is nearly unchanged during the process evolution, while the AID undergoes variation of about 3dB. This means that the reader will be able to monitor the level of the sugar with 0.3dB/cm sensitivity of the AID and with negligible variation of the read range.

IV. CONCLUSION

The design of RFID radio sensors can be optimized by jointly considering communication and sensing features. The optimization can be guided by using innovative nomograms able to represent the key parameters of the direct and the reverse link. The proposed methodology can be also applied to the backscattered power and similar sensing-communication charts can be produced. Other application examples will be discussed during the Conference.

REFERENCES

- [1] Marrocco, G., "Pervasive electromagnetics: sensing paradigms by passive RFID technology", *Wireless Communications, IEEE*, vol.17, no.6, pp.10-17, December 2010
- [2] K. V. S. Rao, P. V. Nikitin, S. F. Lam, "Impedance Matching Concepts in RFID Transponder Design", *Proceeding of Fourth IEEE Workshop on Automatic Identification Advanced Technologies*, pp.39-42, 2005
- [3] C. Occhiuzzi, G. Marrocco, "Sensing the human body by implanted RFID tags," *Proceedings of the Fourth European Conference on Antennas and Propagation (EuCAP)*, pp.1-5, 12-16 April 2010

A NEW LOCALIZATION METHOD FOR UHF-RFID SMART SHELVES

A. D'Alessandro⁽¹⁾, A. Buffi⁽¹⁾, P. Nepa⁽¹⁾ and G. Isola⁽²⁾

⁽¹⁾ Department of Information Engineering, University of Pisa
Via G. Caruso 16, 56122, Pisa, Italy
[a.dalessandro](mailto:a.dalessandro@iet.unipi.it), [a.buffi](mailto:a.buffi@iet.unipi.it), [p.nepa](mailto:p.nepa@iet.unipi.it)@iet.unipi.it

⁽²⁾ CAEN RFID s.r.l.
Via Vetraia 11, 55049, Viareggio (LU), Italy
g.isola@caen.it

Abstract

A new localization method for UHF-RFID smart shelves is presented, with reference to a pharmacy drawer for drug storage. Exploiting RSSI (Received Signal Strength Indicator) information during drawer opening and closing movements, tagged item location is estimated. During drawer movements, the relative position of tag and reader antenna changes, allowing for uncorrelated RSSI measurements. Measurements in a real scenario are carried out with commercial tags and reader antennas. Location performance is presented in terms of the probability of making a correct decision, when the drawer is subdivided into two regions.

Index Terms—Smart shelves, UHF RFID, localization.

I. INTRODUCTION

RFID technology has been recently employed in retail and pharmaceutical industries to get automatic real-time inventory, tracking of misplaced items and unattended billing at cashiers [1]. It can be used in many applications such as Item Level Tagging (ILT) with smart shelves, proximity point readers or conveyor belts. In addition to classical solutions with HF-RFID systems that exploits the near-field inductive coupling, UHF-RFID systems have been developed. Thanks to the EPC-Global Class1 Gen2 standard, UHF-RFID systems allow for easy-fabrication, low-cost, scalability and simultaneous multiple-tag detection. In addition to UHF-RFID systems employing reader and tag antennas operating in the far-field region, Near-Field (NF) UHF-RFID systems have been also designed [2]. In this paper, a localization method for UHF-RFID smart shelves is presented with reference to applications such as pharmacy drawers or hospital drug cabinets [3]. Starting from measurements in a drawer with drug boxes, a location algorithm has been developed, and it is described in Section II. The main idea is to exploit RSSI (Received Signal Strength Indicator) measurements during the drawer opening and closing operations, to locate tagged items through a linear classification algorithm. Localization capability in terms of percentage of correct decision probability is shown in Section III.

II. THE LOCALIZATION METHOD

The new localization method for RFID smart drawers is illustrated with reference to a measurement campaign in a real scenario. A 86x44 cm²

wood drawer has been filled with 42 empty drug boxes of different size (Fig. 1). Each box has been tagged with an UPM Raflatac Rafsec G2 tag [4]. The employed reader is the CAEN RFID R4300P ION model [5]. The reader input power has been set to 500mW and it is able to detect up to 100 tag/sec. The reader antenna (WANTENNAX007 CAEN RFID [5]) is a linearly polarized antenna, with a gain of 8dBi. Tagged boxes inside the drawer have been subdivided into two regions (named as region A and region B in Fig. 1) and RSSI measurements have been carried out for different positions of the reader antenna along the drawer sides (a polarization matching condition between reader and tag antennas has been considered). A 3D scatter-plot of measured RSSI values is shown in Fig. 2. For a given tagged box, each point corresponds to three RSSI measured values (each one corresponding to a different position of the reader antenna with respect to the drawer).

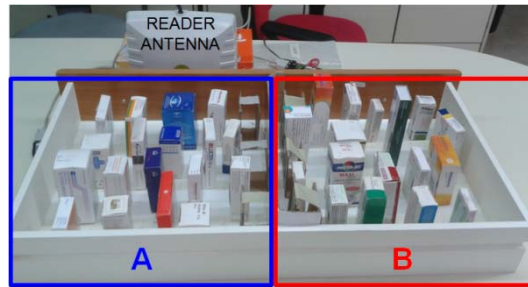


FIG. 1 – A 86x44 cm² drawer with 42 tagged empty drug boxes and a linearly polarized reader antenna.

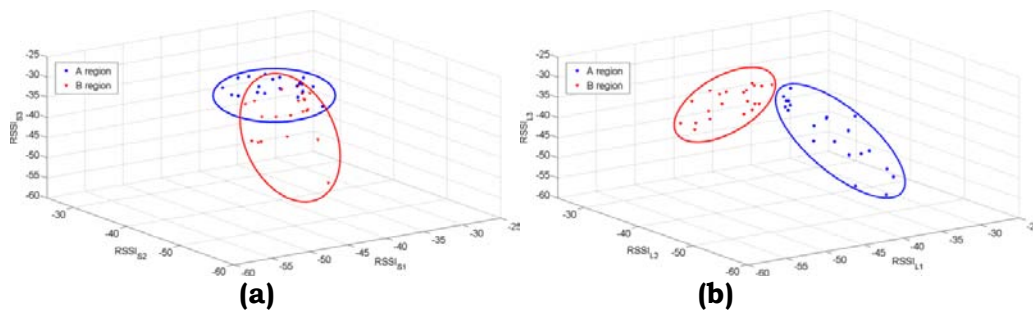


FIG. 2 – Scatter-plot of measured RSSI values for three different reader antenna position during its movement along **(a)** the drawer short side and **(b)** the drawer long side.

In particular, Fig. 2a represents measured RSSI values for three different antenna positions during its movement along the drawer shorter side; the point clouds related to tags in region A (blue circle) and region B (red circle) are partly overlapped, so indicating that it is not possible to distinguish among tagged boxes located in region A and those located in region B. On the other hand, if the antenna moves parallel to the longer side of the drawer (Fig. 2b), the point clouds are clearly separated, and this shows that localization of tagged items is possible.

III. ALGORITHM DESCRIPTION

The proposed classification method exploits a conventional algorithm with linear discriminating analysis (LDA), which uses six reference tags. Two different arrangements for the reference tags have been considered: tags aligned along the longer size, in the middle of the drawer (Fig. 3a); tags aligned at the boundary between regions A and B (Fig. 3b).

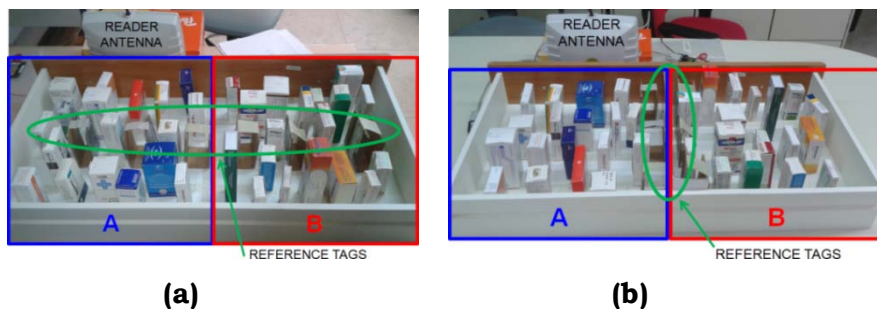


FIG. 3 – Drawer scenario with 42 tagged empty drug boxes: **(a)** reference tags aligned along the longer size of the drawer, in the middle, and **(b)** reference tags aligned at the boundary between the two regions.

For each tagged box, a number of RSSI samples are collected during the drawer movement (drawer shift with respect to the reader antenna). Then, such RSSI samples have been averaged on a proper number of time sub-intervals, in such a way to get the same number of decision variables at the classifier for all tagged items. For a scenario as that in Fig. 3, with reference tags aligned along the longer size in the middle of the drawer (Fig. 3a), the decision probability matrix $\underline{P} = \{p_{ij}\}$ is shown in Fig. 4a. Each column represents the number of tags actually belonging to i -region and classified as belonging to the j -region (normalized with respect to the number of tags belonging to the i -region). So, the diagonal terms represent the correct classifications, while the others are associated to misclassified tags. If three mean RSSI values are employed at the classifier (and for a uniform tag distribution in the two regions), the total correct decision probability is around $P_C=78\%$ for the above test case. For the configuration with reference tags aligned along the boundary between the two regions (Fig. 3b), the decision probability matrix is represented in Fig. 4b and the total correct decision probability is around $P_C=94\%$. To test the reliability of the above performance, different random distributions of tagged items inside the drawer have been considered. The mean correct decision probability \overline{P}_C has been recalculated as soon as a new scenario has been tested. A number of eighteen test cases has been considered, allowing for a convergence of the \overline{P}_C value. After initial fluctuations, the \overline{P}_C assumes a limit value of around 77% for the configuration with reference tags aligned along the longer size of the drawer, and a limit value of around 95% when the reference tags are aligned at the boundary between the two regions.

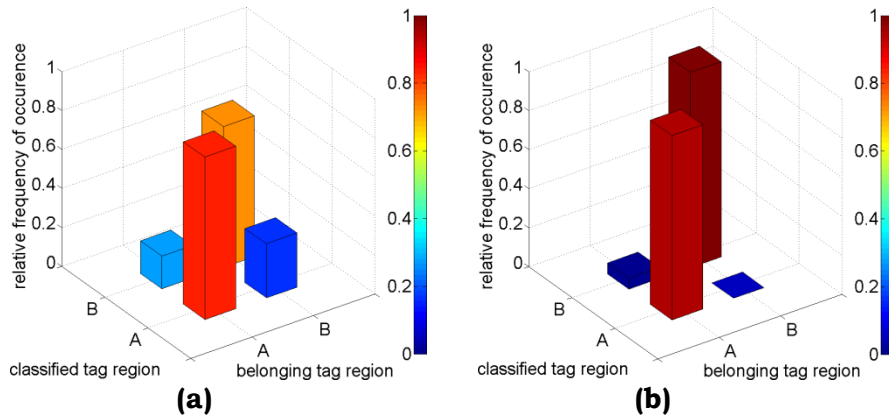


FIG. 4 – Correct decision probability related to the drawer scenarios in Fig. 3:
(a) reference tags aligned along the longer size of the drawer, in the middle and
(b) reference tags aligned at the boundary between the two regions.

IV. CONCLUSIONS

A new localization method for UHF-RFID smart shelves has been presented. By exploiting the collection of RSSI samples during drawer opening and closing movements, tagged item location can be identified. The proposed method represents a valuable alternative to localization approaches that use a set of reader antennas distributed along the drawer sides, as it reduces cost and complexity of the whole RFID smart shelf. System performance has been shown in terms of correct decision probability of tagged item position, with reference to a scenario with two classification regions. Work is in progress to test the proposed method for a random orientation between tags and reader antenna (polarization mismatching). Guidelines for choosing the proper number of classification regions and reference tags will be also provided.

ACKNOWLEDGEMENT

The author would like to thank CAEN RFID for the technical support and for providing the devices used during the measurement campaign.

REFERENCES

- [1] C. R. Medeiros, J. R. Costa, and C. A. Fernandes, “RFID Reader Antennas for Tag Detection in Self-Confined Volumes at UHF”, *IEEE Antennas and Propagation Magazine*, Vol. 53, No. 2, pp. 39-50, April 2011.
- [2] F. Fuschini, C. Piersanti, L. Sydanheimo, L. Ukkonen, and G. Falciasecca, “Electromagnetic Analyses of Near Field UHF RFID Systems”, *IEEE Transactions on Antennas and Propagation*, Vol. 58, No. 5, pp. 1759-1769, May 2010.
- [3] <http://www.mepsrealtime.com>.
- [4] http://www.tags.co.kr/UHF/STM/3001107_SD2.pdf.
- [5] <http://www.caenrfid.it/rfid>.

EQUIVALENT IMPEDANCE RETRIEVAL OF PLANAR SURFACES BY OPEN RESONATOR TECHNIQUE

S. Costanzo, G. Di Massa, O. H. Moreno

DEIS – University of Calabria
Via P. Bucci, 87036 Rende (CS), Italy
costanzo@deis.unical.it

Abstract

The use of an open resonator system with an optimized coupling transition to the feeding waveguide is proposed in this work to accurately characterize the equivalent impedance of planar surfaces from return loss measurements. A modeling circuit derived from a complete modal expansion is adopted to optimize the coupling as well as taking into account for the cavity losses. Two application contexts are considered as validation examples, namely the complex permittivity retrieval of thin substrates and the phase response characterization of microstrip reflectarrays. For both applications, successful K-band experimental results are presented.

Index Terms – Dielectric characterization, open resonator, reflectarray phase response characterization.

I. INTRODUCTION

The accurate modeling of dielectric and impedance features is an essential need for the efficient design of microstrip circuits and antennas. The increasing demand for miniaturization and high-frequency operation strongly imposes the accurate characterization of low-loss thin dielectric surfaces, both in the form of simple laminated substrates, as well as in more complex configurations of microstrip grids to be used for reflectarray/transmitarray structures. Open resonator methods give the most powerful tool to accurately retrieve the equivalent impedance properties of low-loss thin dielectric surfaces. In the standard resonator approach, approximate empirical formulas are adopted to obtain the surface impedance characterization from the knowledge of measured resonant parameters, such as the frequency shift and the cavity quality factor. Information from different sample thicknesses and/or positioning are generally adopted to increase the accuracy in the surface parameters extraction, which is performed in terms of a transcendental equation having multiple roots [1]. In this work, an equivalent circuit formulation is adopted to accurately model the open resonator behavior in the presence of the test surface. On the basis of a complete modal analysis as proposed in [2], the adopted circuit approach leads to optimize the coupling between the cavity and the exciting waveguide, while including, at the same time, a proper modeling of the cavity losses, which gives a significant improvement when compared to the traditional open resonator approach [1].

II. EQUIVALENT CIRCUIT FORMULATION

The open resonator system adopted for the equivalent impedance characterization is illustrated in Fig. 1(a). It consists of a spherical mirror of radius R_0 , which is used to produce a Gaussian beam impinging on the grounded test surface at a distance l . A feeding rectangular waveguide of standard height b is adopted for the cavity excitation, and a transition is properly designed to optimize the coupling with the cavity.

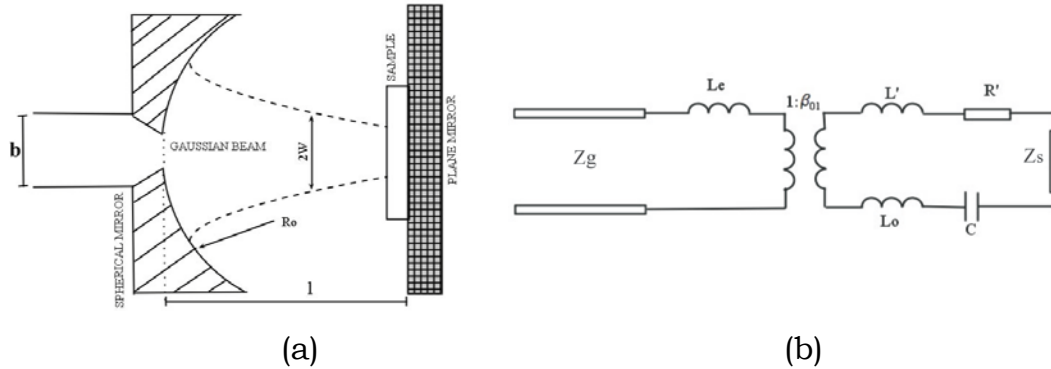


FIG. 1 – (a) Open resonator system and (b) equivalent circuit for the impedance characterization of planar surfaces.

At this purpose, the approach proposed in [2] is adopted, which is based on a complete eigenfunctions analysis leading to the equivalent circuit of Fig. 1(b). The relative circuit parameters, accurately defined in [2], properly model the cavity losses, thus leading to an accurate characterization of the open resonator behavior in the presence of the unknown test surface, whose equivalent impedance Z_s can be easily derived from return loss measurements performed at the waveguide input, under empty and loaded cavity conditions. As a matter of fact, the insertion of the test surface sample produces a shift in the resonant frequency of the cavity, from which the imaginary part of impedance Z_s can be retrieved. At the same time, an amplitude reduction of the reflection coefficient is obtained in the presence of the test sample, which in turns is related to the real part of impedance Z_s . In the following paragraphs, a more detailed description of the impedance reconstruction method is provided for two specific application contexts, namely the complex permittivity retrieval of thin dielectric substrates and the phase response characterization of microstrip reflectarrays.

III. APPLICATION EXAMPLE: DIELECTRIC CHARACTERIZATION

The insertion of a grounded dielectric substrate having complex permittivity $\epsilon = \epsilon' - j\epsilon''$ leads to an equivalent impedance Z_s , easily expressed as:

$$Z_s = jZ_d \operatorname{tg}(k_d h - \phi_G) \quad (1)$$

where Z_d and k_d give the characteristic impedance and the propagation constant of the dielectric slab h , while ϕ_G is the phase shift caused by the impinging Gaussian beam [3]. Equation (1) can be easily splitted into its real and imaginary parts, which are related to the unknown terms ϵ' and ϵ'' . From the return loss measurements, the information relative to the resonant frequency shift and the loaded quality factor are derived, which are used to retrieve the imaginary and the real parts of impedance Z_s , respectively. In the final stage, the complex permittivity is reconstructed from the above information [3]. To test the validity of the proposed approach, a K-band open resonator system is designed, with a waveguide-to-cavity transition properly dimensioned for optimizing the coupling on the basis of the equivalent circuit in Fig. 1(b). A standard dielectric substrate Diclad 527, whose nominal parameters are reported in Table I, is used as test example.

TABLE I – NOMINAL AND RETRIEVED DIELECTRIC PARAMETERS (DICLAD 527)

h [mm]	ϵ' (Nominal)	$\tan \delta$ (Nominal)	ϵ' (Retrieved)	$\tan \delta'$ (Retrieved)
0.762	2.55	0.0018	2.535	0.002

The measured return loss with empty and dielectric loaded cavity is shown in Fig. 2, and the relative frequency shift and amplitude reduction are used to properly retrieve the dielectric parameters (ϵ' , $\tan\delta$) reported in Table I.

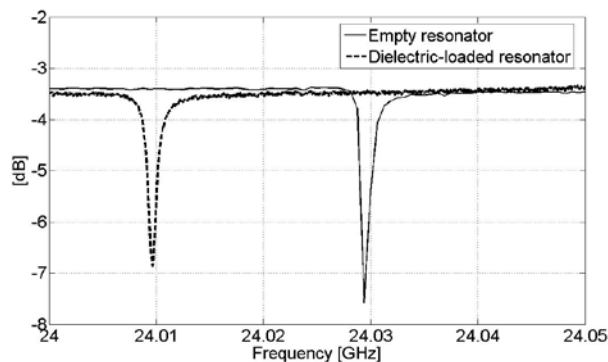


FIG. 2 – Measured return loss with empty and dielectric loaded resonator.

IV. APPLICATION EXAMPLE: REFLECTARRAY CHARACTERIZATION

The phase response of reflectarray elements can be characterized by inserting a periodic array of identical radiators into the open resonator system of Fig. 1(a). Due to the small thickness h of the usually adopted substrates, and assuming neglecting dielectric losses, an equivalent known inductance can be considered to represent the slab, whose parallel with an L,C circuit modeling the reflecting grid gives the unknown equivalent impedance Z_s . From the knowledge of the cavity resonant frequencies in the presence of the array grid, parameters L,C

are derived by applying the resonant conditions of the equivalent circuit in Fig. 1(b). The procedure is then repeated for different size of the reflectarray element to fully characterize its phase response [4]. The outlined approach is tested on a K-band reflectarray grid of variable size patches (Fig. 3(a)). Resonant frequencies are measured for different values of the patch side D , and the equivalent circuit of Fig. 1(b) is applied to reconstruct the phase response in Fig. 3(b), where an excellent agreement can be observed with results coming from Ansoft Designer simulations.

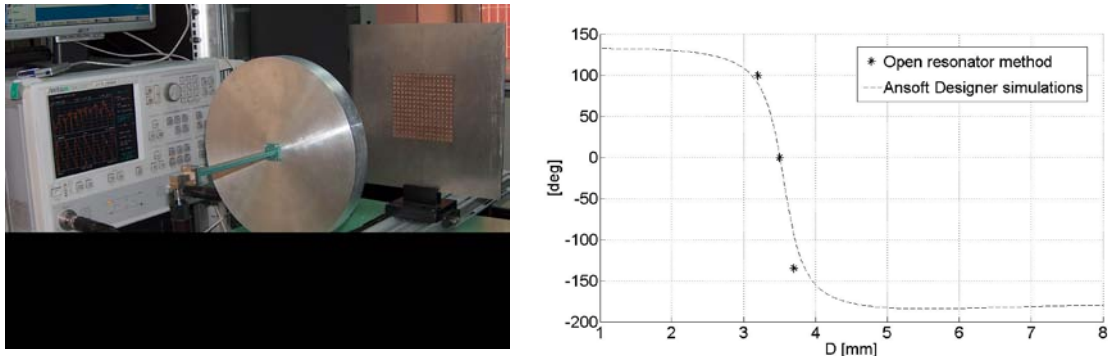


FIG. 3 – (a) K-band open resonator system and (b) reconstructed phase response vs patch side D .

V. CONCLUSION

A simple equivalent circuit approach has been adopted to accurately predict the behavior of open resonator systems loaded with planar dielectric surfaces. The equivalent impedance of the test surface is easily derived from the resonant information included in the return loss measurements. Successful K-band experimental validations on complex permittivity reconstruction and reflectarray phase response characterization have been discussed.

REFERENCES

- [1] P. K. Yu, and A. L. Cullen, "Measurement of permittivity by means of an open resonator. I Theoretical," *Proc. R. Soc. Lond*, vol. A 380, pp. 49-71, 1982.
- [2] O. M. Bucci, and G. Di Massa, "Open resonator powered by rectangular waveguide," *IEE Proc. H*, vol. 139, pp. 323-329, 1992.
- [3] G. Di Massa, S. Costanzo, and O. H. Moreno, "Accurate circuit model of open resonator system for dielectric material characterization," *Journal of Electrom. Waves Applicat.*, vol. 26, pp. 783-794, 2012.
- [4] G. Di Massa, S. Costanzo, and O. H. Moreno, "Open resonator system for reflectarray elements characterization," submitted to *Int. Journal of Antennas Propagat.*, special issue on *Reflectarray Antennas: Analysis and Synthesis Techniques*, ed. by S. Costanzo, R. Gillard and M. Arrebola, 2012.

WIRELESS POWER TRANSMISSION LINKS: EXPERIMENTAL RESULTS AT THE ELECTROMAGNETIC LABORATORY OF LECCE

G. Monti, L. Tarricone, F. Congedo, P. Arcuti

⁽¹⁾ Engineering for Innovation Department, University of Salento
Via per Monteroni, 73100 Lecce, Italy
{giuseppina.monti, luciano.tarricone, fabrizio.congedo, paola.arcuti}@unisalento.it

Abstract

This paper presents some results concerning the design of wireless links for power transmission developed at the Electromagnetic Laboratory of Lecce. More in detail, a system for far-field communications using a rectifying antenna (rectenna) and one for near-field communications using inductively coupled resonators are presented. In both cases experimental results are given and discussed.

Index Terms – Wireless Power Transmission; Rectenna; Inductive Power Transmission; Implantable Biomedical Devices.

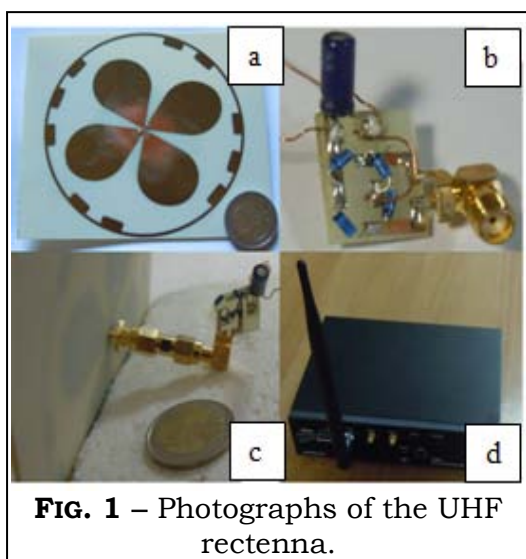


FIG. 1 – Photographs of the UHF rectenna.

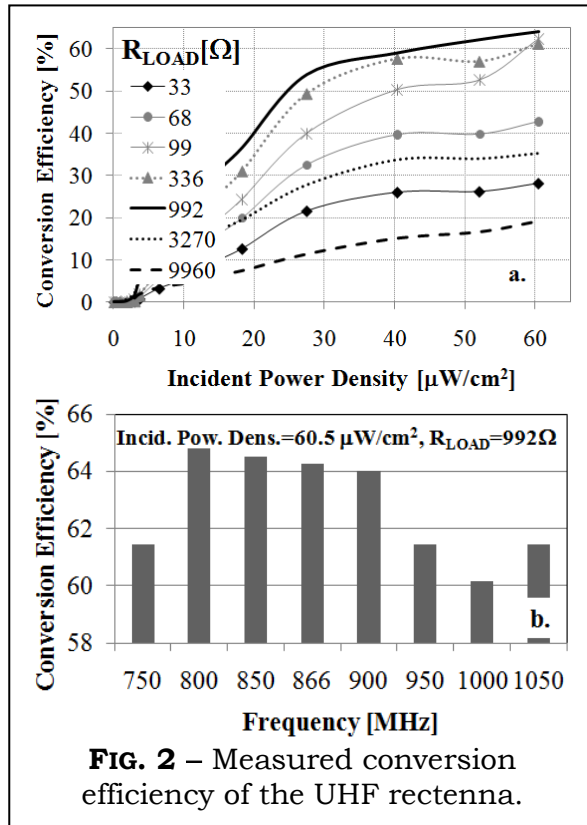
I. INTRODUCTION

The basic idea of Wireless Power Transmission (WPT, [1]) is to wirelessly transmit power, thus representing an enabling technology for the development of energy-autonomous systems. Two main strategies can be identified for implementing WPT, depending on whether the wireless link uses resonant systems coupled by their far- or near- electromagnetic (EM) field. In the first case (far-field communications) a rectifying

antenna (rectenna) consisting of an antenna and a rectifier is used to receive the EM wave and to convert it into DC power [2]. While, in the second case (near-field communications) electrically or magnetically coupled systems are used [3].

In this paper some experimental results referring to the two above described WPT strategies are presented. More specifically, a compact rectenna working in the UHF (Ultra High Frequency) band and an inductive link using planar resonators will be presented.

The paper is structured as follows: a brief description and experimental results of the UHF rectenna and of the inductive link are given in section II and III, respectively. Finally, some conclusions are drawn in section IV.



II. UHF RECTENNA

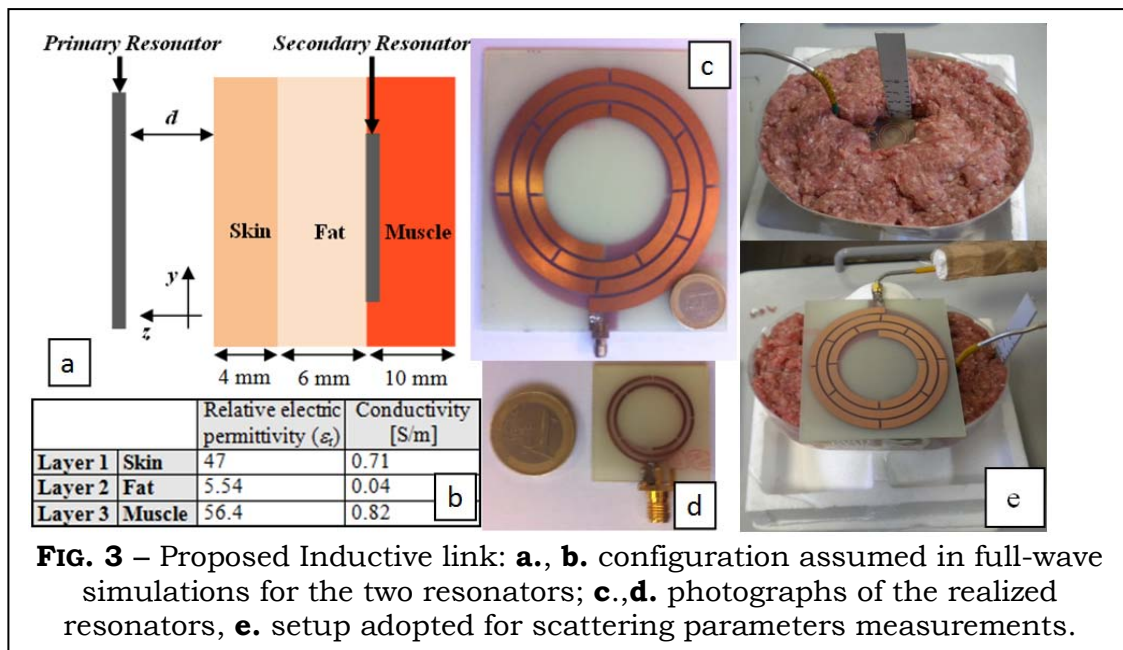
Some photographs of the UHF rectenna are given in Fig. 1. The rectifier is a full-wave bridge rectifier which consists of four Schottky diodes in a bridge configuration (the diodes are 1N 6263 of ST Microelectronics, see Fig. 1b). A capacitor of 1 μF in shunt configuration with the load has been also used. The aim of this capacitor is to block the RF signal with respect to the load. As for the antenna, it consists of two crossed bowties loaded with an annular ring (see Fig. 1a). The substrate is a 1.6 mm thick FR4 laminate with a relative permittivity of 3.7 and a loss tangent of 0.019. From

full-wave simulations this antenna exhibits a gain higher than 3 dB over the entire frequency range of interest (i.e., [860, 950] MHz).

Measurements of the RF-to-DC conversion efficiency of the proposed rectenna were performed by using a Software-Defined Radio (SDR) platform. More specifically, in order to generate the microwave signal incident on the rectenna, the software toolkit GNU-Radio and a Universal Software Radio Peripheral (USRP) were used (see Fig. 1d); the USRP was equipped with a FLEX900 daughterboard which supports operating frequencies in the range of [750-1050] MHz [4]. Experimental data were taken for different values of: the resistive load, the power density and the frequency of the microwave signal incident on the antenna. Data collected this way have been used to calculate the RF-to-DC conversion efficiency according to the following definition:

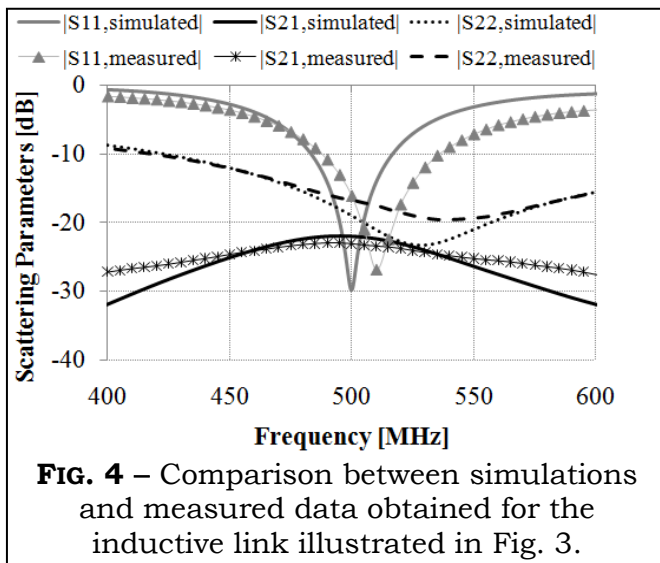
$$\eta_{RFtoDC} = P_{OUT,DC} / S_{RF} A_G = (V_{DC}^2 / R_{LOAD}) (1 / S_{RF} A_G)$$

where S_{RF} is the power density incident on the antenna, V_{DC} is the DC output voltage, R_{LOAD} is the resistive load. A_G is the geometric area of the antenna ($\sim 72 \text{ cm}^2$). Corresponding results are summarized in Fig. 2. Figure 2a shows the conversion efficiency measured at 866 MHz; it can be seen that a maximum of about 65% was measured with an incident power density of $60.5 \mu\text{W}/\text{cm}^2$ and a resistive load of 992 Ω . Figure 2b shows results obtained by varying the frequency of the signal generated by the USRP; it can be noticed that values greater than 60% were obtained over the entire operating frequency range of the FLEX900 daughterboard (i.e., [750, 1050] MHz).



III. INDUCTIVE LINK FOR POWER TRANSMISSION

In this section results referring to a 500 MHz inductive link for powering implantable biomedical devices are presented. The proposed wireless link consists of two planar resonators: a primary resonator that is connected to a power source and operates outside the body and a secondary resonator that is placed inside the body and it is connected to an implanted device (see Fig. 3a). Photographs of the realized resonators are given in Figs. 3c and 3d; the occupied area is $110 \times 115 \text{ mm}^2$ for the primary resonator and $30.4 \times 30.4 \text{ mm}^2$ for the secondary resonator. Each resonator consists of two segmented spiral loops realized on the top and bottom face of a low-cost FR4 substrate ($\epsilon_r=3.7$, $\tan(\delta)=0.025$) with a thickness of 1.6 mm. More in details, referring to applications that use devices implanted under the skin to a maximum depth of 1 cm, the parameters of the secondary resonator were optimized by considering the resonator inserted in a stratified medium consisting of the following three layers: a first layer of skin, a second layer of fat and a third layer of muscle (see Figs. 3a-3b). In order to experimentally evaluate the performance of the proposed inductive link in the presence of human tissues, we used minced pork [5]. In fact, in the frequency range of interest minced pork exhibits values of electric parameters very close to the ones corresponding to the human skin and muscle [5], [6]. The experimental setup adopted for measurements is illustrated in Fig. 3e; the secondary resonator was placed inside minced pork at a depth $d_1=1 \text{ cm}$, while the primary resonator was placed at a distance $d_2=2 \text{ cm}$ with respect to the minced pork surface (the overall distance between the two resonators was 3 cm). Corresponding results



are given in Fig. 4 and compared with numerical data calculated by using the stratified medium illustrated in Fig. 3a. It is evident that they are in a good agreement (port 1 and 2 are connected to the primary and the secondary resonator, respectively). From measurements, the value calculated at 500 MHz for the S_{21} parameter is of about -23 dB.

IV. CONCLUSION

In this paper two wireless links for power transmission applications have been presented: a system using an UHF rectenna and an inductive link for powering implantable biomedical devices. In both cases experimental results have been reported and discussed demonstrating that the systems here presented are optimum candidates to be used in near- and far-field communications, respectively.

REFERENCES

- [1] N. Tesla, "Apparatus for transmitting electrical energy," U.S. Patent, 1119732, 1914.
- [2] G. Monti, L. Tarricone, M. Spartano, "X-Band Planar rectenna", *Antennas and Wireless Propagation Letters*, vol. 10, pp. 1116-1119, 2011.
- [3] M. Dionigi, M. Mongiardo, "CAD of wireless resonant energy links (WREL) realized by coils," *2010 IEEE MTT-S*, May 2010, Anaheim, CA, USA.
- [4] Ettus Research LLC website: <http://www.ettus.com>.
- [5] F. J. Huang, C. M. Lee, C. L. Chang, L. K. Chen, T. C. Yo, C. H. Luo, "Rectenna Application of Miniaturized Implantable Antenna Design for Triple-band Biotelemetry Communication," *IEEE Trans. On Antenna and Propagation*, vol. 59(7), pp. 2646-265, July 2011.
- [6] S. Gabriel, R.W. Lau, C. Gabriel, "The dielectric properties of biological tissues: II. Measurements in the frequency range 10 Hz to 20 GHz," *Phys. Med. Biol.*, vol. 41, pp. 2251-2269, 1996.

TIME-MODULATED ARRAYS FOR NEXT GENERATION COGNITIVE RADIO SYSTEMS – POTENTIALITIES AND ENVISAGED SOLUTIONS

P. Rocca

ELEDIA Research Center @ DISI, University of Trento
Via Sommarive 5, Povo 38123 Trento, Italy
paolo.rocca@disi.unitn.it

Abstract

The potentialities and opportunities offered by time-modulated arrays as antenna systems for cognitive radio applications is analyzed and discussed in this paper. The easy reconfiguration of the radiation characteristics and the possibility to exploit the self-generated harmonic radiations for multiple channel communication purposes are obtained by simply controlling the on-off switching sequence modulating the static array excitations. The optimization of the radiation features are achieved by means of a customized optimization procedure based on an evolutionary strategy.

Index Terms – Cognitive radio, MIMO systems, Reconfigurable arrays, Switching strategy, Time-modulated arrays.

I. INTRODUCTION

Nowadays, there is a growing interest in the design and synthesis of wireless antenna systems for cognitive radio (CR) [1] able to first sense the electromagnetic environment and then reconfigure the radiation characteristics to operate according to the desired/requested functionality. Such systems are based on the idea of software-defined radio which exploits smart antenna devices equipped with radio-frequency (RF) switches [2] able to rapidly adapt to the scenario at hand and to provide both nulling as well as beam-forming capabilities within the available frequency band. One of the key advantages is the ability to quickly reconfigure the antenna front-end completely via software.

In this framework, there has been recently a renewed interest towards time-modulated arrays (TMAs) which are antenna systems controlled by means of a set of RF switches included in the beam forming network which are used to modulate, through a periodic time sequence, a classical phased array architecture. One of the main advantages of TMAs is the use of time as an additional degree of freedom in the design process. The idea, firstly conceived in [3], has been then significantly extended over the years both from the theoretical [4], methodological [5], applicative [6], and experimental [7] viewpoint. Such an interest is also due to the advances in the last few years in the realization of fast RF switches [8] and the introduction of efficient strategies for the reduction of the harmonic radiations [9], the so-called sideband radiation (SR) [4], caused by the on-off periodic commutations of the switches.

On the contrary, it has been also observed that the SR can be suitably exploited to generate independent beams at the harmonic frequencies [10]. Such beams can be used to transmit the information over different channels or to receive multiple signals from different directions as in MIMO receiver. Both applications are enabled by the use of TMAs and can be exploited in CR systems. In this paper, the reception of multiple signals by means of a single TMA is presented and discussed.

II. MATHEMATICAL FORMULATION

Let us consider a time-modulated linear array (TMLA) with N isotropic sensors and uniform inter-element spacing d . The on-off behavior of the RF switches is described by the rectangular pulse functions $U_n(t)$, $n = 1, \dots, N$ of period T_p which modulate the complex static excitations $I_n = A_n e^{j\phi_n}$, $n = 1, \dots, N$, being A_n and ϕ_n the amplitude and phase weights, respectively. It turns out that the n -th is on when $U_n(t) = 1$ and is off when $U_n(t) = 0$. By assuming $T_p \gg T_0 = 1/f_0$ where f_0 is the antenna working frequency, each $U_n(t)$ can be expanded into a Fourier series [3]. Accordingly, the array factor turns out being composed by an (ideally) infinite number of harmonic terms spaced in the frequency domain by $\omega_p = 2\pi/T_p$ [4]. Mathematically, it is described by the following relationship

$$F(\vartheta, t) = \sum_{h=-\infty}^{+\infty} e^{jh\omega_p t} F_h(\vartheta) = \sum_{h=-\infty}^{+\infty} e^{jh\omega_p t} \sum_{n=1}^N I_n u_{nh} e^{j\beta d(n-1)u} \quad (1)$$

where $F_h(\vartheta)$ is the array factor of the pattern generated at the h -harmonic with β the free-space wave-number and u_{nh} the Fourier coefficients associated to the n -th rectangular pulse functions.

When a set of S signals impinge on the antenna from different directions ϑ_i , $i = 1, \dots, S$ and with strength s_i , $i = 1, \dots, S$, it is possible to optimize the pulse sequence $U_n(t)$, $n = 1, \dots, N$ such that the corresponding Fourier coefficients generate S harmonic beams, each one having a maximum in the direction of one signal while nulls in the directions of arrival of the others. Accordingly, it is possible to define a suitable functional to be maximized [11] which allows to maximize the signal to noise plus interference ratio (SINR) on each harmonic channel.

III. NUMERICAL RESULTS

As a representative example, let us consider a TMLA made of $N = 20$ elements with half-wavelength inter-element spacing (i.e., $d = \lambda/2$) and uniform amplitude excitations $A_n = 1$, $n = 1, \dots, N$. Two signals $S = 2$

with equal power (i.e., $s_1 = s_2$) impinge on the antenna from directions $s_1 = 50[\text{deg}]$ and $s_2 = 30[\text{deg}]$. By considering the proposed approach [11], signal $i = 1$ is received with the beam generated at the carrier frequency ($h = 0$) and signal $i = 2$ with the first superior harmonic beam ($h = 1$). Figure 1 reports the pulse sequence achieved at the end of the optimization process [Fig. 1(a)] and the values of the phase weights [Fig. 1(b)] used to steer the beam at $h = 0$ towards the direction of signal $i = 1$. Differently, the shaping and the steering of the beam at the first harmonic are obtained by means of the optimized on-off sequence ($h=1$ - Fig. 2). It is possible to observe that the two generated beams are characterized by a peak value in the direction of the corresponding signals and deep nulls towards the signal received on the other harmonic. Moreover, also the sidelobe level of the two beams is kept low, in this case below -25dB , according to the adopted optimization strategy [11]. This allows to reduce the effect of noise or other undesired signals. Finally, Fig. 3 shows the behavior of the SINR during the optimization process. At convergence, the SINR achieved on the two channels is close to 32dB with an increment of more than 10dB with respect to the initial solution.

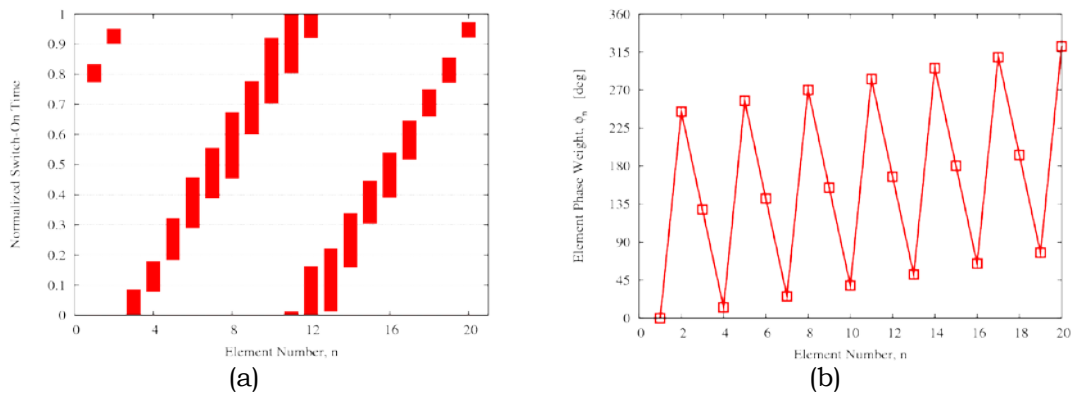


FIG. 1 – Optimized pulse sequence (a) and values of the element phases (b).

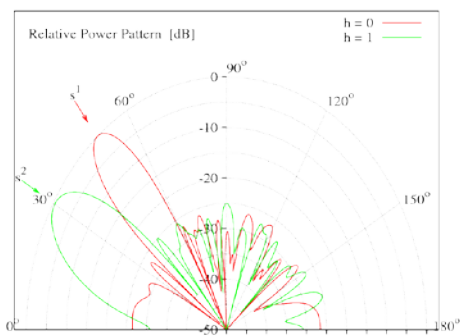


FIG. 2 – Radiation patterns at $h=0$ and $h=1$ obtained by controlling the antenna with the pulse sequence and phase weights reported in Fig. 1.

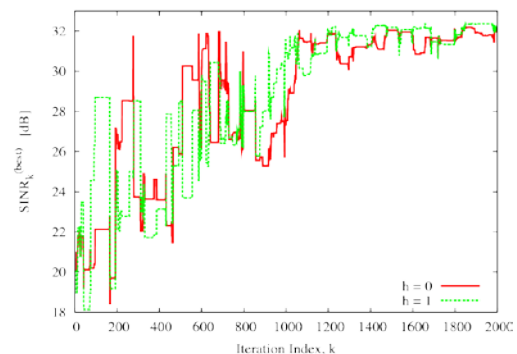


FIG. 3 – Behavior of the SINR throughout the optimization process.

IV. CONCLUSION

In this paper, the use TMAs as antenna systems for cognitive radio has been discussed and possible solutions envisaged. A representative example regarding the reception of multiple signals at different harmonic channels has been studied and a preliminary result reported to show the effectiveness of the approach.

Although further investigation are certainly required and experimental validation needed, TMAs seem to be a potential candidate for a class of future communication and radar systems where the fast, easy, and efficient reconfiguration of the radiation features is required and where the use of multiple channels can provide an added values to improve the robustness and effectiveness of the wireless system.

REFERENCES

- [1] S. Haykin, "Cognitive radio: brain-empowered wireless communications," *IEEE J. Selected Areas Comm.*, vol. 23(2), pp. 201-220, Feb. 2005.
- [2] Y. Tawk, J. Costantine, S. Hemmady, G. Balakrishnan, K. Avery, and C. G. Christodoulou, "Demonstration of a cognitive radio front end using an optically pumped reconfigurable antenna system (OPRAS)," *IEEE Trans. Antennas Propag.*, vol. 60(2), pp. 1075-1083, Feb. 2012.
- [3] H. E. Shanks and R. W. Bickmore, "Four-dimensional electromagnetic radiators," *Canad. J. Phys.*, vol. 37, pp. 263-275, Mar. 1959.
- [4] J. C. Brégains, J. Fondevila, G. Franceschetti, and F. Ares. "Signal radiation and power losses of time-modulated arrays," *IEEE Trans. Antennas Propag.*, vol. 56(6), pp. 1799-1804, Jun. 2008.
- [5] L. Poli, P. Rocca, L. Manica, and A. Massa, "Pattern synthesis in time-modulated linear arrays through pulse shifting," *IET Microw., Antennas Propag.*, vol. 4(9), pp. 1157-1164, 2010.
- [6] G. Li, S. Yang, and Z. Nie, "A study on the application of time modulated antenna arrays to airborne pulsed doppler radar," *IEEE Trans. Antennas Propag.*, vol. 57(5), pp. 1578-1582, May 2009.
- [7] A. Tennant, "Experimental two-element time-modulated direction finding array," *IEEE Trans. Antennas Propag.*, vol. 58(3), pp. 986-988, Mar. 2010.
- [8] M. G. Labate, A. Buonanno, M. D'Urso, G. Calzolaio, A. Vacca, L. Zeni, G. Leone, and G. Riccardo, "Photoconductive switches for radar systems exploiting time domain," *Proc. 5th European Conf. Antennas Propag. (EUCAP)*, Rome, Italy, 11-15 Apr. 2011, pp. 2244-2245.
- [9] L. Poli, P. Rocca, L. Manica, and A. Massa, "Handling sideband radiations in time-modulated arrays through particle swarm optimization," *IEEE Trans. Antennas Propag.*, vol. 58(4), pp. 1408-1411, Apr. 2010.
- [10] L. Poli, P. Rocca, G. Oliveri, and A. Massa, "Harmonic beamforming in time-modulated linear arrays," *IEEE Trans. Antennas Propag.*, vol. 59, no. 7, pp. 2538-2545, Jul. 2011.
- [11] P. Rocca, L. Poli, E. T. Bekele, and A. Massa, "Time-modulation for MIMO systems - Potentials and trends," *Proc. 6th European Conf. Antennas Propag. (EUCAP)*, Prague, Czech Republic, 26-30 March 2012, pp. 2.

ARRAY DESIGN IN THE CORRELATION DOMAIN: A NEW PARADIGM

F. Viani

ELEDIA Research Center @DISI, University of Trento
 Via Sommarive 5, I-38123 Trento, Italy
federico.viani@disi.unitn.it

Abstract

A new paradigm for the design of antenna arrays is proposed in which the constraints and objectives are formulated in the “autocorrelation domain” rather than in terms of pattern features. Such an approach is motivated by the known relations between the radiating properties of antenna arrays and the autocorrelation of the associated weighting sequences. Thanks to such a property, the introduced framework enables the exploitation of already developed sequences with known correlation features coming from combinatorial theory. Moreover, it enables the formulation of new design problems which do not require the evaluation of array patterns for their solution. A preliminary example is reported to point out the potentialities of the proposed correlation-domain paradigm.

Index Terms– Linear Arrays, Array Synthesis, Autocorrelation.

I. INTRODUCTION AND MOTIVATION

The problem of designing arrays with prescribed radiating features represents a fundamental challenge in applied electromagnetics since its origin [1]. A vast number of techniques have been developed to tackle this problem depending on the available degrees-of-freedom, the expected performances, and the geometries at hand [1]. Despite these large differences, most existing design techniques share the approach of evaluating the figures of merit of the array through the computation of its radiated pattern [1]-[4]. Accordingly, many array design techniques require several *array factor* computations to achieve the final design [3][4], thus resulting in computationally expensive procedures.

Nevertheless, some alternatives to the above guideline can be considered as well. Indeed, it is known that the radiating properties of an array can be inferred or estimated starting from the knowledge of the autocorrelation of the associated “weighting sequence” [5]-[7]. Such a property, which has been mainly employed to derive analytical designs for thinned arrays [5]-[7] starting from binary sequences with known autocorrelation [8], has actually a much wider range of applicability as it does not depend on the thinned nature of the arrangement at hand [7]. In fact, one could observe that evaluating an array in the correlation domain, as it is done in radioastronomy applications thanks to the Van Cittert-Zernike theorem [9][10], could allow classical design problems to be solved by exploiting “autocorrelation synthesis” approaches already

developed in code theory, cryptography, and combinatorics [5][6]. Moreover, the formulation of array constraints in the correlation domain could enhance the computational efficiency of array optimization tools thanks to the reduced complexity (proportional to $N \log(N)$, N being the size of the problem) in the figures-of-merit computation.

Accordingly, a new paradigm is proposed in this work for the synthesis of antenna arrays through formulation of the design constraints in the *correlation domain* instead of the *radiation domain*. The proposed approach can be applied to arbitrary design targets/constraints, provided that they are suitably transformed according to the provided guidelines. A preliminary example concerning the design of a thinned arrangement is presented to assess the features and potentialities of the proposed paradigm.

II. SYNTHESIS PROBLEM IN THE CORRELATION DOMAIN

Consider a linear array of N equally spaced isotropic elements with complex-valued weights w_n ($n=0, \dots, N-1$) whose array factor is equal to

$$F(u) = \sum_{n=0}^{N-1} w_n \exp(2\pi j n d u) \quad (1)$$

where d is the lattice spacing in wavelengths, and u is the direction cosine [1]. Thanks to the fact that [7]

$$\left| F\left(\frac{q}{dN}\right) \right|^2 = A(q), \quad q = 0, \dots, N-1 \quad (2)$$

where $A(q)$ is the autocorrelation function of the weighting sequence, which can be computed as

$$A(q) = \sum_{n=1}^N w_n w_{(n+q) \bmod N} \quad (3)$$

(“mod” standing for the modulus operator), it turns out that the array synthesis problem can be formulated in the correlation domain as follows

Array Synthesis Problem – Given the target tolerance ε , the array size N , and the lattice spacing d , find w_n ($n=0, \dots, N-1$) such that

$$\Omega = \sum_{q=1}^N |A(q) - A_T(q)| < \varepsilon$$

where

$$A_T(q) = \left| F_T\left(\frac{q}{dN}\right) \right|^2, \quad q = 0, \dots, N-1 \quad (4)$$

is the target autocorrelation and $F_T(u)$ is the target array factor. It is worth remarking that the above formulation can be seen as a “power synthesis” one, as the phase of $F_T(u)$ is neglected. Moreover, although only a set of pattern samples are actually enforced during the synthesis

[see Eq. (4)], suitable methods exist to estimate the “error” in the pattern domain without requiring the computation of $F(u)$ [6]-[8].

III. APPLICATION TO GA-BASED THINNED ARRAY SYNTHESIS

Without loss of generality, let us consider the design of a $N=90$ thinned array (i.e., $w_n \in \{0,1\}$) with a prescribed three-level autocorrelation function $A_T(q)$ in order to achieve a desired sidelobe level, as detailed in [6]. Accordingly, the following target autocorrelation is assumed

$$A_T(q) = \begin{cases} K & \text{for } q = 0 \\ L & \text{for } Q \text{ values of } q \\ L - 1 & \text{otherwise} \end{cases} \quad (5)$$

where K is the number of non-zero w_n values, and L is the “high autocorrelation level” which is assumed by $A_T(q)$ in Q points [8].

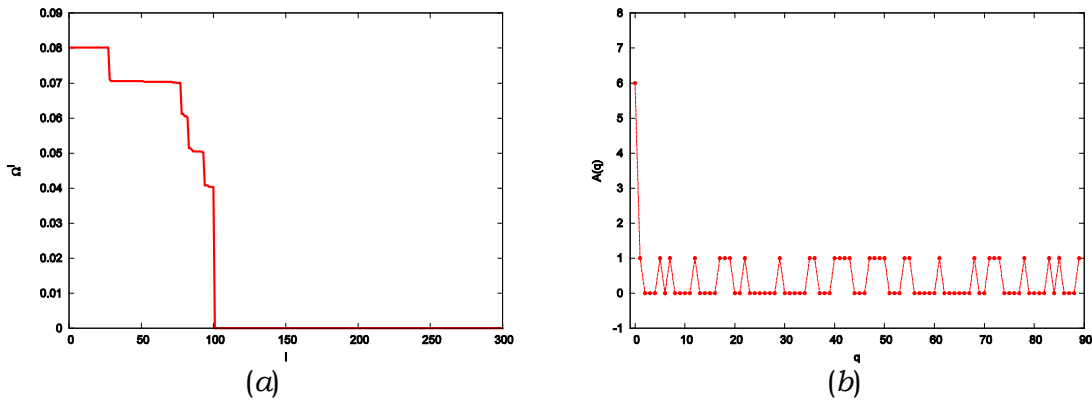


FIG. 1– Example of Correlation-Domain Design - Behaviour of the normalized matching function during the GA evolution (a) and final autocorrelation (b).

Since no known sequence exists which comply with (5), a Genetic Algorithm (GA)-based procedure is considered [11][12] to minimize Ω according to the above problem formulation. Towards this end, the following parameters have been assumed: a population of size P equal to 50, a cross-over rate equal to 0.9, a mutation probability equal to 0.01, and a number of GA generations equal to $I=300$.

The plots of Ω as a function of the GA iteration i [Fig. 1(a)] indicate that the procedure is able to converge to the desired three-level correlation [$K=6, L=1$ - Fig. 1(b)] in less than 100 iterations, each one requiring the computation of $P \times N \log(N)$ operations. On the contrary, the design of a thinned array using the same methodology but formulated in the “pattern domain” [12] with about $N=90$ elements would require more than 500 iterations each one having a complexity of about $P \times U \log(U)$ operations, $U \gg N$ being the number of pattern samples required to fully characterize the array [12]. Such a result points out the capability of the

proposed correlation-domain formulation to significantly improve the numerical efficiency of array synthesis techniques.

IV. CONCLUSIONS

The problem of array synthesis is solved with a new paradigm. The fundamental idea, which is enabled by to the relationships between the array factor and the properties of the array weighting sequence, is to formulate the synthesis objectives in terms of correlation instead of pattern features. Such a choice is motivated by the fact that (i) it enables the use of previously synthesized sequences with known correlation properties, and (ii) it allows the computationally efficient solution of new design problems formulated in such a transformed domain. The discussed preliminary example remarks the potentialities of the proposed paradigm over classical formulations.

REFERENCES

- [1] C. A. Balanis, *Antenna Theory: Analysis and Design*, 2nd ed. New York: Wiley, 1997
- [2] B. Steinberg, "The peak sidelobe of the phased array having randomly located elements," *IEEE Transactions on Antennas and Propagation*, vol. 20, no. 2, pp. 129-136, Mar 1972.
- [3] R. L. Haupt, "Thinned arrays using genetic algorithms," *IEEE Transactions on Antennas and Propagation*, vol. 42, no. 7, pp. 993-999, July 1994.
- [4] D. S. Weile and E. Michielssen, "Integer coded Pareto genetic algorithm design of constrained antenna arrays," *Electronics Letters*, vol. 32, no. 19, pp. 1744-1745, Sep. 1996.
- [5] D. G. Leeper, "Isophoric arrays-massively thinned phased arrays with well-controlled sidelobes," *IEEE Transactions on Antennas and Propagation*, vol. 47, no. 12, pp. 1825-1835, Dec. 1999.
- [6] G. Oliveri, M. Donelli, and A. Massa, "Linear array thinning exploiting almost difference sets," *IEEE Trans. Antennas Propag.*, vol. 57, no. 12, pp. 3800-3812, Dec. 2009.
- [7] G. Oliveri, L. Manica, and A. Massa, "ADS-Based guidelines for thinned planar arrays," *IEEE Trans. Antennas Propag.*, vol. 58, pp. 1935-1948, June. 2010.
- [8] K. T. Arasu, C. Ding, T. Helleseth, P. V. Kumar, H. M. Martinsen, "Almost difference sets and their sequences with optimal autocorrelation," *IEEE Transactions on Information Theory*, vol. 47, no. 7, pp. 2934-2943, Nov 2001.
- [9] G. Oliveri, F. Caramanica, and A. Massa, "Hybrid ADS-based techniques for radio astronomy array design," *IEEE Transactions on Antennas and Propagation*, vol. 59, no. 6, pp. 1817-1827, June 2011.
- [10] J. W. Goodman, *Statistical Optics*, New York: Wiley, 1985.
- [11] G. Oliveri, M. Donelli, and A. Massa, "Genetically-designed arbitrary length almost difference sets," *Electronic Letters*, vol. 45, no. 23, pp. 1182-1183, November 2009.
- [12] G. Oliveri, and A. Massa, "Genetic algorithm (GA)-enhanced almost difference set (ADS)-based approach for array thinning," *IET Microwaves, Antennas & Propagation*, vol. 5, no. 3, pp. 305-315, Feb. 2011.

SURVEILLANCE OF WIDE ZONES WITH UNATTENDED GROUND SENSORS: FROM DETECTION TO ALERT

D. Pavone⁽¹⁾, G. Sorrentino⁽²⁾, A. Buonanno⁽²⁾, M. D'Urso⁽²⁾

- ⁽¹⁾ OPTEL - Consorzio Nazionale di Ricerca per le Tecnologie Optoelettroniche dell'Inp, Via Circumvallazione Esterna di Napoli, zona ASI, I-80014 Giugliano di Napoli, Napoli, Italy. d.pavone@optel.it
- ⁽²⁾ SELEX Sistemi Integrati S.p.A., Via Circumvallazione Esterna di Napoli, zona ASI, I-80014 Giugliano di Napoli, Napoli, Italy. giosorrentino@selex-si.com;

Abstract

In this paper, we describe the experimental work and present an algorithm for vehicle and human detection using seismic sensors. For the vehicle detection, we propose a real-time algorithm able to calculate an adaptive threshold in order to lower the false alarm probability. For the human detection, instead, when the persons moving over ground, they generate a succession of impacts. Even in noisy environments, statistical measures of the seismic amplitude distribution, such as kurtosis, can be used to identify a footstep.

Index Terms – Detection, Seismic, Median Filter, Moment Statistic.

I. INTRODUCTION

Modern battles are increasingly being fought in complex urban environments. Surveillance in these areas is very difficult to perform using traditional stand-off sensors. An approach with growing popularity is to use large numbers of the ground sensors distributed (or unattended) in the area of interest. These sensors are typically very resource limited both in terms of processing capability and battery life. Consequently many traditional approaches to detection, classification, and tracking need to be reconsidered in this environment. In this paper we will describe a vehicle-human detection algorithm which provides robust performance under these conditions which is also general enough to be applicable to a wide variety of sensor domains and environmental conditions.

II. VEHICLE DETECTION ALGORITHM FOR THE ACOUSTIC-SEISMIC SENSOR

Previous research has demonstrated that acoustic and seismic background noise can be highly non-stationary and non-Gaussian [1]. Given the wide variation in noise background and target signatures, it's clear that we need a very robust detection algorithm that can quickly adapt to changing conditions. A common approach is to use an order statistic constant false alarm rate (OS-CFAR) detection algorithm. One advantage of this approach is that it can be very efficiently implemented using a *median filter*. The data was collected using a SM-7 10 Hz Geophone with a minimum sample rate of 64 samples for second. We collect data in continuous snippets. We then calculate the median of the absolute value of each snippet. The median filter provides additional robustness against non-Gaussian data as well as being computationally

efficient [2]. The median of each snippet is then used in a secondary running median filter. This gives us an estimate of the noise background. An additional running median filter is also performed on the deviation between the current snippet median level and the long term noise estimate. This gives us an approximate measure of the mean and standard deviation of background distribution. We can then use these estimates as a basis for a CFAR detector. Estimation of the mean and standard deviation allows the use of a CFAR detector. We choose between the two hypothesis H_0 = no target present and H_1 = target present using

$$\begin{array}{c}
 H_1 \\
 > \\
 m_n - b > T\sigma \\
 < \\
 H_0
 \end{array} \tag{1}$$

where m_n is the median of the absolute value of the n^{th} snippet, b is the current background estimate, T is a user defined threshold (typically 3.0), and finally, σ is the median deviation of the background. To reduce false alarms we further require 3 snippets to exceed the detection threshold before declaring a detection event. Moreover, the algorithm is robust against the unexpected “spike” false alarm.

III. HUMAN DETECTION ALGORITHM FOR THE SEISMIC-ACOUSTIC SENSOR

A footstep signature is caused by the impact on the ground. Each footstep has a characteristic shape that can be used to distinguish it from other noise. The most striking feature of the footstep when comparing time series data for footsteps to other seismic signatures is the series of sharp "spikes" generated by each impact. This differs from the random noise induced by the winds over the ground and from vehicle noise. We make recognize the footstep signal considering a statistical measure of the amplitude of the signature, the kurtosis. Kurtosis is ratio of the 4th to 2nd moment of the amplitude distribution of the signature. For each snippet, composed from N samples of data, the kurtosis is calculated:

$$Kur = \left(\frac{\sum_i (x_i - \mu)^4}{N - 1} \right) / \left(\frac{\sum_i (x_i - \mu)^2}{N - 1} \right)^2$$

where μ is the computed mean over N samples. The kurtosis value compared for a sample sequence is much higher in the presence of impulsive events than it is in the presence of Gaussian or sinusoidal signatures [3]. Note that the method depends only on the shape of the signature and not the amplitude. When the vehicle is close to the sensor, the vehicle signature dominates, and the kurtosis is ~3, while as the vehicle moves away the kurtosis increases [3]. The kurtosis itself varies with target, time and distance and its value for vehicles and background noise the kurtosis is low. in the human detection, the Kurtosis threshold value, in order to declare the detection has been fixed at 6.5 [3].

IV. EXPERIMENTAL RESULTS

This section will demonstrate the algorithm presented in previous sections. The field test consisted of vehicle and personnel pass-bys closed (two meters) at two sensors on the paved road. The seismic signals acquired with 44.100 sample/sec are showed respectively in Fig. 2a and in Fig.4a. After, these signals have been sampled with a sampling frequency of 64 Hz because this value is a good compromise between accuracy (low false alarm) and power consumed (due at processing of data acquired). The data have been collected in continuous snippets, each of duration of half second and analyzed 5 snippets at time. In this situation, the threshold will update every 5 snippets that is every 2.5 second. The block diagram of the algorithm for the vehicle-human detection is showed in Fig.1.

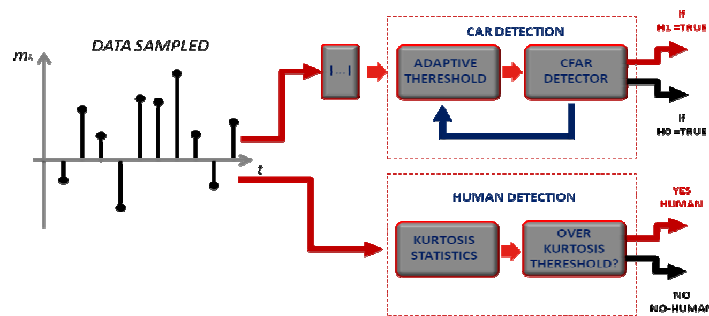


FIG. 1 – Block diagram of the algorithm for the vehicle-human detection.

An example of the detection process is show in Fig. 2-3. In particular, in Fig.3a shows the estimated background noise level and the noise threshold for vehicle detection while in Fig. 3b the relative kurtosis function varying the number of samples for second. The final detection result is shown in Fig.2b where the red lines represent the human detection while the black linen that for the vehicle. The results demonstrate that, although a few sample for second, the algorithm present only two false alarm (at 130). Fewer than 64 sample for second the algorithm manifest numerous false errors while, increasing the number of the samples, the performance improves at the expense of the higher power consumption.

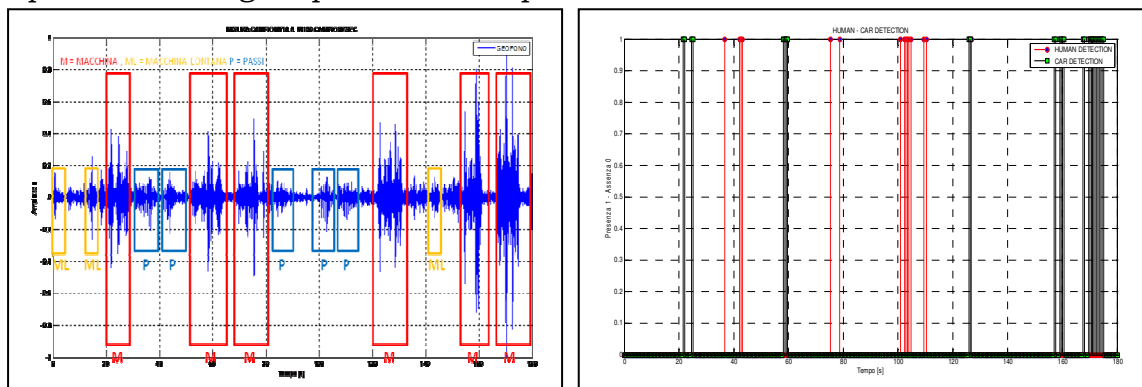


FIG. 2 – (a) Geophone signal during the transit of the vehicle and the personnel and (b) the relative detection by the algorithm presented.

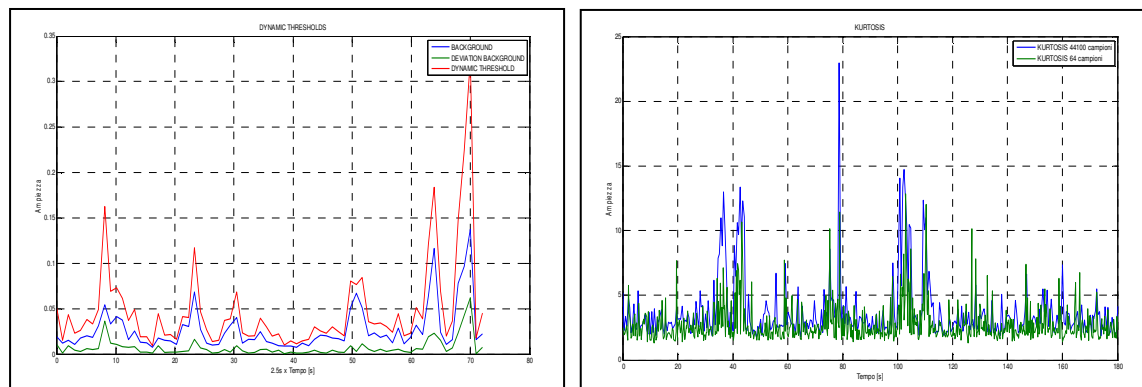


FIG. 3 – (a) Background estimate and dynamic threshold for the vehicle detection and (b) the trend of the Kurtosis changing the sample rate for the human detection considering a seismic signal.

V. CONCLUSIONS

We have demonstrated a robust, low power detection algorithm, for personnel and vehicle that operating under realistic conditions. The power consumption could easily be reduced at the cost of a slight drop in probability of detection. The use of the median filters increases the robustness of the detectors under highly non homogeneous conditions. A walker can be detected by computing the kurtosis of the seismic signature. Future research will include the possibility to use a cadence, that can also be computed from the signature, and used in combination with kurtosis to detect footsteps in the seismic record.

REFERENCES

- [1] A. Quach and K. Lo, "Automatic target detection using a ground-based passive acoustic sensor," *Proceedings of the 1999 Conference on Information, Decision and Control*, pp. 187–192, 1999.
- [2] A.M. Zoubir, V. Koivunen, Y. Chakhchoukh, and M. Muma, "Robust Estimation in Signal Processing", *IEEE Signal Processing Magazine*, Jul. 2012
- [3] G. Succi, G. Prado, R. Gampert, T. Pedersen, and H. Dhalival, "Footstep Detection and Tracking," *Proceedings of SPIE*, 4393, pp.22-29, April 2001.

DIGITAL MULTIPLE BEAMS RADARS FOR AIRPORT MONITORING AND SURVEILLANCE

A. Buonanno⁽¹⁾, P. Vinetti⁽¹⁾, M. G. Labate⁽¹⁾, M. D'Urso⁽¹⁾, M. Albertini⁽²⁾, L. Russo⁽²⁾

⁽¹⁾ SELEX Sistemi Integrati S.p.A., Giugliano in Campania, Italy
anbuonanno@selex-si.com; pvinetti@selex-si.com; mdurso@selex-si.com

⁽²⁾ Space Engineering S.p.A., Rome, Italy

Abstract

Phased array radar is very important in modern radar development, and sub-array clustering for digital multiple beams is a fundamental enabling technology in phased array radar. Full digitization of each antenna T/R module in large phased array radar is typically impracticable, and digitization at sub-array level can provide digital beamforming capability to address high performance requirements of modern multifunctional radar. The paper discusses a novel approach to effective design the antenna front end of a MFC radar.

Index Terms – radar systems, phased array, digital beamforming.

I. INTRODUCTION

Electronically scanned phased array radar [1] technology comprising several thousand RF T/R modules and associated RF Beam Forming (BF) is employed in the present generation of high performance military radars. In some cases these radars are further enhanced by a level of digital beamforming at subarray level. This level of digitisation can provide a number of advanced spatial processing features such as adaptive digital beamforming, adaptive angle estimation and space-time processing against clutter. This has a number of key challenges that make it unrealisable at present. The first is the cost of thousands of digitisers, another is processing the huge data rate that would come off of such an array and another is the distribution of thousands of local oscillator feeds. The middle ground then is to employ, 'high levels of digitisation'. 'High levels of digitisation' allows extra spatial digital processing capabilities such as multiple beam clusters and wideband LFM waveform processing. At this high level of digitization the array aperture is sampled adequately to achieve acceptable low sidelobes for offset beams and LFM beam correction. This paper firstly reviews the issues and benefits of various levels on digitisation in a Digital Array Radar for airport Surveillance and Monitoring. Element level digitisation provides for total flexibility of digital beamforming. It would provide for any number of simultaneous multiple beams to be formed in any desired look direction. It also provides for considerable flexibility of beam shape. No RF phase shifting is required to 'steer' beams as all beamforming is provided within the DSP. Such complete flexibility is,

however, not generally an essential requirement for radars. Apart from anything else, if the transmit energy is shared over a number of simultaneous beams, then the power per beam is proportionally less. The benefits provided by a high level of digitisation are discussed in the following bullet.

- Ability to generate a cluster of beams: scanning the search volume with a cluster of beams and simultaneously processing each beam provide a significant speed improvement. This mode does of course suppose that an appropriately broad transmit beam is employed to cover the beam cluster. Although this can result in less transmit power per angular sector, some radar modes are time limited rather than power limited.
- Implementation of wideband LFM (stretch) operation without the need for analogue RF time delay units. In present wideband LFM radars, RF Time Delay Unit (TDUs) are employed at element level to prevent the beam from squinting. TDU's are large an expensive. Digitising with sub-array enables LFM correction in the DSP.
- Ability to employ complex spatial angle estimation techniques, e.g. adaptive monopulse, super-resolution, maximum likelihood algorithms. These angle estimation techniques allow also coping with jammers by enabling adaptive BF.

The further degrees of freedom provided by per-element digital control enable expansion on radar function and performance, but they impose heavy requirements on digital processing in terms of wider bandwidths and higher dynamic ranges of analog to digital conversion chain. This processing need is commonly met with expensive, high throughput architectures that trade off scalability for functionality due to current technology limitations and/or restrictions imposed by the architecture itself. This work proposes a novel synthesis approach to the design of the antenna front-end for Multifunctional (MFC) radar, allowing a significant reduction of active T/R modules by means of a proper thinning procedure and, simultaneously, enabling the introduction of a proper digitisation level by means of an effective clustering into sub-array of the antenna, taking into account practical implementation constraints.

II. APPLICATION TO MULTIFUNCTIONAL RADAR

The design of a MFC radars operating into the short-medium range (up to 110 km) devoted to Air Traffic Control (ATC) and weather forecast missions has been considered. Naturally, dealing with MFC systems, where different independent functions are integrated into single equipment, makes the operational scenario, to deal with, significantly variable on the basis of the considered mission and, accordingly, the design of the overall system more complex. On the other side, concentrating more capabilities into a unique apparatus allows a

reduction of the cost of the final product if compared to two separated solutions. Furthermore, it reduces the number of systems deployed on the area (i.e. airport) and managed by the competent authorities, providing remarkable benefits in terms of logistics and maintenance.

The proposed MFC radar is based on a full Active Electronically Scanned Array (AESA) architecture, and the design of the antenna front-end has been accomplished by an innovative approach based on the steps described in the following.

The Antenna front-end design procedure is detailed in the following.

A baseline architecture is determined by pattern specifications. A full planar array, with elements half wavelength spaced, is dimensioned by matching the power pattern specifications (beamwidth, side lobe level and power). A thinning procedure is applied on the full array in order to refine the baseline solution and reduce the overall number of elements.

Thinning is applied by taking into account transmission (Tx) pattern specifications (which provides typically less degree of freedom in pattern generation – isophoric excitation). Fig. 1(a) illustrates the results of thinning on the full array: white pixel refer to switched off elements, while black ones refer to active. A 1D clustering is introduced in order to group T/R modules into sub-array. As showed in Fig. 1(b) clustering operates onto the azimuth dimension. Clustering strategy takes into account the power of the signal received by the sub-array, in order to ensure the proper dynamic to the related Analog-to-Digital Converter (ADC). Once given the sub-array clustering the Rx power pattern synthesis aimed at reducing quantization lobes (grating lobes arising from sub-array architecture) is faced by means of a synthesis based on a proper convex formulation [2], which ensure optimal solution by means of local optimization.

The above approach has allowed a reduction of 22.5% (thinned antenna has nearly 10.000 elements against nearly 12.500 elements of the full array). The radiating performance of the final array is comparable with that of the baseline solution and, accordingly, it ensures the required antenna performance for the considered applications. Fig. 2(a) and fig. 2(b) show the 2D power pattern of the synthesized Tx beam and the reference broadside Rx beam, respectively. It's worth noting that, since a sub-array architecture has been introduced, scanning the angular region requires analog RF phase correction for the generation of a reference beam. Fig. 3 shows the elevation cut of the power with the Tx beam and the simultaneous 10 Rx beams.

III. CONCLUSIONS

A novel approach for the design of a complex large AESA antenna for MFC radars has been proposed. The approach has demonstrated to be effective in reducing the number of TRMs by a proper thinning procedure and in clustering into sub-array the array enabling a digital

BF capability, taking into account power pattern specifications and signal power issues of the ADC chain.

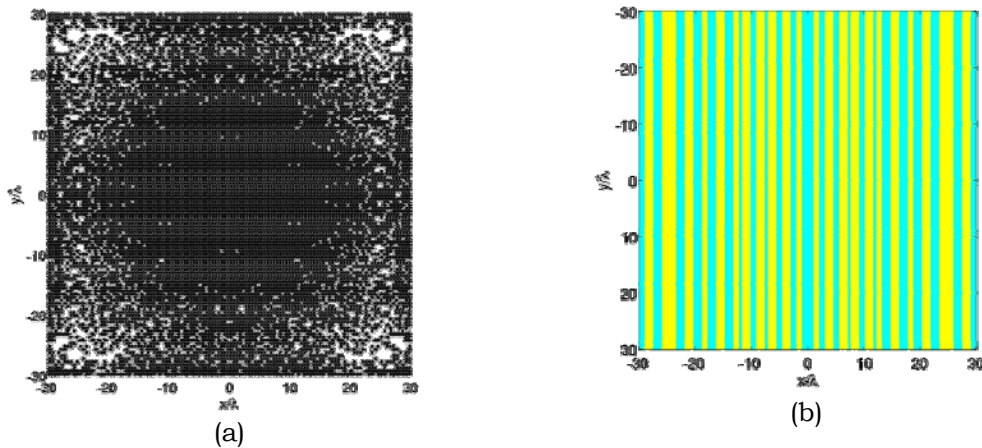


FIG. 1 – Antenna layout: (a) Thinned antenna layout; (b) Clustering layout.

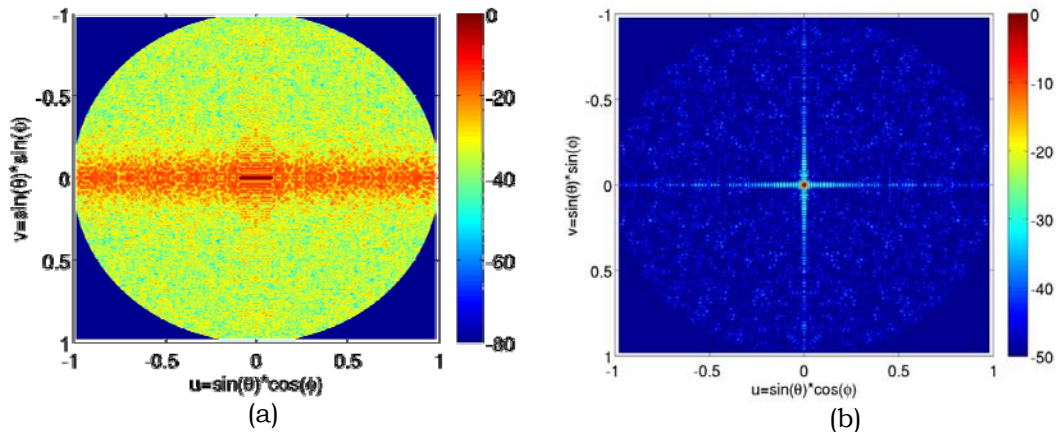


FIG. 2 – Antenna layout: (a) Tx isophoric beam; (b) Rx reference beam.

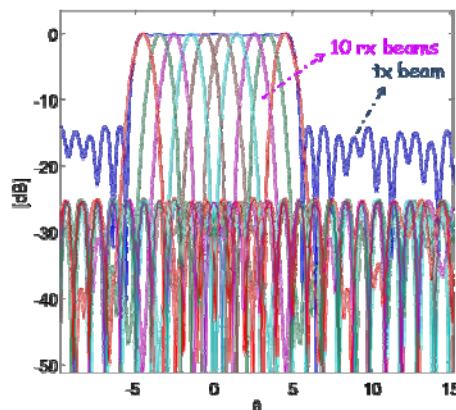


FIG. 3 –Beams in the elevation plane: Tx and the 10 simultaneous Rx beams.

REFERENCES

- [1] R.J. Mailloux, “Phased Array Handbook”, 2nd Ed., Artec House, 2005.
- [2] O. M. D’Urso, T. Isernia, “Solving some array synthesis problem by using an hybrid approach”, IEEE Trans. Ant. Prop., 55, 3, 2007.

Poster session III

D. Riccio and G. Ruello

A novel approach for the sampling of fractal surfaces in remote sensing

S. Meschino, L. Pajewski, M. Pastorino, A. Randazzo, and G. Schettini

Sub-array processing techniques applied to the detection of buried targets

Y. Pei, S. Yi, J. Zhou, R. Notarpietro, P. Savi, and M. Pini

GNSS reflectometry for Earth's surface monitoring exploiting an open-loop approach

S. Pompili, A. Di Carlofelice, P. Romano, and C. Sciannella

Spaceborne microwave interferometric radiometers: lunar sub-surface remote sensing, inverse problems and electromagnetic diagnostics

L. Pulvirenti, M. Chini, F.S. Marzano, N. Pierdicca, S. Mori, and L. Guerriero

Detection of floods and heavy rain using COSMO-SkyMed data

F. Nunziata and M. Montuori

Reflection symmetry to observe metallic targets at sea by a dual-polarimetric SAR

G. Di Martino, A. Iodice, D. Riccio, and G. Ruello

Electromagnetic characterization of speckle in SAR images

G. Olivieri

Contrast source bayesian compressive imaging by a minimum norm formulation

M. Muzi

Resolution of MEG inverse problem via reweighted ℓ_1 minimization algorithm

A. Di Carlofelice, E. Di Giampaolo, and P. Tognolatti

Electromagnetic propagation inside a module of international space station: a numerical analysis

G. Bellizzi and O.M. Bucci

Criterion for the optimal choice of the operative conditions in magnetic nanoparticle hyperthermia: uncertainty analysis

B. Bisceglia, E. Avallone, A. Buonerba, E. Caliendo, F. Chiadini, A. Grassi, L. Incarnato, A. Scaglione, and L. Guerriero

Microwave treatment of tuff-stones. Structural analysis

P. Marracino, M. Migliorati, A. Paffi, M. Liberti, G. d'Inzeo, and F. Apollonio

Signal transduction on enzymes: the effect of electromagnetic field stimuli on superoxide dismutase (SOD)

M. Cavagnaro, S. Franco, V. Lopresto, and R. Pinto

Characterization of a microwave thermal ablation process

G. Monti, L. Tarricone, M. Dionigi, and M. Mongiardo

Artificial transmission line for wireless power transmission

M. Dal Forno, P. Craievich, R. Vescovo, and C. Serpico

Microwave design studies of linear accelerators for free electron laser photoinjectors

G.L. Ravera and S. Ceccuzzi

Analysis of the FAST ICRH antenna straps array with water load using HFSS code

M. Barbuto, A. Monti, D. Ramaccia, F. Bilotti, A. Toscano, and L. Vegni

Metamaterial activities at microwave and optical frequencies at “Roma Tre” University

A NOVEL APPROACH FOR THE SAMPLING OF FRACTAL SURFACES IN REMOTE SENSING

D. Riccio, G. Ruello⁽¹⁾

⁽¹⁾ DIBET, University of Naples Federico II
Via Claudio 21, 80125 Naples, Italy
{daniele.riccio, ruello}@unina.it

Abstract

Fractal geometry is widely recognized as the most suitable instrument for describing shape of natural surfaces. The fractional Brownian motion is widely used for the description of the second order statistics of natural surfaces. In many applications, the backscattered field is of interested (instead of its averages); this computation needs appropriately describing the properties of surfaces as required by the correct representation and of the backscattered. Therefore, it arises the needs for the synthesis of fBm surfaces. In this paper we propose an innovative physical based approach for determining the conditions under which a Weierstrass-Mandelbrot predictable process can be considered as an appropriate a convenient spectral sampling of an fBm whenever the surface description its backscattered electromagnetic field are in order.

Index Terms – Electromagnetic scattering, fractals.

I. INTRODUCTION

The use of fractal geometry improved the electromagnetic scattering models and the relative instruments for radar image interpretation [1]-[2]. In particular, the fractional Brownian motion (fBm), a continuous, not differential stochastic regular process, described in terms of the pdf of its increments, is diffusely adopted in conjunction with the most used electromagnetic scattering methods, allowing the evaluation of the second order statistics of the field scattered by fractal surfaces [2].

In many applications, a first order statistical description of the electromagnetic field scattered by a fractal surface is required. Therefore, several synthesis techniques of fBm surfaces have been proposed, based on different approaches (displaced interpolation, spectral synthesis, wavelet methods and so on [3]). One of the most efficient techniques is based on the use of Weierstrass-Mandelbrot (WM) functions as spectral synthesis functions. In fact, a WM function is a predictable stochastic process that allows an easy and controllable modeling of deterministic and stochastic processes, as a function of few physical parameters [2].

The choice of the appropriate WM parameters for the representation of an fBm process with assigned roughness, is still an open problem. In this paper we propose a physical approach for determining all the synthesis parameters. In particular, we focus our attention on the parameter that governs the frequency spacing between the surface

tones, which is crucial for determining the minimum number of WM tones for describing an fBm process, and whose evaluation is still object of scientific discussion. In Section 2 we introduce the fBm and WM functions and we present the metric, and the physical criterion for determining the minimum distance under which WM and fBm processes can be considered indistinguishable. In Section 3 we present the results and the synthesis problem for the backscattered field evaluation.

II. FRACTAL SURFACES

The fBm is a regular process defined in terms of the pdf of its increments. In particular, a stochastic process $z(x,y)$ is an fBm surface if, for every x, y, x', y' , it satisfies the following relation [2]:

$$\Pr\{z(x,y) - z(x',y') < \bar{\zeta}\} = \frac{1}{\sqrt{2\pi s\tau^H}} \int_{-\infty}^{\bar{\zeta}} \exp\left(-\frac{\zeta^2}{2s^2\tau^{2H}}\right) d\zeta, \quad (1)$$

where τ is the distance between the points (x,y) and (x',y') , Pr stands for “probability” and the two parameters that control the fBm are the Hurst coefficient H ($0 < H < 1$), related to the fractal dimension D by means of the relation $D=3-H$ and the standard deviation s , measured in m^{1-H} , of the surface increments at unitary distance.

A mathematical WM is a superposition of infinite sinusoidal tones with periods spaced by an irrational factor. Natural surfaces exhibit a fractal behavior in a wide but finite range of scales. Therefore, a physical WM [4] can be obtained by using the 2-D band-limited (i.e. with a finite number of tones, P) WM function $z(x,y)$:

$$z(x,y) = b \sum_{p=0}^{P-1} C_p \nu^{-Hp} \sin\left[k_0 \nu^p (x \cos \psi_p + y \sin \psi_p) + \phi_p\right]. \quad (2)$$

The WM is described in terms of five parameters. The amplitude scaling factor b and the Hurst coefficient H can be classified as the intrinsic parameters, because they define the roughness of the surface. The fundamental tone wavenumber k_0 , the highest tone wavenumber k_{\max} and the irrational frequency scaling factor ν are the extrinsic parameters, dependent on the observation system. In remote sensing applications, the extrinsic parameters are determined by the properties of the sensor. In the radar case, the highest scale that contribute to the field is given by the illuminated area, and it determines the k_0 value; the scales under fractions of wavelength give a negligible contribution to the field-surface interaction, and this set the k_{\max} value.

The frequency factor ν value set the number of tones used to describe the surface. The closer to 1 its value is, the higher the number of tones needed to represent the surface. The choice of the ν value is crucial for

determining the WM properties and, as a consequence, the properties of the corresponding scattered field. In literature, to the author's knowledge, the choice of the frequency factor value is still an open problem.

III. PHYSICAL MODELS FOR FRACTAL SAMPLING

A significant equivalence between the WM and fBm processes was found in the spectral domain. The fBm exhibits the typical power law spectrum [4], and the spectrum of the WM process is evaluated by applying the Wiener – Kintchine theorem [2]. The spectral powers of these two stochastic processes were compared in concentric annular regions of radii $(k_p \nu^{0.5}, k_p \nu^{0.5})$. It was proved that, for every ν value, the power of the fBm and the WM processes coincides if the amplitude factor b is appropriately evaluated as a function of the fBm spectral parameters and the ν value [2]. The obtained relation is an integral condition, that ensures that the power obtained by integration of the power-density spectrum associated to the two processes is the same. For every ν value, an appropriate b value that allows to fulfill this condition always exists. As an example, in Figure 1, the spectra of WM and fBm processes with the same fractal parameters ($s=0.01, H=0.8$) are compared for two ν values. This comparison reveals that the equivalence of the power is not sufficient for determining the equivalence of the two processes. In the graphs of Fig. 1 it is evident that the local spectral difference falls off for decreasing ν values.

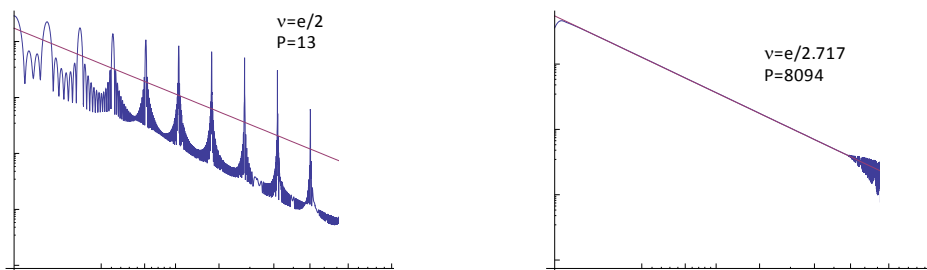


FIG. 1 – Spectral comparison between fBm (purple line) and WM (blue line) for $\nu=e/2$ (left) and $\nu=e/2.717$ (right).

In this paper, we propose to define the distance between the two processes as the absolute difference between the fBm and the WM spectra, integrated in the bandwidth of interest. Once this norm has been defined, it is possible to define a distance threshold under which the two processes can be considered undistinguishable. Such a procedure allows the evaluation of the minimum ν value, that will be function of the surface roughness and the required precision.

It turns out that tens WM tones are needed to represent an fBm with precision of the order of the surface overall amplitude. In terms of

scattered field, it means that we need hundreds of thousands of modes to represent the field, and this is unacceptable for numerical computation of the scattered field with general purpose computers. Anyway, the electromagnetic field scattered from a fractal surface is an integral of contributions coming from different parts over the whole surface. Therefore, different criteria can be adopted for the sampling of the field. In this case, we work in the space domain, where we can easily define the difference between the processes as the distance between the radar cross sections. Hence, our idea is to employ reliability of the backscattered field as a measure for similarity of the surface representations. The resulting number of tones turns out to be reduced by one order of magnitude, with an exponential decrease of the number of modes needed for representing the backscattered field. The presented method is the first physical approach for determining the sampling of fBm surfaces by means of WM functions.

IV. CONCLUSION

In this paper an innovative physical approach for synthesis of fBm surfaces and their backscattered field is presented. It is shown that the synthesis procedure are firmly linked. The surface synthesis is performed in the spectral domain. The power law spectrum of the fBm is the target function, the WM tones are the synthesis functions and a distance criterion was appropriately defined. The proposed procedure allows the evaluation of the minimum frequency spacing parameter that allows the required precision with the minimum complexity. The same rationale (definition of target and synthesis functions and of a proper metric) has been performed in the spatial domain for comparing the electromagnetic field scattered by fBm and WM surfaces.

The proposed approach provides the solution for the a very efficient representation of a fractal surface, that holds details at any scale, whenever a reliable evaluation of its backscattered field is of interest.

REFERENCES

- [1] B. B. Mandelbrot, *The Fractal Geometry of Nature*, New York: W.H. Freeman & C., 1983.
- [2] G. Franceschetti, D. Riccio, *Scattering, Natural Surfaces and Fractals*, Academic Press, Burlington, MA (USA), 2007.
- [3] W. M. Krueger, S. D. Jost and K. Rossi, "On Synthesizing Discrete Fractional Brownian Motion with Applications to Image Processing", *Graphical Models and Image Processing*, vol. 58, no.4, pp. 334-344, 1996.
- [4] Austin R. T., England A. W., Wakefield G. H., "Special Problems in the Estimation of Power-Law Spectra as Applied to Topographical Modeling", *IEEE Trans. Geosci. And Remote Sensing*, vol. 32, pp. 928-939, July 1994.

SUB-ARRAY PROCESSING TECHNIQUES APPLIED TO THE DETECTION OF BURIED TARGETS

S. Meschino⁽¹⁾, L. Pajewski⁽¹⁾, M. Pastorino⁽²⁾,
A. Randazzo⁽²⁾, and G. Schettini⁽¹⁾

- ⁽¹⁾ Applied Electronics Department, “Roma Tre” University
Via della Vasca Navale 84, 00146 Rome, Italy
{smeschino; pajewski; schettin}@uniroma3.it
- ⁽²⁾ Department of Naval, Electrical, Electronic, and
Telecommunication Engineering, University of Genoa
Via Opera Pia 11A, 16145 Genova, Italy
{matteo.pastorino; andrea.randazzo}@unige.it

Abstract

A sub-array processing (SAP) technique for the localization of conductive buried objects is proposed. A Direction of Arrival (DoA) approach is implemented by using two different methodologies: a bearing algorithm based on the conventional MULTIPLE SIGNAL CLASSIFICATION (MUSIC) implementation is compared with a Kernel-based technique, such as Support Vector Machines (SVM). An array of sensors is considered and partitioned in sub-arrays. A dominant DoA is found for each sub-array. By triangulating the DoAs, a crossing pattern is derived and it is statistically processed in order to estimate the object position.

Index Terms – Buried object detection, sub-array processing, direction of arrival estimation.

I. INTRODUCTION

Localization of buried objects is a very important topic in near-surface probing applications [1]. Many techniques have been proposed for the solution of the electromagnetic inverse scattering problem by buried obstacles. Methods based on Born, Rytov [2], or Kirchhoff [3] approximations, microwave-holography algorithms [4], diffraction tomography techniques [5], and stochastic approaches (as the SVM and Markov chains [6-7]) can be employed. The use of neural networks has been also introduced, showing good performances [8]. In this context, we followed the Direction-Of-Arrival (DoA) technique proposed in [9], by performing a comparison between MUSIC and SVM approaches.

By assuming that the field backscattered by cylinders buried in the ground behaves like a narrowband source, and that the objects are placed in the far zone of the antennas, the received field can be considered as a plane wave. In order to localize also objects placed close to the air-ground interface, the array can be partitioned in sub-arrays, so that for each sub-array the far-field condition is fulfilled. Applying DoA methods, a dominant DoA for each sub-array can be found and, by triangulating the whole set of DoAs, a crossing pattern can be obtained, showing the object location. Since the backscattered signal is supposed to be affected by zero-mean Gaussian noise, some sparse crossings, determined by false DoAs, are also present. They are removed by using a statistical procedure [9]. Finally, the cylinder position is estimated.

II. OUTLINE OF THE APPROACH

A set of M_{PEC} PEC circular cylinders is considered, having radii a_m and buried at depths h_m ($m=1, \dots, M_{\text{PEC}}$) in a homogeneous half space characterized by a relative dielectric permittivity ϵ_r (Fig. 1). The cross sections of the cylinders are centered at (x_m^c, z_m^c) . The scenario is illuminated by a plane wave and the scattered electric field is measured by means of N_{array} antennas uniformly spaced along the air-ground interface. The distance between two adjacent antennas is denoted as d .

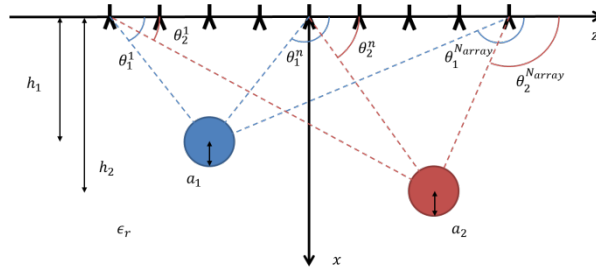


FIG. 1 – Geometrical configuration.

The Cylindrical Wave Approach (CWA) [10] is used to numerically compute the electric field scattered by the cylinders and propagated back to the antennas through the air-ground interface.

The collected electric field samples are processed in order to extract information about the location of the cylinder.

The following model is used for the estimation of the DoAs of M waves on a sub-array of N antennas

$$\mathbf{y} = \begin{bmatrix} y_1 \\ \vdots \\ y_N \end{bmatrix} = \mathbf{A} \begin{bmatrix} s_1 \\ \vdots \\ s_M \end{bmatrix} + \begin{bmatrix} n_1 \\ \vdots \\ n_N \end{bmatrix} = \mathbf{A}\mathbf{s} + \mathbf{n} \quad (1)$$

where s_m ($m = 1, \dots, M$) are the outputs of the first element of the sub-array assumed as reference, n_i ($i = 1, \dots, N$) are the output noises of sub-array elements, the steering matrix is $\mathbf{A} = [\mathbf{a}(\theta_1) \ \mathbf{a}(\theta_2) \ \dots \ \mathbf{a}(\theta_M)]$ being $\mathbf{a}(\theta) = [1, e^{-jkd \sin \theta}, \dots, e^{-jk(N-1)d \sin \theta}]^t$ the steering vector ($(\cdot)^t$ denotes transposition and $k = \omega(\epsilon_r \epsilon_0 \mu_0)^{0.5}$ is the wavenumber in the hosting medium), and θ_m ($m = 1, \dots, M$) are the DoAs of the impinging waves. The covariance matrix is computed, defined as $\mathbf{R} = E\{\mathbf{y}\mathbf{y}^H\} = \mathbf{A}\mathbf{R}_{ss}\mathbf{A}^H + \mathbf{R}_{nn}$, being $\mathbf{R}_{ss} = E\{\mathbf{s}\mathbf{s}^H\}$ and $\mathbf{R}_{nn} = E\{\mathbf{n}\mathbf{n}^H\}$ the source and noise correlation matrices and $(\cdot)^H$ the Hermitian transposition.

The MUSIC algorithm [12] extracts information about the DoAs by exploiting the properties of noise eigensystem, i.e., the $(N - M)$ eigenvectors corresponding to the smallest eigenvalues. In particular, it results that the quantity $[\mathbf{a}^H(\theta)\mathbf{E}\mathbf{E}^H\mathbf{a}(\theta)]$, being \mathbf{E} the subspace spanned by the noise eigenvectors, vanishes for $\theta = \theta_m$. DoAs are obtained by computing the “peaks” of the MUSIC pseudospectrum $P(\theta)$ given by:

$$P(\theta) = [\mathbf{a}^H(\theta)\mathbf{E}\mathbf{E}^H\mathbf{a}(\theta)]^{-1} \quad (2)$$

The SVR method [13] computes the DoAs by using Support Vector Machines [14], which are trained by considering a set of L_{train} samples

of the input/output values of the mapping (i.e., L_{train} values of the DOA, $\tilde{\theta}_m^l$, $l = 1, \dots, L_{train}$, with the corresponding values of the covariance matrix, \mathbf{R}_{train}^l , $l = 1, \dots, L_{train}$). In particular, the m th DOA is computed as

$$\theta_m = \sum_{l=1}^{L_{train}} (\alpha_l - \alpha'_l) \psi(\mathbf{z}_{train}^l, \mathbf{z}) + b \quad (3)$$

where α_l , α'_l , and b are parameters obtained during the training stage, \mathbf{z} and \mathbf{z}_{train}^l are arrays containing the elements of the covariance matrices of the training samples and of the current measured values, respectively, and ψ is a Gaussian kernel.

A triangularization algorithm is applied to all the DoAs found by sub-arrays. The DOA crossings are modeled by Poisson distributions and a testing procedure is employed in order to extract the window set belonging to the scatterer. The cylinder-axis coordinates are estimated, by averaging the crossing coordinates in the scatterer region.

III. NUMERICAL RESULTS

An example of the results provided by the previously described approach is reported in the following. A single metallic cylinder of radius $a = \lambda$ (being λ the free-space wavelength) is buried at depth $h = 2.5\lambda$ in a medium characterized by $\epsilon_r = 9$. The center of the cylinder has an offset of $z = 2.5\lambda$ with respect to the center of the receiving array. A set of $N_{array} = 51$ antennas is used to collect the scattered electric field and it is partitioned into 17 sub-arrays composed by $N = 3$ elements. The electric field values computed by the CWA have been corrupted by a Gaussian noise with zero mean value and variance 0.25. The SVM is trained by using $L_{train} = 180$ uniformly-distributed DoAs and by setting the hyper-parameters [14] to $C = 100$, $\epsilon = 10^{-6}$, and $\gamma = 0.5$. The false-alarm probability is set equal to 10^{-6} and the region of interest is divided in square windows of side $\lambda/2$.

Figs. 2(a) and 2(b) show the DoAs (represented as the directions of the plotted lines) and the crossing patterns provided by the two considered approaches (MUSIC- and SVR-based ones, respectively). As expected, in both cases the DoA lines intersect near the center of the cylinder. The crossing are more crowded near the cylinder. The relative localization errors are comparable for both the approaches ($e = 0.41$ MUSIC-based one and $e = 0.47$ for the SVR-based one).

IV. CONCLUSION

In this work a sub-array procedure for the estimation of the position of buried conductive cylindrical objects is considered. The localization problem is solved by employing a DoA estimation approach. A statistical technique is applied for the extraction of the coordinates of the objects. Two different bearing algorithms are implemented and compared, based on MUSIC and SVM methods, respectively. Future research activities will be devoted to the extension of the procedure to lossy media.

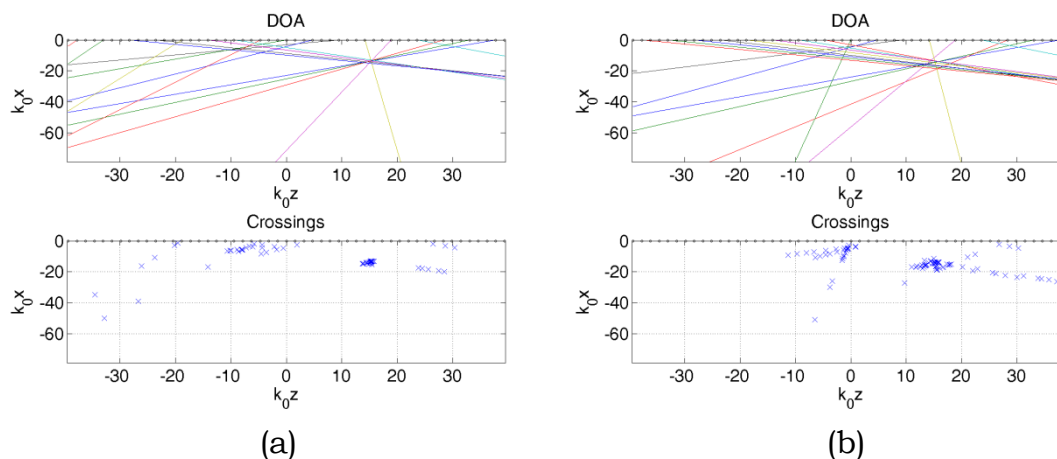


Fig. 2 – DOAs and crossing patterns for (a) MUSIC and (b) SVR.

REFERENCES

- [1] D. J. Daniels, *Ground Penetrating Radars*, 2nd ed. London, U.K.: IEE, 2004.
- [2] W. B. Beydoun and A. Tarantola, "First Born and Rytov approximations: Modeling and inversion conditions in a canonical example," *J. Acoust. Soc. Am.*, vol. 83, no. 3, pp. 1045-1055, Mar. 1988.
- [3] F. Soldovieri, A. Brancaccio, G. Prisco, G. Leone, and R. Pierri, "A kirchhoff based shape reconstruction algorithm for the multimono-static configuration: the realistic case of buried pipes," *IEEE Trans. Geosci. Remote Sensing*, vol. 46, no. 10, pp. 3031-3038, Oct. 2008.
- [4] N. Osumi and K. Keno, "Microwave holographic imaging methods with improved resolution," *IEEE Trans. Antennas Propagat.*, vol. AP-32, no. 10, pp. 1018-1026, Oct. 1984.
- [5] L. Chommeloux, C. Pichot, J.C. Bolomey, "Electromagnetic modeling for microwave imaging of cylindrical buried inhomogeneities," *IEEE Trans. Microwave Theory Tech.*, vol. MTT-34, no. 10, pp. 1064-1076, Oct. 1986.
- [6] A. Massa, A. Boni, and M. Donelli, "A classification approach based on svm for electromagnetic subsurface sensing," *IEEE Trans. Geosci. Remote Sensing*, vol. 43, no. 9, pp. 2084-2093, Sept. 2005.
- [7] S. Caorsi, C. L. Gagnani, S. Medicina, M. Pastorino, G. Zunino, "Microwave imaging based on a Markov random field model," *IEEE Trans. Antennas Propagat.*, vol. AP-42, no.3, pp. 293-303, Mar. 1994.
- [8] E. Bermani, S. Caorsi, M. Raffetto, "An inverse scattering approach based on a neural network technique for the detection of dielectric cylinders buried in a lossy half-space," *Prog. Electromagn. Res.*, vol. 26, pp. 69-90, 2000.
- [9] A. Şahin, E. L. Miller, "Object detection using high resolution near-field array processing," *IEEE Trans. Geosci. Remote Sensing*, vol. 39, no. 1, pp. 136-141, Jan. 2001.
- [10] M. Di Vico, F. Frezza, L. Pajewski, and G. Schettini, "Scattering by a Finite Set of Perfectly Conducting Cylinders Buried in a Dielectric Half-Space: a Spectral-Domain Solution," *IEEE Trans. Antennas Propagat.*, vol. 53, pp. 719-727, Feb. 2005.
- [11] L.C. Godara, *Smart Antennas*, CRC Press LLC, Boca Raton 2004.
- [12] S. Meschino, L. Pajewski, and G. Schettini, "Use of a Sub-Array Statistical Approach for the Detection of a Buried Object," *Near Surface Geophysics*, vol. 8, no. 5, pp. 365-375, Oct. 2010.
- [13] M. Pastorino and A. Randazzo, "A Smart Antenna System for Direction of Arrival Estimation based on a Support Vector Regression," *IEEE Trans. Antennas Propagat.*, vol. 53, no. 7, pp. 2161-2168, July 2005.
- [14] V. Vapnik, *Statistical Learning Theory*. New York: Wiley, 1998.

GNSS REFLECTOMETRY FOR EARTH'S SURFACE MONITORING EXPLOITING AN OPEN-LOOP APPROACH

Y. Pei⁽¹⁾, S. Yi⁽¹⁾, J. Zhou⁽¹⁾, R. Notarpietro⁽¹⁾, P. Savi⁽¹⁾, M. Pini⁽²⁾

(1) Politecnico di Torino, Dip. di Elettronica e Telecomunicazioni

(2) Istituto Superiore Mario Boella

Corso Duca degli Abruzzi 24, 10129 Torino, Italy

riccardo.notarpietro@polito.it

Abstract - *In the framework of the regional Italian project SMAT-F1, an experimental campaign using small aircraft flying an area above Vercelli (Piedmont, North Italy) was performed to remotely sense rice fields' flooding state by applying Global Navigation Satellites System Reflectometry (GNSS-R) technique. Both direct and reflected GPS signals (the latest exploiting a bistatic configuration) were collected by the receivers mounted on the aircraft. The reflected signal was processed using Delay Doppler Maps and Delay Waveforms (DM) to evaluate Signal to Noise Ratio (SNR) in order to investigate the correlation with soil moisture. Final results not only indicated high spatial correlation between powers measured considering two close specular tracks observed from two GPS satellites, but also shown great agreement between processed SNRs and the surface conditions, including flooding or not, fields or boundaries.*

Index Terms – GNSS reflectometry, Soil moisture, Delay Doppler Maps.

I. INTRODUCTION

As it is well known, Global Navigation Satellite Systems (GNSS) signals, commonly processed for navigation purposes, can also be used to characterize media where they propagate in. Applications can be found for the remote sensing of the atmosphere - for example the total integrated wet part of troposphere, its three/four dimensional distribution using tomographic algorithms - or the extraction of very accurate and high resolved atmospheric refractivity vertical profile using the GNSS Radio Occultation technique (see [1] for an overview). Moreover, the reflected and scattered GNSS signals have potential to remotely sense the Earth's surface, considering the so-called GNSS Reflectometry (GNSS-R), where a GNSS receiver can be used in a bistatic configuration. The technique is becoming more and more important from the last decades, although it needs refinements and further validation in many cases. This paper presents an analysis on GNSS reflected signals measured on rice fields for flooding detection considering an open loop approach for the processing of raw data collected by a fully software GPS receiver.

II. DESCRIPTION OF THE SYSTEM AND OF THE MEASUREMENT CAMPAIGN

During the regional SMAT-F1 project [2], GNSS signals were collected after reflection and scattering from rice fields and used to monitor the fields' flooding status. A prototype based on a Software Defined Radio solution was developed, using a navigation software receiver, the NGene Software receiver, developed by NAVSAS group of Politecnico di Torino [3]. The instrument is highly reconfigurable, since it collects raw I and Q IF samples of the incoming signals (both for the direct and the

reflected one). A sampling frequency of 8.1838 MHz is used, giving about 8 samples per C/A code chip. The architecture is shown in Fig.1.

FIG. 1 – Architecture of software defined radio.

During a measurement campaign on May 2011, an experiment was performed by flying over an area above Vercelli (Piedmont region, North Italy). The receiving system was placed on board a small aircraft in order to track reflections from rice fields. Since rice fields were flooded during that month, they were a perfect scenario to study reflection phenomena.

The receiving system consists of two antennas; one pointed toward the zenith was able to receive direct RHCP (Right Handed Circular Polarization) GPS signals used for positioning purposes. The other antenna was pointing in the nadir direction and was used for receiving reflected signals. The geometry of reflections was analyzed and all the satellites with elevation lower than 33° were discarded, since below this elevation the specular reflections did not enter inside the half power beamwidth of the LHCP nadir looking antenna. On board the aircraft, a video camera was placed to see which fields were really flooded during the acquisition. The panoramic view extracted from the video was superimposed on Google Maps, together with the specular reflection points.

The RHCP data were processed using the NGene software receiver to give the positions of the aircraft and of the GPS satellites. These positions were further used to calculate the positions of specular points (a spherical flat Earth was considered). The reflected LHCP raw data were instead processed by generating Delay Doppler Maps and Delay Waveforms to evaluate Signal to Noise Ratio (SNR) using an “open loop” approach. Delay Doppler Maps (DDM) are the output of the autocorrelation between received signal and local replica of GPS C/A code in both delay (range) and Doppler frequency domain. A Delay Waveform (DW) is a row of the DDM (extracted considering a constant Doppler frequency). In a closed loop receiver (like the NGene one), the DW containing the correlation absolute maxima is used to derive the peak value and the values associated to the previous and the following autocorrelation lags. These are enough for tracking purposes and to allow the receiver to compute the final position. We instead preferred to look for and to store the entire autocorrelation function (the entire DW row) for each millisecond of data (which is the GPS C/A code length). This DW row is characterized by a certain Doppler shift and is the one containing the peak of the autocorrelation function. In the next millisecond, only autocorrelations evaluated for the nearest Doppler shifts are computed, avoiding the evaluation of the entire DDM.

This is something similar to an “open loop” approach, which makes available the entire autocorrelation function and not only its peak, which is automatically identified in the closed loop approach. In future operations, this open loop approach will be necessary to remotely sense other characteristics of the surface, such as wind over sea or sea state, considering reflections above oceans [4].

Usually, single DDMs and DWs generated from a period of GPS C/A code (1 ms) cannot be used to detect the reflected signal power, since this signal power is too attenuated by the surface, and SNR is consequently too low. Therefore, several summations (incoherent integration) are needed in order to reveal the real signal shape and to eliminate the fading noise effects. After a few experiments and comparisons, a final incoherent integration over 500 ms time intervals has been chosen to process the whole data set. Therefore, a set of continuous SNR values was obtained every 0.5 s. Such data can be exploited to evaluate average surface condition (soil moisture).

III. RESULTS

During the planned flight measurement campaign, reflections of signals transmitted by several GPS satellites were observed. Using the method described in the previous section, the total data set acquired during the experiment was processed. For each available satellite, and with a 0.5 s sample time, a SNR value related to the reflected power is recorded. Aircraft positions derived by processing the navigation data (using the NGene Software Receiver) were interpolated for each sample time, and the corresponding specular points were computed and georeferenced. At each specular point position was associated the SNR evaluated considering the open loop approach. An example of the results obtained is shown in Fig. 2 and Fig. 3.

FIG. 2 – Total SNR results during the whole flight from satellite 5, 8 and 26. Black curve indicates the flight track. See Fig.3 for the details related to red rectangular zoom.

In order to show some further details, SNRs recorded in the area included in the red rectangle in Fig. 2 are given in Fig. 3. Here SNRs related to reflected signals from two different satellites (8th and 26th) were georeferenced and shown on a Google map. Dark (blue) color corresponds to dry fields while light (red) colors are associated with high humidity fields (flooding ones). First of all, it has to be noticed the high spatial correlation between the two tracks since they are close to each other and are expected to have similar behaviors of SNRs. Moreover, SNR values seem to have good correlation also with the flooding state of the fields. In the image at the bottom of Fig. 3, the picture taken from video camera is superimposed on Google map. In this case, sun glitters

allows recognizing flooded areas. Finally, these results also showed a high sensitivity with boundaries between two flooded fields.

FIG. 3 – Specular reflection point tracks with SNR from satellite 8 and 26 superimposed on Google Maps (top and center) and on an image taken by the video camera (bottom)

IV. CONCLUSIONS

The result of this measurement campaign is encouraging, since it gives an accurate SNR output which seems to be very sensitive and coherent with the surface's soil moisture changes. Moreover, this experiment allows us to implement the possibility to extract the entire autocorrelation function related to the reflected signal in an "open loop" fashion, which will be necessary for measuring other parameters than the soil moisture. Future work is needed to improve the remote sensing algorithms necessary to derive geophysical information of the surface around the specular point.

ACKNOWLEDGEMENT

Authors are grateful to Regione Piemonte for funding the SMAT-F1 project; ISMB and Digisky for the development of the experimental campaign over rice fields and to NAVSAS group for providing the NGene receiver.

REFERENCES

- [1] R. Notarpietro, M. Cucca and S. Bonafoni, "GNSS Signals: A Powerful Source for Atmosphere and Earth's Surface Monitoring," *Remote Sensing of Planet Earth*, ed. by Y. Chemin, 2012, pp. 171-200.
- [2] SMATF1, <http://www.smatf1.polito.it/>
- [3] M. Fantino, A. Molino, P. Mulassano, M. Nicola, and M. Pini, "N-Genie: A GPS and Galileo Fully Software Receiver," *Proceedings of SDR-Italy'09 Workshop – From Software Defined Radio to Cognitive Networks*, Pisa, Italy, July 2-3, 2009.
- [4] S. Gleason, "Remote Sensing of Ocean, Ice and Land Surfaces Using Bistatically Reflected GNSS Signals From Low Earth Orbit," PhD Dissertation, University of Surrey, 2006.

SPACEBORNE MICROWAVE INTERFEROMETRIC RADIOMETERS: LUNAR SUB-SURFACE REMOTE SENSING, INVERSE PROBLEMS AND ELECTROMAGNETIC DIAGNOSTICS

S. Pompili^(1,2), A. Di Carlofelice⁽¹⁾, P. Romano⁽³⁾, C. Sciannella⁽⁴⁾

⁽¹⁾ Dept. of Electrical and Information Engineering, University of L'Aquila, Via Giovanni Gronchi 18, 67100 L'Aquila, Italy

⁽²⁾ Observation Systems and Radar Business Unit, Thales Alenia Space Italia, Via Saccomuro 24, 00131 Rome, Italy

⁽³⁾ Adaptive Micronano Wave Systems Group, Lausanne, Switzerland

⁽⁴⁾ Dept. of Information Engineering, "La Sapienza" University of Rome, Via Eudossiana 18, 00184 Rome, Italy

Abstract

In this paper we propose a mission concept, called Lunar Interferometric Radiometer by Aperture Synthesis (LIRAS), which addresses the high-resolution mapping and vertical sounding of the Moon sub-surface for planetary analysis and studies. This is done by taking advantage of the antenna aperture synthesis technique applied to a multi-frequency microwave passive payload. The final objectives of this study are to demonstrate the technical feasibility of the LIRAS project and then, with the aid of microwave simulations of Moon soil behavior and the synthetic antenna aperture, to present its preliminary design.

Index Terms – Interferometry, remote sensing of the Moon, microwave radiometry, synthetic aperture radiometry.

I. INTRODUCTION

There is nowadays a renewed and growing interest in returning to the Moon. The current target of the envisaged lunar missions is to establish a permanent presence in order to start a new era of Moon exploration and exploitation. To pursue this aim, some products of interest such as the characterization of the surface microwave (MW) emissivity, the sub-surface thermal properties and the anomalies of regolith layer, can help the space mission designers to choose lunar sites where focus their attention. Satellite MW radiometry can represent a tool to satisfy these requirements exploiting the advantage of being a passive instrument.

This work aims to describe the Lunar Interferometric Radiometer by Aperture Synthesis (LIRAS) mission concept that takes advantage from the Soil Moisture and Ocean Salinity (SMOS) mission for earth observation purposes [1], [2]. The paper is organized into four sections: Section II briefly describes the basic concept of the LIRAS system design, Section III presents the LIRAS L-band imaging simulator and Section IV where conclusions are drawn.

II. PRELIMINARY PAYLOAD DESIGN

The LIRAS mission is devoted to the design of a small satellite at an orbit height of about 100 km, with a revisiting time period less than one

Lunar month and equipped with two multi-frequency MW radiometers: a high-resolution synthetic aperture radiometer and a real aperture radiometer. For sub-surface sounding purposes the envisaged frequencies are at 1 GHz and 3 GHz, whereas for near-surface probing two frequencies at 12 GHz and 24 GHz are foreseen [3]:

- 1) *Sub-Surface Sounding Payload (SS-PL)*: the S and L-band channels will be implemented through a Y-shaped interferometric array with three arms less than 2.5 m long, obtaining spatial resolutions less than 5 km at surface, penetration depth within the first 5 m in the lunar sub-surface and an imaging swath of at least 100 km.
- 2) *Near-Surface Mapping Payload (NS-PL)*: the Ku and K-band channels will be implemented through nadir pointing real-aperture corrugated conical horn antennas with a spatial resolution less than 20 km.

Heritage has been considered for the design process. The SS-PL has been designed sizing its equipment on SMOS Microwave Imaging Radiometer using Aperture Synthesis (MIRAS) payload [1]. For the NS-PL preliminary baseline design the ESA's European Student Moon Orbiter (ESMO) mission has been considered, since one of the possible scientific payloads embarked by ESMO is a real aperture multi-frequency radiometer: Microwave Radiometric Sounder (MiWaRS) [4].

III. LIRAS IMAGING SIMULATOR

The design of the aperture synthesis L-band radiometer, that establishes the maximum size of the payload, has been obtained with the aid of the Matlab® simulation tool. Since the LIRAS spacecraft orbit is a Moon frozen orbit, a performance trade-off has been carried out in order to optimize both number of receivers and inter-element spacing to meet performance requirements throughout the entire orbit [5]. For simulations following “worst-cases” have been considered: (a) a minimum height of 70 km; (b) a maximum height of 130 km.

Simulations have been carried out by considering MIRAS operational parameters, listed in Table I, and under the hypothesis of identical receiver pre-detection sections, absence of spatial decorrelation effects and computing the radiometric resolution considering baseline redundancy effects [6].

The minimum number of receiving antenna elements has been identified as 10 Lightweight Cost-Effective MW receivers (LICEF) on each side of the Y-shaped array, whose minimum baseline, d , equals 0.8λ . This choice differs from the spacing which has been selected for MIRAS, where single antenna receiving elements are spaced 0.89λ [1].

TABLE I - OPERATIONAL PARAMETERS USED FOR THE SIMULATIONS.

Symbol	Quantity	Value
f_0	<i>central frequency</i>	1.413 GHz
B	<i>bandwidth</i>	20 MHz
T_{REC}	<i>equivalent receiver noise temperature</i>	80 K
G	<i>equivalent gain of LICEF antennas</i>	0 dBi
T_b	<i>Uniform target brightness temperature scene</i>	245 K

The advantages of a smaller spacing are: (1) larger swath width and (2) larger alias-free field of view. The swath may be defined as:

$$swath = 2 \cdot H \cdot \operatorname{tg}\left(\frac{FOV}{2}\right) \propto H \cdot \frac{\lambda}{D} \quad (1)$$

where H is the orbital height and FOV is the field of view of the instrument, directly proportional to wavelength (λ) and inversely proportional to minimum baseline (D). Concerning the second point, since discrete sampling produces spatial periodicity, it can be proven that sampling frequencies above the Nyquist frequency limit, which is $\lambda/3$ for hexagonally shaped sampling grids [7], produce periodically overlapping instantaneous FOVs. The spacing $d = 0.8\lambda = 16.99$ cm derived from simulations meets the spatial resolution requirement for a configuration of 30 LICEF receivers in worst case ($H = 130$ km) by providing optimum FOV extension, reducing the aliased area and still providing enough physical space to accommodate LICEF receivers whose diameter is equal to 16.5 cm $= 0.78\lambda$.

The radiometric resolution ΔT calculated by simulating tool is:

$$\Delta T = \left[\frac{T_{sys}}{\sqrt{2B\tau}} \right] \frac{A_{syn}}{NA_e} \quad (2)$$

where B is the system bandwidth, τ the integration time, T_{sys} the system noise temperature, A_{syn} the synthesized equivalent area and N and A_e parameters depending on number and physical dimensions of the LICEF antennas. According to mission requirements, ΔT shall be maintained within 0.5 K. Since the spacecraft experiences large height variations during its orbital time [7], both spatial and radiometric resolutions can be maintained for the same antenna configuration only by means of digital signal processing of the final data product (Fig. 1a).

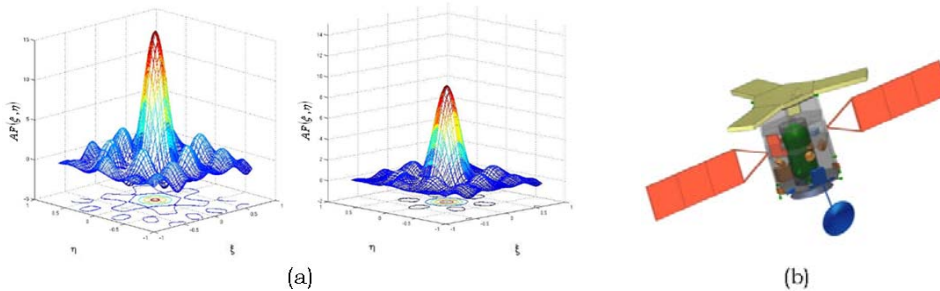


FIG. 1 – (a) Simulation of the Array Factor, or AF, for a Y-shaped array using Rectangular (left) and Triangular weighting function (right). Radiometric resolution is progressively improved at the expense of spatial resolution using increasingly tapered functions. (b) Spacecraft deployed configuration.

The data-rate calculation assumes that the instrument is capable of quantizing each pixel with 10 bits: the dynamic of T_b values emitted by the Moon in the low MW frequency region extends from ca. 90 K to 360 K and is quantized according to radiometric resolution at 0.5 K steps. According to satellite velocity ($v = 1.58 \cdot 10^3$ m/s) and τ , the data-rate is:

$$DR = \frac{2 \cdot N_{bit} \cdot N_V}{\tau} \quad (3)$$

where N_V is the number of non redundant samples which may be calculated as $N_V = 6N_{el}^2 + 6N_{el} + 1$ for a Y-shaped thinned array.

IV. CONCLUSION

Some major advantages of the performed studies may be synthesized as follows. 1) The heritage based and simple design considerations allow designing a system characterized by a low amount of novel elements. 2) The aperture synthesis principle adopted in LIRAS requires to deploy single one-piece antenna arms [Fig. 1b]. With respect to SMOS payload three-tiled antenna arms configuration the LIRAS deployment system provides implicit robustness. 3) The antenna configuration has been optimized in terms of component number and mass budget in a way allowing to accommodate a further real aperture radiometer. 4) The real aperture radiometer provides data products which both may be considered as ancillary data to the interferometric measurements, complementing in depth measurements with near surface sounding and representing also a “stand-alone” scientific product.

ACKNOWLEDGEMENT

This work was supported by ASI in collaboration with engineers of TAS-I and professors of University “La Sapienza” of Rome and University of L’Aquila. The pre-feasibility study was carried out at the Concurrent Design Facility of the University of Rome “La Sapienza” in the frame of the IX edition of the “Master in Satelliti e Piattaforme Orbitanti”.

REFERENCES

- [1] SMOS Team, “MIRAS SMOS Payload”, *ESA SMOS Information Day*, University of Porto, 2003.
- [2] C.S. Ruf, C. T. Swift, A. B. Tanner and D. M. Le Vine, “Interferometric synthetic aperture microwave radiometry for remote sensing of the Earth”, *IEEE Trans. Geosci. Remote Sensing*, Vol. 26, No 5, pp. 597-611, 1988.
- [3] F. S. Marzano, P. Tognolatti, M. Montopoli, A. Di Carlofelice, “Lunar Imaging Radiometer by Aperture Synthesis for thermo-morphological sub-surface mapping”, *Mission Requirements Document*, v02/06, May 2011.
- [4] R. Walker and M. Cross, “The European student moon orbiter (ESMO) project attracting and training a new generation of Lunar explorers”, *Acta Astronautica*, vol.66, pp.1177–1188, 2010.
- [5] MasterSat9 Team, “Study Report LIRAS”, *MasterSat Concurrent Design Facility (CDF)*, University of Rome, June 2011.
- [6] M. Scigliano, C. Sciannella, S. D’Addio, P. Angeletti and G. Schettini, “Analysis of the effect of baseline redundancy on synthetic aperture interferometric radiometers performance”, *IEEE Antennas and Propagation Society Int. Symposium (APSURSI)*, 2010.
- [7] A. Camps, I. Corbella, J. Barà and F. Torres, “Radiometric Sensitivity Computation in Aperture Synthesis Interferometric Radiometry”, *IEEE Trans. Geoscience and Remote Sensing*, v.36, n.2, March 1998.

DETECTION OF FLOODS AND HEAVY RAIN USING COSMO-SKYMED DATA

Luca Pulvirenti⁽¹⁾, Marco Chini⁽²⁾, Frank S. Marzano⁽¹⁾, Nazzareno Pierdicca⁽¹⁾, S. Mori⁽¹⁾, Leila Guerriero⁽³⁾

⁽¹⁾ Dept. Information Engineering, Electronics and Telecommunications, Sapienza University of Rome, Italy

⁽²⁾ Istituto Nazionale di Geofisica e Vulcanologia, Rome, Italy

⁽³⁾ Dept. Computer Science, Systems and Production, TorVergata University of Rome, Italy

Abstract

This paper presents a severe weather event that occurred in Northwestern Italy observed from space by the ©COSMO SkyMed X-band radar developed by ASI. The study presents a methodology to detect water surfaces, as well as areas in which heavy rain is present. The methodology is based on a combined use of electromagnetic scattering models and image processing techniques and uses also ancillary data, such as optical images, land cover maps and a digital elevation model (DEM).

Index Terms – Synthetic Aperture radar, propagation, surface scattering, flood mapping.

I. INTRODUCTION

When X-band SARs are used to monitor severe weather events, in which both heavy precipitation and flooded areas are present in the observed scenario, the attenuation of the radar signal due to precipitation implies that the microwave radar signature of rain can be similar to that of water surfaces, so that the discrimination among permanent water bodies, flooded areas and areas affected by significant rainfall is not easy and may need to use ancillary data, as well as a certain amount of supervision [1]. The shadowing effects due to the topography, as well as the possible presence of wet snow that absorbs X-band radiation further complicate the classification of a SAR image aiming at detecting floods.

This paper presents a case study regarding a recent severe weather event that occurred in Northwestern Italy and caused 6 casualties in the city of Genoa; heavy rainfall occurred in some areas of the Liguria and Piedmont regions from November 3, 2011 till November 8, 2011 and numerous flash floods were reported. The event was monitored by using a number of CSK images provided by the Italian Space Agency (ASI) within the framework of the OPERA project.

This study presents a methodology to detect either permanent water bodies or flooded areas, as well as areas in which heavy rain is present.

II. THE AVAILABLE DATA

©Cosmo-SkyMed (CSK) was programmed to continuously monitor the Northwestern Italy event starting from November 4, 2011 until November 8, 2011 and the images were promptly delivered to the OPERA team. Among the large number of CSK data that have been analyzed, Fig. 1 shows those acquired on November 5, 2011 at 05:15 UTC and on November 8, 2011 at 05:21 UTC, in Spotlight mode, at horizontal polarization and with an incidence angle of 37.5° and 43.2° , respectively. In the left panel of Fig. 1, the inland large dark areas correspond to zones affected by attenuation of the radar signal, while, in the right panel, the dark areas in the upper left part of the CSK image likely correspond to snow, while some small flooded areas near the Po River are also present (see the zoomed images in Fig. 1). It can be noted that the radar return of all the aforementioned regions is very similar, thus confirming that the classification of a SAR observation of a severe weather event may be a difficult task. The CSK data have been calibrated and geocoded by means of the ENVI/SARSCAPE© software and the SRTM DEM to derive the backscattering coefficient σ^0 . Besides the DEM, as ancillary data we have also used a Land Cover map derived from the European Corine Land Cover project and a Landsat-7 (L7) optical image. As for the former, the level-1 legend has been considered to discriminate between a limited set of macro-classes, such as agricultural areas (mainly bare at the time of the event), urban settlements and forests. The L7 image was taken on November 24, 2011 and was downloaded from the U. S. Geological Survey website (<http://glovis.usgs.gov/>). Both the L7 image and the land cover map have been co-registered with the CSK imagery and a pixel size of 10 m has been chosen for all the co-registered data. A MODIS image was also used to verify the presence of snow.

III. THE METHODOLOGY

Both water surfaces and areas affected by the attenuation of the radar signal caused by intense rain are characterized by low backscatter (i.e., appear dark in the SAR imagery, see Fig. 1). Actually, it is well known that the presence of wind or of vegetation emerging above the water surface tends to increase radar backscattering, thus complicating the detection of inundated pixels. For this case study, phenomena of large increase of σ^0 due to the presence of floodwater were not detected, so that we have limited ourselves to search for low backscatter (dark) areas. We have firstly applied a segmentation algorithm based on mathematical morphology, such as that proposed in [2], in order to divide the SAR image into separate objects that are homogeneous with respect to pixel intensity. Then, the mean value of σ^0 has been computed for each object and compared to the outputs of the electromagnetic scattering models developed by the Tor Vergata

University of Rome for agricultural areas (bare soil has been assumed in this case) and for forests [3-4]. For agricultural areas we have searched for objects whose mean σ^0 was less than a threshold value derived from model simulations under flooded conditions (see [5]), obtained by replacing the soil with a semi-infinite layer having the dielectric constant of water and a negligible roughness.

Once the dark areas in a SAR image have been identified, considering the characteristics of the landscape in Northern Italy, they can in principle belong to the classes of “water bodies”, “heavy rain”, “shadowing”, or “wet snow”. Here we focus on the method we developed to automatically discriminate between the first two classes, that represents the most difficult task, while shadowing can be identified through a local incidence angle (θ_l) map that we have derived from the DEM as done in [6], while snow might be identified through information about the freezing level, or by computing the Normalized Difference Snow Index from an optical image in clear sky conditions close in time to the SAR ones.

First of all, we have made the simple hydraulic consideration that standing water is generally present in flat regions, so that only areas in which θ_l is not very different from the nominal one (θ) can be flooded. Areas in which there is intense rainfall can be hardly detected if θ_l is very large (and different from θ), because the small backscattering can be in principle ascribed either to rain or to topography. Consequently, dark objects with large θ_l adjacent to areas of heavy rain have been associated to the class “heavy rain”, while isolated dark objects with large θ_l have been considered affected by shadowing. Dark objects lying in forested and also urban areas have been associated to the class “heavy rain”, since in this case floodwater tends to increase σ^0 .

Among objects having θ_l similar to θ , to discriminate between “heavy rain” and “water surfaces” we have taken into account the shape of the objects, which are expected to be different for atmospheric targets (rain cells) and surface targets (flooded land). To this aim we have processed the optical L7 image by a K-means clustering algorithm in order to single out the different objects that are present in the scenario. Then, an edge detector such as the Sobel filter has been applied to identify the boundaries of the agricultural fields. The edge detector has been also applied to the outputs of the map of dark areas produced by the segmentation of the SAR images and by the comparison with the model outputs. Basing on the idea that flooded areas have generally the shape of the land objects under dry conditions, we have labeled as water surfaces the dark areas whose edges match the boundaries of the agricultural fields identified through the K-means algorithm. Fig.2 shows the results of our methodology applied to the CSK images of November 5 and November 8, 2011.

ACKNOWLEDGEMENT

This work has been supported by the Italian Space Agency (ASI) under contract No. I/048/07/0.

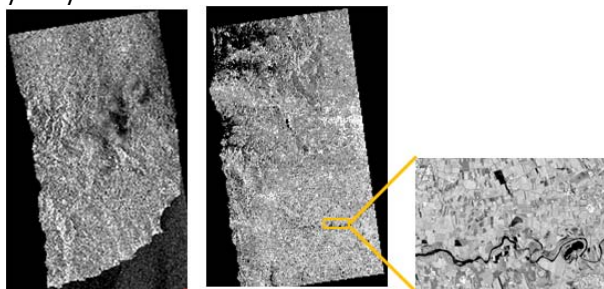


FIG. 1 - CSK images acquired on November 5 (left panel) and November 8 (right panel), 2011.

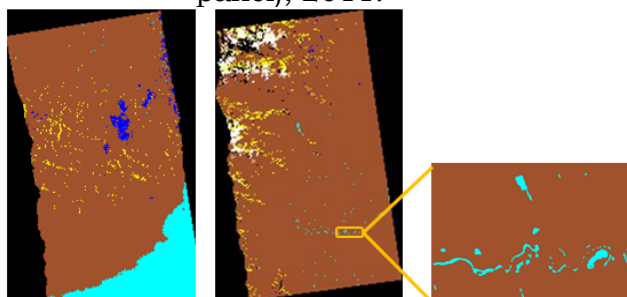


FIG. 2 - Results of the classification of the images shown in Fig. 1. Blue: heavy rain, cyan: water surfaces (permanent water bodies or flooded areas), yellow: shadowing, white: possible snow cover, brown: dry conditions, black: no data.

REFERENCES

- [1] F. S. Marzano, S. Mori, M. Chini, L. Pulvirenti, N. Pierdicca, M. Montopoli, and J. A. Weinman, "Potential of high-resolution detection and retrieval of precipitation fields from X-band spaceborne synthetic aperture radar over land," *Hydrology and Earth System Sciences*, vol. 15, pp. 859-875, 2011.
- [2] L. Pulvirenti, M. Chini, N. Pierdicca, L. Guerriero, and P. Ferrazzoli, "Flood monitoring using multi-temporal COSMO-SkyMed data: image segmentation and signature interpretation," *Remote Sensing of Environment*, vol. 115, pp. 990-1002, 2011.
- [3] M. Bracaglia, P. Ferrazzoli, and L. Guerriero, "A fully polarimetric multiple scattering model for crops," *Remote Sensing of Environment*, vol. 54, pp. 170-179, 1995.
- [4] P. Ferrazzoli, and L. Guerriero, "Radar sensitivity to tree geometry and woody volume: a model analysis," *IEEE Transaction on Geoscience and Remote Sensing* vol. 33, pp. 360-371, 1995.
- [5] L. Pulvirenti, N. Pierdicca, M. Chini, and L. Guerriero, "An algorithm for operational flood mapping from Synthetic Aperture Radar (SAR) data based on the fuzzy logic," *Natural Hazards and Earth System Sciences*, vol. 11, pp. 529-540, 2011.
- [6] L. Pulvirenti, N. Pierdicca, and F. S. Marzano, "Prediction of the Error Induced by Topography in Satellite Microwave Radiometric Observations," *IEEE Transaction on Geoscience and Remote Sensing* vol. 49, pp. 3180-3188, 2011.

REFLECTION SYMMETRY TO OBSERVE METALLIC TARGETS AT SEA BY A DUAL-POLARIMETRIC SAR

F. Nunziata and A. Montuori

Università di Napoli Parthenope,
Dipartimento per le Tecnologie
Centro Direzionale, isola C4 - 80143, Napoli, Italy.
ferdinando.nunziata@uniparthenope.it

Abstract

A polarimetric model to observe metallic targets at sea in polarimetric Synthetic Aperture Radar (SAR) data is proposed. The model gives an understanding of the different symmetry properties that characterize sea surface with and without metallic targets in terms of the correlation between like- and cross-polarized channels. Experiments undertaken over C-band Single Look Complex (SLC) RADARSAT-2 SAR data confirm the soundness of the approach.

Index Terms – Polarimetry, SAR, ship detection.

I. INTRODUCTION

Synthetic Aperture Radar (SAR) observation of metallic targets, i.e. ships and oil rigs, at sea relies on the fact that their backscattered signal causes a bright spot over SAR images. However, the information provided by the sole backscattered intensity, collected by a single-polarization SAR, is not generally sufficient to effectively observe metallic targets. To conceive more effective observation techniques, the interest towards polarimetric approaches is very much increased, supported also by new high-performances polarimetric SARs, e.g. the ones operated on-board of the ALOS, RADARSAT-2, TerraSAR-X and COSMO-SkyMed missions.

In order to reduce false alarms, recently, promising results have been obtained by employing physically-based polarimetric techniques [1]. However, these algorithms often are quite complex to be implemented operationally and the choice of a suitable threshold is a non-trivial issue.

In this study, a new physically-based approach is proposed to observe man-made metallic targets in polarimetric SAR data. The approach exploits the intrinsic symmetry properties that characterize sea surface with and without metallic targets. Symmetry is a powerful concept that applies in various scientific areas such as quantum mechanics and crystallography. It has also applicative relevance in electromagnetics, in antennas and scattering [2]. At more basic level, symmetries in electromagnetics include those in the Maxwell equations (e.g. duality and reciprocity [2]), those in geometric symmetry (e.g. rotation, reflection, translation, similarity [2]), and combination of these. An important symmetry property that characterizes natural

background scenarios is reflection symmetry [2]. Sea surface, being a distributed natural scene, is expected to satisfy reflection symmetry. When dealing with man-made metallic targets, being complex and man-made structures, they are expected to break reflection symmetry.

In this study, the correlation between like- and cross-polarized scattering amplitudes is exploited as a measure of the departure from the reflection symmetry. Hence, first the sensitivity of the proposed indicator to metallic targets at sea is investigated; then, a simple and very effective technique is proposed to observe targets at sea in polarimetric SAR data.

II. METHODOLOGY

The most logical way to deal with polarimetric scattering from a distributed and depolarizing target is by using the second-order products of the scattering matrix [3]. This can be accomplished by using the covariance matrix that, under the backscatter alignment (BSA) convention and when reciprocity holds, is given by:

$$\mathbf{C} = \begin{pmatrix} \langle |S_{hh}|^2 \rangle & \sqrt{2} \langle S_{hh} S_{hv}^* \rangle & \langle S_{hh} S_{vw}^* \rangle \\ \sqrt{2} \langle S_{hv} S_{hh}^* \rangle & \langle |S_{nv}|^2 \rangle & \sqrt{2} \langle S_{nv} S_{vw}^* \rangle \\ \langle S_{vw} S_{hh}^* \rangle & \sqrt{2} \langle S_{vw} S_{nv}^* \rangle & \langle |S_{vw}|^2 \rangle \end{pmatrix}, \quad (1)$$

$\langle . \rangle$ stands for ensemble average and S_{pq} is the generic the scattering matrix elements with $\{p, q\} = \{h, v\}$. \mathbf{C} is a 3×3 Hermitian semi-definite positive matrix which consists of 9 independent parameters and has real and non-negative eigenvalues and orthogonal eigenvectors. Up to now, no hypothesis has been made on the scattering system but the linearity and the reciprocity. Therefore the 3×3 covariance matrix (1) is obtained. However, the number of independent parameters is reduced when symmetry properties are satisfied. This is the case of naturally distributed scenarios that generally satisfy reflection symmetry [4]. It can be shown that a distributed scene, which satisfies this symmetry property, is characterized by the following covariance matrix:

$$\mathbf{C} = \begin{pmatrix} \langle |S_{hh}|^2 \rangle & 0 & \langle S_{hh} S_{vw}^* \rangle \\ 0 & \langle |S_{nv}|^2 \rangle & 0 \\ \langle S_{vw} S_{hh}^* \rangle & 0 & \langle |S_{vw}|^2 \rangle \end{pmatrix}, \quad (2)$$

It should be noted that a direct consequence of reflection symmetry is that the correlation between like- and cross-polarized scattering amplitudes vanishes:

$$\langle S_{hh} S_{nv}^* \rangle = \langle S_{nv} S_{vw}^* \rangle = 0, \quad (3)$$

Hence, the modulus of the correlation between like- and cross-polarized scattering amplitudes r :

$$r = \left| \left\langle \dot{\mathbf{S}}_{rh}^* \dot{\mathbf{S}}_{rv}^* \right\rangle \right|, \quad (4)$$

is the natural norm to measure the departure from the reflection symmetry case. When r tends to 0, the observed scene is characterized by the symmetry property and (2) applies, while for larger r values, departure from reflection symmetry is achieved and (1) applies.

It is now important to read reflection symmetry in marine physical terms. Sea surface, being a natural distributed target, is expected to satisfy reflection symmetry. As a matter of fact, $r \approx 0$ should apply. When dealing with man-made metallic objects, due to their complex shape that consists of plane, dihedral, and trihedral structures, as well as dihedral corner reflectors and thin wires, reflection symmetry is not expected to be still satisfied, therefore, r values significantly larger than the free sea surface one are expected.

III. EXPERIMENTS

In this section, the physical consistency of the proposed polarimetric model and the effectiveness of the polarimetric target detection approach are investigated. Actual polarimetric Single Look Complex (SLC) SAR data, acquired by the C-band RADARSAT-2 satellite mission, are considered.

A meaningful experiment, accomplished over a dual-polarimetric HH-HV SAR data related to the acquisition of 13 May 2011 at 16:40:10 UTC (Product ID: PDS 01780080, image ID: 133029), is shown and discussed. The SAR data has been acquired off the Taranto coast, Italy. The incidence angle ranges between 30° and 37°. The squared modulus related to an excerpt of the HH-polarized SLC SAR data is shown in Fig.1 (a), where 3 targets, labeled as T1 to T3, are present. Large marine-related features are also visible (see bright strips in Fig.1(a)) that make target detection a very challenging task. First, the sensitivity of the model to sea surface with and without targets is investigated by evaluating r (4) within region of interests (ROIs) belonging to the three targets (T1-T3) and to sea surface (not shown). r values are listed in Table 1. It can be noted that sea surface and targets call for completely different and well-distinguishable (roughly two order of magnitude) r values. This implies that sea surface is well described by (2) while targets call for (1). Since targets and sea r values are well-separated and no feature associated with the marine strips is present in the r image, a fixed empirical threshold (equal to 0.002) has been employed to obtain the logical true-and-false binary output of Fig.1(c). It can be noted that all the targets have been correctly observed and no false alarm is present.

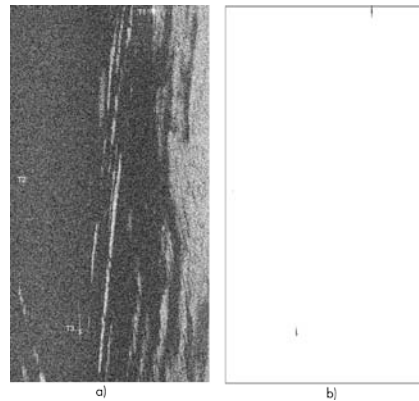


FIG. 1 – RADARSAT-2 dual-polarimetric SLC SAR data related to the acquisition of 13 May 2011 at 16:40:10 UTC. (a) Excerpt of the HH-polarized squared modulus SAR data. (b) r -based filter’s output.

TABLE I - R VALUES MEASURED WITHIN THE ROIS OF FIG. 1(A)

ROI	Target	Sea
1	0.5323	0.005
2	0.1850	0.003
3	0.4568	0.007

IV. CONCLUSION

A polarimetric model is proposed that gives an understanding of the symmetry properties of sea surface with and without targets in terms of the correlation between the like- and cross-polarized channels of a dual-polarization radar. The model’s sensitivity is verified against actual dual-polarimetric C-band RADARSAT-2 SAR data. Then, a simple and very effective technique is proposed to observe targets at sea.

ACKNOWLEDGEMENT

RADARSAT-2 data are obtained under the SOAR project entitled “Multi-polarization approaches for oil spills and vessel detection in polarimetric SAR data.” Italian Space Agency is also acknowledged for partially funding this study.

REFERENCES

- [1]H.Zhaoying, C.Jinsong, “A review of ship detection algorithms in polarimetric SAR images,” Proc. Signal Processing, 2004, vol.3, pp.2155-2158, 2004.
- [2]C.E.Baum and H.N.Kritikos, Eds.,Electromagnetic symmetry. New York: Taylor & Francis, 1995.
- [3]S.R.Cloud, Polarisation: Applications in remote sensing. Oxford University Press, Great Britain, 2009.
- [4]S.V.Nghiem,S.H.Yueh,R.Kwok,andF.K.Li, “Symmetry properties in polarimetric remote sensing,” Radio Sci.,vol.27, no.5, pp.693-711, 1992.

Electromagnetic Characterization of Speckle in SAR Images

G. Di Martino⁽¹⁾, A. Iodice⁽¹⁾, D. Riccio⁽¹⁾, G. Ruello⁽¹⁾

⁽¹⁾ DIBET, University of Naples Federico II
Via Claudio 21, 80125 Naples, Italy
{gerardo.dimartino,iodice,daniele.riccio,ruello}@unina.it

Abstract

New generation space-borne SAR sensors are acquiring images at very high resolution and their statistics, in many actual situations, do not match with those predicted by the fully developed speckle model. Most of the models for non-fully developed speckle are based on the concept of interference between scatterers within the radar resolution cell. The approach proposed in the present paper provides the analytical dependence of the number of scatterers on surface roughness and sensor parameters. The illuminated surface is represented here using fractal geometry.

Index Terms – Electromagnetic scattering, fractals, Synthetic Aperture Radar.

I. INTRODUCTION

Synthetic Aperture Radar (SAR) single look images present the well-known phenomenon of speckle, due to the fact that a resolution cell is usually larger than the wavelength λ of the incident electromagnetic field. The speckle phenomenon is usually described as a stochastic process and the received signal is modeled as the coherent sum of the returns coming from independent scatterers randomly distributed in the resolution cell [1]-[3]. According to this model, the key parameter for the statistical characterization of the speckle is the number of independent scatterers per resolution cell N . As a matter of fact, under the hypothesis of $N \gg 1$, the central limit theorem can be applied thus obtaining a Gaussian complex circular field, with a Rayleigh distributed amplitude and a phase uniformly distributed in $[0, 2\pi]$. In this case the speckle is defined as *fully developed*. For low resolution SAR sensors, whose resolution cell area is of the order of tenth of square meters (very large compared to the centimeter wavelength), the Rayleigh amplitude model (or, equivalently, the Exponential intensity model) well matches actual data. Note that this model is very attractive because only the knowledge of the mean square value of the cell return is required for speckle description, regardless of an accurate characterization of the scatterers.

However, with the increasing availability of space-borne very high resolution SAR data, for which the hypothesis of a resolution cell size much larger than the wavelength cannot be safely assumed, the statistics of SAR images can depart from those predicted by the

Rayleigh model. In the past decades the K-distribution has been positively used to model the statistical behavior of SAR images as a function of the number of scatterers per resolution cell [3]. However, in this case a comprehensive physical and statistical characterization of the scatterers is required to describe the speckle phenomenon.

In this paper we present a new model for the speckle, well-suited for SAR images of natural terrain. It is based on a physical description of the scatterers in the resolution cell. In particular, a relation between the number of equivalent scatterers per resolution cell and the physical properties of the surface and of the sensor is provided. The illuminated surface is modeled as a fractional Brownian motion (fBm) process [4].

II. SPECKLE STATISTICAL MODEL

Most of the models available in literature describe the return from a resolution cell as the coherent sum of N electromagnetic returns [2]-[3]:

$$E = V e^{j\phi} = \sum_{i=1}^N V_i e^{j\phi_i}, \quad (1)$$

where $V_i e^{j\phi_i}$ is the contribution due to the i -th scatterer. Hence, the field E is a function of the number N of scatterers and, according to this value, the speckle can be Exponentially or K-distributed. In particular, the Exponential distribution can be regarded as a particular case of the K-distribution for $N \gg 1$ [3]. Whenever the hypothesis of a large number of independent scatterers per resolution cell is no longer valid, we have to face the problem of studying the coherent sum of a finite number of fields. As a matter of fact, while in the Exponential case no characterization of the scatterers is necessary, conversely in the K-distribution case the number of independent scatterers per resolution cell is needed in order to obtain the expression of the speckle pdf [3].

III. SURFACE MODEL

The use of an adequate model for the description of natural surfaces is crucial to gain a reliable modeling. To this purpose, it has been demonstrated [4]-[5] that the use of the fBm is quite appropriate. A stochastic process $z(x,y)$ is an fBm surface if, for every x, x', y, y' it satisfies the following relation:

$$\Pr\{z(x,y) - z(x',y') < \bar{\xi}\} = \frac{1}{\sqrt{2\pi} T^{1-H} \tau^H} \int_{-\infty}^{\bar{\xi}} \exp\left(-\frac{\xi^2}{2T^{2-2H} \tau^{2H}}\right) d\xi, \quad (2)$$

where τ is the distance between the points (x,y) and (x',y') and the two parameters that control the fBm behavior are the *Hurst coefficient* H and the *topothesis* T [m] [4]. In this case the structure function can be inferred directly from the incremental process characterization (2):

$$Q(\tau) \triangleq \langle |z(x, y) - z(x', y')|^2 \rangle = T^2 - 2H\tau^{2H}. \quad (3)$$

IV. ELECTROMAGNETIC CHARACTERIZATION OF SPECKLE

The SAR image is the superposition of the reflectivity function $\gamma(\bullet)$, weighted by the overall (i.e., including the focusing) unit response $g(\bullet)$:

$$i(x_0, y_0) = S e^{-j2kR} \iint e^{j2k_x x} e^{j2k_y y} e^{j2k_z z(x, y)} g(x_0 - x, y_0 - y) dx dy. \quad (4)$$

The function $g(\bullet)$ is assumed to be negligible outside an area A centered around (x_0, y_0) , here defined as the “resolution cell” [2]. The reflectivity function $\gamma(x, y)$ can be expressed as the product of a polarization factor S - dependent on soil complex permittivity and reasonably assumed constant within a resolution cell - and a (two-way) propagation factor $e^{-j2kR} e^{j2\mathbf{k}\cdot\mathbf{r}}$, which accounts for the phase contributions coming from the points of the resolution cell located in position $\mathbf{r} = x\hat{x} + y\hat{y} + z(x, y)\hat{z}$. Here, $\mathbf{k} = k_x\hat{x} + k_y\hat{y} + k_z\hat{z}$ is the electromagnetic propagation vector, so that $\|\mathbf{k}\| = k = 2\pi/\lambda$ [m⁻¹] [1], and R is the distance of the sensor from the origin of the reference system.

In order to move toward the simplified model (1), we can subdivide the resolution cell into smaller domains, each representing a single “equivalent scatterer”, so that returns pertaining to a single domain are correlated, whereas returns from different domains are uncorrelated. To obtain a proper evaluation of the equivalent scatterer size, we define the scatterer radius τ_M as the distance between the two generic surface points (x, y) and (x', y') such that the correlation between returns from the two points, i.e.,

$$\langle e^{j2k_z z(x, y)} e^{-j2k_z z(x', y')} \rangle = \langle e^{-j2k_z (z(x', y') - z(x, y))} \rangle = e^{-\frac{(2k_z)^2}{2} Q(\tau)}, \quad (5)$$

falls below a given threshold, say e^{-t} , with t of the order of unity. It is straightforward to verify that the required value of τ_M is such that:

$$Q(\tau_M) = \frac{t}{2k_z^2}. \quad (6)$$

The structure function (3) can be used into (6), thus obtaining the following dimension for the equivalent scatterers:

$$\tau_M = \left(\frac{\sqrt{t}}{\sqrt{2}k_z T^{1-H}} \right)^{\frac{1}{H}}. \quad (7)$$

Finally, we can evaluate N as the ratio between the cell area and $\pi\tau_M^2$. In Fig.1 N is plotted as a function of T assuming the parameters of the Cosmo-SkyMed high resolution SAR sensor, i.e. a resolution cell

area of 1 m², a wavelength of 3.1 cm and a look angle of 30°. As shown by the graph the number of scatterers per resolution cell is below 10 in some practical situations. Note that the range for T and H has been chosen in accordance to typical values of natural surfaces [4].

V. CONCLUSION

A novel approach for the characterization of the equivalent scatterers within a SAR resolution cell has been presented. The provided results can be used for the statistical description of speckle in high resolution SAR images and for data simulation purposes.

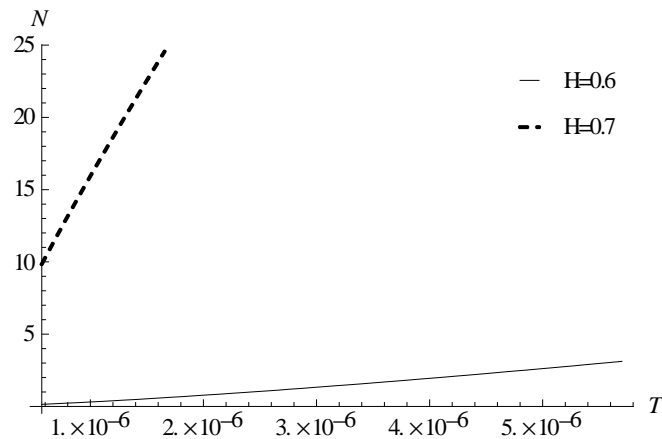


FIG. 1 – Plot of N as a function of T [m] assuming the Cosmo-SkyMed parameters reported in the text of the paper.

ACKNOWLEDGEMENT

This work has been supported by the EU-FP7 project "Development of Pre-Operational Services for Highly Innovative Maritime Surveillance Capabilities" (DOLPHIN).

REFERENCES

- [1] P. Beckman, A. Spizzichino, *The Scattering of Electromagnetic Waves from Rough Surfaces*, New York: Pergamon Press, 1963.
- [2] J. W. Goodman, "Some fundamental properties of speckle", *J. Opt. Soc. Am.*, vol. 66, no. 11, pp. 806-814, Nov. 1976.
- [3] E. Jakeman and P. N. Pusey, "A Model for Non-Rayleigh Sea Echo", *IEEE Trans. Antennas Propag.*, vol. 24, no. 6, pp. 1145-1150, Nov. 1976.
- [4] G. Franceschetti, D. Riccio, *Scattering, Natural Surfaces and Fractals*. Burlington, MA: Academic, 2007.
- [5] B.B. Mandelbrot, *The Fractal Geometry of Nature*. New York: Freeman, 1983.

CONTRAST SOURCE BAYESIAN COMPRESSIVE IMAGING BY A MINIMUM NORM FORMULATION

G. Oliveri

ELEDIA Research Center @DISI, University of Trento

Via Sommarive 5, I-38123 Trento, Italy

giacomo.oliveri@disi.unitn.it

Abstract

The problem of imaging sparse dielectric profiles from scattered field data is solved by means of a new multi-task Bayesian Compressive Sensing (MT-BCS) approach under the contrast-source-inversion (CSI) formulation. The proposed strategy is devoted to a twofold objective: on the one hand, to effectively exploit the a-priori knowledge on the sparseness of the objects of interest, and, on the other hand, to suitably manage the complex nature of the unknowns during the solution process. Towards this end, a minimum-norm current expansion is adopted. A set of preliminary numerical results are reported to assess the features of the arising method.

Index Terms– Multi-Task Bayesian Compressive Sensing (MT-BCS), Microwave Imaging, Minimum-Norm Currents.

I. INTRODUCTION

The problem of retrieving the dielectric features of sparse objects located in inaccessible domains starting from non-invasive electromagnetic measurements at microwave frequencies is gathering an increasing attention from the methodological viewpoint [1]. Indeed, since in many practical cases unknown profiles can be assumed as “sparse” in a suitable expansion basis [1]-[3], several techniques have been introduced in the last years to effectively solve such problems [1]-[4].

In this framework, Compressive Sensing (CS) strategies have been firstly proposed to effectively solve imaging problems within Contrast-Source-Inversion (CSI) framework [5][6] in a “sparseness-regularized” sense (i.e., exploiting the *a-priori* knowledge of the sparseness of the solution during the retrieval process) [1]. Because of the features of the associated formulations [5]-[8], algorithms able to overcome the limitations of classical L_1 -regularized CS techniques, namely Bayesian Compressive Sensing methodologies (BCS) [1]-[4][9], have been investigated, and their performance have been compared with those of deterministic and stochastic imaging methods [1]. Thanks to their effectiveness and accuracy, these approaches have then been extended to Contrast-Field-Inversion formulations [2][3] as well as to other CSI problems [4].

Nevertheless, these techniques share a common limitation which can significantly affect their accuracy. Indeed, BCS strategies require the discretized unknown (i.e., the “contrast source” coefficients in the CSI

case) to be real-valued. Accordingly, state-of-the-art BCS imaging approaches are formulated so that the real- and imaginary-parts of the unknown current coefficients are treated as independent (i.e., stored in two *separate* real-valued vectors). Unfortunately, such a strategy neglects the complex nature of contrast sources (i.e., the relationships among the location of non-zero entries of the real and imaginary parts of the unknown currents).

This work is aimed at presenting an innovative formulation for the sparse two-dimensional CSI problem which is able to effectively manage the relations between the real and imaginary part of the unknown contrast sources. Towards this end, a minimum-norm current expansion will be employed to reformulate the unique imaging problem into two *correlated* ones, which are subsequently solved by means of a multi-task Bayesian Compressive Sensing (MT-BCS) strategy [9]. The features of the arising approach are preliminarily validated through a set of numerical experiments.

II. PROBLEM FORMULATION AND PROPOSED APPROACH

Consider a set of V time-harmonic incident transverse-magnetic (TM) waves $I_\nu(\underline{r})$ ($\nu=1, \dots, V$) impinging on an investigation domain D which contains a lossless sparse object modeled through the contrast function $\tau(\underline{r})=\varepsilon(\underline{r})-1$ ($\underline{r} \in D$) ($\varepsilon(\underline{r})$ being its dielectric permittivity) embedded in a lossless background with wavenumber k . In this scenario, the *scattered* field $F_\nu(\underline{r})=E_\nu(\underline{r})-I_\nu(\underline{r})$ complies with the “data” equation

$$F_\nu(\underline{r}_m) = -k^2 \int_{\Omega} g(\underline{r}_m, \underline{r}') J_\nu(\underline{r}') d\underline{r}', \quad \underline{r}_m \in O \quad (1)$$

where \underline{r}_m ($m=1, \dots, M$) is the position of the m -th measurement probe, O is the observation domain, $J_\nu(\underline{r}) = \tau(\underline{r})E_\nu(\underline{r})$ is the (unknown) contrast source, $E_\nu(\underline{r})$ is the *total* field, and $g(\underline{r}, \underline{r}')$ is the 2D Green’s function [1]. To solve (1) starting from the knowledge of $F_\nu(\underline{r}_m)$, its discretized version (using a suitable expansion basis of size N [1]) is firstly computed as

$$\underline{F}_\nu = \mathbf{G} \underline{J}_\nu \quad \nu = 1, \dots, V \quad (2)$$

where $\underline{F}_\nu \in C^M$ and $\underline{J}_\nu \in C^N$ are the complex-valued field and current vectors, and \mathbf{G} is the Green’s matrix [1] which is processed according to singular value decomposition (SVD) to yield [6]

$$\mathbf{G} = \mathbf{U} \Psi \mathbf{V}^H \quad (3)$$

Ψ being the diagonal matrix storing the singular values ψ_n , ($n=1, \dots, N$). The minimum-norm current distribution $\underline{J}_\nu^{MN} = \mathbf{V} \Psi_T^{-1} \mathbf{U}^H \underline{F}_\nu$, obtained by substituting the thresholded version of (3) (Ψ_T being the “truncated Ψ ” where the ψ_n below a threshold have been removed) into (2) is then used compute the “real” and “imaginary” scattered fields as

$$\begin{cases} \underline{F}_\nu|_{\Re} = \mathbf{G} \Re \left\{ \underline{J}_\nu^{MN} \right\} \\ \underline{F}_\nu|_{\Im} = \mathbf{G} \Im \left\{ \underline{J}_\nu^{MN} \right\} \end{cases} \quad \nu = 1, \dots, V \quad (4)$$

By recasting the (2) in a Bayesian framework, the following split formulation is finally obtained

$$\begin{cases} \Re\{\hat{\underline{J}}_\nu\} = \arg \left[\max_{\underline{J}_\nu} \wp(\underline{J}_\nu | \underline{F}_\nu |_{\Re}) \right] \\ \Im\{\hat{\underline{J}}_\nu\} = \arg \left[\max_{\underline{J}_\nu} \wp(\underline{J}_\nu | \underline{F}_\nu |_{\Im}) \right] \end{cases} \quad \nu = 1, \dots, V \quad (5)$$

which can be solved by taking into account the relationships between $\Re\{\underline{J}_\nu\}$ and $\Im\{\underline{J}_\nu\}$ through the *MT-BCS* formulation described in [4][9]. Once $\hat{\underline{J}}_\nu = \Re\{\hat{\underline{J}}_\nu\} + j\Im\{\hat{\underline{J}}_\nu\}$ has been computed, the discretized version of $\tau(\underline{r})$ can be evaluated by using the “state equation” as shown in [1].

III. PRELIMINARY NUMERICAL VALIDATION

For the numerical experiments, a 3λ -sided D has been subdivided in $N=324$ cells and illuminated by $V=27$ plane waves coming from $\theta_\nu=2\pi(\nu-1)/(V-1)$, and $M=27$ equally spaced probes have been employed to collect the data within O (i.e., circle of radius 3λ). The plots of the retrieved profiles when dealing with two squares with $\tau=1.0$ [Fig. 1(a)] show that the proposed approach [“*MT-BCS*” - Fig. 1(c)] overcomes the state-of-the-art method [“*ST-BCS*” - Fig. 1(b)] introduced in [1] in terms of accuracy, achieving a satisfactory fidelity despite the low *SNR* (Fig. 1). The improved quality of the reconstruction is also confirmed by the corresponding total error $\xi_{TOT} = \left[\int |\hat{\tau}(\underline{r}) - \tau(\underline{r})| d\underline{r} \right] / \left[\int (\tau(\underline{r}) + 1) d\underline{r} \right]$ which is resumed in Fig. 2 for different *SNR* and τ values. Indeed, thanks to the considered formulation, the proposed algorithm outperforms that in [1] whatever the noise level and contrast of the reference profile.

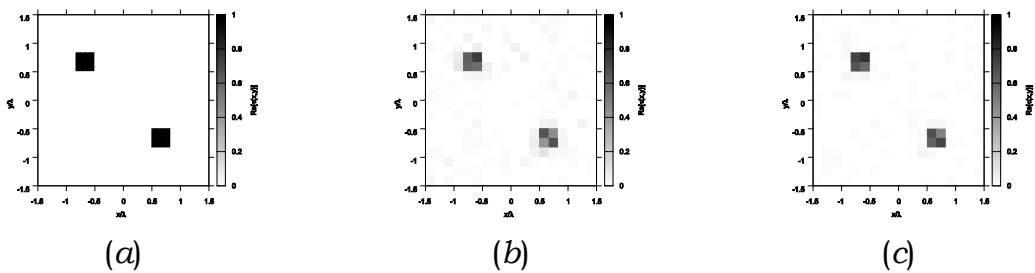


FIG. 1– Comparative Assessment - Actual (a), *ST-BCS* (b), and *MT-BCS* (c) retrieved contrast when *SNR*=10 [dB].

IV. CONCLUSIONS

An innovative *MT-BCS* approach is proposed to image sparse dielectric profiles taking into account the *a-priori* information on the complex nature of the unknown contrast sources during the inversion process.

Towards this end, a minimum-norm-current expansion is adopted. A set of preliminary results is presented to show the effectiveness of the introduced algorithm with respect to state-of-the-art *BCS* approaches.

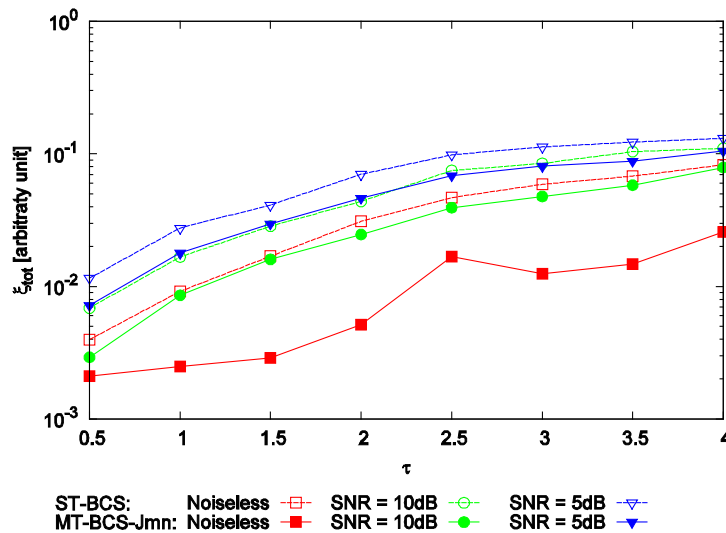


FIG. 2– Comparative Assessment – Behavior of ξ_{tot} as a function of τ for different SNR values.

REFERENCES

- [1] G. Oliveri, P. Rocca, and A. Massa, "A Bayesian Compressive sampling-based inversion for imaging sparse scatterers," *IEEE Trans. Geosci. Remote Sens.*, vol. 49, no. 10, pp. 3993-4006, Oct. 2011.
- [2] L. Poli, G. Oliveri, and A. Massa, "Microwave imaging within the first-order Born approximation by means of the contrast-field Bayesian compressive sensing," *IEEE Trans. Antennas Propag.*, in press.
- [3] G. Oliveri, L. Poli, P. Rocca, and A. Massa, "Bayesian compressive optical imaging within the Rytov approximation", *Opt. Lett.*, in press.
- [4] L. Poli, G. Oliveri, P. Rocca, and A. Massa, "Bayesian Compressive Sensing approaches for the reconstruction of two-dimensional sparse scatterers under TE illuminations", *IEEE Trans. Geosci. Remote Sens.*, submitted.
- [5] C. Gilmore, A. Abubakar, W. Hu, T. M. Habashy, and P. M. van der Berg, "Microwave biomedical data inversion using the finite-difference contrast source inversion method," *IEEE Trans. Antennas Propag.*, vol. 57, no. 5, pp. 1528-1538, May 2009.
- [6] P. Rocca, M. Donelli, G. L. Gragnani, and A. Massa, "Iterative multi-resolution retrieval of non-masurable equivalent currents for the imaging of dielectric objects," *Inv. Prob.*, vol. 25, 2009.
- [7] S. Kharkovsky and R. Zoughi, "Microwave and millimeter wave nondestructive testing and evaluation – Overview and recent advances," *IEEE Instrum. Meas. Mag.*, vol. 10, pp.26-38, Apr. 2007.
- [8] T. Isernia, V. Pascazio, R. Pierri, "On the local minima in a tomographic imaging technique," *IEEE Trans. Geosci. Remote Sens.*, vol. 39, no. 7, pp. 1596-1607, Jul. 2001.
- [9] S. Ji, D. Dunson, and L. Carin, "Multitask compressive sensing," *IEEE Trans. Signal Process.*, vol. 57, no. 1, pp. 92-106, Jan. 2009.

Resolution of MEG inverse problem via Reweighted ℓ_1 Minimization Algorithm

M. Muzi ^(1,2)

¹ Institute of Advanced Biomedical Imaging, "G. d'Annunzio" University Foundation, University "G. d'Annunzio" Chieti-Pescara, Italy

² Department of Neuroscience and Imaging, University "G. d'Annunzio" Chieti-Pescara, Italy
marco.muzi@unich.it

Abstract

The MagnetoEncephaloGraphy (MEG) inverse problem consists in the estimate of the cerebral current dipole distribution generating the induction magnetic field measured by a MEG device. In this work, a nouvelle approach to solve the MEG inverse problem under the hypothesis of a sparse solution is presented. This approach solves a recursive sequence of constrained weighted ℓ_1 -minimization problems. The weights used for the next iteration are computed from the values of the current solution acting, de facto, as an "auto-regularization" of the problem that improves the accuracy of the source estimate. The proposed method is tested on extensive simulation and on real MEG data.

Index Terms – MEG, inverse, ℓ_1 norm optimization, neuronal activity.

I. INTRODUCTION

Magnetoencephalography (MEG) [1] is a noninvasive technique for mapping brain activity by recording the magnetic field produced by electrical currents naturally occurring in the brain.

The MEG inverse problem consists in estimating the cerebral current distribution that produces the magnetic field measured outside the scalp. The problem is generally ill posed and ill conditioned.

Under suitable conditions (e.g. during a task), we can suppose that the recorded signal is due to the contribution of few brain regions which can be modeled by a sparse representation of current dipoles. Under this hypothesis it is possible to assume that the solution is obtainable by solving a suitable ℓ_1 -minimization problem,[3]. However, ill-conditionedness makes the computed solution prone to uncorrectness: this forces the adoption of regularization schemes.

II. METHODS AND RESULT

The procedure to solve the MEG inverse problem can be divided into several step.

The first step is the definition and discretization of the source domain together with the estimation of the MEG sensor spatial

configuration. In this work, a standard anatomical model is used, [6], in which a set of sources lying on the normal to the cortical surface is defined. The sources are modeled as current dipoles with known position and unknown orientation and amplitude. The sensors configuration is taken from the MEG system operating at the Institute of Advanced Biomedical Technologies [8].

The second step is the definition of the lead field matrix, described as follows. The contribution to the field due to the cortical current dipoles and to the eddy current on the scalp surface is treated as described in [9] and a linear relation (Eq. (1)) between source intensity and measured magnetic field is obtained:

$$B = LJ \quad (1)$$

Let be: $B \in \mathbb{R}^n$: array of magnetic field amplitude values measured at a given instant; $L \in \mathbb{R}^{n,m}$: the lead field matrix; $J \in \mathbb{R}^{n,m}$: array of unknown current dipoles amplitude. In this work, according to the MEG system and head model used, $n=139$ and $m=19998$. The problem is obviously ill posed. The reciprocal of the condition number is near 10^{-38} . The problem is also ill conditioned.

The third step consists in the choice of the problem solver. In this work, the basis pursuit approach is chosen, since under the hypothesis of sparse solution it is possible to search for the correct solution despite ill posedness of problem [4]. In practice, the basic problem has the following form (Eq. 2):

$$\min_{x \in \mathbb{R}^m} \|J\|_1 \quad \text{subject to} \quad B = LJ \quad (2)$$

where $\|J\|_1 = \sum_{i=1}^m |J_i|$ is the definition of ℓ_1 norm and J_i is the i -th component of dipole amplitude array.

The solution is computed by a primal-dual minimization algorithm. In this work, in order to mitigate the ill conditionedness of the problem, the algorithm described in [10] was adopted.

The algorithm consists in solving a recursive sequence of problems as described in Eq. (3), where the weighting matrix W^l used for the actual iteration are computed from the inverse values of the previous solution.

$$\min_{x \in \mathbb{R}^m} \|W^l J\|_1 \quad \text{subject to} \quad B = LJ \quad (3)$$

This approach, de facto, acts as an "auto-regularization" of the problem that improves the accuracy of the source estimate.

We tested the proposed method on extensive simulations, evaluating the average value and standard deviation of Dipole Localization Error and Spatial Dispersion as suggested in [2]; and on real MEG data recorded during non painful electric stimulation of right median nerve.

The results of the inverse problem solution via reweighted ℓ_1 -minimum norm (rew l1 min norm) are compared with sLORETA (sLOR) [5], and standard ℓ_1 -minimum (l1 min norm) norm approaches. Figure 1 shows the normalized amplitude for the sources active at 35 ms after stimulation; while in Table I responses of the simulation are reported

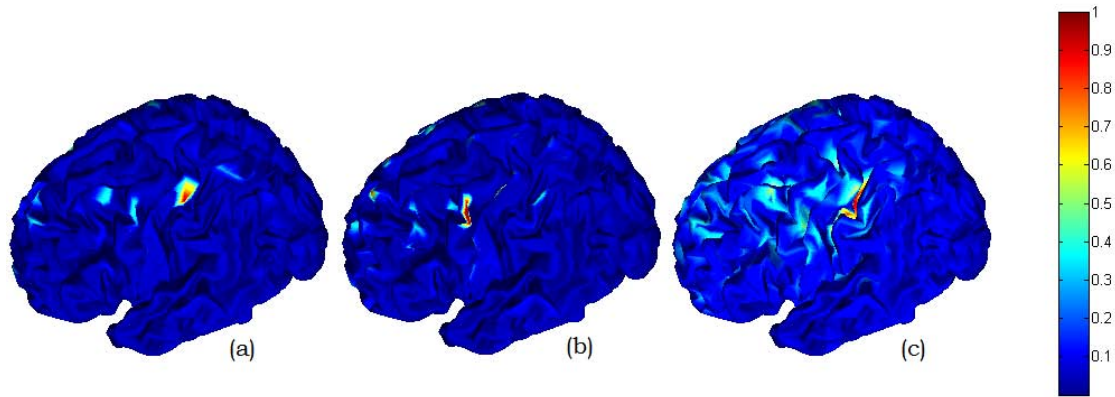


FIG. 1 – Representation of estimated current dipole amplitude on the cortex surface by: (a) Reweighted ℓ_1 -minimum norm algorithm; (b) ℓ_1 -minimum norm algorithm; (c) sLORETA. Values scales are normalized to somatosensory peak value for a better comparison.

TABLE I -

Method	DLE [cm]	SD [cm]
rew l1 min norm	0.67+/-0.06	0.12+/-0.06
l1 min norm	1.0+/-0.8	5+/-8
sLOR	1.4+/-1.0	2+/-1.2

As shown in Fig.1(a) and Fig.2(b) the main Activation Area (AA) is localized on the left somatosensory area in all cases, as expected.

III. CONCLUSION

Benefits obtainable from the use of ℓ_1 -minimum norm approach, instead ℓ_2 -minimum norm approach, in presence of sparse ill posed problem are well known [4], [10]. The main intent of this study is to evaluate the effective improvement obtainable by the application of this tools to the MEG inverse problem, or generally to heavily ill conditioned, and ill posed, magnetic inverse problem resolution. The replacement of

problem (2) with (3) guarantees, as expected (see Table I), a better result in term of definition and localization of cerebral activation area. The obtained results show an effective improvement of the estimate, also for real data. The next steps will be to relax sparsity solution hypothesis, so to extend the proposed method also on non properly sparse solution(as in the case of the study of the resting state or more complex tasks), and to further investigate ℓ_1 -minimum norm algorithm potentiality.

ACKNOWLEDGEMENT

The author would like to thank Ing. Laura Marzetti and Prof. Vittorio Pizzella for the guide and help offered during the progress of the study and for their constructive comments.

REFERENCES

- [1] M. Hamalainen, R. Hari, R.J. Ilmonieni, J.Knuutila, and O.V. Lounasmaa, "Magnetoencephalography: theory, instrumentation, and applications to noninvasive studies of the working human brain", *Rev. Mod. Phys.*, Vol. 65, No.2, 1993, pp. 414-487.
- [2] O. Hauk, D. G. Wakeman, R. Henson. "Comparison of noise-normalized minimum norm estimates for MEG analysis using multiple resolution metrics", *NeuroImage*, 54 (2011), pp. 1966-1974.
- [3] D.L. Donoho and B.F. Logan, "Signal recovery and the large sieve", *SIAM J. Appl. Math.*, Vol. 52, No.2, 1992, pp. 577-591.
- [4] S.S. Chen, D.L. Donoho and M.A. Saunders, "Atomic Decomposition by Basis Pursuit", *SIAM Review*, Vol. 43, No. 1, 2001, pp. 129-159.
- [5] R.D. Pascual-Marqui, "Standardized low resolution brain electromagnetic tomography (sLORETA): technical details", *Met. Find. Exp. Clin. Pharm.*, 2002, pp. 91-107.
- [6] VS Fonov, AC Evans, RC McKinstry, CR Almli and DL Collins, "Unbiased nonlinear average age-appropriate brain templates from birth to adulthood" *NeuroImage*, Vol. 47, Supp. 1, July 2009, Pag. S102 Organization for Human Brain Mapping 2009 Annual Meeting.
- [8] S. Della Penna, C. Del Gratta, C. Granata, A. Pasquarelli, V. Pizzella, R. Rossi, M. Russo, K. Torquati and, S. N. Ernè, "Biomagnetic System for clinical use", *Philosophical Magazine Part B*, (2000), 80: 5, pp. 937-948.
- [9] G. Nolte, "The Magnetic lead field theorem in the quasi-static approximation and its use for magnetoencephalography forward calculation in realistic volume conductors", *Phys. Med. Biol.*, Vol. 48, 2003, pp. 3637-3652.
- [10] E. J. Candès, M.B. Wakin and S. P. Boyd, "Enhancing Sparsity by Reweighted ℓ_1 Minimization", *J Fourier Anal. Appl.*, 2008, pp. 877-905.

ELECTROMAGNETIC PROPAGATION INSIDE A MODULE OF INTERNATIONAL SPACE STATION: A NUMERICAL ANALYSIS

A. Di Carlofelice, E. Di Giampaolo and P. Tognolatti

Dept. of Electrical Engineering and Information,
University of L'Aquila,
Via G. Gronchi, 18, 67100, L'Aquila, Italy
alessandro.dicarlofelice@univaq.it

Abstract

A numerical investigation of the electromagnetic pollution produced inside a model of a module of the International Space Station (ISS) by a radar UWB is shown. In particular, the work investigates possible narrowband interference and the level of the background noise introduced by an UWB radar because these phenomena may decrease the QoS of existing wireless networks and apparatus. This study is part of the project "Non Invasive Monitoring by Ultra wide band Radar of Respiratory Activity of people inside a spatial environment" (NIMURRA) which refers to a feasibility study of a ultra wide band (UWB) radar applied to the breath activity monitoring of astronauts.

Index Terms – Electromagnetic pollution, UWB, NIMURRA, Optical Geometric, ISS.

I. INTRODUCTION

The project NIMURRA is focused on the development of a new kind of UWB radar for the monitoring of the breathing of people inside the crew quarters of the International Space Station (ISS). In fact, rest and sleep have been consistently reported as being of poor quality in microgravity, both by American astronauts and Russian cosmonauts [1], [2] but up to now only few studies have addressed the combined action of microgravity and rest on respiration and chest wall. An UWB radar, placed on the cabin wall at the level of the nipples and the umbilicus, i.e non-contacting, is able to retrieve physiological parameters of both cardiac and breathing activity.

The work here shown concerns a numerical investigation of the electromagnetic pollution produced inside a model of a module of the ISS by an UWB source.

II. GEOMETRICAL MODEL

Starting from information gathered in different publications and documents [3],[4], it is estimated the size of this container to be about 1m x 1m x 2m, its sides are partially occluded by the racks hosted in the node. Because of the complex structure of the walls, it is not possible to make a realistic model of the crew quarters suitable to be used with geometrical optics, therefore an approximated model has been used consisting of a box having walls partially made of perfect electric conductors as shown in Fig. 1. The centre aisle is modelled with a rectangular box 6137.2 mm long, and cross-section 2133.6 mm high and 2133.6 mm width. The walls are flat and perfectly conducting even though some appendages can be introduced somewhere to simulate the

presence of some equipments. A section of the modelled environment is shown in Fig.1.

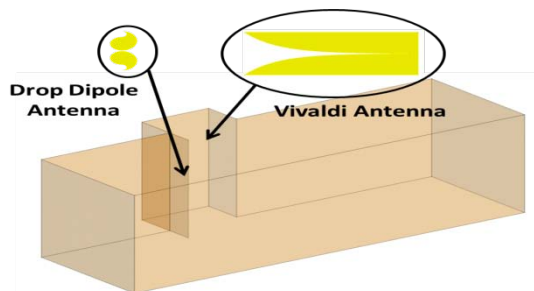


FIG. 1 GO model of the CQ and isle. Positions of UWB antennas are also shown.

This model, although very simple, is from an electromagnetic point of view as a worst case because it does not have any loss (that is not possible in the real case) and gets worse the cavity-like behaviour of the aisle. The absence of furniture makes the reflection of the signals more strong than that of furnished case [5].

III. ELECTROMAGNETIC MODEL

The source of the field is a Vivaldi antenna, modelled separately by means of a method of moments. The Vivaldi antenna is a kind of UWB antenna which is often used in UWB radar systems, UWB communication systems and so on. The Vivaldi antenna has a lot of good radiation performances including end-fire radiation pattern, UWB voltage standing wave ratio, low profile and light weigh.

This antenna is not optimized for the whole frequency band used in this computation.

Inside the geometrical optics model, this antenna is modelled as a point source emitting a set of spherical harmonics. The number of harmonics depends on the frequency but it is sufficiently large to allow the point source to radiate more than 99.9% of the radiated power at each frequency. The EIRP radiated at each frequency is set to -41.5 dBm in agreement with the FCC rules.

A miniaturized drop-shaped dipole antenna, instead, is used for an analysis of the field in time-domain.

IV. NUMERICAL RESULTS

From a numerical standpoint the above described model has a big computational charge because of the largeness of the environment (i.e. the number of observation points), the number of spherical harmonics and the number of high-order reflections to be considered. For this reason, the first investigation concerns the choice of the suitable number of reflections and the suitable spatial resolution. Simulation for 5, 7 and 9 reflections have been performed at frequency 2.4 GHz and for spatial resolution of $\lambda/2$, $\lambda/4$ and $\lambda/8$ (i.e. the field is calculated at points of a grid with mesh $\lambda/2$, $\lambda/4$ and $\lambda/8$, respectively). This calculation is used for evaluating the maximum significant number of reflections and the suitable density of field points. To this purpose, the

near E-field is computed inside a cell of dimension $5\lambda \times 5\lambda$ (i.e. to reduce the computation time) and the average E-field on this cell is calculated.

All cases computed by varying the field points density and the number of reflections are shown in Table I.

From Table I it is apparent that as the spatial resolution moves from $\lambda/2$ to $\lambda/8$ the differences among the average E-fields are negligible. Instead, as regards the choice of the number of reflections, it can be seen that from 5 to 7 reflections, the average E-field has increased of about 25%, while in going from 7 to 9, the field remains unchanged. For this reason, the spatial resolution was set at $\lambda/2$ in order to save computational time and memory, while the number of reflections was set to 7.

TABLE I - COMPARISON OF AVERAGE E-FIELD IN THE CELL, FOR DIFFERENTE NUMBER OF REFLECTIONS

5 REFLECTIONS	
Spatial Resolution	Average Field in the cell ($5\lambda \times 5\lambda$) (V/m)
Lambda/2	0.0012966
Lambda/4	0.0012932
Lambda/8	0.0012951
7 REFLECTIONS	
Lambda/2	0.0016942
Lambda/4	0.0016942
Lambda/8	0.0016911
9 REFLECTIONS	
Lambda/2	0.0017191
Lambda/4	0.0016593
Lambda/8	0.0016478

Figure 3 shows the E-field (in dBV/m) in the geometrical model for three different cut planes at 2.4GHz. It is apparent the maximum magnitude is near the point source, while outside the black circle is always less than -40 dBV/m. Figure 4, instead, shows the three component of E-field in time-domain in point P, shown in fig. 3 and located at 3.8 meters from the antenna.

I. CONCLUSION

A numerical investigation of the electromagnetic propagation inside a model of a module of the ISS with annexed crew quarters has been shown. Calculations were performed at two different frequencies and with a different number of reflections. Numerical results show that a number of 7 reflections is sufficient to obtain accurate calculation because the discrepancy with respect to 9 reflections is less than 2%. The average field (average on a surface of $5\lambda \times 5\lambda$) instead is not sensitive to the density of the field points provide that the mesh is less than $\lambda/2$. The field inside the model results to be lower than -40dBV/m when the EIRP of the antenna is -41.5 dBm, which is the maximum allowable EIRP for FCC rules.

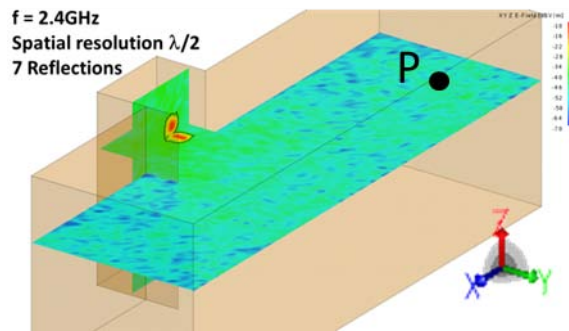


FIG. 3 E-Field, computed with 7 reflections, for three different plane at 2.4GHz with a spatial resolution of $\lambda/2$.

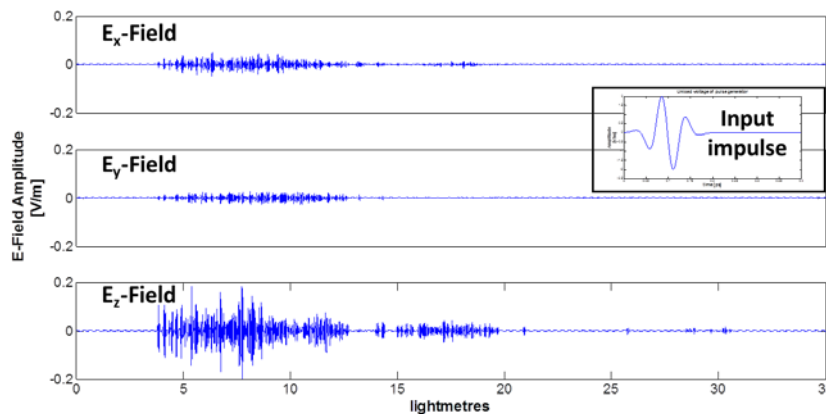


FIG. 4 Time-domain behavior of the electric field components in P when drop dipole is used. The impulse signal used to feed the antenna is also shown.

ACKNOWLEDGEMENT

This work is partially supported by ASI under contract NIMURRA. The authors wish to thank Stefano Pisa from La Sapienza University of Rome, for his coordinating activities in NIMURRA project.

REFERENCES

[1] P.A. Santy, H. Kapanka, J.R. Davis, D.F. Stewart, "Analysis of sleep on Shuttle missions," *Aviat Space Environ Med*, vol. 59, pp.1094–1097, 1988.
 [2] C. Stampi, "Sleep and circadian rhythms in space," *J Clin Pharmacol*, vol. 34, pp. 518–534, 1994.
 [3] J.L. Broyan, S. M. Cad, D. A. Welsh, "International Space Station Crew Quarters Ventilation and Acoustic Design Implementation", 40th International Conference on Environmental Systems, American Institute of Aeronautics and Astronautics pp. 1-14, 2010.
 [4] International Space Station (ISS) Interactive Reference Guide, <http://www.nasa.gov/externalflash/ISSRG/pdfs/harmony.pdf>.
 [5] S. U. Hwu, Y.C. Loh, C. C. Sham, "Space Station Wireless Local Area Network Signal Characteristics Modelling and Measurements", *IEEE 25th Digital Avionics Systems Conference*, pp. 1-8, 2006.

CRITERION FOR THE OPTIMAL CHOICE OF THE OPERATIVE CONDITIONS IN MAGNETIC NANOPARTICLE HYPERTHERMIA: UNCERTAINTY ANALYSIS

G. Bellizzi⁽¹⁾, O.M. Bucci⁽²⁾

(1) DIBET-Università di Napoli Federico II, Via Claudio 21,80125,
Napoli, Italy

(2) IREA-Consiglio Nazionale delle Ricerche, Via Diocleziano 328,
80124, Napoli, Italy
bucci@unina.it

Abstract

The aim of the paper is to assess the robustness of a recently proposed criterion, for the optimal choice of the operational conditions in Magnetic NanoParticle Hyperthermia (MNP), against the uncertainty on the knowledge of the thermal properties of the exposed tissues. In particular, the uncertainty on the induced temperature rise due to a rough knowledge of the thermal properties is analytically evaluated and the obtained results are compared to those numerically computed in the case of tumors hosted in a homogeneous healthy tissue.

Index Terms – Magnetic nanoparticle hyperthermia, Pennes bioheat equation, optimization criterion, uncertainty analysis.

I. INTRODUCTION

MNP is an emerging modality of hyperthermia, which achieves the selective heating of the cancerous tissue, above a therapeutic threshold, by inserting into it magnetic nanoparticles (MNP) and applying a radiofrequency magnetic field (MF). Currently, one of the main challenges in MNP is to maximize the Specific Absorption Rate (SAR) of the used MNP in order to achieve the therapeutic heating of the tumor and the desired spatial selectivity of the treatment with an amount of MNP as small as possible. Since the SAR depends on the amplitude and frequency of the applied MF, say H and f , as well as on the MNP core size, say d , SAR can be optimized by properly setting the values of such parameters. An effective optimization criterion to get this has been recently proposed [1] and its effectiveness numerically tested. The aim of this paper is to assess the robustness of the criterion against the uncertainty on the knowledge of the thermal properties of the irradiated tissues. In particular, the uncertainty on the induced temperature rise due to a rough knowledge of the thermal properties is analytically evaluated and the obtained results are compared to those numerically computed in the case of spherical tumors hosted in homogeneous healthy tissue.

II. OPTIMIZATION CRITERION

Since the goal of hyperthermia is to selectively heat the tumor, the starting point of the criterion is to describe the thermal balance within the irradiated tissues. Here, we exploit the Pennes Bioheat equation [1]:

$$\bar{\nabla} \cdot (k(\underline{r}) \bar{\nabla} T(\underline{r})) - c_b w(\underline{r})(T(\underline{r}) - T_b) + p_{met}(\underline{r}) + p(\underline{r}) = 0 \quad (1)$$

where T is the induced temperature field, k the thermal conductivity, w the blood perfusion rate, c_b the specific heat capacity of blood, T_b the temperature of blood ($T_b=37$ °C), p_{met} the metabolic heat generation rate and p the heat generation rate due to the applied field (the dependence on the position vector \underline{r} expresses spatial inhomogeneity). The term $p(\underline{r})$ in Eq.(1) can be conveniently expressed as follows:

$$p(\underline{r}) = p_m \tilde{h}^2(\underline{r})/2 + p_e \tilde{\sigma}(\underline{r}) \tilde{e}^2(\underline{r})/2 \quad (2)$$

where p_m and p_e are the spatial averages of the magnetic and electric power densities dissipated respectively into the tumor (due to the MNP and the MF) and over the irradiated region (due to the induced Electric Field, EF), while h , e and σ are well-defined, dimensionless, functions taking into account the spatial non uniformity of the MF, of the EF and of the electric conductivity of the exposed tissue. Moreover, it is reasonably assumed that a constant temperature $T=T_b$ is kept at boundary of the irradiated region (boundary condition). From Eq.(1)-(2), it follows that $T(\underline{r})$ can be controlled and shaped by properly setting the values of p_m and p_e , which, due to the linearity, can be easily estimated through a linear inversion, once the desired temperature constraints have been assigned.

Since p_m and p_e depend on H , f and d , the proposed criterion determines the optimal values of H , f , d , and the corresponding minimum MNP-concentration, C_{min} , to be supplied, by firstly estimating p_m and p_e such that $T(\underline{r})$ meets the assigned constraints. In particular, we require that $T(\underline{r})$ is larger than the therapeutic threshold all over the tumor and smaller than a safety threshold outside a transition region containing the tumor, whose extension represents the desired level of spatial selectivity. Once p_m and p_e have been evaluated, the optimal values of H , f , d and C_{min} are determined by exploiting the relations existing among these quantities and the estimated p_m and p_e [1].

III. UNCERTAINTY ANALYSIS

As described in Section II, the application of the criterion requires the knowledge of the thermal parameters, k and w , of the irradiated tissues,

which is unavoidably affected by uncertainty. Therefore, the induced temperature rise is affected by uncertainty which has to be estimated in order to assess the effectiveness of the criterion. To this end, we assume that $k \in k_0(1+\delta_k)$ and $w \in w_0(1+\delta_w)$ where k_0 and w_0 are the expected values of k and w , while δ_k and δ_w are the relative uncertainties. Denoting with T_0 , T_k , T_w the induced temperature fields for $k=k_0$ and $w=w_0$, $k=k_0(1+\delta_k)$ and $w=w_0$, $k=k_0$ and $w=w_0(1+\delta_w)$ respectively, from Eq.(1) one has:

$$\bar{\nabla} \cdot (k_0 \bar{\nabla} T_0) - c_b w_0 (T_0 - T_b) + p_{met} + p = 0 \quad (3)$$

$$(1 + \delta_k) \bar{\nabla} \cdot (k_0 \bar{\nabla} T_k) - c_b w_0 (T_k - T_b) + p_{met} + p = 0 \quad (4)$$

$$\bar{\nabla} \cdot (k_0 \bar{\nabla} T_w) - (1 + \delta_w) c_b w_0 (T_w - T_b) + p_{met} + p = 0 \quad (5)$$

where the values of p_m and p_e appearing in the term p of Eq. (3)-(5) are estimated for $k=k_0$ and $w=w_0$. By multiplying both sides of Eq.(3) once by $(1+\delta_k)$ and another by $(1+\delta_w)$ and subtracting the two equations so obtained from Eq.(4) and (5) respectively, one gets:

$$(1 + \delta_k) \bar{\nabla} \cdot (k_0 \bar{\nabla} \delta T_k) - c_b w_0 \delta T_k + \delta_k (c_b w_0 (T_0 - T_b) - p_{met} - p) = 0 \quad (6)$$

$$\bar{\nabla} \cdot (k_0 \bar{\nabla} \delta T_w) - (1 + \delta_w) c_b w_0 \delta T_w - \delta_w (\bar{\nabla} \cdot (k_0 \bar{\nabla} T_0) + p_{met} + p) = 0 \quad (7)$$

where $\delta T_k = T_k - T_0$ and $\delta T_w = T_w - T_0$. Finally, by summing Eq.(6) and (7), with $\delta_k = \delta_w = \delta$, and taking Eq.(3) into account, it results:

$$\bar{\nabla} \cdot (k_0 \bar{\nabla} \delta T) - c_b w_0 \delta T - \delta (p_{met} + p) + \delta (\bar{\nabla} \cdot (k_0 \bar{\nabla} \delta T_k) - c_b w_0 \delta T_w) = 0 \quad (8)$$

where $\delta T = \delta T_k + \delta T_w$ is the uncertainty on the induced temperature rise when $\delta_k = \delta_w = \delta$, in the worst case of δ_k and δ_w having the same sign. As can be seen from Eq.(8), δT satisfies the same thermal problem of the temperature rise $T_0 - T_b$, except for the last term, which, for small δ , can be neglected as compared to the term $\delta(p_{met} + p)$, being of higher order in δ . Accordingly, for the linearity of the problem, it results $\delta T = \delta(T_0 - T_b)$.

IV. NUMERICAL ANALYSIS

To test the reliability of the obtained expression for δT , we have performed a numerical analysis considering as test case a spherical tumor of radius 7.5 mm located at the center of a cylindrical healthy tissue of radius 50 mm. The tissue is assumed homogeneous with

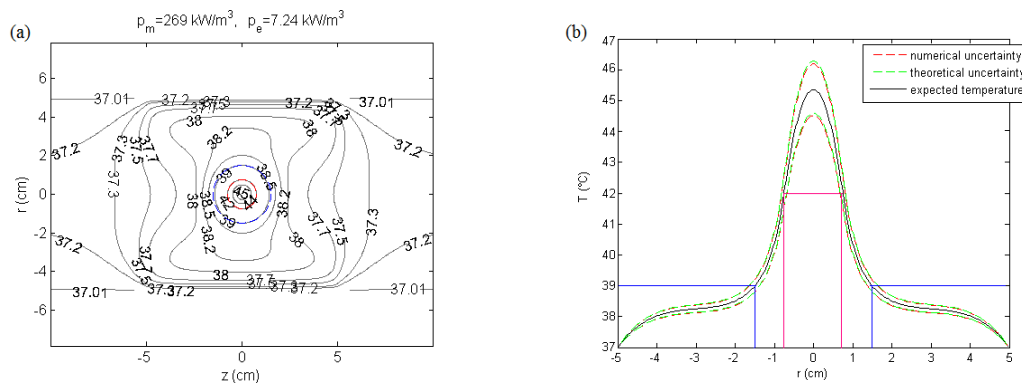


FIG. 1 – (a) Isothermal curves of the temperature field induced over the irradiated tissues; (b) radial profile of temperature in the plane containing the tumor center.

$k_0=0.6$ W/m/°K, $\omega_0=1$ kg/m³/s and $p_{met}=1$ kW/ m³ [1]. As first step of the analysis, by using the proposed criterion, we have estimated the values p_m and p_e such that the resulting temperature field, $T_0(\underline{r})$, meets assigned constraints, which are $T_0(\underline{r})\geq 42^\circ\text{C}$ all over the tumor (red circle in Fig. 1a) and $T_0(\underline{r})\leq 39^\circ\text{C}$ outside the transition region (blue circle of radius 15 mm in Fig. 1a). The isothermal lines of $T_0(\underline{r})$ are shown in Fig. 1a, together with the estimated p_m and p_e . As can be seen, the temperature constraints are completely fulfilled. As second step, by using the estimated p_m and p_e as heat source, we have computed the induced temperature fields assuming a relative uncertainty $\delta=10\%$ on both the above values of k_0 and ω_0 . The obtained radial profiles of temperature, in the plane containing the tumor center, are shown in Fig. 1b (dashed red lines) together with the expected temperature profile, T_0 , (black line) and the profiles of $T_0\pm\delta T$ (dashed green lines), with δT given in Section II. As can be seen, there is a satisfactory agreement between the predicted and the numerically computed profiles of uncertainty, which proves the goodness of the analytical estimation of δT . Moreover, as foreseen, δT is proportional to the relative uncertainty, δ , which proves the robustness of the proposed optimization criterion.

V. CONCLUSION

In this paper the robustness of a proposed optimization criterion in MNPH has been assessed against the uncertainty on the knowledge of the thermal parameters of the involved tissue. Both analytical and the numerical results have shown that the criterion is very robust having an error on the estimated temperature rise which is proportional to the relative error on the thermal parameters.

REFERENCES

- [1] G. Bellizzi and O. M. Bucci, “On the optimal choice of the exposure conditions and the nanoparticle feature in magnetic nanoparticle hyperthermia” *Int. J. Hyperthermia*, vol. 26(4), pp. 389-403, June 2010.

MICROWAVE TREATMENT OF TUFF-STONES. STRUCTURAL ANALYSIS

B. Bisceglia⁽¹⁾, E. Avallone⁽²⁾, A. Buonerba⁽³⁾, E. Caliendo⁽²⁾,
F. Chiadini⁽¹⁾, A. Grassi⁽³⁾, L. Incarnato⁽²⁾, A. Scaglione⁽¹⁾, L. Guerriero⁽⁴⁾

⁽¹⁾ Department of Electronic and Computer Engineering,
University of Salerno, Via Ponte Don Melillo, Fisciano (SA), Italy
[bbisceglia*fchiadini*ascaglione}@unisa.it](mailto:{bbisceglia*fchiadini*ascaglione}@unisa.it)

⁽²⁾ Department of Industrial Engineering,
University of Salerno, Via Ponte Don Melillo, Fisciano (SA), Italy
eavallon*incarnato}@unisa.it emiliacaliendo@virgilio.it

⁽³⁾ Department of Chemistry and Biology
University of Salerno, Via Ponte Don Melillo, Fisciano (SA), Italy
abuonerba*grassi}@unisa.it

⁽⁴⁾ Dipartimento di Restauro e Costruzione dell'Architettura e
dell'Ambiente, II Università di Napoli
luigi.guerriero@unina2.it

Abstract

Non destructive and non invasive techniques are irreplaceable in order to preserve and to restore cultural heritage objects in its structure and shape. Microwave (MW) non invasive disinfection methods allow to intervene on the heritage goods with no alteration of the state of preservation. It is important to demonstrate that the MW treatment does not alter the structure of the goods, since this can influence its physical, chemical and mechanical properties.

Aim of this work is to investigate about alterations of the structure of tuff-stones after MW disinfection.

The effects have been investigated by several techniques, such as X-ray diffraction, infrared spectroscopy and thermogravimetric analysis. The results show that the structure is not much influenced by MW treatment.

Index Terms – Tuff-stones, microwaves, disinfection, works of art.

I. INTRODUCTION

Historical structures are valuable documents that present the achievements of the past in terms of architectural, constructional technologies and functional systems. It is essential to keep their authenticity and to provide their survival for posterity [1].

Stone decay takes many different forms: physical and chemical mechanisms are considered the main factors. Living organisms also contribute to the decay of stone and similar materials and their study presents numerous features of interest [1].

Stone-cleaning processes often involved harsh acidic treatments. Damaged architectural stone was either replaced or repaired with little regard to the materials' compatibility with the stone, appearance matching, or the durability of the treatment. The unsuitability of many of these treatments encouraged research efforts to develop new materials and procedures for the preservation of stone [2].

Electromagnetic waves can be used for diagnostic and conservation of works of art [3]. Some important results are available in literature considering the whole interval from X-rays up to radiofrequencies paying particular attention to non-invasive and transportable instrumentation [4].

MW-treated and untreated yellow and grey tuff specimens collected from ancient buildings located in the environs of Salerno (Nocera Inferiore) have been characterized by means of different experimental techniques, in order to establish whether such a treatment could induce structural modification that might impair durability of such materials. Preliminary analysis have been also carried out on mortar specimen and baked clay.

II. MATERIALS AND METHODS

Isotropic exposure of the samples was carried out in an aluminum made cubic (120 cm side long) reverberating enclosure equipped with two rectangular (90 x 20 cm) mode stirrers rotating at different velocities (0.4 and 1.1 rps respectively).

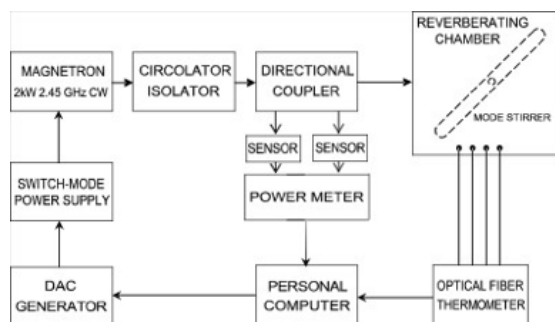


FIG. 1 – MW exposure system

A 2.45 GHz, 2 kW CW magnetron, powered by a switch-mode power supply, was used to provide microwave energy. This system allows the magnetron to work at different power levels ranging from a few watts to 2 kW. The measurement of the power incident on and reflected from the reverberating chamber is performed using a dual directional coupler connected to a dual channel power meter. (Fig. 1)

Tuff samples were collected from ancient buildings in the surrounding area of Salerno (Italy) and afterwards shaped as cubic specimen ($l=5$ cm) by mean of a power saw.

The samples were MW treated with an Incident Power (measured at the Input port of reverberation chamber) of 400÷900 W for 60÷180 sec.

In order to evaluate the chemical composition and the effect of the MW treatment on crystal structure thermogravimetric measurements, FT-IR and X-ray diffraction analysis were carried out on the untreated and treated tuff samples. The variation of the aesthetical properties induced by the treatments was verified by colorimetric analysis.

Moreover water capillary sorption, total water absorption by total immersion and uniaxial compression strength test have been performed in order to check both transport properties and durability of tuff samples.

III. RESULTS AND DISCUSSION

X-ray patterns indicate no detectable differences in crystalline phases for treated and untreated tuff samples (both yellow and grey), thus the MW treatment did not induce any crystal modification. Thermogravimetric analysis, along with FT-IR investigation, confirmed that the MW treatment did not induce any structural breakdown. FT-IR spectra are reported in Fig. 2.

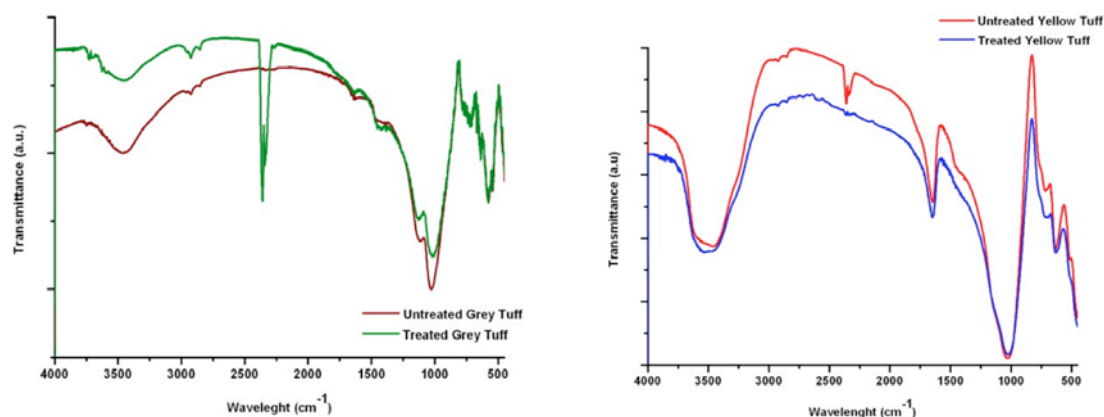


FIG. 2 – FT IR spectra of tuff samples
(grey: 700 W, 9 min; yellow: 500 W, 3 min)

Colorimetric analysis showed that following the MW treatments, tuff samples did not change their aesthetical properties.

Transport properties (Fig. 3, water capillary sorption) revealed just a slight difference in the water uptake for treated yellow tuff, which could be ascribed to the more porous nature of the stone.

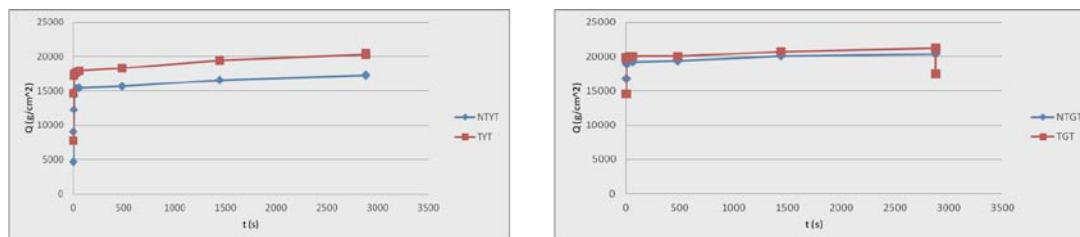


FIG. 3 – Curves of water capillary rise vs square root of time relative to yellow and grey tuffs

IV. CONCLUSION

No relevant modifications can be relieved between treated and untreated samples.

MWs constitute a good tool for non destructive art and archeological disinfection work. The exposure of samples validate expectant potential application of MW non invasive techniques. These data are useful in order to obtain treatment protocols.

REFERENCES

- [1] E. Doehne and C. Price, "Stone Conservation: An Overview of Current Research", 2nd Ed., The Getty Conservation Institute, L.A. 2010.
- [2] M. Bacci, "Exploitation of the entire electro-magnetic spectrum in art conservation studies", 35th International Conference on Infrared, Millimeter and Terahertz Waves, Rome, Italy, September 5-10, 2010.
- [3] B. Bisceglia, R. De Leo, S. Von Gratowski, V. Meriakri and A.P. Pastore, "Innovative systems for cultural heritage conservation. Millimeter waves application for non-invasive monitoring and treatment of works of art", Journal of Microwave Power and Electromagnetic Energy, 45(1)36-48, 2011.
- [4] Ö. Özaka and H. Böke, "Properties of Roman bricks and mortars used in Serapis temple in the city of Pergamon", Materials Characterization 60(2009) 995-1000.

Signal Transduction on Enzymes: the Effect of Electromagnetic Field stimuli on Superoxide Dismutase (SOD)

P. Marracino, M. Migliorati, A. Paffi, M. Liberti, G. d'Inzeo, F. Apollonio

Italian Inter-University Centre for the Study of Electromagnetic Fields and Biosystems (ICEmB) at "Sapienza" University of Rome, Rome 00184, Italy.

marracino@die.uniroma1.it

Abstract

Protein functions and characteristics can highly differ from physiological conditions in presence of chemical, mechanical or electromagnetic stimuli. In this work we provide a rigorous picture of electric field effects on proteins behavior investigating, at atomistic details, the possible ways in which an external signal can be transduced into biochemical effects.

Index Terms – signal transduction, molecular simulations, enzymes, microwaves

I. INTRODUCTION

Under physiological conditions, proteins, enzymes and peptides spend most of their life-time in the native conformation, facilitating their biological functions. Several authors have demonstrated, through molecular dynamic simulations, that microwave electromagnetic (EM) fields may excite macromolecular vibrational modes and alter protein conformation, even including denaturation and stability [1].

Similarly from experimental side, it is demonstrated that nanosecond Pulsed Electric Fields (nsPEFs) with intensities up to several MV/m, can interact with proteins and genetic materials [2]. nsPEFs are signals whose frequency spectrum extends well in the microwave region with a quite large bandwidth, similarly to what happens to ultra-wideband technology signals. Due to their particular frequency content, nsPEF, may solicit on proteins a coupling with different frequencies in the microwave region.

In this context it seems appropriate to study the EM signal transduction on proteins through the approach based on molecular simulations. As a case study we have selected SOD enzyme, an important defense in nearly all cells, which has been widely investigated both theoretically and experimentally, even in presence of EM perturbation, in a wide range of frequencies [3], [4]. Our idea is to theoretically study the sensitivity of SOD enzyme to different EM stimuli, in particular 1 and 2.45 GHz continuous wave (CW) and a Gaussian pulse centered at 2.45 GHz with a bandwidth of 2 GHz, resulting in a pulse duration in time of less than 8 ns, with the perspective to possibly act on SOD activity in a controlled and efficient way.

II. MODELS AND METHODS

We carried out molecular dynamic simulations of a single SOD enzyme in water using GROMACS package [5]. The simulated system consisted of a rectangular box (7-nm side), in which we placed a single SOD enzyme, 10480 Single Point Charge (SPC) water molecules and 9 sodium counterions resulting in a typical density of 1000 kg/m³. Trajectories were propagated up to 80 ns in a NVT ensemble using an integration step of 2 fs, fixing the SOD centre of mass. The temperature was kept constant at 300 K. We introduced different signals, two continuous waves (1 GHz and 2.45 GHz) and a complete pulse (see Fig. 1), each with two different intensities of 10⁹ and 10⁸ V/m. The time-signal of Fig. 1 is obtained considering a gaussian pulse in the frequency domain with central frequency equal to 2.45 GHz and bandwidth of 2 GHz. In classical simulations the magnetic field force is several order of magnitude smaller than that of the electric component [1], so hereinafter only electric field will be considered.

To evaluate the structural properties of SOD we adopted the Covariance Matrix Method. Diagonalization of the 3x3 Covariance Matrix provides the eigenvectors, which represent the directions along which the overall system fluctuates with a positional mean square fluctuation given by the corresponding eigenvalues. Since polarization effects are expected in exposure conditions, we have also taken into account the dipole moment of the whole enzyme. Time courses of the observables were first numerically filtered through an Hamming pass-band filter, with the low cut-off frequency of 500 MHz and the high one of 5 GHz. Then the average periodogram was calculated over 10 segments of the trace. Regarding the gaussian pulse, spectrograms were adopted to represent how the spectral density of a signal varies with time.

III. RESULTS

In Fig. 3 we present a comparison between the unexposed simulation (panel A) and the {2.45 GHz, 10⁹ V/m} CW exposed simulation (panel B). It appears quite clear that high exogenous electric field, even with duration of few nanoseconds, can alter SOD native conformation, inducing a sharp stretching along the electric field direction (in our case the x-axis in the external coordinate system). The CW signal at {1 GHz, 10⁹ V/m} produces the same result, conversely, neither CW signals at lower intensities ($\leq 10^8$ V/m) nor the pulse, produced evident modifications in SOD geometry during the 60 ns trajectories (data not shown). In its native state SOD enzyme possesses a dipole moment of about 80-120 Debye. Dipole moment is a good observable to study polarization effect induced by the exogenous field, even at those intensities not affecting other observables. The spectral representation of dipole moment can, in principle, clarify the entity of signal transduction, as confirmed by the density spectra profiles shown in Fig. 4 for 10⁸ V/m and pulsed signals. We can observe a sharp effect at 1

and 2.45 GHz even for such a lower intensity. Surprisingly the 10^9 V/m Gaussian pulse seems to exhibit a similar behavior to those of the 10^8 V/m, with a peak at 2.45 GHz about 20 dB below the one of almost 10^6 Debye²/Hz, due to the {2.45 GHz, 10^9 V/m} signal. This mismatch can be explained considering that only for a small fraction of the total simulation time (60 ns) the signal is on (Fig. 1), hence providing a duty cycle of about 14%. Therefore the representation via the density power spectrum may be misleading. A possible alternative analysis is the signal representation via a spectrogram. In Fig. 5 we show two spectrograms for unexposed and exposed (to the pulse) conditions: in panel A we can appreciate the native spectra components possessed by SOD enzyme, while in panel B the high components around 2.45 GHz are pronounced mainly within the first ten ns. Moreover it is quite evident that the signal pulse is able to increase the frequency content of the SOD enzyme spectra even below the 2.45 GHz, since as it was expected, due to its wide frequency band, it is able to solicit the protein vibrational modes which are in the frequency range of [0.5-1.5] GHz.

IV. CONCLUSIONS

Molecular dynamics simulations are a useful tool to investigate the interaction of EM fields with enzyme molecules. Classical observables like covariance matrix and dipole moment are able to provide information on major effects as denaturation or large conformational changes. Nonetheless signal transduction of the fields into the molecular system is still detectable for field intensities, which do not induce relevant molecular variations, when using a proper spectral analysis. Finally more sophisticated time-frequency techniques seem to be the best approach for investigating such a transduction for short nanosecond pulses.

V. REFERENCES

- [1] N. J. English, G. Y. Solomentsev, and P. O'Brien, "Nonequilibrium molecular dynamics study of electric and low-frequency microwave fields on hen egg white lysozyme", *The Journal of Chemical Physics*, 2009, 131, 035106
- [2] S. J. Beebe and K. H. Schoenbach, "Nanosecond Pulsed Electric Fields: A New Stimulus to Activate Intracellular Signaling", *J Biomed Biotechnol.* 2005; 2005(4): 297–300
- [3] M. Pellegrino, F. Apollonio, M. Liberti, A. Amadei, A. di Nola, G. d'Inzeo, "Molecular simulations of biochemical processes in presence of a MW signal", *IEEE Antennas and Propagation Society International Symposium*, luglio 2008 San Diego, CA, 1-4.
- [4] G. Guler, N. Seyhan and A. Aricioglu, "Effects of Static and 50 Hz Alternating Electric Fields on Superoxide Dismutase Activity and TBARS Levels in Guinea Pigs", *Gen. Physiol. Biophys.*, 2006, 25, 177–193
- [5] D. Van Der Spoel, E. Lindahl, B. Hess, G. Groenhof, A. E. Mark, H. J. Berendsen, "GROMACS: fast, flexible, and free". *J Comput Chem*, 2005, 26 (16): 1701–18

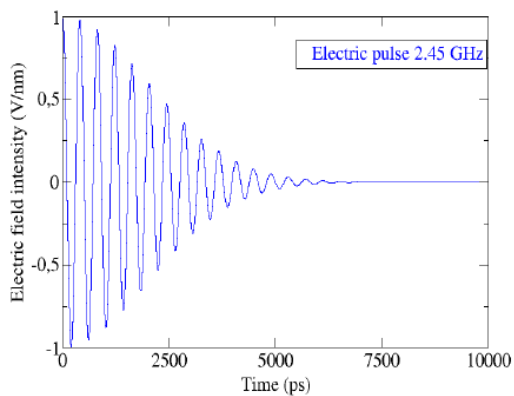


Figure 1. Time trend of the exogenous electric pulse (first 10 ns). The time-signal is obtained considering a gaussian pulse in the frequency domain with $f_0=2.45$ GHz, BW= 2 GHz and amplitude of 10^9 V/m.

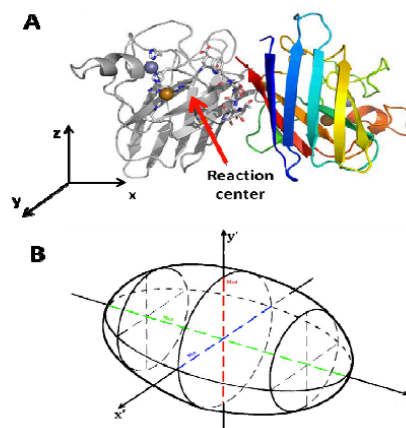


Figure 2. Panel A, molecular representation of SOD enzyme as obtained by VMD software (<http://www.ks.uiuc.edu/Research/vmd/>) in the external coordinate system $\{x,y,z\}$. Panel B, ellipsoidal region approximating SOD enzyme, as stated by covariance matrix method; to note the internal coordinate system $\{x',y',z'\}$ determined by SOD eigenvectors.

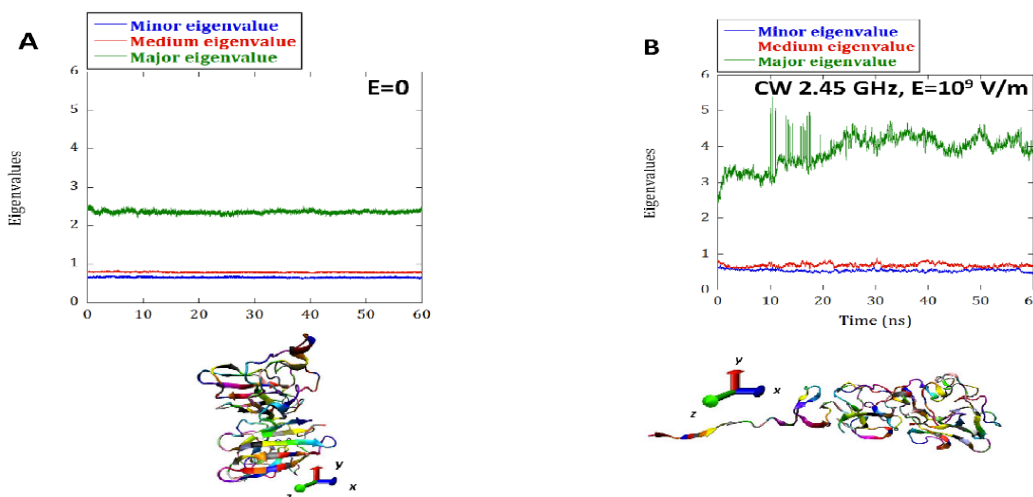


Figure 3. Panel A, time course of the three eigenvalues in unexposed conditions. To note the equilibrium condition during the simulation and the compact globular shape of SOD enzyme. During the application of the CW {2.45 GHz, 10^9 V/m} signal SOD major eigenvalue is stretched up to 200% of the physiological value.

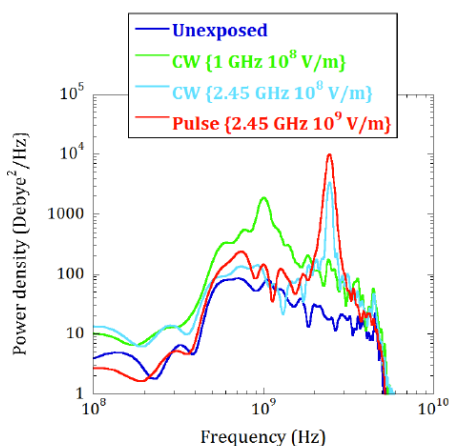


Figure 4. Power density spectrum of dipole component along SOD major axis.

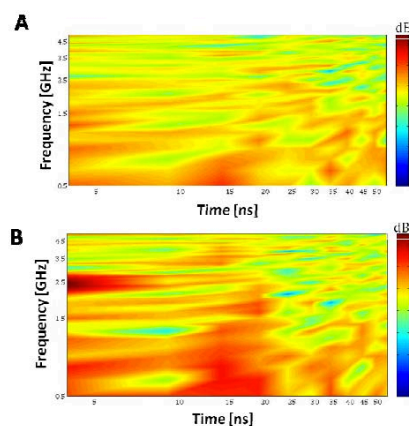


Figure 5. Spectrograms of unexposed (panel A) and exposed (panel B) simulations

CHARACTERIZATION OF A MICROWAVE THERMAL ABLATION PROCESS

M. Cavagnaro⁽¹⁾, S. Franco⁽¹⁾, V. Lopresto⁽²⁾, R. Pinto⁽²⁾

⁽¹⁾ DIET, Sapienza University of Rome
Via Eudossiana 18, 00184 Rome, Italy
cavagnaro@die.uniroma1.it

⁽²⁾ UT BIORAD, ENEA Casaccia Research Centre,
via Anguillarese 301, 00123, Rome, Italy
vanni.lopresto@enea.it

Abstract

Experimental measurements and numerical simulations are conducted with the aim of developing a numerical tool able to predict the very high temperature increases found in microwave thermal ablation procedures. Measurements of the temperature increase close to the microwave antenna have been performed. Measured data have been compared with numerical results obtained solving the bio-heat equation (BHE). The influence of the liquid refrigerating the antenna is put into evidence.

Index Terms – ablation procedures, numerical simulations, measurements.

I. INTRODUCTION

Microwave (MW) thermal ablation is a therapeutic technique used to remove un-healthy tissue by way of a high temperature increase provoked by the absorption of an electromagnetic field at microwave frequencies. Thermal ablation is obtained when the temperature of the target tissue increases up to about 60 °C [1]. The most recent applications of microwave thermal ablation are the treatment of tumours, and in particular, of liver tumours.

In microwave thermal ablation therapies, an antenna is inserted into the body up to the target area. Then, the antenna is fed with microwave power, with values up to 100 W for about 10 – 20 minutes. At the end of the treatment, an ablated area, defined as the area of tissue where temperature exceeded 60 °C, with a radial extension from the antenna up to about 5-6 cm can be obtained [2]. Numerical simulations can be used to design the microwave antenna, as well as to support the development of clinical protocols. Simulations solve the electromagnetic problem, governed by the Maxwell's equations, and the thermal one, defined by the bio-heat equation (BHE) [2]. However, measurements are needed to validate numerical data.

In this work, recent developments on the modelling of a microwave thermal ablation procedures will be presented. In particular, in previous works the dielectric properties of ex-vivo liver tissue have been measured as a function of the temperature [3]. Moreover, measurements of the temperature close to a microwave ablation antenna have been performed, considering several values of the

radiated power. This paper focuses on the numerical model of the ablation procedure, taking into account the experimental results, and considering the antenna cooling system. Numerical and experimental results will be compared in order to evidence the limits of the electromagnetic and thermal models.

II. METHODS AND MODELS

The experimental set-up (Fig. 1) is realized confining the liver tissue into a plastic box to help reproducibility of the positioning both of the microwave antenna and the considered sensors. The antenna is a asymmetric coaxial dipole with a mini-choke [2], and it is equipped with an internal cooling system: water, from a thermostatic bath at controlled temperature, circulates into the antenna up to the choke section, with a constant velocity. The antenna was supplied with a continuous wave signal at 2.45 GHz from a MW power generator (HS Amica, HS Hospital Service S.p.A., Rome, Italy). A two-channels power meter (Agilent E4419B, Agilent Technologies Inc., Santa Clara, CA, USA) was used to monitor, through a dual-coaxial directional coupler (Narda 3022, Narda Microwave–East, Hauppauge, NY, USA), the powers supplied to and reflected by the MW ablation antenna. Measurements of the temperatures close to the radiating antenna have been performed using a two channels fibre-optic thermometer (Luxtron 712, Luxtron Corp., Santa Clara, CA, USA) and a four-channels thermocouple thermometer (TC Misure e Controlli s.r.l., Turin, Italy) positioned orthogonally with respect to the antenna axis. Measurements of the dielectric properties were performed using an open-ended coaxial probe (Agilent 85070E, Agilent Technologies Inc., Santa Clara, CA, USA) connected to a vector network analyser (HP 8735C, Hewlett Packard Corp., Palo Alto, CA, USA), remotely controlled by a dedicated software running on a personal computer, through a general-purpose interface bus.

Simulations have been performed solving the electromagnetic problem by way of the Finite Difference Time Domain (FDTD) method, and the thermal problem by way of an FD solution of the BHE [4].

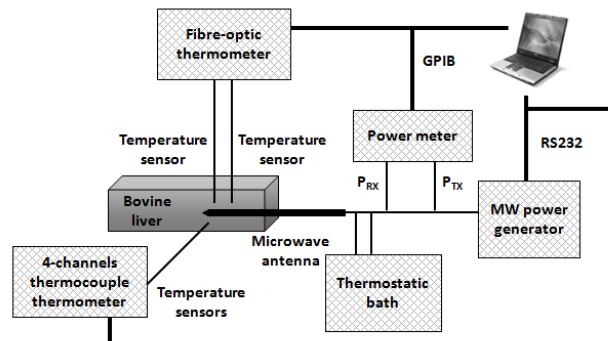


FIG. 1 – Experimental set-up for the measurements of temperature during a microwave ablation procedure.

The codes exploit the cylindrical symmetry of the problem. They have been validated with reference to ablation procedures against numerical and experimental data [2], [4]. In this paper, besides the code which implements the standard BHE [2], [4], a code implementing the BHE modified in order to take into account the mechanisms of water vaporization [5] will be used. The quantities numerically evaluated are the temperature as a function of time, and the thermal lesion dimension, defined as the area where the tissue temperature exceeded 60 °C. Particular care has been devoted to the evaluation of the influence of the antenna cooling system on the obtained results.

III. RESULTS

Fig. 2 shows temperature increments obtained close to the antenna tip at 5 mm distance from the antenna surface, for 20 W radiated for 10 min. The values measured by the Luxtron and thermocouple probes are reported together with the data simulated considering the standard and the modified BHE. An optimum agreement can be noted between the measured data and those simulated with the modified BHE.

Finally, fig. 3 shows the temperature increments evaluated at 5 mm from the antenna surface, in a section close to the antenna cooling system. From the figure it can be noted that, as expectable, the main parameter governing the heat exchange between the antenna and the surrounding tissue is the temperature difference between the liquid (T_{liq}) and the tissue (T_{set-up}) and the convection coefficient (H).

IV. CONCLUSIONS

In this paper the characterization of a microwave ablation procedure is considered, with particular emphasis on the development of a

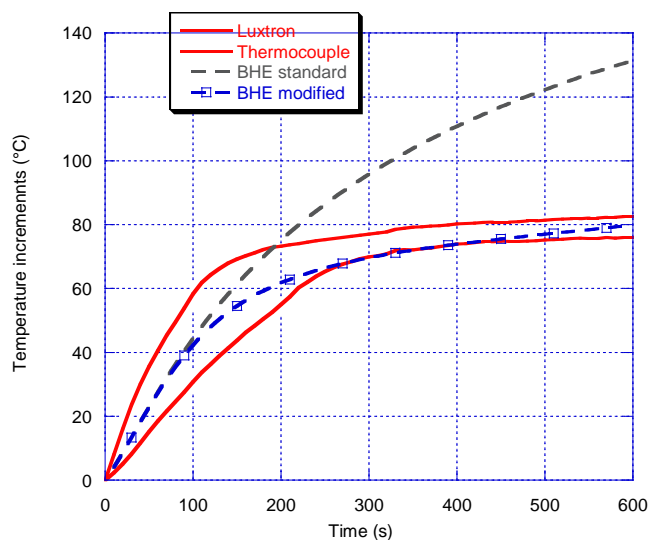


FIG. 2 – Temperature increments measured and simulated during a microwave ablation procedure (20 W, 10 min).

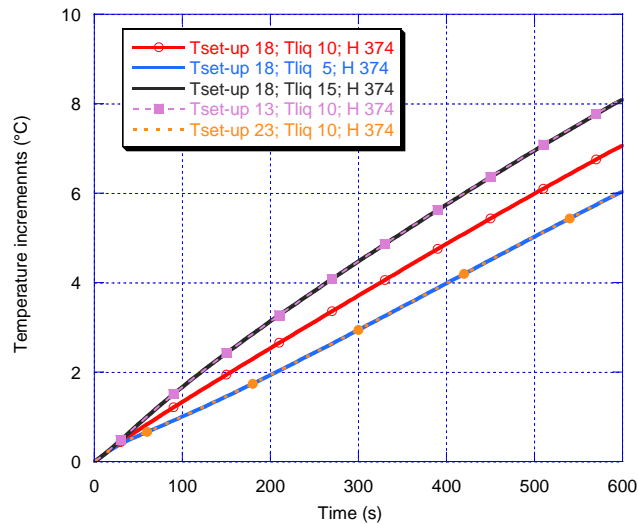


FIG. 3 – Effect of the cooling system on the numerically evaluated temperature increases.

numerical tool to be used in the design of the antennas and in the definition of clinical protocols.

ACKNOWLEDGEMENT

The Authors acknowledge the HS Hospital Service R&D unit for having made available the microwave antennas, and the colleague Sergio Mancini for his technical support essential to accomplish the measurements.

REFERENCES

- [1] M. G. Skinner, M. N. Iizukay, M. C. Koliosz, and M. D. Sherary, “A theoretical comparison of energy sources—microwave, ultrasound and laser—for interstitial thermal therapy,” *Phys. Med. Biol.*, vol. 43, pp. 3535–3547, 1998.
- [2] M. Cavagnaro, C. Amabile, P. Bernardi, S. Pisa, and N. Tosoratti, “A minimally invasive antenna for microwave ablation therapies: design, performances, and experimental assessment,” *IEEE Trans. Biomed. Eng.*, vol. 58, pp. 949-959, 2011.
- [3] V. Lopresto, R. Pinto, G. A. Lovisolo, and M. Cavagnaro, “Changes in the dielectric properties of ex vivo bovine liver during microwave thermal ablation at 2.45 GHz,” accepted *Phys. Med. Biol.*, 2012.
- [4] P. Bernardi, M. Cavagnaro, J. C. Lin, S. Pisa, and E. Piuzzi, “Distribution of SAR and temperature elevation induced in a phantom by a microwave cardiac ablation catheter,” *IEEE Trans. Microw. Theory Tech. (Special Issue on Medical Applications and Biological Effects of RF/Microwaves)*, vol. 52(8), pp. 1978–1986, Aug. 2004.
- [5] Yang D, Converse M C, Mahvi D M and Webster J G 2007b Expanding the Bioheat Equation to Include Tissue Internal Water Evaporation During Heating *IEEE Trans. on Biomed. Eng.* 54 1382-8

ARTIFICIAL TRANSMISSION LINE FOR WIRELESS POWER TRANSMISSION

G. Monti⁽¹⁾, L. Tarricone⁽¹⁾, M. Dionigi⁽²⁾, M. Mongiardo⁽²⁾

⁽¹⁾ Engineering for Innovation Department, University of Salento
Via per Monteroni, 73100 Lecce, Italy

⁽²⁾ Electronic and Information Engineering Department,
University of Perugia, 06125 Perugia, Italy
giuseppina.monti@unisalento.it, luciano.tarricone@unisalento.it
marco.dionigi@unipg.it, mauro.mongiardo@unipg.it

Abstract

In this paper a periodic network for wireless power transmission applications is presented. More in detail, the system here proposed consists of N inductively coupled LC unit cells. By using an artificial transmission line approach, useful design equations are derived and discussed. It is demonstrated that the wireless power link here presented exhibits a pass-band characterized by negative values of the phase propagation constant (i.e., a double negative pass-band). Comparisons with experimental data are also reported, thus validating the proposed analytical model.

Index Terms – Wireless Power Transmission; Inductive Coupling; Artificial Transmission Line; Double Negative Media.

I. INTRODUCTION

In the last years several studies have been dedicated to the use of inductively coupled systems [1-6] for wireless power transmission (Wireless Resonant Energy Link-WREL).

Traditionally, these systems are investigated by using a coupled mode theory [3]. More recently, some CAD procedures based on a network approach have been proposed [4, 5].

It has also been noted that, by using further resonators as relay elements, it is possible to extend the range for WREL [6]. The resulting typical coil resonator system is shown in Fig. 1, where it is possible to observe a cascade of inductive coils, each loaded with a capacitor, placed along a line. However, this arrangement closely resembles those used in magneto-inductive waveguides [7, 8] where the split-ring resonator is a metallic loop loaded by a small bulk capacitor. It was shown [7, 8] that an array of such loops can act as waveguides propagating magneto-inductive (MI) waves within a narrow band around the element's resonant frequency.

In this paper, a WREL consisting of a periodic network with inductively coupled unit cells is considered and analyzed by using an Artificial Transmission Line (ATL) approach [9-10]. Some useful design formulas are derived and discussed. In particular, it will be demonstrated that the analyzed WREL exhibits a double-negative (DNG) pass-band.

The paper is structured as follows: in section II the WREL system here considered is presented and analyzed by using an artificial transmission line approach; some circuital simulation results and experimental data are also given. Some conclusions are drawn in section III.

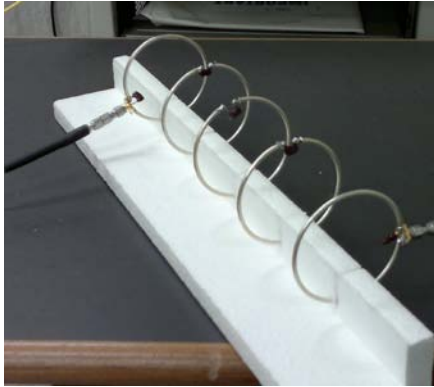


FIG. 1 – Photograph of the type of WREL system analyzed in this paper: the first and last resonators are coupled via relay elements (synchronous resonators).

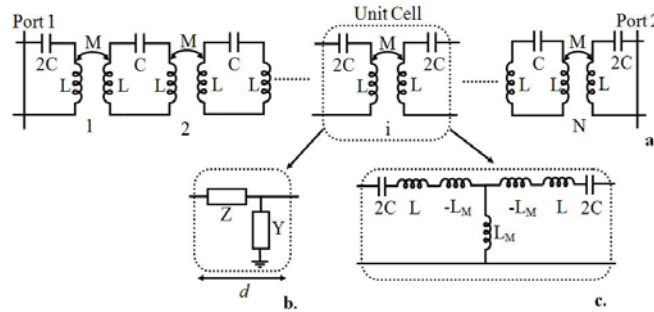


FIG. 2 – Schematic representation of the periodic network analyzed in this paper. **a.** Cascade of N inductively coupled LC unit cells, **b.** unit cell representation using a generic series impedance and shunt admittance, **c.** equivalent circuit of the unit cell; L_M is the mutual inductance ($L_M=ML$).

II. ANALYTICAL APPROACH AND RESULTS

The periodic network here proposed for WPT applications is illustrated in Fig. 2a; it consists of N identical unit cells. In the frequency range where the unit cell phase-shift is much smaller than 2π , the network acts as an ATL which is a transmission line described by an effective phase propagation constant and characteristic impedance ($\beta_{eff}d = \sqrt{-ZY}$, $Z_{0,eff} = \sqrt{Z/Y}$). Referring to the unit cell shown in Fig. 2a and to the corresponding equivalent circuit illustrated in Fig. 2c, it can be derived:

$$\begin{cases} \phi_{unit_cell} = \beta_{eff}d = \sqrt{2\frac{(1-M)}{M}} \sqrt{\left(\frac{1}{\hat{f}^2} - 1\right)} \\ Z_{0,eff} = \omega L \sqrt{2M(1-M)} \sqrt{\left(\frac{1}{\hat{f}^2} - 1\right)} \end{cases}, \hat{f} = \frac{f}{f_0}, f_0 = \frac{1}{2\pi\sqrt{2LC(1-M)}}. \quad (1)$$

It is evident that β_{eff} assumes imaginary values for frequencies above f_0 . Furthermore, from transmission line theory it can be shown that the

propagation along the line is equivalent to the propagation in a medium with constitutive parameters given by:

$$\mu_{eff} = \frac{Z}{j\omega} = L(1-M) \left(1 - \frac{1}{\hat{f}^2} \right), \varepsilon_{eff} = \frac{Y}{j\omega} = -\frac{1}{\omega^2 ML}. \quad (2)$$

Eq. (2) shows that the propagation along the ATL is equivalent to the propagation in a medium with negative values of both the electric permittivity and the magnetic permeability (i.e., a Double Negative-DNG medium) for frequencies below f_0 , whereas it is equivalent to the propagation in a medium with negative values of the electric permittivity for frequencies above f_0 . As a consequence, f_0 is an upper bound for the propagation along the ATL: the propagation is allowed only for frequencies below f_0 and it is characterized by negative values of β_{eff} .

In order to verify results obtained by using the ATL approach and summarized in (1) and (2), some measurements and circuital simulations have been performed. The analyzed system is the one of Fig. 1, which consists of 5 inductively coupled resonators. Each resonator is a loop loaded by a lumped capacitor. Referring to Fig. 2, the system is equivalent to an ATL consisting of 4 unit cells. As for the unit cell parameters, loops have a diameter of 74 mm and a mutual distance of 70 mm, thus resulting in a value of 79.6 nH and of 6.94 nH for L and L_M (i.e., $M=0.044$), respectively. The loading capacitor has a capacitance of 132 pF. Fig. 3a compares results obtained for this system by using the ATL approach with measurements; it can be noticed that a good

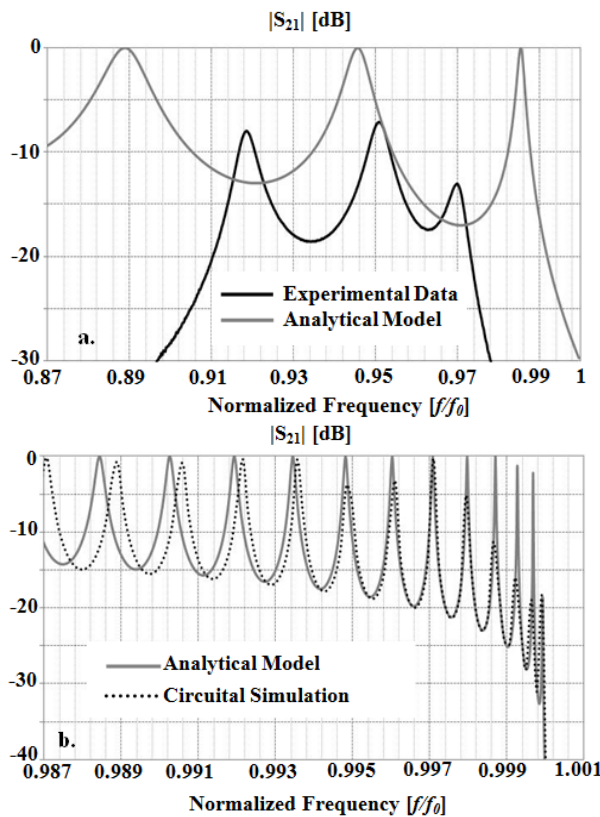


FIG. 3 – Validation of the ATL analytical model by means of comparisons with measurements (a.) and circuital simulations (b.).

agreement has been obtained, considering that the ATL model is lossless. The system has been also investigated by means of circuital simulations; corresponding results are illustrated in Fig. 3b. More in detail, Fig. 3b compares analytical and circuital results obtained for the transmission coefficient of a WREL consisting of 56 unit cells (N). Referring to Fig. 2, the unit cell parameters are: $2C=33$ pF, $L=169.2$ nH,

$M=0.1$. A perfect agreement has been obtained in the upper part of the bandwidth where the unit cell phase shift is much smaller than 2π .

III. CONCLUSION

A Wireless Resonant Link (WREL) consisting of a cascade of N identical unit cells has been considered and analyzed by using an artificial transmission line approach. It is demonstrated that the use of inductively coupled resonators as unit cell results in a WREL with a bandwidth characterized by negative values of the phase propagation constant. Experimental and circuit results validating the proposed analytical approach have been also reported.

REFERENCES

- [1] C. G. Kim, D. H. Seo, J. S. You, J. H. Park, and B. H. Cho, "Design of a contactless battery charger for cellular phone," *IEEE Trans. Ind. Electron.*, vol. 48, No. 6, pp. 1238-1247, December 2001.
- [2] T. Sekitani, M. Takamiya, Y. Noguchi, S. Nakano, Y. Kato, T. Sakurai, and T. Someya, "A large-area wireless power-transmission sheet using printed organic transistors and plastic MEMS switches," *Nature Mater.*, vol. 6, pp. 413-417, June 2007.
- [3] A. Karalis, J.D. Joannopoulos, M. Soljacic, "Efficient wireless nonradiative mid-range energy transfer," *Annals of Physics*, Elsevier, 323, pp. 24-48, 2008.
- [4] M. Dionigi, M. Mongiardo, R. Sorrentino and C. Tomassoni, "Networks Methods for Wireless Resonant Energy Links (WREL) Computations," ICEAA, Turin, Italy, 2009.
- [5] M. Dionigi, M. Mongiardo, "CAD of Efficient Wireless Power Transmission systems," *IEEE Microwave Symposium Digest (MTT)*, 5-10 June 2011, pp. 1-4.
- [6] M. Dionigi, A. Costanzo, M. Mongiardo, "Network Methods for the Analysis and Design of Resonant Wireless Power Transfer Systems," Chapter of the book "Wireless Energy Transfer Based on Electromagnetic Resonance - Principles and Engineering Explorations," <http://www.intechweb.org/>, 2011.
- [7] E. Shamonina, V.A. Kalinin, K.H. Ringhofer, and L. Solymar, "Magneto-inductive waveguide," *Electron. Lett.*, 2002, 38, pp. 371-373.
- [8] M. C. K. Wiltshire, E. Shamonina, I.R. Young, and L. Solymar, "Dispersion characteristics of magneto-inductive waves: comparison between theory and experiment," *Electron Lett.*, 39, pp. 215-217, 2003.
- [9] G. Monti, L. Tarricone, "Compact Broadband Monolithic 3-dB Coupler by using Artificial Transmission Lines," *Microwave and Optical Technology Letters*, vol. 50, 10, pp.: 2662-2667, Oct. 2008.
- [10] G. Monti, L. Tarricone, "Dual-Band Artificial Transmission Lines Branch-Line Coupler," *Int. Journal of RF and Microwave Computer-Aided Engineering*, vol. 18, iss. 1, pp.: 53-62, Sept. 2007.

MICROWAVE DESIGN STUDIES OF LINEAR ACCELERATORS FOR FREE ELECTRON LASER PHOTOINJECTORS

M. Dal Forno⁽¹⁾, P. Craievich^{(2)*}, R. Vescovo⁽¹⁾, C. Serpico⁽²⁾

⁽¹⁾ Department of Engineering and Architecture,
University of Trieste
Via A. Valerio 10, 34127 Trieste, Italy
massimo.dalforno@phd.units.it, vescovo@units.it

⁽²⁾ Sincrotrone Trieste S.C.p.A., 34149 Basovizza, Trieste, Italy

Abstract

The front-end injection systems of the FERMI@Elettra linac [1] produce high brightness electron beams that define the performance of the Free Electron Laser (FEL). The photoinjector mainly consists of a radiofrequency (RF) gun and of two S-band RF structures which accelerate the beam. Accelerating structures endowed with a single feed coupler cause deflection and degradation of the electron beam properties, due to the electromagnetic field asymmetry. Presently, a dual feed coupler is adopted to symmetrize the coupler field. In this paper, a new type of single feed structure with movable short circuit is proposed. It has the advantage of having only one waveguide input, and the dipolar component of the coupler field is reduced. With the racetrack geometry, the quadrupolar component is reduced as well.

Index Terms – Travelling wave linear accelerator, single feed with movable short, racetrack geometry, coupler asymmetry, electron beam dynamics.

I. INTRODUCTION

The two FERMI@Elettra [1] accelerating sections of the injector work at 2.998 GHz and operate with a 16 MeV/m gradient. The main challenge in the microwave design of such structures is that of obtaining a high gradient of acceleration without degrading the beam emittance, which is a constrained parameter in FELs. The couplers of the accelerating structure have field asymmetries that are responsible for the deflection of the electron beam [2-3]. Such asymmetries can be reduced by using dual feeding or a dual feed with the racetrack geometry [4]. In this paper we evaluate the performances of a new type of single feed coupler endowed with an adjustable short-circuit on the opposite side. The latter approach provides the same field magnitude distribution as that of the dual feed structure. The results of the microwave design with Ansoft HFSS [5] are shown.

II. BEAM DYNAMICS IN THE COUPLER

A travelling wave accelerating structure is endowed with two couplers, the input and the output coupler (Fig. 1), used for feeding the structure and for collecting the residual power, respectively.

* Now working at Paul Scherrer Institute (PSI), Switzerland.

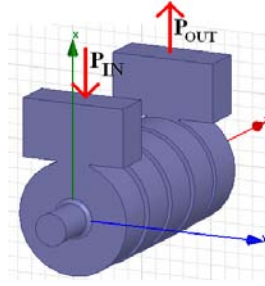


FIG. 1 – Single feed travelling wave accelerating structure.

The couplers introduce a field asymmetry. The longitudinal electric field can be decomposed into multipoles, where the monopole is the accelerating mode, while the other modes (such as the dipole and the quadrupole mode) are unwanted and cause degradation of the beam quality. In a first-order approximation, the electric field of the coupler is given by [2]:

$$E_z = \left[E_{z,0} + \frac{\Delta E_d}{2a} x \right] \exp\left(j \frac{\Delta \varphi_d}{2a} x \right) \quad (1)$$

which expresses the accelerating field in presence of the dipole field. The Panofsky-Wenzel theorem [3] shows that the electron beam receives a transversal kick. The transversal momentum (Δp_{\perp}) is given by:

$$\Delta p_{\perp} = j \frac{q}{\omega} \int_0^l \nabla_{\perp} E_z dz \quad (2)$$

where q is the electron charge, ω is the angular frequency, l the coupler length. The transversal dynamics of the particle can be evaluated by substituting (1) into (2), obtaining:

$$\Delta p_x = \frac{q \cdot E_{z,0} \cdot l}{\omega} \left(\frac{\overline{\Delta \varphi_d}}{2a} \cos(\varphi_{RF}) + \frac{\overline{\Delta E_d}}{2a E_{z,0}} \sin(\varphi_{RF}) \right) \quad (3)$$

where $\overline{\Delta \varphi_d}$ is the phase gradient of E_z , and $\overline{\Delta E_d}$ is the amplitude gradient, both quantities averaged along the z -axis of the coupler taking into account the transit factor [2]; φ_{RF} is the RF phase.

The field asymmetry can be evaluated by measuring the variation of the electric field along the coupler midplane. Assuming that the dipole field is predominant and varies as a cosinusoidal function of the azimuthal angle ϕ , the contribution of the dipole can be evaluated as follows:

$$\frac{\Delta E_d}{E_{z,0}} = \frac{|E_z(x=a)| - |E_z(x=-a)|}{|E_z(x=0, y=0)|}, \quad \Delta \varphi_d = \angle E_z(x=a) - \angle E_z(x=-a) \quad (4a)$$

where $E_{z,0}$ is the magnitude of the E_z field at $x=0, y=0$.

On the contrary, if the quadrupole field is predominant and varies as $\cos(2\phi)$, the quadrupole contribution can be evaluated as follows:

$$\frac{\Delta E_q}{E_{z,0}} = \frac{|E_z(x=a)| - |E_z(y=a)|}{|E_z(x=0, y=0)|}, \quad \Delta \varphi_q = \angle E_z(x=a) - \angle E_z(y=a) \quad (4b)$$

The general multipole decomposition is performed by expanding the amplitude and the phase of the field component E_z in the midplane. This gives the following Fourier coefficients C_k^{mag} (referred to the magnitude of E_z) and C_k^{arg} (referred to the phase of E_z):

$$C_k^{mag} = \frac{1}{2\pi} \int_0^{2\pi} \left| E_z \left(\phi, r = a, z = \frac{l}{2} \right) \right| e^{jk\phi} d\phi \quad (5a)$$

$$C_k^{arg} = \frac{1}{2\pi} \int_0^{2\pi} \angle E_z \left(\phi, r = a, z = \frac{l}{2} \right) e^{jk\phi} d\phi \quad (5b)$$

Eqs. (4) and (5) are related as follows:

$$\Delta E_d / E_{z,0} = \frac{4 \cdot |C_1^{mag}|}{|E_z(x=0, y=0)|}, \quad \Delta \varphi_d = 4 \cdot \left(|C_1^{arg}| - \angle E_z(x=0) \right) \quad (6a)$$

$$\Delta E_q / E_{z,0} = \frac{4 \cdot |C_2^{mag}|}{|E_z(x=0, y=0)|}, \quad \Delta \varphi_q = 4 \cdot \left(|C_2^{arg}| - \angle E_z(x=0) \right) \quad (6b)$$

Such values can be easily calculated from the simulation results.

III. MICROWAVE DESIGN AND EVALUATION OF THE PERFORMANCES

This section shows the different coupler geometries that have been studied and analyzed. The proposed solutions are the following:

1. Single feed
2. Dual feed
3. Dual feed with racetrack
4. Single feed with movable short-circuit
5. Single feed with movable short-circuit and racetrack

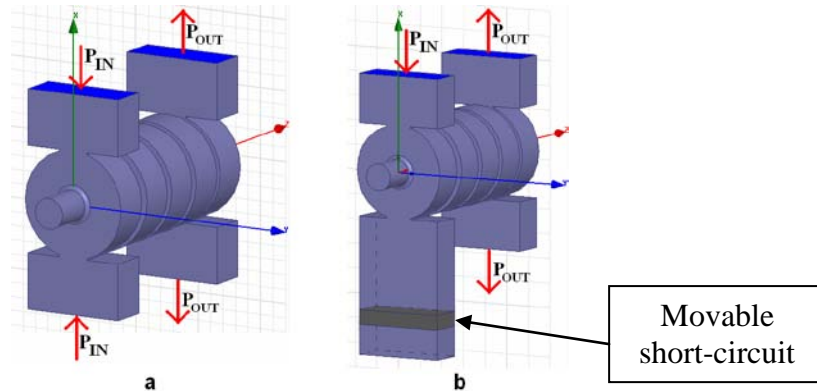


FIG. 2 – Dual feed (a) and Single feed with movable short-circuit (b).

Fig. 2 shows the difference between dual feed (2a) and single feed with movable short (2b). The advantage of the solution “Single feed with movable short”, is that of providing a dipole-free coupler field avoiding the power splitter. In fact, although traditional dual feed structures can be well designed, they can have a dipole field, due to the phase and amplitude differences produced by the waveguide path existing between the power splitter and the input couplers windows.

The design of the single feed with movable short-circuit has been performed with Ansoft HFSS [5], by iteratively changing the short circuit position to minimize the dipole component, matching the coupler at each time, by changing the coupler dimensions. Table I summarizes the results achieved for the four structures.

TABLE I – RESULTS OF THE ASYMMETRIES

	Single feed	Dual feed	Dual feed racetrack	Single feed with movable short	Single feed with movable short + racetrack
$\Delta E_d/E_{z,0}$	6%	0	0	0.01%	0.01%
$\Delta\phi_d$	0.6°	0°	0°	0.6°	0.6°
$\Delta E_q/E_{z,0}$	1.2%	1.6%	-0.01%	2.3%	0.01%
$\Delta\phi_q$	0.1°	0.12°	0.12°	0.13°	0.12°

Column 5 shows that the magnitude gradient of the dipole electric field is strongly reduced in the case of symmetric coupler with one waveguide input. Column 6 shows that both the magnitude gradient of the dipole electric field and the magnitude gradient of the quadrupole electric field, are strongly reduced in the case of single feed input with movable short and racetrack.

IV. CONCLUSION

This paper shows that a single feed coupler with movable short-circuit can provide the same performance as a dual feed structure, with reference to the electric field amplitude. The dipolar component of the electric field magnitude is therefore reduced. The racetrack geometry can be applied to the single feed with movable short, reducing the quadrupolar component as well.

ACKNOWLEDGEMENT

The authors wish to thank G. Penco (Sincrotrone Trieste S.C.p.A.) for his contribution in the understanding of the effects on the beam dynamics. The PhD of M. Dal Forno in the Department of Engineering and Architecture of the University of Trieste, Italy, is supported by Sincrotrone Trieste S.C.p.A., Italy.

REFERENCES

- [1] C. J. Bocchetta et al., “FERMI@Elettra Conceptual Design Report”, Sincrotrone Trieste, Tech. Rep. ST/F-TN-07/12, 2007.
- [2] G. A. Loew et al., “The Stanford Two-Mile Accelerator”, 1968 W. A. Benjamin, Inc, New York, pag. 146-148.
- [3] W.K. H. Panofsky and W. Wenzel, “Some Consideration concerning the Transverse Deflection of Charged Particles in Radio-Frequency Fields”, Rev. Sci. Instr., 27, 967, 1956.
- [4] Z. Li et al., “Coupler design for the LCLS injector S-Band structures”, Proceedings of PAC 05, TPPT031, Knoxville, Tennessee, 16-20 May 2005.
- [5] Ansoft HFSS, <http://www.ansoft.com/products/hf/hfss/>.

ANALYSIS OF THE FAST ICRH ANTENNA STRAPS ARRAY WITH WATER LOAD USING HFSS CODE

G.L. Ravera⁽¹⁾, S. Ceccuzzi^(1,2)

⁽¹⁾ Euratom-ENEA Association for fusion, C.R. Frascati
Via Enrico Fermi 45, 00044, Frascati, Italy

⁽²⁾ Applied Electronics Department, “Roma Tre” University
Via della Vasca Navale 84, 00146 Rome, Italy
ravera@frascati.enea.it

Abstract

FAST (Fusion Advanced Studies Torus) is a compact tokamak with high toroidal magnetic field (8.5 T) and plasma current (up to 8 MA), proposed as a Satellite Tokamak for accompanying the International Thermonuclear Experimental Torus (ITER) programme. The project foresees an Ion Cyclotron Resonance Heating (ICRH) able to couple a RF power of 30 MW in the 60 – 90 MHz frequency range with six antennas. Each antenna consists of eight straps arranged in a four rows by two columns array. Its performances can be simulated with a good accuracy, using a commercial code as HFSS, replacing the magnetized plasma with a high permittivity dielectric. Salty water solution can advantageously be used as dummy load. The relevant parameters of the FAST ICRH eight straps antenna have been carefully evaluated in a large range of straps' loading by varying the distance between straps and dummy load. Power handling capability (given a maximum voltage sustainable in the cables), mutual coupling between straps and RF potentials have been studied.

Index Terms – FAST, ICRH antenna, RF potentials.

I. INTRODUCTION

In FAST the ICRH power produces a fast ion population with energy above the half MeV range allowing to investigate α -particle behaviour in burning plasmas [1]. The high RF power in pulsed regime (pulse lengths up to 150 s every 2 h) will be coupled to the plasma by means of six antennas located in different equatorial ports of the machine. The antenna performances have been investigated by means of the HFSS code substituting the actual load, namely a highly magnetized plasma, with a salty water tank positioned at changeable distance from the straps. The maximization of the antenna performances corresponds to the minimization of mutual coupling between straps as well as RF potentials [2]. The latter, responsible of the impurity production, are computed by the integrals of the value or of the absolute value of the RF electric field components parallel (E_{\parallel}) to the magnetic field lines in front of the antenna.

II. DESCRIPTION OF THE HFSS MODEL WITH SALTED WATER DIELECTRIC

The maximum voltage sustainable is 38 kV for a rigid coaxial cable with characteristic impedance $Z_0 = 30 \Omega$, inner radius $r_a = 60.6 \text{ mm}$ and outer radius $r_b = 100 \text{ mm}$, assuming a standard dry air breakdown field of 2.42 MV m^{-1} and a safety factor of 2. The FAST ICRH antenna structure, shown in Fig.1a, consists of a single cavity containing eight straps (length = 275 mm, width = 140 mm, thickness = 8 mm, relative distance = 280 mm), short strip lines terminated on a background plane, arranged in four rows. They are protected against disruptive plasma interactions by a Faraday Shield (FS), not shown in the figure, made of 28 conducting bars, with rectangular cross section (2 x 1.5) cm. A dummy load able to simulate the peculiar plasma electric characteristics is a salty water solution with conductivity $0.5 \Omega^{-1} \text{ m}^{-1}$. The relative permittivity of this solution has a real part $k_d' = 81$ and an imaginary part $k_d'' = 120$. The salty solution, contained in a plexiglass tank with wall thickness $L_p = 2 \text{ cm}$, assures the absorption of the whole RF power also in a tank with limited depth. In addition, by properly changing antenna-dielectric distance, it is possible to verify the performances of the RF system in plasma-like loading conditions as pioneered by [3]. The water tank (Fig. 1b) is as wide as the antenna cavity and $L_d = 22 \text{ cm}$ deep. A vacuum layer (thickness L_w) is interposed between the straps and the dielectric slab. The simulations have been carried out by using a flat geometry for the antenna mouth, by setting the characteristic impedance of the eight coaxial cables (P1 to P8 are the input ports of the HFSS model) to $Z_0 = 30 \Omega$ and by varying L_w in the range 10 – 250 mm. Dipole phasing (0, π) is preset between the two columns of four straps.

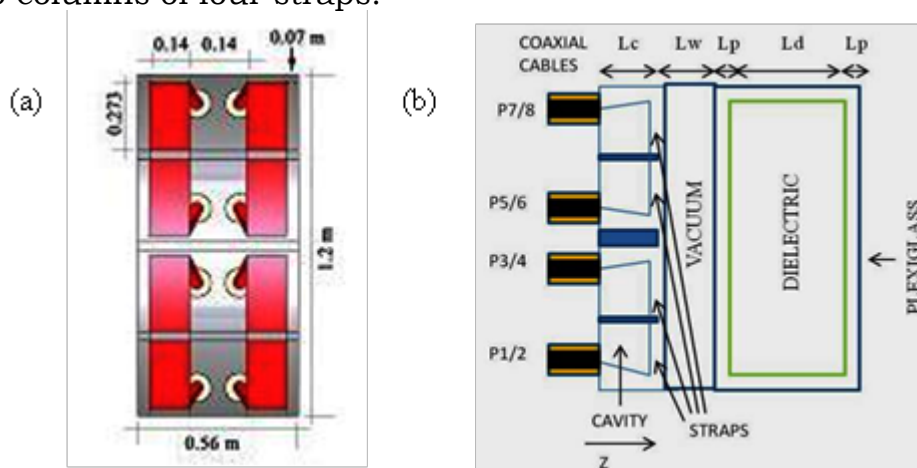


FIG. 1 – a) ICRH antenna structure. b) Layout of the salty water contained in a plexiglass tank with thickness L_p and positioned in front of the straps.

III. SIMULATION RESULTS

The first consideration concerns the geometrical asymmetry between central and outer straps which produces in the whole considered

frequency range, a different reflection for each group of straps, as shown in Fig. 2. The reflection decreases with the frequency and, as consequence of this asymmetry, it is lower for outer straps.

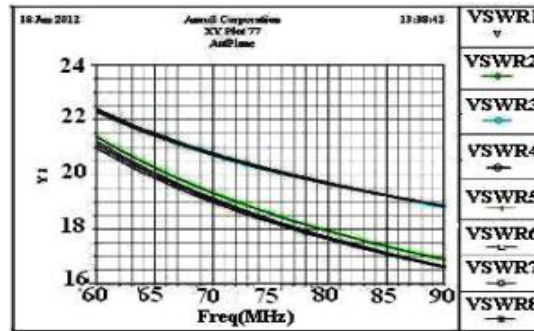


FIG. 2 – VSWR of eight straps for $L_w = 45$ mm and $Z_0 = 30\Omega$.

The coupling efficiency of the launcher can be expressed by $g_{\min i}$, which is the conductance in a voltage anti-node of the standing wave for all the straps ($i=1,\dots,8$). Optimizing the power coupled by a single straps for a given maximum voltage ($V_{\max i}$) corresponds to maximizing $g_{\min i}$:

$$P_i = 0.5 \times g_{\min i} \times V_{\max i}^2 \quad (1)$$

where

$$g_{\min i} = \frac{1}{VSWR_i \times Z_0} \quad (2)$$

Given a $V_{\max} = 38$ kV the value of P_i , slightly higher for outer straps, is represented against L_w in Fig. 3. A different procedure to evaluate P_i consists in setting the maximum intensity of electric field ($E_{\max} = 12.65$ kV/cm) corresponding to V_{\max} in the matched transmission line between strap and matching system. For $L_w = 70$ mm the P_i , computed from Eq (1) and (2), is about 0.95 MW while imposing E_{\max} the mutual coupling effects in the antenna array are taken into account and P_i decreases to 0.7 MW. So it is relevant to investigate the entity of vertical coupling (between straps of the same column) and horizontal coupling (between straps on the same row) considering for outer and central straps the related cross terms of the 8×8 scattering matrix.

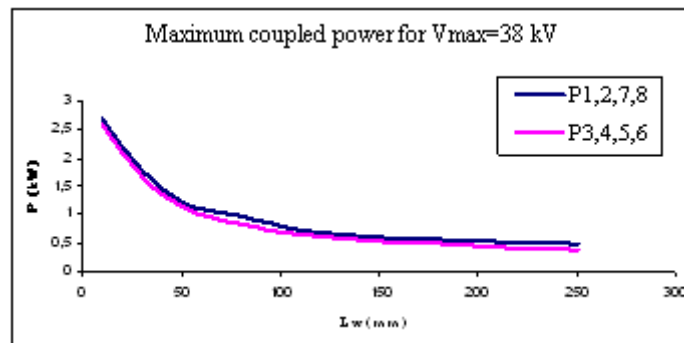


FIG. 3 – Maximum power coupled determined by $g_{\min i}$.

The toroidal coupling for outer and central straps is respectively about -20.5 dB and -21.5 dB independently from the distance L_w , while the poloidal coupling, comparable for outer and central straps, undergoes an excursion between -18 dB and -28 dB increasing L_w from 10 mm to 250 mm. RF potentials, normalized to 1 MW of power coupled, computed at 5 mm in front of the launcher for $L_w = 45$ mm, are reported respectively in Fig. 4 as a function of poloidal position. Peak values are located at the top and bottom of the antenna.

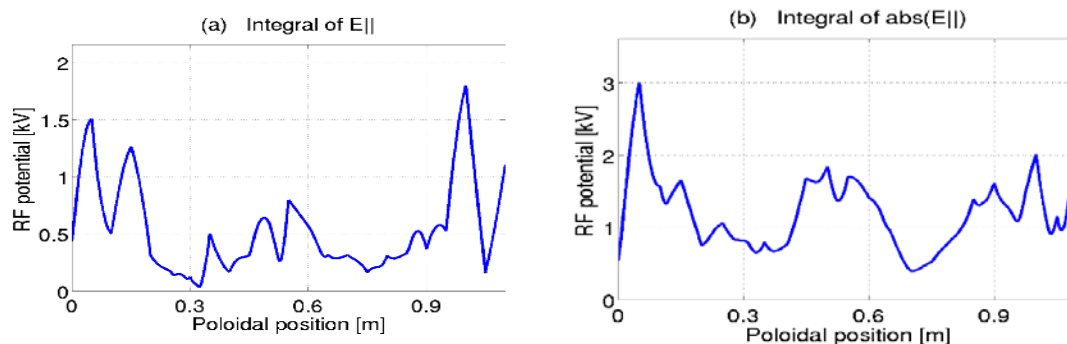


FIG. 4 – RF potentials at $f = 75$ MHz: a) integrals of E_{\parallel} b) integrals of absolute E_{\parallel} at 5 mm in front of the straps.

IV. CONCLUSION

Power handling capability, entity of mutual coupling and preliminary analysis of RF potentials for the FAST ICRH eight straps antenna array in front of a salty water dielectric have been successfully performed. To increase the P_{\max} over 5.6 MW, a modification of the antenna design will be necessary in order to reduce the mutual coupling and to minimize the reflection.

REFERENCES

- [1] A. Cardinali, G. Calabrò, C. Di Troia, M. Marinucci, B. Baiocchi, R. Bilato, M. Brambilla, S. briguglio, G. Fogaccia,, P. Mantica, G. Vlad, and F. Zonca, "Role of Combined NNBI and ICRH Heating in FAST H-node plasmas" *Proceedings of the 19th Topical Conference Radio Frequency Power in Plasmas*, Newport (USA), jun. 1- 3 2011, vol. 1406 , pp. 353-356.
- [2] S. Ceccuzzi, R. Cesario, A. Krivska, F. Mirizzi, G.L. Ravera, A.A. Tuccillo, R. Maggiore, D. Milanesio, V. Bobkov, F. Braun, J-M. Noterdaeme, I. Zammuto and ASDEX Upgrade team, "Assessment of ion cyclotron antenna performance in ASDEX Upgrade using TOPICA", *15th Intl.l Symp. on Applied Electromagnetics and Mechanics Proc.*, Sep. 7-9 2011, Naples, Italy, 2pp.
- [3] A.M. Messiaen, P. Dumortier, R. Koch, P. Lamalle, F. Louche, J.L. Martini, M. Vervier , "Realization of a test facility for the ITER ICRH antenna plug-in by means of a mock-up with salted water load," *Fusion Engineering and Design*, vol. 74, pp.367–375, 2005.

METAMATERIAL ACTIVITIES AT MICROWAVE AND OPTICAL FREQUENCIES AT "ROMA TRE" UNIVERSITY

M. Barbuto, A. Monti, D. Ramaccia, F. Bilotti, A. Toscano, L. Vegni

Applied Electronics Department, "Roma Tre" University
Via della Vasca Navale 84, 00146 Rome, Italy
mbarbuto@uniroma3.it; amonti@uniroma3.it; dramaccia@uniroma3.it

Abstract

In this contribution, we review some research activities recently developed at "Roma Tre" University in the field of metamaterials. In particular, we present several innovative devices with intriguing and unconventional features, working at both microwave and optical frequencies.

Index Terms – Metamaterials, cloaking, non-Foster elements, nano-antennas.

I. INTRODUCTION

In this paper, we review our most recent results in metamaterial (MTM) research. In the first section, we present an overview of different MTM-based devices operating at microwave frequencies, whereas the second section is devoted to the applications in optics.

II. MICROWAVES

A. Annular MTM lens for broadband shortened horn antennas

High-directivity horn antennas are typically heavy and rather bulky. The availability of compact horns with gain performances comparable to regular and optimum horns, would represent a remarkable achievement in the field. Here, we report on a shortened horn antenna loaded with an annular MTM lens [1]. Thanks to the phase-compensation enabled by the lens, the broadside gain is comparable to the one of a two-times longer optimum horn (see Fig.1)

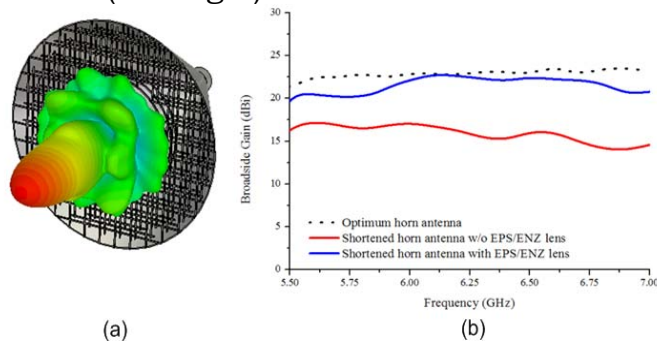


FIG. 1 – (a) 3D gain pattern at 6 GHz; (b) broadside gain vs frequency.

B. Self-filtering horn antennas

In order to reduce the noise captured by a receiving horn antenna for satellite applications, we have designed a MTM-inspired filtering module

consisting of a double-sided omega particle printed on a dielectric slab (Fig. 2(a)) and placed at the horn throat. The radiating performances of the proposed antenna are comparable to the ones of a regular horn radiator in the pass-band of the filtering module (Fig. 2 (b)).

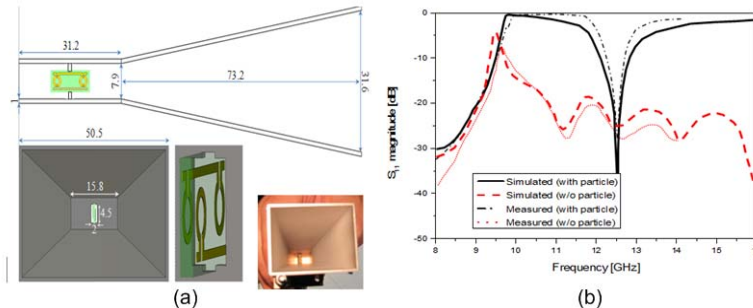


FIG. 2 – (a) Geometrical sketch; (b) matching properties vs frequency.

C. Reduction of the blockage effect and enhanced antenna co-siting strategies

In a recent work [3], we have analyzed the possibility to apply the mantle cloak technique to reduce the observability of receiving antennas. We consider the case of two dipoles resonating at slightly different frequencies placed in close proximity ($\lambda_0/10$ at 3 GHz). Impedance matching and radiation pattern of each dipole are seriously affected by the presence of the other antenna in the near-field region (Fig. 3(b)). Electrical and radiative features are restored by covering each antenna with a proper mantle cloak (Fig. 3(c)).

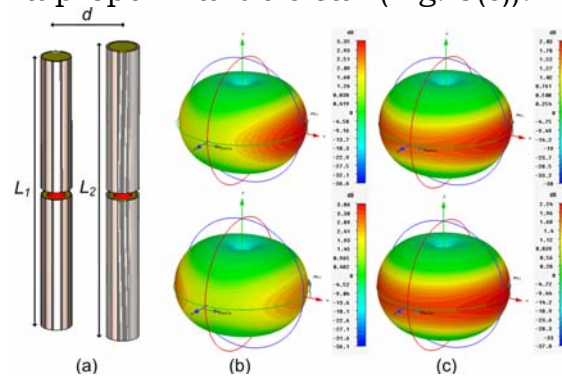


FIG. 3 - (a) Two half-wave dipoles resonating at slightly different frequencies covered with a proper mantle cloak; (b) 3D gain pattern in the uncloaked scenario; (c) 3D gain pattern in the cloaked scenario.

D. Linear-to-circular polarization transformer

We have recently proposed a polarization transformer [4] (Fig. 4(a)) consisting of a circular metallic screen with a sub-wavelength aperture through which two sets of connected circularly polarized electrically small antennas are placed. This structure has been used to close an open-ended circular waveguide in order to transform linear polarization into a circular one. Matching and polarization properties are reported in Figs. 4(b) and 4(c), respectively

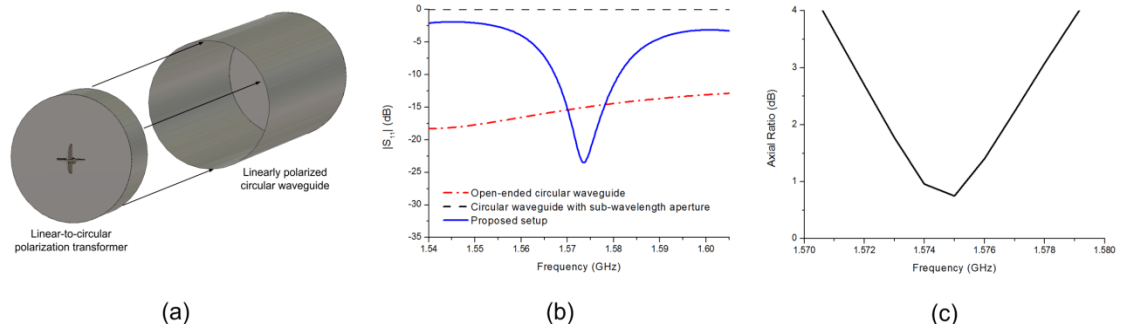


FIG. 4 – (a) Geometrical sketch; (b) Matching and (c) polarization properties vs frequency.

E. MTM-inspired antenna loaded with non-Foster elements

We have also proposed the use of Non-Foster active circuits to increase the operation bandwidth of MTM-inspired components. In [5] we have demonstrated a 7 times improvement of the operation bandwidth of an electrically small SRR-loaded monopole antenna by loading the SRR with a proper active circuit. Actual implementation with commercial elements and the matching properties are reported in Fig. 5.

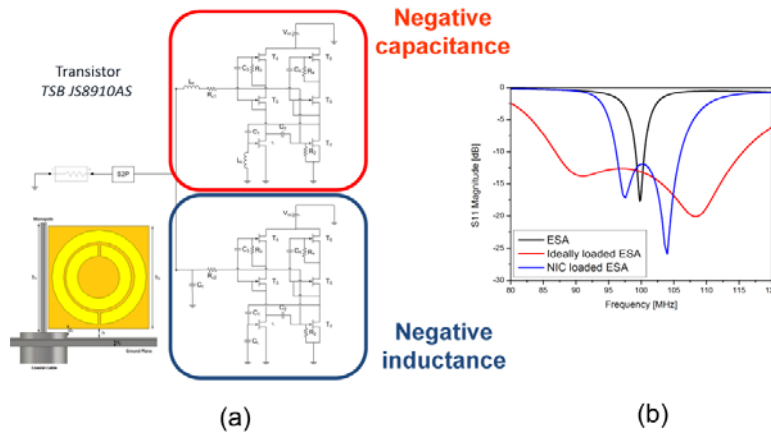


FIG. 5 - (a) SRR-loaded monopole antenna and active non-Foster circuit used; (b) matching properties of the SRR-loaded monopole antenna in the unloaded case and in the loaded case.

III. OPTICS

A. Broadband optical horn nano-antenna

We have proposed the new concept of an horn nano-antenna working at near infrared frequencies [6]. The antenna consists of an Ag-air-Ag nano-transmission line terminated in a tapered horn. This antenna is matched and radiates efficiently over a broad frequency range (Fig. 6), making it suitable for application in different fields (optical wireless communications and energy harvesting).

B. Optical cloaking

We have recently proposed a scattering cancellation based cover [7-8] working at optical frequencies, constituted by a periodic arrangement of core-shell nano-particles. The cover, used to cloak a cylinder (Fig. 7a) consists in 117 core-shell nano-spheres organized in 9 columns of 13 elements. The core of the sphere is made of silica and the shell of silver.

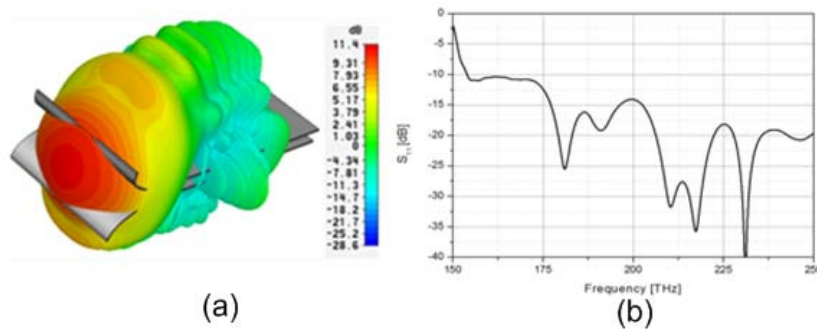


FIG. 6 – (a) 3D gain pattern at 200 THz; (b) matching properties vs frequency.

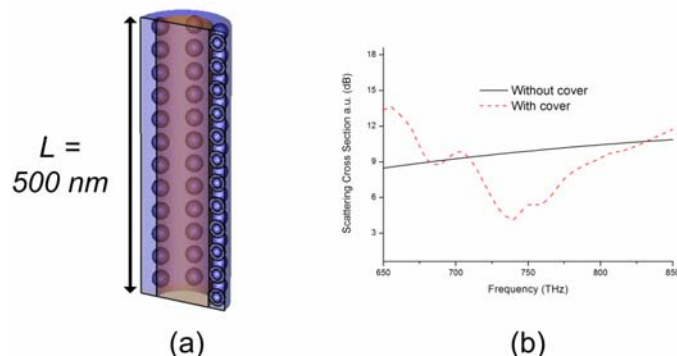


FIG. 7 - (a) Dielectric cylinder ($\epsilon_r = 2$) covered by an arrangement of core-shell nano-spheres; (b) scattering cross-section of the object.

REFERENCES

- [1] D.Ramaccia, F. Scattone, F. Bilotti, and A. Toscano, “Design of a broadband shortened horn loaded with a flat wire-medium annular lens,” *Proc. of Metamaterials 2012*, St. Petersburg, Russia, 16-23 September, 2012.
- [2] F. Bilotti, L. Di Palma, D. Ramaccia, and A. Toscano, “Self-filtering low-noise horn antenna for satellite applications,” *IEEE Antennas Wireless Propagat. Lett.*, vol. 11, pp. 354-357, 2012.
- [3] A. Monti, A. Toscano, and F. Bilotti, “Metasurface mantle cloak for antenna applications,” *Proc. 2012 IEEE AP-S*, Chicago, USA, 8-14 July, 2012.
- [4] M. Barbuto, F. Bilotti, and A. Toscano, “Linear-to-circular polarization transformer using electrically small antennas,” *Proc. 2012 IEEE AP-S*, Chicago, USA, 8-14 July, 2012.
- [5] M. Barbuto, A. Monti, F. Bilotti, and A. Toscano, “Design of a non-Foster actively loaded metamaterials-inspired antenna,” *Proc. of Metamaterials 2011*, Barcelona, Spain, 10-15 October, 2011.
- [6] D. Ramaccia, F. Bilotti, A. Toscano, and A. Massaro, “Efficient and wideband horn nano-antennas,” *Opt. Lett.*, vol. 36, no.10, pp. 1743-1745, 2011.
- [7] A. Monti, F. Bilotti, and A. Toscano, “Optical cloaking of cylindrical objects by using covers made of core-shell nanoparticles,” *Opt. Lett.*, vol. 36, pp. 4479-4481, 2011.
- [8] A. Monti, F. Bilotti, A. Toscano, and L. Vegni, “Possible implementation of epsilon-near-zero metamaterials working at optical frequencies,” *Opt. Comm.*, Vol. 285, pp. 3412-3418, 2012